Aus der Abteilung für Mikrogravitation und Translationale Regenerative Medizin
der Medizinischen Fakultät

der Otto-von-Guericke-Universität Magdeburg

Einbeziehung gravitationsbiologischer Methoden in die biomedizinische Grundlagenforschung

---

Habilitationsschrift

zur Erlangung des akademischen Grades

Dr. rer. nat. habil.
(*doctor rerum naturalium habilitatus*)

an der Medizinischen Fakultät
der Otto-von-Guericke-Universität Magdeburg

---

vorgelegt von
Dr. rer. nat. Marcus Krüger
aus Forchheim

Magdeburg, 2024

meinen Eltern,

meinen Lehrern, Mentoren, Studenten, Kollegen und Freunden,
die mich immer wieder inspiriert und daran erinnert haben,
dass Neugier zu den wichtigsten Eigenschaften eines Wissenschaftlers gehört

Die Wissenschaft von heute
ist die Technik von morgen

EDWARD TELLER (1908-2003)

Danksagung

Dass die Habilitationsschrift nun in dieser Form existiert, habe ich vor allem Frau **Prof. Dr. med. Daniela Grimm** und Herrn **Prof. Dr. med. Manfred Infanger** zu verdanken. Sie waren es, die mich 2016 in Magdeburg empfangen und mich (als Biologen) in das spannende Arbeitsfeld der biomedizinischen Gravitationsforschung eingeführt haben. Vielen Dank für die stets offene Tür, die unzähligen wissenschaftlichen Diskussionen und die Freiheit, Projekte auch selbständig gestalten zu können.

Darüber hinaus möchte ich mich auch bei allen derzeitigen und ehemaligen **Mitgliedern der Forschungsabteilung für Mikrogravitation und Translationale Regenerative Medizin** für die angenehme Zusammenarbeit, für kritische Diskussionen, Anregungen, Kuchen, und viele fachliche, aber auch weniger fachliche Gespräche bedanken. Hervorheben möchte ich **Markus Wehland** und **Herbert Schulz,** die mit mir nicht nur geforscht, sondern auch die Lehre in der Weltraummedizin bestritten haben. **Viviann Sandt** danke ich für die perfekte Organisation der Labore und die tatkräftige Unterstützung bei vielen Experimenten. Nicht zu vergessen die bereits Ehemaligen **Sascha Kopp** und **Jessica Pietsch**, die mich bei den ersten Schritten in der Weltraumforschung begleitet und unterstützt haben.

Und dann wären da natürlich noch „meine“ Doktorand(inn)en, Masterandinnen und Praktikantinnen der letzten Jahre, **Daniela Melnik**, **José Luis Cortes Sanchez**, **Shannon Marchal**, **Anna Sophie Heinrich, Laura Schuttpelz, Lena Nieke, Nadine Becker** und **Jenny Graf**, die durch die engagierte und hilfreiche Mitarbeit an ihren Projekten auch wertvolle Beiträge zu dieser Arbeit geliefert haben. Man denkt immer, dass während der Ausbildung die Weitergabe von Wissen, Ratschlägen und Tipps unidirektional ist. Mittlerweile bin ich überzeugt, dass beide Seiten davon profitieren. Ich hoffe, dass ihr einen guten Start in eure Wissenschaftskarriere hattet.

Ein produktives Forschungsumfeld steht und fällt mit den Kollegen. Auch hier hatte ich Glück. Die Zusammenarbeit mit **anderen Abteilungen, Lehrstühlen, Instituten und Kliniken** war immer angenehm und gewinnbringend. Dazu beigetragen haben u.a. Stefan Kahlert, Hermann-Josef Rothkötter, Anna Dittrich, Fred Schaper, Fabian Wohlfromm, Inna Lavrik, Heike Walles, Cornelia Wiese-Rischke, Thorsten Walles, Katrin Vogel, Monika Brunner-Weinzierl, Michael Kreißl, Klaudija Janic, Julian Thiele, Thorsten Halle, Elmar Woschke und Andreas Wienert. Ebenfalls nicht zu vergessen sind die vielen organisatorischen Dienste, die eine gute Forschung an der Medizinischen Fakultät erst möglich gemacht haben. Besonders zu erwähnen sind dabei unsere Sekretärinnen, **Diana Großmann** (MTRM) und **Elke Ponath** (KCHP), die freundlichen Mitarbeiterinnen und Mitarbeiter in der **Drittmittelverwaltung**, in der **Zentralapotheke**, beim **Zentralen Einkauf** und in der **Medizintechnik**.

Und ganz besonders danke ich auch meinen Eltern, meiner Familie und meinen Freunden, die mich nicht zuletzt immer wieder zur Fertigstellung dieser Arbeit motiviert haben :-)

INHALTSVERZEICHNIS

INHALTSVERZEICHNIS V

VERWENDETE ABKÜRZUNGEN..... VIII

VORWORT 1

PUBLIKATIONEN DIESER HABILITATIONSSCHRIFT 2

SYNTHESE 5

1. Einleitung: Eine gravitationsbiologische Sicht der Evolution 5

2. Weltraummedizin.....6

2.1 Krankheitsbilder bei Astronauten 6

2.2 Molekularbiologische Gravitationsforschung – vom Astronauten zum Patienten auf der Erde 8

3. Plattformen für Mikrogravitationsforschung 9

3.1 Fallturm.....9

3.2 Parabelflug.....9

3.3 Höhenforschungsraketen.....10

3.4 Orbitale Plattformen: Satelliten, Raumfähren, Raumstationen.....13

4. Erzeugung von mikrogravitations-ähnlichen Bedingungen im Labor 13

4.1 Klinostat 14

4.2 Rotating Wall Vessel.....14

4.3 Random Positioning Machine 15

4.4 Magnetische Levitation 16

5. Die struktur- und molekularbiologische Basis für schwerkraftabhängige Effekte in humanen Zellen.....16

5.1 Potenzielle Gravisensoren eurakyotischer Zellen 16

5.2 Zeitfenster für die zelluläre Antwort auf Gravitationsänderungen.....18

6. Durch Gravitationsänderungen induzierte Effekte in humanen Zellen.....19

6.1 Reorganisation des Zytoskeletts 19

6.2 Zelladhäsion 20
6.3 Intrazelluläre Signalwege 21
6.4 Zell-Zell-Kommunikation 23
6.5 Sphäroidbildung auf der Random Positioning Machine 25

7. Die RPM-Zellkultur als *ex vivo*-Metastasierungsmodell 29
7.1 RPM-generierte Tumorsphäroide als „2,5D“-Zellkultur 30
7.2 Tumorsphäroidbildung auf der RPM – Parallelen zur Metastasierung 35
7.3 Mucin-1 als Schlüsselprotein der RPM-induzierten Tumorsphäroidbildung 35
7.4 Pharmazeutische Beeinflussung der RPM-induzierten Sphäroidbildung 37
7.5 Lymphsystem *vs.* Weltraum: Subpopulationen der RPM-Zellkultur 39

8. Gewebekonstruktion (Tissue Engineering) mithilfe von Mikrogravitations-Bioreaktoren 40
8.1 Endothel 41
8.2 Knochen- und Knorpelstrukturen 44
8.3 Fibroblasten 47

9. Zusammenfassung und Fazit 48

LITERATURVERZEICHNIS 51

EIDESSTATTLICHE VERSICHERUNG 68

ORIGINALE DER PUBLIKATIONEN 69

1. Fighting Thyroid Cancer with Microgravity Research 69
2. Breast Cancer Cells in Microgravity: New Aspects for Cancer Research 90
3. Thyroid cancer cells in space during the TEXUS-53 sounding rocket mission – The THYROID Project 112
4. Microgravity Affects Thyroid Cancer Cells during the TEXUS-53 Mission Stronger than Hypergravity 125
5. Fluid and Bubble Flow Detach Adherent Cancer Cells to Form Spheroids on a Random Positioning Machine 145
6. Real Microgravity Influences the Cytoskeleton and Focal Adhesions in Human Breast Cancer Cells 172
7. Simulated Microgravity Influences VEGF, MAPK, and PAM Signaling in Prostate Cancer Cells 197

8. Dexamethasone Selectively Inhibits Detachment of Metastatic Thyroid Cancer Cells during Random Positioning 223

9. Dexamethasone Inhibits Spheroid Formation of Thyroid Cancer Cells Exposed to Simulated Microgravity 248

10. The Formation of Stable Lung Tumor Spheroids during Random Positioning Involves Increased Estrogen Sensitivity 272

11. Morphological and Molecular Changes in Juvenile Normal Human Fibroblasts Exposed to Simulated Microgravity 289

12. Decreased E-Cadherin in MCF7 Human Breast Cancer Cells Forming Multicellular Spheroids Exposed to Simulated Microgravity 311

13. Proteins Involved in Spheroid Formation and Angiogenesis in Endothelial Cells After Long-Term Exposure to Simulated Microgravity 321

14. Short-term Microgravity Influences Cell Adhesion in Human Breast Cancer Cells 338

15. Cytokine Release and Focal Adhesion Proteins in Normal Thyroid Cells Cultured on the Random Positioning Machine 365

16. Alterations of growth and focal adhesion molecules in human breast cancer cells exposed to the Random Positioning Machine 379

17. Three-dimensional growth of prostate cancer cells exposed to simulated microgravity 396

18. Changes in Human Foetal Osteoblasts Exposed to the Random Positioning Machine and Bone Construct Tissue Engineering 417

19. Changes in Exosome Release in Thyroid Cancer Cells after Prolonged Exposure to Real Microgravity in Space 443

20. Changes in Exosomal miRNA Composition in Thyroid Cancer Cells after Prolonged Exposure to Real Microgravity in Space 462

21. Growth of Endothelial Cells in Space and in Simulated Microgravity – A Comparison on the Secretory Level 486

22. Growing blood vessels in space: Preparation studies of the SPHEROIDS project using related ground-based studies 508

WISSENSCHAFTLICHER LEBENSLAUF 514

VERWENDETE ABKÜRZUNGEN

2D / 3D	zweidimensional / dreidimensional
Abb.	Abbildung
CRISPR	Clustered Regularly Interspaced Short Palindromic Repeats
CTC	Zirkulierende Tumorzelle (circulating tumor cell)
DLR	Deutsches Zentrum für Luft- und Raumfahrt
EET	Epithelial-endotheliale Transition
EMT	Epithelial-mesenchymale Transition
ESA	Europäische Weltraumagentur (International Space Station)
et al.	und andere (*et alia*)
EZM, ECM	Extrazelluläre Matrix
FA	Fokale Adhäsion
FDA	Fluoresceindiacetat
FLIM	Fluoreszenzlebenszeit-Mikroskopie
FLUMIAS	Fluorescence Microscopy Analysis System
GBF	Ground-based facility (bodengestützte Anlage zur Simulation von Schwerelosigkeit)
GFR	Wachstumsfaktor-Rezeptor (growth factor receptor)
HARV	High Aspect Rotating Wall Vessel
ISS	Internationale Raumstation (International Space Station)
MCTS	Multizelluläres Tumorsphäroid
miRNA	Micro-RNA
mRNA	Messenger-RNA
NASA	National Aeronautics and Space Administration (US Weltraumbehörde)
NP	Kernpore (nulear pore)
NSCLC	Nicht-kleinzelliges Lungenkarzinom (non-small-cell lung cancer)
OXPHOS	Oxidative Phosphorylierung
PAS	Periodsäure-Schiff-Reaktion (Färbung)
RCCS	Rotating Cell Culture System
RPM	Random Positioning Machine
RWV	Rotating Wall Vessel
SANS	Spaceflight-Associated Neuro-Ocular Syndrome
STS	Space Transportation System
TEXUS	Technologische Experimente unter Schwerelosigkeit
TF	Transkriptionsfaktor

Einheiten

°C	Grad Celsius
d	Tag
g	Erdbeschleunigung
Gy	Gray (J/kg)
h	Stunde
L	Liter
m	Meter
M	molar (mol/L)
min	Minute
mmHg	Millimeter-Quecksilbersäule
Pa	Pascal
rpm	Umdrehungen pro Minute
s	Sekunde

Formelzeichen (zugehörige Einheiten)

F	Kraft (N)
τ	Fluoreszenz-Lebensdauer (s)

Vorsätze

M	Mega	(10^6)
k	Kilo	(10^3)
m	Milli	(10^{-3})
µ	Mikro	(10^{-6})
n	Nano	(10^{-9})
p	Piko	(10^{-12})
f	Femto	(10^{-15})

Zelltypen

HMVEC	Mikrovaskuläre Endothelzellen (dermal)
HSVEC	Endothelzellen der Vena saphena magna
HUVEC	Endothelzellen der Nabelschnurvene
NHDF	Normale humane Fibroblasten (dermal)

VORWORT

Die molekularbiologische bzw. biomedizinische Weltraumforschung ist ein sehr weites und interdisziplinäres Feld. Im Labor bedarf es nicht nur der Anpassung der üblichen Zellkultur an (simulierte) Mikrogravitationsbedingungen, für Parabelflug-, Raketen- und ISS-Experimente ist oftmals sogar das Design neuer Hardware nötig. Weltraumbiologen/-mediziner arbeiten daher an den Schnittstellen von Medizin, Biologie, Physik, Materialwissenschaften, Maschinenbau, Elektrotechnik und Informatik. Ebenso weitgefächert sind die Inhalte der in dieser Arbeit verwendeten Publikationen, die wortwörtlich zwischen „Himmel“ und Erde entstanden sind.

Aufgrund der thematischen Breite soll diese kumulative Habilitationsschrift vor allem die Errungenschaften der gravitationsbiologischen Forschung für die Biomedizin in den letzten Jahren in Form einer Synthese zusammenfassen. Sie umfasst Publikationen verschiedener Themenschwerpunkte, die im Rahmen der interdisziplinären Weltraumforschung zunächst an der Universitätsklinik für Plastische, Ästhetische und Handchirurgie (KCHP) und später in der neu gegründeten Abteilung für Mikrogravitation und Translationale Regenerative Medizin (MTRM) der Medizinischen Fakultät der Otto-von-Guericke-Universität Magdeburg entstanden sind. Die vollständige Publikationsliste des Habilitanden wurde diesem Habilitationsantrag in einem separaten Dokument beigefügt. Sie umfasst 86 Publikationen, darunter 14 Erst- sowie 16 Letztautorenschaften.

Für ein besseres Verständnis der erhobenen Forschungsdaten werden zunächst die theoretischen Hintergründe der Gravitationsforschung (Kapitel 1), der Weltraummedizin und der molekularbiologischen Gravitationsforschung (Kapitel 2) sowie die Möglichkeiten der Forschung unter Mikrogravitationsbedingungen (Kapitel 3-5) kurz vorgestellt. Die Gesamtergebnisse werden in den Kapiteln 6-8 in ihrem wissenschaftlichen Kontext beschrieben und enden mit einer Zusammenfassung und Schlussfolgerungen in Kapitel 9.

PUBLIKATIONEN DIESER HABILITATIONSSCHRIFT

Gegenstand dieser kumulativen Habilitationsschrift ist der Inhalt der nachfolgend aufgelisteten 22 Publikationen, zu denen 4 Erst- und 5 Letztautorenschaften. Damit wird die nach der Habilitationsordnung gegebene Möglichkeit „*zur Vorlage publizierter Forschungsergebnisse, die in ihrer Gesamtheit eine einer Habilitationsschrift gleichwertige wissenschaftliche Leistung darstellen*“ genutzt. Die empfohlene Anzahl von 10 Publikationen wird aufgrund des thematischen Zusammenhangs der genannten Arbeiten und des weit gefassten Anwendungsfeldes der Gravitationsforschung überschritten. Die Publikationen wurden nach der Reihenfolge ihrer Erwähnung im Text fortlaufend nummeriert.

(1) **Krüger M**, Melnik D, Kopp S, Buken C, Sahana J, Bauer J, Wehland M, Hemmersbach R, Corydon TJ, Infanger M & Grimm D. (2019) Fighting Thyroid Cancer with Microgravity Research. *Int. J. Mol. Sci. 20(10):2553*. doi:10.3390/ijms20102553.

(2) Nassef, MZ, Melnik D, Kopp S, Sahana J, Infanger M, Lützenberg R, Relja B, Wehland M, Grimm D & **Krüger M**. (2020) Breast Cancer Cells in Microgravity: New Aspects for Cancer Research. *Int. J. Mol. Sci. 21(19):7345.* doi:10.3390/ijms21197345.

(3) Kopp S*, **Krüger M***, Feldmann S, Oltmann H, Schütte A, Schmitz B, Bauer J, Schulz H, Saar K, Huebner N, Wehland M, Nassef MZ, Melnik D, Meltendorf S, Infanger M & Grimm D. (2018) Thyroid cancer cells in space during the TEXUS-53 sounding rocket mission – The THYROID Project. *Sci. Rep. 8(1):10355.* doi:10.1038/s41598-018-28695-1.

(4) Kopp S, **Krüger M**, Bauer J, Wehland M, Corydon TJ, Sahana J, Nassef MZ, Melnik D, Bauer TJ, Schulz H, Schütte A, Schmitz B, Oltmann H, Feldmann S, Infanger M & Grimm D. (2018) Microgravity Affects Thyroid Cancer Cells during the TEXUS-53 Mission Stronger than Hypergravity. *Int. J. Mol. Sci. 19(12):4001*. doi:10.3390/ijms19124001.

(5) Cortés-Sánchez JL, Melnik D, Sandt V, Kahlert S, Marchal S, Johnson IRD, Calvaruso M, Liemersdorf C, Wuest SL, Grimm D & **Krüger M**. (2023) Fluid and Bubble Flow Detach Adherent Cancer Cells to Form Spheroids on a Random Positioning Machine. *Cells 12(22):2665.* doi:10.3390/cells12222665.

(6) Nassef MZ, Kopp S, Wehland M, Melnik D, Sahana J, **Krüger M**, Corydon TJ, Oltmann H, Schmitz B, Schütte A, Bauer, TJ, Infanger M & Grimm D. (2019) Real Microgravity Influences the Cytoskeleton and Focal Adhesions in Human Breast Cancer Cells. *Int. J. Mol. Sci. 20(13):3156*. doi:10.3390/ijms20133156.

(7) Hybel TE, Dietrichs D, Sahana J, Corydon TJ, Nassef MZ, Wehland M, **Krüger M**, Magnusson NE, Bauer J, Utpatel K, Infanger M, Grimm D & Kopp S. (2020) Simulated

Microgravity Influences VEGF, MAPK, and PAM Signaling in Prostate Cancer Cells. *Int. J. Mol. Sci. 21(4):1263*. doi:10.3390/ijms21041263

(8) Melnik D, Cortés-Sánchez JL, Sandt V, Kahlert S, Kopp S, Grimm D & **Krüger M**. (2023) Dexamethasone Selectively Inhibits Detachment of Metastatic Thyroid Cancer Cells during Random Positioning. *Cancers 15(6):1641*. doi:10.3390/cancers15061641

(9) Melnik D, Sahana J, Corydon TJ, Kopp S, Nassef MZ, Wehland M, Infanger M, Grimm D & **Krüger M**. (2020) Dexamethasone Inhibits Spheroid Formation of Thyroid Cancer Cells Exposed to Simulated Microgravity. *Cells 9(2):367*. doi:10.3390/cells9020367.

(10) Barkia B, Sandt V, Melnik D, Cortés-Sánchez JL, Marchal S, Baselet B, Baatout S, Sahana J, Grimm D, Wehland M, Schulz H, Infanger M, Kraus A* & **Krüger M***. (2024) The Formation of Stable Lung Tumor Spheroids during Random Positioning Involves Increased Estrogen Sensitivity. *Biomolecules 4(10):1292.* doi:10.3390/biom14101292.

(11) Buken C, Sahana J, Corydon TJ, Melnik D, Bauer J, Wehland M, **Krüger M**, Balk S, Abuagela N, Infanger M & Grimm D. (2019) Morphological and Molecular Changes in Juvenile Normal Human Fibroblasts Exposed to Simulated Microgravity. *Sci. Rep. 9(1):11882.* doi:10.1038/s41598-019-48378-9.

(12) Sahana J, Nassef MZ, Wehland M, Kopp S, **Krüger M**, Corydon TJ, Infanger M, Bauer J & Grimm D. (2018) Decreased E-Cadherin in MCF7 Human Breast Cancer Cells Forming Multicellular Spheroids Exposed to Simulated Microgravity. *Proteomics 18(13):e1800015.* doi:10.1002/pmic.201800015.

(13) Dittrich A, Grimm D, Sahana J, Bauer J, **Krüger M**, Infanger M & Magnusson NE. (2018) Key Proteins Involved in Spheroid Formation and Angiogenesis in Endothelial Cells After Long-Term Exposure to Simulated Microgravity. *Cell. Physiol. Biochem. 45(2):429-445*. doi:10.1159/000486920.

(14) Nassef MZ, Kopp S, Melnik D, Corydon TJ, Sahana J, **Krüger M**, Wehland M, Bauer TJ, Liemersdorf C, Hemmersbach R, Infanger M & Grimm D. (2019) Short-term Microgravity Influences Cell Adhesion in Human Breast Cancer Cells. *Int. J. Mol. Sci. 20(22):5730.* doi:10.3390/ijms20225730.

(15) Warnke E, Pietsch J, Kopp S, Bauer J, Sahana J, Wehland M, **Krüger M**, Hemmersbach R, Infanger M, Lützenberg R & Grimm D. (2017) Cytokine Release and Focal Adhesion Proteins in Normal Thyroid Cells Cultured on the Random Positioning Machine. *Cell. Physiol. Biochem. 43(1):257-270.* doi:10.1159/000480368.

(16) Sahana J, Corydon TJ, Wehland M, **Krüger M**, Kopp S, Melnik D, Relja B, Kahlert S, Infanger M & Grimm D. (2021) Alterations of growth and focal adhesion molecules in human

breast cancer cells exposed to the Random Positioning Machine. *Front. Cell Dev. Biol. 9:672098*. doi:10.3389/fcell.2021.672098.

(17) Dietrichs D, Grimm D, Sahana J, Melnik D, Corydon T, Wehland M, **Krüger M**, Vermeesen R, Baselet B, Baatout S, Hybel T, Kahlert S, Schulz H, Infanger M & Kopp S. (2022) Three-dimensional growth of prostate cancer cells exposed to simulated microgravity. *Front. Cell Dev. Biol. 10:841017*. doi:10.3389/fcell.2022.841017.

(18) Mann V, Grimm D, Corydon TJ, **Krüger M**, Wehland M, Riwaldt S, Sahana J, Kopp S, Bauer J, Reseland JE, Infanger M, Lian AM, Okoro E & Sundaresan A. (2019) Changes in Human Foetal Osteoblasts Exposed to the Random Positioning Machine and Bone Construct Tissue Engineering. *Int. J. Mol. Sci. 20(6):1357.* doi:10.3390/ijms20061357.

(19) Wise PM, Neviani P, Corydon TJ, Wehland M, Braun M, **Krüger M**, Infanger M & Grimm D. (2021) Changes in Exosome Release in Thyroid Cancer Cells after Prolonged Exposure to Real Microgravity in Space. *Int. J. Mol. Sci. 22(4):2132*. doi:10.3390/ijms22042132.

(20) Wise PM, Neviani P, Riwaldt S, Corydon TJ, Wehland M, Braun M, **Krüger M**, Infanger M & Grimm D. (2021) Changes in Exosomal miRNA Composition in Thyroid Cancer Cells after Prolonged Exposure to Real Microgravity in Space. *Int. J. Mol. Sci. 22(23):12841.* doi:10.3390/ijms222312841.

(21) **Krüger M**, Pietsch J, Bauer J, Kopp S, Carvalho DTO, Baatout S, Moreels M, Melnik D, Wehland M, Egli M, Sahana J, Kobberø SD, Corydon TJ, Nebuloni S, Gass S, Evert M, Infanger M & Grimm D. (2019) Growth of Endothelial Cells in Space and in Simulated Microgravity – A Comparison on the Secretory Level. *Cell. Physiol. Biochem. 52(5):1039-1060.* doi:10.33594/000000071.

(22) **Krüger M***, Kopp S*, Wehland M, Bauer J, Baatout S, Moreels M, Egli M, Corydon TJ, Infanger M & Grimm D. (2019) Growing blood vessels in space: Preparation studies of the SPHEROIDS project using related ground-based studies. *Acta Astronaut. 159:267-272*. doi:10.1016/j.actaastro.2019.03.074.

*) geteilte Autorenschaft

SYNTHESE

1. Einleitung: Eine gravitationsbiologische Sicht der Evolution

Die Gravitation (Schwerkraft) ist die einzige Grundkraft, die über die gesamte Evolutionsgeschichte der Erde nahezu konstant war. Demnach ist es nicht überraschend, dass sich das Leben auf unserem Planeten an die Gravitation angepasst und teilweise auch nach ihr ausgerichtet hat (Adamopoulos *et al.*, 2021). Zusammengefasst bestimmt die Schwerkraft die Form und Größe von Organismen, die Entwicklung von Skelett und Stützorganen sowie den Energiehaushalt (Dubinin & Vaulina, 1976); die Gravitation wird daher manchmal sogar als „Architekt des menschlichen Designs“ bezeichnet. Die Knochen sind die wichtigste Stützstruktur unseres Körpers, zusammen mit dem Musculus transversus abdominis und einer Reihe weiterer Muskeln, die zur Gesamtstabilität beitragen (De Troyer *et al.*, 1990). Dieses skelettale Konstrukt ermöglicht uns, aufrecht zu stehen und der Erdanziehung zu trotzen. Unsere Muskeln sind über Sehnen flexibel mit den Knochen verbunden, wodurch wir uns trotz Schwerkraft frei bewegen können. Unser Herz ist so konstruiert, dass es das Blut gegen die Erdanziehung nach oben zum Gehirn pumpt. Venenklappen in unseren Beinen öffnen sich als Einwegventile, wenn unsere Beinmuskeln kontrahieren, und schließen sich anschließend wieder, um zu verhindern, dass das Blut in Richtung der Schwerkraft zurück nach unten fließt (Tansey *et al.*, 2019). Die Art und Weise, wie wir Nahrung zu uns nehmen und Abfallprodukte ausscheiden hängt überwiegend von der Schwerkraft ab (Yang *et al.*, 2020), ebenso die Position eines Fötus in Bezug auf den Geburtskanal und der eigentliche Geburtsvorgang (Stark *et al.*, 2023). Auch die Art und Weise, wie ein Baby von seiner Mutter gesäugt wird, die Ausrichtung der weiblichen Brust (Mills *et al.*, 2016), und die Richtung des Milchflusses sind gravitationsabhängig. Darüber hinaus lassen viele unserer Körperfunktionen einen Schwerkraftbezug unmittelbar erkennen, darunter Schwere- und Gleichgewichtssinn (Vestibularapparat) (Smetacek, 2002), verschiedene Stütz-Strukturen (Knochen, Knorpel) sowie Bewegungen, die der Schwerkraft entgegengerichtet sind, um Stabilität zu erhalten (Haltungssinne). Die Gravitation ist also eine wichtige Kraft, an die unser Körper evolutiv adaptiert ist.

Welche Bedeutung die Gravitation tatsächlich für die Funktion und Gesundheit des menschlichen Körpers hat, wird deutlich, wenn man sich vor Augen führt, was mit Menschen geschieht, wenn die Schwerkraft aufgehoben wird. Studien an Astronauten haben gezeigt, dass die Schwerkraft nicht nur eine Kraft ist, sondern auch als Signal dient, das dem Körper vermittelt, wie er sich verhalten soll. In Schwerelosigkeit verringert sich die Knochendichte um 1 bis 2% pro Monat (Man *et al.*, 2022). Muskeln schwinden aufgrund von Nichtnutzung sogar um 5% pro Woche (Juhl *et al.*, 2021). Wenn Astronauten von Langzeitaufenthalten im Weltraum zurückkehren, müssen sie nicht selten auf Bahren abtransportiert werden, da es ihnen aufgrund des Kraftverlustes zu schwerfällt, in der Schwerkraft aufrecht zu stehen.

Des Weiteren beeinflusst die Gravitation die Verteilung von Körperflüssigkeiten und damit die Funktion des Herz-Kreislauf-Systems. Sie sorgt dafür, dass das Blut in unserem Körper ein optimales Blutdruckniveau aufrechterhält. Im Stehen beträgt der Blutdruck in unseren Füßen bis zu 200 mmHg, während im Gehirn hingegen nur 60-80 mmHg herrschen. Das Herz ist daran gewöhnt, gegen die Gravitation zu arbeiten; Pumpleistung und Gravitationseffekte gleichen sich aus. In der ersten Zeit in Schwerelosigkeit gleicht sich der Blutdruck im ganzen Körper auf etwa 100 mmHg an. Das Gesicht schwillt mit Flüssigkeit an („puffy face“), die Beine werden durch die Flüssigkeitsverschiebung dünner („bird legs“) (Baran *et al.*, 2021). Der Anstieg des Blutdrucks löst über die Barorezeptoren im Sinus caroticus einen Alarm aus, dass der Körper zu viel Blut hat. Auch wenn der Blutdruck durch Regulationsmaßnahmen in den ersten zwei bis drei Tagen an Schwerelosigkeit teiladaptiert, führt dies zu einer Verringerung des Blutvolumens um 22% (Castillo, 2012). Durch Hypovolämie verringert sich die Herztätigkeit, wodurch es schließlich zu einer Herzatrophie kommt.

Dies soll nur ein kleines Beispiel sein, wie abhängig einige unsere Körperfunktionen von der Gravitation sind. Da sich alle bisher bekannten zellbiologischen Prozesse unter dem Einfluss der Schwerkraft entwickelt haben, können selbst kleine Schwankungen der Gravitation erhebliche Auswirkungen auf die Funktion von Zellen, Geweben und Organen haben. Schaut man über den Tellerrand humaner Forschung hinaus, sind komplexe physiologische Vorgänge, wie die Frühentwicklung von Wirbeltieren, in Schwerelosigkeit ebenfalls beeinträchtigt und führen oftmals zu nicht lebensfähigen Föten (Li *et al.*, 2021; Ma *et al.*, 2008; Schenker & Forkheim, 1998).

Mit dem Ziel zukünftiger Weltraumexploration ist es zwingend erforderlich, die Auswirkungen der Schwerelosigkeit auf den menschlichen Organismus zu verstehen und Lösungsansätze für zu erwartende Gesundheitsrisiken zu entwickeln. Die Gravitationsbiologie bietet Werkzeuge und Methoden, um Effekte von Gravitationsänderungen auf biologische Systeme zu untersuchen (Hemmersbach *et al.*, 2006). Die aus dieser Forschung gewonnenen Resultate bringen aber teilweise auch unerwartete und überraschende Erkenntnisse zutage, die nicht nur für die Weltraumforschung wichtig sind, sondern auch die Grundlagenforschung (patho)physiologischer Prozesse auf der Erde voranbringen.

2. Weltraummedizin

2.1 Krankheitsbilder bei Astronauten

Befindet sich der menschliche Körper im Weltraum, führt das nach einiger Zeit zur Beeinträchtigung der physiologischen Funktionen (Abb. 1). Einige Effekte (insb. bei Muskeln, Herz und Knochen) sind dabei auf eine geringere Beanspruchung in Schwerelosigkeit zurückzuführen und können durch ein adäquates Trainingsprogramm für Astronauten reduziert werden (Lambrecht *et al.*, 2017; S. J. Lee *et al.*, 2020; Parafati *et al.*, 2023). Das sogenannte Spaceflight-Associated

Neuro-Ocular Syndrome (SANS) umfasst Symptome wie verschwommenes Sehen und Veränderungen der Augenstruktur. Diese Veränderungen werden durch einen erhöhten intrakraniellen Druck verursacht, der durch Mikrogravitation begünstigt wird (Mader *et al.*, 2011). Die langfristigen Folgen von SANS sind noch nicht vollständig verstanden, stellen jedoch ein erhebliches Gesundheitsrisiko dar. Bekannt ist ebenfalls, dass die erhöhte Weltraumstrahlung außerhalb der Erdatmosphäre zu multiplen Effekten, wie erhöhtem Risiko genetischer Mutationen, Verbrennungen oder zu Veränderungen in der Mikroarchitektur von Geweben führen kann (Chancellor *et al.*, 2014). Wie sich das Zusammenspiel von veränderter Gravitation und erhöhter Strahlenbelastung während Weltraumaufenthalten auf das humane Immun- und Nervensystem auswirkt, ist weiterhin Gegenstand intensiver Untersuchungen und zum gegenwärtigen Zeitpunkt noch nicht vollständig erklärbar. Völlig unbekannt sind bisher sogar die Auswirkungen auf die Entstehung und das Fortschreiten von Krebserkrankungen, da bisher noch kein Astronaut an Krebs erkrankt ist (Stand von heute) bzw. kein Astronaut mit Krebsleiden im Weltall war. Die Weltraumstrahlung jenseits der Erdatmosphäre erhöht theoretisch das Risiko für die maligne Transformation von Zellen (Guo *et al.*, 2022; National Academies of Sciences & Medicine, 2021). Daher sollte die Krebsforschung unter Weltraumbedingungen auch weiterhin nicht komplett außer Acht gelassen werden (Afshinnekoo *et al.*, 2020; Hamm *et al.*, 1998).

Mit dem wieder aufgekommenen Interesse an der Mond- und Marsexploration sowie kommerziellem Weltraumtourismus rückt die Weltraummedizin in den Fokus der Forschung. Wissenschaftler wollen verstehen, was genau mit unserem Körper nach Verlassen der Erde passiert, um rechtzeitig eventuelle Maßnahmen ergreifen zu können.

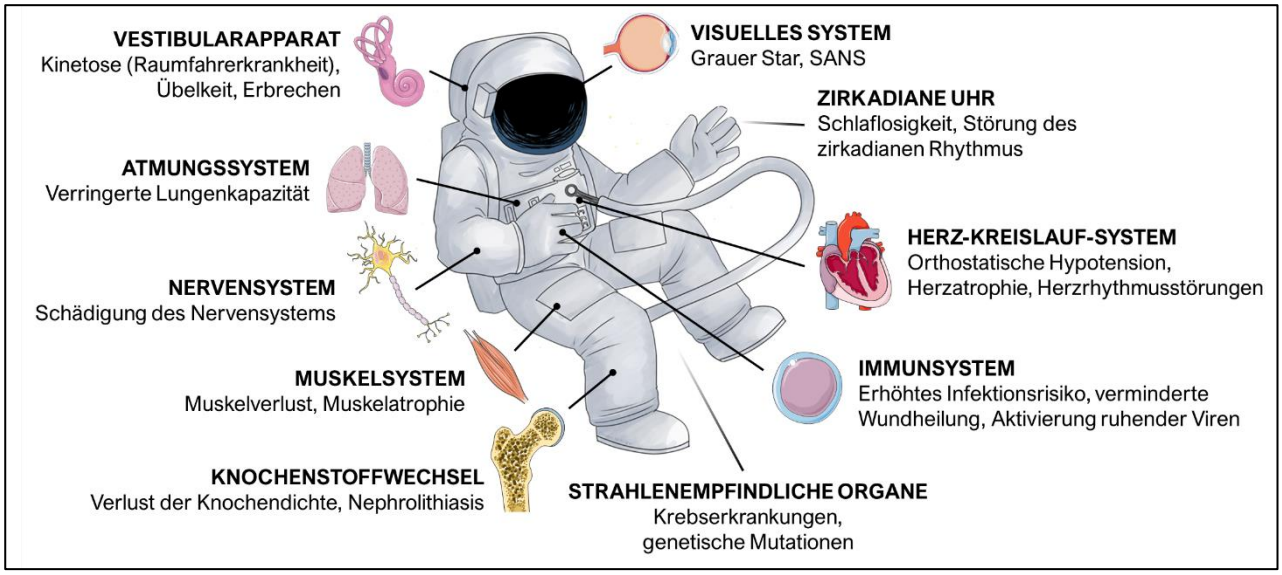


Abbildung 1: Übersicht der gesundheitlichen Auswirkungen eines Weltraumaufenthalts bei Astronauten. Die Abbildung wurde übersetzt und verändert nach einem eigenen Entwurf für (Moroni *et al.*, 2022). SANS: Spaceflight-Associated Neuro-Ocular Syndrome.

2.2 Molekularbiologische Gravitationsforschung – vom Astronauten zum Patienten auf der Erde

Die Forschung zu den Auswirkungen von Schwerelosigkeit auf biologische Systeme hat in den letzten zwei Jahrzehnten erheblich an Bedeutung gewonnen. Während der Space-Shuttle-Mission STS-90 im Jahr 1998 wurden Primärkulturen menschlicher Nierenrindenzellen sechs Tage lang an Bord der Raumfähre Columbia kultiviert, bevor sie zur Analyse zur Erde zurückkehrten. Es zeigte sich, dass die Expression von 1632 der 10.000 analysierten Gene im Vergleich zu Bodenkontrollen verändert war (Hammond *et al.*, 2000). Dies war das erste Experiment, welches zeigte, dass eine Umgebung mit reduzierter Schwerkraft eine Vielzahl von Genen von *in vitro* kultivierten Zellen beeinflussen kann. Seitdem wurden zahlreiche unterschiedliche Zelltypen, Gewebe und Organismen unter dem Einfluss veränderter Schwerkraft von Forschern aus der ganzen Welt untersucht. Vor allem die Errichtung der Internationalen Raumstation (ISS) eröffnete neue Möglichkeiten für die biologische Gravitationsforschung, insb. für Langzeit-Beobachtungen. Experimente in Mikrogravitation ermöglichen es, zelluläre und molekulare Mechanismen zu analysieren, die unter normalen Laborbedingungen nicht beobachtet werden können. Zahlreiche Studien haben gezeigt, dass sich Zellwachstum, Genexpression und Signaltransduktion in Mikrogravitation signifikant verändern. Insbesondere die Regulation von Genen, die für das Zellwachstum und die Differenzierung zuständig sind, wurde intensiv untersucht (Corydon *et al.*, 2023). Experimente an Bord der ISS lieferten unlängst wichtige Daten über die Auswirkungen von Mikrogravitation auf das muskuloskelettale System (Ha *et al.*, 2023; Kim *et al.*, 2024). Auch die Auswirkungen auf das Immunsystem (Akiyama *et al.*, 2020; Crucian *et al.*, 2018; Hicks *et al.*, 2023) und den Metabolismus (Bergouignan *et al.*, 2016) sind wesentliche Forschungsfelder, die tiefere Einblicke in die biochemischen Anpassungsmechanismen unseres Organismus bieten.

Die Ergebnisse der Gravitationsforschung haben auch Auswirkungen auf die Medizin auf der Erde. Durch Mikrogravitation induzierte Veränderungen können als Modell für pathologische Prozesse dienen, wie sie beispielsweise bei Immobilität, Alterung oder bestimmten Erkrankungen auftreten (Bradbury *et al.*, 2020). Die Erkenntnisse über Zellphysiologie und Genexpression können zur Entwicklung neuer therapeutischer Ansätze in der regenerativen Medizin beitragen. So dienen die Daten beispielsweise zur Entwicklung gezielter Therapien zur Bekämpfung von Osteoporose oder Muskelschwund (Ballerini *et al.*, 2020; Ha *et al.*, 2023; Lee *et al.*, 2020). Auch die Onkologie profitiert von der Gravitationsforschung (Becker & Souza, 2013). Krebszellen wachsen in Mikrogravitation dreidimensional und zeigen dadurch ein ähnliches Verhalten wie *in vivo*. In solchen Ansätzen können Tumorzellen und deren Wachstumsprozesse *in vitro* genauer untersucht werden. 2018 wurde beispielsweise die Angiex-Therapie, die Tumore durch den Entzug ihrer Blutversorgung bekämpfen soll, u.a. an Krebszellen an Bord der ISS getestet[1]. Mikrogravitationsexperimente können auch zu besseren oder neuartigen Behandlungsansätzen führen, die präziser und weniger

[1] https://www.nasa.gov/missions/station/space-station-leads-to-breakthroughs-in-human-health-on-earth/

toxisch sind. Ebenso kann die Entwicklung neuer Krebsmedikamente durch die Gravitationsforschung beschleunigt werden, in dem auf ungewöhnliche Weise neue, noch unbekannte Targets gefunden werden (Topal & Zamur, 2021). Zwei eigene Übersichtsartikel beschreiben die bisherigen Erkenntnisse der Mikrogravitationsforschung an Schilddrüsen- **(Publikation 1)** und Brustkrebs **(Publikation 2)**.

3. Plattformen für Mikrogravitationsforschung

Als Mikrogravitation (µ*g*) wird im Allgemeinen der Zustand der angenäherten „Schwerelosigkeit" beschrieben, in dem ein Beobachter die auf der Erde konstant wirkende Beschleunigung g_0 nicht verspürt (Messerschmid *et al.*, 1997). Nach den Gesetzen der Physik ist jedes Objekt schwerelos, das sich im freien Fall befindet; das wird bei Experimenten in µ*g* meistens angestrebt. Allerdings ist die Schwerelosigkeit auch beim freien Fall nicht vollkommen, da die Fallbewegung beispielsweise durch den Luftwiderstand beeinflusst wird. Die verbleibende Restschwere bezeichnet man als Mikrogravitation. Auf der Internationalen Raumstation ISS herrschen auf etwa 400 km Flughöhe immer noch 0,88*g*. Da sich die ISS jedoch im freien Fall „um die Erde herum" befindet, ist in ihrem Bezugssystem die Fallbeschleunigung nahezu 0*g*. Neben der ISS gibt es noch eine Reihe weiterer Plattformen, auf denen biologische Experimente unter Mikrogravitationsbedingungen möglich sind (▤ Tafel 1A).

3.1 Fallturm

Falltürme, wie beim Zentrum für Angewandte Raumfahrttechnologie und Mikrogravitation (ZARM) der Universität Bremen, ermöglichen eine qualitativ hochwertige Kurzzeit-Mikrogravitation, die durch den Fall in einem evakuierten Turm für wenige Sekunden erreicht wird. Der Bremer Fallturm bietet Experimentatoren in der 120 m langen Fallröhre 4,74 s Mikrogravitation mit $\Delta g < 10^{-6} g$. Bei der Verwendung des 2004 im Kellerschacht des Turms installierten und weltweit einzigartigen Katapults, welches die Experiment-Kapsel in 0,25 s mit 168 km/h auf eine Vertikalparabel schießt, sind sogar 9,3 s möglich (ZARM, Universität Bremen). Für Biowissenschaftler reicht die kurze Zeitspanne in Mikrogravitation allerdings nur für die Untersuchung weniger (biophysikalischer) Phänomene aus, wie z.B. Ionenverschiebungen über Membranen. Fallturm-Experimente haben aber anschaulich demonstriert, wie schnell einige humane Zellen auf Mikrogravitation reagieren können (Striebel *et al.*, 2023).

3.2 Parabelflug[1]

Bei Parabelflugmanövern können längere Mikrogravitationsphasen (15-22 s) erreicht werden, die jedoch von zwei Hypergravitationsphasen (1,5-2,5*g*) flankiert sind. Meist werden während eines

[1] Die Daten von drei DLR-Parabelflugkampagnen sind in die Publikationen dieser Habilitationsschrift eingeflossen.

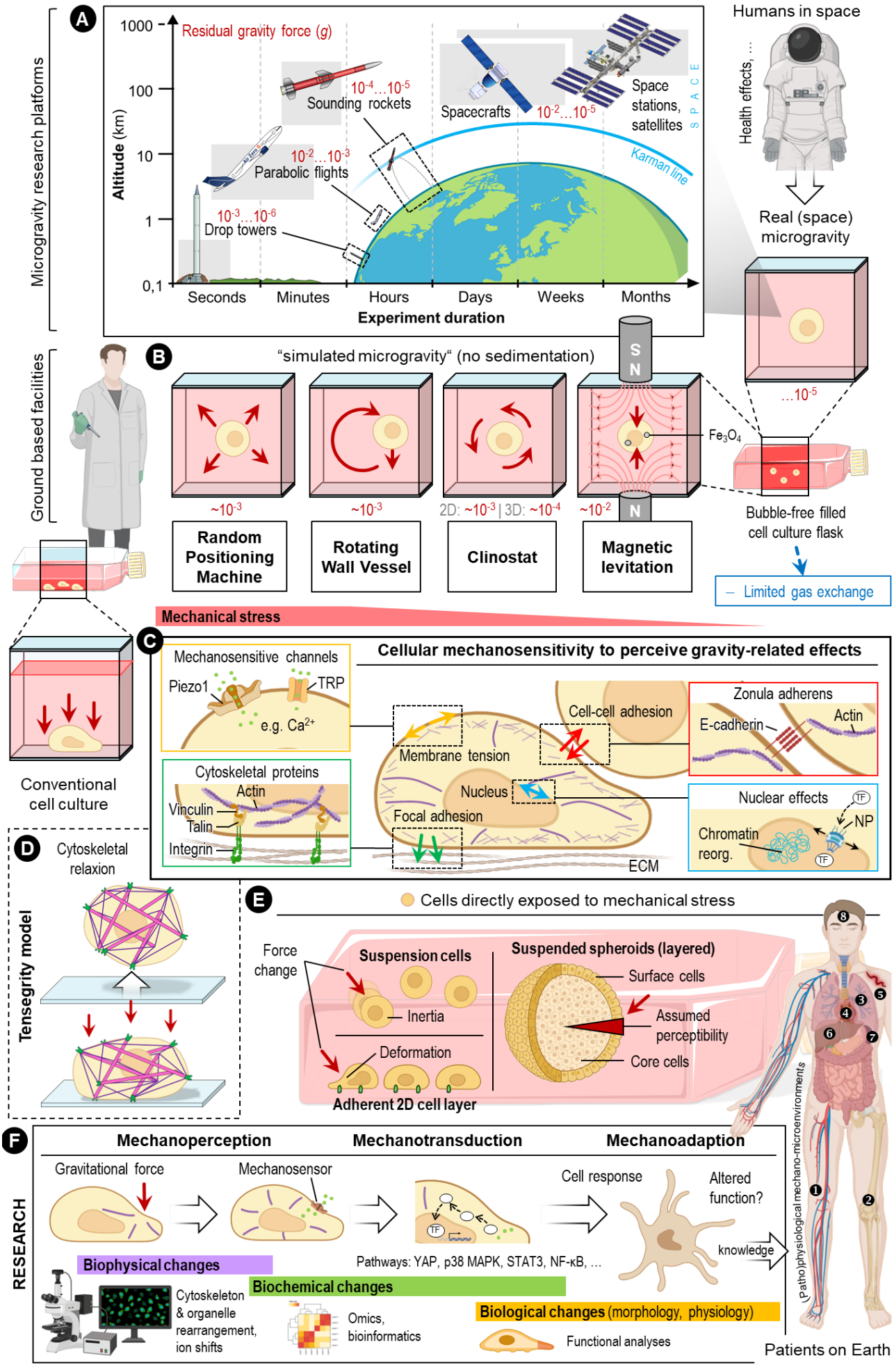
Parabelflugs mehrere solcher Parabeln in kurzen zeitlichen Abständen hintereinander geflogen. Die unterschiedlichen Gravitationsbedingungen während eines solchen Parabelflugs müssen daher bei der Analyse der erhaltenen Daten berücksichtigt werden. Parabelflüge eignen sich sehr gut, Reaktionen auf Gravitationsänderungen in biologischen Systemen zu analysieren. Da das speziell ausgestattete Flugzeug (z.B. der umgebaute Airbus A310 AirZeroG von Novespace, Bordeaux, Frankreich) atmosphärischen Faktoren ausgesetzt und auch nicht komplett frei von Vibrationen ist, ist die Qualität der Mikrogravitation während der Flugparabel etwas geringer (~$10^{-2}g$), Anpassungen der Parabelform ermöglichen jedoch auch gezielt die Erzeugung von Mond- und Marsgravitation. Des Weiteren sind Parabelflüge die einzige Plattform, bei denen die Experimentatoren zusammen mit dem Experiment in Mikrogravitation gebracht werden und dieses dann auch aktiv steuern bzw. beeinflussen können. Darüber hinaus sind auch größere Experimentaufbauten möglich (Ruyters & Friedrich, 2006).

3.3 Höhenforschungsraketen[1]

Unbemannte Höhenforschungsraketen können wissenschaftliche Experimente mitsamt Messinstrumenten in Höhen zwischen 45 bis zu 1.200 km befördern. Bei dem europäischen TEXUS-Programm (Technologische Experimente unter Schwerelosigkeit) erreichen die ballistischen, zweistufigen Raketen dabei eine Mikrogravitationszeit von ca. 6 Minuten bei ~$10^{-4}g$. Die Flugbahn entspricht auch hier einer Parabel mit einer Gipfelhöhe bei etwa 250 km. Die von Platzbedarf und Gewicht begrenzten Experimente werden während des Fluges in übereinanderliegenden, autonomen Modulen innerhalb der Rakete durchgeführt. Während dieser Zeit haben die Wissenschaftler vom Kontrollzentrum aus die Möglichkeit, ihre Versuche durch Telecommanding und Videoübertragung zu steuern und zu überwachen. Die Daten werden während des Fluges per Telemetrie übermittelt oder nach Bergung der wissenschaftlichen Nutzlast. Um Omics-Analysen adhärenter Zellen während eines Raketenflugs zu ermöglichen, werden automatisierte Zellkulturkammern zur Versorgung und Fixierung der Zellen konstruiert **(Publikation 3)**.

Während des Raketenstarts sind die Experimente für kurze Zeit einer Hypergravitation von 12-13*g* ausgesetzt. Eine mit Schilddrüsenkarzinomzellen durchgeführte Genexpressionsstudie zeigte jedoch, dass die Mikrogravitationsphase des Fluges einen größeren Effekt auf die Zellen hat als die initiale Hypergravitationsphase **(Publikation 4)**.

[1] Die Daten von zwei Raketenmissionen (TEXUS-53 und TEXUS-54) sind in die Publikationen dieser Habilitationsschrift eingeflossen.


A
Microgravity research platforms
Residual gravity force (g)
1000
100
10
1
0,1
Altitude (km)
Sounding rockets
10-4…10-5
Parabolic flights
10-2…10-3
Drop towers
10-3…10-6
Spacecrafts
10-2…10-5
Space stations, satellites
SPACE
Karman line
Seconds
Minutes
Hours
Days
Weeks
Months
Experiment duration
Humans in space
Health effects, …
Real (space) microgravity
…10-5
Ground based facilities
B
"simulated microgravity" (no sedimentation)
~10-3
~10-3
2D: ~10-3 | 3D: ~10-4
~10-2
S
N
N
Fe3O4
Random Positioning Machine
Rotating Wall Vessel
Clinostat
Magnetic levitation
Bubble-free filled cell culture flask
– Limited gas exchange
Mechanical stress
C
Cellular mechanosensitivity to perceive gravity-related effects
Mechanosensitive channels
Piezo1
TRP
e.g. Ca2+
Cytoskeletal proteins
Actin
Vinculin
Talin
Integrin
Membrane tension
Focal adhesion
Cell-cell adhesion
Zonula adherens
E-cadherin
Actin
Nucleus
Nuclear effects
TF
NP
Chromatin reorg.
ECM
Conventional cell culture
D
Cytoskeletal relaxion
Tensegrity model
E
Cells directly exposed to mechanical stress
Force change
Suspension cells
Inertia
Deformation
Adherent 2D cell layer
Suspended spheroids (layered)
Surface cells
Assumed perceptibility
Core cells
F
RESEARCH
Mechanoperception
Mechanotransduction
Mechanoadaption
Gravitational force
Mechanosensor
Cell response
Altered function?
knowledge
Pathways: YAP, p38 MAPK, STAT3, NF-κB, …
Biophysical changes
Cytoskeleton & organelle rearrangement, ion shifts
Biochemical changes
Omics, bioinformatics
Biological changes (morphology, physiology)
Functional analyses
(Patho)physiological mechano-microenvironments
Patients on Earth

◄ TAFEL 1: ZELLBIOLOGISCHE FORSCHUNG IN MIKROGRAVITATION. (**A**) Plattformen für Forschung in realer Mikrogravitation (µ*g*). Das Diagramm stellt die Dauer, in der sich das Experiment (in Summe) unter Mikrogravitationsbedingungen befindet gegen die Höhe der verwendeten Plattform über dem Meeresspiegel dar. Die vorhandene „Restschwerkraft" bei der Verwendung dieser Plattformen ist in Rot angegeben. Ebenso dargestellt ist die Karman-Linie, die Grenze zwischen Erde und Weltraum (100 km ü. NN). (**B**) Mechanismen der Simulation von Mikrogravitation für biologische Experimente im Labor. Gemeinsam ist allen Methoden die Verhinderung der Sedimentation planktonischer Zellen. Die durch Pfeile angedeuteten Kräfte und Bewegungen der Mikrogravitations-Simulatoren, denen die Zellen ausgesetzt sind, verdeutlichen bereits, dass „simulierte Mikrogravitation" nicht exakt den Bedingungen in realer Mikrogravitation entspricht (Bild rechts). Für die magnetische Levitation werden in den meisten Fällen Fe_3O_4-Nanopartikel in die Zellen eingebracht, die dann in einem Magnetfeld in Schwebe gehalten werden. Der rote Balken zeigt den auftretenden mechanischen Stress bei der Verwendung der jeweiligen Simulatoren an. Die Qualität der simulierten Mikrogravitation ist in Rot angegeben. Bei der Verwendung von handelsüblichen Zellkulturflaschen ist zu beachten, dass für Rotations-Simulatoren die Zellkulturflasche luftblasenfrei gefüllt sein muss, was die Oberfläche für den Gasaustausch reduziert (blaue Box). (**C**) Die Zelle nutzt verschiedene Strukturen und Proteine, um gravitationsbezogene, mechanische Effekte wahrzunehmen. Hierzu gehören mechanosensitive Ionenkanäle (gelb), die sich durch mechanische Einflüsse öffnen, Zell-Zell- (rot) und Zell-Matrix-Verbindungsproteine (grün). Auch der Zellkern selbst wird durch mechanische Einflüsse beeinflusst (blau): es öffnen sich Kernporen (NP) zum erleichterten Ein-/Austritt von Transkriptionsfaktoren (TF) und Chromatin wird reorganisiert. Eine der wichtigsten Strukturen für gravitationsbezogene Effekte ist das (Aktin-)Zytoskelett (violett) samt seiner Verbindungsproteine (z.B. Vinculin, Talin, Paxillin, FAK, ZO-1). (**D**) Das „Tensegrity-Modell" dient zur Beschreibung des Zytoskelett-Verhaltens von Einzelzellen in Mikrogravitation. Nach dem Wegfall der gravitationsabhängen mechanischen Einwirkung auf die Zelle entspannt sich das gesamte Gerüst aus Filamenten und es kommt zur Verschiebung von Zell-EZM- und Zell-Zell-Kontakten. (**E**) Die Wahrnehmung äußerer Kräfte (rote Pfeile) ist abhängig von den verwendeten Zellkulturbedingungen. Während adhärente, zweidimensional wachsende Zellen mechanisch verformt werden, unterliegen Suspensionszellen nur der Trägheit, was zu Scherungen führt. Bei 3D-Zellkulturen werden sehr wahrscheinlich nur die äußeren, umweltexponierten Zellen mechanisch beeinflusst. Die Mechano-Wahrnehmung nimmt im Sphäroid von außen nach innen ab. (**F**) Die Reaktion von Zellen auf mechanische Einflüsse, wie sie auch bei Gravitationsänderungen auftreten, läuft in verschiedenen, aufeinanderfolgenden Phasen ab, die mit unterschiedlichen Methoden analysiert werden können. Unmittelbar nach dem mechanischen Reiz kommt es zu den biophysikalischen Effekten der Mechanoperzeption (insb. Verformungen). Diese können mikroskopisch beobachtet werden. Oftmals lösen Ionenverschiebungen anschließend die biochemische Signaltransduktion aus, die mit den verschiedenen Omics-Methoden untersucht werden kann. Die biologischen Effekte, wie die mechanoadaptierte, veränderte Zellmorphologie, -physiologie und -funktion, leiten die letzte Phase der Zellantwort ein. In dieser Phase bieten sich zelluläre Funktionstests an.

Die Tafel in ihrer Gesamtheit beschreibt den Weg, wie die Auswirkungen der Schwerelosigkeit auf den menschlichen Körper (oben) in der Weltraummedizin Forschungsfragen aufwerfen, die aufgrund der begrenzen Verfügbarkeit von realer Mikrogravitation die Entwicklung von µ*g*-Simulationsmethoden vorantreiben, welche zur intensiven Erforschung der Auswirkungen von Gravitationsänderungen auf Zellen genutzt werden. Von der Forschung auf diesem Gebiet kann letztendlich auch die Medizin auf der Erde profitieren (unten), insbesondere wenn (patho)physiologische Mechano-Mikroumgebungen im Körper beteiligt sind (1: Angiogenese, 2: Osteoporose/Osteoarthritis, 3: Lungenfibrose, 4: Herzfibrose, 5: Wundheilung, 6: Leberfibrose, 7: Nierenfibrose, 8: Neuroregeneration).

*Teilabbildungen A und B wurden verändert nach **Publikation 1**, Teilabbildung D wurde verändert nach **Publikation 2**.*

Die Tafel wurde mit Elementen aus BioRender und Servier Medical Art erstellt.

3.4 Orbitale Plattformen: Satelliten, Raumfähren, Raumstationen[1]

Der Goldstandard für Mikrogravitations-Experimente besteht darin, das Untersuchungsobjekt in eine Erdumlaufbahn zu bringen, wie z.B. auf die ISS, auf Raumfähren oder Satelliten. Objekte in der Umlaufbahn befinden sich ständig im freien Fall und unterliegen daher keinen Schwerkrafteffekten. Die ISS bietet eine Reihe von Forschungseinrichtungen in einer einzigartigen Laborumgebung, in denen Weltraumeffekte bereits auf viele Aspekte unseres täglichen Lebens untersucht wurden. Auf orbitalen Plattformen sind vor allem Langzeitexperimente unter Weltraumbedingungen möglich, die aufgrund der exponierten Lage in der Erdatmosphäre jedoch gleichzeitig auch immer höherer Weltraumstrahlung ausgesetzt sind (effektive Dosis an Bord der ISS: ca. 0,3 mGy/Tag) (Shavers *et al.*, 2024). Orbitale Plattformen bieten daher „Gesamtpakete“ für Forschung unter Weltraumbedingungen.

4. Erzeugung von mikrogravitations-ähnlichen Bedingungen im Labor

In den letzten Jahrzehnten wurden mehrere technische Geräte mit unterschiedlichen physikalischen Konzepten entwickelt, um Mikrogravitation auf der Erde zu „simulieren“ (Beysens & van Loon, 2015; Herranz *et al.*, 2013). Gemein ist den „gound-based facilities“ (GBFs), wie sie von der Europäischen Raumfahrtagentur ESA bezeichnet werden (Brungs *et al.*, 2016; Jost *et al.*, 2005), die Verhinderung der Sedimentation von Zellen und Zellaggregaten, wodurch diese in einem Schwebezustand gehalten werden (▤ Tafel 1B). Die Auswirkungen der Erdgravitation werden durch diese Methoden nicht verringert bzw. ausgeschaltet, sondern durch andere physikalische Effekte geschickt überdeckt. Wie bei jedem Kompromiss gibt es dabei Nebeneffekte, auf die bei der Vorstellung der jeweiligen Geräte noch näher eingegangen wird. Daher ist der Begriff „simulierte Mikrogravitation“ sicher nicht optimal gewählt und es sollte besser von „simulierten Effekten der Mikrogravitation“ gesprochen werden, die jedoch zelltypspezifisch und abhängig vom gewählten Untersuchungssystem sind. Daher könnte man die GBFs ebenso zu den Mikrogravitations-Analoga zählen, zu denen u.a. Strategien wie das Hindlimb-Unloading (Nager), Dry Immersion- (Mensch), und Bedrest-Studien (Mensch) gehören; Methoden, bei denen nicht unbedingt die Erzeugung mikrogravitationsähnlicher Bedingungen im Vordergrund steht, sondern von vergleichbaren physiologischen Effekten (Ferranti *et al.*, 2021). Da die zellulären Effekte oftmals vom Betriebsmodus der GBFs abhängig sind, wurden zur besseren Vergleichbarkeit und Wahrung der Reproduzierbarkeit gravitationsbiologischer Experimente mit den Bonner Kriterien Anfang der 2010er Jahre GBF-Betriebsparameter festgelegt, die zusammen mit den Resultaten publiziert werden sollten. Dazu zählen verwendeter Gerätetyp, Rotationsmodus, Winkelgeschwindigkeiten sowie die höchsten erreichten Winkelbeschleunigungen (Hammond & Allen, 2011).

[1] Mit *SPHEROIDS* (Endothelzellen), *CellBox-1* und *CellBox-2* (Schilddrüsenkrebszellen) sind auch drei ISS-Experimente Gegenstand der Publikationen dieser Habilitationsschrift.

Aufgrund der hohen Kosten und begrenzten Möglichkeiten für Experimente unter realen Mikrogravitationsbedingungen stellen Mikrogravitations-Biorektoren eine perfekte Option zur Prüfung von Hypothesen oder zur Durchführung von Vor- und vergleichenden Studien dar. Außerdem ermöglichen diese Technologien mehr als nur Endpunktanalysen sowie einfache Wiederholbarkeit der Experimente.

4.1 Klinostat

Klinostaten sind Rotations-Bioreaktoren, die sich mit konstanter Geschwindigkeit um eine (2D-Klinostaten) oder zwei Achsen (3D-Klinostaten) drehen. Unter optimalen Experimentbedingungen erzeugen sie nach einigen zügigen Rotationen („fast running clinostats“, ca. 60 rpm) annäherungsweise einen Zustand der „Bewegungslosigkeit“ von Partikeln relativ zur umgebenden Flüssigkeit (Klaus, 2001). Das funktioniert gut bei kleinen Objekte, wie z.B. Einzelzellen (Briegleb, 1992). Ein Klinostat wird daher normalerweise für Experimente mit planktonischen Objekten eingesetzt, die eine ruhige, stressfreie Zellumgebung erfordern, wie sie auch unter realer Mikrogravitation vorzufinden ist. Bei unsachgemäßem Betrieb kommt es jedoch schnell zu hohen Scherkräften.

4.2 Rotating Wall Vessel

Die Rotating Wall Vessel (RWV; kommerziell auch gerne als Rotary Cell Culture System, RCCS, oder als High Aspect Rotating-Wall Vessel, HARV, bezeichnet) wurde in den frühen 1990er Jahren von der amerikanischen National Aeronautics and Space Administration (NASA) entwickelt (Schwarz *et al.*, 1992). Genau genommen handelt es sich bei der RWV um ein spezielles zylindrisches Zellkulturgefäß (5-20 cm Durchmesser), welches über einen Riemenantrieb in eine horizontale Drehung versetzt wird (10-20 rpm). Technisch ist die RWV den 2D-Klinostaten zuzuordnen, allerdings ist das Innere der Zellkulturkammer nicht komplett scherungsfrei, schafft aber eine scherungsarme Kulturumgebung mit gleichmäßigem Flüssigkeitsaustausch (Gao *et al.*, 1997), was eine dreidimensionale Aggregation der Zellen forciert. Die RWV wird daher über die Gravitationsbiologie hinaus gerne zur Erzeugung von 3D-Zellkulturen eingesetzt. Zusätzlich wird während des Experiments der Gasaustausch über eine Silikonmembran ermöglicht. Dadurch liefert die RWV durch interne Flüssigkeitsumwälzung nicht nur ausreichend Nährstoffe, sondern auch die notwendige Sauerstoffzufuhr für die Entwicklung und Polarisierung von Zellen, was dem Tissue Engineering zugutekommt. Initial werden die Zellen für RWV-Experimente auf Mikrocarrier-Beads oder in einer speziellen Matrix kultiviert, es ist aber auch der direkte Einsatz von Zellsuspensionen möglich (Hammond & Hammond, 2001). Suspensionszellen sind durch den „endlosen freien Fall“ in der rotierenden RWV allerdings ständig von einer Flüssigkeitsströmung umgeben (Liu *et al.*, 2004).

Als Weiterentwicklung der RWV ist der ClinoStar® der Firma CelVivo (Dänemark) zu nennen. Bei diesem Gerät ist zum einen der CO_2-Inkubator schon um die Kulturgefäße herumgebaut, die neben einer semipermeablen Membran zum Gasaustausch auch ein Befeuchtungssystem mit

Wasserperlen beinhalten. Zum anderen kann das 3D-Wachstum während der Experimente für alle 6 Kulturkammern über eine Kamera beobachtet werden.

4.3 Random Positioning Machine

Bei der Random Positioning Machine (RPM) handelt es sich um eine spezielle Version des 3D-Klinostaten, bei der im „real random"-Normalbetrieb die Rotationsrichtung und -geschwindigkeit der beiden Achsen über einen Zufalls-Algorithmus so gesteuert wird, dass der über die Zeit gemittelte Gravitationsvektor in Summe <0,01*g* beträgt. Damit verbunden ist einer der wichtigsten Unterschiede zum 3D-Klinostaten, dass die Drehrichtung der auf der RPM installierten Zellkulturflaschen variiert und keine konstante Geschwindigkeit aufweist, was wiederum Einfluss auf die Flüssigkeitsbewegungen innerhalb einer luftblasenfrei gefüllten Zellkulturflasche hat. Mit dem Thema „Scherkräfte auf der RPM" haben sich bereits einige Arbeitsgruppen befasst (Hauslage *et al.*, 2017; Leguy *et al.*, 2017; Wuest *et al.*, 2015; Wuest *et al.*, 2017).

Eine modifizierte RPM ist die Inkubator-RPM (iRPM), bei der ein kompletter CO_2-Inkubator zwischen den zwei Rahmen aufgehängt ist und über einen Zufallsalgorithmus rotiert wird. Die am MTRM vorhandene, nicht-kommerzielle iRPM2 (entwickelt von Prof. Jörg Sekler, Fachhochschule Nordwestschweiz) ermöglicht die Untersuchung von größeren Proben und Probenmengen zur gleichen Zeit (Benavides Damm *et al.*, 2014).

Besonders beliebt ist die RPM für die Kultivierung adhärenter Zellen, die als Monolayer unter den Bedingungen simulierter Mikrogravitation untersucht werden sollen. Solche Experimente fordern das Prinzip der Mikrogravitations-Simulation (▤ Tafel 1B) natürlich besonders heraus, da die Zellen ihre Position am Boden der Zellkulturflasche nicht ändern können und durch die Rotation – den Scherkräften der Flüssigkeitsströmung ausgeliefert – vor allem „zufallspositioniert" werden. Diese Zufallspositionierung ist bereits ausreichend, um interessante Effekte in den Zellkulturen auszulösen, die teilweise ähnliche Ergebnisse hervorbringen, wie sie mit derselben Zelllinie nach Raketenflügen und/oder Weltraumaufenthalten beobachtet werden (Ma *et al.*, 2014).

In einer Studie mit Schilddrüsenkarzinomzellen wurden die komplexen Bewegungen der RPM in unterschiedliche Rotationen und Orientierungen der Zellkulturflaschen aufgesplittet. Hierbei wurde deutlich, dass die RPM-Bewegung effektiv mehr ist als eine einfache Rotation um eine Achse oder die Summe aller Ausrichtungen der Zellkulturflasche **(Publikation 5)**. Die in den Krebszellen ausgelösten Effekte durch die RPM konnten weder durch Klinorotation noch durch statische, räumliche Reorientierung der Zellen nachgeahmt werden. Während die Rotation mathematisch unabhängig von der Rotationsgeschwindigkeit früher oder später immer zur „über die Zeit gemittelten Mikrogravitation" führt, waren die zellulären Effekte sehr wohl abhängig von der Rotationsgeschwindigkeit. Hier spielen vor allem die vorhin erwähnten mikrofluidischen Effekte innerhalb der Zellkulturflasche eine Rolle, die durch die Zufallspositionierung entstehen **(Publikation 5)**.

4.4 Magnetische Levitation

Magnetische Levitation ist eine nicht-rotationsbasierte Methode, die ebenfalls zur Simulation von Mikrogravitation eingesetzt wird (Kamal *et al.*, 2016; Sanavandi & Guo, 2021; Sarabi *et al.*, 2022). Ihr Prinzip beruht darauf, dass sich Körper je nach ihrer Ladung oder Polarität gegenseitig abstoßen können und die Schwerkraft dadurch ausgeglichen wird. Hierfür werden die Zellen zunächst meist mit ferromagnetischen Nanopartikeln (enthalten Fe_3O_4) beladen, die anschließend in einem Magnetfeld stabilisiert werden und auf diese Weise die Sedimentation der Zellen verhindern. Die „magnetisierten" Zellen sind während der Levitation zwar keinen Scherkräften ausgesetzt, allerdings ist ein Einfluss der eingesetzten Partikel auf die Zellphysiologie zwar unwahrscheinlich, jedoch nicht komplett ausgeschlossen (Aljarrah *et al.*, 2012; Souza *et al.*, 2010). Starke Magnetfelder können auch Störeffekte in Zellen hervorrufen, die zu Fehlinterpretationen der Effekte in „simulierter Mikrogravitation" führen können (Hemmersbach *et al.*, 2014).

5. Die struktur- und molekularbiologische Basis für schwerkraftabhängige Effekte in humanen Zellen

5.1 Potenzielle Gravisensoren eurakyotischer Zellen (siehe auch Tafel 1C)

5.1.1 Mechanosensorische Strukturen

Albrecht-Bühler hat in den 1990er Jahren bereits postuliert, dass das Gewicht einer einzelnen Zelle normaler Größe im Vergleich zu anderen zellulären Kräften zu gering ist, als dass sie zwischen oben und unten unterscheiden könnten. Tierische Zellen nehmen nach seiner Hypothese Änderungen im Gravitationsvektor daher nur indirekt (von außen) wahr (Albrecht-Buehler, 1991). Während bei pflanzlichen Zellen intrazelluläre Strukturen höherer Dichte (stärkehaltige Statolithen) existieren, die im Zytoplasma durch die Erdanziehung sedimentieren (Takahashi *et al.*, 2021), ist bei tierischen Zellen bisher kein solches, zellinternes System bekannt. Wenn Statolithen vorkommen, wie z.B. in sensorischen Organen im Innenohr, dann sind diese extrazellulär und sedimentieren von außen auf die perzipierende Zelle und lenken dadurch beispielsweise berührungssensitive Zilien aus (Hudspeth & Corey, 1977). Das Konzept der zytoplasmatischen Bewegung von Organellen höherer bzw. geringerer Dichte im Schwerefeld der Erde ist bei tierischen Zellen bisher nicht nachgewiesen, aber auch nicht komplett ausgeschlossen. Der Zellkern hat beispielsweise eine geringere Dichte als das umgebende Zytoplasma (Kim & Guck, 2020). Durch die Aufhängung des Zellkerns an Mikrofilamenten des Zytoskeletts können zelluläre Effekte hervorgerufen oder – analog zu Pflanzenzellen – membranständige Ionenkanäle beeinflusst werden (Uhler & Shivashankar, 2017; Wang *et al.*, 2009).

5.1.2 Zytoskelett

Von einigen Forschern wird das Zytoskelett (Aktinfilamente (Mikrofilamente), Mikrotubuli, Intermediärfilamente, Verbindungsproteine) als möglicher Gravisensor vorgeschlagen (Hughes-Fulford, 2003; Vorselen *et al.*, 2014), da es sehr sensitiv auf jegliche Verformung der Zelle reagiert und mechanische Einwirkungen sehr schnell innerhalb der Zelle bis hin zur Chromatin-Organisation verteilen kann. Das „Tensegrity-Modell“ (aus engl. tension = Spannung und integrity = Zusammenhalt) veranschaulicht, wie das Fehlen von äußeren Kräften in einer Mikrogravitationsumgebung zu einer Entspannung der zytoskelettdurchspannten Zelle führen und so zellweite Veränderungen hervorrufen kann (▤ Tafel 1D) (Ingber, 1999). Zytoskelett-Untersuchungen sind daher oft im Fokus der Gravitationsforschung (Corydon *et al.*, 2016; Wu *et al.*, 2022).

5.1.3 Zelladhäsionsproteine

Transmembrane Zelladhäsionsproteine fungieren als bidirektionale Schnittstelle zwischen extrazellulären mechanischen Kräften und zellulären Reaktionen. Sie übertragen physikalische Spannungen über die Membran hinweg ins Zellinnere (outside-in), wo sie über Verbindungsproteine mit dem Zytoskelett verbunden sind. Zusätzlich wird die Zelladhäsion anhand intrazellulärer Bedingungen beeinflusst (inside-out). Damit sind Adhäsionsproteine nicht nur strukturelle Gerüste, sondern Signalzentren, die in der Lage sind, verschiedene Reaktionen nach angewandten externen Reizen zu koordinieren. Aufgrund dieser Tatsache spielen sie auch bei Gravitationseffekten eine wichtige Rolle. Trotz zahlreicher Studien sind die Mechanismen, durch die sich die Schwerelosigkeit auf die Zelladhäsion auswirkt, noch nicht vollständig bekannt und müssen weiter untersucht werden (Lin *et al.*, 2020).

Die vier Hauptklassen der Zelladhäsionsproteine sind Integrine, Cadherine (E-Cadherin, N-Cadherin, VE-Cadherin), die Immunglobulin-Superfamilie (ICAM, VCAM, PECAM) und Selektine (E-Selektin, L-Selektin, P-Selektin). Integrine gehen Verbindungen mit verschiedenen Proteinen der EZM ein (u.a. Fibronektin, Vitronektin) (Sun *et al.*, 2016), während Cadherine adaptive, dimere Zell-Zell-Verbindungen formen (Leckband & de Rooij, 2014). Immunglobuline und Selektine dienen funktionell spezifischen Adhäsionen zwischen verschiedenen Zelltypen, wie Immun-, Endothel- und Tumorzellen (Läubli & Borsig, 2010; Matthäus *et al.*, 2017; Witz, 2008).

5.1.4 Membranen und mechanosensitive Ionenkanäle

Biologische Membranen sind selbst mechanoresponsive Strukturen, die in ihrer Flüssig-Mosaik-Struktur Mechanosensoren beinhalten, welche bei gravitationsbedingter Deformation angesprochen werden. Zu den bekanntesten gehören Piezo- und TRP-Kanäle (transient receptor potential), die sich bei mechanischer Verformung öffnen und den Einstrom von Ionen erlauben, was wiederum zu einer Veränderung des Membranpotentials führt und die Signalübertragung aktiviert (Cox *et al.*,

2024; Delmas *et al.*, 2022; Fang *et al.*, 2021). Mittlerweile gibt es mehrere Hinweise, dass einige G-Protein-gekoppelte Rezeptoren (GPCRs), neben Licht und chemischen Liganden, auch durch mechanische Einflüsse aktiviert werden können (Goodman *et al.*, 2023). Sieber *et al.* gingen nach ihren Membranstudien unter verschiedenen Schwerkraftbedingungen sogar noch einen Schritt weiter: Sie führten die Hypothese ein, dass eine Vielzahl von Ionenkanälen in ihren Eigenschaften vom physikalischen Zustand der Membran abhängig ist, deren Fluidität sich in Mikrogravitation beispielsweise erhöht (Sieber *et al.*, 2014).

5.1.5 Zellkern

Die auf die Zellen einwirkenden Kräfte werden über die Komponenten des Zytoskeletts von der extrazellulären Umgebung auf die verschiedenen Zellorganellen übertragen. Der Zellkern besitzt die größte Steifigkeit (Kirby & Lammerding, 2018) und kann bei mechanischen Einflüssen erhebliche Formveränderungen erfahren, die in Folge veränderte Genexpressionsmuster hervorrufen (Alisafaei *et al.*, 2019; Humphrey *et al.*, 2014). Die biophysikalische Mechanosensitivität beinhaltet stressbedingte Veränderungen von Proteinkonformationen (Interaktion mit Bindungspartnern), die Verlagerung von Transkriptionsregulatoren, die Konformation und Organisation von Chromosomen und die Dehnung/Ruptur der Kernmembran (Cho *et al.*, 2017; Kirby & Lammerding, 2018; Pennacchio *et al.*, 2021). Der Zellkern ist demnach eine wichtige Mechanosensor-Organelle und steuert gleichzeitig die Reaktion der Zelle auf mechanische (Schwerkraft-)Einflüsse (Neelam *et al.*, 2020; Vahlensieck *et al.*, 2021).

5.2 Zeitfenster für die zelluläre Antwort auf Gravitationsänderungen

Die Reaktion einer Zelle auf Gravitationsänderungen umfasst drei aufeinanderfolgende Phasen (▤ Tafel 1F), die schließlich in der funktionellen Adaption enden. Die biophysikalische Phase (Phase I, Sekunden bis Minuten) beinhaltet die mechanische Wahrnehmung von Schwerkraft(effekten) durch spezialisierte Sensoren, wie Statolithen in Pflanzen oder mechanosensitive Ionenkanäle in tierischen Zellen, aber auch durch die mechanische Veränderung von Zytoskelett und Zellstruktur. Die folgende, biochemische Phase (Phase II, Stunden bis Tage) umfasst die Aktivierung von Signaltransduktionswegen und Veränderungen der Genexpression, die infolge mechanischer Reize ausgelöst werden. Diese Reaktionen sind oftmals wichtig für die spätere Anpassung von Zellfunktionen an die veränderte Schwerkraft. In der biologischen Phase (Phase III, Tage bis Wochen) entwickeln sich strukturelle und funktionelle Veränderungen in Zellen oder Geweben, wie etwa die Modifikation von Zellproliferation, -morphologie, -metabolismus, und -differenzierung. Anhand dieser Phasen existieren Zeitfenster, in denen sich jeweils vorübergehend bestimmte Vorgänge in der Zelle mit unterschiedlichen Methoden beobachten lassen.

6. Durch Gravitationsänderungen induzierte Effekte in humanen Zellen

6.1 Reorganisation des Zytoskeletts

Die Struktur des Zytoskeletts ist eng mit der Zellform verknüpft (Flusberg *et al.*, 2001). Zahlreiche Studien zeigen, dass sowohl reale als auch simulierte Mikrogravitationsbedingungen zu einer signifikanten Veränderung der Struktur und Dynamik von Aktinfilamenten und Mikrotubuli führen. Das von Vorselen *et al.* 2014 vorgeschlagene Modell der Zytoskelettveränderungen in Mikrogravitation hat heute noch Gültigkeit und beinhaltet die Verkürzung von Mikrotubuli und den Verlust ihrer radialen Organisation hin zu einer perinukleären Anordnung. Aktinfilamente akkumulieren perinukleär und/oder cortikal und Aktin-Stressfasern reduzieren sich in Anzahl, Länge und Dicke (Vorselen *et al.*, 2014).

Da sich das Zytoskelett unter veränderten Gravitationsbedingungen entsprechend dem Tensegrity-Modell spontan ändern kann (▤ Tafel 1D), bieten sich zur Untersuchung der Zytoskelettstruktur v.a. Live-Beobachtungen der Zellen beim Übergang unterschiedlicher Gravitationsphasen an. Während der TEXUS-54-Mission wurden doppelt transfizierte MCF-7-Mammakarzinomzellen untersucht, bei denen Lifeact-GFP zur Visualisierung von F-Aktin und mCherry-Tubulin zur Visualisierung der Mikrotobuli zum Einsatz kamen **(Publikation 6)**. Mithilfe des für TEXUS-Raketen angepassten FLUMIAS-Mikroskops (Fluorescence Microscopy Analysis System) (Corydon *et al.*, 2016) konnten die lebenden Zellen während des Fluges live beobachtet werden. In den 7 Minuten in realer Mikrogravitation wurden bei den Zellen kurzfristig auftretende lokale Aktin-Akkumulierungen sowie die Ausbildung von Filopodien und Lamellipodien beobachtet. Das Mikrotubuligerüst lockerte sich nach etwa 2,5 Minuten auf **(Publikation 6)**. Ähnlich schnelle Veränderungen des Zytoskeletts konnten auch bei anderen Zelltypen, wie z.B. Schilddrüsenkarzinomzellen (Corydon *et al.*, 2016) oder Makrophagen (Thiel *et al.*, 2019), in Mikrogravitation gezeigt werden. Die perinukleäre Clusterbildung der Mikrotubuli trat bei Endothelzellen z.B. schon nach 22 s Mikrogravitation während eines Parabelflugs auf (Grosse *et al.*, 2012). Die rapide Reorganisation des Zytoskeletts unter Mikrogravitationsbedingungen spiegelt auch die spontane Anpassungsfähigkeit humaner Zellen wider, da das Zytoskelett wiederum Zelladhäsion, -proliferation und verschiedene Signaltransduktionswege beeinflusst (Tietze *et al.*, 2020). Ein 4-stündiges RPM-Experiment mit zweidimensional wachsenden FTC-133-Schilddrüsenkarzinomzellen zeigte eine ähnliche Akkumulierung von F-Aktin wie ein Durchflussexperiment mit 25 mPa Scherstress, was auf einen ähnlichen mechanischen Einfluss auf die Zellen schließen lässt **(Publikation 5)**. Bei längeren Experimenten in simulierter Mikrogravitation konnten immer wieder veränderte Zytoskelettstrukturen im Vergleich zu statischen Kontrollen beobachtet werden **(Publikation 7)**, die nicht nur auf eine räumliche Verschiebung beschränkt waren, sondern auch die Anzahl und Länge der Filamente betrafen. Hierzu sollte allerdings angemerkt werden, dass es sich bei der Polymerisation/Depolymerisation von Zytoskelett-Filamenten um eine dynamisch regulierte Zellantwort handelt, während sich spontane Änderungen

beim Eintritt in Mikrogravitation auf die einfache physikalische Wiederherstellung des mechanischen Gleichgewichts zurückführen lassen. Die Prozesse, die zur Veränderung der Zytoskelettmorphologie unter Mikrogravitationsbedingungen führen, sind also zu Beginn andere als im späteren Verlauf.

6.2 Zelladhäsion und extrazelluläre Matrix

Zellen kommunizieren über das Zytoskelett und Zelloberflächen-Adhäsionsproteine mit der EZM und den benachbarten Zellen. Werden Tumorzellen in Mikrogravitation als Monolayer kultiviert, regulieren sie Adhäsionsproteine wie E-Cadherin und Integrin-β1 meist herunter (Li *et al.*, 2009) **(Publikationen 6, 8-10)**. Diese Beobachtung wurde auch bei einigen gutartigen Zellen gemacht, darunter juvenile dermale Fibroblasten **(Publikation 11)** und Keratinozyten (Ranieri *et al.*, 2017), und sie wurde dadurch in Verbindung mit der mikrogravitations-induzierten Sphäroidbildung gebracht. In Sphäroid-Kulturen selbst gab es (am Beispiel von FTC-133-Zellen) eine zeitlich verzögerte Zunahme der *CDH1*- und *ITGB1*-mRNA nach drei Tagen Zufallspositionierung **(Publikation 9)**. Auch Langzeit-RPM-Kulturen (7/14 Tage) mit sehr dichten Monolayern besitzen mehr E-Cadherin **(Publikation 12)**. Das verdeutlicht noch einmal, dass die Interaktion von Zellen mit anderen Zellen und/oder mit der EZM in 2D- und 3D-Kulturen ganz unterschiedlich durch Gravitationsänderungen beeinflusst werden und „Gravitationsstress“ vermutlich zellkulturabhängig wahrgenommen wird. Darauf deuten auch Experimente mit unterschiedlich langen Präinkubationszeiten vor der Zufallspositionierung hin **(Publikation 5)**.

Etwas anders verhält es sich bei Endothelzellen: Sowohl bei immortalisierten Ea.hy926-Zellen als auch bei primären mikrovaskulären Endothelzellen (HMVEC) gab es eine Zunahme von Integrin-β1 in einer RPM-Zellkultur (Abb. 5B). Auch ICAM-1 und VCAM-1 wurden bei RPM-2D-Zellkulturen von Ea.hy926-Zellen verstärkt exprimiert **(Publikation 13)**. Ein zweistündiger Parabelflug führte bei MDA-MB-231-Mammakarzinomzellen ebenfalls zur gesteigerten Expression von ICAM-1, VCAM-1 und CD44 verglichen mit entsprechenden Bodenkontrollen **(Publikation 14)**. Zuvor gab es bereits einen ähnlichen Effekt bei FTC-133-Zellen während der TEXUS-53-Mission **(Publikation 4)**. Keiner dieser Effekte konnte allerdings durch eine zweistündige RPM-Exposition simuliert werden. Die Expression von *ICAM1* wurde in MCF-7-Zellen aber durch ein flugzeugähnliches Vibrationsmuster (Vibraplex), die von *CD44* durch Hypergravitation (1,8*g*, Zentrifuge) erhöht **(Publikation 14)**. Da die Expression von Adhäsionsproteinen stark von der Mechano-Umgebung der Zellen abhängig ist (äußere mechanische Einflüsse, Festigkeit und Struktur des Substrats, etc.), die sich bei den Studien unterschieden haben könnte, ist es schwierig, Ergebnisse aus unterschiedlichen Studien direkt miteinander zu vergleichen. Die Daten geben jedoch Anhaltspunkte für weitere Forschung.

Viele Zellen produzieren unter mechanischer Belastung verstärkt EZM, wobei die Modifikation der sezernierten Matrix durch Gravitationsänderungen zelltypabhängig ist. Die EZM-Komponenten sind entscheidend für Wachstum, Differenzierung und Apoptose von Zellen. In RPM-Zellkulturen wurden erhöhte Fibronektin-Mengen bei Fibroblasten **(Publikation 11)**, Endothelzellen **(Publikation 12)**, Schilddrüsenepithelzellen **(Publikationen 15)** und triple-negativen Mammakarzinomzellen

(Publikation 16) nachgewiesen, nicht jedoch bei anderen Tumorzellen wie FTC-133-Schilddrüsenkarzinom- **(Publikation 9)** oder PC-3-Prostatakarzinomzellen **(Publikation 17)**. Die Kollagenmenge wurde durch die RPM in PC-3-Zellen **(Publikation 7)**, Schilddrüsenepithelzellen **(Publikation 8)** und Chondrozyten **(Publikation 11)** erhöht**.** Die Lamininbildung wurde durch die RPM in fötalen Osteoblasten angeregt **(Publikation 18)**. Auch wenn bei den Auswirkungen der RPM auf die EZM kein direktes Muster erkennbar ist, so hat eine Umgestaltung der EZM meist einen anhaltenden Effekt auf die Morphologie und die Funktionen von Zellen. Die mechanischen Eigenschaften der EZM sind für viele biologische Prozesse entscheidend. So definiert die Steifigkeit der EZM den Widerstand gegen Verformung von Zellen und Geweben (Gewebeelastizität). Insbesondere die Verformbarkeit von Krebszellen steht in Zusammenhang mit dem invasiven Verhalten und könnte daher eine entscheidende Rolle bei der Metastasierung spielen (Ishihara & Haga, 2022).

6.3 Intrazelluläre Signalwege

Intrazelluläre Signalwege bilden das Verbindungsstück zwischen der Wahrnehmung von gravitationsbedingten Signalen und zellulären Reaktionen (Signaltransduktion). Da sowohl die Anzahl an Signalwegen in der Zelle als auch die Interaktion verschiedener Signalwege untereinander (crosstalk) sehr komplex und auch noch nicht vollständig untersucht ist, soll hier nur auf die wichtigsten Signalwege eingegangen werden, die auch eine Rolle in den verwendeten Publikationen spielen.

6.3.1 p38 MAPK-Signalweg

Die p38-mitogenaktivierte Proteinkinase (MAPK) ist an einer Signalkaskade beteiligt, welche die zelluläre Reaktionen auf Zytokine und Stress kontrolliert (Whitmarsh, 2010). In gravitationsbiologischen Experimenten wurde p38 schon im Zusammenhang mit der Immunsuppression in Mikrogravitation (Wang *et al.*, 2015; Wang *et al.*, 2020), sowie der RWV-vermittelten Chondrogenese (Yu *et al.*, 2011) gebracht.

Wir haben p38 erstmals in RPM-exponierten Krebszellen untersucht. FTC-133-Zellen reagierten auf die RPM in einer dreitägigen Kultur mit einer starken Aktivierung (Kernverschiebung) von p38 **(Publikation 8)**. Der Effekt konnte pharmazeutisch durch Dexamethason revertiert werden. Im Gegensatz dazu hatte die RPM bei gutartigen Nthy-ori 3-1-Schilddrüsenepithelzellen kaum Einfluss auf p38 **(Publikation 8)**. Bei RPM-Ergebnissen handelt es sich immer um Momentaufnahmen, und wie Untersuchungen zu weiteren Zeitpunkten zeigten, ist der Effekt in FTC-133-Zellen nach 4 h Zufallspositionierung genau umgekehrt (zytoplasmatische Translokation von p38) **(Publikation 5)**. Bei Calu-3-Lungenkarzinomzellen war ebenfalls keine Kernverschiebung von p38 nach dreitägiger RPM-Kultur zu erkennen **(Publikation 10)**. Diese Daten scheinen zunächst widersprüchlich zu sein, deuten aber an, dass der p38-Signalweg sehr dynamisch in Abhängigkeit von den Zellkulturbedingungen sowie von den Eigenschaften der eingesetzten Zellen zu reagieren scheint.

Eine Lebendzellbeobachtung (auf der RPM bisher noch nicht möglich) wäre eine adäquatere Untersuchungsmethode für die p38 Signalübertragung unter Mikrogravitationsbedingungen.

6.3.2 NF-κB-Signalweg

Die Bedeutung des NF-κB-Signalwegs (nuclear factor 'kappa-light-chain-enhancer' of activated B-cells) kam vor allem nach den Arbeiten von Kopp *et al.* an MCF-7 Mammakarzinomzellen auf der RPM auf. In den Experimenten verdichteten sich die Hinweise, dass NF-κB eine wichtige Rolle in der RPM-induzierten Sphäroidbildung spielt (Kopp *et al.*, 2018). Die Aktivierung des klassischen NF-κB-Signalwegs konnten wir in anderen Krebszellen (FTC-133, Calu-3) bisher nicht bestätigen **(Publikationen 9,10)**, so dass es sich bei den Beobachtungen in MCF-7-Zellen wahrscheinlich um einen zellspezifischen Effekt handelt.

6.3.3 STAT3-Signalweg

Der Transkriptionsfaktor STAT3 (signal transducer and activator of transcription 3) wurde mit der Hochregulierung der Expression von Adhäsionsproteinen wie z.B, ICAM-1 in menschlichen Nabelvenen-Endothelzellen (HUVECs) unter Weltraumbedingungen in Verbindung gebracht (Muid *et al.*, 2013). Wir konnten in RPM-Experimenten mit Calu-3-Zellen zuletzt keine Kerntranslokation von STAT3 beobachten, obwohl es ebenfalls eine Zunahme der *ICAM1* mRNA gab **(Publikation 10)**.

6.3.4 Hippo-Signalweg (YAP/TAZ)

Der Hippo-Signalweg mit seinen Transkriptionsfaktoren YAP1 (yes-associated protein 1) und TAZ (transcriptional co-activator with PDZ-binding motif) ist einer der bekanntesten Mechanosignalwege, der u.a. auch mit weltrauminduzierten Leberdysfunktion (Li *et al.*, 2023) und der Regulation vom Stammzellen in Mikrogravitation zusammenhängt (Arun *et al.*, 2019; Lv *et al.*, 2023). Da YAP/TAZ auch im Organ- und Tumorwachstum involviert ist (Low *et al.*, 2014), haben wir YAP1 in FTC-133-Zellen untersucht, die auf der RPM kultiviert wurden. Hier zeigte sich jedoch, dass die Kern/Zytoplasma-Verteilung von YAP1 stärker von der Zelldichte abhängt als von der RPM selbst **(Publikationen 5, 8)**.

6.3.5 Wnt-Signalweg

Der Einfluss von Mikrogravitation auf den Wnt-Signalweg wurde bisher vor allem in Kulturen von Knochen- und Knorpelzellen beschrieben (Aissiou *et al.*, 2023; Fan *et al.*, 2022; Yang *et al.*, 2015), bei denen er auch eine wichtige Rolle in der Pathogenese von Osteoarthritis spielt.

Wir konnten in einem FTC-133-Experiment auf der RPM erstmals eine Kerntranslokation von β-Catenin in Tumorzellen beobachten **(Publikation 9)**, was downstream ein wichtiger Schritt im Wnt-Signalweg ist. Sahana *et al.* haben anschließend aus ihren β-Catenin-Daten von RPM-kultivierten

MCF-7 Zellen geschlossen, dass das Wnt-Signaling eine zentrale Rolle in der mikrogravitationsabhängigen Sphäroidbildung zu spielen scheint **(Publikation 16)**. Diese Experimente waren der Ausgangspunkt für das geplante *CANCEROIDS*-Weltraumexperiment, bei dem die Translokation von β-Catenin in MCF-7-Zellen mit Lebendzellmikroskope an Bord der ISS untersucht werden soll. Das Experiment soll laut aktuellem Plan Ende 2026 stattfinden; im ersten Durchlauf mit dem neu entwickelten FLUMIAS-ISS Mikroskop.

6.4 Zellkommunikation

6.4.1 Signalmoleküle: Zytokine, Chemokine, Wachstumsfaktoren

Die unter Mikrogravitationsbedingungen am häufigsten beeinflussten Signalmoleküle umfassen Zytokine (IL-6, TNF), Chemokine (IL-8, CCL2/MCP-1) sowie Wachstumsfaktoren (CTGF, EGF, VEGF). Die Expression von Zytokinen, wie IL-6 (Interleukin-6), wurde vor Kurzem als frühe Reaktion von Prostatakrebszellen auf Gravitationsänderungen in Parabelflugmanövern beschrieben (Schulz *et al.*, 2022). In Chondrozyten ist IL-6 als Antwort auf Scherstress schon länger bekannt (Wang *et al.*, 2010). Erste Arbeiten von Warnke *et al.* deuteten darauf hin, dass die Zytokinausschüttung bei GBF-Experimenten ebenfalls eine Reaktion auf mechanischen Stress sein könnte. Während es auf der RPM (turbulente Strömung) eine verstärkte Zytokinausschüttung bei FTC-133 Zellen gab, war sie auf dem Klinostaten (± unidirektionale Strömung) verringert (Warnke *et al.*, 2014). Vor allem in stressexponierten 2D-Kulturen auf der RPM scheint die erhöhte IL-6-Produktion zelltypunabhängig zu sein und wurde bei Krebszellen **(Publikationen 10)**, Fibroblasten **(Publikationen 11)** und Endothelzellen **(Publikationen 13)** nachgewiesen. Bei einer direkten Vergleichsstudie zwischen Tumor- und gutartigen Zellen wurde aber deutlich, dass nicht alle Zellen IL-6 zur gleichen Zeit exprimieren. Nach drei Tagen auf der RPM war das *IL6* mRNA-Level nur bei 2D wachsenden FTC-133 Zellen erhöht, nicht aber bei entsprechend kultivierten Nthy-ori 3-1-Zellen **(Publikation 8)**. Langzeit-Experimente von Kopp *et al.* zeigten, dass die IL-6 Expression bei Nthy-ori 3-1-Zellen auf der RPM später einsetzt (Kopp *et al.*, 2015).

Die verstärkte Sekretion von IL-8 (Interleukin-8) und VEGF-A (vaskulär-endothelialer Wachstumsfaktor A) tritt bei gutartigen Zellen meistens dann auf, wenn Sphäroide gebildet werden (siehe auch Kapitel 6.5) **(Publikationen 11,13)**. Von IL-8 ist bekannt, dass die Expression durch Flüssigkeitsscherung aktiviert werden kann (Sun *et al.*, 2019) und dass die Anwesenheit von IL-8 (zumindest bei Tumorsphäroiden) die Proliferation steigert (Uddin *et al.*, 2020). Gegensätzliche Daten existieren zur VEGF-A-Expression. Bei einer RPM-Kultur von PC-3-Tumorzellen war die VEGF-A-Konzentration im Zellkulturüberstand geringer als bei statischen Kontrollen **(Publikation 7)**. Generell lässt sich für Tumorzellen sagen, dass die VEGF-A-Sekretion abnimmt, wenn der Monolayer höheren Stressbedingungen ausgesetzt wird. Im Gegensatz dazu nimmt die VEGF-A-Expression in der Sphäroid-Kultur bei geringem Stress ebenfalls ab, steigt aber bei hohem Stresslevel an **(Publikationen 5, 9)**. Die VEGF-A-Regulation in den Tumorsphäroiden entspricht

somit der *in vivo* (Sarkar *et al.*, 2020). Die Menge an sekretiertem VEGF-A ist bei einer RPM-Zellkultur scheinbar auch vom Populationsverhältnis von Monolayer zu Sphäroiden abhängig.

CTGF (Bindegewebe-Wachstumsfaktor) wird ebenfalls als Antwort auf mechanischen Stress sekretiert (Schild & Trueb, 2002), wobei bei Endothelzellen auch die Art des Scherstresses ausschlaggebend ist: In HUVECs wurde CTGF durch laminare Scherbelastung signifikant herunterreguliert; in Zellen, die einer ungleichmäßigen Scherbelastung ausgesetzt waren, jedoch induziert (Cicha *et al.*, 2008). Wir fanden bei 2D FTC-133-Zellen, die der turbulenten Strömung der RPM ausgesetzt waren, eine erhöhte *CTGF*-Expression **(Publikation 9)**, jedoch nicht in den Zellen der freischwebenden Sphäroide (Warnke *et al.*, 2014). Das CTGF-Level war auch in den Proben des Weltraumexperiments SimBox erhöht (Ma *et al.*, 2014).

In mikrogravitationsexponierten Zellen sind zahlreiche Faktoren auf der Ebene des Transkriptoms, Proteoms und Sekretoms verändert. Nicht alle von ihnen haben direkten Einfluss auf die veränderte Funktion der Zellen. Die Zuordnung der Gravitationseffekte auf molekularer Ebene zu den verschiedenen biologischen und phänotypischen Prozessen wird eine der Herausforderungen der kommenden Jahre sein.

6.4.2 Exosomen

Nach ihrer Entdeckung wurde zunächst angenommen, dass extrazelluläre Vesikel ausschließlich der Entsorgung unerwünschter Zellbestandteile dienen. Eine Untergruppe der extrazellulären Vesikel (30-150 nm Größe), die bei Fusion des multivesikulären Körpers mit der Plasmamembran aus den Zellen freigesetzt werden, wurden später als „Exosomen“ definiert. Durch die nähere Erforschung der Exosomen wurde sehr schnell klar, dass sie auf die interzelluläre Signalübertragung spezialisiert sind, indem sie Proteine, Nukleinsäuren, Lipide aber auch Stoffwechselprodukte von Donorzellen zu benachbarten Empfängerzellen oder sogar zu entfernten Organen transportieren. Es wurde bereits gezeigt, dass Exosomen an der Entwicklung und Ausbreitung von Tumorerkrankungen beteiligt sind, da sie Informationen zwischen Tumorzellen oder zu anderen Zellen übertragen können (Kalluri & LeBleu, 2020).

Mit Unterstützung der ExtraCellular Vesicle Core Facility am Children's Hospital Los Angeles konnte für das CellBox-1 ISS-Experiment (FTC-133 Schilddrüsenkrebszellen) erstmals eine Exosomenanalyse aus den gesammelten Zellkulturüberständen durchgeführt werden. Die Ergebnisse zeigen bei den Weltraumproben bereits Unterschiede in der Anzahl der sezernierten Exosomen sowie in der Verteilung der Subpopulationen in Bezug auf ihre Oberflächenproteine. Insbesondere wurde eine Veränderung der Tetraspanin-Oberflächenexpression beobachtet **(Publikation 19)**. Eine zusätzliche Array-Analyse zeigte außerdem, dass sich die Exosomen der Weltraumproben in 100 regulatorischen Mikro-RNAs (miRNAs) unterschieden **(Publikation 20)**. Die neu gewonnenen Daten waren ein erster vielversprechender Schritt in einen neuen Bereich der Mikrogravitationsforschung, der zukünftig dazu beitragen kann, die bei Mikrogravitations-experimenten beobachteten molekularen und phänotypischen Effekte besser erklären zu können.

Die Tatsache, dass Weltraumaufenthalte bei Zellkulturexperimenten die Exosomenbeladung und -sezernierung beeinflussen, macht die Effekte von Weltraumflügen allerdings systemisch. Es muss gar nicht jede einzelne Zelle des Körpers Gravitationsänderungen wahrnehmen und darauf reagieren, wenn von einigen gravisensitiven Zellen über Zell-Kommunikationssyteme, wie Exosomen, wichtige regulatorische Faktoren ausgeschüttet werden, die daraufhin andere Zellen in anderen Bereichen des Organismus beeinflussen.

6.5 Sphäroidbildung auf der Random Positioning Machine

Frühe RWV-Versuche mit embryonischen Stammzellen, die in einem EZM-reichen Matrigel kultiviert wurden, zeigten, verglichen mit denen, die statisch kultiviert wurden, die verstärkte Bildung von drüsen- und röhrenförmigen Strukturen, von denen viele ein Lumen mit polarisiertem Epithel und Mikrovilli enthielten. Dies deutet darauf hin, dass die 3D-Kultur in simulierter Mikrogravitation die Bildung geschichteter und organisierter gewebeartiger Strukturen begünstigt (Philp *et al.*, 2005). Mittlerweile haben zahlreiche Studien belegt, dass Mikrogravitation die Bildung von 3D-Zellaggregaten, sogenannten Sphäroiden, fördert. Die RPM-induzierte Aggregatbildung wurde im Rahmen dieser Arbeit sowohl bei gutartigen **(Publikationen 11, 13)**, als auch bei bösartigen Zellen beobachtet **(Publikationen 5, 9, 10, 16, 17)**, allerdings mit unterschiedlicher Geschwindigkeit, Menge und Qualität der gebildeten Strukturen. Eines der angestrebten Ziele ist daher, ein allgemeines Modell der mikrogravitations-induzierten Sphäroidbildung zu entwickeln, mit dem sich die bisherigen Beobachtungen erklären, sowie zukünftige Anwendungen besser vorhersagen und nutzen lassen. Tafel 2 zeigt die Zusammenstellung der bisherigen Erkenntnisse.

6.5.1 Sphäroidbildung als zweistufiger Prozess

Mit **Publikation 5** konnte gezeigt werden, dass es sich bei der Sphäroidbildung adhärent wachsender Zellen auf der RPM um einen zweistufigen Prozess handelt (Abb. 2). Er erfordert zunächst eine Ablösung (detachment) der zweidimensional wachsenden Zellen. Diese wird hauptsächlich durch die Flüssigkeitsströmung bedingt, die durch die Rotation der Zellkulturflasche entsteht, und durch Luftblasen in der Flasche verstärkt wird. Sobald die Zellen sich in Suspension befinden, verhindert die Zufallspositionierung (Rotation der Zellkulturflasche) die Sedimentation, und es kommt zur Bildung von 3D-Aggregaten (Abb. 2, **Publikation 5)**.

Die Ablösung der Monolayer-Zellen scheint dabei vom Gleichgewicht zwischen den zellspezifischen Adhäsionskräften (abhängig von der Zelldichte, der Menge der Matrix und den Adhäsionsproteinen) und den physikalischen Scherkräften der Zellkultur (Durchflussrate, Luftblasen, Oberflächenbeschaffenheit der Zellkulturflasche) abzuhängen.

Es konnte gezeigt werden, dass die Intensität der Scherung sowie das Auftreten von Luftblasen Einfluss auf die Anzahl der abgelösten Krebszellen hat **(Publikation 5)**. Offen bleibt jedoch die Frage, warum sich nur einige und nicht alle Zellen lösen. Eine mögliche Lösung hierfür könnte der Eintritt der sich ablösenden Zellen in die Mitose liefern, bei dem die fokalen Adhäsionen

vorübergehend verschwinden (Li & Burridge, 2019). Dafür würde zumindest sprechen, dass überwachsene Zellkulturen mit reduzierter Proliferation weniger zur Sphäroidbildung neigen – sowohl in realer Mikrogravitation als auch auf der RPM (Riwaldt, Bauer, *et al.*, 2015; Riwaldt, Pietsch, *et al.*, 2015). Allerdings wäre der Umkehrschluss, dass nur proliferierende 2D-Zellkulturen die beschriebenen Sphäroide bilden können und ausdifferenzierte Zellen davon ausgenommen sind.

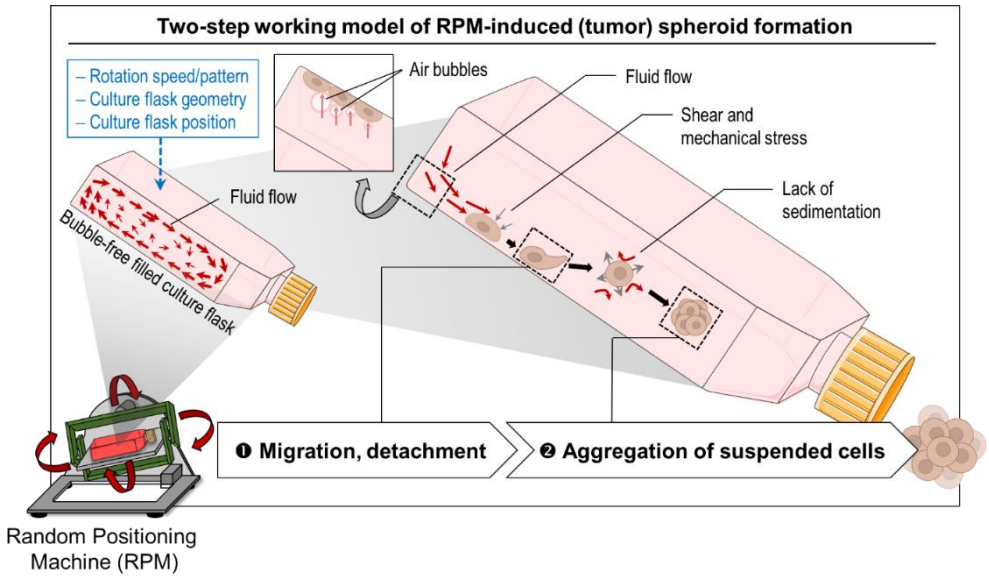


Abbildung 2: Die RPM-induzierte Sphäroidbildung ist ein zweistufiger Prozess. Flüssigkeitsbewegungen während der Rotation (rote Pfeile) führen zur Ablösung 2D wachsender Zellen. Die Intensität dieser Scherungen ist abhängig von der Rotationsbewegung selbst, von der Geometrie der Zellkulturflasche sowie von der Position der Flasche auf der RPM. Luftblasen in der Zellkulturflasche können diesen Effekt verstärken (kleines Bild). Nach der Ablösung führt die Verhinderung der Sedimentation zur Sphäroidbildung. Die Abbildung wurde verändert nach **(Publikation 5)**. Die Abbildung wurde mit Elementen aus BioRender und Servier Medical Art erstellt.

6.5.2 Ablösung adhärenter Zellen: Ein Zeitfenster für erfolgreiche Sphäroidbildung

Anders als bei der RWV oder Klinostaten werden RPM-Experimente mit adhärenten Zellen meist mit Monolayern begonnen. Hierbei ist wichtig zu erwähnen, dass der Adhäsionsvorgang in mehreren Schritten abläuft (▤ Tafel 2A): Während zunächst durch Sedimentation elektrostatische Wechselwirkungen zwischen der ausgesäten Zelle und Substrat auftreten (Phase I) (Hong *et al.*, 2006), führt die Integrinbindung zur Anheftung der Zelle auf dem Substrat. Zu diesem Zeitpunkt ist die Zelle noch zur Migration befähigt. Bei Krebszellen, die durch verstärkte Expression von Antiadhäsionsproteinen wie Mucin-1 und durch erhöhte Produktion von Matrix-Metalloproteinasen (MMPs, **Publikation 8**) einen EZM-Umsatz haben, ist diese Phase verlängert. Die Ausbreitung auf dem Substrat führt zu einer Abflachung der Zellhöhe und einer Vergrößerung der Kontaktfläche (Phase II). Eine Reorganisation von F-Aktin an den Zellgrenzen sowie die Ausbildung von fokalen Adhäsionen erhöht die Adhäsionskraft (Phase III) (Khalili & Ahmad, 2015). Die zunehmende Anzahl an fokalen Adhäsionen wird schließlich durch Aktin-Stressfasern stabilisiert (Phase IV). In dieser letzten Phase sind die Adhäsionskräfte der Zelle so stark, dass Zellen durch die RPM-Scherung nicht mehr abgelöst werden können. Dies zeigte sich bei RPM-Experimenten mit längerer Prä-Adhäsionsphase (48 h statt 24 h), die unter identischen RPM-Einstellungen kaum noch Sphäroide

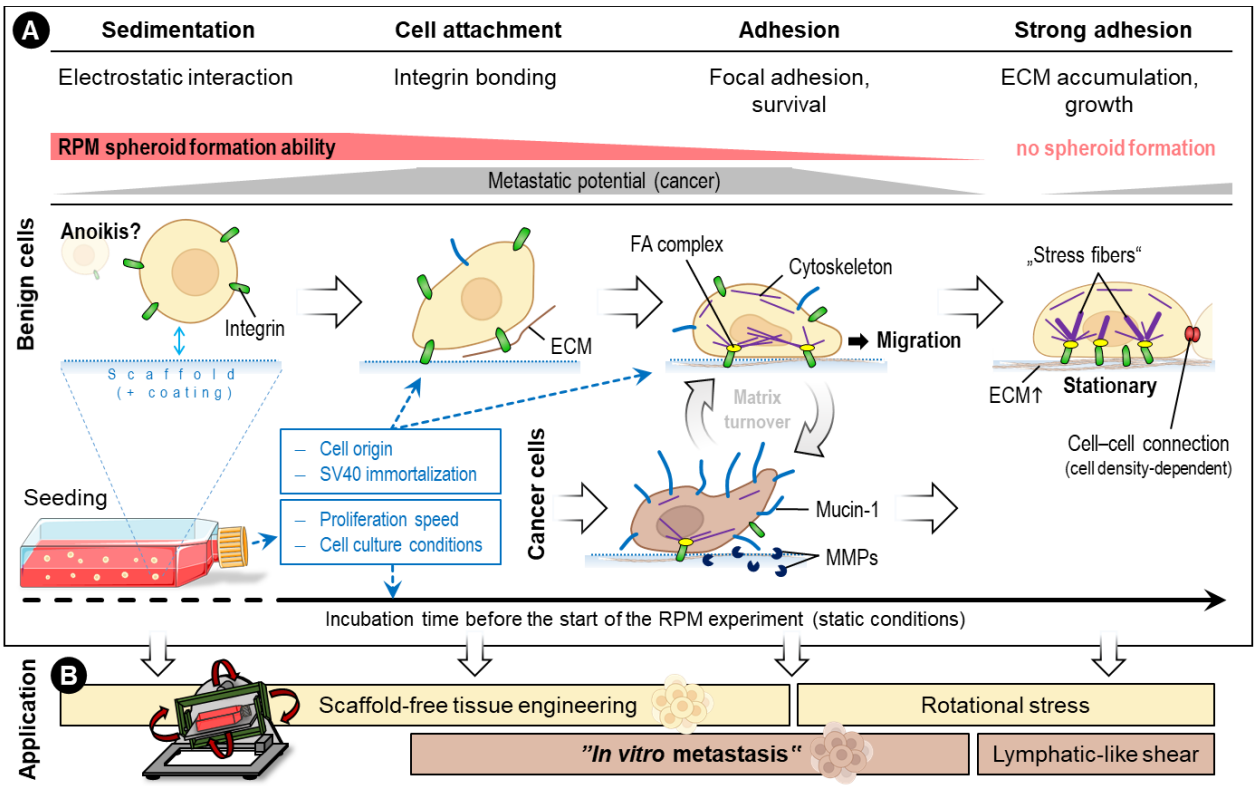
von FTC-133-Zellen hervorbrachten **(Publikation 5)**. Ein ähnliches Phänomen trat auch bei Experimenten in realer Mikrogravitation auf. Vor der CellBox-1-Mission gab es Verzögerungen des Raketenstarts und es bildeten sich während der zwei Wochen im Orbit ebenfalls keine Sphäroide (Riwaldt, Bauer, *et al.*, 2015; Riwaldt, Pietsch, *et al.*, 2015).

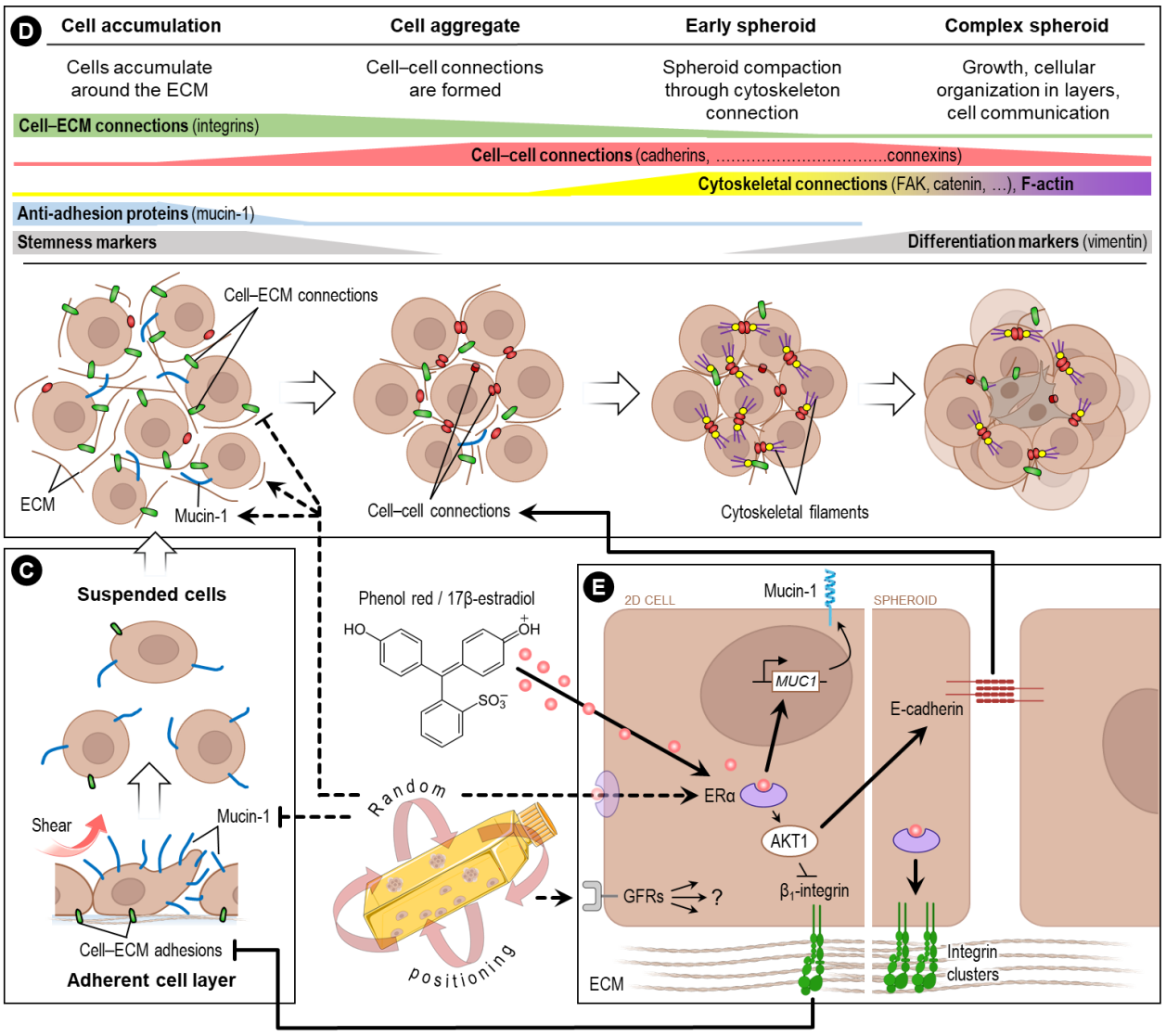
Aus den gewonnenen Daten lässt sich also schließen, dass es einen Zeitrahmen für die Initiation der Sphäroidbildung auf der RPM gibt, der für Ansätze in der Krebsforschung und/oder zum Tissue Engineering genutzt werden kann (▤ Tafel 2B). Bei der Verwendung gutartiger Zellen sollte dieser Zeitrahmen aufgrund von Anoikis nicht unter-, aber aufgrund der zeitlich begrenzten Ablösbarkeit der Zellen auch nicht überschritten werden.

6.5.3 Sphäroid-Stabilität

Die Bildung von 3D-Aggregaten beinhaltet mehrere Phasen, die auch unter Mikrogravitationsbedingungen auftreten (▤ Tafel 2C/D): Zunächst akkumulieren Zellen in Suspension um sezernierte EZM-Proteine, woran vorwiegend Integrine beteiligt sind (Phase I). Die Aggregation (Phase II) erfolgt durch die Expression von Zell-Zell-Verbindungsproteinen (Cadherine) (Lin & Chang, 2008) und dem Verschwinden von Antiadhäsionsproteinen (Mucine). Die anschließende Verknüpfung der Adhäsionsproteine an F-Aktin führt zu einer Kompaktierung und Stabilisierung der Sphäroidstruktur (Madhavan *et al.*, 2023), die anschließend nicht mehr so leicht aufgebrochen werden kann (Phase III) (Kouroupis & Correa, 2021; Smyrek *et al.*, 2019). Das stabilisierte Sphäroid wächst nun in der typischen, mehrschichtigen Struktur weiter (Phase IV). Zellpolarität und lokale Differenzierung führen zur Expression spezifischer Differenzierungsmarkers, wie z.B. Vimentin.

Besonders die ersten beiden Phasen der Sphäroidbildung sind kritisch für eine erfolgreiche Bildung von stabilen und integren Sphäroiden auf der RPM. E-Cadherin-negative Mammakarzinomzellen (MDA-MB-231), bilden lockerere Sphäroide auf der RPM als E-Cadherin-positive (Sahana *et al.*, 2023). Die Verwendung eines inhibitorischen E-Cadherin-Antikörpers führte bei MCF-7-Zellen nach einer 14-tägigen RPM-Kultur zwar zu mehr, aber auch kleineren Sphäroiden verglichen mit einer unbehandelten Zellkultur **(Publikation 12)**. Hier scheint die fehlende Funktionalität von E-Cadherin, die nach dem vorgeschlagenen Sphäroidbildungs-Modell zur Kompaktierung von Sphäroiden beiträgt, die Integrität der Zellaggregate zu verringern, welche dann durch die Scherkräfte während der Zufallspositionierung „zerschlagen“ werden. Studien mit Calu-3-Zellen deuten darauf hin, dass Mucin-1 nicht nur ein wichtiger Faktor bei der Initiierung der Sphäroidbildung (Ablösung der Zellen) ist, sondern auch zur Stabilität der anschließend gebildeten Sphäroide beiträgt, was eine Voraussetzung für deren Integrität unter den Scherstressbedingungen der RPM ist **(Publikation 10)**.


A
Sedimentation
Cell attachment
Adhesion
Strong adhesion
Electrostatic interaction
Integrin bonding
Focal adhesion, survival
ECM accumulation, growth
RPM spheroid formation ability
no spheroid formation
Metastatic potential (cancer)
Benign cells
Anoikis?
Integrin
Scaffold (+ coating)
ECM
FA complex
Cytoskeleton
Migration
„Stress fibers"
ECM↑
Stationary
Cell–cell connection (cell density-dependent)
Matrix turnover
Cell origin
SV40 immortalization
Proliferation speed
Cell culture conditions
Seeding
Cancer cells
Mucin-1
MMPs
Incubation time before the start of the RPM experiment (static conditions)
B
Application
Scaffold-free tissue engineering
Rotational stress
"In vitro metastasis"
Lymphatic-like shear


D
Cell accumulation
Cell aggregate
Early spheroid
Complex spheroid
Cells accumulate around the ECM
Cell–cell connections are formed
Spheroid compaction through cytoskeleton connection
Growth, cellular organization in layers, cell communication
Cell–ECM connections (integrins)
Cell–cell connections (cadherins, ...connexins)
Cytoskeletal connections (FAK, catenin, ...), F-actin
Anti-adhesion proteins (mucin-1)
Stemness markers
Differentiation markers (vimentin)
Cell–ECM connections
ECM
Mucin-1
Cell–cell connections
Cytoskeletal filaments
C
Suspended cells
Shear
Mucin-1
Cell–ECM adhesions
Adherent cell layer
Phenol red / 17β-estradiol
HO
OH
SO3−
Random
positioning
E
2D CELL
SPHEROID
Mucin-1
MUC1
E-cadherin
ERα
AKT1
GFRs
?
β1-integrin
ECM
Integrin clusters

◄ TAFEL 2: MODELL DER SPHÄROIDBILDUNG AUF DER RANDOM POSITIONING MACHINE. (**A**) Der Adhäsion von Zellen an ein Substrat ist ein mehrstufiger Prozess. Sie beginnt mit der elektrostatischen Interaktion zwischen Zelle und Oberfläche des Zellkulturgefäßes. Integrine binden entweder direkt an das Material oder an sezernierte EZM-Proteine (Anlagerung). Die Adhäsion beinhaltet schließlich die Ausbildung von Adhäsionskomplexen (fokale Adhäsionen, FA) unter Beteiligung des Zytoskeletts. In dieser Phase sind Zellen noch zur Migration befähigt; Krebszellen verbleiben durch ihren dynamischen EZM-Umbau längere Zeit in dieser Phase. Bei der starken Adhäsion werden die Adhäsionskomplexe mit Aktin-Stressfasern stabilisiert und binden die Zellen fest an eine größere Menge von EZM-Proteinen. Die Adhäsion in dieser Phase ist so stark, dass keine Migration mehr stattfindet und Zellen auf der RPM nicht mehr für die Sphäroidbildung abgelöst werden können. Inwiefern Zelleigenschaften und Zellkulturbedingungen diesen Ablauf beeinflussen und ggf. verzögern können (blaue Boxen), ist noch nicht vollständig erforscht. (**B**) Die Anwendungen der RPM hängen vom „Adhäsionsgrad“ der Zellen ab. Experimente zum Tissue Engineering sowie das später noch genauer besprochene Metastasierungsmodell setzen Zellen voraus, die durch die Scherkräfte der RPM abgelöst werden können, um 3D-Strukturen zu bilden. Befinden sich die Zellen erst einmal in der letzten Adhäsionsphase („überwachsen“), sind nur noch Monolayer-Experimente mit der RPM möglich, mit denen sich jedoch gut die mechanischen Einflüsse der RPM (Scherstress, Kompression) auf Zellen untersuchen lassen. (**C**) Die Sphäroidbildung setzt zunächst das Ablösen adhärenter Zellen durch die Scherkräfte der RPM voraus. Das Vorhandensein von Antiadhäsionsproteinen, wie Mucin-1, erleichtert die Ablösung der 2D-Zellen und hat einen positiven Effekt auf die spätere Sphäroidbildung. (**D**) Auch die Bildung der dreidimensionalen Sphäroide findet in mehreren aufeinanderfolgenden Phasen statt. Zunächst akkumulieren die Zellen um gebildete EZM-Proteine. Über Zell-EZM- (Integrine) und Zell-Zell-Verbindungsproteine (Cadherine) aggregieren die Zellen um die EZM-Elemente herum zu einer semistabilen Zellgruppe. Anschließend werden weitere Zell-Zell-Verbindungen gebildet, die mit intrazellulären Verbindungsproteinen (Vinculin, Talin, β-Catenin, etc.) am Zytoskelett befestigt werden. Es entsteht ein stabiles, kompakteres Sphäroid, das sich im weiteren Verlauf der Zellkultur in konzentrischen Schichten organisiert. Durch die Interaktion und Kommunikation zwischen den Zellen kommt es zur Polarisierung und eventuell auch zur Differenzierung einzelner Zellen Die Zell-Zell- und Zell-EZM-Verbindungsproteine werden in dieser letzten Phase nach Bedarf gebildet oder abgebaut. (**E**) Am Beispiel von Calu-3-Lungenkarzinomzellen wurde der Einfluss von Östrogenen (Phenolrot, 17β-Estradiol) im Zellkulturmedium in Kombination mit der RPM genauer untersucht. Die molekularen Effekte der RPM sind mit gestrichelten Pfeilen dargestellt, die Effekte der Östrogene mit durchgezogenen Linien. Die RPM erhöht die Östrogensensitivität in Calu-3-Zellen durch eine erhebliche Steigerung der *ESR1*-Expression (Östrogenrezeptor alpha). Es zeigte sich, dass Östrogene (rote Kreise) in dieser Zelllinie zum einen die Mucin-1-Expression in den 2D-Zellen, zum anderen die Menge an E-Cadherin in den Sphäroiden steigern. Beide Effekte tragen dazu bei, dass sich zahlenmäßig mehr und v.a. stabilere Sphäroide bilden können. Somit hat auch die Zellkulturchemie einen wichtigen Einfluss auf die Sphäroidbildung auf der RPM.

*Teilabbildungen C-E wurden verändert nach **Publikation 10**.*

Die Tafel wurde mit Elementen aus BioRender und Servier Medical Art erstellt.

Des Weiteren konnten wir an Calu-3-Zellen zeigen, dass die Zufallspositionierung die Östrogenempfindlichkeit einer Zellkultur durch Hochregulierung der *ESR1*-Expression (Östrogenrezeptor alpha) steigern kann. Demnach steigern Östrogene (17β-Estradiol, Phenolrot) im Zellkulturmedium die gebildete Menge von E-Cadherin in den Sphäroidzellen (kompaktere Sphäroide) und die Mucin-1-Expression in den Monolayer-Zellen (leichtere Ablösung) (▤ Tafel 2E). Die erfolgreiche Bildung von Sphäroiden hängt folglich nicht ausschließlich von zelltypspezifischen Eigenschaften und den mechanischen Einflüssen der RPM ab, sondern wird teilweise auch von der chemischen Zusammensetzung des verwendeten Mediums bestimmt **(Publikation 10)**.

7. Die RPM-Zellkultur als *ex vivo*-Metastasierungsmodell

Die RPM ist nach wie vor eines der wichtigsten Arbeitsgeräte in der biomedizinischen Gravitationsforschung, auch wenn sie zusätzlich zur „simulierten Mikrogravitation“ eine Reihe an Nebeneffekten auslöst. Über die Jahre hinweg hat sich gezeigt, dass das Ablösen adhärenter Krebszellen auf der RPM nicht nur analog zu Weltraumexperimenten auftritt, es hat auch noch Ähnlichkeit mit einem anderen pathophysiologischen Prozess, bei dem sich adhärent wachsende Zellen ablösen: der Metastasierung (Grimm *et al.*, 2022). Neben der phänotypischen Parallele bestätigte auch eine *in silico*-Analyse von Genexpressionsdaten des Mammakarzinoms bereits eine positive Assoziation zwischen der realen Umgebung des metastatischen Mikrotumors und RPM-induzierten Tumorsphäroiden im Hinblick auf die EZM, das Zytoskelett, die Morphologie, verschiedene Schlüsselproteine des zellulären Signalweges und verschiedene andere Komponenten (Sahana *et al.*, 2023).

7.1 RPM-generierte Tumorsphäroide als „2,5D“-Zellkultur

Die Zellen des menschlichen Körpers wachsen eingebettet in einer strukturgebenden EZM, umgeben von einem biochemischen Mikromilieu mit vielfältigen regulatorischen Funktionen. Dadurch erhalten Organe, aber auch Tumore, nicht nur ihre dreidimensionale, „natürliche“ Form, sondern werden auch in ihrer Funktionsweise beeinflusst. Unter klassischen Zellkulturbedingungen wachsen adhärente Tumorzellen in 2D-Schichten, die Bedingungen vorgeben, welche *in vivo* so nicht vorkommen. In soliden Tumoren liegen beispielsweise Konzentrationsgradienten im Gehalt von Nährstoffen, Sauerstoff oder Metaboliten vor, die Einfluss auf das Zellwachstum und -stoffwechsel haben.

Multizelluläre Tumorsphäroide (MCTS) werden seit den 1970er Jahren untersucht und sind seitdem stetig weiterentwickelt worden (Gencoglu *et al.*, 2018; Sutherland *et al.*, 1971; Sutherland *et al.*, 1986). Die Tumorzellen behalten im MCTS ihre morphologischen und funktionellen Eigenschaften, sodass mit ihnen die *in vivo* Situation avaskulärer Mikroregionen und Mikrometastasen eines soliden Tumors sehr gut imitiert werden kann (Tafel 3B) (Fennema *et al.*, 2013; Hirschhaeuser *et al.*, 2010). In den MCTS wird mehr EZM gebildet und es entsteht, wie im Tumor, eine zelluläre Heterogenität. Aufgrund guter Versorgung mit Sauerstoff und Nährstoffen über das Medium bilden sich in der Randzone des MCTS proliferierende Zellen mit der Fähigkeit zu differenzieren. So imitieren Zellen der MCTS-Peripherie Tumorzellen, die *in vivo* an Kapillaren angrenzen (Tafel 3B). Mit zunehmender Entfernung vom Medium und gleichzeitiger Ansammlung von Abfallprodukten befinden sich ruhende Zellen im mittleren Teil und nekrotische Zellen im Sphäroidkern. Bis zu einem Durchmesser von 150-200 µm sind MCTS gut durch Diffusion versorgt. Der für avaskuläres Tumorgewebe typische, nekrotische Kern bildet sich ab einer Größe von etwa 400 µm (Friedrich *et al.*, 2009). Dieser ist üblicherweise von einem Gürtel aus lebenden Zellen umgeben. Bedingt durch eingeschränkte Einwärts-/Auswärtsdiffusion kommt es zur

Unterversorgung mit Sauerstoff und Nährstoffen, einer Ansammlung von Abfallprodukten und einem verringerten pH-Wert (Tafel 3B) (Acker *et al.*, 1987; Carlsson & Acker, 1988).

Diverse Studien haben Anpassungen des Zell-Metabolismus an umgebungsbedingten physiologischen Stress im Inneren des MCTS gezeigt, aber auch, dass die Sensitivität von Tumorzellen für diese Stresssituationen recht unterschiedlich sein kann (Bredel-Geissler *et al.*, 1992; Freyer *et al.*, 1990; Freyer *et al.*, 1991; Teutsch *et al.*, 1995; Walenta *et al.*, 1990). Dies hängt mit dem sehr variablen Energiestoffwechsel von Tumorzellen zusammen, der sowohl unter aeroben als auch unter anaeroben Bedingungen funktioniert. MCTS beinhalten ein komplexes Netzwerk aus Zell-Zell- und Zell-Matrix-Interaktionen und verfügen teilweise über eine ausgedehnte EZM. Diese Komponenten beeinflussen nicht nur die Verteilung und Funktion biologischer Regulatoren (z.B. Wachstumsfaktoren, Zytokine) (Winters *et al.*, 2006), sondern auch die Penetration und Aktivität von Wirkstoffen (Goodman *et al.*, 2007). Die konzentrische Anordnung heterologer Zellpopulationen in Sphäroiden und das Auftreten eines pathophysiologischen Gradienten entsprechen der Situation in Mikrometastasen, vaskulärer Tumoren oder interkapillären Tumorregionen. Im Gegensatz zu Tumorgewebe *in vivo*, befinden sich allerdings die innersten Zellen eines MCTS im Ruhezustand („outside-in"-Situation). Sie sterben letztendlich durch Apoptose oder Nekrose und bilden dadurch sekundär einen nekrotischen Kern (Tafel 3B).

MCTS können generiert werden, indem initial adhärent wachsende Tumorzellen auf nicht adhäsiven Oberflächen (z.B. liquid overlay), in Hanging Drop-Techniken oder in (rotierenden) Bioreaktoren wie den GBFs kultiviert werden. An MCTS werden heutzutage wichtige Abläufe zum Verständnis des Tumorwachstums wie Signaltransduktion, unterschiedliches Expressionsverhalten innen und außen, Metabolismus und Differenzierung untersucht (vgl. Tafel 3A) (Lin & Chang, 2008). Darüber hinaus werden sie genutzt, um therapeutische Fragestellungen zu untersuchen, die sich mit metabolischen und proliferativen Gradienten befassen; beispielsweise die Effekte in chronisch hypoxischen Tumorzellen, aber auch die Rolle von Zell-Zell- und Zell-Matrix-Interaktionen bei der Radio- und Chemotherapie (Costa *et al.*, 2016; Fennema *et al.*, 2013). Da MCTS, genauso wie Tumore *in vivo*, Permeabilitätsunterschiede aufweisen, können Wirkstoffe besser untersucht und möglicherweise als Therapeutikum auch schneller ausgeschlossen werden, wenn die Moleküle nicht alle Zellen erreichen (Breslin & O'Driscoll, 2013; LaBarbera *et al.*, 2012). MCTS sind somit zu wertvollen Werkzeugen in der Krebsforschung geworden (Jubelin *et al.*, 2022; Sharma *et al.*, 2024).

Auf der RPM gebildete MCTS von Brustkrebszellen eignen sich gut für Migrations- und Invasionsstudien, wie Experimente mit unterschiedlich aggressiven Brustkrebszellen zeigten **(Publikation 16)**. Die RPM-Tumorsphäroide unterscheiden sich von MCTS, die mit anderen (statischen) Methoden erzeugt wurden in einigen Eigenschaften (Tafel 3C/D), darunter weniger Nekrose im Zentrum (Kopp *et al.*, 2015) **(Publikation 1)**, aber auch schnelleres Wachstum und eine durchgehend höhere Stoffwechselaktivität (Abb. 3A). Mikroskopische Aufnahmen von gefärbten Ultradünnschnitten zeigten am Beispiel von Prostata-MCTS eine lockere Packung der Zellen in GBF-gebildeten MCTS verglichen mit statisch gebildeten (Abb. 3B). Ein kürzlich durchgeführtes

Experiment zeigte eine zügigere Diffusion von Fluoresceindiacetat (FDA) in PC-3-Prostata-MCTS, die auf verschiedenen GBFs erzeugt wurden (Abb. 3C). Der beobachtete Effekt ist also geräteunabhängig und kann daher der „simulierten Mikrogravitation“ zugeschrieben werden. Für ihn gibt es zwei mögliche Begründungen: Die größeren interzellulären Abstände der Zellen im GBF-Sphäroid ermöglichen eine zügigere, parazelluläre Aufnahme von FDA bis tiefer in das Sphäroid hinein (▤ Tafel 3D). Ebenso kann die RPM zu einer erhöhten Membranfluidität führen, die schon bei früheren Studien anderer Forschergruppen beschrieben wurde (Kohn & Hauslage, 2019; Sieber *et al.*, 2014). Beide Möglichkeiten würden dazu führen, dass auch andere im Zellkultur-Medium gelöste Faktoren (Nährstoffe, Wachstumsfaktoren, etc.) leichter in die GBF-exponierten Zellen aufgenommen werden und diese auf verschiedene Weise intrazellulär beeinflussen können, was sich z.B. in einem schnellen Wachstum oder einer besseren Versorgung des Sphäroidkerns zeigen würde (▤ Tafel 3C), was auch tatsächlich von uns beobachtet wurde. Was in eine Richtung funktioniert, sollte dann auch in die andere Richtung funktionieren: Auf GBFs müsste es daher eine erhöhte Diffusion zytoplasmatischer Proteine/Moleküle in den Zellkulturüberstand geben, die auch wiederum die restliche Zellkultur beeinflussen können. Konkret nachgewiesen wurde dieser Effekt bisher noch nicht. Höhere Zytokinkonzentrationen in GBF-Zellkulturen verglichen mit statischen Kontrollen widerlegen diese Theorie zumindest nicht **(Publikationen 10, 13)**. Auf diesem Gebiet sind in Zukunft also noch weitere Erkenntnisse zu erwarten.

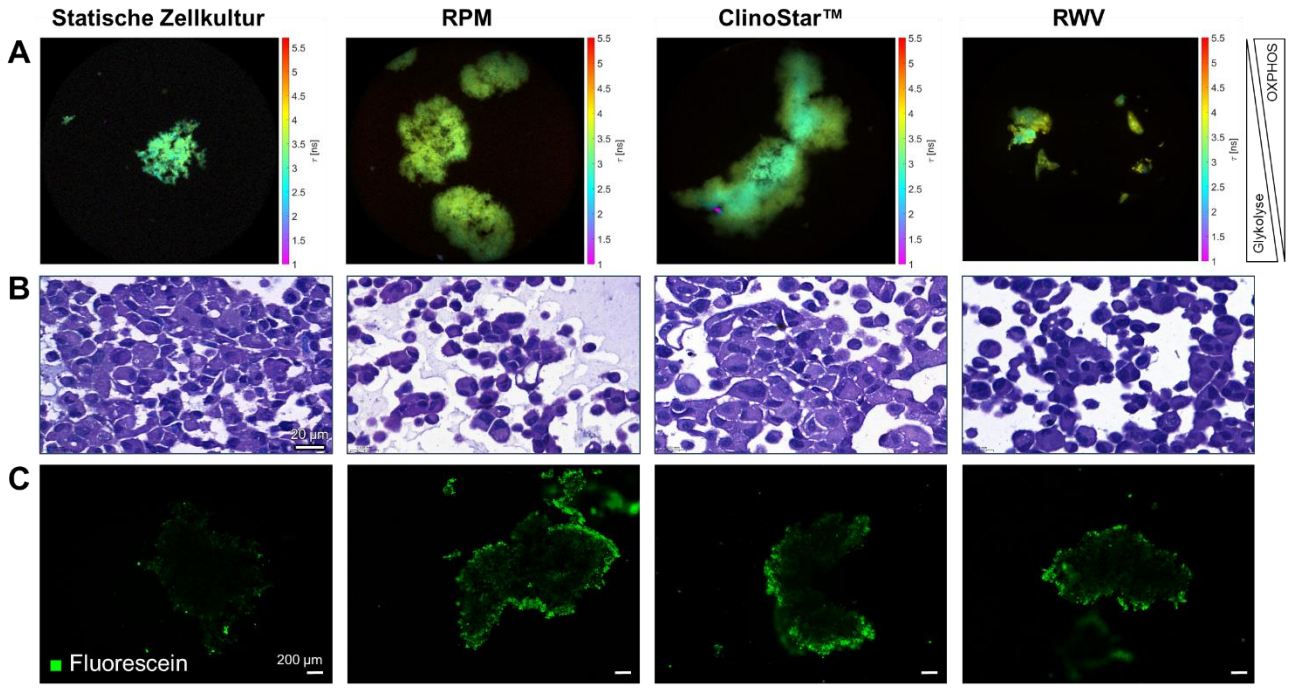
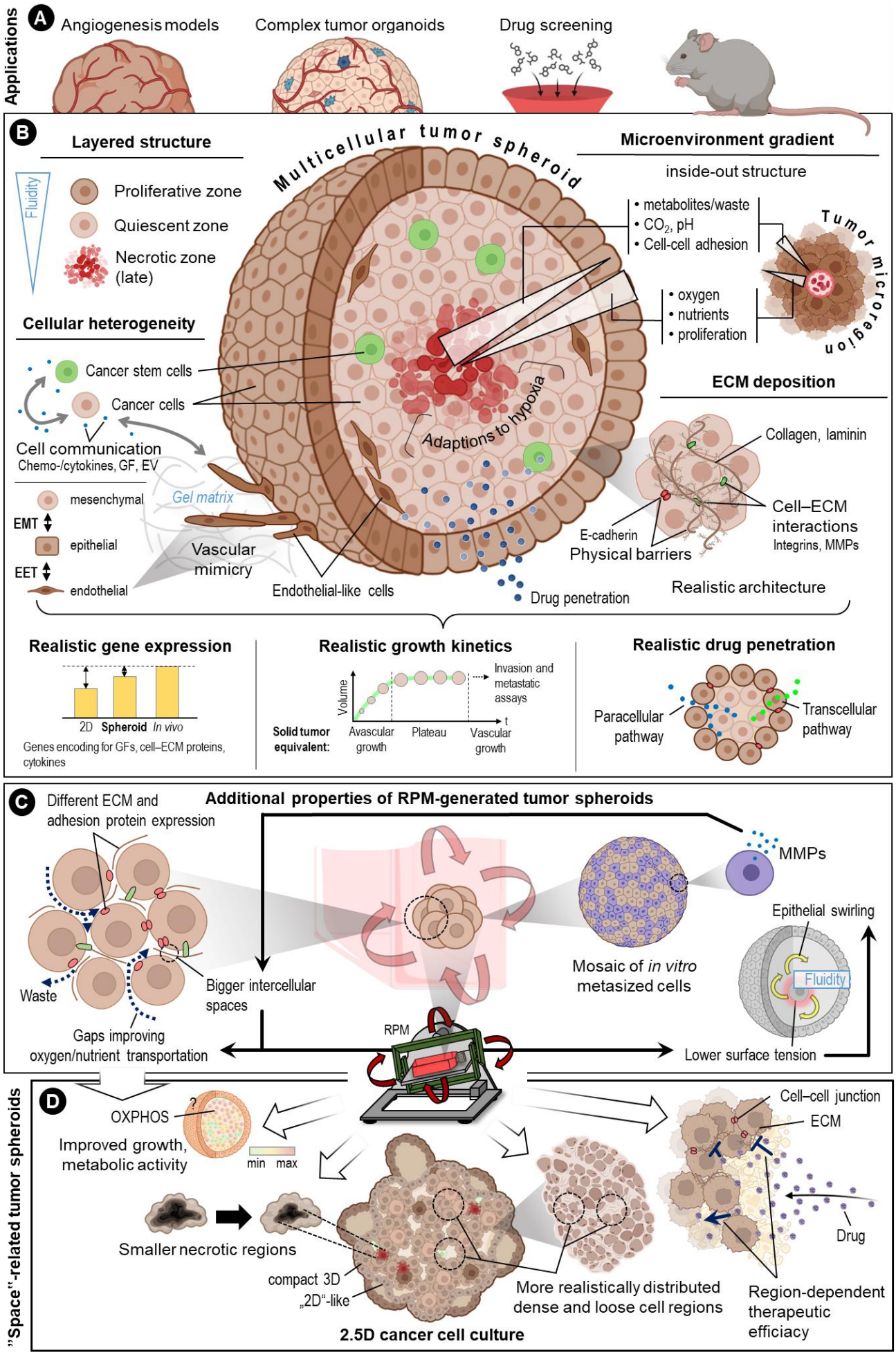


Abbildung 3: Eigenschaften von PC-3-Tumorsphäroiden (Prostatakarzinom), die auf unterschiedlichen GBFs erzeugt wurden. (**A**) Stoffwechselaktivität gemessen als markierungsfreie Stoffwechsel-Bildgebung der NADH-Fluoreszenz-Lebenszeit mittels FLIM (Fluoreszenzlebensdauer-Mikroskopie). Anhand der Fluoreszenz-Lebenszeit lassen sich Tendenzen des Zellmetabolismus erkennen (mehr glykolytisch oder mehr oxidative Phosphorylierung, OXPHOS). (**B**) PAS-Färbung (Periodsäure-Schiff-Reaktion) von histologischen Schnitten aus drei Tage lang gewachsenen PC-3-Sphäroiden verschiedener Herstellungsmethoden. Messbalken: 20 µm. (**C**) Fluoresceinnachweis in PC-3-Sphäroiden nach 4,5-minütiger Inkubation mit Fluoresceindiacetat im Zellkulturmedium. Messbalken: 200 µm.


Applications
A
Angiogenesis models
Complex tumor organoids
Drug screening
B
Layered structure
Fluidity
Proliferative zone
Quiescent zone
Necrotic zone (late)
Multicellular tumor spheroid
Microenvironment gradient
inside-out structure
• metabolites/waste
• CO_2, pH
• Cell-cell adhesion
Tumor microregion
• oxygen
• nutrients
• proliferation
Cellular heterogeneity
Cancer stem cells
Cancer cells
Cell communication
Chemo-/cytokines, GF, EV
mesenchymal
EMT
epithelial
EET
endothelial
Gel matrix
Vascular mimicry
Endothelial-like cells
Adaptions to hypoxia
ECM deposition
Collagen, laminin
Cell–ECM interactions
Integrins, MMPs
E-cadherin
Physical barriers
Drug penetration
Realistic architecture
Realistic gene expression
2D Spheroid In vivo
Genes encoding for GFs, cell–ECM proteins, cytokines
Realistic growth kinetics
Volume
Invasion and metastatic assays
t
Solid tumor equivalent:
Avascular growth
Plateau
Vascular growth
Realistic drug penetration
Paracellular pathway
Transcellular pathway
C
Different ECM and adhesion protein expression
Additional properties of RPM-generated tumor spheroids
MMPs
Epithelial swirling
Fluidity
Waste
Bigger intercellular spaces
Gaps improving oxygen/nutrient transportation
Mosaic of in vitro metasized cells
RPM
Lower surface tension
"Space"-related tumor spheroids
D
OXPHOS
?
Improved growth, metabolic activity
min
max
Cell–cell junction
ECM
Drug
Smaller necrotic regions
compact 3D
„2D"-like
More realistically distributed dense and loose cell regions
Region-dependent therapeutic efficiacy
2.5D cancer cell culture

◄ **TAFEL 3: TUMORSPHÄROIDE.** (**A**) Multizelluläre Tumorsphäroide (MCTS) bieten zahlreiche Vorteile gegenüber konventionellen 2D-Zellkulturen. Sie sind ein geeignetes Untersuchungsmodell für verschiedene physiologische und pharmazeutische Fragestellungen, darunter die Neoangiogenese und Proliferation von Tumoren, sowie die Entwicklung und das Austesten neuer Krebsmedikamente. Da die Ergebnisse verlässlicher und realistischer zu *in vivo*-Anwendungen sind, tragen MCTS ebenfalls dazu bei, Tierversuche zu reduzieren (3R[1]). (**B**) MCTS sind komplexe Strukturen, die verschiedene Aspekte von Tumor-Mikroregionen in Geweben aufweisen Sie besitzen eine geschichtete Struktur mit Zonen proliferierender, ruhender und nekrotischer Zellen im MCTS-Kern (abhängig von der Sphäroidgröße). MCTS weisen Stoffwechselprodukt- und Versorgungsgradienten auf, die einer inside-out-Struktur echter Tumoren entsprechen. Eine gewebeerealistische Menge und Zusammensetzung der EZM führt zu einer intrasphäroidalen Zellheterogenität mit entsprechender Zellkommunikation und Zell-ECM-Interaktionen. Durch diese Heterogenität der Zellen können in Teilbereichen der MCTS auch biologische Prozesse wie epithelial-mesenchymale Transition (EMT) oder epithelial-endotheliale Transition (EET, meist in Matrix) beobachtet werden. Die EZM-Verteilung führt zu physikalischen Barrieren, die ebenfalls eine realistische Aufnahme und Verteilung von Medikamenten ermöglichen. Wachstumsverhalten und Genexpressionsmuster entsprechen eher denen *in vivo* als denen von 2D-Zellkulturen. (**C**) RPM-generierte MCTS unterscheiden sich von statisch generierten Sphäroiden in einigen morphologischen Eigenschaften. Sie wachsen nicht ausschließlich konstant, sondern bestehen aus einem Mosaik von aggregierten und neu abgelösten Zellen aus der 2D-Population. Die Sphäroidzellen sind durch eine modifizierte EZM und Menge an Zelladhäsionsproteinen weniger dicht gepackt. Das ermöglicht eine einfachere parazelluläre Aufnahme von Sauerstoff und Nährstoffen bis tief in das Sphäroid hinein. Durch die entsprechend höhere Fluidität im Sphäroidinneren kann es auch zum „epithelial swirling“ kommen, was die Komplexität des MCTS weiter erhöht. (**D**) Die spezifischen Eigenschaften von RPM-Tumorsphäroiden spiegeln sich auch in ihrer Funktionalität wider. Insbesondere führt die lockerere Packung der Zellen zu einer besseren Versorgung des Sphäroidkerns, was sich wiederum in einem schnelleren Wachstum und einem verbesserten Stoffwechsel zeigt (es gibt Hinweise, dass die oxidative Phosphorylierung in RPM-generierten MCTS stärker vertreten ist; dieser Aspekt muss allerdings noch weiter untersucht werden). Ebenfalls bedingt durch die bessere Nährstoff- und Sauerstoffversorgung ist die reduzierte Neigung zur zentralen Nekrose. Die komplex-heterogene Zell- und EZM-Verteilung führt zu einem sehr realistischen Mix aus dichteren und weniger dichten Sphäroidregionen. Dies hat wiederum Einfluss auf die Therapierbarbeit der Sphäroidzellen mit lokalen Effekten. Da sie sowohl Eigenschaften einer 2D-Zellkultur als auch von einer 3D-Zellkultur vereinen, könnten RPM-generierte MCTS auch als „2,5D-Zellkultur“ bezeichnet werden.

Die Tafel wurde mit Elementen aus BioRender und Servier Medical Art erstellt.

[1] Ziel des **3R-Prinzips** ist es, Tierversuche vollständig zu vermeiden (Replacement) und die Zahl der Tiere (Reduction) und ihr Leiden (Refinement) in Versuchen auf das unerlässliche Maß zu beschränken.

7.2 Tumorsphäroidbildung auf der RPM – Parallelen zur Metastasierung

Nicht nur die Bildung von MCTS auf der RPM ähnelt dem Wachstum von Metastasen, es gibt weitere Parallelen zwischen der RPM-Zellkultur adhärenter Krebszellen und der Metastasierung im menschlichen Körper (▤ Tafel 4) (Fares *et al.*, 2020).

Ablösung der Zellen *vs.* Dissemination: In beiden Fällen sind physikalische Kräfte involviert. Während bei wachsenden Tumoren der Außendruck auf die Tumorzellen im Gewebe zunimmt, produziert die RPM vor allem Scherkräfte, die zur Ablösung der adhärenten Zellen von ihrem Substrat führen **(Publikation 5)**. In dieser Phase bilden Tumore *in vivo* vermehrt IL-6, VEGF sowie MMPs, die zur EMT beitragen (Basson *et al.*, 2015). In der adhärenten Zellpopulation auf der RPM werden ebenfalls IL-6 und MMPs ausgeschüttet **(Publikation 17)**. Teilweise wird mehr Mucin-1 produziert und Wachstumsfaktorrezeptoren (GFRs) werden nach oben reguliert. Die Zellen steigern die Produktion von EZM-Faktoren und Integrinen **(Publikationen 8, 10)**.

Suspensionszellen *vs.* zirkulierende Tumorzellen (CTCs): In beiden Fällen werden die Zellen mit der Strömung des Blutflusses bzw. der Rotationszellkultur transportiert. Krebszellen produzieren Mucin-1, um sich vor Anoikis zu schützen (Horm & Schroeder, 2013) **(Publikation 8)**. Zirkulierende Tumorzellen besitzen mehr GFRs (wie EGFR, epidermal growth factor receptor), was die Sensitivität für Wachstumsfaktoren erhöht.

Tumorsphäroide *vs.* CTC-Cluster: Manchmal kommt es bei zirkulierenden Tumorzellen zur Clusterbildung. Ein wichtiger Trigger dafür ist die DNA-Hypomethylierung in den Zellen. Die aggregatbildenden Tumorzellen bilden verstärkt Adhäsionsproteine (ICAM-1, CD44, Plakoglobin) und sekretieren mehr IL-8 (Schuster *et al.*, 2021). RPM-generierte Tumorsphäroide sekretieren in dieser Phase ebenfalls IL-8, aber auch VEGF-A **(Publikationen 8, 17)**. E-Cadherin ist ein wichtiges Adhäsionsprotein in der Bildung kompakter Sphäroide **(Publikationen 10, 12)**. Stoffwechsel-Bildgebungsdaten deuten auf einen höheren Anteil oxidativer Phosphorylierung in den MCTS hin (Abb. 3A).

Re-adhäsion *vs.* Kolonisierung: Nach dem Erreichen einer geeigneten metastatischen Nische kommt es *in vivo* zur Extravasation und anschließenden Bildung einer Metastase. Es zeigte sich, dass in Metastasen mehr Integrin-β1 vorhanden ist als im Primärtumor (Meder *et al.*, 2024) und nach neuesten Erkenntnissen wird auch hier die oxidative Phosphorylierung zur Energiegewinnung aktiviert (Davis *et al.*, 2020; Uslu *et al.*, 2024). Beim Stoppen der RPM sedimentieren die gebildeten Tumorsphäroide und es kommt zum Auswachsen einer neuen 2D-Zellpolulation (Abb. 4A). Interessanterweise können aus Metastasen isolierte Krebszellen (z.B. MDA-MB-231) auch während der Rotation readhärieren. Diese Zellen exprimieren ebenfalls etwas mehr Integrin-β1 als die Zellen, die in der RPM-Kultur adhärent bleiben (115±11% vs. 100±15%; Abb.4B).

Die RPM-Zellkultur zeigte für die von uns untersuchen, v.a. metastatischen Tumorzellen einige Parallelen zur Metastasierung. Das Modell ist aber eventuell nicht auf alle Tumortypen übertragbar.

So fanden Sabbatini *et al.* bei Gliom-Zellen keine MCTS-Bildung und einige der (wenigen) untersuchten Faktoren sprachen in diesem Fall eher für eine anti-metastatische Wirkung der RPM (Sabbatini *et al.*, 2023). Hier wird weitere Forschung zeigen, wie generalisiert das Modellsystem angewendet werden kann.

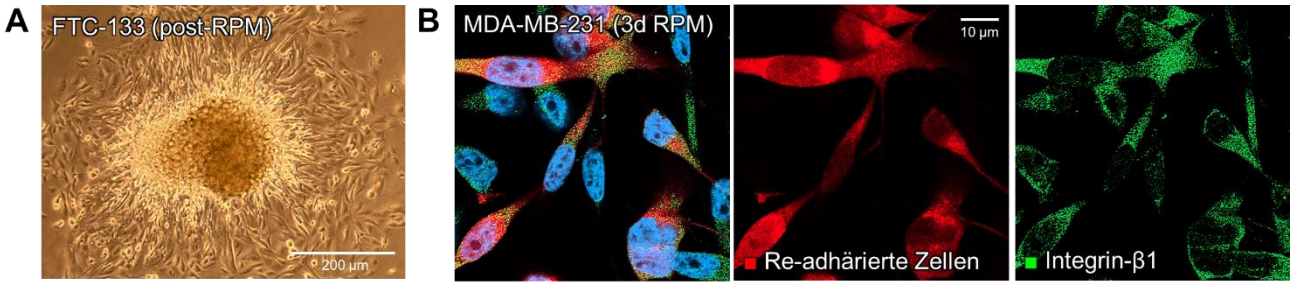


Abbildung 4: Readhäsion von Tumorzellen in einer RPM-Zellkultur. (**A**) Nach dem Ausschalten der RPM sedimentieren die gebildeten Tumorsphäroide (hier: FTC-133) und wachsen wieder als 2D-Kultur aus. Messbalken: 200 µm. (**B**) Zellen, die aus Metastasen gewonnen wurden (hier: MDA-MB-231), readhärieren bereits während der Zufallspositionierung. Die Bilder zeigen eine Mischkultur aus adhärenten bleibenden (ungefärbt) und adhärierten Brustkrebszellen aus einer Suspensionskultur (rot) nach 3 Tagen auf der RPM. Integrin-β1 ist grün gefärbt, die Zellkerne (DAPI) blau. Messbalken: 10 µm.

7.3 Mucin-1 als Schlüsselprotein der RPM-induzierten Tumorsphäroidbildung

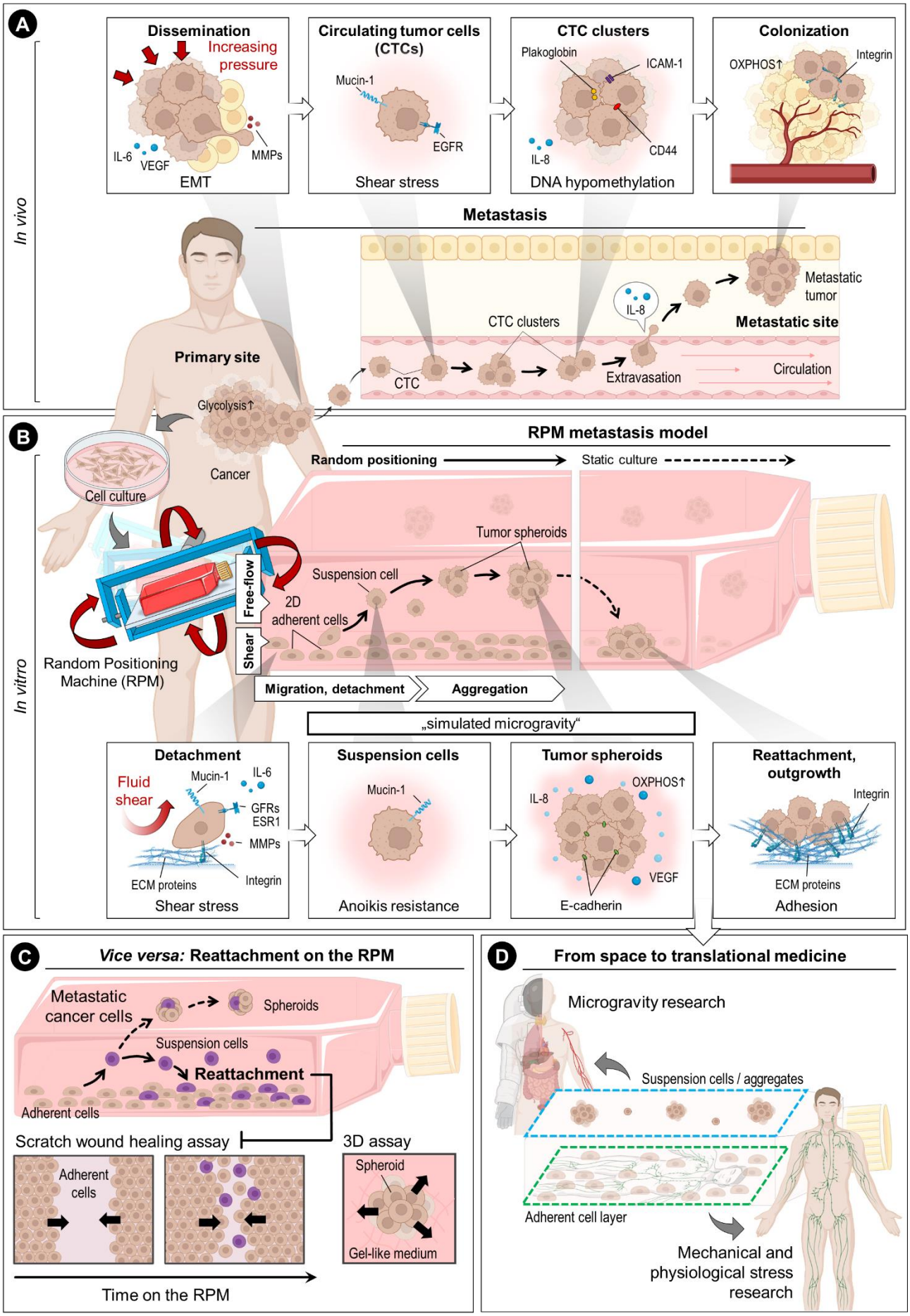
Lange Zeit war eine der wichtigsten Fragen in der RPM-Forschung, warum nur bestimmte adhärente Zellen durch Zufallspositionierung Sphäroide bilden, während andere, insbesondere primäre Zellen, ausschließlich als 2D-Zellrasen weiterwachsen. Was bisher kaum untersucht und verstanden war, rückte wieder in den Fokus unserer Forschung, als sich die RPM-induzierte Sphäroidbildung durch Zugabe von pharmazeutischen Wirkstoffen gezielt für einige Zelltypen ausschalten ließ. Wir konnten zeigen, dass die Sphäroidbildung metastasierter Schilddrüsenkarzinomzellen (FTC-133, WRO) durch die Zugabe von Dexamethason selektiv gehemmt wird **(Publikationen 8, 9)**, wohingegen die Sphäroidbildung gutartiger Schilddrüsenepithelzellen (Nthy-ori 3-1) oder der aus einem Rezidiv isolierten Schilddrüsenkarzinomzellen (ML-1) (Schönberger *et al.*, 2000) nicht dadurch beeinflusst wurde **(Publikation 8)**. Bei der Auswertung der Daten wurde deutlich, dass sowohl Nthy-ori 3-1 als auch ML-1 Zellen auf der RPM das antiadhäsive Transmembran-Glykoprotein Mucin-1 vermehrt exprimieren. Diese Zunahme kann durch die räumliche Einschränkung von Mucin-1 mit Adhäsionsproteinen (Cadherine, Integrine) dazu beitragen, dass diese Zellen während der dynamischen RPM-Zellkultur weniger stark adhärent sind und infolgedessen 3D-Strukturen ausbilden. Eine Hemmung durch den Mucin-1-Inhibitor GO-203 unterdrücke die Sphäroidbildung von Nthy-ori 3-1 Zellen auf der RPM. Darüber hinaus zeigte ein Vergleich am MTRM verfügbarer Zelllinien eine gute Korrelation zwischen der Mucin-1-Expression auf Proteinebene und der Fähigkeit dieser Zellen, Sphäroide auf der RPM zu bilden. Somit kann allein über das Vorhandensein von Mucin-1 oftmals schon im Vornherein erahnt werden, wie gut erfolgreich 3D-Aggregate erhalten werden können **(Publikationen 8, 10)**. Da Mucin-1 in bösartigen Zellen meist überexprimiert vorliegt

(Horm & Schroeder, 2013; Jing *et al.*, 2019; Lan *et al.*, 2022), kann dies auch die besonders gute Bildung von Tumorsphäroiden in einer RPM-Zellkultur erklären.

7.4 Pharmazeutische Beeinflussung der RPM-induzierten Sphäroidbildung

Bei *ex vivo*-Vorversuchen in der Entwicklung neuer Krebsmedikamente verlassen sich schätzungsweise >80% der Forscher der Einfachheit immer noch auf 2D-Kulturen (Lv *et al.*, 2017). Allerdings spiegeln diese Systeme die Antwort von Zellen im Mikromilieu (wie in Geweben und Tumoren *in vivo*) nur unzureichend bzw. gar nicht wider, was zur Folge hat, dass die Prognose für eine klinische Antwort auf neue Wirkstoffe eher begrenzt ist. In der Tat ist das Fehlen aussagekräftiger präklinischer Modelle eine bedeutende Ursache für die niedrige Erfolgsquote in der Wirkstoffentwicklung (Bertotti & Trusolino, 2013; Kamb, 2005). Viel zu oft scheitern vielversprechende Substanzen in der späteren klinischen Entwicklung. Darum erscheint es sinnvoll, die Möglichkeiten komplexerer *in vitro*-Funktionsmodelle zu nutzen, um die *in vivo*-Situation besser nachzuahmen (Hickman *et al.*, 2014). Für die pharmazeutische Forschung an der Metastasierungskaskade wird sich bisher auf eine Vielzahl einzelner Methoden verlassen, die alle nur einen kleinen Schritt des Gesamtprozesses abbilden (Wakefield *et al.*, 2023).

Dass Mikrogravitations-Experimente oftmals eine noch nicht verstandene, pharmazeutische „Wundertüte“ sind, zeigen Experimente mit der RWV. Die Zellantworten auf die Chemotherapien wurden durch die RWV sehr heterogen beeinflusst; eine konkrete Aussage über die Effekte war schwierig (McKinley *et al.*, 2023; Prasanth *et al.*, 2020). Die ersten pharmazeutischen Tests mit dem RPM-Metastasierungmodell wurden mit FTC-133-Zellen und Dexamethason durchgeführt, das die Sphäroidbildung von FTC-133-Zellen auf der RPM hemmt **(Publikation 8)**. FTC-133-Zellen wurden aus einer Metastase isoliert. Wie viele andere metastasierte Karzinomzellen, die EMT durchlaufen haben (Martin, 2014; Martin & Jiang, 2009; Salvador *et al.*, 2016), besitzen FTC-133 und die ebenfalls aus einer Metastase gewonnenen WRO-Zellen (UCLA RO-82-W-1) eine im Vergleich zu normalen Schilddrüsenepithelzellen verringerte Menge an Tight Junctions **(Publikation 8)**. Dadurch werden die adhärenten Zellen unter den Flüssigkeitsscherkräften einer RPM-2D-Zellkultur leichter abgelöst. Aus Metastasen isolierte Karzinomzellen bilden daher besonders einfach Sphäroide während der Zufallspositionierung. Die pharmazeutische Behandlung mit Dexamethason inhibierte im Falle von FTC-133-Zellen die Sphäroidbildung durch eine Wiederherstellung einer „normalen“ Menge an Tight Junctions **(Publikation 8)**. Eine Glucocorticoid-induzierte Bildung und Reorganisation von Tight Junctions wurde bereits beschrieben (Zettl *et al.*, 1992). Unsere Studie zeigte allerdings erstmals, dass es funktionelle Parallelen zwischen der Hemmung von Metastasen durch Glucocorticoide *in vivo* (Hayashi *et al.*, 1994; Omland & Fosså, 1989) und der Hemmung der RPM-induzierten MCTS-bildung durch Dexamethason *in vitro* gibt.


A
In vivo
Dissemination
Increasing pressure
IL-6
VEGF
MMPs
EMT
Circulating tumor cells (CTCs)
Mucin-1
EGFR
Shear stress
CTC clusters
Plakoglobin
ICAM-1
CD44
IL-8
DNA hypomethylation
Colonization
OXPHOS↑
Integrin
Metastasis
Primary site
Glycolysis↑
Cancer
CTC clusters
IL-8
Metastatic tumor
Metastatic site
CTC
Extravasation
Circulation
B
In vitro
RPM metastasis model
Random positioning
Static culture
Cell culture
Random Positioning Machine (RPM)
Free-flow
Shear
2D adherent cells
Suspension cell
Tumor spheroids
Migration, detachment
Aggregation
„simulated microgravity“
Detachment
Fluid shear
Mucin-1
IL-6
GFRs
ESR1
MMPs
ECM proteins
Integrin
Shear stress
Suspension cells
Mucin-1
Anoikis resistance
Tumor spheroids
IL-8
OXPHOS↑
VEGF
E-cadherin
Reattachment, outgrowth
Integrin
ECM proteins
Adhesion
C
Vice versa: Reattachment on the RPM
Metastatic cancer cells
Spheroids
Suspension cells
Reattachment
Adherent cells
Scratch wound healing assay
Adherent cells
3D assay
Spheroid
Gel-like medium
Time on the RPM
D
From space to translational medicine
Microgravity research
Suspension cells / aggregates
Adherent cell layer
Mechanical and physiological stress research

◄ **TAFEL 4: DAS RPM-METASTASIERUNGSMODELL.** (**A**) Der Prozess der Metastasierung beginnt mit der Dissemination von Zellen des Primärtumors, die wahrscheinlich durch den wachsenden Tumor aufgrund eines steigenden Gewebedrucks epithelial-mesenchymale Transition (EMT) durchlaufen. Bei diesem Vorgang verlieren epitheliale Zellen ihre Zellpolarität und -verbindungen und verwandeln sich in mesenchymale Zellen. Die abgespalteten Zellen migrieren durch das angrenzende Gewebe, bis sie Anschluss an das Gefäßsystem finden. Über Intravasation gelangen die Zellen in den Blutkreislauf oder in das Lymphsystem, wo sie als zirkulierende Tumorzellen (CTCs) mit der Strömung transportiert werden. Teilweise kommt es zur Clusterbildung von CTCs, verbunden mit der Expression bestimmter Adhäsionsmoleküle. An geeigneten Stellen (metastatische Nische) verlassen die CTCs das Gefäßsystem (Extravasation). Die metastatische Nische wird kolonisiert und die Zellen wachsen zu einer Metastase heran, die sich in einigen Eigenschaften vom Primärtumor unterscheiden kann. (**B**) *In vitro* werden Krebszellen auf der RPM zunächst als Monolayer eingesetzt; die Kulturflaschen sind luftblasenfrei gefüllt. Meist lösen sich einzelne Zellen innerhalb eines Tages durch Scherkräfte ab, die durch die Rotation der Zellkulturflasche entstehen. Das Verhältnis von Adhäsions- und Antiadhäsionsproteinen sowie die Menge an EZM bestimmen die Rate der Zellablösung. Die abgelösten Zellen werden durch die Zufallspositionierung an der erneuten Sedimentation gehindert. Sie wachsen mit der Zeit zu Tumorsphäroiden heran, die durch Cadherine Stabilität verliehen bekommen und strukturell bereits Ähnlichkeiten mit Mikrometastasen haben. Nach dem Stopp der RPM sedimentieren die Tumorsphäroide und können am Boden der Zellkulturflasche wieder auswachsen. (**C**) Krebszellen, die aus Metastasen isoliert worden, readhärieren bereits teilweise während der Zufallspositionierung. Die neu adhärierten Zellen besitzen dabei eine größere Menge an Integrin als die ursprüngliche 2D-Zellpopulation und können sich auch in anderen Zelleigenschaften von ihren unterscheiden. Das Phänomen der Readhäsion kann in einigen Fällen die Ergebnisse funktionaler Assays, wie Scratch-Assays, verfälschen. Daher bieten sich für Migrations- und Invasionsstudien mit metastasierten Zellen auf der RPM eher 3D-Matrix-Kulturen an. (**D**) Die beiden Subpopulationen, die in einer RPM-Zellkultur adhärenter Zellen koexistieren, sind unterschiedlichen Zellkulturbedingungen ausgesetzt. Während der 2D-Monolayer den physikalischen Effekten einer rotierenden Zellkulturflasche ausgeliefert ist, befinden sich die Suspensionszellen und Sphäroide in einem stressärmeren Schwebezustand, welcher der Vorstellung von Mikrogravitation am nächsten kommt. Der Monolayer kann jedoch für andere Untersuchungen zu Effekten von mechanischem Stress genutzt werden. Interessanterweise liegen die Scherkräfte bei normalem RPM-Betrieb in einer ähnlichen Größenordnung wie physiologisch relevante Scherwerte des Lymphsystems.

Die Tafel wurde mit Elementen aus BioRender und Servier Medical Art erstellt.

7.5 Lymphsystem *vs.* Weltraum: Subpopulationen der RPM-Zellkultur

Ausgehend von einer zweidimensionalen Zellschicht bilden sich durch die rotationsinduzierte Ablösung einzelner Zellen auf der RPM in der Regel innerhalb eines Tages MCTS. Im weiteren Verlauf der RPM-Zellkultur koexistieren die 2D-Zellschicht und die Sphäroide parallel und führen zu unterschiedlichen biologischen und funktionellen Phänotypen.

Dass Flüssigkeitsbewegungen in der Zellkulturflasche mit den RPM-induzierten Effekten in der 2D Population zusammenhängen, verdeutlichte ein Perfusionsexperiment. Mehrere der RPM-Effekte auf Genexpressions- und Proteinebene konnten in zweidimensional wachsenden FTC-133-Zellen ebenfalls in einem mediendurchströmten Ein-Kanal-Objektträger erzeugt werden **(Publikation 5)**. Da diese Scherungen nur bei der 2D-Population auftreten, muss zwischen den beiden Subpopulationen der RPM-Kultur (2D, MCTS) unterschieden werden. Scherungen treten in realer Mikrogravitation nicht auf, daher ist die Suspensionspopulation beim Vergleich zu Weltraumexperimenten zu bevorzugen (Tafel 4D). Die 2D-Population bietet dafür andere Vorteile. Der durch die RPM induzierte Stress scheint Zellen dazu zu verleiten, sich wie Tumorzellen zu

verhalten (Bonetto *et al.*, 2024). Während des RPM-Betriebs erfährt die adhärente Zellpopulation Scherkräfte, welche in der Größenordnung denen des menschlichen Lymphsystems gleichen (Huang *et al.*, 2018). Demnach könnte die 2D-Zellkultur auf der RPM mit einigen Modifikationen auch als Modell für lymphatischen Stress (z.B. im Rahmen der Metastasierung) dienen (▤ Tafel 4D).

Der Prozess der Sphäroidbildung ist bisher nur in eine Richtung beschrieben. Wir haben allerdings unlängst den umgekehrten Fall bei aggressiven MDA-MB-231-Mammakarzinomzellen beobachtet. Ausgehend von einer dreidimensionalen Sphäroidkultur bildete sich während der Rotation der RPM eine zweidimensionale Subpopulation auf dem Boden der Zellkulturflasche (▤ Tafel 4C). Damit konnten wir nachweisen, dass die Ablösung adhärenter Krebszellen im Gleichgewicht mit der Re-Adhäsion von bereits suspendierten Zellen steht, die sich biologisch und funktionell in einem bisher noch unbekannten Maße von den nicht adhärent bleibenden Zellen unterscheiden. Es entsteht ein biologisches Mosaik adhärenter Zellen (Abb. 4B). Da die 2D-Subpopulation einer RPM-Zellkultur in der Regel als Gegenstück zu den sich in Suspension befindenden, Sphäroid-bildenden Zellen analysiert wird, sollte dieser Aspekt bei der Interpretation biologischer RPM-Daten zukünftig berücksichtigt werden. Die Re-Adhäsion kann auch zu Verfälschung der Daten funktioneller Assays (wie z.B. Scratch-Assays) führen. Bei gutartigen Zellen, die nicht zu sehr zur RPM-induzierten Sphäroidbildung neigen, mögen diese Methoden gut funktionieren und sicherlich aussagekräftige Ergebnisse liefern (Cialdai *et al.*, 2017; Radstake *et al.*, 2023), bei sich leicht ablösenden Krebszellen sollten diese Experimente jedoch mit einiger Vorsicht durchgeführt werden.

8. Gewebekonstruktion (Tissue Engineering) mithilfe von Mikrogravitations-Bioreaktoren

Die Vermeidung der Sedimentation durch Rotationsbewegungen führt bei adhärent wachsenden Zellen in vielen Fällen automatisch zur Aggregatbildung. Die auf diese Weise erzeugten Sphäroide oder Organoide haben – im Vergleich zum 3D-Bioprinting – den Vorteil, dass sie ohne artifizielle Stützstrukturen (engl. scaffolds) auskommen und daher ähnlicher zu natürlich gewachsenen Geweben sind. Diese Eigenschaft macht sie besonders interessant für die Gewebeersatz-Forschung (Aleshcheva *et al.*, 2016; Cui *et al.*, 2023; Grimm *et al.*, 2018; Grimm *et al.*, 2014). Ebenso zeichnen sich RPM-generierte Sphäroide durch eine besonders *in vivo*-nahe Morphologie und biochemische Zusammensetzung aus. Da das 3D-Wachstum insbesondere für mechanisch hochsensitive Zellen wie Endothelzellen (Kapitel 8.1), Osteoblasten, Chondrozyten, (Kapitel 8.2) und Fibroblasten (Kapitel 8.3) beschrieben wurde, lässt sich vermuten, dass die vielfältigen mechanischen Einwirkungen der RPM-Zellkultur (eine Mischung aus Scher- und Dehnungsstress sowie wiederholter Kompression; siehe ▤ Tafel 5A/B) einen positiven Einfluss auf die Kultur dieser Zelltypen haben, welcher in den folgenden Kapiteln noch genauer beleuchtet wird.

8.1 Endothel

Endothelzellen bilden als einzellige Lage die innerste Zellschicht von Lymph- und Blutgefäßen. Sie sind in verschiedenste physiologische Prozesse involviert, darunter der Stoff- und Gasaustausch zwischen Gewebe und Blut, die Regulation des Blutdrucks (über die Produktion von Stickstoffmonoxid), die Hemmung und Aktivierung von Gerinnungsprozessen (Erhaltung der Fließfähigkeit des Blutes) sowie Entzündungsvorgänge (Augustin & Koh, 2024).

8.1.1 Zwei Typen von Endothel-Sphäroiden

Bei der RPM-Kultur von Endothelzellen wird ein sehr interessanter Phänotyp sichtbar. Während auch hier die bereits beschriebenen, globulären Sphäroide entstehen, bilden sich nach mindestens 7-tägiger Kultur auch längliche, tubuläre Sphäroidstrukturen aus, die ein Lumen besitzen und damit Ähnlichkeiten mit der Intima von Gefäßen zeigen (Grimm *et al.*, 2009; Infanger *et al.*, 2006). Weshalb sich bestimmte Endothelzellen zu diesen besonderen Aggregaten zusammenlagern, ist bisher nicht geklärt. Es scheint, dass die Mikrogravitations-Zellkultur bei einigen Zelltypen eine Art „Positionierungsgedächtnis“ aktivieren kann und sich dadurch physiologisch relevante Strukturen ausbilden können. Das zelltypspezifische Aggregationsmuster während einer RPM-Zellkultur wurde aber nicht nur bei vaskulären Endothelzellen, sondern auch bei lymphatischen Endothelzellen und bei Glioblastom-Zellen sowie bei Hepatozyten (Yoffe *et al.*, 1999) beobachtet.

In der Studie „*Key Proteins Involved in Spheroid Formation and Angiogenesis in Endothelial Cells After Long-Term Exposure to Simulated Microgravity*“ **(Publikation 13)** wurde die endothelähnliche Zelllinie Ea.hy926 für bis zu 35 Tage auf einer RPM kultiviert – bisher das längste bekannte RPM-Experiment mit diesem Modell-Zelltyp. Über diese Zeit hinweg hatten sich *de novo* tubuläre Strukturen mit Längen im Millimeterbereich gebildet die anschließend getrennt von den globulären Endothelzell-Sphäroiden untersucht wurden.

Dass die RPM in für dieses Zellkultur-Modell eine sehr gute Simulation für mikrogravitations-induzierten Effekte bietet, wird durch die Ergebnisse des *SPHEROIDS*-Projekts gestützt. Im Rahmen dieses Projekts wurden Ea.hy926-Zellen während eines 14-tägigen Weltraumflugs zur ISS in einer speziell entwickelten Hardware kultiviert. Auch hier hatten sich am Ende der Mission sphärische und tubuläre 3D-Strukturen gebildet, die anschließend histologisch und biochemisch untersucht wurden (Pietsch *et al.*, 2017) **(Publikation 21)**.

Warum Ea.hy926-Zellen im Vergleich zu anderen (primären) Endothelzellen besonders stark zur Sphäroidbildung unter Mikrogravitationsbedingungen neigen, kann zum jetzigen Zeitpunkt nur vermutet werden. Im Gegensatz zu den Primärzellen sekretieren Ea.hy926-Zellen größere Mengen von VEGF-A und IL-8 und könnten damit einen autokrinen Induktionsmechanismus anstoßen (▤ Tafel 5C) **(Publikation 13)**. VEGF-A ist ein Zusatz in den meisten Spezial-Kulturmedien für Endothelzellen und wurde schon vor längerer Zeit als wichtiger Faktor für die Sphäroidbildung identifiziert (Infanger *et al.*, 2006).

8.1.2 Endothel-Sphäroidbildung: Antiadhäsion und Anoikis-Schutz durch Mucin-1?

Das 3D-Wachstum von Endothelzellen auf der RPM funktioniert besonders gut mit Ea.hy926-Zellen, während mikrovaskuläre Endothelzellen der Haut (HMVEC) nach aktuellen Studien kaum und Endothelzellen der Vena saphena magna (HSVEC) gar nicht zur Sphäroidbildung neigen **(Publikation 22)**. Hier bleibt allerdings fraglich, inwieweit Ea.hy926-Zellen, die als somatische Hybridzelllinie aus HUVECs und alveolaren Lungenadenokarzinom-Zellen (einem Thioguanin-resistenten A549-Klon) hergestellt wurden (Edgell *et al.*, 1983), auch Eigenschaften beider Ursprungszelllinien vereinen. Die stärkere Sphäroidbildung von Ea.hy926-Zellen bei einem 3D-Klinostaten-Experiment mit erhöhter Glukosekonzentration (Jokšienė *et al.*, 2023) kann durchaus auch auf den Krebsursprung zurückzuführen sein. Auch die Entstehung tubulärer Sphäroide könnte mit dem Tumor-Erbe und der epithelial-endothelialen Transition (EET) in Verbindung gebracht werden (vaskulares Mimikry; Wechman *et al.*, 2020; Abb. 5C). Wir konnten kürzlich zeigen, dass Ea.hy926-Zellen verglichen mit HMVECs eine höhere Menge des Tumormarkers Mucin-1 aufweisen (Abb. 5A, Tafel 5C), was die stärkere Tendenz zur RPM-induzierten Sphäroidbildung erklären könnte. Bei Endothelzellen kann Mucin-1 gleich durch zwei Effekte die Sphäroidbildung begünstigen: durch die bereits beschriebene Antiadhäsionswirkung und durch eine Mucin-Schicht bedingten Schutz von Anoikis (Wilson *et al.*, 2019). Ob diese Eigenschaft von den A549-Zellen, oder den HUVECs vererbt wurde, ist nicht klar, da HUVECs als eine der sehr wenigen Endothel-Vertreter ebenfalls Mucin-1 exprimieren (Porowska *et al.*, 2010). Interessanterweise haben Cheng *et al.* gezeigt, dass die Interaktion zwischen HUVECs und Lungenkarzinomzellen, den Ausgangs-Zelltypen von Ea.hy926-Zellen, die Morphologie von HUVECs beeinflussen können, so dass diese einen eher höhere Motilität verbunden mit einer anderen Organisation des Aktin-Zytoskeletts (mehr Filopodien) und verstärkter Bildung tubulärer Sphäroide aufweisen (Cheng *et al.*, 2017). Die co-kultivierten HUVECs zeigten eine höhere Expression von *CXCL8*, *ICAM1* und *VCAM1*, ein Verhalten, das auch für die Ea.hy926-Sphäroidzellen auf der RPM beschrieben wurde **(Publikation 13)**.

Auch wenn Ea.hy926-Zellen keine „echten“ Endothelzellen sind, die besser nicht zum vaskulären Tissue Engineering in der regenerativen Medizin herangezogen werden sollten, so könnten diese Zellen unter Zufallspositionierung eventuell aber als Modell für Tumorangiogenese dienen. In den beschriebenen Co-Kultur-Experimenten korrelierten die Gensignaturen der HUVECs mit der klinischen Prognose bei Patienten, die an einem nicht-kleinzelligen Lungenkarzinom (NSCLC) leiden (Cheng *et al.*, 2017). Für eine abschließende Bewertung der RPM als Tumorangiogenese-Modell ist die Datenlage derzeit jedoch noch zu gering.

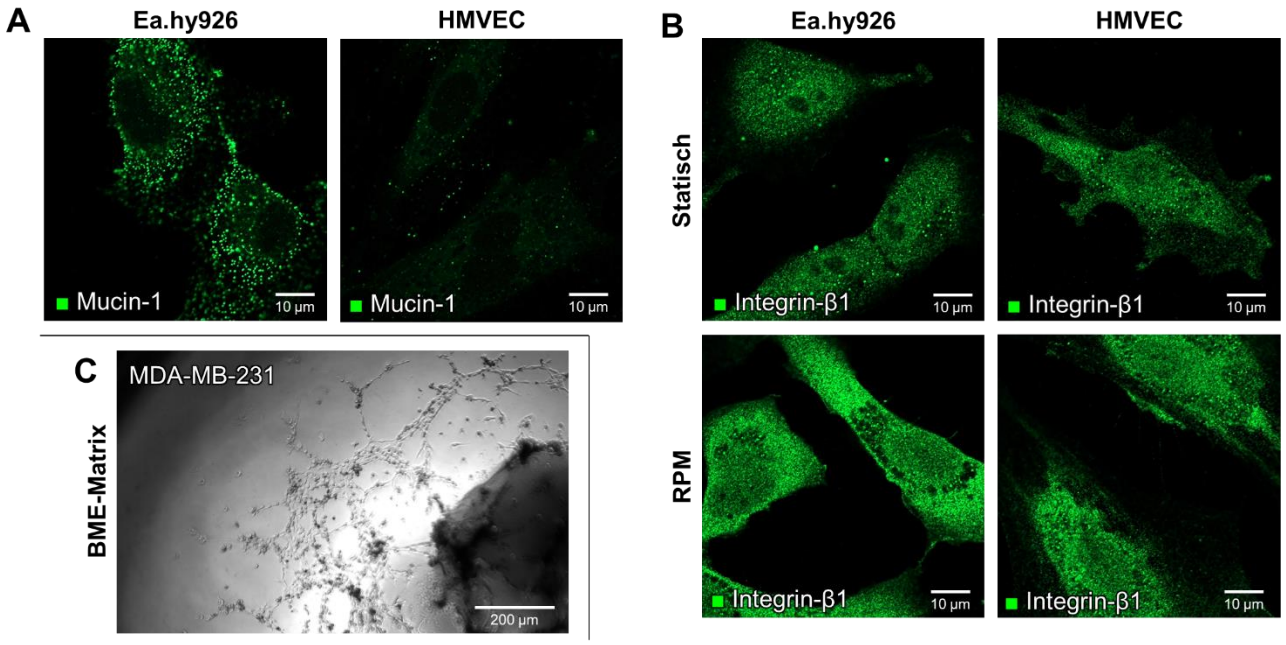


Abbildung 5: Antiadhäsions- und Adhäsionsproteine bei verschiedenen Endothelzellen. (**A**) Im Gegensatz zu mikrovaskulären Endothelzellen (HMVEC) exprimiert die Hybridzelllinie Ea.hy926 (HUVEC×A549) größere Mengen des Antiadhäsionsprotein Mucin-1 (grün), das auch bei Tumorzellen die Sphäroidbildung begünstigt. Die Bilder stammen aus einer dreitätigen statischen Zellkultur. (**B**) Bei der Integrin-β1-Expression (grün) verhalten sich beide Zelltypen gleich: Die Proteinmengen sind ähnlich und auf der RPM konnte nach drei Tagen sowohl bei Ea.hy926-Zellen als auch bei HMVECs eine Zunahme an Integrin-β1 beobachtet werden. (**C**) Tumorsphäroide von MDA-MB-231-Zellen, eingebettet in BME-Matrix (Basalmembran-Extrakt), wachsen teilweise spontan als tubuläre Strukturen in die Matrix ein. Dieses Verhalten ähnelt dem vaskularen Mimikry und könnte zusammen mit der RPM-induzierten Bildung tubulärer Strukturen von Ea.hy926-Zellen wertvolle Erkenntnisse zur Angio- und Neuangiogenese liefern.

8.1.3 Funktionalität von RPM-kultivierten Endothelzellen

Auch bei der zweidimensionalen Kultur von Endothelzellen beeinflusst die RPM deren Funktionalität. Eine wichtige Aufgabe ist die Interaktion mit peripheren mononukleären Blutzellen (PBMCs), wie Monozyten, welche durch Zelladhäsionsmoleküle (ICAM-1, VCAM-1, CD44, E-/P-Selektine) vermittelt wird. Zufallspositionierte Ea.hy926-Zellen erhöhen die Expression dieser Zelladhäsionsmoleküle ähnlich wie bei einer Durchfluss-Zellkultur (▤ Tafel 5C). Die RPM scheint demnach einen positiven physiologischen Effekt auf 2D-Kulturen von Endothelzellen auszuüben und ihren funktionellen Phänotyp zu bewahren. Interessanterweise führte die RPM-Zellkultur in handelsüblichen Zellkulturflaschen zur Bildung von zwei Subpopulationen von Ea.hy926-Zellen, die sich in Zellgröße und gebildeter ICAM-1-Menge unterschieden haben (kleinere Zellen bildeten mehr ICAM-1). Wenn man davon ausgeht, dass beide Effekte scherungsabhängig sind, würden diese vorläufigen Daten mit den Simulationsexperimenten von Wuest *et al.* korrelieren, dass nicht alle Monolayer-Zellen auf der RPM denselben Scherkräften ausgesetzt sind (Wuest *et al.*, 2017).

8.2 Knochen- und Knorpelstrukturen

8.2.1 Osteoblasten auf der RPM: Kompression zur Differenzierung, Scherkräfte zur Apoptose-Suppression

Osteoblasten sind spezialisierte Knochenzellen, die für die Osteogenese verantwortlich sind. Sie synthetisieren und sezernieren organische Knochenmatrixproteine (Osteoid), die sowohl im sich entwickelnden Skelett als auch während des Knochenumbaus mineralisiert werden (Tanaka *et al.*, 2005). Fötale menschliche Osteoblasten (hFOB 1.19) wurden verwendet, um die Möglichkeit der RPM-Zellkultur zur Herstellung von Knochen-Konstrukten zu erörtern. Eine 7- bzw. 14-tägige Zufallspositionierung führte zur Bildung von Sphäroiden mit knochenspezifischer Morphologie **(Publikation 18)**. In dem 14-Tage-Experiment erhöhte die RPM induzierte vor allem die Expression von Fibronektin, Kollagen I und Osteopontin in der Stress-exponierten 2D-Subpopulation sowie von Laminin in den frei beweglichen Sphäroiden. Des Weiteren führte die gesamte Rotationskultur zur verstärkten Sekretion von Osteopontin, Osteocalcin und Osteoprotegerin **(Publikation 18)**.

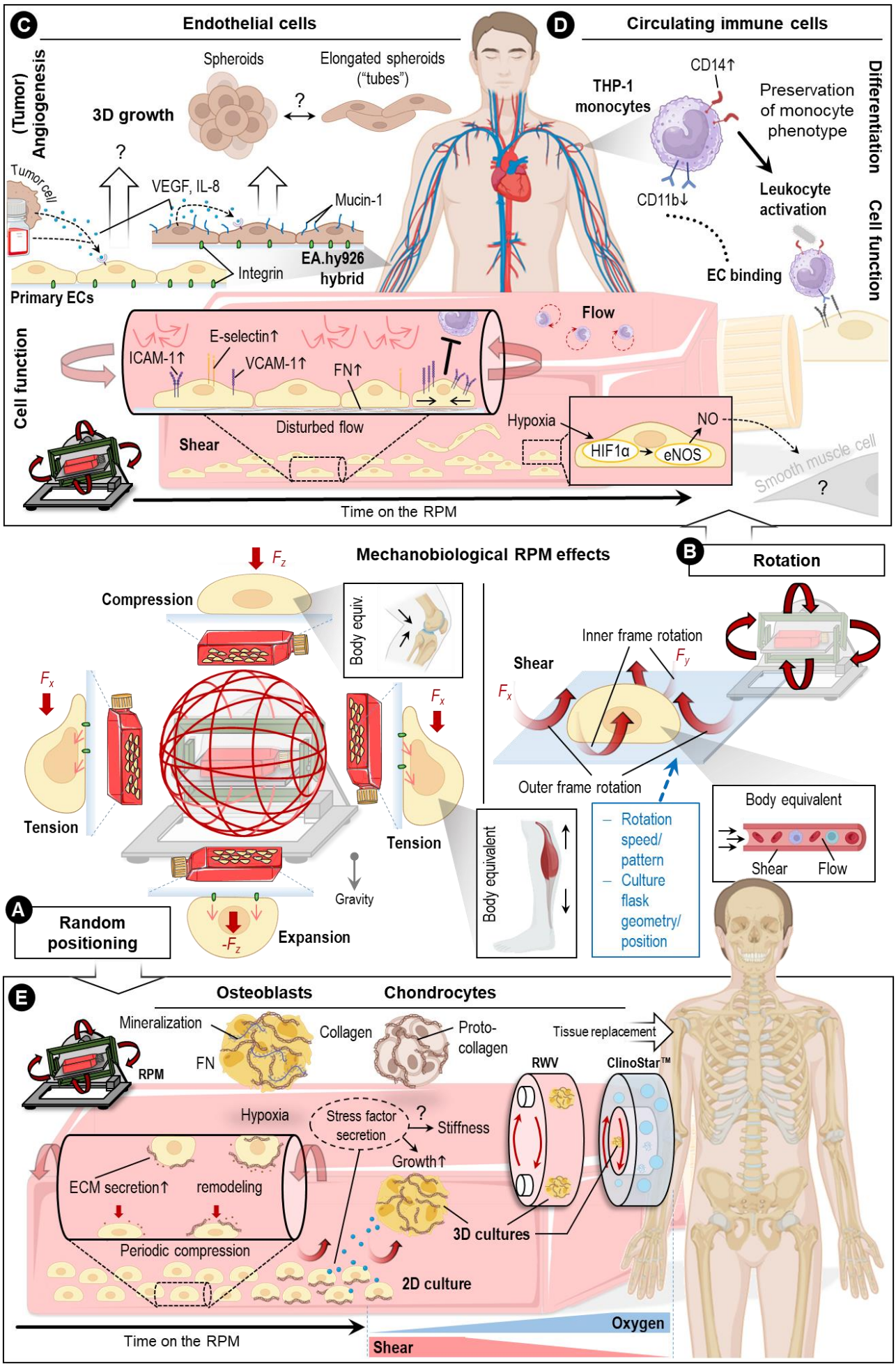
Es ist bekannt, dass mechanische Einflüsse, Dehnung und v.a. zyklische Kompression, wie sie auch durch die Rotation der 2D-Zellkultur auf der RPM stattfindet, eine wichtige Rolle bei der Osteroblasten-Differenzierung (Chen *et al.*, 2017) und Osteogenese spielen (Fedeli *et al.*, 2022; Radstake *et al.*, 2023). In Kompressions-Experimenten mit Osteoblasten wurde eine Hochregulation der Expression von Kollagen I, Osteocalcin und Osteopontin beschrieben (Rath *et al.*, 2008). Scherkräfte, die ebenfalls während der RPM-Kultur auftreten, scheinen die Apoptose von Osteroblasten zu verringern (Radstake *et al.*, 2023).

Die Osteoblasten-Forschung auf GBFs befindet sich noch relativ am Anfang. Es gibt aber bereits Hinweise, dass die RPM eine Kombination aus verschiedenen physikalischen Einflüssen bietet, die sich positiv auf das Tissue Engineering von Knochen-Konstrukten auswirken (▤ Tafel 5E).

8.2.2 Chondrozyten auf der RPM: 2D-Subpopulation fördert Sphäroidentwicklung

Gelenkknorpel befindet sich *in vivo* in einem komplexen und dynamisch-mechanischen Umfeld, das durch Druck- und Scherspannungen entlang mehrerer Achsen sowie durch hydrostatische und osmotische Drücke gekennzeichnet ist (Eschweiler *et al.*, 2021). Das biomechanische Umfeld bestimmt zum Teil die Entwicklung und Reifung der nativen Strukturarchitektur durch eine klassische Struktur-Funktions-Beziehung (Williams *et al.*, 2008). Knorpel-Konstrukte, die unter Mikrogravitation kultiviert werden, zeigen eine geringere Zelldichte sowie erhöhte Mengen an Kollagen II/I, während der Aggrecan/Versican-Anteil geringer ist als bei Kulturen in unter normalen (statischen) Gravitationsbedingungen (Stamenković *et al.*, 2010).

Die chondrogene Kultur in Mikrogravitations-Bioreaktoren führte stets zu einer besseren Qualität der erzeugten Knorpel-Konstrukte verglichen mit statischen Kulturmethoden (Luo *et al.*, 2011; Wu *et al.*, 2013; Yuge *et al.*, 2006), was darauf hindeutet, dass die rotationsbedingte Mikroumgebung auf diesen Maschinen einen positiven Effekt auf die Knorpelneubildung hat.


C
Endothelial cells
(Tumor) Angiogenesis
Spheroids
Elongated spheroids ("tubes")
3D growth
?
?
Tumor cell
VEGF, IL-8
Mucin-1
Integrin
EA.hy926 hybrid
Primary ECs
D
Circulating immune cells
THP-1 monocytes
CD14↑
CD11b↓
Preservation of monocyte phenotype
Leukocyte activation
EC binding
Differentiation
Cell function
Flow
Cell function
ICAM-1↑
E-selectin↑
VCAM-1↑
FN↑
Disturbed flow
Shear
Hypoxia
HIF1α
eNOS
NO
Smooth muscle cell
?
Time on the RPM
Mechanobiological RPM effects
B
Rotation
Compression
Body equiv.
Inner frame rotation
Shear
Outer frame rotation
Body equivalent
Shear
Flow
Body equivalent
– Rotation speed/ pattern
– Culture flask geometry/ position
Tension
Tension
Gravity
Expansion
A
Random positioning
E
Osteoblasts
Chondrocytes
Mineralization
FN
Collagen
Proto-collagen
Tissue replacement
RPM
RWV
ClinoStar™
Hypoxia
Stress factor secretion
?
Stiffness
Growth↑
ECM secretion↑
remodeling
Periodic compression
3D cultures
2D culture
Time on the RPM
Oxygen
Shear

◄ TAFEL 5: EFFEKTE DER RANDOM POSITIONING MACHINE BEIM SCAFFOLD-FREIEN TISSUE ENGINEERING. (**A**) Durch die unterschiedliche Ausrichtung einer luftblasenfrei gefüllten Zellkulturflasche während der RPM-Rotation, sind die Zellen des Monolayers unterschiedlichen mechanischen Kräften ausgesetzt. Je nach Orientierung werden die Zellen durch die auf sie wirkende Gewichtskraft des Mediums (*F*, rote Pfeile) komprimiert oder gedehnt. Durch den Bewegungsalgorithmus der RPM-Steuerung passiert das periodisch in allen Richtungen des dreidimensionalen Raums (F_x, F_y, F_z). (**B**) Durch die Rotation wird auch das Zellkulturmedium in der Kulturflasche in Bewegung versetzt, was Scherkräfte erzeugt, die ebenfalls auf die Zellen wirken. Die Richtung der Scherkräfte ist dabei auch vom Rotationsmuster der RPM abhängig und wird ebenfalls durch die Position der Zellkulturflasche auf der RPM beeinflusst (blaue Box). Zufallspositionierung und rotationsbedingte Scherkräfte sind die mechanischen Hauptkräfte, die auf einer 2D-Zellkultur einwirken und haben entsprechende Pendants im menschlichen Körper. Bei der Gelenkbewegung werden Zellen mechanisch komprimiert, bei der Muskeldehnung mechanisch gestreckt und die Zellen des Blutkreislaufs sind stetig Scherkräften ausgesetzt (kleine Boxen). (**C**) Die auf der RPM erzeugten (turbulenten) Scherkräfte haben daher auch die größte physiologische Wirkung auf 2D-wachsende Endothelzellen. RPM-kultivierte Endothelzellen exprimieren verstärkt Adhäsionsproteine (insb. ICAM-1, VCAM-1)[1]. Ebenso wird mehr Fibronektin (FN) sezerniert und die Zellen schrumpfen. Bei längeren Experimenten wird vermehrt Stickstoffmonoxid (NO) gebildet, was eventuell mit beginnender Hypoxie zusammenhängen könnte, die durch die verringerte Gasaustauschfläche, die bei luftblasenfrei gefüllten Zellkulturflaschen zwangsläufig in Kauf genommen wird. Ein zweiter beobachteter Effekt ist die Bildung von Endothelsphäroiden (rund und langgestreckt/tubulär), die vor allem bei Ea.hy926-Zellen beobachtet wurde. Bisher ist noch nicht endgültig geklärt, welche Voraussetzungen für das RPM-induzierten 3D-Wachstum nötig sind, es könnten aber die Mengen an exprimiertem Mucin-1 sowie im Medium vorhandenen Mengen an VEGF-A und IL-8 entscheidend sein, die von Ea.hy926-Zellen autokrin/parakrin sekretiert werden. (**D**) Im Gegensatz zu den adhärenten Endothelzellen, befinden sich zirkulierende Immunzellen (hier am Beispiel von THP-1-Monozyten) in Suspension und bewegen sich mit der von der RPM generierten Flüssigkeitsströmung mit. Bei diesen Zellen ist die Datenlage zum aktuellen Zeitpunkt noch sehr dünn, aber deutet sich an, dass die RPM-Kultur zumindest vorübergehend zu einem aktiveren Phänotyp führt, da Aktivierungsmarker (CD14) vorübergehend hochreguliert werden. Ebenfalls unterschiedlich zu Endothelzellen: Adhäsionsproteine (CD11b) werden herunterreguliert. Die Effekte auf die Immun-Endothelzell-Interaktionen sind gerade Thema intensiver Forschung. (**E**) Bei der Kultur von Knochen- und Knorpel-Konstrukten spielt wahrscheinlich die RPM-generierte zyklische Kompression und Dehnung der Osteoblasten und Chondrozyten eine wichtige Rolle. Beide Zelltypen reagieren sensitiv auf mechanische Verformung, produzieren als Monolayer verstärkt EZM und sekretieren Stressfaktoren (Wachstumsfaktoren, Zytokine), die dann als Signalstoffe schließlich einen positiven Einfluss auf die Entwicklung der Sphäroide hat. Die RPM ist der einzige Mikrogravitations-Bioreaktor, bei dem 2D- und 3D-wachsende Zellen zusammen in demselben Zellkulturgefäß kultiviert werden.

Die Tafel wurde mit Elementen aus BioRender und Servier Medical Art erstellt.

Parallelen zwischen simulierter Mikrogravitation und zyklischem hydrostatischem Druck wurden bereits von Nordberg *et al.* in der Modulation von LRP-Rezeptoren (lipoprotein receptor-related protein) von Chrondrozyten gefunden (Nordberg *et al.*, 2019). Der Einfluss von Scherstress auf Knorpelzellen umfasste eine veränderte Expression von Aggrecan und Kollagen II, veränderte Sekretion des oligomeren Knorpelmatrixproteins (COMP), Induktion von Apoptose-Signalen sowie eine veränderte Menge an Integrin (Sharifi & Gharravi, 2019).

Auf der RWV begannen entdifferenzierte Chondrozyten zu redifferenzieren und eine knorpelspezifische extrazelluläre Matrix innerhalb von 12 Wochen zu produzieren (Marlovits *et al.*,

[1] Auf Transkriptionsebene gibt es bei fast allen Zellen temporäre RPM-Effekte, die manchmal ein anderes Bild vermuten lassen (vgl. z.B. Grenon *et al.*, 2013). Da es sich hierbei meist um Momentaufnahmen handelt und das Proteom am ehesten die Funktionalität der Zellen widerspiegelt, werden Proteinlevel gezeigt.

2003). Auf der RPM konnten bereits nach 28 Tagen bis zu 2 mm große Chondrozyten-Sphäroide mit Protokollagen-Fibrillen nachgewiesen werden, einem der wichtigsten Bestandteile von Knorpel. Der Hauptunterschied zu den anderen Mikrogravitations-Simulatoren ist die initiale 2D-Zellkultur, die unter dem dynamischen Stress der RPM verstärkt *IL6*, *RUNX2*, *RUNX3*, *SOX6*, *SOX9* und *MMP13* exprimiert (Wehland *et al.*, 2020). Eine gesteigerte Expression von *IL6*, *SOX9* und *RUNX2* fanden Steinwerth *et al.* beispielsweise nicht in einer RWV-Suspensionskultur primärer Chondrozyten (Steinwerth *et al.*, 2024). SOX9 ist ein wichtiger Transkriptionsfaktor während der Chondrogenese (Lefebvre & Dvir-Ginzberg, 2017). IL-6 wurde vor allem als wichtiger sekretierter Faktor in der chondrogenen Differenzierung mesenchymaler Stammzellen beschrieben und führte zu der Vermutung, dass IL-6 zur Homöostase und Selbstreparatur des Knorpels beiträgt (Kondo *et al.*, 2015). Darüber hinaus sezernieren Konstrukte humaner Chondrozyten unter zyklischer Kompression mehr Glykosaminoglykane (z.B. Chondroitinsulfat) (Démarteau *et al.*, 2003), was nach 24-stündiger Exposition in 2D wachsenden Chondrozyten auf der RPM ebenfalls nachgewiesen wurde (Ulbrich *et al.*, 2010).

Zusammenfassend vereint die Kombination aus mechanisch beeinflusster 2D-Zellkultur und freischwebender 3D-Kultur auf der RPM vorteilhafte Bedingungen für das Knorpelwachstum (▤ Tafel 5A/E). Die RPM kann daher für zelluläre Knorpelregenerationsansätze in der Trauma- und Osteoarthritis-Therapie eingesetzt werden.

8.3 Fibroblasten

Fibroblasten sind mesenchymalen Ursprungs, befinden sich im Bindegewebe und sind hauptverantwortlich für die Sezernierung der EZM in Geweben. Kollagen ist eines der wichtigsten Fibroblasten-Produkte und sorgt zusammen den ebenfalls gebildeten Proteoglykanen für eine erhöhte Festigkeit der EZM. Gewebeschäden können über zelluläre Zytokinausschüttung die Proliferation und Matrix-Synthese von Fibroblasten anregen, was sich meist positiv auf die Reparatur solcher Schäden auswirkt, beim Überschuss jedoch schnell zur pathologischen Fibrose führt. Ebenso reagieren die Fibroblasten selbst auf mechanische Einflüsse mit einer verstärkten EZM-Produktion (Breen, 2000; Le Bellego *et al.*, 2009; Ludwig *et al.*, 2004; Manuyakorn, 2014; Manuyakorn *et al.*, 2016).

8.3.1 Juvenile dermale Fibroblasten bilden Sphäroide auf der RPM

Auf der RPM bildeten Fibroblasten, die aus menschlicher neonataler Vorhaut isoliert wurden (juvenile NHDF-Zellen), ebenfalls Sphäroide **(Publikation 11)**. Dieses Verhalten konnte bei adulten, dermalen Fibroblasten (HFIB-D, provitro) unter den gleichen Kulturbedingungen nicht beobachtet werden (persönl. Mitteilung M. Isensee) und wurde auch von anderen RPM-Forschergruppen bisher nicht beschrieben (Fedeli *et al.*, 2022; Radstake *et al.*, 2023). In unserer Studie konnten wir bei den RPM-kultivierten juvenilen NHDF-Zellen eine erhöhte Produktion von Fibronektin, Laminin und Kollagen IV, sowie der Matrix-remodellierenden Proteine MMP-1, MMP-3 und TIMP-1 (TIMP

Metallopeptidase Inhibitor 1) nachweisen **(Publikation 11)**, was grundsätzlich der Antwort von Fibroblasten auf mechanische Einwirkungen entspricht (zum Vergleich: in „stressärmeren“ RWV-Kulturen mit adulten Fibroblasten auf Cytodex™-Mikroträgern verringerte sich die Menge an gebildeten Kollagenen I und III und es kam zu vermehrter Apoptose (Yue *et al.*, 2023)). Die veränderte Matrix-Zusammensetzung ließ jedoch keine Aussagen auf das Sphäroidbildungsverhalten zu. Fibroblasten werden als mesenchymale Zellen normalerweise als Mucin-1-negativ angesehen, was zwar unsere Beobachtungen bei adulten Fibroblasten untermauert, nicht aber die NHDF-Sphäroide. In der Literatur finden sich allerdings Berichte, dass juvenile NHDF-Zellen unerwarteterweise Mucin-1 exprimieren (Kumar *et al.*, 2014), was unserem Modell der RPM-induzierten Sphäroidbildung entsprechen würde.

8.3.2 RPM-Forschung mit Fibroblasten

Die Rotation der Zellkultur führt auch bei dermalen Fibroblasten zu unterschiedlichen Effekten. Während die „Aktivierung“ der Fibroblasten am wahrscheinlichsten durch die wiederholte Kompression der 2D wachsenden Zellen erklärt werden kann (Kalli *et al.*, 2018), können die unterschiedlichen Scherstress-Intensitäten in der Zellkulturflasche (Wuest *et al.*, 2017) **(Publikation 5)** Zellpolarität, Migrationsverhalten und Adhäsion der Fibroblasten beeinflussen (Lei *et al.*, 2020).

Durch diese unterschiedlichen induzierten Effekte liefert die RPM eine geeignete Methode, das Fibroblastenverhalten mitsamt seinen Kontrollmechanismen *in vitro* zu erforschen. Die Erkenntnisse aus diesen Studien können nicht nur direkte therapeutische Ansätze bei Krankheiten wie Krebs und Fibrose aufzeigen, sondern auch Fortschritte bei zukünftigen regenerativen Therapien ermöglichen. Während zufallspositionierte 2D-Kulturen dermaler Fibroblasten proliferativ und wenig apoptotisch bleiben und „aktivierte“ Zellen mit breiten Lamellipodien und Stressfasern beinhalten (Radstake *et al.*, 2023), zeigen Fibroblasten in verschiedenen 3D-Kulturen eine Vielzahl von Merkmalen, vom „aktivierten“ Phänotyp, wie er in 2D-Kulturen und bei Myofibroblasten zu beobachten ist (Granato *et al.*, 2017), bis hin zu einem „Ruhezustand“, der wahrscheinlich besser den meisten Fibroblasten *in vivo* entspricht (Salmenperä *et al.*, 2016). Choi *et al.* nutzen zuletzt einen RPM-ähnlichen 3D-Klinostaten um bereits vorgeformte Sphäroide aus Fibroblasten und Keratinozyten weiter zu kultivieren (Choi *et al.*, 2021). Nach drei Tagen waren die Fibroblasten-Sphäroide stärker kompaktiert als die Kontrollgruppe unter statischen Bedingungen (1*g*), was von dem Autorenteam als Modell für die bei Astronauten beobachtete Hautverdünnung vorgeschlagen wurde (Farkas & Farkas, 2021). Heterogene Sphäroide aus beiden Zelltypen besaßen nach 7 Tagen Klinorotation allerdings einen größeren Anteil an Kollagen.

9. Zusammenfassung und Fazit

Die Herausforderungen in der Gravitationsbiologie sind oft genauso groß und komplex wie der Weltraum selbst. Selbst bei etablierten Methoden lernen wir ständig dazu, passen die Protokolle an

und verbessern die Versuchsaufbauten. Mikrogravitations-Simulatoren wie die RPM bieten eine vergleichsweise kostengünstigere und schnell verfügbare Möglichkeit für gravitationsbiologische Experimente. Allerdings sind längst nicht alle Prozesse auf Mikrogravitations-Bioreaktoren verstanden. Insbesondere die RPM induziert eine Reihe an mechanodynamischen Effekten, die in Summe zwar zu ähnlichen Resultaten führen können, wie sie auch bei Experimenten in realer Mikrogravitation gefunden wurden. Ob der Weg dorthin aber derselbe ist wie im Weltraum, ist bisher nicht bekannt.

Der Hauptfokus dieser Forschung lag auf der Sphäroidbildung verschiedener adhärenter Zellen, die sowohl in „simulierter“ als auch in realer Mikrogravitation auftritt. Bei dem von uns am häufigsten genutzten Mikrogravitationsbioreaktor, der RPM, sind wir einen großen Schritt weitergekommen. Wir konnten zeigen, dass die Sphäroidbildung in zwei Schritten abläuft, dass Scherkräfte bei der Ablösung der Zellen eine wichtige Rolle spielen und dass Zellen selbst gewisse Bedingungen erfüllen müssen (Mucin-1), damit die Sphäroidbildung erfolgreich verläuft. Und in realer Mikrogravitation? Da hier keine Scherkräfte vorkommen, die zur Ablösung der Zellen beitragen können, muss der erste Schritt der Sphäroidbildung anders ablaufen. Aufgrund der seltenen Möglichkeiten für Langzeit-Experimente und dem Fehlen geeigneter Untersuchungsmethoden für diese Fragestellung, lassen sich dazu bisher nur Vermutungen anstellen. Eine mögliche Erklärung haben wir durch verschiedene räumliche Ausrichtungen der Zellkultur bekommen. Auch in der Kopfüber-Zellkultur lösen sich Zellen ab, die im Anschluss Sphäroide bilden können. Da wir nicht wissen und beeinflussen können, wie die Experiment-Hardware in der Trägerrakete zum Gravitationsvektor der Erde ausgerichtet war, solange sie noch unter dem Einfluss der Schwerkraft stand, könnten sich schon vor dem Eintritt in Mikrogravitation Zellen gelöst haben, die dann im Orbit die Sphäroide gebildet haben (CellBox-2). Da eine solche Ablösung bei überwachsenen Zellkulturen nicht vorkommt, würde das auch die ausgebliebene Sphäroidbildung bei CellBox-1 erklären.

Ein weiteres bedeutendes Resultat war die Erkenntnis, dass es mehr biologische Parallelen zwischen der Metastasierung *in vivo* und der Sphäroidbildung auf der RPM gibt, was zu einer besseren Bewertbarkeit des „*in vivo*-Metastasierungsmodells“ beiträgt und nun die Möglichkeit einräumt, dass in Zukunft eine *ex vivo*-Methode zur Erforschung der Metastasierung und geeigneter Therapien existiert. Eine pharmazeutische Behandlung von Schilddrüsentumorzellen mit Dexamethason brachte schon vielversprechende erste Ergebnisse mit *in vivo*-ähnlichen Effekten.

Die aus der Tumorforschung mit der RPM gewonnenen Erkenntnisse können auch teilweise auf das scaffold-freie Tissue Engineering übertragen werden. Hier profitieren v.a. mechanosensitive Zellen (Endothelzellen, Osteoblasten, Chondrozyten, Fibroblasten) von den mechanischen „Nebenwirkungen“ der RPM-Zellkultur (Scherung, Kompression, Dehnung). Für sie bietet die RPM-Kultur eine einzigartige und komplexe Mikroumgebung, die schließlich zu 3D-Konstrukten führt, die mit anderen Methoden nicht so einfach hergestellt werden können. Gewisse Parallelen existieren auch hier zur Tumorzellkultur, beispielsweise, dass Mucin-1 förderlich für die Bildung von 3D-Strukturen ist. GBF-Zellkulturen, insbesondere auch mit Stammzellen, können und werden bereits

in verschiedenen medizinischen Bereichen genutzt, darunter in der regenerativen Medizin, in der Arzneimittelentwicklung und in der Erforschung von Krankheitsmodellen. Anwendung finden sie zum Beispiel bei der Untersuchung von Wachstumsmustern, der Empfindlichkeit gegenüber Medikamenten und bei der Entwicklung neuer Wirkstoffe (zusammengefasst in Nishimura, 2023).

Was die vorgeschlagene „2,5D-Zellkultur“ bei RPM-gebildeten Sphäroiden angeht, bedarf es in Zukunft noch weiterer Forschung, um die Eigenschaften und Möglichkeiten einer optimalen Nutzung besser einordnen zu können. Interessant wäre, zu überprüfen, wie sich bereits vorgeformte Tumorsphäroide in Mikrogravitation verhalten, ob es dort ebenfalls zu einer Auflockerung der Struktur und dadurch zu einer besseren Therapier-/Kontrollierbarkeit der Tumormodelle unter Weltraumbedingungen kommt.

Auch über unsere Forschung hinaus, öffnet die Gravitationsforschung neue Horizonte und bietet eine Plattform für innovative Anwendungen. Studien haben gezeigt, dass die Kristallisation von Proteinen in Mikrogravitation zu hochqualitativen Kristallen führt, die bei der Strukturaufklärung helfen können (Jackson *et al.*, 2024). Diese Erkenntnisse sind besonders relevant für die Arzneimittelentwicklung, da verbesserte Kristalle genauere Informationen über die Zielstrukturen von Medikamenten liefern. Die kontinuierliche Zusammenarbeit zwischen Raumfahrtorganisationen und biowissenschaftlichen Institutionen wird entscheidend sein, um die Potenziale dieser einzigartigen Forschungsumgebung vollständig auszuschöpfen.

Die molekularbiologische Gravitationsforschung ist nach über 25 Jahren immer noch relativ am Anfang. Langzeit-Weltraumexperimenten (reale Mikrogravitation), die ausreichend Zeit zur Bildung von Sphäroiden bieten (beispielsweise auf der ISS), hatten bisher immer das Problem, dass nur Endpunktanalysen bei Omics-Untersuchungen möglich waren. Das wird sich mit dem geplanten FLUMIAS-ISS-Mikroskop der Deutschen und Europäischen Weltraumagenturen (DLR/ESA) ändern, das ab Ende 2026 auf der ISS für wissenschaftliche Experimente zur Verfügung stehen soll. Zukünftige Missionen, wie geplante Flüge zum Mond/Mars oder neue Strategien für Raumfahrzeuge (van Loon *et al.*, 2024), werden die Möglichkeit bieten, noch umfassendere Daten zu sammeln. Gleichzeitig könnte die Kombination von Weltraumforschung mit modernsten Technologien wie CRISPR (Clustered Regularly Interspaced Short Palindromic Repeats) zur Genomeditierung und Bioinformatik neue Wege in der medizinischen Forschung eröffnen (Alon *et al.*, 2023). Somit hat die molekularbiologische Gravitationsforschung nicht nur das Potenzial, das Verständnis biologischer Anpassungen an veränderte Schwerkraftbedingungen zu vertiefen, sondern auch bedeutsame Fortschritte in der Medizin zu fördern. Manche Erkenntnisse, die von Wissenschaftlern mit ihren GBFs und Astronauten im Weltraum gewonnen werden, kommen am Ende auch der Patientenversorgung auf der Erde zugute, was eine vielversprechende Schnittstelle zwischen Raumfahrt und Gesundheitswissenschaften darstellt. Auf diese Weise kann aus der Wissenschaft von heute tatsächlich die Technik von morgen werden.

LITERATURVERZEICHNIS

Acker, H., Carlsson, J., Mueller-Klieser, W., & Sutherland, R. M. (1987). Comparative pO_2 measurements in cell spheroids cultured with different techniques. *Br. J. Cancer*, *56*(3), 325-327. doi:10.1038/bjc.1987.197

Adamopoulos, K., Koutsouris, D., Zaravinos, A., & Lambrou, G. I. (2021). Gravitational Influence on Human Living Systems and the Evolution of Species on Earth. *Molecules*, *26*(9), 2784. doi:10.3390/molecules26092784

Afshinnekoo, E., Scott, R. T., MacKay, M. J., Pariset, E., Cekanaviciute, E., Barker, R., Gilroy, S., Hassane, D., Smith, S. M., Zwart, S. R., Nelman-Gonzalez, M., Crucian, B. E., Ponomarev, S. A., Orlov, O. I., Shiba, D., Muratani, M., Yamamoto, M., Richards, S. E., Vaishampayan, P. A. & Beheshti, A. (2020). Fundamental Biological Features of Spaceflight: Advancing the Field to Enable Deep-Space Exploration. *Cell*, *183*(5), 1162-1184. doi:10.1016/j.cell.2020.10.050

Aissiou, A. K., Jha, S., Dhunnoo, K., Ma, Z., Li, D. X., Ravin, R., Kunze, M., Wong, K., & Adesida, A. B. (2023). Transcriptomic response of bioengineered human cartilage to parabolic flight microgravity is sex-dependent. *npj Microgravity*, *9*(1), 5. doi:10.1038/s41526-023-00255-6

Akiyama, T., Horie, K., Hinoi, E., Hiraiwa, M., Kato, A., Maekawa, Y., Takahashi, A., & Furukawa, S. (2020). How does spaceflight affect the acquired immune system? *npj Microgravity*, *6*, 14. doi:10.1038/s41526-020-0104-1

Albrecht-Buehler, G. (1991). Possible mechanisms of indirect gravity sensing by cells. *ASGSB Bull*, *4*(2), 25-34.

Aleshcheva, G., Bauer, J., Hemmersbach, R., Slumstrup, L., Wehland, M., Infanger, M., & Grimm, D. (2016). Scaffold-free Tissue Formation Under Real and Simulated Microgravity Conditions. *Basic Clin. Pharmacol. Toxicol.*, *119*(S3), 26-33. doi:10.1111/bcpt.12561

Alisafaei, F., Jokhun, D. S., Shivashankar, G. V., & Shenoy, V. B. (2019). Regulation of nuclear architecture, mechanics, and nucleocytoplasmic shuttling of epigenetic factors by cell geometric constraints. *Proc. Natl. Acad. Sci. USA*, *116*(27), 13200-13209. doi:10.1073/pnas.1902035116

Aljarrah, K., Mhaidat, N. M., Al-Akhras, M. A. H., Aldaher, A. N., Albiss, B. A., Aledealat, K., & Alsheyab, F. M. (2012). Magnetic nanoparticles sensitize MCF-7 breast cancer cells to doxorubicin-induced apoptosis. *World J. Surg. Oncol.*, *10*(1), 62. doi:10.1186/1477-7819-10-62

Alon, D. M., Mittelman, K., Stibbe, E., Countryman, S., Stodieck, L., Doraisingam, S., Leal Martin, D. M., Hamo, E. R., Pines, G., & Burstein, D. (2023). CRISPR-based genetic diagnostics in microgravity. *Biosens. Bioelectron.*, *237*, 115479. doi:10.1016/j.bios.2023.115479

Arun, R. P., Sivanesan, D., Patra, B., Varadaraj, S., & Verma, R. S. (2019). Simulated microgravity increases polyploid giant cancer cells and nuclear localization of YAP. *Sci. Rep.*, *9*(1), 10684. doi:10.1038/s41598-019-47116-5

Augustin, H. G., & Koh, G. Y. (2024). A systems view of the vascular endothelium in health and disease. *Cell*, *187*(18), 4833-4858. doi:10.1016/j.cell.2024.07.012

Ballerini, A., Chua, C. Y. X., Rhudy, J., Susnjar, A., Di Trani, N., Jain, P. R., Laue, G., Lubicka, D., Shirazi-Fard, Y., Ferrari, M., Stodieck, L. S., Cadena, S. M., & Grattoni, A. (2020). Counteracting Muscle Atrophy on Earth and in Space via Nanofluidics Delivery of Formoterol. *Adv. Therap.*, *3*(7), 2000014. doi:10.1002/adtp.202000014

Baran, R., Marchal, S., Garcia Campos, S., Rehnberg, E., Tabury, K., Baselet, B., Wehland, M., Grimm, D., & Baatout, S. (2021). The Cardiovascular System in Space: Focus on In Vivo and In Vitro Studies. *Biomedicines*, *10*(1). doi:10.3390/biomedicines10010059

Basson, M. D., Zeng, B., Downey, C., Sirivelu, M. P., & Tepe, J. J. (2015). Increased extracellular pressure stimulates tumor proliferation by a mechanosensitive calcium channel and PKC-β. *Mol. Oncol.*, *9*(2), 513-526. doi:10.1016/j.molonc.2014.10.008

Becker, J. L., & Souza, G. R. (2013). Using space-based investigations to inform cancer research on Earth. *Nat. Rev. Cancer*, *13*(5), 315-327. doi:10.1038/nrc3507

Benavides Damm, T., Walther, I., Wüest, S. L., Sekler, J., & Egli, M. (2014). Cell cultivation under different gravitational loads using a novel random positioning incubator. *Biotechnol. Bioeng.*, *111*(6), 1180-1190. doi:10.1002/bit.25179

Bergouignan, A., Stein, T. P., Habold, C., Coxam, V., O' Gorman, D., & Blanc, S. (2016). Towards human exploration of space: The THESEUS review series on nutrition and metabolism research priorities. *npj Microgravity*, *2*(1), 16029. doi:10.1038/npjmgrav.2016.29

Bertotti, A., & Trusolino, L. (2013). From bench to bedside: does preclinical practice in translational oncology need some rebuilding? *J. Natl. Cancer. Inst.*, *105*(19), 1426-1427. doi:10.1093/jnci/djt253

Beysens, D. A., & van Loon, J. J. W. A. (2015). *Generation and Applications of Extra-Terrestrial Environments on Earth* (D. A. Beysens & J. J. W. A. van Loon, Eds. 1st Edition ed.). River Publishers. doi:10.1201/9781003338277

Bonetto, V., Pagano, C. A., Sabbatini, M., Magnelli, V., Donadelli, M., Marengo, E., & Masini, M. A. (2024). Microgravity as a Tool to Investigate Cancer Induction in Pleura Mesothelial Cells. *Curr. Issues Mol. Biol.*, *46*(10), 10896-10912.

Bradbury, P., Wu, H., Choi, J. U., Rowan, A. E., Zhang, H., Poole, K., Lauko, J., & Chou, J. (2020). Modeling the Impact of Microgravity at the Cellular Level: Implications for Human Disease [Mini Review]. *Front. Cell Dev. Biol.*, *8*. doi:10.3389/fcell.2020.00096

Bredel-Geissler, A., Karbach, U., Walenta, S., Vollrath, L., & Mueller-Klieser, W. (1992). Proliferation-associated oxygen consumption and morphology of tumor cells in monolayer and spheroid culture. *J. Cell Physiol.*, *153*(1), 44-52. doi:10.1002/jcp.1041530108

Breen, E. C. (2000). Mechanical strain increases type I collagen expression in pulmonary fibroblasts in vitro. *J. Appl. Physiol. (1985)*, *88*(1), 203-209. doi:10.1152/jappl.2000.88.1.203

Bremen University. The Bremen Drop tower. Online verfügbar: https://www.zarm.uni-bremen.de/de/fallturm/allgemeine-informationen.html (aufgerufen am 01.11.2024)

Breslin, S., & O'Driscoll, L. (2013). Three-dimensional cell culture: the missing link in drug discovery. *Drug Discov. Today*, *18*(5), 240-249. doi:10.1016/j.drudis.2012.10.003

Briegleb, W. (1992). Some qualitative and quantitative aspects of the fast-rotating clinostat as a research tool. *ASGSB Bull.*, *5*(2), 23-30.

Brungs, S., Egli, M., Wuest, S. L., M. Christianen, P. C., W. A. van Loon, J. J., Ngo Anh, T. J., & Hemmersbach, R. (2016). Facilities for Simulation of Microgravity in the ESA Ground-Based Facility Programme. *Microgravity Sci. Technol.*, *28*(3), 191-203. doi:10.1007/s12217-015-9471-8

Carlsson, J., & Acker, H. (1988). Relations between pH, oxygen partial pressure and growth in cultured cell spheroids. *Int. J. Cancer*, *42*(5), 715-720. doi:10.1002/ijc.2910420515

Castillo, M. (2012). Imaging in space exploration. *AJNR Am. J. Neuroradiol.*, *33*(2), 201-202. doi:10.3174/ajnr.A2795

Chancellor, J. C., Scott, G. B., & Sutton, J. P. (2014). Space Radiation: The Number One Risk to Astronaut Health beyond Low Earth Orbit. *Life (Basel)*, *4*(3), 491-510. doi:10.3390/life4030491

Chen, X., Guo, J., Yuan, Y., Sun, Z., Chen, B., Tong, X., Zhang, L., Shen, C., & Zou, J. (2017). Cyclic compression stimulates osteoblast differentiation via activation of the Wnt/β-catenin signaling pathway. *Mol. Med. Rep.*, *15*(5), 2890-2896. doi:10.3892/mmr.2017.6327

C**heng, H.-W., Chen, Y.-F., Wong, J.-M., Weng, C.-W., Chen, H.-Y., Yu, S.-L., Chen, H.-W., Yuan, A., & Chen, J. J. W.** (2017). Cancer cells increase endothelial cell tube formation and survival by activating the PI3K/Akt signalling pathway. *J. Exp. Clin. Cancer Res.*, *36*(1), 27. doi:10.1186/s13046-017-0495-3

Cho, S., Irianto, J., & Discher, D. E. (2017). Mechanosensing by the nucleus: From pathways to scaling relationships. *J. Cell Biol.*, *216*(2), 305-315. doi:10.1083/jcb.201610042

Choi, D. H., Jeon, B., Lim, M. H., Lee, D. H., Ye, S.-K., Jeong, S.-Y., & Kim, S. (2021). 3D cell culture using a clinostat reproduces microgravity-induced skin changes. *npj Microgravity*, *7*(1), 20. doi:10.1038/s41526-021-00148-6

Cialdai, F., Vignali, L., Morbidelli, L., Colciago, A., Celotti, F., Santi, A., Caselli, A., Cirri, P., & Monici, M. (2017). Modeled Microgravity Affects Fibroblast Functions Related to Wound Healing. *Microgravity Sci. Technol.*, *29*(1), 121-132. doi:10.1007/s12217-016-9532-7

Cicha, I., Goppelt-Struebe, M., Muehlich, S., Yilmaz, A., Raaz, D., Daniel, W. G., & Garlichs, C. D. (2008). Pharmacological inhibition of RhoA signaling prevents connective tissue growth factor induction in endothelial cells exposed to non-uniform shear stress. *Atherosclerosis*, *196*(1), 136-145. doi:10.1016/j.atherosclerosis.2007.03.016

Corydon, T. J., Kopp, S., Wehland, M., Braun, M., Schütte, A., Mayer, T., Hülsing, T., Oltmann, H., Schmitz, B., Hemmersbach, R., & Grimm, D. (2016). Alterations of the cytoskeleton in human cells in space proved by life-cell imaging. *Sci. Rep.*, *6*, 20043. doi:10.1038/srep20043

Corydon, T. J., Schulz, H., Richter, P., Strauch, S. M., Böhmer, M., Ricciardi, D. A., Wehland, M., Krüger, M., Erzinger, G. S., Lebert, M., Infanger, M., Wise, P. M., & Grimm, D. (2023). Current Knowledge about the Impact of Microgravity on Gene Regulation. *Cells*, *12*(7). doi:10.3390/cells12071043

Costa, E. C., Moreira, A. F., de Melo-Diogo, D., Gaspar, V. M., Carvalho, M. P., & Correia, I. J. (2016). 3D tumor spheroids: an overview on the tools and techniques used for their analysis. *Biotechnol. Adv.*, *34*(8), 1427-1441. doi:10.1016/j.biotechadv.2016.11.002

Cox, C. D., Poole, K., & Martinac, B. (2024). Re-evaluating TRP channel mechanosensitivity. *Trends Biochem. Sci.*, *49*(8), 693-702. doi:10.1016/j.tibs.2024.05.004

Crucian, B. E., Choukèr, A., Simpson, R. J., Mehta, S., Marshall, G., Smith, S. M., Zwart, S. R., Heer, M., Ponomarev, S., Whitmire, A., Frippiat, J. P., Douglas, G. L., Lorenzi, H., Buchheim, J. I., Makedonas, G., Ginsburg, G. S., Ott, C. M., Pierson, D. L., Krieger, S. S., . . . Sams, C. (2018). Immune System Dysregulation During Spaceflight: Potential Countermeasures for Deep Space Exploration Missions. *Front. Immunol.*, *9*, 1437. doi:10.3389/fimmu.2018.01437

Cui, Y., Liu, W., Zhao, S., Zhao, Y., & Dai, J. (2023). Advances in Microgravity Directed Tissue Engineering. *Adv. Healthc. Mater.*, *12*(23), 2202768. doi:10.1002/adhm.202202768

Davis, R. T., Blake, K., Ma, D., Gabra, M. B. I., Hernandez, G. A., Phung, A. T., Yang, Y., Maurer, D., Lefebvre, A., Alshetaiwi, H., Xiao, Z., Liu, J., Locasale, J. W., Digman, M. A., Mjolsness, E., Kong, M., Werb, Z., & Lawson, D. A. (2020). Transcriptional diversity and bioenergetic shift in human breast cancer metastasis revealed by single-cell RNA sequencing. *Nat. Cell Biol.*, *22*(3), 310-320. doi:10.1038/s41556-020-0477-0

De Troyer, A., Estenne, M., Ninane, V., Van Gansbeke, D., & Gorini, M. (1990). Transversus abdominis muscle function in humans. *J. Appl. Physiol. (1985)*, *68*(3), 1010-1016. doi:10.1152/jappl.1990.68.3.1010

Delmas, P., Parpaite, T., & Coste, B. (2022). PIEZO channels and newcomers in the mammalian mechanosensitive ion channel family. *Neuron*, *110*(17), 2713-2727. doi:10.1016/j.neuron.2022.07.001

Démarteau, O., Wendt, D., Braccini, A., Jakob, M., Schäfer, D., Heberer, M., & Martin, I. (2003). Dynamic compression of cartilage constructs engineered from expanded human articular chondrocytes. *Biochem. Biophys. Res. Commun.*, *310*(2), 580-588. doi:10.1016/j.bbrc.2003.09.099

Dubinin, N. P., & Vaulina, E. N. (1976). The evolutionary role of gravity. *Life Sci. Space Res.*, *14*, 47-55.

Edgell, C. J., McDonald, C. C., & Graham, J. B. (1983). Permanent cell line expressing human factor VIII-related antigen established by hybridization. *Proc. Natl. Acad. Sci. USA*, *80*(12), 3734-3737. doi:10.1073/pnas.80.12.3734

Eschweiler, J., Horn, N., Rath, B., Betsch, M., Baroncini, A., Tingart, M., & Migliorini, F. (2021). The Biomechanics of Cartilage-An Overview. *Life (Basel)*, *11*(4). doi:10.3390/life11040302

Fan, C., Wu, Z., Cooper, D. M. L., Magnus, A., Harrison, K., Eames, B. F., Chibbar, R., Groot, G., Huang, J., Genth, H., Zhang, J., Tan, X., Deng, Y., & Xiang, J. (2022). Activation of Focal Adhesion Kinase Restores Simulated Microgravity-Induced Inhibition of Osteoblast Differentiation via Wnt/B-Catenin Pathway. *Int. J. Mol. Sci.*, *23*(10), 5593.

Fang, X.-Z., Zhou, T., Xu, J.-Q., Wang, Y.-X., Sun, M.-M., He, Y.-J., Pan, S.-W., Xiong, W., Peng, Z.-K., Gao, X.-H., & Shang, Y. (2021). Structure, kinetic properties and biological function of mechanosensitive Piezo channels. *Cell Biosci.*, *11*(1), 13. doi:10.1186/s13578-020-00522-z

Fares, J., Fares, M. Y., Khachfe, H. H., Salhab, H. A., & Fares, Y. (2020). Molecular principles of metastasis: a hallmark of cancer revisited. *Signal Transduct. Target. Ther.*, *5*(1), 28. doi:10.1038/s41392-020-0134-x

Farkas, Á., & Farkas, G. (2021). Effects of Spaceflight on Human Skin. *Skin Pharmacol. Physiol.*, *34*(5), 239-245. doi:10.1159/000515963

Fedeli, V., Cucina, A., Dinicola, S., Fabrizi, G., Catizone, A., Gesualdi, L., Ceccarelli, S., Harrath, A. H., Alwasel, S. H., Ricci, G., Pedata, P., Bizzarri, M., & Monti, N. (2022). Microgravity Modifies the Phenotype of Fibroblast and Promotes Remodeling of the Fibroblast-Keratinocyte Interaction in a 3D Co-Culture Model. *Int. J. Mol. Sci.*, *23*(4). doi:10.3390/ijms23042163

Fennema, E., Rivron, N., Rouwkema, J., van Blitterswijk, C., & de Boer, J. (2013). Spheroid culture as a tool for creating 3D complex tissues. *Trends Biotechnol.*, *31*(2), 108-115. doi:10.1016/j.tibtech.2012.12.003

Ferranti, F., Del Bianco, M., & Pacelli, C. (2021). Advantages and Limitations of Current Microgravity Platforms for Space Biology Research. *Appl. Sci.*, *11*(1), 68.

Flusberg, D. A., Numaguchi, Y., & Ingber, D. E. (2001). Cooperative control of Akt phosphorylation, bcl-2 expression, and apoptosis by cytoskeletal microfilaments and microtubules in capillary endothelial cells. *Mol. Biol. Cell*, *12*(10), 3087-3094. doi:10.1091/mbc.12.10.3087

Freyer, J. P., Fink, N. H., Schor, P. L., Coulter, J. R., Neeman, M., & Sillerud, L. O. (1990). A system for viably maintaining a stirred suspension of multicellular spheroids during NMR spectroscopy. *NMR Biomed.*, *3*(5), 195-205. doi:10.1002/nbm.1940030502

Freyer, J. P., Schor, P. L., Jarrett, K. A., Neeman, M., & Sillerud, L. O. (1991). Cellular energetics measured by phosphorous nuclear magnetic resonance spectroscopy are not correlated with chronic nutrient deficiency in multicellular tumor spheroids. *Cancer Res.*, *51*(15), 3831-3837.

Friedrich, J., Seidel, C., Ebner, R., & Kunz-Schughart, L. A. (2009). Spheroid-based drug screen: considerations and practical approach. *Nat. Protoc.*, *4*(3), 309-324. doi:10.1038/nprot.2008.226

Gao, H., Ayyaswamy, P. S., & Ducheyne, P. (1997). Dynamics of a microcarrier particle in the simulated microgravity environment of a rotating-wall vessel. *Microgravity Sci. Technol.*, *10*(3), 154-165.

Gencoglu, M. F., Barney, L. E., Hall, C. L., Brooks, E. A., Schwartz, A. D., Corbett, D. C., Stevens, K. R., & Peyton, S. R. (2018). Comparative Study of Multicellular Tumor Spheroid Formation Methods and Implications for Drug Screening. *ACS Biomater. Sci. Eng.*, *4*(2), 410-420. doi:10.1021/acsbiomaterials.7b00069

Goodman, M. B., Haswell, E. S., & Vásquez, V. (2023). Mechanosensitive membrane proteins: Usual and unusual suspects in mediating mechanotransduction. *J. Gen. Physiol.*, *155*(3). doi:10.1085/jgp.202213248

Goodman, T. T., Olive, P. L., & Pun, S. H. (2007). Increased nanoparticle penetration in collagenase-treated multicellular spheroids. *Int. J. Nanomed.*, *2*(2), 265-274.

Granato, G., Ruocco, M. R., Iaccarino, A., Masone, S., Calì, G., Avagliano, A., Russo, V., Bellevicine, C., Di Spigna, G., Fiume, G., Montagnani, S., & Arcucci, A. (2017). Generation and analysis of spheroids from human primary skin myofibroblasts: an experimental system to study myofibroblasts deactivation. *Cell Death Discov.*, *3*(1), 17038. doi:10.1038/cddiscovery.2017.38

Grenon, S. M., Jeanne, M., Aguado-Zuniga, J., Conte, M. S., & Hughes-Fulford, M. (2013) Effects of gravitational mechanical unloading in endothelial cells: association between caveolins, inflammation and adhesion molecules. *Sci Rep. 3*,1494. doi:10.1038/srep01494

Grimm, D., Egli, M., Krüger, M., Riwaldt, S., Corydon, T. J., Kopp, S., Wehland, M., Wise, P., Infanger, M., Mann, V., & Sundaresan, A. (2018). Tissue Engineering Under Microgravity Conditions–Use of Stem Cells and Specialized Cells. *Stem Cells Dev.*, *27*(12), 787-804. doi:10.1089/scd.2017.0242

Grimm, D., Infanger, M., Westphal, K., Ulbrich, C., Pietsch, J., Kossmehl, P., Vadrucci, S., Baatout, S., Flick, B., Paul, M., & Bauer, J. (2009). A Delayed Type of Three-Dimensional Growth of Human Endothelial Cells Under Simulated Weightlessness. *Tissue Eng. Part A*, *15*(8), 2267-2275. doi:10.1089/ten.tea.2008.0576

Grimm, D., Schulz, H., Krüger, M., Cortés-Sánchez, J. L., Egli, M., Kraus, A., Sahana, J., Corydon, T. J., Hemmersbach, R., Wise, P. M., Infanger, M., & Wehland, M. (2022). The Fight against Cancer by Microgravity: The Multicellular Spheroid as a Metastasis Model. *Int. J. Mol. Sci.*, *23*(6). doi:10.3390/ijms23063073

Grimm, D., Wehland, M., Pietsch, J., Aleshcheva, G., Wise, P., van Loon, J., Ulbrich, C., Magnusson, N. E., Infanger, M., & Bauer, J. (2014). Growing tissues in real and simulated microgravity: new methods for tissue engineering. *Tissue Eng. Part B Rev.*, *20*(6), 555-566. doi:10.1089/ten.TEB.2013.0704

Grosse, J., Wehland, M., Pietsch, J., Ma, X., Ulbrich, C., Schulz, H., Saar, K., Hübner, N., Hauslage, J., Hemmersbach, R., Braun, M., van Loon, J., Vagt, N., Infanger, M., Eilles, C., Egli, M., Richter, P., Baltz, T., Einspanier, R., . . . Grimm, D. (2012). Short-term weightlessness produced by parabolic flight maneuvers altered gene expression patterns in human endothelial cells. *Faseb J.*, *26*(2), 639-655. doi:10.1096/fj.11-194886

Guo, Z., Zhou, G., & Hu, W. (2022). Carcinogenesis induced by space radiation: A systematic review. *Neoplasia*, *32*, 100828. doi:10.1016/j.neo.2022.100828

Ha, P., Kwak, J. H., Zhang, Y., Shi, J., Tran, L., Liu, T. P., Pan, H. C., Lee, S., Kim, J. K., Chen, E., Shirazi-Fard, Y., Stodieck, L. S., Lin, A., Zheng, Z., Dong, S. N., Zhang, X., Wu, B. M., Ting, K., & Soo, C. (2023). Bisphosphonate conjugation enhances the bone-specificity of NELL-1-based systemic therapy for spaceflight-induced bone loss in mice. *npj Microgravity*, *9*(1), 75. doi:10.1038/s41526-023-00319-7

Hamm, P. B., Billica, R. D., Johnson, G. S., Wear, M. L., & Pool, S. L. (1998). Risk of cancer mortality among the Longitudinal Study of Astronaut Health (LSAH) participants. *Aviat. Space Environ. Med.*, *69*(2), 142-144.

Hammond, T., & Allen, P. (2011). The Bonn Criteria: Minimal Experimental Parameter Reporting for Clinostat and Random Positioning Machine Experiments with Cells and Tissues. *Microgravity Sci. Technol.*, *23*(2), 271-275. doi:10.1007/s12217-010-9226-5

Hammond, T. G., Benes, E., O'Reilly, K. C., Wolf, D. A., Linnehan, R. M., Taher, A., Kaysen, J. H., Allen, P. L., & Goodwin, T. J. (2000). Mechanical culture conditions effect gene expression: gravity-induced changes on the space shuttle. *Physiol. Genomics*, *3*(3), 163-173. doi:10.1152/physiolgenomics.2000.3.3.163

Hammond, T. G., & Hammond, J. M. (2001). Optimized suspension culture: the rotating-wall vessel. *Am. J. Physiol. Renal Physiol.*, *281*(1), F12-25. doi:10.1152/ajprenal.2001.281.1.F12

Hauslage, J., Cevik, V., & Hemmersbach, R. (2017). Pyrocystis noctiluca represents an excellent bioassay for shear forces induced in ground-based microgravity simulators (clinostat and random positioning machine). *npj Microgravity*, *3*(1), 12. doi:10.1038/s41526-017-0016-x

Hayashi, R., Hanyu, N., & Moriyama, S. (1994). Efficacy of steroid therapy on liver metastasis of thymic carcinoid. *Intern. Med.*, *33*(1), 45-47. doi:10.2169/internalmedicine.33.45

Hemmersbach, R., Simon, A., Waßer, K., Hauslage, J., Christianen, P. C., Albers, P. W., Lebert, M., Richter, P., Alt, W., & Anken, R. (2014). Impact of a high magnetic field on the orientation of gravitactic unicellular organisms--a critical consideration about the application of magnetic fields to mimic functional weightlessness. *Astrobiology*, *14*(3), 205-215. doi:10.1089/ast.2013.1085

Hemmersbach, R., von der Wiesche, M., & Seibt, D. (2006). Ground-based experimental platforms in gravitational biology and human physiology. *Signal Transduct.*, *6*(6), 381-387. doi:10.1002/sita.200600105

Herranz, R., Anken, R., Boonstra, J., Braun, M., Christianen, P. C., de Geest, M., Hauslage, J., Hilbig, R., Hill, R. J., Lebert, M., Medina, F. J., Vagt, N., Ullrich, O., van Loon, J. J., & Hemmersbach, R. (2013). Ground-based facilities for simulation of microgravity: organism-

specific recommendations for their use, and recommended terminology. *Astrobiology*, *13*(1), 1-17. doi:10.1089/ast.2012.0876

Hickman, J. A., Graeser, R., de Hoogt, R., Vidic, S., Brito, C., Gutekunst, M., & van der Kuip, H. (2014). Three-dimensional models of cancer for pharmacology and cancer cell biology: capturing tumor complexity in vitro/ex vivo. *Biotechnol. J.*, *9*(9), 1115-1128. doi:10.1002/biot.201300492

Hicks, J., Olson, M., Mitchell, C., Juran, C. M., & Paul, A. M. (2023). The Impact of Microgravity on Immunological States. *Immunohorizons*, *7*(10), 670-682. doi:10.4049/immunohorizons.2200063

Hirschhaeuser, F., Menne, H., Dittfeld, C., West, J., Mueller-Klieser, W., & Kunz-Schughart, L. A. (2010). Multicellular tumor spheroids: an underestimated tool is catching up again. *J. Biotechnol.*, *148*(1), 3-15. doi:10.1016/j.jbiotec.2010.01.012

Hong, S., Ergezen, E., Lec, R., & Barbee, K. A. (2006). Real-time analysis of cell–surface adhesive interactions using thickness shear mode resonator. *Biomaterials*, *27*(34), 5813-5820. doi:10.1016/j.biomaterials.2006.07.031

Horm, T. M., & Schroeder, J. A. (2013). MUC1 and metastatic cancer. *Cell Adh. Migr.*, *7*(2), 187-198. doi:10.4161/cam.23131

Huang, Q., Hu, X., He, W., Zhao, Y., Hao, S., Wu, Q., Li, S., Zhang, S., & Shi, M. (2018). Fluid shear stress and tumor metastasis. *Am. J. Cancer Res.*, *8*(5), 763-777.

Hudspeth, A. J., & Corey, D. P. (1977). Sensitivity, polarity, and conductance change in the response of vertebrate hair cells to controlled mechanical stimuli. *Proc. Natl. Acad. Sci. USA*, *74*(6), 2407-2411. doi:10.1073/pnas.74.6.2407

Hughes-Fulford, M. (2003). Function of the cytoskeleton in gravisensing during spaceflight. *Adv. Space Res.*, *32*(8), 1585-1593. doi:10.1016/s0273-1177(03)90399-1

Humphrey, J. D., Dufresne, E. R., & Schwartz, M. A. (2014). Mechanotransduction and extracellular matrix homeostasis. *Nat. Rev. Mol. Cell Biol.*, *15*(12), 802-812. doi:10.1038/nrm3896

Infanger, M., Kossmehl, P., Shakibaei, M., Baatout, S., Witzing, A., Grosse, J., Bauer, J., Cogoli, A., Faramarzi, S., Derradji, H., Neefs, M., Paul, M., & Grimm, D. (2006). Induction of three-dimensional assembly and increase in apoptosis of human endothelial cells by simulated microgravity: Impact of vascular endothelial growth factor. *Apoptosis*, *11*(5), 749-764. doi:10.1007/s10495-006-5697-7

Ingber, D. (1999). How cells (might) sense microgravity. *Faseb J.*, *13*(9001), S3-S15. doi:10.1096/fasebj.13.9001.s3

Ishihara, S., & Haga, H. (2022). Matrix Stiffness Contributes to Cancer Progression by Regulating Transcription Factors. *Cancers*, *14*(4), 1049.

Jackson, K., Hoff, R., Wright, H., Wilkinson, A., Brewer, F., Williams, A., Whiteside, B., Macbeth, M. R., & Wilson, A. M. (2024). An Analysis of Protein Crystals Grown under Microgravity Conditions. *Crystals*, *14*(7), 652.

Jing, X., Liang, H., Hao, C., Yang, X., & Cui, X. (2019). Overexpression of MUC1 predicts poor prognosis in patients with breast cancer. *Oncol. Rep.*, *41*(2), 801-810. doi:10.3892/or.2018.6887

Jokšienė, J., Sahana, J., Wehland, M., Schulz, H., Cortés-Sánchez, J. L., Prat-Duran, J., Grimm, D., & Simonsen, U. (2023). Effects of High Glucose on Human Endothelial Cells Exposed to Simulated Microgravity. *Biomolecules*, *13*(2). doi:10.3390/biom13020189

Jost, P. D., Binot, R. A., & Schmitt, D. A. (2005). ESA ground based facilities. ESA Special Publication, Cologne, Germany.

Jubelin, C., Muñoz-Garcia, J., Griscom, L., Cochonneau, D., Ollivier, E., Heymann, M.-F., Vallette, F. M., Oliver, L., & Heymann, D. (2022). Three-dimensional in vitro culture models in oncology research. *Cell Biosci.*, *12*(1), 155. doi:10.1186/s13578-022-00887-3

Juhl, O. J., Buettmann, E. G., Friedman, M. A., DeNapoli, R. C., Hoppock, G. A., & Donahue, H. J. (2021). Update on the effects of microgravity on the musculoskeletal system. *npj Microgravity*, *7*(1), 28. doi:10.1038/s41526-021-00158-4

Kalli, M., Papageorgis, P., Gkretsi, V., & Stylianopoulos, T. (2018). Solid Stress Facilitates Fibroblasts Activation to Promote Pancreatic Cancer Cell Migration. *Ann. Biomed. Eng.*, *46*(5), 657-669. doi:10.1007/s10439-018-1997-7

Kalluri, R., & LeBleu, V. S. (2020). The biology, function, and biomedical applications of exosomes. *Science*, *367*(6478). doi:10.1126/science.aau6977

Kamal, K. Y., Herranz, R., van Loon, J. J. W. A., Christianen, P. C. M., & Medina, F. J. (2016). Evaluation of Simulated Microgravity Environments Induced by Diamagnetic Levitation of Plant Cell Suspension Cultures. *Microgravity Sci. Technol.*, *28*(3), 309-317. doi:10.1007/s12217-015-9472-7

Kamb, A. (2005). What's wrong with our cancer models? *Nat. Rev. Drug Discov.*, *4*(2), 161-165. doi:10.1038/nrd1635

Khalili, A. A., & Ahmad, M. R. (2015). A Review of Cell Adhesion Studies for Biomedical and Biological Applications. *Int. J. Mol. Sci.*, *16*(8), 18149-18184. doi:10.3390/ijms160818149

Kim, K., & Guck, J. (2020). The Relative Densities of Cytoplasm and Nuclear Compartments Are Robust against Strong Perturbation. *Biophys. J.*, *119*(10), 1946-1957. doi:10.1016/j.bpj.2020.08.044

Kim, S., Ayan, B., Shayan, M., Rando, T. A., & Huang, N. F. (2024). Skeletal muscle-on-a-chip in microgravity as a platform for regeneration modeling and drug screening. *Stem Cell Rep.*, *19*(8), 1061-1073. doi:10.1016/j.stemcr.2024.06.010

Kirby, T. J., & Lammerding, J. (2018). Emerging views of the nucleus as a cellular mechanosensor. *Nat. Cell Biol.*, *20*(4), 373-381. doi:10.1038/s41556-018-0038-y

Klaus, D. M. (2001). Clinostats and bioreactors. *Gravit. Space Biol. Bull.*, *14*(2), 55-64.

Kohn, F. P. M., & Hauslage, J. (2019). The gravity dependence of pharmacodynamics: the integration of lidocaine into membranes in microgravity. *npj Microgravity*, *5*(1), 5. doi:10.1038/s41526-019-0064-5

Kondo, M., Yamaoka, K., Sakata, K., Sonomoto, K., Lin, L., Nakano, K., & Tanaka, Y. (2015). Contribution of the Interleukin-6/STAT-3 Signaling Pathway to Chondrogenic Differentiation of Human Mesenchymal Stem Cells. *Arthritis Rheumatol.*, *67*(5), 1250-1260. doi:10.1002/art.39036

Kopp, S., Sahana, J., Islam, T., Petersen, A. G., Bauer, J., Corydon, T. J., Schulz, H., Saar, K., Huebner, N., Slumstrup, L., Riwaldt, S., Wehland, M., Infanger, M., Luetzenberg, R., & Grimm, D. (2018). The role of NFκB in spheroid formation of human breast cancer cells cultured on the Random Positioning Machine. *Sci. Rep.*, *8*(1), 921. doi:10.1038/s41598-017-18556-8

Kopp, S., Warnke, E., Wehland, M., Aleshcheva, G., Magnusson, N. E., Hemmersbach, R., Corydon, T. J., Bauer, J., Infanger, M., & Grimm, D. (2015). Mechanisms of three-dimensional

growth of thyroid cells during long-term simulated microgravity. *Sci. Rep.*, *5*, 16691. doi:10.1038/srep16691

Kouroupis, D., & Correa, D. (2021). Increased Mesenchymal Stem Cell Functionalization in Three-Dimensional Manufacturing Settings for Enhanced Therapeutic Applications [Review]. *Frontiers in Bioeng. Biotechnol.*, *9*. doi:10.3389/fbioe.2021.621748

Kumar, P., Ji, J., Thirkill, T. L., & Douglas, G. C. (2014). MUC1 Is Expressed by Human Skin Fibroblasts and Plays a Role in Cell Adhesion and Migration. *Biores. Open Access*, *3*(2), 45-52. doi:10.1089/biores.2013.0045

LaBarbera, D. V., Reid, B. G., & Yoo, B. H. (2012). The multicellular tumor spheroid model for high-throughput cancer drug discovery. *Expert Opin. Drug Discov.*, *7*(9), 819-830. doi:10.1517/17460441.2012.708334

Lambrecht, G., Petersen, N., Weerts, G., Pruett, C., Evetts, S., Stokes, M., & Hides, J. (2017). The role of physiotherapy in the European Space Agency strategy for preparation and reconditioning of astronauts before and after long duration space flight. *Musculoskelet. Sci. Pract.*, *27*, S15-S22. doi:10.1016/j.math.2016.10.009

Lan, Y., Ni, W., & Tai, G. (2022). Expression of MUC1 in different tumours and its clinical significance (Review). *Mol. Clin. Oncol.*, *17*(6), 161. doi:10.3892/mco.2022.2594

Läubli, H., & Borsig, L. (2010). Selectins promote tumor metastasis. *Semin. Cancer Biol.*, *20*(3), 169-177. doi:10.1016/j.semcancer.2010.04.005

Le Bellego, F., Perera, H., Plante, S., Chakir, J., Hamid, Q., & Ludwig, M. S. (2009). Mechanical strain increases cytokine and chemokine production in bronchial fibroblasts from asthmatic patients. *Allergy*, *64*(1), 32-39. doi:10.1111/j.1398-9995.2008.01814.x

Leckband, D. E., & de Rooij, J. (2014). Cadherin Adhesion and Mechanotransduction. *Annu. Rev. Cell Dev. Biol.*, *30*(Volume 30, 2014), 291-315. doi:10.1146/annurev-cellbio-100913-013212

Lee, S.-J., Lehar, A., Meir, J. U., Koch, C., Morgan, A., Warren, L. E., Rydzik, R., Youngstrom, D. W., Chandok, H., George, J., Gogain, J., Michaud, M., Stoklasek, T. A., Liu, Y., & Germain-Lee, E. L. (2020). Targeting myostatin/activin A protects against skeletal muscle and bone loss during spaceflight. *Proc. Natl. Acad. Sci. USA*, *117*(38), 23942-23951. doi:10.1073/pnas.2014716117

Lee, S. J., Lehar, A., Meir, J. U., Koch, C., Morgan, A., Warren, L. E., Rydzik, R., Youngstrom, D. W., Chandok, H., George, J., Gogain, J., Michaud, M., Stoklasek, T. A., Liu, Y., & Germain-Lee, E. L. (2020). Targeting myostatin/activin A protects against skeletal muscle and bone loss during spaceflight. *Proc. Natl. Acad. Sci. USA*, *117*(38), 23942-23951. doi:10.1073/pnas.2014716117

Lefebvre, V., & Dvir-Ginzberg, M. (2017). SOX9 and the many facets of its regulation in the chondrocyte lineage. *Connect. Tissue Res.*, *58*(1), 2-14. doi:10.1080/03008207.2016.1183667

Leguy, C. A. D., Delfos, R., Pourquie, M. J. B. M., Poelma, C., Westerweel, J., & van Loon, J. J. W. A. (2017). Fluid dynamics during Random Positioning Machine micro-gravity experiments. *Adv.Space Res.*, *59*(12), 3045-3057. doi:10.1016/j.asr.2017.03.009

Lei, X., Liu, B., Wu, H., Wu, X., Wang, X. L., Song, Y., Zhang, S. S., Li, J. Q., Bi, L., & Pei, G. X. (2020). The effect of fluid shear stress on fibroblasts and stem cells on plane and groove topographies. *Cell Adh. Migr.*, *14*(1), 12-23. doi:10.1080/19336918.2020.1713532

Li, F., Ye, Y., Lei, X., & Zhang, W. (2021). Effects of Microgravity on Early Embryonic Development and Embryonic Stem Cell Differentiation: Phenotypic Characterization and Potential Mechanisms. *Front. Cell Dev. Biol.*, *9*, 797167. doi:10.3389/fcell.2021.797167

Li, J., Zhang, S., Chen, J., Du, T., Wang, Y., & Wang, Z. (2009). Modeled microgravity causes changes in the cytoskeleton and focal adhesions, and decreases in migration in malignant human MCF-7 cells. *Protoplasma*, *238*(1-4), 23-33. doi:10.1007/s00709-009-0068-1

Li, W., Shu, X., Zhang, X., Zhang, Z., Sun, S., Li, N., & Long, M. (2023). Potential Roles of YAP/TAZ Mechanotransduction in Spaceflight-Induced Liver Dysfunction. *Int. J. Mol. Sci.*, *24*(3). doi:10.3390/ijms24032197

Li, Y., & Burridge, K. (2019). Cell-Cycle-Dependent Regulation of Cell Adhesions: Adhering to the Schedule. *BioEssays*, *41*(1), 1800165. doi:10.1002/bies.201800165

Lin, R. Z., & Chang, H. Y. (2008). Recent advances in three-dimensional multicellular spheroid culture for biomedical research. *Biotechnol. J.*, *3*(9-10), 1172-1184. doi:10.1002/biot.200700228

Lin, X., Zhang, K., Wei, D., Tian, Y., Gao, Y., Chen, Z., & Qian, A. (2020). The Impact of Spaceflight and Simulated Microgravity on Cell Adhesion. *Int. J. Mol. Sci.*, *21*(9). doi:10.3390/ijms21093031

Liu, T., Li, X., Sun, X., Ma, X., & Cui, Z. (2004). Analysis on forces and movement of cultivated particles in a rotating wall vessel bioreactor. *Biochem. Eng. J.*, *18*(2), 97-104. doi:10.1016/S1369-703X(03)00171-2

Low, B. C., Pan, C. Q., Shivashankar, G. V., Bershadsky, A., Sudol, M., & Sheetz, M. (2014). YAP/TAZ as mechanosensors and mechanotransducers in regulating organ size and tumor growth. *FEBS Lett.*, *588*(16), 2663-2670. doi:10.1016/j.febslet.2014.04.012

Ludwig, M. S., Ftouhi-Paquin, N., Huang, W., Pagé, N., Chakir, J., & Hamid, Q. (2004). Mechanical strain enhances proteoglycan message in fibroblasts from asthmatic subjects. *Clin. Exp. Allergy*, *34*(6), 926-930. doi:10.1111/j.1365-2222.2004.01980.x

Luo, W., Xiong, W., Qiu, M., Lv, Y., Li, Y., & Li, F. (2011). Differentiation of mesenchymal stem cells towards a nucleus pulposus-like phenotype utilizing simulated microgravity In vitro. *J. Huazhong Univ. Sci. Technolog.*, *31*(2), 199-203. doi:0.1007/s11596-011-0252-3

Lv, D., Hu, Z., Lu, L., Lu, H., & Xu, X. (2017). Three-dimensional cell culture: A powerful tool in tumor research and drug discovery. *Oncol. Lett.*, *14*(6), 6999-7010. doi:10.3892/ol.2017.7134

Lv, W., Peng, X., Tu, Y., Shi, Y., Song, G., & Luo, Q. (2023). YAP Inhibition Alleviates Simulated Microgravity-Induced Mesenchymal Stem Cell Senescence via Targeting Mitochondrial Dysfunction. *Antioxidants*, *12*(5), 990.

Ma, B.-H., Cao, Y.-J., Zheng, W.-B., Lu, J.-R., Kuang, H.-b., Lei, X.-H., Lv, Y.-H., Zhang, T., & Duan, E.-K. (2008). Real-time micrography of mouse preimplantation embryos in an orbit module on SJ-8 satellite. *Microgravity Sci. Technol.*, *20*, 127-136.

Ma, X., Pietsch, J., Wehland, M., Schulz, H., Saar, K., Hübner, N., Bauer, J., Braun, M., Schwarzwälder, A., Segerer, J., Birlem, M., Horn, A., Hemmersbach, R., Waβer, K., Grosse, J., Infanger, M., & Grimm, D. (2014). Differential gene expression profile and altered cytokine secretion of thyroid cancer cells in space. *Faseb J.*, *28*(2), 813-835. doi:10.1096/fj.13-243287

Mader, T. H., Gibson, C. R., Pass, A. F., Kramer, L. A., Lee, A. G., Fogarty, J., Tarver, W. J., Dervay, J. P., Hamilton, D. R., Sargsyan, A., Phillips, J. L., Tran, D., Lipsky, W., Choi, J., Stern, C., Kuyumjian, R., & Polk, J. D. (2011). Optic disc edema, globe flattening, choroidal folds, and hyperopic shifts observed in astronauts after long-duration space flight. *Ophthalmology*, *118*(10), 2058-2069. doi:10.1016/j.ophtha.2011.06.021

Madhavan, M., Jaiswal, D., Karlberg, S., Duggan, A., Almarshad, H.A., Claffey, K. P. & Hoshino K. (2023) Electron microscopy imaging and mechanical characterization of T47D multicellular tumor spheroids–Older spheroids reduce interstitial space and become stiffer. *Plos One 18(5), e0286291*. doi:10.1371/journal.pone.0286291

Man, J., Graham, T., Squires-Donelly, G., & Laslett, A. L. (2022). The effects of microgravity on bone structure and function. *npj Microgravity*, *8*(1), 9. doi:10.1038/s41526-022-00194-8

Manuyakorn, W. (2014). Airway remodelling in asthma: role for mechanical forces. *Asia Pac. Allergy*, *4*(1), 19-24. doi:10.5415/apallergy.2014.4.1.19

Manuyakorn, W., Smart, D. E., Noto, A., Bucchieri, F., Haitchi, H. M., Holgate, S. T., Howarth, P. H., & Davies, D. E. (2016). Mechanical Strain Causes Adaptive Change in Bronchial Fibroblasts Enhancing Profibrotic and Inflammatory Responses. *Plos One*, *11*(4), e0153926. doi:10.1371/journal.pone.0153926

Marlovits, S., Tichy, B., Truppe, M., Gruber, D., & Schlegel, W. (2003). Collagen Expression in Tissue Engineered Cartilage of Aged Human Articular Chondrocytes in a Rotating Bioreactor. *Int. J. Artif. Organs*, *26*(4), 319-330. doi:10.1177/039139880302600407

Martin, T. A. (2014). The role of tight junctions in cancer metastasis. *Semin. Cell Dev. Biol.*, *36*, 224-231. doi:10.1016/j.semcdb.2014.09.008

Martin, T. A., & Jiang, W. G. (2009). Loss of tight junction barrier function and its role in cancer metastasis. *Biochim. Biophys. Acta - Biomembr.*, *1788*(4), 872-891. doi:10.1016/j.bbamem.2008.11.005

Matthäus, C., Langhorst, H., Schütz, L., Jüttner, R., & Rathjen, F. G. (2017). Cell-cell communication mediated by the CAR subgroup of immunoglobulin cell adhesion molecules in health and disease. *Mol. Cell. Neurosci.*, *81*, 32-40. doi:10.1016/j.mcn.2016.11.009

McKinley, S., Taylor, A., Peeples, C., Jacob, M., Khaparde, G., Walter, Y., & Ekpenyong, A. (2023). Simulated Microgravity-Induced Changes to Drug Response in Cancer Cells Quantified Using Fluorescence Morphometry. *Life*, *13*(8), 1683.

Meder, L., Orschel, C. I., Otto, C. J., Koker, M., Brägelmann, J., Ercanoglu, M. S., Dähling, S., Compes, A., Selenz, C., Nill, M., Dietlein, F., Florin, A., Eich, M.-L., Borchmann, S., Odenthal, M., Blazquez, R., Hilberg, F., Klein, F., Hallek, M., . . . Ullrich, R. T. (2024). Blocking the angiopoietin-2–dependent integrin β-1 signaling axis abrogates small cell lung cancer invasion and metastasis. *JCI Insight*, *9*(10). doi:10.1172/jci.insight.166402

Messerschmid, E., Bertrand, R., & Pohlemann, F. (1997). Mikrogravitation. In *Raumstationen: Systeme und Nutzung* (pp. 291-320). Springer Berlin Heidelberg. doi:10.1007/978-3-662-09676-5_8

Mills, C., Sanchez, A., & Scurr, J. (2016). Estimating the gravity induced three dimensional deformation of the breast. *J. Biomech.*, *49*(16), 4134-4137. doi:10.1016/j.jbiomech.2016.10.012

Moroni, L., Tabury, K., Stenuit, H., Grimm, D., Baatout, S., & Mironov, V. (2022). What can biofabrication do for space and what can space do for biofabrication? *Trends Biotechnol.*, *40*(4), 398-411. doi:10.1016/j.tibtech.2021.08.008

Muid, S., Froemming, G. R., Ali, A. M., & Nawawi, H. (2013). Interleukin-6 and intercellular cell adhesion molecule-1 expression remains elevated in revived live endothelial cells following spaceflight. *Malays. J. Pathol.*, *35*(2), 165-176.

National Academies of Sciences, Education & Medicine. (2021). *Space Radiation and Astronaut Health: Managing and Communicating Cancer Risks*. The National Academies Press. doi:10.17226/26155

Neelam, S., Richardson, B., Barker, R., Udave, C., Gilroy, S., Cameron, M. J., Levine, H. G., & Zhang, Y. (2020). Changes in Nuclear Shape and Gene Expression in Response to Simulated Microgravity Are LINC Complex-Dependent. *Int. J. Mol. Sci.*, *21*(18), 6762.

Nishimura, Y. (2023). Technology using simulated microgravity. *Regen. Ther.*, *24*, 318-323. doi:10.1016/j.reth.2023.08.001

Nordberg, R. C., Mellor, L. F., Krause, A. R., Donahue, H. J., & Loboa, E. G. (2019). LRP receptors in chondrocytes are modulated by simulated microgravity and cyclic hydrostatic pressure. *Plos One*, *14*(10), e0223245. doi:10.1371/journal.pone.0223245

Omland, H., & Fosså, S. D. (1989). Spontaneous regression of cerebral and pulmonary metastases in renal cell carcinoma. *Scand. J. Urol. Nephrol.*, *23*(2), 159-160. doi:10.3109/00365598909180834

Parafati, M., Giza, S., Shenoy, T. S., Mojica-Santiago, J. A., Hopf, M., Malany, L. K., Platt, D., Moore, I., Jacobs, Z. A., Kuehl, P., Rexroat, J., Barnett, G., Schmidt, C. E., McLamb, W. T., Clements, T., Coen, P. M., & Malany, S. (2023). Human skeletal muscle tissue chip autonomous payload reveals changes in fiber type and metabolic gene expression due to spaceflight. *npj Microgravity*, *9*(1), 77. doi:10.1038/s41526-023-00322-y

Pennacchio, F. A., Nastały, P., Poli, A., & Maiuri, P. (2021). Tailoring Cellular Function: The Contribution of the Nucleus in Mechanotransduction [Mini Review]. *Front. Bioeng. Biotechnol.*, *8*. doi:10.3389/fbioe.2020.596746

Philp, D., Chen, S. S., Fitzgerald, W., Orenstein, J., Margolis, L., & Kleinman, H. K. (2005). Complex Extracellular Matrices Promote Tissue-Specific Stem Cell Differentiation. *Stem Cells*, *23*(2), 288-296. doi:10.1634/stemcells.2002-0109

Pietsch, J., Gass, S., Nebuloni, S., Echegoyen, D., Riwaldt, S., Baake, C., Bauer, J., Corydon, T. J., Egli, M., Infanger, M., & Grimm, D. (2017). Three-dimensional growth of human endothelial cells in an automated cell culture experiment container during the SpaceX CRS-8 ISS space mission – The SPHEROIDS project. *Biomaterials*, *124*, 126-156. doi:10.1016/j.biomaterials.2017.02.005

Porowska, H., Paszkiewicz-Gadek, A., Wosek, J., Wnuczko, K., Rusak, M., & Szczepański, M. (2010). Expression of MUC1 mucin in human umbilical vein endothelial cells (HUVEC). *Folia Histochem. Cytobiol.*, *48*(3), 417-424. doi:10.2478/v10042-010-0027-x

Prasanth, D., Suresh, S., Prathivadhi-Bhayankaram, S., Mimlitz, M., Zetocha, N., Lee, B., & Ekpenyong, A. (2020). Microgravity Modulates Effects of Chemotherapeutic Drugs on Cancer Cell Migration. *Life (Basel)*, *10*(9). doi:10.3390/life10090162

Radstake, W. E., Gautam, K., Miranda, S., Van Rompay, C., Vermeesen, R., Tabury, K., Verslegers, M., Dowson, A., Gorissen, J., van Loon, J., Savage, N. D. L., Baatout, S., & Baselet, B. (2023). Gravitational effects on fibroblasts' function in relation to wound healing. *npj Microgravity*, *9*(1), 48. doi:10.1038/s41526-023-00286-z

Ranieri, D., Proietti, S., Dinicola, S., Masiello, M. G., Rosato, B., Ricci, G., Cucina, A., Catizone, A., Bizzarri, M., & Torrisi, M. R. (2017). Simulated microgravity triggers epithelial mesenchymal transition in human keratinocytes. *Sci. Rep.*, *7*(1), 538. doi:10.1038/s41598-017-00602-0

Rath, B., Nam, J., Knobloch, T. J., Lannutti, J. J., & Agarwal, S. (2008). Compressive forces induce osteogenic gene expression in calvarial osteoblasts. *J. Biomech.*, *41*(5), 1095-1103. doi:10.1016/j.jbiomech.2007.11.024

Riwaldt, S., Bauer, J., Pietsch, J., Braun, M., Segerer, J., Schwarzwälder, A., Corydon, T. J., Infanger, M., & Grimm, D. (2015). The Importance of Caveolin-1 as Key-Regulator of Three-Dimensional Growth in Thyroid Cancer Cells Cultured under Real and Simulated Microgravity Conditions. *Int. J. Mol. Sci.*, *16*(12), 28296-28310. doi:10.3390/ijms161226108

Riwaldt, S., Pietsch, J., Sickmann, A., Bauer, J., Braun, M., Segerer, J., Schwarzwälder, A., Aleshcheva, G., Corydon, T. J., Infanger, M., & Grimm, D. (2015). Identification of proteins involved in inhibition of spheroid formation under microgravity. *Proteomics*, *15*(17), 2945-2952. doi:10.1002/pmic.201500067

Ruyters, G., & Friedrich, U. (2006). From the Bremen Drop Tower to the international space station ISS – Ways to weightlessness in the German space life sciences program. *Signal Transduct.*, *6*(6), 397-405. doi:10.1002/sita.200600108

Sabbatini, M., Bonetto, V., Magnelli, V., Lorusso, C., Dondero, F., & Masini, M. A. (2023). Microgravity as an Anti-Metastatic Agent in an In Vitro Glioma Model. *Biophysica*, *3*(4), 636-650.

Sahana, J., Cortés-Sánchez, J. L., Sandt, V., Melnik, D., Corydon, T. J., Schulz, H., Cai, Z., Evert, K., Grimm, D., & Wehland, M. (2023). Long-Term Simulation of Microgravity Induces Changes in Gene Expression in Breast Cancer Cells. *Int. J. Mol. Sci.*, *24*(2). doi:10.3390/ijms24021181

Salmenperä, P., Karhemo, P. R., Räsänen, K., Laakkonen, P., & Vaheri, A. (2016). Fibroblast spheroids as a model to study sustained fibroblast quiescence and their crosstalk with tumor cells. *Exp. Cell Res.*, *345*(1), 17-24. doi:10.1016/j.yexcr.2016.05.005

Salvador, E., Burek, M., & Förster, C. Y. (2016). Tight Junctions and the Tumor Microenvironment. *Curr. Pathobiol. Rep.*, *4*, 135-145. doi:10.1007/s40139-016-0106-6

Sanavandi, H., & Guo, W. (2021). A magnetic levitation based low-gravity simulator with an unprecedented large functional volume. *npj Microgravity*, *7*(1), 40. doi:10.1038/s41526-021-00174-4

Sarabi, M. R., Yetisen, A. K., & Tasoglu, S. (2022). Magnetic levitation for space exploration. *Trends Biotechnol.*, *40*(8), 915-917. doi:10.1016/j.tibtech.2022.03.010

Sarkar, S., Peng, C. C., & Tung, Y. C. (2020). Comparison of VEGF-A secretion from tumor cells under cellular stresses in conventional monolayer culture and microfluidic three-dimensional spheroid models. *Plos One*, *15*(11), e0240833. doi:10.1371/journal.pone.0240833

Schenker, E., & Forkheim, K. (1998). Mammalian mice embryo early development in weightlessness environment on STS 80 space flight. *Israel Aerospace Medicine Institute Report*, *5*.

Schild, C., & Trueb, B. (2002). Mechanical Stress Is Required for High-Level Expression of Connective Tissue Growth Factor. *Exp. Cell Res.*, *274*(1), 83-91. doi:10.1006/excr.2001.5458

Schönberger, J., Bauer, J., Spruss, T., Weber, G., Chahoud, I., Eilles, C., & Grimm, D. (2000). Establishment and characterization of the follicular thyroid carcinoma cell line ML-1. *J. Mol. Med. (Berl)*, *78*(2), 102-110. doi:10.1007/s001090000085

Schulz, H., Dietrichs, D., Wehland, M., Corydon, T. J., Hemmersbach, R., Liemersdorf, C., Melnik, D., Hübner, N., Saar, K., Infanger, M., & Grimm, D. (2022). In Prostate Cancer Cells

Cytokines Are Early Responders to Gravitational Changes Occurring in Parabolic Flights. *Int. J. Mol. Sci.*, *23*(14). doi:10.3390/ijms23147876

Schuster, E., Taftaf, R., Reduzzi, C., Albert, M. K., Romero-Calvo, I., & Liu, H. (2021). Better together: circulating tumor cell clustering in metastatic cancer. *Trends Cancer*, *7*(11), 1020-1032. doi:10.1016/j.trecan.2021.07.001

Schwarz, R. P., Goodwin, T. J., & Wolf, D. A. (1992). Cell culture for three-dimensional modeling in rotating-wall vessels: An application of simulated microgravity. *Journal Tissue Cult. Methods*, *14*(2), 51-57. doi:10.1007/BF01404744

Sharifi, N., & Gharravi, A. M. (2019). Shear bioreactors stimulating chondrocyte regeneration, a systematic review. *Inflamm. Regen.*, *39*(1), 16. doi:10.1186/s41232-019-0105-1

Sharma, K., Dey, S., Karmakar, R., & Rengan, A. K. (2024). A comprehensive review of 3D cancer models for drug screening and translational research. *Cancer Innov.*, *3*(1), e102. doi:10.1002/cai2.102

Shavers, M., Semones, E., Tomi, L., Chen, J., Straube, U., Komiyama, T., Shurshakov, V., Li, C., & Rühm, W. (2024). Space agency-specific standards for crew dose and risk assessment of ionising radiation exposures for the International Space Station. *Zeitschrift für Medizinische Physik*, *34*(1), 14-30. doi:10.1016/j.zemedi.2023.06.005

Sieber, M., Hanke, W., & Kohn, F. (2014). Modification of Membrane Fluidity by Gravity. *Open J. Biophys.*, *4*, 105-111. hdoi:10.4236/ojbiphy.2014.44012

Smetacek, V. (2002). Balance: Mind-grasping gravity. *Nature*, *415*(6871), 481-481. doi:10.1038/415481a

Smyrek, I., Mathew, B., Fischer, S. C., Lissek, S. M., Becker, S., & Stelzer, E. H. K. (2019). E-cadherin, actin, microtubules and FAK dominate different spheroid formation phases and important elements of tissue integrity. *Biol. Open*, *8*(1). doi:10.1242/bio.037051

Souza, G. R., Molina, J. R., Raphael, R. M., Ozawa, M. G., Stark, D. J., Levin, C. S., Bronk, L. F., Ananta, J. S., Mandelin, J., Georgescu, M. M., Bankson, J. A., Gelovani, J. G., Killian, T. C., Arap, W., & Pasqualini, R. (2010). Three-dimensional tissue culture based on magnetic cell levitation. *Nat. Nanotechnol.*, *5*(4), 291-296. doi:10.1038/nnano.2010.23

Stamenković, V., Keller, G., Nesic, D., Cogoli, A., & Grogan, S. P. (2010). Neocartilage formation in 1 g, simulated, and microgravity environments: implications for tissue engineering. *Tissue Eng. Part A*, *16*(5), 1729-1736. doi:10.1089/ten.tea.2008.0624

Stark, M., Mynbaev, O., Malvasi, A., & Tinelli, A. (2023). Inviting Newton to Visit the Delivery Room. The Role of Gravity During Childbirth. *Int. J. Womens Health*, *15*, 1059-1061. doi:10.2147/ijwh.S405077

Steinwerth, P., Bertrand, J., Sandt, V., Marchal, S., Sahana, J., Bollmann, M., Schulz, H., Kopp, S., Grimm, D., & Wehland, M. (2024). Structural and Molecular Changes of Human Chondrocytes Exposed to the Rotating Wall Vessel Bioreactor. *Biomolecules*, *14*(1), 25.

Striebel, J., Kalinski, L., Sturm, M., Drouvé, N., Peters, S., Lichterfeld, Y., Habibey, R., Hauslage, J., El Sheikh, S., Busskamp, V., & Liemersdorf, C. (2023). Human neural network activity reacts to gravity changes in vitro. *Front. Neurosci.*, *17*, 1085282. doi:10.3389/fnins.2023.1085282

Sun, L., Wen, J., Wang, L., Wen, Q., Wu, J., & Bie, M. (2019). Fluid shear stress-induced IL-8/CXCR signaling in human ovarian cancer cells. *Transl. Cancer Res.*, *8*(4), 1591-1601. doi:10.21037/tcr.2019.08.22

Sun, Z., Guo, S. S., & Fässler, R. (2016). Integrin-mediated mechanotransduction. *J. Cell Biol.*, *215*(4), 445-456. doi:10.1083/jcb.201609037

Sutherland, R. M., McCredie, J. A., & Inch, W. R. (1971). Growth of multicell spheroids in tissue culture as a model of nodular carcinomas. *J. Natl. Cancer. Inst.*, *46*(1), 113-120.

Sutherland, R. M., Sordat, B., Bamat, J., Gabbert, H., Bourrat, B., & Mueller-Klieser, W. (1986). Oxygenation and differentiation in multicellular spheroids of human colon carcinoma. *Cancer Res.*, *46*(10), 5320-5329.

Takahashi, K., Takahashi, H., Furuichi, T., Toyota, M., Furutani-Seiki, M., Kobayashi, T., Watanabe-Takano, H., Shinohara, M., Numaga-Tomita, T., Sakaue-Sawano, A., Miyawaki, A., & Naruse, K. (2021). Gravity sensing in plant and animal cells. *npj Microgravity*, *7*(1), 2. doi:10.1038/s41526-020-00130-8

Tanaka, Y., Nakayamada, S., & Okada, Y. (2005). Osteoblasts and osteoclasts in bone remodeling and inflammation. *Curr. Drug Targets Inflamm. Allergy*, *4*(3), 325-328. doi:10.2174/1568010054022015

Tansey, E. A., Montgomery, L. E. A., Quinn, J. G., Roe, S. M., & Johnson, C. D. (2019). Understanding basic vein physiology and venous blood pressure through simple physical assessments. *Adv. Physiol. Educ.*, *43*(3), 423-429. doi:10.1152/advan.00182.2018

Teutsch, H. F., Goellner, A., & Mueller-Klieser, W. (1995). Glucose levels and succinate and lactate dehydrogenase activity in EMT6/Ro tumor spheroids. *Eur. J. Cell Biol.*, *66*(3), 302-307.

Thiel, C. S., Tauber, S., Lauber, B., Polzer, J., Seebacher, C., Uhl, R., Neelam, S., Zhang, Y., Levine, H., & Ullrich, O. (2019). Rapid Morphological and Cytoskeletal Response to Microgravity in Human Primary Macrophages. *Int. J. Mol. Sci.*, *20*(10). doi:10.3390/ijms20102402

Tietze, S., Hofmann, A., Wolk, S., & Reeps, C. (2020). Grundlagen der zellulären Mechanotransduktion. *Gefässchirurgie*, *25*(4), 244-248. doi:10.1007/s00772-020-00648-x

Topal, U., & Zamur, C. (2021). Microgravity, Stem Cells, and Cancer: A New Hope for Cancer Treatment. *Stem Cells Int.*, *2021*(1), 5566872. doi:10.1155/2021/5566872

Uddin, M. M., Gaire, B., & Vancurova, I. (2020). Interleukin-8 Induces Proliferation of Ovarian Cancer Cells in 3D Spheroids. *Methods Mol. Biol*,. *2108*, 117-124. doi:10.1007/978-1-0716-0247-8_10

Uhler, C., & Shivashankar, G. V. (2017). Regulation of genome organization and gene expression by nuclear mechanotransduction. *Nat. Rev. Mol. Cell Biol.*, *18*(12), 717-727. doi:10.1038/nrm.2017.101

Ulbrich, C., Westphal, K., Pietsch, J., Winkler, H. D., Leder, A., Bauer, J., Kossmehl, P., Grosse, J., Schoenberger, J., Infanger, M., Egli, M., & Grimm, D. (2010). Characterization of human chondrocytes exposed to simulated microgravity. *Cell. Physiol. Biochem.*, *25*(4-5), 551-560. doi:10.1159/000303059

Uslu, C., Kapan, E., & Lyakhovich, A. (2024). Cancer resistance and metastasis are maintained through oxidative phosphorylation. *Cancer Lett.*, *587*, 216705. doi:10.1016/j.canlet.2024.216705

Vahlensieck, C., Thiel, C. S., Zhang, Y., Huge, A., & Ullrich, O. (2021). Gravitational Force-Induced 3D Chromosomal Conformational Changes Are Associated with Rapid Transcriptional Response in Human T Cells. *Int. J. Mol. Sci.*, *22*(17). doi:10.3390/ijms22179426

van Loon, J. J. W. A., Lobascio, C., Boscheri, G., Goujon, C., Voglino, S., Zeminiani, E., González-Cinca, R., & Ewald, R. (2024). Benefits of a rotating – Partial gravity – Spacecraft. *Acta Astronaut.*, *220*, 403-415. doi:10.1016/j.actaastro.2024.04.041

Vorselen, D., Roos, W. H., MacKintosh, F. C., Wuite, G. J., & van Loon, J. J. (2014). The role of the cytoskeleton in sensing changes in gravity by nonspecialized cells. *Faseb J.*, *28*(2), 536-547. doi:10.1096/fj.13-236356

Wakefield, L., Agarwal, S., & Tanner, K. (2023). Preclinical models for drug discovery for metastatic disease. *Cell*, *186*(8), 1792-1813. doi:10.1016/j.cell.2023.02.026

Walenta, S., Dötsch, J., & Mueller-Klieser, W. (1990). ATP concentrations in multicellular tumor spheroids assessed by single photon imaging and quantitative bioluminescence. *Eur. J. Cell Biol.*, *52*(2), 389-393.

Wang, C., Chen, H., Luo, H., Zhu, L., Zhao, Y., Tian, H., Wang, R., Shang, P., & Zhao, Y. (2015). Microgravity activates p38 MAPK-C/EBPβ pathway to regulate the expression of arginase and inflammatory cytokines in macrophages. *Inflamm. Res.*, *64*(5), 303-311. doi:10.1007/s00011-015-0811-3

Wang, J., Han, C., Lu, Z., Ge, P., Cui, Y., Zhao, D., Yang, X., Wu, B., Qiang, L., Zhang, Y., Chai, Q., Lei, Z., Li, L., Hua Liu, C., & Zhang, L. (2020). Simulated microgravity suppresses MAPK pathway-mediated innate immune response to bacterial infection and induces gut microbiota dysbiosis. *Faseb J.*, *34*(11), 14631-14644. doi:10.1096/fj.202001428R

Wang, N., Tytell, J. D., & Ingber, D. E. (2009). Mechanotransduction at a distance: mechanically coupling the extracellular matrix with the nucleus. *Nat. Rev. Mol. Cell Biol.*, *10*(1), 75-82. doi:10.1038/nrm2594

Wang, P., Zhu, F., Lee, N. H., & Konstantopoulos, K. (2010). Shear-induced interleukin-6 synthesis in chondrocytes: roles of E prostanoid (EP) 2 and EP3 in cAMP/protein kinase A- and PI3-K/Akt-dependent NF-kappaB activation. *J. Biol. Chem.*, *285*(32), 24793-24804. doi:10.1074/jbc.M110.110320

Warnke, E., Pietsch, J., Wehland, M., Bauer, J., Infanger, M., Görög, M., Hemmersbach, R., Braun, M., Ma, X., Sahana, J., & Grimm, D. (2014). Spheroid formation of human thyroid cancer cells under simulated microgravity: a possible role of CTGF and CAV1. *Cell Commun. Signal.*, *12*(1), 32. doi:10.1186/1478-811X-12-32

Wechman, S. L., Emdad, L., Sarkar, D., Das, S. K., & Fisher, P. B. (2020). Vascular mimicry: Triggers, molecular interactions and in vivo models. *Adv. Cancer Res.*, *148*, 27-67. doi:10.1016/bs.acr.2020.06.001

Wehland, M., Steinwerth, P., Aleshcheva, G., Sahana, J., Hemmersbach, R., Lützenberg, R., Kopp, S., Infanger, M., & Grimm, D. (2020). Tissue Engineering of Cartilage Using a Random Positioning Machine. *Int. J. Mol. Sci.*, *21*(24). doi:10.3390/ijms21249596

Whitmarsh, A. J. (2010). A central role for p38 MAPK in the early transcriptional response to stress. *BMC Biol.*, *8*, 47. doi:10.1186/1741-7007-8-47

Williams, G. M., Klisch, S. M., & Sah, R. L. (2008). Bioengineering Cartilage Growth, Maturation, and Form. *Pediatr. Res.*, *63*(5), 527-534. doi:10.1203/PDR.0b013e31816b4fe5

Wilson, R. B., Solass, W., Archid, R., Weinreich, F.-J., Königsrainer, A., & Reymond, M. A. (2019). Resistance to anoikis in transcoelomic shedding: the role of glycolytic enzymes. *Pleura and Peritoneum*, *4*(1). doi:10.1515/pp-2019-0003

Winters, B. S., Raj, B. K. M., Robinson, E. E., Foty, R. A., & Corbett, S. A. (2006). Three-dimensional culture regulates Raf-1 expression to modulate fibronectin matrix assembly. *Mol. Biol. Cell*, *17*(8), 3386-3396. doi:10.1091/mbc.e05-09-0849

Witz, I. P. (2008). The selectin-selectin ligand axis in tumor progression. *Cancer Metastasis Rev.*, *27*(1), 19-30. doi:10.1007/s10555-007-9101-z

Wu, X., Li, S. H., Lou, L. M., & Chen, Z. R. (2013). The effect of the microgravity rotating culture system on the chondrogenic differentiation of bone marrow mesenchymal stem cells. *Mol. Biotechnol.*, *54*(2), 331-336. doi:10.1007/s12033-012-9568-x

Wu, X. T., Yang, X., Tian, R., Li, Y. H., Wang, C. Y., Fan, Y. B., & Sun, L. W. (2022). Cells respond to space microgravity through cytoskeleton reorganization. *Faseb J.*, *36*(2), e22114. doi:10.1096/fj.202101140R

Wuest, S. L., Richard, S., Kopp, S., Grimm, D., & Egli, M. (2015). Simulated microgravity: critical review on the use of random positioning machines for mammalian cell culture. *Biomed. Res. Int.*, *2015*, 971474. doi:10.1155/2015/971474

Wuest, S. L., Stern, P., Casartelli, E., & Egli, M. (2017). Fluid Dynamics Appearing during Simulated Microgravity Using Random Positioning Machines. *Plos One*, *12*(1), e0170826. doi:10.1371/journal.pone.0170826

Yang, J.-Q., Jiang, N., Li, Z.-P., Guo, S., Chen, Z.-Y., Li, B.-B., Chai, S.-B., Lu, S.-Y., Yan, H.-F., Sun, P.-M., Zhang, T., Sun, H.-W., Yang, J.-W., Zhou, J.-L., Yang, H.-M., & Cui, Y. (2020). The effects of microgravity on the digestive system and the new insights it brings to the life sciences. *Life Sci. Space Res.*, *27*, 74-82. doi:10.1016/j.lssr.2020.07.009

Yang, X., Sun, L.-W., Liang, M., Wang, X.-N., & Fan, Y.-B. (2015). The Response of wnt/ß-Catenin Signaling Pathway in Osteocytes Under Simulated Microgravity. *Microgravity Sci. Technol.*, *27*(6), 473-483. doi:10.1007/s12217-015-9439-8

Yoffe, B., Darlington, G. J., Soriano, H. E., Krishnan, B., Risin, D., Pellis, N. R., & Khaoustov, V. I. (1999). Cultures of human liver cells in simulated microgravity environment. *Adv. Space Res.*, *24*(6), 829-836. doi:10.1016/s0273-1177(99)00079-4

Yu, B., Yu, D., Cao, L., Zhao, X., Long, T., Liu, G., Tang, T., & Zhu, Z. (2011). Simulated microgravity using a rotary cell culture system promotes chondrogenesis of human adipose-derived mesenchymal stem cells via the p38 MAPK pathway. *iochem. Biophys. Res. Commun.*, *414*(2), 412-418. doi:10.1016/j.bbrc.2011.09.103

Yue, Y., Yang, J. Q., Lu, S. Y., Ge, J., Nie, H. Y., Liu, K. G., Liu, F., Li, H., Yan, H. F., Zhang, T., Sun, P. M., Sun, H. W., Yang, J. W., Zhou, J. L., & Cui, Y. (2023). Simulated microgravity altered the proliferation, apoptosis, and extracellular matrix formation of L929 fibroblasts and the transforming growth factor-β1/Smad3 signaling pathway. *Skin Res. Technol.*, *29*(5), e13341. doi:10.1111/srt.13341

Yuge, L., Kajiume, T., Tahara, H., Kawahara, Y., Umeda, C., Yoshimoto, R., Wu, S. L., Yamaoka, K., Asashima, M., Kataoka, K., & Ide, T. (2006). Microgravity potentiates stem cell proliferation while sustaining the capability of differentiation. *Stem Cells Dev.*, *15*(6), 921-929. doi:10.1089/scd.2006.15.921

Zettl, K. S., Sjaastad, M. D., Riskin, P. M., Parry, G., Machen, T. E., & Firestone, G. L. (1992). Glucocorticoid-induced formation of tight junctions in mouse mammary epithelial cells in vitro. *Proc. Natl. Acad. Sci. USA*, *89*(19), 9069-9073. doi:10.1073/pnas.89.19.9069

EIDESSTATTLICHE VERSICHERUNG

gemäß der Habilitationsordnung der Medizinischen Fakultät der Otto-von-Guericke-Universität Magdeburg

Hiermit erkläre ich, Marcus Krüger, geboren am 09.05.1980 in Forchheim, dass ich die der Medizinischen Fakultät zur Habilitation eingereichte Habilitationsschrift mit dem Titel

Einbeziehung gravitationsbiologischer Methoden in die biomedizinische Grundlagenforschung

In der Abteilung für Mikrogravitation und Translationale Regenerative Medizin

- ohne sonstige Hilfe durchgeführt und bei der Abfassung keine anderen als die dort aufgeführten Hilfsmittel benutzt habe,
- bei der Abfassung der Habilitationsschrift keine Rechte Dritter verletzt wurden,
- die Habilitationsschrift bisher an keiner in- oder ausländischen Hochschule/Universität zur Habilitation eingereicht habe,
- mir die geltende Habilitationsordnung bekannt ist.

Ich übertrage der Medizinischen Fakultät der Otto-von-Guericke-Universität Magdeburg das Recht, weitere Kopien meiner Habilitationsschrift herzustellen und zu vertreiben.

Magdeburg, den 15.11.2024

(Dr. rer. nat. Marcus Krüger)

International Journal of
Molecular Sciences

MDPI

Review

Fighting Thyroid Cancer with Microgravity Research

Marcus Krüger [1], Daniela Melnik [1], Sascha Kopp [1], Christoph Buken [1,2], Jayashree Sahana [2], Johann Bauer [3], Markus Wehland [1], Ruth Hemmersbach [4], Thomas J. Corydon [2,5], Manfred Infanger [1] and Daniela Grimm [1,2,6,*]

1 Clinic for Plastic, Aesthetic and Hand Surgery, Otto von Guericke University, 39120 Magdeburg, Germany; marcus.krueger@med.ovgu.de (M.K.); daniela.melnik@med.ovgu.de (D.M.); sascha.kopp@med.ovgu.de (S.K.); christoph.buken@gmx.de (C.B.); markus.wehland@med.ovgu.de (M.W.); manfred.infanger@med.ovgu.de (M.I.)
2 Department of Biomedicine, Aarhus University, 8000 Aarhus C, Denmark; jaysaha@biomed.au.dk (J.S.); corydon@biomed.au.dk (T.J.C.)
3 Max Planck Institute of Biochemistry, 82152 Martinsried, Germany; jbauer@biochem.mpg.de
4 Institute of Aerospace Medicine, Gravitational Biology, German Aerospace Center (DLR), Linder Höhe, 51147 Cologne, Germany; ruth.hemmersbach@dlr.de
5 Department of Ophthalmology, Aarhus University Hospital, 8200 Aarhus N, Denmark
6 Gravitational Biology and Translational Regenerative Medicine, Faculty of Medicine and Mechanical Engineering, Otto von Guericke University, 39120 Magdeburg, Germany
* Correspondence: dgg@biomed.au.dk; Tel.: +45-8716-7693; Fax: +45-8612-8804

Received: 17 April 2019; Accepted: 23 May 2019; Published: 24 May 2019



Abstract: Microgravity in space or simulated by special ground-based devices provides an unusual but unique environment to study and influence tumour cell processes. By investigating thyroid cancer cells in microgravity for nearly 20 years, researchers got insights into tumour biology that had not been possible under normal laboratory conditions: adherently growing cancer cells detach from their surface and form three-dimensional structures. The cells included in these multicellular spheroids (MCS) were not only altered but behave also differently to those grown in flat sheets in normal gravity, more closely mimicking the conditions in the human body. Therefore, MCS became an invaluable model for studying metastasis and developing new cancer treatment strategies via drug targeting. Microgravity intervenes deeply in processes such as apoptosis and in structural changes involving the cytoskeleton and the extracellular matrix, which influence cell growth. Most interestingly, follicular thyroid cancer cells grown under microgravity conditions were shifted towards a less-malignant phenotype. Results from microgravity research can be used to rethink conventional cancer research and may help to pinpoint the cellular changes that cause cancer. This in turn could lead to novel therapies that will enhance the quality of life for patients or potentially develop new preventive countermeasures.

Keywords: three-dimensional growth; spheroids; aggressiveness; metastasis; signal transduction; cytokines; target

1. Introduction

For cancer biologists, microgravity-based research is still an unusual terrain. Microgravity (μg) provides a physical condition that is not possible on Earth and interestingly, this condition may be ripe for studying cancer [1,2]. The use of μg for cancer research was born at the end of the last millennium. During the STS-90 (Space Transportation System) mission in 1998, primary cultures of human renal cortical cells were cultured for six days aboard the space shuttle Columbia before they returned to Earth for analysis. Hammond et al. [3] reported an alteration of 1632 of the 10,000 analyzed genes relative to ground controls. This was the first experiment to show that reduced gravity can affect a

wide range of genes of in vitro cultured cells. These findings led to the speculation that weightlessness could also trigger cancer cells to change the expression of numerous proteins, which could be the basis for the development of new targets for drugs.

Inside the human body, the cells normally grow surrounded by a structure-supporting extracellular matrix together with a regulating biochemical microenvironment, which allows organs, as well as tumours, to maintain their three-dimensional (3D) shapes. Under normal laboratory conditions, adherent cells in vitro do not behave similarly to how they would react in vivo in the body: They grow two-dimensionally (2D), spreading out into monolayers on Petri dishes or polystyrene surfaces, which poses problems for scientists who study cancer by examining genetic changes affecting cell growth and development [4]. During the last decades, scientists have developed several laboratory methods to mimic the 3D growth of cancer cells.

Scaffold-based, spinner flask, liquid-overlay and hanging drop techniques were used to gain multicellular spheroids (MCS). But from a certain size, these MCS showed necrosis inside [5]. Under µ*g* conditions, cells can arrange themselves scaffold-free into large MCS without any signs of necrosis [6]. MCS can help to develop new cancer treatment strategies, which might be later translated into in vivo models. Today they represent a useful model for studying angiogenesis mechanisms and performing pharmacological testing of chemotherapeutic agents such as tyrosine kinase inhibitors (lenvatinib, sunitinib, sorafenib etc.), which are often used in metastatic cancer therapy [7]. In addition, they can be applied in toxicological and radiation experiments [8,9].

Thyroid cancer is the most common form of endocrine malignancy. Over the past four decades, incidence rates have increased worldwide [10]. According to the Global Cancer Statistics GLOBOCAN, 567,233 new cases were diagnosed in the world population, and 41,071 people died from thyroid cancer in 2018 [11]. Poorly differentiated thyroid tumours are aggressive and metastasize early, resulting in poor prognosis. Also, differentiated (papillary or follicular) thyroid cancer, that is usually well treatable, could—in its recurrent form—become less-differentiated by diminishing its iodine uptake capability. Thus, current treatment options for recurrent differentiated thyroid cancer are extremely limited and patients show remarkably reduced survival. Scientists have searched intensely for new ways/methods to identify targets for novel drugs—and some of them have considered to use experimentation in altered gravity conditions (Figure 1) [12,13].

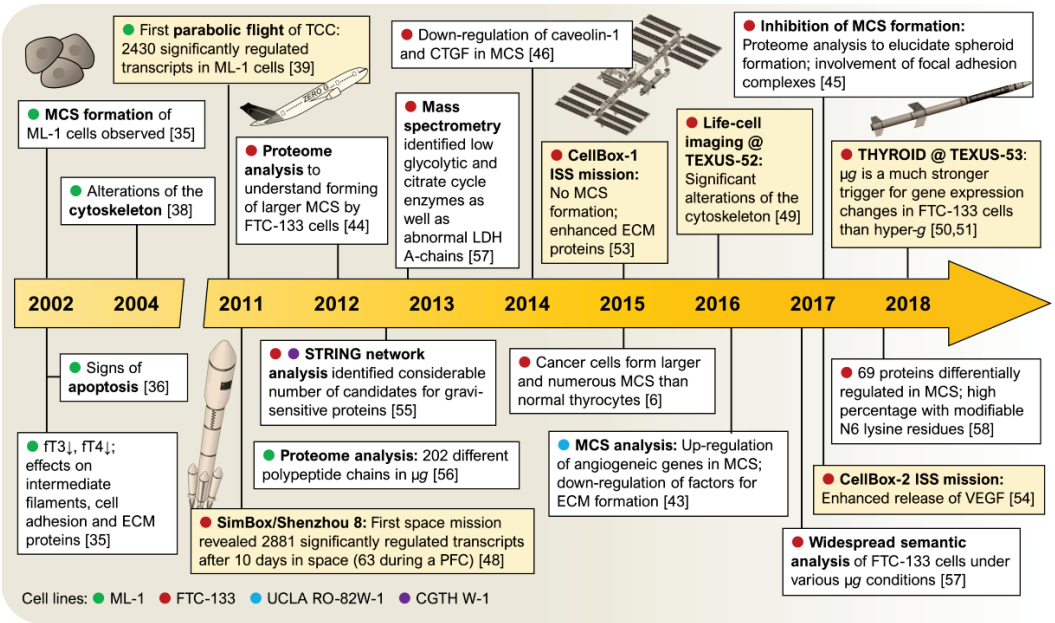


Figure 1. Timeline: research on thyroid cancer in microgravity. White squares: studies in simulated µ*g*; yellow squares: studies in real µ*g*. PFC: parabolic flight campaign, TCC: thyroid cancer cells.

2. Ground-Based Techniques Allow Microgravity Research on Earth

Experiments in real μg (parabolic flights, sounding rocket flights, experiments on satellites, space vehicles or space stations (Figure 2A)) are rare and expensive. For this reason, different ground-based facilities have been developed to simulate μg on Earth [1]. Devices such as the fast-rotating clinostat (FRC) [14], the rotating wall vessel (RWV) [15] or the random positioning machine (RPM) [16,17] allow cost-efficient preparations of spaceflights as well as intensive research in stand-alone studies (Figure 2B). The ground-based facilities have been shown to imitate μg effects for several (but for not all) experimental conditions [18,19].

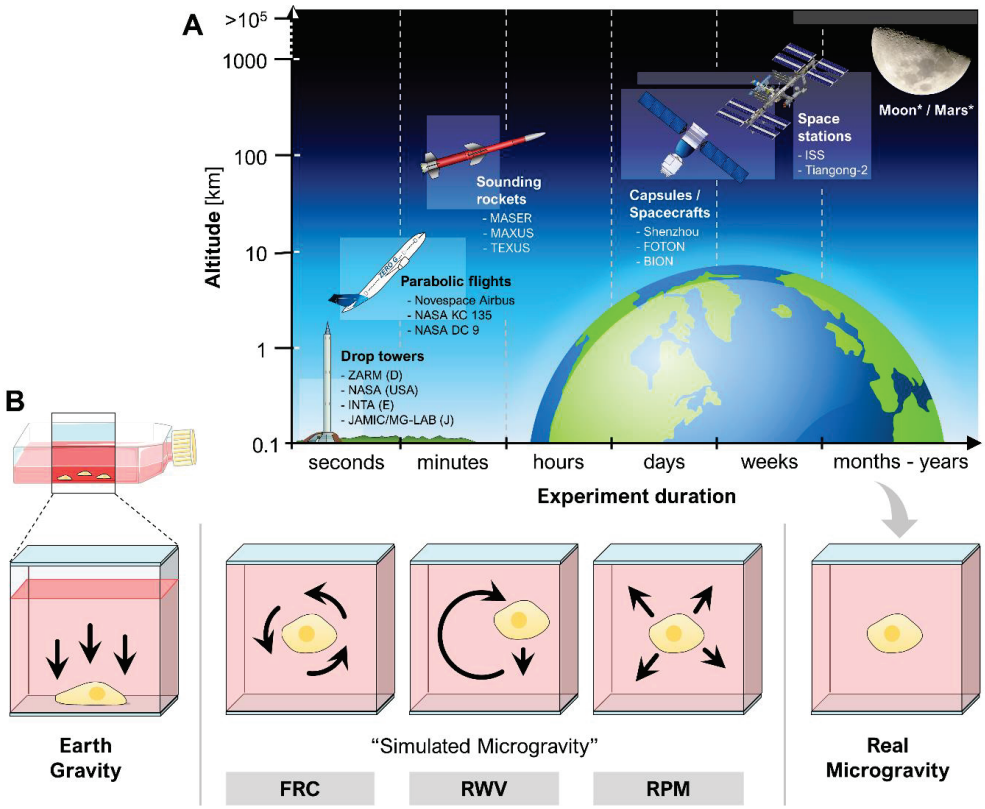


Figure 2. (**A**) Currently available and future (*) platforms for research in real μg. The highlighted boxes indicate altitude and duration ranges of the experiments; (**B**) Different ground-based facilities to simulate μg on Earth. Arrows indicate gravitational forces (Earth gravity) or movements to annulling gravity ("simulated μg"). Parts of the figure were drawn by using pictures from Servier Medical Art, licensed under a Creative Commons Attribution 3.0 Unported License (https://creativecommons.org/licenses/by/3.0/).

3. The Behaviour of Normal Thyrocytes in Microgravity

The structural feature of the thyroid tissue is the thyroid follicle. These follicles are formed by the cells that produce the thyroid hormones triiodothyronine (T3) and thyroxine (T4) and are called follicular epithelial cells or thyrocytes. In vivo, the thyrocytes are arranged in a single layer (epithelium) and surround the lumen of the follicles. In cross sections, the follicles of the healthy thyroid gland are round or oval. Microgravity changes the thyroid follicles [20]. The follicles reveal larger thyrocytes and show an elevation of cyclic adenosine monophosphate (cAMP), thyrotropin-receptors and caveolin-1 [20,21]. Earlier in vitro and in vivo experiments demonstrated that thyrocytes respond to μg and hypergravity conditions [22–26]. Kossmehl et al. [23] showed that normal HTU-5 cells (obtained without transfection) [27] exposed to clinorotation revealed signs of apoptosis, as demonstrated by activation of caspase-3, increases in Fas and Bax and elevation of 85-kDa apoptosis-related

cleavage fragments resulting from enhanced poly(ADP-ribose) polymerase activity. Apoptosis was found for various different cell types exposed to altered gravity conditions [28–31]. Results of the TEXUS (German: 'Technologische EXperimente Unter Schwerelosigkeit')-44 sounding rocket mission with FRTL-5 cells onboard showed that in real μ*g*, normal thyroid cells do not respond to thyroid-stimulating hormone (TSH) treatment and present an irregular shape with condensed chromatin, a modification of the cell membrane with shedding of the TSH receptor in the supernatant, as well as elevated sphingomyelin-synthase and Bax protein [22]. With the help of a rotary cell culture system, differentiated thyroid neofollicles were located in close proximity after two weeks of culture [24]. A time-dependent increase in human thyroglobulin was detected in the cell culture supernatant. Exposure of thyrocytes in a rotary cell culture system under the presence of keratinocyte growth factor (KGF) allowed the formation of artificial human thyroid organoids. They structurally resembled natural thyroid tissue [24]. In addition, Nthy-ori 3-1 thyrocytes were able to form 3D spheroids when exposed to an FRC or an RPM [25]. This cell line was originally obtained from normal human primary thyrocytes transfected with a plasmid containing an origin-defective large T antigen SV40 genome [32]. Although Nthy-ori 3-1 cells remain non-tumorigenic, they possess a few specific features such as a strongly diminished thyroglobulin production and the presence of tri-tetraploid clones. Nthy-ori 3-1 cells were exposed for 24 h and 72 h to an RPM. After a 24-h RPM-exposure, they started to detach and to form 3D aggregates. The spheroids increased in number and size over time (72 h), while adherent cells decreased [26]. Nthy-ori 3-1 cells secreted various cytokines in connection with focal adhesion proteins and revealed positively or negatively interacting proteins, strengthening the onset of MCS formation. The interleukins (IL)-6, IL-8 and TIMP-1 seemed to be involved in this process [26]. Long-term RPM-exposure of Nthy-ori 3-1 cells demonstrated no signs of necrosis in the centre of the spheroids [6]. The non-malignant thyroid cells did not express receptors for vascular endothelial growth factor (VEGFRs) in a measurable amount [6] but they reacted with an up-regulation of downstream signalling molecules, which hinted either to a delayed reaction to the simulated μ*g* or to further signalling molecules, which are involved in 3D-aggregate formation. The multipotent IL-6 could be a candidate that influences the cytoskeleton via β-actin [6]. IL-6 is known to be involved in angiogenesis and metastasis not only in thyroid cancer but also in several other cancer types. Elevated IL-6 concentrations could be explained by mechanically triggered activation of the specific surface receptor CD44 [33]. It was suggested that the CD44-IL-6-connection plays a possible role in gravity perception [6]. At least in pancreatic cancer cells, IL-6 stimulation activates the small GTPase cell division cycle 42 (Cdc42) and thus promotes the formation of pre-migratory, actin-based filopodia [34].

In summary, normal thyrocytes revealed changes in the cytoskeleton, shredding of their membranes, alterations in gene expression, protein synthesis and secretion and showed an increased amount of apoptosis and a change in growth behaviour.

4. Research on Thyroid Cancer Cells in Microgravity

Research on thyroid cancer cells using μ*g* conditions became a more and more interesting topic [1]. Nearly 20 years of μ*g* research in this field provided a deeper insight into the growth behaviour and signalling mechanisms of thyroid cancer (Figure 3). Since the first experiments in 2002, many studies have been conducted both in real and simulated μ*g* environments using different model cell lines (ML-1, FTC-133 and UCLA RO-82W-1) and different research platforms (see also Figure 1).

- Ground-Based Studies

Growth of 3D-aggregates (Figures 3 and 4A) during random positioning was observed very early [35] and it was found that apoptosis is involved in MCS formation [23,36]. Programmed cell death of μ*g*-exposed cells was also confirmed for other cell types [30,37]. In this setting, nuclear factor kappa-light-chain-enhancer of activated B cells (NFκB) was identified as a key player [37]. Furthermore, simulated μ*g* affected gene expression patterns and the structure of the cytoskeleton already very early after exposure to μ*g* [38,39]. In addition to alterations of the F-actin morphology (Figure 4B,C), 30 min

of clinorotation induced a disorganization of vimentin, cytokeratin and microtubules. However, these changes were nearly reversed after 48 h [40]. This finding clearly supported the hypothesis that the cytoskeleton may sense gravity in eukaryotic cells [41]. μ*g* also increased the amount of extracellular matrix (ECM) proteins in a time-dependent manner [40]. Based on the proteome data of different μ*g* experiments, Bauer et al. [42] postulated that the stability of the ECM has a great influence on MCS formation under μ*g*.

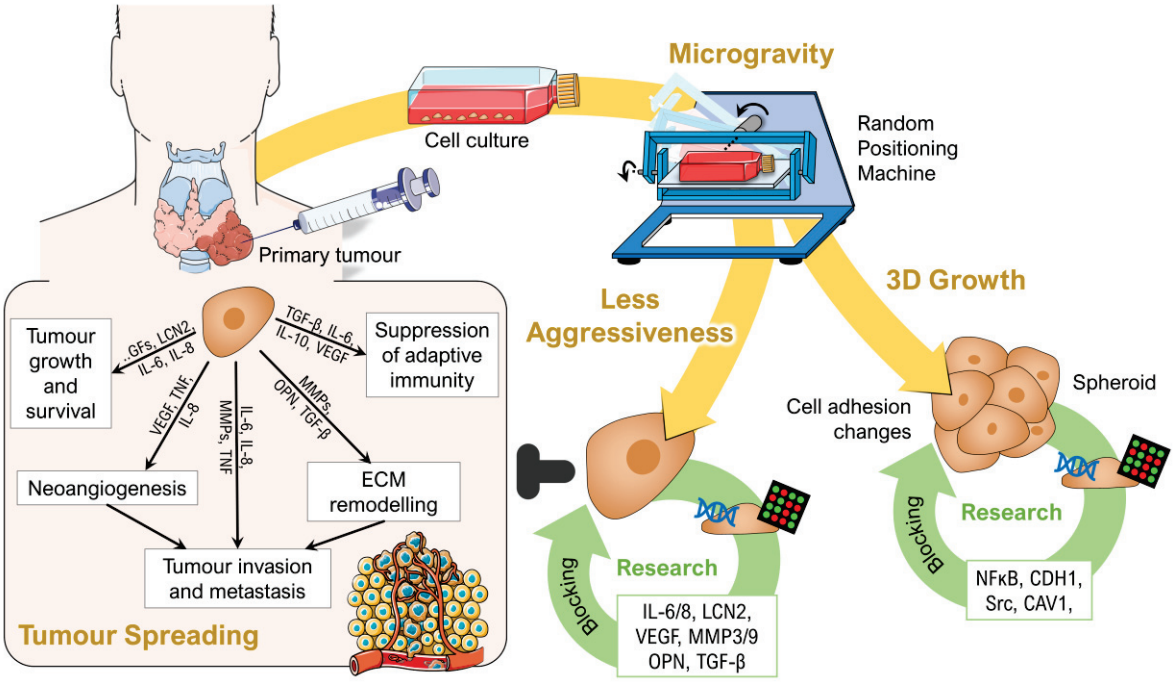


Figure 3. Overview: Current research on thyroid cancer using (simulated) microgravity. Parts of the figure were drawn by using pictures from Servier Medical Art, licensed under a Creative Commons Attribution 3.0 Unported License (https://creativecommons.org/licenses/by/3.0/).

For scientists, it is very important to understand why and how MCS were formed. A 24 h-RPM-experiment with UCLA RO-82W-1 cells showed that genes of products involved in angiogenesis were up-regulated in MCS whereas gene products involved in ECM formation were down-regulated [43]. Especially FTC-133 follicular thyroid cancer cells formed larger and numerous spheroids compared to normal thyrocytes [6]. It is assumed that these cells express surface proteins that bind fibronectin, strengthening 3D cell cohesion [44]. An intense proteome analysis of FTC-133 cells to elucidate MCS formation revealed that paxillin, vinculin (Figure 4D,E) and focal adhesion kinase (FAK or PTK2) may be positioned within the focal adhesion complex in a way that favours cell detachment from the bottom of a culture flask and mutual attachment [45]. Caveolin-1 and connective tissue growth factor (CTGF) were down-regulated in spheroids [46].

Different transcription factors, especially the sex-determining region Y-related high-mobility group box (SOX) proteins, are deeply involved in cancer development and metastasis but for thyroid cancer only a few studies have addressed this topic so far. Also, the influence of μ*g* on SOX expression is still unclear. In a first experiment, FTC-133 cells were analyzed after 10 days on the RPM. The cell line did not express *SOX2*, *SOX5*, *SOX6* and *SOX7* but was positive for SOX9 and SOX11. RPM-exposure had only a marginal effect on the expression of the SOX genes both in adherently growing cells and in the MCS cells [47].

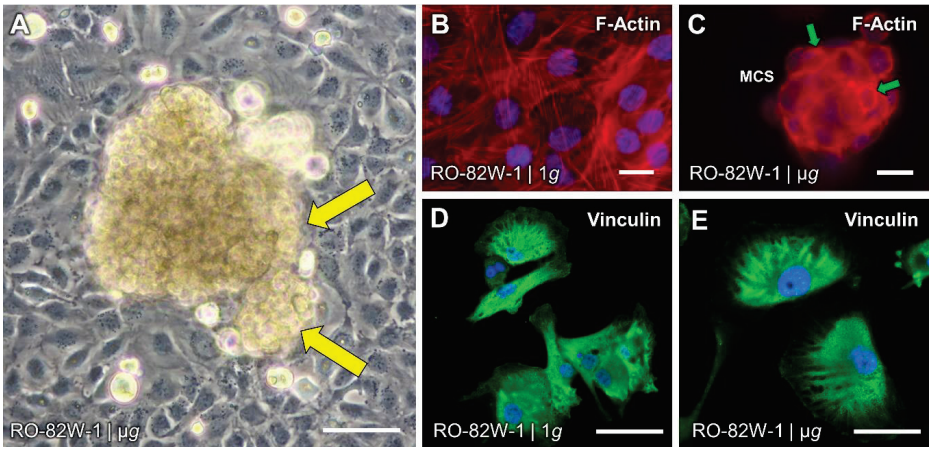


Figure 4. Simulated microgravity affects morphology and growth of thyroid cancer cells: (**A**) Multicellular spheroid (MCS) of UCLA RO-82W-1 cells, observed after three days on a random positioning machine (RPM). Yellow arrows indicate proliferating areas; (**B**,**C**) Fluorescence staining of F-actin (red) in UCLA RO-82W-1 cells that were grown for three days in normal gravity (**B**) or on an RPM (**C**). Small MCS were visible with increased F-actin deposits at the outer membranes of the MCS surface (green arrows); (**D**,**E**) Immunofluorescence of vinculin (green) in UCLA RO-82W-1 cells. DAPI-stained nuclei are shown in blue. Scale bars: 50 µm.

- Parabolic and Sounding Rocket Flights

Alternating phases of real µ*g* (ca. 22 s), hypergravity and normal gravity during a parabolic flight provide optimal conditions for investigating morphological and genetic alterations directly in the transition from hypergravity to µ*g*. A parabolic flight changed the morphology of the F-actin/cytokeratin cytoskeleton of ML-1 cells as well as the expression status of genes involved in forming the cytoskeleton and ECM [39]. Interestingly, the gene expression during the parabolic flight (and thus several changes in gravity conditions) was often regulated in the opposite direction compared to the RPM or space [48].

Several sounding-rocket flights allowed further short-term experiments in real µ*g* (about 6 min) during the last years. The focus of these analyses was the very early mechanisms of cells exposed to real µ*g* aiming to detect the first steps that later lead to cell detachment and MCS formation. FTC-133 cells expressing the LifeAct-GFP marker protein for the visualization of F-actin were flown on TEXUS-52 in 2015 and observed with live-cell imaging using the confocal FLUMIAS (Fluorescence-Microscopic Analysis Systems for Space Application) microscope. They proved significant structural alterations of the actin cytoskeleton as well as effects on the gene expression of genes involved in cytoskeleton forming (*EZR*) and signalling (*SEPT11*) [49]. With the *THYROID* project on the TEXUS-53 mission in 2016, Kopp et al. [50] investigated the effects of short-term µ*g* and hypergravity on the transcriptome and proteome of FTC-133 cells. They identified a possible role of epidermal growth factor (EGF) and vascular endothelial growth factor (VEGF) for spheroid formation in µ*g*. In addition, they found that µ*g* is a stronger regulator of gene expression than hypergravity, which shortly occurs during the launch of the rocket [51].

- Space Missions

The long-term experiments in real µ*g* provided a deeper insight into the growth behaviour of thyroid cancer cells in weightlessness excluding any additional shear forces as they might be induced in ground-based facilities. This helped to evaluate whether µ*g* was the trigger for the effects observed in RPM experiments on Earth. After the SimBox/Shenzhou-8 mission in 2011, it became clear that space-flown follicular thyroid cancer cells changed their proliferation, cell adhesion, growth behaviour, and the post-flight results indicated that the cells shifted toward a less-aggressive phenotype [48]. Another interesting finding was that the confluence status of a cell culture could influence MCS

formation. Preincubation of FTC-133 cells for five days before exposure to μ*g* during the CellBox-1 mission completely inhibited the spheroid formation suggesting that the cell density together with high amounts of ECM proteins and caveolin-1 are of great importance for 3D growth [52,53]. The CellBox-2 mission in 2017 allowed to investigate the effects of real μ*g* on the transcriptome and proteome of FTC-133 cells. The cells formed MCS in space and interestingly, these spheroids differed from MCS generated on an RPM by an enhanced release of VEGF [54]. As VEGF has a key role in neoangiogenesis, the enhanced production suggests a different angiogenic potential of thyroid cancer cells in space.

- Supporting Semantic Analyses

Genomic and proteomic analyses performed after exposing healthy and malignant thyroid cells to devices simulating μ*g* or to space or orbit flights unveiled a number of genes and proteins, which may play a role when the cells adapt to μ*g* [55–57]. Semantic analyses of these genes and proteins enabled the identification of groups of interacting cellular entities and members of distinct pathways [58,59]. A group of gravisensitive genes was detected, which altered their transcription when exposed to μ*g*. They code for proteins, which are either secreted into the culture supernatant, inserted in the cell membrane or located within the cytoplasm. Within the first 24 h of culturing the cells on an RPM, genes coding for secreted proteins were up-regulated but those coding for membrane or cytoplasmic proteins were down-regulated. After prolonged incubation, up-regulation of genes coding for membrane and cytoplasm proteins was also observed. According to information retrievable from the literature, these proteins form a network of interaction. They can either mutually influence their gene expression, form complexes or regulate their activity. Interestingly, this interaction network not only includes the products of gravisensitive genes but it also comprises proteins detected in culture supernatants by multianalyte profiling technology upon the cells' exposure to μ*g* [6,25,43,52].

Another group of related proteins was found when a deep proteome analysis was evaluated. This analysis was performed comparatively on thyroid FTC-133 cells, which were either incubated under normal gravity conditions or on the RPM, where they were split into two populations, one continuing to grow adherently, while the other one started to grow within a 3D aggregate. The evaluation showed 104 proteins of the integrin signalling pathway. In cells forming 3D aggregates during three days of culture on the RPM, the levels of caveolin-1 and p130cas proteins were reduced but arf-GAP with SH3 domain (ASAP1) production was enhanced. The results confirmed that caveolin-1 plays an important role in spheroid formation [52] and challenged the speculation that the positions of the proteins paxillin, vinculin and focal adhesion kinase may be changed by μ*g* within the focal adhesion complex in a way that favours cell detachment from the bottom of a culture flask. Preliminary hints towards a μ*g*-dependent change of intracellular vinculin distribution had already been observed during a recent TEXUS flight [45,51]. Taking together, in vitro studies on thyroid cells exposed to microgravity suggested that groups of proteins are affected by μ*g* which interact over the membrane barrier and provided first insights in the mechanisms of tissue cells leaving the site of growth to migrate to another one as observed in metastasis [60].

4.1. Spheroids as a 3D Tumour Model

Both thyroid cancer cells and normal thyrocytes formed MCS [43,61], when they were cultivated in (simulated) μ*g*. Follicular thyroid cancer cells detached from the cell culture flask bottom and assembled to compact 3D aggregates within a short time [35]. The tumour MCS were described to mimic small metastases that are not as complex as the primary tumour but could resemble a part of their organ of origin, reflecting a pathophysiological 'inside-out' situation (Figure 5) [62]. The ECM of MCS differed in amount and composition from the corresponding monolayer cultures comprising a complex 3D network of cell-cell and cell-matrix interactions. These differences might facilitate the penetration and action of drugs and affect the distribution and function of other physiological molecules such as hormones and growth factors. Thus, the composition of MCS fundamentally determines the regulation of cell growth, differentiation and apoptosis [62].

An important task is to clarify the mechanisms for spheroid formation. Several factors are involved in this process in addition to their role in metastasis and spreading of cancer cells in vivo (Tables 1 and 2). Some of these factors may serve as future targets in cancer therapy.

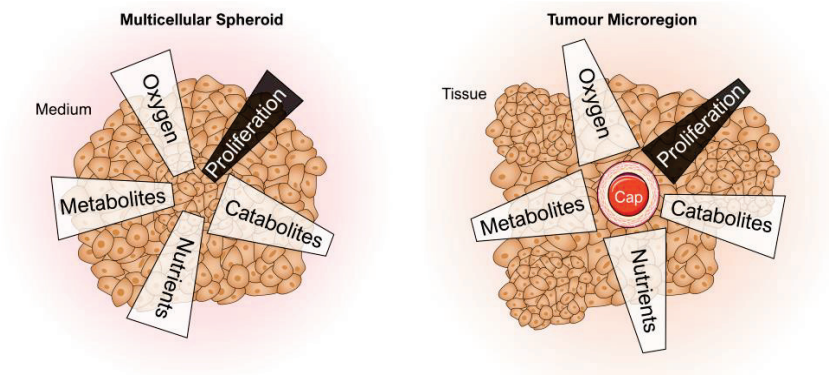


Figure 5. Schematic of the analogy between a multicellular spheroid (**left**) and a tumour (**right**) to illustrate the pathophysiological inside-out situation described by Kunz-Schughart [62]. Cap: capillary. Parts of the figure were drawn by using pictures from Servier Medical Art, licensed under a Creative Commons Attribution 3.0 Unported License (https://creativecommons.org/licenses/by/3.0/).

Table 1. Selected articles addressing the mechanisms of spheroid formation of thyroid cancer cells exposed to real or simulated μ*g*.

Cell Line	Condition	Findings	Ref.
FTC-133	Space ISS (5d) preincubation (12d)	Factors involved in inhibition of 3D growth: caveolin-1, VCAM-1 and activated protein kinase Cα recruited in caveolae	[52]
FTC-133	Space ISS (5d) preincubation (12d)	Proteins involved in the inhibition of 3D growth: extracellular matrix proteins, phosphorylated profilin 1	[53]
FTC-133	Space (10d) Shenzhou 8	*IL6*, *CXCL8*, *IL15*, *SPP1*, *VEGFA*, *VEGFD*, *FGF17*, *MMP2*, *MMP3*, *TIMP1*, *PRKAA* and *PRKCA*	[48]
FTC-133	Space (10d) Shenzhou 8	*CTGF* and *EGF*	[63]
FTC-133	RPM 3d, (2d) preincubation (5d) preincubation	Vinculin, paxillin, focal adhesion kinase 1 and adenine diphosphate (ADP)-ribosylation factor 6	[45]
FTC-133, Nthy-ori 3-1	RPM (14d)	VEGF, FLT-1. FLK-1, CD44, Copine 1, TGM2, IL-6, IL-8, IL-17, OPN, neutrophil gelatinase-associated lipocalin (NGAL, LCN2)	[6]
ML-1, RO82-W-1	RPM (3d), FRC (7d)	ML-1 cells: elevated release of IL-6 and monocyte chemoattractant protein (MCP-1)	[64]

Table 2. Genes involved in spheroid formation.

Pathway/Function	Genes
Cell adhesion	*VCAM1*, *CD44*, *CDH1*
Angiogenesis	*VEGFD*, *VEGFA*, *FLK1*
Apoptosis	*TGFB1*
Caveolae	*CAV1*
Extracellular matrix	*SPP1*, *MMP2*, *MMP3*, *TIMP1*, *FN1*, *COL1A1*
Inflammation	*IL6*, *CXCL8*, *IL17*
NFκB signalling	*NFKB1*
Protein kinases	*PRKAA*, *PRKCA*
Cytoskeleton	*ACTB*, *TUBB*, *FN1*

An interesting finding was that caveolin-1 is a key factor for the inhibition of spheroid formation when confluent monolayers are exposed to μg [52]. The results of a pathway analysis using the data of these articles (Table 1) are given in Figure 6.

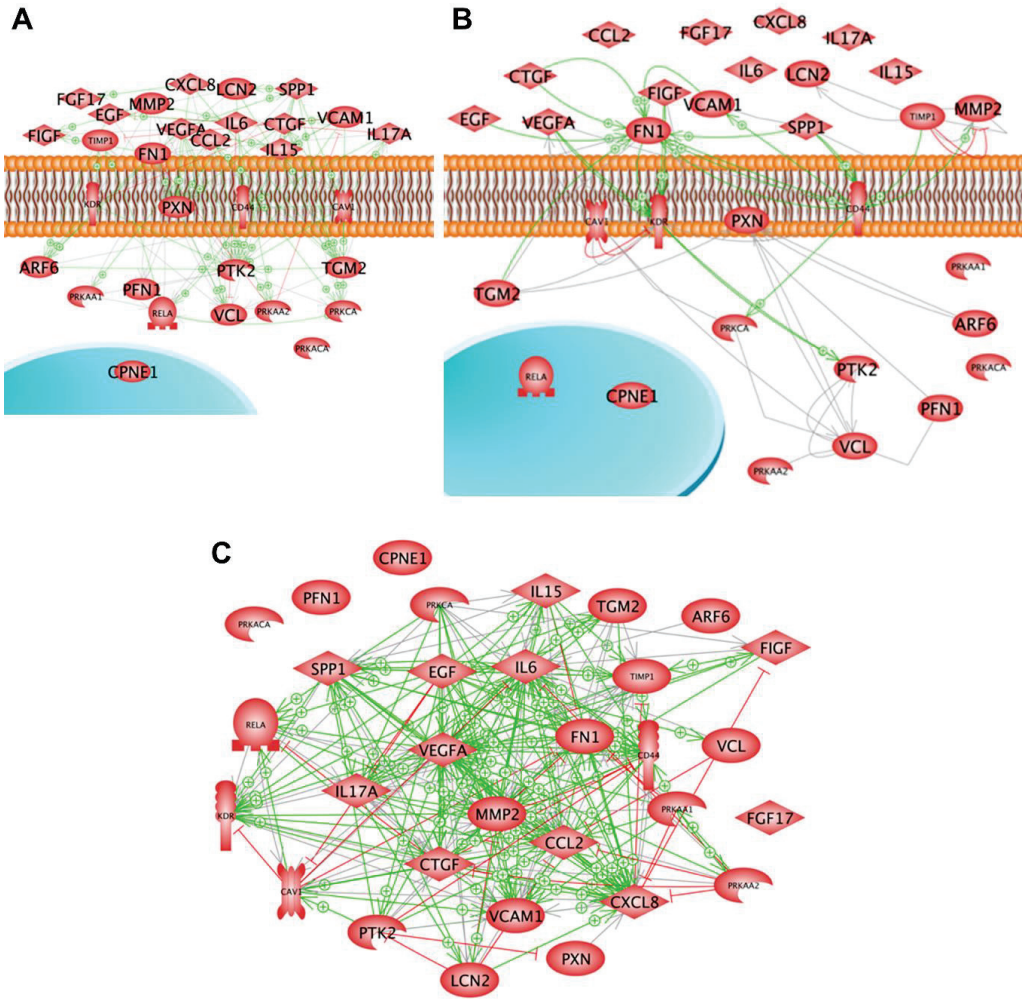


Figure 6. Semantic analysis of factors involved in spheroid formation: (**A**) Protein-protein regulation of follicular thyroid cancer cells exposed to μg; (**B**) Direct protein interactions; (**C**) Gene interaction of various differentially regulated genes of thyroid cancer cells exposed to μg conditions. Connecting lines indicate binding, arrows show directed interaction; green lines with '+' signs point to an enhancing effect, red lines with perpendicular bars indicate inhibition. Networks were built up using Pathway Studio v.11 (Elsevier, Amsterdam, The Netherlands).

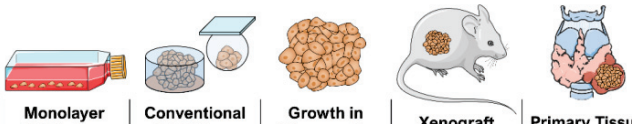
Ten of numerous studies on the behaviour of thyroid cells revealed proteins and genes coding for proteins that appear to be key proteins in spheroid formation. The studies were performed at very different time points on different populations of thyroid cells, culturing the cells either on an RPM, a clinostat or in space. The 31 proteins recognized as being important in MCS formation were, besides copine-1, all members of the networks of interaction according to the literature evaluated by the Elsevier Pathway Studio.

As demonstrated in Figure 6, various factors are involved in the formation of spheroids. The next step would be to study them in more detail. A first step was done by targeting E-cadherin in MCF-7 breast cancer cells [65]. The proto-oncogene tyrosine-protein kinase c-Src was detected in MCF-7 MCS. Anti-E-cadherin antibodies had enhanced the amount of MCS. The agent PP2, blocking the E-cadherin reducer SRC, prevented MCS formation completely [65].

Figure 6A,B show protein interaction networks. Looking at the mutual regulation of the proteins, it can be seen that 29 proteins form a network influencing the activity of each other (see Figure 6A). In most cases, the influence is stimulating (green arrows). Only a few red lines with little perpendicular bars at their ends indicate inhibition. PTK2, the focal adhesion kinase, seems to play a central role in this system, as most of the arrows point to its icon. As the icon of VEGF-A is a starting point for a considerable number of green arrows, one may conclude that VEGF-A is a strong initiator of spheroid formation. Interestingly, 21 of the proteins investigated bind physically to each other forming complexes (connecting lines) or triggering the partner's activity (green arrows) (Figure 6B). In two cases, TIMP1-MMP2 and CAV1-KDR inhibition were indicated (red lines with the perpendicular bar at the side of inhibited protein). In this system of binding, fibronectin seems to play a central role.

Figure 6C shows that 27 of the proteins recognized as being important in spheroid formation influence each other's mRNA expression. As shown by the high number of arrows the mutual gene expression regulation is very intensive. Again, most proteins favoured the expression of the partner protein's mRNA (green arrows). Still a considerable number inhibits (red line with perpendicular bar at the end). In this system *VEGFA*, *KDR*, *IL6* and *CXCL8* are indicated as dominant target genes as many arrows point to their icons. Noteworthy is that many green arrows start at the SPP1 icon. This suggests that osteopontin is a major trigger of spheroid formation.

Figure 7 provides a comparative overview of the current cell (culture) models used for cancer research. It visualizes possibilities and limits of the different model types including µ*g*-grown tumour spheroids. The µ*g*-based method is able to provide a large number of MCS in a short time and is suitable for long-term experiments (no necrotic cores) as well as for cocultures. MCS were used for a variety of experimental studies using radiotherapy, chemotherapy, radioimmunotherapy, cell- and antibody-based immunotherapy, hyperthermia, gene therapy and photodynamic treatment [66]. Further, they serve as an invaluable experimental and theoretical model for basic research on proliferation, viability, energy metabolism, nutrient metabolism, invasion, cell-cell interactions and extracellular matrix composition helping to better estimate in vivo antitumor treatment modalities [66]. But although thyroid cancer cells grow in 3D structures in µ*g*, MCS do not possess blood vessels that can provide oxygen and nutrients. Therefore, the MCS size remains limited.



	Monolayer Cell Culture	Conventional 3D Culture	Growth in Microgravity	Xenograft	Primary Tissue
Techniques		Spinnerflask, Hanging drop, Liquid overlay	'Simulated' µ*g*, Real µ*g* (see Fig. 2)		
Model type	in vitro, 2D	in vitro, 3D	in vitro, 3D	in vivo, 3D	in vitro, 3D
Reproducibility	✓	✓	✓ for s-µ*g*	✓	
Long-term studies	✓		✓	✓	
Cocultures	✓	✓	✓		
Drug testing	✓	✓	✓	✓	✓
Radiation experiments	✓	✓	✓	✓	✓
Toxicity screens	✓	✓	✓		

Figure 7. Comparison of different cell culture models for thyroid cancer research. s-µ*g*: simulated microgravity. Parts of the figure were drawn by using pictures from Servier Medical Art, licensed under a Creative Commons Attribution 3.0 Unported License (https://creativecommons.org/licenses/by/3.0/).

4.2. Growth of Thyroid Cancer Cells in Microgravity–A Temporary Mimicry of Metastasis?

When a (progressive) tumour spreads from its primary site to another part of the organism this process is called metastasis. Metastatic cancer is characterized by the same type of cancer cells as

the primary cancer. The tumour starts to extend and invades into the structures and tissues in its surrounding area. The first description of a thyroid metastasis was made by Rudolf Virchow in 1871, who found metastatic thyroid cells inside a testis [67]. Thyroid cancer mostly spreads to the lymph nodes, lungs, bone and occasionally to the brain. Follicular thyroid cancer tends to spread to distant sites via the blood vessels (hematogenously), as opposed to papillary thyroid cancer, which metastasizes through the lymphatic system (lymphogenously), usually to local lymph nodes. As angioinvasion is associated with the risk of recurrence, the differentiation of lymphatic and angioinvasion is of high importance [68]. Survival and growth of metastases at the new sites needs angiogenesis: The tumour forms a new blood supply by building new blood vessels. Metastasis is responsible for more than 90% of all the cancer-associated deaths. Approximately 30% of patients suffering from thyroid cancer develop metastases [69] and the incidence of distant metastasis after thyroidectomy remains between 7% and 23% [70]. In rare cases metastasis is associated with malignant ascites (especially described for medullary thyroid cancer [71]). Metastatic ascites containing multicellular spheroids can promote chemo-resistance and recurrence [72]. Model mechanisms relating to how single cells aggregate to form MCS once detached are important. MCS have been used in developmental biology and experimental cancer research for many years [73]. They are used as in vitro models of tumour microregions and as early avascular stage of tumour growth [62,66,74].

Progression and aggression of cancer are known to be closely connected to mechanical stress [75] resulting in alterations of cytoskeletal structures, cellular shape, proliferation, differentiation, cell adhesion, survival/death and migration [76,77]. The loss of gravity can also be a stressor for adherently growing cells that may be induced by tensegrity (tensional integrity) after gravitational unloading [78,79]. Interestingly, there are many parallels between the detachment of single cells from the primary tumour during metastasis and the detachment of adherently growing cells in μ*g* (Table 3). Whereas metastasis is forced, among other factors, by the external pressure from the growing tumour [76], a possible physical trigger for cell detachment in μ*g* is the lapse of gravity.

Research using MCS focused on mechanisms involved in proliferation, invasion and metastasis. μ*g* conditions have been shown to induce 3D growth of benign and malignant cells [72]. A great advantage of μ*g*-engineered MCS is that they do not develop a necrotic centre when cultured for several weeks [6,80]. Interestingly, results hint to a re-differentiation of follicular thyroid cancer cells in space to a less-aggressive phenotype (see chapter 4.4.) [48]. These findings are supported by recent data obtained with melanoma cells types exposed to μ*g*. BL6-10 cells did not form multicellular spheroids but revealed comparable results, as clinostat-simulated μ*g* reduced proliferation, adhesion and invasiveness in vitro and decreased tumour lung metastasis in vivo. Clinorotation also down-regulated metastasis-related integrin α6β4, MMP9 and Met72 molecules. Further, it significantly reduced the formation of focal adhesions and activation of the focal adhesion kinase (FAK), Rho family proteins (RhoA, Rac1 and Cdc42) and mTORC1 kinase but activated AMPK and ULK1 kinases [81]. Clinostat-exposure of the cells inhibited focal adhesions and induced inhibition of FAK and RhoA signalling and the mTORC1 pathway, which resulted in the activation of the AMPK pathway and thus reducing melanoma cell proliferation and metastasis. μ*g* further changed the cytoskeleton and nuclear positioning, leading to enhanced cell apoptosis by suppressing the FAK/RhoA-regulated mTORC1/NFκB and ERK1/2 pathways [82]. Similar data were found by Grosse et al. [61] investigating follicular thyroid cancer (FTC-133) cells. Especially invasive follicular thyroid cancer is known to show an extensive vascular invasion [68]. FTC-133 cells grown on the RPM showed higher levels of NFκB p65 protein and apoptosis than controls grown under normal gravity (1*g*), a result also found earlier in endothelial cells [31]. *IL6*, *CXCL8*, *CD44* and *SPP1* were significantly up-regulated in adherent cells but not in MCS, while *ERK1/2*, *CAV2*, *TLN1* and *CTGF* were significantly down-regulated in adherent cells. Simultaneously, the expression of *ERK2*, *IL6*, *CAV2*, *TLN1* and *CTGF* was reduced in 3D MCS compared to 1*g* samples. The signalling elements IL-6, IL-8, OPN, TLN1 and CTGF were involved together with NF-κB p65 in the RPM-dependent thyroid carcinoma cell MCS formation. Similar findings were reported with glioma cells exposed to μ*g* [83]. Simulated μ*g* induced apoptosis of U251 cells. The FAK/RhoA/Rock and

FAK/Nek2 signalling events were attenuated by simulated μ*g* to destabilize the actin cytoskeleton and centrosome disjunction, which caused G2/M arrest and inhibition of cell viability and migration [83]. The FAK/RhoA/Rock and FAK/Nek2 pathways are affected by simulated μ*g* and might serve as future targets. In addition, an earlier study showed that simulated μ*g* reduced the metastatic potential of human lung adenocarcinoma cells by diminishing the expression of antigen MKI67 and MMP2, thereby inhibiting cell proliferation, migration and invasion [84]. In addition, MMP2 was reduced in the thyroid cancer space samples [48], supporting the results of Chang et al. [84] that simulated μ*g* exerts an antiproliferative effect on lung cancer cells.

Table 3. Comparison between exposure to μ*g* and metastasis.

	Microgravity (Detachment)	**Metastases (Detachment)**
Physical Trigger	Lapse of gravity (tensegrity, mechanical stress)	Pressure from growing tumour
Cytoskeleton	Formation of filopodia and lamellipodia [49]	Formation of filopodia and lamellipodia [85]
	PFN↑ [6], phosphorylated profilin-1 prevented MCS formation [43]	Profilin 1↓ [86]
Cell Adhesion	Blockage of E-cadherin leads to enhanced spheroid formation of MCF-7 breast cancer cells [65]	E-cadherin↓ [87]
ECM	*MMP9*↑ [43]; OPN↑ [61]	MMP9↑ [88]; OPN↑ [89]
Cytokines	IL-6↑, IL-8↑ [6]	IL-6↑ [87]; IL-8 enhances metastatic potential [90]
Growth Factors	VEGF-A↑ [48]	VEGF↑ facilitates metastasis through the VEGF-VEGFR1 signalling pathway [91]
Others	CD44↑ [61]	CD44↑ [92]

↓ down-regulation; ↑ up-regulation; AD: adherent cells; MCS: multicellular spheroids.

4.3. Reduced Aggressiveness of Thyroid Cancer Cells after Long-Term Exposure to Real Microgravity

When thyroid cancer cells had been examined after cultivation on an RPM at various time-points results suggested that μ*g* initiated a re-differentiation of dedifferentiated FTC-133 cells after long-term RPM-exposure (Figure 8) [6]. The exact mechanisms behind this transformation are still unknown. After 7 and 14 days, expression of angiogenic factors like VEGF-A was significantly down-regulated, whereas the expression of apoptotic factors was increased. This suggested that exposure to simulated μ*g* enabled selective programmed cell death, which identified the cells more differentiated compared to those grown under normal conditions [6]. Similar results were obtained from the SimBox/Shenzhou-8 mission when FTC-133 cells were cultured on an unmanned spacecraft for two weeks. Space-flown cells were shifted towards a less-malignant phenotype by down-regulation of *VEGFA* and up-regulation of *VEGFD* and *IL15* [48]. *IL6*, *CXCL8*, *SPP1*, *PRKAA* and *PRKCA* mRNAs were all reduced both in adherent cells and MCS grown in space. As VEGF-A was found increased and VEGF-D serum levels were reported to be reduced in patients suffering from high-stage thyroid cancer [93,94], the authors concluded that μ*g* possibly triggers some antitumor pathways involving IL-15 [48]. Consistent with these results a down-regulation of *VEGFA* was also found in the space-flown cells after the CellBox-2 mission, whereas the mRNA level of *VEGFA* stayed rather constant during a respective RPM experiment [54]. This VEGF discrepancy was often observed when results of simulated μ*g* experiments were compared with data from real μ*g* studies. Here it should be noted that VEGF gene expression is also up-regulated by the cells as a result of mechanical stress. It may be that fluid shear stress caused by random positioning [19,95,96] contributed to higher *VEGFA* mRNA levels of the RPM samples. In contrast to the space studies, the short-term exposure to real μ*g* during a parabolic flight suggested an increased malignancy of the FTC-133 cells [48].

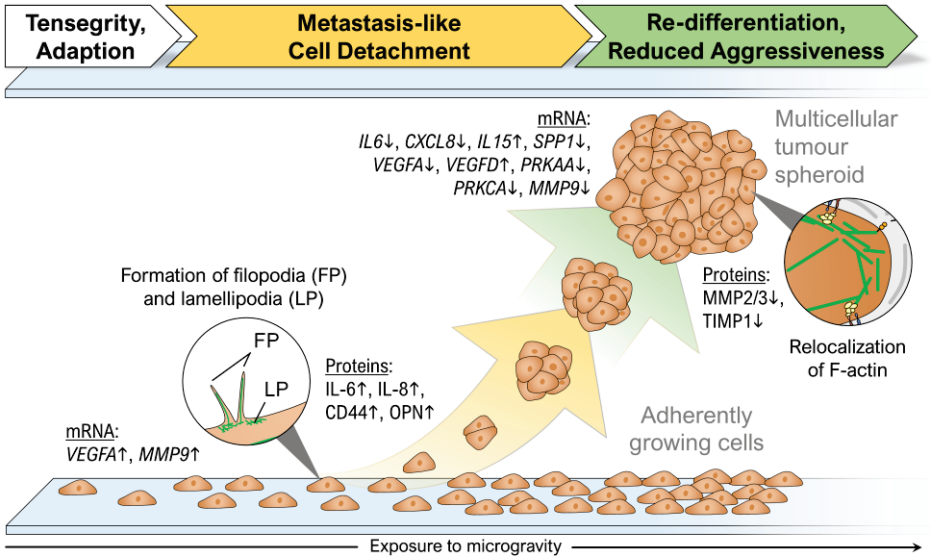


Figure 8. From metastasis-like cell detachment to lower aggressiveness: the transformation of thyroid cancer cells during their exposure to microgravity. The green lines show F-actin filaments. ↓ down-regulation/decrease, ↑ up-regulation/increase.

4.4. Drug Targeting

Using proteome analysis, Pietsch et al. [97] were able to detect the expression of 37 proteins previously not found in thyroid cells. Of special interest is the plastin-2, which plays a crucial role in the development of thyroid tumours, as well as the interferon-induced 17 kDa protein precursor, which is coded by the *ISG15* gene [42]. This protein may be conjugated to target proteins by the E1 and E2 enzymes. Of the more than 150 yet known target proteins [98], we found 71 in the thyroid cells investigated [42]. During incubation on the RPM the protein's accumulation decreased [45,56]. However, when mRNA expression was analyzed, after thyroid cells had been cultured for 10 days in space or on the RPM, a considerable up-regulation of the gene expression was observed [42,48,63]. ISG15 plays a role in antiviral immunity [99]. Recently a drug (Q63) was described, which exerted antiviral activity by down-regulation of ISG15 [100]. Even in cancer research ISG15 has attracted attention. It was recognized to be a prognostic marker in human breast cancer [101]. Studies on MCF7 cells suggested that the protein plays a role in stabilization of MCS generated on an RPM [65]. How the latter findings apply to thyroid cancer remains to be determined.

Bauer et al. [59] detected 69 proteins, which are significantly accumulated in thyroid cancer cells in the transition from 2D cell growth in normal gravity to spheroid growth in μ*g*. These factors seem to be part of an overarching mechanism and therefore they are very interesting candidates for targeted tumour therapy. Reduction or inhibition of metastasis by knock-down or knock-out of one of these factors would decisively improve cancer therapy as well as patient survival. After the exploratory phase researchers have now begun with the functional analysis of previously detected genes. Using pharmacological targeting or silencing of individual genes, they are able to inhibit selected signalling pathways. MCF-7 breast cancer cells which were incubated with the NFκB inhibitor dexamethasone showed dose-dependent inhibition of spheroid formation [37]. The artificial glucocorticoid dexamethasone functionally inhibits NFκB and NFκB-dependent gene expression. Based on these results in μ*g* research, it was proved that NFκB plays a crucial role in spheroid formation in breast cancer tumours. Further studies with the Src inhibitor PP2 and an anti-E-cadherin antibody also showed an influence on the spheroid formation of MCF-7 cells [65]. While the presence of PP2 completely inhibited spheroids, the E-cadherin antibody stimulated the formation of 3D structures. Both drugs had no effect on cell viability and all cells survived after pharmacological intervention.

Similar attempts are planned for thyroid cancer research in the near future. The pharmacological substances that appear to be suitable are listed in Table 4.

Table 4. Potential drugs targeting the proteins that were found to be influenced by μ*g*.

Drug	Target	Ref.
PP2 (4-amino-5-(4-chlorophenyl)-7-(dimethylethyl) pyrazolo[3,4-d]pyrimidine)	Proto-oncogene tyrosine-protein kinase Src	[102]
Daidzein	Caveolin-1	[103]
Camptothecin	Ubiquitin-like protein ISG15	[104]
SP600125	Mitogen-activated protein kinase 8	[105]
mNOX-E36	C-C motif chemokine 2	[106]
Dexamethasone, BAY 11-7082	NFκB p65	[107]
GSK2256098, MPAP	Focal adhesion kinase 1	[108]
MT189	Paxillin	[109]
Baicalein	Ezrin	[110]
Curcumin	HMOX-1	[111]
DX52-1	Radixin	[112]
TM5441	Plasminogen activator inhibitor 1	[113]
UK370106	Stromelysin, (MMP3)	[114]
Oseltamivir	Sialidase	[115]

5. Summary and Perspectives

Microgravity alters growth, cell adhesion, migration, proliferation, the cytoskeleton, extracellular matrix and focal adhesion of human cells in vitro. A large number of differentially regulated genes and altered protein synthesis and secretion are detectable in benign and malignant cells exposed to real or simulated μ*g*. The model system 'Multicellular Spheroid' is suitable to mimic metastasis of solid tumours and can be used for drug testing in pharmacology or as a coculture model to study processes like metastasis or angiogenesis. The investigation of the underlying mechanisms of spheroid formation also delivers valuable information about the in vivo cancer progression and metastasis.

Research in the fields of space medicine and gravitational biology makes it possible to find new proteins in organ tissues and changes in protein synthesis and secretion. Altered gravity conditions provide a new technology which is helpful to detect changes in proteins which may represent new targets for drug development in cancer. A large number of proteins which may serve as promising targets and available drugs are listed in Table 4. In order to address cancer growth and regulation, further μ*g* studies should be performed. We recently investigated changes of SOX transcription factors on FTC-133 follicular thyroid cancer cells exposed to the RPM and determined the mRNA expression of *SOX9* and *SOX11* in adherently growing and MCS cells [47]. The SOX family is involved in the progression and metastasis of cancer cells. Its expression in thyroid cancer is not clarified until today and requires further investigation. Studies focusing on the role of SOX family members and in particular the SoxF group in radioactive iodine-refractory differentiated thyroid cancer cells are of high interest. Recent results in the field of cancer research in μ*g* taught us that focal adhesions play an important role in the inhibition of proliferation and metastasis in melanoma cells [81]. Therefore, intensive research in thyroid cancer investigating focal adhesions should be performed in μ*g* by applying live-cell imaging with the FLUMIAS microscope [49] onboard the ISS or on sounding rockets.

Microgravity research is just one part of cancer research but might enable a significant step toward better treatments. Some years ago, with the help of simulated μ*g* various proteins were detected in thyroid tissue for the first time [97]. Some of them are targeted today. In addition, the compounds

given in Table 4 are currently under investigation. The results may truly provide hope for thyroid cancer patients.

Author Contributions: All authors contributed to the review and searched literature. Conceptualization, M.K. and D.G.; Investigation, D.M., C.B., J.S. and T.J.C.; writing—original draft preparation, M.K., J.B. and D.G.; review and editing. M.K., D.G., R.H. and J.B.; visualization, M.K., J.B. and S.K.; project administration, D.G.; funding acquisition, D.G., M.I., R.H.

Funding: This research was funded by the German Space Agency (DLR, grants 50WB1124, 50WB1524 and 50WB1924), by the Otto von Guericke University Magdeburg, Germany and by the Aarhus University, Denmark.

Acknowledgments: We would like to thank Markus Braun and Michael Becker from the German Aerospace Center (DLR, Bonn) for supporting our studies for many years. We also thank the engineers of Airbus Defence and Space for developing the perfect hardware for our spaceflights and sounding rocket flights and for their wonderful support. Last but not least we would like to thank the team of PRS & EJE (Letchworth Garden City, UK) for academic proofreading of the manuscript.

Conflicts of Interest: The authors declare no conflict of interest.

Abbreviations

2D	Two-dimensional
3D	Three-dimensional
ACTB	β-Actin
AD	Adherent cells
AMPK	5′Adenosine monophosphate-activated protein kinase
CAV1/2	Caveolin-1, -2,
CD44	Cluster of differentiation 44
CTGF	Connective tissue growth factor
CXCL	C-X-C motif
ECM	Extracellular matrix
EGF	Epidermal growth factor
ERK1/2	Extracellular signal-regulated kinase 1,2
FGF17	Fibroblast growth factor 17
FLK1	Fetal liver kinase 1
FLUMIAS	Fluorescence-microscopic analysis systems for space application
FLT1	Fms-related tyrosine kinase 1
FN1	Fibronectin
FRC	Fast-rotating clinostat
IL	Interleukin
KDR	Kinase insert domain receptor
MCS	Multicellular spheroid
MMP	Matrix metalloproteinase
μg	Microgravity
Nek2	Serine/threonine-protein kinase Nek2
NFκB	Nuclear factor κ-light-chain-enhancer of activated B cells
OPN	Osteopontin
PRKAA	Protein kinase, AMP-activated, α catalytic subunit
PRKCA	Protein kinase Cα
RhoA	Ras homolog gene family, member A
RPM	Random positioning machine
RWV	Rotating wall vessel
SOX	Sex determining region Y-related high-mobility group box proteins
TGF-β	Transforming growth factor β
TIMP1	Tissue inhibitor of metalloproteinases 1
TLN1	Talin 1
TSH	Thyroid-stimulating hormone
TUBB	β-tubulin
VEGF	Vascular endothelial growth factor

References

1. Becker, J.L.; Souza, G.R. Using space-based investigations to inform cancer research on earth. *Nat. Rev. Cancer* **2013**, *13*, 315–327. [CrossRef]
2. Jhala, D.V.; Kale, R.K.; Singh, R.P. Microgravity alters cancer growth and progression. *Curr. Cancer Drug Targets* **2014**, *14*, 394–406. [CrossRef] [PubMed]
3. Hammond, T.G.; Benes, E.; O'Reilly, K.C.; Wolf, D.A.; Linnehan, R.M.; Taher, A.; Kaysen, J.H.; Allen, P.L.; Goodwin, T.J. Mechanical culture conditions effect gene expression: Gravity-induced changes on the space shuttle. *Physiol. Genom.* **2000**, *3*, 163–173. [CrossRef] [PubMed]
4. Duval, K.; Grover, H.; Han, L.-H.; Mou, Y.; Pegoraro, A.F.; Fredberg, J.; Chen, Z. Modeling physiological events in 2d vs. 3d cell culture. *Physiology* **2017**, *32*, 266–277. [CrossRef]
5. Groebe, K.; Mueller-Klieser, W. On the relation between size of necrosis and diameter of tumor spheroids. *Int. J. Radiat. Oncol. Biol. Phys.* **1996**, *34*, 395–401. [CrossRef]
6. Kopp, S.; Warnke, E.; Wehland, M.; Aleshcheva, G.; Magnusson, N.E.; Hemmersbach, R.; Corydon, T.J.; Bauer, J.; Infanger, M.; Grimm, D. Mechanisms of three-dimensional growth of thyroid cells during long-term simulated microgravity. *Sci. Rep.* **2015**, *5*, 16691. [CrossRef]
7. Aleshcheva, G.; Bauer, J.; Hemmersbach, R.; Slumstrup, L.; Wehland, M.; Infanger, M.; Grimm, D. Scaffold-free tissue formation under real and simulated microgravity conditions. *Basic Clin. Pharmacol. Toxicol.* **2016**, *119*, 26–33. [CrossRef]
8. Zanoni, M.; Piccinini, F.; Arienti, C.; Zamagni, A.; Santi, S.; Polico, R.; Bevilacqua, A.; Tesei, A. 3d tumor spheroid models for in vitro therapeutic screening: A systematic approach to enhance the biological relevance of data obtained. *Sci. Rep.* **2016**, *6*, 19103. [CrossRef]
9. Al-Ramadan, A.; Mortensen, A.C.; Carlsson, J.; Nestor, M.V. Analysis of radiation effects in two irradiated tumor spheroid models. *Oncol. Lett.* **2018**, *15*, 3008–3016. [CrossRef] [PubMed]
10. La Vecchia, C.; Malvezzi, M.; Bosetti, C.; Garavello, W.; Bertuccio, P.; Levi, F.; Negri, E. Thyroid cancer mortality and incidence: A global overview. *Int. J. Cancer* **2015**, *136*, 2187–2195. [CrossRef]
11. Bray, F.; Ferlay, J.; Soerjomataram, I.; Siegel, R.L.; Torre, L.A.; Jemal, A. Global cancer statistics 2018: Globocan estimates of incidence and mortality worldwide for 36 cancers in 185 countries. *CA Cancer J. Clin.* **2018**, *68*, 394–424. [CrossRef]
12. Albi, E.; Krüger, M.; Hemmersbach, R.; Lazzarini, A.; Cataldi, S.; Codini, M.; Beccari, T.; Ambesi-Impiombato, F.S.; Curcio, F. Impact of gravity on thyroid cells. *Int. J. Mol. Sci.* **2017**, *18*, 972. [CrossRef] [PubMed]
13. Braddock, M. From target identification to drug development in space: Using the microgravity assist. *Curr. Drug Discov. Technol.* **2019**. [CrossRef]
14. Eiermann, P.; Kopp, S.; Hauslage, J.; Hemmersbach, R.; Gerzer, R.; Ivanova, K. Adaptation of a 2-d clinostat for simulated microgravity experiments with adherent cells. *Microgravity Sci. Technol.* **2013**, *25*, 153–159. [CrossRef]
15. Klaus, D.M. Clinostats and bioreactors. *Gravit. Space Biol. Bull.* **2001**, *14*, 55–64.
16. Borst, A.G.; van Loon, J.J.W.A. Technology and developments for the random positioning machine, rpm. *Microgravity Sci. Technol.* **2008**, *21*, 287. [CrossRef]
17. van Loon, J.J.W.A. Some history and use of the random positioning machine, rpm, in gravity related research. *Adv. Space Res.* **2007**, *39*, 1161–1165. [CrossRef]
18. Herranz, R.; Anken, R.; Boonstra, J.; Braun, M.; Christianen, P.C.; de Geest, M.; Hauslage, J.; Hilbig, R.; Hill, R.J.; Lebert, M.; et al. Ground-based facilities for simulation of microgravity: Organism-specific recommendations for their use and recommended terminology. *Astrobiology* **2013**, *13*, 1–17. [CrossRef]
19. Wuest, S.L.; Richard, S.; Kopp, S.; Grimm, D.; Egli, M. Simulated microgravity: Critical review on the use of random positioning machines for mammalian cell culture. *Biomed. Res. Int.* **2015**, *2015*, 971474. [CrossRef]
20. Albi, E.; Curcio, F.; Lazzarini, A.; Floridi, A.; Cataldi, S.; Lazzarini, R.; Loreti, E.; Ferri, I.; Ambesi-Impiombato, F.S. How microgravity changes galectin-3 in thyroid follicles. *Biomed. Res. Int* **2014**, *2014*, 5. [CrossRef]
21. Masini, M.A.; Albi, E.; Barmo, C.; Bonfiglio, T.; Bruni, L.; Canesi, L.; Cataldi, S.; Curcio, F.; D'Amora, M.; Ferri, I.; et al. The impact of long-term exposure to space environment on adult mammalian organisms: A study on mouse thyroid and testis. *PLoS ONE* **2012**, *7*, e35418. [CrossRef] [PubMed]

22. Albi, E.; Ambesi-Impiombato, F.S.; Peverini, M.; Damaskopoulou, E.; Fontanini, E.; Lazzarini, R.; Curcio, F.; Perrella, G. Thyrotropin receptor and membrane interactions in frtl-5 thyroid cell strain in microgravity. *Astrobiology* **2011**, *11*, 57–64. [CrossRef] [PubMed]
23. Kossmehl, P.; Shakibaei, M.; Cogoli, A.; Infanger, M.; Curcio, F.; Schönberger, J.; Eilles, C.; Bauer, J.; Pickenhahn, H.; Schulze-Tanzil, G.; et al. Weightlessness induced apoptosis in normal thyroid cells and papillary thyroid carcinoma cells via extrinsic and intrinsic pathways. *Endocrinology* **2003**, *144*, 4172–4179. [CrossRef] [PubMed]
24. Martin, A.; Zhou, A.; Gordon, R.E.; Henderson, S.C.; Schwartz, A.E.; Schwartz, A.E.; Friedman, E.W.; Davies, T.F. Thyroid organoid formation in simulated microgravity: Influence of keratinocyte growth factor. *Thyroid* **2000**, *10*, 481–487. [CrossRef]
25. Warnke, E.; Kopp, S.; Wehland, M.; Hemmersbach, R.; Bauer, J.; Pietsch, J.; Infanger, M.; Grimm, D. Thyroid cells exposed to simulated microgravity conditions – comparison of the fast rotating clinostat and the random positioning machine. *Microgravity Sci. Technol.* **2016**, *28*, 247–260. [CrossRef]
26. Warnke, E.; Pietsch, J.; Kopp, S.; Bauer, J.; Sahana, J.; Wehland, M.; Krüger, M.; Hemmersbach, R.; Infanger, M.; Lützenberg, R.; et al. Cytokine release and focal adhesion proteins in normal thyroid cells cultured on the random positioning machine. *Cell Physiol. Biochem.* **2017**, *43*, 257–270. [CrossRef] [PubMed]
27. Curcio, F.; Ambesi-Impiombato, F.S.; Perrella, G.; Coon, H.G. Long-term culture and functional characterization of follicular cells from adult normal human thyroids. *Proc. Natl. Acad. Sci. USA* **1994**, *91*, 9004–9008. [CrossRef]
28. Lewis, M.L.; Reynolds, J.L.; Cubano, L.A.; Hatton, J.P.; Lawless, B.D.; Piepmeier, E.H. Spaceflight alters microtubules and increases apoptosis in human lymphocytes (jurkat). *FASEB J.* **1998**, *12*, 1007–1018. [CrossRef]
29. Uva, B.M.; Masini, M.A.; Sturla, M.; Bruzzone, F.; Giuliani, M.; Tagliafierro, G.; Strollo, F. Microgravity-induced apoptosis in cultured glial cells. *Eur. J. Histochem.* **2002**, *46*, 209–214. [CrossRef]
30. Battista, N.; Meloni, M.A.; Bari, M.; Mastrangelo, N.; Galleri, G.; Rapino, C.; Dainese, E.; Agro, A.F.; Pippia, P.; Maccarrone, M. 5-lipoxygenase-dependent apoptosis of human lymphocytes in the international space station: Data from the roald experiment. *FASEB J.* **2012**, *26*, 1791–1798. [CrossRef]
31. Infanger, M.; Kossmehl, P.; Shakibaei, M.; Baatout, S.; Witzing, A.; Grosse, J.; Bauer, J.; Cogoli, A.; Faramarzi, S.; Derradji, H.; et al. Induction of three-dimensional assembly and increase in apoptosis of human endothelial cells by simulated microgravity: Impact of vascular endothelial growth factor. *Apoptosis* **2006**, *11*, 749–764. [CrossRef] [PubMed]
32. Lemoine, N.R.; Mayall, E.S.; Jones, T.; Sheer, D.; McDermid, S.; Kendall-Taylor, P.; Wynford-Thomas, D. Characterisation of human thyroid epithelial cells immortalised in vitro by simian virus 40 DNA transfection. *Br. J. Cancer* **1989**, *60*, 897–903. [CrossRef] [PubMed]
33. Vistejnova, L.; Safrankova, B.; Nesporova, K.; Slavkovsky, R.; Hermannova, M.; Hosek, P.; Velebny, V.; Kubala, L. Low molecular weight hyaluronan mediated cd44 dependent induction of il-6 and chemokines in human dermal fibroblasts potentiates innate immune response. *Cytokine* **2014**, *70*, 97–103. [CrossRef] [PubMed]
34. Razidlo, G.L.; Burton, K.M.; McNiven, M.A. Interleukin-6 promotes pancreatic cancer cell migration by rapidly activating the small gtpase cdc42. *J. Biol. Chem.* **2018**, *293*, 11143–11153. [CrossRef] [PubMed]
35. Grimm, D.; Kossmehl, P.; Shakibaei, M.; Schulze-Tanzil, G.; Pickenhahn, H.; Bauer, J.; Paul, M.; Cogoli, A. Effects of simulated microgravity on thyroid carcinoma cells. *Life Space Life Earth* **2002**, *501*, 39–42.
36. Kossmehl, P.; Shakibaei, M.; Cogoli, A.; Pickenhahn, H.; Paul, M.; Grimm, D. Simulated microgravity induces programmed cell death in human thyroid carcinoma cells. *J. Gravit. Physiol.* **2002**, *9*, 295–296. [PubMed]
37. Kopp, S.; Sahana, J.; Islam, T.; Petersen, A.G.; Bauer, J.; Corydon, T.J.; Schulz, H.; Saar, K.; Huebner, N.; Slumstrup, L.; et al. The role of nfkappab in spheroid formation of human breast cancer cells cultured on the random positioning machine. *Sci. Rep.* **2018**, *8*, 921. [CrossRef]
38. Infanger, M.; Kossmehl, P.; Shakibaei, M.; Schulze-Tanzil, G.; Cogoli, A.; Faramarzi, S.; Bauer, J.; Curcio, F.; Paul, M.; Grimm, D. Longterm conditions of mimicked weightlessness influences the cytoskeleton in thyroid cells. *J. Gravit. Physiol.* **2004**, *11*, P169–P172.
39. Ulbrich, C.; Pietsch, J.; Grosse, J.; Wehland, M.; Schulz, H.; Saar, K.; Hübner, N.; Hauslage, J.; Hemmersbach, R.; Braun, M.; et al. Differential gene regulation under altered gravity conditions in follicular thyroid cancer cells: Relationship between the extracellular matrix and the cytoskeleton. *Cell Physiol. Biochem.* **2011**, *28*, 185–198. [CrossRef]

40. Infanger, M.; Kossmehl, P.; Shakibaei, M.; Bauer, J.; Kossmehl-Zorn, S.; Cogoli, A.; Curcio, F.; Oksche, A.; Wehland, M.; Kreutz, R.; et al. Simulated weightlessness changes the cytoskeleton and extracellular matrix proteins in papillary thyroid carcinoma cells. *Cell Tissue Res.* **2006**, *324*, 267–277. [CrossRef]
41. Vorselen, D.; Roos, W.H.; MacKintosh, F.C.; Wuite, G.J.; van Loon, J.J. The role of the cytoskeleton in sensing changes in gravity by nonspecialized cells. *FASEB J.* **2014**, *28*, 536–547. [CrossRef]
42. Bauer, J.; Wehland, M.; Pietsch, J.; Sickmann, A.; Weber, G.; Grimm, D. Annotated gene and proteome data support recognition of interconnections between the results of different experiments in space research. *Microgravity Sci. Technol.* **2016**, *28*, 357–365. [CrossRef]
43. Riwaldt, S.; Bauer, J.; Wehland, M.; Slumstrup, L.; Kopp, S.; Warnke, E.; Dittrich, A.; Magnusson, N.E.; Pietsch, J.; Corydon, T.J.; et al. Pathways regulating spheroid formation of human follicular thyroid cancer cells under simulated microgravity conditions: A genetic approach. *Int. J. Mol. Sci.* **2016**, *17*, 528. [CrossRef]
44. Pietsch, J.; Sickmann, A.; Weber, G.; Bauer, J.; Egli, M.; Wildgruber, R.; Infanger, M.; Grimm, D. A proteomic approach to analysing spheroid formation of two human thyroid cell lines cultured on a random positioning machine. *Proteomics* **2011**, *11*, 2095–2104. [CrossRef]
45. Bauer, J.; Kopp, S.; Schlagberger, E.M.; Grosse, J.; Sahana, J.; Riwaldt, S.; Wehland, M.; Luetzenberg, R.; Infanger, M.; Grimm, D. Proteome analysis of human follicular thyroid cancer cells exposed to the random positioning machine. *Int. J. Mol. Sci.* **2017**, *18*, 546. [CrossRef]
46. Warnke, E.; Pietsch, J.; Wehland, M.; Bauer, J.; Infanger, M.; Görög, M.; Hemmersbach, R.; Braun, M.; Ma, X.; Sahana, J.; et al. Spheroid formation of human thyroid cancer cells under simulated microgravity: A possible role of ctgf and cav1. *Cell Commun. Signal.* **2014**, *12*, 32. [CrossRef]
47. Grimm, D.; Bauer, J.; Wise, P.; Krüger, M.; Simonsen, U.; Wehland, M.; Infanger, M.; Corydon, T.J. The role of sox family members in solid tumours and metastasis. *Semin. Cancer Biol.* **2019**. [CrossRef]
48. Ma, X.; Pietsch, J.; Wehland, M.; Schulz, H.; Saar, K.; Hübner, N.; Bauer, J.; Braun, M.; Schwarzwälder, A.; Segerer, J.; et al. Differential gene expression profile and altered cytokine secretion of thyroid cancer cells in space. *FASEB J.* **2014**, *28*, 813–835. [CrossRef]
49. Corydon, T.J.; Kopp, S.; Wehland, M.; Braun, M.; Schutte, A.; Mayer, T.; Hulsing, T.; Oltmann, H.; Schmitz, B.; Hemmersbach, R.; et al. Alterations of the cytoskeleton in human cells in space proved by life-cell imaging. *Sci. Rep.* **2016**, *6*, 20043. [CrossRef]
50. Kopp, S.; Krüger, M.; Feldmann, S.; Oltmann, H.; Schütte, A.; Schmitz, B.; Bauer, J.; Schulz, H.; Saar, K.; Huebner, N.; et al. Thyroid cancer cells in space during the TEXUS-53 sounding rocket mission-the thyroid project. *Sci. Rep.* **2018**, *8*, 10355. [CrossRef]
51. Kopp, S.; Krüger, M.; Bauer, J.; Wehland, M.; Corydon, T.J.; Sahana, J.; Nassef, M.Z.; Melnik, D.; Bauer, T.J.; Schulz, H.; et al. Microgravity affects thyroid cancer cells during the TEXUS-53 mission stronger than hypergravity. *Int. J. Mol. Sci.* **2018**, *19*, 4001. [CrossRef] [PubMed]
52. Riwaldt, S.; Bauer, J.; Pietsch, J.; Braun, M.; Segerer, J.; Schwarzwälder, A.; Corydon, T.J.; Infanger, M.; Grimm, D. The importance of caveolin-1 as key-regulator of three-dimensional growth in thyroid cancer cells cultured under real and simulated microgravity conditions. *Int. J. Mol. Sci.* **2015**, *16*, 28296–28310. [CrossRef]
53. Riwaldt, S.; Pietsch, J.; Sickmann, A.; Bauer, J.; Braun, M.; Segerer, J.; Schwarzwälder, A.; Aleshcheva, G.; Corydon, T.J.; Infanger, M.; et al. Identification of proteins involved in inhibition of spheroid formation under microgravity. *Proteomics* **2015**, *15*, 2945–2952. [CrossRef]
54. Melnik, D.; Krüger, M.; Kopp, S.; Wehland, M.; Bauer, J.; Infanger, M.; Grimm, D. Microgravity-based modulation of VEGF expression in human thyroid carcinoma cells. *Front. Physiol.* **2019**, *9*. [CrossRef]
55. Pietsch, J.; Riwaldt, S.; Bauer, J.; Sickmann, A.; Weber, G.; Grosse, J.; Infanger, M.; Eilles, C.; Grimm, D. Interaction of proteins identified in human thyroid cells. *Int. J. Mol. Sci.* **2013**, *14*, 1164–1178. [CrossRef] [PubMed]
56. Pietsch, J.; Bauer, J.; Weber, G.; Nissum, M.; Westphal, K.; Egli, M.; Grosse, J.; Schönberger, J.; Eilles, C.; Infanger, M.; et al. Proteome analysis of thyroid cancer cells after long-term exposure to a random positioning machine. *Microgravity Sci. Technol.* **2011**, *23*, 381–390. [CrossRef]
57. Pietsch, J.; Sickmann, A.; Weber, G.; Bauer, J.; Egli, M.; Wildgruber, R.; Infanger, M.; Grimm, D. Metabolic enzyme diversity in different human thyroid cell lines and their sensitivity to gravitational forces. *Proteomics* **2012**, *12*, 2539–2546. [CrossRef] [PubMed]
58. Bauer, J.; Grimm, D.; Gombocz, E. Semantic analysis of thyroid cancer cell proteins obtained from rare research opportunities. *J. Biomed. Inform.* **2017**, *76*, 138–153. [CrossRef]

59. Bauer, J.; Wehland, M.; Infanger, M.; Grimm, D.; Gombocz, E. Semantic analysis of posttranslational modification of proteins accumulated in thyroid cancer cells exposed to simulated microgravity. *Int. J. Mol. Sci.* **2018**, *19*, 2257. [CrossRef]
60. Bauer, J.; Cohly, H.H.P.; Sahana, J.; Grimm, D. Preparative enrichment of human tissue cells capable to change a site of growth in vitro or in vivo-recent developments. *Prep. Biochem. Biotechnol.* **2018**, *48*, 954–960. [CrossRef]
61. Grosse, J.; Wehland, M.; Pietsch, J.; Schulz, H.; Saar, K.; Hübner, N.; Eilles, C.; Bauer, J.; Abou-El-Ardat, K.; Baatout, S.; et al. Gravity-sensitive signaling drives 3-dimensional formation of multicellular thyroid cancer spheroids. *FASEB J.* **2012**, *26*, 5124–5140. [CrossRef]
62. Kunz-Schughart, L.A. Multicellular tumor spheroids: Intermediates between monolayer culture and in vivo tumor. *Cell Biol. Int.* **1999**, *23*, 157–161. [CrossRef]
63. Pietsch, J.; Ma, X.; Wehland, M.; Aleshcheva, G.; Schwarzwälder, A.; Segerer, J.; Birlem, M.; Horn, A.; Bauer, J.; Infanger, M.; et al. Spheroid formation of human thyroid cancer cells in an automated culturing system during the shenzhou-8 space mission. *Biomaterials* **2013**, *34*, 7694–7705. [CrossRef]
64. Svejgaard, B.; Wehland, M.; Ma, X.; Kopp, S.; Sahana, J.; Warnke, E.; Aleshcheva, G.; Hemmersbach, R.; Hauslage, J.; Grosse, J.; et al. Common effects on cancer cells exerted by a random positioning machine and a 2d clinostat. *PLoS ONE* **2015**, *10*, e0135157. [CrossRef]
65. Sahana, J.; Nassef, M.Z.; Wehland, M.; Kopp, S.; Krüger, M.; Corydon, T.J.; Infanger, M.; Bauer, J.; Grimm, D. Decreased e-cadherin in mcf7 human breast cancer cells forming multicellular spheroids exposed to simulated microgravity. *Proteomics* **2018**, *18*, e1800015. [CrossRef]
66. Kunz-Schughart, L.A.; Freyer, J.P.; Hofstaedter, F.; Ebner, R. The use of 3-d cultures for high-throughput screening: The multicellular spheroid model. *J. Biomol. Screen* **2004**, *9*, 273–285. [CrossRef]
67. Willis, R.A. Metastatic tumours in the thyreoid gland. *Am. J. Pathol.* **1931**, *7*, 187–208.183.
68. Schmidbauer, B.; Menhart, K.; Hellwig, D.; Grosse, J. Differentiated thyroid cancer-treatment: State of the art. *Int. J. Mol. Sci.* **2017**, *18*, 1292. [CrossRef]
69. Wang, L.Y.; Palmer, F.L.; Nixon, I.J.; Thomas, D.; Patel, S.G.; Shaha, A.R.; Shah, J.P.; Tuttle, R.M.; Ganly, I. Multi-organ distant metastases confer worse disease-specific survival in differentiated thyroid cancer. *Thyroid* **2014**, *24*, 1594–1599. [CrossRef]
70. Parameswaran, R.; Shulin Hu, J.; Min En, N.; Tan, W.B.; Yuan, N.K. Patterns of metastasis in follicular thyroid carcinoma and the difference between early and delayed presentation. *Ann. R. Coll. Surg. Engl.* **2017**, *99*, 151–154. [CrossRef]
71. Rosa, M. Cytological features of medullary thyroid carcinoma in ascitic effusion. *Diagn Cytopathol.* **2017**, *45*, 1030–1032. [CrossRef]
72. Al Habyan, S.; Kalos, C.; Szymborski, J.; McCaffrey, L. Multicellular detachment generates metastatic spheroids during intra-abdominal dissemination in epithelial ovarian cancer. *Oncogene* **2018**, *37*, 5127–5135. [CrossRef]
73. Mueller-Klieser, W. Multicellular spheroids. A review on cellular aggregates in cancer research. *J. Cancer Res. Clin. Oncol.* **1987**, *113*, 101–122. [CrossRef]
74. Hamilton, G. Multicellular spheroids as an in vitro tumor model. *Cancer Lett.* **1998**, *131*, 29–34. [CrossRef]
75. Northcott, J.M.; Dean, I.S.; Mouw, J.K.; Weaver, V.M. Feeling stress: The mechanics of cancer progression and aggression. *Front. Cell Dev. Biol.* **2018**, *6*, 17. [CrossRef]
76. Butcher, D.T.; Alliston, T.; Weaver, V.M. A tense situation: Forcing tumour progression. *Nat. Rev. Cancer* **2009**, *9*, 108–122. [CrossRef]
77. Yu, H.; Mouw, J.K.; Weaver, V.M. Forcing form and function: Biomechanical regulation of tumor evolution. *Trends Cell Biol.* **2011**, *21*, 47–56. [CrossRef]
78. Ingber, D.E.; Wang, N.; Stamenovic, D. Tensegrity, cellular biophysics and the mechanics of living systems. *Rep. Prog. Phys.* **2014**, *77*, 046603. [CrossRef]
79. Ingber, D. How cells (might) sense microgravity. *FASEB J.* **1999**, *13*, 3–15. [CrossRef]
80. Dittrich, A.; Grimm, D.; Sahana, J.; Bauer, J.; Krüger, M.; Infanger, M.; Magnusson, N.E. Key proteins involved in spheroid formation and angiogenesis in endothelial cells after long-term exposure to simulated microgravity. *Cell Physiol. Biochem.* **2018**, *45*, 429–445. [CrossRef]

81. Tan, X.; Xu, A.; Zhao, T.; Zhao, Q.; Zhang, J.; Fan, C.; Deng, Y.; Freywald, A.; Genth, H.; Xiang, J. Simulated microgravity inhibits cell focal adhesions leading to reduced melanoma cell proliferation and metastasis via fak/rhoa-regulated mtorc1 and ampk pathways. *Sci. Rep.* **2018**, *8*, 3769. [CrossRef] [PubMed]
82. Zhao, T.; Li, R.; Tan, X.; Zhang, J.; Fan, C.; Zhao, Q.; Deng, Y.; Xu, A.; Lukong, K.E.; Genth, H.; et al. Simulated microgravity reduces focal adhesions and alters cytoskeleton and nuclear positioning leading to enhanced apoptosis via suppressing fak/rhoa-mediated mtorc1/nf-kappab and ERK1/2 pathways. *Int. J. Mol. Sci.* **2018**, *19*, 1994. [CrossRef]
83. Deng, B.; Liu, R.; Tian, X.; Han, Z.; Chen, J. Simulated microgravity inhibits the viability and migration of glioma via fak/rhoa/rock and fak/nek2 signaling. *In Vitro Cell Dev. Biol. Anim.* **2019**, *55*, 260–271. [CrossRef] [PubMed]
84. Chang, D.; Xu, H.; Guo, Y.; Jiang, X.; Liu, Y.; Li, K.; Pan, C.; Yuan, M.; Wang, J.; Li, T.; et al. Simulated microgravity alters the metastatic potential of a human lung adenocarcinoma cell line. *In Vitro Cell Dev. Biol. Anim.* **2013**, *49*, 170–177. [CrossRef] [PubMed]
85. Yamaguchi, H.; Condeelis, J. Regulation of the actin cytoskeleton in cancer cell migration and invasion. *Biochim. Biophys. Acta* **2007**, *1773*, 642–652. [CrossRef] [PubMed]
86. Ding, Z.; Joy, M.; Bhargava, R.; Gunsaulus, M.; Lakshman, N.; Miron-Mendoza, M.; Petroll, M.; Condeelis, J.; Wells, A.; Roy, P. Profilin-1 downregulation has contrasting effects on early vs late steps of breast cancer metastasis. *Oncogene* **2014**, *33*, 2065–2074. [CrossRef]
87. Miao, J.W.; Liu, L.J.; Huang, J. Interleukin-6-induced epithelial-mesenchymal transition through signal transducer and activator of transcription 3 in human cervical carcinoma. *Int. J. Oncol.* **2014**, *45*, 165–176. [CrossRef]
88. Klassen, L.M.B.; Chequin, A.; Manica, G.C.M.; Biembengut, I.V.; Toledo, M.B.; Baura, V.A.; de, O.P.F.; Ramos, E.A.S.; Costa, F.F.; de Souza, E.M.; et al. *Mmp9* gene expression regulation by intragenic epigenetic modifications in breast cancer. *Gene* **2018**, *642*, 461–466. [CrossRef]
89. Wai, P.Y.; Kuo, P.C. Osteopontin: Regulation in tumor metastasis. *Cancer Metastasis Rev.* **2008**, *27*, 103–118. [CrossRef]
90. Luca, M.; Huang, S.; Gershenwald, J.E.; Singh, R.K.; Reich, R.; Bar-Eli, M. Expression of interleukin-8 by human melanoma cells up-regulates mmp-2 activity and increases tumor growth and metastasis. *Am. J. Pathol.* **1997**, *151*, 1105–1113.
91. Liu, W.; Xu, J.; Wang, M.; Wang, Q.; Bi, Y.; Han, M. Tumor-derived vascular endothelial growth factor (vegf)-a facilitates tumor metastasis through the vegf-vegfr1 signaling pathway. *Int. J. Oncol.* **2011**, *39*, 1213–1220. [CrossRef] [PubMed]
92. Sottnik, J.L.; Theodorescu, D. Cd44: A metastasis driver and therapeutic target. *Oncoscience* **2016**, *3*, 320–321. [CrossRef] [PubMed]
93. Nersita, R.; Matrone, A.; Klain, M.; Scavuzzo, F.; Vitolo, G.; Abbondanza, C.; Carlino, M.V.; Giacco, V.; Amato, G.; Carella, C. Decreased serum vascular endothelial growth factor-d levels in metastatic patients with differentiated thyroid carcinoma. *Clin. Endocrinol.* **2012**, *76*, 142–146. [CrossRef]
94. Hsueh, C.; Lin, J.D.; Wu, I.C.; Chao, T.C.; Yu, J.S.; Liou, M.J.; Yeh, C.J. Vascular endothelial growth factors and angiopoietins in presentations and prognosis of papillary thyroid carcinoma. *J. Surg. Oncol.* **2011**, *103*, 395–399. [CrossRef]
95. Hauslage, J.; Cevik, V.; Hemmersbach, R. Pyrocystis noctiluca represents an excellent bioassay for shear forces induced in ground-based microgravity simulators (clinostat and random positioning machine). *NPJ Microgravity* **2017**, *3*, 12. [CrossRef]
96. Wuest, S.L.; Stern, P.; Casartelli, E.; Egli, M. Fluid dynamics appearing during simulated microgravity using random positioning machines. *PLoS ONE* **2017**, *12*, e0170826. [CrossRef]
97. Pietsch, J.; Kussian, R.; Sickmann, A.; Bauer, J.; Weber, G.; Nissum, M.; Westphal, K.; Egli, M.; Grosse, J.; Schonberger, J.; et al. Application of free-flow ief to identify protein candidates changing under microgravity conditions. *Proteomics* **2010**, *10*, 904–913. [CrossRef] [PubMed]
98. Zhao, C.; Denison, C.; Huibregtse, J.M.; Gygi, S.; Krug, R.M. Human isg15 conjugation targets both ifn-induced and constitutively expressed proteins functioning in diverse cellular pathways. *Proc. Natl. Acad. Sci. USA* **2005**, *102*, 10200–10205. [CrossRef] [PubMed]
99. Morales, D.J.; Lenschow, D.J. The antiviral activities of isg15. *J. Mol. Biol.* **2013**, *425*, 4995–5008. [CrossRef] [PubMed]

100. Yao, X.; Guo, S.; Wu, W.; Wang, J.; Wu, S.; He, S.; Wan, Y.; Nandakumar, K.S.; Chen, X.; Sun, N.; et al. Q63, a novel denv2 rdrp non-nucleoside inhibitor, inhibited denv2 replication and infection. *J. Pharmacol. Sci.* **2018**, *138*, 247–256. [CrossRef]
101. Bektas, N.; Noetzel, E.; Veeck, J.; Press, M.F.; Kristiansen, G.; Naami, A.; Hartmann, A.; Dimmler, A.; Beckmann, M.W.; Knüchel, R.; et al. The ubiquitin-like molecule interferon-stimulated gene 15 (isg15) is a potential prognostic marker in human breast cancer. *Breast Cancer Res.* **2008**, *10*, R58. [CrossRef]
102. Hanke, J.H.; Gardner, J.P.; Dow, R.L.; Changelian, P.S.; Brissette, W.H.; Weringer, E.J.; Pollok, B.A.; Connelly, P.A. Discovery of a novel, potent and src family-selective tyrosine kinase inhibitor. Study of lck- and fynt-dependent t cell activation. *J. Biol. Chem.* **1996**, *271*, 695–701. [CrossRef]
103. Sharma, S.; Singh, M.; Sharma, P.L. Ameliorative effect of daidzein: A caveolin-1 inhibitor in vascular endothelium dysfunction induced by ovariectomy. *Indian J. Exp. Biol.* **2012**, *50*, 28–34.
104. Liu, M.; Hummer, B.T.; Li, X.; Hassel, B.A. Camptothecin induces the ubiquitin-like protein, isg15 and enhances isg15 conjugation in response to interferon. *J. Interferon Cytokine Res.* **2004**, *24*, 647–654. [CrossRef]
105. Zhang, W.; Sun, J.; Luo, J. High expression of rab-like 3 (rabl3) is associated with poor survival of patients with non-small cell lung cancer via repression of mapk8/9/10-mediated autophagy. *Med. Sci. Monit.* **2016**, *22*, 1582–1588. [CrossRef]
106. Baeck, C.; Wehr, A.; Karlmark, K.R.; Heymann, F.; Vucur, M.; Gassler, N.; Huss, S.; Klussmann, S.; Eulberg, D.; Luedde, T.; et al. Pharmacological inhibition of the chemokine ccl2 (mcp-1) diminishes liver macrophage infiltration and steatohepatitis in chronic hepatic injury. *Gut* **2012**, *61*, 416–426. [CrossRef]
107. Dai, Y.; Rahmani, M.; Dent, P.; Grant, S. Blockade of histone deacetylase inhibitor-induced rela/p65 acetylation and nf-kappab activation potentiates apoptosis in leukemia cells through a process mediated by oxidative damage, xiap downregulation and c-jun n-terminal kinase 1 activation. *Mol. Cell. Biol.* **2005**, *25*, 5429–5444. [CrossRef]
108. Zhang, J.; He, D.H.; Zajac-Kaye, M.; Hochwald, S.N. A small molecule fak kinase inhibitor, gsk2256098, inhibits growth and survival of pancreatic ductal adenocarcinoma cells. *Cell Cycle* **2014**, *13*, 3143–3149. [CrossRef]
109. Xu, L.; Wang, W.; Meng, T.; Ma, L.P.; Tong, L.J.; Shen, J.K.; Wang, Y.Q.; Miao, Z.H. New microtubulin inhibitor mt189 suppresses angiogenesis via the jnk-vegf/vegfr2 signaling axis. *Cancer Lett.* **2018**, *416*, 57–65. [CrossRef]
110. Wu, B.; Li, J.; Huang, D.; Wang, W.; Chen, Y.; Liao, Y.; Tang, X.; Xie, H.; Tang, F. Baicalein mediates inhibition of migration and invasiveness of skin carcinoma through ezrin in a431 cells. *BMC Cancer* **2011**, *11*, 527. [CrossRef]
111. Kreutz, D.; Sinthuvanich, C.; Bileck, A.; Janker, L.; Muqaku, B.; Slany, A.; Gerner, C. Curcumin exerts its antitumor effects in a context dependent fashion. *J. Proteom.* **2018**, *182*, 65–72. [CrossRef] [PubMed]
112. Persson, A.; Lindberg, O.R.; Kuhn, H.G. Radixin inhibition decreases adult neural progenitor cell migration and proliferation in vitro and in vivo. *Front. Cell Neurosci.* **2013**, *7*, 161. [CrossRef] [PubMed]
113. Placencio, V.R.; Ichimura, A.; Miyata, T.; DeClerck, Y.A. Small molecule inhibitors of plasminogen activator inhibitor-1 elicit anti-tumorigenic and anti-angiogenic activity. *PLoS ONE* **2015**, *10*, e0133786. [CrossRef] [PubMed]
114. Kim, H.J.; Kang, G.J.; Kim, E.J.; Park, M.K.; Byun, H.J.; Nam, S.; Lee, H.; Lee, C.H. Novel effects of sphingosylphosphorylcholine on invasion of breast cancer: Involvement of matrix metalloproteinase-3 secretion leading to wnt activation. *Biochim. Biophys. Acta* **2016**, *1862*, 1533–1543. [CrossRef]
115. O'Shea, L.K.; Abdulkhalek, S.; Allison, S.; Neufeld, R.J.; Szewczuk, M.R. Therapeutic targeting of neu1 sialidase with oseltamivir phosphate (tamiflu(r)) disables cancer cell survival in human pancreatic cancer with acquired chemoresistance. *Onco Targets Ther.* **2014**, *7*, 117–134. [CrossRef]



© 2019 by the authors. Licensee MDPI, Basel, Switzerland. This article is an open access article distributed under the terms and conditions of the Creative Commons Attribution (CC BY) license (http://creativecommons.org/licenses/by/4.0/).

International Journal of
Molecular Sciences

MDPI

Review

Breast Cancer Cells in Microgravity: New Aspects for Cancer Research

Mohamed Zakaria Nassef [1,†], Daniela Melnik [1,†], Sascha Kopp [1,2], Jayashree Sahana [3], Manfred Infanger [1,2], Ronald Lützenberg [1], Borna Relja [4], Markus Wehland [1,2], Daniela Grimm [1,2,3] and Marcus Krüger [1,2,*]

1 Department of Microgravity and Translational Regenerative Medicine, Clinic for Plastic, Aesthetic and Hand Surgery, Otto von Guericke University, 39106 Magdeburg, Germany; nassefmohamedzakaria@gmail.com (M.Z.N.); daniela.melnik@med.ovgu.de (D.M.); sascha.kopp@med.ovgu.de (S.K.); manfred.infanger@med.ovgu.de (M.I.); ronald.luetzenberg@med.ovgu.de (R.L.); markus.wehland@med.ovgu.de (M.W.); daniela.grimm@med.ovgu.de (D.G.)
2 Research Group "Magdeburger Arbeitsgemeinschaft für Forschung unter Raumfahrt- und Schwerelosigkeitsbedingungen" (MARS), Otto von Guericke University, 39106 Magdeburg, Germany
3 Department of Biomedicine, Aarhus University, 8000 Aarhus C, Denmark; jaysaha@biomed.au.dk
4 Experimental Radiology, Department of Radiology and Nuclear Medicine, Otto von Guericke University, 39120 Magdeburg, Germany; borna.relja@med.ovgu.de
* Correspondence: marcus.krueger@med.ovgu.de; Tel.: +49-391-6757471
† These authors contributed equally to this work.

Received: 28 July 2020; Accepted: 2 October 2020; Published: 5 October 2020



Abstract: Breast cancer is the leading cause of cancer death in females. The incidence has risen dramatically during recent decades. Dismissed as an "unsolved problem of the last century", breast cancer still represents a health burden with no effective solution identified so far. Microgravity (μ*g*) research might be an unusual method to combat the disease, but cancer biologists decided to harness the power of μ*g* as an exceptional method to increase efficacy and precision of future breast cancer therapies. Numerous studies have indicated that μ*g* has a great impact on cancer cells; by influencing proliferation, survival, and migration, it shifts breast cancer cells toward a less aggressive phenotype. In addition, through the de novo generation of tumor spheroids, μ*g* research provides a reliable in vitro 3D tumor model for preclinical cancer drug development and to study various processes of cancer progression. In summary, μ*g* has become an important tool in understanding and influencing breast cancer biology.

Keywords: metastasis; proliferation; apoptosis; cell adhesion; cytoskeleton; in vitro 3D tumor model; cancer therapeutic targets

1. Learning from Space

After humans managed to leave Earth's surface, the era of microgravity (μ*g*) research began. Since the middle of the 20th century, researchers have been investigating how μ*g* affects the human body. Many astronauts and cosmonauts have reported various side effects after long-term space missions in orbit, to the Moon or onboard the International Space Station, Tiangong or the Mir station. They included cardiovascular changes, reduction in bone density, muscle atrophy, and risk of kidney stone formation [1–7]. Many of these health issues are attributed to the effects of μ*g* on cellular properties. Gravity was near constant during billions of years of evolution on Earth (estimated to be stabilized to 9.8 m/s^2 after hypothesized mass-changing events such as the Late Heavy Bombardment during Earth formation). Therefore, there is little or no genetic memory in organisms on how to

respond to force changes in the low gravity range. Hence, it is likely that terrestrial life adapting to μ*g* will reveal many novel mechanisms that could be helpful in biomedical research [8–10].

The relationship between a μ*g* environment and tumorigenesis is a further great concern that has attracted the attention of the academic world [11–14]. During a stay in space, the immune system of astronauts is affected to varying degrees, resulting in a reduced function of immune cells as well as a reduced ability to control mutated cells [15], among other effects of space radiation. In addition, μ*g* induces alterations in gene expression, signal transduction, proliferation and morphology in a variety of tumor cells by influencing the 'mechanical tumor microenvironment' [16,17]. Moreover, thyroid cancer cells were found to develop a more differentiated and less aggressive phonotype when cultured in space [18]. A very important point, however, is that these results were obtained in cancer cell monocultures. For example, μ*g* was also observed to suppress the activity of immune cells, which itself increases the risk of cancer development [16]. To our knowledge, no cancer-bearing organisms has been sent into space as of yet, neither were mice with tumor xenografts studied in orbit. Therefore, further research has to focus on the complex molecular interplay in vivo that determines physiological and biological responses to μ*g*.

When cancer cells grow in μ*g*, they start detaching from their substrate and form three-dimensional (3D) aggregates known as multicellular spheroids (MCS) [19]. Cancer biologists have recognized the importance of μ*g*-generated MCS for cancer research [20]. Due to their close resemblance to the in vivo growth of human tumors, MCS are a promising model to study metastasis and to investigate potential cancer drugs [21–23]. In summary, μ*g* can change the growth, migration and invasion ability of cancer cells, and thus displays an interesting tool for cancer research [24–26].

This review will summarize the current knowledge about the effects of μ*g* on human breast cancer cells. Breast cancer is the most invasive cancer in women. Tumor heterogeneity is a major problem limiting the efficacy of targeted cancer therapies. Therefore, fighting breast cancer requires to "think outside-the-box". We address the importance of μ*g* research as a tool that can be used to develop new 3D in vitro model systems for drug screening or even discover novel breast cancer medications.

2. Breast Cancer

According to the latest global GLOBOCAN statistics from 2018 [27], breast cancer was responsible for 11.6% of total cancer deaths in both sexes as the second leading cause of cancer death. This year's cancer statistics by the American Cancer Society shows that breast cancer alone accounts for 30% of all new cancer incidents (and 5% of cancer deaths) in women in the Unites States [28]. Breast cancer represents both a health and an economical burden with a rising number of cases predicted every year. Cancer research is the best approach to fight this malignancy of the disease and to identify novel targets which could be used for the development of new medications. Environmental and lifestyle factors are considered to be the main reasons for developing breast cancer, whereas genetic predisposition accounts for only 10% of cases [29]. Late maternal age at first pregnancy, early menarche, late onset of menopause and lack of breast-feeding account as environmental and lifestyle factors [30]. Other factors such as obesity, physical inactivity and alcohol use were found to increase the risk of developing breast cancer [31]. Mutations in high penetrance genes such as breast cancer 1 (*BRCA1*), breast cancer 2 (*BRCA2*), phosphatase and tensin homolog (*PTEN*), tumor protein P53 (*TP53*), E-cadherin (*CDH1*) and serine/threonine kinase 11 (*STK11*) lead to an increased life-time risk of developing breast cancer up to 80% [32]. Furthermore, mutations in moderate-penetrance genes such as BRCA1 interacting protein C-terminal helicase 1 (*BRIP1*), ataxia telangiectasia mutated (*ATM*), partner and localizer of BRCA2 (*PALB2*), and checkpoint kinase 2 (*CHEK2*) are associated with a two-fold increased risk of developing breast cancer [32]. Women with family history of breast cancer are recommended a genetic evaluation. Next Generation Sequencing is currently the tool of choice for investigation of genetic disorders in breast cancer [29,32].

How breast cancer transformation is initiated is not clear; however, it is divided into seven subtypes based on its molecular characteristics. These seven subtypes are luminal A, luminal B, basal

like/triple-negative, human epidermal growth factor receptor (HER)2-enriched, molecular apocrine, claudin-low and normal breast cancer-like [33–36]. The biological classification of breast cancer improved therapy guidelines and contributed to developing new therapy approaches for each subtype. Moreover, breast cancer is considered hormone-receptor-positive when it possesses estrogen receptor (ER) and/or progesterone receptor (PR), whereas a tumor is considered as triple negative breast cancer when lacking in ER, PR and HER2 expression. Triple negative breast cancer is associated with particularly poor prognosis, as it does not respond to hormonal therapy [29].

Early stage breast cancer is curable in 70-80% of cases, while advanced breast cancer is virtually incurable [29]. Metastasis is the cause of death in almost all breast cancer patients [37]. Breast cancer spreads in the bones, lungs, liver, and rarely to the brain. Metastatic breast cancer patients receive treatment with the aim of relieving symptoms and prolonging life-expectancy [29]. Therefore, it is of utmost importance to diagnose breast cancer in the early stages prior to metastasis. The diagnosis is achieved through biopsies, mammography, ultrasound and breast magnetic resonance imaging. Treatment options include surgery, radiotherapy, chemotherapy and molecular treatment [38–40]. The therapy is tailored according to the stage and progression of the disease in the individual patient [29]. To improve the disease outcome, intensive research studies are mandatory to gain a better understanding of the pathogenesis of the disease and to identify novel targets.

Common breast cancer cell lines that have been used in μ*g* research to date are listed in Table 1.

Table 1. Features of different breast cancer cell lines used in microgravity studies (modified from [41]).

Cell Line	Tumor	Subtype	ER	PR	HER2	Characteristic Expression
AU565	AC	HER2 enriched	-	-	+	EGFR, HER3, HER4, p53
BT-20	IDC	Triple-negative	-	-	-	Wnt-3, Wnt-7B
MCF-7	IDC	Luminal A	+	+	-	Wnt-7B, IGFBP2, -4, -5
MDA-MB-231	IDC	Claudin-low	-	-	-	EGFR, TGFα, Wnt-7B
MDA-MB-468	AC	Triple-negative	-	-	-	EGFR, TGFα

AC, adenocarcinoma; EGFR, epidermal growth factor receptor; HER, human epidermal growth factor receptor; IDC, invasive ductal carcinoma; IGFBP, insulin-like growth factor-binding protein; TGFα, transforming growth factor alpha.

3. Breast Cancer Cells Exposed to Microgravity

3.1. The Microgravity Environment

The nature of gravity was first described by Sir Isaac Newton over 300 years ago. Gravity is an attractive force, which is always present between two objects that have a mass, most apparent when one mass is very large (like Earth). Near the Earth's surface, the acceleration of an object toward the ground (9.8 m/s^2), caused by gravity alone, is called "normal gravity" or 1*g*. The condition of microgravity (μ*g*) is frequently used as a synonym for weightlessness or "zero-*g*"; however, *g*-forces are not actually zero but rather very small. Physically, μ*g* is achieved when the absolute sum of all mass-dependent accelerations is below a noise level of 10^{-4} (per definition, 1 μ*g* = 1×10^{-6} g) [42,43]. Real microgravity (r-μ*g*) for more than a few minutes can only be reached in space. Shorter durations of r-μ*g* can be attained in drop towers (<10 s), on parabolic (~22 s) or sounding rocket flights (up to 13 min), whenever an object is in free fall (the properties and r-μ*g* qualities of the different flight platforms are described in Section 3.3). In simulation experiments in laboratories on Earth, the magnitude of the Earth gravity vector cannot be changed. However, its influence can be altered with a simulator resulting in a "functional near-weightlessness" or vector-averaged, "simulated" microgravity (s-μ*g*) [42,43]. Multiple experiments demonstrated that cells and unicellular organisms behave differently under μ*g* conditions (both real and simulated) compared to similar cells exposed to the normal gravity of Earth. Therefore, by removing the effects of gravitational force, it is possible to study the fundamental processes of life down to the cellular level in different organisms [43]. Microgravity is suggested to be a mechanical

stressor for adherent cells induced through tensegrity [44]. It is known that mechanical stress influences the aggression and progression of cancer [45]. This is elucidated by changes of cancer cell behavior (e.g., cell survival, proliferation, differentiation) and structure (e.g., cellular shape, alteration in the cytoskeleton) [46].

3.2. Cellular Studies in Simulated Microgravity

In recent decades, several devices with different physical concepts have been engineered to simulate μ*g* on Earth. Due to high costs and limited options for experiments in space, s-μ*g* represents a perfect option to test hypotheses or to perform preliminary/preparatory and comparative studies. Moreover, these technologies enable multi-time-point experiments and multiple repetitions.

Various rotational simulators diminish the impact of gravity on biological samples by randomizing the direction of the gravity vector over time, such as 2D/3D clinostats (rotation around one or two axes), the Random Positioning Machine (RPM; a special version of a 3D clinostat, where both frames can operate with different speeds and in different directions) and the NASA-developed Rotating Wall Vessel (RWV) bioreactor, commercially known as Rotary Cell Culture System (RCCS) [43]. Suspending cells in a magnetic field offers another innovative way to study their properties and establish 3D cultures under s-μ*g*, called diamagnetic levitation [47,48].

3.2.1. Growth Behavior

Like other adherent cell types, breast cancer cells exposed to s-μ*g* grow into two distinct populations, characterized by hugely different morphologies. The first population consists of cells adherent to the substrate roughly preserving their native, spindle profile. The other population comprises small, rounded cells, which are grouped and linked to each other forming MCS floating in the supernatant (Figure 1a) [49]. These MCS represent a valuable 3D in vitro model system to study different aspects of cancer biology and for drug screening (see Section 4). Masiello et al. [49] suggested that during MCS formation in s-μ*g*, non-adherent cells are grouped in discrete clusters establishing tight cell–cell contacts. Thus, their solidity is higher compared to isolated, adherent cells on the RPM. The multiple cell adhesion is suggested to "stabilize" cell shape, by mutually reinforcing their stiffness [49].

Kopp et al. [50] intensely investigated MCF-7 cells for several days on an RPM. After 24 h, the first MCS were observed; MCS continued to increase in number and complexity until day 5. Most interestingly, the MCS showed a duct-like shape resembling human epithelial breast cells in vivo. Using the additional experimental omics data gained from these experiments, a Pathway Studio analysis identified that genes influenced by s-μ*g* are involved in the regulation of cell shape, cell tip formation and membrane-to-membrane docking [50]. Furthermore, the capability of MCF-7 cells to form MCS on the RPM depended on the intracellular distribution of the nuclear factor 'kappa-light-chain-enhancer' of activated B-cells (NF-κB) p65 subunit [51]. After 24 h of exposure to s-μ*g*, NF-κB was predominantly localized in the cytoplasm of adherent cells. In contrast, NF-κB was found in the nuclei of MCS cells. The glucocorticoid dexamethasone targeting NF-κB, suppressed MCS formation of MCF-7 cells in a dose-dependent manner [51]. An interaction analysis of 47 investigated genes suggested that heme oxygenase 1 (HMOX-1) and NF-κB variants are activated, when MCS are formed [51]. AU-565 cells indicated enhanced cell repair, modified cell adhesion and phenotypic preservation after 24 h on the RPM [52]. A large proteomics analysis determined the role of the cell junction protein E-cadherin in MCS formation of RPM-exposed cells [53]. E-cadherin was significantly reduced in MCS in comparison to conventionally cultured cells. This decrease in E-cadherin was also observed when MCF-7 cells were exposed to r-μ*g* phases (31 × 22 s) during a parabolic flight [54]. After blocking E-cadherin with antibodies MCS formation was promoted in MCF-7 cells [53]. In contrast, MCS formation was prevented by c-Src (proto-oncogene tyrosine-protein kinase c-Src) inhibition. This finding highlighted the importance of E-cadherin in s-μ*g*-induced MCS formation [53]. Moreover, several studies have detected ubiquitin-like protein ISG15, which is highly expressed in different cancers [53,55–58]. It is also known as a prognostic marker in human breast cancer [59] and it might play an important role in

the stabilization on MCS [53]. By analyzing omics data and semantic searches, Bauer et al. [60] found that the process of linking cells to each other or to the extracellular matrix (ECM) in (s-)μ*g* also includes the sialylation of extracellular domains of adhesion proteins.

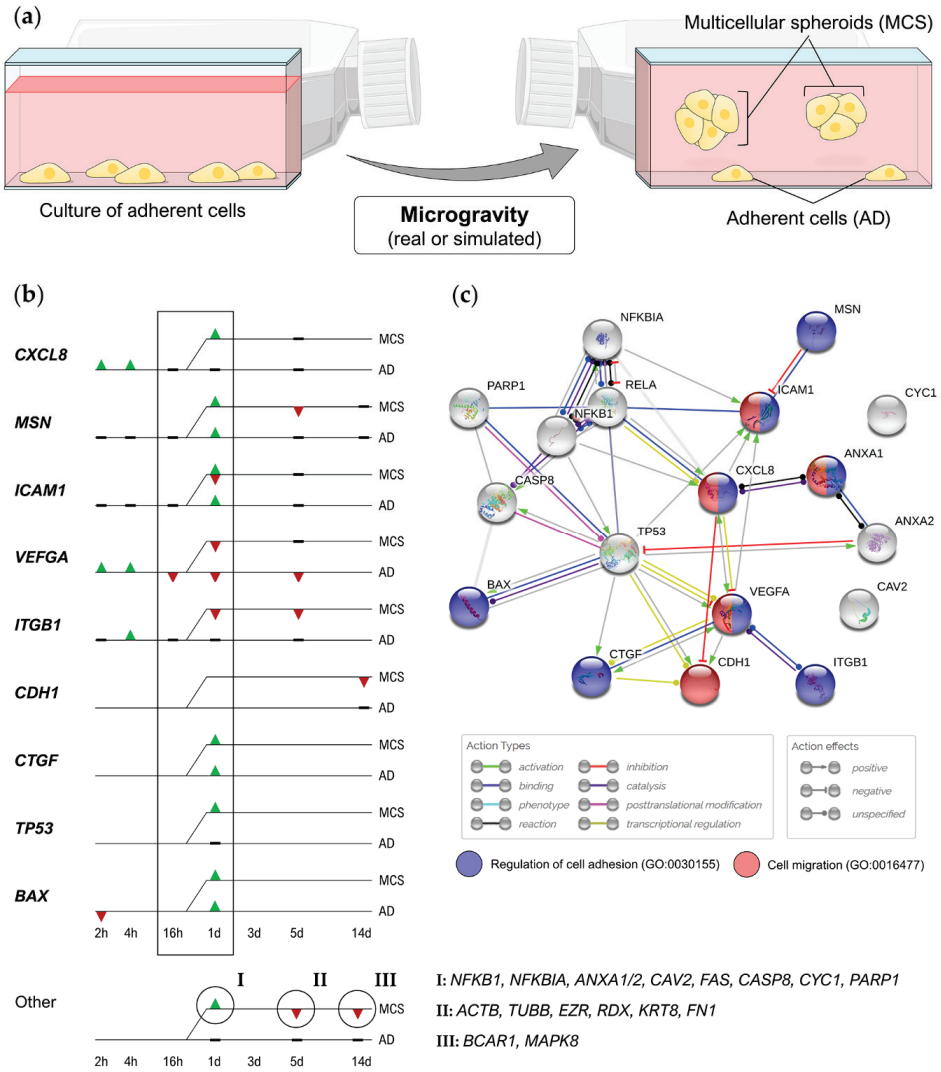


Figure 1. (**a**) Under μ*g* conditions, breast cancer cells grow into two distinct populations, characterized by hugely different morphologies. (**b**) Genes regulated in s-μ*g*-induced multicellular spheroids (MCS) formation of MCF-7 cells [50,51,53]. First MCS were detectable after 24 h of random positioning. ▲, upregulation; ▼, downregulation; (**c**) STRING (Search Tool for the Retrieval of Interacting Genes/Proteins) interaction network of proteins encoded by the regulated genes. Biological processes that are important both in cancer progression and in MCS formation are colorized. Blue, regulation of cell adhesion (Gene Ontology process GO:0030155); red, cell migration Gene Ontology process GO: 0016477). Gene symbols: *ACTB*, β-actin; *ANXA1/2*, annexin 1/2; *BAX*, Bcl-2-associated X protein; *BCAR1*, breast cancer anti-estrogen resistance protein 1; *CASP8*, caspase-8; *CAV2*, caveolin 2; *CDH1*, E-cadherin; *CTGF*, connective tissue growth factor; *CXCL8*, interleukin-8; *CYC1*, cytochrome c1; *EZR*, ezrin; *FAS*, Fas cell surface death receptor; *FN1*, fibronectin; *ICAM1*, intercellular adhesion molecule 1; *IKBKG*, inhibitor of NF-κB kinase regulatory subunit gamma; *ITGB1*, integrin-β1; *KRT8*, cytokeratin; *MSN*, moesin; *NFKB1*, nuclear factor kappa B subunit 1; *NFKBIA*, NF-κB inhibitor A; *PARP1*, poly [ADP-ribose] polymerase 1; *RDX*, radixin; *TP53*, tumor protein p53; *TUBB*, β-tubulin; *VEGFA*, vascular endothelial growth factor A. Parts of the figure are drawn using pictures from Servier Medical Art (https://smart.servier.com), licensed under a Creative Commons Attribution 3.0 Unported License (https://creativecommons.org/licenses/by/3.0).

Although these studies offered valuable information about the underlying mechanism of MCS formation in s-μ*g* (Figure 1b,c), the full mechanism remains to be unraveled. However, similar regulation of some genes (*CXCL8*, *VEGFA*, *TP53*, etc.) has been found in various malignant and non-malignant cell types that have been exposed to s-μ*g* [50,61–64]. This suggests a general mechanism of MCS formation in s-μ*g*, although different culture conditions and time points hamper to compare the existing results directly with each other.

In addition to the common use of rotatory-based s-μ*g*, different breast cancer cells (MCF-7, MDA-MB-231 and MDA-MB-468) also formed vital 3D aggregates when cultured (shear-force-free) under magnetic levitation. Levitated MCS showed high N-cadherin expression and enhanced epidermal growth factor receptor activity [65,66]. However, levitation research on breast cancer is just beginning and further studies are necessary to compare the effects of magnetic levitation with that of rotating bioreactors.

3.2.2. Cytoskeleton Architecture

When human cells are exposed to μ*g* (both simulated and real; see also Section 3.3.1) the cytoskeleton undergoes a dramatic reorganization, resulting in the activation of various genes which can trigger different biochemical pathways [67–69]. Hereby, the complex interplay between tensional forces and the cytoskeleton architecture modulates several essential cell functions such as proliferation, differentiation, apoptosis or ECM remodeling. The cytoskeleton is therefore often referred to as a gravity sensor [70].

Particularly for tumor cells, it has been reported that actin arrangement and remodeling can be related to their metastatic potential [71]. Invasive MDA-MB-231 cells showed a large rearrangement of F-actin after 24 h of RPM exposure. These rearrangements were almost stable and could been observed even after 72 h on the RPM [49]. Interestingly, the cytoskeleton changes greatly differed between the two cell populations: in adherent MDA-MB-231 cells, the complex cytosolic actin network disappeared, and actin was mostly localized on the cell border. In MCS cells, the F-actin network was completely disrupted [49]. Li et al. [72] described that non-invasive MCF-7 cells exposed to a clinostat did not display their typical radial actin array during 7 days of observation. These cells seemed to re-adapt to the s-μ*g* environment as part of the newly formed actin structures (e.g., lamellipodia) were reversed after 48 h. This is in accordance with the findings of Chiotaki et al. [73] who described that MDA-MB-231 cells appear to require a stable actin cytoskeleton to maintain a consistent nuclear periphery, while this is not the case for MCF-7 cells. Kopp et al. [50] further reported that both MCF-7 cell populations showed an accumulation of F-actin at the cell borders in addition to pronounced holes in the F-actin network after 5 days on the RPM. Stress fibers were only visible in adherent cells, indicating a higher mechanical load on these cells during random positioning. Molecular analyses revealed that *ACTB* and *TUBB* genes, as well as mRNAs of ezrin (*EZR*) and radixin (*RDX*) linking actin to the plasma membrane, were downregulated in the MCS cells [50]. Similar effects were observed when AU565 breast adenocarcinoma cells (which overexpress HER2/neu) were exposed to the RPM: actin filaments accumulated at the cell border after 5 days. At the same time, gene expression of transforming protein RhoA (*RHOA*) was upregulated [74]. The involvement of RhoA in s-μ*g*-induced actin (re-)organization seems to be cell type-specific, since the *RHOA* mRNA levels were unaltered in RPM-exposed MCF-7 cells [50].

Microtubules were disrupted in adherent MCF-7 cells after 4 h of clinorotation, but were partly reestablished by 48 h [72]. In adherent MDA-MB-231 cells grown on the RPM for 24–72 h microtubules were disorganized, with a more evident thickening in perinuclear position, whereas in MCS cells, the tubulin network was completely disrupted showing a slight diffuse fluorescence throughout the entire cytoplasm [49]. Considering that microtubule-associated tumor suppressors (such as breast cancer 1, BRCA1) can have major impact on cancer aggressiveness and clinical outcome [75], microtubule rearrangement through s-μ*g* can indeed be a tool to influence the latter.

The intermediate filament vimentin is selectively expressed in aggressive breast cancer cell lines such as MDA-MB-231 correlating with increased migration and invasion abilities of these cancer cells [76]. After exposing MDA-MB-231 cells to the RPM for 3 days, the vimentin network was disrupted in both adherent and MCS cells. Vimentin formed dense aggregates close to the nucleus [49] and thereby maybe influencing nuclear shape, mechanics and chromatin organization [77]. In AU565 cells the VIM gene was upregulated after 5 days on the RPM [74].

In summary, there are many indications that mechanical stimuli created by s-μ*g*, cytoskeletal structure, and cellular behavior are tightly linked. Studying the mechanisms that underlie these processes will contribute to identify key molecular targets guiding to new therapeutics based on the tumor mechanobiology.

3.2.3. Cell Cycle and Proliferation

Influence of s-μ*g* on the cell cycle was found in MCF-7 cultured on a clinostat, as cells in G2/M phase were significantly increased after 24 h and 48 h of clinorotation [78]. Chen et al. [79] investigated MCF-7 and MDA-MB-231 cells for 5 days on an RCCS. Simulated μ*g* did not affect the overall growth rate of these cancer cells, but the authors reported a significant accumulation of adherent cells in the S phase of the cell cycle. The induction of cell cycle arrest on the RCCS can most likely be attributed to the inhibition of cyclin D1 [79], a master regulator of the cell cycle that is required for re-entry into G1-phase after quiescence. Cyclin D1 overexpression is reported in >50% of human breast cancers and dysregulation of cyclin D1 expression or function contributes to altered cell cycle control during breast cancer development [80]. Masiello et al. [49] analyzed both cell populations of RPM-treated MDA-MB-231 cells in detail. A slight increase in the S phase distribution of adherent cells could be observed. However, non-adherent cells showed an impressive decrease in the S phase distribution paired with an accumulation of cells in the G2/M phase both after 24 and 72 h, demonstrating a persistent inhibition of cell growth. Furthermore, a significant decrease in cyclin D1 levels was recorded in MCS, whereas cyclin D1 levels were higher in adherent cells [49]. Considering that proper functioning of the mitotic process requires a correct arrangement of the tubulin meshwork [81], disorganization of tubulin microfilaments in non-adherent cells (either directly caused by s-μ*g* or by s-μ*g*-induced cyclin D1 repression) may help in elucidating the cell cycle arrest. Though, when Zheng et al. [82] cultured MCF-7 MCS encapsulated in 3D collagen-alginate hydrogels on an RCCS, neither the cytoskeleton distribution nor the assembly of mitotic spindle were altered by rotary culture. Nevertheless, cells in S and G2/M phase were significantly increased compared to the control group. This study also indicated that the RCCS promotes the proliferation of encapsulated MCF-7 MCS cells by inducing the ERK1/2 pathway [82].

3.2.4. Apoptosis

Qian et al. [78] reported that clinorotation induced apoptosis in MCF-7 cells after 72 h. However, they did not conduct a molecular analysis to explain their observation. Studies using the RPM often revealed contrasting behaviors of MCF-7 cells: an increase in apoptosis after 24 h [51], but no obvious change in apoptosis-related proteins after 48 h [83]. The investigations by Masiello et al. [49] may explain the different results through the presence of different cell populations. The authors found that the apoptotic process was particularly enhanced in non-adherent MDA-MB-231 cells on the RPM (increase in pro-apoptotic effectors after 24 and 72 h), in contrast to adherent cells which displayed only minor changes in apoptosis. Similarly, Nassef and coauthors [84] detected no apoptosis in adherent MDA-MB-231 cells after short-term exposure to the RPM, but the cells responded to s-μ*g* with transcriptional downregulation of both anti-apoptotic annexin A2 and pro-apoptotic Bax (Bcl-2-associated X protein) after 2 h. Bcl-2 (B-cell lymphoma 2) plays an important role in tumor development by regulating the endogenous apoptosis pathway which can inhibit apoptosis [85]. This way, it can counteract the pro-apoptotic stress occurring during tumorigenesis. Recently, Jiang et al. [86] described that apoptosis of MDA-MB-231 cells was promoted by RCCS culture (7 days) by decreased

expression of the anti-apoptotic Bcl-2 as well as increased expression of the pro-apoptotic Fas protein, further accompanied by the appearance of a large number of lysosomal and vacuolar structures.

This leads to assume that a s-μ*g* environment can induce apoptotic processes in cancer cells including breast cancer cells. Their regulation in MDA-MB-231 cells comprises an interplay between different cell signaling pathways, mainly involving the activation of p-ERK and p-AKT expression. Both p-AKT and p-ERK were significantly reduced in suspended (apoptosis-sensitive) cells but increased in the adherent (apoptosis-resistant) cell population exposed to an RPM [49]. Unravelling the underlying molecular mechanisms of apoptosis control might indeed bear a potential for new targets in cancer drug discovery. However, some overly enthusiastic reports about killing breast cancer cells in s-μ*g* have to be evaluated critically [87].

3.2.5. Cell Adhesion and Migration Ability

Microgravity causes disorganization in the focal adhesions (FAs) of adherently growing cancer cells, which is most likely connected to MCS formation (suspension cell population) and crucial for cell migration including metastasis. Creating cell movement requires the maturation of FAs, which serve as traction points to propel the cell forward [88]. An important step during the maturation process is binding and clustering of integrins to establish a physical and functional link between the cytoskeleton and the ECM [89]. Li et al. [72] detected that the number of FAs generated in s-μ*g* was reduced and these FAs were less mature (clustered) than those established under normal gravity conditions. In addition, s-μ*g* attenuated the expression of integrin-β1 and integrin-β4 and affected adhesion signaling by decreasing FAK, PYK2, and ILK kinase activity in MCF-7 cells [72]. Chen [90] later proposed that both decreased integrin expression and downregulated FA kinase activities are key processes in suppression of breast cancer cell migration under s-μ*g*. Most recently, Shi et al. [91] performed experiments with MCF-7 cells on an RWV and reported that EMT transcription factors (Snail, Twist, and ZEB1) are also involved in the alteration of cell adhesion properties under s-μ*g*. This might be a possible response of breast cancer cells to stress changes, in regulating the expressions of adhesion proteins and thus adapting their adhesion state to the altered mechanical (s-μ*g*) environment [91].

Cell migration is a fundamental process in the development of multicellular organisms [92]. Even in adult organisms, the migration of specialized cells is still essential, e.g., for proper immune response, wound repair, and tissue homeostasis. However, during metastasis, this process converts to the characteristically malignant behavior of tumor cells. The s-μ*g* environment is known to change the migration and invasion ability of various tumor cells [93,94]. For MCF-7 cells, Qian et al. [78] found that the invasive ability decreased after clinostat exposure together with a reduced expression of matrix-metallopeptidases (MMP-2, MMP-9) and vinculin. A transwell migration assay showed that the migration of MDA-MB-231 cells was also significantly reduced after 72 h on an RCCS [86]. The authors concluded that the decrease in MMP-9 expression in MDA-MB-231 cells might be closely related to a decrease in migration ability in s-μ*g*.

3.2.6. Matrix Composition and Stiffening

The development of tumor tissue is often associated with ECM accumulation after the transition from the avascular growth phase of cancer cells [95]. As a result, the tumor tissue is often much stiffer than the host tissue [96]. Elastic modules of human breast cancer lesions were measured one order of magnitude higher (10–42 kPa) than the typical elastic modules of normal breast tissue (3.25 kPa) [97]. The cultivation of MCF-7 cells on the RPM induced changes in the ECM, including laminin and fibronectin. In particular, fibronectin was downregulated after 5 days in adherent cells cultured on the RPM, whereas laminin was reduced in MCS cells indicating a reduction of ECM stiffness and tumorigenicity in MCF-7 cells after s-μ*g* treatment [50]. Data gained from breast cancer cells in conventional 3D suspension culture suggest that increased cellular fibronectin could promote the initial attachment of cancer cells to secondary sites during metastasis [98]. However, there have

been no comparative studies in shear force-free r-μ*g* so far to elucidate (possible) effects of mechanical stress on the ECM composition.

3.2.7. Cancer Cell Metabolism

In an early study, Coinu et al. [83] demonstrated that the metabolic activity of MCF-7 cells was attenuated after a 2-day exposure to an RPM. They found reductions in glucose and methionine uptake and decreased thymidine incorporation as an effect of s-μ*g*. A gene array analysis of MCF-7 cells after RPM-treatment revealed a > 2-fold change of only 23 genes and among them several were coding for proteins that are affected by oxygen levels or regulate glycolysis [51]. Comparing ERα positive MCF-7 and ERα negative MDA-MB-231 cells on an RCCS, Zheng et al. [99] reported an important role in protecting cells from oxidative stress damage under s-μ*g*. Later studies investigating both cell lines on the RCCS revealed changes in energy metabolism as well as increases in intracellular lactic acid and lactate dehydrogenase activity. Chen et al. [79] reported that several metabolic pathways were affected after 5 days of s-μ*g* including a number of pathways involved in glycometabolism (e.g., glycolysis, Krebs cycle, pentose phosphate pathway, and glycerol-phosphate and malate-aspartate shuttles). The authors suggested that different types of cancer cells can reprogram their metabolism to fulfill particular demands after long-term exposure to s-μ*g*, including processes involved in cell proliferation, metastasis, immunological escape and survival, thus shifting their aggressive phenotype [79]. Metabolic reprogramming is regarded as a characteristic of tumor cells [100]. Van der Heiden et al. [101] explained that the elevated expression of glycolytic enzymes in cancer cells, the molecular basis of the Warburg effect, is connected to the increased stability of hypoxia inducible factor 1α (HIF1α), which presents the master transcriptional regulator of glycolysis. Although the exact molecular mechanisms are still unknown, data have shown that glycolysis can not only be induced by hypoxia (and HIF1α), but also by high levels of adrenomedullin under s-μ*g* conditions [79]. This finding represents a novel mechanism of glycolysis activation and further aspect to understand the Warburg effect in MCF-7 and MDA-MB-231 cells.

3.2.8. Cancer Treatment

Recently, Hekmat et al. [102] demonstrated that s-μ*g* can affect the antiproliferative effect of TiO_2 nanoparticles on MDA-MB-231 cells. After 48 h of clinorotation in the presence of the sterilized nanoparticles, cell viability decreased noticeably without changing morphology. So far this was the first study investigating the influence of s-μ*g* on the effects of breast cancer treatment. However, results from leukemic cells have already indicated that s-μ*g* is able to modulate the cancer cell response to chemotherapy [103]. Authors proposed that (s-)μ*g* can be a powerful additional treatment for cancer cells and an immunomodulatory tool for the development of new immunotherapies, offering to open up new horizons to novel strategies for breast cancer therapy [102,103].

3.3. Cellular Studies in Real Microgravity

In addition to drop towers, which enable a very short r-μ*g* phase of a few seconds, there are different orbital and sub-orbital platforms to perform experiments in r-μ*g*: Parabolic flights are frequently offered and the easiest to participate in and therefore considered the platform of choice for researchers to gain access to r-μ*g* experiments. However, repeating r-μ*g*-phases during the flight are flanked by hypergravity phases and interrupted by 1*g*-phases, making it difficult to identify the effects solely attributed to r-μ*g* [104]. In addition, airplane vibration is often transferred onto the experiment and represents a further mechanical stimulus for the cells. Sounding rocket flights provide a longer, vibration-free r-μ*g*-phase (in Europe, MAXUS sounding rocket flights with r-μ*g* times of up to 13 min are achievable so far), after a phase of strong hypergravity (peak acceleration ~13*g*, depending on the rocket/motor combination) during the launch [105]. For long-term studies in r-μ*g*, remote-controlled experiments on satellites (e.g., Bion, Photon) or automated experiments onboard the ISS are currently available alternatives.

3.3.1. Cell Ultrastructure / Cytoskeleton

The first ultrastructural studies with MCF-7 cells in r-μ*g* were executed by Vassy et al. [106,107] during the Photon 12 mission (CNES, 1999). The cells were fixed after 1.5, 22, and 48 h after launching and responded to r-μ*g* by prolonging cycling and mitosis. Moreover, the cells exhibited a loose perinuclear cytokeratin network and chromatin structure, reduced cell proliferation and altered microtubule structure. Life-cell imaging during the TEXUS-54 sounding rocket flight (DLR, 2018) confirmed a fast rearrangement of the tubulin network in MCF-7 cells (within 150 s in r-μ*g*), together with a disturbance of actin bundles and appearance of cortical filopodia- and lamellipodia-like structures in the actin cytoskeleton (Figure 2a) [54]. An emerging role for microtubules in metastasis has long been suggested and there is increasing interest in the crosstalk between tubulin interacting proteins and actin [108]. The actin cytoskeleton is involved in many processes that are essential for normal physiology [109], but it is known that the actin cytoskeletal architecture can suppress the invasion of ER^+ breast cancer cells [110]. Some years ago, Mouneimne and coworkers [111] analyzed cancerous tissue and cell samples and found that ER can suppress the invasiveness of breast cancer cells by regulating the expression of actin-binding proteins which affect the formation of actin-driven cell membrane protrusions via suppressive cortical actin bundles. Especially the Ena/VASP-like (EVL) protein has been characterized to promote the generation of these bundles as well as the formation of stress fibers leading to transient cell stiffening. This stability is important during premalignant tumor growth [112]. Even if EVL has not been investigated in μ*g* yet, μ*g* certainly influences the cytoskeletal architecture of breast cancer cells in a way that can impact tumor cell migration and proliferation, and therefore provide an important tool to study metastasis or to develop novel therapeutics against aggressive and metastatic disease [108].

3.3.2. Cell Adhesion and Invasiveness

Changes in gene expression occur very quickly after breast cancer cells are exposed to altered gravity conditions. Both cell lines, MCF-7 and MDA-MB-231, responded to short-term r-μ*g* by modifications in the expression of invasiveness factors and adherence genes (Figure 2b) [54,84]. Enhanced levels of VEGF-A and interleukin-8 together with a down-regulation of vinculin, integrin-β1 and E-cadherin indicated the shift to a more invasive function of MCF-7 cells exposed to short-term r-μ*g* during parabolic flight maneuvers. In MDA-MB-231 cells, the adhesion molecules ICAM-1 (intercellular adhesion molecule 1) and VCAM-1 (vascular cell adhesion molecule 1) were increased after 31 r-μ*g* phases of a parabolic flight. In contrast, there was no expression change of ICAM-1 and VCAM-1 in MDA-MB-231 cells cultured on the RPM for 2 h (total duration of the parabolic flight) [84]. These results may indirectly reflect different biological effects caused by r- and s-μ*g*. The effect may also depend on the duration of r-μ*g* exposure. Thyroid cancer cells showed signs of increased invasiveness after being exposed to short-term r-μ*g* on a parabolic flight, but developed a less aggressive phenotype after being cultured in space for 10 days [18]. However, to our knowledge, no long-term r-μ*g* experiments have been performed on human breast cancer cells as of yet. Table 2 provides an overview of all previous studies investigating breast cancer cells exposed to μ*g*.

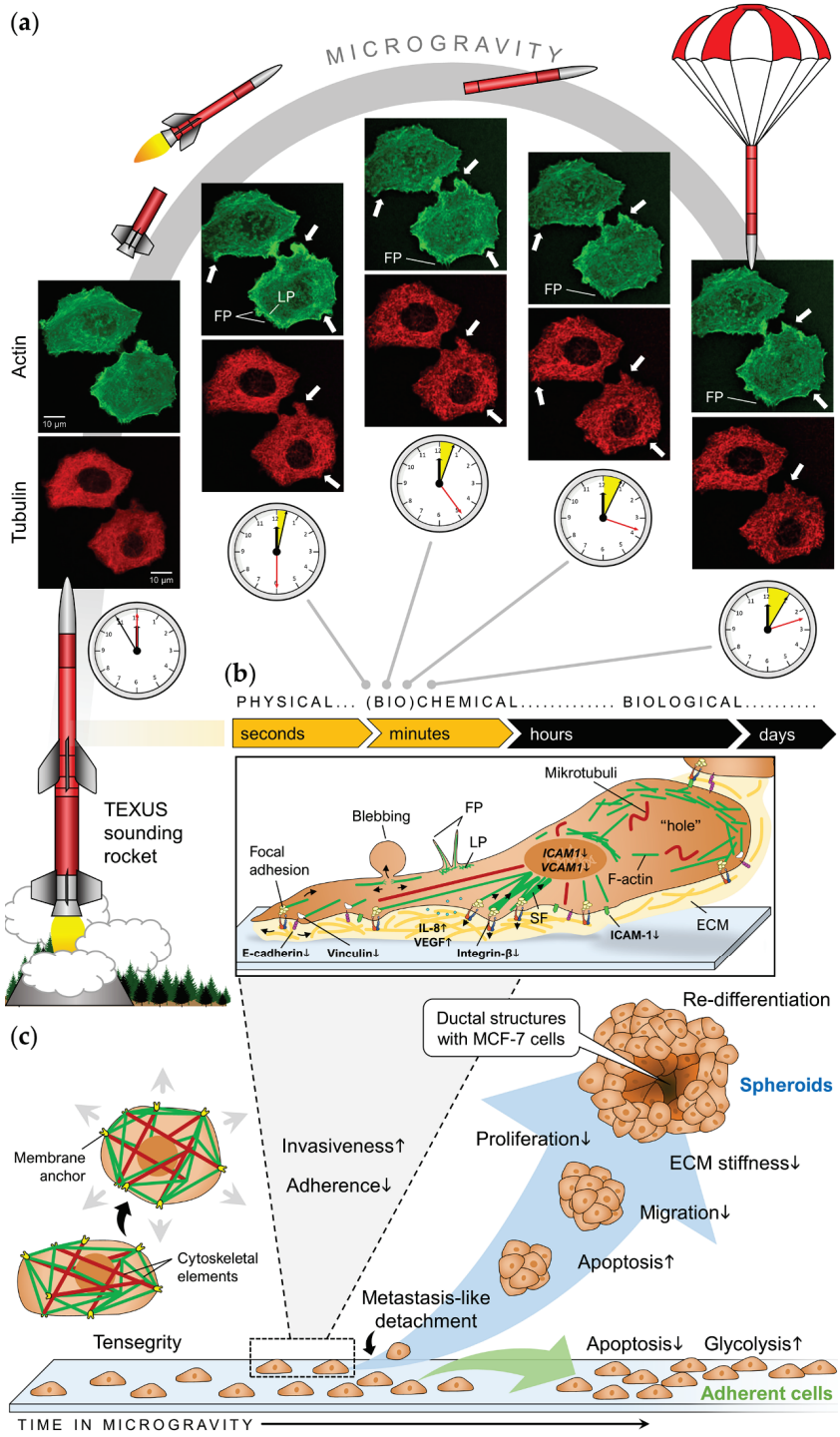


Figure 2. (**a**) Time course images of MCF-7 cells taken on board of the TEXUS-54 sounding rocket during microgravity in comparison to a control image taken 5 min prior to launch. The arrows indicate changes in F-actin (green channel) or α-tubulin (red channel). F-actin cytoskeleton shows appearance of filopodia- and lamellipodia-like structures, accumulation of F-actin, while α-tubulin shows a loose structure and rearrangement of the cytoskeleton. (**b**) Subsequent cellular alterations of adherently growing breast cancer cells after exposure to r-µ*g* (modified from [54]). F-actin is shown as green lines, the extracellular matrix (ECM) in yellow. The effects observed on parabolic and sounding rocket flights were observed in a time-range from a few seconds until minutes. (**c**) Downstream key processes in both cell populations of human breast cancer cells during long-term exposure to s-µ*g*. FP, filopodia; LP, lamellipodia; SF, stress fibers.

Table 2. Studies reporting the effects of microgravity on human breast cancer cells.

Cell Line	µg Condition (Duration)	Findings	Ref.
MCF-7	Clinostat (24–72 h)	Alterations of cell invasion, migration, adhesion, cell cycle and vinculin expression	[78]
	RPM (2 h–5 d)	After 24 h: compact spheroids; after 5 d: duct-like spheroids; downregulation of *ACTB*, *TUBB*, *EZR*, *RDX*, *FN1*, *VEGFA*, *FLK1*, *CASP3*, *CASP9*, *PRKCA*	[50]
	RPM (24 h)	Translocation of RelA into the nucleus, upregulation of *ANXA1*, *ANXA2*, *CTGF*, *CAV2*, *ICAM1*, *FAS*, *CASP8*, *BAX*, *TP53*, *CYC1*, *PARP1*	[51]
	RPM (48 h)	Reduction of glucose uptake, methionine uptake/incorporation, thymidine incorporation, proliferation, and metabolic machinery	[83]
	RPM (14 d)	Downregulation of *CDH1* and E-cadherin protein in MCS	[53]
	PFC (31 × 22 s)	Upregulation of *KRT8*, *RDX*, *TIMP1*, *CXCL8*; downregulation of *VCL* and E-cadherin protein	[54]
	Sounding rocket (6 min)	Disturbance of F-actin bundles, appearance of filopodia- and lamellipodia-like structures; rearrangement of the tubulin network.	[54]
	Satellite (1.5–24 h)	Prolonged cycling/mitosis, loose perinuclear cytokeratin network and chromatin structure, reduced cell proliferation; altered microtubule structure	[106,107]
MDA-MB-231	RPM (24–72 h)	Reorganized cytoskeleton; alterations in ERK, AKT and survivin signaling pathways	[49]
	RPM (2 h)	Downregulation of *ANXA2*, *BAX*	[84]
	RCCS (7 d)	Impaired cell cycle and ultrastructure, increased apoptosis, decreased migration ability and decreased expression of *BCL2*, *MMP9*	[86]
	PFC (31 × 22 s)	Upregulation of *NFKB1*, *RELA*, *ERK1*, *ICAM1*, *NFKBIA*, *NFKBIB*, *FAK1*, *SPP1*, *CD44*; reduced levels of RelA, osteopontin, increased levels of ICAM-1, VCAM-1; changes in cell adhesion	[84]
AU565	RPM (24 h)	Upregulation of *BRCA1*, *VCAM1*; downregulation of *KRAS*, *VIM*; enhanced cell repair, modified cell adhesion	[52]
	RPM (5 d)	Upregulation of *VIM*, *RHOA*, *BRCA1*, *MAPK*, *ERBB2*; downregulation of *VEGFA*	[74]

MCS, multicellular spheroid; PFC, parabolic flight campaign; RCCS, Rotary Cell Culture System; RPM, Random Positioning Machine. AKT, protein kinase B; ERK, extracellular-signal regulated kinase; RelA, transcription factor p65. Gene symbols: *ACTB*, β-actin; *ANXA*, annexin; *BAX*, Bcl-2-associated X protein; *BCL2*, B-cell lymphoma 2; *BRCA1*, breast cancer 1, early-onset; *CASP*, caspase; *CAV2*, caveolin-2; *CD44*, cluster of differentiation 44; *CDH1*, E-cadherin; *CTGF*, connective tissue growth factor; *CXCL8*, interleukin-8; *CYC1*, cytochrome c1; *ERBB2*, v-erb-b2 erythroblastic leukemia viral oncogene homolog 2 (=HER2); *ERK1*, extracellular-signal regulated kinase 1; *EZR*, ezrin; *FAK1*, focal adhesion kinase 1; *FAS*, Fas cell surface death receptor; *FN1*, fibronectin; *FLK1*, fetal liver kinase 1, *ICAM1*, intercellular adhesion molecule 1; *KRAS*, Kirsten rat sarcoma; *KRT8*, cytokeratin; *MAPK*, mitogen-activated protein kinase; *MMP9*, matrix metallopeptidase 9; *NFKB1*, nuclear factor kappa B subunit 1; *NFKBIA*, NF-κB inhibitor alpha; *NFKBIB*, NF-κB inhibitor beta; *PARP1*, poly [ADP-ribose] polymerase 1; *PRKCA*, protein kinase C alpha; *RDX*, radixin; *RELA*, transcription factor p65; *RHOA*, Ras homolog family member A; *SPP1*, osteopontin; *TIMP1*, tissue inhibitor of metalloproteinases; *TP53*, tumor protein p53; *TUBB*, β-tubulin; *VCAM1*, vascular cell adhesion molecule 1; *VCL*, vinculin; *VEGFA*, vascular endothelial growth factor A; *VIM*, vimentin.

4. Microgravity-Generated 3D Breast Cancer Models

4.1. Homogenous Tumor Spheroids

Multicellular architecture is one of the defining characteristics of breast cancer. Unfortunately, most in vitro tumor models fail to reconstruct tumor architecture or are unable to predict in vivo cellular responses to therapeutics accurately [113]. However, this architecture is known to drive the tumor progression through cell/cell- and cell/matrix-contacts, forced depolarization and reduced tensional homeostasis [114]. Moreover, it leads to the formation of a complex microenvironment characterized by metabolic, catabolic and oxygen gradients, which can only be resembled in 3D cell culture [115].

Studies have repeatedly shown that various types of human cells form scaffold-free 3D aggregates after exposure to s-μ*g* or r-μ*g* [19,64,115–118]. This behavior has also been observed for breast cancer cells already after the first 24 h. An unexpected finding was the formation of glandular MCF-7 spheroids after at least 5 days on the RPM (Figures 2c and 3a), containing duct-like structures with unicellular borders and polarized cells [50]. To form these structures, cells must adapt various processes such as cell/cell- and cell/matrix communication, directed apoptosis, differentiation, and polarization (Figure 3b). Especially for cell polarity, cytoskeletal filaments and associated proteins, that are influenced by μ*g*, may play a significant role [119].

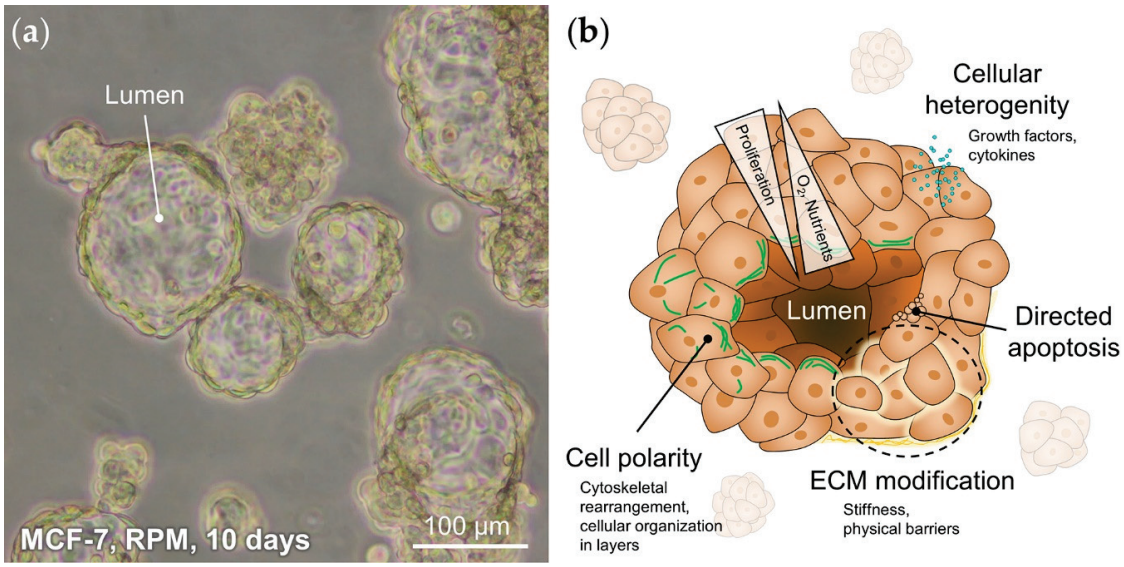


Figure 3. (**a**) Glandular MCF-7 spheroids grown in s-μ*g* for 10 days. (**b**) Schematic diagram and special features of a glandular breast cancer spheroid.

After generation in (s-)μ*g*, these MCS are suitable for studies with chemotherapy, gene therapy, cell- and antibody-based immunotherapy, etc., under normal laboratory conditions [120]. The special 3D architecture of MCS might facilitate the penetration and action of cancer drugs more closely mimicking the situation of a breast tumor in the human body. This way, MCS could help to investigate and understand cell aggregation and to improve the penetration and action of drugs for cancer therapy. However, due to avascular growth, the size of homogenous tumor MCS is still limited.

4.2. Heterogeneous Breast Tumor Models

Tumor heterogeneity is one of the hallmarks of breast cancer malignancy. Breast tumors often contain morphologically and molecularly different cell populations (intratumor heterogeneity), resulting in different behavior, presentation, and prognosis [121]. In order to meet these requirements for a 3D tumor model, Vamvakidou et al. [122] generated a coculture-based 3D tumor model out of MDA-MB-231, MCF-7, and ZR-751 cells. The different cell lines were cocultured in an RWV and formed

a large number of heterogeneous aggregates. The most important feature was the temporal-spatial organization of the MCS, including the presence of central necrotic areas and higher levels of cell proliferation at the MCS periphery [122].

In a bioreactor experiment that was carried out in 1998 during the last Mir increment, breast cancer cells were co-cultured with a fibroblast layer, made up of angiogenic cells. This was the very first attempt to investigate vascularization of a solid tumor in r-μ*g*. In the tissue that returned from space half a year later, vascularization was initiated [123]. Some years later, Kaur et al. [124] used s-μ*g* to generate a 3D breast cancer model, which consisted of cancer cells (UACC-893, BT-20, or MDA-MB-453) and fibroblasts. Co-cultures resulted in the generation of 'histoids' with cancer cells invading fibroblast spheroids.

In another approach, different breast cancer cell lines (MCF-7, MDA-MB-231, and MDA-MB-468) were co-cultured with fibroblasts and then magnetically levitated. The data of Jaganathan and coworkers [125] indicated that the formed 3D aggregates were advantageous due to the ability to: (1) form large MCS within 24 h (millimeter in diameter); (2) resemble tumor cell architecture and density; (3) accurately mimic properties of the in vivo tumor microenvironment; and (4) test drug efficiency in an in vitro model that is comparable to in vivo breast tumors [125].

Heterogenous spheroids grown in s-μ*g* provide a high-throughput in vitro model that could help to understand early stages of cancer development. Furthermore, they can be used as a drug testing or a drug delivery system [122].

4.3. Advantages of Microgravity-Generated Spheroids

Reproducibility and physiological relevance are two essential features for in vitro test systems used in drug development [126]. MCS are conventionally generated using bioprinting or with several culture methods such as liquid overlay, hanging drop and hydrogel-based cultures [127–129]. One of the important elements required in most techniques for MCS generation is the presence of a synthetic or naturally-derived scaffold that should mimic the ECM [130,131]. However, the addition of an artificial scaffold may impede cell growth and affect cell interactions. In addition, the growing in vivo environment cannot be reconstructed by the static concentration of the scaffold [132]. In μ*g*, cells promote 3D self-assembly without using an artificial scaffold and without the need of external surface for support enabling the simulation of changing in vivo environment. Another advantage of studying cells in μ*g*, sedimentation and buoyancy demonstrated to be neglectable in μ*g* so that it is possible to observe the minimal alterations in biological and physical systems [19]. Microgravity-generated MCS with other cell types do not develop necrosis even when cultured for several weeks in s-μ*g* and therefore are suitable for long-term experiments [50,133]. In comparison to other current technologies the s-μ*g*-based method reproducibly provides a large number of MCS in a short time. Furthermore, due to the ability to reach large diameters (up to 0.5 mm) in a short time, the s-μ*g* MCS model exhibits the condition of in vivo lesions more accurate, including the occurrence of hypoxic regions inside the 3D aggregates. Long-term studies over months need to be performed to study the appearance of necrosis in the MCS.

5. Summary and Perspectives

Previous studies indicate that μ*g*, both real and simulated, has a significant impact on breast cancer cells. Changes in cell proliferation, survival, apoptosis and growth behavior had been observed both in triple-negative MDA-MB-231 cells and well-differentiated MCF-7 cells exposed to the s-μ*g* [49–51,84]. Gravity-sensitive signaling is required for the very early (24 h) formation of MCS during random positioning. Molecular analyses revealed that inflammatory cytokines (IL-8), NF-κB p65, cell adhesion molecules (ICAM-1, VCAM-1), and growth factors (TGF-β, VEGF-A) seem to be involved in MCS formation in breast cancer cells on the RPM [84]. Particularly, inflammatory cytokines are key players in tumor initiation, promotion, angiogenesis, and metastasis regulating both the induction and the protection in breast cancer [134]. Using the liquid overlay technique, it was shown that interleukins IL-8

and IL-6 can directly induce MCS formation of thyroid cancer cells grown on agarose at 1*g* [129]. IL-8 was upregulated early in MCF-7 cells exposed to short-term r-μ*g* during parabolic flight maneuvers and might start the signaling process for MCS formation [54]. The regulation of IL-6 has not been investigated in breast cancer cells exposed to μ*g* so far, but was it was found elevated in other cancer cells under these conditions [116,135]. In addition, MCF-7 cells overexpressing IL-6 initiated EMT and exhibited a more invasive phenotype [136]. Since MCS formation represents a valuable in vitro metastasis model, targeting cytokines and/or NF-κB might be a promising approach for breast cancer treatment. Genetic alterations related to the cytoskeleton, cell adhesion, ECM and cytokines have been detected with other malignant and non-malignant human cells in a similar way. This may hint towards an overarching mechanism of MCS formation in cancer cells that has to be validated in future studies.

Today's technologies are constantly providing new insights into the development and biology of breast cancer. The quest for treatment options is advancing just as quickly. So, what is the significance of μ*g* research? On one hand, epidemiological studies have shown an increased breast cancer incidence in female commercial flight attendants (which are exposed to similar occupational conditions as astronauts thought to raise the risk of developing breast cancer without considering further risk factors for cancer such as ionizing radiation) [137], on the other hand, the aggressiveness of cancer cells seems to be reduced in vitro after s-μ*g* exposure [18]. To explain this discrepancy, it is worth mentioning that different biological systems were investigated in these studies and effects found in vitro do not always reflect the complex situation in vivo which also comprises cell/cell interactions and the crosstalk between different body systems in space (disrupted melatonin homeostasis, changes in immune function, etc.). Sending patients into space will certainly not be the cure for breast cancer. Strictly speaking, a lot of research focused on cancer development and progression in space is still needed, especially within the context of planned long-term missions to the moon and Mars. However, μ*g* research offers a unique in vitro tool to investigate biomechanical effects in cancer biology. Microgravity is not directly an option for cancer treatment but supports cancer research in two ways: First, μ*g* research provides a reliable in vitro 3D tumor model for preclinical cancer drug development; second, it has unraveled some remarkably interesting aspects of cancer cell biology. These can be used in other approaches to increase efficacy and precision of future cancer therapies and thus enhance survivability and quality of life for breast cancer patients.

Author Contributions: Conceptualization, M.K., M.Z.N. and D.M.; writing—original draft preparation, M.Z.N., M.K., D.M. and J.S.; writing—review and editing, M.K., S.K., D.G., M.W., R.L. and B.R.; visualization, M.K. and M.Z.N.; funding acquisition, D.G. and M.I. All authors have read and agreed to the published version of the manuscript.

Funding: This research was funded by Deutsches Zentrum für Luft- und Raumfahrt (DLR), BMWi project 50WB1924 and Aarhus University (D.G., J.S.). The APC was funded by the Open Access Publication Fonds of the Otto von Guericke University Magdeburg.

Acknowledgments: The authors thank Petra Wise for the English language review of this manuscript.

Conflicts of Interest: The authors declare no conflict of interest.

Abbreviations

2D	Two-dimensional
3D	Three-dimensional
ECM	Extracellular matrix
ER	Estrogen receptor
HER2	Human epidermal growth factor receptor
μ*g*	Microgravity (r-μ*g*, real microgravity; s-μ*g*, simulated microgravity)
MCS	Multicellular spheroids
RCCS	Rotary Cell Culture System
RPM	Random Positioning Machine
RWV	Rotating Wall Vessel
PR	Progesterone receptor

References

1. White, R.J.; Averner, M. Humans in space. *Nat. Cell Biol.* **2001**, *409*, 1115–1118. [CrossRef] [PubMed]
2. Charles, J.B.; Lathers, C.M. Cardiovascular adaptation to spaceflight. *J. Clin. Pharmacol.* **1991**, *31*, 1010–1023. [CrossRef] [PubMed]
3. Grimm, D.; Grosse, J.; Wehland, M.; Mann, V.; Reseland, J.E.; Sundaresan, A.; Corydon, T.J. The impact of microgravity on bone in humans. *Bone* **2016**, *87*, 44–56. [CrossRef] [PubMed]
4. Pietsch, J.; Bauer, J.; Egli, M.; Infanger, M.; Wise, P.; Ulbrich, C.; Grimm, D. The effects of weightlessness on the human organism and mammalian cells. *Curr. Mol. Med.* **2011**, *11*, 350–364. [CrossRef]
5. Smith, S.; Zwart, S.R.; Heer, M.; Hudson, E.K.; Shackelford, L.; Morgan, J.L. Men and women in space: Bone loss and kidney stone risk after long-duration spaceflight. *J. Bone Miner. Res.* **2014**, *29*, 1639–1645. [CrossRef]
6. VanDenburgh, H.; Chromiak, J.; Shansky, J.; Del Tatto, M.; Lemaire, J. Space travel directly induces skeletal muscle atrophy. *FASEB J.* **1999**, *13*, 1031–1038. [CrossRef]
7. Zayzafoon, M.; Meyers, V.E.; McDonald, J. Microgravity: The immune response and bone. *Immunol. Rev.* **2005**, *208*, 267–280. [CrossRef]
8. Demontis, G.C.; Germani, M.M.; Caiani, E.G.; Barravecchia, I.; Passino, C.; Angeloni, D. Human pathophysiological adaptations to the space environment. *Front. Physiol.* **2017**, *8*, 547. [CrossRef]
9. Ploutz-Snyder, L. Evaluating countermeasures in spaceflight analogs. *J. Appl. Physiol.* **2016**, *120*, 915–921. [CrossRef]
10. Prasad, B.; Richter, P.; Vadakedath, N.; Mancinelli, R.; Krüger, M.; Strauch, S.M.; Grimm, D.; Darriet, P.; Chapel, J.-P.; Cohen, J.; et al. Exploration of space to achieve scientific breakthroughs. *Biotechnol. Adv.* **2020**, *43*, 107572. [CrossRef]
11. Nimon, J. Running the Race to Cure Cancer from Space. Available online: https://www.nasa.gov/mission_pages/station/research/news/cancer_research_in_space (accessed on 26 May 2020).
12. Greicius, T. Fighting Cancer with Space Research. Available online: https://www.nasa.gov/feature/jpl/fighting-cancer-with-space-research (accessed on 26 May 2020).
13. Elkavich, A. Cancer Research on the Space Station. Available online: https://www.issnationallab.org/blog/cancer-research-on-the-space-station/ (accessed on 26 May 2020).
14. Krüger, M.; Bauer, J.; Grimm, D. *Cancer Research in Space*; Springer Science and Business Media LLC: Berlin/Heidelberg, Germany, 2017; pp. 87–106.
15. Crucian, B.E.; Chouker, A.; Simpson, R.J.; Mehta, S.; Marshall, G.; Smith, S.M.; Zwart, S.R.; Heer, M.; Ponomarev, S.; Whitmire, A.; et al. Immune system dysregulation during spaceflight: Potential countermeasures for deep space exploration missions. *Front. Immunol.* **2018**, *9*, 1437. [CrossRef] [PubMed]
16. Jhala, D.; Kale, R.K.; Singh, R.P. Microgravity alters cancer growth and progression. *Curr. Cancer Drug Targets* **2014**, *14*, 394–406. [CrossRef] [PubMed]
17. Arun, R.P.; Sivanesan, D.; Patra, B.; Varadaraj, S.; Verma, R.S. Simulated microgravity increases polyploid giant cancer cells and nuclear localization of YAP. *Sci. Rep.* **2019**, *9*, 10684. [CrossRef] [PubMed]
18. Ma, X.; Pietsch, J.; Wehland, M.; Schulz, H.; Saar, K.; Hübner, N.; Bauer, J.; Braun, M.; Schwarzwälder, A.; Segerer, J.; et al. Differential gene expression profile and altered cytokine secretion of thyroid cancer cells in space. *FASEB J.* **2013**, *28*, 813–835. [CrossRef]
19. Aleshcheva, G.; Bauer, J.; Hemmersbach, R.; Slumstrup, L.; Wehland, M.; Infanger, M.; Grimm, D. Scaffold-free tissue formation under real and simulated microgravity conditions. *Basic Clin. Pharmacol. Toxicol.* **2016**, *119*, 26–33. [CrossRef]
20. Becker, J.L.; Souza, G.R. Using space-based investigations to inform cancer research on Earth. *Nat. Rev. Cancer* **2013**, *13*, 315–327. [CrossRef]
21. Achilli, T.-M.; Meyer, J.; Morgan, J.R. Advances in the formation, use and understanding of multi-cellular spheroids. *Expert Opin. Biol. Ther.* **2012**, *12*, 1347–1360. [CrossRef]
22. Huang, B.-W.; Gao, J.-Q. Application of 3D cultured multicellular spheroid tumor models in tumor-targeted drug delivery system research. *J. Control. Release* **2018**, *270*, 246–259. [CrossRef]
23. Mehta, G.; Hsiao, A.Y.; Ingram, M.; Luker, G.D.; Takayama, S. Opportunities and challenges for use of tumor spheroids as models to test drug delivery and efficacy. *J. Control. Release* **2012**, *164*, 192–204. [CrossRef]

24. Chang, D.; Xu, H.; Guo, Y.; Jiang, X.; Liu, Y.; Li, K.; Pan, C.; Yuan, M.; Wang, J.; Li, T.; et al. Simulated microgravity alters the metastatic potential of a human lung adenocarcinoma cell line. *Vitr. Cell. Dev. Biol. Anim.* **2013**, *49*, 170–177. [CrossRef]
25. Deng, B.; Liu, R.; Tian, X.; Han, Z.; Chen, J. Simulated microgravity inhibits the viability and migration of glioma via FAK/RhoA/Rock and FAK/Nek2 signaling. *Vitr. Cell. Dev. Biol. Anim.* **2019**, *55*, 260–271. [CrossRef] [PubMed]
26. Krüger, M.; Melnik, D.; Kopp, S.; Buken, C.; Sahana, J.; Bauer, J.; Wehland, M.; Hemmersbach, R.; Corydon, T.J.; Infanger, M.; et al. Fighting thyroid cancer with microgravity research. *Int. J. Mol. Sci.* **2019**, *20*, 2553. [CrossRef] [PubMed]
27. Bray, F.; Ferlay, J.; Soerjomataram, I.; Siegel, R.L.; Torre, L.A.; Jemal, A. Global cancer statistics 2018: GLOBOCAN estimates of incidence and mortality worldwide for 36 cancers in 185 countries. *CA A Cancer J. Clin.* **2018**, *68*, 394–424. [CrossRef] [PubMed]
28. Siegel, R.L.; Mph, K.D.M.; Jemal, A. Cancer statistics, 2020. *CA A Cancer J. Clin.* **2020**, *70*, 7–30. [CrossRef]
29. Harbeck, N.; Penault-Llorca, F.; Cortes, J.; Gnant, M.; Houssami, N.; Poortmans, P.; Ruddy, K.; Tsang, J.; Cardoso, F. Breast cancer. *Nat. Rev. Dis. Prim.* **2019**, *5*, 66. [CrossRef]
30. Britt, K.L.; Ashworth, A.; Smalley, M.J. Pregnancy and the risk of breast cancer. *Endocr. Relat. Cancer* **2007**, *14*, 907–933. [CrossRef]
31. Danaei, G.; Hoorn, S.V.; Lopez, A.D.; Murray, C.J.; Ezzati, M. Causes of cancer in the world: Comparative risk assessment of nine behavioural and environmental risk factors. *Lancet* **2005**, *366*, 1784–1793. [CrossRef]
32. Shiovitz, S.; Korde, L.A. Genetics of breast cancer: A topic in evolution. *Ann. Oncol.* **2015**, *26*, 1291–1299. [CrossRef]
33. Dai, X.; Li, T.; Bai, Z.; Yang, Y.; Liu, X.; Zhan, J.; Shi, B. Breast cancer intrinsic subtype classification, clinical use and future trends. *Am. J. Cancer Res.* **2015**, *5*, 2929–2943.
34. Farmer, P.; Bonnefoi, H.; Becette, V.; Tubiana-Hulin, M.; Fumoleau, P.; Larsimont, D.; MacGrogan, G.; Bergh, J.; Cameron, D.; Goldstein, D.; et al. Identification of molecular apocrine breast tumours by microarray analysis. *Oncogene* **2005**, *24*, 4660–4671. [CrossRef]
35. Prat, A.; Parker, J.S.; Karginova, O.; Fan, C.; Livasy, C.; Herschkowitz, J.I.; He, X.; Perou, C.M. Phenotypic and molecular characterization of the claudin-low intrinsic subtype of breast cancer. *Breast Cancer Res.* **2010**, *12*, 1–18. [CrossRef] [PubMed]
36. Nahed, A.S.; Shaimaa, M.Y.; Soliman, N.A.; Yussif, S.M. Ki-67 as a prognostic marker according to breast cancer molecular subtype. *Cancer Biol. Med.* **2016**, *13*, 496. [CrossRef]
37. Cardoso, F.; Senkus, E.; Costa, A.; Papadopoulos, E.; Aapro, M.; André, F.; Harbeck, N.; Lopez, B.A.; Barrios, C.; Bergh, J.; et al. 4th ESO–ESMO International Consensus Guidelines for Advanced Breast Cancer (ABC 4). *Ann. Oncol.* **2018**, *29*, 1634–1657. [CrossRef] [PubMed]
38. Berry, D.; Cronin, K.A.; Plevritis, S.K.; Fryback, D.G.; Clarke, L.; Zelen, M.; Mandelblatt, J.S.; Yakovlev, A.Y.; Habbema, J.D.F.; Feuer, E.J. Effect of screening and adjuvant therapy on mortality from breast cancer. *N. Engl. J. Med.* **2005**, *353*, 1784–1792. [CrossRef] [PubMed]
39. McDonald, E.S.; Clark, A.S.; Tchou, J.; Zhang, P.; Freedman, G.M. Clinical diagnosis and management of breast cancer. *J. Nucl. Med.* **2016**, *57*, 9–16. [CrossRef]
40. Peart, O. Breast intervention and breast cancer treatment options. *Radiol. Technol.* **2015**, *86*, 535.
41. Dai, X.; Cheng, H.; Bai, Z.; Li, J. Breast Cancer Cell Line Classification and its relevance with breast tumor subtyping. *J. Cancer* **2017**, *8*, 3131–3141. [CrossRef]
42. Albrecht-Buehler, G. The simulation of microgravity conditions on the ground. *ASGSB Bull. Publ. Am. Soc. Gravit. Space Biol.* **1992**, *5*, 3–10.
43. Herranz, R.; Anken, R.; Boonstra, J.; Braun, M.; Christianen, P.C.; De Geest, M.; Hauslage, J.; Hilbig, R.; Hill, R.J.; Lebert, M.; et al. Ground-based facilities for simulation of microgravity: Organism-specific recommendations for their use, and recommended terminology. *Astrobiology* **2013**, *13*, 1–17. [CrossRef]
44. Ingber, D.E.; Wang, N.; Stamenović, D. Tensegrity, cellular biophysics, and the mechanics of living systems. *Rep. Prog. Phys.* **2014**, *77*, 046603. [CrossRef]
45. Northcott, J.M.; Dean, I.S.; Mouw, J.K.; Weaver, V.M. Feeling stress: The mechanics of cancer progression and aggression. *Front. Cell Dev. Biol.* **2018**, *6*, 17. [CrossRef] [PubMed]
46. Yu, H.; Mouw, J.K.; Weaver, V.M. Forcing form and function: Biomechanical regulation of tumor evolution. *Trends Cell Boil.* **2011**, *21*, 47–56. [CrossRef] [PubMed]

47. Qian, A.R.; Yin, D.C.; Yang, P.F.; Lv, Y.; Tian, Z.C.; Shang, P. Application of diamagnetic levitation technology in biological sciences research. *IEEE Trans. Appl. Supercond.* **2013**, *23*, 3600305. [CrossRef]
48. Anil-Inevi, M.; Yaman, S.; Yildiz, A.A.; Meşe, G.; Yalcin-Ozuysal, O.; Tekin, H.C.; Ozcivici, E. Biofabrication of in situ Self Assembled 3D cell cultures in a weightlessness environment generated using magnetic levitation. *Sci. Rep.* **2018**, *8*, 7239. [CrossRef] [PubMed]
49. Masiello, M.G.; Cucina, A.; Proietti, S.; Palombo, A.; Coluccia, P.; D'Anselmi, F.; DiNicola, S.; Pasqualato, A.; Morini, V.; Bizzarri, M. Phenotypic switch induced by simulated microgravity on MDA-MB-231 breast cancer cells. *BioMed Res. Int.* **2014**, *2014*, 1–12. [CrossRef] [PubMed]
50. Kopp, S.; Slumstrup, L.; Corydon, T.J.; Sahana, J.; Aleshcheva, G.; Islam, T.; Magnusson, N.E.; Wehland, M.; Bauer, J.; Infanger, M.; et al. Identifications of novel mechanisms in breast cancer cells involving duct-like multicellular spheroid formation after exposure to the random positioning machine. *Sci. Rep.* **2016**, *6*, 26887. [CrossRef] [PubMed]
51. Kopp, S.; Sahana, J.; Islam, T.; Petersen, A.G.; Bauer, J.; Corydon, T.J.; Schulz, H.; Saar, K.; Huebner, N.; Slumstrup, L.; et al. The role of NFκB in spheroid formation of human breast cancer cells cultured on the Random Positioning Machine. *Sci. Rep.* **2018**, *8*, 921. [CrossRef]
52. Strube, F.; Infanger, M.; Dietz, C.; Romswinkel, A.; Kraus, A. Short-term effects of simulated microgravity on morphology and gene expression in human breast cancer cells. *Physiol. Int.* **2019**, *106*, 311–322. [CrossRef]
53. Sahana, J.; Nassef, M.Z.; Wehland, M.; Kopp, S.; Krüger, M.; Corydon, T.J.; Infanger, M.; Bauer, J.; Grimm, D. Decreased E-cadherin in MCF7 human breast cancer cells forming multicellular spheroids exposed to simulated microgravity. *Proteomics* **2018**, *18*. [CrossRef]
54. Nassef, M.Z.; Kopp, S.; Wehland, M.; Melnik, D.; Sahana, J.; Krüger, M.; Corydon, T.J.; Oltmann, H.; Schmitz, B.; Schütte, A.; et al. Real microgravity influences the cytoskeleton and focal adhesions in human breast cancer cells. *Int. J. Mol. Sci.* **2019**, *20*, 3156. [CrossRef]
55. Andersen, J.B.; Aaboe, M.; Borden, E.C.; Goloubeva, O.G.; Hassel, B.A.; Ørntoft, T.F. Stage-associated overexpression of the ubiquitin-like protein, ISG15, in bladder cancer. *Br. J. Cancer* **2006**, *94*, 1465–1471. [CrossRef] [PubMed]
56. Desai, S.D.; Haas, A.L.; Wood, L.M.; Tsai, Y.-C.; Pestka, S.; Rubin, E.H.; Saleem, A.; Nur-E-Kamal, A.; Liu, L.F. Elevated expression of ISG15 in tumor cells interferes with the ubiquitin/26S proteasome pathway. *Cancer Res.* **2006**, *66*, 921–928. [CrossRef] [PubMed]
57. Padovan, E.; Terracciano, L.; Certa, U.; Jacobs, B.; Reschner, A.; Bolli, M.; Spagnoli, G.C.; Borden, E.C.; Heberer, M. Interferon stimulated gene 15 constitutively produced by melanoma cells induces e-cadherin expression on human dendritic cells. *Cancer Res.* **2002**, *62*, 3453–3458. [PubMed]
58. Weichselbaum, R.R.; Ishwaran, H.; Yoon, T.; Nuyten, D.S.A.; Baker, S.W.; Khodarev, N.; Su, A.W.; Shaikh, A.Y.; Roach, P.; Kreike, B.; et al. An interferon-related gene signature for DNA damage resistance is a predictive marker for chemotherapy and radiation for breast cancer. *Proc. Natl. Acad. Sci. USA* **2008**, *105*, 18490–18495. [CrossRef]
59. Bektas, N.; Noetzel, E.; Veeck, J.; Press, M.F.; Kristiansen, G.; Naami, A.; Hartmann, A.; Dimmler, A.; Beckmann, M.W.; Knüchel, R.; et al. The ubiquitin-like molecule interferon-stimulated gene 15 (ISG15) is a potential prognostic marker in human breast cancer. *Breast Cancer Res.* **2008**, *10*, R58. [CrossRef]
60. Bauer, T.J.; Gombocz, E.; Wehland, M.; Bauer, J.; Infanger, M.; Grimm, D. Insight in adhesion protein sialylation and microgravity dependent cell adhesion-An omics network approach. *Int. J. Mol. Sci.* **2020**, *21*, 1749. [CrossRef]
61. Aleshcheva, G.; Sahana, J.; Ma, X.; Hauslage, J.; Hemmersbach, R.; Egli, M.; Infanger, M.; Bauer, J.; Grimm, D. Changes in morphology, gene expression and protein content in chondrocytes cultured on a random positioning machine. *PLoS ONE* **2013**, *8*, e79057. [CrossRef]
62. Aleshcheva, G.; Wehland, M.; Sahana, J.; Bauer, J.; Corydon, T.J.; Hemmersbach, R.; Frett, T.; Egli, M.; Infanger, M.; Grosse, J.; et al. Moderate alterations of the cytoskeleton in human chondrocytes after short-term microgravity produced by parabolic flight maneuvers could be prevented by up-regulation of BMP-2 and SOX-9. *FASEB J.* **2015**, *29*, 2303–2314. [CrossRef]
63. Corydon, T.J.; Kopp, S.; Wehland, M.; Braun, M.; Schütte, A.; Mayer, T.; Hülsing, T.; Oltmann, H.; Schmitz, B.; Hemmersbach, R.; et al. Alterations of the cytoskeleton in human cells in space proved by life-cell imaging. *Sci. Rep.* **2016**, *6*, 20043. [CrossRef]

64. Warnke, E.; Pietsch, J.; Wehland, M.; Bauer, J.; Infanger, M.; Görög, M.; Hemmersbach, R.; Braun, M.; Ma, X.; Sahana, J.; et al. Spheroid formation of human thyroid cancer cells under simulated microgravity: A possible role of CTGF and CAV1. *Cell Commun. Signal.* **2014**, *12*, 32. [CrossRef]
65. Bumpers, H.L.; Janagama, D.G.; Manne, U.; Basson, M.D.; Katkoori, V. Nanomagnetic levitation three-dimensional cultures of breast and colorectal cancers. *J. Surg. Res.* **2015**, *194*, 319–326. [CrossRef] [PubMed]
66. Bumpers, H.; Janagama, D.; Manne, U.; Basson, M.; Katkoori, V. Development of magnetic levitation 3-D cultures of breast and colon cancer cells using carbon encapsulated cobalt magnetic nanoparticles. *J. Surg. Res.* **2014**, *186*, 515. [CrossRef]
67. Cogoli, A. Signal transduction in T lymphocytes in microgravity. *Gravit. Space Biol. Bull. Publ. Am. Soc. Gravit. Space Biol.* **1997**, *10*, 5–16.
68. Hatton, J.P.; Gaubert, F.; Lewis, M.L.; Darsel, Y.; Ohlmann, P.; Cazenave, J.; Schmitt, D. The kinetics of translocation and cellular quantity of protein kinase C in human leukocytes are modified during spaceflight. *FASEB J.* **1999**, *13*, S23–S33. [CrossRef] [PubMed]
69. Hammond, T.G.; Benes, E.; O'Reilly, K.C.; Wolf, D.A.; Linnehan, R.M.; Taher, A.; Kaysen, J.H.; Allen, P.L.; Goodwin, T.J. Mechanical culture conditions effect gene expression: Gravity-induced changes on the space shuttle. *Physiol. Genom.* **2000**, *3*, 163–173. [CrossRef]
70. Vorselen, D.; Roos, W.H.; Mackintosh, F.C.; Wuite, G.J.L.; Van Loon, J.J.W.A. The role of the cytoskeleton in sensing changes in gravity by nonspecialized cells. *FASEB J.* **2013**, *28*, 536–547. [CrossRef]
71. Xu, W.; Mezencev, R.; Kim, B.; Wang, L.; McDonald, J.F.; Sulchek, T. Cell stiffness is a biomarker of the metastatic potential of ovarian cancer cells. *PLoS ONE* **2012**, *7*, e46609. [CrossRef]
72. Li, J.; Zhang, S.; Chen, J.; Du, T.; Wang, Y.; Wang, Z. Modeled microgravity causes changes in the cytoskeleton and focal adhesions, and decreases in migration in malignant human MCF-7 cells. *Protoplasma* **2009**, *238*, 23–33. [CrossRef]
73. Chiotaki, R.; Polioudaki, H.; Theodoropoulos, P.A. Differential nuclear shape dynamics of invasive andnon-invasive breast cancer cells are associated with actin cytoskeleton organization and stability. *Biochem. Cell Boil.* **2014**, *92*, 287–295. [CrossRef]
74. Strube, F.; Infanger, M.; Wehland, M.; Delvinioti, X.; Romswinkel, A.; Dietz, C.; Kraus, A. Alteration of cytoskeleton morphology and gene expression in human breast cancer cells under simulated microgravity. *Cell J* **2019**, *22*, 106–114.
75. Rodrigues-Ferreira, S.; Molina, A.; Nahmias, C. Microtubule-associated tumor suppressors as prognostic biomarkers in breast cancer. *Breast Cancer Res. Treat.* **2019**, *179*, 267–273. [CrossRef] [PubMed]
76. Hendrix, M.J.; Seftor, E.A.; Seftor, R.E.; Trevor, K.T. Experimental co-expression of vimentin and keratin intermediate filaments in human breast cancer cells results in phenotypic interconversion and increased invasive behavior. *Am. J. Pathol.* **1997**, *150*, 483–495. [PubMed]
77. Keeling, M.C.; Flores, L.R.; Dodhy, A.H.; Murray, E.R.; Gavara, N. Actomyosin and vimentin cytoskeletal networks regulate nuclear shape, mechanics and chromatin organization. *Sci. Rep.* **2017**, *7*, 5219. [CrossRef] [PubMed]
78. Qian, A.; Zhang, W.; Xie, L.; Weng, Y.; Yang, P.; Wang, Z.; Hu, L.; Xu, H.; Tian, Z.; Shang, P. Simulated weightlessness alters biological characteristics of human breast cancer cell line MCF-7. *Acta Astronaut.* **2008**, *63*, 947–958. [CrossRef]
79. Chen, L.; Yang, X.; Cui, X.; Jiang, M.; Gui, Y.; Zhang, Y.; Luo, X. Adrenomedullin is a key protein mediating rotary cell culture system that induces the effects of simulated microgravity on human breast cancer cells. *Microgravity Sci. Technol.* **2015**, *27*, 417–426. [CrossRef]
80. Velasco-Velázquez, M.A.; Li, Z.; Casimiro, M.; Loro, E.; Homsi, N.; Pestell, R.G. Examining the role of cyclin D1 in breast cancer. *Futur. Oncol.* **2011**, *7*, 753–765. [CrossRef]
81. Carminati, J.L.; Stearns, T. Microtubules orient the mitotic spindle in yeast through dynein-dependent interactions with the cell cortex. *J. Cell Biol.* **1997**, *138*, 629–641. [CrossRef]
82. Zheng, H.; Tian, W.; Yan, H.; Yue, L.; Zhang, Y.; Han, F.; Chen, X.; Li, Y. Rotary culture promotes the proliferation of MCF-7 cells encapsulated in three-dimensional collagen-alginate hydrogels via activation of the ERK1/2-MAPK pathway. *Biomed. Mater.* **2012**, *7*, 015003. [CrossRef]

83. Coinu, R.; Chiaviello, A.; Galleri, G.; Franconi, F.; Crescenzi, E.; Palumbo, G. Exposure to modeled microgravity induces metabolic idleness in malignant human MCF-7 and normal murine VSMC cells. *FEBS Lett.* **2006**, *580*, 2465–2470. [CrossRef]
84. Nassef, M.Z.; Kopp, S.; Melnik, D.; Corydon, T.J.; Sahana, J.; Krüger, M.; Wehland, M.; Bauer, T.J.; Liemersdorf, C.; Hemmersbach, R.; et al. Short-term microgravity influences cell adhesion in human breast cancer cells. *Int. J. Mol. Sci.* **2019**, *20*, 5730. [CrossRef]
85. Li, H.; Wang, H.; Deng, K.; Han, W.; Hong, B.; Lin, W. The ratio of Bcl-2/Bim as a predictor of cisplatin response provides a rational combination of ABT-263 with cisplatin or radiation in small cell lung cancer. *Cancer Biomark.* **2019**, *24*, 51–59. [CrossRef] [PubMed]
86. Jiang, N.; Chen, Z.; Li, B.; Guo, S.; Li, A.; Zhang, T.; Fu, X.; Si, S.; Cui, Y. Effects of rotary cell culture system-simulated microgravity on the ultrastructure and biological behavior of human MDA-MB-231 breast cancer cells. *Precis. Radiat. Oncol.* **2019**, *3*, 87–93. [CrossRef]
87. Bizzarri, M. Fake news from the outer space. *J. Biol. Sci.* **2020**, *3*, 2. [CrossRef]
88. Nagano, M.; Hoshino, D.; Koshikawa, N.; Akizawa, T.; Seiki, M. Turnover of focal adhesions and cancer cell migration. *Int. J. Cell Biol.* **2012**, *2012*, 1–10. [CrossRef] [PubMed]
89. Zamir, E.; Geiger, B. Molecular complexity and dynamics of cell-matrix adhesions. *J. Cell Sci.* **2001**, *114*, 3583–3590. [PubMed]
90. Chen, J. Tumor Cells in Microgravity. In *Into Space-A Journey of How Humans Adapt and Live in Microgravity*; Russomano, T., Rehnberg, L., Eds.; IntechOpen: London, UK, 2018; pp. 77214–105772.
91. Shi, S.; Li, Q.; Cao, Q.; Diao, Y.; Zhang, Y.; Yue, L.; Wei, L. EMT transcription factors are involved in the altered cell adhesion under simulated microgravity effect or overloading by regulation of E-cadherin. *Int. J. Mol. Sci.* **2020**, *21*, 1349. [CrossRef] [PubMed]
92. Franz, C.M.; Jones, G.E.; Ridley, A.J. Cell migration in development and disease. *Dev. Cell* **2002**, *2*, 153–158. [CrossRef]
93. Shi, Z.-X.; Rao, W.; Wang, H.; Wang, N.-D.; Si, J.-W.; Zhao, J.; Li, J.-C.; Wang, Z.-R. Modeled microgravity suppressed invasion and migration of human glioblastoma U87 cells through downregulating store-operated calcium entry. *Biochem. Biophys. Res. Commun.* **2015**, *457*, 378–384. [CrossRef]
94. Chung, J.H.; Ahn, C.B.; Son, K.H.; Yi, E.; Son, H.S.; Kim, H.-S.; Lee, S.H.; Ho, C.J.; Bum, A.C.; Hui, S.K.; et al. Simulated microgravity effects on nonsmall cell lung cancer cell proliferation and migration. *Aerosp. Med. Hum. Perform.* **2017**, *88*, 82–89. [CrossRef]
95. Chaudhuri, O.; Koshy, S.T.; Da Cunha, C.B.; Shin, J.-W.; Verbeke, C.S.; Allison, K.H.; Mooney, D.J. Extracellular matrix stiffness and composition jointly regulate the induction of malignant phenotypes in mammary epithelium. *Nat. Mater.* **2014**, *13*, 970–978. [CrossRef]
96. Stylianopoulos, T.; Munn, L.L.; Jain, R.K. Reengineering the physical microenvironment of tumors to improve drug delivery and efficacy: From mathematical modeling to bench to bedside. *Trends Cancer* **2018**, *4*, 292–319. [CrossRef] [PubMed]
97. Samani, A.; Zubovits, J.T.; Plewes, D. Elastic moduli of normal and pathological human breast tissues: An inversion-technique-based investigation of 169 samples. *Phys. Med. Biol.* **2007**, *52*, 1565–1576. [CrossRef] [PubMed]
98. Park, H.-J.; Helfman, D.M. Up-regulated fibronectin in 3D culture facilitates spreading of triple negative breast cancer cells on 2D through integrin β-5 and Src. *Sci. Rep.* **2019**, *9*, 19950. [CrossRef] [PubMed]
99. Zheng, H.-X.; Tian, W.; Yan, H.-J.; Jiang, H.-D.; Liu, S.-S.; Yue, L.; Han, F.; Wei, L.-J.; Chen, X.-B.; Li, Y. Expression of estrogen receptor α in human breast cancer cells regulates mitochondrial oxidative stress under simulated microgravity. *Adv. Space Res.* **2012**, *49*, 1432–1440. [CrossRef]
100. De Mas‡, I.M.; Aguilar‡, E.; Jayaraman, A.; Polat, I.H.; Martín-Bernabé, A.; Bharat, R.; Foguet, C.; Milà, E.; Papp, B.; Centelles, J.J.; et al. Cancer cell metabolism as new targets for novel designed therapies. *Futur. Med. Chem.* **2014**, *6*, 1791–1810. [CrossRef]
101. Heiden, M.G.V.; Locasale, J.W.; Swanson, K.D.; Sharfi, H.; Heffron, G.J.; Amador-Noguez, D.; Christofk, H.R.; Wagner, G.; Rabinowitz, J.D.; Asara, J.M.; et al. Evidence for an alternative glycolytic pathway in rapidly proliferating cells. *Science* **2010**, *329*, 1492–1499. [CrossRef]
102. Hekmat, A.; Rabizadeh, M.; Safavi, M.; Hajebrahimi, Z. The comparison of the apoptosis effects of titanium dioxide nanoparticles into MDA-MB-231 cell line in microgravity and gravity conditions. *Nanomed. J.* **2019**, *6*, 120–127. [CrossRef]

103. Prasanth, D.; Suresh, S.; Prathivadhi-Bhayankaram, S.; Mimlitz, M.; Zetocha, N.; Lee, B.; Ekpenyong, A. Microgravity modulates effects of chemotherapeutic drugs on cancer cell migration. *Life* **2020**, *10*, 162. [CrossRef]
104. Shelhamer, M. Parabolic flight as a spaceflight analog. *J. Appl. Physiol.* **2016**, *120*, 1442–1448. [CrossRef]
105. Kopp, S.; Krüger, M.; Feldmann, S.; Oltmann, H.; Schütte, A.; Schmitz, B.; Bauer, J.; Schulz, H.; Saar, K.; Huebner, N.; et al. Thyroid cancer cells in space during the TEXUS-53 sounding rocket mission-The THYROID Project. *Sci. Rep.* **2018**, *8*, 10355. [CrossRef]
106. Vassy, J.; Portet, S.; Beil, M.; Millot, G.; Fauvel-Lafève, F.; Karniguian, A.; Gasset, G.; Irinopoulou, T.; Calvo, F.; Rigaut, J.P.; et al. The effect of weightlessness on cytoskeleton architecture and proliferation of human breast cancer cell line MCF-7. *FASEB J.* **2001**, *15*, 1104–1106. [CrossRef] [PubMed]
107. Vassy, J.; Portet, S.; Beil, M.; Millot, G.; Fauvel-Lafève, F.; Gasset, G.; Schoevaert, D. Weightlessness acts on human breast cancer cell line MCF-7. *Adv. Space Res.* **2003**, *32*, 1595–1603. [CrossRef]
108. Fife, C.M.; McCarroll, J.A.; Kavallaris, M. Movers and shakers: Cell cytoskeleton in cancer metastasis. *Br. J. Pharmacol.* **2014**, *171*, 5507–5523. [CrossRef] [PubMed]
109. Hohmann, T.; Dehghani, F. The cytoskeleton-A complex interacting meshwork. *Cells* **2019**, *8*, 362. [CrossRef] [PubMed]
110. Padilla-Rodriguez, M.; Parker, S.S.; Adams, D.G.; Westerling, T.; Puleo, J.I.; Watson, A.W.; Hill, S.M.; Noon, M.; Gaudin, R.; Aaron, J.; et al. The actin cytoskeletal architecture of estrogen receptor positive breast cancer cells suppresses invasion. *Nat. Commun.* **2018**, *9*, 1–16. [CrossRef]
111. Mouneimne, G.; Hansen, S.D.; Selfors, L.M.; Petrak, L.; Hickey, M.M.; Gallegos, L.L.; Simpson, K.J.; Lim, J.; Gertler, F.B.; Hartwig, J.H.; et al. Differential remodeling of actin cytoskeleton architecture by profilin isoforms leads to distinct effects on cell migration and invasion. *Cancer Cell* **2012**, *22*, 615–630. [CrossRef]
112. Tavares, S.; Vieira, A.F.; Taubenberger, A.; Araújo, M.; Martins, N.P.; Bras-Pereira, C.; Polonia, A.; Herbig, M.; Barreto, C.; Otto, O.; et al. Actin stress fiber organization promotes cell stiffening and proliferation of pre-invasive breast cancer cells. *Nat. Commun.* **2017**, *8*, 15237. [CrossRef]
113. Reynolds, D.S.; Tevis, K.M.; Blessing, W.A.; Colson, Y.L.; Zaman, M.H.; Grinstaff, M.W. Breast cancer spheroids reveal a differential cancer stem cell response to chemotherapeutic treatment. *Sci. Rep.* **2017**, *7*, 10382. [CrossRef]
114. Paszek, M.J.; Zahir, N.; Johnson, K.R.; Lakins, J.N.; Rozenberg, G.I.; Gefen, A.; Reinhart-King, C.A.; Margulies, S.S.; Dembo, M.; Boettiger, D.; et al. Tensional homeostasis and the malignant phenotype. *Cancer Cell* **2005**, *8*, 241–254. [CrossRef]
115. Friedrich, J.; Ebner, R.; Kunz-Schughart, L.A. Experimental anti-tumor therapy in 3-D: Spheroids-old hat or new challenge? *Int. J. Radiat. Boil.* **2007**, *83*, 849–871. [CrossRef]
116. Grosse, J.; Wehland, M.; Pietsch, J.; Schulz, H.; Saar, K.; Hübner, N.; Eilles, C.; Bauer, J.; Abou-El-Ardat, K.; Baatout, S.; et al. Gravity-sensitive signaling drives 3-dimensional formation of multicellular thyroid cancer spheroids. *FASEB J.* **2012**, *26*, 5124–5140. [CrossRef] [PubMed]
117. Pietsch, J.; Ma, X.; Wehland, M.; Aleshcheva, G.; Schwarzwälder, A.; Segerer, J.; Birlem, M.; Horn, A.; Bauer, J.; Infanger, M.; et al. Spheroid formation of human thyroid cancer cells in an automated culturing system during the Shenzhou-8 Space mission. *Biomaterials* **2013**, *34*, 7694–7705. [CrossRef] [PubMed]
118. Pietsch, J.; Sickmann, A.; Weber, G.; Bauer, J.; Egli, M.; Wildgruber, R.; Infanger, M.; Grimm, D. A proteomic approach to analysing spheroid formation of two human thyroid cell lines cultured on a random positioning machine. *Proteomics* **2011**, *11*, 2095–2104. [CrossRef] [PubMed]
119. Li, R.; Gundersen, G.G. Beyond polymer polarity: How the cytoskeleton builds a polarized cell. *Nat. Rev. Mol. Cell Biol.* **2008**, *9*, 860–873. [CrossRef]
120. Kunz-Schughart, L.A.; Freyer, J.P.; Hofstaedter, F.; Ebner, R. The use of 3-D cultures for high-throughput screening: The multicellular spheroid model. *J. Biomol. Screen.* **2004**, *9*, 273–285. [CrossRef]
121. Ellsworth, R.E.; Blackburn, H.L.; Shriver, C.D.; Soon-Shiong, P.; Ellsworth, D.L. Molecular heterogeneity in breast cancer: State of the science and implications for patient care. *Semin. Cell Dev. Boil.* **2017**, *64*, 65–72. [CrossRef]
122. Vamvakidou, A.P.; Mondrinos, M.J.; Petushi, S.P.; Garcia, F.U.; Lelkes, P.I.; Tozeren, A. Heterogeneous breast tumoroids: An in vitro assay for investigating cellular heterogeneity and drug delivery. *J. Biomol. Screen.* **2006**, *12*, 13–20. [CrossRef]
123. Freeman, M. *Challenges of Human Space Exploration*; Springer: London, UK, 2000.

124. Kaur, P.; Ward, B.; Saha, B.; Young, L.; Groshen, S.; Techy, G.; Lu, Y.; Atkinson, R.; Taylor, C.R.; Ingram, M.; et al. Human breast cancer histoid. *J. Histochem. Cytochem.* **2011**, *59*, 1087–1100. [CrossRef]
125. Jaganathan, H.; Gage, J.; Leonard, F.; Srinivasan, S.; Souza, G.R.; Dave, B.; Godin, B. Three-dimensional in vitro co-culture model of breast tumor using magnetic levitation. *Sci. Rep.* **2014**, *4*, 6468. [CrossRef]
126. Keller, F.; Rudolf, R.; Hafner, M. Towards optimized breast cancer 3D spheroid mono-and co-culture models for pharmacological research and screening. *J. Cell. Biotechnol.* **2019**, *5*, 89–101. [CrossRef]
127. Cui, X.; Hartanto, Y.; Zhang, H. Advances in multicellular spheroids formation. *J. R. Soc. Interface* **2017**, *14*, 20160877. [CrossRef] [PubMed]
128. Froehlich, K.; Haeger, J.-D.; Heger, J.; Pastuschek, J.; Photini, S.M.; Pfarrer, C.; Mrowka, R.; Schleußner, E.; Yan, Y.; Lupp, A.; et al. Generation of multicellular breast cancer tumor spheroids: Comparison of different protocols. *J. Mammary Gland. Biol. Neoplasia* **2016**, *21*, 89–98. [CrossRef] [PubMed]
129. Svejgaard, B.; Wehland, M.; Ma, X.; Kopp, S.; Sahana, J.; Warnke, E.; Aleshcheva, G.; Hemmersbach, R.; Hauslage, J.; Grosse, J.; et al. Common effects on cancer cells exerted by a random positioning machine and a 2D clinostat. *PLoS ONE* **2015**, *10*, e0135157. [CrossRef] [PubMed]
130. Lukashev, M. ECM signalling: Orchestrating cell behaviour and misbehaviour. *Trends Cell Boil.* **1998**, *8*, 437–441. [CrossRef]
131. Talukdar, S.; Mandal, M.; Hutmacher, D.W.; Russell, P.; Soekmadji, C.; Kundu, S.C. Engineered silk fibroin protein 3D matrices for in vitro tumor model. *Biomaterials* **2011**, *32*, 2149–2159. [CrossRef]
132. Leonard, F.; Godin, B. 3D In Vitro model for breast cancer research using magnetic levitation and bioprinting method. *Breast Cancer* **2016**, *1406*, 239–251. [CrossRef]
133. Dittrich, A.; Grimm, D.; Sahana, J.; Bauer, J.; Krüger, M.; Infanger, M.; Magnusson, N.E. Key proteins involved in spheroid formation and angiogenesis in endothelial cells after long-term exposure to simulated microgravity. *Cell. Physiol. Biochem.* **2018**, *45*, 429–445. [CrossRef]
134. Esquivel-Velázquez, M.; Ostoa-Saloma, P.; Arreola, M.I.P.; Nava-Castro, K.E.; Castro, J.I.; Morales-Montor, J. The role of cytokines in breast cancer development and progression. *J. Interf. Cytokine Res.* **2015**, *35*, 1–16. [CrossRef]
135. Kopp, S.; Warnke, E.; Wehland, M.; Aleshcheva, G.; Magnusson, N.E.; Hemmersbach, R.; Corydon, T.J.; Bauer, J.; Infanger, M.; Grimm, D. Mechanisms of three-dimensional growth of thyroid cells during long-term simulated microgravity. *Sci. Rep.* **2015**, *5*, 16691. [CrossRef]
136. Sullivan, N.J.; Sasser, A.K.; Axel, A.E.; Vesuna, F.; Raman, V.; Ramirez, N.; Oberyszyn, T.M.; Hall, B.M. Interleukin-6 induces an epithelial-mesenchymal transition phenotype in human breast cancer cells. *Oncogene* **2009**, *28*, 2940–2947. [CrossRef]
137. Barr, Y.R.; Bacal, K.; Jones, J.A.; Hamilton, D.R. Breast cancer and spaceflight: Risk and management. *Aviat. Space Environ. Med.* **2007**, *78*, 26–37.



© 2020 by the authors. Licensee MDPI, Basel, Switzerland. This article is an open access article distributed under the terms and conditions of the Creative Commons Attribution (CC BY) license (http://creativecommons.org/licenses/by/4.0/).

www.nature.com/scientificreports

SCIENTIFIC REPORTS

OPEN

Thyroid cancer cells in space during the TEXUS-53 sounding rocket mission – The THYROID Project

Received: 23 March 2018
Accepted: 28 June 2018
Published online: 09 July 2018

Sascha Kopp[1], Marcus Krüger[1], Stefan Feldmann[2], Hergen Oltmann[2], Andreas Schütte[2], Burkhard Schmitz[2], Johann Bauer[3], Herbert Schulz[4], Kathrin Saar[5], Norbert Huebner[5], Markus Wehland[1], Mohamed Zakaria Nassef[1], Daniela Melnik[1], Stefan Meltendorf[6], Manfred Infanger[1] & Daniela Grimm[1,7,8]

Human follicular thyroid cancer cells (FTC-133) were sent to space via a sounding rocket during the TEXUS-53 mission to determine the impact of short-term microgravity on these cells. To enable cell culture and fixation in real microgravity, an automated experiment container (EC) was constructed. In order to ensure safe cell culture, cell-chambers consisting of polycarbonate (PC) material were used. They were highly biocompatible as proved by measuring cell survival using Annexin V flow cytometry. In the follow-up experiment, FTC-133 cells were sent to space via a sounding rocket and were fixed before and after the microgravity (µ*g*) phase with RNA*later*. In addition, cells were tested for reactions on hypergravity (hyper-*g*) as much as 18 *g* to determine whether worst case acceleration during launch can have an influence on the cells. We investigated genes belonging to biological processes such as cytoskeleton, cell adhesion, tumor growth, angiogenesis and apoptosis. Pathway analyses revealed central functions of *VEGFA* and *EGF*. *EGF* upregulates aspartate beta-hydroxylase (*ASPH*) which is influencing *CASP3*. Hyper-*g* induced a significant up-regulation of *TUBB1*, *VIM*, *RDX*, *CAV1*, *VEGFA* and *BCL2*. FTC-133 cells grown in an automated EC exposed to µ*g* revealed moderate gene expression changes indicating their survival in orbit.

Thyroid cancer is the most common malignancy of the endocrine system. The incidence of this cancer type continues to rise steadily worldwide[1]. According to GLOBOCAN, 298,102 new cases were diagnosed in the world population and 39,769 people died from thyroid cancer in 2012. Thyroid cancer comprises a group of tumors with different features[2]. Whereas differentiated thyroid cancer (DTC; papillary or follicular) types are well treatable and usually curable, poorly differentiated tumors are aggressive, metastasize early and have a much poorer prognosis[3]. Unfortunately, recurrent DTC can become less-differentiated, lack iodine uptake capability and is radioiodine refractory. Patients with this cancer type have a remarkably reduced survivability and treatment options for DTC are extremely limited. Therefore, new ideas in terms of drug development are needed to fill this treatment gap[3,4].

Alterations of gravity have been shown to remarkably influence growth and biological processes of malignant cancer cells[5–10]. Thus, altered gravity experiments became a promising method to improve our understanding of thyroid cancer biology, and may be useful to detect interesting target proteins for future cancer treatment.

[1]Clinic for Plastic, Aesthetic and Hand Surgery, Otto-von-Guericke-University Magdeburg, Leipziger Str. 44, D-39120, Magdeburg, Germany. [2]Airbus Defence and Space GmbH, Airbus-Allee 1, D-28199, Bremen, Germany. [3]Max-Planck Institute of Biochemistry, D-82152, Martinsried, Germany. [4]Cologne Center for Genomics, University of Cologne, D-50931, Cologne, Germany. [5]Max-Delbrück-Center for Molecular Medicine, D-13092, Berlin-Buch, Germany. [6]Experimental Pediatrics and Neonatology, University Hospital, Otto-von-Guericke University Magdeburg, Leipziger Str. 44, D-39120, Magdeburg, Germany. [7]Department of Biomedicine, Aarhus University, Wilhelm Meyers Allé 4, DK-8000, Aarhus C, Denmark. [8]Gravitational Biology and Translational Regenerative Medicine, Faculty of Medicine and Mechanical Engineering, Otto-von-Guericke-University Magdeburg, D-39120, Magdeburg, Germany. Sascha Kopp and Marcus Krüger contributed equally to this work. Correspondence and requests for materials should be addressed to D.G. (email: dgg@biomed.au.dk)

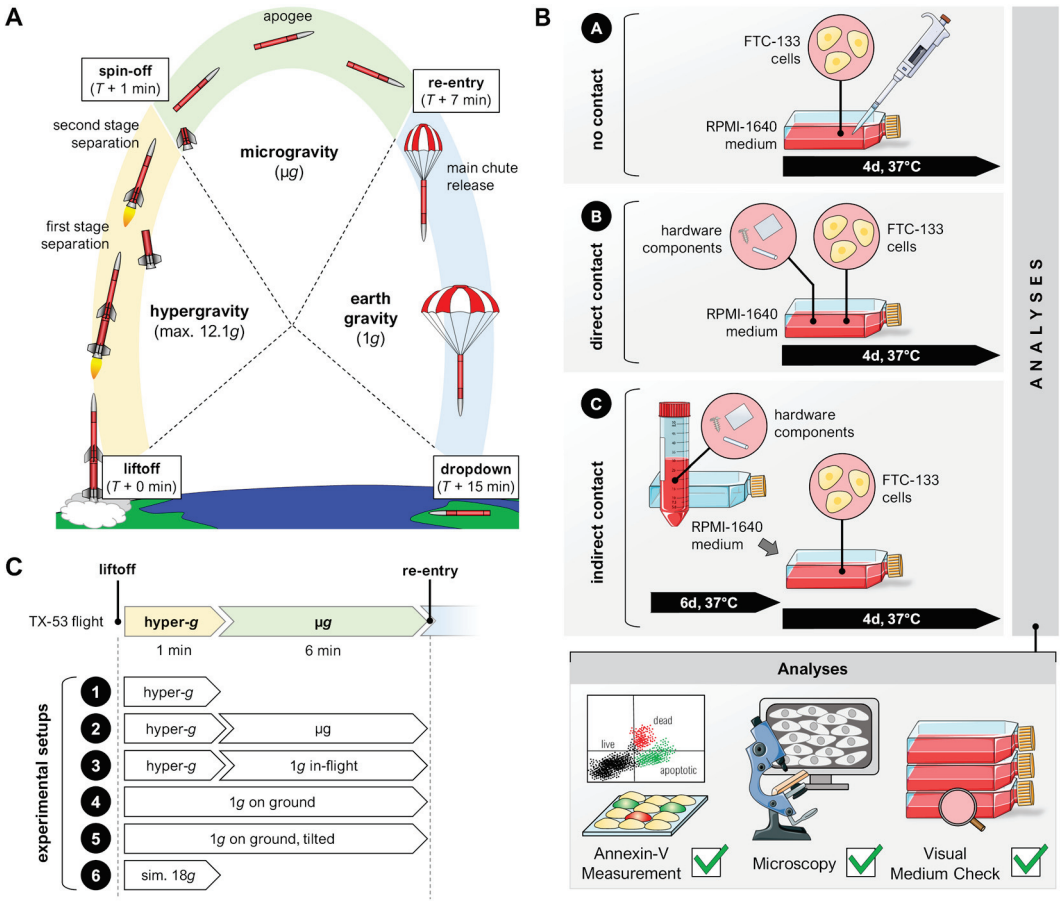


Figure 1. Experimental setup of the study for a rocket mission. (**A**) rocket flight; (**B**) biocompatibility experiments; (**C**) different experiment groups. Parts of the figure were drawn by using pictures from Servier Medical Art. Servier Medical Art by Servier is licensed under a Creative Commons Attribution 3.0 Unported License (https://creativecommons.org/licenses/by/3.0/).

Dedifferentiated thyroid cancer cells of the cell line FTC-133 had already been exposed to short-term microgravity (22 seconds) during parabolic flights and to long-term microgravity attained during the SIMBOX/Shenzhou-8 mission and the CELLBOX-1 mission[11–14].

While parabolic flights offer an accumulation of 31 parabolas each with 22 sec of microgravity (μ*g*) and 40 sec of 1.8 *g*, a space mission offers up to a 14-day or longer phase of microgravity[12,15–19].

FTC-133 cells were fixed with RNA*later* and paraformaldehyde respectively during these missions, after the μ*g*-phases and were then analyzed post-flight in the respective laboratories. While short-term μ*g*-exposure resulted in gene expression changes which could be interpreted as an increase in tumor cell malignancy, cultivation of the same cell line in space for 10 days resulted in a gene expression profile hinting to a highly decreased malignancy in addition to three-dimensional (3D) growth[11,12].

Furthermore, FTC-133 cells expressing Lifeact-GFP marker protein were investigated during a sounding rocket mission using a compact fluorescence microscope (FLUMIAS) for fast live-cell imaging under real microgravity, revealing rapid cytoskeletal changes[18]. To examine the underlying mechanisms of these changes we exposed FTC-133 cells to 6 minutes of μ*g* during a sounding rocket mission (Fig. 1).

Based on data from these experiments we participated in the sounding rocket mission with the acronym TEXUS 53 (*Technologische Experimente unter Schwerelosigkeit*) in January 2016. The launch center was the Esrange Space Center in Kiruna, Sweden, which is operated by the Swedish Space Corporation. Requirements for the rocket flight were manifold. Firstly, the cell culture chambers to be used had to be adaptable to the changed conditions of a use in space, but also be biocompatible with the human thyroid cancer cells and the liquids utilized. Secondly, the cell chambers needed a sufficient growth area in order to harvest sufficient material for further analyses together with a significant number of replicates. In addition, an onboard 1*g*-centrifuge was necessary to discriminate between μ*g*-effects on the cells, launch and vibrations effects. Finally, the cell chambers had to be flushed with the fixative RNA*later* via a remote controlled operation at the time points of interest.

The major aim of this study was therefore to develop the experimental hardware for adherent cells, suitable to be operated during a rocket flight in real microgravity. Consequently, a cell container combined with a module allowing automatic fluid exchange and entrainment of replacement culture medium and fixatives was developed. This manuscript is comprised of a chronological description of this experiment and the post-flight evaluation of the resulting samples. It is completed by the investigation of the cells' gene expression in real microgravity (r-μ*g*) and hyper-*g*.

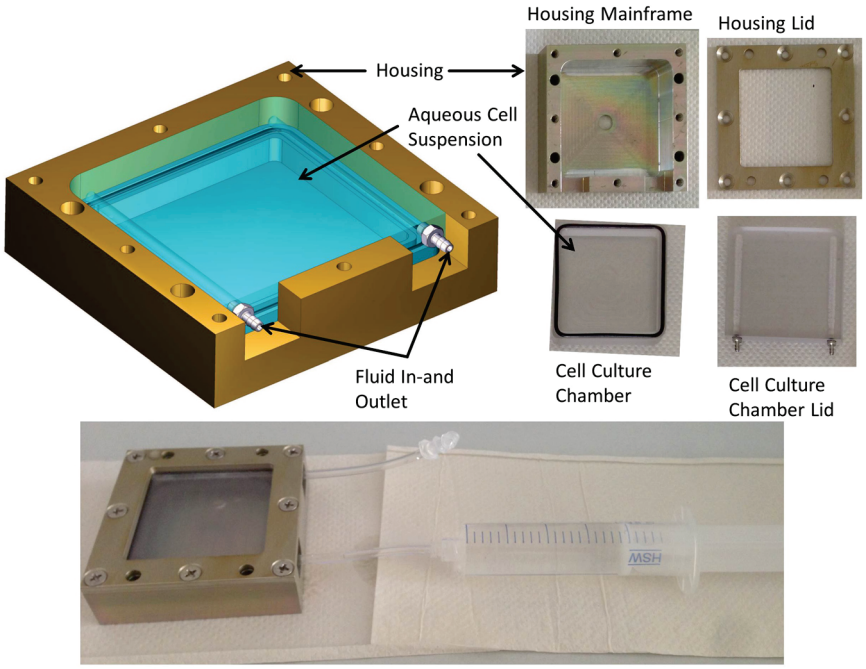


Figure 2. Components of the culture chamber (CC). The CC is composed of four parts. Cell culture chamber and lid are in direct contact to the cells. Housing and lid are used to keep the CC together.

Results

To examine the mechanisms of gene expression changes of FTC-133 cells during the 6-min lasting µg-phase of a sounding rocket mission (Fig. 1A), it was necessary to recover RNA-stabilized cells after the mission. Therefore, the company Airbus Defence and Space designed, assembled and operated a hardware suitable to save the treated cells until return and from material which passed the biocompatibility test (Fig. 1B). The hardware is thermo-controlled to 37 °C and easy access to the hardware in the rocket is possible by separate openings in the outer structure so that EUs could be installed at the latest possible time before launch. The experimental setup is given in detail in Fig. 1C.

Biocompatibility Test. FTC-133 thyroid cancer cells used for the TX-53 mission were grown without contact to the cell chamber (CC) material, with direct contact to the CC material, or in conditioned medium previously incubated with CC material (Fig. 1B). The examined medium did not show any pH changes due to the PC material. In addition, microscopic analysis of the cells presented comparable cell numbers and viability, with the cells keeping their characteristic morphology. To ensure cell viability in the PC environment, Annexin-V was investigated via flow cytometry. All three scenarios presented cell viabilities between 83% and 95%, while the number of apoptotic and necrotic cells was low (data not shown).

Construction of the experiment container and their role in the sounding rocket mission. *Cell chambers.* The CCs provided a growth area allowing harvesting sufficient material for further analyses together with a significant number of replicates (Fig. 2). They are composed of two parts (Fig. 2). The cell holding chamber consists of two pieces milled from a PC block (blue). The lower part is 0.5 cm deep and has a cell growth area of 5 × 5 cm. The bottom was not special treated, as viability test and cell number determination presented good biocompatibility. The lid is also composed of PC. It holds two vertical tubes, which are studded with small holes pointing to the inner side of the cell chamber. The tubes are used for fluid in- and outlet. An O-ring embedded into the border of the lower chamber ensures proper sealing.

The PC culture chambers are embedded into an aluminum housing (gold). The housing lid presses the two PC pieces together when screwed on. It holds, in addition to the screw holes, four holes, which are used to connect the culture chambers to the fixation unit. All parts of the culture chamber are autoclavable and were disinfected prior to cell seeding.

Experimental Unit and Rigid platform. One experimental unit (EU) consists of two spring-loaded syringes and can hold two culture chambers (Fig. 3). The syringe is not only holding the fixative, but also is used as the reservoir for the medium, which leaves the cell cultivation chamber when triggered. The loaded syringes are connected to the culture chambers via silicon tubing. The triggers of the loaded system are valves, which squeeze the tubing to keep the pressure in the syringes. By releasing the squeeze on the tube, the spring pushes the fixative into the culture chamber, while the medium is guided through the outlet and into the back of the syringe. Syringes can be triggered separately, allowing fixation on various time points. Three experimental units are mounted to the rigid platform resulting in six cell culture chambers.

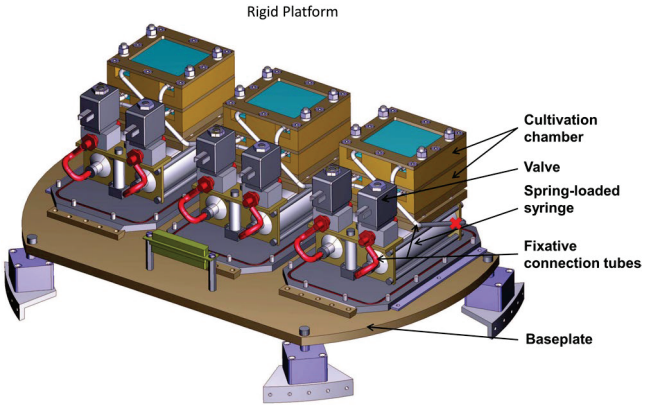


Figure 3. Rigid platform with three experimental units. One unit is composed of two CCs (gold) connected with a silicon tube (red) to two spring-loaded fixative syringes (light grey) which are triggered by two valves (dark grey) accordingly.

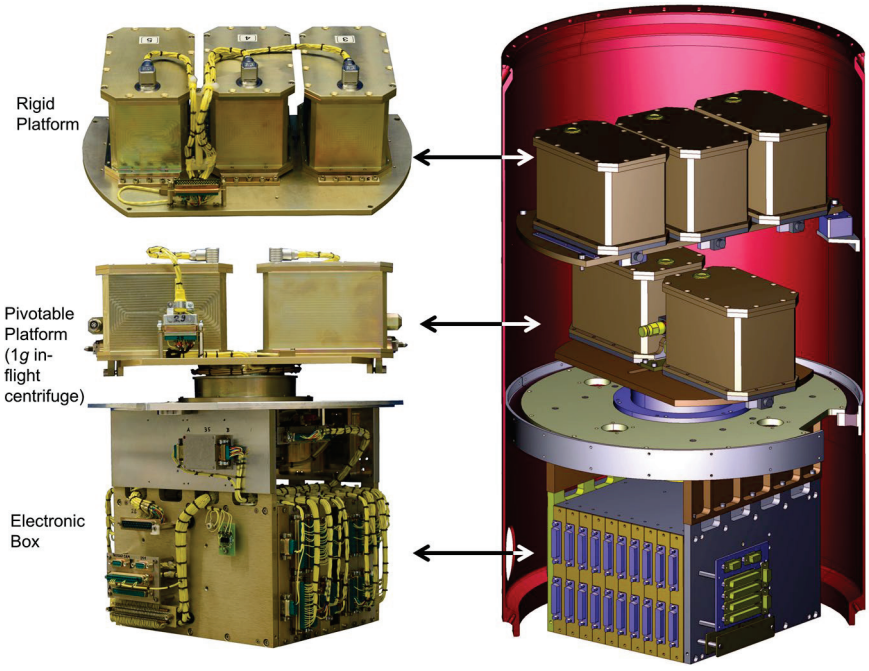


Figure 4. TEXUS 53 THYROID experiment. Left side: both platforms and electronic box. Right side: CAD drawing of integrated experiment module with external structure (red).

The EUs were prepared by Airbus Defence and Space. After assembling the parts and connecting the CCs, the EUs were introduced into a pressure resistant envelope and tested for pressure leakage in an evacuation chamber to exclude pressure-leakage.

Pivotal platform. Experimental units, as described above, are also mounted on the pivotal platform (Fig. 4). The pivotal platform is connected to a motor, which enables centrifugation of samples at 1 *g* during rocket flight. The centrifuge is started immediately after entrance into microgravity, giving the researcher the opportunity to distinguish between accumulative effects of hyper-*g* during takeoff and 1 *g*, and hyper-*g* in addition to µg. The centrifuge holds two experimental units, resulting in four samples. Due to the orientation of the cells on the centrifuge, they are exposed to hyper-*g* vertically while they feel 1 *g* horizontally (Supplemental Fig. 1). This increased the need for additional controls, referred to as 1 *g* in-flight simulation. In parallel to the rocket flight, experimental units on ground were either placed in a 90 degree tilted position to simulate the horizontal stimulation of the in-flight centrifuge or a non-tilted position as regular control for 6 minutes and were afterwards remote controlled chemically fixed.

Impact of microgravity and hypergravity on gene expression. In order to gain reliable information about alteration of gene expression patterns the experimental groups depicted in Fig. 1C were prepared for the sounding rocket experiment as described under Material and Methods. After the mission, gene array experiments were performed. In addition, qPCR analyses were done on target gene products which were differentially regulated in real microgravity during parabolic flight mission and space experiments[11,12,14,18]. To achieve a high comparability, we included the results of all possible scenarios described in the material section. These data are given in Fig. 5.

We tested for expression changes in cytoskeletal and associated genes such as β-actin (*ACTB*), β-tubulin (*TUBB*), vimentin (*VIM*), ezrin (*EZR*), radixin (*RDX*), and moesin (*MSN*). In addition, the extracellular matrix gene laminin (*LAMA1*) and the membrane associated genes caveolin 1 (*CAV1*), talin 1 (*TLN1*) and integrin beta 1 (*ITGB1*) were investigated. Furthermore, the expression of the signaling cytokines epithelial growth factor (*EGF*) and vascular endothelial growth factor A (*VEGFA*) was determined. Finally, we focused on the apoptosis involved factors bcl2 (*BCL2*), bax (*BAX*) and caspase 3 (*CASP3*). Beside *TUBB1* all these genes form a network of interaction. These genes and their products are influencing each other at gene and protein levels (Figs 6,7). Central functions are exerted by the genes of the cytokines *EGF* and *VEGFA* (Fig. 6), which are usually secreted in the culture supernatant (Fig. 7). They have either enhancing (green arrows) or down-regulating (red lines) effects on the genes of the cytoskeletal proteins actin, vimentin, ezrin, and integrin beta 1, and of the scaffolding protein caveolin-1 as well as on those of the apoptotic factors CASP3, BAX and BCL-2. The cytoskeletal proteins and apoptotic factors investigated are located within the cells. They are affected by the cytokine EGF in an indirect manner (Fig. 7, dashed) via corresponding membrane inserted receptors. But amongst themselves, they may influence each other indirectly via additional proteins (Fig. 7, dashed lines) or directly by physical interaction (solid arrows) or even complex formation (solid lines) as shown for zinc transporter 1, BCL2, moesin and integrin-beta-1 (Fig. 7).

All scenarios introduced before were tested for expression of the mentioned factors. We first determined the expression changes during worst-case hyper-*g* scenario produced by a centrifuge for 1 min (referred to as Hyper-*g* Con and Hyper-*g* Sim). We found a significant up-regulation of *TUBB1*, *RDX*, *VIM*, *CAV1*, *VEGFA* and *BCL2* (Fig. 5A,B,C,E,G and H). *MSN* and *TLN1* (data not shown) as well as *LAMA1* and *EGF* (Fig. 5D,F) presented a non-significant up-regulation in this scenario while *ACTB*, *EZR*, *ITGB1* (data not shown) like *BAX* and *CASP3* (Fig. 5I,J) gene expression remained unchanged. These results reveal an up-regulating influence of VEGF-A on the *BCL2* gene (green arrow) and a down-regulating effect on BAX (red line) (Figs 6, 7). But unregulated BAX suggests that the effect of VEGF-A down-regulating the expression of this factor is balanced by an effect of EGF favoring BAX expression. In contrast, up-regulated *BCL2* seems to be due to a positive effect of EGF and VEGF-A. Both cytokines appear also to be involved in up-regulation of vimentin.

The control scenarios (referred to as TX53 1 *g* ground, TX53 1 *g* IF, TX53 IFS ground) and the hyper-*g* (referred to as TX53 Hyper-*g*) did not reveal significant variations. Even the gene array experiment on the cells of these scenarios did not reveal any gene that changed at least two-fold (Table 1). Only an ANOVA analysis over the gene array results on cells obtained from theses 4 scenarios suggests variation of eight genes (Table 1). None of the detected genes were identical to those selected for the experiments on the basis of earlier experiments. However, two of these genes fit within the interaction network of the well-known candidates for gravi-sensitivity among other (Figs 6, 7). The most significantly regulated gene was *ASPH* undergoing 5% FDR. It up-regulates *EGF* and its product aspartate beta-hydroxylase supports the action of CASP3 (Figs 6, 7).

Unfortunately, an issue happened during the installation of one of the pressure resistant envelopes which produced a kink in the fixative tubing (Fig. 3, indicated by a red cross) and prevented proper fixation. Due to the non-transparent cabin there was no possibility to check for any kinks in the tubing after installation and before takeoff. Therefore, the cells harvested from the µg samples did not allow a significant microarray gene analysis. qPCR experiments showed that the gene expression in µ*g*-samples is markedly, but not significantly down-regulated in most of the tested gene products (Fig. 5).

Only *VEGFA* remained clearly unregulated in µ*g* samples. Though it seems to lack an anti-apoptotic effect, as the tendency of regulation of *BCL2* seems to be opposite in µg as compared to hyper-*g* (Fig. 5). Under the microgravity condition, the genes of the cytoskeletal proteins show though not significant but clear tendencies of down-regulation. Especially ezrin and radixin, which are both under the regulation of *EGF*, appear most clearly down-regulated.

Discussion

Cell biology in real microgravity is currently a hot topic in space research[20]. To perform cell culture experiments in space a functioning, automated hardware is necessary. Several biological experiments with plants, mice or mammalian cells have been performed under microgravity conditions[11,13,19,21]. A few articles published the concept of experimental units for application on the ISS and in space[19,22–24].

In this study, we describe the successful construction of a hardware container suitable to transport and culture human cells in real microgravity realized by the sounding rocket mission TEXUS 53 and the cell biological experiment THYROID. Using this hardware, we investigated the molecular biological changes of human follicular thyroid cancer cells (FTC-133 cell line) exposed to r-µ*g* and hyper-*g* during a sounding rocket mission. The aim of this project was to monitor changes in gene expression occurring during short-term µ*g* in thyroid cancer cells measured by microarray analysis and following quantitative rtPCR.

These studies might help to further understand the observed impact of µ*g* on biological processes and the formation of 3D aggregates of normal and malignant cells[6,8,25,26], explaining the mechanisms underlying the µ*g*-induced changes in growth behavior, differentiation, proliferation, cell adhesion, migration as well as the increased apoptosis and alterations of the cytoskeleton and extracellular matrix proteins[25].

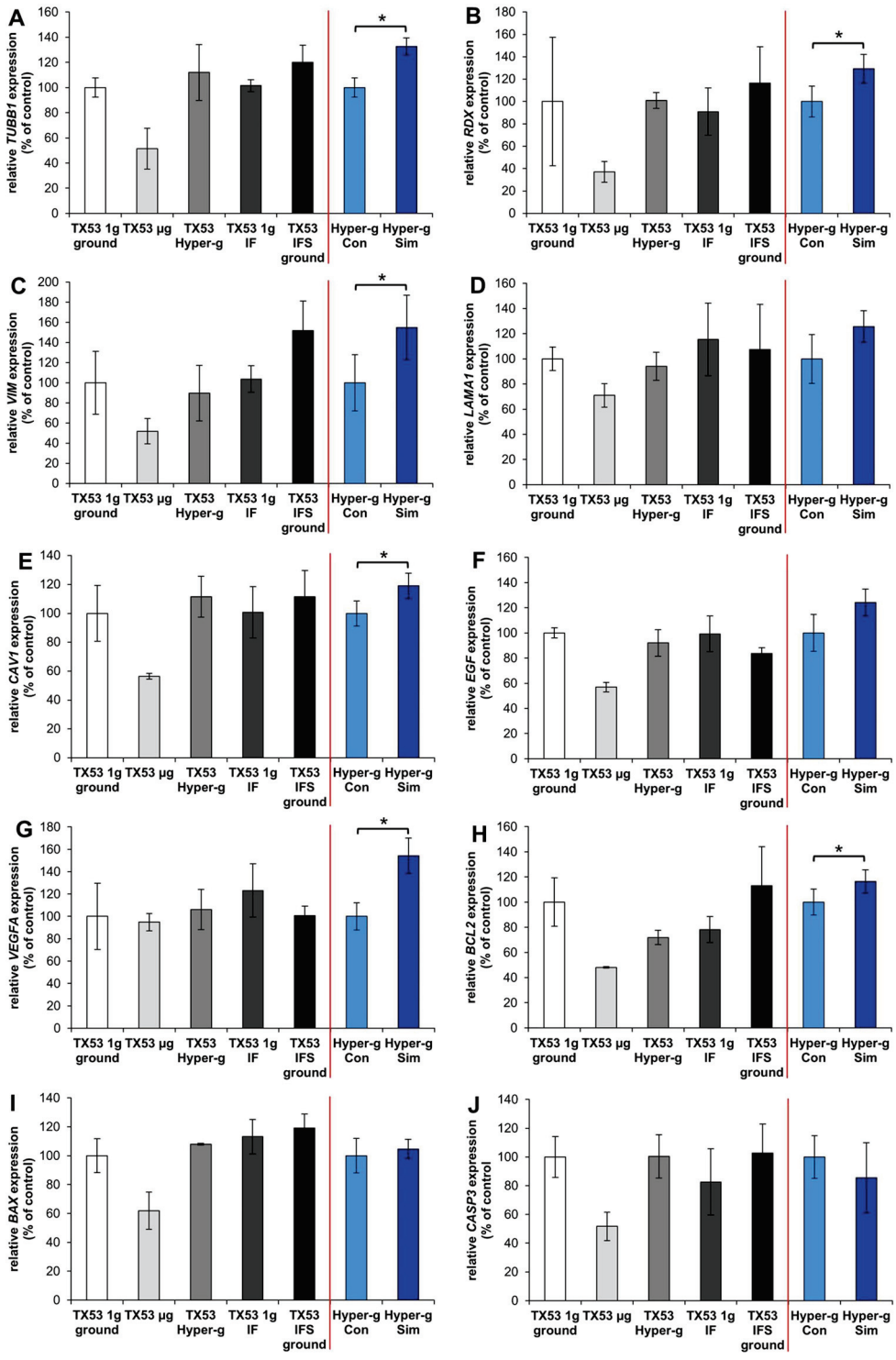


Figure 5. Gene expression of selected genes involved in several biological processes. (**A**) Beta-tubulin (*TUBB1*), (**B**) Radixin (*RDX*), (**C**) Vimentin (*VIM*), (**D**) Laminin alpha 1 (*LAMA1*), (**E**) Caveolin 1 (*CAV1*), (**F**) Epidermal growth factor (*EGF*), (**G**) Vascular endothelial growth factor (*VEGFA*), (**H**) Bcl-2 (*BCL2*), (**I**) Bax (*BAX*), (**J**) Caspase-3 (*CASP3*) and data not shown Beta-actin (*ACTB*), Ezrin (*EZR*), Moesin (*MSN*), Talin 1 (*TLN1*), Integrin beta 1 (*ITGB1*) were analysed after exposure to various conditions. TX53 1 *g* ground is the ground control during the mission (n = 3); TX53 µ*g* describes the sample which was exposed to the launch acceleration and the following µ*g*-phase (n = 2); TX53 Hyper-*g* describes the sample which was only effected by launch acceleration (n = 3); TX53 1 *g* IF describes the sample which was first exposed to the launch acceleration and then centrifuged at 1 *g* during the µ*g*-phase (n = 3); TX53 IFS ground presents the simulation of the inflight centrifuge as the samples were stimulated horizontally (n = 3); Hyper-*g* control (n = 5) and hyper-*g* simulation (n = 5) present control and simulation of worst case acceleration possible during a sounding rocket launch. All values are given as mean ± standard deviation. *$p < 0.05$.

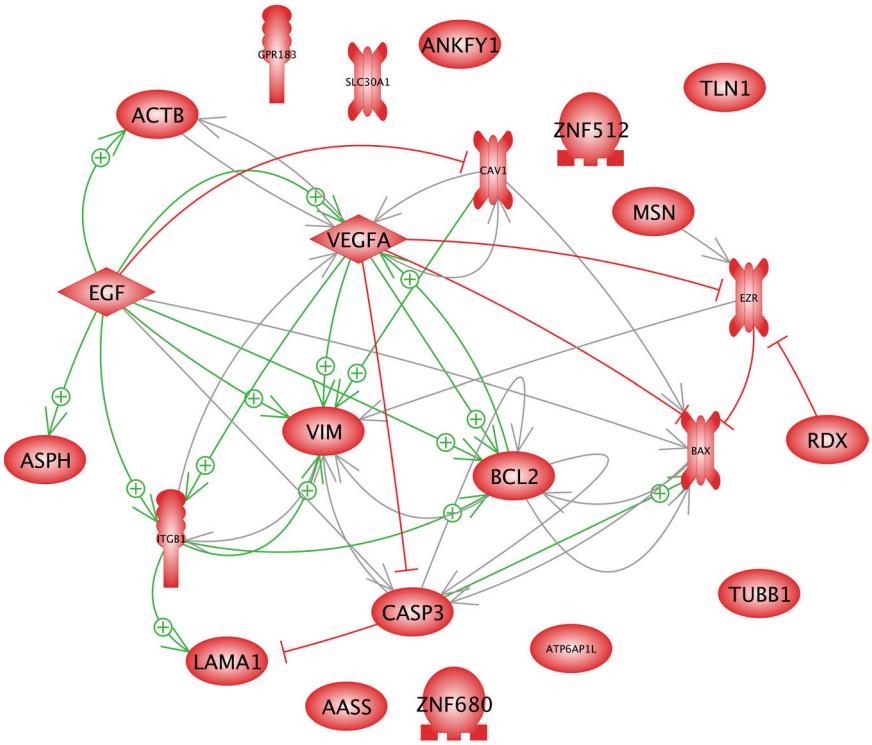


Figure 6. Interaction of investigated gene and gene products at gene level. Green arrows indicate up-regulation, red arrow mean down-regulation.

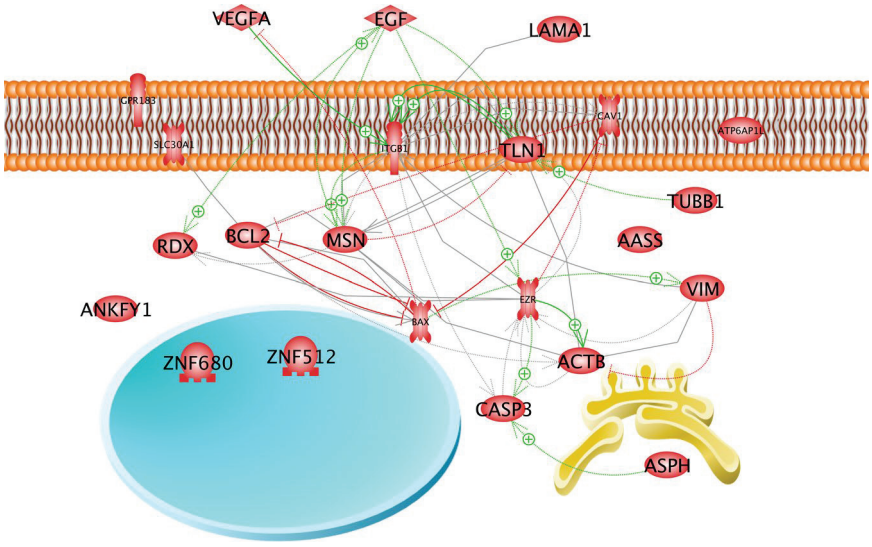


Figure 7. Interaction of investigated proteins and their localization within the cell. Blue circle indicates nucleus, yellow figure indicates ER, pink shows the membrane. Solid lines indicate binding, solid arrows indicate regulation by direct interaction, dashed arrows indicate indirect regulation via other cellular components.

	1d		4d	
Container	Initial #	Final #	Initial #	Final #
T25	3×10^6 (100%)	387500 (12.9%)	1.5×10^6 (100%)	1.1×10^6 (73.3%)
H/W	3×10^6 (100%)	187500 (6.25%)	1.5×10^6 (100%)	863000 (57.5%)
T25	2×10^6 (100%)	1.6×10^6 (80%)		
H/W	2×10^6 (100%)	$1{,}73 \times 10^6$ (86.25%)		

Table 1. Cell number determination.

In 2011, we investigated FTC-133 thyroid cancer cells during a parabolic flight campaign (PFC) and during the Sino-German Shenzhou-8/SIMBOX space mission[12]. A microarray analysis performed after the PFC delivered 63 moderately regulated transcripts after 22 s of r-μ*g*, while 2881 significantly regulated (>2 fold) transcripts were recognized after 10 days on the RPM or in space[12]. The latter results showed genes of various biological processes such as apoptosis, cytoskeleton, cell adhesion/extracellular matrix, angiogenesis and others differentially regulated under altered gravity conditions[12]. Interestingly, a microarray analysis performed after another PFC with experiments on thyroid cancer ML-1 cells revealed 102 significantly (>2 fold) down-regulated, and 46 up-regulated genes[27], which also coded for proteins involved in biological processes mentioned above. In addition, they revealed sensitivity of *ASPH* and *EBI2* genes found also in this microarray analysis together with *ZNF512*, which had been noticed earlier in chondrocytes recovered from PFC[28].

Here, we focused on selected genes also belonging to these processes mentioned above and investigated the low-differentiated FTC-133 follicular thyroid cancer cells exposed sounding rocket flight, which includes 1 min of extreme hyper-*g* and 6 min of μ*g*.

The cytoskeletal genes *ACTB*, *TUBB1* and *VIM* were down-regulated by μ*g*, whereas hyper-*g* during the flight did not alter the gene expression of these genes. In contrast, a centrifugation of the cells on Earth induced an up-regulation of the *VIM* and *TUBB1* mRNAs, indicating that factors like launch stress and vibration may impact the cytoskeleton.

The ERM protein group comprises the three proteins ezrin, radixin and moesin and is known to crosslink actin with the cellular plasma membranes regulating biological processes like reorganization of actin cytoskeleton, cell survival, membrane dynamics, cell adhesion and migration[29]. In a preceding set of experiments actin bundles changed rapidly when a sounding rocket entered the μg-phase and an accumulation of F-actin at the outer membranes of different cell types was detectable after parabolic flights (PF). Simultaneously *EZR* was down-regulated in cells expressing Lifeact-GFP, but up-regulated in normal FTC-133, while RDX and MSN remained un-changed in both types of cells[18]. In the present study, after 6 min of μ*g* *EZR*, *RDX* and *MSN* mRNAs were down-regulated compared to all other groups.

This may be caused by enhanced hyper-*g* during the launch phase as a similar increase of *EZR*, *MNS*, and *RDX* is observed under 1.8 *g* conditions[18]. Of the three ERM genes, *EZR* was most strikingly down-regulated. This gene change resembles the result obtained after PF of endothelial cells, where *EZR* was down-regulated only, but *MSN* and *RDX* remained unchanged[30]. The relationship was turned around in 7-day simulated (s)-μ*g* cultures, when the *EZR* gene was mostly up-regulated[31].

Interestingly, we detected a slight reduction of the *LAMA1* gene expression in the μ*g* group. This cell adhesion molecule and extracellular matrix protein is known to be altered when different cell types are exposed to s-μ*g* conditions[8,9,18,32,33]. A reduction was reported in adult retinal pigment epithelium cells and increases in dental pulp stem cells[32,33]. During the PFC FTC-133 cells exhibited no change in *LAMA1* gene expression after 31 parabolas[18]. Laminins are important for cell adhesion, the shape of the cells, phenotype, their differentiation, and movement.

The *CAV1* mRNA expression was reduced in microgravity samples. CAV-1 is a known member of several pathways such as caveolar-mediated endocytosis signaling, endothelial nitric oxide synthase (eNOS) signaling, integrin signaling, and others. Its role in spheroid formation is not clear. The *CAV1* mRNA was elevated in thyroid ML-1 cells and in chondrocytes after a PF[27,34] as well as in 24-hour mechanical-unloading-exposed human umbilical venous endothelial cells, which was associated with a decrease in the length and width of the cells[35]. After a 5- and 7-day cultivation of EA.hy926 cells, this gene was down-regulated[31]. We recently demonstrated that caveolin protein is reduced in multicellular spheroids and elevated in adherent cells[36], indicating that caveolin is a key regulator for growth and spheroid formation.

Talin (*TLN1*) is normally detectable in large amounts in focal adhesions and links integrins to the actin cytoskeleton[37]. Talin interacts directly with β-integrin (Fig. 7)[38], therefore we analyzed the gene expression of *TLN1*. The *TLN1* mRNA expression was reduced in microgravity samples and unaltered in all other groups. It is known that TLN1 is involved in RPM-dependent thyroid cancer spheroid formation[15]. Regarding the findings described above, the *TLN1* gene expression might point to the time frame in which the detachment and subsequent formation of MCS occurs.

In addition, we observed a reduced amount of epidermal growth factor (*EGF*) mRNA in μ*g*- samples. In a spaceflight experiment, EGF has shown to be involved in the scaffold-free formation of three-dimensional (3D) aggregates by FTC-133 cells with altered expression of *EGF* and *CTGF* genes under r- μ*g*[11]. The multicellular spheroids contained increased amounts of *EGF* mRNA compared to control cells.

Another growth factor known to be important for 3D growth is Vascular Endothelial Growth Factor (VEGF) which had demonstrated an influence on the ITGB1-LAMA1-TLN1 complex (Fig. 7, solid grey lines)[39,40]. VEGF was only up-regulated by centrifugation compared to control cells and was not altered during the rocket flight. In endothelial cells VEGF was unregulated after a PF[31]. But in chondrocytes VEGF-A was enhanced after simulation of the hyper-g phases of a PF[28]. After 10 days in space a down-regulation of *VEGFA* was detectable in adherent cells and spheroids[12]. These data were confirmed by a RPM experiment. In contrast, data obtained from a parabolic flight mission revealed no change in the gene expression of VEGF-A[12], which support the results of this study. From these findings, it is obvious that its gene expression is altered at later time points by microgravity suggesting a role for VEGF-A in growth and proliferation of the spheroids.

It is known from earlier studies that apoptosis is involved in cell detachment and formation of spheroids[10,15], therefore we investigated *BCL2*, *BAX* and *CASP3* mRNAs. *BAX* and *BCL2* genes were down-regulated in the μ*g* group.

The gene array experiments revealed eight genes that changed at least two-fold, none of the detected genes were identical to those selected for the experiments on the basis of earlier experiments. However, two of these genes fit within the interaction network of the well-known candidates for gravi-sensitivity.

Taken together, this sounding rocket flight carrying a cell biological experiment in an automatic functioning hardware has demonstrated its suitability for realizing cell biology studies under microgravity conditions even though some minor adaptations have to be introduced.

Moreover, the data show that the expression of key genes observed during earlier experiments at various time points is altered after six minutes of r-μ*g*. Hence, it further expands our knowledge of time-dependence of response of these genes to μ*g*. *EZR* seems to be fast responding to changes of gravity. While the *CAV-1* gene is up-regulated in a very early phase and down-regulated afterwards, gravity-dependent reactions of the *VEGFA* gene begin later starting with a transient up-regulation followed by down-regulation.

Future studies should be performed to investigate phosphorylation of proteins and morphological changes of the cells with the help of a laser scanning microscope suitable for space experiments.

Conclusions

The results of all completed experiments enabled the construction of a reliable container for thyroid cell culture during a sounding rocket mission, which flew successfully in January 2016.

The developed automatic cell culturing system was demonstrated to be suitable for sounding rocket experiments with human adherent cells and can be used for future cell biological experiments by space researchers.

But the hardware needs improvement by guiding the tubing through an aluminum tube at critical positions in order to avoid future adversities. These cell culture experiments in real microgravity are necessary to increase our knowledge about the alterations of cells exposed to microgravity. This information is important to protect our health because in the near future, many humans will travel in space and missions are planned to the Moon and Mars.

Material and Methods

Cell cultures. The human thyroid cancer cell line FTC-133 is well-established and was flown in space several times prior to this sounding rocket flight (Fig. 1A)[11,13]. The cell line is derived from a lymph node metastasis of a follicular thyroid carcinoma. Even though the cell line retained some thyrocyte functions like responsiveness to thyrotropin, a number of chromosomal changes and p53 mutations were detected[41].

The cells were cultured in RPMI 1640 medium (Life Technologies) supplemented with 10% FBS and 100 U/mL penicillin and 100 μg/mL streptomycin (Sigma). Cultivation took place in a humidified incubator at 37 °C and 5% CO_2.

Biocompatibility tests. The hardware used was designed and constructed by Airbus Defence and Space. In order to prove the biocompatibility of the CCs, FTC-133 cells were seeded into vented T25 cm^2 cell culture flasks at a density of 10^6 cells per flask, giving them a minimum of 24 hours to adhere.

To test the biocompatibility of the cell chamber material, three scenarios were applied:

In scenario S1 the cells were harvested and analyzed after four days of cultivation without contact to other materials (control samples; Fig. 1B(A)).

In S2 the polycarbonate (PC) material of the culture chamber (CC) was placed into the cell culture flasks to assure direct contact between the cells and the material. After exposure for four days the cells were harvested and analyzed (Fig. 1B(B)). Finally, in S3 the FTC-133 cells were incubated for 4 days with conditioned medium, previously exposed to the culturing chambers' PC material for six days (Fig. 1B(C)).

After these tests, the apoptotic status of the cells was assessed using the Annexin V-FITC Apoptosis Detection Kit I (BD Bioscience) as previously described[11,19,42].

The stained cells were analyzed using a FACSCanto II (Becton Dickinson), data analysis was attained by Flowing Software (Version 2.5.1). Each measurement was composed of a count of 6 × 5000 cells. To visually examine cell viability, cells were observed and photographed using an Axiovert 25 Microscope (Carl Zeiss Microscopy, LLC, USA) and a Canon EOS 550D camera (Canon GmbH, Krefeld, Germany).

Determination of the appropriate cell number. To test which cell number had to be seeded per cell culture flask to result in an appropriate amount of RNA for downstream analyzes, the optimal cell density was determined. As sounding rocket launches are restricted to suitable weather conditions and postponements are common, we also included the possibility of delays. Table 1 summarizes the different tests. The cells were seeded with a defined cell density into the CCs with growth areas of 25 cm^2 or into T25 cm^2 flasks and incubated for either one or four days. After reaching the time point of interest, the cells were harvested by trypsinization, counted by Neubauer technique and stained with trypan blue to determine the cell viability.

Experimental setup. To allow for statistical analysis, the experiments shown in Fig. 1 were carried out in triplicates: three samples were fixed with RNA*later* (Sigma) one min after launch (referred to as TX53 hyper-*g*). Three samples were located on the in-flight centrifuge and were fixed prior to reentry of the rocket (referred to as TX53 1 *g* in-flight) and finally, four samples should have been fixed after the microgravity (μ*g*) phase. However, only two samples were triggered. In addition to the flight samples, ground controls and hypergravity (hyper-*g*) simulations were conducted. Two different ground controls must be taken into account, which resulted from the positioning of the cells on the in-flight centrifuge. During the flight the cells were stimulated vertically at 1 *g* on a centrifuge. To simulate this stimulation, the hardware was positioned at a 90 degree angle. Controls were performed in parallel to the rocket flight, in ground-based hardware with an automated fixation unit (Fig. 1C).

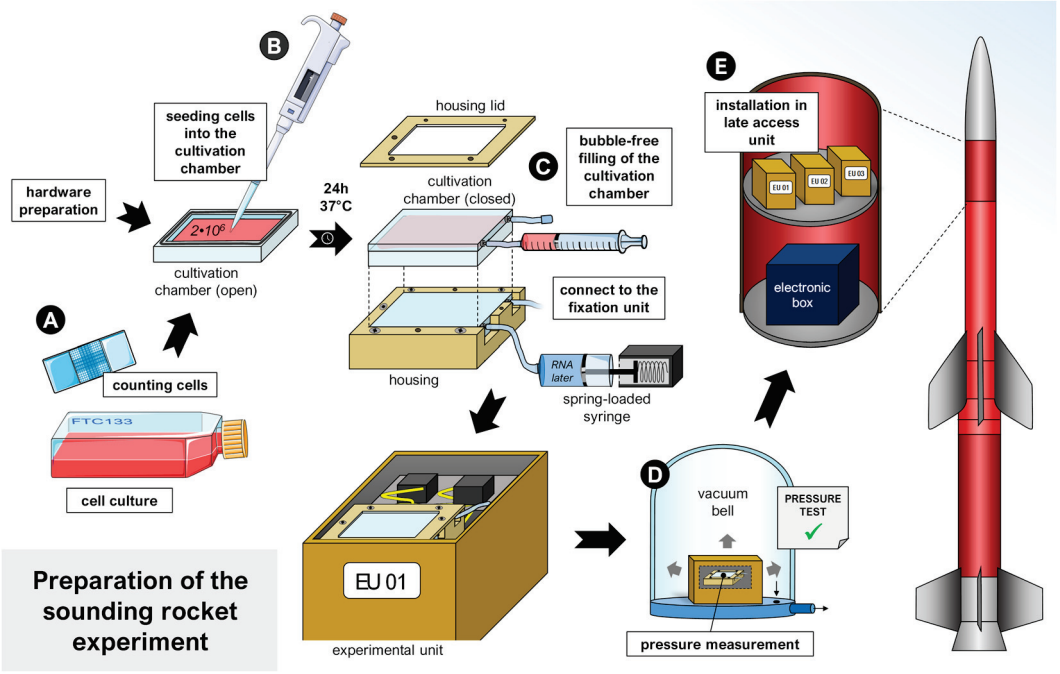


Figure 8. Preparation of the sounding rocket experiment at the laboratory of the Swedish Space Corporation (SSC) at the Esrange launch center, Kiruna, Sweden. (**A**) cell culture: (**B**) cell seeding with defined cell number in cultivation chamber; (**C**) bubble-free filling of the cultivation chamber; (**D**) installed chamber in the experimental unit and pressure measurement; (**E**) installation in late access unit. Parts of the figure were drawn by using pictures from Servier Medical Art. Servier Medical Art by Servier is licensed under a Creative Commons Attribution 3.0 Unported License (https://creativecommons.org/licenses/by/3.0/).

Cell cultures prior to launch at ESRANGE. The FTC-133 cells were set up one week before launch (Fig. 8A). As sounding rocket launches are restricted to suitable weather conditions and postponements are common, we also included the possibility of delays and repeated the setup procedure during the following days.

One day prior to the scheduled rocket launch, the cells were seeded into the CCs (Fig. 8B). Therefore, adherent FTC-133 cells were harvested from culture flasks via trypsinization and counted via the Neubauer technique (Fig. 8A). As a result to the previous determination of the optimal cell number, 2×10^6 cells per CC were directly seeded in 6 mL medium (Fig. 8B). CCs were stored inside their housing in a 37 °C incubator overnight to allow cell adhesion.

On launch day, the culture medium was exchanged and the chambers were filled entirely, bubble-free (Fig. 8C). The flasks were connected to spring-loaded syringes, which were equipped with a solenoid valve and filled with RNA*later*, and subsequently installed in the experimental units (EUs). A pressure test was performed following assembly: The EUs were placed in a vacuum bell with low pressure while sensors logged the inside pressure of the EUs, which should not change during this procedure (Fig. 8D). Upon passing this test, the EUs were installed on the rigid platforms of the rocket as late access units (Fig. 8E). Then the EUs were incubated at 37 °C until handover to Airbus Defence and Space.

Sounding rocket flight. A sounding rocket flight is composed of different stressors[18]. During launch the rocket reached a maximum linear acceleration of 12.1 *g* (Fig. 1A, Supplemental Table 1). In addition to the acceleration, the rocket is spin stabilized during ascent, which also influences the cell chamber in case bubbles are present. T + 1 min after launch, the first and the second stage of the rocket motors are separated from the payload and the payload rotation is stopped via a yo-yo de-spin mechanism. This is followed by a nearly six-minute-phase of microgravity during which the payload describes a high parabola and reaches an apogee of approx. 260 km. Shortly after re-entry into Earth atmosphere, a parachute system is released to de-accelerate the payload and let it glide safely back to the ground. Typically, 90 minutes after landing, the payload is recovered which allows fast retrieval of the samples. Because the flight is rather short, all procedures on board are automatically executed. Supplemental Table 1 shows all data gathered during the flight.

Hyper-g simulation. Cells were handled similar to the cell samples prior to launch. FTC-133 cells were seeded into T25 cm^2 cell culture flasks at a density of 2×10^6 cells and given 24 hours to adhere to the bottom of the flasks. The next day the samples were run at $18 \times g$ for 1 min at 31 °C in a Heraeus Multifuge 3SR + (Thermo Scientific), in microtiter plate buckets (127 × 85 mm) to simulate the worst-case scenario during rocket launch acceleration. After each run, cells were fixed with RNA*later* for downstream analysis. 4 cell culture flasks were centrifuged at combined for a total of 4 times. Controls were placed in the same centrifuge for 1 min without centrifugation.

Factor	Primer name	Sequence 5′-3′
18 S	*18S-F*	GGAGCCTGCGGCTTAATTT
	18S-R	CAACTAAGAACGGCCATGCA
Actin Beta	*ACTB-F*	TGCCGACAGGATGCAGAAG
	ACTB-R	GCCGATCCACACGGAGTACT
Apoptosis Regulator BAX; *BAX*	*BAX-F*	GTCAGCTGCCACTCGGAAA
	BAX-R	AGTAACATGGAGCTGCAGAGGAT
Apoptosis Regulator BCL-2; *BCL2*	*BCL2-F*	TCAGAGACAGCCAGGAGAAATCA
	BCL2-R	CCTGTGGATGACTGAGTACCTGAA
Caspase 3	*CASP3-F*	CTCCAACATCGACTGTGAGAAGTT
	CASP3-R	GCGCCAGCTCCAGCAA
Caveolin-1	*Cav1-F*	CCTCCTCACAGTTTTCATCCA
	Cav1-R	TGTAGATGTTGCCCTGTTCC
Endothelial Growth Factor	*EGF-F*	TGCCAGCTGCACAAATACAGA
	EGF-R	TCTTACGGAATAGTGGTGGTCATC
Ezrin	*EZR-F*	GCAATCCAGCCAAATACAACTG
	EZR-R	CCACATAGTGGAGGCCAAAGTAC
Laminin Alpha 1	*LAMA1-F*	TGACTGACCTGGGTTCAGGA
	LAMA1-R	TGCTAGCACTCCTTGCTTCC
Moesin	*MSN-F*	GAAATTTGTCATCAAGCCCATTG
	MSN-R	CCATGCACAAGGCCAAGAT
Radixin	*RDX-F*	GAAAATGCCGAAACCAATCAA
	RDX-R	GTATTGGGCTGAATGGCAAATT
Integrin Beta 1	*ITGB1-F*	GAAAACAGCGCATATCTGGAAATT
	ITGB1-R	CAGCCAATCAGTGATCCACAA
Talin-1	*TLN1-F*	GATGGCTATTACTCAGTACAGACAACTGA
	TLN1-R	CATAGTAGACTCCTCATCTCCTTCCA
Tubulin Beta 1	*TUBB1-F*	CTGGACCGCATCTCTGTGTACTAC
	TUBB1-R	GACCTGAGCGAACAGAGTCCAT
Vascular Endothelial Growth Factor A	*VEGFA-F*	GCGCTGATAGACATCCATGAAC
	VEGFA-R	CTACCTCCACCATGCCAAGTG
Vimentin	*VIM-F*	TTCAGAGAGAGGAAGCCGAAAAC
	VIM-R	AGATTCCACTTTGCGTTCAAGGT

Table 2. Primers used for quantitative real-time PCR. All sequences are given in the 5′-3′direction.

Post-flight cell harvest. After the rocket flight, the cell samples were received fixed in RNA*later*. To harvest the cell material for post-flight analyses, the supernatant was removed and 1 mL of fresh RNA*later* was added. Using a small cell scraper, the cells were detached and brought into solution. The solution was transferred into 2 mL tubes. The cultivation area was washed twice with 1 mL RNA*later*, the solution transferred into the corresponding tubes. The cell suspension was kept at 4 °C until further analysis.

Quantitative real time PCR. The RNA extraction was performed using the RNAeasy mini kit (Qiagen GmbH, Hilden, Germany) according to the manufacturer's protocol. Concentrations were determined via Nanodrop 2000 (Thermofisher Scientific), as described previously[12,18].

Complementary DNA was produced using the First Strand cDNA Synthesis Kit (Thermo Fisher Scientific) following manufacturer's instructions. qrtPCR was performed using the SYBR® Select Master Mix (Applied Biosystems, Darmstadt, Germany) and the 7500 Fast Real-Time PCR System (Applied Biosystems) to determine the expression levels of target genes, shown in Table 2. Selective primers were designed using PubMed primer blast, with a focus to span exon-exon boundaries where applicable, and on a T_m of 60 °C. The designed primers were synthesized by TIB Molbiol (Berlin, Germany). Samples were measured in triplicates and normalized to the 18 S rRNA as housekeeping control. The comparative threshold cycle ($\Delta\Delta$CT) method was used for relative quantification of transcription levels, with 1 *g* set as 100%.

Microarray analysis. The same RNA samples as used for the qPCR were examined via microarray analysis. Samples were analyzed via the Illumina HumanWG-6_V2_0_R3 array, which was normalized using the BeadStudio Gene Expression Module v3.3.7, in addition to quantile normalization without background correction. After the quantile normalization and exclusion of low or not expressed genes (minimum Illumina detection p-value > 0.05) a parametric ANOVA was applied to compare the conditions 1*g*-on-ground, 1*g*-in-flight, 1*g*-on-ground-in-flight simulation and hyper-*g*-inflight. µ*g* samples were not included into the measurement as a sample number of 2 is statistically irrelevant. Probes which undergo 5% FDR (Reference) are usually selected as

SYMBOL	P	Q	Log2 expression (standard deviation)			
			1 *g* in flight centrifuge	1 *g* on ground	1 *g* on ground infl. sim.	hyper-*g* in flight
ASPH	6.25E-07	**0.017**	7.30 (0.016)	7.16 (0.020)	7.33 (0.009)	7.45 (0.026)
ZNF512	1.50E-05	0.125	8.31 (0.011)	8.61 (0.042)	8.52 (0.036)	8.28 (0.053)
ATP6AP1L	1.54E-05	0.125	7.02 (0.022)	7.09 (0.028)	7.01 (0.006)	6.88 (0.021)
ZNF680	1.80E-05	0.125	7.71 (0.014)	7.64 (0.038)	7.64 (0.018)	7.83 (0.007)
EBI2	4.53E-05	0.243	8.53 (0.076)	8.26 (0.109)	8.44 (0.056)	8.91 (0.057)
SLC30A1	6.14E-05	0.243	8.14 (0.045)	8.10 (0.099)	8.17 (0.084)	8.62 (0.040)
AASS	7.44E-05	0.243	7.25 (0.033)	7.31 (0.013)	7.31 (0.013)	7.16 (0.017)
ANKFY1	9.87E-05	0.243	7.01 (0.016)	6.87 (0.026)	6.94 (0.010)	6.88 (0.028)

Table 3. Genes differentially expressed at a significance level of $P < 10^{-4}$ in the ANOVA over the four conditions: 1*g*-on-ground, 1*g*-in-flight, 1*g*-on-ground-in-flight simulation and hyper-*g*-inflight. Significances are printed in bold.

differential expressed, however, only one of the measured genes, the aspartate beta-hydroxylase (ASPH) reached this condition (Table 3).

Pathway analysis. To investigate mutual regulation of genes and to visualize localization and interactions between proteins, we entered the relevant UniProtKB entry numbers in the Pathway Studio v.11 software (Elsevier Research Solutions, Amsterdam, The Netherlands). Graphs were generated for gene expression and protein regulation and binding. The method was described previously[36,43].

Statistical evaluation. Statistical evaluation was performed using SPSS 15.0 (SPSS, Inc., Chicago, IL, USA). The Mann-Whitney-U-Test was used to compare 1 *g* and μ*g* conditions, as well as 1 *g* and hyper-*g* conditions. All data is presented as mean ± standard deviation (SD) with a significance level of $*p < 0.05$.

References

1. La Vecchia, C. *et al.* Thyroid cancer mortality and incidence: a global overview. *Int J Cancer* **136**, 2187–2195, https://doi.org/10.1002/ijc.29251 (2015).
2. Sherman, S. I. Thyroid carcinoma. *Lancet* **361**, 501–511 (2003).
3. Laursen, R. *et al.* Effects and Role of Multikinase Inhibitors in Thyroid Cancer. *Curr Pharm Des* **22**, 5915–5926 (2016).
4. Ancker, O. V., Wehland, M., Bauer, J., Infanger, M. & Grimm, D. The Adverse Effect of Hypertension in the Treatment of Thyroid Cancer with Multi-Kinase Inhibitors. *Int J Mol Sci* **18**, https://doi.org/10.3390/ijms18030625 (2017).
5. Becker, J. L. & Souza, G. R. Using space-based investigations to inform cancer research on Earth. *Nat Rev Cancer* **13**, 315–327, https://doi.org/10.1038/nrc3507 (2013).
6. Warnke, E. *et al.* Spheroid formation of human thyroid cancer cells under simulated microgravity: a possible role of CTGF and CAV1. *Cell Commun Signal* **12**, 32, https://doi.org/10.1186/1478-811X-12-32 (2014).
7. Svejgaard, B. *et al.* Common Effects on Cancer Cells Exerted by a Random Positioning Machine and a 2D Clinostat. *PloS one* **10**, e0135157, https://doi.org/10.1371/journal.pone.0135157 (2015).
8. Kopp, S. *et al.* Mechanisms of three-dimensional growth of thyroid cells during long-term simulated microgravity. *Sci Rep* **5**, 16691, https://doi.org/10.1038/srep16691 (2015).
9. Kopp, S. *et al.* Identifications of novel mechanisms in breast cancer cells involving duct-like multicellular spheroid formation after exposure to the Random Positioning Machine. *Sci Rep* **6**, 26887, https://doi.org/10.1038/srep26887 (2016).
10. Kopp, S. *et al.* The role of NFkappaB in spheroid formation of human breast cancer cells cultured on the Random Positioning Machine. *Sci Rep* **8**, 921, https://doi.org/10.1038/s41598-017-18556-8 (2018).
11. Pietsch, J. *et al.* Spheroid formation of human thyroid cancer cells in an automated culturing system during the Shenzhou-8 Space mission. *Biomaterials* **34**, 7694–7705, https://doi.org/10.1016/j.biomaterials.2013.06.054 (2013).
12. Ma, X. *et al.* Differential gene expression profile and altered cytokine secretion of thyroid cancer cells in space. *FASEB J* **28**, 813–835, https://doi.org/10.1096/fj.13-243287 (2014).
13. Riwaldt, S. *et al.* Identification of proteins involved in inhibition of spheroid formation under microgravity. *Proteomics* **15**, 2945–2952, https://doi.org/10.1002/pmic.201500067 (2015).
14. Riwaldt, S. *et al.* The Importance of Caveolin-1 as Key-Regulator of Three-Dimensional Growth in Thyroid Cancer Cells Cultured under Real and Simulated Microgravity Conditions. *Int J Mol Sci* **16**, 28296–28310, https://doi.org/10.3390/ijms161226108 (2015).
15. Grosse, J. *et al.* Gravity-sensitive signaling drives 3-dimensional formation of multicellular thyroid cancer spheroids. *FASEB J* **26**, 5124–5140, https://doi.org/10.1096/fj.12-215749 (2012).
16. Thiel, C. S. *et al.* Stability of gene expression in human T cells in different gravity environments is clustered in chromosomal region 11p15.4. *NPJ microgravity* **3**, 22, https://doi.org/10.1038/s41526-017-0028-6 (2017).
17. Thiel, C. S. *et al.* Dynamic gene expression response to altered gravity in human T cells. *Sci Rep* **7**, 5204, https://doi.org/10.1038/s41598-017-05580-x (2017).
18. Corydon, T. J. *et al.* Alterations of the cytoskeleton in human cells in space proved by life-cell imaging. *Sci Rep* **6**, 20043, https://doi.org/10.1038/srep20043 (2016).
19. Pietsch, J. *et al.* Three-dimensional growth of human endothelial cells in an automated cell culture experiment container during the SpaceX CRS-8 ISS space mission - The SPHEROIDS project. *Biomaterials* **124**, 126–156, https://doi.org/10.1016/j.biomaterials.2017.02.005 (2017).
20. Albi, E. *et al.* Impact of Gravity on Thyroid Cells. *Int J Mol Sci* **18**, https://doi.org/10.3390/ijms18050972 (2017).
21. Kiss, J. Z. *et al.* Biocompatibility studies in preparation for a spaceflight experiment on plant tropisms (TROPI). *Adv Space Res* **39**, 1154–1160, https://doi.org/10.1016/j.asr.2006.12.017 (2007).
22. Brinckmann, E. ESA hardware for plant research on the International Space Station. *Adv Space Res* **36**, 1162–1166, https://doi.org/10.1016/j.asr.2005.02.019 (2005).
23. Brinckmann, E. Spaceflight opportunities on the ISS for plant research — The ESA perspective. *Adv Space Res* **24**, 779–788, https://doi.org/10.1016/S0273-1177(99)00413-5 (1999).

24. Kern, V. D. *et al*. Life sciences flight hardware development for the International Space Station. *Adv Space Res* **27**, 1023–1030 (2001).
25. Grimm, D. *et al*. Simulated microgravity alters differentiation and increases apoptosis in human follicular thyroid carcinoma cells. *FASEB J* **16**, 604–606 (2002).
26. Albi, E. *et al*. Thyrotropin receptor and membrane interactions in FRTL-5 thyroid cell strain in microgravity. *Astrobiology* **11**, 57–64, https://doi.org/10.1089/ast.2010.0519 (2011).
27. Ulbrich, C. *et al*. Differential gene regulation under altered gravity conditions in follicular thyroid cancer cells: relationship between the extracellular matrix and the cytoskeleton. *Cell Physiol Biochem* **28**, 185–198, https://doi.org/10.1159/000331730 (2011).
28. Wehland, M. *et al*. Differential gene expression of human chondrocytes cultured under short-term altered gravity conditions during parabolic flight maneuvers. *Cell Commun Signal* **13**, 18, https://doi.org/10.1186/s12964-015-0095-9 (2015).
29. Ponuwei, G. A. A glimpse of the ERM proteins. *J Biomed Sci* **23**, 35, https://doi.org/10.1186/s12929-016-0246-3 (2016).
30. Wehland, M. *et al*. The impact of altered gravity and vibration on endothelial cells during a parabolic flight. *Cell Physiol Biochem* **31**, 432–451, https://doi.org/10.1159/000343380 (2013).
31. Ma, X. *et al*. Genomic approach to identify factors that drive the formation of three-dimensional structures by EA.hy926 endothelial cells. *PloS one* **8**, e64402, https://doi.org/10.1371/journal.pone.0064402 (2013).
32. Corydon, T. J. *et al*. Reduced Expression of Cytoskeletal and Extracellular Matrix Genes in Human Adult Retinal Pigment Epithelium Cells Exposed to Simulated Microgravity. *Cell Physiol Biochem* **40**, 1–17, https://doi.org/10.1159/000452520 (2016).
33. He, L. *et al*. Increased proliferation and adhesion properties of human dental pulp stem cells in PLGA scaffolds via simulated microgravity. *Int Endod J* **49**, 161–173, https://doi.org/10.1111/iej.12441 (2016).
34. Aleshcheva, G. *et al*. Moderate alterations of the cytoskeleton in human chondrocytes after short-term microgravity produced by parabolic flight maneuvers could be prevented by up-regulation of BMP-2 and SOX-9. *FASEB J* **29**, 2303–2314, https://doi.org/10.1096/fj.14-268151 (2015).
35. Grenon, S. M., Jeanne, M., Aguado-Zuniga, J., Conte, M. S. & Hughes-Fulford, M. Effects of gravitational mechanical unloading in endothelial cells: association between caveolins, inflammation and adhesion molecules. *Sci Rep* **3**, 1494, https://doi.org/10.1038/srep01494 (2013).
36. Bauer, J. *et al*. Proteome Analysis of Human Follicular Thyroid Cancer Cells Exposed to the Random Positioning Machine. *Int J Mol Sci* **18**, https://doi.org/10.3390/ijms18030546 (2017).
37. Vignoud, L., Albiges-Rizo, C., Frachet, P. & Block, M. R. NPXY motifs control the recruitment of the alpha5beta1 integrin in focal adhesions independently of the association of talin with the beta1 chain. *J Cell Sci* **110**(Pt 12), 1421–1430 (1997).
38. Warnke, E. *et al*. Cytokine Release and Focal Adhesion Proteins in Normal Thyroid Cells Cultured on the Random Positioning Machine. *Cell Physiol Biochem* **43**, 257–270, https://doi.org/10.1159/000480368 (2017).
39. Shao, B. *et al*. Signal-dependent slow leukocyte rolling does not require cytoskeletal anchorage of P-selectin glycoprotein ligand-1 (PSGL-1) or integrin alphaLbeta2. *J Biol Chem* **287**, 19585–19598, https://doi.org/10.1074/jbc.M112.361519 (2012).
40. Ariel, A. *et al*. Induction of T cell adhesion to extracellular matrix or endothelial cell ligands by soluble or matrix-bound interleukin-7. *Eur J Immunol* **27**, 2562–2570, https://doi.org/10.1002/eji.1830271015 (1997).
41. Goretzki, P. E., Frilling, A., Simon, D. & Roeher, H. D. Growth regulation of normal thyroids and thyroid tumors in man. *Recent results in cancer research. Fortschritte der Krebsforschung. Progres dans les recherches sur le cancer* **118**, 48–63 (1990).
42. Grosse, J. *et al*. Radiolabeled annexin V for imaging apoptosis in radiated human follicular thyroid carcinomas–is an individualized protocol necessary? *Nucl Med Biol* **36**, 89–98, https://doi.org/10.1016/j.nucmedbio.2008.10.004 (2009).
43. Riwaldt, S. *et al*. Pathways Regulating Spheroid Formation of Human Follicular Thyroid Cancer Cells under Simulated Microgravity Conditions: A Genetic Approach. *Int J Mol Sci* **17**, 528, https://doi.org/10.3390/ijms17040528 (2016).

Acknowledgements

The authors would like to thank the German Space Agency (DLR; (DG) BMWi project 50WB1524). The authors also would like to thank Mr. Y. Kozinski for his through language review of the manuscript.

Author Contributions

S.K. conducted and analyzed the experiments for the biocompatibility tests; A.S., H.O., S.F. and B.S. were responsible for the EU design and construction; S.K., M.W. performed the rocket experiment in Kiruna; S.K., M.K. and S.M. performed the hyper-*g* experiments; S.K., M.K., M.Z.N. and D.M. performed the qPCR; J.B. performed the pathway analyses; K.S. and N.H. performed the microarray; H.S. analyzed the data of the gene array. M.I. and D.G. designed the experimental requirements; S.K., D.G., J.B., H.S., and M.K. wrote the manuscript.

Additional Information

Supplementary information accompanies this paper at https://doi.org/10.1038/s41598-018-28695-1.

Competing Interests: The authors declare no competing interests.

Publisher's note: Springer Nature remains neutral with regard to jurisdictional claims in published maps and institutional affiliations.

Open Access This article is licensed under a Creative Commons Attribution 4.0 International License, which permits use, sharing, adaptation, distribution and reproduction in any medium or format, as long as you give appropriate credit to the original author(s) and the source, provide a link to the Creative Commons license, and indicate if changes were made. The images or other third party material in this article are included in the article's Creative Commons license, unless indicated otherwise in a credit line to the material. If material is not included in the article's Creative Commons license and your intended use is not permitted by statutory regulation or exceeds the permitted use, you will need to obtain permission directly from the copyright holder. To view a copy of this license, visit http://creativecommons.org/licenses/by/4.0/.

© The Author(s) 2018

International Journal of
Molecular Sciences

MDPI

Article

Microgravity Affects Thyroid Cancer Cells during the TEXUS-53 Mission Stronger than Hypergravity

Sascha Kopp [1], Marcus Krüger [1], Johann Bauer [2], Markus Wehland [1], Thomas J. Corydon [3,4], Jayashree Sahana [3], Mohamed Zakaria Nassef [1], Daniela Melnik [1], Thomas J. Bauer [1], Herbert Schulz [5], Andreas Schütte [6], Burkhard Schmitz [6], Hergen Oltmann [6], Stefan Feldmann [6], Manfred Infanger [1] and Daniela Grimm [1,3,7,*]

1 Clinic for Plastic, Aesthetic and Hand Surgery, Otto von Guericke University Magdeburg, Leipziger Str. 44, D-39120 Magdeburg, Germany; sascha.kopp@med.ovgu.de (S.K.); marcus.krueger@med.ovgu.de (M.K.); markus.wehland@med.ovgu.de (M.W.); mohamed.nassef@med.ovgu.de (M.Z.N.); daniela.melnik@med.ovgu.de (D.M.); thomas.bauer@med.ovgu.de (T.J.B.); manfred.infanger@med.ovgu.de (M.I.)
2 Max Planck Institute of Biochemistry, D-82152 Martinsried, Germany; jbauer@biochem.mpg.de
3 Department of Biomedicine, Aarhus University, Wilhelm Meyers Allé 4, DK-8000 Aarhus C, Denmark; corydon@biomed.au.dk (T.J.C.); jaysaha@biomed.au.dk (J.S.)
4 Department of Ophthalmology, Aarhus University Hospital, Aarhus, 8000 Aarhus C, Denmark
5 Cologne Center for Genomics, University of Cologne, D-50931 Cologne, Germany; herbert.schulz@uni-koeln.de
6 Airbus Defence and Space GmbH, Airbus-Allee 1, D-28199 Bremen, Germany; andreas.schuette@airbus.com (A.S.); burkhard.schmitz@airbus.com (B.S.); hergen.oltmann@airbus.com (H.O.); stefan.feldmann@airbus.com (S.F.)
7 Gravitational Biology and Translational Regenerative Medicine, Faculty of Medicine and Mechanical Engineering, Otto-von-Guericke-University Magdeburg, D-39120 Magdeburg, Germany
* Correspondence: dgg@biomed.au.dk; Tel.: +45-871-67693

Received: 15 November 2018; Accepted: 9 December 2018; Published: 12 December 2018



Abstract: Thyroid cancer is the most abundant tumor of the endocrine organs. Poorly differentiated thyroid cancer is still difficult to treat. Human cells exposed to long-term real (r-) and simulated (s-) microgravity (μ*g*) revealed morphological alterations and changes in the expression profile of genes involved in several biological processes. The objective of this study was to examine the effects of short-term μ*g* on poorly differentiated follicular thyroid cancer cells (FTC-133 cell line) resulting from 6 min of exposure to μ*g* on a sounding rocket flight. As sounding rocket flights consist of several flight phases with different acceleration forces, rigorous control experiments are mandatory. Hypergravity (hyper-*g*) experiments were performed at 18*g* on a centrifuge in simulation of the rocket launch and s-μ*g* was simulated by a random positioning machine (RPM). qPCR analyses of selected genes revealed no remarkable expression changes in controls as well as in hyper-*g* samples taken at the end of the first minute of launch. Using a centrifuge initiating 18*g* for 1 min, however, presented moderate gene expression changes, which were significant for *COL1A1*, *VCL*, *CFL1*, *PTK2*, *IL6*, *CXCL8* and *MMP14*. We also identified a network of mutual interactions of the investigated genes and proteins by employing *in-silico* analyses. Lastly, μ*g*-samples indicated that microgravity is a stronger regulator of gene expression than hyper-*g*.

Keywords: Microgravity; hypergravity; random positioning machine; thyroid cancer; sounding rocket; cytoskeleton; focal adhesion; extracellular matrix

1. Introduction

Thyroid cancer (TC) is one of the most abundant neoplasms of the endocrine organs [1]. Thyroid carcinomas are malignant tumors of the thyroid gland and are classified into differentiated TC (papillary TC, follicular TC and Hürthle cell cancer), medullary TC; and anaplastic TC. The American Cancer Society recently estimated that in the US in 2018 about 2,060 persons died from TC [1].

Thyroid cells as well as differentiated TC cells are capable of taking up iodine [2]. When radioactive iodine (RAI; ^{131}I) is given, it concentrates in the thyroid. The radiation will destroy the thyroid gland and any other benign and malignant thyroid cells. RAI-treatment is used to ablate any thyroid tissue in the organism. Unfortunately, undifferentiated TC cells lost the ability to take up iodine which increases the need to find new therapeutically valuable treatments [3], for example by targeting tumor angiogenesis [2,4].

Microgravity (μ*g*) offers a very special culture environment for cells enabling three-dimensional (3D) growth. This environment is suitable for tissue engineering purposes, while exposing cells to an unknown stress and thereby forcing them to react and adapt to this new condition [5–7].

Normal and benign thyroid cells have been examined after cultivation on a random positioning machine (RPM) at various time-points [8–10]. The results suggest that RPM-exposure changed differentiation and growth behavior of poorly differentiated malignant FTC-133 cells after long-term RPM-exposure [8]. Comparable results were obtained from the Simbox/Shenzhou-8 mission, when FTC-133 cells were cultured on an unmanned spacecraft for 10 days [11].

Furthermore, the cytoskeleton underwent changes in structure and organization by exposure to μ*g*. This was demonstrated during parabolic flights as well as a TEXUS (TX) sounding rocket mission, where a novel live-cell imaging approach using the FLUMIAS microscope revealed the occurrence of "holes" in the F-actin-network and in lamellipodia- and filopodia-like structures [12]. According to the tensegrity model, meaning that cells gain their structure through a pervasive tensional force, the cytoskeleton might play an important role in the mechano- and gravisensing process of human cells [13,14]. It is proposed that the cytoskeleton acts as a mediator and conductor of signals from the extracellular space into the nucleus due to it being hardwired to specific cell surface proteins, such as integrins, which are involved in focal adhesion formation and cell-cell interaction [15,16], as well as to cytoplasmic transduction molecules [13]. Proteins involved in the linkage of the cytoskeleton to membrane proteins and the ECM are most prominently talin, vinculin or the ERM proteins [17–19].

To determine the impact of r-μ*g* on the cells after the 1-min long hyper-*g* phase during launch-, FTC-133 cells were exposed to 6 min of r-μ*g* during the TEXUS-(TX) 53 mission [20] and in parallel to 1 min of 18*g* on a centrifuge (see Figure 1 of [20]). In addition, we compared the effects of the short-term r-μ*g* with a 6-min cultivation on the RPM (s-μ*g*), focusing on extracellular matrix (ECM) proteins, the cytoskeleton, cell adhesion, focal adhesion and cytokines.

The expression of genes and the accumulation of proteins, which were known to be highly sensitive to altered gravity conditions were analyzed. Furthermore, we have conducted an *in-silico* analysis including data from the literature to identify possible mutual interaction networks between the analyzed proteins, as successfully practiced earlier [21,22].

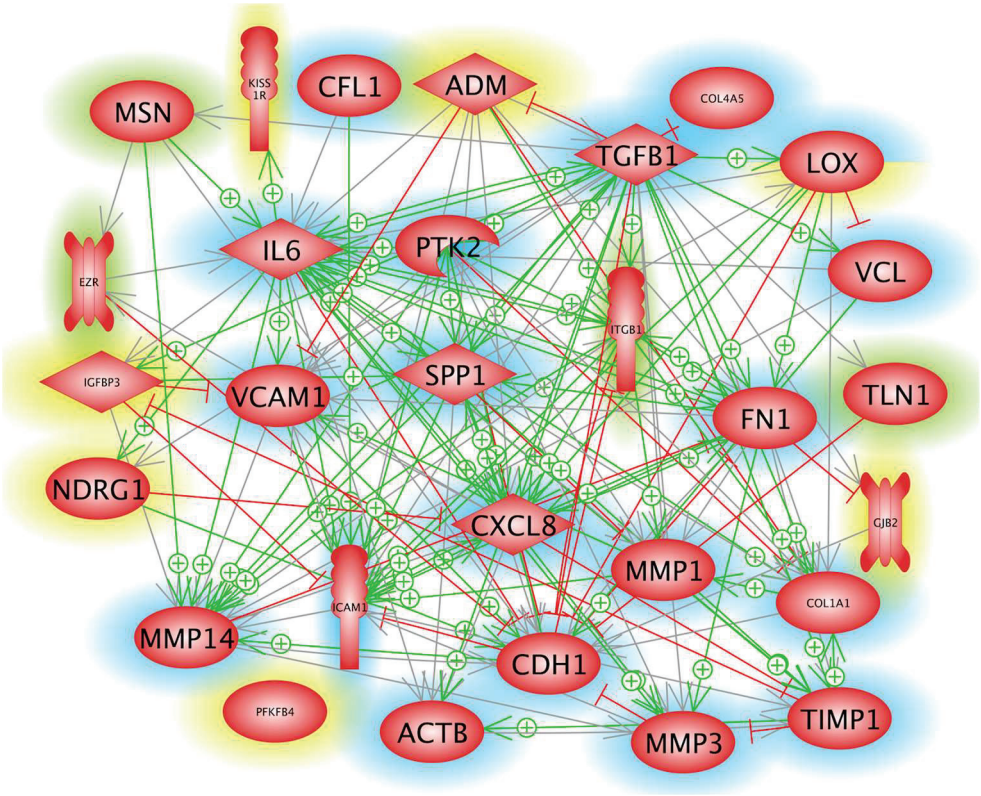


Figure 1. Network of interaction and mutual influence of the identified entities on a gene expression level. The genes, whose icons are marked with a green or blue rim have been found in recent studies referenced or mentioned in the preceding paper [20], respectively. The genes displayed with yellow icons attracted our attention when the two µ*g*-samples were investigated by gene array analysis, although the result lacked significance due to the fact of only two samples being available per experiments. Green arrows with a plus sign indicate expression or enhanced expression of a gene to which an arrow points to and red lines with a terminal crossbar show suppression or reduced expression of the gene near the crossbar. Grey arrows point to interaction with unknown effects as of now.

2. Results

After the samples' return to the laboratory, quantitative real-time PCR (qPCR) and pathway analyses were performed. The studies were done on the samples collected during the TX53 mission as described in [20] as well as on samples exposed to 18*g* (worst case) hyper-g on a centrifuge, or cultured for 6-min of s-µ*g* exposure on an RPM. We focused on the F-actin cytoskeleton, the ECM, focal adhesion, cell adhesion molecules, and cytokines. Various genes belonging to these groups and recently found to be differentially expressed during long-term spaceflights and RPM-experiments (Table 1) were investigated.

The genes listed in Table 1 were complemented with a number of additional genes known to be involved in cell-cell and cell-substrate adhesion. The *in-silico* evaluation of the selected genes revealed a self-contained network. These genes, indicated by a green or blue rim, form a network of mutual influence (Figure 1, icons with red rim), with *TGFB1*, *ITGB1*, *SPP1*, *IL-6*, *IL8*, *FN1*, *COL1A1*, *CDH1*, *and MMP14* being nodal points of this network. Additionally, many arrows start at *TGFB1*, *LOX* and *PTK2*, meaning that these entities are effectors in the system. Interestingly, the 6 genes marked with a yellow rim fit rather well into the network. These genes caught our attention during a preliminary evaluation of the microarray analysis of the two µ*g*-samples available, because they were at least 1.7-fold enhanced in comparison to the controls.

Table 1. Summary of previously found regulations in selected molecular targets due to gravitational alterations. ↑ indicates upregulation; ↓ indicates downregulation; double arrow indicates significant alterations; → indicates no regulation, blank was not examined.

Cell Line	*g*-Condition		*FN1*	*COL1A1*	*COL4A5*	*SPP1*	Reference
FTC-133	Space	10 days				↓	[11]
	RPM	1 day				AD↑↑ MCS↑	[23]
		7 days		↓		↑↑	[8]
		14 days		↓		↑↑	[8]
	PFC	31P				WT↑↑	[11]
	hyper-*g*	2 h					[11]
Nthy-ori 3-1	RPM	4 h	AD↑				[9]
		1 day	AD↑ MCS↓				[9]
		3 days	AD→ MCS→				[9]
		7 days		↑↑			[8]
		14 days		↑↑		↑↑	[8]
Cell line	***g*-Condition**		***ICAM1***	***VCAM1***	***IL6***	***CXCL8***	**Reference**
FTC-133	Space	10 days			↓	↓	[11]
	RPM	1 day			AD↑↑ MCS↓↓	AD↑↑ MCS↑	[23]
		7 days			↑↑	AD↑↑ MCS↓↓	[8]
		14 days			↑↑	AD↑↑ MCS→	[8]
	PFC	31 P			WT↑↑	WT↑↑	[11]
	hyper-g	2 h					[11]
Nthy-ori 3-1	RPM	4 h					[9]
		1 day					[9]
		3 days					[9]
		7 days			↑↑	AD↑↑ MCS↓↓	[8]
		14 days			↑↑	AD↑↑ MCS↑↑	[8]

Regarding the products of these genes (Figure 2), three groups can be distinguished: There are extracellular proteins, membrane proteins and intracellular proteins. As indicated above, the proteins whose icons are marked with a green or blue rim, are gene products found in recent studies referenced or mentioned in the preceding paper [20], respectively. On the protein level, however, the most important nodal points are fibronectin and integrin β 1. Intracellularly, they are connected to VCL, MSN and ACTB, which are involved in forwarding signals, generated by cells' binding to the ECM, towards the nucleus.

2.1. Impact of Microgravity on the Regulation of Genes Whose Products Act Extracellularly

Immunofluorescence staining (IFS) showed that the ECM protein fibronectin was redistributed in RPM-samples compared to control cells (Figure 3A,B). The *FN1* gene expression was not significantly altered (Figure 3C). In addition, fibronectin expression did not change in FTC-133 cells exposed to the RPM for 6 min (Figure 3D). *COL1A1* mRNA, however, was significantly upregulated in hyper-*g* samples compared with corresponding controls (Figure 3E), whereas the *COL4A5* mRNA remained stable in all groups (Figure 3F). The expression of the structural protein collagen IV was not significantly changed by short-term μ*g* as compared to the corresponding control (Figure 3G).

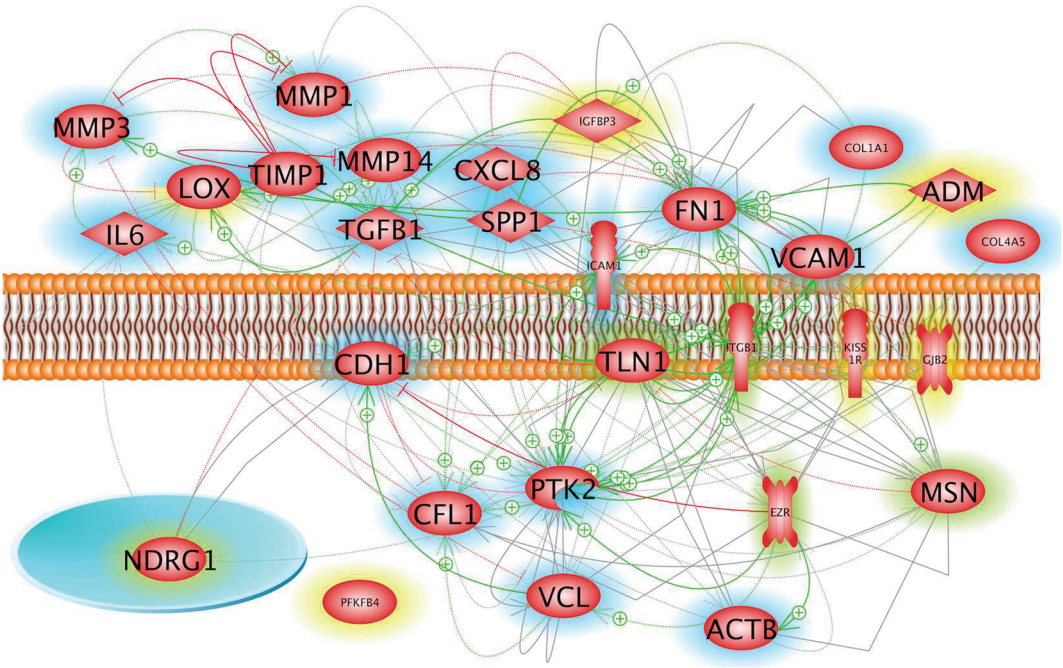


Figure 2. Localization and interaction of the products of genes mentioned above. The icons of genes products found in recent studies referenced or mentioned in the preceding paper [20], are marked with a green or blue rim, respectively. The genes products marked by yellow icons attracted our attention when the µ*g* samples (2) were evaluated by gene array analysis, although the results lacked significance due to the fact that only two samples per experiments were available. Green arrows with plus sign indicate stimulation and red lines with terminal crossbar show inhibition. Grey arrows indicate direct (solid line) or indirect (dashed line) interaction with unknown effect. Grey lines show protein–protein complex formation.

Moreover, we studied the ECM protein and cell adhesion molecule osteopontin. The secreted phosphoprotein 1 (*SPP1*) gene expression, determined in post-flight and hyper-*g* samples was slightly, but not significantly elevated (Figure 3H). RPM-exposure of the FTC-133 cells did not induce significant changes in the amount of protein in both groups (Figure 3I). qPCR of *TGFB1* mirrored these findings (Figure 3J).

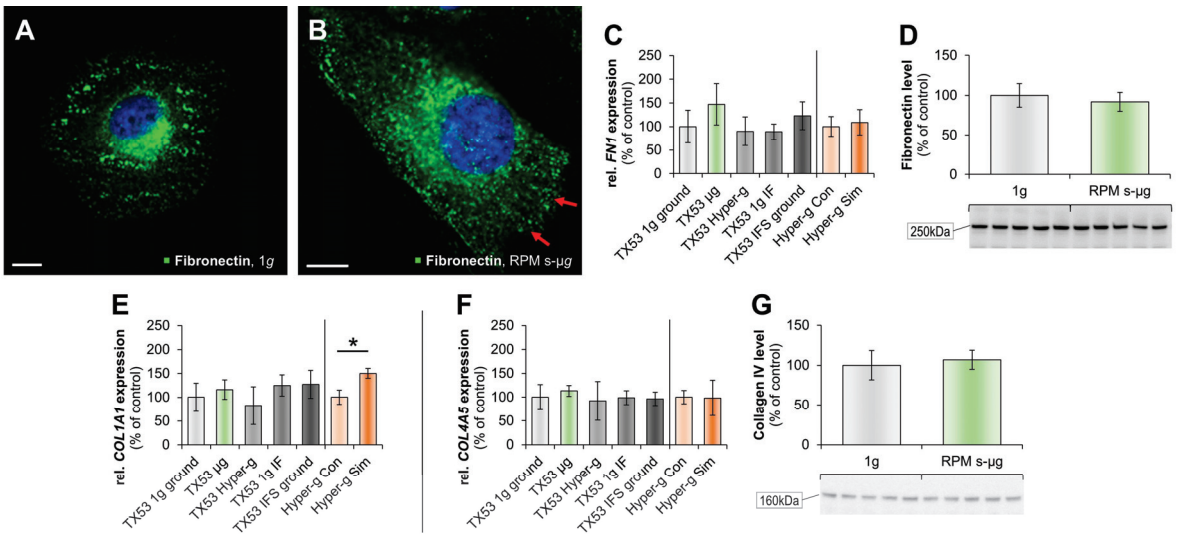


Figure 3. *Cont.*

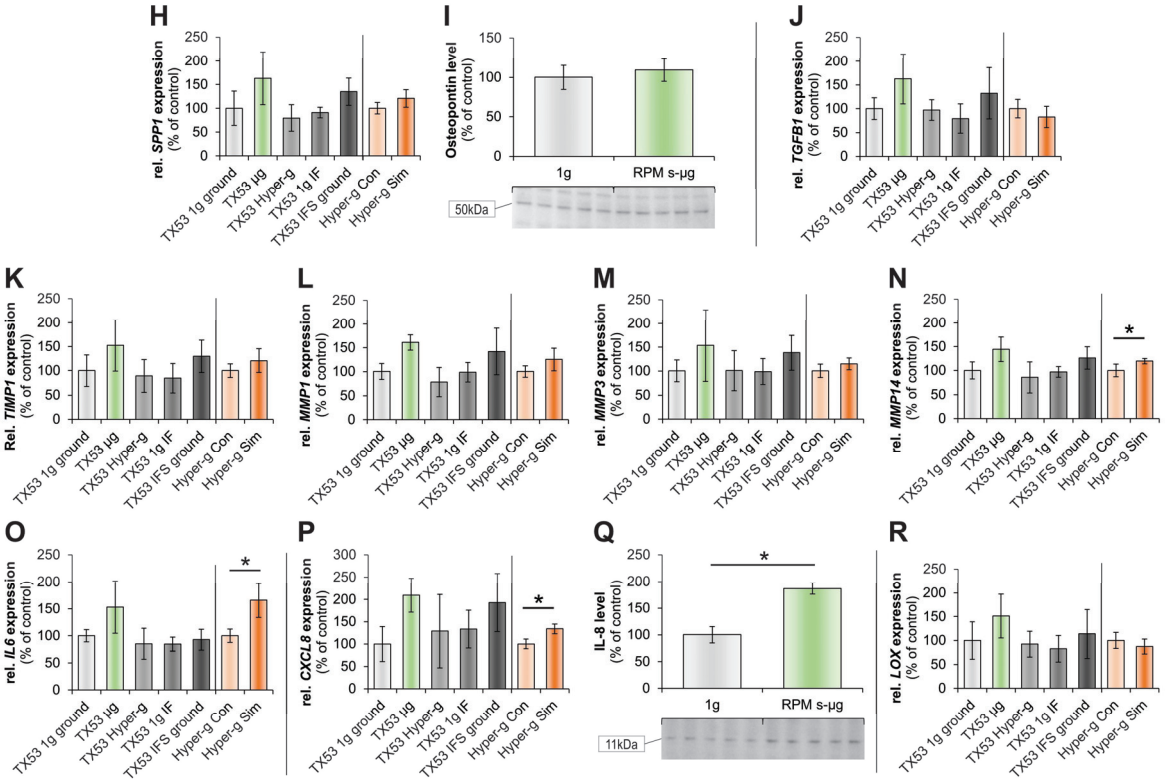


Figure 3. IFS of fibronectin (green) and nucleus (blue) (**A**,**B**); scale bar 10 µm; red arrow redistributed fibronectin, qPCR analyses of *FN1* (**C**), *Col1A1* (**E**), *Col4A5* (**F**), *SPP1* (**H**), *TGB1* (**J**), *TIMP1* (**K**), *MMP1* (**L**), *MMP3* (**M**), *MMP14* (**N**), *IL-6* (**O**), *CXCL8* (**P**) and *LOX* (**R**), and WB of fibronectin (**D**), collagen IV (**G**), osteopontin (**I**), and IL-8 (**Q**). "TX53" indicates samples collected from the sounding rocket mission, whereas "Hyper-g" presents data from a parallel experiment simulating the worst case-possible launch acceleration. IF: in-flight; Con: control; Sim: simulated; RPM: random positioning machine; 6min s-µ*g*; * $p < 0.05$ vs.1*g*.

Finally, we determined the gene expression patterns of tissue inhibitor of metalloproteinase 1 (*TIMP1*) and matrix metalloproteinases *MMP1*, *MMP3* and *MMP14* (Figure 3K-N). *TIMP1*, *MMP1*, and *MMP3* genes were slightly elevated in r-µ*g*, whereas the *MMP14* mRNA was elevated in r-µ*g* and significantly elevated in hyper-*g* samples (Figure 3N).

Earlier studies investigating the impact of µ*g* on human cells and the synthesis and secretion of the two cytokines interleukin-6 (IL-6) and interleukin-8 (IL-8 or synonymous CXC-motif-chemokine 8, (CXCL8)) have shown their involvement in 3D spheroid formation [24]. The release and expression of both cytokines was altered in space in FTC-133 cells [24]. Here we show that both, the *IL6* and *CXCL8* mRNA are elevated in the r-µ*g* and 18*g* centrifugation groups compared to controls (Figure 3O,P), while the IL8 protein expression was significantly enhanced during 6 min on the RPM (Figure 3Q). The *LOX* mRNA expression was elevated in r-µ*g* samples, but remained unaltered in all other groups (Figure 3R).

2.2. Influence of Microgravity on Genes of Membrane Proteins and Their Accumulation

The F-actin staining of RPM-exposed FTC-133 cells revealed stress fibers (yellow arrows) and lamellipodia together with filopodia (blue arrows) compared to controls (Figure 4A,B). In addition, F-actin accumulated at the cell membrane (Figure 4B). The beta-actin protein was reduced in RPM-samples compared to static 1*g*-controls (Figure 4C).

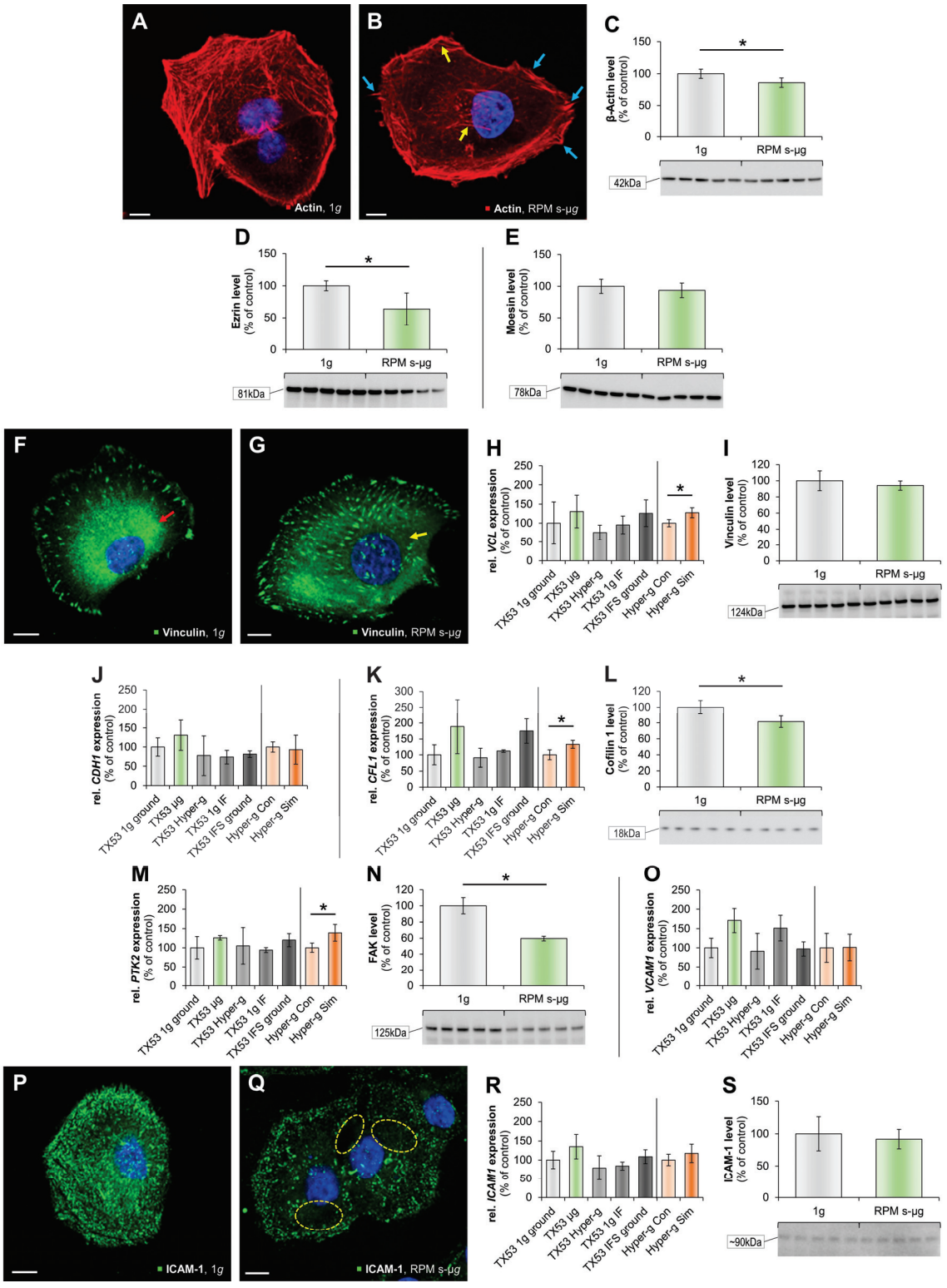


Figure 4. Histological staining of F-actin (red) and the nucleaus (blue) (**A**,**B**); yellow arrows: stress fibers and blue arrows: filopodia and lamellipodia; IFS of vinculin (green) and nucleus (blue) (**F**,**G**); red arrow: compact vinculin in 1*g* around the nucleus and yellow arrow: redistributed vinculin in RPM-samples; ICAM-1 (green) and nucleus (blue); yellow circles: areas with no ICAM1-positivity in RPM-samples (**P**,**Q**); scale bar 10 µm. qPCR analyses of *VCL* (**H**), *CDH1* (**J**), *CFL1* (**K**), *PTK2* (**M**), V*CAM1* (**O**), *ICAM1* (**R**), and WB of ACTB (**C**), ezrin (**D**), moesin (**E**), VCL (**I**), cofilin (**L**), FAK (**N**), ICAM1 (**S**). "TX53" indicates samples collected during the sounding rocket mission, whereas "Hyper-g" presents data from a parallel experiment aiming on the worst case-possible launch acceleration. IF: in-flight; Con: control; Sim: simulated; RPM: random positioning machine; 6min s-µ*g*; * $p < 0.05$ vs.1*g*, scale bars: 10 µm.

In a further step, we found a reduction for the protein ezrin in s-μ*g* (Figure 4D), but no significant changes for moesin (Figure 4E) [20].

Immunofluorescence staining of vinculin showed a normal distribution of this cytoskeletal protein, present in adherence-type cell junctions in the FTC-133 cells, at 1*g* (Figure 4F). A clear disorganization of vinculin was visible in RPM-exposed FTC-133 cells (Figure 4G). *VCL* was not changed in the flight samples, but significantly elevated by 18*g* centrifugation (Figure 4H). Vinculin expression was not changed after RPM-exposure compared to 1*g* (Figure 4I). Vinculin regulates the E-cadherin expression and is involved in mechanosensing by the E-cadherin complex. Therefore, we evaluated the *CDH1* mRNA expression, which was not altered in any of the samples (Figure 4J).

Vinculin and E-cadherin are known to be involved in cell morphology and locomotion. Another F-actin-binding protein is cofilin. The *CFL1* gene was elevated in r-μ*g*, and significantly enhanced in hyper-*g* samples (Figure 4K), indicating its role in the dynamics and organization of the F-actin cytoskeletal network. Western blot analysis of cofilin revealed a significant reduction in the RPM sample (Figure 4L). Focal adhesions are multiprotein structures connecting the ECM and the cytoskeleton.

Focal adhesion kinase 1 (FAK1 or protein tyrosine kinase 2 (PTK2)) is important for cell migration and its inhibition decreases mobility and metastasis. The *PTK2* mRNA was not altered in the TEXUS samples, but elevated by 18*g* centrifugation compared to the corresponding control (Figure 4M). The FAK1 protein content was significantly reduced in RPM samples (Figure 4N)

Finally, we measured the gene expression of the cell adhesion molecules vascular cell adhesion molecule 1 (*VCAM1*) (Figure 4O) and intercellular adhesion molecule 1 (*ICAM1*) (Figure 4R). Both proteins were upregulated in r-μ*g*, but not significantly changed in hyper-*g* (Figure 4O,R). ICAM-IFS visualized changes between the two groups (1*g* vs. RPM-exposure) (Figure 4P,Q). In RPM-samples ICAM1 IFS revealed holes and a lower density of ICAM-positive areas (Figure 4Q), but the ICAM1 protein concentration remained stable during 6 min on the RPM (Figure 4S).

Due to a kink in a fixative tubing one culture chamber was not filled with fixative, meaning that one μ*g*-chamber was not fixed with RNA*later* at the end of the 6-min μ*g*-phase [20]. Therefore, the cells harvested from the residual two μ*g*-samples did not allow a significant microarray gene analysis. In order to obtain preliminary hints on possible gene regulation within the six early minutes of μ*g*, we compared the result of microarray analysis of the three 1*g*-samples with the average values of two measurements of the μ*g*-samples. Of the 27,600 genes analyzed, eight genes appeared to be down-regulated, while seven seemed to be upregulated. While no further indication was found for the relevance of the apparent down-regulation, the comparison pointed to the possibility that *LOX*, *ADM*, *IGFBP3*, *NDRG1*, *KISS1R*, *GJB2*, *PFKFB4* genes could at least be upregulated1.7-fold after 6 min of μ*g*. The speculation is supported by the result that besides *PFKFB4* these genes and their products are members of the networks shown in Figures 1 and 2. In addition, several earlier studies have shown that all these genes or their products are gravisensitive and are downregulated during a prolonged stay in weightlessness [11,24–26].

3. Discussion

The exposure of thyroid cells to r- and s-μ*g* led to promising results in regard to re-differentiation of TC cells [8,11,23,27–29]. Especially a 10-day long-term sojourn in μ*g* during an unmanned space mission revealed gene expression changes suggesting a re-differentiation of the TC cells compared to their ground controls [11]. In this study, we could advance this theory and learned that up- and downregulation of a given gene may be a time-dependent process.

3.1. Impact of Microgravity on the Cytoskeleton

It is still unknown how cells are able to sense μ*g*. An interesting and often discussed candidate for sensing and conduction of μ*g* is the cellular cytoskeleton [30–33]. For this reason, we focused here on important cytoskeletal factors, associated focal adhesion complex molecules, and actin-binding proteins, which are all interconnected at the protein level (Figure 2).

The actin cytoskeleton network is one of the most intensively investigated structures in μ*g*. It is involved in cell shape, migration and stress response, among others [34]. In previous studies we found that the β-actin expression in TC cells as well as in other cell types is remarkably regulated during short- and long-term exposure to s-μ*g* and r-μ*g* [8,11,23,27]. Following short-term r-μ*g* the *ACTB* gene expression was upregulated in a matter of seconds, for example [27]. These findings were emphasized by live-cell imaging during a sounding rocket flight, where F-actin cytoskeleton re-arrangements were monitored immediately after entering the μ*g*-phase [12]. Here, we investigated FTC-133 follicular TC cells exposed to a 6-min RPM-exposure and found similar changes which support the findings from the previous rocket mission TX52.

During the TEXUS mission, the *ACTB* gene expression was constant in all controls as well as after 1 min of hyper-*g*, either on the rocket or in the control-experiment [20]. However, the μ*g*-samples presented a distinct downregulation of *ACTB*, which is in line with findings from short-term experiments during a parabolic flight mission [12]. In contrast, after 7-day and 14-day-exposure of FTC-133 cells on the RPM, *ACTB* was found to be highly upregulated [8]. This indicates a strong regulatory effect on the cells as they start to form 3D cell aggregates [8].

Ezrin (EZR) and moesin (MSN) are part of a focal adhesion complex and interconnect the plasma membrane to the cytoskeleton [35]. Moesin forms a complex with ezrin and is able to bind to actin [36,37]. These proteins are strikingly involved in the surface structure adhesion, migration and have been associated with some human cancers [38,39]. Ezrin and moesin have also been found to be modulated in previous μ*g*-experiments with thyroid cells [12,28]. During a 24 h-exposure study on the RPM with the thyroid cancer cell line UCLA RO82-W-1, the *EZR* gene expression was significantly downregulated [28]. That is in alignment with the findings from the TEXUS flight, as only the expression in μ*g*-samples was downregulated while controls and hyper-*g* probes were not affected [20] and corresponds to the reduction of ezrin protein during 6 min on the RPM (Figure 4D). Interestingly, the *MSN* gene expression was slightly downregulated in μ*g*-samples and upregulated in hyper-*g* experiments. *MSN* was not found to be modulated during parabolic flights using microarray analyses [27]. However, a 24 h exposure on the RPM presented a downregulation in adherently growing cells, comparable to the present study [28].

3.2. Real Microgravity Changes the Extracellular Matrix

Furthermore, we investigated the ECM with a focus on fibronectin. Earlier detailed proteomic analyses have shown that FTC-133 cells express surface proteins that bind fibronectin, strengthening 3D growth [40]. These results are in agreement with our current data. We observed upregulated *FN1* mRNA in r-μ*g* samples. In a former study, ML1 follicular TC cells were exposed to parabolic flight conditions. It was demonstrated that the *COL4A5* mRNA was downregulated under r-μ*g*, whereas *OPN* and *FN1* were significantly upregulated after 31 parabolas [27]. After six min r-μ*g* the *SPP1* gene expression was clearly elevated in r-μ*g* samples (Figure 3H), but the *COL4A5* mRNA kept a stable expression during the TEXUS flight (Figure 3F), indicating that the duration of μ*g* exposure might play a role in the upregulation of this basement membrane gene. In addition, ML1 TC cells exposed to the RPM revealed an increased synthesis of collagen type I and III, fibronectin, laminin and chondroitin sulfate [41].

Lysyl oxidase (LOX; protein-lysine 6-oxidase), is a protein that is encoded by the *LOX* gene. LOX upregulation in cancer cells is of importance in tumorigenesis and may promote progression of the primary tumor. qPCR analysis displayed a *LOX* upregulation in the TEXUS r-μ*g* group compared to all other groups (Figure 3R), the findings were confirmed by microarray technology. The LOX enzyme supports the cross-linking of collagen and elastin, which are both ECM components [42] and *LOX* gene expression was identified as promoting culture flask adherence of EA.hy926 cells [25]. During the Sino/German Simbox/Shenzhou-8 spaceflight mission, where the ECM linker LOX was virtually switched off, very large multicellular spheroids were formed [43].

The collagen homeostasis is maintained via collagen synthesis and degradation by the TC cells and is influenced by matrix metalloproteinases (MMPs). The MMPs themselves are regulated by TIMPs [44]. Little is known about matrix metalloproteinases and follicular TC. TIMP-1 was identified as a biomarker candidate for papillary TC [45]. Recently, the TIMP-1 secretion of space-flown FTC-133 cells was measured as 2.8-fold elevated. In parallel, the MMP-3 release was 5.94-fold elevated in ISS space samples compared to 1*g*-samples [46]. These results contradict earlier results. Following the SimBox/Shenzhou-8 space mission we detected a reduced MMP-3 secretion in both, RPM-samples and in space-flown samples [11]. The ECM plays a key role in tissue maintenance and integrity [47]. MMPs degrade the ECM and are involved in cancer progression and MMP activity is regulated by TIMPs [48]. The mode of action of TIMPs in cancer is yet not known, but there are reports about tumor suppression and tumor progression properties [49]. Here we found an increase in *TIMP1*, *MMP1*, *MMP3* and *MMP14* mRNA expression in r-μ*g*-samples (Figure 3K–N), indicating an activation in orbit. These results support the data obtained from the ISS spaceflight in 2014 [46].

We detected an upregulation of the *TGFB1* gene expression in the r-μ*g* group as compared to 1*g*-control cells (Figure 3J). No change was found after centrifugation. TGF-β_1 is a growth factor and a multifunctional cytokine. It is involved in biological processes like cell proliferation, adhesion and differentiation, and is therefore, a target in cancer therapy [50].

3.3. Alteration of Focal Adhesion Proteins

Focal adhesions or cell–matrix adhesions mediate cell signaling in response to ECM adhesion and serve as mechanical linkages to the ECM. Focal adhesions are known to be important gravisensors [51,52]. To determine alterations in focal adhesion proteins, we focused on vinculin as a first point of interest. Vinculin has a vital role in mechanotransduction with integrins at focal adhesion sites [53]. Vinculin also directly interacts with talin, integrins and actin, hence allowing a proper cellular migration and orchestrating focal adhesion [54]. In addition, vinculin is a component of the adherence junctions and mediates cellular and extracellular signals. The *VCL* gene expression was not altered by μ*g*, but elevated by centrifugation (Figure 4H). Structure and morphology of vinculin was visualized by IFS (Figure 4F,G). Interesting changes were visible by RPM-exposure (Figure 4G). Vinculin was disarranged in s-μ*g*, indicating a clear reaction to the low-gravity condition.

Another important focal adhesion factor is the cytosolic and mechanosensitive protein talin-1 (TLN1). It links integrin directly and indirectly via vinculin to the cytoskeleton. Integrins bind to talin and talin binds to vinculin and thus influence cell adhesion. In addition, the integrin receptors are involved in the attachment of adherent cells to the ECM. Talin is a mechanosensitive protein and is connecting integrins and the actin-cytoskeleton. It links actin to the integrin-β_1, which is inserted in the plasma membrane [55]. It is especially enriched in regions of cell-cell contacts and adhesion to substrate [56]. Because of its function, it is of high interest when cells transit from a two-dimensional (2D) cell growth to a 3D cell growth in μ*g*. These 3D-aggregates or multicellular spheroids resemble the in vivo situation much closer than conventional cell cultures, making them extremely valuable for cancer research [6,57]. A downregulation of *TLN1* in the early state of μ*g* might be an indication for detachment of the cells from the substrate [20]. On the background that talin has a vinculin-binding site and can recruit vinculin, it forms a complex with integrins and is thus inducing cell adhesion.

Integrin-β_1 (*ITGB1*) is a subunit of a plasma membrane associate receptor family which primarily detects ECM components [58]. It is bound to and activated by talin [59]. *ITGB1* was not regulated in any experimental condition [20]. This is in in alignment with findings from short-term μ*g*-experiments conducted during parabolic flight missions as *ITGB1* was not regulated as well [27]. Interestingly, *ITGB1* was regulated when human Nthy-ori-3-1 cells were exposed to a RPM for 24 h suggesting that the regulation is cell type-, time- or μ*g*-origin-dependent [29].

In a next step, we focused on E-cadherin. Cadherins are Ca^{2+} -dependent cell adhesion molecules in the cell-cell adherence junction, which belongs to the plasma membrane and is connected to cytoskeletal actin filaments [60]. E-cadherin's intracellular domains are connected to the cytoskeleton

and its stability is regulated by catenin D1 [61], which can affect cell-cell adhesion [62]. E-cadherin is downregulated in tumors and multicellular MCF-7 breast cancer spheroids engineered by a 14-day RPM exposure and are known to be involved in metastasis [63]. The loss of E-cadherin expression in association with the epithelial–mesenchymal transition occurs frequently during tumor metastasis. The regulation of the adhesive activity of E-cadherin present at the cell surface by an inside-out signaling mechanism is important in cancer [64]. In this experiment, we found a slight increase in *CDH1* mRNA in the r-μ*g* group, but no changes in all other groups (Figure 4J). This is an interesting finding because the E-cadherin (*CDH1*) expression in cancer cells exposed to r-μ*g* is an unknown area. Proteomic pathway analyses demonstrated changes in papillary TC which were associated with the disruption of cell contacts (loss of E-cadherin), actin cytoskeleton dynamics and loss of differentiation markers, all hallmarks of an invasive phenotype [65].

We focused on the actin-binding protein cofilin, which disassembles actin filaments and influences the actin dynamics [66]. We determined the *CFL1* gene expression and found an elevation in the r-μ*g* group compared with the respective controls (Figure 4K). In addition, the gene was upregulated by 18*g*-centrifugation, while the protein concentration was reduced after 6 min on the RPM (Figure 4L). Little is known concerning the impact of cofilin in follicular TC. An interesting proteomic analysis was published recently [66]. The authors investigated the fine needle aspiration fluid protein patterns of papillary thyroid carcinomas. A statistically significant upregulation of cofilin-1 was detected among others [67]. Cofilin-1 is determining the direction of cell migration and has importance for metastasis in papillary thyroid cancer [68]. Future experiments will be necessary to study cofilin-1 in follicular thyroid cancer in detail.

Furthermore, we studied focal adhesion kinase 1 (protein tyrosine kinase 2, PTK2), which plays an important part during cell migration. Interestingly, *FAK1/PTK2* gene expression did not change by the sounding rocket flight, but it was upregulated by centrifugation. Recently, we showed that FTC-133 cells growing in monolayers or in spheroids after RPM-exposure incorporate vinculin, paxillin, focal adhesion kinase 1, and adenine diphosphate (ADP)-ribosylation factor 6 in different ways into the focal adhesion complex [69].

In summary, we were able show that focal adhesion proteins are important gravi-sensors and link the information to the ECM and the cytoskeleton.

In addition, we investigated the cell adhesion molecules ICAM-1 and VCAM-1. We had learned from the ISS CellBox-1 space mission that VCAM-1, TIMP1, protein kinase C_α and others are involved in the inhibition of spheroid formation under r-μ*g* [46]. Interestingly, both *ICAM1* and *VCAM1* mRNA expressions were slightly elevated in r-μ*g*-samples. They were not significantly altered after 18*g*-centrifugation or RPM-exposure. This finding might be due to the short μ*g*-exposure time.

3.4. Impact of altered gravity on cytokines

Centrifugation with 18*g* hyper-*g* and simulating the 31 parabolas of a parabolic flight induced the gene expression of *IL6* and *CXCL8* in ML1 TC cells [26]. Here, we found a similar result. Short-term 18*g*-centrifugation upregulated both *IL6* and *CXCL8* mRNAs. In addition, there was an increase detectable in both genes in the r-μ*g* group. These results confirmed earlier data, when TC cells were exposed to the RPM. We did observe that the *IL6* gene expression was enhanced in FTC-133 thyroid cancer cells, which remained adherent for 24 h on the RPM [23]. Similar results were obtained when human follicular epithelial thyroid Nthy-ori 3-1 cells were incubated for up to 72 h on the RPM [9]. Both cytokines have shown to have a 3D growth-promoting effect on follicular cancer spheroids [24]. In summary, the cytokines IL-6 and IL-8 are involved in migration and growth in thyroid cancer, and both are sensitive to altered gravity conditions. They seem to be involved in the initiation of MCS formation via focal adhesion proteins of benign cells [9] and cancer cells.

Taken together, our findings suggest that μ*g* is a much stronger trigger for gene expression changes than hyper-*g*. This enables us to adjust some controls in favor of μ*g*-samples in future space missions, which will result in increased scientific output and saves resources.

4. Materials and Methods

4.1. Cell Cultures

Cell culture and preparation of the experiments were performed as previously described in detail [20]. In short, FTC-133 poorly differentiated follicular thyroid cancer cells (Sigma Aldrich, St. Louis, MO, USA) were seeded into cell culture chambers at a defined density of 10^6 cells/chamber one day prior to the rocket launch (Figure 5A). These cell culture chambers were placed into late access unites, which ensured introduction into the rocket very close to launch (Figure 5B). During flight the cells were exposed to a variety of stressors, besides an on-flight 1*g*-centrifuge (Figure 5C). To discriminate between effects of μ*g* and the different stressors the cell culture chambers were fled with RNAlater (Thermofisher Scientific, Waltham, MA, USA) fixative at defined time points (Figure 5D), resulting in samples to be analyzed for gene expression changes back in the home laboratory. Furthermore, FTC-133 cells were exposed to worst case-hyper-*g* on a centrifuge for 1 min which could have been the case during sounding rocket launch [20].

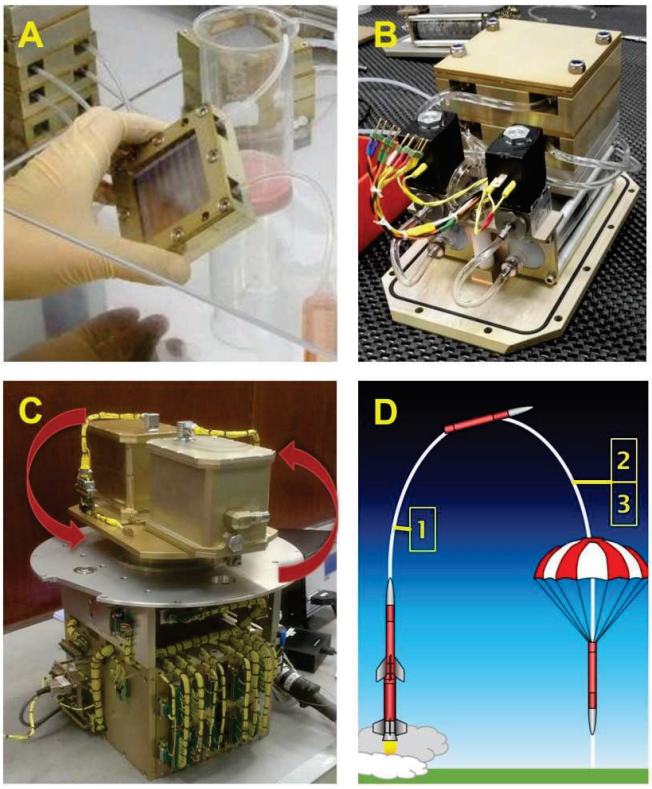


Figure 5. Workflow during the TEXUS-53 mission. Cell culture chamber were filled with cells (**A**) and afterwards placed into the late access unite (**B**). During flight a 1*g*-centrifuge (**C**) served as one control besides others. Red arrows indicate the rotation direction of the centrifuge. The cells were fixed at defined time points 1, 2, 3 (**D**).

4.2. TEXUS Sounding Rocket Mission

Investigated conditions ranged from different 1*g*-controls, to hyper-*g*- and μ*g*-samples as described before [20]. In short, during a sounding rocket flight the launch phase of 1 min can reach an acceleration of up to 12*g* which could have an effect on the cells (sample: TX53 Hyper-*g*). After the launch, the payload enters a 6 min μ*g*-phase during which one part of the samples are kept on a 1*g*-centrifuge (sample: In-flight 1*g*-centrifuge), as a control, while the other part is exposed to μ*g* (sample: TX53 μ*g*). Shortly before re-entering the Earth atmosphere samples are fixed as described before. In addition to the flight samples, on ground 1*g* controls were performed with the cells kept horizontal (sample: TX53

Ground Control) and vertical (sample: TX53 In-flight 1*g* sim.). The vertical control was done due to the special arrangement of the cells on the in-flight centrifuge. Finally, a worst-case hyper-*g* experiment was performed keeping the cells on a centrifuge with 18*g* for 1 min (sample: Hyper-*g* 1 min).

4.3. Random Positioning Machine

Simulated μ*g* (s-μ*g*) was performed on the desktop RPM (Airbus Defence and Space (ADS), Leiden, The Netherlands) located in a standard incubator (37 °C and 5% CO_2) as previously described [70].

In brief, the RPM was operated in real random mode with random interval and direction with a maximum speed of 12.5 revolutions per minute. In each case sample flasks were placed onto the middle frame with a maximum distance of 7 cm to the center of rotation providing a μ*g* quality in the range of 10^{-4}–10^{-2} *g* (n = 5 samples each group/run) [10,71]. Samples were run on the RPM for 6 min to mimic the μ*g*-phase of the sounding rocket flight. The RPM-samples and the corresponding static 1*g*-control flasks were completely filled with medium. The 1*g*-samples were placed in the incubator next to the RPM (n = 5 samples each group/run).

4.4. F-actin Staining

F-actin was visualized by means of rhodamine-phalloidin staining (Molecular Probes®, Eugene, OR, USA). The nuclei were stained with Hoechst 33342 (Molecular Probes®). The method was published earlier [72,73].

4.5. Confocal Laser Scanning Microscopy (CLSM)

The stained samples were examined using a confocal laser scanning microscope (LSM 780, Zeiss, Jena, Germany) using 40× oil-immersion objective with a NA of 1.3 [74].

4.6. Immunofluorescence of Fibronectin, Vinculin and ICAM-1

Immunofluorescence staining was performed to visualize changes in fibronectin, vinculin and ICAM-1 proteins. After the experiments, the cells were washed three times with PBS and afterwards fixed in 4% PFA (Sigma-Aldrich) for 30 min at room temperature. The primary antibodies (fibronectin, (Invitrogen, Carlsbad, CA, USA), mouse, dilution 1:100, vinculin (Abcam, Cambridge, UK), mouse, dilution 1:200, ICAM1, (Cell Signaling Technology, Danvers, MA, USA), rabbit, dilution 1:200) were applied for 24 h. Then the slides were washed three times with PBS before incubation with secondary antibodies (AF488 conjugated anti-mouse/rabbit: 1:500, both Cell Signaling Technology) for 2 h. Nuclei were stained with DAPI (4′,6-diamidino-2-phenylindole) (Invitrogen) and mounted with Vectashield. Afterwards the slides were investigated by CLSM (LSM 780, Zeiss, Jena, Germany).

4.7. Western Blot Analysis

Western blotting was performed as described earlier [72,73]. In each experiment (performed three times) five different culture flasks were subjected to either s-μ*g* or 1*g*. At the end of the experiment cells were collected and solubilized in lysis buffer. Following lysis and centrifugation, aliquots of 30 μ*g* were subjected to SDS-PAGE and Western blotting. For the RPM-samples five lanes representing the AD cells and five lanes representing AD static 1*g*-control cells were loaded. The samples were loaded on Criterion XT 4–12% precast gels (BioRad, Hercules, CA, USA) and run for 1h at 150 volts. Proteins were then transfer with a TurboBlot (Biorad) (100 V, 30 min) to a PVDF membrane. Glycerine aldehyde-3-phosphate-dehydrogenase (GAPDH) was used as a loading control.

Membranes were then blocked 2 h in TBS-T containing 0.3% I-Block (Applied Biosystems, Foster City, CA, USA). For detection of the selected antigens (see Table 2) the membranes were incubated overnight at room temperature in TBS-T and 0.3% I-Block solutions of the antibodies. Following three washing steps of 5 min membranes were incubated additionally 2 h at room temperature secondary with a Horseradish peroxidase (HRP)-linked antibody (Cell Signaling Technology Inc., Danvers, MA,

USA) diluted 1:4000 in TBS-T and 0.3% I-Block. The respective protein bands were visualized using BioRad Clarity Western ECL (BioRad) and images were captured with Image Quant LAS 4000 mini (GE Healthcare Life Science, Freiburg, Germany). Images of stained membranes were captured on Syngene PXi 4EZ image analysis system (Synoptics, Cambridge, UK) and analyzed using the ImageJ software (U.S. National Institutes of Health, Bethesda, MD, USA; http://rsb.info.nih.gov/ij/) for densitometric quantification of the respective bands and total protein load.

Table 2. Antibodies for Western blot analyses.

Antibodies	Company/No	Species	MW (kDa)	Dilution
Collagen type I	Sigma/C2456	Ms	~130	1:500
B-actin	Sigma/A5316	Ms	42	1:2000
Fibronectin	Invitrogen/MA1198	Ms	250	1:1000
Osteopontin	Sigma/07264	Rb	50	1:1000
Cofilin	#ab 42824	Rb	20	1:2000
IL-8	Abcam/ab7747	Rb	11	1:500
Collagen type IV	Abcam/ab52235	Rb	160	1:1000
Ezrin	Cell Signaling #3145	Rb	81	1:500
Moesin	Cell Signaling #3150	Rb	78	1:500
Vinculin	Abcam/ab18058	Ms	124	1:1000
ICAM 1	Cell Signaling #4915S	Rb	89–92	1:500
GAPDH	Abcam/ab9384	Rb	37	1: 1000

4.8. Postflight qPCR Analysis

qPCR analysis was performed as previously described [42]. In short, samples from the mission were transported and stored in RNA*later*. In addition, samples from hyper-g experiments were investigated. RNA was isolated from cells using the RNAeasy kit (Qiagen, Venlo, The Netherlands) following the manufactures instructions. After concentration determination via Nanodrop 2000, cDNA was produced using the first strand cDNA kit (Thermo Scientific, Waltham, MA, USA). qPCR was performed using the FAST SYBR® Select Master Mix (Applied Biosystem) and the 7500 Fast Real-Time PCR System (Applied Biosystems) to determine the expression levels of the target genes (Table 3). The selected primers were designed to span exon-exon junctions and to have a Tm of 60 °C using NCBI Primer Blast and were synthesized by TIB Molbiol (Berlin, Germany). Samples were normalized to 18S rRNA and measured in triplicates. We used the comparative threshold cycle ($\Delta\Delta C_T$) method for relative quantification of transcription levels, with "TX53 Ground Control" set as 100%.

4.9. In-silico Analyses

In-silico analyses were performed as described by Bauer et al. [22]. To investigate the mutual interactions of detected proteins, the UniProt accession numbers of the selected targets were induced in a Pathway Studio v.11 software (Elsevier Research Solutions, Amsterdam, The Netherlands) [63,69].

4.10. Microarray Analysis

Microarray analyses were performed as described by Kopp et al. [20].

4.11. Statistics

Statistical evaluation was performed using SPSS 15.0 (SPSS, Inc., Chicago, IL, USA). The Mann-Whitney-U-Test was used to compare the different conditions. All data is presented as mean ± standard deviation (SD) with a significance level of * $p < 0.05$.

Table 3. Primer sequences for qPCR.

Gene	Primer Name	Sequence
18S-rRNA	18S-F 18S-R	GGAGCCTGCGGCTTAATTT CAACTAAGAACGGCCATGCA
ACTB	ACTB-F ACTB-R	TGCCGACAGGATGCAGAAG GCCGATCCACACGGAGTACT
CDH1	CDH1-F CDH1-R	GCTGGACCGAGAGAGTTTCC CAGCTGTTGCTGTTGTGCTT
CFL	CFL-F CFL-R	GAAGGAGGATCTGGTGTTTATCTTCT CCTTGGAGCTGGCATAAATCAT
COL1A1	COL1A1-F COL1A1-R	ACGAAGACATCCCACCAATCAC CGTTGTCGCAGACGCAGAT
COL4A5	COL4A5-F COL4A5-R	GGTACCTGTAACTACTATGCCAACTCCTA CGGCTAATTCGTGTCCTCAAG
EZR	EZR-F EZR-R	GCAATCCAGCCAAATACAACTG CCACATAGTGGAGGCCAAAGTAC
FAK1/PTK2	FAK1-F FAK1-R	TGTGGGTAAACCAGATCCTGC CTGAAGCTTGACACCCTCGT
FN1	FN1-F FN1-R	AGATCTACCTGTACACCTTGAATGACA CATGATACCAGCAAGGAATTGG
ICAM-1	ICAM1-F ICAM1-R	CGGCTGACGTGTGCAGTAAT CTTCTGAGACCTCTGGCTTCGT
IL6	IL6-F IL6-R	CGGGAACGAAAGAGAAGCTCTA GAGCAGCCCCAGGGAGAA
IL8/CXCL8	IL8-F IL8-R	TGGCAGCCTTCCTGATTTCT GGGTGGAAAGGTTTGGAGTATG
ITGB1	ITGB1-F ITGB1-R	GAAAACAGCGCATATCTGGAAATT CAGCCAATCAGTGATCCACAA
LOX	LOX-F LOX-R	TGGGAATGGCACAGTTGTCA AGCCACTCTCCTCTGGGTGTT
MMP1	MMP1-F MMP1-R	GTCAGGGGAGATCATCGGG GAGCATCCCCTCCAATACCTG
MMP3	MMP3-F MMP3-R	ACAAAGGATACAACAGGGACCAA TAGAGTGGGTACATCAAAGCTTCAGT
MMP14	MMP14-F MMP14-R	ACTTTATGGGGGTGAGTCAGG GATGTTGGGCCCATAGGTGG
MSN	MSN-F MSN-R	GAAATTTGTCATCAAGCCCATTG CCATGCACAAGGCCAAGAT
PFN1	PFN-F PFN-R	GGGAATTTAGCATGGATCTTCGT ACCGTGGACACCTTCTTTGC
SSP1	SSP1-F SSP1-R	CGAGGTGATAGTGTGGTTTATGGA CGTCTGTAGCATCAGGGTACTG
TGFB1	TGFB1-F TGFB1-R	CACCCGCGTGCTAATGGT AGAGCAACACGGGTTCAGGTA
TIMP1	TIMP1-F TIMP1-R	GCCATCGCCGCAGATC GCTATCAGCCACAGCAACAACA
TLN1	TLN1-F TLN1-R	GATGGCTATTACTCAGTACAGACAACTGA CATAGTAGACTCCTCATCTCCTTCCA
VCAM-1	VCAM1–F VCAM1-R	CATGGAATTCGAACCCAAACA GGCTGACCAAGACGGTTGTATC
VCL	VCL-F VCL-R	GTCTCGGCTGCTCGTATCTT GTCCACCAGCCCTGTCATTT

All sequences are given in 5′–3′ direction.

5. Conclusions

Taken together, simulated hyper-*g* induced the gene expression of *COL1A1*, *VCL*, *CFL1*, *PTK2*, *IL6*, *CXCL8* and *MMP14*.

Unfortunately, after the TX53 mission, we noticed that only two r-μ*g* samples were fixed with RNA*later* [20], so that no statistical evaluation was possible. qPCR measured elevated mRNA of the ECM genes *FN1*, *SPP1*, *TGFB1*, *TIMP1*, *MMP1*, *MMP3*, *MMP14*. In addition, the cell adhesion genes *ICAM1* and *VCAM1*, the focal adhesion factors *CFL1* and *CDH1* as well as cytokines *IL6* and *CXCL8* were upregulated in r-μ*g* samples. All these factors have demonstrated their gravi-sensitivity. *FN1* and *TIMP1* are recently proposed as potential target genes in papillary TC [75]. Downregulation of E-cadherin plays a role in metastasis, and the restoration of E-cadherin inhibits tumor growth. Antibodies reducing E-cadherin activity favor MCS formation, and PP2, blocking the E-cadherin reducer SRC prevents MCS formation *in vitro* [63]. Therefore, E-cadherin seems to be an interesting target in follicular TC. Future detailed investigations focusing on E-cadherin/β-catenin signaling will be performed.

Furthermore, we were able to show that μ*g* achieved by a sounding rocket flight is a strong trigger for gene expression changes in FTC-133 cells. Future studies during TEXUS sounding rocket missions will be performed in order to increase the number of samples.

Author Contributions: Sounding rocket flight, A.S., B.S., H.O., and S.F.; Conceptualization, D.G. and J.B.; methodology, S.K., M.Z.N., J.S., T.J.B., and D.M.; Software, H.S. and J.B.; Validation, D.G., T.J.C., S.K., M.K. and D.M.; Formal analysis, S.K., J.S., and M.W.; Investigation, S.K.; Resources, M.I.; Writing—Original draft preparation, S.K., T.J.C, M.K., D.G., J.B.; Project administration, D.G.; funding acquisition, D.G. and M.I..

Funding: This research was funded by the German Space Agency (DLR; BMWi project 50WB1524).

Acknowledgments: We like to thank Otfried Joop and Markus Braun (German Space Agency DLR, Bonn) for their support and for giving us the possibility to attend the TEXUS mission in Kiruna, Sweden. This paper was presented at the 69th International Astronautical Congress, 1–5 October 2018, Bremen, Germany. www.iafastro.org.

Conflicts of Interest: The authors declare no conflict of interest. The funders had no role in the design of the study; in the collection, analyses, or interpretation of data; in the writing of the manuscript, or in the decision to publish the results.

Abbreviations

μ*g*	Microgravity
2D	two-dimensional
3D	three-dimensional
AD	adherently growing
ADS	Airbus Defence and Space
CDH1	Cadherin-1/E-cadherin
CFL1	Cofilin
COL1A1/COL4A5	Collagen 1A1/Collagen 4A5
CXCL8	Interleukin 8
ECM	Extracellular Matrix
ERM	Ezrin-Radixin-Moesin
FN1	Fibronectin 1
ICAM1	Intercellular adhesion molecule 1
IL6	Interleukin 6
IMS	Immunofluorescence staining
ITGB1	Integrin beta-1
LOX	Protein-lysine 6-oxidase
MCS	Multicellular spheroids
MMPs	Matrix metalloproteinases
PTK2/FAK1	Focal adhesion kinase 1
qPCR	Quantitative PCR
r-	real-

RAI	Radioiodine therapy
RPM	Random Positioning Machine
s-	simulated-
SPP1	Secreted Phosphoprotein 1 / Osteopontin
TC	Thyroid cancer
TGFB1	Transforming growth factor beta-1
TIMP1	Metallopeptidase (proteinase) inhibitor 1
TX	TEXUS
VCAM1	Vascular cell adhesion protein 1
ADM	Adrenomedullin
GJB2	Gap junction beta-2 protein
PFKFB4	6-phosphofructo-2-kinase/fructose-2,6-biphospatase 4
KISS1R	KiSS-1 receptor
NDRG1	Protein NDRG1
IGFBP3	Insulin-like growth factor-binding protein 3

References

1. Bray, F.; Ferlay, J.; Soerjomataram, I.; Siegel, R.L.; Torre, L.A.; Jemal, A. Global cancer statistics 2018: Globocan estimates of incidence and mortality worldwide for 36 cancers in 185 countries. *CA Cancer J. Clin.* **2018**, *68*, 394–424. [CrossRef] [PubMed]
2. Ancker, O.V.; Wehland, M.; Bauer, J.; Infanger, M.; Grimm, D. The adverse effect of hypertension in the treatment of thyroid cancer with multi-kinase inhibitors. *Int. J. Mol. Sci.* **2017**, *18*, 625. [CrossRef] [PubMed]
3. Omur, O.; Baran, Y. An update on molecular biology of thyroid cancers. *Crit. Rev. Oncol. Hematol.* **2014**, *90*, 233–252. [CrossRef] [PubMed]
4. Laursen, R.; Wehland, M.; Kopp, S.; Pietsch, J.; Infanger, M.; Grosse, J.; Grimm, D. Effects and role of multikinase inhibitors in thyroid cancer. *Curr. Pharm. Des.* **2016**, *22*, 5915–5926. [CrossRef] [PubMed]
5. Grimm, D.; Egli, M.; Kruger, M.; Riwaldt, S.; Corydon, T.J.; Kopp, S.; Wehland, M.; Wise, P.; Infanger, M.; Mann, V.; et al. Tissue engineering under microgravity conditions-use of stem cells and specialized cells. *Stem Cells Dev.* **2018**, *27*, 787–804. [CrossRef] [PubMed]
6. Grimm, D.; Wehland, M.; Pietsch, J.; Aleshcheva, G.; Wise, P.; van Loon, J.; Ulbrich, C.; Magnusson, N.E.; Infanger, M.; Bauer, J. Growing tissues in real and simulated microgravity: New methods for tissue engineering. *Tissue Eng. Part B Rev.* **2014**, *20*, 555–566. [CrossRef] [PubMed]
7. Strauch, S.M.; Grimm, D.; Corydon, T.J.; Krüger, M.; Bauer, J.; Lebert, M.; Wise, P.; Infanger, M.; Richter, P. Current knowledge about the impact of microgravity on the proteome. *Expert Rev. Proteom.* **2018**, 1–12. [CrossRef] [PubMed]
8. Kopp, S.; Warnke, E.; Wehland, M.; Aleshcheva, G.; Magnusson, N.E.; Hemmersbach, R.; Corydon, T.J.; Bauer, J.; Infanger, M.; Grimm, D. Mechanisms of three-dimensional growth of thyroid cells during long-term simulated microgravity. *Sci. Rep.* **2015**, *5*, 16691. [CrossRef] [PubMed]
9. Warnke, E.; Pietsch, J.; Kopp, S.; Bauer, J.; Sahana, J.; Wehland, M.; Krüger, M.; Hemmersbach, R.; Infanger, M.; Lützenberg, R.; et al. Cytokine release and focal adhesion proteins in normal thyroid cells cultured on the random positioning machine. *Cell. Physiol. Biochem.* **2017**, *43*, 257–270. [CrossRef] [PubMed]
10. Warnke, E.; Pietsch, J.; Wehland, M.; Bauer, J.; Infanger, M.; Görög, M.; Hemmersbach, R.; Braun, M.; Ma, X.; Sahana, J.; et al. Spheroid formation of human thyroid cancer cells under simulated microgravity: A possible role of CTGF and CAV1. *Cell Commun. Signal.* **2014**, *12*, 32. [CrossRef]
11. Ma, X.; Pietsch, J.; Wehland, M.; Schulz, H.; Saar, K.; Hübner, N.; Bauer, J.; Braun, M.; Schwarzwälder, A.; Segerer, J.; et al. Differential gene expression profile and altered cytokine secretion of thyroid cancer cells in space. *FASEB J.* **2014**, *28*, 813–835. [CrossRef] [PubMed]
12. Corydon, T.J.; Kopp, S.; Wehland, M.; Braun, M.; Schütte, A.; Mayer, T.; Hulsing, T.; Oltmann, H.; Schmitz, B.; Hemmersbach, R.; et al. Alterations of the cytoskeleton in human cells in space proved by life-cell imaging. *Sci. Rep.* **2016**, *6*, 20043. [CrossRef] [PubMed]
13. Ingber, D. How cells (might) sense microgravity. *FASEB J.* **1999**, *13*, S3–S15. [CrossRef] [PubMed]

14. Ingber, D.E.; Wang, N.; Stamenovic, D. Tensegrity, cellular biophysics, and the mechanics of living systems. *Rep. Prog. Phys.* **2014**, *77*, 046603. [CrossRef] [PubMed]
15. Schoenwaelder, S.M.; Burridge, K. Bidirectional signaling between the cytoskeleton and integrins. *Curr. Opin. Cell Biol.* **1999**, *11*, 274–286. [CrossRef]
16. Yamada, K.M.; Geiger, B. Molecular interactions in cell adhesion complexes. *Curr. Opin. Cell Biol.* **1997**, *9*, 76–85. [CrossRef]
17. Calderwood, D.A.; Shattil, S.J.; Ginsberg, M.H. Integrins and actin filaments: Reciprocal regulation of cell adhesion and signaling. *J. Biol. Chem.* **2000**, *275*, 22607–22610. [CrossRef] [PubMed]
18. McClatchey, A.I. Erm proteins at a glance. *J. Cell Sci.* **2014**, *127*, 3199–3204. [CrossRef] [PubMed]
19. Schwartz, M.A. Integrins and extracellular matrix in mechanotransduction. *Cold Spring Harb. Perspect. Biol.* **2010**, *2*, a005066. [CrossRef]
20. Kopp, S.; Krüger, M.; Feldmann, S.; Oltmann, H.; Schütte, A.; Schmitz, B.; Bauer, J.; Schulz, H.; Saar, K.; Huebner, N.; et al. Thyroid cancer cells in space during the texus-53 sounding rocket mission—The thyroid project. *Sci. Rep.* **2018**, *8*, 10355. [CrossRef]
21. Bauer, J.; Grimm, D.; Gombocz, E. Semantic analysis of thyroid cancer cell proteins obtained from rare research opportunities. *J. Biomed. Inform.* **2017**, *76*, 138–153. [CrossRef] [PubMed]
22. Bauer, J.; Wehland, M.; Infanger, M.; Grimm, D.; Gombocz, E. Semantic analysis of posttranslational modification of proteins accumulated in thyroid cancer cells exposed to simulated microgravity. *Int. J. Mol. Sci.* **2018**, *19*, 2257. [CrossRef] [PubMed]
23. Grosse, J.; Wehland, M.; Pietsch, J.; Schulz, H.; Saar, K.; Hubner, N.; Eilles, C.; Bauer, J.; Abou-El-Ardat, K.; Baatout, S.; et al. Gravity-sensitive signaling drives 3-dimensional formation of multicellular thyroid cancer spheroids. *FASEB J.* **2012**, *26*, 5124–5140. [CrossRef] [PubMed]
24. Svejgaard, B.; Wehland, M.; Ma, X.; Kopp, S.; Sahana, J.; Warnke, E.; Aleshcheva, G.; Hemmersbach, R.; Hauslage, J.; Grosse, J.; et al. Common effects on cancer cells exerted by a random positioning machine and a 2d clinostat. *PLoS ONE* **2015**, *10*, e0135157. [CrossRef] [PubMed]
25. Ma, X.; Wehland, M.; Schulz, H.; Saar, K.; Hübner, N.; Infanger, M.; Bauer, J.; Grimm, D. Genomic approach to identify factors that drive the formation of three-dimensional structures by ea.Hy926 endothelial cells. *PLoS ONE* **2013**, *8*, e64402. [CrossRef]
26. Ma, X.; Wehland, M.; Aleshcheva, G.; Hauslage, J.; Wasser, K.; Hemmersbach, R.; Infanger, M.; Bauer, J.; Grimm, D. Interleukin-6 expression under gravitational stress due to vibration and hypergravity in follicular thyroid cancer cells. *PLoS ONE* **2013**, *8*, e68140. [CrossRef]
27. Ulbrich, C.; Pietsch, J.; Grosse, J.; Wehland, M.; Schulz, H.; Saar, K.; Hubner, N.; Hauslage, J.; Hemmersbach, R.; Braun, M.; et al. Differential gene regulation under altered gravity conditions in follicular thyroid cancer cells: Relationship between the extracellular matrix and the cytoskeleton. *Cell. Physiol. Biochem.* **2011**, *28*, 185–198. [CrossRef]
28. Riwaldt, S.; Bauer, J.; Wehland, M.; Slumstrup, L.; Kopp, S.; Warnke, E.; Dittrich, A.; Magnusson, N.E.; Pietsch, J.; Corydon, T.J.; et al. Pathways regulating spheroid formation of human follicular thyroid cancer cells under simulated microgravity conditions: A genetic approach. *Int. J. Mol. Sci.* **2016**, *17*, 528. [CrossRef]
29. Warnke, E.; Kopp, S.; Wehland, M.; Hemmersbach, R.; Bauer, J.; Pietsch, J.; Infanger, M.; Grimm, D. Thyroid cells exposed to simulated microgravity conditions—Comparison of the fast rotating clinostat and the random positioning machine. *Microgravity Sci. Technol.* **2016**, *28*, 247–260. [CrossRef]
30. Buravkova, L.B.; Romanov, Y.A. The role of cytoskeleton in cell changes under condition of simulated microgravity. *Acta Astronaut.* **2001**, *48*, 647–650. [CrossRef]
31. Crawford-Young, S.J. Effects of microgravity on cell cytoskeleton and embryogenesis. *Int. J. Dev. Biol.* **2006**, *50*, 183–191. [CrossRef] [PubMed]
32. Hughes-Fulford, M. Function of the cytoskeleton in gravisensing during spaceflight. *Adv. Space Res.* **2003**, *32*, 1585–1593. [CrossRef]
33. Vorselen, D.; Roos, W.H.; MacKintosh, F.C.; Wuite, G.J.; van Loon, J.J. The role of the cytoskeleton in sensing changes in gravity by nonspecialized cells. *FASEB J.* **2014**, *28*, 536–547. [CrossRef] [PubMed]
34. Huber, F.; Schnauss, J.; Ronicke, S.; Rauch, P.; Muller, K.; Futterer, C.; Kas, J. Emergent complexity of the cytoskeleton: From single filaments to tissue. *Adv. Phys.* **2013**, *62*, 1–112. [CrossRef] [PubMed]
35. Tsukita, S.; Yonemura, S.; Tsukita, S. Erm proteins: Head-to-tail regulation of actin-plasma membrane interaction. *Trends Biochem. Sci.* **1997**, *22*, 53–58. [CrossRef]

36. Neisch, A.L.; Fehon, R.G. Ezrin, radixin and moesin: Key regulators of membrane-cortex interactions and signaling. *Curr. Opin. Cell Biol.* **2011**, *23*, 377–382. [CrossRef]
37. Pearson, M.A.; Reczek, D.; Bretscher, A.; Karplus, P.A. Structure of the erm protein moesin reveals the ferm domain fold masked by an extended actin binding tail domain. *Cell* **2000**, *101*, 259–270. [CrossRef]
38. Barros, F.B.A.; Assao, A.; Garcia, N.G.; Nonogaki, S.; Carvalho, A.L.; Soares, F.A.; Kowalski, L.P.; Oliveira, D.T. Moesin expression by tumor cells is an unfavorable prognostic biomarker for oral cancer. *BMC Cancer* **2018**, *18*, 53. [CrossRef]
39. Bartova, M.; Hlavaty, J.; Tan, Y.; Singer, C.; Pohlodek, K.; Luha, J.; Walter, I. Expression of ezrin and moesin in primary breast carcinoma and matched lymph node metastases. *Clin. Exp. Metastasis* **2017**, *34*, 333–344. [CrossRef]
40. Pietsch, J.; Sickmann, A.; Weber, G.; Bauer, J.; Egli, M.; Wildgruber, R.; Infanger, M.; Grimm, D. A proteomic approach to analysing spheroid formation of two human thyroid cell lines cultured on a random positioning machine. *Proteomics* **2011**, *11*, 2095–2104. [CrossRef]
41. Grimm, D.; Bauer, J.; Kossmehl, P.; Shakibaei, M.; Schöberger, J.; Pickenhahn, H.; Schulze-Tanzil, G.; Vetter, R.; Eilles, C.; Paul, M.; et al. Simulated microgravity alters differentiation and increases apoptosis in human follicular thyroid carcinoma cells. *FASEB J.* **2002**, *16*, 604–606. [CrossRef] [PubMed]
42. Levene, C.I.; Carrington, M.J. The inhibition of protein-lysine 6-oxidase by various lathyrogens. Evidence for two different mechanisms. *Biochem. J.* **1985**, *232*, 293–296. [CrossRef] [PubMed]
43. Bauer, J.; Wehland, M.; Pietsch, J.; Sickmann, A.; Weber, G.; Grimm, D. Annotated gene and proteome data support recognition of interconnections between the results of different experiments in space research. *Microgravity Sci. Technol.* **2016**, *28*, 357–365. [CrossRef]
44. Arpino, V.; Brock, M.; Gill, S.E. The role of timps in regulation of extracellular matrix proteolysis. *Matrix Biol.* **2015**, *44–46*, 247–254. [CrossRef]
45. Hawthorn, L.; Stein, L.; Varma, R.; Wiseman, S.; Loree, T.; Tan, D. TIMP1 and SERPIN-A overexpression and TFF3 and CRABP1 underexpression as biomarkers for papillary thyroid carcinoma. *Head Neck* **2004**, *26*, 1069–1083. [CrossRef]
46. Riwaldt, S.; Bauer, J.; Pietsch, J.; Braun, M.; Segerer, J.; Schwarzwälder, A.; Corydon, T.J.; Infanger, M.; Grimm, D. The importance of caveolin-1 as key-regulator of three-dimensional growth in thyroid cancer cells cultured under real and simulated microgravity conditions. *Int. J. Mol. Sci.* **2015**, *16*, 28296–28310. [CrossRef]
47. Marastoni, S.; Ligresti, G.; Lorenzon, E.; Colombatti, A.; Mongiat, M. Extracellular matrix: A matter of life and death. *Connect. Tissue Res.* **2008**, *49*, 203–206. [CrossRef]
48. Chaudhary, A.K.; Pandya, S.; Ghosh, K.; Nadkarni, A. Matrix metalloproteinase and its drug targets therapy in solid and hematological malignancies: An overview. *Mutat. Res.* **2013**, *753*, 7–23. [CrossRef]
49. Kraiem, Z.; Korem, S. Matrix metalloproteinases and the thyroid. *Thyroid* **2000**, *10*, 1061–1069. [CrossRef]
50. Kingsley, D.M. The TGF-β superfamily: New members, new receptors, and new genetic tests of function in different organisms. *Genes Dev.* **1994**, *8*, 133–146. [CrossRef]
51. Geiger, B.; Spatz, J.P.; Bershadsky, A.D. Environmental sensing through focal adhesions. *Nat. Rev. Mol. Cell Biol.* **2009**, *10*, 21–33. [CrossRef] [PubMed]
52. Zhao, T.; Li, R.; Tan, X.; Zhang, J.; Fan, C.; Zhao, Q.; Deng, Y.; Xu, A.; Lukong, K.E.; Genth, H.; et al. Simulated microgravity reduces focal adhesions and alters cytoskeleton and nuclear positioning leading to enhanced apoptosis via suppressing FAK/RhoA-mediated mTORC1/NF-κB and ERK1/2 pathways. *Int. J. Mol. Sci.* **2018**, *19*, 1994. [CrossRef] [PubMed]
53. Spanjaard, E.; de Rooij, J. Mechanotransduction: Vinculin provides stability when tension rises. *Curr. Biol.* **2013**, *23*, R159–R161. [CrossRef] [PubMed]
54. Humphries, J.D.; Wang, P.; Streuli, C.; Geiger, B.; Humphries, M.J.; Ballestrem, C. Vinculin controls focal adhesion formation by direct interactions with talin and actin. *J. Cell Biol.* **2007**, *179*, 1043–1057. [CrossRef] [PubMed]
55. Tadokoro, S.; Shattil, S.J.; Eto, K.; Tai, V.; Liddington, R.C.; de Pereda, J.M.; Ginsberg, M.H.; Calderwood, D.A. Talin binding to integrin β tails: A final common step in integrin activation. *Science* **2003**, *302*, 103–106. [CrossRef] [PubMed]
56. Critchley, D.R. Biochemical and structural properties of the integrin-associated cytoskeletal protein talin. *Annu. Rev. Biophys.* **2009**, *38*, 235–254. [CrossRef] [PubMed]

57. Aleshcheva, G.; Bauer, J.; Hemmersbach, R.; Slumstrup, L.; Wehland, M.; Infanger, M.; Grimm, D. Scaffold-free tissue formation under real and simulated microgravity conditions. *Basic Clin. Pharmacol. Toxicol.* **2016**, *119* (Suppl. 3), 26–33. [CrossRef]
58. Goodfellow, P.J.; Nevanlinna, H.A.; Gorman, P.; Sheer, D.; Lam, G.; Goodfellow, P.N. Assignment of the gene encoding the β-subunit of the human fibronectin receptor (β-FNR) to chromosome 10p11.2. *Ann. Hum. Genet.* **1989**, *53*, 15–22. [CrossRef]
59. Bouaouina, M.; Lad, Y.; Calderwood, D.A. The N-terminal domains of talin cooperate with the phosphotyrosine binding-like domain to activate β1 and β3 integrins. *J. Biol. Chem.* **2008**, *283*, 6118–6125. [CrossRef]
60. Van Roy, F.; Berx, G. The cell–cell adhesion molecule E-cadherin. *Cell. Mol. Life Sci.* **2008**, *65*, 3756–3788. [CrossRef]
61. Reynolds, A.B. P120-catenin: Past and present. *Biochim. Biophys. Acta* **2007**, *1773*, 2–7. [CrossRef] [PubMed]
62. Ishiyama, N.; Ikura, M. The three-dimensional structure of the cadherin-catenin complex. In *Adherens Junctions: From Molecular Mechanisms to Tissue Development and Disease*; Subcellular Biochemistry; Springer: Dordrecht, The Netherlands, 2012; Volume 60, pp. 39–62.
63. Sahana, J.; Nassef, M.Z.; Wehland, M.; Kopp, S.; Krüger, M.; Corydon, T.J.; Infanger, M.; Bauer, J.; Grimm, D. Decreased E-cadherin in MCF7 human breast cancer cells forming multicellular spheroids exposed to simulated microgravity. *Proteomics* **2018**, *18*, e1800015. [CrossRef] [PubMed]
64. Petrova, Y.I.; Schecterson, L.; Gumbiner, B.M. Roles for E-cadherin cell surface regulation in cancer. *Mol. Biol. Cell* **2016**, *27*, 3233–3244. [CrossRef] [PubMed]
65. Martinez-Aguilar, J.; Clifton-Bligh, R.; Molloy, M.P. Proteomics of thyroid tumours provides new insights into their molecular composition and changes associated with malignancy. *Sci. Rep.* **2016**, *6*, 23660. [CrossRef] [PubMed]
66. McGough, A.; Pope, B.; Chiu, W.; Weeds, A. Cofilin changes the twist of F-actin: Implications for actin filament dynamics and cellular function. *J. Cell Biol.* **1997**, *138*, 771–781. [CrossRef]
67. Giusti, L.; Iacconi, P.; Ciregia, F.; Giannaccini, G.; Donatini, G.L.; Basolo, F.; Miccoli, P.; Pinchera, A.; Lucacchini, A. Fine-needle aspiration of thyroid nodules: Proteomic analysis to identify cancer biomarkers. *J. Proteome Res.* **2008**, *7*, 4079–4088. [CrossRef]
68. Maimaiti, Y.; Jie, T.; Jing, Z.; Changwen, W.; Pan, Y.; Chen, C.; Tao, H. Aurora kinase a induces papillary thyroid cancer lymph node metastasis by promoting cofilin-1 activity. *Biochem. Biophys. Res. Commun.* **2016**, *473*, 212–218. [CrossRef]
69. Bauer, J.; Kopp, S.; Schlagberger, E.M.; Grosse, J.; Sahana, J.; Riwaldt, S.; Wehland, M.; Luetzenberg, R.; Infanger, M.; Grimm, D. Proteome analysis of human follicular thyroid cancer cells exposed to the random positioning machine. *Int. J. Mol. Sci.* **2017**, *18*, 546. [CrossRef]
70. Kopp, S.; Sahana, J.; Islam, T.; Petersen, A.G.; Bauer, J.; Corydon, T.J.; Schulz, H.; Saar, K.; Huebner, N.; Slumstrup, L.; et al. The role of NFκB in spheroid formation of human breast cancer cells cultured on the Random Positioning Machine. *Sci. Rep.* **2018**, *8*, 921. [CrossRef]
71. Wuest, S.L.; Richard, S.; Kopp, S.; Grimm, D.; Egli, M. Simulated microgravity: Critical review on the use of random positioning machines for mammalian cell culture. *BioMed Res. Int.* **2015**, *2015*, 971474. [CrossRef]
72. Aleshcheva, G.; Sahana, J.; Ma, X.; Hauslage, J.; Hemmersbach, R.; Egli, M.; Infanger, M.; Bauer, J.; Grimm, D. Changes in morphology, gene expression and protein content in chondrocytes cultured on a random positioning machine. *PLoS ONE* **2013**, *8*, e79057. [CrossRef] [PubMed]
73. Aleshcheva, G.; Wehland, M.; Sahana, J.; Bauer, J.; Corydon, T.J.; Hemmersbach, R.; Frett, T.; Egli, M.; Infanger, M.; Grosse, J.; et al. Moderate alterations of the cytoskeleton in human chondrocytes after short-term microgravity produced by parabolic flight maneuvers could be prevented by up-regulation of BMP-2 and SOX-9. *FASEB J.* **2015**, *29*, 2303–2314. [CrossRef] [PubMed]
74. Nyegaard, M.; Rendtorff, N.D.; Nielsen, M.S.; Corydon, T.J.; Demontis, D.; Starnawska, A.; Hedemand, A.; Buniello, A.; Niola, F.; Overgaard, M.T.; et al. A novel locus harbouring a functional CD164 nonsense mutation identified in a large danish family with nonsyndromic hearing impairment. *PLoS Genet.* **2015**, *11*, e1005386. [CrossRef] [PubMed]
75. Zhang, K.; Liu, J.; Li, C.; Peng, X.; Li, H.; Li, Z. Identification and validation of potential target genes in papillary thyroid cancer. *Eur. J. Pharmacol.* **2018**, *843*, 217–225. [CrossRef] [PubMed]



© 2018 by the authors. Licensee MDPI, Basel, Switzerland. This article is an open access article distributed under the terms and conditions of the Creative Commons Attribution (CC BY) license (http://creativecommons.org/licenses/by/4.0/).

cells

MDPI

Article

Fluid and Bubble Flow Detach Adherent Cancer Cells to Form Spheroids on a Random Positioning Machine

José Luis Cortés-Sánchez [1], Daniela Melnik [1,2], Viviann Sandt [1], Stefan Kahlert [3], Shannon Marchal [1], Ian R. D. Johnson [4], Marco Calvaruso [5], Christian Liemersdorf [6], Simon L. Wuest [7], Daniela Grimm [1,2,8] and Marcus Krüger [1,2,*]

1 Department of Microgravity and Translational Regenerative Medicine, Otto-von-Guericke University, 39106 Magdeburg, Germany; jose.cortes@ovgu.de (J.L.C.-S.); daniela.melnik@med.ovgu.de (D.M.); viviann.sandt@med.ovgu.de (V.S.); shannon.marchal@med.ovgu.de (S.M.); daniela.grimm@med.ovgu.de (D.G.)
2 Research Group "Magdeburger Arbeitsgemeinschaft für Forschung unter Raumfahrt- und Schwerelosigkeitsbedingungen" (MARS), Otto-von-Guericke University, 39106 Magdeburg, Germany
3 Institute of Anatomy, University Hospital Magdeburg, 39120 Magdeburg, Germany; stefan.kahlert@med.ovgu.de
4 Research in Space Environments Group, UniSA Clinical and Health Sciences, University of South Australia, Adelaide, SA 5000, Australia; ian.johnson@unisa.edu.au
5 Institute of Bioimaging and Molecular Physiology, National Research Council (IBFM-CNR), 90015 Cefalù, Italy; marco.calvaruso@ibfm.cnr.it
6 Department of Gravitational Biology, Institute of Aerospace Medicine, German Aerospace Center, 51147 Cologne, Germany; christian.liemersdorf@dlr.de
7 Institute of Medical Engineering, Lucerne University of Applied Sciences and Arts, 6052 Hergiswil, Switzerland; simon.wueest@hslu.ch
8 Department of Biomedicine, Aarhus University, 8000 Aarhus C, Denmark
* Correspondence: marcus.krueger@med.ovgu.de; Tel.: +49-391-67-57471

check for updates

Citation: Cortés-Sánchez, J.L.; Melnik, D.; Sandt, V.; Kahlert, S.; Marchal, S.; Johnson, I.R.D.; Calvaruso, M.; Liemersdorf, C.; Wuest, S.L.; Grimm, D.; et al. Fluid and Bubble Flow Detach Adherent Cancer Cells to Form Spheroids on a Random Positioning Machine. *Cells* **2023**, *12*, 2665. https://doi.org/10.3390/cells12222665

Academic Editor: Alexander E. Kalyuzhny

Received: 30 October 2023
Revised: 10 November 2023
Accepted: 17 November 2023
Published: 20 November 2023

Copyright: © 2023 by the authors. Licensee MDPI, Basel, Switzerland. This article is an open access article distributed under the terms and conditions of the Creative Commons Attribution (CC BY) license (https://creativecommons.org/licenses/by/4.0/).

Abstract: In preparing space and microgravity experiments, the utilization of ground-based facilities is common for initial experiments and feasibility studies. One approach to simulating microgravity conditions on Earth is to employ a random positioning machine (RPM) as a rotary bioreactor. Combined with a suitable low-mass model system, such as cell cultures, these devices simulating microgravity have been shown to produce results similar to those obtained in a space experiment under real microgravity conditions. One of these effects observed under real and simulated microgravity is the formation of spheroids from 2D adherent cancer cell cultures. Since real microgravity cannot be generated in a laboratory on Earth, we aimed to determine which forces lead to the detachment of individual FTC-133 thyroid cancer cells and the formation of tumor spheroids during culture with exposure to random positioning modes. To this end, we subdivided the RPM motion into different static and dynamic orientations of cell culture flasks. We focused on the molecular activation of the mechanosignaling pathways previously associated with spheroid formation in microgravity. Our results suggest that RPM-induced spheroid formation is a two-step process. First, the cells need to be detached, induced by the cell culture flask's rotation and the subsequent fluid flow, as well as the presence of air bubbles. Once the cells are detached and in suspension, random positioning prevents sedimentation, allowing 3D aggregates to form. In a comparative shear stress experiment using defined fluid flow paradigms, transcriptional responses were triggered comparable to exposure of FTC-133 cells to the RPM. In summary, the RPM serves as a simulator of microgravity by randomizing the impact of Earth's gravity vector especially for suspension (i.e., detached) cells. Simultaneously, it simulates physiological shear forces on the adherent cell layer. The RPM thus offers a unique combination of environmental conditions for in vitro cancer research.

Keywords: rotating bioreactor; simulated microgravity; cancer cell; shear stress; cell detachment; in vitro metastasis

1. Introduction

One of the most exciting aspects of biomedical research using microgravity provided by real microgravity platforms, such as International Space Station (ISS), is the formation of three-dimensional spheroids or organoids that seem to be enhanced under microgravity conditions lacking sedimentation [1–4]. These 3D cell cultures are more relevant to an organism's complex biology than traditional two-dimensional monocultures of cells and provide a potential means to minimize animal experiments. Cancer cells exposed to microgravity may also provide models for metastasis events [5,6]. Whilst orbital labs such as the ISS provide the gold standard for microgravity research, the logistics and extensive costs prohibit easy access to real microgravity on orbital platforms. Even unmanned orbital (satellites) or sub-orbital platforms, such as sounding rocket flights, are very rare and extremely costly approaches. Further gravity research platforms like parabolic flights or drop towers cannot provide sufficient time under microgravity conditions to address questions regarding, e.g., developmental processes. Therefore, rotating bioreactors such as 2D clinostats, rotating wall vessels, or the random positioning machine (RPM, Figure 1A) have become essential tools to provide simulated microgravity environments for cellular biomedical research on Earth [7]. The rotational motion of the fluid environment allows suspension cells to experience simulated free-fall conditions avoiding sedimentation over longer durations. For some cell systems, therefore, these microgravity simulations can provide data comparable to experiments conducted on orbital platforms in real microgravity. Interestingly, exposure of certain types of adherent cells to simulated microgravity induces characteristic spheroid formation in some cell types (Figure 1B). However, it is not evident what induces the detachment of cells from the growth surface and their aggregation toward spheroid formation. The genomic, transcriptomic, and proteomic data even on a single cell type are heterogeneous across various platforms simulating microgravity or the respective culturing conditions [8,9]. Previously, it was argued that the effects of microgravity on individual cells are primarily indirect, and that the mass of a single cell is too low to directly sense changes in the gravity vector [10]. Instead, forces acting from the outside, such as the hydrostatic pressure of the medium or the local microenvironment, should change how the cell responds to the microgravity environment. The RPM induces biologically relevant shear forces [11–14] that affect human cancer cells in adherent cell layers. Suspension cancer cells in the same culture experience lower shear and are therefore affected differently. Currently, the studies on the RPM-based cellular behavior of human cancer-derived cell lines are not fully concise. Therefore, a generalized model of RPM-induced metastasis does not exist at the moment. In the current study, we aimed to understand which influences lead to cell detachment and spheroid formation under different modes of action on an RPM. The outcome might aid in the identification of metastasis traits at the onset of and in the course of cancer spheroid formation.

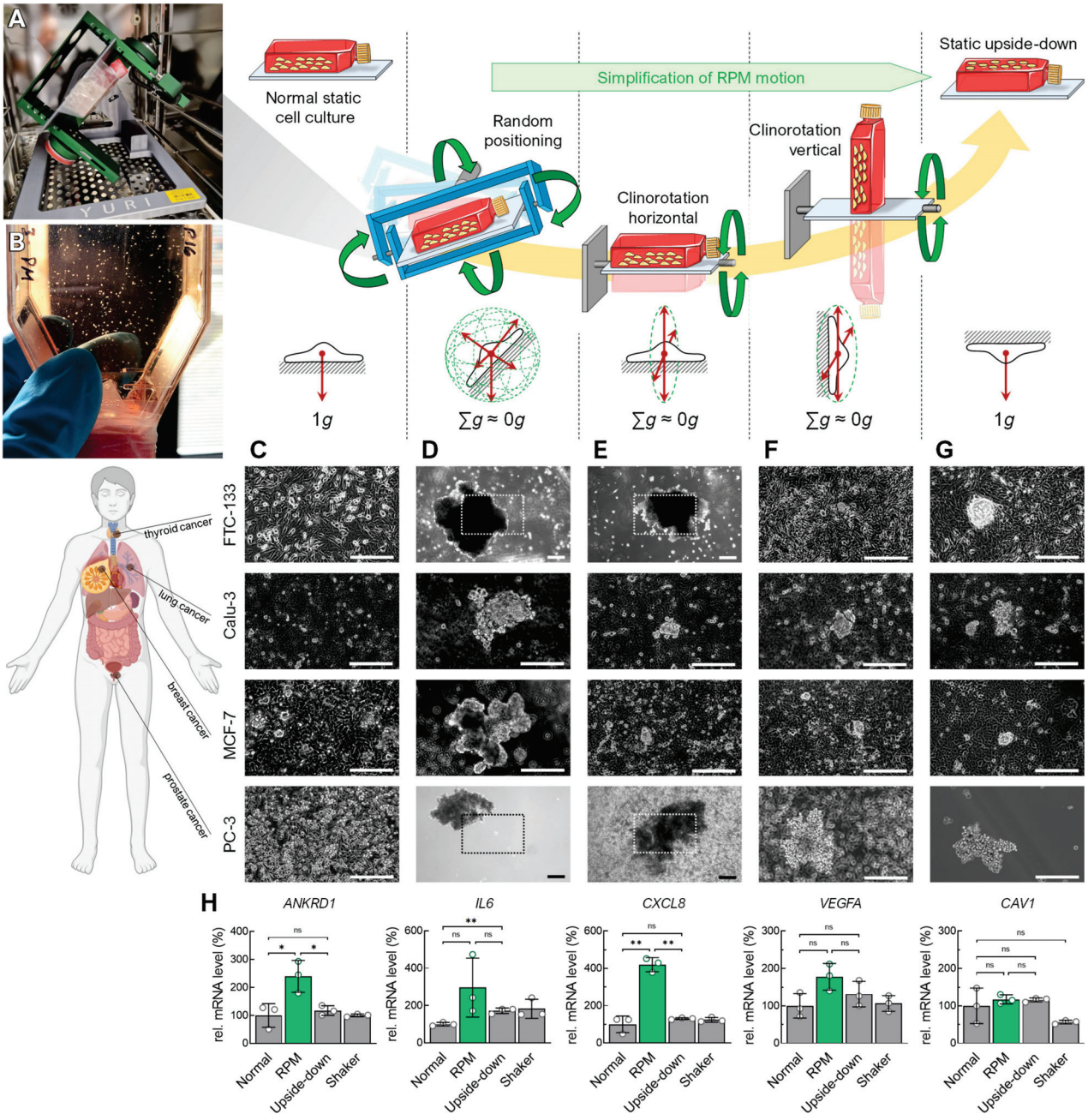


Figure 1. Spheroid formation of various adherent human carcinoma cell lines differently oriented with respect to Earth's gravity vector for 72 h. Rotational movements of the cell culture flasks are indicated with green arrows. (**A**) Benchtop RPM in an incubator during an experiment with a T25 flask attached. (**B**) Visible spheroids formed after 3 days of random positioning in a cell culture flask. (**C**) Standard static cell culture. (**D**) Random positioning in real random mode. (**E**) RPM clinorotation mode with horizontal orientation of the T25 flask. (**F**) RPM clinorotation mode with vertical orientation of the T25 flask. (**G**) Upside-down static cell culture. (**H**) RNA expression changes in specific genes in FTC-133 cells that have been described previously to play a role in spheroid formation on the RPM. The plots show the mean ± SD $\Delta\Delta C_T$ values of three cell cultures performed in triplicate together with the individual data points. Scale bars: 300 µm. The outlined areas reflect the magnification of the field of view in most images except for larger spheroids formed in FTC-133 and PC-3 cells in RPM and horizontal clinorotation mode. * Independent sample *t*-test $p \leq 0.05$, ** $p \leq 0.01$, ^{ns} non-significant. Parts of the figure were drawn by using pictures from Biorender.com and from Servier Medical Art.

2. Materials and Methods

2.1. Cell Lines and Cell Culture

The human follicular thyroid carcinoma FTC-133 cell line (passages 8–18) was purchased from Sigma-Aldrich (St. Louis, MO, USA). The MCF-7 mammary carcinoma cells (passages 5–9) and PC-3 prostate carcinoma cells (passages 36–40) were purchased from ATCC (Manassas, VA, USA). The Calu-3 lung carcinoma cell line (passage 19) was a kind gift from Prof. Heike Walles, the University of Magdeburg. The FTC-133, MCF-7, and PC-3 cells were cultured in the RPMI 1640 medium (Life Technologies, Carlsbad, CA, USA) supplemented with 10% fetal calf serum (FCS; Sigma-Aldrich, St. Louis, MO, USA) and 1% penicillin/streptomycin (Life Technologies) at 37 °C and 5% CO_2. The Calu-3 cells were cultured in the DMEM/F12 medium + 2.5 mM L-glutamine + 29 mM sodium bicarbonate (Life Technologies) supplemented with 10% FCS and 1% penicillin/streptomycin. The cells were routinely checked using visual inspection and maintained at a maximum confluence of 90% for up to 2 to 4 days before passaging. At 24 h before each experiment, a cell density of 1×10^6 cells (40,000 cells/cm^2) per flask was seeded in uncoated T25 cell culture flasks (Sarstedt, Nümbrecht, Germany) to allow cells to adhere. For immunofluorescence staining, uncoated glass coverslips (Carl Roth, Karlsruhe, Germany) were fixed using sterilized vaseline (Edeka, Hamburg, Germany) in a T25 flask before seeding a cell density of 1×10^6. For the cell cultures in channel slides, 20,000 cells/cm^2 (microscopy) or 40,000 cells/cm^2 (qPCR) were seeded in a µ-Slide I Luer Glass Bottom 0.8 (ibidi, Gräfelfing, Germany).

2.2. Rotating Cell Cultures

For the experiments (4 h, 24 h, 72 h), a desktop RPM 2.0 (Yuri, Meckenbeuren, Germany) was used in a HERAcell CO_2 incubator (Thermo Scientific) at 37 °C, 5% CO_2 without humidification. The medium was not specially pretreated. For random positioning, the RPM was operated in real random mode (two frames) at three different speed ranges: average speed 25°/s (range: 21–30°/s), average speed 60°/s (range: 50–70°/s), and average speed 90°/s (range: 80–100°/s). The RPM was operated in one frame mode for clinorotation with a constant speed of 60°/s. Before starting the rotation, the cell culture flasks were filled completely with medium, avoiding bubbles (any remaining bubbles were carefully removed using a pipette tip before closing the culture flask). Static controls were placed next to the RPM in the same incubator at the same environmental conditions.

2.3. Orbital Shaker Cell Cultures (FTC-133)

For the shaker experiments (72 h) with the FTC-133 cells, a Stuart SSM1 Orbital Shaker (Cole-Parmer, Vernon Hills, IL, USA) was used in a HERAcell CO_2 incubator at 37 °C, 5% CO_2 without humidification. The shaker was operated using fully filled T25 flasks at a speed of 60 rpm.

2.4. Flow Channel Cell Cultures (FTC-133)

An ISM827 Reglo peristaltic pump system (Ismatec, Grevenbroich, Germany) was used for the experiments (4 h, 24 h). The system consisted of a medium reservoir containing 70 mL of cell culture medium. Carbogen (5% CO_2 in O_2; Air Liquide, Düsseldorf, Germany) was continuously injected into the reservoir to supply CO_2 and O_2 to the cell culture. On top of the flask, a syringe attached to an empty flask served as a foam trap for the sterile filter of the exhaust gas. The medium was pumped in a closed loop from a reservoir via a channel slide with defined dimensions ($50 \times 5 \times 0.8$ mm) (ibidi) at a rate of 0.5 or 1 mL/min creating a calculated shear stress of 12.5 and 25 mPa [15]. To mimic the shear stress induced by bubbles, medium supplemented with defined bubbles was pumped via channel slides. A second peristaltic pump connected was added to the inlet tubing upstream the slide via a Y-adaptor. In this setup, one bubble was pumped every second.

The effect of an oscillating fluid flow was investigated in an oscillatory flow configuration ibidi pump system (ibidi), in which one cycle consisted of a change in flow direction

every 7.5 s and a flow rate of 1 mL/min (corresponding to 25 mPa of shear stress [15]). A brightfield image of the same slide area was acquired for live visualization every 5 min.

2.5. Serum Starvation and Pharmaceutical Treatment (FTC-133)

After 24 h of seeding, the FTC-133 cells were washed once using phosphate-buffered saline (PBS; Life Technologies), synchronized for 4 h in RPMI 1640 with 0.25% FCS and 1% penicillin/streptomycin, following cultivation with RPMI 1640 medium supplemented with 1 µM ethanol-soluble dexamethasone (Sigma-Aldrich) for 72 h, as described in [16]. The synchronization procedure was also used to reduce the amount of nutrients present before an experiment.

2.6. Phase Contrast Microscopy

The cells were routinely visually inspected and imaged using an Olympus CKX53 inverted microscope in phase contrast mode and a magnification of 10× (NA: 0.25) or 20× (NA: 0.4; Olympus, Tokyo, Japan). An Axiovert 200M microscope at brightfield mode at a magnification of 40× (NA: 0.6; Carl Zeiss, Oberkochen, Germany) was used for live visualization during the flow experiments in channel slides.

2.7. Cell Tracking and Migration Analysis (FTC-133)

For cell tracking, the Manual Tracking Plugin in Fiji v1.54f (ImageJ, imagej.net) was used. The exported file for tracking was processed using Chemotaxis and Migration Tool 2.0 (ibidi). For each condition, three independent FTC-133 cell cultures in the channel slides (see section Flow Channel Cell Cultures) were observed for 24 h. To determine the migratory ability of the cells, the average cell position at the end of the observation was determined for individual cells ($n > 40$ cells/condition), as well as the distance traveled in µm and the time to detachment in min.

2.8. Immunofluorescence Microscopy (FTC-133)

The cells were cultured as described above. For fixation, the cells were washed thrice using 0.1 M phosphate buffer (PB; Na_2HPO_4/NaH_2PO_4; Carl Roth), fixed for 15 min at 4 °C in 4% paraformaldehyde (PFA; Carl Roth), and then washed with PB for 3 × 15 min on a shaker. The cells were stored in 0.1 M PB at 4 °C for a maximum of one day before staining. The cell membrane was permeabilized using 0.2% Triton X-100 (Carl Roth) and washed thrice with 0.1 M PB. Non-specific binding sites were blocked using 3% bovine serum albumin (BSA, Carl Roth) in 0.1 M PB for 1 h at room temperature (RT). Subsequently, the cells were labeled with the primary antibodies diluted in 0.1 M PB containing 1% BSA (listed in Table S1) overnight at 4 °C. The next day, the cells were washed two times using 0.1 M PB. The cells were incubated with the secondary Alexa Fluor™ 488 (AF488)-conjugated (Invitrogen, Life Technologies) or Alexa Fluor™ 647 (AF647)-conjugated (Invitrogen, Life Technologies) antibodies (Table S1) at a dilution of 1:500 (MRTF-A) or 1:1000 at RT for 1 h. For F-actin staining, Alexa Fluor™ 568 Phalloidin (Invitrogen, Life Technologies) was added at a dilution of 1:400 for 1 h, and then the sample was washed thrice with 0.1 M PB. The cells were washed again three times using 0.1 M PB and mounted using Fluoroshield™ with DAPI (4′,6-diamidino-2-phenylindole) to stain the nuclear DNA (Sigma-Aldrich). The slides were examined using a ZEISS LSM 800 confocal laser scanning microscope (Carl Zeiss). To ensure comparability for intensity quantification, all the images were acquired with the same settings using the ZEISS Airyscan detector and ZEN 3.4 software (Carl Zeiss). The Airyscan processing settings were optimized for each antibody–wavelength combination and manually applied to the corresponding samples. To check for non-specific binding of the secondary antibody and thus a false negative signal, the secondary antibodies were applied to separate samples of the same condition without the primary antibody.

2.9. Immunofluorescence Analysis

To determine the localization of the transcription factors, we searched for the nuclear signal in the Z-position of the fluorescence image. The Z-position was used where the size of the nucleus was largest and the intensity of the nuclear signal was strongest. The cytoplasmic part of the signal was determined at the same Z-position. In this way, a correct measurement of the ratio between the nucleus and cytoplasm was ensured. Only 1 Z-position per file was used.

The resulting file was used in Fiji software v1.54f (ImageJ, imagej.net) to quantify the relative protein expression levels based on the sample's fluorescence intensity using the Image Calculator tool. The relative intensities were measured according to the method of Shihan et al. [17]. To determine the ratio of protein localization between the nucleus and cytoplasm (N/C ratio), the mean fluorescence intensities of the protein of interest were measured for the nuclear area and the cytoplasm area. Using the Freehand Selection tool, the nuclear area was determined based on the DAPI signal. The total cell area was determined by selecting the background without cells and subtracting it from the total area. The cytoplasmic area was determined by subtracting the nuclear area from the cell area. The intensity measured in the cytoplasmic area is the average signal from the cytoplasms of all cells in this image. The signal intensity from the nuclear area was divided by the signal intensity of the cytoplasmic area. This corresponds to the individual N/C ratio for the respective image.

2.10. mRNA Isolation and Quantitative Real-Time PCR (FTC-133)

The procedure was performed in the same way as described in [18]. To obtain sufficient mRNA out of the cells grown in channel slides, a higher cell number of 40,000 cells/cm^2 and a µ-Slide, 0.8 Luer, ibiTreat (ibidi) were used. The primer sequences used in the quantitative real-time PCR can be found in the Supplementary Materials (Table S2). The samples were measured in triplicate and evaluated by using the comparative threshold cycle ($\Delta\Delta C_T$) method. 18S rRNA was used as the housekeeper reference due to its stable expression in dynamic FTC-133 cell cultures [18].

2.11. Statistical Analysis

Statistical evaluation was performed using SPSS Statistics v29 (IBM, Armonk, NY, USA). The non-parametric Mann–Whitney U test was used to compare samples (biological replicates) from different culture conditions. For experiments in which only a few samples were available (<5 biological replicates), an independent sample *t*-test was used. All data are presented as mean ± standard deviation (SD). In most plots, the individual data points are shown additionally. The sample size for each experiment is provided in the figure legends.

3. Results

3.1. Alteration of the Gravity Vector

The operating principle of rotating microgravity simulators is based on a continuous change in the Earth's gravitational vector direction on the cells. We aligned diverse human carcinoma cell lines (FTC-133, Calu-3, MCF-7, PC-3) in various positions with respect to the Earth's gravitational vector field (Figure 1). In general, these cells grow as monolayers in standard (static) cell culture (Figure 1C). Although MCF-7 cells sometimes tend to form multiple cell layers, the cells remain adhered to their surface. Exposed to the RPM, the adherent cancer cells formed spheroids above the cell layer within 3 days (Figure 1D).

To determine which orientations or movements of the cell cultures contribute to spheroid formation during random positioning, and whether a particular gravity vector orientation is sufficient to form three-dimensional aggregates, we examined rotating cell cultures mounted horizontally (Figure 1E) or vertically (Figure 1F) on an RPM operated in 2D clinostat mode. After 3 days, the FTC-133 cells aligned parallel to the rotational axis formed spheroids, whereas the cells oriented perpendicular to the rotational axis remained

adherent. Calu-3, MCF-7, and PC-3 cells formed smaller spheroids in the perpendicularly oriented rotation than in the other rotations (Figure 1F). Interestingly, we also observed the formation of spheroids from all cell lines in a static, inverted cell culture (Figure 1G). These occurred in low-density cultures, making three-dimensional growth due to overgrowth an unlikely cause. Here, we detected new cell growth on the opposite (lower) side of the culture flask, caused by cell detachment from the cell layer and sedimentation. Spheroid formation from an inverted vessel suggested that the cells must hang "upside down" for a time for spheroids to form. The spheroids were more prominent in the rotating cell cultures, especially on the RPM. Accordingly, simply inverting the cell culture flasks only partially replaced random positioning for spheroid formation. This is also reflected in the upregulation of certain typical genes (e.g., *ANKRD1*, *IL6*, *CXCL8*) in FTC-133 cells that have been described previously as involved in RPM-induced spheroid formation (Figure 1H) [19–21]. To verify whether better mixing of the culture medium on the RPM (60°/s) compared to the static cell cultures could explain these RPM-specific gene regulatory effects, an additional experiment was performed using normal-orientated cell cultures on a rocket shaker (60 rpm). The shaker had only a minor effect on *CAV1* expression and cannot explain the molecular effects found in the RPM cultures (Figure 1H).

Since the FTC-133 cell line showed the greatest differences in spheroid formation at different orientations and is a well-characterized cell culture model in altered gravity conditions [3,22,23], we used this cell line for further studies. Next, we imitated the different orientations of cell culture flasks occurring on the RPM with static and rotating cell cultures (Figure 2). The RPM positions the cell culture flask via rotation in all spatial directions (Figure 2A). Both the cells and the culture medium surrounding them are subjected to gravity. In a completely filled T25 cell culture flask (h = 24 mm), the cell layer experiences 240 Pa ($p = \rho \times a \times h$) of hydrostatic pressure at a normal orientation. This pressure compresses the cells and the nuclei, which can also promote the nuclear transport of transcription factors (Figure 2B) [24]. In an upright cell culture flask, there is a gradient in hydrostatic pressure increasing from top to bottom.

In an inverted cell culture, there is no hydrostatic pressure from the cell culture medium on the cells, making this orientation the most "force-free". Cells in the inverted and at the top of the upright-oriented culture flasks showed lower F-actin filament density than in normal culture (Figure 2C). This could be related to the lower impact of mechanical forces lacking a large medium column, with corresponding hydrostatic pressure above the adherent cells. These results could support the idea that cells do not sense the gravity vector directly due to the low mass of their organelles but instead sense the indirect effects of gravity on larger structures, such as the surrounding culture medium [10]. There was minimal change in the nuclear or cytoplasmic distribution of the mechanosensitive transcription factors YAP1, p38 MAPK, or MRTF-A in the static cell cultures of different orientations (Figure 2D–F). These factors are important players in mechanosignaling, helping cells to recognize and respond to mechanical forces and adapt to changes in their microenvironment.

A cell culture on the RPM is not only subjected to different positions but also to different rotations, resulting in fluid shear forces and periodic compressions of the cell. These effects should be mimicked using two different types of 2D clinorotation produced by utilizing only one rotational axis of the RPM (Figure 2G). The F-actin density was similar in the clinorotation and RPM samples, indicated by some stress fibers (Figure 2H). A translocation to the cytoplasm was observed for YAP1 when the cells were exposed to random positioning (Figure 2I), and a statistically significant alteration in p38 MAPK subcellular localization when the cell culture flask was rotated with horizontal orientation (Figure 2J). We observed stark, but highly variable, differences in the nuclear/cytoplasmic fluorescence ratio for MRTF-A; compared to normal cell culture, more nuclear distribution was observed after clinorotation regardless of the flask orientation, and more cytoplasmic distribution was observed after random positioning (Figure 2K).

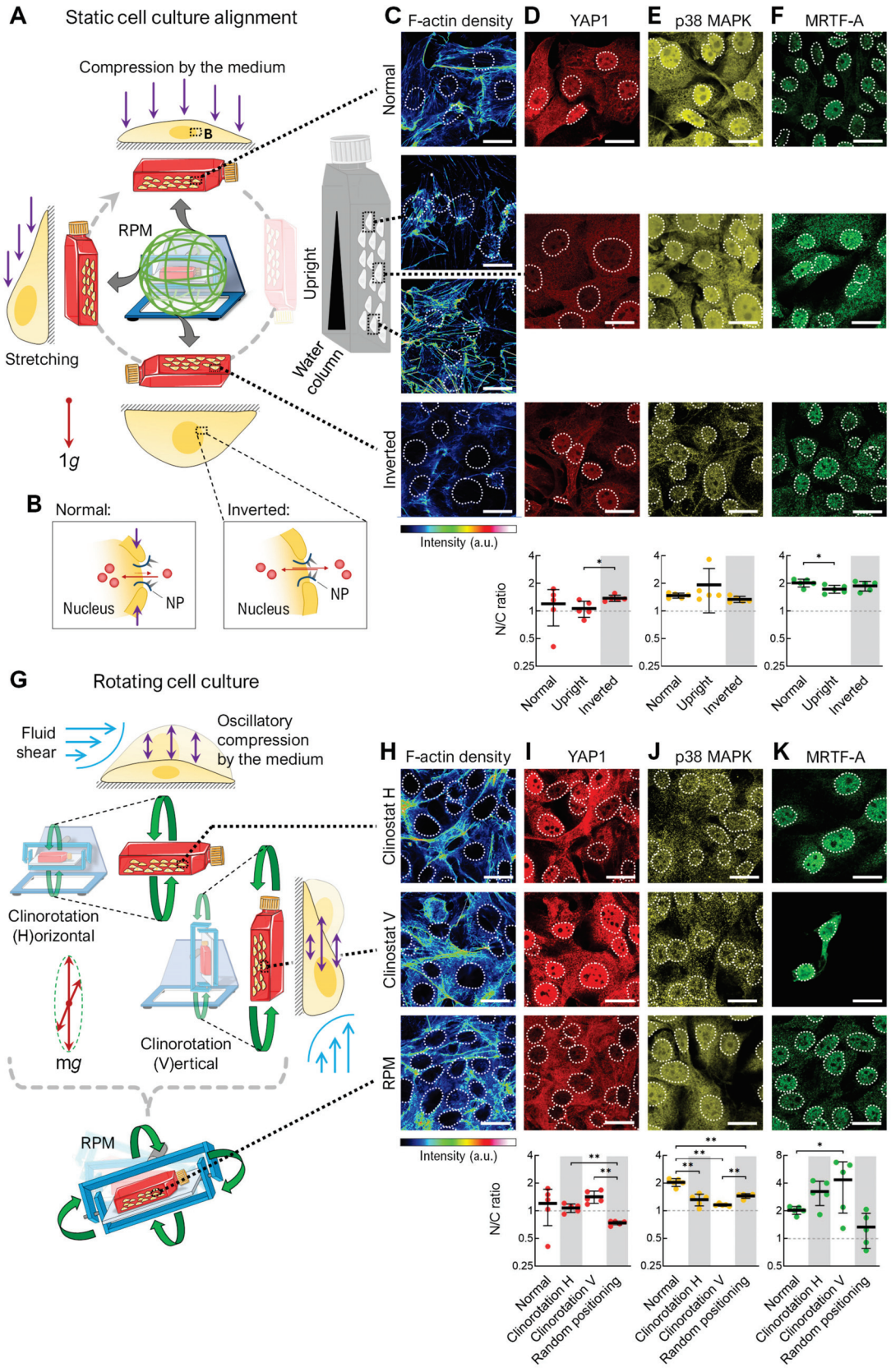


Figure 2. F-actin density and transcription factor localization in the remaining adherent cells in differently oriented and rotated cell culture flasks. (**A**) Static cell cultures in different orientations: normal cell culture, upright flasks, and inverted flasks. (**B**) Effect of cell compression on nuclear

transport of transcription factors (red circles) via nuclear pores (NP). (**C**) F-actin density (phalloidin staining) and immunofluorescence of the mechanoresponsive transcription factors (**D**) YAP1, (**E**) p38 MAPK, and (**F**) MRTF-A after 72 h (n = 5 for each condition; one representative picture is shown). Outlines of the nuclei as indicated using DAPI staining (not shown) depicted as dashed lines. (**G**) Rotating cell cultures: horizontal clinorotation (60°/s), vertical clinorotation (60°/s), and random positioning (average speed 60°/s). (**H**) F-actin density. (**I**) YAP1, (**J**) p38 MAPK, and (**K**) MRTF-A localization after 72 h (n = 5 for each condition; one representative picture is shown). Outlines of the nuclei are shown as dashed lines. (Below) The relative mean nuclear–cytoplasmic (N/C) ratio of transcription factors was measured for at least 15 cells (5 pictures per condition). Static cell culture was set as reference. The experimental conditions where the spheroid formation was observed are shaded gray. Scale bars: 300 µm. The fluorescence images in this figure were optimized to visualize protein localization and unsuitable for comparative protein level quantification. * Mann–Whitney $p \leq 0.05$, ** $p \leq 0.01$. Parts of the figure were drawn by using pictures from Servier Medical Art.

In summary, rotating cell cultures, including RPM cultures, have a stronger effect on transcription factor translocation than static cell cultures, further emphasizing the importance of flow shear on the RPM. However, it should be noted that in the cell cultures in which spheroids are formed (Figure 2, gray-shaded areas), there is no uniform nucleation of the transcription factors studied. This may indicate that these signaling pathways are not involved in spheroid formation or that the cells are already adapted to the culture conditions after 72 h.

An RPM experiment with different angular velocities showed that the time-averaged cancellation of the gravity vector alone could not form spheroids (Figure 3). In microgravity experiments, the RPM typically operates at an average frame speed of 60°/s, resulting in fluid flow in the cell culture flask [14,25] (Figure 3A). In addition to the usually applied real random mode at a velocity of 60°/s, we performed experiments at velocities of ~25°/s and ~90°/s. All operating speeds resulted in a calculated time-averaged milligravity (~0.01 g) within a few hours (Figure 3B–D). Slower random positioning of the FTC-133 cells (average speed 25°/s) failed to induce cell detachment or spheroid formation (Figure 3E). Using higher RPM speeds (average speed 90°/s), much smaller spheroids formed compared to the typical angular velocity of 60°/s.

Assuming that a balance between cell confluency and fluid flow was needed to efficiently induce spheroid formation, we let the cells attach for 24 or 48 h prior to RPM exposure in all three angular velocities. Indeed, a longer period of cell attachment before RPM exposure affected the spheroid formation ability. The FTC-133 cells that adhered for 48 h did not form spheroids at any RPM speed (Figure 3F), except for one single small spheroid (110 µm) found at 90°/s (Figure 3F, insert). This effect of a prolonged adhesion phase before the start of the experiment was also observed in the PC-3 cells (not shown) and during the CellBox-1 mission, in which the cells became confluent due to a delay in the rocket launch and did not form spheroids during the experiment on the ISS [26]. We demonstrated that only under spheroid-forming conditions on the RPM was the expression of certain genes upregulated (e.g., *IL6*, *CXCL8*, *ICAM1*, *KRT8*) that have previously been described as targets of various mechanosignaling pathways (including p38 MAPK, NFκB, MEK/ERK) in human cells, among others (Figure 3G) [19,20]. Hence, both the fluid flow generated by the RPM and the adhesion force of the cells are important parameters for spheroid formation.

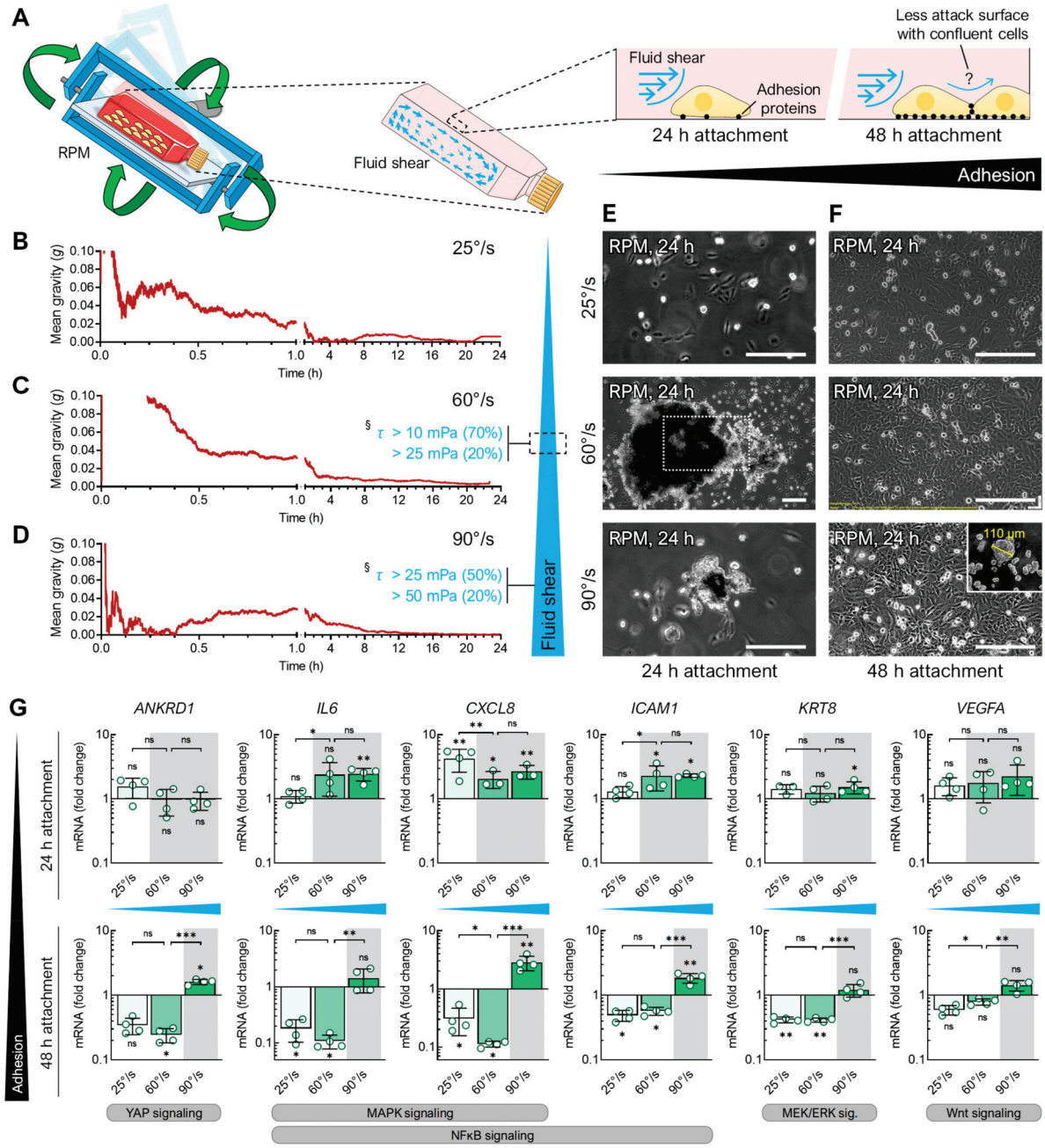


Figure 3. Spheroid formation of FTC-133 cells exposed to the RPM at different angular velocities for 24 h. (**A**) Illustration of fluid shear within cell culture flasks on the RPM. Time-averaged residual gravity levels and shear forces were calculated at RPM average velocities of (**B**) 25°/s, (**C**) 60°/s, and (**D**) 90°/s. Spheroid formation was examined in FTC-133 cultures that had previously been allowed to adhere to the bottom of the cell culture flask for (**E**) 24 h or (**F**) 48 h. The outlined area reflects the magnification of the field of view in most images except for larger spheroids compared at 60°/s after 24 h of normal cell growth followed by 24 h of exposure to the RPM. (**G**) Expression changes (compared to static cell culture) in gene transcripts known to be responsive to shear stress after 24 h exposure to the RPM operated with different velocities. The plots show the mean ± SD $\Delta\Delta C_T$ values of four cell cultures performed in triplicate together with the individual data points. The experimental conditions where spheroid formation was observed are shaded gray. Scale bars: 300 µm. * Independent sample *t*-test $p \leq 0.05$, ** $p \leq 0.01$, *** $p \leq 0.001$, ^{ns} non-significant vs. static control. § Shear stress τ according to Wuest et al. [14]. Parts of the figure were drawn by using pictures from Servier Medical Art.

3.2. Fluid Shear

Live-cell imaging on the RPM is not yet possible; therefore, we used a flow channel slide experiment to simulate the effects of RPM-induced fluid shear stress (Figure 4). Adherent FTC-133 cells were cultured in a channel slide connected to a peristaltic pump that perfused the medium through the channel at 0.5 and 1 mL/min speeds (Figure 4A,B). The fluid flow in the chosen dimensions of the channel slide (50 × 5 × 0.8 mm) produced shear stresses on the cells in the order of 12.5 and 25 mPa [15]. This stress was supposed to be similar to the fluid shear stress predicted to be observed on the walls of T25 cell culture flasks on the RPM at an average speed of 60°/s [14]. Both fluid flows significantly decreased the cell confluency within 20–24 h (confluency change at 0.5 mL/min: −11%, 1.0 mL/min: −38%) (Figure 4C). Time-lapse imaging showed cell detachment (Figure 4D, Video S1), migration, and rolling across the surface in the same direction as the media flow (Figure 4E). More cells detached at a flow rate of 1 mL/min, with initial cell detachment occurring after 12 h of flow exposure. This is consistent with prior observations of spheroid formation occurring after 16–24 h on the RPM [27–29]. Finally, the cells rounded off, detached, and were transported away by the flow. This observation over an extended period suggests that the detachment of the cell could be part of a biological process. In non-perfused cell cultures, no detachment was observed (Figure 4C), and the cell motility was significantly reduced (Figure 4F). Cell detachment is an essential step in RPM-induced spheroid formation; previous studies have shown that detached FTC-133 cells (i.e., suspension cultures) can form spheroids on the RPM. Interestingly, the proliferation of adherent cells was slightly higher at a flow rate of 1 mL/min compared with 0.5 mL/min, until approximately 12 h after the start of the experiment (Figure 4C,D).

3.3. Air Bubbles

From previous RPM experiments, we knew that the observation of air bubbles at the end of an RPM experiment (including their size and number, compare Figure S1) influences the number of adherent cells remaining, depending on the cell line and flask configuration used (Figure 5A). In a recent study, we described that FTC-133 cells cultured on the RPM in the presence of 1 µM dexamethasone (to avoid cell clustering) did not show spheroid formation [16]. However, when additional air bubbles were added to the cell culture flasks containing an FTC-133 cell culture (bubble diameter: 0.5–8.3 mm at the end of the experiment), spheroid formation occurred on the RPM even during treatment with 1 µM dexamethasone (Figure 5B). The air bubbles in a cell culture flask on the RPM thus appeared to be able to detach even "stickier" cells. RPM experiments usually are initiated using completely filled cell culture flasks devoid of air bubbles using de-gassed culture media. Therefore, it is challenging to determine when and where bubbles originate from (Figure S1). They occur sporadically, even without cells, which indicates an incomplete de-gassing of the medium and/or, e.g., temperature fluctuations during the filling of the flasks. Furthermore, repeated biological or technical replicates (identical cells, flasks, medium, treatment, and cell number) resulted in differing numbers and sizes of bubbles present at the end of the RPM experiment. In various experiments, we found a correlation between the formation of spheroids and the presence of bubbles in culture flasks. The size and geometry of the culture vessel also played a role in RPM-induced spheroid formation. For example, we have not observed air bubble movements and spheroid formation of adherent cancer cells in channel slides. In a µ-well slide experiment, only one single bubble was formed that moved around the interior edges of the cuboid chamber and did not disturb the cells (Figure 5A).

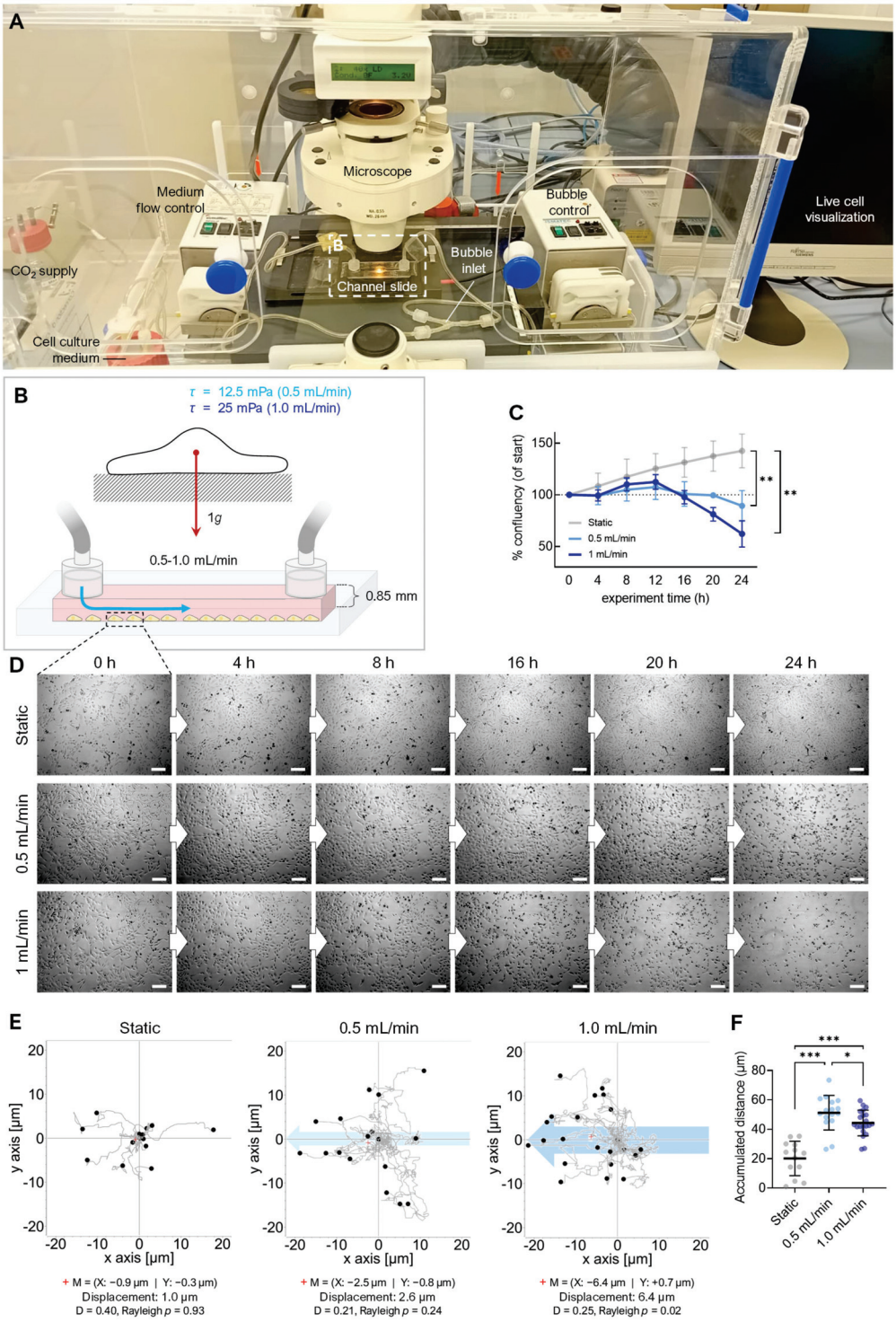


Figure 4. Effect of fluid flow on detachment of adherent FTC-133 cells. (**A**) Setup of the flow experiment. (**B**) Flow schematics. (**C**) Confluency of cell cultures over 24 h (n = 3). (**D**) Snapshots from the brightfield time-lapse recordings of one representative experiment with different flow speeds. (**E**) Migration traces of single cells in the flow channel perfused with different flow rates. The blue arrow indicates the direction of flow, and the position of cells (n > 40 cells for each condition) after 24 h is indicated by black circles. The red cross (+) indicates the mean value (M) of spatial cell migration (values are given below the plot). D: directness. (**F**) Cumulative migration distances of cells over 24 h at different flow rates. Scale bars: 300 µm. * Independent sample t-test (**C**) or Mann–Whitney (**F**) $p \leq 0.05$, ** $p \leq 0.01$, *** $p \leq 0.001$.

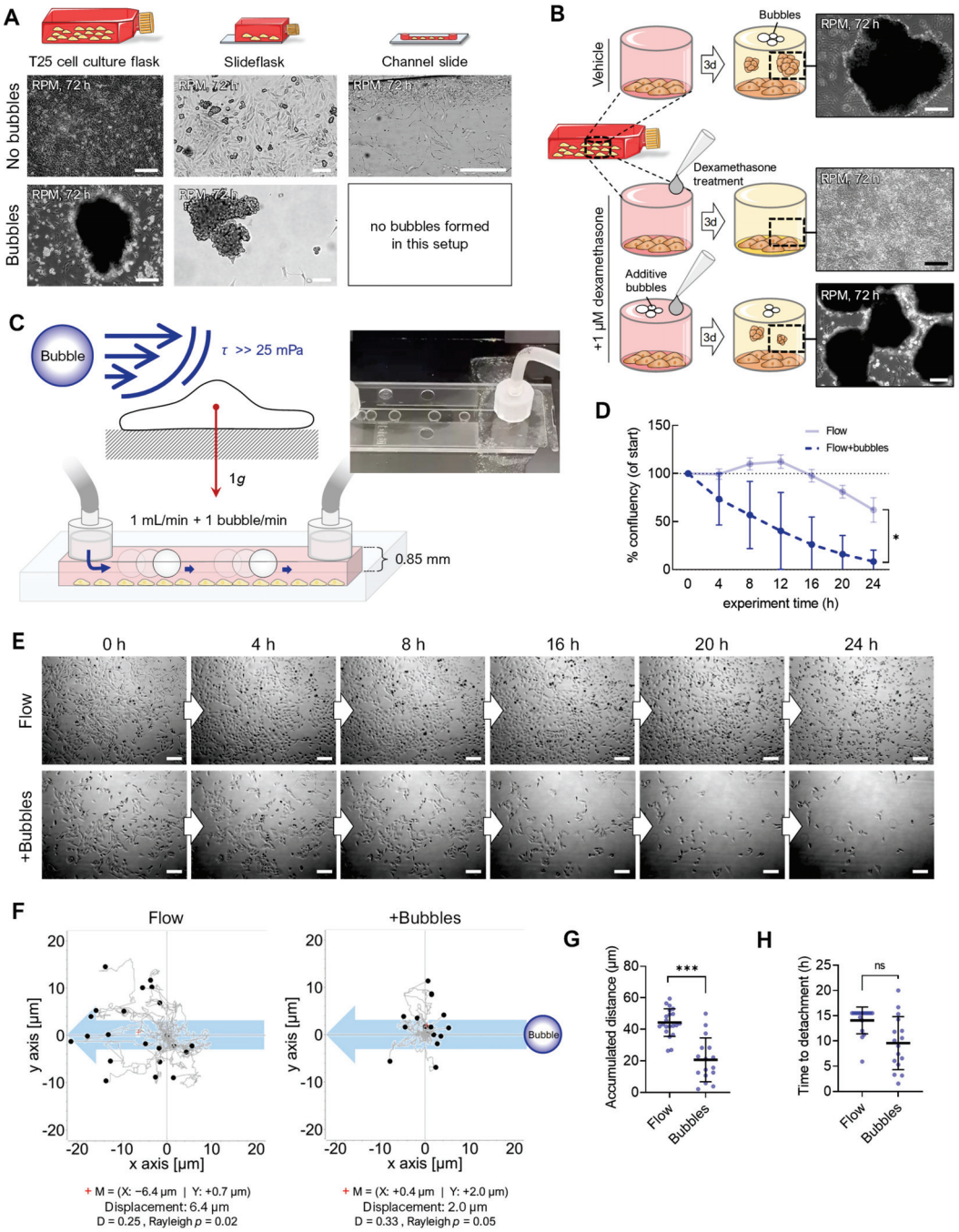


Figure 5. Enhancing effect of air bubbles on detachment of adherent FTC-133 cells. (**A**) Spheroid formation on the RPM depends on the culture flask geometry and the presence of air bubbles during the experiment. (**B**) Air bubbles were able to counteract the inhibitory effect of dexamethasone on the spheroid formation of FTC-133 cells on the RPM. (**C**) Setup of the bubble experiment. (**D**) Confluence of cell cultures over 24 h (n = 3). (**E**) Snapshots from the time-lapse recordings of one representative experiment with a flow rate of 1 mL/min without and with 1 bubble/min. (**F**) Migration traces of single cells in the flow channel. The blue arrow indicates the flow direction, and black circles indicate the position of cells after 24 h (n > 40 cells for each condition). The red cross (+) indicates the mean value (M) of spatial cell migration (values are given below the plot). D: directness. (**G**) Cumulative migration distances of cells over 24 h at a 1 mL/min flow rate with and without air bubbles. (**H**) Experiment time until initial cell detachment. Scale bars: 300 µm. * Independent sample t-test (**D**) or Mann–Whitney (**G**,**H**) $p \leq 0.05$, *** $p \leq 0.001$, ^{ns}, not significant. Parts of the figure were drawn by using pictures from Servier Medical Art.

Consequently, we modified the channel experiment, and air bubbles were pumped into the flowing medium at one bubble per second (bubble diameter: 5 mm; Figure 5C), using the same flow rate as in the shear flow experiments (1 mL/min). The cells detached at an earlier timepoint than without bubbles (Figure 5D,E; Video S2), suggesting bubble-enhanced cell detachment due to enhanced mechanical forces above 25 mPa (confluency change with bubbles: −92%, without bubbles: −38%). In addition, we observed significantly reduced cell migration (20.7 µm vs. 44.3 µm) when bubbles were present (Figure 5F,G). This could also be related to a faster detachment of the cells during migration (Figure 5H).

3.4. Flow Versus Random Positioning—Mechanobiology of Cell Detachment

After recognizing that fluid flow, as it occurs during the usual operation of the RPM in cell culture flasks, leads to the enhanced migration and detachment of adherent FTC-133 cells, we directly compared the mechanobiological responses of cells to flow- and RPM-induced shear forces (Figure 6). Because the number of cells in the channel slides decreased rapidly (compare Figure 5), we chose an examination time point 4 h after the start of the experiment. This also bypasses a possible adaptation of the cells that could be observed within 3 days. Shear forces might act differently on the same cell type depending on the culture vessel (T25 flasks and channel slides) and the corresponding possible exposure to fluid motions (Figure 6A). Nevertheless, in both culture conditions, we observed an increase in the F-actin density (Figure 6B) and altered localization (nuclear or cytoplasmic) of certain mechanosensitive transcription factors. Whilst both experimental approaches resulted in an altered nuclear protein content of RelA and p38 MAPK, the difference was only statistically significant for cells on the RPM (Figure 6C–E). Specifically, a decrease in nuclear p38 was observed on the RPM after 4 h, while an increase was observed in the flow channel (Figure 6D). MRTF-A nuclear localization was slightly decreased in the flow channel (Figure 6E). Subcellular localization of β-catenin remained unchanged. Conversely, the amount of β-catenin in the RPM cells was significantly increased (Figure 6F). Whilst there was no change in the nuclear levels of YAP1 on the RPM, YAP1 localization became more cytoplasmic in the cells under both exposure to RPM and flow (Figure 6G).

To investigate the mechanosignaling pathways, we investigated the mRNA expression of a panel of genes previously observed to be differentially expressed under simulated microgravity conditions [18]. The expression of these target genes was similar on the RPM and in the flow channel (Figure 6H). We found that *IL6*, *CXCL8*, and *ANKRD1* were upregulated in both RPM and flow conditions. We serum-starved T25 cell cultures for 4 h before starting the RPM. This procedure better mimicked the lower nutrient availability in the channel slides after the 24 h attachment phase and further approximated the gene expression changes to those of the cells from the flow channel experiment (Figure 6H, light grey bars). *CCN2*, *ICAM1*, *SNAI1*, *FN1*, and *VCL* showed similar regulatory behavior in both experimental setups.

The direction of the fluid flow in the RPM culture and the channel slide differs and changes continuously during random positioning. To test the effects of a discontinuous fluid flow on the cells, we utilized an oscillatory fluid flow of 1 mL/min and a flow direction change every 7.5 s (Figure 7A). Unlike a unidirectional flow, fewer cells detach when exposed to an oscillating flow (Figure 7B). In addition, β-catenin was significantly reduced in the nucleus after 4 h, whilst RelA, MRTF-A, and YAP1 were increasingly localized in the nucleus (Figure 7C). Thus, MRTF-A and YAP1 show a similar behavior as in cells exposed to the RPM, in contrast to β-catenin and RelA. qPCR confirmed that the SRF target gene *VCL* was upregulated, and the Wnt/β-catenin target genes *FN1*, *SNAI1*, and *VEGFA* were uniformly downregulated (Figure 7D).

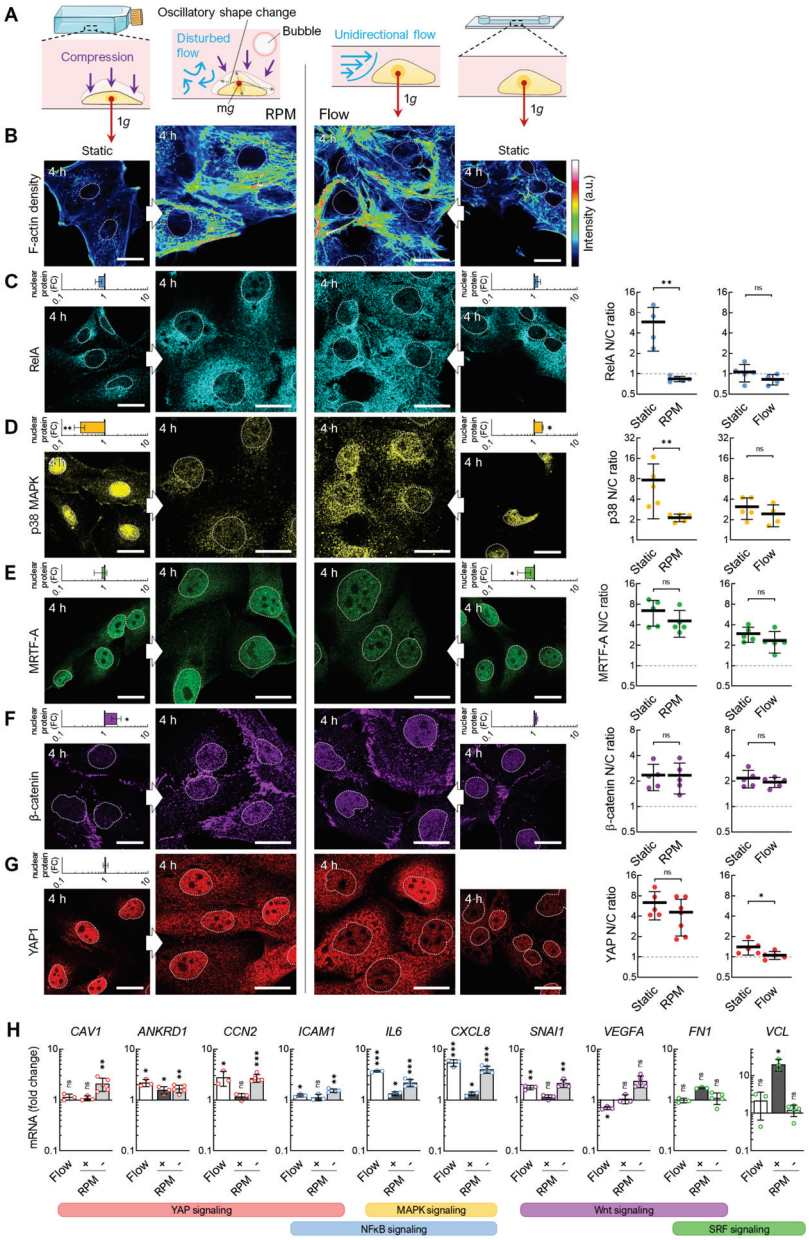


Figure 6. Transcription factor levels in random positioning compared to continuous flow. (**A**) Fluid motions acting on cells within different cell culture vessels. (**B**) Actin density and immunofluorescence of the mechanoresponsive transcription factors (**C**) RelA, (**D**) p38 MAPK, (**E**) MRTF-A, (**F**) β-catenin, and (**G**) YAP1 after 4 h. Outlines of the nuclei are shown as dashed lines. The small graphs indicate fold changes (FC) in nuclear protein levels compared to static cell cultures (n = 5 for each condition; one representative picture is shown). (Right) The mean nuclear/cytoplasmic (N/C) ratio of transcription factor localizations was measured for five overview images from independent experiments, each showing at least three cells. (**H**) Gene expression response after 4 h exposure to the RPM (60°/s) and continuous flow (1 mL/min). The plots show the mean ± SD ΔΔCt values of 3–5 independent experiments performed in triplicate. To mimic the channel slide's low medium and nutrient volume, the RPM experiment was performed once identically to the flow ("+", dark gray bars) experiment and once with a prior starvation phase ("−", light gray bars). Scale bars: 300 µm. The fluorescence images in this figure were optimized to visualize protein localization and unsuitable for comparative protein level quantification. * Mann–Whitney (**G**) or independent sample t-test (**H**) $p \leq 0.05$, ** $p \leq 0.01$, *** $p \leq 0.001$, ^{ns} non-significant vs. static control. Parts of the figure were drawn using pictures from Servier Medical Art.

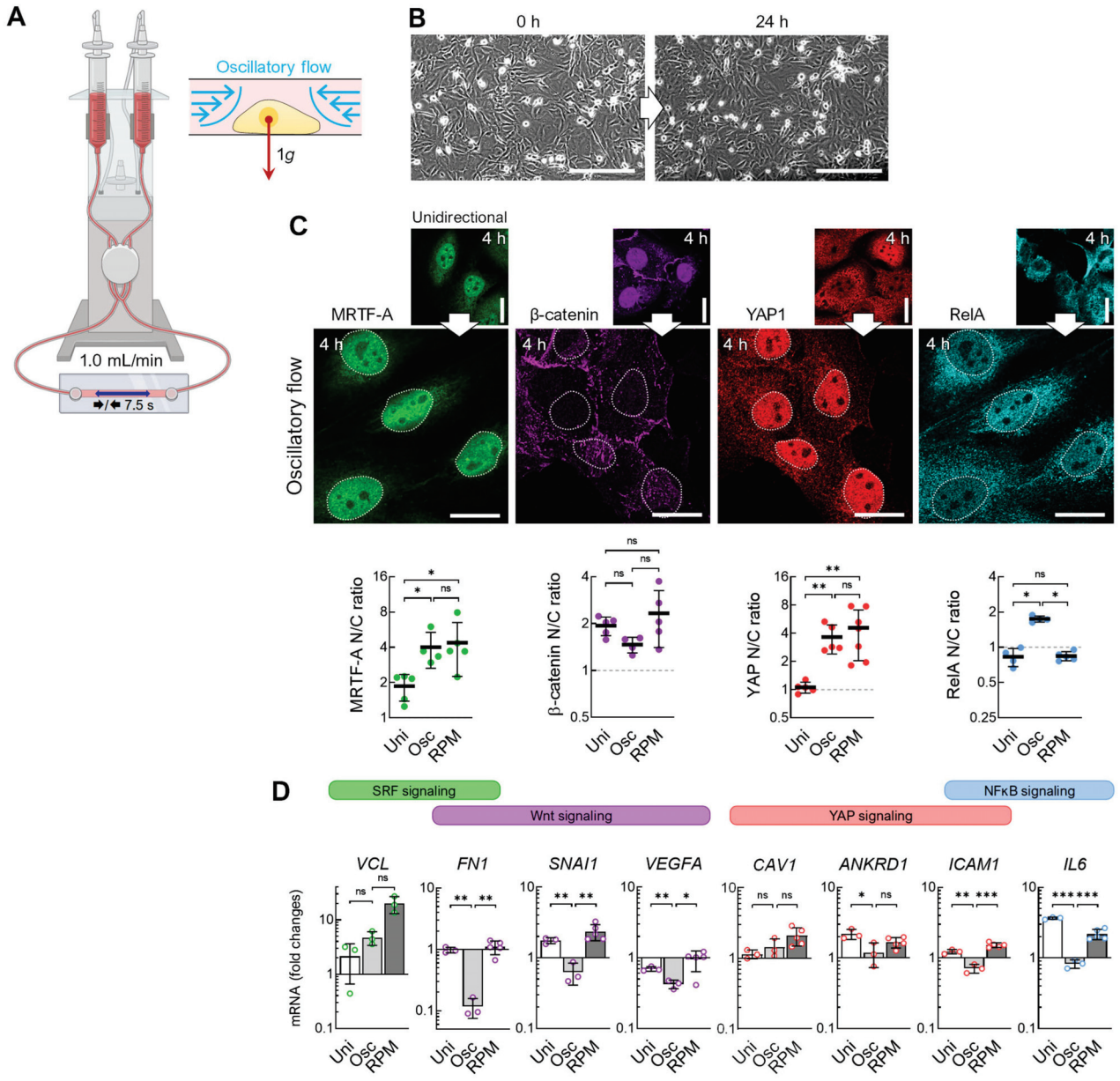


Figure 7. Transcription factor effects in response to oscillatory flow compared with continuous flow. (**A**) Setup for an oscillatory flow experiment (1 mL/min, direction change every 7.5 s). (**B**) Snapshots of cells in the channel before the start of the experiment and after 24 h of oscillating flow show reduced detachment of cells. (**C**) Nuclear transport of transcription factors after 4 h oscillatory flow ($n = 5$ for each condition; one representative picture is shown). (Below) Fold changes in nuclear protein levels compared to unidirectional flow. The mean nuclear/cytoplasmic (N/C) ratio of transcription factor localizations was measured for five overview images from independent experiments, each showing at least three cells. (**D**) Gene expression response after 4 h exposure to the oscillatory flow (Osc) compared to unidirectional flow (Uni) and to RPM culture ($n = 3$–5). Scale bars: 300 µm. The fluorescence images in this figure were optimized to visualize protein localization and unsuitable for comparative protein level quantification. * Mann–Whitney (**C**) or independent sample *t*-test (**D**) $p \leq 0.05$, ** $p \leq 0.01$, *** $p \leq 0.001$, ^{ns} non-significant. Parts of the figure were drawn using pictures from Biorender.com (accessed on 30 October 2023).

In summary, FTC-133 cells cultured on the RPM and those cultured in a flow channel show similar behavior regarding actin condensation, the translocation of mechanorespon-

sive transcription factors, and the expression of the target genes of the mechanosignaling pathways. An oscillatory flow showed greater similarity in the translocation of MRTF-A and YAP1 and lower similarity in the translocation of β-catenin and RelA to the cells on the RPM.

4. Discussion

Microgravity enables entirely new approaches to cell biology studies, including cancer research on a cellular level (reviewed in [5,30,31]). It is well established among gravitational researchers that it is impossible to simulate an exact microgravity environment in the laboratory. Nevertheless, depending on the device and the cell system chosen, ground-based facilities can produce results that closely resemble those of space experiments [32–34]. Therefore, simulated microgravity bioreactors may be a useful tool for space scientists. However, devices like the RPM have been a biological "black box", and most of the molecular and cellular processes that lead to exciting discoveries remain uncharacterized. In this study, we aimed to shed light on the cellular processes involved in cultivating adherent cancer cells on the RPM and understand how and why tumor spheroids form during culture in random positioning conditions.

4.1. Adherent Cells in Rotating Bioreactors

Investigation of gravitational biology is the most common reason for using rotating bioreactors. This requires that cells perceive changes in the direction of the gravity vector. While this property has already been proven for larger unicellular organisms (such as *Paramecium* or *Euglena*) [35–37], there has not been a clear answer for smaller human cells. Early calculations by Albrecht-Bühler suggest that the volume within a human cell is too small for the cell to sense gravitational changes [10]. Albrecht-Bühler instead assumed that the mass of the surrounding cell culture medium, which is also subject to gravity, triggers an indirect gravitational perception by exerting external pressure on the cell.

Restructuring of the cytoskeleton is often suggested as an early response to changes in the gravity vector [38]. Typical rearrangements of the cytoskeleton (reduced stress fibers, the formation of lamellipodia, etc.) were also observed by Ju et al. in their comparative study with different human cell types in response to simulated microgravity on a 3D clinostat. However, they observed the same cytoskeletal changes in an inverted cell culture, which they concluded must be a general response of mammalian cells to gravitational changes [39]. These effects could also be explained by the large column of culture medium above the cells in a standard orientated culture flask, which is not present in an inverted flask. However, it should be noted that the liquid column itself causes a hydrostatic pressure difference of 2.4 mbar in a 2.4 cm thick ($p = \rho \times a \times h$) completely filled T25 cell culture flask, which is in the order of magnitude of daily air pressure fluctuations. A possible (and maybe additive) influence of air pressure on cell culture observations should be investigated in a further study. Nevertheless, these results could explain the relaxation of tension the cell sensed, which may have induced the cytoskeletal changes observed. This could lead to the assumption that human cells in in vitro culture might sense only the indirect effects of gravity. In the meantime, however, other studies have appeared indicating that at least some human cells might be able to perceive gravity directly. Luna et al. [40] exposed human mesenchymal stem cells to different angular velocities on a clinostat and observed a rounder, less spread morphology as a function of the rotation speed. This angular frequency dependence suggested that the ability of a human cell to perceive the changing gravity vector depends on the rate of perturbation [40]. It is important to note that a slide, not a T25 culture flask, was used in this experiment to avoid the possible effects of shear forces and movement of the cell culture medium.

Clinorotation is usually associated with lower shear forces, which should result in a lower F-actin density in clinorotated cells compared with cells on the RPM. This was not observed in our experiments (Figure 2H); however, our goal was to study RPM motion and not to generate perfect clinorotation. One explanation for this discrepancy could be

the use of adherent cells instead of suspension cells. In addition, the rotation axis of an RPM operated in clinostat mode is much more offset compared with a slideflask/channel slide clinostat, resulting in low centrifugal forces (about 0.01 *g* on the cell layer, assuming a 10 cm offset and a rotation speed of 60°/s).

Even assuming that human cells are gravisensitive and can sense gravity directly, the question remains as to which subcellular structures are responsible. Vorselen's theory of the cytoskeleton as one of the first gravity responders in non-specialized cells [41] is still relevant, but is weakened by the fact that structural changes in the cytoskeleton happen in response to any mechanical influence on the cell, even with indirect perception of gravity. This is particularly evident as we observed changes in F-actin not only in response to the spatial orientation of the cell culture but also in response to the fluid flow without changing the gravitational vector (Figure 2). Also, the fact that MRTF-A and YAP1 are predominantly nuclear-localized in the rotating and flow cell cultures suggests that RhoA-dependent active actin remodeling occurred during fluid shear (Figures 2 and 6).

Zhang et al. [42] also compared different orientations of cell culture flasks for investigating the effect of the gravity vector on the mechanical remodeling of adherent murine MC3T3-E1 preosteoblast cells. Their results proposed a biomechanical model for integrating the mechanosensation of nucleus displacement with cytoskeletal remodeling and reorganization of the focal adhesion complex triggered by the gravity vector. If the mechanical stability of orientation-varied adherent cells could be explained, among other things, by the sedimentation of cell nuclei, this finding would suggest that gravisensing mechanisms in plant cells (sedimentation of statoliths) could also apply to mammalian cells in a distinct way. These results could explain why adherent cells adapt to a new physical culture condition after a period of time, which we saw in FTC-133 when comparing the results after 4 and 72 h (Figure 1). While we detected a significant translocation of p38 into the cytoplasm in RPM-exposed cells after 4 h, this was no longer the case after 72 h (Figure 2).

4.2. Flow Shear

Previous studies with thyroid cancer cells on the RPM show that the first spheroids form between 12 and 24 h. Our experiments have shown that FTC-133 cells begin to detach after about 12 h in a flow channel, which should have a similar fluid flow to a culture flask on the RPM. This process would be consistent with the timings observed on the RPM. We have also seen that the spheroid formation of FTC-133 cells depends on the RPM rotational speed, which should be proportional to the expected shear forces. Interestingly, by doubling the flow rate in the flow channel, we did not observe earlier detachment of the cells. Only in the presence of air bubbles did the cells' detachment occur from the beginning of the experiment.

We operated the RPM at different speeds to determine how shear stress affects biological experiments. After 8 h, the time-averaged gravity vector in all experimental setups was around 0.01 *g*, implying a "microgravity" condition. However, what distinguishes each setup from the others are the shear forces generated, which have already been calculated by Wuest et al. [14] for cell culture flasks on the RPM. Since the spheroid formation depended on the rotation speed, the microgravity simulation alone cannot be responsible for this process. When placed in a T25 flask at an average speed of 60°/s (commonly used in RPM microgravity simulation experiments), an estimated 70% of adherent cells experience a shear stress of at least 10 mPa. Further, 20% of the cells experience even higher rates of 25 mPa or more [14]. We mimicked these shear forces in a flow channel for ease of study and obtained a similar gene signature response to RPM experiments of the same length after 4 h.

Not all cells are exposed to the same shear forces on the RPM, which may have resulted in the lower fold changes in gene expression in the RPM-exposed cells compared to the cells from the flow channel. According to the simulations by Wuest et al. [14], only 20% of the cell monolayer was exposed to forces of the same magnitude as in the channel slide. There

were a few differences in the nuclear levels of the transcription factors p38, MRTF-A, and β-catenin, suggesting that the mechanosignaling of cells on the RPM cannot be replicated using a simple flow experiment. An oscillatory flow mimicked the changing shear stress direction found on the RPM better than a unidirectional flow but could not explain the difference. This further illustrates that the detachment of adherent cells, essential for spheroid formation on the RPM, can be mimicked by the shear forces from fluid flows and suggests that adherent cell layers on the RPM are subjected to higher mechanical stress before spheroids form. This is also supported by the fact that genes overexpressed in the adherent RPM cell population were upregulated in cancer cells exposed to shear stress (Figure 6F). Recently, advances in the study of the effects of low shear stress on cancer cells have been published [43–45]. Of particular interest for random positioning research are the low shear stress rates of 10–25 mPa that are expected during normal RPM operation. The physiological shear values of the lymphatic system (10–20 mPa), for example, can be found in this range [43], which is of critical importance for experiments with metastatic cancer cells or those isolated from lymphatic system metastases such as FTC-133. Work by Lee et al. [44] showed that low shear stress can activate YAP-dependent motility programs in metastatic cancer cell lines. In 2022, Kim et al. [45] showed that the cell motility in prostate cancer cell lines depends on the Piezo1–Src–YAP axis at low shear stress.

Triggered by the fluid flow inside the flow channel, we observed that the cells detach, migrate, and roll across the surface in the same direction as the media flow. At some point, the cells rounded out, detached, and were carried away by the flow. This observation over an extended period suggests that the increased detachment of the cells induced by flow is a biological process. Cells can sense flow-induced shear stress depending on its intensity and direction in a YAP-dependent manner that promotes cell motility [44]. We confirmed that the shear forces also contribute to the increased proliferation in RPM cell cultures [46,47]. We observed that cell confluency increased more rapidly at a higher flow rate of 1 mL/min compared with 0.5 mL/min until approximately 12 h after the start of the experiment.

Numerous research groups have reported alterations in gene and protein expression related to focal adhesion components, including integrins, as well as changes in the activity of focal adhesion kinase components, when employing rotating bioreactors to simulate microgravity [41]. These changes may be attributable to the cellular motility within this environment and can be more appropriately understood as a general cellular response to low shear stress.

4.3. Air Bubbles

First of all, it must be said that most studies pay enough attention to remove air bubbles in their experiments in order not to generate misleading results. It is therefore unusual to introduce additional air bubbles into a culture vessel. The bubble experiment (Figure 5) was primarily designed to investigate the effects of relatively large air bubbles on the cells. Despite particular care during filling, air bubbles in culture flasks on the RPM cannot be completely avoided, especially during longer experiments of $\geq$24 h. We have investigated a number of possible causes for the occurrence of bubbles in RPM experiments (compare Figure S1). However, it is most likely a combination of several effects. The correlation between the occurrence of air bubbles and the formation of spheroids, which we have seen in many RPM experiments, could be supported by the flow channel experiments in this study (Figure 5). The movement of air bubbles over the cell layer resulted in the rapid detachment of cells. This helps produce a larger amount of spheroids but results in much greater mechanical stress on the adherent cell population. Air bubbles also cause significant problems in microfluidic devices, and it is usually recommended to avoid them [48]. Bubbles in motion can have different effects depending on their size. They can interact directly with the cells and turbulent flow can be generated behind rising bubbles. Bubbles' effects on cell damage have been discussed for suspended cell populations. Cells can become trapped in the circulating fluid behind a rising bubble ("bubble wake") and are thereby dragged along by the bubble. For small bubbles, these microeddies can be

sufficiently intense to even create cell damage [49]. However, as soon as bubbles have formed in a culture flask on the RPM, they immediately hit the flask wall due to buoyancy and travel with rather high velocities along the wall with each revolution. These bubbles create high velocity gradients, and thereby high shear forces, in the liquid film between the bubble and cells [50].

4.4. Cell Density

Another interesting observation in our study was the influence of the cell pre-incubation time on RPM-induced spheroid formation. A longer pre-cultivation prior to RPM start resulted in a reduced formation to an absence of formation of 3D aggregates. It has previously been described that overgrown cell cultures no longer form spheroids under microgravity conditions [26]. In the case of a very dense cell culture, one possible explanation could be that there is no lateral surface of attack for shear forces due to the lack of space between the cells. Another explanation could be that cells detach during mitosis when they are less attached to the substrate (rounding of the cell). At low density, cells continue to divide and are at higher risk of detaching. At high density, the cells may go into a senescent state and stop dividing. Thus, the risk of detachment is lower. The results of the inverted flask experiments suggest that FTC-133 cells regularly detach from the surface, which would not be noticeable in a normally positioned cell culture (Figure 2). In cancer cells, this property can contribute to the formation of new metastases. However, further investigations are required to determine whether prior cell migration, cell–cell or cell–matrix contact formation, or mitosis is necessary for detachment (Figure 4). Our observations suggest that this is the case, as the detached cells migrated in the flow channel before their final detachment. The free space between the cells allows them to migrate according to the YAP nuclear status (Figure 2). YAP signaling is involved in contact inhibition of cell proliferation and growth [51] and allows the cell to maintain a motile environment by limiting the maturation of focal adhesions and restricting cytoskeletal tension [52]. Once a cell culture reaches confluence, YAP localization is completely cytoplasmic, and cells cease motility and possibly subsequent detachment in an RPM cell culture.

4.5. Spheroid Formation on the RPM

Our experiments indicated that the spheroid formation of adherent cells on the RPM is likely to be a two-step process (Figure 8A). In the first step, the cells are detached from their monolayer. Responsible for this are mainly fluid shear and the mechanical forces of migrating air bubbles during random positioning. Our fluid channel experiment mimicked fluid flow at a comparable scale to the RPM regular operation [14] and induced similar translocation of mechanosensitive transcription factors and a comparable signature of activated mechanoresponsive genes in FTC-133 cells. After detachment, the cells on the RPM are suspended in free-fall due to the appropriate rotational speed, preventing their sedimentation and two-dimensional outgrowth. In this phase, the cells aggregate into three-dimensional aggregates. The work of Melnik et al. [18] has shown that FTC-133 cells, when used as a suspension on the RPM, also form spheroids. Therefore, starting an RPM experiment with a layer of adherent cells is not essential for generating and studying spheroids. In other devices for microgravity research, such as the ClinoStar (CelVivo, Denmark) or the rotating wall vessel bioreactor (Synthecon, TX, USA), cells are also seeded in suspension before floating spheroids develop under rotation. However, using adherent cells in an RPM experiment allows for additional studies. For example, not all cells detach equally due to random positioning. A balance of adhesion and anti-adhesion proteins was discussed as responsible for this behavior [18]. In addition, metastatic cancer cells tolerate the suspension phase better due to the anoikis (cell death due to loss of cell–matrix contact) resistance they usually develop during the metastasis formation multistep process [53], as a prolonged culture phase before the start of random positioning inhibited the detachment of FTC-133 cells (Figure 3). After a two-day pre-attachment phase, the only conditions that obtained spheroids were higher angular velocities, which were only

able to induce the formation of a single small spheroid (ca. 110 µm) (Figure 3). The cells exhibited no transcriptional response to RPM treatment until higher velocities were applied. However, whether this inertia was related to increased "stickiness" due to a plentiful secreted extracellular matrix, to a higher level of adhesion proteins, or simply to the physical protection against flow shear caused by being embedded into a cell layer cannot be deduced from our data.

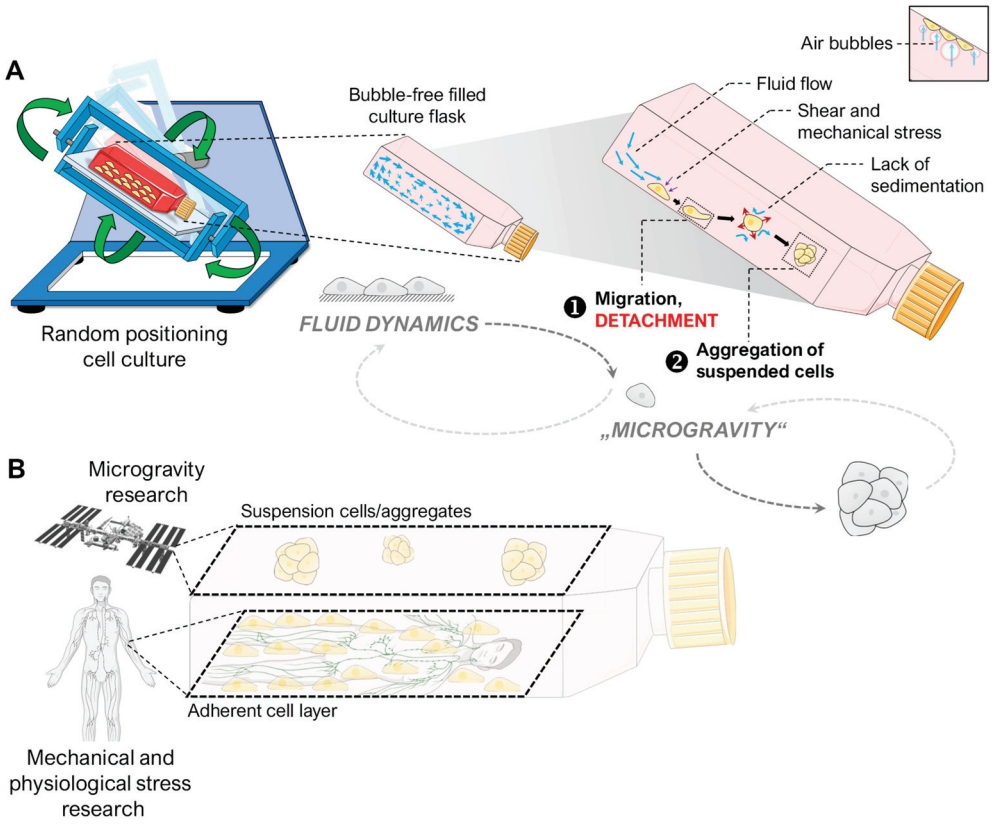


Figure 8. (**A**) Illustration of the hypothesized processes occurring with adherent cells in an initially air-bubble-free cell culture flask on the RPM, finally leading to spheroid formation. We observed that RPM-induced spheroid formation is a two-step process. First, the adherent cells detach due to mechanical stress (e.g., fluid flow, air bubbles). Then, "simulated microgravity" (free-fall) leads to the formation of three-dimensional spheroids by preventing the sedimentation of suspended cells. The small picture indicates the amplifying mechanical effect of air bubbles. (**B**) The two cell populations (adherent cell layer and suspension cells) of an RPM cell culture of adherent cells are subjected to different mechanical forces. While the suspension cells are held in a mostly stress-free suspension, the cell layer experiences shear forces similar to those in the human lymphatic system. Parts of the figure were drawn by using pictures from Biorender.com and from Servier Medical Art.

4.6. Implications for Future Experiments in Gravitational Biology

4.6.1. "Simulated Microgravity"

The RPM continues to be a suitable bioreactor to simulate microgravity effects for some cell model systems on Earth. To achieve optimal results in cell culture experiments, it is vital to have a thorough understanding of the internal dynamics of random positioning. Attention to these dynamics ensures that experiments are well planned and yield accurate and reliable results. For a suspended object, the RPM can simulate free-fall, the main effect experienced by astronauts and organisms on the ISS or during parabolic flights. An adherent cell population on the RPM is subject to shear forces that detach the cells after some time, leaving them to float free in the culture medium. Without sedimentation, if they can resist anoikis, they may aggregate and form spheroids.

It must be considered that the adherent cell layer and the suspension cells are exposed to very different mechanical forces, especially when air bubbles are present. Meaningful results will only be achieved with careful design of RPM-based experiments. The cellular effect triggered by fluid motion can be several orders of magnitude higher than the effect triggered by gravity alteration. Thus, it is not necessary to design a gravity-focused RPM experiment with a prior adhesion period leading to a two-dimensional cell layer. Instead, initiation with suspension cultures could prove a possible alternative. In 2022, Masini et al. [54] successfully performed a long-term experiment with suspended cancer cells on the RPM. They found that under the influence of the RPM, the behavior and metabolism of tumor cells led to the acquisition of an aggressive and metastatic stem cell-like phenotype.

The size and geometry of the cell culture vessel also play a role, as they directly influence the turbulence of the medium generated during random positioning. In the current study, we also observed this effect when using different culture flasks for the FTC-133 cells. In large flasks, the medium has a higher rotational energy. In small channel slides, the adhesive forces dominate, and the medium has hardly any chance to reach its full speed. Lower shear stress in the slide flasks or channel slides resulted in fewer or no spheroids, respectively, even though the RPM program or random speed and random direction velocities used were the same.

4.6.2. Real Microgravity

Spheroid formation of adherently growing human cells was also observed in several space experiments. In the ISS experiments SimBox [1], SPHEROIDS [2], and CellBox-2 [3], the formation of 3D aggregates in real microgravity has been reported. Since the detachment of cells has not yet been observed in microgravity, it cannot be completely ruled out that cells detach from their substrate during the microgravity phase. Nevertheless, it is possible that the appearance of these spheroids was triggered by a specific orientation of the flight hardware (e.g., by flipping) in combination with the formation of air bubbles (compare Figure S1). In our study, we were able to show that an upside-down-orientated cell culture flask with air bubbles led to the formation of spheroids after some time (Figure 2). Since it is unknown and not determinable in which orientation the flight hardware was stored between the handover and the rocket launch, a similar effect in the CellBox-2 experiment cannot be excluded. Accordingly, spheroids could have formed even before arrival on the ISS, e.g., due to accelerations or vibrations during the launch phase. FTC-133 cells were also used in the space experiment, and numerous air bubbles could be seen in the culture chamber at the end of the experiment (Figure S1B). Live cell observation during space experiments would help to determine when spheroids are formed during spaceflights. In future experiments on spheroid formation in real microgravity, special care must be taken to avoid air bubbles, e.g., using a bubble trap in the loop system or specific culture flask geometries that minimize the described bubble effect (e.g., channel or chamber slides).

4.6.3. Cell Models

While individual suspension cells are directly exposed to direct or indirect gravitational effects on the RPM, this is not necessarily true for cells inside cell clusters or multicellular organisms. While the cells of multicellular plants with statoliths still have intracellular perception mechanisms for gravity [55], mammalian cells have established perception of external structures exposed to gravity (e.g., otoliths). The cells used for the gravitational perception of environmental stimuli are mostly located on the internal or external surfaces of the organism, sometimes combined into sensory tissues or organs. The task of perceiving gravity is delegated to a higher organizational level (organ or system). Cells embedded into mostly non-gravity-sensitive tissue are likely to respond only to the mechanical deformation of the surrounding tissue but not to changes in the gravity vector. This may also be true for position-fixed adherent cells in a monolayer on the RPM. In 2022, ElGindi et al. [56] provided evidence of the more influential role of the local microenvironment in comparison to the general gravity vector. Their experiments showed that a 3D

microenvironment attenuated the changes in the transcriptome of T cells mediated by the RPM. The research group also exposed dendritic cells to the RPM in two different types of extracellular matrices (loose and stiff) [57]. The effects of random positioning at the transcriptome level were smaller when the cells were cultured in the denser matrix. Both studies indicate the major influence of the microenvironment on mammalian cell biology. This is also supported by the different effects at the transcriptional and protein levels found in numerous comparative analyses of the two cell populations (adherent cells, AD, and multicellular spheroids, MCS) in RPM experiments with human cells [8,19,46,58]; although both populations are by definition subjected to "simulated microgravity", the adherent cell layer is more exposed to mechanical fluid flow, whereas the spheroid cells float in a suspension with lower shear and are also primarily embedded into a protective stable tissue aggregate. Here, the cell microenvironment probably has a greater influence than the constantly changing gravitational vector and can influence cell signaling, proliferation, and apoptosis [59–61]. One possible approach to answering this ambiguous question is the planned project by Larose and colleagues to study spheroids and organoids under real microgravity conditions. This will open up the possibility of testing the extent to which microgravity affects the three-dimensional constructs of cancer cells [62].

Albrecht-Bühler [10] once commented that the microgravity simulation requires more than averaging the gravity vector in clinorotation. In addition, Einstein [63] stated that: "The gravitational field has only a relative existence in a way similar to the electric field generated by magnetoelectric induction. Because for an observer falling freely from the roof of a house there exists—at least in his immediate surroundings—no gravitational field". After more than 100 years, we can confirm this at least for human cells. While probably only isolated cells free-falling in vacuum could experience microgravity directly (a theoretical consideration), the indirect effects of altered gravity are perceived and processed differently by cells, depending on their type, origin, and cell culture conditions, and the characteristics of the "microgravity simulator" used. Conversely, this also means that a free-fall simulator is not always required to mimic the cellular effects of exposure to microgravity. A cell type-specific combination of mechanical stimuli could be sufficient.

4.7. Study Limitations

It should be noted that we have a heterogeneous cell population on the RPM (because not all cells are subjected to the same shear forces). Since we saw that not all cells detached simultaneously during flow exposure, we can hypothesize that cells may regulate some molecular factors before detaching from the surface. Unfortunately, we could only perform endpoint analyses from the localization of transcription factors and gene expression. Live cell observation of the cells on the RPM would provide more accurate information on spontaneous and/or short-term changes and adaptations. Some researchers suspect that the vibrations inside an incubator prevent/slow cell attachment to plastic flask surfaces. In the current study, we did not investigate the influence of vibrations, but started the experiments after a preceding 24(-48) h attachment phase of the cells.

5. Conclusions

Spheroid formation of adherently growing cells on the RPM is a two-step process. It requires detachment of the cells, caused mainly by fluid flow (triggered by the rotation of the cell culture flask), and air bubbles can enhance it. Once the cells are in suspension, random positioning prevents sedimentation, and 3D aggregate formation occurs.

The detachment itself seems to depend on the balance between the cell-specific adhesion forces (depending on the cell density, amount of matrix, and adhesion proteins) and the physical shear forces of the cell culture (flow rate, bubbles, surface conditions of the cell culture flask). In the current study, a fluid flow experiment mimicked several RPM-induced effects in adherent FTC-133 cells. During regular operation of the RPM, shear forces act in a range similar to that of the human lymphatic system. Thus, the RPM serves as a free-fall simulator for (detached) suspension cells in gravitational research, but it also

simulates the shear forces of the human organism on the adherent cell layer, providing a unique combination of study conditions for cancer research (Figure 8B). To ensure that, experiments with the RPM must be well planned and the results interpreted accordingly.

Supplementary Materials: The following supporting information can be downloaded at https://www.mdpi.com/article/10.3390/cells12222665/s1: Figure S1: Occurrence of air bubbles under different cell culture conditions and handling of cell culture flasks; Table S1: Antibodies used for immunofluorescence analyses; Table S2: Primer sequences for quantitative real-time PCR; Video S1: 24 h time-lapse video of FTC-133 cells exposed to a fluid flow of 1 mL/min inside a channel slide; Video S2: 24 h time-lapse video of FTC-133 cells exposed to a fluid flow of 1 mL/min with 1 bubble/min inside a channel slide.

Author Contributions: Conceptualization, J.L.C.-S. and M.K.; methodology, J.L.C.-S., V.S., S.K., D.M. and M.K.; software, J.L.C.-S.; formal analysis, J.L.C.-S. and M.K.; investigation, J.L.C.-S., D.M., V.S. and S.M.; resources, D.G.; writing—original draft preparation, J.L.C.-S. and M.K.; writing—review and editing, J.L.C.-S., S.L.W., C.L., I.R.D.J., M.C., S.K., S.M., D.M., D.G. and M.K.; visualization, J.L.C.-S. and M.K.; supervision, M.K.; funding acquisition, D.G. All authors have read and agreed to the published version of the manuscript.

Funding: This work was supported by the German Space Agency at DLR (Deutsches Zentrum für Luft- und Raumfahrt, grant number 50WB2219). J.L.C.-S. received financial support from the CONACyT-DAAD scholarship (CVU: 1059612).

Institutional Review Board Statement: Not applicable.

Informed Consent Statement: Not applicable.

Data Availability Statement: The data presented in this study are available in the electronic Supplementary Materials. The complete raw data are available on request.

Acknowledgments: We would like to thank ibidi GmbH, especially Charlotte Öri, for kindly providing the ibidi pump system as a demo test for the oscillatory flow. We would also like to thank Hermann-Josef Rothkötter (Institute of Anatomy, Magdeburg) for the opportunity to perform some experiments at his institute.

Conflicts of Interest: The authors declare no conflict of interest.

References

1. Pietsch, J.; Ma, X.; Wehland, M.; Aleshcheva, G.; Schwarzwälder, A.; Segerer, J.; Birlem, M.; Horn, A.; Bauer, J.; Infanger, M.; et al. Spheroid Formation of Human Thyroid Cancer Cells in an Automated Culturing System during the Shenzhou-8 Space Mission. *Biomaterials* **2013**, *34*, 7694–7705. [CrossRef] [PubMed]
2. Pietsch, J.; Gass, S.; Nebuloni, S.; Echegoyen, D.; Riwaldt, S.; Baake, C.; Bauer, J.; Corydon, T.J.; Egli, M.; Infanger, M.; et al. Three-Dimensional Growth of Human Endothelial Cells in an Automated Cell Culture Experiment Container during the SpaceX CRS-8 ISS Space Mission—The SPHEROIDS Project. *Biomaterials* **2017**, *124*, 126–156. [CrossRef] [PubMed]
3. Melnik, D.; Krüger, M.; Schulz, H.; Kopp, S.; Wehland, M.; Bauer, J.; Baselet, B.; Vermeesen, R.; Baatout, S.; Corydon, T.J.; et al. The CellBox-2 Mission to the International Space Station: Thyroid Cancer Cells in Space. *Int. J. Mol. Sci.* **2021**, *22*, 8777. [CrossRef] [PubMed]
4. Freed, L.E.; Langer, R.; Martin, I.; Pellis, N.R.; Vunjak-Novakovic, G. Tissue Engineering of Cartilage in Space. *Proc. Natl. Acad. Sci. USA* **1997**, *94*, 13885–13890. [CrossRef] [PubMed]
5. Kim, H.; Shin, Y.; Kim, D.-H. Mechanobiological Implications of Cancer Progression in Space. *Front. Cell Dev. Biol.* **2021**, *9*, 740009. [CrossRef] [PubMed]
6. Becker, J.L.; Souza, G.R. Using Space-Based Investigations to Inform Cancer Research on Earth. *Nat. Rev. Cancer* **2013**, *13*, 315–327. [CrossRef]
7. Brungs, S.; Egli, M.; Wuest, S.L.; Christianen, P.C.M.; van Loon, J.J.W.A.; Anh, T.J.N.; Hemmersbach, R. Facilities for Simulation of Microgravity in the ESA Ground-Based Facility Programme. *Microgravity Sci. Technol.* **2016**, *28*, 191–203. [CrossRef]
8. Kopp, S.; Slumstrup, L.; Corydon, T.J.; Sahana, J.; Aleshcheva, G.; Islam, T.; Magnusson, N.E.; Wehland, M.; Bauer, J.; Infanger, M.; et al. Identifications of Novel Mechanisms in Breast Cancer Cells Involving Duct-like Multicellular Spheroid Formation after Exposure to the Random Positioning Machine. *Sci. Rep.* **2016**, *6*, 26887. [CrossRef]
9. Shi, S.; Li, Q.; Cao, Q.; Diao, Y.; Zhang, Y.; Yue, L.; Wei, L. EMT Transcription Factors Are Involved in the Altered Cell Adhesion under Simulated Microgravity Effect or Overloading by Regulation of E-Cadherin. *Int. J. Mol. Sci.* **2020**, *21*, 1349. [CrossRef]
10. Albrecht-Buehler, G. Possible Mechanisms of Indirect Gravity Sensing by Cells. *ASGSB Bull.* **1991**, *4*, 25–34.

11. Hauslage, J.; Cevik, V.; Hemmersbach, R. Pyrocystis Noctiluca Represents an Excellent Bioassay for Shear Forces Induced in Ground-Based Microgravity Simulators (Clinostat and Random Positioning Machine). *NPJ Microgravity* **2017**, *3*, 12. [CrossRef] [PubMed]
12. Leguy, C.A.D.; Delfos, R.; Pourquie, M.J.B.M.; Poelma, C.; Westerweel, J.; van Loon, J.J.W.A. Fluid Dynamics during Random Positioning Machine Micro-Gravity Experiments. *Adv. Space Res.* **2017**, *59*, 3045–3057. [CrossRef]
13. Wuest, S.L.; Richard, S.; Kopp, S.; Grimm, D.; Egli, M. Simulated Microgravity: Critical Review on the Use of Random Positioning Machines for Mammalian Cell Culture. *BioMed Res. Int.* **2015**, *2015*, 971474. [CrossRef] [PubMed]
14. Wuest, S.L.; Stern, P.; Casartelli, E.; Egli, M. Fluid Dynamics Appearing during Simulated Microgravity Using Random Positioning Machines. *PLoS ONE* **2017**, *12*, e0170826. [CrossRef] [PubMed]
15. Ibidi GmbH. Application Note 11, Shear Stress and Shear Rates for Ibidi µ-Slides Based on Numerical Calculations. 2022. Available online: https://ibidi.com/img/cms/support/AN/AN11_Shear_stress.pdf (accessed on 29 October 2023).
16. Melnik, D.; Sahana, J.; Corydon, T.J.; Kopp, S.; Nassef, M.Z.; Wehland, M.; Infanger, M.; Grimm, D.; Krüger, M. Dexamethasone Inhibits Spheroid Formation of Thyroid Cancer Cells Exposed to Simulated Microgravity. *Cells* **2020**, *9*, 367. [CrossRef] [PubMed]
17. Shihan, M.H.; Novo, S.G.; Le Marchand, S.J.; Wang, Y.; Duncan, M.K. A Simple Method for Quantitating Confocal Fluorescent Images. *Biochem. Biophys. Rep.* **2021**, *25*, 100916. [CrossRef] [PubMed]
18. Melnik, D.; Cortés-Sánchez, J.L.; Sandt, V.; Kahlert, S.; Kopp, S.; Grimm, D.; Krüger, M. Dexamethasone Selectively Inhibits Detachment of Metastatic Thyroid Cancer Cells during Random Positioning. *Cancers* **2023**, *15*, 1641. [CrossRef]
19. Kopp, S.; Warnke, E.; Wehland, M.; Aleshcheva, G.; Magnusson, N.E.; Hemmersbach, R.; Corydon, T.J.; Bauer, J.; Infanger, M.; Grimm, D. Mechanisms of Three-Dimensional Growth of Thyroid Cells during Long-Term Simulated Microgravity. *Sci. Rep.* **2015**, *5*, 16691. [CrossRef]
20. Riwaldt, S.; Bauer, J.; Pietsch, J.; Braun, M.; Segerer, J.; Schwarzwälder, A.; Corydon, T.J.; Infanger, M.; Grimm, D. The Importance of Caveolin-1 as Key-Regulator of Three-Dimensional Growth in Thyroid Cancer Cells Cultured under Real and Simulated Microgravity Conditions. *Int. J. Mol. Sci.* **2015**, *16*, 28296–28310. [CrossRef]
21. Corydon, T.J.; Schulz, H.; Richter, P.; Strauch, S.M.; Böhmer, M.; Ricciardi, D.A.; Wehland, M.; Krüger, M.; Erzinger, G.S.; Lebert, M.; et al. Current Knowledge about the Impact of Microgravity on Gene Regulation. *Cells* **2023**, *12*, 1043. [CrossRef]
22. Ma, X.; Pietsch, J.; Wehland, M.; Schulz, H.; Saar, K.; Hübner, N.; Bauer, J.; Braun, M.; Schwarzwälder, A.; Segerer, J.; et al. Differential Gene Expression Profile and Altered Cytokine Secretion of Thyroid Cancer Cells in Space. *FASEB J.* **2014**, *28*, 813–835. [CrossRef] [PubMed]
23. Kopp, S.; Krüger, M.; Feldmann, S.; Oltmann, H.; Schütte, A.; Schmitz, B.; Bauer, J.; Schulz, H.; Saar, K.; Huebner, N.; et al. Thyroid Cancer Cells in Space during the TEXUS-53 Sounding Rocket Mission—The THYROID Project. *Sci. Rep.* **2018**, *8*, 10355. [CrossRef] [PubMed]
24. Kalukula, Y.; Stephens, A.D.; Lammerding, J.; Gabriele, S. Mechanics and Functional Consequences of Nuclear Deformations. *Nat. Rev. Mol. Cell Biol.* **2022**, *23*, 583–602. [CrossRef]
25. Brungs, S.; Hauslage, J.; Hemmersbach, R. Validation of Random Positioning Versus Clinorotation Using a Macrophage Model System. *Microgravity Sci. Technol.* **2019**, *31*, 223–230. [CrossRef]
26. Riwaldt, S.; Pietsch, J.; Sickmann, A.; Bauer, J.; Braun, M.; Segerer, J.; Schwarzwälder, A.; Aleshcheva, G.; Corydon, T.J.; Infanger, M.; et al. Identification of Proteins Involved in Inhibition of Spheroid Formation under Microgravity. *Proteomics* **2015**, *15*, 2945–2952. [CrossRef]
27. Kopp, S.; Sahana, J.; Islam, T.; Petersen, A.G.; Bauer, J.; Corydon, T.J.; Schulz, H.; Saar, K.; Huebner, N.; Slumstrup, L.; et al. The Role of NFκB in Spheroid Formation of Human Breast Cancer Cells Cultured on the Random Positioning Machine. *Sci. Rep.* **2018**, *8*, 921. [CrossRef]
28. Dietrichs, D.; Grimm, D.; Sahana, J.; Melnik, D.; Corydon, T.J.; Wehland, M.; Krüger, M.; Vermeesen, R.; Baselet, B.; Baatout, S.; et al. Three-Dimensional Growth of Prostate Cancer Cells Exposed to Simulated Microgravity. *Front. Cell Dev. Biol.* **2022**, *10*, 841017. [CrossRef]
29. Grosse, J.; Wehland, M.; Pietsch, J.; Schulz, H.; Saar, K.; Hübner, N.; Elles, C.; Bauer, J.; Abou-El-Ardat, K.; Baatout, S.; et al. Gravity-sensitive Signaling Drives 3-dimensional Formation of Multicellular Thyroid Cancer Spheroids. *FASEB J.* **2012**, *26*, 5124–5140. [CrossRef]
30. Sahebi, R.; Aghaei, M.; Halvaei, S.; Alizadeh, A. The Role of Microgravity in Cancer: A Dual-Edge Sword. *Multidiscip. Cancer Investig.* **2017**, *1*, 1–5. [CrossRef]
31. Medha, M.; Roy, A. Microgravity: New Aspect for Breast Cancer Treatment, a Review. *Acta Astronaut.* **2022**, *190*, 62–73. [CrossRef]
32. Herranz, R.; Anken, R.; Boonstra, J.; Braun, M.; Christianen, P.C.M.; de Geest, M.; Hauslage, J.; Hilbig, R.; Hill, R.J.A.; Lebert, M.; et al. Ground-Based Facilities for Simulation of Microgravity: Organism-Specific Recommendations for Their Use, and Recommended Terminology. *Astrobiology* **2013**, *13*, 1–17. [CrossRef] [PubMed]
33. Topal, U.; Zamur, C. Microgravity, Stem Cells, and Cancer: A New Hope for Cancer Treatment. *Stem Cells Int.* **2021**, *2021*, 5566872. [CrossRef] [PubMed]
34. Choi, D.H.; Jeon, B.; Lim, M.H.; Lee, D.H.; Ye, S.-K.; Jeong, S.-Y.; Kim, S. 3D Cell Culture Using a Clinostat Reproduces Microgravity-Induced Skin Changes. *NPJ Microgravity* **2021**, *7*, 20. [CrossRef] [PubMed]
35. Häder, D.-P.; Hemmersbach, R. Euglena, a Gravitactic Flagellate of Multiple Usages. *Life* **2022**, *12*, 1522. [CrossRef] [PubMed]
36. Roberts, A.M. The Mechanics of Gravitaxis in Paramecium. *J. Exp. Biol.* **2010**, *213*, 4158–4162. [CrossRef] [PubMed]

37. Hemmersbach, R.; Häder, D.P. Graviresponses of Certain Ciliates and Flagellates. *FASEB J.* **1999**, *13*, S69–S75. [CrossRef] [PubMed]
38. Lichterfeld, Y.; Kalinski, L.; Schunk, S.; Schmakeit, T.; Feles, S.; Frett, T.; Herrmann, H.; Hemmersbach, R.; Liemersdorf, C. Hypergravity Attenuates Reactivity in Primary Murine Astrocytes. *Biomedicines* **2022**, *10*, 1966. [CrossRef]
39. Ju, Z.; Thomas, T.N.; Chiu, Y.-J.; Yamanouchi, S.; Yoshida, Y.; Abe, J.-I.; Takahashi, A.; Wang, J.; Fujiwara, K.; Hada, M. Adaptation and Changes in Actin Dynamics and Cell Motility as Early Responses of Cultured Mammalian Cells to Altered Gravitational Vector. *Int. J. Mol. Sci.* **2022**, *23*, 6127. [CrossRef]
40. Luna, C.; Yew, A.G.; Hsieh, A.H. Effects of Angular Frequency during Clinorotation on Mesenchymal Stem Cell Morphology and Migration. *NPJ Microgravity* **2015**, *1*, 15007. [CrossRef]
41. Vorselen, D.; Roos, W.H.; MacKintosh, F.C.; Wuite, G.J.L.; van Loon, J.J.W.A. The Role of the Cytoskeleton in Sensing Changes in Gravity by Nonspecialized Cells. *FASEB J.* **2014**, *28*, 536–547. [CrossRef]
42. Zhang, C.; Zhou, L.; Zhang, F.; Lü, D.; Li, N.; Zheng, L.; Xu, Y.; Li, Z.; Sun, S.; Long, M. Mechanical Remodeling of Normally Sized Mammalian Cells under a Gravity Vector. *FASEB J.* **2017**, *31*, 802–813. [CrossRef] [PubMed]
43. Huang, Q.; Hu, X.; He, W.; Zhao, Y.; Hao, S.; Wu, Q.; Li, S.; Zhang, S.; Shi, M. Fluid Shear Stress and Tumor Metastasis. *Am. J. Cancer Res.* **2018**, *8*, 763–777. [PubMed]
44. Lee, H.J.; Diaz, M.F.; Price, K.M.; Ozuna, J.A.; Zhang, S.; Sevick-Muraca, E.M.; Hagan, J.P.; Wenzel, P.L. Fluid Shear Stress Activates YAP1 to Promote Cancer Cell Motility. *Nat. Commun.* **2017**, *8*, 14122. [CrossRef] [PubMed]
45. Kim, O.-H.; Choi, Y.W.; Park, J.H.; Hong, S.A.; Hong, M.; Chang, I.H.; Lee, H.J. Fluid Shear Stress Facilitates Prostate Cancer Metastasis through Piezo1-Src-YAP Axis. *Life Sci.* **2022**, *308*, 120936. [CrossRef] [PubMed]
46. Calvaruso, M.; Militello, C.; Minafra, L.; La Regina, V.; Torrisi, F.; Pucci, G.; Cammarata, F.P.; Bravatà, V.; Forte, G.I.; Russo, G. Biological and Mechanical Characterization of the Random Positioning Machine (RPM) for Microgravity Simulations. *Life* **2021**, *11*, 1190. [CrossRef] [PubMed]
47. Jha, R.; Wu, Q.; Singh, M.; Preininger, M.K.; Han, P.; Ding, G.; Cho, H.C.; Jo, H.; Maher, K.O.; Wagner, M.B.; et al. Simulated Microgravity and 3D Culture Enhance Induction, Viability, Proliferation and Differentiation of Cardiac Progenitors from Human Pluripotent Stem Cells. *Sci. Rep.* **2016**, *6*, 30956. [CrossRef] [PubMed]
48. Zhao, X.; Ma, C.; Park, D.S.; Soper, S.A.; Murphy, M.C. Air Bubble Removal: Wettability Contrast Enabled Microfluidic Interconnects. *Sens. Actuators B Chem.* **2022**, *361*, 131687. [CrossRef]
49. Chisti, Y. Animal-Cell Damage in Sparged Bioreactors. *Trends Biotechnol.* **2000**, *18*, 420–432. [CrossRef]
50. Huang, W.; Yun, H.; Huang, W.; Zhang, B.; Lyu, X. On the Influences of Air Bubbles on Water Flow in a Two-Dimensional Channel. *Math. Probl. Eng.* **2021**, *2021*, 6818673. [CrossRef]
51. Gumbiner, B.M.; Kim, N.-G. The Hippo-YAP Signaling Pathway and Contact Inhibition of Growth. *J. Cell Sci.* **2014**, *127*, 709–717. [CrossRef]
52. Mason, D.E.; Collins, J.M.; Dawahare, J.H.; Nguyen, T.D.; Lin, Y.; Voytik-Harbin, S.L.; Zorlutuna, P.; Yoder, M.C.; Boerckel, J.D. YAP and TAZ Limit Cytoskeletal and Focal Adhesion Maturation to Enable Persistent Cell Motility. *J. Cell Biol.* **2019**, *218*, 1369–1389. [CrossRef] [PubMed]
53. Khan, S.U.; Fatima, K.; Malik, F. Understanding the Cell Survival Mechanism of Anoikis-Resistant Cancer Cells during Different Steps of Metastasis. *Clin. Exp. Metastasis* **2022**, *39*, 715–726. [CrossRef] [PubMed]
54. Masini, M.A.; Bonetto, V.; Manfredi, M.; Pastò, A.; Barberis, E.; Timo, S.; Vanella, V.V.; Robotti, E.; Masetto, F.; Andreoli, F.; et al. Prolonged Exposure to Simulated Microgravity Promotes Stemness Impairing Morphological, Metabolic and Migratory Profile of Pancreatic Cancer Cells: A Comprehensive Proteomic, Lipidomic and Transcriptomic Analysis. *Cell. Mol. Life Sci.* **2022**, *79*, 226. [CrossRef] [PubMed]
55. Häder, D.-P.; Braun, M.; Hemmersbach, R. Gravity Sensing, Graviorientation and Microgravity. In *Gravitational Biology I*; SpringerBriefs in Space Life Sciences; Springer International Publishing: Cham, Switzerland, 2018; pp. 1–11, ISBN 9783319938936.
56. ElGindi, M.; Sapudom, J.; Laws, P.; Garcia-Sabaté, A.; Daqaq, M.F.; Teo, J. 3D Microenvironment Attenuates Simulated Microgravity-Mediated Changes in T Cell Transcriptome. *Cell. Mol. Life Sci.* **2022**, *79*, 508. [CrossRef] [PubMed]
57. ElGindi, M.; Sapudom, J.; Garcia Sabate, A.; Chesney Quartey, B.; Alatoom, A.; Al-Sayegh, M.; Li, R.; Chen, W.; Teo, J. Effects of an Aged Tissue Niche on the Immune Potency of Dendritic Cells Using Simulated Microgravity. *NPJ Aging* **2023**, *9*, 14. [CrossRef] [PubMed]
58. Svejgaard, B.; Wehland, M.; Ma, X.; Kopp, S.; Sahana, J.; Warnke, E.; Aleshcheva, G.; Hemmersbach, R.; Hauslage, J.; Grosse, J.; et al. Common Effects on Cancer Cells Exerted by a Random Positioning Machine and a 2D Clinostat. *PLoS ONE* **2015**, *10*, e0135157. [CrossRef] [PubMed]
59. Liu, Q.; Luo, Q.; Ju, Y.; Song, G. Role of the Mechanical Microenvironment in Cancer Development and Progression. *Cancer Biol. Med.* **2020**, *17*, 282–292. [CrossRef]
60. Jokela, T.A.; LaBarge, M.A. Integration of Mechanical and ECM Microenvironment Signals in the Determination of Cancer Stem Cell States. *Curr. Stem Cell Rep.* **2021**, *7*, 39–47. [CrossRef]
61. Mierke, C.T. Bidirectional Mechanical Response between Cells and Their Microenvironment. *Front. Phys.* **2021**, *9*, 749830. [CrossRef]

62. Larose, T.L. Tumors in Space: Preparation for Spaceflight. In *Preparation of Space Experiments*; Pletser, V., Ed.; IntechOpen: London, UK, 2020; ISBN 9781789851380.
63. Einstein, A. Grundgedanken Und Methoden Der Relativitätstheorie in Ihrer Entwicklung Dargestellt. In *The Berlin Years: Writings*; Janssen, M., Lehner, C., Buchwald, D., Eds.; Princeton University Press: Princeton, NJ, USA, 1918; Volume 7.

Disclaimer/Publisher's Note: The statements, opinions and data contained in all publications are solely those of the individual author(s) and contributor(s) and not of MDPI and/or the editor(s). MDPI and/or the editor(s) disclaim responsibility for any injury to people or property resulting from any ideas, methods, instructions or products referred to in the content.

International Journal of
Molecular Sciences

MDPI

Article

Real Microgravity Influences the Cytoskeleton and Focal Adhesions in Human Breast Cancer Cells

Mohamed Zakaria Nassef [1], Sascha Kopp [1], Markus Wehland [1], Daniela Melnik [1], Jayashree Sahana [2], Marcus Krüger [1], Thomas J. Corydon [2,3], Hergen Oltmann [4], Burkhard Schmitz [4], Andreas Schütte [4], Thomas J. Bauer [1], Manfred Infanger [1] and Daniela Grimm [1,2,5,*]

1 Clinic for Plastic, Aesthetic and Hand Surgery, Otto von Guericke University Magdeburg, D-39120 Magdeburg, Germany
2 Department of Biomedicine, Aarhus University, DK-8000 Aarhus C, Denmark
3 Department of Ophthalmology, Aarhus University Hospital, DK-8000 Aarhus C, Denmark
4 Airbus Defence and Space GmbH, Airbus-Allee 1, D-28199 Bremen, Germany
5 Gravitational Biology and Translational Regenerative Medicine, Faculty of Medicine and Mechanical Engineering, Otto von Guericke University Magdeburg, D-39120 Magdeburg, Germany
* Correspondence: dgg@biomed.au.dk; Tel.: +45-871-69693

Received: 23 May 2019; Accepted: 26 June 2019; Published: 28 June 2019



Abstract: With the increasing number of spaceflights, it is crucial to understand the changes occurring in human cells exposed to real microgravity (r-μ*g*) conditions. We tested the effect of r-μ*g* on MCF-7 breast cancer cells with the objective to investigate cytoskeletal alterations and early changes in the gene expression of factors belonging to the cytoskeleton, extracellular matrix, focal adhesion, and cytokines. In the Technische Experimente unter Schwerelosigkeit (TEXUS) 54 rocket mission, we had the opportunity to conduct our experiment during 6 min of r-μ*g* and focused on cytoskeletal alterations of MCF-7 breast cancer cells expressing the Lifeact-GFP marker protein for the visualization of F-actin as well as the mCherry-tubulin fusion protein using the Fluorescence Microscopy Analysis System (FLUMIAS) for fast live-cell imaging under r-μ*g*. Moreover, in a second mission we investigated changes in RNA transcription and morphology in breast cancer cells exposed to parabolic flight (PF) maneuvers (31st Deutsches Zentrum für Luft- und Raumfahrt (DLR) PF campaign). The MCF-7 cells showed a rearrangement of the F-actin and tubulin with holes, accumulations in the tubulin network, and the appearance of filopodia- and lamellipodia-like structures in the F-actin cytoskeleton shortly after the beginning of the r-μ*g* period. PF maneuvers induced an early up-regulation of *KRT8, RDX, TIMP1, CXCL8* mRNAs, and a down-regulation of *VCL* after the first parabola. E-cadherin protein was significantly reduced and is involved in cell adhesion processes, and plays a significant role in tumorigenesis. Changes in the E-cadherin protein synthesis can lead to tumor progression. Pathway analyses indicate that VCL protein has an activating effect on *CDH1*. In conclusion, live-cell imaging visualized similar changes as those occurring in thyroid cancer cells in r-μ*g*. This result indicates the presence of a common mechanism of gravity perception and sensation.

Keywords: microgravity; breast cancer cells; cytoskeleton; tubulin; F-actin; focal adhesion; E-cadherin; vinculin; live-cell imaging

1. Introduction

Cancer is a burden of mankind with a high morbidity and mortality and is responsible for an estimated 9.6 million deaths, according to the World Health Organization (WHO) Global Cancer Observatory (GLOBOCAN) data indicated in 2018 [1]. The GLOBOCAN statistics from 2018 published

that breast cancer is the most common cancer in women and the second leading cause of cancer deaths worldwide [1]. More women are diagnosed with breast cancer in 2019 than with any other cancer, besides skin cancer. In 2019, an estimated 268,600 women in the United States will be diagnosed with invasive breast cancer, and 62,930 women with in situ breast cancer [2]. In addition, an estimated 2670 men in the United States will be diagnosed with breast cancer.

Due to the high mortality, new ways must be taken to find new approaches and therapeutic strategies in cancer research. Experiments performed in the space environment are not typically the main topic of cancer researchers [3]. However, a stay in orbit on the International Space Station (ISS) provides physical conditions that are not achievable on Earth. Studying the mechanisms of microgravity-dependent cellular and molecular changes is necessary to improve space medicine and to develop new treatment strategies for cancer patients [4].

Gravity is the most familiar force in human life [5]. In space, the gravity force is lowered, resulting in microgravity (μg). Although human cells do not have a gravity sensor, they can still sense μg through the cytoskeleton [6]. The response of cells to early μg, together with changes in actin and microtubules, has been reported for different kinds of cells [7–10]. Moreover, human thyroid cancer cells have demonstrated a response to early μg by alterations in the cytoskeleton such as disturbance of F-Actin bundles, formation of lamellipodia- and filopodia-like structures and cellular detachment [11]. When cells are subjected to μg for a longer duration, they tend to form three-dimensional (3D) aggregates, so-called multicellular spheroids (MCS) [12].

There are several options to study cells real microgravity (r-μg), such as parabolic flights, sounding rockets missions, unmanned BION and photon spaceflights or a spaceflight in orbit or to the ISS with a commercial carrier. The Technische Experimente unter Schwerelosigkeit (TEXUS, TX) sounding rocket program, offered by the Deutsches Zentrum für Luft- und Raumfahrt (DLR, German Aerospace Center), offers researchers six minutes of μg to conduct their experiments [11,13,14]. We participated in the TX54 mission with the main objective of study cytoskeletal alterations of breast cancer cells in r-μg. Moreover, we attended the 31st DLR parabolic flight campaign (PFC) and investigated morphological changes and focused on the gene expression of selected genes of interest. The Michigan cancer foundation (MCF)-7 cell line was chosen as a suitable candidate for both the TX 54 mission and the PFC. As an alternative to conducting experiment in r-μg, which often is very expensive and time consuming, researchers may choose to investigate biological processes in simulated μg. The simulation of μg is achievable by using the rotating wall vessel (RWV), the random positioning machine (RPM), a 2D or 3D clinostat, and magnetic levitation [15]. These special conditions had been applied to study changes in cell growth and the function of different benign cell types and cancer cells, and may to some extent resemble the findings provided by r-μg [16].

The MCF-7 cell line had been investigated for several times under altered μg conditions in space and on Earth. The MCF-7 cell line showed a robust behavior in μg, and MCF-7 cells had been tested in space in a Photon capsule [17]. The MCF-7 cells reacted by exhibiting alterations in microtubules [17]. In addition, the MCF-7 cells exerted a loosening of the perinuclear cytokeratin network [18]. RPM-exposure experiments of the MCF-7 cells revealed changes in their growth behavior.

In this paper, we report for the first-time live-cell imaging of breast cancer cells on board a sounding rocket (TX 54). Live-cell imaging was performed with a spinning-disc Fluorescence Microscopy Analysis System (FLUMIAS) [11]. The objective of this study was first to focus on changes in the microtubule and F-actin cytoskeleton. Second, we investigated the changes in expression, distribution and localization of selected proteins by indirect immunofluorescence of fixed cells during μg. Third, we examined MCF-7 cells exposed to PF maneuvers and addressed changes in the gene expression patterns of genes encoding for components of the cytoskeleton, the extracellular matrix (ECM), focal adhesion molecules and cytokines.

2. Results

The TEXUS program is an established DLR-sponsored sounding rocket program which offers researchers precious μ*g* time to test their hypotheses [19]. The sounding rocket has the advantage of providing a relatively longer time (6 min) period of r-μ*g* compared to the parabolic flights. Moreover, it has only one period of hypergravity (hyper-*g*) and vibration at the beginning prior to the r-μ*g* phase.

2.1. TEXUS 54 Sounding Rocket Mission: "Live-Cell Imaging of Human Breast Cancer Cells in Short-Term Weightlessness"

The cytoskeleton is a highly dynamic structure playing a crucial role in adaptation and cell signaling processes in μ*g*. We first examined human MCF-7 breast cancer cells on a sounding rocket and studied the early cytoskeletal alterations (F-actin, α-tubulin).

MCF-7 cells exhibited three forms of growth when cultured for 24 days and five days under s-μ*g* conditions. One part grew adherently on the cell culture flask bottom, a second group formed duct-like multicellular spheroids and a third group revealed compact spheroids on the RPM after a five-day exposure, whereas after 24h only adherent cells and compact MCS were visible [20,21]. The MCF-7 cells were transfected with a Sleeping Beauty transposon-based (pSB-LAGICT) expression construct to visualize F-actin and α-tubulin. The LAGICT (LifeAct-eGFP-IRES-mCherry-Tubulin) expression cassette enables simultaneous examination of F-actin and α-tubulin, through co-expression of Lifeact GFP and mCherry-tubulin fusion proteins, respectively. Transfected MCF-7 cells were examined with the FLUMIAS microscope with 488 nm and 568 nm diode lasers prior to launch and during r-μ*g*. All the images taken at r-μ*g* were compared to control images (Figure 1) which were taken before launch. We showed that MCF-7 cells respond to r-μ*g* within four minutes and demonstrate similar changes as the FTC-133 thyroid cancer cells studied in previous campaigns [11]. This indicates a general gravitational mechanism in human cancer cells. During the r-μ*g* phase of the TEXUS flight, various changes in the cytoskeleton were seen, including a clear influence on the F-actin bundles and the appearance of filopodia/lamellipodia-like structures (Figure 1).

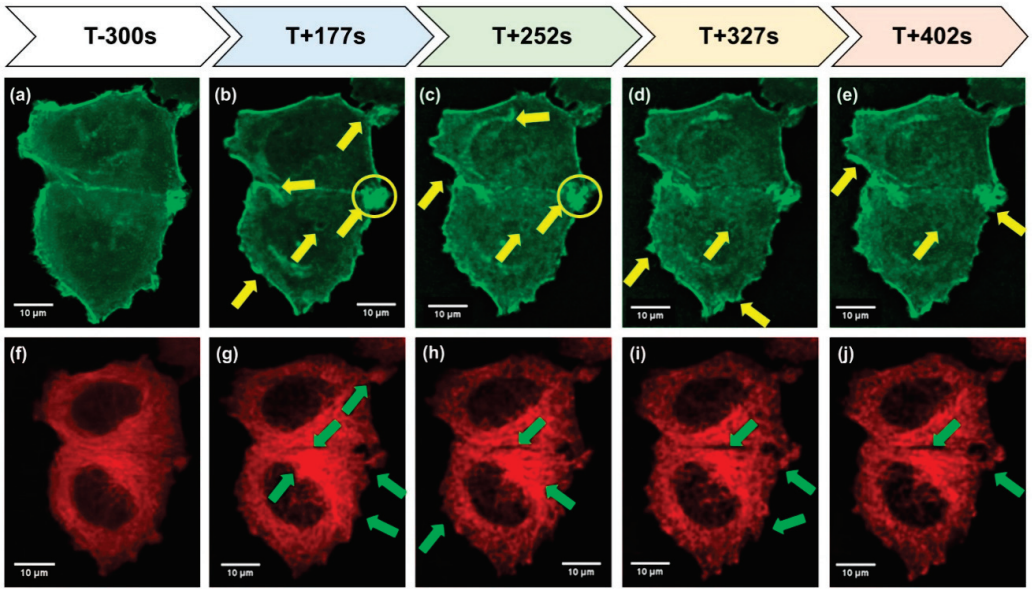


Figure 1. Time course and images of FLUMIAS on TEXUS 54 (40×/1.2). The MCF-7 breast cancer cells 5 min before launch (T-300 s) of the rocket and during the r-μ*g* phase (T + 177s–T + 402s). The yellow arrows show the changes in F-actin (**a**–**e**; green fluorescence). The yellow circles include an area with F-actin accumulations. Filopodia and lamellipodia are found after 150s, which are more pronounced with time. The green arrows indicate changes in α-tubulin (**f**–**j**; red fluorescence). The tubulin network reveals holes after 150s and a looser structure.

2.2. Immunostaining of MCF 7 Cells Exposed to r-µg during the TEXUS 54 Sounding Rocket Mission and Fixed in Orbit

In addition to the live-cell imaging studies of the transfected MCF-7 cells, regular MCF-7 cells were seeded into 18-well Ibidi slides which were fixed with 4% PFA at the end of the *µg* period and the hyper-g period. These slides were compared to a control slide fixed with 4% PFA on ground. Thus, we had the opportunity to investigate the changes in expression and distribution of the designated proteins. We tested the antibodies MMP9, VEGFA (c-term), IL-6 and IL-8. Phalloidin rhodamine and DAPI stains were used additionally for all the slides from the TX 54 mission.

Upon visual inspection of the microscopic images, there was no apparent difference in the protein distribution between the different conditions for all the tested antibodies (Figure 2a–l). In order to provide an indication on whether the level of the visualized proteins may have changed, the microscopic images were analyzed at the end of the hyper-*g* and µ*g* phases in comparison to the controls by using the ImageJ program. At the end of the hyper-*g* phase, the analysis indicated that the level of F-actin was increased (Figure 2c,f,i,l,o) compared to the controls (Figure 2a,d,g,j), while the level of MMP9 (Figure 2a,c), IL-6 (Figure 2g,i) and IL-8 (Figure 2j,l) apparently was reduced (Figure 2m,p,q). VEGF exhibited no changes at the end of hyper-*g* phase (Figure 2d,f,n). Furthermore, the microscopic images at the end of the r-µ*g* phase were also investigated in comparison to the controls. The levels of VEGF and F-actin appeared to be increased (Figure 2n,o), while the levels of MMP9, IL-6 and IL-8 apparently were unchanged (Figure 2m,p,q).

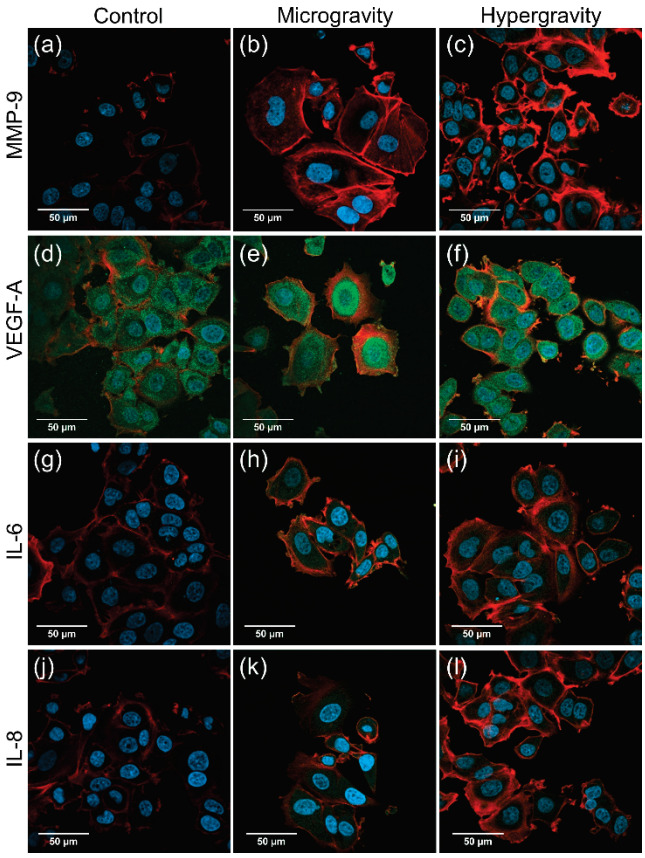


Figure 2. *Cont.*

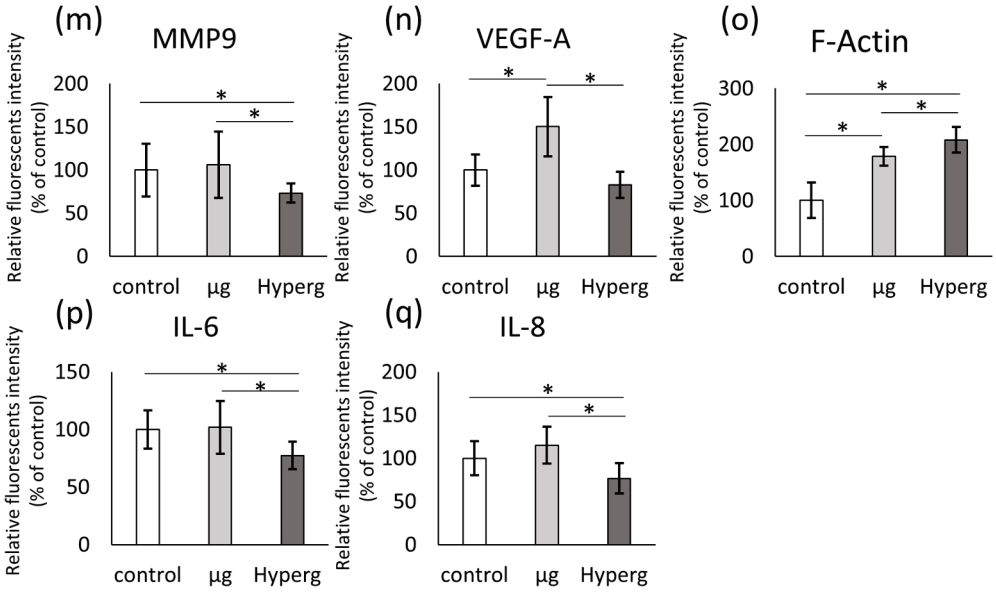


Figure 2. Indirect immunofluorescence staining of PFA-fixed cells from the TEXUS 54 sounding rocket mission. 2500 MCF-7 cells were seeded into each well of the 18 well Ibidi slides. The cells were fixed either at the end of the hyper-*g* period or at the end of the µ*g* period. The two conditions were compared to 1*g*-ground control samples. The confocal laser scanning microscopy images (**a**–**l**) show either MMP9, VEGF-A, IL-6 or IL-8 in green, DAPI (in blue) and F-Actin (in red). Scale bar is equal to 50 µm. The intensity of the staining was quantified by ImageJ (**m**–**q**). All data are shown as mean ± SD, n = 10–14, with significance indicated by * $p < 0.05$.

2.3. Results of the 31st DLR Parabolic Flight Campaign: "Effects Of Short-Term Microgravity on Human Breast Cancer Cells"

The PFCs were organized by the DLR in close collaboration with the company Novespace, Bordeaux-Mérignac, France. A parabolic flight consisted of 31 consecutive parabolas. Each parabola contains two phases of 1.8 *g* hyper-*g* spanning one phase of 10^{-2} *g* r-µ*g*. The first phase of a parabola begins with flying at 45 degrees for 22 s known as pull-up, followed by decreasing thrust and following the trajectory of a parabola for 22 s of free-fall. Thus, the r-µ*g* phase lasts for the 22 s of the free-fall. The last phase is known as pull-out which begins pulling out the plane to fly back on a horizontal line trajectory. The pull-up phase lasts for 22 s with hyper-*g* of 1.8 *g* [16,22,23]. Not only does the parabolic flight have the advantage of offering valuable r-µ*g* time to researchers, but also it gives the scientists access to their experiment on board of the flight.

The 31st DLR PFC took place in March 2018 at the company Novespace at the Bordeaux-Mérignac airport in France. The breast cancer cells (MCF-7 cell line) were examined after parabola 1 (P1) and after 31 parabolas (P31). At the same time, the ground control experimentation took place in the laboratories of Novespace. Subsequently, the fixed cells were transported to the Otto von Guericke University Magdeburg, Germany, where they were examined by molecular biology. We performed qPCR, Western blot and pathway analyses. The results are shown in the following Figures 3–10. Figures 3–8 each show the following groups: static ground controls (1*g*), P1 and P31.

2.3.1. Studies on Cytoskeletal Genes

Figure 3 gives the expression of the cytoskeletal genes and Figure 4 shows the levels of the corresponding proteins. There were no changes after P1 for the *ACTB*, *TUBB*, *EZR*, *RDX* and *MSN* mRNAs. However, there was a significant up-regulation of *KRT8* after P1 and P31 compared to 1*g* (Figure 3c) and of *RDX* after P31 (Figure 3e). The cytokeratin protein synthesis was also significantly increased after the first parabola but returned to control levels after 31 parabolas (Figure 4c).

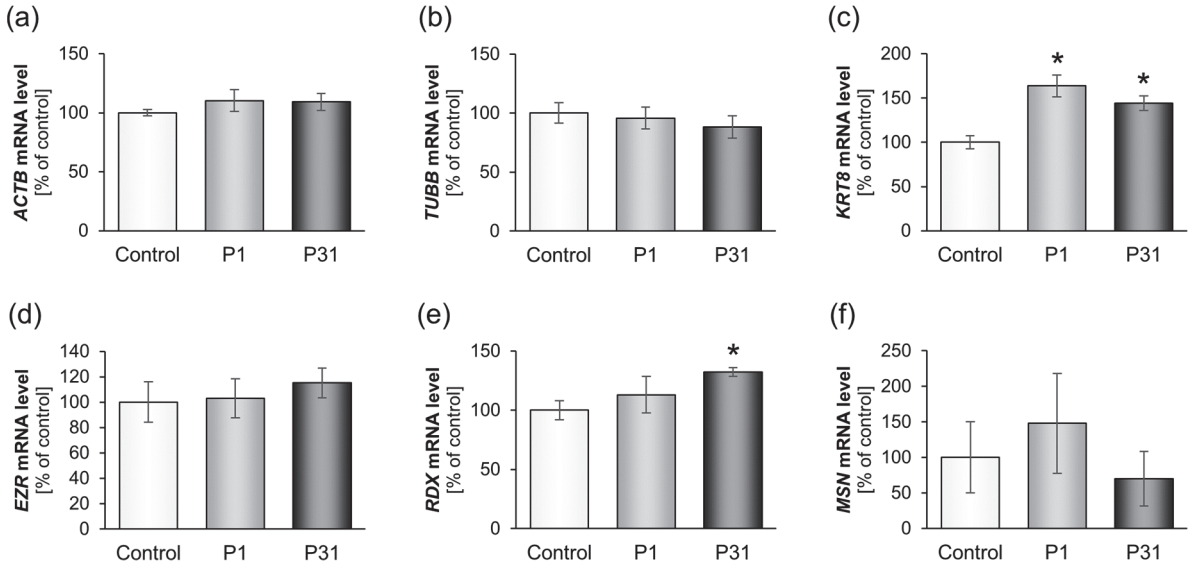


Figure 3. Influence of short-term microgravity on the gene expression (mRNA) of cytoskeletal factors. The data are given as mean ± standard deviation. * $p < 0.05$ vs. Control.

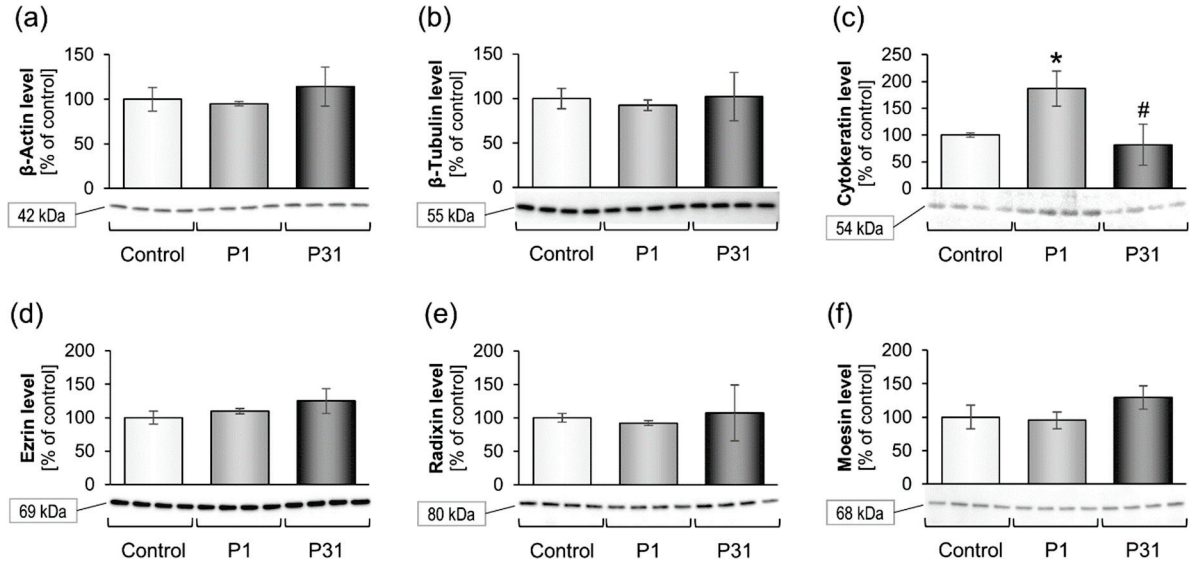


Figure 4. Influence of short-term microgravity on the protein accumulation of cytoskeletal factors. The data are given as mean ± standard deviation. * $p < 0.05$ vs. Control; # $p < 0.05$ vs. P1.

2.3.2. Altered Expression of Genes of the Focal Adhesion Complex

Furthermore, we examined the mRNA expression and protein content of focal adhesion molecules (Figures 5 and 6). The *VCL* gene and corresponding vinculin protein were significantly reduced under r-μ*g* (Figures 5a and 6a). *TLN1*, *ITGB1*, *CDH1*, *PTK2*, *CAV1* and *CAV2* remained unchanged under r-μ*g*, while the E-cadherin protein (Figure 6c) as well as β_1-integrin protein (Figure 6b) were significantly reduced. FAK1 protein was elevated after P1 (Figure 6d).

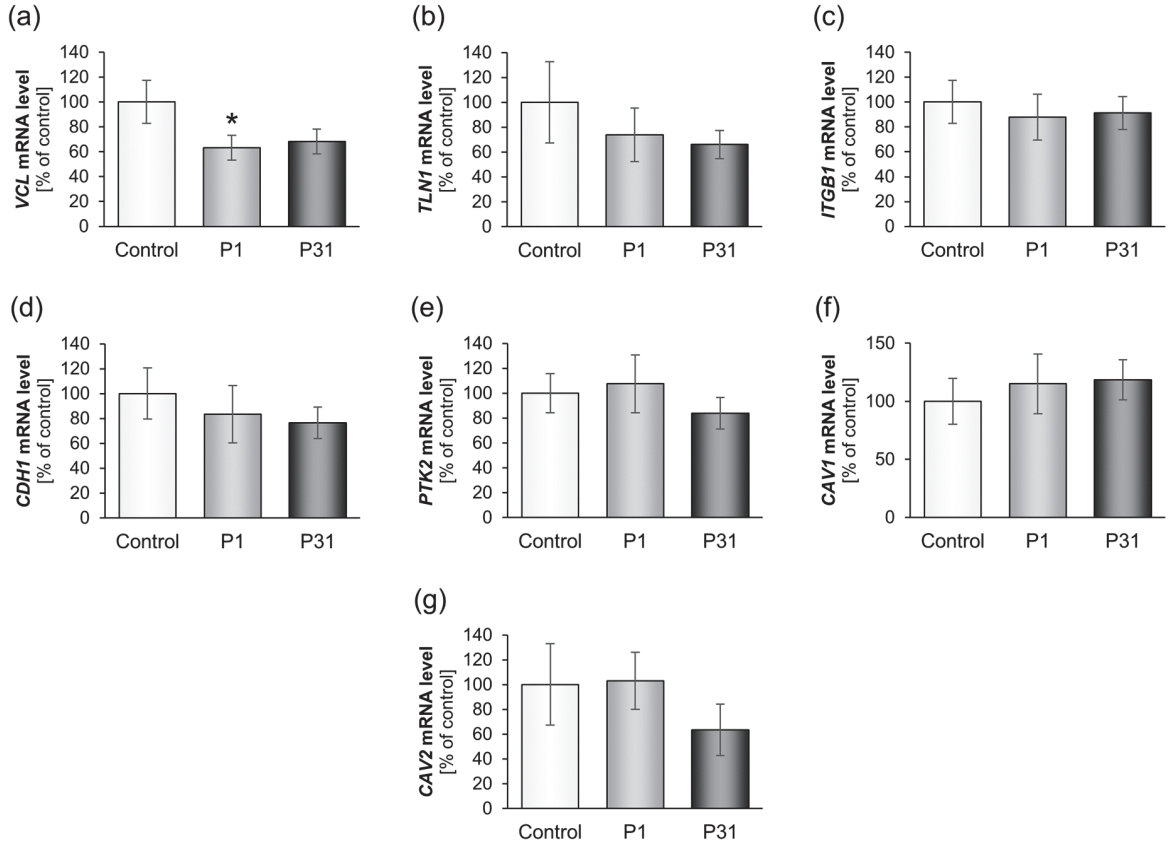


Figure 5. Influence of short-term microgravity on the expression (mRNA) of focal adhesion complex components. The data is given as mean ± standard deviation. * $p < 0.05$ vs. Control.

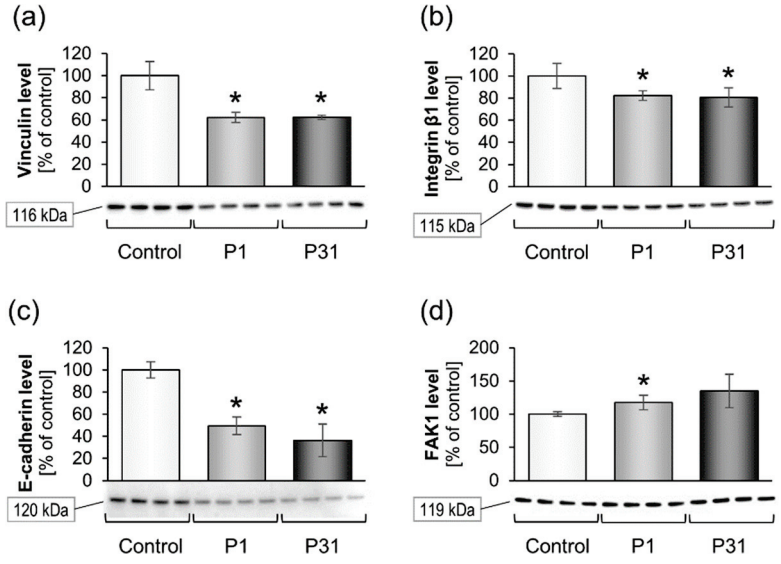


Figure 6. Influence of short-term microgravity on the protein accumulation of focal adhesion complex components. The data is given as mean ± standard deviation. * $p < 0.05$ vs. Control.

2.3.3. Changes of Extracellular Matrix and Cytokine Gene Expression

The results on the extracellular matrix proteins are shown in Figures 7 and 8. There were no changes in the gene expression for *LAMA1*, *LAMA3*, *COL1A1*, *FN1*, *MMP9* and *PAI1* (*SERPINE1*). The *TIMP1* mRNA was significantly elevated after P31 compared with ground control samples (Figure 7e). In addition, we investigated the expression of the cytokines IL-6 and IL-8, which play

a major role in spheroid formation. The *IL6* mRNA was not significantly changed, but there was a tendency of an up-regulation after P1 and P31 (Figure 7h). In contrast, *CXCL8* was significantly up-regulated after P1, and slightly elevated after P31 (Figure 7i). A similar behavior showed the corresponding IL-8 protein synthesis, which was significantly increased after P1 and P31 (Figure 8). Moreover, a significant elevation of the *VEGFA* mRNA was detectable (Figure 7j).

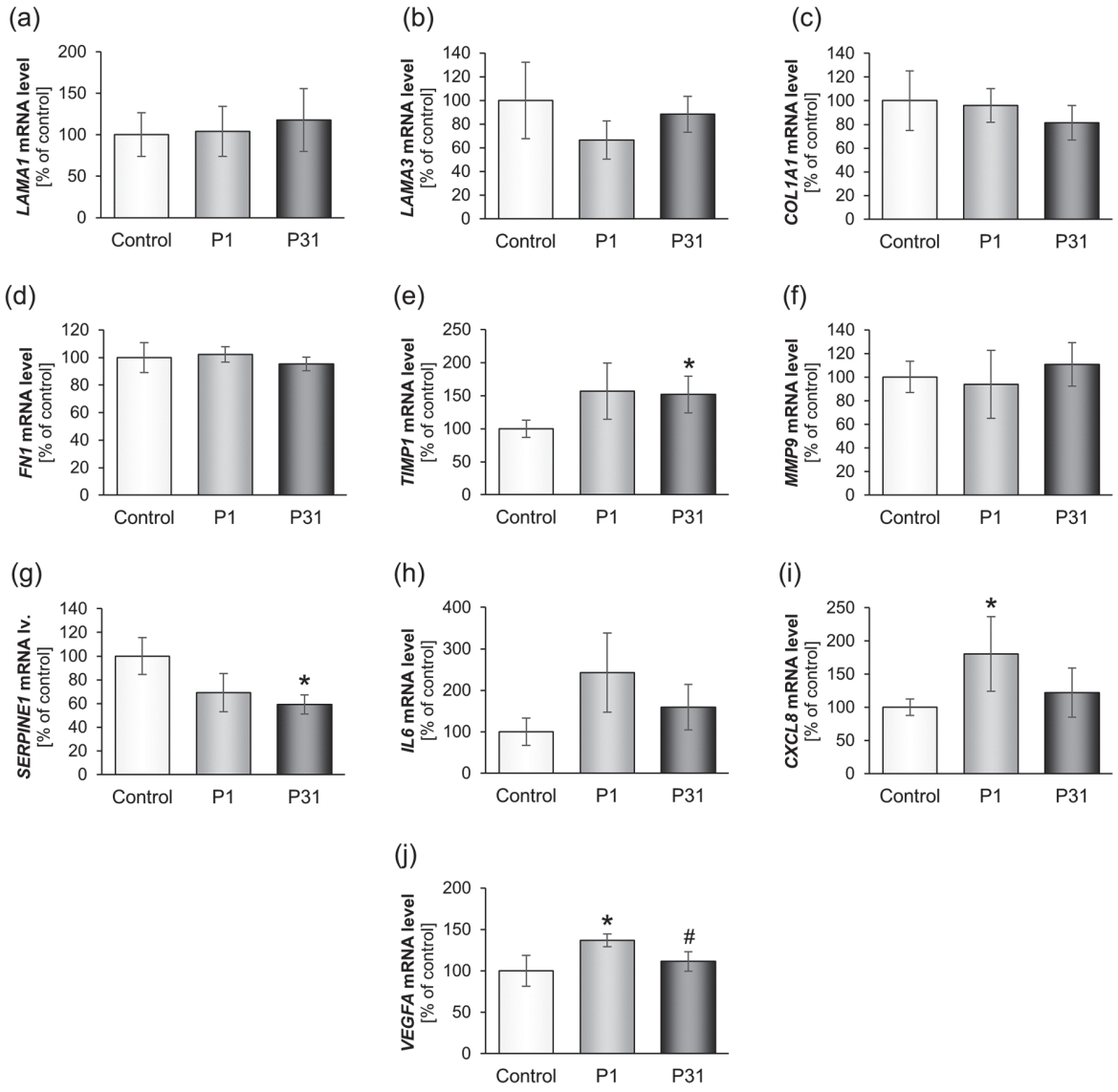


Figure 7. Influence of short-term microgravity on expression of different ECM and cytokine genes. * $p < 0.05$ vs. Control; # $p < 0.05$ vs. P1.

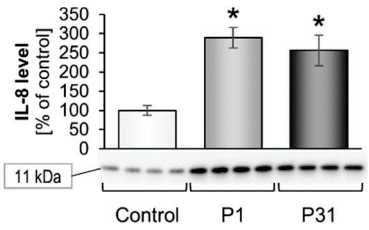


Figure 8. Influence of short-term microgravity on the protein accumulation of IL-8. The data is given as mean ± standard deviation. * $p < 0.05$ vs. Control.

2.3.4. Pathway Analyses

The results of the pathway analysis given in Figure 9 indicate a clear role for *ITGB1*, *FN1*, *TLN1*, *CDH1*, *PTK2* and *VCL* in gravity sensing of MCF-7 breast cancer cells exposed to short-term r-μg.

FN1, *VEGFA*, *TLN1* and *TIMP1* proteins are positively influencing β_1-integrin which is inducing *PTK2* and fibronectin. *TLN1* is interacting with *PTK2* and *FN1*. Vinculin is activating E-cadherin, whereas ezrin has a negative influence on *CDH1*. Moreover, *TIMP1* is inhibiting *MMP9*.

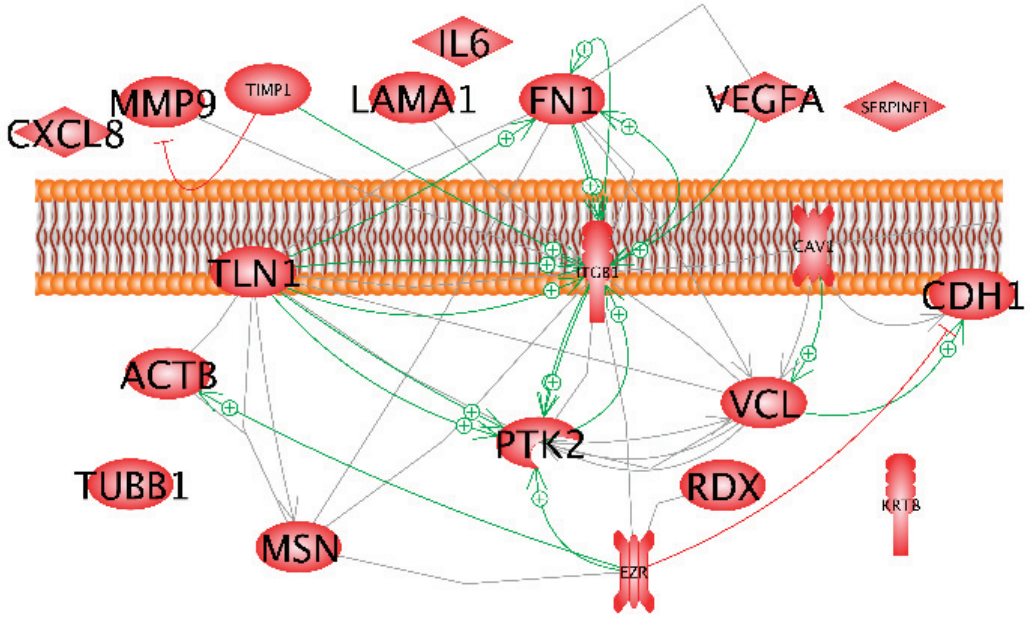


Figure 9. Interaction and localization of proteins detected in the cells by Western blot (red margins). Solid lines indicate the bond. Filled arrows show the directional interaction and dashed arrows show the influence. + Signs indicate activity − inducing effect and red lines indicate inhibition.

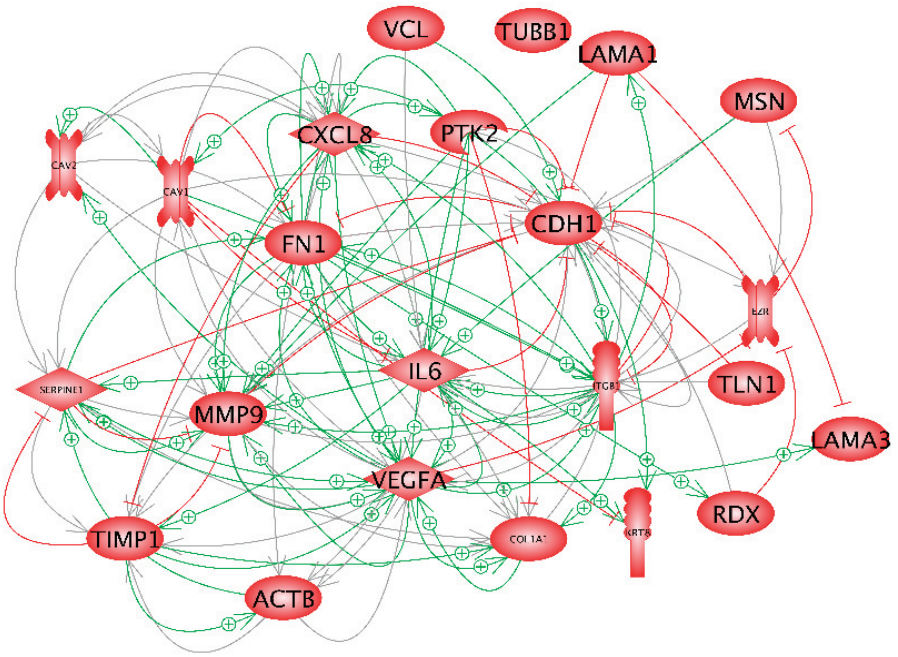


Figure 10. Mutual interactions of expression of the genes examined with qPCR and shown in Figures 2–4. + Signs indicate an activity-enhancing effect and red lines indicate inhibition. The interaction networks were created using Elsevier Pathway Studio v11.

The interaction network shown in Figure 10 indicates a fast significant up-regulation of *KRT8*, *RDX*, *TIMP1* and *CXCL8*, while *VCL* is down-regulated. Simultaneously, *TLN1* and *CDH1* indicate a slight but non-significant reduction of gene expression. Considering the red lines together with the qPCR results cell adhesion via *CDH1* seems to be attenuated. Various genes demonstrate an inhibitory effect on *CDH1* (Figure 9).

3. Discussion

In this study we investigated MCF-7 breast cancer cells in real microgravity using two experimental platforms offered by a sounding rocket mission and a parabolic flight. Live-cell imaging visualized similar changes as those occurring in thyroid cancer cells, when they were exposed to r-μg. Our results now indicate the presence of a common cellular mechanism for sensing gravity. After entering microgravity, the MCF-7 cells showed a rearrangement of F-actin and tubulin comprising holes, accumulations in the tubulin network, and the appearance of filopodia- and lamellipodia-like structures. Up-regulation of *VEGF* and down-regulation of E-cadherin during parabolic flight maneuvers indicated a temporary change to a more invasive phenotype of MCF-7 cells. This finding also supports earlier data gained from thyroid cancer cells and may hint at a general cellular answer of cancer cells to short-term microgravity.

There is evidence that in vitro cell cultures respond to altered gravity conditions. Studies suggest that this response might be involved in the physiological changes and fundamental health problems of humans during spaceflight [24]. Microgravity alters adhesion, migration, proliferation, differentiation, growth, signaling and gene expression [25]. The cytoskeleton is discussed as the initial gravity sensor [26]. For example, bone cells exposed to r- and s-μg show changes in their cytoskeleton and focal adhesions, two major mechanosensitive structures [27,28]. Similar results were obtained when investigating thyroid cancer and melanoma cells cultured under μg-conditions [14,29].

Live-cell imaging of benign and tumor cells is possible using the FLUMIAS microscope which was flown on parabolic flight missions, sounding rocket missions and a more advanced version to the ISS [11,30].

3.1. Cytoskeletal Alterations Visualized during the TEXUS 54 Mission

The principal aim of our experiment onboard the TX 54 sounding rocket was to investigate the effect of r-μg on the cytoskeleton of human breast cancer cells.

During the flight, MCF-7 cells exhibited alterations in the F-actin and microtubule cytoskeleton. The appearance of filopodia- and lamellipodia-like structures shortly after the beginning of the r-μg period is comparable to the results which we have obtained with FTC-133 thyroid cancer cells during the TX 52 mission [11]. This data indicates that the gravi-sensing is similar in both cancer types. We could visualize impressing changes of alpha-tubulin during the r-μg phase. This supports earlier results [20]. Investigating suspensions of purified tubulin, Moos et al. [31] found a significant difference between microtubules assembled in the 30 s μg phase and the 2g hyper-g phase of a PF. These data reveal that microtubule polymerization is altered by altered gravity. These results were substantiated by sounding rocket [32] and shuttle flight [33] experiments.

In addition, an immunofluorescence staining on MCF-7 cells was performed. The cell fixation was done automatically during the r-μg phase of the TX 54 mission. The quantitative analysis of VEGF exhibited an up-regulation of the protein in the r-μg condition compared to the controls. We also measured an accumulation of F-actin. While VEGFA was up-regulated only in the r-μg condition, F-actin was increased in both the hyper-g and r-μg conditions. The significant up-regulation of a protein in both μg and hyper-g conditions indicates that hyper-g was the main inducer for the up-regulation, because the hyper-g period precedes the μg period. The F-actin content was elevated in A431 epidermoid carcinoma cells after a 7-min μg-exposure during a sounding rocket flight [34]. Boonstra concluded that the actin microfilament system is sensitive to altered gravity conditions

and that its remodeling may affect signal transduction [34]. Reflecting our results, we can support this hypothesis.

Therefore, we can conclude that only VEGF showed a clear up-regulation in r-μ*g* compared to the control. This data fits to earlier results obtained during a PF mission, where *VEGF* was significantly up-regulated after P1 and P31 [16]. VEGF is a key inducer of angiogenesis and enhances spreading and metastasis [35,36]. Serum VEGF was significantly elevated in patients with metastatic differentiated thyroid cancer but not in those with poorly differentiated thyroid cancer metastases [37]. The release of VEGF by FTC-133 exposed to space conditions during the Shenzhou-8 spaceflight was high but not significantly different in 1*g* samples and r-μ*g* samples, but the gene expression of *VEGFA* was down-regulated after a 10-day mission [16].

3.2. MCF-7 Breast Cancer Cells Exposed to PF Maneuvers during the 31st DLR PFC

Earlier experiments investigating chondrocytes, endothelial cells, and thyroid cancer cells revealed that a short-term r-μ*g*-exposure (22 s) during PF maneuvers induced early cytoskeletal changes and an altered gene expression pattern in these different cell types [22,38,39]. These studies showed that the gravi-response of cancer and benign cells occurred very early, within the first few seconds [22,38,39]. Several gravi-sensitive signaling elements, such as AMP-activated protein kinase alpha 1 and integrins are involved in the reaction of endothelial cells to altered gravity conditions [38]. Down-regulated *MTSS1* and up-regulated *LIMA1* were key factors stabilizing the cytoskeleton of tumor cells under μ*g* conditions [39].

ECM proteins, focal adhesion and cytoskeletal components form a dynamic network interacting with signaling molecules as an adaptive response to altered gravity. These focal adhesions are integrin-containing structures that form mechanical links between intracellular actin bundles and the extracellular space of a cell. Focal adhesions are dynamic protein complexes through which the cytoskeleton of a cell connects to the ECM. The adhesion dynamics play a central role in cellular migration. Focal complexes are formed at the leading edge of the cell in lamellipodia.

We had first investigated the gene expression of cytoskeletal factors. Most cytoskeletal genes were not significantly altered but there was a significant up-regulation of the *KRT8* mRNA after P1 and P31. This finding is similar to earlier results with thyroid cancer cells [39].

Studying the genes of the focal adhesion complex we found a decrease in E-cadherin protein as well as β_1-integrin protein. Changes in the focal adhesion complex were also found in cells exposed to s-μ*g* and r-μ*g*. Tan et al. [29] reported about a reduction in focal adhesions in melanoma cells exposed to s-μ*g*. In space on board the SJ-10 satellite, the mechanosensitive molecules β_1-integrin, β-actin, α-tubulin, and others were elevated, whereas among others vinculin was down-regulated in bone marrow-derived mesenchymal stem cells [40]. In addition, the authors observed an accumulation of microtubules and vimentin through the altered expression and location of focal adhesion complexes [40].

Several ECM genes such as *FN1* were not altered during short-term μ*g* in MCF-7 breast cancer cells. This is different to the results which we obtained from low-differentiated ML-1 thyroid cancer cells [39]. During this PFC we detected an up-regulation of the *FN1* mRNA, which indicates a cancer type-specific reaction to μ*g*.

β_1-integrin, fibronectin, and PTK2 play essential roles, when cells bind to the extracellular matrix. β_1-integrin is involved in the proliferation and differentiation as well as in the development of epithelial tissues [41]. It is important for adhesion dynamics and essential for the control of cell migration and, therefore, is a marker for a poor prognosis in breast cancer [41]. β_1-integrin forms heterodimers with various α-types integrins. Some of these dimers are able to bind to fibronectin. After binding, signals are forwarded to FAK1 (Focal adhesion kinase 1 coded by *PTK2*) and talin (TLN1) [42].

Binding of β_1-integrin to fibrillar fibronectin promotes the phosphorylation of STAT3, which is known to participate in the induction of the epithelial mesenchymal transition [43]. In addition, β_1-integrin facilitates the secretion of fibronectin in a way which is poorly understood. Fibronectin remaining intracellular is directly interacting with the actin cytoskeleton [43], which is changed when the

cells are exposed to microgravity [20]. Moreover, β_1-integrin controls the VE-cadherin localization and blood vessel stability in the mouse retina [44]. VEGF can promote angiogenesis through up-regulation and/or activation of integrins [45]. The VEGF activity is dependent on β_1-integrin function.

FAK1 and talin are members of the focal adhesion complexes. Talin mediates cell-cell adhesion linking the integrins to the actin cytoskeleton and in the activation of integrins [46]. Talin was differentially regulated in AD and MCS of thyroid cancer cells exposed to simulated microgravity [47]. FAK1 is a cytoplasmic protein tyrosine, kinase which is found to be concentrated in the focal adhesions. It promotes the organization of the fibronectin matrix and fibrillar adhesions [48]. In addition, FAK1 triggers the recruitment of talin to nascent adhesions independently of integrin. It plays a key role in the migration process and FAK1 inhibition decreases mobility and metastasis. The β1-Integrin-FAK pathway is involved in cell survival and on the role of FAK in breast cancer development and progression [49]. In this study, the *PTK2* mRNA was stable in the breast cancer cells, but the corresponding protein showed an elevation after P1 (Figure 6d). This is different to the data obtained with thyroid cancer cells, where the *PTK2* mRNA in FTC-133 thyroid cancer cells was differentially expressed in the TEXUS samples, but the FAK1 protein content was significantly reduced in RPM samples [14].

The pathway analysis of the investigated genes revealed important roles of *CDH1* and *VEGFA* in the network. These genes are under the influence of IL-6 and IL-8, which both exert inhibitory effects on CDH1 and promoting effects on VEGFA. IL-6 promotes e-cadherin repression [50] and treating human gastric carcinoma cells with exogenous IL-8 decreased expression of E-cadherin mRNA [51]. IL-6 and IL-8 induce the expression of VEGF [52,53]. The *CDH1* gene encodes e-cadherin, which establishes cell-cell junctions [54]. After a 2-week RPM-exposure, E-cadherin, was diminished in MCF-7 MCS cells, where proteins of the E-cadherin autodegradation pathway were enhanced as well as c-Src (proto-oncogene tyrosine-protein kinase c-Src) [55]. Blocking the E-cadherin activity by specific antibodies promoted spheroid formation. As indicated by the high number of red lines shown in Figure 10, *CDH1* gene expression is strongly controlled by a number of proteins. Of the investigated components, only vinculin has a positive modulatory influence (green arrow) [56].

But, in addition to IL-6 and IL-8, EZR, talin, PTK2, ITGB1 and MMP9 were already found to have inhibitory effects. E-cadherin and EZR are involved in tumor growth. In a patient study, the ezrin expression was upregulated, while that of E-cadherin was decreased in breast cancer as compared to the control specimen. Ezrin expression was negatively correlated to the E-cadherin expression in a subpopulation of breast cancer patients with a high expression of ezrin [ezrin(high)] and a low expression of E-cadherin [E-cad(low)] [57]. Talin regulates the stability of E-cadherin transcriptional repressors [58]. An increased expression of E-cadherin was observed after reducing the level of β_1-integrin in B16-F10 melanoma cells [59]. Treatment with recombinant MMP-9 or transient expression of MMP-9 is sufficient to reduce E-cadherin levels in differentiated ovarian tumor cells [60].

VEGFA encodes the vascular endothelial growth factor, which supports (neo)-vascularization of healthy and malignant tissues [61]. As mentioned above, IL-6 and IL-8 favor its expression. In addition, human astrocytoma cells expressed increased levels of fibronectin and VEGF upon transformation with a versican G3 construct [62] and VEGF expression was positively linked to MMP-9 levels in gastric carcinoma [63]. Overexpression of TIMP1 and PAI-1 in endothelial cells blocks vascular tube regression [64].

3.3. Microgravity-Induced Cytoskeleton Changes and Potent Physiological Responses

The cytoskeleton directs a number of essential cell functions, such as maintenance of cell shape, support of vacuole formation or fixation of organelles. The cytoskeleton is dynamic and not static, and it can disassemble and reassemble to contribute to cell mobility (Figure 11). It is involved in migration which is necessary for tissue repair and tumor spreading, progression and metastasis [65]. It is important for cellular signaling.

In this study, we demonstrate for the first time using live-cell imaging in real μ*g* that MCF-7 cells reveal a rearrangement of the F-actin and microtubule cytoskeleton with holes, accumulations in the tubulin network, and the appearance of filopodia- and lamellipodia-like structures in the F-actin cytoskeleton (Figure 1). In lamellipodia are ribs of actin called microspikes spreading beyond the lamellipodium frontier are then called filopodia, which are involved in cell adhesion and migration, healing processes and others. The initiation and elongation of filopodia is depending on polymerization, convergence and crosslinking of actin filaments [66]. Filopodia and filopodia-like structures are involved in 3D cell migration and thus in tumor dissemination, growth and metastasis [67]. Filopodia are normally situated at the front of invading cancer cells [68,69] and filopodia-like structures promote cancer cell survival at metastatic sites [70,71]. In Figure 11 the possible mechanism is demonstrated how these μ*g*-induced alterations of the cytoskeleton are involved in 3D growth and in the formation of multicellular spheroids, which resemble in vivo microtumors and metastases [65].

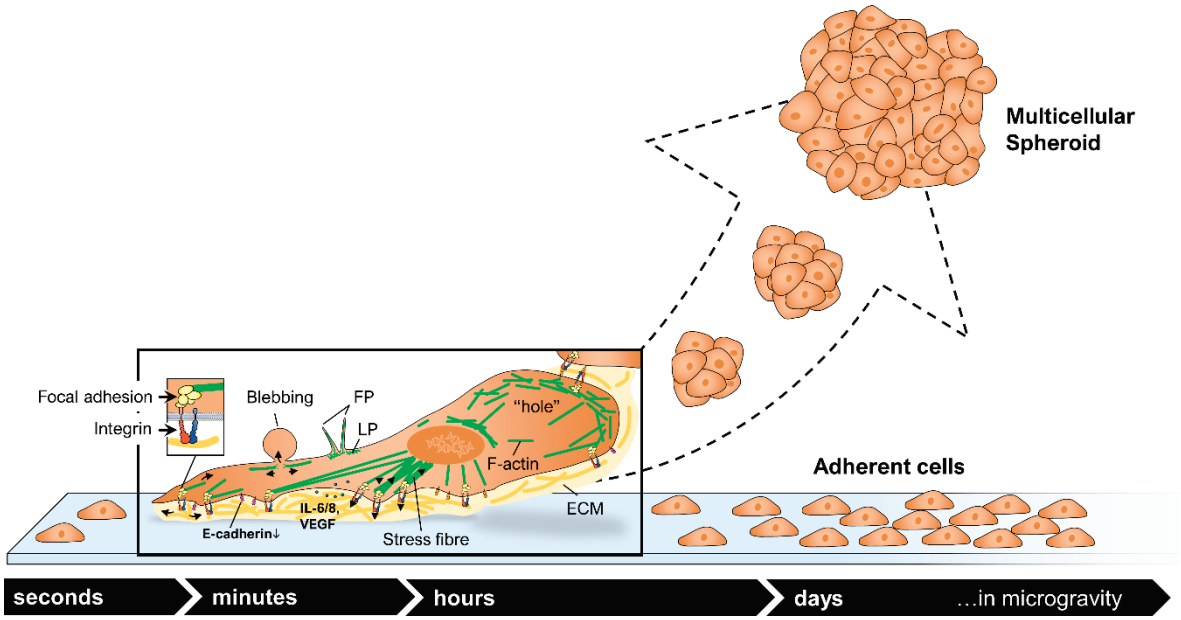


Figure 11. Alterations of adherently growing cancer cells after exposure to microgravity (modified from [65]). The figure in the box shows changes at the microscopic level. F-actin is displayed as green lines, the ECM in yellow. FP: filopodia, LP: lamellipodia.

In this study PF maneuvers induced a downregulation of *VCL* mRNA and the corresponding protein in MCF-7 breast cancer cells. Pathway analyses indicated that VCL protein has an activating effect on *CDH1*. E-cadherin is involved in cell adhesion and in tumorigenesis. Changes in the E-cadherin protein synthesis can lead to tumor progression. In addition, blockage of E-cadherin and a down-regulation of *CDH1* leads to enhanced spheroid formation of MCF-7 breast cancer cells [55,65].

r-μ*g*-induced changes in the cytoskeleton and/or in focal adhesion components of human cells as for example cancer cells and normal cells like osteoblasts, chondrocytes and cancer cells are the two major mechanosensitive responses [8,14,28]. The cytoskeleton responds to changes in the mechanical environment because of its connection to the ECM through focal adhesions. Exposure of human cells to *μg* impaired their cytoskeleton stability and reduced cellular tension, as well as focal adhesion formation and stability [8].

The ECM-membrane receptors-cytoskeleton system is known to be involved in cancer and metastasis [72]. Growth factor receptors, adhesion proteins and ion channels in association with the sub-membranous system of the actin cytoskeleton control the actin microfilament's force generating capacity. Perturbations of the actin microfilament system in cell motility and migration and their role in cancer pathophysiology are currently a hot topic [72].

The exact mechanisms how the cells transform the mechanical signal (microgravity) into a biochemical signal is still not known. The widely acknowledged tensegrity model hypothesis proposed by Ingber [73] explains that the cells are hardwired by the cytoskeleton components. The cells are spanned open and are under continuous tension [26,73]. An imbalance between adhesion and the cytoskeleton network might induce a cell shape change and has a direct impact on cell signaling [26,73]. This theory is supported by data of cytoskeletal changes in various benign and malignant cell types after short-term exposure to microgravity [11,16,21,22,38,74].

When microgravity conditions influence human adherent MCF-7 breast cancer cells, the microtubules (tubulin) rapidly reorient themselves and actin stress fibers increase in density in order to reinforce their mechanical strength. These changes in the F-actin and in microtubule network are followed by changes in adhesion, shedding of membrane receptors, cell detachment, migration, growth behavior, differentiation, and apoptosis [12,20,38,75]. These physiological changes have been detected in real microgravity and on Earth using various μ*g*-simulation devices [15].

In summary, an early up-regulation of *KRT8, RDX, TIMP1, CXCL8*, and down-regulation of *VCL* were found after the PF maneuvers. E-cadherin protein was reduced after the PF maneuvers. This result is very important because E-cadherin is not only involved in the cell adhesion process but plays a significant role in tumorigenesis. Changes in the E-cadherin protein can lead to tumor progression. VCL protein has an activating effect on *CDH1* (Figure 9). However, many of the genes investigated lead to an inhibition of *CDH1* (Figure 10). *CXCL8* is also important for tumor progression and the early up-regulation of the cytokine supports this thesis.

4. Materials and Methods

4.1. Cell Culture

The MCF-7 breast cancer cells were purchased from the American Type Culture Collection (MCF7, ATCC® HTB-22™). They were cultured in RPMI 1640 (Life Technologies, Paisley, UK), 10 % FCS (Sigma Aldrich, Steinheim, Germany) and 1% penicillin/ streptomycin (Life Technologies, New York, NY, USA). The Lifeact-eGFP-IRES-mCherry-Tubulin MCF-7 expressing cells were cultured in the same medium, in addition to G418 (Geneticin) to allow the growth of the stably transfected cells. The cells were cultured in T-75 flasks and the cells were harvested and seeded into other flasks every 3-5 days to prevent confluence.

4.2. Construction of An Expression Cassette to Visualize F-actin and α-tubulin

We constructed a pcDNA3.1 LifeAct-eGFP-IRES-mCherry-Tubulin (pLAGICT) expression cassette for visualization of F-acting and α-tubulin. In order to construct this expression cassette, pUC57 plasmid was ordered from GenScript. The required cassette LifeAct-eGFP-IRES-mCherry-Tubulin was excised from the pUC57 plasmid with NotI/XbaI restriction enzymes. The excised part was further purified by gel extraction and ligated into pcDNA3.1 (+) (Invitrogen, Carlsberg, CA, USA). The constructed plasmid was transformed into ultra-competent *Escherichia coli* cells to produce more copies of the plasmid. QIAprep spin column (Qiagen, Hilden, Germany) was used to extract the plasmid from the bacteria. More details about the construction of the expression cassette are mentioned in [11,76].

4.3. Generation of MCF 7 Cells Expressing Lifeact-eGFP-IRES-mCherry-Tubulin

The MCF-7 cell line was stably transfected using a Sleeping Beauty (SB) transposon-based vector containing the LAGICT expression cassette for the visualization of F-actin and α-tubulin as described in [11,77,78]. In brief, LifeAct-eGFP-IRES-mCherry-Tubulin was excised from the pLAGICT plasmid with NotI/XbaI restriction enzymes, and sub-cloned into a Sleeping Beauty transposon-based vector pT2/CMV-linker-SV40-Neo [78,79] containing a linker enabling insertion of the NotI-LAGICT-Xba1 fragment excised from the pLAGICT vector. The resulting plasmid, pT2/CMV-LAGICT-SV40-Neo, was

entitled pSB-LAGICT. In order to provide stable expression of the LifeAct-eGFP-IRES-mCherry-Tubulin expression cassette, MCF-7 cells were co-transfected with pSB-LAGICT and pCMV-SB100X [78], using X-tremeGENE 9 transfection (Roche, Basel, Switzerland) reagent according to the manufacturer's protocol [77]. Afterwards, the transfected cells were cultured in medium containing G418 (Geneticin) to allow growth of stably transfected cells only. A fluorescence microscope was used to validate the efficiency of the transfection.

4.4. Live Cell Imaging by the FLUMIAS Microscope

Approximately 7000 MCF-7 cells were seeded into one channel of an ibiTreat µ-slide VI 0.4 (Ibidi, Gräfelfingen, Germany). The slide was temperature controlled and loaded into the FLUMIAS microscope (developed by FEI Munich GmbH [11]) shortly before the launch (Figure 12). Five minutes prior to launch three z-stacks were obtained from pre-selected cells as a ground control. About 75s after launch the microgravity phase was reached, and the microscope started recording the pre-selected cells. Three z-stacks were taken every one minute with 125 ms exposure time. The thickness of the z-stack was 21 µm with 0.5 µm step size. The procedure was repeated four times with a total number of five active phases covering 6 min of microgravity.

After recovery of the image data, a single image was extracted from each z-stack taken during microgravity to allow analysis of all images in the focal plane. The extracted images were deconvolved by Huygens Essential Scientific Volume Imaging software 4.3 and compared to a control image taken on ground.

4.5. TEXUS 54 Sounding Rocket Mission

The late access unit (Figure 13) was transferred into the payload, along with the cells shortly before launch. The sounding rocket, used in the TEXUS 54 mission, was composed of the payload and a Brazilian two-stage solid propellant VSB 30 rocket. The rocket was launched on the 13th of May 2018 from ESRANGE space center in Kiruna, Sweden. After launch, the sounding rocket reached an altitude of ~260 km. And it entered microgravity 75 s later after launch. The microgravity phase of $< 10^{-4}$ g lasted for ~353 s. Following the microgravity phase, the rocket went back to Earth by a parachute-mediated deceleration. The payload was recovered after landing by a helicopter (Figure 13).

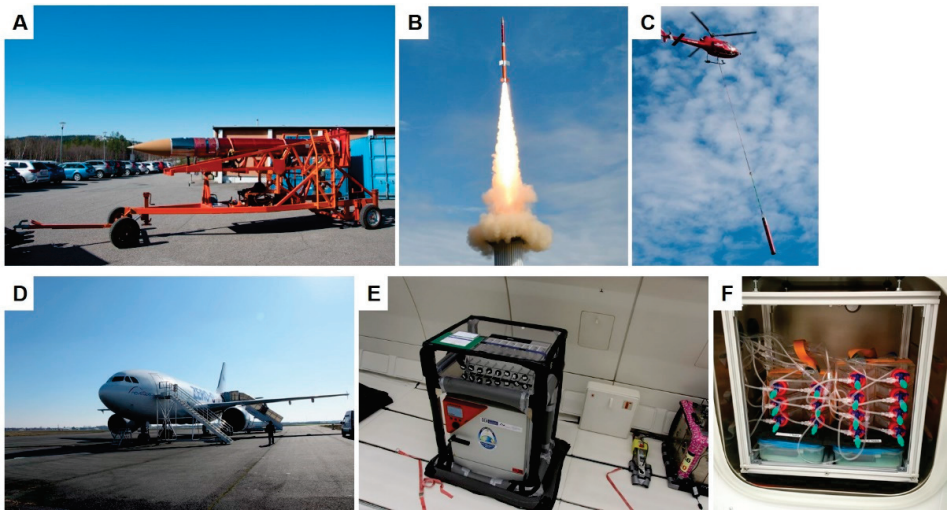


Figure 12. Shows the vehicles and experimental setups of the µg-experiments. (**A**): TX 54 rocket transportation to the launch tower. (**B**): Launch of the TX 54 rocket (courtesy of Airbus, Defense & Space). (**C**): retrieval of the TX 54 rocket with a helicopter. (**D**): Airbus 310 aircraft used for the parabolic flight. (**E**): The incubator used for the experiment. (**F**): Inside of the incubator prior to take off of the flight.

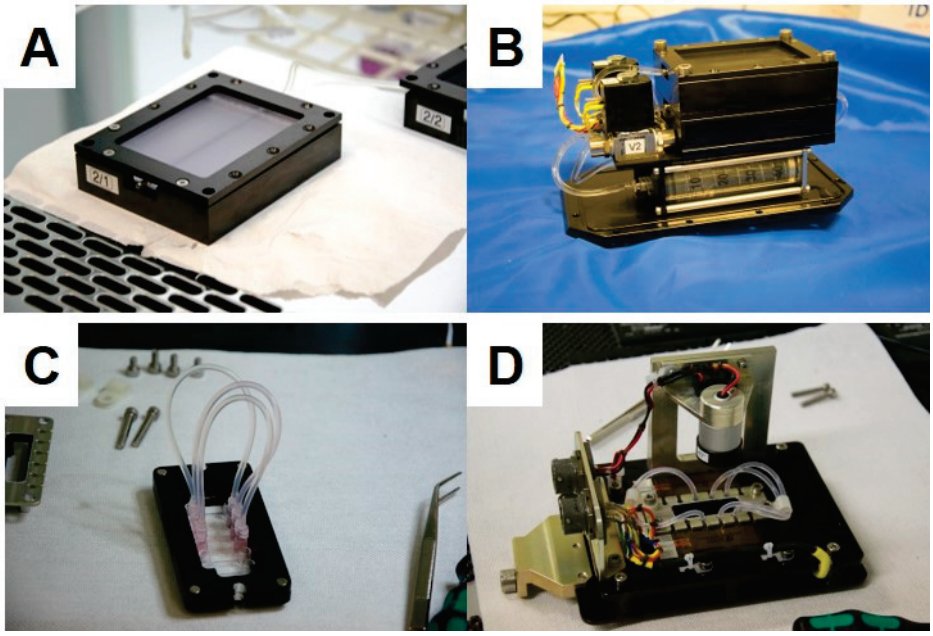


Figure 13. Late access units of the FLUFIX (**A**,**B**) and FLUMIAS (**C**,**D**).

4.6. FLUFIX and Immunocytochemistry of MCF-7 Fixed Cells during TEXUS 54

The MCF 7 cells were cultured in 18 well Ibidi slides. Approximately 2500 cells were seeded into each well. 4 slides were cultured on ground at 1*g* to be used as a control. Furthermore, there were four 18 well Ibidi slides on board of the rocket. The cells, on board of the rocket, were fixed with 4% paraformaldehyde (PFA) at two time points. Two Ibidi slides were fixed at the end of the hyper gravity phase and the other two slides were fixed at the end of the microgravity phase. The ground control slides were fixed with 4% PFA in parallel to the launch of the rocket. The slides were recovered and transferred back to the lab in 4% PFA.

To discard excess PFA, the cells were washed with DPBS three times. Afterwards, the slides were washed with 0.3% Triton X in DPBS for 10 min with agitation which was followed by washing with DPBS. To prevent non-specific binding, the slides were incubated in 3% BSA for one hour. Primary antibodies were added to the slides overnight at 4 °C (Table 1). The following day, the slides were washed with DPBS and the secondary antibody Alex Fluor 488 anti-mouse/anti-rabbit was added for one hour (Table 1). The slides were washed again with DPBS and Alexa Fluor 568 phalloidin was added for one hour, followed by washing with DPBS and mounting with Fluoroshield with DAPI (Sigma). For the slides to be ready for examination, they were incubated overnight at 4 °C. Carl ZEISS LSM 800 Confocal laser scanning microscope was used to examine the cells. Three lasers were used to examine the slides: 488 nm, 561 nm and 405 nm for visualization of Alexa 488, Alexa 568 and DAPI, respectively.

The microscopic images were quantitatively analyzed by ImageJ 1.52b (U.S. National Institutes of Health, Bethesda, MD, USA) to detect the difference in protein expression between different conditions. The intensity of the fluorescence in every photo was measured by ImageJ after the areas of interest were defined by the wand (tracing) tool. Furthermore, all the values were normalized to background fluorescence.

4.7. 31st DLR Parabolic Flight Campaign

The parabolic flights were performed from the Bordeaux–Mérignac Airport between 6 and 9 March 2018. The cells were transferred on board of the Airbus 310 to a 37 °C pre-warmed incubator shortly before take-off and they were incubated at 37 °C for the whole time of the flight. The parabolic flight consisted of 31 parabolas. Each parabola had an initial phase of hyper gravity (1.8 *g*) for 22 s during pull up, followed by a microgravity phase for 22 s. At the end of the parabola, there is a second

phase of hyper gravity for 22 s during pull out. The flight maneuver is repeated 31 times per flight day [11] (Figure 12).

Table 1. Names, types, classes, companies, and dilutions of all the antibodies that were used for immunostaining.

Antibody Name	Class	Type	Company	Reference no.	Dilution
Matrix Metallopeptidase 9 (MMP9) (2C3)	mouse monoclonal AB	Primary Antibody	Santa Cruz	sc-21733	(1:100)
interleukin 6 (IL6) (E-4)	mouse monoclonal AB	Primary Antibody	Santa Cruz	sc-28343	(1:100)
interleukin 8 (IL8) (C-11)	mouse monoclonal AB	Primary Antibody	Santa Cruz	sc-376750	(1:100)
Vascular Endothelial Growth Factor (VEGF) (c-term)	Rabbit monoclonal	Primary Antibody	Epitomics, Inc	#1909-1	(1:250)
Alexa fluor plus 488 goat anti-mouse IgG (H + L)	Goat polyclonal	Secondary Antibody	Invitrogen by Thermo Fischer Scientific	A32723	(1:400)
Alexa fluor 488 F(ab') 2 frangment of goat anti-rabbit igG (H + L)	Goat polyclonal	Secondary Antibody	Invitrogen by Thermo Fischer Scientific	A11070	(1:500)
Alexa Fluor 568 phalloidin	bicyclic peptide toxin	Toxin	Invitrogen by Thermo Fischer Scientific	A12380	one unit in 200 µL per slide
Fluoroshield with DAPI	fluorescent stain	fluorescent stain	Sigma Life science	F6057	no dilution

4.8. RNA Isolation and qPCR

During the parabolic flights, the MCF-7 cells were fixed with RNA*later* (Invitrogen by Thermo Fischer Scientific) at the end of the first parabola (P1) and the end of the last parabola (P31). The cells were cultured in T-75 cell culture flasks (75 cm^2, SARSTEDT) with 10 mL medium in each flask. Each flask had a fixed three-way connector on the lid which was connected with 140 cm tubing to a 50 mL syringe filled with RNA*later*. The RNA*later* was injected manually into the flasks at the designated times. Additional MCF-7 cells were incubated on ground to serve as a ground control. The ground control cells were fixed with RNA*later* in parallel to the samples on board of the flight. After landing, the medium and RNA*later* mixture were thrown away and replaced with 3-5 mL of fresh RNA*later*. Cells were harvested with 25 cm scraper (SARSTEDT) and incubated with RNA*later* at 4 °C in 15 mL tubes until RNA isolation.

All the falcon tubes were centrifuged (2500 g for 10 min at 4 °C), followed by discarding the supernatant. The RNA was isolated afterwards by the RNeasy Mini Kit (Qiagen) according to the manufacturer's protocol. The quality of the RNA was evaluated with a spectrophotometer. The RNA was converted to cDNA with a High Capacity cDNA reverse Transcription Kit according to the manufacturer's protocol (Applied Biosystems, Darmstadt, Germany). The the final volume of the reverse transcription reaction mix was 20 µL with 1 µ*g* total RNA added to each reaction mix. The primers were designed using Primer Blast (primer designing tool from NCBI).

A total volume of 13 µL SYBR green reaction mix (Applied Biosystems) was pipetted in each well in a 96 well plate. 1 µL of cDNA was added to each reaction mix with a concentration of 100 µM forward and reverse primers. 7500 Fast Real-Time PCR System (Applied Biosystems) was used to determine the transcription level of targeted genes (Table 2). The program consisted of initial 20 s holding stage of 95 °C followed by cycling stage. The cycling stage consisted of 40 cycles of 3 s at 95 °C and 30 s at 60 °C. A melt curve stage was implemented at the end which consisted of 15 s at 95 °C and 60 s at 60 °C. The data were collected and analyzed by the ΔΔCT method; 18s and TBP were used as reference genes [21].

Table 2. List of all the primer sequences used in the quantitative PCR. All the sequences are listed from 5′–3′ direction.

Factor	Primer Name	Sequence 5′–3′
18S	18s-F	GGAGCCTGCGGCTTAATTT
	18s-R	CAACTAAGAACGGCCATGCA
ACTB	ACTB-F	TGCCGACAGGATGCAGAAG
	ACTB-R	GCCGATCCACACGGAGTACT
CAV1	CAV1-F	CCTCCTCACAGTTTTCATCCA
	CAV1-R	TGTAGATGTTGCCCTGTTCC
CAV2	CAV2-F	GATCCCCACCGGCTCAAC
	CAV2-R	CACCGGCTCTGCGATCA
COL1A1	COL1A1-F	ACGAAGACATCCCACCAATCAC
	COL1A1-R	CGTTGTCGCAGACGCAGAT
EZR	EZR-F	GCAATCCAGCCAAATACAACTG
	EZR-R	CCACATAGTGGAGGCCAAAGTAC
FN1	FN1-F	TGAGGAGCATGGTTTTAGGAGAA
	FN1-R	TCCTCATTTACATTCGGCGTATAC
ICAM1	ICAM1-F	CGGCTGACGTGTGCAGTAAT
	ICAM1-R	CTTCTGAGACCTCTGGCTTCGT
IL6	IL6-F	CGGGAACGAAAGAGAAGCTCTA
	IL6-R	GAGCAGCCCCAGGGAGAA
CXCL8	IL8-F	TGGCAGCCTTCCTGATTTCT
	IL8-R	GGGTGGAAAGGTTTGGAGTATG
KRT8	KRT8-F	GATCTCTGAGATGAACCGGAACA
	KRT8-R	GCTCGGCATCTGCAATGG
LAMA1	LAMA1-F	TGACTGACCTGGGTTCAGGA
	LAMA1-R	TGCTAGCACTCCTTGCTTCC
LAMA3	LAMA3-F	AAAGCAAGAAGTCAGTCCAGC
	LAMA3-R	TCCCATGAAGACCATCTCGG
MMP9	MMP9-F	CCTGGAGACCTGAGAACCAATC
	MMP9-R	TTCGACTCTCCACGCATCTCT
MSN	MSN-F	GAAATTTGTCATCAAGCCCATTG
	MSN-R	CCATGCACAAGGCCAAGAT
TBP	TBP-F	GTGACCCAGCATCACTGTTTC
	TBP-R	GCAAACCAGAAACCCTTGCG
TIMP1	TIMP1-F	GCCATCGCCGCAGATC
	TIMP1-R	GCTATCAGCCACAGCAACAACA
TLN1	TLN1-F	GATGGCTATTACTCAGTACAGACAACTGA
	TLN1-R	CATAGTAGACTCCTCATCTCCTTCCA
TUBB	TUBB-F	CTGGACCGCATCTCTGTGTACTAC
	TUBB-R	GACCTGAGCGAACAGAGTCCAT
VEGFA	VEGFA-F	GCGCTGATAGACATCCATGAAC
	VEGFA-R	CTACCTCCACCATGCCAAGTG
VCL	VCL-F	GTCTCGGCTGCTCGTATCTT
	VCL-R	GTCCACCAGCCCTGTCATTT
PTK2	FAK1-F	TGTGGGTAAACCAGATCCTGC
	FAK1-R	CTGAAGCTTGACACCCTCGT
RDX	RDX-F	GAAAATGCCGAAACCAATCAA
	RDX-R	GTATTGGGCTGAATGGCAAATT
PAI1	PAI1-F	AGGCTGACTTCACGAGTCTTTCA
	PAI1-R	CACTCTCGTTCACCTCGATCTTC
CDH1	CDH1-F	GCTGGACCGAGAGAGTTTCC
	CDH1-R	CAGCTGTTGCTGTTGTGCTT
ITGB1	ITGB1-F	GAAAACAGCGCATATCTGGAAATT
	ITGB1-R	CAGCCAATCAGTGATCCACAA

4.9. Western Blot Analysis

Western blot analysis, gel electrophoresis, trans-blotting, and densitometry were carried out following routine protocols as described previously [38–40]. Following lysis and centrifugation, aliquots of 30 µ*g* were subjected to SDS-PAGE and Western blotting. The samples attained at the end of the P1 and P31 are compared to 1*g* control samples. Each condition is represented with 4 samples with a total number of 12 samples for all the conditions. The samples were loaded on Criterion XT 4–12% precast gels (Bio-Rad, Hercules, CA, USA) and run for 1h at 150 volts. Proteins were then transferred with a TurboBlot (Bio-Rad) (100 V, 30 min) to a PVDF membrane. Glyceraldehyde -3-phosphate-dehydrogenase (GAPDH) was used as a loading control. Membranes were then blocked for two hours in TBS-T containing 0.3% I Block (Applied Biosystems, Foster City, CA, USA). For detection of the selected antigens (see Table 3), the membranes were incubated overnight at room temperature in TBS-T and 0.3% I Block solutions of the antibodies. Following three washing steps of 5 min, membranes were incubated for additional two hours at room temperature with secondary antibody horseradish peroxidase (HRP)-linked antibody (Cell Signaling Technology Inc., Danvers, MA, USA) diluted 1:4000 in TBS-T and 0.3% I-Block. The respective protein bands were visualized using Bio-Rad Clarity Western ECL (Bio-Rad) and images were captured with Image Quant LAS 4000 mini (GE Healthcare Life Science, Freiburg, Germany). Images of stained membranes were captured on Syngene PXi 4EZ image analysis system (Synoptics, Cambridge, UK) and analyzed using the ImageJ software for densitometric quantification of the respective bands and total protein load [22].

Table 3. List of the names, sources, companies, molecular weight and dilutions of all the antibodies that were used for Western blots.

Antibody Name	Source	Company	Reference no.	MW kDa	Dilution
Anti-Cyclophilin B	Rabbit monoclonal	Abcam	#178397	24	1: 1000
Anti-Cytokeratin	Mouse monoclonal	Sigma	#C1801	68	1: 1000
Anti-E Cadherin	Mouse monoclonal	Abcam	ab1416	97	1:500
Anti-FAK	Rabbit monoclonal	Abcam	ab40794	125	1:1000
Anti-IL-8	Rabbit polyclonal	Abcam	ab7747	11	1:500
Anti-Integrin beta 1	Rabbit monoclonal	Abcam	#134179	88	1: 1000
Anti-Laminin	Rabbit polyclonal	Sigma	#L9393	220	1: 1000
Anti-PAI1	Rabbit polyclonal	Abcam	Ab66705	45	1:1000
Anti-Vinculin	Mouse monoclonal	Abcam	Ab18058	124	1:1000
Anti-β-Actin	Mouse monoclonal	Sigma	A5316	42	1:2000
Beta Tubulin Antibody	Rabbit Polyclonal	Santa Cruz Biotechnology	sc-9104	55	1: 1000
Ezrin	Rabbit polyclonal	Cell Signaling	#3145	81	1:500
Fibronectin	Mouse monoclonal	Invitrogen	#MA5-11981	250	1:1000
GAPDH (14C10)	Rabbit monoclonal	Cell signaling	#5014S	37	1:1000
MMP9	Mouse monoclonal	ThermoFisher	#MA5-14220	92	1: 500
Moesin (Q480)	Rabbit polyclonal	Cell signaling	#3150	78	1:500
Radixin	Rabbit monoclonal	Cell Signaling	#2636S	80	1: 1000
TIMP1	Mouse monoclonal	ThermoFisher	#MA5-13688	28	1: 500

4.10. Immunostaining of Fixed MCF-7 Cells Collected during the 31st Parabolic Flight Campaign

Approximately 20,000 MCF-7 cells were seeded into Ibidi slide flasks two days prior to the flight day. Four flasks were fixed at the end of the first parabola and additional four flasks were fixed at the end of the 31st parabola. Four slide flasks were cultured in parallel on ground to act as a control. Cells were fixed with 4% PFA and transferred to the lab to continue the staining procedure. MMP9, IL 6 and IL-8 were used as primary Antibodies. Alexa Fluor plus 488 goat anti-mouse IgG was used as a secondary antibody. DAPI and phalloidin were used additionally in all the slides (Table 1). The immunostaining procedure was performed as mentioned earlier [22].

4.11. Statistical Analysis

GraphPad prism 7.01 (GraphPad Software, Inc., California, USA) was used to analyze the data. The nonparametric Mann–Whitney U test was used as a statistical test of significance. The difference between groups was considered significant when the P-value was less than 0.05.

5. Conclusions

The FLUMIAS microscope has now been shown to be an elegant device suitable for live-cell imaging in real microgravity [11,30]. We could show for the first time, significant changes in the F-actin and microtubule cytoskeleton on living MCF-7 breast cancer cells in orbit. MCF-7 cells sense microgravity early and focal adhesion proteins are involved in this process. The actin cytoskeleton is contributing to adhesion and migration of the cancer cells. The early formation of lamellipodia and filopodia is the right step in this direction [66]. Early increases in *VEGFA* and *CXCL8* gene expression as well as the down-regulation of *VCL* mRNA and the reduced E-cadherin protein indicate a change to a more invasive function of the MCF-7 cells exposed to short-term microgravity which supports earlier data with thyroid cancer cells exposed to parabolic flight maneuvers [16]. Our future plan is to investigate these cells for a longer time in space to investigate the behavior of breast cancer cells on the ISS.

Author Contributions: Sounding rocket flight, A.S., B.S., and H.O.; Conceptualization, D.G., T.J.C. and S.K.; methodology, S.K., M.Z.N., D.M., T.J.B., T.J.C. and J.S..; Software, T.J.B. and S.K.; Validation, D.G., T.J.C., S.K., M.K. and D.M.; Formal analysis, S.K., J.S., and M.W.; Investigation, S.K.; Resources, M.I.; Writing—Original draft preparation, S.K., T.J.C, D.G., M.K., M.W.; Project administration, D.G.; funding acquisition, D.G. and M.I.

Funding: This research was funded by the German Space Agency (DLR; BMWi projects 50WB1524; 50WB1924).

Acknowledgments: We like to thank Otfried Joop, Michael Becker and Markus Braun (German Aerospace Center DLR, Bonn) for their support and for giving us the possibility to attend the TEXUS mission in Kiruna, Sweden and the 31st DLR Parabolic Flight Campaign in Bordeaux-Mérignac, France.

Conflicts of Interest: The authors declare no conflict of interest.

Abbreviations

2D	two-dimensional
3D	three-dimensional
ACTB	Beta-actin
CAV1	Caveolin-1
CAV2	Caveolin-2
CDH1	E-cadherin
COL1A1	Collagen type 1 alpha 1
CXCL8	Interleukin 8
DAPI	4’,6-diamidino-2-phenylindole
DLR	German Aerospace Center
ECM	Extracellular matrix
ESRANGE	European Space and Sounding Rocket Range
EZR	Ezrin
FLUMIAS	spinning-disc Fluorescence Microscopy Analysis System
FN1	Fibronectin
FTC-133	Follicular thyroid cancer cell line 133
GFP	Green fluorescent protein
GLOBOCAN	Global Cancer Observatory
IL-6	Interleukin 6
IL-8	Interleukin 8
ISS	International Space Station
ITGB1	Integrin beta 1
KRT8	Cytokeratin 8

LAMA1	Laminin alpha 1
LAMA3	Laminin alpha 3
LIMA1	LIM domain and actin-binding protein 1
MCF-7	Michigan cancer foundation
MCS	Multicellular spheroids
MMP9	Matrix metalloproteinases 9
MSN	Moesin
MTSS1	Metastasis suppressor protein 1
P	Parabola
PAI1	Plasminogen activator inhibitor 1
PF	Parabolic flight
PFA	Paraformaldehyde
PFC	Parabolic flight campaign
pLAGICT	pcDNA3.1 LifeAct-eGFP-IRES-mCherry-Tubulin
pSB-LAGICT	Sleeping Beauty LifeAct-eGFP-IRES-mCherry-Tubulin
PTK2	Protein tyrosine kinase 2; Focal adhesion kinase 1
r-μg	real microgravity
RDX	Radixin
RPM	Random positioning machine
s-μg	simulated microgravity
SB	Sleeping beauty
TIMP1	Metalloproteinase inhibitor 1
TLN1	Talin-1
TUBB	Beta tubulin
TX (TEXUS)	'Technische Experimente unter Schwerelosigkeit'
VCL	Vinculin
VEGFA	Vascular endothelial growth factor A
WHO	World health organization

References

1. Bray, F.; Ferlay, J.; Soerjomataram, I.; Siegel, R.L.; Torre, L.A.; Jemal, A. Global cancer statistics 2018: Globocan estimates of incidence and mortality worldwide for 36 cancers in 185 countries. *CA Cancer J. Clin.* **2018**, *68*, 394–424. [CrossRef] [PubMed]
2. Cancer.net. Breast cancer: Statistics. Available online: https://www.cancer.net/cancer-types/breast-cancer (accessed on 14 May 2019).
3. Becker, J.L.; Souza, G.R. Using space-based investigations to inform cancer research on earth. *Nat. Rev. Cancer* **2013**, *13*, 315–327. [CrossRef] [PubMed]
4. Grimm, D.; Wehland, M.; Pietsch, J.; Aleshcheva, G.; Wise, P.; van Loon, J.; Ulbrich, C.; Magnusson, N.E.; Infanger, M.; Bauer, J. Growing tissues in real and simulated microgravity: New methods for tissue engineering. *Tissue Eng. Part B Rev.* **2014**, *20*, 555–566. [CrossRef] [PubMed]
5. Grimm, D.; Bauer, J.; Wise, P.; Kruger, M.; Simonsen, U.; Wehland, M.; Infanger, M.; Corydon, T.J. The role of sox family members in solid tumours and metastasis. *Semin. Cancer Biol.* **2019**. [CrossRef] [PubMed]
6. Vorselen, D.; Roos, W.H.; MacKintosh, F.C.; Wuite, G.J.; van Loon, J.J. The role of the cytoskeleton in sensing changes in gravity by nonspecialized cells. *FASEB J.* **2014**, *28*, 536–547. [CrossRef] [PubMed]
7. Corydon, T.J.; Mann, V.; Slumstrup, L.; Kopp, S.; Sahana, J.; Askou, A.L.; Magnusson, N.E.; Echegoyen, D.; Bek, T.; Sundaresan, A.; et al. Reduced expression of cytoskeletal and extracellular matrix genes in human adult retinal pigment epithelium cells exposed to simulated microgravity. *Cell Physiol Biochem* **2016**, *40*, 1–17. [CrossRef] [PubMed]
8. Hughes-Fulford, M. Function of the cytoskeleton in gravisensing during spaceflight. *Adv. Space Res.* **2003**, *32*, 1585–1593. [CrossRef]
9. Maier, J.A.; Cialdai, F.; Monici, M.; Morbidelli, L. The impact of microgravity and hypergravity on endothelial cells. *Biomed. Res. Int.* **2015**, *2015*, 434803. [CrossRef]

10. Carlsson, S.I.; Bertilaccio, M.T.; Ballabio, E.; Maier, J.A. Endothelial stress by gravitational unloading: Effects on cell growth and cytoskeletal organization. *Biochim. Biophys. Acta* **2003**, *1642*, 173–179. [CrossRef]
11. Corydon, T.J.; Kopp, S.; Wehland, M.; Braun, M.; Schutte, A.; Mayer, T.; Hulsing, T.; Oltmann, H.; Schmitz, B.; Hemmersbach, R.; et al. Alterations of the cytoskeleton in human cells in space proved by life-cell imaging. *Sci. Rep.* **2016**, *6*, 20043. [CrossRef]
12. Kopp, S.; Warnke, E.; Wehland, M.; Aleshcheva, G.; Magnusson, N.E.; Hemmersbach, R.; Corydon, T.J.; Bauer, J.; Infanger, M.; Grimm, D. Mechanisms of three-dimensional growth of thyroid cells during long-term simulated microgravity. *Sci. Rep.* **2015**, *5*, 16691. [CrossRef] [PubMed]
13. Kopp, S.; Kruger, M.; Feldmann, S.; Oltmann, H.; Schutte, A.; Schmitz, B.; Bauer, J.; Schulz, H.; Saar, K.; Huebner, N.; et al. Thyroid cancer cells in space during the texus-53 sounding rocket mission—the thyroid project. *Sci. Rep.* **2018**, *8*, 10355. [CrossRef] [PubMed]
14. Kopp, S.; Kruger, M.; Bauer, J.; Wehland, M.; Corydon, T.J.; Sahana, J.; Nassef, M.Z.; Melnik, D.; Bauer, T.J.; Schulz, H.; et al. Microgravity affects thyroid cancer cells during the texus-53 mission stronger than hypergravity. *Int. J. Mol. Sci.* **2018**, *19*. [CrossRef] [PubMed]
15. Grimm, D.; Egli, M.; Kruger, M.; Riwaldt, S.; Corydon, T.J.; Kopp, S.; Wehland, M.; Wise, P.; Infanger, M.; Mann, V.; et al. Tissue engineering under microgravity conditions-use of stem cells and specialized cells. *Stem Cells Dev.* **2018**, *27*, 787–804. [CrossRef] [PubMed]
16. Ma, X.; Pietsch, J.; Wehland, M.; Schulz, H.; Saar, K.; Hübner, N.; Bauer, J.; Braun, M.; Schwarzwälder, A.; Segerer, J.; et al. Differential gene expression profile and altered cytokine secretion of thyroid cancer cells in space. *FASEB J.* **2014**, *28*, 813–835. [CrossRef] [PubMed]
17. Vassy, J.; Portet, S.; Beil, M.; Millot, G.; Fauvel-Lafeve, F.; Gasset, G.; Schoevaert, D. Weightlessness acts on human breast cancer cell line mcf-7. *Adv Space Res* **2003**, *32*, 1595–1603. [CrossRef]
18. Vassy, J.; Portet, S.; Beil, M.; Millot, G.; Fauvel-Lafeve, F.; Karniguian, A.; Gasset, G.; Irinopoulou, T.; Calvo, F.; Rigaut, J.P.; et al. The effect of weightlessness on cytoskeleton architecture and proliferation of human breast cancer cell line mcf-7. *FASEB J.* **2001**, *15*, 1104–1106. [CrossRef] [PubMed]
19. Tewinkel, M.; Burfeindt, J.; Rank, P.; Volkmann, D. Automatic fixation facility for plant seedlings in the texus sounding rocket programme. *Microgravity Sci. Technol.* **1991**, *4*, 216–220. [PubMed]
20. Kopp, S.; Slumstrup, L.; Corydon, T.J.; Sahana, J.; Aleshcheva, G.; Islam, T.; Magnusson, N.E.; Wehland, M.; Bauer, J.; Infanger, M.; et al. Identifications of novel mechanisms in breast cancer cells involving duct-like multicellular spheroid formation after exposure to the random positioning machine. *Sci. Rep.* **2016**, *6*, 26887. [CrossRef]
21. Kopp, S.; Sahana, J.; Islam, T.; Petersen, A.G.; Bauer, J.; Corydon, T.J.; Schulz, H.; Saar, K.; Huebner, N.; Slumstrup, L.; et al. The role of nfkappab in spheroid formation of human breast cancer cells cultured on the random positioning machine. *Sci. Rep.* **2018**, *8*, 921. [CrossRef]
22. Aleshcheva, G.; Wehland, M.; Sahana, J.; Bauer, J.; Corydon, T.J.; Hemmersbach, R.; Frett, T.; Egli, M.; Infanger, M.; Grosse, J.; et al. Moderate alterations of the cytoskeleton in human chondrocytes after short-term microgravity produced by parabolic flight maneuvers could be prevented by up-regulation of bmp-2 and sox-9. *FASEB J.* **2015**, *29*, 2303–2314. [CrossRef] [PubMed]
23. Wehland, M.; Ma, X.; Braun, M.; Hauslage, J.; Hemmersbach, R.; Bauer, J.; Grosse, J.; Infanger, M.; Grimm, D. The impact of altered gravity and vibration on endothelial cells during a parabolic flight. *Cell Physiol. Biochem.* **2013**, *31*, 432–451. [CrossRef] [PubMed]
24. Pietsch, J.; Gass, S.; Nebuloni, S.; Echegoyen, D.; Riwaldt, S.; Baake, C.; Bauer, J.; Corydon, T.J.; Egli, M.; Infanger, M.; et al. Three-dimensional growth of human endothelial cells in an automated cell culture experiment container during the spacex crs-8 iss space mission - the spheroids project. *Biomaterials* **2017**, *124*, 126–156. [CrossRef] [PubMed]
25. Strauch, S.M.; Grimm, D.; Corydon, T.J.; Kruger, M.; Bauer, J.; Lebert, M.; Wise, P.; Infanger, M.; Richter, P. Current knowledge about the impact of microgravity on the proteome. *Expert. Rev. Proteomics* **2018**, 1–12. [CrossRef] [PubMed]
26. Hader, D.P.; Braun, M.; Grimm, D.; Hemmersbach, R. Gravireceptors in eukaryotes-a comparison of case studies on the cellular level. *NPJ Microgravity* **2017**, *3*, 13. [CrossRef] [PubMed]
27. Guignandon, A.; Faure, C.; Neutelings, T.; Rattner, A.; Mineur, P.; Linossier, M.T.; Laroche, N.; Lambert, C.; Deroanne, C.; Nusgens, B.; et al. Rac1 gtpase silencing counteracts microgravity-induced effects on osteoblastic cells. *FASEB J.* **2014**, *28*, 4077–4087. [CrossRef] [PubMed]

28. Mann, V.; Grimm, D.; Corydon, T.J.; Kruger, M.; Wehland, M.; Riwaldt, S.; Sahana, J.; Kopp, S.; Bauer, J.; Reseland, J.E.; et al. Changes in human foetal osteoblasts exposed to the random positioning machine and bone construct tissue engineering. *Int. J. Mol. Sci.* **2019**, *20*. [CrossRef]
29. Tan, X.; Xu, A.; Zhao, T.; Zhao, Q.; Zhang, J.; Fan, C.; Deng, Y.; Freywald, A.; Genth, H.; Xiang, J. Simulated microgravity inhibits cell focal adhesions leading to reduced melanoma cell proliferation and metastasis via fak/rhoa-regulated mtorc1 and ampk pathways. *Sci. Rep.* **2018**, *8*, 3769. [CrossRef]
30. Thiel, C.S.; Tauber, S.; Seebacher, C.; Schropp, M.; Uhl, R.; Lauber, B.; Polzer, J.; Neelam, S.; Zhang, Y.; Ullrich, O. Real-time 3d high-resolution microscopy of human cells on the international space station. *Int. J. Mol. Sci.* **2019**, *20*. [CrossRef]
31. Moos, P.J.; Graft, K.; Edwards, M.D.; Stodieck, L.S.; Einhorn, R.; Luttges, M.W. Gravity-induced changes in microtubule formation. *USGS Bull.* **1988**, *2*, 55.
32. Papaseit, C.; Pochon, N.; Tabony, J. Microtubule self-organization is gravity-dependent. *Proc. Natl. Acad. Sci. USA* **2000**, *97*, 8364–8368. [CrossRef] [PubMed]
33. Piepmeier, E.H.; Kalns, J.E.; McIntyre, K.M.; Lewis, M.L. Prolonged weightlessness affects promyelocytic multidrug resistance. *Exp. Cell Res.* **1997**, *237*, 410–418. [CrossRef] [PubMed]
34. Boonstra, J. Growth factor-induced signal transduction in adherent mammalian cells is sensitive to gravity. *FASEB J.* **1999**, *13*, S35–S42. [CrossRef]
35. Leung, D.W.; Cachianes, G.; Kuang, W.J.; Goeddel, D.V.; Ferrara, N. Vascular endothelial growth factor is a secreted angiogenic mitogen. *Science* **1989**, *246*, 1306–1309. [CrossRef] [PubMed]
36. Luo, M.; Hou, L.; Li, J.; Shao, S.; Huang, S.; Meng, D.; Liu, L.; Feng, L.; Xia, P.; Qin, T.; et al. Vegf/nrp-1axis promotes progression of breast cancer via enhancement of epithelial-mesenchymal transition and activation of nf-kappab and beta-catenin. *Cancer Lett.* **2016**, *373*, 1–11. [CrossRef] [PubMed]
37. Tuttle, R.M.; Fleisher, M.; Francis, G.L.; Robbins, R.J. Serum vascular endothelial growth factor levels are elevated in metastatic differentiated thyroid cancer but not increased by short-term tsh stimulation. *J. Clin. Endocrinol. Metab.* **2002**, *87*, 1737–1742. [CrossRef]
38. Grosse, J.; Wehland, M.; Pietsch, J.; Ma, X.; Ulbrich, C.; Schulz, H.; Saar, K.; Hubner, N.; Hauslage, J.; Hemmersbach, R.; et al. Short-term weightlessness produced by parabolic flight maneuvers altered gene expression patterns in human endothelial cells. *FASEB J.* **2012**, *26*, 639–655. [CrossRef]
39. Ulbrich, C.; Pietsch, J.; Grosse, J.; Wehland, M.; Schulz, H.; Saar, K.; Hubner, N.; Hauslage, J.; Hemmersbach, R.; Braun, M.; et al. Differential gene regulation under altered gravity conditions in follicular thyroid cancer cells: Relationship between the extracellular matrix and the cytoskeleton. *Cell Physiol. Biochem.* **2011**, *28*, 185–198. [CrossRef] [PubMed]
40. Lu, D.; Sun, S.; Zhang, F.; Luo, C.; Zheng, L.; Wu, Y.; Li, N.; Zhang, C.; Wang, C.; Chen, Q.; et al. Microgravity-induced hepatogenic differentiation of rbmscs on board the sj-10 satellite. *FASEB J.* **2019**, *33*, 4273–4286. [CrossRef]
41. dos Santos, P.B.; Zanetti, J.S.; Ribeiro-Silva, A.; Beltrao, E.I. Beta 1 integrin predicts survival in breast cancer: A clinicopathological and immunohistochemical study. *Diagn Pathol.* **2012**, *7*, 104. [CrossRef]
42. Theodosiou, M.; Widmaier, M.; Bottcher, R.T.; Rognoni, E.; Veelders, M.; Bharadwaj, M.; Lambacher, A.; Austen, K.; Muller, D.J.; Zent, R.; et al. Kindlin-2 cooperates with talin to activate integrins and induces cell spreading by directly binding paxillin. *Elife* **2016**, *5*, e10130. [CrossRef] [PubMed]
43. Shinde, A.; Libring, S.; Alpsoy, A.; Abdullah, A.; Schaber, J.A.; Solorio, L.; Wendt, M.K. Autocrine fibronectin inhibits breast cancer metastasis. *Mol. Cancer Res.* **2018**, *16*, 1579–1589. [CrossRef] [PubMed]
44. Yamamoto, H.; Ehling, M.; Kato, K.; Kanai, K.; van Lessen, M.; Frye, M.; Zeuschner, D.; Nakayama, M.; Vestweber, D.; Adams, R.H. Integrin beta1 controls ve-cadherin localization and blood vessel stability. *Nat. Commun.* **2015**, *6*, 6429. [CrossRef] [PubMed]
45. Lee, T.H.; Seng, S.; Li, H.; Kennel, S.J.; Avraham, H.K.; Avraham, S. Integrin regulation by vascular endothelial growth factor in human brain microvascular endothelial cells: Role of alpha6beta1 integrin in angiogenesis. *J. Biol. Chem.* **2006**, *281*, 40450–40460. [CrossRef] [PubMed]
46. Das, M.; Ithychanda, S.; Qin, J.; Plow, E.F. Mechanisms of talin-dependent integrin signaling and crosstalk. *Biochim Biophys Acta* **2014**, *1838*, 579–588. [CrossRef] [PubMed]
47. Grosse, J.; Wehland, M.; Pietsch, J.; Schulz, H.; Saar, K.; Hubner, N.; Eilles, C.; Bauer, J.; Abou-El-Ardat, K.; Baatout, S.; et al. Gravity-sensitive signaling drives 3-dimensional formation of multicellular thyroid cancer spheroids. *FASEB J.* **2012**, *26*, 5124–5140. [CrossRef] [PubMed]

48. Ilic, D.; Kovacic, B.; Johkura, K.; Schlaepfer, D.D.; Tomasevic, N.; Han, Q.; Kim, J.B.; Howerton, K.; Baumbusch, C.; Ogiwara, N.; et al. Fak promotes organization of fibronectin matrix and fibrillar adhesions. *J. Cell Sci.* **2004**, *117*, 177–187. [CrossRef]
49. Guan, J.L. Integrin signaling through fak in the regulation of mammary stem cells and breast cancer. *IUBMB Life* **2010**, *62*, 268–276. [CrossRef]
50. Sullivan, N.J.; Sasser, A.K.; Axel, A.E.; Vesuna, F.; Raman, V.; Ramirez, N.; Oberyszyn, T.M.; Hall, B.M. Interleukin-6 induces an epithelial-mesenchymal transition phenotype in human breast cancer cells. *Oncogene* **2009**, *28*, 2940–2947. [CrossRef]
51. Kitadai, Y.; Haruma, K.; Mukaida, N.; Ohmoto, Y.; Matsutani, N.; Yasui, W.; Yamamoto, S.; Sumii, K.; Kajiyama, G.; Fidler, I.J.; et al. Regulation of disease-progression genes in human gastric carcinoma cells by interleukin 8. *Clin. Cancer Res.* **2000**, *6*, 2735–2740.
52. Cohen, T.; Nahari, D.; Cerem, L.W.; Neufeld, G.; Levi, B.Z. Interleukin 6 induces the expression of vascular endothelial growth factor. *J. Biol. Chem.* **1996**, *271*, 736–741. [CrossRef] [PubMed]
53. Martin, D.; Galisteo, R.; Gutkind, J.S. Cxcl8/il8 stimulates vascular endothelial growth factor (vegf) expression and the autocrine activation of vegfr2 in endothelial cells by activating nfkappab through the cbm (carma3/bcl10/malt1) complex. *J. Biol. Chem.* **2009**, *284*, 6038–6042. [CrossRef] [PubMed]
54. Lecuit, T.; Yap, A.S. E-cadherin junctions as active mechanical integrators in tissue dynamics. *Nat. Cell Biol.* **2015**, *17*, 533–539. [CrossRef] [PubMed]
55. Sahana, J.; Nassef, M.Z.; Wehland, M.; Kopp, S.; Kruger, M.; Corydon, T.J.; Infanger, M.; Bauer, J.; Grimm, D. Decreased e-cadherin in mcf7 human breast cancer cells forming multicellular spheroids exposed to simulated microgravity. *Proteomics* **2018**, *18*, e1800015. [CrossRef] [PubMed]
56. Hazan, R.B.; Kang, L.; Roe, S.; Borgen, P.I.; Rimm, D.L. Vinculin is associated with the e-cadherin adhesion complex. *J. Biol. Chem.* **1997**, *272*, 32448–32453. [CrossRef] [PubMed]
57. Yu, Z.; Sun, M.; Jin, F.; Xiao, Q.; He, M.; Wu, H.; Ren, J.; Zhao, L.; Zhao, H.; Yao, W.; et al. Combined expression of ezrin and e-cadherin is associated with lymph node metastasis and poor prognosis in breast cancer. *Oncol. Rep.* **2015**, *34*, 165–174. [CrossRef] [PubMed]
58. Thapa, N.; Tan, X.; Choi, S.; Wise, T.; Anderson, R.A. Pipkigamma and talin couple phosphoinositide and adhesion signaling to control the epithelial to mesenchymal transition. *Oncogene* **2017**, *36*, 899–911. [CrossRef] [PubMed]
59. Dudek, M.C.; Wong, K.E.; Bassa, L.M.; Mora, M.C.; Ser-Dolansky, J.; Henneberry, J.M.; Crisi, G.M.; Arenas, R.B.; Schneider, S.S. Antineoplastic effects of rhodiola crenulata treatment on b16-f10 melanoma. *Tumour Biol.* **2015**, *36*, 9795–9805. [CrossRef] [PubMed]
60. Cowden Dahl, K.D.; Symowicz, J.; Ning, Y.; Gutierrez, E.; Fishman, D.A.; Adley, B.P.; Stack, M.S.; Hudson, L.G. Matrix metalloproteinase 9 is a mediator of epidermal growth factor-dependent e-cadherin loss in ovarian carcinoma cells. *Cancer Res.* **2008**, *68*, 4606–4613. [CrossRef] [PubMed]
61. Grunewald, M.; Avraham, I.; Dor, Y.; Bachar-Lustig, E.; Itin, A.; Jung, S.; Chimenti, S.; Landsman, L.; Abramovitch, R.; Keshet, E. Vegf-induced adult neovascularization: Recruitment, retention, and role of accessory cells. *Cell* **2006**, *124*, 175–189. [CrossRef]
62. Zheng, P.S.; Wen, J.; Ang, L.C.; Sheng, W.; Viloria-Petit, A.; Wang, Y.; Wu, Y.; Kerbel, R.S.; Yang, B.B. Versican/pg-m g3 domain promotes tumor growth and angiogenesis. *FASEB J.* **2004**, *18*, 754–756. [CrossRef] [PubMed]
63. Zheng, H.; Takahashi, H.; Murai, Y.; Cui, Z.; Nomoto, K.; Niwa, H.; Tsuneyama, K.; Takano, Y. Expressions of mmp-2, mmp-9 and vegf are closely linked to growth, invasion, metastasis and angiogenesis of gastric carcinoma. *Anticancer Res.* **2006**, *26*, 3579–3583. [PubMed]
64. Davis, G.E.; Bayless, K.J.; Mavila, A. Molecular basis of endothelial cell morphogenesis in three-dimensional extracellular matrices. *Anat. Rec.* **2002**, *268*, 252–275. [CrossRef] [PubMed]
65. Krüger, M.; Melnik, D.; Kopp, S.; Buken, C.; Sahana, J.; Bauer, J.; Wehland, M.; Hemmersbach, R.; Corydon, T.J.; Infanger, M.; et al. Fighting thyroid cancer with microgravity research. *Int. J. Mol. Sci.* **2019**, *20*. [CrossRef]
66. Mattila, P.K.; Lappalainen, P. Filopodia: Molecular architecture and cellular functions. *Nat. Rev. Mol. Cell Biol.* **2008**, *9*, 446–454. [CrossRef] [PubMed]
67. Jacquemet, G.; Hamidi, H.; Ivaska, J. Filopodia in cell adhesion, 3d migration and cancer cell invasion. *Curr. Opin. Cell Biol.* **2015**, *36*, 23–31. [CrossRef] [PubMed]

68. Jacquemet, G.; Green, D.M.; Bridgewater, R.E.; von Kriegsheim, A.; Humphries, M.J.; Norman, J.C.; Caswell, P.T. Rcp-driven alpha5beta1 recycling suppresses rac and promotes rhoa activity via the racgap1-iqgap1 complex. *J. Cell Biol.* **2013**, *202*, 917–935. [CrossRef]
69. Paul, N.R.; Allen, J.L.; Chapman, A.; Morlan-Mairal, M.; Zindy, E.; Jacquemet, G.; Fernandez del Ama, L.; Ferizovic, N.; Green, D.M.; Howe, J.D.; et al. Alpha5beta1 integrin recycling promotes arp2/3-independent cancer cell invasion via the formin fhod3. *J. Cell Biol.* **2015**, *210*, 1013–1031. [CrossRef]
70. Shibue, T.; Brooks, M.W.; Inan, M.F.; Reinhardt, F.; Weinberg, R.A. The outgrowth of micrometastases is enabled by the formation of filopodium-like protrusions. *Cancer Discov* **2012**, *2*, 706–721. [CrossRef]
71. Shibue, T.; Brooks, M.W.; Weinberg, R.A. An integrin-linked machinery of cytoskeletal regulation that enables experimental tumor initiation and metastatic colonization. *Cancer Cell* **2013**, *24*, 481–498. [CrossRef]
72. Lindberg, U.; Karlsson, R.; Lassing, I.; Schutt, C.E.; Höglund, A.S. The microfilament system and malignancy. *Semin. Cancer Biol.* **2008**, *18*, 2–11. [CrossRef] [PubMed]
73. Ingber, D. How cells (might) sense microgravity. *FASEB J.* **1999**, *13*, S3–S15. [CrossRef] [PubMed]
74. Aleshcheva, G.; Sahana, J.; Ma, X.; Hauslage, J.; Hemmersbach, R.; Egli, M.; Infanger, M.; Bauer, J.; Grimm, D. Changes in morphology, gene expression and protein content in chondrocytes cultured on a random positioning machine. *PLoS One* **2013**, *8*, e79057. [CrossRef] [PubMed]
75. Grimm, D.; Bauer, J.; Kossmehl, P.; Shakibaei, M.; Schoberger, J.; Pickenhahn, H.; Schulze-Tanzil, G.; Vetter, R.; Eilles, C.; Paul, M.; et al. Simulated microgravity alters differentiation and increases apoptosis in human follicular thyroid carcinoma cells. *FASEB J.* **2002**, *16*, 604–606. [CrossRef] [PubMed]
76. Aronovich, E.L.; McIvor, R.S.; Hackett, P.B. The sleeping beauty transposon system: A non-viral vector for gene therapy. *Hum. Mol. Genet.* **2011**, *20*, R14–R20. [CrossRef] [PubMed]
77. Askou, A.L.; Aagaard, L.; Kostic, C.; Arsenijevic, Y.; Hollensen, A.K.; Bek, T.; Jensen, T.G.; Mikkelsen, J.G.; Corydon, T.J. Multigenic lentiviral vectors for combined and tissue-specific expression of mirna- and protein-based antiangiogenic factors. *Mol. Ther. Methods Clin. Dev.* **2015**, *2*, 14064. [CrossRef] [PubMed]
78. Pihlmann, M.; Askou, A.L.; Aagaard, L.; Bruun, G.H.; Svalgaard, J.D.; Holm-Nielsen, M.H.; Dagnaes-Hansen, F.; Bek, T.; Mikkelsen, J.G.; Jensen, T.G.; et al. Adeno-associated virus-delivered polycistronic microrna-clusters for knockdown of vascular endothelial growth factor in vivo. *J. Gene Med.* **2012**, *14*, 328–338. [CrossRef]
79. Staunstrup, N.H.; Sharma, N.; Bak, R.O.; Svensson, L.; Petersen, T.K.; Aarenstrup, L.; Kristiansen, K.; Bolund, L.; Mikkelsen, J.G. A sleeping beauty DNA transposon-based genetic sensor for functional screening of vitamin d3 analogues. *BMC Biotechnol.* **2011**, *11*, 33. [CrossRef]



© 2019 by the authors. Licensee MDPI, Basel, Switzerland. This article is an open access article distributed under the terms and conditions of the Creative Commons Attribution (CC BY) license (http://creativecommons.org/licenses/by/4.0/).

International Journal of
Molecular Sciences

MDPI

Article

Simulated Microgravity Influences VEGF, MAPK, and PAM Signaling in Prostate Cancer Cells

Trine Engelbrecht Hybel [1], Dorothea Dietrichs [2], Jayashree Sahana [1], Thomas J. Corydon [1,3], Mohamed Z. Nassef [2,4], Markus Wehland [2,4], Marcus Krüger [2,4], Nils E. Magnusson [5], Johann Bauer [6], Kirsten Utpatel [7], Manfred Infanger [2,4], Daniela Grimm [1,2,4,8,*] and Sascha Kopp [2,4,*]

1 Department of Biomedicine, Aarhus University, 8000 Aarhus C, Denmark; trihyb@rm.dk (T.E.H.); jaysaha@biomed.au.dk (J.S.); corydon@biomed.au.dk (T.J.C.)
2 Clinic for Plastic, Aesthetic and Hand Surgery, Otto von Guericke University Magdeburg, 39120 Magdeburg, Germany; dorothea.dietrichs@st.ovgu.de (D.D.); mohamed.nassef@med.ovgu.de (M.Z.N.); markus.wehland@med.ovgu.de (M.W.); marcus.krueger@med.ovgu.de (M.K.); manfred.infanger@med.ovgu.de (M.I.)
3 Department of Ophthalmology, Aarhus University Hospital, 8200 Aarhus N, Denmark
4 Research Group "Magdeburger Arbeitsgemeinschaft für Forschung unter Raumfahrt-und Schwerelosigkeitsbedingungen" (MARS), Otto von Guericke University, Universitätsplatz 2, 39106 Magdeburg, Germany
5 Diabetes and Hormone Diseases—Medical Research Laboratory, Department of Clinical Medicine, Faculty of Health, Aarhus University, 8200 Aarhus N, Denmark; nm@clin.au.dk
6 Max Planck Institute of Biochemistry, 82152 Martinsried, Germany; jbauer@biochem.mpg.de
7 Institute for Pathology, University of Regensburg, 95053 Regensburg, Germany; kirsten.utpatel@ukr.de
8 Department of Microgravity and Translational Regenerative Medicine, Otto von Guericke University, Pfälzer Platz, 39106 Magdeburg, Germany
* Correspondence: dgg@biomed.au.dk (D.G.); sascha.kopp@med.ovgu.de (S.K.); Tel.: +45-871-67693 (D.G.); +49-391-6721267 (S.K.)

Received: 23 November 2019; Accepted: 11 February 2020; Published: 13 February 2020

check for updates

Abstract: Prostate cancer is one of the leading causes of cancer mortality in men worldwide. An unusual but unique environment for studying tumor cell processes is provided by microgravity, either in space or simulated by ground-based devices like a random positioning machine (RPM). In this study, prostate adenocarcinoma-derived PC-3 cells were cultivated on an RPM for time periods of 3 and 5 days. We investigated the genes associated with the cytoskeleton, focal adhesions, extracellular matrix, growth, survival, angiogenesis, and metastasis. The gene expression of signaling factors of the vascular endothelial growth factor (VEGF), mitogen-activated protein kinase (MAPK), and PI3K/AKT/mTOR (PAM) pathways was investigated using qPCR. We performed immunofluorescence to study the cytoskeleton, histological staining to examine the morphology, and a time-resolved immunofluorometric assay to analyze the cell culture supernatants. When PC-3 cells were exposed to simulated microgravity (s-µg), some cells remained growing as adherent cells (AD), while most cells detached from the cell culture flask bottom and formed multicellular spheroids (MCS). After 3-day RPM exposure, PC-3 cells revealed significant downregulation of the *VEGF*, *SRC1*, *AKT*, *MTOR*, and *COL1A1* gene expression in MCS, whereas *FLT1*, *RAF1*, *MEK1*, *ERK1*, *FAK1*, *RICTOR*, *ACTB*, *TUBB*, and *TLN1* mRNAs were not significantly changed. *ERK2* and *TLN1* were elevated in AD, and *FLK1*, *LAMA3*, *COL4A5*, *FN1*, *VCL*, *CDH1*, and *NGAL* mRNAs were significantly upregulated in AD and MCS after 3 days. After a 5-day culture in s-µg, the PC-3 cells showed significant downregulations of *VEGF* mRNA in AD and MCS, and *FN1*, *CDH1*, and *LAMA3* in AD and *SCR1* in MCS. In addition, we measured significant upregulations in *FLT1*, *AKT*, *ERK1*, *ERK2*, *LCN2*, *COL1A1*, *TUBB*, and *VCL* mRNAs in AD and MCS, and increases in *FLK1*, *FN1*, and *COL4A5* in MCS as well as *LAMB2*, *CDH1*, *RAF1*, *MEK1*, *SRC1*, and *MTOR* mRNAs in AD. *FAK1* and *RICTOR* were not altered by s-µg.

In parallel, the secretion rate of VEGFA and NGAL proteins decreased. Cytoskeletal alterations (F-actin) were visible, as well as a deposition of collagen in the MCS. In conclusion, RPM-exposure of PC-3 cells induced changes in their morphology, cytoskeleton, and extracellular matrix protein synthesis, as well as in their focal adhesion complex and growth behavior. The significant upregulation of genes belonging to the PAM pathway indicated their involvement in the cellular changes occurring in microgravity.

Keywords: microgravity; prostate cancer; VEGF signaling; cytoskeleton; focal adhesion; extracellular matrix

1. Introduction

Space research and investigations on cell signaling processes in the growth and development of cells exposed to microgravity (μg) is currently a hot topic in cancer research and regenerative medicine [1–5]. Prostate cancer is the fifth leading cause of cancer mortality in men, with the second highest cancer incidence worldwide. It is the most frequently diagnosed cancer in more than half of the countries in the world. In 2018, 1,276,106 cases of prostate cancer and 358,989 deaths were recorded worldwide [6]. Therefore, it is important to increase the current knowledge and develop novel treatment strategies for prostate cancer.

According to the 2016 World Health Organization (WHO) classification of tumors of the prostate, one of the main groups of prostate carcinomas are epithelial tumors, including the subtype acinar adenocarcinoma [7], which is by far the most common type of prostate carcinoma [8,9]. Initially, this carcinoma is local and confined to the prostate. If not detected early, it can progress to advanced stages, characterized by local invasion of the vesicular glands. The cancer can eventually progress to metastatic disease, usually resulting in death [9]. Moreover, the disease can change to a state of androgen independence, increasing the difficulty of treatment [9].

Many studies have shown that changes in gravity have extensive effects on cell functions [10–12]. Microgravity can induce alterations in morphology, growth, and protein biosynthesis and secretion [10], depending on the responding cell type [12]. In addition, cell cultures in μg can be performed scaffold-free to engineer three-dimensional (3D) aggregates, including multicellular spheroids (MCS), tissues, and tubular structures [13–15]. These organoids can be used for research in space medicine [13,16] and for testing the delivery and efficacy of drugs [17].

However, real μg can only be experienced during spaceflights, unmanned Bion flights, suborbital flights, rocket flights, parabolic flights, or with the help of a drop tower [18]. As these opportunities are rare and costly, devices have been developed to simulate μg on Earth, including the random positioning machine (RPM), rotating wall vessel (RWV), and the two-dimensional (2D) or 3D clinostat [16,18].

An RPM consists of two independently rotating frames, each moving at a randomized speed and direction [16]. By placing a sample of sufficiently small objects or cells in the middle of the RPM, the gravity vector perceived by the sample is averaged to zero over time; thus, the objects are exposed to simulated μg (s-μg) [16,19]. It has been shown for various cell types, including thyroid [20] and breast cancer cells [21], that cultivation on an RPM results in MCS formation [16].

This method facilitates long-term scaffold-free 3D-aggregate formation with the advantage of a lack of necrosis. This makes it possible to conduct long-term experiments where huge spheroids can be produced [22]. Experiments with follicular thyroid cancer cells cultured in a scaffold-free manner on an RPM for 14 days [23] and endothelial cells exposed to s-μg for 28 and 35 days revealed no necrosis. The endothelial cells grew in a large number of 3D organoids and tubular structures [15,24]. The liquid overlay and spinner flask techniques and other 1 g methods provide specific environments for 3D formation [25]. Unfortunately, after two weeks the spheroids revealed a necrotic center [26].

MCS are spherical cell clusters containing networks of cell–cell and cell–matrix interactions [17]. They are similar to in vivo tissue regarding the complexity of cell types, cell–cell interactions, extracellular matrix (ECM) deposition, and chemical gradients [17]. The concentration of oxygen and nutrients is highest in the outer layers, while metabolic wastes accumulate in the center [17,27], which resembles the conditions in avascular tumors but is "inside-out" compared to tumors containing capillaries in the center [28]. It has been shown that when MCS are formed from cancer cells, they mimic tumors formed in vivo [29] better than monolayers of cells [28]. Therefore, they can be used as in vitro model systems and for high-throughput screening assays [30] to measure the responses of tumors to potential anticancer drugs [28–30]. This increases the opportunity for cell-based research in drug development [30] and can be used as an addition to in vivo models and/or to reduce animal experiments [28].

Various studies have shown that μg can affect the secretion of vascular endothelial growth factors (VEGFs) in different cell types [15,23,31]. VEGFs are signaling molecules important for the process of angiogenesis [32]. Abnormal angiogenesis is one of the hallmarks of cancer [33], and overexpression of VEGF-A has been implicated in pathological angiogenesis in tumors and other diseases, causing the development of dysfunctional and disorganized types of blood vessels [32]. In tumors, neoangiogenesis changes blood flow, oxygenation, and interstitial fluid pressure, creating an abnormal microenvironment, increasing cancer progression, and decreasing the efficacy of treatment [33]. Anti-VEGF treatment has been developed and successfully utilized as cancer treatment [33,34].

The actions of VEGF-A are mediated through the molecule binding to its two receptors, VEGFR-1/fetal liver kinase 1 (FLT1) and VEGFR-2 Fms-related tyrosine kinase 1 (FLK1). Upon VEGF-A binding to VEGFR-2, phosphorylation of specific tyrosine residues leads to recruitment of downstream effector proteins and initiation of specific signaling pathways [35]. The extracellular signal regulated kinase 1/2 (ERK1/2)/rapidly accelerated fibrosarcoma (raf)-mitogen-activated protein kinase kinase 1 (MEK1)-mitogen-activated protein kinase (MAPK) pathway is activated, leading to increased proliferation [35,36]. Apoptosis is inhibited through the steroid receptor coactivator (SRC) proto-oncogene, non-receptor tyrosine kinase (Src)/phosphoinositide 3-kinase (PI3K)/protein kinase B (PKB, also known as Akt) signaling pathway, leading to increased cell survival [35,37]. Mammalian target of rapamycin (mTOR) signaling, which includes mTOR complex 2 (mTORC2), containing the subunits mTOR and rapamycin-insensitive companion of mTOR (RICTOR), is activated through the PI3K/Akt signaling pathway, regulating processes such as cell growth and differentiation [38]. VEGF signaling through VEGFR-2 also leads to activation of focal adhesion kinase (FAK), which stimulates increased vascular permeability [39] as well as migration and anti-apoptosis via Src [40]. Moreover, p38MAPK is activated, affecting cell motility through actin cytoskeleton reorganization [35].

In comparison to other VEGFRs, the signaling functions of VEGFR-1 are less well characterized [41]. It has been associated with the ERK/MAPK, PI3K/AKT, and p38MAPK signaling pathways [42]. Furthermore, VEGFR-1 has been shown to bind VEGF with a higher affinity than VEGFR-2 and thereby have a negative impact on angiogenesis caused by VEGFR-2 [41].

Previous findings showed 3D growth patterns of PC-3 cells when cultured in an RWV culture system [14]. Spheroid formation followed within a few hours after reducing gravitational conditions, and expression of cell adhesion molecules (CD44 and E-cadherin) was increased in the MCS. In parallel, Zhau and co-workers established a 3D human prostatic cancer model by co-culturing prostate fibroblasts with prostate cancer cells under s-μg conditions using an RWV system [43]. Using a similar setup, Clejan and colleagues studied the effects of RWV cultivation on DU-145 human prostate carcinoma cells [44]. Notably, after 6 days of RWV growth, the activation of the PI3K pathway was observed. From this study the authors concluded that RWV cultivation provides a 3D growth model of prostate cancer that imitates in vivo tissue growth. In addition, Margolis et al. reported long-term maintenance (minimum of 28 days) of benign explanted human prostate tissue grown in culture medium in an RWV [45]. This study investigated the impact of s-μg on PC-3 prostate cancer cells in vitro.

The principal aims of this study are to (i) investigate the changes and behavior of PC-3 prostate cancer cells exposed to s-µg created by an RPM; (ii) test, based on previous findings, the hypothesis that exposure of PC-3 cells to s-µg induces the formation of MCS and alters the expression of genes related to angiogenesis, metastasis, the cytoskeleton, the ECM, and focal adhesions (FAs); and (iii) focus on the VEGF, MAPK, and PI3K/AKT/mTOR (PAM) signaling pathways.

2. Results

2.1. Morphology and Cell Growth

In order to examine whether PC-3 cells will form MCS when cultured under s-µg conditions, cell culture flasks containing PC-3 cells were placed on the RPM for 3 and 5 days; 1 g controls were cultured in parallel.

The 1 g control cells (Figure 1A,D) kept dividing throughout the experiment, reaching 100% confluence. The cells on the RPM (Figure 1B,C,E,F) were exposed to s-µg conditions. Only a few cells remained adherent, growing as a 2D monolayer (AD), while the majority detached and aggregated to MCS. After 3 days (Figure 1B,C), there were numerous MCS floating in the medium. In addition, a smaller number of loose aggregates could be found among the spheroids. After 5 days (Figure 1E,F), the spheroids had grown significantly. The size, shape, and density varied among the spheroids, as well as among the cell culture flasks used in the same experiment.

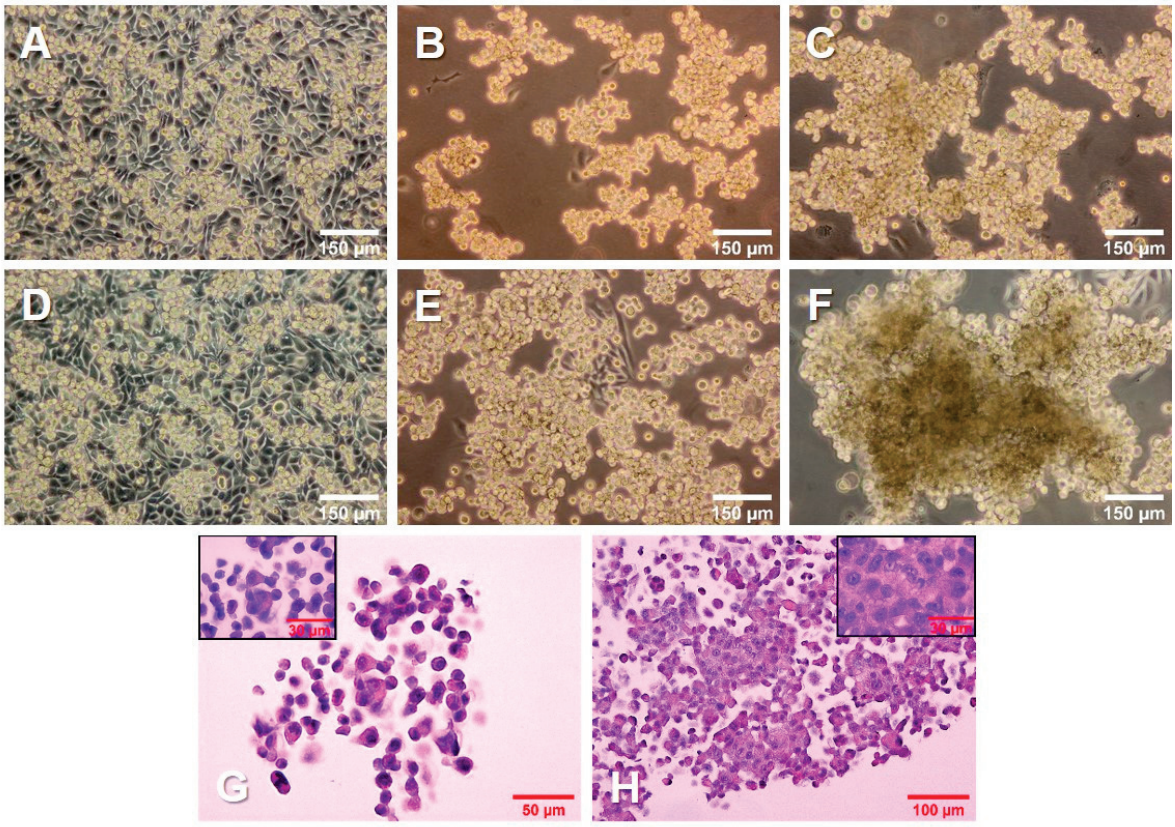


Figure 1. Growth of PC-3 prostate cancer cells in simulated microgravity. PC-3 cells were cultured (**A**,**D**) under 1 g conditions or (**B**,**C**,**E**,**F**) on an RPM for 3 days (**A**–**C**) and 5 days (**D**–**F**). (**G**,**H**) PC-3 cells growing in MCS, stained with hematoxylin and eosin (HE) after a 3-day (**G**) and 5-day (**H**) RPM exposure, respectively.

Hematoxylin–eosin (HE) staining of spheroids grown after 3 days (Figure 1G) and 5 days (Figure 1H) on the RPM presented a condensation of cells together with an increased amount of ECM.

In addition, the cells in all groups were viable and did not undergo apoptosis or necrosis, as seen from the normal cell shape, cytoplasm staining, and intact nuclei.

2.2. VEGF, MAPK, and PAM Signaling Pathways

Quantitative real-time polymerase chain reaction (qPCR) analysis was performed to examine the gene expression of relevant genes of the VEGF, MAPK, and PAM signaling pathways. The qPCR data revealed a significant decrease in the amount of *VEGFA* mRNA in MCS compared to 1 g controls after 3 days and 5 days (Figure 2A).

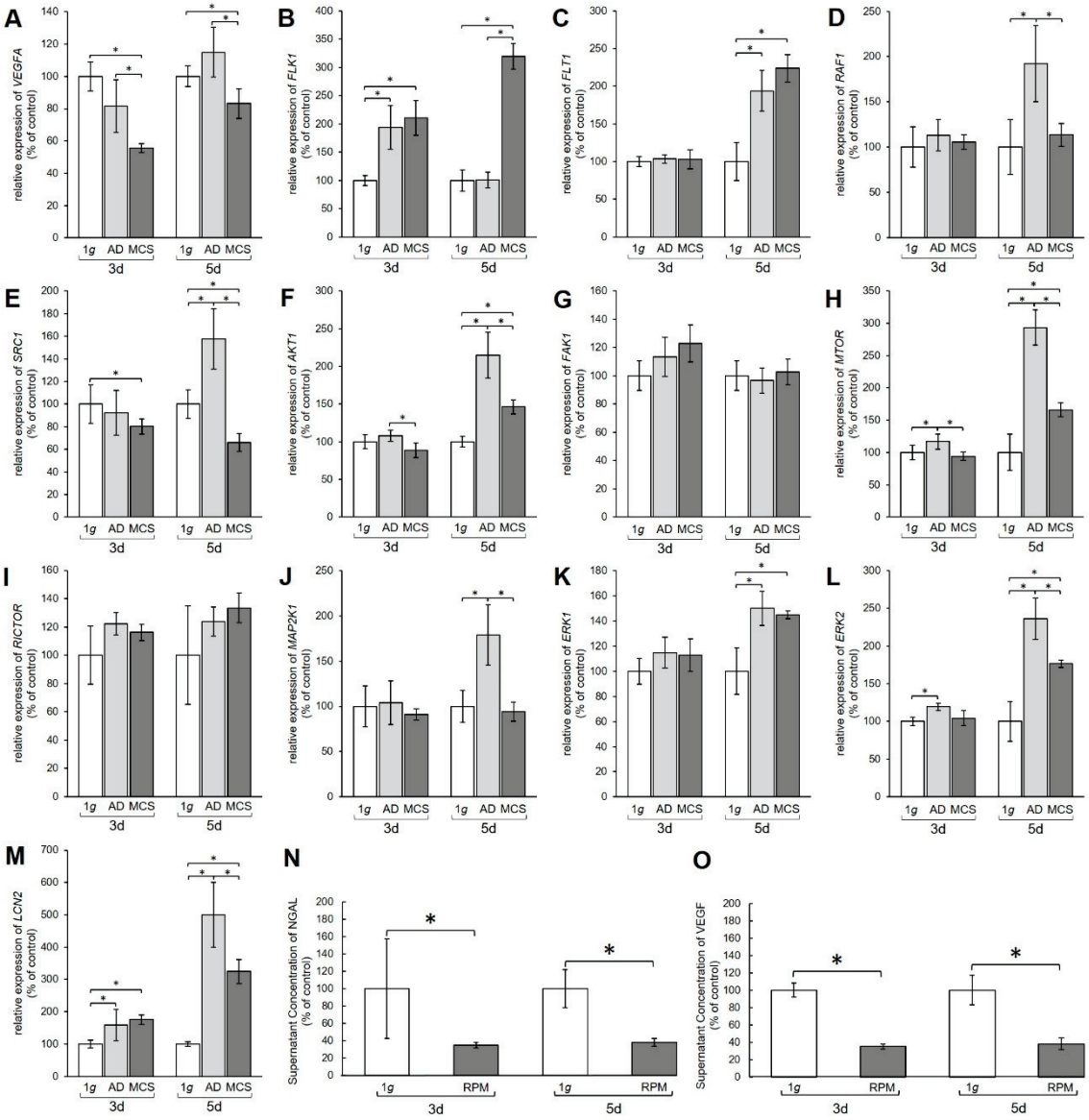


Figure 2. Gene expression of various proteins from the vascular endothelial growth factor (VEGF) signaling pathway. Results show relative mRNA transcription levels from (**A**) *VEGFA*, (**B**) *FLK1*, (**C**) *FLT1*, (**D**) *RAF1*, (**E**) *SRC1*, (**F**) *AKT1*, (**G**) *FAK1*, (**H**) *MTOR*, (**I**) *RICTOR*, (**J**) *MAP2K1*, (**K**) *ERK1*, (**L**) *ERK2*, and (**M**) *LCN2* genes. Results are shown as percentages of 3-day and 5-day 1 g controls. Time-resolved immunofluorometric assay (TRIFMA) results show amounts of (**N**) NGAL and (**O**) VEGF proteins in the supernatant taken from 3-day and 5-day flasks containing PC-3 cells, shown as percentages of 3-day and 5-day 1 g controls. * $p < 0.05$.

The mRNA levels of the VEGFA receptors *FLK1* and *FLT* also showed changes (Figure 2B,C). After 3 days the *FLK1* gene expression was significantly upregulated in both AD and MCS compared to 1 g. After 5 days the *FLK1* mRNA level in AD was unchanged, while MCS showed an increase compared to 1 g and AD (Figure 2B). The *FLT1* mRNA was unchanged after 3 days, but clearly upregulated in both 5-day AD and MCS groups compared with 1 g controls (Figure 2C).

Furthermore, the MAPK pathway was affected by the s-µg conditions. The *RAF1* mRNA was not changed after 3 days, but significantly increased in AD cells after 5 days (Figure 2D). The *SRC1* mRNA expression was significantly downregulated in 3-day MCS compared to corresponding 1 g samples, whereas a 5-day exposure induced upregulation of *SRC1* mRNA in AD and downregulation in MCS compared with 1 g controls and AD samples (Figure 2E). *AKT1* was downregulated in MCS compared to AD, but not significantly changed compared with 1 g after a 3-day RPM exposure. After 5 days, we measured an upregulation of the *AKT1* gene in AD and MCS compared with 1 g (Figure 2F). Interestingly, the *FAK1* gene expression was not significantly changed in all samples (Figure 2G). *MTOR* mRNA was significantly elevated in AD after 3 days and further enhanced after 5 days in both AD and MCS samples (Figure 2H). *RICTOR* gene expression was not differentially displayed in all groups (Figure 2I). Similarly, there was also no change in *MAP2K1* mRNA after 3 days, whereas after 5 days *MAP2K1* mRNA was significantly upregulated in AD cells (Figure 2J). *ERK1* was not changed in 3-day samples, but significantly enhanced in AD and MCS after 5 days (Figure 2K). *ERK2* was upregulated in AD samples after 3 days and, like *ERK1*, clearly upregulated in AD and MCS after 5 days (Figure 2L).

The transcription level of the lipocalin 2/NGAL protein neutrophil gelatinase-associated lipocalin (*LCN2*) gene, however, was increased in both AD and MCS compared to 1 g after 3 and 5 days, but decreased from AD to MCS after 5 days (Figure 2M). Furthermore, the amount of VEGF and NGAL protein secreted from the PC-3 cells into the medium was examined using time-resolved immunofluorometric assay (TRIFMA) (Figure 2N,O). Secreted amounts of VEGF and NGAL were significantly decreased after both 3 and 5 days of RPM-exposure.

2.3. Cytoskeleton

The effect of RPM exposure on the cytoskeleton was examined by qPCR analysis for the genes encoding β-actin and β-tubulin. In addition, F-actin and β-actin were visualized by immunofluorescence (IF). A redistribution of F-actin was observed in PC-3 cells when exposed to s-µg for 3 and 5 days (Figure 3A–C and Figure 3D–F, respectively). AD cells showed an accumulation of cortical actin compared to 1 g control cells. After 3 days, the formation of filopodia and lamellipodia could be observed (Figure 3B). After 5 days, filopodia, lamellipodia, and cortical stress fibers were prominent (Figure 3E). F-actin was accumulated at the cell membrane in MCS after both 3 and 5 days (Figure 3C,F). IF staining for β-actin (Figure 3G–L) did not show a clear difference in the distribution of the protein, although the AD at 3 days (Figure 3H) showed some membrane blebbing. *ACTB* gene expression revealed a significant upregulation in MCS compared to AD after 3 days (Figure 3M), while *TUBB* presented no expression changes (Figure 3N). After 5 days, *ACTB* and *TUBB* mRNAs were increased in both AD and MCS compared to 1 g control cells, and were lower in MCS than AD (Figure 3M,N).

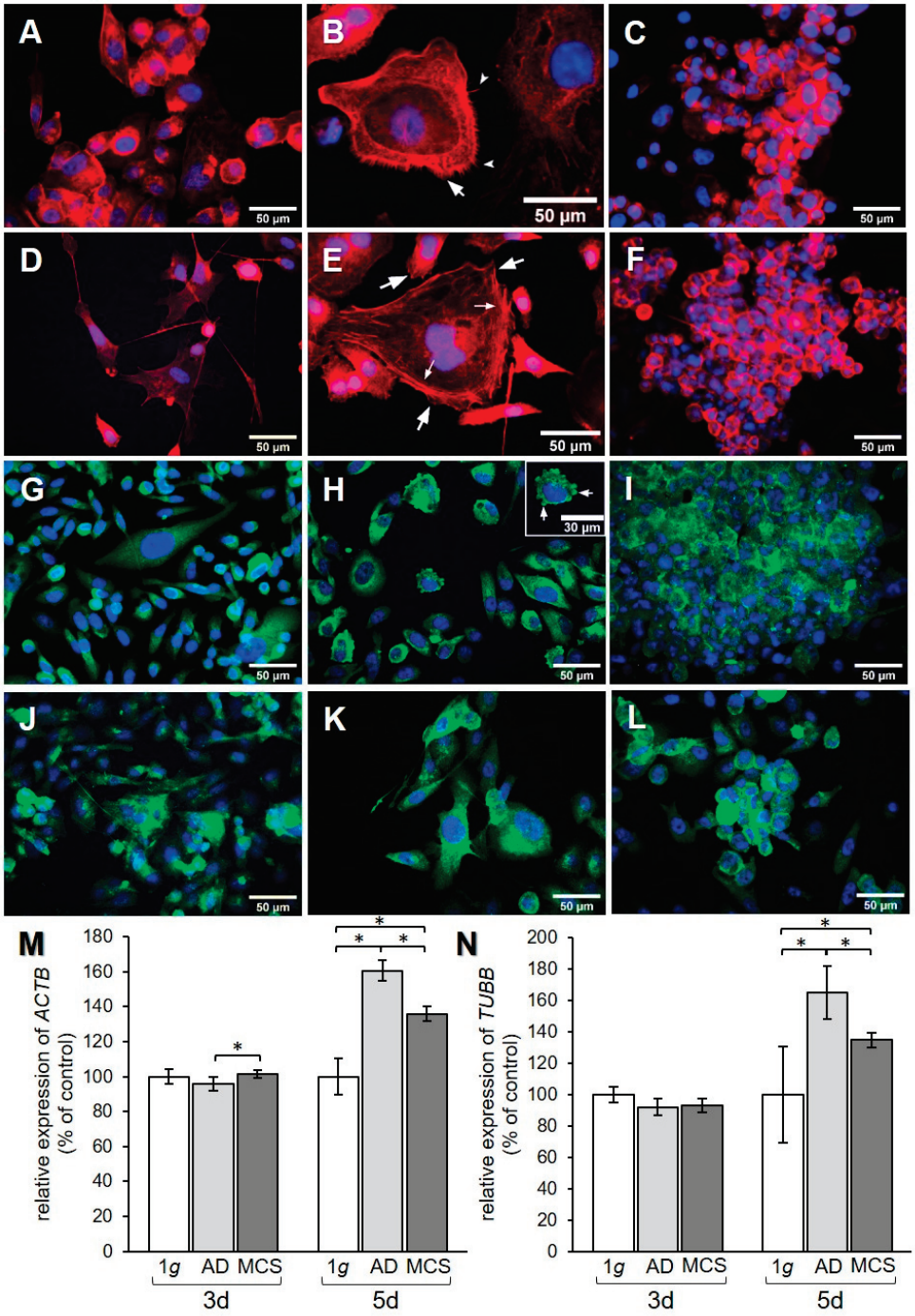


Figure 3. Investigation of the cytoskeleton. F-actin visualized by means of phalloidin and immunofluorescence (IF) staining for β-actin. F-actin pictures show (**A**) 3-day 1 g control, (**B**) 3-day AD, (**C**) 3-day MCS, (**D**) 5-day 1 g, (**E**) 5-day AD, and (**F**) 5-day MCS. Big arrows in (**B**) and (**E**) point to lamellipodia, notched arrows in (**B**) point to filopodia, and small arrows in (**E**) point to stress fibers. β-actin pictures show (**G**) 3-day 1 g control, (**H**) 3-day AD, (**I**) 3-day MCS, (**J**) 5-day 1 g, (**K**) 5-day AD, and (**L**) 5-day MCS. Arrows in (**H**) point to membrane blebbing. Relative mRNA transcription levels of (**M**) *ACTB* and (**N**) *TUBB* genes in 3-day and 5-day samples were analyzed by qPCR. * $p < 0.05$.

2.4. Extracellular Matrix

To examine the effect of s-µg on the ECM, the regulation of collagen, laminin, and fibronectin at the mRNA level and collagen deposition were investigated (Figure 4).

Sirius red staining of PC-3 cells revealed that 1 g cell samples (Figure 4A,D) and AD (Figure 4B,E) were negative for extracellular collagen after 3 and 5 days. However, collagen was found in RPM-exposed samples and was detectable in MCS. After 3-day exposure, a rim of collagen was formed around the cells in the MCS (Figure 4C). After 5 days, larger amounts of collagen were detectable in the center of the MCS, as demonstrated by the prominent red structures (Figure 4F).

qPCR data of the *COL1A1* gene expression revealed a decrease of this gene in MCS compared to both 1 g and AD after 3 days. After 5 days, an upregulation of *COL1A1* mRNA was measured in both AD and MCS compared to 1 g controls (Figure 4G). The gene expression of *COL4A5* was increased after 3 days in AD and MCS compared to 1 g, but decreased in MCS compared to AD. After 5 days, the *COL4A5* mRNA level was strongly elevated in MCS, while no difference was found between AD and 1 g (Figure 4H). The mRNA expression of the genes for the laminin α3 and β2 subunits was investigated. The mRNA level of the *LAMA3* gene was upregulated in AD and MCS compared to 1 g after 3 days, while the *LAMA3* mRNA level in MCS was lower than in AD. After 5 days, the *LAMA3* mRNA in AD was decreased compared to both 1 g and MCS, while MCS did not show a difference compared to 1 g (Figure 4I).

The *LAMB2* mRNA level in AD and MCS was unchanged after 3 days compared to 1 g. *LAMB2* was downregulated in MCS compared to AD. After 5 days, the *LAMB2* mRNA transcription was very high in AD compared to both 1 g and MCS (Figure 4J). The qPCR data for *FN1* showed an increase in AD and MCS cells compared to 1 g after 3 days (Figure 4K). After 5 days, the *FN1* mRNA level was decreased in AD samples compared to both 1 g and MCS (Figure 4K).

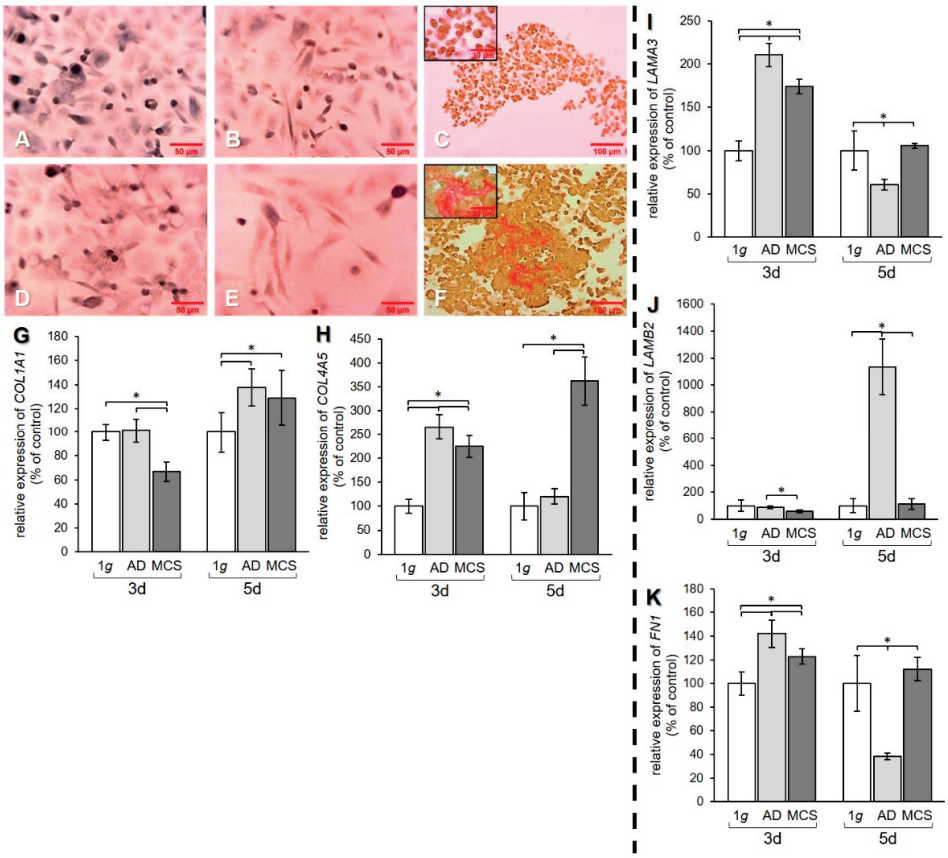


Figure 4. Investigation of ECM components. Collagen deposition in PC-3 cells stained with Sirius red (SR) after (**A**–**C**) 3 days and (**D**–**F**) 5 days. 1 g control cells (**A**,**D**) AD (**B**,**E**) and MCS (**C**,**F**). Depositions of collagen I and III are stained in red. qPCR results show relative mRNA transcription levels of (**G**) *COL1A1*, (**H**) *COL4A5*, (**I**) *LAMA3*, (**J**) *LAMB2*, and (**K**) *FN1* genes in 3-day and 5-day AD and MCS. * $p < 0.05$.

2.5. Altered Expression of Genes of the Focal Adhesion Complex

Finally, we examined the effect of s-μg-exposure of PC-3 cells on the transcription of genes involved in FA.

TLN1 gene expression was upregulated mRNA level after 3 days in AD, but not in MCS compared to 1 g, whereas after 5 days no significant changes were measured (Figure 5A). The mRNA expression of *VCL* was significantly elevated in AD and MCS samples compared to 1 g controls. This elevation of *VCL* was further enhanced after 5 days in both AD and MCS (Figure 5B). Moreover, the *CDH1* gene expression was clearly upregulated after an RPM-exposure in 3-day AD and MCS samples. In contrast, the *CDH1* mRNA expression was downregulated in AD after 5 days, while the *CDH1* level was still upregulated in MCS compared to both 1 g and AD (Figure 5C).

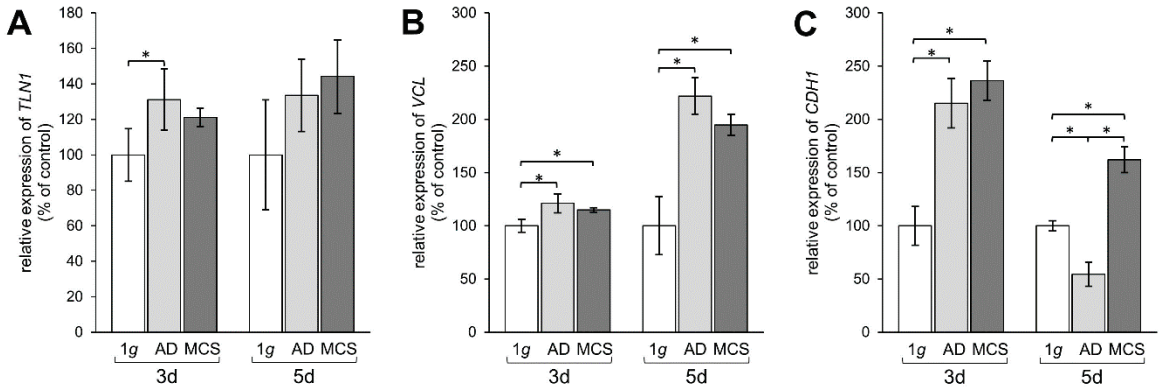


Figure 5. Investigation of gene expression of focal adhesion molecules talin-1, vinculin, and E-cadherin. qPCR results show relative mRNA transcription levels of (**A**) *TLN1*, (**B**) *VCL*, and (**C**) *CDH1* genes in 3-day and 5-day samples. * $p < 0.05$.

2.6. Interaction of Genes Investigated by Pathway Analysis

The various genes analyzed by qPCR (Figure 6A) were differentially regulated in μg samples (AD and RPM). Figure 6A presents a summary of the qPCR data, already described in Figures 2–5, and gives a comparable overview on the results. A closer look at the 3-day samples reveals that most genes involved in VEGF signaling (blue bars) are upregulated in AD samples compared to 1 g, while the gene expression in MCS presents a more heterogeneous pattern. Notably, *VEGFA*, *FLK1*, and *LCN2* are equally regulated in AD and MCS samples after 3 days. After a 5-day RPM-exposure, most of the investigated VEGF signaling molecules are significantly upregulated in AD samples. In comparison, 5-day MCS samples presented a significant regulation, which is in contrast to 3-day samples. Remarkably, *VEGFA* is not regulated in 5-day AD samples compared to 1 g. In addition, *LCN2* is strongly upregulated in all conditions. The cytoskeletal molecules of interest (green bars) are not regulated after 3 days. However, after 5 days, both conditions are upregulated. The investigated ECM molecules (violet bars) after a 3-day RPM-exposure present a comparable image in AD and MCS samples. After 5 days, AD cells show a heterogeneous expression image, while *LAMB2* is strikingly upregulated. In MCS, however, collagens are clearly enhanced, while *LAMB2* is not changed compared to the controls. Genes of the focal adhesion molecule complex (orange bars), especially *CDH1* mRNA, are highly upregulated in both 3-day conditions. Even though *CDH1* is still significantly upregulated, it seems to be reduced in 5-day conditions.

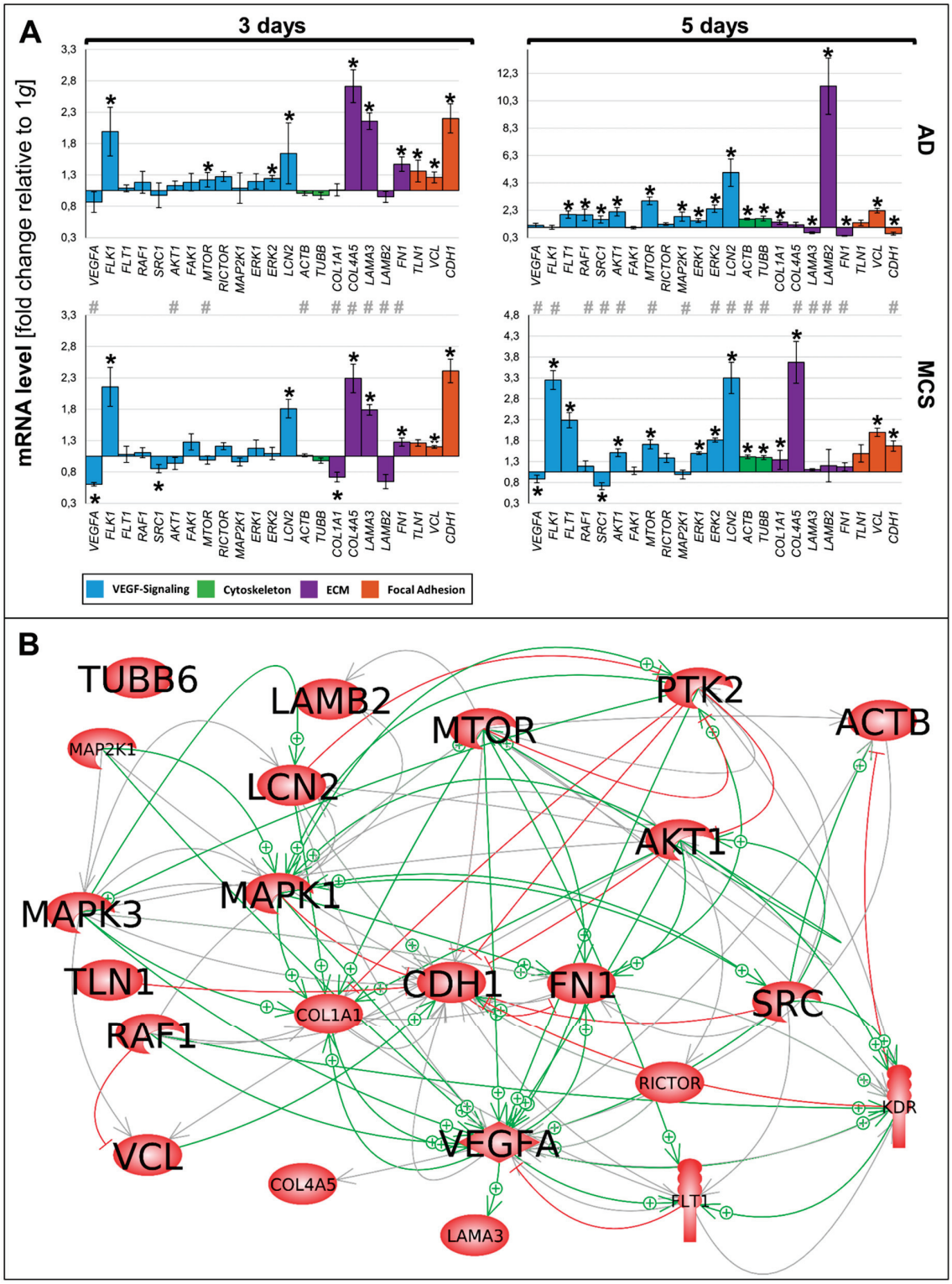


Figure 6. (**A**) Summary of gene expression fold change measured by qPCR of 3- and 5-day RPM-exposed PC-3 samples. Results determined in AD and MCS in relation to 1 g are shown. Color-coded bars represent genes of related biological processes. * $p < 0.01$ 1 g vs. AD/MCS, # $p < 0.01$ AD vs. MCS. (**B**) Interaction network of selected items at gene expression level; 22 of 23 selected genes analyzed by qPCR contribute to the network comprising 114 relations. Green arrows indicate activation and red arrows indicate inhibition. Gray lines signify that interactions take place whose effects have not been clarified. The interaction network was built using Elsevier Pathway Studio plus.

The 23 genes of interest were investigated in regard to their 114 possible interaction and mutual expression dependence. A pathway analysis of these items, represented in molecular action mode, is shown in Figure 6B. It can be seen that the components investigated are members of a complicated network, which includes the central factors *CDH1*, *VCL*, *TLN1*, *FN1*, *VEGFA*, *KDR*, *RAF1*, *ERK1/2*, *MAP2K1*, *MTOR*, *AKT1*, *PTK2*, and *SRC1*. Of these components, *CDH1* seemed to be the main node point.

3. Discussion

In this study, we focused on the changes induced in PC-3 cells when they were cultured under s-μg conditions. Possible simulation devices included RPM, RVW, and 2D clinostat. The RPM was chosen as this device rotates samples around two axes, thus enabling the cells to float freely and randomly in the medium, which increases the chances of interactions and MCS formation [16]. In addition, the RPM provides efficient diffusion of nutrients, gases, and waste through a small fluid flow [16]. The optimal method would be to cultivate the cells on a spaceflight, as this would provide real μg. In contrast, simulation devices average the gravity level to near zero without neutralizing it [18] and expose the cells to small fluid shear forces [46], which might slightly decrease the reproducibility in real μg. However, previous studies have noted that in many cases s-μg produces results similar to real μg [47]. Genes and proteins involved in the regulation of cancer cell proliferation and metastasis, such as IL6, IL8, and VEGFA, were similarly regulated under RPM and spaceflight conditions [47]. Therefore, in the future, it would be interesting to expose PC-3 cells to real μg to compare its effects to our results, as only space experiments can validate results obtained on devices on Earth [18].

When PC-3 cells were placed on the RPM, some of the cells remained adherent, while others detached and formed multicellular tumor-like spheroids. After 5 days, only a few cells remained growing adherently, while the majority were growing in MCS. Notably, variations in the shape, size, and density of the spheroids were observed. This could be due to variations in placement on the RPM. Nevertheless, various cell types exposed to s-μg have grown as multicellular spheroids and also as an adherent monolayer. Examples are thyroid cancer cells [20], breast cancer cells [21], and nonmalignant cells, such as endothelial cells [15].

3.1. Signaling Pathways Involved in Three-Dimensional Growth

3.1.1. VEGF Signaling

We examined the expression of genes belonging to the VEGF signaling pathway and found that the gene expression of *VEGFA* was downregulated after 3 and 5 days of exposure, except in 5-day AD. Accordingly, significant decreases in the amount of secreted VEGF and NGAL were found. This points toward development of a less-aggressive phenotype as a result of cultivation on the RPM, as VEGFA has been implicated in pathological angiogenesis and tumor development [32,48], while NGAL induces *VEGFA* expression [49], among other cancer-promoting functions [50–52]. The *LCN2* gene expression, on the other hand, was increased in all groups, potentially due to a counterregulatory mechanism. Possibly, mRNA levels increase in order to compensate the elevated protein secretion of NGAL protein in the supernatant. The development of a less-aggressive phenotype is supported by the findings in thyroid cancer cells [22,47] and human adult retinal pigment epithelium cells [31]. In contrast, the VEGF and NGAL secretion was elevated in endothelial cells exposed to μg [15]. Future studies should explore this μg-induced shift in greater detail. This can be elucidated by investigating the regulation of other genes and proteins linked to metastasis and proliferation of cancer cells, such as interleukin 6 (IL6), IL8, osteopontin, and fibroblast growth factor 17 [22,47].

In contrast to these findings, we found the expression of genes for the VEGF receptors *FLT1* and *FLK1* to be upregulated after 5 days in MCS, which might indicate a counterregulatory effect of the two VEGF receptors. Furthermore, we found a significant regulation of downstream signaling molecules,

with a general trend to upregulate the gene expression. This was especially evident after 5 days on the RPM.

3.1.2. MAPK Signaling

Factors of the MAPK signaling pathway are known to be involved in 3D growth and metastasis [1]. The biological process of the epithelial–mesenchymal transition (EMT) is known to increase migration and spreading of cancer cells, progression of the cell cycle, and resistance to apoptosis and chemotherapy [53]. Thus, we focused on *RAF1* mRNA expression. RAF1 acts as a regulatory link between the membrane-associated Ras GTPases and the MAPK/ERK cascade and functions as a switch determining, among others, proliferation, differentiation, and oncogenic transformation of human cells. Its main cellular role is in phosphorylation and activation of the MAP kinase kinases MEK1 and MEK2 [54].

In this study we found *RAF1* to be upregulated in AD cells but not in MCS. This indicates its activation by s-µg and its possible involvement in spheroid formation (Figure 2D). As RAF1 activation initiates a mitogen-activated protein kinase cascade, we also determined *MAP2K1* (also known as *MEK1*) gene expression. *MAP2K1* gene expression was comparable to the *RAF1* mRNA level and was significantly elevated in 5-day AD cells (Figure 2J). In a next step, we determined the expression of *ERK1* and *ERK2.* The ERK subfamily consists of typical (ERK 1/2/5) and atypical (ERK 3/4/7/8) members. ERKs are known to regulate EMT and promote tumor progression [54]. *ERK1/2* gene expression was significantly upregulated after 5 days in AD and MCS compared to 1 g samples (Figure 2K,L). Both ERK1 and ERK2 seem to be involved in 3D aggregation in µg.

3.1.3. PI3K/AKT/mTOR (PAM) Signaling

Tee et al. showed that the PAM signaling pathway is frequently mutated in prostate cancer [55]. The PAM pathway is involved in the regulation of growth, metabolism, and migration [55]. In our experiment, the *AKT* gene expression was enhanced in AD and MCS samples after a 5-day RPM-exposure of prostate cancer cells. Activated AKT phosphorylates a host of proteins involved in cell growth, including mTOR [56]. Interestingly, we observed an upregulation of the *MTOR* gene expression in AD after 3 days and in all RPM-exposed cell samples after 5 days. According to the clinicaltrials.gov database, various inhibitors of this pathway are currently being tested in 36 phase I/II clinical trials for prostate cancer, either as monotherapy or in combination with conventional chemotherapies [57].

Finally, we focused on the *SRC1* gene, which belongs to the p160 family of SRCs. SRCs promote cancer cell proliferation, survival, metabolism, migration, invasion, and metastasis. In prostate cancer, *SRC1* is highly expressed [58]. We found an upregulated *SRC1* gene in AD cells after 5 days, indicating its involvement in migration and 3D formation.

Together with MAP1K2, SRC-1 regulates the transcriptional activity of STAT3 [59]. In addition, it blocks upregulation of the VEGF-A receptors [60] and inhibits expression of E-cadherin [61]. On the other side, SRC-1 activates FAK1 [62], which strengthens vinculin, containing focal adhesion complexes [63] that link cells to fibronectin or other components of the ECM [64] and include talin-1 as a hinge between the cytoskeleton and the extracellular space [65]. Downregulation of talin favors activation of the MAPK1/MAPK3 pathway [66].

3.2. Changes in the Cytoskeleton and the Extracellular Matrix

In this study we observed s-µg-induced changes in the F-actin network of the cells. The formation of lamellipodia and filopodia in our cells under s-µg might indicate that the cells are trying to adhere better to the ECM to resist the s-µg conditions, because these structures are involved in migration and adherence of cells to the substrate [67]. In addition, the stress fibers also present might have formed in order to compensate for changes in adhesion and cell morphology [68].

The cortical F-actin accumulation is consistent with earlier findings in endothelial cells, although the latter also showed perinuclear accumulation [12]. An increase in the density of F-actin was also found in A431 cells, although the actin filaments became less organized [69]. Just like PC-3 cells, human fetal osteoblasts showed formation of filopodia and lamellipodia [70]. In contrast, osteoblasts had reduced cortical actin and fewer stress fibers [71]. It is clear from these examples that the changes in F-actin induced by µg depend on the cell type.

Moreover, we found that the mRNA level of *ACTB* was increased after 5 days. This is in accordance with similar findings in follicular thyroid cancer cells [72]. In addition, our qPCR analysis showed an increased *TUBB* mRNA level in PC-3 cells exposed to s-µg, which is similar to earlier results in endothelial cells [73].

In general, we found a tendency of elevated ECM components at the mRNA level when PC-3 cells were exposed to s-µg on the RPM. The mRNA levels of the *COL1A1*, *COL4A5*, *LAMA3*, *LAMB2*, and *FN1* genes were upregulated or unchanged, with only a few exceptions. In addition, collagen deposition was found in spheroids. A possible explanation for this finding could be that the cells try to increase the ECM to resist the s-µg conditions, because the ECM provides structural support for the cells [74], which they lack after detaching because of the RPM-exposure. Our results concerning the ECM fit the findings of a study of human fetal osteoblasts exposed to s-µg, where the cells showed collagen deposition in spheroids and increased *FN1* and *LAMA1* gene expression [70]. However, the gene expression of *COL4A5*, *FN1*, and *LAMB2* was reduced in s-µg-exposed adult retinal pigment epithelial cells [31]. Thus, regulation of ECM compounds because of µg-exposure must depend on the cell type.

We found an increase in the focal adhesion component *VCL* mRNA. It is plausible that this change occurs because the cells are trying to resist the s-µg conditions and hold onto the ECM, although this does not match the generally unchanged amounts of *TLN1* gene expression in our experiment. In contrast to the results of this study, FTC-133 cells exposed to µg showed no change in *VCL* expression and decreased *TLN* mRNA [75]. Thus, PC-3 cells and FTC-133 cells show a different regulation of FA gene expression and, possibly, synthesis or secretion of proteins.

Finally, we detected a general upregulation of the *CDH1* gene expression. In conjunction with our observations on the secretion of VEGF and NGAL described above, this could also indicate a tendency toward a less-aggressive phenotype, as *CDH1* is a tumor suppressor gene, and inactivation of E-cadherin is involved in the development of prostate cancer [76,77]. E-cadherin was enhanced in papillary thyroid carcinoma cells [78], but decreased in human breast cancer cells [79] exposed to s-µg conditions. Thus, E-cadherin acts depending on the cell type.

3.3. Interaction Network of Selected Genes Evaluated by Pathway Analysis

In the pathway analysis various interactions were found, but *VCL*, *FN1*, *mTOR*, *SRC1*, and *VEGFA* are indicated as dominant target genes, as many arrows point to their icons (Figure 6B).

There are interactions between vinculin and fibronectin. *FN1* and *VCL1* were both upregulated in MCS after 3- and 5-day RPM-exposure (Figures 4K and 5B). Similar findings were reported after 24- and 48-h clinostat-exposures of poorly differentiated follicular thyroid cancer cells exhibiting increased expression of vinculin and among other ECM proteins as well as fibronectin in MCS compared with 1 g controls [11]. A recent paper reported that FN1 KO podocytes showed significant downregulated FA molecules (talin, vinculin, and paxillin) and reduced cell spreading, indicating an important role of FN1 in adhesion [80]. FN1 plays a key role in the adaptation of podocytes to mechanical stress. Moreover, this supports the hypothesis that its interaction with vinculin is an adaptive mechanism to protect µg-exposed prostate cancer cells and other cell types.

In addition, there is an interaction between vinculin and MAPK1 (ERK2). Both factors are involved in transmitting and transducing environmental signals to biochemical cascades. The protein kinases are known to regulate the activity of FA proteins [81]. Vinculin also interacts with MAPK3 (ERK1). Macrophages grown on polished surfaces changed from spherical to well-spread cells. These

morphological changes were associated with an altered distribution of vinculin [82]. The pFAK, pSrc, pERK1/2 levels were associated with cell shape and a more spread morphology [82].

There is an interesting interaction between FN1 and MAPK3 (ERK2). Treatment of PC-3 cells with 1 μM FN1 resulted in a decrease of activated ERK1/2 [83]. In clear-cell renal cancer, eight differentially expressed genes were identified as biomarkers, including *VEGFA*, *FLT1*, *FN1*, and others [84]. Both fibronectin and VEGF are known to stimulate blood vessel formation. Patient data showed that circulating fibronectin modulates blood vessel formation and tumor growth by modifying the amount of and response to VEGF [85]. In addition, measuring the fibronectin level can serve as a prognostic biomarker for prostate cancer and possibly others.

The *SRC1* mRNA was significantly downregulated in MCS after 3- and 5-day RPM-exposure of prostate cancer cells (Figure 2E), whereas *VCL* was elevated in MCS in our experimental setting (Figure 5B). Moreover, *CDH1* mRNA expression was enhanced in PC-3 MCS after 3 and 5 days on the RPM (Figure 5C). The product of the human SRC gene, *c-Src*, is overexpressed and often activated in many human cancers. The relationship between Src activation and cancer progression appears to be significant [86].

Interestingly, the exposure of PC-3 cells induced a decrease in *SRC1*, which supports the hypothesis that the PC-3 cells showed a more moderate expansion behavior as compared to MCF-7 breast cancer cells. In contrast, in MCF-7 breast cancer spheroids, c-Src was elevated and E-cadherin was reduced [79]. MCS formation could be prevented by inhibition of c-Src and enhanced by blocking of E-cadherin. These results suggest that the balance of proteins that up- or downregulate E-cadherin mediates the tendency of breast cancer cells to form MCS during s-μg-exposure [79].

In addition, there was another detectable interaction between SRC and laminin subunit alpha-3 (LAMA3). *LAMA3* gene expression was upregulated in AD and MCS after a 3-day RPM-exposure of the cells. It also was shown earlier that the recently identified Lm3B11, consisting of laminin α3B (encoded by *LAMA3*), β1, and γ1 chains, stimulated the phosphorylation of Src and Akt more strongly than other laminins in vascular basement membranes [87]. This unique activity of Lm3B11 appears to be favorable to the process of angiogenesis.

SRC has been found to play a crucial role in VEGF-dependent vascular permeability involved in angiogenesis. Chou et al. showed that the two main VEGFRs, kinase insert domain-containing receptor/fetal liver kinase-1 (KDR/Flk-1) and Fms-like tyrosine kinase-1 (Flt-1), interact with SRC. VEGF stimulation elevated SRC activity associated with activated KDR/Flk-1 in endothelial cells [88]. The gene expression of *VEGFA* was downregulated, whereas both VEGFA-receptor genes, *KDR* and *FLT1*, were upregulated in all 5-day RPM samples, which might indicate a counterregulatory effect (Figure 2A–C). In colon cancer cells, SRC induced VEGF, thus enhancing angiogenesis [89,90]. The relationship between Src and VEGF appears to be somewhat reciprocal [86]. VEGF-induced activity is negated with the inhibition of Src activity. Src also appears to provide a link in VEGF signaling of MAPK pathways, contributing to spreading and metastasis [90].

In PC-3 prostate cancer cells, we found a significant downregulation of *VEGFA* mRNA and protein secretion, indicating a lower metastatic potential of the cells when exposed to microgravity. These results are similar to those obtained from low-differentiated follicular thyroid cancer cells in space [47], where we also found a downregulation of both VEGFA gene and protein secretion.

The PI3K/AKT/mTOR signaling pathway plays a key role in cancer metastasis. The activation of a mitogenic pathway involving a feedback mechanism between mTOR and PI3K/ERK1/2 is important for the tumorigenesis of glioblastoma multiforme [91] and may be involved in 3D spheroid formation in s-μg. The MAPK and PI3K/AKT/mTOR pathways regulate cell survival, proliferation, and motility. In addition to their independent signaling programs, the pathways engage in an extensive crosstalk to both positively and negatively regulate each other. Encouragingly, co-inhibition of both pathways has been successful in reducing tumor growth in xenograft cancer models and, importantly, also in genetically engineered mouse models [92,93]. mTOR catalyzes the phosphorylation of multiple targets such as AKT, protein kinase C (PKC), and others, thereby regulating various biological processes such

as tumor growth and metastasis. Many mTOR inhibitors have been developed to treat cancer. While some of them have been approved to treat human cancer, more mTOR inhibitors are being evaluated in clinical trials. In addition, current research is designed to optimize the use of VEGF/VEGF receptor inhibitors and mTOR inhibitors for combination or sequential treatment of patients with advanced cancer [94,95].

In short, the s-μg conditions created by the RPM caused differential regulations of the expression of the VEGF, MAPK, and PAM pathway-involved genes *VEGFA*, *FLK1*, *FLT1*, *RAF1*, *SRC1*, *AKT1*, *MTOR*, *MAP2K1*, *ERK1*, and *ERK2*, as well as the genes *ACTB*, *TUBB*, *COL1A1*, *COL4A5*, *LAMA3*, *LAMB2*, *FN1*, *TLN1*, *VCL*, and *CDH1*, involved in signal transduction in the cytoskeleton, ECM, and FAs. Furthermore, a redistribution of F-actin was found in the cells, as well as a deposition of collagen in MCS and decreased secretion of VEGF and NGAL. Thus, s-μg resulted in the regulation of proteins and genes involved in angiogenesis, cell morphology, migration, attachment, ECM, and 3D growth. Possibly, some changes are due to attempts to resist the alterations in μg. Moreover, the PC-3 cells formed spheroids when cultured in s-μg conditions. These 3D constructs might be useful in future studies on the effects of anticancer drugs, as they more closely mimic the cellular environment in actual metastasis, including, for example, the need for diffusion of the drug into the core of the spheroid as opposed to monolayer cell cultures. A future project could be to examine the effects of drugs targeting the proteins regulated in the PC-3 cells when exposed to μg. This was done, for example, with dexamethasone targeting NFκB in breast cancer cells [21], and possible drug investigations are planned for thyroid cancer cells in μg [22]. In addition, it is also important to apply different signaling pathway inhibitors as well as an agonist to investigate the role of μg in prostate cells. Further examination of prostate cancer cells in weightlessness may thus contribute to investigations concerning treatment options and possibly reduce animal experiments in the field of prostate cancer.

4. Materials and Methods

4.1. Cell Culturing and Microgravity Simulation on the RPM

The human prostatic carcinoma cell line PC-3 was established from a human prostatic adenocarcinoma metastatic to bone, enabling investigations concerning the changes involved in advanced prostate cancer as well as response to treatment [96]. PC-3 cells (ECACC 90112714) were thawed from a frozen aliquot preserved in liquid nitrogen. They were seeded in T75 flasks (Sarstedt, Nümbrecht, Germany) with RPMI 1640 medium (Gibco, Fisher Scientific, Schwerte, Germany) containing 14% fetal bovine serum (FBS) (Sigma-Aldrich) and 1% penicillin/streptomycin (Gibco, Fisher Scientific, Schwerte, Germany). Afterwards, the medium was changed when necessary, using RPMI 1640 medium with 7% FBS and 1% penicillin/streptomycin. When the cells had grown appropriately, they were subcultured in T25 flasks (Sarstedt) and slideflasks (Thermo Scientific, Waltham, MA, USA) and left in 1 g conditions until reaching approximately 60% confluence.

After reaching 60% confluence, all flasks were filled completely with RPMI medium containing 10% FBS and 1% penicillin/streptomycin. Filling the flasks completely and without air bubbles was important to reduce shear stress and disturbance of the cells. Half of the flasks were mounted on the middle frame of the RPM. The other half were placed beside the RPM in 1 g conditions as controls. The RPM used in this experiment (a desktop model from Airbus, Defense and Space, Leiden, the Netherlands) was, along with all flasks, placed in an incubator at 37 °C and 5% CO_2. Then, the RPM was started, exposing the cells to s-μg conditions for the chosen time periods (3 or 5 days). The RPM simulates μg with a calculated residual acceleration of approximately ~10^{-3} g [97]. The maximal distance to the rotation center was chosen to be 7 cm, and the rotational acceleration was 20°/s^2. The device was described in detail by Grimm et al. [98].

4.2. Sample Collection

Three groups were collected from the RPM experiments: 1 g, AD, and MCS. In addition, aliquots of medium (cell supernatants) were collected for the TRIFMA experiment.

The control cells were collected from the T25 flasks exposed to 1 g conditions. First, several aliquots of medium from the flasks were collected. The rest of the medium was discarded, the cells were washed with 5 mL of phosphate-buffered saline (PBS) and then scraped off the bottom of each flask with a cell scraper, and another 5 mL PBS (Gibco, Fisher Scientific, Schwerte, Germany). The cell suspensions were transferred to tubes and subsequently centrifuged. After discarding the supernatant, the cell pellets were resuspended in PBS and transferred to reaction tubes.

MCS were collected from the T25 flasks from the RPM. First, the flasks were left until the spheroids had all fallen to the bottom. Then, several aliquots of medium were collected, after which the flasks were shaken to allow the MCS to redistribute themselves in the liquid. The medium was transferred to new tubes and centrifuged. The supernatant was discarded and the pellets containing the MCS were resuspended in PBS and transferred to Eppendorf tubes.

AD were collected from the RPM flasks by scraping the cells in PBS, then transferred to Eppendorf tubes.

Following the collection, all Eppendorf tubes were centrifuged, the supernatant was discarded, and pellets were snap-frozen in liquid nitrogen and stored at −80 °C. The supernatant aliquots were frozen and stored at −20 °C. All centrifugation steps were performed at 3000 rpm and 4 °C for 10 min.

4.3. RNA Isolation

RNA isolation was done using the RNeasy Mini Kit (Qiagen, Hilden, Germany). The samples were thawed and kept on ice. First, 10 µL of β-mercaptoethanol (BME) was added to 1 mL of lysis buffer (RTL), followed by the addition of 600 µL of this mixture to each sample. The samples were incubated for 2 min and the cells were lysed by applying shear force while passing them through a 20 G needle. Finally, 600 µL of 70% ethanol was added to each sample.

Then 700 µL of each sample was transferred to RNeasy Mini spin columns and 700 µL of Buffer RW1 and 500 µL of Buffer RPE were added. Between these steps the samples were centrifuged for 15 s at 8000× *g*, and flow-through was discarded. Then 500 µL of Buffer RPE was added again, this time followed by centrifugation for 2 min at 8000× *g*, and flow-through was discarded. Finally, the samples were centrifuged for 1 min to dry the membrane and remove any remaining ethanol.

The RNeasy spin columns were placed in new collection tubes, followed by the addition of 35 µL of RNase-free water directly to the membrane. The RNA was eluted from the membrane by centrifugation for 1 min at 8000× *g*.

4.4. Quantitative Real-Time Polymerase Chain Reaction

Before performing qPCR, primers were designed using NCBI Primer Blast, which were selective for cDNA by spanning exon–exon junctions and had a melting temperature of around 60 °C. The primers were synthesized by TIB Molbiol (Berlin, Germany). The primers used are listed in Table 1.

Table 1. List of primer sequences used in quantitative PCR. All sequences are listed in the 5′–3′ direction.

Factor	Primer Name	Sequence 5′–3′
18S-rRNA	18s-F	GGAGCCTGCGGCTTAATTT
	18s-R	CAACTAAGAACGGCCATGCA
Actin-beta (***ACTB***)	ACTB-F	TGCCGACAGGATGCAGAAG
	ACTB-R	GCCGATCCACACGGAGTACT
RAC-alpha Serine/threonine-protein kinase (***AKT1***)	Akt1-F	CTTCTATGGCGCTGAGATTGTG
	Akt1-R	CAGCATGAGGTTCTCCAGCT
Collagen 1 alpha 1 (***COL1A1***)	COL1A1-F	ACGAAGACATCCCACCAATCAC
	COL1A1-R	CGTTGTCGCAGACGCAGAT
Collagen 4 alpha 5 (***COL4A5***)	COL4A5-F	GGTACCTGTAACTACTATGCCAACTCCTA
	COL4A5-R	CGGCTAATTCGTGTCCTCAAG
E-cadherin (***CDH1***)	CDH1-F	GCTGGACCGAGAGAGTTTCC
	CDH1-R	CAGCTGTTGCTGTTGTGCTT
Extracellular signal-regulated kinase 1 (***ERK1***)	ERK1-F	ACCTGCGACCTTAAGATTTGTGA
	ERK1-R	AGCCACATACTCCGTCAGGAA
Extracellular signal-regulated kinase 2 (***ERK2***)	ERK2-F	TTCCAACCTGCTGCTCAACA
	ERK2-R	TCTGTCAGGAACCCTGTGTGAT
Focal adhesion kinase 1 (Protein-tyrosin kinase 2) (FAK1 (***PTK2***))	FAK1-F	TGTGGGTAAACCAGATCCTGC
	FAK1-R	CTGAAGCTTGACACCCTCGT
Fibronectin (***FN1***)	FN1-F	TGAGGAGCATGGTTTTAGGAGAA
	FN1-R	TCCTCATTTACATTCGGCGTATAC
Laminin alpha 3 (***LAMA3***)	LAMA3-F	AAAGCAAGAAGTCAGTCCAGC
	LAMA3-R	TCCCATGAAGACCATCTCGG
Laminin β2 (***LAMB2***)	LAMB2-F	TGCTCATGGTCAATGCTAATCTG
	LAMB2-R	TCTATCAATCCTCTTCCTTGGACAA
Mitogen-activated protein kinase kinase 1 (***MAP2K1***)	MAP2K1-F	CGTTACCCGGGTCCAAAATG
	MAP2K1-R	TCCAAGTTGGTCTCCGCA
Mechanistic target of rapamycin kinase (***MTOR***)	MTOR-F	ATCTTGGCCATAGCTAGCCTC
	MTOR-R	ACAACTGGGTCATTGGAGGG
Neutrophil gelatinase-associated lipocalin (NGAL, ***LCN2***)	LCN2-F	AGGGAGTACTTCAAGATCACCCTCTA
	LCN2-R	AGAGATTTGGAGAAGCGGATGA
Raf-1 proto-oncogene, serine/threonine kinase (***RAF1***)	RAF1-F	GGGAGCTTGGAAGACGATCAG
	RAF1-R	ACACGGATAGTGTTGCTTGTC
Rapamycin-insensitive companion of MTOR (***RICTOR***)	RICTOR-F	GGAAGCCTGTTGATGGTGAT
	RICTOR-R	GGCAGCCTGTTTTATGGTGT
Steroid receptor coactivator-1 (***SRC1***)	SRC1-F	CCACCTTTGTGGCCCTCTAT
	SRC1-R	CCTCTGTGTTGTTGACAATCTGG
Talin-1 (***TLN1***)	TLN1-F	GATGGCTATTACTCAGTACAGACAACTGA
	TLN1-R	CATAGTAGACTCCTCATCTCCTTCCA
Tubulin-beta (***TUBB***)	TUBB-F	CTGGACCGCATCTCTGTGTACTAC
	TUBB-R	GACCTGAGCGAACAGAGTCCAT
Vascular endothelial growth factor A (***VEGFA***)	VEGFA-F	GCGCTGATAGACATCCATGAAC
	VEGFA-R	CTACCTCCACCATGCCAAGTG
Vascular endothelial growth factor receptor 1 (***FLT1***)	FLT1-F	CCCTCGCCGGAAGTTGTAT
	FLT1-R	GATAATTAACGAGTAGCCACGAGTCAA
Vascular endothelial growth factor receptor 2 (***FLK1***)	FLK1-F	TCTTCTGGCTACTTCTTGTCATCATC
	FLK1-R	GATGGACAAGTAGCCTGTCTTCAGT
Vinculin (***VCL***)	VCL-F	GTCTCGGCTGCTCGTATCTT
	VCL-R	GTCCACCAGCCCTGTCATTT

The first step was to generate cDNA from the RNA using the high capacity cDNA reverse transcription kit (Applied Biosystems, Foster City, CA, USA). The RNA concentrations of all samples were measured using a NanoDrop. The results were used to calculate the amount of RNA and

nuclease-free water needed to obtain 1 μg of RNA in a final volume of 10 μL. The nuclease-free water was pipetted into wells on a 96-well plate, followed by addition of RNA, then 10 μL of master mix was added to each well. This contained RT buffer, dNTP mix, RT random primers, reverse transcriptase, and nuclease-free water. The plate was sealed and centrifuged briefly to eliminate any air bubbles and spin down liquid. The thermal cycler was run using the following program: primer annealing for 10 min at 25 °C reverse transcription for 120 min at 37 °C and enzyme deactivation for 5 min at 85 °C. After this, 50 μL of nuclease-free water was added to each well to obtain a working volume of 70 μL for the next steps.

The qPCR was carried out using FAST SYBR™ Green Master Mix (Applied Biosystems) and the 7500 Fast Real-Time PCR System (Applied Biosystems). First, a master mix was prepared for measurement of all samples in triplicate as well as 3 no-template controls (NTCs). The master mix contained MM Buffer, reverse primer, forward primer, and water. Then, a sub-master mix was prepared for each sample by mixing 42 μL of master mix and 3 μL of cDNA. For each sample, 13 μL of the sub-master mix was pipetted into a 96-well plate in triplicate. NTCs were added to the last 3 wells. The plate was sealed, centrifuged briefly, and stored at 4 °C. When ready to use, the plate was placed in the instrument, and the thermal cycling conditions were set: 95 °C for 20 s, 95 °C for 3 s, and 60 °C for 30 s. The reaction volume was set to 15 μL and the program was run.

In the following analysis the samples were normalized to 18S rRNA. The comparative threshold cycle ($\Delta\Delta C_T$) method was utilized to obtain the relative transcription levels; 1 g controls were defined as 100%.

4.5. Immunofluorescence

Staining experiments were performed on cells grown in slideflasks that had been cultured on the RPM for 3 or 5 days and their corresponding 1 g controls in order to investigate the change in distribution of F-actin and β-actin.

When the flasks were taken off the RPM, the medium was discarded and the cells were washed three times with PBS and afterwards fixed with 4% paraformaldehyde (PFA; Sigma-Aldrich, St. Louis, MO, USA) in PBS. All slides were stored at 4 °C until ready to use. When ready, the PFA was removed and the slides were washed with PBS, followed by the addition of 0.1% Triton X-100 (Sigma-Aldrich, St. Louis, MO, USA), which was left for 15 min. Then, the slides were removed from the flasks and placed in a dark and moist chamber. Rhodamine–phalloidin (for F-actin; Sigma, P1951, diluted 1:250) or primary antibody (for β-actin; Sigma, A5316, diluted 1:1000) diluted in 0.5% bovine serum albumin (BSA) (Merck, Darmstadt, Germany) in PBS was pipetted onto each slide. For β-actin, the incubation was left overnight, and the next day secondary antibody (anti-mouse IgG Fab2 Alexa Fluor® 488 Molecular Probes 2 mg/mL #4408S, diluted 1:500) diluted in PBS was added. The secondary antibody was left on the slides for a minimum of 4 h.

Finally, the slides were prepared with Fluoroshield™ mounting medium containing 4′,6′-diamidino-2-phenylindole (DAPI) (Sigma-Aldrich, St. Louis, MO, USA). The slides were sealed by putting a coverslip on top and stored in a dark box at 4 °C. Between steps, the slides were washed with cold PBS.

4.6. Histochemical Staining

Histological staining was performed on 3- and 5-day 1 g controls and RPM slides using hematoxylin-eosin (HE) and Sirius red (SR) stains as described earlier [99,100].

The histological staining was done on cells on slides and on MCS on separate slides. After culturing the cells on the RPM for 3 or 5 days, the MCS were collected from the slides with a pipette, washed three times in PBS, and then fixed in 4% PFA. Then they were embedded in paraffin, followed by sectioning into 3 μm sections with a microtome. For 1 g and RPM AD samples, the medium was discarded and the slides were washed three times with PBS, and afterwards 4% PFA was applied. The

slides and sectioned spheroids were stained with HE or SR. HE staining was used to evaluate the cell morphology, while SR staining was used to investigate the collagen content.

4.7. Microscopy

All flasks containing viable cells were examined throughout growth as well as before and after RPM-exposure with a Leica phase contract microscope. Pictures were taken using a Canon EOS 550D camera. All cells stained by immunofluorescence were examined with a Leica DFC310 FX fluorescence microscope. Pictures were taken at 20×, 40×, and 100× magnification using the LAS V3.7 software. The pictures were not taken using the same settings, as the signal intensities were not quantified. The pictures were instead used to examine the locations of the proteins. Immersion oil (Sigma-Aldrich, St. Louis, MO, USA) was applied to the slides when using the higher resolution.

4.8. Time-Resolved Immunofluorometric Assay

TRIFMA was performed as described earlier [101,102]. In brief, microtiter 96-well plates were coated overnight at 4 °C with primary antibodies dissolved in PBS. They were specific for either NGAL (1 µg/mL) or VEGF (2 µg/mL). All wells were then incubated with blocking buffer (1% Tween-20 in PBS) for 2 h.

The samples were diluted 1:2 in assay buffer to a total of 100 µL and added to the plates. The assay buffer used was PBS supplemented with 0.05% Tween-20. In addition, recombinant standards (VEGF and NGAL) were added to the plate (100 µL per well). Negative control samples, containing 100 µL of assay buffer without added supernatant, were also added to the plates. All samples were added to the plates in duplicate to increase the precision of the results.

The Fluorescence was measured using a time-resolved fluorometer (PerkinElmer, Waltham, MA, USA). The concentrations of VEGF and NGAL were determined using a 4-parameter standard curve fit implemented in WorkOut 2.5 data analysis software (PerkinElmer, Waltham, MA, USA).

4.9. Pathway Analysis

To investigate the mutual regulation of genes and visualize localization and interactions between proteins, we entered relevant UniProtKB entry numbers in the Pathway Studio plus software (Elsevier Research Solutions, Amsterdam, The Netherlands). Graphs were generated for gene expression and protein regulation and binding. The method was described previously [103].

4.10. Statistical Analysis

All statistical evaluations were performed using IBM SPSS Statistics 23 (IBM Deutschland GmbH, Ehningen, Germany). The Mann–Whitney U-test was utilized to evaluate the statistical significance of the changes in expression levels following RPM exposure, thus comparing 1 g control to AD and MCS. A significance level of 0.05 was used. The standard deviation was calculated and presented together with the mean values as percentages in bar plots.

5. Conclusions

Prostate cancer cells (PC-3 cell line) exposed to s-µg conditions generated by an RPM grew as adherent cells and in the form of 3D MCS. The RPM-exposed cells revealed alterations in the cytoskeleton, as well as gene expression changes of cytoskeletal and FA factors and ECM components. The VEGF, MAPK, and PAM signaling pathways are involved in 3D formation of prostate cancer cells. The majority of the factors are upregulated, indicating their impact on growth and progression of these cells.

Overall, our study suggests that these pathways drive the regulation of metastasis, survival, and angiogenesis of prostate cancer cells.

Author Contributions: RPM experiments: T.E.H. and J.S.; conceptualization, D.G., T.J.C., and S.K.; methodology, S.K., M.Z.N., D.D., and J.S.; software, J.B., M.W., and S.K.; validation, D.G., T.J.C., S.K., and M.K.; formal analysis, M.Z.N., S.K., J.S., D.D., and M.W.; investigation, T.E.H., N.E.M., M.Z.N., J.S., M.E., and S.K.; resources, M.I. and K.U.; writing—original draft preparation, T.E.H., S.K., T.J.C., D.G., and J.B.; project administration, D.G.; funding acquisition, D.G. and M.I. All authors have read and agree to the published version of the manuscript.

Funding: This research was funded by the German Space Agency (DLR; BMWi project 50WB1924) and Aarhus University (DG).

Acknowledgments: We would like to thank Christa Baumann, Institute of Pathology, University of Regensburg, University Hospital, Regensburg, Germany for performing the paraffin sections, and HE and Sirius red staining.

Conflicts of Interest: The authors declare no conflict of interest.

Abbreviations

AD	Adherent cell(s)
BME	β-mercaptoethanol
BSA	Bovine serum albumin
DAPI	4′,6-diamidino-2-phenylindole
ECM	Extracellular matrix
EMT	Epithelial–mesenchymal transition
ERK	Extracellular signal regulated kinase
FA	Focal adhesion
FAK	Focal adhesion kinase
FLK1	Fms-related tyrosine kinase 1
FLT1	Fetal liver kinase 1
FBS	Fetal bovine albumin
HE	Hematoxylin–eosin
HRP	Horseradish peroxidase
IF	Immunofluorescence
MAPK	Mitogen-activated protein kinase
MCS	Multicellular spheroid(s)
MEK1	Mitogen-activated protein kinase kinase 1
mTOR	Mammalian target of rapamycin
mTORC2	mTOR complex 2
μg	Microgravity
NGAL (LCN2)	Neutrophil gelatinase-associated lipocalin (lipocalin 2)
NTC	No-template control
1 g	Normal gravity
PAM	PI3K/AKT/mTOR
PBS	Phosphate-buffered saline
PBST	Phosphate-buffered saline with Tween
PFA	Paraformaldehyde
PI3K	Phosphoinositide 3-kinase
PKB	Protein kinase B
qPCR	Quantitative real-time polymerase chain reaction
RAF	Rapidly accelerated fibrosarcoma
RICTOR	Rapamycin-insensitive companion of mTOR
RIPA	Radioimmunoprecipitation assay
RPM	Random positioning machine
rpm	Rounds per minute
RWV	Rotating wall vessel
SR	Sirius red
SRC (Src)	Steroid receptor coactivator (proto-oncogene, non-receptor tyrosine kinase)
S-μg	Simulated microgravity
TBST	Tris-buffered saline with Tween

VEGF	Vascular endothelial growth factor
VEGFR	Vascular endothelial growth factor receptor
WHO	World Health Organization
TRIFMA	Time-resolved immunofluorometric assay
2D	Two-dimensional
3D	Three-dimensional

References

1. Nassef, M.Z.; Kopp, S.; Melnik, D.; Corydon, T.J.; Sahana, J.; Krüger, M.; Wehland, M.; Bauer, T.J.; Liemersdorf, C.; Hemmersbach, R.; et al. Short-Term Microgravity Influences Cell Adhesion in Human Breast Cancer Cells. *Int. J. Mol. Sci.* **2019**, *20*, 5730. [CrossRef] [PubMed]
2. Fukazawa, T.; Tanimoto, K.; Shrestha, L.; Imura, T.; Takahashi, S.; Sueda, T.; Hirohashi, N.; Hiyama, E.; Yuge, L. Simulated microgravity enhances CDDP-induced apoptosis signal via p53-independent mechanisms in cancer cells. *PLoS ONE* **2019**, *14*, e0219363. [CrossRef] [PubMed]
3. Camberos, V.; Baio, J.; Bailey, L.; Hasaniya, N.; Lopez, L.V.; Kearns-Jonker, M. Effects of Spaceflight and Simulated Microgravity on YAP1 Expression in Cardiovascular Progenitors: Implications for Cell-Based Repair. *Int. J. Mol. Sci.* **2019**, *20*, 2742. [CrossRef] [PubMed]
4. Qin, W.; Liu, L.; Wang, Y.; Wang, Z.; Yang, A.; Wang, T. Mir-494 inhibits osteoblast differentiation by regulating BMP signaling in simulated microgravity. *Endocrine* **2019**, *65*, 426–439. [CrossRef] [PubMed]
5. Deng, B.; Liu, R.; Tian, X.; Han, Z.; Chen, J. Simulated microgravity inhibits the viability and migration of glioma via FAK/RhoA/Rock and FAK/Nek2 signaling. *In Vitro Cell. Dev. Biol. Anim.* **2019**, *55*, 260–271. [CrossRef] [PubMed]
6. Bray, F.; Ferlay, J.; Soerjomataram, I.; Siegel, R.L.; Torre, L.A.; Jemal, A. Global cancer statistics 2018: GLOBOCAN estimates of incidence and mortality worldwide for 36 cancers in 185 countries. *CA Cancer J. Clin.* **2018**, *68*, 394–424. [CrossRef]
7. Humphrey, P.A.; Moch, H.; Cubilla, A.L.; Ulbright, T.M.; Reuter, V.E. The 2016 WHO Classification of Tumours of the Urinary System and Male Genital Organs-Part B: Prostate and Bladder Tumours. *Eur. Urol.* **2016**, *70*, 106–119. [CrossRef]
8. Humphrey, P.A. Histological variants of prostatic carcinoma and their significance. *Histopathology* **2012**, *60*, 59–74. [CrossRef]
9. Abate-Shen, C.; Shen, M.M. Molecular genetics of prostate cancer. *Genes. Dev.* **2000**, *14*, 2410–2434. [CrossRef]
10. Feng, M.; Peng, J.; Song, C.; Wang, Y. Mammalian cell cultivation in space. *Microgravity Sci. Technol.* **1994**, *7*, 207–210.
11. Grimm, D.; Bauer, J.; Kossmehl, P.; Shakibaei, M.; Schoberger, J.; Pickenhahn, H.; Schulze-Tanzil, G.; Vetter, R.; Eilles, C.; Paul, M.; et al. Simulated microgravity alters differentiation and increases apoptosis in human follicular thyroid carcinoma cells. *FASEB J.* **2002**, *16*, 604–606. [CrossRef]
12. Grimm, D.; Wise, P.; Lebert, M.; Richter, P.; Baatout, S. How and why does the proteome respond to microgravity? *Expert Rev. Proteom.* **2011**, *8*, 13–27. [CrossRef] [PubMed]
13. Aleshcheva, G.; Bauer, J.; Hemmersbach, R.; Slumstrup, L.; Wehland, M.; Infanger, M.; Grimm, D. Scaffold-free Tissue Formation Under Real and Simulated Microgravity Conditions. *Basic Clin. Pharmacol. Toxicol.* **2016**, *119* (Suppl. 3), 26–33. [CrossRef] [PubMed]
14. Ingram, M.; Techy, G.B.; Saroufeem, R.; Yazan, O.; Narayan, K.S.; Goodwin, T.J.; Spaulding, G.F. Three-dimensional growth patterns of various human tumor cell lines in simulated microgravity of a NASA bioreactor. *In Vitro Cell. Dev. Biol. Anim.* **1997**, *33*, 459–466. [CrossRef] [PubMed]
15. Dittrich, A.; Grimm, D.; Sahana, J.; Bauer, J.; Kruger, M.; Infanger, M.; Magnusson, N.E. Key Proteins Involved in Spheroid Formation and Angiogenesis in Endothelial Cells After Long-Term Exposure to Simulated Microgravity. *Cell. Physiol. Biochem.* **2018**, *45*, 429–445. [CrossRef]
16. Grimm, D.; Wehland, M.; Pietsch, J.; Aleshcheva, G.; Wise, P.; van Loon, J.; Ulbrich, C.; Magnusson, N.E.; Infanger, M.; Bauer, J. Growing tissues in real and simulated microgravity: New methods for tissue engineering. *Tissue Eng. Part B Rev.* **2014**, *20*, 555–566. [CrossRef]
17. Mehta, G.; Hsiao, A.Y.; Ingram, M.; Luker, G.D.; Takayama, S. Opportunities and challenges for use of tumor spheroids as models to test drug delivery and efficacy. *J. Control. Release* **2012**, *164*, 192–204. [CrossRef]

18. Herranz, R.; Anken, R.; Boonstra, J.; Braun, M.; Christianen, P.C.; de Geest, M.; Hauslage, J.; Hilbig, R.; Hill, R.J.; Lebert, M.; et al. Ground-based facilities for simulation of microgravity: Organism-specific recommendations for their use, and recommended terminology. *Astrobiology* **2013**, *13*, 1–17. [CrossRef]
19. Hoson, T.; Kamisaka, S.; Masuda, Y.; Yamashita, M.; Buchen, B. Evaluation of the three-dimensional clinostat as a simulator of weightlessness. *Planta* **1997**, *203*, S187–S197. [CrossRef]
20. Warnke, E.; Pietsch, J.; Wehland, M.; Bauer, J.; Infanger, M.; Gorog, M.; Hemmersbach, R.; Braun, M.; Ma, X.; Sahana, J.; et al. Spheroid formation of human thyroid cancer cells under simulated microgravity: A possible role of CTGF and CAV1. *Cell. Commun. Signal.* **2014**, *12*, 32. [CrossRef]
21. Kopp, S.; Sahana, J.; Islam, T.; Petersen, A.G.; Bauer, J.; Corydon, T.J.; Schulz, H.; Saar, K.; Huebner, N.; Slumstrup, L.; et al. The role of NFkappaB in spheroid formation of human breast cancer cells cultured on the Random Positioning Machine. *Sci. Rep.* **2018**, *8*, 921. [CrossRef] [PubMed]
22. Kruger, M.; Melnik, D.; Kopp, S.; Buken, C.; Sahana, J.; Bauer, J.; Wehland, M.; Hemmersbach, R.; Corydon, T.J.; Infanger, M.; et al. Fighting Thyroid Cancer with Microgravity Research. *Int. J. Mol. Sci.* **2019**, *20*, 2553. [CrossRef] [PubMed]
23. Kopp, S.; Warnke, E.; Wehland, M.; Aleshcheva, G.; Magnusson, N.E.; Hemmersbach, R.; Corydon, T.J.; Bauer, J.; Infanger, M.; Grimm, D. Mechanisms of three-dimensional growth of thyroid cells during long-term simulated microgravity. *Sci. Rep.* **2015**, *5*, 16691. [CrossRef] [PubMed]
24. Grimm, D.; Infanger, M.; Westphal, K.; Ulbrich, C.; Pietsch, J.; Kossmehl, P.; Vadrucci, S.; Baatout, S.; Flick, B.; Paul, M.; et al. A delayed type of three-dimensional growth of human endothelial cells under simulated weightlessness. *Tissue Eng. Part A* **2009**, *15*, 2267–2275. [CrossRef]
25. Svejgaard, B.; Wehland, M.; Ma, X.; Kopp, S.; Sahana, J.; Warnke, E.; Aleshcheva, G.; Hemmersbach, R.; Hauslage, J.; Grosse, J.; et al. Common Effects on Cancer Cells Exerted by a Random Positioning Machine and a 2D Clinostat. *PLoS ONE* **2015**, *10*, e0135157. [CrossRef]
26. Soranzo, C.; Della Torre, G.; Ingrosso, A. Formation, growth and morphology of multicellular tumor spheroids from a human colon carcinoma cell line (LoVo). *Tumori* **1986**, *72*, 459–467. [CrossRef]
27. Cui, X.; Hartanto, Y.; Zhang, H. Advances in multicellular spheroids formation. *J. R. Soc. Interface* **2017**, *14*. [CrossRef]
28. Kunz-Schughart, L.A. Multicellular tumor spheroids: Intermediates between monolayer culture and in vivo tumor. *Cell. Biol. Int.* **1999**, *23*, 157–161. [CrossRef]
29. Mueller-Klieser, W. Method for the determination of oxygen consumption rates and diffusion coefficients in multicellular spheroids. *Biophys. J.* **1984**, *46*, 343–348. [CrossRef]
30. Kunz-Schughart, L.A.; Freyer, J.P.; Hofstaedter, F.; Ebner, R. The use of 3-D cultures for high-throughput screening: The multicellular spheroid model. *J. Biomol. Screen.* **2004**, *9*, 273–285. [CrossRef]
31. Corydon, T.J.; Mann, V.; Slumstrup, L.; Kopp, S.; Sahana, J.; Askou, A.L.; Magnusson, N.E.; Echegoyen, D.; Bek, T.; Sundaresan, A.; et al. Reduced Expression of Cytoskeletal and Extracellular Matrix Genes in Human Adult Retinal Pigment Epithelium Cells Exposed to Simulated Microgravity. *Cell. Physiol. Biochem.* **2016**, *40*, 1–17. [CrossRef]
32. Nagy, J.A.; Dvorak, A.M.; Dvorak, H.F. VEGF-A and the induction of pathological angiogenesis. *Annu. Rev. Pathol.* **2007**, *2*, 251–275. [CrossRef]
33. Goel, S.; Duda, D.G.; Xu, L.; Munn, L.L.; Boucher, Y.; Fukumura, D.; Jain, R.K. Normalization of the vasculature for treatment of cancer and other diseases. *Physiol. Rev.* **2011**, *91*, 1071–1121. [CrossRef]
34. Carmeliet, P.; Jain, R.K. Molecular mechanisms and clinical applications of angiogenesis. *Nature* **2011**, *473*, 298–307. [CrossRef]
35. Peach, C.J.; Mignone, V.W.; Arruda, M.A.; Alcobia, D.C.; Hill, S.J.; Kilpatrick, L.E.; Woolard, J. Molecular Pharmacology of VEGF-A Isoforms: Binding and Signalling at VEGFR2. *Int. J. Mol. Sci.* **2018**, *19*, 1264. [CrossRef]
36. Takahashi, T.; Ueno, H.; Shibuya, M. VEGF activates protein kinase C-dependent, but Ras-independent Raf-MEK-MAP kinase pathway for DNA synthesis in primary endothelial cells. *Oncogene* **1999**, *18*, 2221–2230. [CrossRef] [PubMed]
37. Gerber, H.P.; McMurtrey, A.; Kowalski, J.; Yan, M.; Keyt, B.A.; Dixit, V.; Ferrara, N. Vascular endothelial growth factor regulates endothelial cell survival through the phosphatidylinositol 3′-kinase/Akt signal transduction pathway. Requirement for Flk-1/KDR activation. *J. Biol. Chem.* **1998**, *273*, 30336–30343. [CrossRef]

38. Conciatori, F.; Bazzichetto, C.; Falcone, I.; Pilotto, S.; Bria, E.; Cognetti, F.; Milella, M.; Ciuffreda, L. Role of mTOR Signaling in Tumor Microenvironment: An Overview. *Int. J. Mol. Sci.* **2018**, *19*, 2453. [CrossRef]
39. Chen, X.L.; Nam, J.O.; Jean, C.; Lawson, C.; Walsh, C.T.; Goka, E.; Lim, S.T.; Tomar, A.; Tancioni, I.; Uryu, S.; et al. VEGF-induced vascular permeability is mediated by FAK. *Dev. Cell.* **2012**, *22*, 146–157. [CrossRef]
40. Abu-Ghazaleh, R.; Kabir, J.; Jia, H.; Lobo, M.; Zachary, I. Src mediates stimulation by vascular endothelial growth factor of the phosphorylation of focal adhesion kinase at tyrosine 861, and migration and anti-apoptosis in endothelial cells. *Biochem. J.* **2001**, *360*, 255–264. [CrossRef]
41. Koch, S.; Claesson-Welsh, L. Signal transduction by vascular endothelial growth factor receptors. *Cold Spring Harb. Perspect. Med.* **2012**, *2*, a006502. [CrossRef]
42. Tchaikovski, V.; Fellbrich, G.; Waltenberger, J. The molecular basis of VEGFR-1 signal transduction pathways in primary human monocytes. *Arterioscler. Thromb. Vasc. Biol.* **2008**, *28*, 322–328. [CrossRef] [PubMed]
43. Zhau, H.E.; Goodwin, T.J.; Chang, S.M.; Baker, T.L.; Chung, L.W. Establishment of a three-dimensional human prostate organoid coculture under microgravity-simulated conditions: Evaluation of androgen-induced growth and PSA expression. *In Vitro Cell. Dev. Biol. Anim.* **1997**, *33*, 375–380. [CrossRef] [PubMed]
44. Clejan, S.; O'Connor, K.; Rosensweig, N. Tri-dimensional prostate cell cultures in simulated microgravity and induced changes in lipid second messengers and signal transduction. *J. Cell. Mol. Med.* **2001**, *5*, 60–73. [CrossRef]
45. Margolis, L.; Hatfill, S.; Chuaqui, R.; Vocke, C.; Emmert-Buck, M.; Linehan, W.M.; Duray, P.H. Long term organ culture of human prostate tissue in a NASA-designed rotating wall bioreactor. *J. Urol.* **1999**, *161*, 290–297. [CrossRef]
46. Leguy, C.A.D.; Delfos, R.; Pourquié, M.; Poelma, C.; Krooneman, J.; Westerweel, J.; van Loon, J.J.W.A. Fluid motion for microgravity simulations in a random positioning machine. *Gravit. Space Biol.* **2011**, *25*, 36–39.
47. Ma, X.; Pietsch, J.; Wehland, M.; Schulz, H.; Saar, K.; Hubner, N.; Bauer, J.; Braun, M.; Schwarzwalder, A.; Segerer, J.; et al. Differential gene expression profile and altered cytokine secretion of thyroid cancer cells in space. *FASEB J.* **2014**, *28*, 813–835. [CrossRef] [PubMed]
48. Viallard, C.; Larrivee, B. Tumor angiogenesis and vascular normalization: Alternative therapeutic targets. *Angiogenesis* **2017**, *20*, 409–426. [CrossRef]
49. Yang, J.; Moses, M.A. Abstract 1293: Neutrophil gelatinase-associated lipocalin regulates the expression of angiogenic cytokines and VEGF in human breast and ovarian cancer cells. *Cancer Res.* **2010**, *70*, 1293. [CrossRef]
50. Iannetti, A.; Pacifico, F.; Acquaviva, R.; Lavorgna, A.; Crescenzi, E.; Vascotto, C.; Tell, G.; Salzano, A.M.; Scaloni, A.; Vuttariello, E.; et al. The neutrophil gelatinase-associated lipocalin (NGAL), a NF-kappaB-regulated gene, is a survival factor for thyroid neoplastic cells. *Proc. Natl. Acad. Sci. USA* **2008**, *105*, 14058–14063. [CrossRef]
51. Sun, Y.; Yokoi, K.; Li, H.; Gao, J.; Hu, L.; Liu, B.; Chen, K.; Hamilton, S.R.; Fan, D.; Sun, B.; et al. NGAL expression is elevated in both colorectal adenoma-carcinoma sequence and cancer progression and enhances tumorigenesis in xenograft mouse models. *Clin. Cancer Res.* **2011**, *17*, 4331–4340. [CrossRef] [PubMed]
52. Zhang, X.F.; Zhang, Y.; Zhang, X.H.; Zhou, S.M.; Yang, G.G.; Wang, O.C.; Guo, G.L.; Yang, G.Y.; Hu, X.Q. Clinical significance of Neutrophil gelatinase-associated lipocalin(NGAL) expression in primary rectal cancer. *BMC Cancer* **2009**, *9*, 134. [CrossRef] [PubMed]
53. Olea-Flores, M.; Zuniga-Eulogio, M.D.; Mendoza-Catalan, M.A.; Rodriguez-Ruiz, H.A.; Castaneda-Saucedo, E.; Ortuno-Pineda, C.; Padilla-Benavides, T.; Navarro-Tito, N. Extracellular-Signal Regulated Kinase: A Central Molecule Driving Epithelial-Mesenchymal Transition in Cancer. *Int. J. Mol. Sci.* **2019**, *20*, 2885. [CrossRef] [PubMed]
54. Eblen, S.T. Extracellular-Regulated Kinases: Signaling From Ras to ERK Substrates to Control Biological Outcomes. *Adv. Cancer Res.* **2018**, *138*, 99–142. [CrossRef] [PubMed]
55. Tee, S.S.; Suster, I.; Truong, S.; Jeong, S.; Eskandari, R.; DiGialleonardo, V.; Alvarez, J.A.; Aldeborgh, H.N.; Keshari, K.R. Targeted AKT Inhibition in Prostate Cancer Cells and Spheroids Reduces Aerobic Glycolysis and Generation of Hyperpolarized [1-(13)C] Lactate. *Mol. Cancer Res.* **2018**, *16*, 453–460. [CrossRef]
56. Cully, M.; You, H.; Levine, A.J.; Mak, T.W. Beyond PTEN mutations: The PI3K pathway as an integrator of multiple inputs during tumorigenesis. *Nat. Rev. Cancer* **2006**, *6*, 184–192. [CrossRef]
57. Available online: https://clinicaltrials.gov/ (accessed on 13 February 2020).

58. Magani, F.; Peacock, S.O.; Rice, M.A.; Martinez, M.J.; Greene, A.M.; Magani, P.S.; Lyles, R.; Weitz, J.R.; Burnstein, K.L. Targeting AR Variant-Coactivator Interactions to Exploit Prostate Cancer Vulnerabilities. *Mol. Cancer Res.* **2017**, *15*, 1469–1480. [CrossRef]
59. Jain, N.; Zhang, T.; Fong, S.L.; Lim, C.P.; Cao, X. Repression of Stat3 activity by activation of mitogen-activated protein kinase (MAPK). *Oncogene* **1998**, *17*, 3157–3167. [CrossRef]
60. Shen, B.Q.; Lee, D.Y.; Gerber, H.P.; Keyt, B.A.; Ferrara, N.; Zioncheck, T.F. Homologous up-regulation of KDR/Flk-1 receptor expression by vascular endothelial growth factor in vitro. *J. Biol. Chem.* **1998**, *273*, 29979–29985. [CrossRef]
61. Fan, P.; Agboke, F.A.; McDaniel, R.E.; Sweeney, E.E.; Zou, X.; Creswell, K.; Jordan, V.C. Inhibition of c-Src blocks oestrogen-induced apoptosis and restores oestrogen-stimulated growth in long-term oestrogen-deprived breast cancer cells. *Eur. J. Cancer* **2014**, *50*, 457–468. [CrossRef]
62. Calalb, M.B.; Polte, T.R.; Hanks, S.K. Tyrosine phosphorylation of focal adhesion kinase at sites in the catalytic domain regulates kinase activity: A role for Src family kinases. *Mol. Cell. Biol.* **1995**, *15*, 954–963. [CrossRef] [PubMed]
63. Dumbauld, D.W.; Shin, H.; Gallant, N.D.; Michael, K.E.; Radhakrishna, H.; Garcia, A.J. Contractility modulates cell adhesion strengthening through focal adhesion kinase and assembly of vinculin-containing focal adhesions. *J. Cell. Physiol.* **2010**, *223*, 746–756. [CrossRef] [PubMed]
64. Bauer, T.J.; Gombocz, E.; Kruger, M.; Sahana, J.; Corydon, T.J.; Bauer, J.; Infanger, M.; Grimm, D. Augmenting cancer cell proteomics with cellular images—A semantic approach to understand focal adhesion. *J. Biomed. Inform.* **2019**, *100*, 103320. [CrossRef] [PubMed]
65. Humphries, J.D.; Wang, P.; Streuli, C.; Geiger, B.; Humphries, M.J.; Ballestrem, C. Vinculin controls focal adhesion formation by direct interactions with talin and actin. *J. Cell. Biol.* **2007**, *179*, 1043–1057. [CrossRef]
66. Chen, P.; Lei, L.; Wang, J.; Zou, X.; Zhang, D.; Deng, L.; Wu, D. Downregulation of Talin1 promotes hepatocellular carcinoma progression through activation of the ERK1/2 pathway. *Cancer Sci.* **2017**, *108*, 1157–1168. [CrossRef]
67. Small, J.V.; Stradal, T.; Vignal, E.; Rottner, K. The lamellipodium: Where motility begins. *Trends Cell. Biol.* **2002**, *12*, 112–120. [CrossRef]
68. Tojkander, S.; Gateva, G.; Lappalainen, P. Actin stress fibers–assembly, dynamics and biological roles. *J. Cell. Sci.* **2012**, *125*, 1855–1864. [CrossRef]
69. Rijken, P.J.; de Groot, R.P.; Kruijer, W.; de Laat, S.W.; Verkleij, A.J.; Boonstra, J. Identification of specific gravity sensitive signal transduction pathways in human A431 carcinoma cells. *Adv. Space Res.* **1992**, *12*, 145–152. [CrossRef]
70. Mann, V.; Grimm, D.; Corydon, T.J.; Kruger, M.; Wehland, M.; Riwaldt, S.; Sahana, J.; Kopp, S.; Bauer, J.; Reseland, J.E.; et al. Changes in Human Foetal Osteoblasts Exposed to the Random Positioning Machine and Bone Construct Tissue Engineering. *Int. J. Mol. Sci.* **2019**, *20*, 1357. [CrossRef]
71. Nabavi, N.; Khandani, A.; Camirand, A.; Harrison, R.E. Effects of microgravity on osteoclast bone resorption and osteoblast cytoskeletal organization and adhesion. *Bone* **2011**, *49*, 965–974. [CrossRef]
72. Ulbrich, C.; Pietsch, J.; Grosse, J.; Wehland, M.; Schulz, H.; Saar, K.; Hubner, N.; Hauslage, J.; Hemmersbach, R.; Braun, M.; et al. Differential gene regulation under altered gravity conditions in follicular thyroid cancer cells: Relationship between the extracellular matrix and the cytoskeleton. *Cell. Physiol. Biochem.* **2011**, *28*, 185–198. [CrossRef] [PubMed]
73. Grosse, J.; Wehland, M.; Pietsch, J.; Ma, X.; Ulbrich, C.; Schulz, H.; Saar, K.; Hubner, N.; Hauslage, J.; Hemmersbach, R.; et al. Short-term weightlessness produced by parabolic flight maneuvers altered gene expression patterns in human endothelial cells. *FASEB J.* **2012**, *26*, 639–655. [CrossRef]
74. Bonnans, C.; Chou, J.; Werb, Z. Remodelling the extracellular matrix in development and disease. *Nat. Rev. Mol. Cell. Biol.* **2014**, *15*, 786–801. [CrossRef] [PubMed]
75. Kopp, S.; Kruger, M.; Bauer, J.; Wehland, M.; Corydon, T.J.; Sahana, J.; Nassef, M.Z.; Melnik, D.; Bauer, T.J.; Schulz, H.; et al. Microgravity Affects Thyroid Cancer Cells during the TEXUS-53 Mission Stronger than Hypergravity. *Int. J. Mol. Sci.* **2018**, *19*, 4001. [CrossRef] [PubMed]
76. Birchmeier, W.; Behrens, J. Cadherin expression in carcinomas: Role in the formation of cell junctions and the prevention of invasiveness. *Biochim. Biophys. Acta* **1994**, *1198*, 11–26. [CrossRef]
77. Semb, H.; Christofori, G. The tumor-suppressor function of E-cadherin. *Am. J. Hum. Genet.* **1998**, *63*, 1588–1593. [CrossRef]

78. Infanger, M.; Kossmehl, P.; Shakibaei, M.; Bauer, J.; Kossmehl-Zorn, S.; Cogoli, A.; Curcio, F.; Oksche, A.; Wehland, M.; Kreutz, R.; et al. Simulated weightlessness changes the cytoskeleton and extracellular matrix proteins in papillary thyroid carcinoma cells. *Cell. Tissue Res.* **2006**, *324*, 267–277. [CrossRef]
79. Sahana, J.; Nassef, M.Z.; Wehland, M.; Kopp, S.; Kruger, M.; Corydon, T.J.; Infanger, M.; Bauer, J.; Grimm, D. Decreased E-Cadherin in MCF7 Human Breast Cancer Cells Forming Multicellular Spheroids Exposed to Simulated Microgravity. *Proteomics* **2018**, *18*, e1800015. [CrossRef]
80. Kliewe, F.; Kaling, S.; Lotzsch, H.; Artelt, N.; Schindler, M.; Rogge, H.; Schroder, S.; Scharf, C.; Amann, K.; Daniel, C.; et al. Fibronectin is up-regulated in podocytes by mechanical stress. *FASEB J.* **2019**. [CrossRef]
81. Garakani, K.; Shams, H.; Mofrad, M.R.K. Mechanosensitive Conformation of Vinculin Regulates Its Binding to MAPK1. *Biophys. J.* **2017**, *112*, 1885–1893. [CrossRef]
82. Ghrebi, S.; Hamilton, D.W.; Douglas Waterfield, J.; Brunette, D.M. The effect of surface topography on cell shape and early ERK1/2 signaling in macrophages; linkage with FAK and Src. *J. Biomed. Mater. Res. A* **2013**, *101*, 2118–2128. [CrossRef]
83. Wei, X.; Zhou, D.; Wang, H.; Ding, N.; Cui, X.X.; Wang, H.; Verano, M.; Zhang, K.; Conney, A.H.; Zheng, X.; et al. Effects of pyridine analogs of curcumin on growth, apoptosis and NF-kappaB activity in prostate cancer PC-3 cells. *Anticancer Res.* **2013**, *33*, 1343–1350. [PubMed]
84. Wu, F.; Wu, S.; Gou, X. Identification of biomarkers and potential molecular mechanisms of clear cell renal cell carcinoma. *Neoplasma* **2018**, *65*, 242–252. [CrossRef] [PubMed]
85. von Au, A.; Vasel, M.; Kraft, S.; Sens, C.; Hackl, N.; Marx, A.; Stroebel, P.; Hennenlotter, J.; Todenhofer, T.; Stenzl, A.; et al. Circulating fibronectin controls tumor growth. *Neoplasia* **2013**, *15*, 925–938. [CrossRef] [PubMed]
86. Irby, R.B.; Yeatman, T.J. Role of Src expression and activation in human cancer. *Oncogene* **2000**, *19*, 5636–5642. [CrossRef]
87. Mori, T.; Ono, K.; Kariya, Y.; Ogawa, T.; Higashi, S.; Miyazaki, K. Laminin-3B11, a novel vascular-type laminin capable of inducing prominent lamellipodial protrusions in microvascular endothelial cells. *J. Biol. Chem.* **2010**, *285*, 35068–35078. [CrossRef]
88. Chou, M.T.; Wang, J.; Fujita, D.J. Src kinase becomes preferentially associated with the VEGFR, KDR/Flk-1, following VEGF stimulation of vascular endothelial cells. *BMC Biochem.* **2002**, *3*, 32. [CrossRef]
89. Fleming, R.Y.; Ellis, L.M.; Parikh, N.U.; Liu, W.; Staley, C.A.; Gallick, G.E. Regulation of vascular endothelial growth factor expression in human colon carcinoma cells by activity of src kinase. *Surgery* **1997**, *122*, 501–507. [CrossRef]
90. Munshi, N.; Groopman, J.E.; Gill, P.S.; Ganju, R.K. c-Src mediates mitogenic signals and associates with cytoskeletal proteins upon vascular endothelial growth factor stimulation in Kaposi's sarcoma cells. *J. Immunol.* **2000**, *164*, 1169–1174. [CrossRef]
91. Albert, L.; Karsy, M.; Murali, R.; Jhanwar-Uniyal, M. Inhibition of mTOR Activates the MAPK Pathway in Glioblastoma Multiforme. *Cancer Genom. Proteom.* **2009**, *6*, 255–261.
92. Kinkade, C.W.; Castillo-Martin, M.; Puzio-Kuter, A.; Yan, J.; Foster, T.H.; Gao, H.; Sun, Y.; Ouyang, X.; Gerald, W.L.; Cordon-Cardo, C.; et al. Targeting AKT/mTOR and ERK MAPK signaling inhibits hormone-refractory prostate cancer in a preclinical mouse model. *J. Clin. Investig.* **2008**, *118*, 3051–3064. [CrossRef]
93. Engelman, J.A.; Chen, L.; Tan, X.; Crosby, K.; Guimaraes, A.R.; Upadhyay, R.; Maira, M.; McNamara, K.; Perera, S.A.; Song, Y.; et al. Effective use of PI3K and MEK inhibitors to treat mutant Kras G12D and PIK3CA H1047R murine lung cancers. *Nat. Med.* **2008**, *14*, 1351–1356. [CrossRef] [PubMed]
94. Bendtsen, M.A.F.; Grimm, D.; Bauer, J.; Wehland, M.; Wise, P.; Magnusson, N.E.; Infanger, M.; Kruger, M. Hypertension Caused by Lenvatinib and Everolimus in the Treatment of Metastatic Renal Cell Carcinoma. *Int. J. Mol. Sci.* **2017**, *18*, 1736. [CrossRef] [PubMed]
95. Nielsen, O.H.; Grimm, D.; Wehland, M.; Bauer, J.; Magnusson, N.E. Anti-Angiogenic Drugs in the Treatment of Metastatic Renal Cell Carcinoma: Advances in Clinical Application. *Curr. Vasc. Pharm.* **2015**, *13*, 381–391. [CrossRef] [PubMed]
96. Kaighn, M.E.; Narayan, K.S.; Ohnuki, Y.; Lechner, J.F.; Jones, L.W. Establishment and characterization of a human prostatic carcinoma cell line (PC-3). *Investig. Urol.* **1979**, *17*, 16–23.
97. Wuest, S.L.; Richard, S.; Kopp, S.; Grimm, D.; Egli, M. Simulated microgravity: Critical review on the use of random positioning machines for mammalian cell culture. *Biomed. Res. Int.* **2015**, *2015*, 971474. [CrossRef]

98. Grimm, D.; Egli, M.; Kruger, M.; Riwaldt, S.; Corydon, T.J.; Kopp, S.; Wehland, M.; Wise, P.; Infanger, M.; Mann, V.; et al. Tissue Engineering Under Microgravity Conditions-Use of Stem Cells and Specialized Cells. *Stem Cells Dev.* **2018**, *27*, 787–804. [CrossRef]
99. Kopp, S.; Slumstrup, L.; Corydon, T.J.; Sahana, J.; Aleshcheva, G.; Islam, T.; Magnusson, N.E.; Wehland, M.; Bauer, J.; Infanger, M.; et al. Identifications of novel mechanisms in breast cancer cells involving duct-like multicellular spheroid formation after exposure to the Random Positioning Machine. *Sci. Rep.* **2016**, *6*, 26887. [CrossRef]
100. Grimm, D.; Jabusch, H.C.; Kossmehl, P.; Huber, M.; Fredersdorf, S.; Griese, D.P.; Kramer, B.K.; Kromer, E.P. Experimental diabetes and left ventricular hypertrophy: Effects of beta-receptor blockade. *Cardiovasc. Pathol.* **2002**, *11*, 229–237. [CrossRef]
101. Grosse, J.; Warnke, E.; Pohl, F.; Magnusson, N.E.; Wehland, M.; Infanger, M.; Eilles, C.; Grimm, D. Impact of sunitinib on human thyroid cancer cells. *Cell. Physiol. Biochem.* **2013**, *32*, 154–170. [CrossRef]
102. Magnusson, N.E.; Hornum, M.; Jorgensen, K.A.; Hansen, J.M.; Bistrup, C.; Feldt-Rasmussen, B.; Flyvbjerg, A. Plasma neutrophil gelatinase associated lipocalin (NGAL) is associated with kidney function in uraemic patients before and after kidney transplantation. *BMC Nephrol.* **2012**, *13*, 8. [CrossRef] [PubMed]
103. Lützenberg, R.; Solano, K.; Buken, C.; Sahana, J.; Riwaldt, S.; Kopp, S.; Kruger, M.; Schulz, H.; Saar, K.; Huebner, N.; et al. Pathway Analysis Hints Towards Beneficial Effects of Long-Term Vibration on Human Chondrocytes. *Cell. Physiol. Biochem.* **2018**, *47*, 1729–1741. [CrossRef] [PubMed]



© 2020 by the authors. Licensee MDPI, Basel, Switzerland. This article is an open access article distributed under the terms and conditions of the Creative Commons Attribution (CC BY) license (http://creativecommons.org/licenses/by/4.0/).

cancers

MDPI

Article

Dexamethasone Selectively Inhibits Detachment of Metastatic Thyroid Cancer Cells during Random Positioning

Daniela Melnik [1,2], José Luis Cortés-Sánchez [1], Viviann Sandt [1], Stefan Kahlert [2,3], Sascha Kopp [2,4], Daniela Grimm [1,2,5] and Marcus Krüger [1,2,*]

[1] Department of Microgravity and Translational Regenerative Medicine, Otto von Guericke University, 39106 Magdeburg, Germany
[2] Research Group "Magdeburger Arbeitsgemeinschaft für Forschung unter Raumfahrt- und Schwerelosigkeitsbedingungen" (MARS), Otto von Guericke University, 39106 Magdeburg, Germany
[3] Institute of Anatomy, Otto von Guericke University, 39120 Magdeburg, Germany
[4] Core Facility Tissue Engineering, Otto von Guericke University, 39106 Magdeburg, Germany
[5] Department of Biomedicine, Aarhus University, 8000 Aarhus, Denmark
* Correspondence: marcus.krueger@med.ovgu.de; Tel.: +49-391-6757471

Simple Summary: Metastasis is the most dangerous feature of advanced cancers. In vitro models of this process could help us to study and understand mechanisms that are not readily accessible in the human body. In our approach, we used random positioning cell cultures to induce cancer cells to spread and form tumor spheroids. In this experimental setup, we show that dexamethasone is able to specifically inhibit the detachment of metastatic thyroid cancer cells. Our results not only show how differently healthy and malignant thyroid cells act and react in this in vitro metastasis model system, but also provide valuable insights into its functioning, possibilities and limitations.

Abstract: We recently reported that synthetic glucocorticoid dexamethasone (DEX) is able to suppress metastasis-like spheroid formation in a culture of follicular thyroid cancer (FTC)-133 cells cultured under random positioning. We now show that this inhibition was selective for two metastatic thyroid carcinoma cells, FTC-133 and WRO, whereas benign Nthy-ori 3-1 thyrocytes and recurrent ML-1 follicular thyroid cancer cells were not affected by DEX. We then compare Nthy-ori 3-1 and FTC-133 cells concerning their adhesion and mechanosignaling. We demonstrate that DEX disrupts random positioning-triggered p38 stress signaling in FTC-133 cells, thereby antagonizing a variety of biological functions. Thus, DEX treatment of FTC-133 cells is associated with increased adhesiveness, which is mainly caused by the restored, pronounced formation of a normal number of tight junctions. Moreover, we show that Nthy-ori 3-1 and ML-1 cells upregulate the anti-adhesion protein mucin-1 during random positioning, presumably as a protection against mechanical stress. In summary, mechanical stress seems to be an important component in this metastasis model system that is processed differently by metastatic and healthy cells. The balance between adhesion, anti-adhesion and cell–cell connections enables detachment of adherent human cells on the random positioning machine—or not, allowing selective inhibition of thyroid in vitro metastasis by DEX.

Keywords: glucocorticoids; thyroid cancer; random positioning; in vitro metastasis; cell adhesion; anti-adhesion; tight junctions; cancer treatment

check for updates

Citation: Melnik, D.; Cortés-Sánchez, J.L.; Sandt, V.; Kahlert, S.; Kopp, S.; Grimm, D.; Krüger, M. Dexamethasone Selectively Inhibits Detachment of Metastatic Thyroid Cancer Cells during Random Positioning. *Cancers* **2023**, *15*, 1641. https://doi.org/10.3390/cancers15061641

Academic Editor: David Wong

Received: 12 February 2023
Revised: 27 February 2023
Accepted: 6 March 2023
Published: 7 March 2023

Copyright: © 2023 by the authors. Licensee MDPI, Basel, Switzerland. This article is an open access article distributed under the terms and conditions of the Creative Commons Attribution (CC BY) license (https://creativecommons.org/licenses/by/4.0/).

1. Introduction

Cancer is considered one of the most life-threatening diseases due to its ability to metastasize. Metastasis is responsible for more than 90% of all cancer-related deaths [1]. The mechanism of cancer metastasis mainly involves six steps: (1) detachment from the primary tumor, (2) intravasation, (3) transport through the bloodstream, (4) entrapment in the endothelial walls of the distant organ, (5) extravasation into the parenchyma of the distant organ, and (6) formation of secondary tumors on the distant organ [2]. In most

cases, the initialization of the metastatic process is thought to be the result of a genetic [3] or epigenetic [4] trigger. However, there is increasing evidence that mechanical stimuli also contribute to metastasis through the interplay of physical forces and biochemical signals (reviewed in [5,6]). In this context, it is important to note that not all cancer cells have the ability to form metastases. It is generally believed that a process similar to epithelial-mesenchymal transition (EMT) is required for cancer cells to metastasize [7], which is associated with a loss of adhesion and stiffness [8]. Early on, Guck et al. [9] demonstrated that human breast cancer cell lines MCF-7 and especially the highly metastatic MDA-MB-231 are more deformable than their epithelial counterpart MCF-10A and opened the field for cancer biophysics. That the invasiveness of cancer cells is indeed correlated with their plastic response was recently reconfirmed by Cho et al. [10] using a novel microfluidic system. Interestingly, metastatic cancer cells seem to change their mechanical properties in response to passive and active mechanical stimuli to a much greater extent than normal cells [11–13].

The random positioning machine (RPM) is a rotating bioreactor originally developed for the study of gravitational biology in cells, tissues and organisms [14,15]. Unlike rotating clinostats, which are primarily designed to prevent sedimentation of suspension cells, the RPM generates shear forces as a side effect [16,17]. Computer simulations showed that the fluid motion inside the cell culture flasks on the RPM never reached or approached a steady state [18]. What is a disadvantage for some may be an advantage for others: adherent cells are stimulated by the RPM to detach from their surface, and in the case of tumor cells, this process mimics spreading in vivo in several aspects (Figure 1) [19–21]. Among the possible explanations for this in vitro metastasis model is that tumor cells respond differently and possibly more sensitively to mechanical stimuli. MDA-MB-231 cells with high metastatic potential were more susceptible to migration under fluid shear forces than the less metastatic MDA-MB-468. The benign MCF-10A cell line had the lowest migration potential under shear forces [22]. Fluid shear stress has also been described to promote invasion through increased secretion of matrix metalloproteinases (MMPs) [23], increased cell motility, and facilitated EMT of adherent tumor cells [24–26]. Ahn et al. [27] indicated that random positioning accelerates the migration of two types of adherent non-small cell lung cancer cells even in a floating environment. However, the exact mechanism of spheroid formation from 2D cultures on the RPM, which was also observed for several healthy cells [28–30], is still unclear.

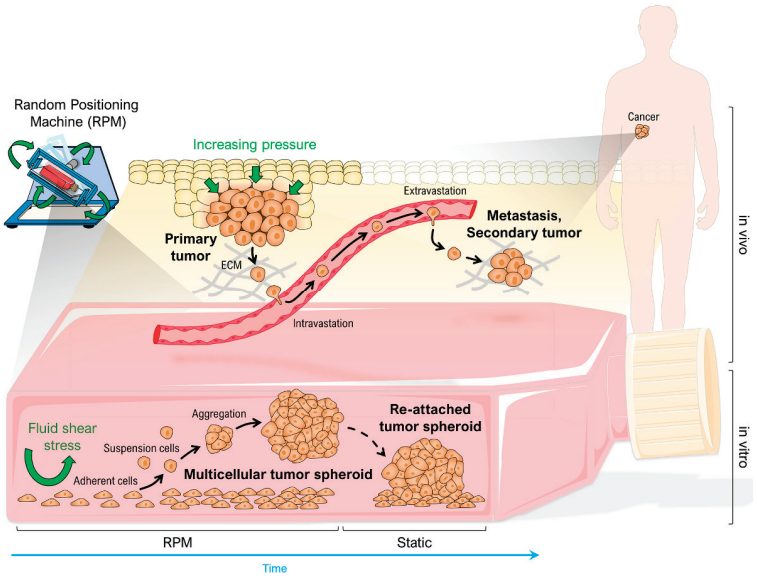


Figure 1. Comparison of metastasis in vivo and random positioning cell culture with adherent growing cancer cells in vitro. Modified from [19]. Parts of the figure were drawn by using pictures from Servier Medical Art, licensed under a Creative Commons Attribution 3.0 Unported License (https://creativecommons.org/licenses/by/3.0/, accessed on 12 February 2023).

Recently, we reported that RPM-induced spheroid formation of FTC-133 thyroid carcinoma cells was inhibited by dexamethasone (DEX) in a concentration-dependent manner and came across a complex regulation network of tumor spheroid formation under dynamic flow that may be influenced by glucocorticoids such as DEX [31]. With the current study, we aimed to reveal and explain the effects of DEX treatment on thyroid cancer cells cultured on the RPM and generally gain a better understanding of the behavior of human cells in a rotational culture.

2. Materials and Methods

2.1. Cell Lines and Cell Culture

The human follicular thyroid carcinoma cell lines FTC-133 (passages 17–25) and WRO (passages 10–16) and the noncancerous follicular epithelial cell line Nthy-ori 3-1 (passages 10–15) were purchased from Sigma-Aldrich (St. Louis, MO, USA). The human follicular thyroid carcinoma cell line ML-1 (passages 5–9) isolated from recurrence [32] was used from a laboratory stock. Cells were cultured in RPMI 1640 medium (Life Technologies, Carlsbad, CA, USA) supplemented with 10% fetal calf serum (FCS; Sigma-Aldrich, St. Louis, MO, USA), and 1% penicillin/streptomycin (Life Technologies) at 37 °C and 5% CO_2 until used for experiments. Twenty-four hours before each experiment, a cell density of 1×10^6 cells per flask were seeded in T25 cell culture flasks (Sarstedt, Nümbrecht, Germany) to allow cells to adhere. T25 flasks equipped with glass coverslips and a reduced cell density of 0.5×10^6 cells were used for immunofluorescence staining.

Breast epithelial cells (MCF-10A; ATCC, Manassas, VA, USA), mammary carcinoma cells (MCF-7; ATCC), and prostate carcinoma cells (PC-3, LnCAP; ATCC) for supplemental experiments were cultured accordingly. The MCF-10A cell line was cultured in DMEM/F12 medium supplemented with 0.5% Mammary Epithelial Growth Supplement (MEGS) (Life Technologies).

2.2. Dexamethasone and Drug Treatment

Ethanol-soluble DEX was purchased from Sigma-Aldrich. Twenty-four hours after seeding, cells were washed once with phosphate-buffered saline (PBS; Life Technologies), synchronized for four hours in RPMI 1640 with 0.25% FCS and 1% Penicillin/Streptomycin, following a cultivation with RPMI 1640 medium supplemented with 0–1000 nM DEX, as described in [31]. This procedure was applied before any drug treatment.

To investigate the selective effect of DEX on metastatic cell lines, we treated FTC-133 and WRO cells with the re-activator of mutant p53 activity, PRIMA-1^{Met} (2-(Hydroxymethyl)-2-(methoxymethyl)-1-azabicyclo [2.2.2]octan-3-one; Sigma-Aldrich). PRIMA-1^{Met} was dissolved in water. Cell cultures were supplemented with 10 µM PRIMA-1^{Met} or 10 µM PRIMA-1^{Met} combined with 1 µM DEX for three days.

To target GR signaling, we used the water-soluble GR antagonist Mifepristone (MIF, Sigma-Aldrich). Based on the highest DEX concentration of 1 µM, FTC-133 cells were cultured for three days in DEX:MIF ratios of 1:1, 1:10 and 1:20. Untreated cells, as well as cells treated with 1 µM DEX or 20 µM MIF, served as controls.

Moreover, we applied the D-amino acid cell-penetrating peptide inhibitor of MUC-1, GO-203 (Selleck Chemicals, Planegg, Germany). A GO-203 stock solution was prepared with sterile water. According to the manufacturer's instructions, we treated Nthy-ori 3-1 cells with 5 µM of GO-203 in combination with 1 µM DEX (Sigma-Aldrich) for three days. To exclude side effects of GO-203, controls supplemented with GO-203 and untreated controls were included.

2.3. Random Positioning

Cell cultures were randomly positioned on a desktop RPM (Dutch Space, Leiden, The Netherlands) inside an incubator or inside an incubator RPM (iRPM 2.0, designed and constructed by Prof. Jörg Sekler, University of Applied Sciences and Arts Northwestern Switzerland [33]), both operated in a real random mode. Before the run, all culture flasks

were filled bubble-free with medium supplemented with the corresponding drug concentrations. Corresponding static controls were each prepared in parallel under the same conditions and stored next to the device in an incubator.

2.4. Static Forced Floating Spheroid Formation

Cells were seeded in 96-well BIOFLOAT™ U-bottom plates (faCellitate, Mannheim, Germany) at a density of 2500 cells per well with culture medium supplemented with 0, 10, 100 and 1000 nM DEX at 37 °C and 5% CO_2. Images were acquired every 24 h for three days using an Invitrogen EVOS™ XL Core Imaging System (Thermo Fisher Scientific, Waltham, MA, USA).

2.5. Trypsin Digestion Adhesion Assay

To investigate the effect of DEX and random positioning on the "stickiness" of adherent FTC-133 and Nthy-ori 3-1 cells, we seeded 0.5×10^6 cells in a Slide Flask (Thermo Fisher Scientific). Cells were treated as described in Section 2.2. After a 24-h attachment period, the Slide Flasks were completely filled with RPMI 1640 medium supplemented with 1 µM DEX for the DEX treatment group and cultured for 24 h under static or RPM conditions. After 24 h, cells were photographed, washed once with PBS, and incubated for 9 min (Nthy-ori 3-1) or 5 min (FTC-133) in prewarmed 0.05% trypsin-EDTA (Life Technologies) at room temperature (RT). The Slide Flasks were moderately hit once, fresh medium was added and removed to stop the trypsin reaction, and the remaining cells were imaged under the microscope.

2.6. Phase Contrast Microscopy

Cells were observed and photographed using an OLYMPUS CKX53 inverted microscope (Olympus, Tokio, Japan) or an Invitrogen™ EVOS™ XL Core Imaging System (Thermo Fisher Scientific).

2.7. Immunofluorescence Microscopy

The adherent cells were washed twice with PBS and fixed by incubation for 30 min at 4 °C in 100% EtOH (Carl Roth, Karlsruhe, Germany), followed by 90 s in ice-cold acetone (Carl Roth) at RT. Cells were stored in 0.5 M sodium azide (Carl Roth) in 0.1 M PBS at 4 °C until observation. Fixed cells were blocked with 3% bovine serum albumin (BSA, Carl Roth) in 0.1 M PBS for 1 h at RT. Subsequently, the cells were labeled with the primary antibodies diluted in 1% BSA (listed in Table S1) overnight at 4 °C. The next day, the cells were washed three times with 0.1 M PBS and incubated with the secondary Alexa Fluor™ 488 (AF488)-conjugated anti-rabbit (Invitrogen, Life Technologies) or Alexa Fluor™ 647 (AF647)-conjugated anti-mouse (Invitrogen, Life Technologies) antibodies at a dilution of 1:500 or 1:1000 at RT for 1 h. Cells were washed again three times with 0.1 M PBS and mounted with Fluoroshield™ with DAPI (4′,6-diamidino-2-phenylindole) (Sigma-Aldrich). The next day, the slides were examined using a ZEISS LSM 800 confocal laser scanning microscope (Carl Zeiss, Oberkochen, Germany). To ensure comparability for intensity quantification, all images were acquired with the same settings using the ZEISS Airyscan detector and ZEN 3.4 software (Carl Zeiss). Images were normalized to the untreated FTC-133 samples cultured under static conditions. Airyscan processing settings were optimized for each antibody/wavelength combination and manually applied to corresponding samples. The resulting file was used in Fiji software v1.53t (ImageJ, imagej.net) to quantify the relative protein amount based on the fluorescence of the sample with the "Image Calculator" tool. Relative intensities were measured according to the method recently described by Shihan et al. [34]. To determine the ratio of protein localization between the nucleus and cytoplasm, the fluorescence intensities of the protein of interest were measured for the nuclear area and the cytoplasm. The nuclear area was determined before using the DAPI signal. For the co-localization measurement of assembled protein complexes, ImageJ image

calculation was used to combine the channels of interest and to subtract the DAPI channel. The amount of protein complexes/co-localization was indicated by the LUT fire setting.

2.8. mRNA Isolation and Quantitative Real-Time PCR

The adherent cells were washed once with PBS and fixed by addition of Invitrogen RNA*later*™ solution (Life Technologies). Cells were harvested using cell scrapers and samples were stored at −20 °C until mRNA extraction. mRNA isolation was performed by using the RNeasy Mini Kit (Qiagen, Venlo, The Netherlands), following the manufacturer's protocol. RNA concentration was determined with a NanoPhotometer® N60 (Implen, Munich, Germany) followed by cDNA synthesis using the High Capacity cDNA Reverse Transcription Kit (Life Technologies). To define the expression level of the genes of interest, quantitative real-time PCR was performed by using the Fast SYBR™ Green Master Mix (Life Technologies) and the QuantStudio™ 3 Real-Time PCR System (Thermo Fisher Scientific). Primer sequences used in the quantitative real-time PCR can be found in the Supplementary Materials (Table S2). The samples were measured in triplicates and evaluated by using the comparative threshold cycle ($\Delta\Delta C_T$) method with 18S rRNA as the housekeeper reference.

2.9. Protein Isolation and Western Blot Analysis

The adherent cells were placed on ice, washed once with ice-cold PBS, and then harvested with ice-cold PBS using cell scrapers. The suspensions were centrifuged at 3000× *g* for 10 min at 4 °C, then the PBS was discarded and the cell pellets were stored at −150 °C.

Proteins were isolated by performing incubation and centrifugation steps in RIPA lysis buffer (Sigma-Aldrich). Protein concentration was measured using the BCA protein assay (Carl Roth). First, 20 µg total protein were loaded onto an SDS-PAGE gel (8%, 10% or 12.5%, 1 mm), run for 20–30 min at 80 V, 90 min at 100 V, and transferred to a nitrocellulose membrane (Carl Roth; 90 min, 100 V). Membranes were blocked with 5% BSA (Carl Roth) in TBS-T for 1 h at RT. To detect proteins of interest, membranes were incubated overnight at 4 °C with a primary antibody diluted in TBS-T containing 5% BSA. GAPDH was used as a loading control. Afterwards, the membranes were washed three times with TBS-T for 5 min and incubated for 1 h at RT with a horseradish peroxidase (HRP)-linked secondary antibody (Invitrogen, Life Technologies) diluted in TBS-T containing 5% BSA. Before the protein bands were visualized by applying Clarity Western ECL Substrate (Bio-Rad, Hercules, CA, USA), the membrane was washed three times with TBS for 5 min. Images were acquired using the ChemiDoc™ XRS+ molecular imager (Bio-Rad) and analyzed using Image Lab™ 6.1 software (Bio-Rad).

For re-staining (e.g., to visualize loading controls of similar size to the protein of interest), membranes were stripped in some Western blots. To remove antibodies, membranes were incubated in stripping buffer (62.5 mM TRIS, 2% SDS, pH 6.8) at 50 °C for 15–20 min and then washed three times with TBS for 5 min.

All antibodies used for Western blot analyses can be found in the Supplementary Materials (Table S1).

2.10. Cell Culture Supernatant Analyses

Oxygen concentration was measured directly in the T25 cell culture flask by fiber-optic oxygen detection using a Microx TX3 transmitter equipped with a flat, broken-tip oxygen microsensor (PreSens, Regensburg, Germany). The sensor was calibrated according to the manufacturer's specifications. Temperature-compensated measurements (37 °C) were recorded using TX3v602 software (PreSens) over a period of 5 min.

2.11. Spheroid Measurement and Quantification

Spheroids were generated through the cultivation of adherent or suspended cells on the RPM. Images of spheroids were taken by using the microscopes described in Section 2.10. These were randomly selected and imaged with the 4× lens. The analysis was done with

ImageJ. First, the spheroids of five images were counted, then outlined with the ImageJ tool "freehand selections" and automatically measured.

2.12. Statistics

Statistical evaluation was performed using SPSS Statistics v28 (IBM, Armonk, NY, USA). The nonparametric Mann–Whitney U test or the independent *t*-test (for Western blot and O_2 saturation analyses due to the smaller number of samples) was used to compare samples from different culture conditions. All data are presented as mean ± standard deviation (SD) with a significance level of $p < 0.05$.

3. Results

As previously reported, FTC-133 spheroid formation was inhibited by DEX in a concentration-dependent manner (Figure 2A).

3.1. Dexamethasone Inhibits Formation but Not Stability of Multicellular Tumor Spheroids

To test spheroid integrity during DEX treatment, we added 1000 nM DEX to a culture of FTC-133 spheroids formed after three days on the RPM and continued random positioning. After three more days, we could see that the spheroids had not disassembled or shrunk, but continued growing in the presence of DEX (Figure 2B). DEX had no influence on the stability of preformed tumor spheroids on the RPM.

3.2. Dexamethasone Selectively Affects Spheroid Formation of Metastatic Thyroid Cancer Cells

In addition to FTC-133 cells, we tested spheroid formation of the normal Nthy-ori 3-1 thyroid epithelial cell line and recurrent ML-1 carcinoma cells derived from a dedifferentiated follicular thyroid carcinoma relapse (Figure 2D) in the presence of different DEX concentrations (0, 10, 100, 1000 nM). Both cell lines formed multicellular spheroids after 72 h on the RPM (Figure 2E). Although the Nthy-ori 3-1 and ML-1 spheroids were much smaller compared to the FTC-133 spheroids, formation was not inhibited by increasing DEX concentrations (Figure 2E). Furthermore, we tested a second metastasis-born thyroid cell line, WRO, that also showed a highly reduced formation of 3D aggregates in the presence of DEX (Figure 2E, bottom line).

The results suggested a selective effect of DEX on the RPM-triggered 3D growth of thyroid carcinoma cells isolated from metastases. Because both FTC-133 and WRO metastatic cell lines have *TP53* mutations, PRIMA-1^{Met} (APR-246) was used to restore mutant p53 activity, thus eliminating the possibility that the observed effect of DEX was due to p53 dysfunction. We demonstrated that the addition of 10 µM PRIMA-1^{Met} did not affect the DEX inhibition of spheroid formation in FTC-133 cells and could not completely reverse the effect in WRO cells (Figure 2F), ruling out the involvement of p53 in this process. Furthermore, PRIMA-1^{Met} alone had no effect on spheroid formation on the RPM.

3.3. Dexamethasone Supresses RPM-Induced Cell Detachment but Not 3D Growth in General

RPM-induced spheroid formation comprises two steps: The detachment of the actually adherent cells from their growth surface and the aggregation/growth of the detached and floating cells in the medium. To find out which step is influenced by DEX, we used ultra-low attachment multi-well plates for comparison, in which spheroids form automatically without mechanical action. After 72 h, spheroids of FTC-133 cells and Nthy-ori 3-1 cells have formed in the wells independently of the used DEX concentration (0–1000 nM) (Figure 2G). Furthermore, FTC-133 cells formed smaller spheroids in the presence of 1000 nM DEX when they were placed directly on the RPM without a prior attachment phase (Figure 2C). The number of these spheroids was comparable with those of the DEX-free samples. We also observed 3D growth when we cultured FTC-133 suspension cells together with DEX on a clinostat. Accordingly, DEX did not prevent the aggregation of the cells itself, but seems to impede the 'metastasis-like' detachment of thyroid cancer cells observed under random positioning.

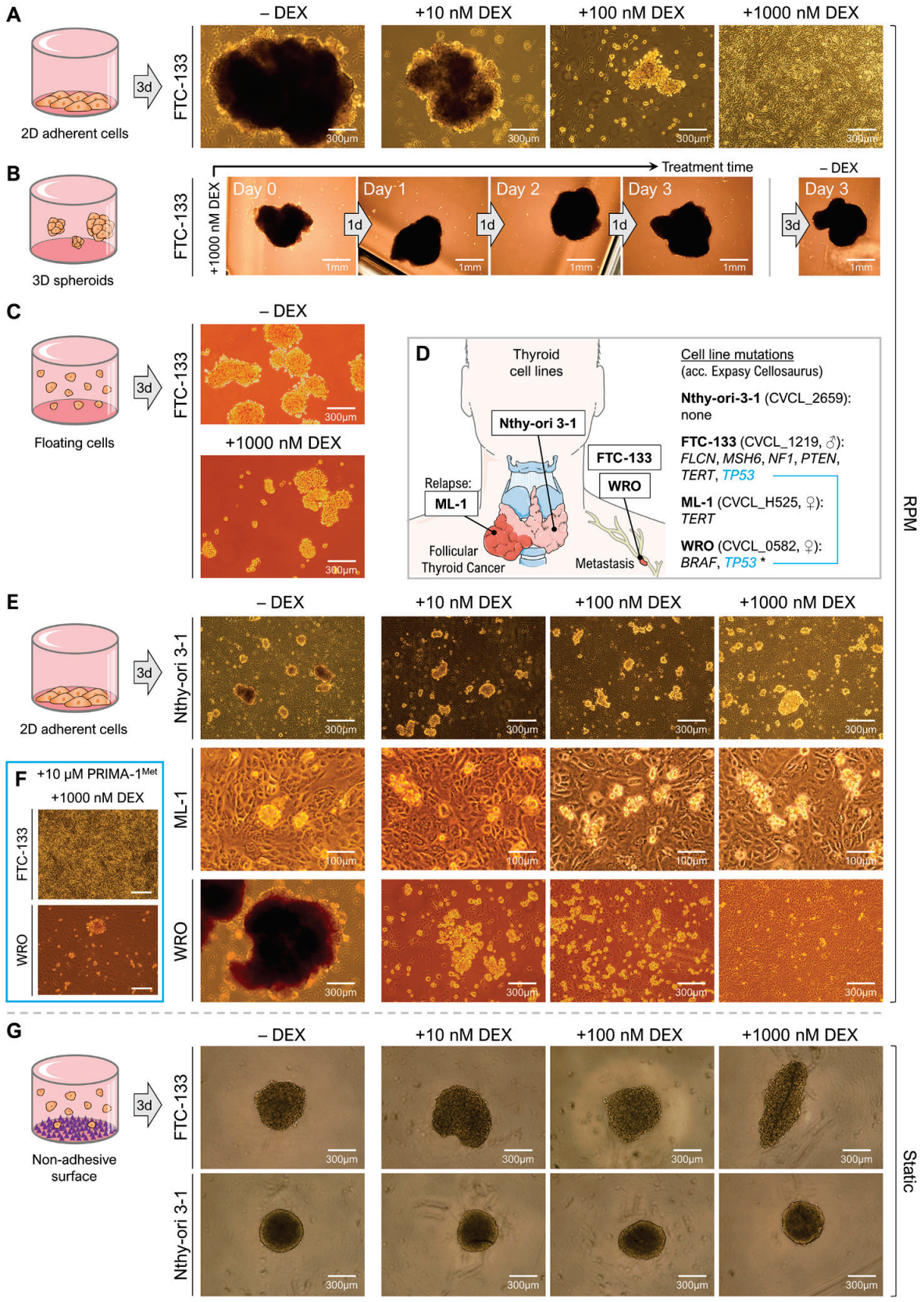


Figure 2. Impact of different DEX concentrations (0, 10, 100, 1000 nM) on spheroid formation and stability of different thyroid epithelial cells after 3 days. (**A**) Spheroid formation of adherent FTC-133 metastasized carcinoma cells after rotation on the RPM; (**B**) stability of preformed FTC-133 spheroids on the RPM in the presence of 1000 nM DEX; (**C**) spheroid formation of FTC-133 suspension

cells; (**D**) origins of the used thyroid cell lines and documented cell line mutations (https://www.cellosaurus.org; accessed on: 2 February 2023). ♂, ♀indicate the gender of the donor. * The *TP53 P223L* mutation in WRO cells is only reported by some authors; (**E**) spheroid formation of adherent Nthy-ori 3-1 thyroid epithelial, ML-1 recurrent and WRO metastasized thyroid carcinoma cells after 3d rotation on the RPM; (**F**) spheroid formation of FTC-133 and WRO cells in the presence of 10 µM of the p53 reactivator PRIMA-1^{Met} and 1000 nM DEX; (**G**) spheroid formation of FTC-133 and Nthy-ori 3-1 cells under static forced floating conditions in ultra-low attachment plates. Parts of subfigure D were drawn by using pictures from Servier Medical Art, licensed under a Creative Commons Attribution 3.0 Unported License (https://creativecommons.org/licenses/by/3.0/, accessed on 12 February 2023).

3.4. Dexamethasone Treatment Alters 'Stickiness' of the Cells

After showing specifically that the spheroid formation of FTC-133 cancer cells versus benign Nthy-ori 3-1 cells is affected by DEX (Figure 3A), we started to investigate the cause in these two cell lines. Considering the different forces of cell adhesion and shear forces on RPM (Figure 3B), DEX treatment of FTC-133 cells must result in adhesion forces being greater than shear forces leading to cell detachment. When treated with a DEX concentration of 1000 nM, spheroid formation of FTC-133 cells was completely suppressed in contrast to Nthy-ori 3-1 cells (Figure 3C, grey area). Spheroid size was also affected by DEX, but since the focus of this study was on the formation of spheroids rather than their later development, this aspect was not further explored here. A trypsinization assay showed that DEX increased the adhesiveness of both cell lines, and that random positioning deceased the adhesiveness of Nthy-ori 3-1 cells.

FTC-133 cells showed a more bipolar or multipolar shape with cellular bridging in the presence of DEX (Figure 3D, yellow arrows). Factors that may increase cell adhesion include extracellular matrix composition (ECM) proteins and cell–cell or cell–ECM junctions.

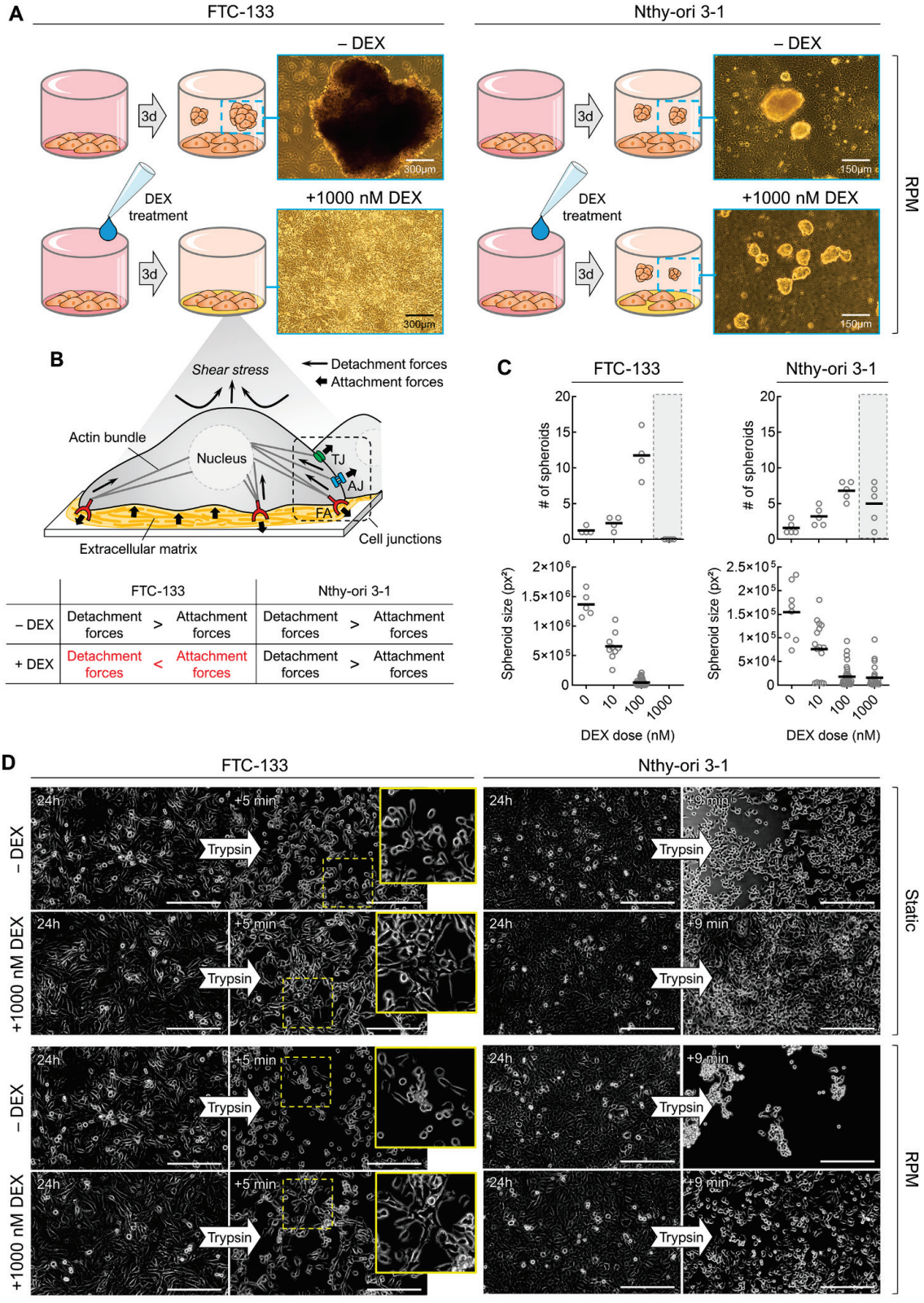
3.4.1. Extracellular Matrix

We examined the ECM composition based on the immunofluorescence of several major components, including fibronectin, collagen I/IV and laminin. Whereas DEX had no effect on fibronectin in FTC-133 cells, we found an 8-fold increase of fibronectin in DEX-treated Nthy-ori 3-1 cells. Moreover, we detected a decrease in fibronectin in RPM-grown FTC-133 cells, which was also present, although to a lesser extent, in Nthy-ori 3-1 cells (Figure 4A,B). In the RPM+DEX samples, the FTC-133 cells produced a slightly lower amount of fibronectin than the Nthy-ori 3-1 cells (Figure 4B).

Collagen I was more highly expressed in FTC-133 cells. Random positioning and DEX treatment alone increased collagen I levels in Nthy-ori 3-1 cells and decreased them simultaneously in FTC-133 (Figure 4C,D). Thus, collagen I levels of both cell lines were almost identical after 72 h of DEX treatment. Interestingly, DEX treatment during random positioning lead to a decrease in collagen I in both malignant and healthy cells (Figure 4D). Collagen IV was only detectable in significant amounts in FTC-133 cells after 72 h. It was less present after random positioning (Figure 4C).

Laminin was significantly reduced by DEX in FTC-133 cells, regardless of culture condition (Figure 4E,F). In Nthy-ori 3-1 cells there was a slight increase of laminin in the DEX-treated RPM group (Figure 4F).

While the amount of MMP-9 was not affected by either RPM or DEX, MMP-2 was decreased after DEX administration in both FTC-133 and Nthy-ori 3-1 cells. Nthy-ori 3-1 cells exhibited generally lower levels of MMP-2 and MMP-9. In particular, MMP-9 was increased 14-fold in FTC-133 cells (Figure 4G,H).



	FTC-133		Nthy-ori 3-1	
– DEX	Detachment forces	>	Detachment forces	>
		Attachment forces		Attachment forces
+ DEX	Detachment forces	<	Detachment forces	>
		Attachment forces		Attachment forces

Figure 3. (**A**) Observed effects of 1000 nM DEX on the RPM-induced spheroid formation of FTC-133 und Nthy-ori 3-1 cells after 3 days; (**B**) putative reasons for the different behavior of the two cell lines. AJ: adherens junction, FA: focal adhesion, TJ: tight junction; (**C**) number and size of spheroids formed after 3 days on the RPM depending on DEX concentration; (**D**) trypsin-based cell detachment assay reveals the general adhesiveness of cells after 24 h of culture in the presence and absence of DEX. The yellow boxes show an enlargement of the outlined section. Scale bars: 300 µm.

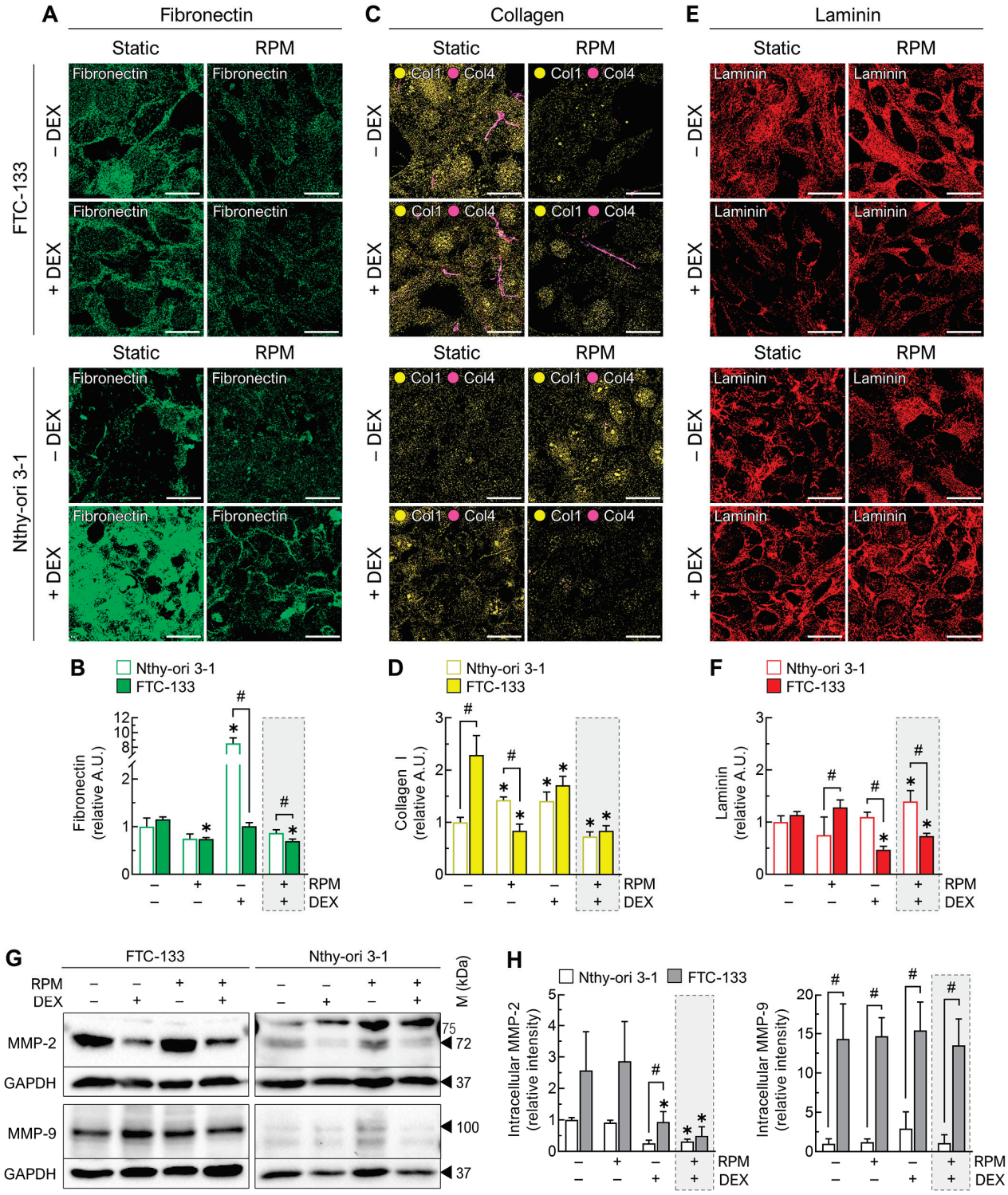


Figure 4. Effect of DEX (1000 nM) and random positioning on the ECM of FTC-133 and Nthy-ori 3-1 cells after 3 days. (**A**) Immunofluorescence of fibronectin; (**B**) fluorescence-based quantification of fibronectin under the different culture conditions ($n = 5$); (**C**) immunofluorescence of collagen I (yellow) and collagen IV (purple); (**D**) fluorescence-based quantification of collagen I under the different culture conditions ($n = 5$); (**E**) immunofluorescence of laminin; (**F**) fluorescence-based quantification of laminin under the different culture conditions ($n = 5$); (**G**) intracellular protein levels of matrix metallopeptidases MMP-2 and MMP-9 indicated by Western blot (see also Supplementary File S1); (**H**) densitometric quantification of Western blot proteins ($n = 3$). Scale bars: 300 µm. * $p < 0.05$ vs. control condition (−DEX/−RPM); # $p < 0.05$.

In summary, we showed that, in FTC-133 cells, three major ECM structural components were reduced by DEX treatment during random positioning. Compared with Nthy-ori 3-1 cells, the ECM components were even more reduced. In addition, FTC-133 cells produced many more collagenases. All this cannot explain the different response of the two cell lines to DEX treatment.

3.4.2. Cell Junctions

The expression of the tight junction (TJ) proteins claudin-1 and ZO-1 (zonula occludens 1) was significantly lower in FTC-133 cells than in Nthy-ori 3-1 cells under normal culture conditions. However, in both cell lines, the levels of the proteins were increased by both DEX and, to a lesser extent, by the RPM (Figure 5A,B). In particular, the expression of ZO-1 was increased 27-fold in FTC-133 in the presence of DEX and 20-fold after exposure to the RPM. In addition, FTC-133 cells showed increased nuclear localization of ZO-1 both on the RPM and after DEX treatment (Figure 5A), indicating the formation and maturation of TJs [35].

Co-localization analysis of claudin-1 and ZO-1 confirmed the enhanced formation of TJs by DEX, which reached the same amount in FTC-133 cells as in Nthy-ori 3-1 cells after 72 h, regardless of culture motion (Figure 5C). This increase in TJs could also explain the cellular bridging and altered shape of FTC-133 cells in the presence of DEX (Figure 3D). Another zonula occludens protein, ZO-2, showed similar regulation to ZO-1 in FTC-133 cells (Figure S1A). Overall, both FTC-133 cells and WRO cells showed very low baseline expression of claudin-1 under static cell culture and strong upregulation during DEX treatment on the RPM (Figure S1B). Therefore, TJ regulation might be related to the inhibition of spheroid formation of both cell lines by DEX (Figure S1C).

E-cadherin expression was generally lower in FTC-133 cells than in Nthy-ori 3-1 cells. Whereas E-cadherin was downregulated mainly by RPM in both cell lines, in FTC-133 cells, both DEX and RPM had a suppressive effect on β-catenin levels (Figure 5D,E). Overall, the amount of adherens junctions (AJs) was higher in FTC-133 cells in the RPM+DEX samples than in standard culture, but still significantly lower than in Nthy-ori 3-1 cells (Figure 5F).

Unlike the benign cells, there was an increase in focal adhesions (FAs) in FTC-133 cancer cells in response to the RPM (Figure 5G–I). In Nthy-ori 3-1 cells, a similar effect was detected in response to DEX. This is also reflected in the amount of the single components, FAK (focal adhesion kinase) and integrin-β1 (Figure 5H). Nevertheless, the combination RPM+DEX did not show any changes in the number of FAs in either cell line (Figure 5I).

In summary, although FTC-133 cells showed a significant increase in claudin-based TJs and cadherin-based AJs after DEX treatment on RPM, the number of cellular junctions examined in these experiments was not higher than that in Nthy-ori 3-1 cells.

3.4.3. Anti-Adhesion Molecules

Because neither the ECM composition nor the number of cellular junctions could explain the different response of the two cell lines to DEX treatment, we further investigated anti-adhesion effects. Thus, we examined the anti-adhesion molecule mucin-1 (MUC1), which is known to inhibit cell–cell and cell–ECM interactions [36,37].

According to the literature [38], the oncoprotein mucin-1 was more highly expressed in FTC-133 cells than in Nthy-ori 3-1 cells under static culture conditions. In FTC-133 cells, neither random positioning nor DEX treatment had any effect on mucin-1 levels (Figure 6A,B). However, immunofluorescence revealed a significant increase of mucin-1 in Nthy-ori 3-1 cells cultured on the RPM (Figure 6A,B). We also confirmed this effect for ML-1 cells (similar response to DEX as Nthy-ori 3-1), but not for WRO cells (similar response to DEX as FTC-133) (Figure S2A). Treatment with 5 μM of the MUC1-inhibitor GO-203 showed that DEX could also suppress RPM-induced spheroid formation of Nthy-ori 3-1 cells after inhibition of mucin-1 (Figure 6D). In addition, we found an attenuated ability for spheroid formation when we cultured Nthy-ori 3-1 cells in the presence of GO-203 on the RPM (Figure 6E,F). Moreover, the amount of mucin-1 in the presence of GO-203 was decreased after 72 h on the RPM (Figure 6G).

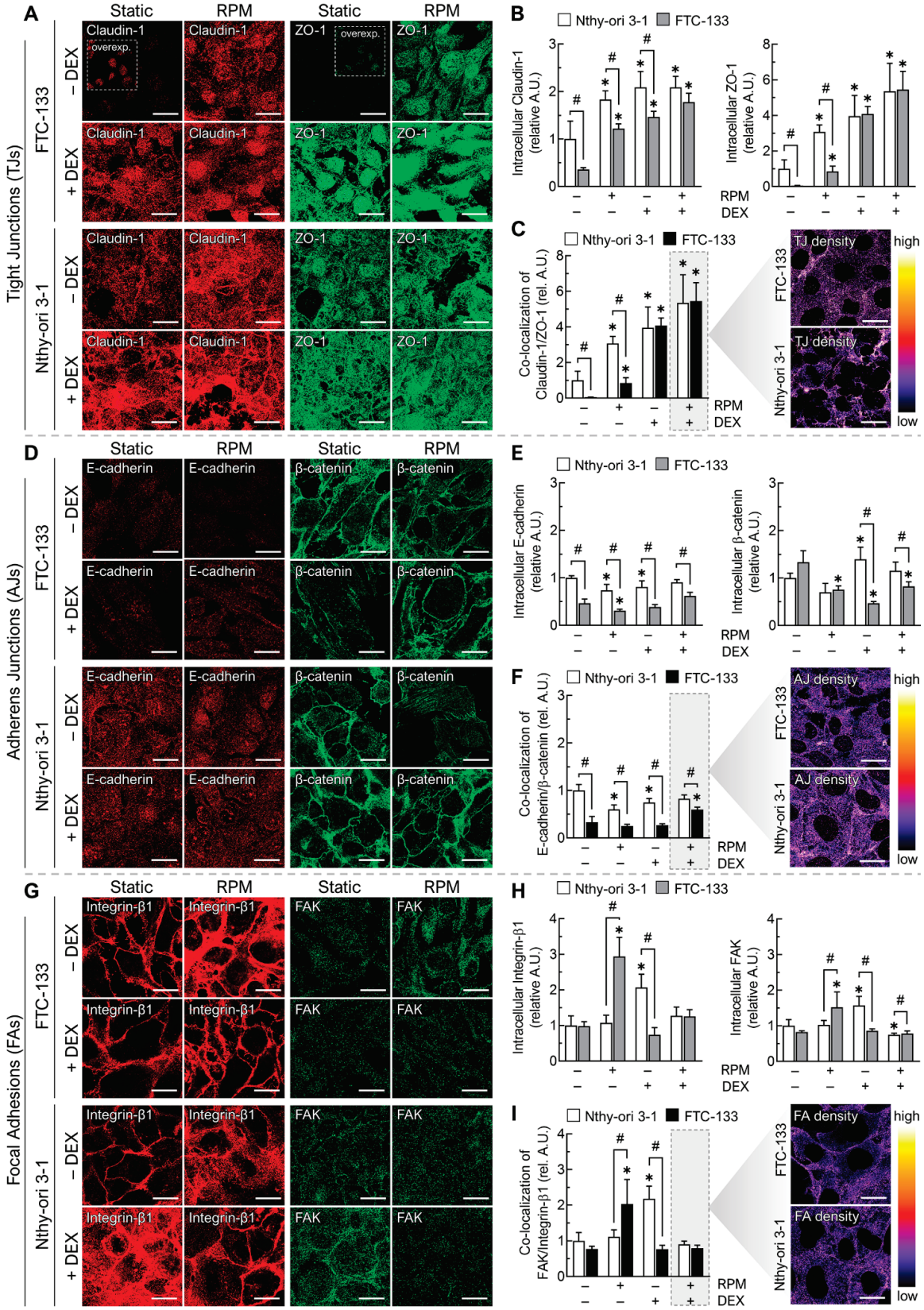


Figure 5. Effect of DEX (1000 nM) and random positioning on the cell junctions of FTC-133 and Nthy-ori 3-1 cells after 3 days. (**A**) Immunofluorescence of claudin-1 (red) and ZO-1 (green). The small inserts show low signal pictures with higher brightness; (**B**) fluorescence-based quantification

of claudin-1 and ZO-1 under the different culture conditions (n = 5); (**C**) co-localization of claudin-1 and ZO-1; (**D**) immunofluorescence of E-cadherin (red) and β-catenin (green); (**E**) fluorescence-based quantification of E-cadherin and β-catenin under the different culture conditions (n = 5); (**F**) co-localization of E-cadherin and β-catenin; (**G**) immunofluorescence of integrin-β1 (red) and FAK (green); (**H**) fluorescence-based quantification of integrin-β1 and FAK under the different culture conditions (n = 5); (**I**) co-localization of integrin-β1 and FAK. Scale bars: 300 µm. * $p < 0.05$ vs. control condition (−DEX/−RPM); # $p < 0.05$.

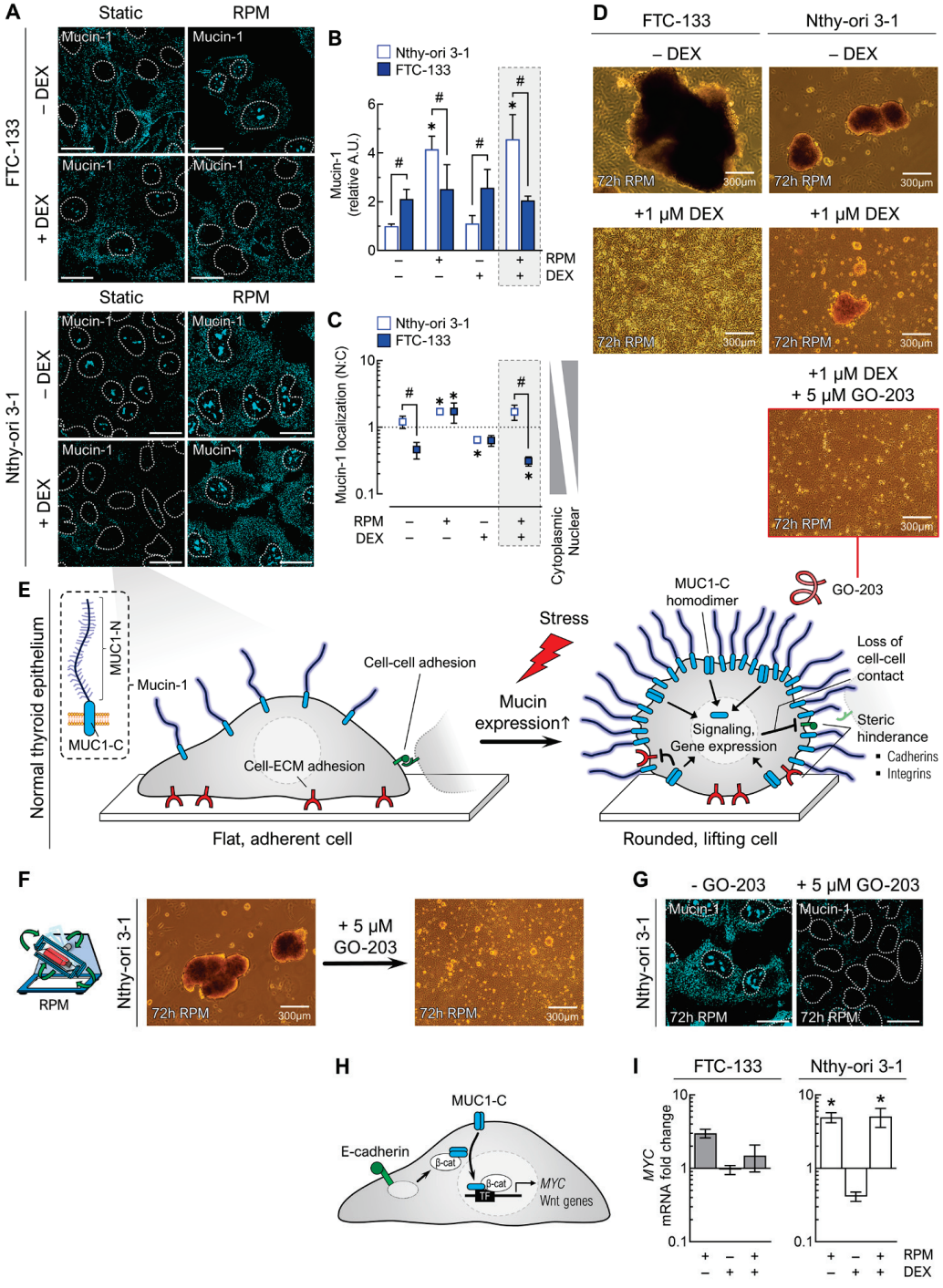


Figure 6. Effect of DEX (1 µM) and random positioning on mucin-1 in FTC-133 and Nthy-ori 3-1 cells after 3 days. (**A**) Mucin-1 immunofluorescence in adherently growing cells. Mucin-1 is shown in turquoise, with the outlines of the nuclei as dashed lines; (**B**) fluorescence-based quantification of

mucin-1 under the different culture conditions (n = 5); (**C**) nuclear localization of mucin-1 (n = 5); (**D**) spheroid formation of FTC-133 and Nthy-ori 3-1 cells in the presence of 1 μM DEX and 5 μM of the MUC1-inhibitor GO-203; (**E**) hypothetical model that could explain the anti-adhesion of Nthy-ori 3-1 cells during RPM-induced increased mucin-1 expression. Mucin-1 is a transmembrane glycoprotein consisting of two subunits, an extracellular, N-terminal highly glycosylated subunit (MUC1-N) and a C-terminal transmembrane subunit (MUC1-C). MUC1-C can form homodimers that affect cellular signaling pathways and gene expression; (**F**) spheroid formation of Nthy-ori 3-1 cells in the presence of 5 μM GO-203; (**G**) MUC-1 immunofluorescence (turquoise) of adherently growing Nthy-ori 3-1 cells in absence and presence of 5 μM GO-203. (**H**) MUC1-C activates the Wnt/β-catenin pathway and induces *MYC* expression. TF: transcription factor. (**I**) Expression levels (mRNA) of the *MYC* gene (n = 5). Scale bars: 300 μm. * $p < 0.05$ vs. control condition (−DEX/−RPM); # $p < 0.05$.

The C-terminal transmembrane subunit of mucin-1 (MUC1-C) can activate the Wnt/β-catenin pathway and induce expression of *MYC* and other Wnt genes (Figure 6H). Consistent with the immunofluorescence data of Nthy-ori 3-1 cells (Figure 6A–C), the expression of *MYC* was significantly increased on the RPM (Figure 6I).

3.5. Dexamethasone Influences Signal Transduction Pathways

3.5.1. Glucocorticoid Receptor Signaling

The main actions of DEX occur through the activation of the glucocorticoid receptor (GR, gene symbol: *NR3C1*), which is activated by phosphorylation and can actively shuttle between cytoplasm and nucleus, where it acts as a transcription factor (Figure 7C) [39]. To verify whether GR effects were responsible for the observed spheroid suppression in FTC-133 cells, we used the competitive GR inhibitor mifepristone (MIF). We found that increasing amounts of MIF (1–20 μM) in the presence of DEX (1 μM) indeed facilitated the (re-)formation of small tumor spheroids.

However, the spheroids in the presence of MIF were smaller than in the vehicle samples (Figure 7A), maybe due to its known anti-proliferative effect. Quantification of the spheroids showed very well the competitive principle of MIF and DEX: with increasing MIF concentration, the number of spheroids formed approaches of the untreated control group (Figure 7B).

With this information, we took a closer look at GR activity under random positioning and DEX treatment. Under static cell culture conditions, expression of the *NR3C1* gene was lower in FTC-133 cells (68.3%) compared to Nthy-ori 3-1 (Figure 7D). Moreover, *NR3C1* transcription in the two cell lines was affected differently by external conditions: While *NR3C1* mRNA levels in FTC-133 cells were increased by DEX, they were decreased in Nthy-ori 3-1 cells by random positioning (Figure 7E).

Western blot showed an increased GR amount in FTC-133 cells on the RPM in the absence of DEX. We also observed a generally lower amount of "activated" p-GR (Ser211) in Nthy-ori 3-1 cells and a strong increase in p-GR after the addition of DEX in both cell lines (Figure 7F,G).

In the absence of DEX, GR was mainly located in the cytoplasm near the nucleus of FTC-133 cells (Figure 7H, yellow arrows). In the presence of DEX, the amount of GR was reduced, but little was translocated to the nucleus (Figure 7H,I). GR translocation was not significantly altered by random positioning after 72 h, suggesting that the RPM has no major influence on normal GR behavior in FTCs. In Nthy-ori 3-1 cells, GR was significantly translocated to the nucleus during DEX treatment (Figure 7H,I).

At the gene expression level, the GR target genes *FKBP5* and *DUSP1* were found to be upregulated in both cell lines in the presence of DEX under both rotational and static conditions (Figure 7J).

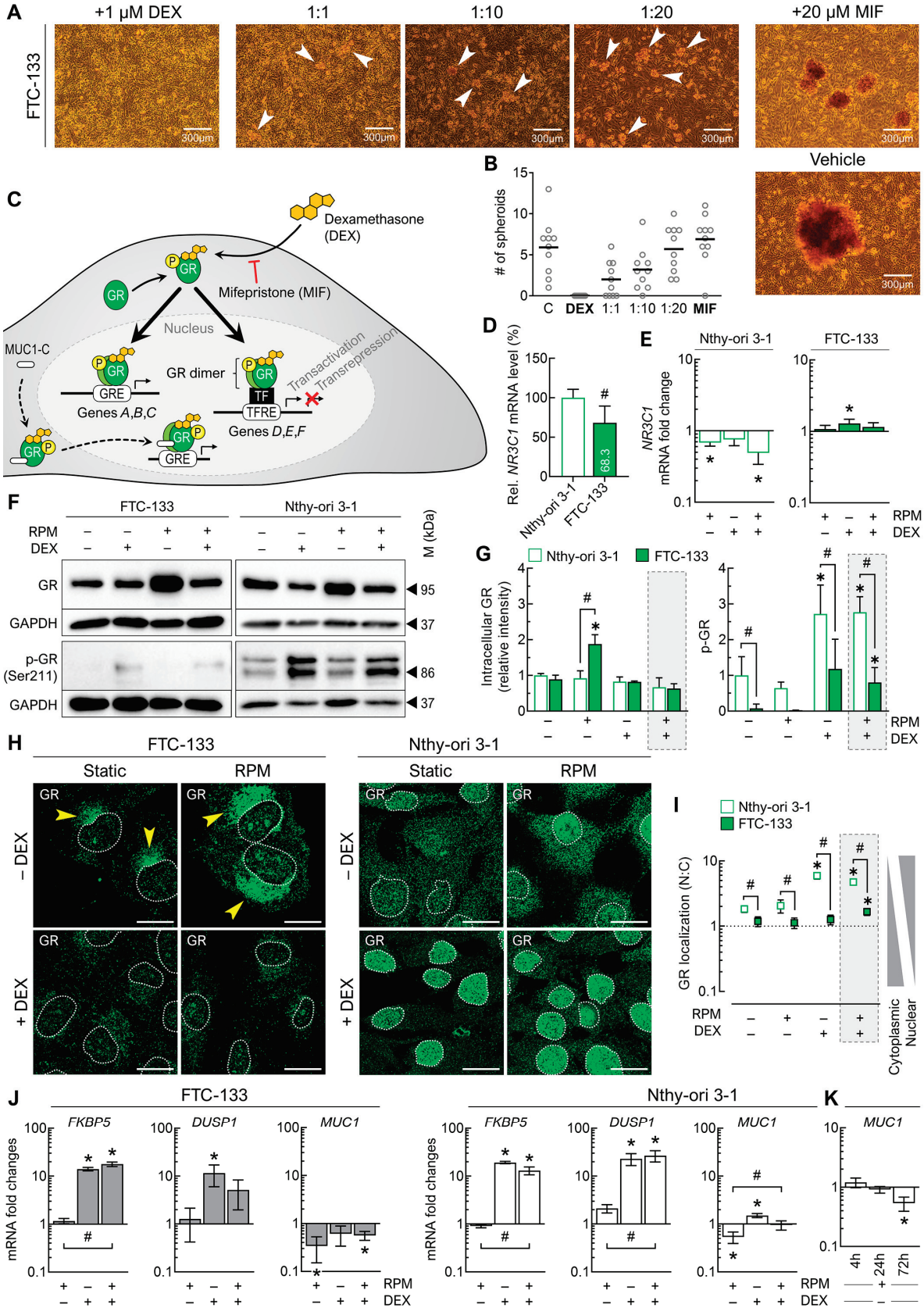


Figure 7. Effect of DEX on the glucocorticoid receptor (GR) and GR signaling in FTC-133 and Nthy-ori 3-1 cells after 3 days. (**A**) Spheroid formation (white arrows) of FTC-133 cells in the presence of 1 µM DEX and different concentrations (1–20 µM) of the competitive GR inhibitor mifepristone (MIF); (**B**) number of FTC-133 spheroids formed on the RPM in the presence of DEX and MIF

(n = 10). (**C**) Simplified schematic representation GR's mechanism of action. The genomic effects of DEX occur through its binding to GR and the movement of DEX-GR to the nucleus, where they can regulate the transcription of genes. GRE: glucocorticoid response element, TF: transcription factor, TFRE: transcription factor response element. (**D**) Expression levels (mRNA) of the *NR3C1* gene (n = 5); (**E**) fold changes of *NR3C1* expression under the different culture conditions (n = 5); (**F**) intracellular protein levels of GR and phosphorylated GR (p-GR) indicated by Western blot (see also Supplementary File S1); (**G**) densitometric quantification of Western blot proteins (n = 3); (**H**) GR immunofluorescence in adherently growing cells. GR is shown in green, with the outlines of the nuclei as dashed lines. In DEX-free FTC-133 cultures, GR is located near the nucleus (yellow arrows). (**I**) Nuclear localization of GR (n = 5); (**J**) fold changes in the expression of some signature genes of the GR pathway under the different culture conditions (n = 5); (**K**) fold changes in *MUC1* expression on the RPM after different time points (n = 5). Scale bars: 300 µm. * $p < 0.05$ vs. control condition (−DEX/−RPM); $^{\#}$ $p < 0.05$.

However, the upregulation of *DUSP1* (encoding dual specificity protein phosphatase 1) in FTC-133 cells on the RPM was lower than in the static cell culture. In addition, one other mutual target gene of GR, *MUC1* (encoding mucin-1), was downregulated in FTC-133 cells primarily by the RPM, whereas in Nthy-ori 3-1 cells it was decreased by random positioning but also upregulated by DEX (Figure 7J). The observed overexpression of mucin-1 protein in Nthy-ori 3-1 cells on the RPM (Figure 6A) could be explained by a transient upregulation of *MUC1* and subsequent negative feedback after 72 h (Figure 7K).

Since a large percentage of GR binding sites is known to be hypoxia-specific [40–42] and we needed to work with completely filled cell culture flasks for random positioning, we also checked whether there was a gene expression response to hypoxia via hypoxia-inducible factor 1α (HIF1A). We found that *HIF1A* expression was upregulated only in Nthy-ori 3-1 cells when the culture flasks were completely filled (Figure S3). This change was independent of RPM exposure or DEX treatment.

3.5.2. Cell Stress Signaling

A crosstalk between GR and p38 mitogen-activated protein kinase (MAPK) was reported earlier [43–45]. p38 (gene symbol: *MAPK14*) can be activated by phosphorylation through mechanical forces [46] and then either accelerates the activation of GR or migrates to the nucleus, where it can itself affect various transcription factors and thus control the expression of numerous genes (Figure 8A). *MAPK14* was expressed about three-fold higher in the cancer cells (Figure 8B), and transcription was upregulated by DEX treatment in both FTC-133 cells and Nthy-ori 3-1 cells. However, downregulation of *MAPK14* by random positioning was also observed in FTCs (Figure 8C).

The p38 protein levels were generally higher in Nthy-ori 3-1 cells compared with FTC-133 cells and were not significantly affected by DEX treatment or the RPM. Phosphorylated p-p38 (Thr180, Tyr182), which can be transferred to the nucleus, was significantly increased in FTC-133 cells on the RPM without DEX and significantly decreased after DEX treatment. In Nthy-ori 3-1 cells, p-p38 levels were not altered by DEX or by random positioning (Figure 8D,E).

Under static cell culture conditions, p38 was mainly located in the cytoplasm of FTC-133 cells, whereas on the RPM, p38 was shifted into the nucleus. This translocation did not occur in the presence of DEX. In contrast, in Nthy-ori 3-1 cells, p38 was shifted into the nucleus only in the presence of DEX (Figure 8F). Thus, we found a strong activation of the p38 pathway during random positioning in FTC-133 cells without DEX and a slight activation of this pathway in Nthy-ori 3-1 cells with DEX (Figure 8G).

Genes under the control of p38 include *IL6*, *CXCL8* and *IL1B*. Consistent with the nuclear localization of p38, all three genes were upregulated on the RPM in FTC-133 cells, and for *IL6* and *CXCL8* we found attenuation of the mRNA levels on the RPM in the presence of DEX. In Nthy-ori 3-1 cells, gene expression was not affected by the RPM alone, but *IL6* and *IL1B* were downregulated on the RPM in the presence of DEX (Figure 8H).

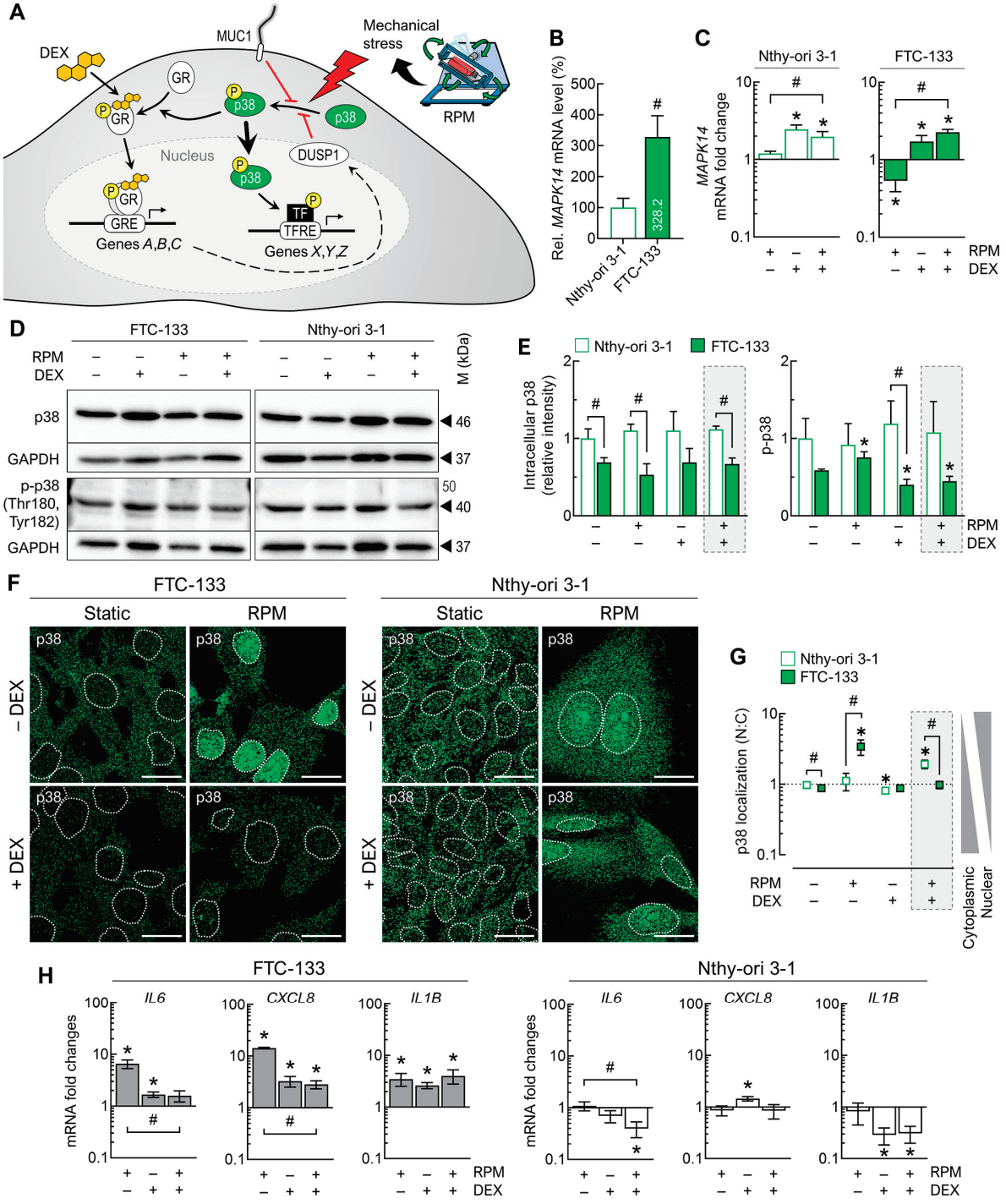


Figure 8. Effect of DEX on p38 MAPK and p38 signaling in FTC-133 and Nthy-ori 3-1 cells after 3 days. (**A**) Simplified schematic representation of p38′s mechanism of action. GRE: glucocorticoid response element, TF: transcription factor, TFRE: transcription factor response element. (**B**) Expression levels (mRNA) of the *MAPK14* gene ($n = 5$); (**C**) fold changes of *MAPK14* expression under the different culture conditions ($n = 5$); (**D**) intracellular protein levels of p38 and phosphorylated p38 (p-p38) indicated by Western blot (see also Supplementary File S1); (**E**) densitometric quantification of Western blot proteins ($n = 3$); (**F**) p38 immunofluorescence in adherently growing cells. p38 is shown in green, with the outlines of the nuclei as dashed lines. (**G**) Nuclear localization of p38 ($n = 5$); (**H**) fold changes in the expression of some mutual signature genes of the p38 pathway under the different culture conditions ($n = 5$). Scale bars: 300 µm. * $p < 0.05$ vs. control condition (−DEX/−RPM); $^{\#}$ $p < 0.05$.

4. Discussion

In this study, we showed that DEX is not only able to suppress RPM-induced spheroid formation of FTC-133 follicular thyroid cancer cells, but this inhibition was selective for two metastatic thyroid carcinoma cells, WRO and FTC-133, whereas benign Nthy-ori 3-1 cells and recurrent ML-1 thyroid cancer cells were not affected by DEX.

4.1. Effects of Dexamethasone

DEX is commonly used in clinical practice to treat side effects such as nausea and vomiting caused by chemotherapy. Wu et al. [47] pointed out that DEX itself is able to inhibit tumor cells in vitro and in vivo. That DEX may also have an anti-metastatic effect is supported by several findings. In a recent study, DEX not only decreased the viability of T47D human breast cancer cells in a time- and dose-dependent manner, but also reduced their cell adhesion and migration. This effect was explained by the altered expression of α-/β-integrin, E-/N-cadherin and MMP-2/-9 in response to DEX treatment [48]. Other authors described a disruption of dynamic cytoskeletal organization in these cells when they were treated with DEX [49]. Lin et al. [50,51] previously observed suppression of ovarian cancer metastasis by DEX. In human bladder cancer cells, suppression of MMP-2, MMP-9 and IL-6 expression, as well as induction of mesenchymal-to-epithelial transition (MET were found in the presence of DEX [52]. Therefore, the described effects of DEX on the RPM metastasis model are not entirely unfounded.

Control of GR by PTEN (phosphatase and tensin homolog) appears to be a fail-safe mechanism for tumor suppression [53]. The loss of PTEN activity in FTC-133 cells might affect GR levels, which could explain the lower translocation of GR into the nucleus of FTC-133 cells in the presence of DEX. In endothelial cells, shear stress led to nuclear localization of GR and consequent expression from the GRE promoter [54,55]. This we could not detect with our thyroid cells on the RPM. While the RPM seems to play a rather minor role in YAP1/Hippo signaling in the adherent cell population, FTC-133 cells responded to random positioning with strong activation of p38. This p38 stress signaling in FTC-133 cells could be inactivated by DEX, maybe due to the kinase activity of GR-induced DUSP1, which was upregulated after DEX treatment. In comparison, Nthy-ori 3-1 cells also activated p38 on the RPM but to a lesser extent and without sensitivity to DEX. Thus, DEX directly interferes with RPM-induced stress signaling via p38 in FTC-133 cells and antagonizes a variety of gene expressions and cell functions according to the multiple transcriptional substrates of p38 [56].

4.2. RPM-Induced Spheroid Formation and Its Inhibition by Dexamethasone

It has been previously reported in the literature that both healthy (Nthy-ori 3-1) and low-differentiated follicular thyroid cancer cells (ML-1, FTC-133, and WRO) form spheroids on the RPM within 24 h [57–62]. All these cells required a lag time of several hours before some of the cells detached from the bottom of the culture flask and assembled into 3D aggregates, while others remained attached. According to the latest comparison by Warnke et al. [58], no striking difference was found between healthy and cancer cells with respect to morphological changes induced by random positioning. It was therefore even more surprising that DEX specifically inhibits the spheroid formation of metastatic thyroid carcinoma cells on the RPM. This suggests that the RPM-induced spheroid formation of the different cell types may not be identical. To date, very few studies have addressed the question of how spheroid formation on the RPM is affected by drugs or the targeted blocking of functional proteins (Table 1). Therefore, it is very difficult to obtain insightful data from this works.

Table 1. Other studies on targeting RPM-induced spheroid formation of cancer cells.

Cell Line	Drug	Main Findings	Reference
FTC-133	Dexamethasone	Inhibition of spheroid formation.	[31]
MCF-7	Dexamethasone Rolipram Olaparib	Reduced spheroid formation. No effects. No effects.	[63]
MCF-7	PP2 anti-E-cadherin	Inhibition of spheroid formation. Increased spheroid formation.	[64]

Some years ago, Lin and Wang [65] summarized the use of glucocorticoids in cancer treatment. In their literature review, they found different effects, in particular that glucocorticoid treatment could promote the growth of malignant solid tumors in certain cancers, while playing a suppressive role in tumor progression and metastasis in other cancers. They concluded that simple cellular experimental models are not sufficient to accurately predict therapeutic outcome in vivo [65]. According to the current literature, space science-derived RPM [66,67] enables a complex, though not yet fully understood, in vitro model for adherent cancer cell metastasis [19–21,68]. Since RPM also promotes 3D growth of other benign cells, it is understandable that there must be some differences between spheroid and tumor spheroid formation, although the visible result is the same in the end. Comparisons between FTC-133 and Nthy-ori 3-1 RPM cell cultures have been performed in the past. Kopp et al. [57] suggested that growth and angiogenic factors may be responsible for the differences in RPM-induced spheroid formation between malignant and healthy thyroid cells. Warnke et al. [58,59] confirmed the involvement of cytokines and focal adhesion proteins during the RPM culture of both cell lines. However, these comparisons were primarily related to gene and protein expression of markers with a focus on the response to altered gravity conditions. In this study, we took a more functional phenotypic approach to explain why benign thyroid cells respond differently to DEX on the RPM treatment than the corresponding carcinoma cells. In this way, we could determine that the adhesion of tumor and healthy thyroid cells on the RPM is affected differently.

We observed, under normal culture conditions, that DEX increased the adhesion of both cell types. This can be explained, on the one hand, by the increased expression of fibronectin (only in Nthy-ori 3-1 cells) and, on the other hand, by an increased formation of TJs, which was particularly observed in metastatic FTC-133 and WRO cells. Glucocorticoid-induced TJ formation and re-organization has been previously described and studied in mouse mammary epithelial cells [69,70] and in preclinical human intestinal models (summarized in [71]). In our experiments, the RPM also increased the expression of TJ proteins claudin-1 and ZO-1, as well as the formation of TJs, which had an enhancing effect when combined with DEX treatment. In a clinorotation experiment with MCF-7 breast cancer cells, Adamian et al. [72] recently observed similar increases in claudin-1 and claudin-3 after 72 h.

It is known that changes in the expression and/or distribution of TJ proteins can lead to a loss of cohesion of the TJ structure. This, in turn, gives cancer cells the ability to invade and ultimately metastasize [73]. In general, low expression of TJs is observed in highly metastatic cancer cells [74], and dedifferentiation of thyroid carcinomas is associated with a decrease in claudin-1, -4, and -7 expression [75]. In FTC-133 cells, our data confirmed low TJ protein expression. However, intracellular localization of claudins is also important, as pure overexpression of non-junctional nuclear claudin-1 in FTC-133 cells led to increased cell migration and invasion [76].

In addition, we also found an increase in AJs in FTC-133 when the cells were treated with DEX on the RPM. AJs have a similar structural organization to TJs: cadherins form contacts with catenins, and these complexes connect the cell surface to the cytoskeleton. In particular, decreased expression or loss of cadherins has been associated with epithelial tumor development, invasion and metastasis [77]. In addition, for the RPM metastasis

model, Sahana et al. [64] found that blocking E-cadherin with an antibody increased the tumor spheroid formation of MCF-7 cells. In thyroid cancer, E-cadherin expression is considered a potential predictive factor for clinical disease progression [78]. Huang et al. [79] reported that the loss of cell adhesion in CGTH W-2 thyroid cancer cells compared with healthy thyrocytes may be due to the incomplete assembly of the cadherin–catenin complexes at the cell membrane. Thus, an increase in assembled AJs, as we have seen from the co-localization of E-cadherin and β-catenin, could also lead to enhanced cell adhesion.

Therefore, it is reasonable to speculate that the increased number of TJs and AJs, especially in FTC-133 cells, could cause a reduction in cell migration after DEX treatment on the RPM, which then leads to the inhibition of tumor spheroid formation. In addition, it would be important to clarify whether the increased occurrence of cell–cell junctions influences the detachment behavior of the cancer cells. It is possible that coherent aggregates of cells, rather than individual cells, detach. For this investigation, an RPM microscope would have to be available, which is currently not the case. Furthermore, this alone does not answer the question of why RPM-induced spheroid formation of healthy Nthy-ori 3-1 cells is not inhibited by DEX, where the amount of ECM proteins and cell junctions is as high or higher than in FTC-133 cells.

4.3. Spheroids from Healthy Cells on the RPM—A Question of Anti-Adhesion?

Cell surface-associated mucins such as mucin-1 are involved in the protection of epithelial surfaces from mechanical stress [80]. This protection program seems to be activated in adherent Nthy-ori 3-1 and ML-1 cells on the RPM, but not in FTC-133 and WRO cells. Because mucin-1 was upregulated in Nthy-ori 3-1 cells only in the RPM samples (not by DEX alone), a hypoxia-induced effect, which has been described in other epithelial cells for other mucins [81], can be excluded here. One possibility could be RPM-induced expression of *MUC1* via STAT3, as recently described in chondrocytes [82]. Due to steric hindrance of mucin-1 and adhesion proteins, overexpressed mucin-1 has an anti-adhesion effect on cells [83]. Intracellularly, it leads to loss of cell–cell contact and induces anchorage-independent growth including resistance to anoikis [84,85]. Both effects could favor the detachment of Nthy-ori 3-1 cells during random positioning, which show much stronger adhesion than metastatic FTC-133 cells under normal culture conditions (Figure 3D). They could even allow the formation of spheroids from cells that would otherwise not detach during random positioning, or undergo anoikis after detachment. Indeed, the absence of such an unexpected mucin-1 increase may explain why not all benign or primary human cells readily form 3D structures on the RPM. Spheroid formation on the RPM is more frequently observed in tumor cells, which tend to spread or migrate and generally have higher mucin expression [86]. One of the best-known example pairs studied so far on the RPM is probably MCF-7 mammary tumor cells and MCF-10A mammary epithelial cells. Monti et al. [86] showed that only MCF-7 cells formed spheroids on the RPM after 72 h. In addition, we found by immunofluorescence analysis that MCF-10A cells expressed very little mucin-1 protein (Figure S2B). Triple-negative MDA-MB-231 cells, which also have very low levels of mucin-1 [87], tend to adhere to culture flasks on the RPM rather than detach (unpublished data). It is also known that *MUC1* gene expression in prostate cancer cells is inhibited by the androgen receptor (AR) [88]. In some of our preliminary experiments, AR-positive LnCAP cells detached less from the growth surface after administration of dihydrotestosterone. Mucin-1 immunofluorescence staining confirmed a decrease in protein amount in the presence of dihydrotestosterone (Figure S2C). In addition, RPM-induced spheroid formation was observed to be absent in some primary endothelial cells. While human umbilical vein endothelial cells (HUVECs) are able to form 3D aggregates, this does not work for human saphenous vein endothelial cells (HSVECs) under RPM conditions [89]. At least for HUVECs, it was demonstrated that mucin-1 is expressed and can be released from the cell membrane [90]. However, we could not find any information about mucin-1 in HSVECs so far.

In this study, we attempted to target mucin-1 pharmaceutically. Although GO-203 is primarily an inhibitor of MUC1-C and thus blocks its intracellular signaling, an auto-inductive effect that has been described for mucin-1 [91] could explain the reduction of (surface) mucin-1 observed after supplementation of GO-203 (Figure 6G).

In summary, it seems important to note that not only adhesion proteins play a role in RPM-induced spheroid formation, but also anti-adhesion proteins.

5. Conclusions

For gravitational biologists, the RPM offers a good platform to study tumor progression or metastasis in vitro and to uncover special targets for cancer therapy [19–21,68]. In this study, we could show that RPM-grown thyroid cancer cells behave differently than corresponding benign epithelial cells when treated with DEX. Comparative analyses showed that the cell detachment process (which is often referred to as 'in vitro metastasis') during random positioning is selectively suppressed by DEX in metastatic cancer cells; on the one hand, due to massive formation of TJs in these cells, and, on the other hand, due to the upregulation of anti-adhesive mucin-1 in their non-metastasis-derived relatives by the RPM. The overall picture of an initially hypothesized anti-metastasis effect of DEX in vitro emerged from an interplay of different effects of the cells, all of which responded differently to RPM cell culture. The balance between adhesion and anti-adhesion appears to allow detachment of adherent human cells on an RPM. This depends on the origin of the cells, their development, and their consequent susceptibility to stress. Therefore, it will continue to be very important to study exactly how human cells behave in rotating bioreactors in order to derive the maximum benefit from these model systems for translational medicine.

Supplementary Materials: The following supporting information can be downloaded at: https://www.mdpi.com/article/10.3390/cancers15061641/s1, Figure S1: Effect of DEX (1000 nM) and random positioning on tight junction proteins after 3 days; Figure S2: Mucin-1 expression in relation to cell adhesion of different cell lines in RPM experiments; Figure S3: Oxygen saturation and hypoxia-induced expression of *HIF1A* in completely filled cell culture flasks; Table S1: Antibodies used for immunofluorescence and Western blot analyses; Table S2: Primer sequences for quantitative real-time PCR. File S1: Full-size Western blots.

Author Contributions: Conceptualization, D.M. and M.K.; methodology, D.M., V.S., J.L.C.-S. and M.K.; software, J.L.C.-S., D.M. and S.K. (Stefan Kahlert); validation, D.M., S.K. (Sascha Kopp) and M.K.; formal analysis, D.M. and J.L.C.-S.; investigation, D.M., V.S. and J.L.C.-S.; resources, D.G.; data curation, D.M. and M.K.; writing—original draft preparation, D.M. and M.K.; writing—review and editing, M.K. and D.G.; visualization, D.M., J.L.C.-S. and M.K.; supervision, M.K.; funding acquisition, D.G. All authors have read and agreed to the published version of the manuscript.

Funding: This research was funded by the German Space Agency at DLR (Deutsches Zentrum für Luft- und Raumfahrt) under grant numbers 50WB1924 and 50WB2219. J.L.C.-S. received financial support from the CONACyT-DAAD scholarship.

Institutional Review Board Statement: Not applicable.

Informed Consent Statement: Not applicable.

Data Availability Statement: The data presented in this study are available in the electronic Supplementary Material. The complete raw data are available on request.

Acknowledgments: We would like to thank Jenny Graf for further insights into mucin-1 expression in additional cell lines.

Conflicts of Interest: The authors declare no conflict of interest. The funders had no role in the design of the study; in the collection, analyses, or interpretation of data; in the writing of the manuscript, or in the decision to publish the results.

References

1. Steeg, P.S. Targeting metastasis. *Nat. Rev. Cancer* **2016**, *16*, 201–218. [CrossRef] [PubMed]
2. Hapach, L.A.; Mosier, J.A.; Wang, W.; Reinhart-King, C.A. Engineered models to parse apart the metastatic cascade. *NPJ Precis. Oncol.* **2019**, *3*, 20. [CrossRef]
3. Lara, O.D.; Wang, Y.; Asare, A.; Xu, T.; Chiu, H.-S.; Liu, Y.; Hu, W.; Sumazin, P.; Uppal, S.; Zhang, L.; et al. Pan-cancer clinical and molecular analysis of racial disparities. *Cancer* **2020**, *126*, 800–807. [CrossRef]
4. Galle, E.; Thienpont, B.; Cappuyns, S.; Venken, T.; Busschaert, P.; Van Haele, M.; Van Cutsem, E.; Roskams, T.; van Pelt, J.; Verslype, C.; et al. DNA methylation-driven EMT is a common mechanism of resistance to various therapeutic agents in cancer. *Clin. Epigenet.* **2020**, *12*, 27. [CrossRef]
5. Wirtz, D.; Konstantopoulos, K.; Searson, P.C. The physics of cancer: The role of physical interactions and mechanical forces in metastasis. *Nat. Rev. Cancer* **2011**, *11*, 512–522. [CrossRef]
6. Northcott, J.M.; Dean, I.S.; Mouw, J.K.; Weaver, V.M. Feeling Stress: The Mechanics of Cancer Progression and Aggression. *Front. Cell Dev. Biol.* **2018**, *6*, 17. [CrossRef]
7. Kumar, S.; Weaver, V.M. Mechanics, malignancy, and metastasis: The force journey of a tumor cell. *Cancer Metastasis Rev.* **2009**, *28*, 113–127. [CrossRef] [PubMed]
8. Kalluri, R.; Weinberg, R.A. The basics of epithelial-mesenchymal transition. *J. Clin. Investig.* **2009**, *119*, 1420–1428. [CrossRef]
9. Guck, J.; Schinkinger, S.; Lincoln, B.; Wottawah, F.; Ebert, S.; Romeyke, M.; Lenz, D.; Erickson, H.M.; Ananthakrishnan, R.; Mitchell, D.; et al. Optical deformability as an inherent cell marker for testing malignant transformation and metastatic competence. *Biophys. J.* **2005**, *88*, 3689–3698. [CrossRef] [PubMed]
10. Yan, Z.; Xia, X.; Cho, W.C.; Au, D.W.; Shao, X.; Fang, C.; Tian, Y.; Lin, Y. Rapid Plastic Deformation of Cancer Cells Correlates with High Metastatic Potential. *Adv. Healthc. Mater.* **2022**, *11*, 2101657. [CrossRef]
11. Baker, E.L.; Lu, J.; Yu, D.; Bonnecaze, R.T.; Zaman, M.H. Cancer Cell Stiffness: Integrated Roles of Three-Dimensional Matrix Stiffness and Transforming Potential. *Biophys. J.* **2010**, *99*, 2048–2057. [CrossRef] [PubMed]
12. Wullkopf, L.; West, A.-K.V.; Leijnse, N.; Cox, T.R.; Madsen, C.D.; Oddershede, L.B.; Erler, J.T. Cancer cells' ability to mechanically adjust to extracellular matrix stiffness correlates with their invasive potential. *Mol. Biol. Cell* **2018**, *29*, 2378–2385. [CrossRef]
13. Gensbittel, V.; Kräter, M.; Harlepp, S.; Busnelli, I.; Guck, J.; Goetz, J.G. Mechanical Adaptability of Tumor Cells in Metastasis. *Dev. Cell* **2021**, *56*, 164–179. [CrossRef] [PubMed]
14. Borst, A.G.; van Loon, J.J.W.A. Technology and Developments for the Random Positioning Machine, RPM. *Microgravity Sci. Technol.* **2008**, *21*, 287. [CrossRef]
15. van Loon, J.J.W.A. Some history and use of the random positioning machine, RPM, in gravity related research. *Adv. Space Res.* **2007**, *39*, 1161–1165. [CrossRef]
16. Hauslage, J.; Cevik, V.; Hemmersbach, R. Pyrocystis noctiluca represents an excellent bioassay for shear forces induced in ground-based microgravity simulators (clinostat and random positioning machine). *NPJ Microgravity* **2017**, *3*, 12. [CrossRef] [PubMed]
17. Leguy, C.A.D.; Delfos, R.; Pourquie, M.J.B.M.; Poelma, C.; Westerweel, J.; van Loon, J.J.W.A. Fluid dynamics during Random Positioning Machine micro-gravity experiments. *Adv. Space Res.* **2017**, *59*, 3045–3057. [CrossRef]
18. Wuest, S.L.; Stern, P.; Casartelli, E.; Egli, M. Fluid Dynamics Appearing during Simulated Microgravity Using Random Positioning Machines. *PLoS ONE* **2017**, *12*, e0170826. [CrossRef]
19. Cortés-Sánchez, J.L.; Callant, J.; Krüger, M.; Sahana, J.; Kraus, A.; Baselet, B.; Infanger, M.; Baatout, S.; Grimm, D. Cancer Studies under Space Conditions: Finding Answers Abroad. *Biomedicines* **2021**, *10*, 25. [CrossRef]
20. Krüger, M.; Melnik, D.; Kopp, S.; Buken, C.; Sahana, J.; Bauer, J.; Wehland, M.; Hemmersbach, R.; Corydon, T.J.; Infanger, M.; et al. Fighting Thyroid Cancer with Microgravity Research. *Int. J. Mol. Sci.* **2019**, *20*, 2553. [CrossRef]
21. Grimm, D.; Schulz, H.; Krüger, M.; Cortés-Sánchez, J.L.; Egli, M.; Kraus, A.; Sahana, J.; Corydon, T.J.; Hemmersbach, R.; Wise, P.M.; et al. The Fight against Cancer by Microgravity: The Multicellular Spheroid as a Metastasis Model. *Int. J. Mol. Sci.* **2022**, *23*, 3073. [CrossRef]
22. Riehl, B.D.; Kim, E.; Lee, J.S.; Duan, B.; Yang, R.; Donahue, H.J.; Lim, J.Y. The Role of Fluid Shear and Metastatic Potential in Breast Cancer Cell Migration. *J. Biomech. Eng.* **2020**, *142*, 101001. [CrossRef] [PubMed]
23. Qazi, H.; Palomino, R.; Shi, Z.D.; Munn, L.L.; Tarbell, J.M. Cancer cell glycocalyx mediates mechanotransduction and flow-regulated invasion. *Integr. Biol.* **2013**, *5*, 1334–1343. [CrossRef] [PubMed]
24. Rizvi, I.; Gurkan, U.A.; Tasoglu, S.; Alagic, N.; Celli, J.P.; Mensah, L.B.; Mai, Z.; Demirci, U.; Hasan, T. Flow induces epithelial-mesenchymal transition, cellular heterogeneity and biomarker modulation in 3D ovarian cancer nodules. *Proc. Natl. Acad. Sci. USA* **2013**, *110*, E1974–E1983. [CrossRef] [PubMed]
25. Liu, S.; Zhou, F.; Shen, Y.; Zhang, Y.; Yin, H.; Zeng, Y.; Liu, J.; Yan, Z.; Liu, X. Fluid shear stress induces epithelial-mesenchymal transition (EMT) in Hep-2 cells. *Oncotarget* **2016**, *7*, 32876–32892. [CrossRef] [PubMed]
26. Choi, H.Y.; Yang, G.M.; Dayem, A.A.; Saha, S.K.; Kim, K.; Yoo, Y.; Hong, K.; Kim, J.H.; Yee, C.; Lee, K.M.; et al. Hydrodynamic shear stress promotes epithelial-mesenchymal transition by downregulating ERK and GSK3β activities. *Breast Cancer Res.* **2019**, *21*, 6. [CrossRef]
27. Ahn, C.B.; Lee, J.-H.; Han, D.G.; Kang, H.-W.; Lee, S.-H.; Lee, J.-I.; Son, K.H.; Lee, J.W. Simulated microgravity with floating environment promotes migration of non-small cell lung cancers. *Sci. Rep.* **2019**, *9*, 14553. [CrossRef]

28. Wehland, M.; Steinwerth, P.; Aleshcheva, G.; Sahana, J.; Hemmersbach, R.; Lützenberg, R.; Kopp, S.; Infanger, M.; Grimm, D. Tissue Engineering of Cartilage Using a Random Positioning Machine. *Int. J. Mol. Sci.* **2020**, *21*, 9596. [CrossRef]
29. Grimm, D.; Infanger, M.; Westphal, K.; Ulbrich, C.; Pietsch, J.; Kossmehl, P.; Vadrucci, S.; Baatout, S.; Flick, B.; Paul, M.; et al. A Delayed Type of Three-Dimensional Growth of Human Endothelial Cells Under Simulated Weightlessness. *Tissue Eng. Part A* **2009**, *15*, 2267–2275. [CrossRef]
30. Buken, C.; Sahana, J.; Corydon, T.J.; Melnik, D.; Bauer, J.; Wehland, M.; Krüger, M.; Balk, S.; Abuagela, N.; Infanger, M.; et al. Morphological and Molecular Changes in Juvenile Normal Human Fibroblasts Exposed to Simulated Microgravity. *Sci. Rep.* **2019**, *9*, 11882. [CrossRef]
31. Melnik, D.; Sahana, J.; Corydon, T.J.; Kopp, S.; Nassef, M.Z.; Wehland, M.; Infanger, M.; Grimm, D.; Krüger, M. Dexamethasone Inhibits Spheroid Formation of Thyroid Cancer Cells Exposed to Simulated Microgravity. *Cells* **2020**, *9*, 367. [CrossRef] [PubMed]
32. Schönberger, J.; Bauer, J.; Spruss, T.; Weber, G.; Chahoud, I.; Eilles, C.; Grimm, D. Establishment and characterization of the follicular thyroid carcinoma cell line ML-1. *J. Mol. Med.* **2000**, *78*, 102–110. [CrossRef] [PubMed]
33. Benavides Damm, T.; Walther, I.; Wüest, S.L.; Sekler, J.; Egli, M. Cell cultivation under different gravitational loads using a novel random positioning incubator. *Biotechnol. Bioeng.* **2014**, *111*, 1180–1190. [CrossRef]
34. Shihan, M.H.; Novo, S.G.; Le Marchand, S.J.; Wang, Y.; Duncan, M.K. A simple method for quantitating confocal fluorescent images. *Biochem. Biophys. Rep.* **2021**, *25*, 100916. [CrossRef] [PubMed]
35. Gottardi, C.J.; Arpin, M.; Fanning, A.S.; Louvard, D. The junction-associated protein, zonula occludens-1, localizes to the nucleus before the maturation and during the remodeling of cell-cell contacts. *Proc. Natl. Acad. Sci. USA* **1996**, *93*, 10779–10784. [CrossRef]
36. Wesseling, J.; van der Valk, S.W.; Hilkens, J. A mechanism for inhibition of E-cadherin-mediated cell-cell adhesion by the membrane-associated mucin episialin/MUC1. *Mol. Biol. Cell* **1996**, *7*, 565–577. [CrossRef]
37. Wesseling, J.; van der Valk, S.W.; Vos, H.L.; Sonnenberg, A.; Hilkens, J. Episialin (MUC1) overexpression inhibits integrin-mediated cell adhesion to extracellular matrix components. *J. Cell Biol.* **1995**, *129*, 255–265. [CrossRef]
38. Nath, S.; Mukherjee, P. MUC1: A multifaceted oncoprotein with a key role in cancer progression. *Trends Mol. Med.* **2014**, *20*, 332–342. [CrossRef]
39. Scheschowitsch, K.; Leite, J.; Assreuy, J. New insights in glucocorticoid receptor signaling—More than just a ligand binding receptor. *Front. Endocrinol.* **2017**, *8*, 16. [CrossRef]
40. Vanderhaeghen, T.; Timmermans, S.; Watts, D.; Paakinaho, V.; Eggermont, M.; Vandewalle, J.; Wallaeys, C.; Van Wyngene, L.; Van Looveren, K.; Nuyttens, L.; et al. Reprogramming of glucocorticoid receptor function by hypoxia. *EMBO Rep.* **2022**, *23*, e53083. [CrossRef]
41. Vanderhaeghen, T.; Beyaert, R.; Libert, C. Bidirectional Crosstalk Between Hypoxia Inducible Factors and Glucocorticoid Signalling in Health and Disease. *Front. Immunol.* **2021**, *12*, 684085. [CrossRef]
42. Yang, N.; Berry, A.; Sauer, C.; Baxter, M.; Donaldson, I.J.; Forbes, K.; Donn, R.; Matthews, L.; Ray, D. Hypoxia regulates GR function through multiple mechanisms involving microRNAs 103 and 107. *Mol. Cell. Endocrinol.* **2020**, *518*, 111007. [CrossRef] [PubMed]
43. Lea, S.; Li, J.; Plumb, J.; Gaffey, K.; Mason, S.; Gaskell, R.; Harbron, C.; Singh, D. P38 MAPK and glucocorticoid receptor crosstalk in bronchial epithelial cells. *J. Mol. Med.* **2020**, *98*, 361–374. [CrossRef]
44. Szatmáry, Z.; Garabedian, M.J.; Vilček, J. Inhibition of Glucocorticoid Receptor-mediated Transcriptional Activation by p38 Mitogen-activated Protein (MAP) Kinase. *J. Biol. Chem.* **2004**, *279*, 43708–43715. [CrossRef]
45. Irusen, E.; Matthews, J.G.; Takahashi, A.; Barnes, P.J.; Chung, K.F.; Adcock, I.M. p38 Mitogen-activated protein kinase–induced glucocorticoid receptor phosphorylation reduces its activity: Role in steroid-insensitive asthma. *J. Allergy Clin. Immunol.* **2002**, *109*, 649–657. [CrossRef]
46. Hoffman, L.; Jensen, C.C.; Yoshigi, M.; Beckerle, M. Mechanical signals activate p38 MAPK pathway-dependent reinforcement of actin via mechanosensitive HspB1. *Mol. Biol. Cell* **2017**, *28*, 2661–2675. [CrossRef]
47. Wu, Y.; Xia, R.; Dai, C.; Yan, S.; Xie, T.; Liu, B.; Gan, L.; Zhuang, Z.; Huang, Q. Dexamethasone inhibits the proliferation of tumor cells. *Cancer Manag. Res.* **2019**, *11*, 1141–1154. [CrossRef] [PubMed]
48. Mohammadi, L.; Mosayyebi, B.; Imani, M.; Rahmati, M. Dexamethasone Reduces Cell Adhesion and Migration of T47D Breast Cancer Cell Line. *Anticancer Agents Med. Chem.* **2022**, *22*, 2494–2501. [CrossRef] [PubMed]
49. Meng, X.G.; Yue, S.W. Dexamethasone disrupts cytoskeleton organization and migration of T47D Human breast cancer cells by modulating the AKT/mTOR/RhoA pathway. *Asian Pac. J. Cancer Prev.* **2014**, *15*, 10245–10250. [CrossRef] [PubMed]
50. Lin, K.-T.; Sun, S.-P.; Wu, J.-I.; Wang, L.-H. Low-dose glucocorticoids suppresses ovarian tumor growth and metastasis in an immunocompetent syngeneic mouse model. *PLoS ONE* **2017**, *12*, e0178937. [CrossRef]
51. Lin, K.-T.; Yeh, Y.-M.; Chuang, C.-M.; Yang, S.Y.; Chang, J.-W.; Sun, S.-P.; Wang, Y.-S.; Chao, K.-C.; Wang, L.-H. Glucocorticoids mediate induction of microRNA-708 to suppress ovarian cancer metastasis through targeting Rap1B. *Nat. Commun.* **2015**, *6*, 5917. [CrossRef]
52. Zheng, Y.; Izumi, K.; Li, Y.; Ishiguro, H.; Miyamoto, H. Contrary Regulation of Bladder Cancer Cell Proliferation and Invasion by Dexamethasone-Mediated Glucocorticoid Receptor Signals. *Mol. Cancer Ther.* **2012**, *11*, 2621–2632. [CrossRef]
53. Yip, H.Y.K.; Chee, A.; Ang, C.-S.; Shin, S.-Y.; Ooms, L.M.; Mohammadi, Z.; Phillips, W.A.; Daly, R.J.; Cole, T.J.; Bronson, R.T.; et al. Control of Glucocorticoid Receptor Levels by PTEN Establishes a Failsafe Mechanism for Tumor Suppression. *Mol. Cell* **2020**, *80*, 279–295.e8. [CrossRef] [PubMed]

54. Ji, J.Y.; Jing, H.; Diamond, S.L. Shear Stress Causes Nuclear Localization of Endothelial Glucocorticoid Receptor and Expression From the GRE Promoter. *Circ. Res.* **2003**, *92*, 279–285. [CrossRef] [PubMed]
55. Nayebosadri, A.; Christopher, L.; Ji, J.Y. Bayesian Image Analysis of Dexamethasone and Shear Stress-Induced Glucocorticoid Receptor Intracellular Movement. *Ann. Biomed. Eng.* **2012**, *40*, 1508–1519. [CrossRef] [PubMed]
56. Whitmarsh, A.J. A central role for p38 MAPK in the early transcriptional response to stress. *BMC Biology* **2010**, *8*, 47. [CrossRef] [PubMed]
57. Kopp, S.; Warnke, E.; Wehland, M.; Aleshcheva, G.; Magnusson, N.E.; Hemmersbach, R.; Corydon, T.J.; Bauer, J.; Infanger, M.; Grimm, D. Mechanisms of three-dimensional growth of thyroid cells during long-term simulated microgravity. *Sci. Rep.* **2015**, *5*, 16691. [CrossRef]
58. Warnke, E.; Pietsch, J.; Kopp, S.; Bauer, J.; Sahana, J.; Wehland, M.; Krüger, M.; Hemmersbach, R.; Infanger, M.; Lützenberg, R.; et al. Cytokine Release and Focal Adhesion Proteins in Normal Thyroid Cells Cultured on the Random Positioning Machine. *Cell. Physiol. Biochem.* **2017**, *43*, 257–270. [CrossRef]
59. Warnke, E.; Pietsch, J.; Wehland, M.; Bauer, J.; Infanger, M.; Görög, M.; Hemmersbach, R.; Braun, M.; Ma, X.; Sahana, J.; et al. Spheroid formation of human thyroid cancer cells under simulated microgravity: A possible role of CTGF and CAV1. *Cell Commun. Signal.* **2014**, *12*, 32. [CrossRef]
60. Svejgaard, B.; Wehland, M.; Ma, X.; Kopp, S.; Sahana, J.; Warnke, E.; Aleshcheva, G.; Hemmersbach, R.; Hauslage, J.; Grosse, J.; et al. Common Effects on Cancer Cells Exerted by a Random Positioning Machine and a 2D Clinostat. *PLoS ONE* **2015**, *10*, e0135157. [CrossRef]
61. Grosse, J.; Wehland, M.; Pietsch, J.; Schulz, H.; Saar, K.; Hübner, N.; Elles, C.; Bauer, J.; Abou-El-Ardat, K.; Baatout, S.; et al. Gravity-sensitive signaling drives 3-dimensional formation of multicellular thyroid cancer spheroids. *FASEB J.* **2012**, *26*, 5124–5140. [CrossRef]
62. Grimm, D.; Bauer, J.; Kossmehl, P.; Shakibaei, M.; Schöberger, J.; Pickenhahn, H.; Schulze-Tanzil, G.; Vetter, R.; Eilles, C.; Paul, M.; et al. Simulated microgravity alters differentiation and increases apoptosis in human follicular thyroid carcinoma cells. *FASEB J.* **2002**, *16*, 604–606. [CrossRef]
63. Kopp, S.; Sahana, J.; Islam, T.; Petersen, A.G.; Bauer, J.; Corydon, T.J.; Schulz, H.; Saar, K.; Huebner, N.; Slumstrup, L.; et al. The role of NFκB in spheroid formation of human breast cancer cells cultured on the Random Positioning Machine. *Sci. Rep.* **2018**, *8*, 921. [CrossRef]
64. Sahana, J.; Nassef, M.Z.; Wehland, M.; Kopp, S.; Krüger, M.; Corydon, T.J.; Infanger, M.; Bauer, J.; Grimm, D. Decreased E-Cadherin in MCF7 Human Breast Cancer Cells Forming Multicellular Spheroids Exposed to Simulated Microgravity. *Proteomics* **2018**, *18*, 1800015. [CrossRef]
65. Lin, K.T.; Wang, L.H. New dimension of glucocorticoids in cancer treatment. *Steroids* **2016**, *111*, 84–88. [CrossRef]
66. Calvaruso, M.; Militello, C.; Minafra, L.; La Regina, V.; Torrisi, F.; Pucci, G.; Cammarata, F.P.; Bravatà, V.; Forte, G.I.; Russo, G. Biological and Mechanical Characterization of the Random Positioning Machine (RPM) for Microgravity Simulations. *Life* **2021**, *11*, 1190. [CrossRef]
67. Wuest, S.L.; Richard, S.; Kopp, S.; Grimm, D.; Egli, M. Simulated microgravity: Critical review on the use of random positioning machines for mammalian cell culture. *Biomed. Res. Int.* **2015**, *2015*, 971474. [CrossRef] [PubMed]
68. Nassef, M.Z.; Melnik, D.; Kopp, S.; Sahana, J.; Infanger, M.; Lützenberg, R.; Relja, B.; Wehland, M.; Grimm, D.; Krüger, M. Breast Cancer Cells in Microgravity: New Aspects for Cancer Research. *Int. J. Mol. Sci.* **2020**, *21*, 7345. [CrossRef] [PubMed]
69. Zettl, K.S.; Sjaastad, M.D.; Riskin, P.M.; Parry, G.; Machen, T.E.; Firestone, G.L. Glucocorticoid-induced formation of tight junctions in mouse mammary epithelial cells in vitro. *Proc. Natl. Acad. Sci. USA* **1992**, *89*, 9069–9073. [CrossRef] [PubMed]
70. Woo, P.L.; Cercek, A.; Desprez, P.Y.; Firestone, G.L. Involvement of the helix-loop-helix protein Id-1 in the glucocorticoid regulation of tight junctions in mammary epithelial cells. *J. Biol. Chem.* **2000**, *275*, 28649–28658. [CrossRef]
71. Tena-Garitaonaindia, M.; Arredondo-Amador, M.; Mascaraque, C.; Asensio, M.; Marin, J.J.G.; Martínez-Augustin, O.; Sánchez de Medina, F. Modulation of intestinal barrier function by glucocorticoids: Lessons from preclinical models. *Pharmacol. Res.* **2022**, *177*, 106056. [CrossRef]
72. Adamian, M.; Hekmat, A.; Hajebrahimi, Z. The Impacts of Simulated Microgravity on The Cell Viability and Claudin-1 and Claudin-3 Expression of MCF-7 Breast Cancer Cells. *J. Sci. Islam. Repub. Iran* **2021**, *32*, 105–114. [CrossRef]
73. Martin, T.A. The role of tight junctions in cancer metastasis. *Semin. Cell Dev. Biol.* **2014**, *36*, 224–231. [CrossRef] [PubMed]
74. Salvador, E.; Burek, M.; Förster, C.Y. Tight Junctions and the Tumor Microenvironment. *Curr. Pathobiol. Rep.* **2016**, *4*, 135–145. [CrossRef] [PubMed]
75. Tzelepi, V.N.; Tsamandas, A.C.; Vlotinou, H.D.; Vagianos, C.E.; Scopa, C.D. Tight junctions in thyroid carcinogenesis: Diverse expression of claudin-1, claudin-4, claudin-7 and occludin in thyroid neoplasms. *Mod. Pathol.* **2008**, *21*, 22–30. [CrossRef] [PubMed]
76. Zwanziger, D.; Badziong, J.; Ting, S.; Moeller, L.C.; Schmid, K.W.; Siebolts, U.; Wickenhauser, C.; Dralle, H.; Fuehrer, D. The impact of CLAUDIN-1 on follicular thyroid carcinoma aggressiveness. *Endocr.-Relat. Cancer* **2015**, *22*, 819–830. [CrossRef] [PubMed]
77. Na, T.-Y.; Schecterson, L.; Mendonsa, A.M.; Gumbiner, B.M. The functional activity of E-cadherin controls tumor cell metastasis at multiple steps. *Proc. Natl. Acad. Sci. USA* **2020**, *117*, 5931–5937. [CrossRef]
78. Zhou, C.; Yang, C.; Chong, D. E-cadherin expression is associated with susceptibility and clinicopathological characteristics of thyroid cancer: A PRISMA-compliant meta-analysis. *Medicine* **2019**, *98*, e16187. [CrossRef]

79. Huang, S.H.; Wu, J.C.; Chang, K.J.; Liaw, K.Y.; Wang, S.M. Distribution of the cadherin-catenin complex in normal human thyroid epithelium and a thyroid carcinoma cell line. *J. Cell. Biochem.* **1998**, *70*, 330–337. [CrossRef]
80. Singh, P.K.; Hollingsworth, M.A. Cell surface-associated mucins in signal transduction. *Trends Cell Biol.* **2006**, *16*, 467–476. [CrossRef] [PubMed]
81. Zhou, X.; Tu, J.; Li, Q.; Kolosov, V.P.; Perelman, J.M. Hypoxia induces mucin expression and secretion in human bronchial epithelial cells. *Transl. Res.* **2012**, *160*, 419–427. [CrossRef]
82. Nakamura, Y.; Saitou, M.; Komura, S.; Matsumoto, K.; Ogawa, H.; Miyagawa, T.; Saitou, T.; Imamura, T.; Imai, Y.; Takayanagi, H.; et al. Reduced dynamic loads due to hip dislocation induce acetabular cartilage degeneration by IL-6 and MMP3 via the STAT3/periostin/NF-κB axis. *Sci. Rep.* **2022**, *12*, 12207. [CrossRef]
83. van Putten, J.P.M.; Strijbis, K. Transmembrane Mucins: Signaling Receptors at the Intersection of Inflammation and Cancer. *J Innate Immun.* **2017**, *9*, 281–299. [CrossRef]
84. Hollingsworth, M.A.; Swanson, B.J. Mucins in cancer: Protection and control of the cell surface. *Nat. Rev. Cancer* **2004**, *4*, 45–60. [CrossRef] [PubMed]
85. Wi, D.H.; Cha, J.H.; Jung, Y.S. Mucin in cancer: A stealth cloak for cancer cells. *BMB Rep.* **2021**, *54*, 344–355. [CrossRef] [PubMed]
86. Monti, N.; Masiello, M.G.; Proietti, S.; Catizone, A.; Ricci, G.; Harrath, A.H.; Alwasel, S.H.; Cucina, A.; Bizzarri, M. Survival Pathways Are Differently Affected by Microgravity in Normal and Cancerous Breast Cells. *Int. J. Mol. Sci.* **2021**, *22*, 862. [CrossRef] [PubMed]
87. Wu, G.; Kim, D.; Kim, J.N.; Park, S.; Maharjan, S.; Koh, H.; Moon, K.; Lee, Y.; Kwon, H.J. A Mucin1 C-terminal Subunit-directed Monoclonal Antibody Targets Overexpressed Mucin1 in Breast Cancer. *Theranostics* **2018**, *8*, 78–91. [CrossRef]
88. Rajabi, H.; Joshi, M.D.; Jin, C.; Ahmad, R.; Kufe, D. Androgen receptor regulates expression of the MUC1-C oncoprotein in human prostate cancer cells. *Prostate* **2011**, *71*, 1299–1308. [CrossRef]
89. Krüger, M.; Kopp, S.; Wehland, M.; Bauer, J.; Baatout, S.; Moreels, M.; Egli, M.; Corydon, T.J.; Infanger, M.; Grimm, D. Growing blood vessels in space: Preparation studies of the SPHEROIDS project using related ground-based studies. *Acta Astronaut.* **2019**, *159*, 267–272. [CrossRef]
90. Porowska, H.; Paszkiewicz-Gadek, A.; Wosek, J.; Wnuczko, K.; Rusak, M.; Szczepański, M. Expression of MUC1 mucin in human umbilical vein endothelial cells (HUVEC). *Folia Histochem. Cytobiol.* **2010**, *48*, 417–424. [CrossRef]
91. Kufe, D.W. MUC1-C oncoprotein as a target in breast cancer: Activation of signaling pathways and therapeutic approaches. *Oncogene* **2013**, *32*, 1073–1081. [CrossRef] [PubMed]

Disclaimer/Publisher's Note: The statements, opinions and data contained in all publications are solely those of the individual author(s) and contributor(s) and not of MDPI and/or the editor(s). MDPI and/or the editor(s) disclaim responsibility for any injury to people or property resulting from any ideas, methods, instructions or products referred to in the content.

cells

MDPI

Article

Dexamethasone Inhibits Spheroid Formation of Thyroid Cancer Cells Exposed to Simulated Microgravity

Daniela Melnik [1], Jayashree Sahana [2], Thomas J. Corydon [2,3], Sascha Kopp [1,4], Mohamed Zakaria Nassef [1], Markus Wehland [1,4], Manfred Infanger [1,4], Daniela Grimm [2,4,5] and Marcus Krüger [1,4,*]

1 Clinic for Plastic, Aesthetic and Hand Surgery, Otto von Guericke University, Leipziger Str. 44, 39120 Magdeburg, Germany; daniela.melnik@med.ovgu.de (D.M.); sascha.kopp@med.ovgu.de (S.K.); mohamed.nassef@med.ovgu.de (M.Z.N.); markus.wehland@med.ovgu.de (M.W.); manfred.infanger@med.ovgu.de (M.I.)
2 Department of Biomedicine, Aarhus University, Hoegh-Guldbergsgade 10, 8000 Aarhus C, Denmark; jaysaha@biomed.au.dk (J.S.); corydon@biomed.au.dk (T.J.C.); dgg@biomed.au.dk (D.G.)
3 Department of Ophthalmology, Aarhus University Hospital, Palle Juul-Jensens Boulevard 99, 8200 Aarhus N, Denmark
4 Research Group "Magdeburger Arbeitsgemeinschaft für Forschung unter Raumfahrt- und Schwerelosigkeitsbedingungen" (MARS), Otto von Guericke University, Universitätsplatz 2, 39106 Magdeburg, Germany
5 Department of Microgravity and Translational Regenerative Medicine, Otto von Guericke University, Pfälzer Platz, 39106 Magdeburg, Germany
* Correspondence: marcus.krueger@med.ovgu.de; Tel.: +49-391-6721-267

Received: 9 December 2019; Accepted: 4 February 2020; Published: 5 February 2020



Abstract: Detachment and the formation of spheroids under microgravity conditions can be observed with various types of intrinsically adherent human cells. In particular, for cancer cells this process mimics metastasis and may provide insights into cancer biology and progression that can be used to identify new drug/target combinations for future therapies. By using the synthetic glucocorticoid dexamethasone (DEX), we were able to suppress spheroid formation in a culture of follicular thyroid cancer (FTC)-133 cells that were exposed to altered gravity conditions on a random positioning machine. DEX inhibited the growth of three-dimensional cell aggregates in a dose-dependent manner. In the first approach, we analyzed the expression of several factors that are known to be involved in key processes of cancer progression such as autocrine signaling, proliferation, epithelial–mesenchymal transition, and anoikis. Wnt/β-catenin signaling and expression patterns of important genes in cancer cell growth and survival, which were further suggested to play a role in three-dimensional aggregation, such as *NFKB2*, *VEGFA*, *CTGF*, *CAV1*, *BCL2*(*L1*), or *SNAI1*, were clearly affected by DEX. Our data suggest the presence of a more complex regulation network of tumor spheroid formation involving additional signal pathways or individual key players that are also influenced by DEX.

Keywords: glucocorticoids; 3D growth; nuclear factor kappa-light-chain-enhancer of activated B-cells (NF-κB); epithelial–mesenchymal transition; anoikis; proliferation

1. Introduction

Glucocorticoids (GCs) are a class of steroid hormones involved in many physiological processes such as metabolism, proliferation, differentiation, and survival of cells [1]. GCs induce their pharmacodynamic effects through binding to glucocorticoid receptors (GRs) [2], which interact downstream with signaling

molecules in the cytoplasm or are able to translocate into the nucleus, where they repress the activity of other transcription factors (such as nuclear factor kappa-light-chain-enhancer of activated B-cells, NF-κB, or activator protein 1, AP-1) or initiate transcription of genes associated with anti-inflammatory and immunosuppressive effects (via binding to specific glucocorticoid response elements, GREs) (Figure 1A) [3,4]. Due to these properties, GCs are utilized in the treatment of a variety of immunological disorder treatments to reduce pain and electrolyte imbalance, but also to enhance the anti-tumor effect of chemotherapeutics and prevent adverse effects caused by cytotoxic agents [5–7]. The synthetic GC dexamethasone (DEX; Figure 1B) is commonly administered as a supportive care co-medication to reduce cancer-related fatigue in patients with advanced disease [8]. DEX was further reported to inhibit proliferation of different cancer cells in vitro and in vivo [9–13]. Effective inhibition of tumor growth was suggested to be associated with downregulation of JAK3/STAT3, hypoxia inducible factor 1α, vascular endothelial growth factor (VEGF), and interleukin-6 [12,14,15]. Nevertheless, the exact mechanism by which DEX suppresses cancer cell growth is still unclear.

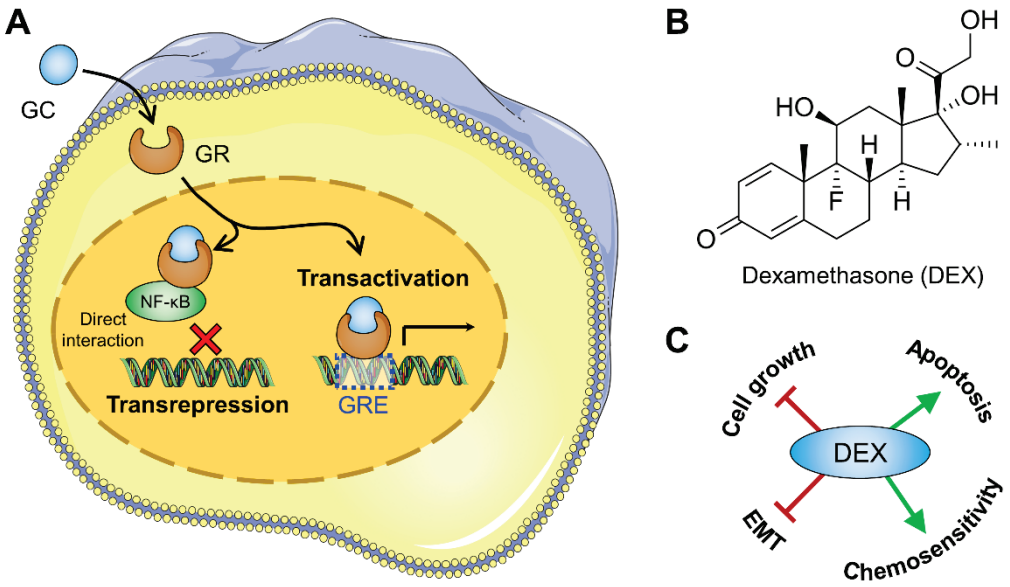


Figure 1. (**A**) Sketch showing the genomic actions of glucocorticoids (GCs) such as dexamethasone (DEX). When bound to DEX, the glucocorticoid receptor (GR) complex translocates into the nucleus and modifies the synthesis of several metabolic proteins. This is done either through directly binding to glucocorticoid response elements (GREs) on the DNA or through influencing the activity of transcription factors (i.e., nuclear factor kappa-light-chain-enhancer of activated B-cells, NF-κB); (**B**) Chemical structure of DEX; (**C**) Described effects of DEX on cancer cells. Parts of the figure are drawn using pictures from Servier Medical Art (https://smart.servier.com), licensed under a Creative Commons Attribution 3.0 Unported License (https://creativecommons.org/licenses/by/3.0).

Over the last 50 years, the incidence of thyroid cancer has increased worldwide and the incidence rate is still on the rise. The result of improved diagnostic procedures, an elevated prevalence of individual risk factors (e.g., obesity), and increased exposure to environmental risk factors (e.g., iodine levels), thyroid cancer is the most common form of endocrine malignancy today [16] and is expected to become the fourth leading type of cancer across the globe [17]. Especially poorly differentiated thyroid tumors are aggressive and tend to metastasize. The prognosis for differentiated thyroid cancer is related to the capability of tumor cells to accumulate radioiodine. Due to de-differentiation, some tumor cells may lose their iodine uptake capability, leaving only extremely limited treatment options, despite intensive searches for new drugs and targets. Therefore, novel approaches to control thyroid cancer progression are required.

Metastasis is the most limiting factor in cancer therapy and responsible for 90% of cancer-related deaths [18]. During the development of metastatic competence, carcinoma cells change their adhesive properties, secrete proteinases, and become motile, which allows them to detach from their primary tumor [19]. Therefore, tumor cells respond to mechanical signals, sensed by integrins or other adhesion receptors [20,21], and chemical signals, sensed by chemokines or growth factor receptors [22] causing changes in their transcriptional profile. The process which enables tumor cells to achieve migration and invasion is called epithelial–mesenchymal transition (EMT) and represents a driving force in tumorigenesis [23]. In the course of EMT, essential proteins for epithelial cell–cell adhesion, such as E-cadherin, are downregulated, thus weakening epithelial tissue integrity and polarization of epithelial cell layers [24]. Under normal circumstances, detached epithelial cells undergo apoptosis, a phenomenon termed anoikis. Cancer cells acquire resistance to anoikis to survive after they have left the primary tumor. In this way, they are able to travel via the circulatory and lymphatic systems disseminating throughout the body. EMT and anoikis resistance are critical steps of the metastatic cascade and potential targets to impact a natural molecular prerequisite for the aggressive metastatic spread of cancer [25,26].

Microgravity (μg) has become a powerful tool in cancer research by enabling metastasis-like cell detachment and formation of three-dimensional (3D) multicellular spheroids (MCS) [27–30]. Experiments in μg contribute to drug discovery by providing an environment which is helpful to detect changes in gene expression and protein synthesis and secretion that occur during the progression from 2D to 3D growth and which might represent new targets for drug development against thyroid cancer. A couple of these proteins were found in follicular thyroid cancer cells by analyzing multiple pilot studies, performed in μg, with the help of semantic methods [31,32]. Some of these potential drugs, including DEX, were recently reviewed [33]. In this study, we investigate the effects of DEX supplementation on the growth of follicular thyroid cancer (FTC) cells exposed to simulated μg produced by a random positioning machine (RPM).

2. Materials and Methods

2.1. Cell Culture

The human follicular thyroid carcinoma cell line FTC-133 was cultured in RPMI-1640 medium (Life Technologies, Carlsbad, CA, USA), supplemented with 10% fetal calf serum (FCS; Sigma-Aldrich, St. Louis, MO, USA), and 1% penicillin/streptomycin (Life Technologies) at 37 °C and 5% CO_2 until use for the experiment. For RPM experiments FTC-133 cells were seeded at a density of 1×10^6 cells per flask either in T25 cell culture flasks (Sarstedt, Nümbrecht, Germany) for mRNA and protein extraction or in slide flasks (Sarstedt) for immunofluorescence staining. Cells were given at least 24 h to attach to the bottom of the flasks.

2.2. Dexamethasone Treatment

Water-soluble DEX (dexamethasone–cyclodextrin complex) was purchased from Sigma-Aldrich. Then, 24 h after seeding, cells were synchronized in RPMI-1640 medium with 0.25% FCS and 1% penicillin/streptomycin for 4 h. Afterwards, the cells were cultured according to Section 2.1, supplemented with DEX concentrations of 10 nM, 100 nM, or 1000 nM [34].

2.3. Random Positioning Machine

The used desktop-RPM (Dutch Space, Leiden, Netherlands) was located in an incubator with 37 °C/5% CO_2 and operated in real random mode, with a constant angular velocity of 60°/s. Before the run, the flasks were filled up completely and air bubble-free with medium to avoid shear stress. The slide and culture flasks were installed on the prewarmed RPM. After 4 h (short-term experiments) or 3 days (long-term experiments), the cells were photographed and fixed with 4% paraformaldehyde (PFA; Carl Roth, Karlsruhe, Germany) for immunostaining. For RNA and protein extraction adherent cells were harvested by adding ice-cold phosphate-buffered saline (PBS; Life Technologies) and using

cell scrapers. The suspensions were centrifuged at 3000× *g* for 10 min at 4 °C followed by discarding the PBS and storage of cell pellets at −150 °C. MCS were collected by centrifuging supernatant at 3000× *g* for 10 min at 4 °C and subsequent storage at −150 °C. Corresponding static controls were prepared in parallel under the same conditions and stored next to the device in an incubator.

2.4. Phase Contrast Microscopy

Cells were observed and photographed using an Axiovert 25 Microscope (Carl Zeiss Microscopy, Jena, Germany) equipped with a Canon EOS 550D camera (Canon, Tokio, Japan).

2.5. Immunofluorescence Microscopy

Immunofluorescence staining was performed to visualize possible translocal alteration of NF-κB proteins and β-catenin by dexamethasone in cells. The PFA-fixed cells were permeabilized with 0.1% Triton™ X-100 for 15 min and blocked with 3% bovine serum albumin (BSA) for 45 min at ambient temperature. Afterwards, the cells were labeled with primary NF-κB p65 rabbit polyclonal antibody #PA1-186 (Invitrogen, Carlsbad, CA, USA) at 1 µg/mL or β-catenin mouse monoclonal antibody #MA1-300 (Invitrogen) at a dilution of 1:200 in 0.1% BSA and incubated overnight at 4 °C in a moist chamber. The next day, cells were washed three times with PBS before incubation with the secondary Alexa Fluor 488 (AF488)-conjugated anti-rabbit (Cell Signaling Technology, Danvers, MA, USA) or anti-mouse antibody (Invitrogen) at a dilution of 1:1000 for 1 h at ambient temperature. Cells were washed again three times with PBS and mounted with Fluoroshield™ with DAPI (4′,6-diamidino-2-phenylindole) (Sigma-Aldrich). The slides were subsequently investigated with a Zeiss LSM 710 confocal laser scanning microscope (Carl Zeiss) [35].

2.6. mRNA Isolation and Quantitative Real-Time PCR

RNA isolation and quantitative real-time PCR were performed according to routine protocols [36–38]. Briefly, RNA was isolated by using the RNeasy Mini Kit (Qiagen, Venlo, Netherlands) according to the manufacturer's protocol and quantified with a spectrophotometer. Afterwards, cDNA was produced with the High Capacity cDNA Reverse Transcription Kit (Applied Biosystems, Foster City, CA, USA) following manufacturer's instructions. To determine the expression level of the target genes shown in Table S1, quantitative real-time PCR was performed applying the Fast SYBR™ Green Master Mix (Applied Biosystems) and the 7500 Fast Real-Time PCR System (Applied Biosystems). Primers were designed to have a $T_m \approx 60$ °C and to span exon/exon boundaries using Primer-BLAST [39] (Supplementary Materials). Primer were synthesized by TIB Molbio (Berlin, Germany). All samples were measured in triplicates and analyzed by the comparative threshold cycle ($\Delta\Delta C_T$) method with 18S rRNA as reference.

2.7. Western Blot Analysis

Western blot analysis was performed with routine protocols as described previously [36]. The control and DEX-treated samples were collected after 4 h and 3 days, solubilized in lysis buffer and compared to the control samples without DEX. Each condition included three batches with a total number of 24 samples (4 h) and 33 samples (3 days), respectively. Following lysis and centrifugation, aliquots of 40 µg total protein were subjected to SDS-PAGE and Western blotting. The samples were loaded onto Criterion XT 4–12% precast gels (Bio-Rad, Hercules, CA, USA), run for 1 h at 150 V and transferred to a polyvinylidene difluoride membrane using TurboBlot (Bio-Rad) (100 V, 30 min). Cyclophilin B was used as a loading control. Membranes were blocked with TBS-T containing 0.3% I-Block (Applied Biosystems) for 2 h at ambient temperature. For detection of the proteins shown in Table S2, the membranes were incubated overnight at 4 °C in TBS-T containing 0.3% I-Block solutions of the antibodies. The next day, membranes were washed three times with TBS-T for 5 min and incubated for 2 h at ambient temperature with a horseradish peroxidase (HRP)-linked antibody (Cell Signaling Technology) diluted 1:1000 in TBS-T with 0.3% I-Block. The respective protein bands were visualized using Clarity ECL Western Blot Substrate (Bio-Rad). Images were captured with

Image Quant LAS 4000 mini (GE Healthcare, Chicago, IL, USA) and analyzed using ImageJ software (imagej.net) for densitometric quantification.

2.8. Terminal Deoxynucleotidyl Transferase dUTP Nick-End Labeling (TUNEL) Assay

The Click-iT™ Plus TUNEL assay (Invitrogen) was used for apoptosis detection. FTC-133 cells were cultured in slide flasks (Sarstedt) under static culture conditions or exposed to the RPM, supplemented without or with 1000 nM DEX. After 4 h or 3 days cells were fixed with 4% PFA and prepared for the evaluation of apoptosis. The staining procedure was performed according to the manufacturer's recommendation. A positive control sample was treated with DNase I (Epicentre, Madison, WI, USA) to induce DNA fragmentation. The stained cells were examined using a Zeiss LSM 800 confocal laser scanning microscope (Carl Zeiss) equipped with an external light source and an objective with a calibrated 630× magnification.

2.9. Ki-67 Proliferation Assay

Cells were cultured and prepared as described in Section 2.5. Cells were labeled with an AF488 recombinant anti-Ki-67 antibody #ab197234 (Abcam, Cambridge, UK) at a dilution of 1:100 in 0.1% BSA and incubated overnight at 4 °C. The next day, cells were washed three times with PBS and mounted with Fluoroshield™ with DAPI (Sigma-Aldrich). The cell proliferation was evaluated by a Zeiss LSM 800 confocal laser scanning microscope (Carl Zeiss) and an objective with a calibrated 230× magnification. Five microscopic images for each condition were analyzed using ImageJ (imagej.net). The percentage of Ki-67 positive cells was counted for each condition and normalized to the control.

2.10. Spheroid Formation Assay

Approximately 1×10^6 cells per flasks were seeded into T25 cell culture flasks (Sarstedt). After 24 h the culture flasks were filled up completely (air bubble-free) with media and were installed on the prewarmed RPM (37 °C, 5% CO_2). To investigate the ability of MCS formation, two RPM running time points were considered: media was completely removed from culture flasks after 24 h and after 48 h exposure to the RPM. Flasks were re-filled with fresh media for a further 24 h run on the RPM. After each run, cells were examined and photographed.

2.11. Statistics

Statistical evaluation was performed using GraphPad Prism 7.01 (GraphPad Software, San Diego, CA, USA). The nonparametric Mann–Whitney U test was used to compare DEX-free with DEX-treated samples as well as static and μg conditions. All data are presented as mean ± standard deviation (SD) with a significance level of $p < 0.05$.

3. Results

Based on the knowledge that NF-κB seems to play a crucial role in spheroid formation of MCF-7 breast cancer cells [34] and that NF-κB subunit p65 (RelA) accumulates in thyroid cancer cells on the RPM [40], we decided to target RelA in μg-grown thyroid cancer cells using DEX. Therefore, we cultured the human follicular thyroid cancer cell line FTC-133 on an RPM in the presence of three different DEX concentrations (10, 100, 1000 nM). After three days on the RPM, the cells showed a DEX dose-dependent inhibition of spheroid formation in μg (Figure 2).

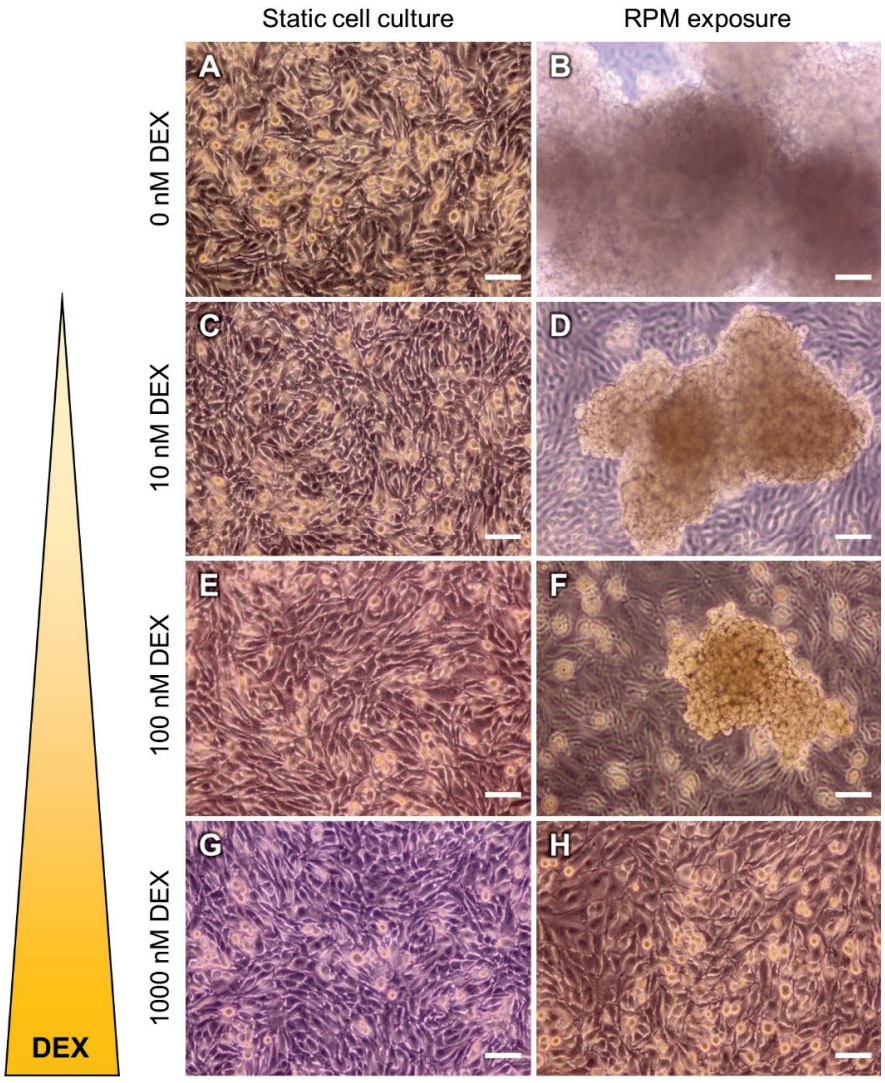


Figure 2. Impact of DEX on the spheroid formation ability of follicular thyroid cancer (FTC)-133 cells exposed to a random positioning machine (RPM). (**A,B**) After three days cells showed a dose-dependent inhibition of spheroid formation when treated with (**C,D**) 10 nM DEX, (**E,F**) 100 nM DEX, or (**G,H**) 1000 nM DEX on the RPM (right column). Scale bars: 100 µm.

3.1. NF-κB Pathway

NF-κB transcription factors play a fundamental role in the tumorigenesis of many cancer types, including thyroid cancer [41,42] and may be a target in the treatment of advanced thyroid cancer [43]. DEX is known to have inhibitory effects on the NF-κB pathway [44].

We investigated the transcription of the NF-κB family members subunit p50 and its precursor p105 (encoded by *NFKB1*) as well as subunit p52 and its precursor p100 (encoded by *NFKB2*). The mRNA levels of both genes were reduced in MCS cells grown for three days on the RPM and *NFKB2* was upregulated in adherently growing (AD) cells, harvested from the RPM (Figure 3A,B). In addition, we found a dose-dependent inhibitory effect of DEX on the mRNA synthesis of *NFKB2* (Figure 3B) and a less pronounced effect on the mRNA synthesis of *NFKB1* (Figure 3A). In contrast to DEX-treated MCF-7 cells [34], RelA was not translocated into the nucleus of FTC-133 cells in a significant amount after DEX supplementation (Figure 3E,F). Furthermore, RelA expression was not significantly altered by DEX on the transcriptional level (Figure 3C). RelA protein was increased after three days on the RPM and seemed to be augmented by DEX treatment in µ*g*-exposed cells (Figure 3D).

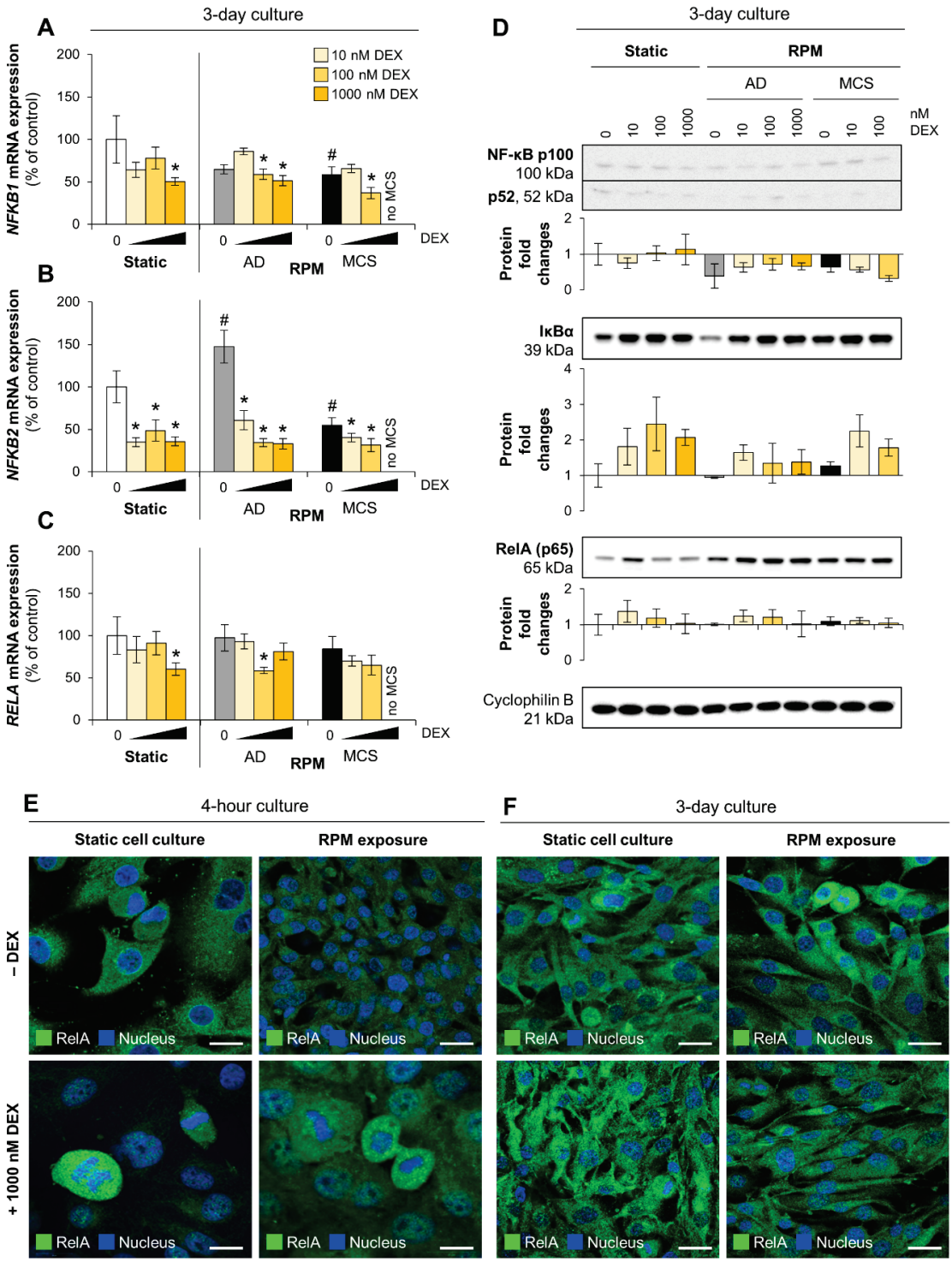


Figure 3. Effect of DEX on NF-κB family members in FTC-133 cells. (**A**) *NFKB1* mRNA expression; (**B**) *NFKB2* mRNA expression; (**C**) *RELA* mRNA expression. Depicted are means of relative mRNA levels ± standard deviations ($n = 5$). *: $p < 0.05$ vs. DEX-free samples. $^{\#}$: $p < 0.05$ vs. static cultures; (**D**) Western blots indicate protein levels of regulated genes after three days. Representatives of each of the three replicates are shown. Diagrams describe relative fold changes to control. AD: adherently growing cells; MCS: multicellular spheroids. (**E**,**F**) Immunofluorescence shows only minor translocation of RelA (green) into the nucleus (blue; 4′,6-diamidino-2-phenylindole (DAPI)-stained) in FTC-133 cells. Scale bars: 20 µm.

NF-κB dimers can be sequestered in the cytoplasm by the inhibitor of κB (IκB) proteins. Therefore, we analyzed the expression of IκBα (encoded by *NFKBIA*), IκBβ (encoded by *NFKBIB*), and IκBε (encoded by *NFKBIE*). The effect of DEX supplementation on *NFKBIA* expression was limited to RPM-exposed cells (Figure 4A), but it tended to upregulate the IκBα protein level in three-day cultures, independent of gravity (Figure 3D). In addition, DEX lowered *NFKBIB* and *NFKBIE* mRNA in cells cultured under normal conditions. The *NFKBIB* mRNA synthesis seemed to be increased (Figure 4B) whereas *NFKBIE* mRNA synthesis was reduced in adherently growing cells on the RPM (Figure 4C). Overall, the mRNA synthesis of all IκB proteins was reduced by long-term exposure to the RPM.

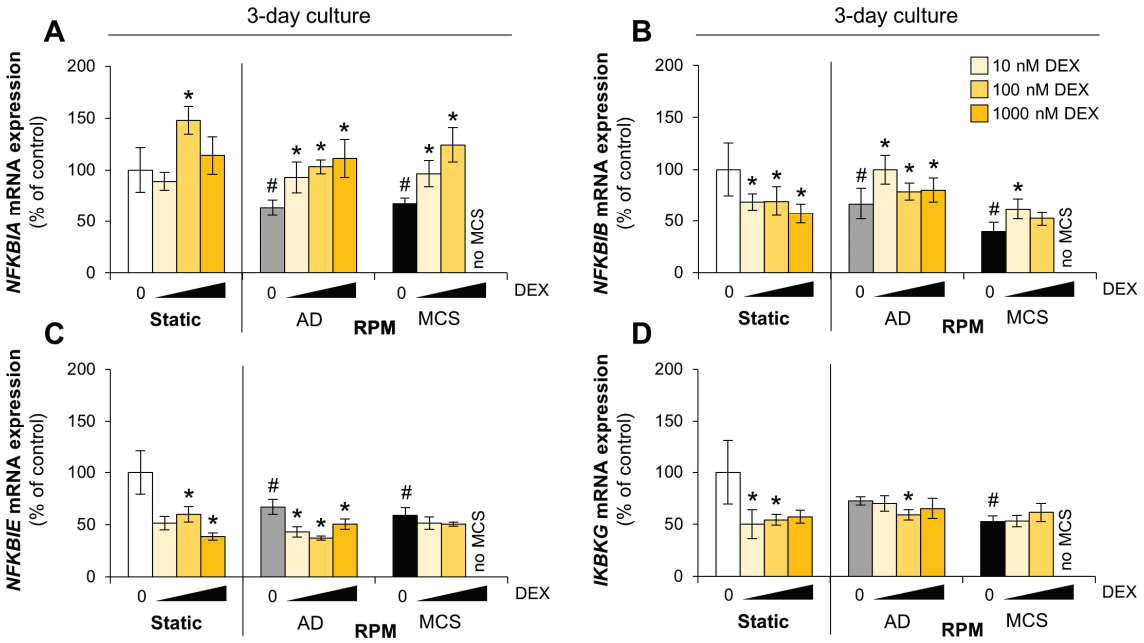


Figure 4. Effect of DEX on NF-κB regulators in FTC-133 cells. (**A**) *NFKBIA* mRNA expression; (**B**) *NFKBIB* mRNA expression; (**C**) *NFKBIE* mRNA expression; (**D**) *IKBKG* mRNA expression. Depicted are means of relative mRNA levels ± standard deviations ($n = 5$). *: $p < 0.05$ vs. DEX-free samples. #: $p < 0.05$ vs. static cultures. AD: adherently growing cells; MCS: multicellular spheroids.

Activation of NF-κB is initiated by the signal-induced degradation of IκB proteins, mainly via activation of IκB kinase (IKK). IKK is composed of the catalytic IKKα/IKKβ heterodimer and the master regulator NEMO (NF-κB essential modulator), also referred as IKKγ (encoded by *IKBKG*). Three-day MCS showed a reduction in *IKBKG* mRNA synthesis. DEX reduced *IKBKG* mRNA synthesis only in static cultured cells after three days. Under all other conditions, transcription was unaffected by DEX supplementation (Figure 4D).

Since NF-κB is obviously not the main target of DEX in suppressing μ*g*-based spheroid formation of FTC-133 cells, we proceeded to illuminate further cancer-related processes which have been reported in connection with DEX (Figure 1C) and that are also involved in the formation of tumor spheroids.

3.2. Growth Factors and Proliferation

Different growth factors are expressed and secreted by cancer cells and contribute to proliferation, survival, and migration. Previous experiments designed to elucidate the growth behavior of cancer cells in μ*g* reveal that especially connective tissue growth factor (CTGF), epidermal growth factor (EGF), transforming growth factor beta (TGF-β), and VEGF were regulated in FTC-133 cells after gravity was omitted [37]. CTGF is a member of the CCN family of secreted, matrix-associated proteins that plays a key role in tumor development, progression, and angiogenesis [45]. CTGF is suggested to regulate cancer cell migration, invasion, angiogenesis, and anoikis [46]. In our experiments, CTGF was

upregulated in adherently growing FTC-133 cells after DEX supplementation (Figure 5A). RPM-exposure also enhanced the *CTGF* mRNA level resulting in an additive effect of µ*g* and DEX supplementation. However, the transcription was lower in MCS cells compared to cells in static cultures after three days (Figure 5A).

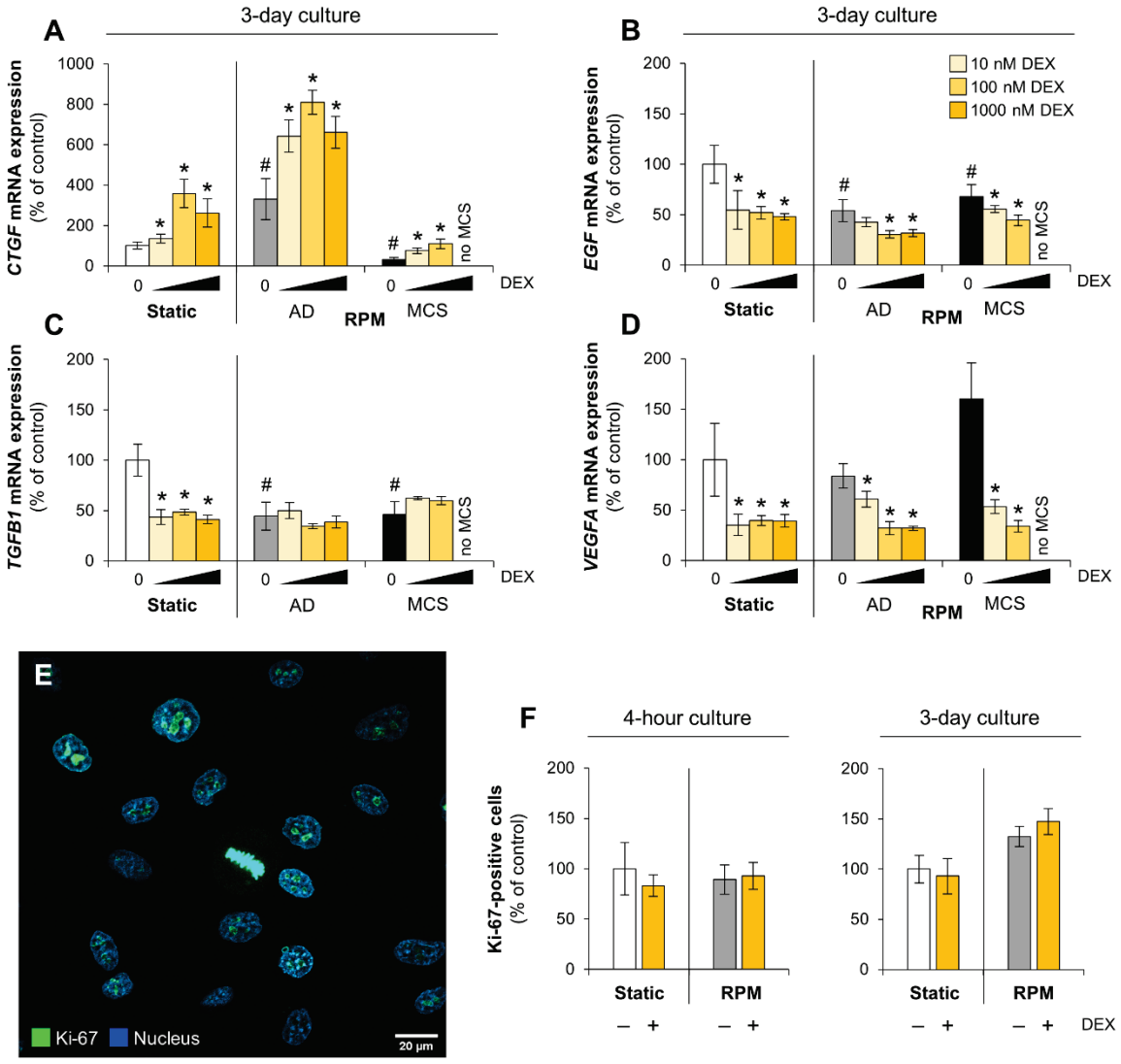


Figure 5. Effect of DEX on autocrine growth factors and proliferation markers in FTC-133 cells. (**A**) *CTGF* mRNA expression; (**B**) *EGF* mRNA expression; (**C**) *TGFB1* mRNA expression; (**D**) *VEGFA* mRNA expression. Depicted are means of relative mRNA levels ± standard deviations (n = 5); (**E**) Immunofluorescence. Nuclear expression of Ki-67 indicates proliferating cells; (**F**) Proliferation analysis using Ki-67. *: $p < 0.05$ vs. DEX-free samples. $^{\#}$: $p < 0.05$ vs. static cultures. AD: adherently growing cells; MCS: multicellular spheroids.

TGF-β and EGF represent two physiological regulators of thyroid cell differentiation and proliferation. Whereas EGF is a strong mitogen for follicular thyroid cells [47], TGF-β has a complicated role in cancer. Initially, TGF-β is a tumor suppressor that inhibits the growth of thyrocytes and induces apoptosis [48]. However, at later stages of tumor progression, TGF-β acts as a potent EMT inducer and then it plays a fundamental role in tumor progression and metastasis formation [49–51]. *EGF* mRNA was downregulated both in presence of DEX and in µ*g* (Figure 5B). *TGFB1* mRNA levels were also lower in µ*g*-grown cells, but DEX decreased *TGFB1* mRNA synthesis only in cells from static cultures (Figure 5C). In addition, DEX suppressed VEGF under normal culture conditions and in both cell populations on the

RPM (Figure 5D). In accordance with previous studies that investigated other follicular thyroid cancer cells on the RPM [52], *VEGFA* expression was somewhat increased in MCS cells after three days.

DEX was previously reported to have anti-proliferative effects on human medullary thyroid cancer cells [53]. To prove this effect with follicular thyroid cancer cells and in the context of μ*g*, we searched for cellular markers for proliferation such as the Ki-67 protein (encoded by *MKI67*) [54]. Ki-67 can be detected during all active phases of the cell cycle (G1, S, G2, and M), but not in resting cells (G0). Thus, the nuclear expression of Ki-67 can be evaluated to study tumor proliferation using immunofluorescence microscopy (Figure 5E). In our experiments, neither μ*g* nor DEX had a significant influence on the proliferation of FTC-133 cells (Figure 5F).

3.3. Epithelial and Mesenchymal Characteristics, Wnt/β-catenin Signaling

To find signs for EMT, that is also influenced by μ*g* in cancer cells [55], different epithelial (E-cadherin) and mesenchymal markers (N-cadherin, vimentin, fibronectin, Snail1) were analyzed. In a four-hour culture the E-cadherin mRNA (encoded by *CDH1*) was reduced in cells incubated with DEX (Figure 6A), without significant changes in E-cadherin protein levels (Figure 6H). After three days on the RPM, we found a difference in the *CDH1* gene expression between the two phenotypes: adherently growing cells showed a lower, whereas MCS showed a higher, *CDH1* expression compared to control cells. The elevated *CDH1* expression in spheroids was significantly reduced by DEX supplementation (Figure 6A).

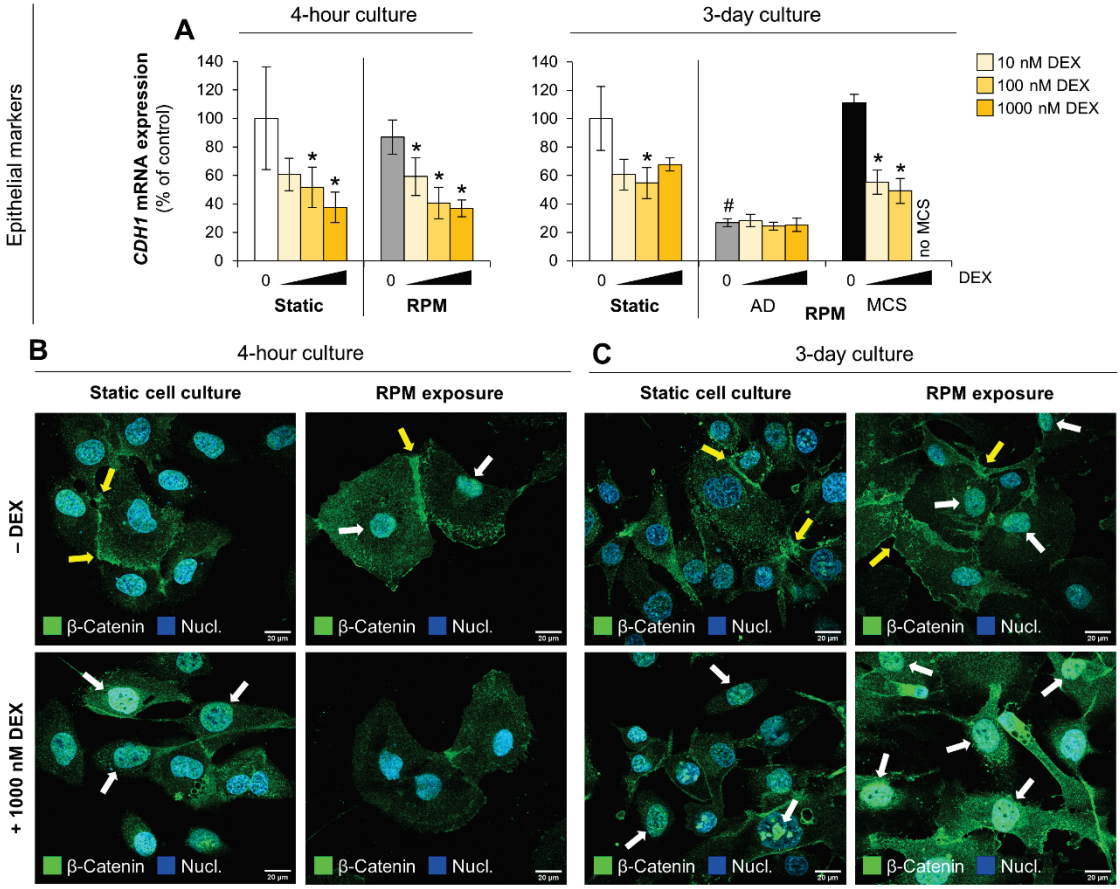


Figure 6. *Cont.*

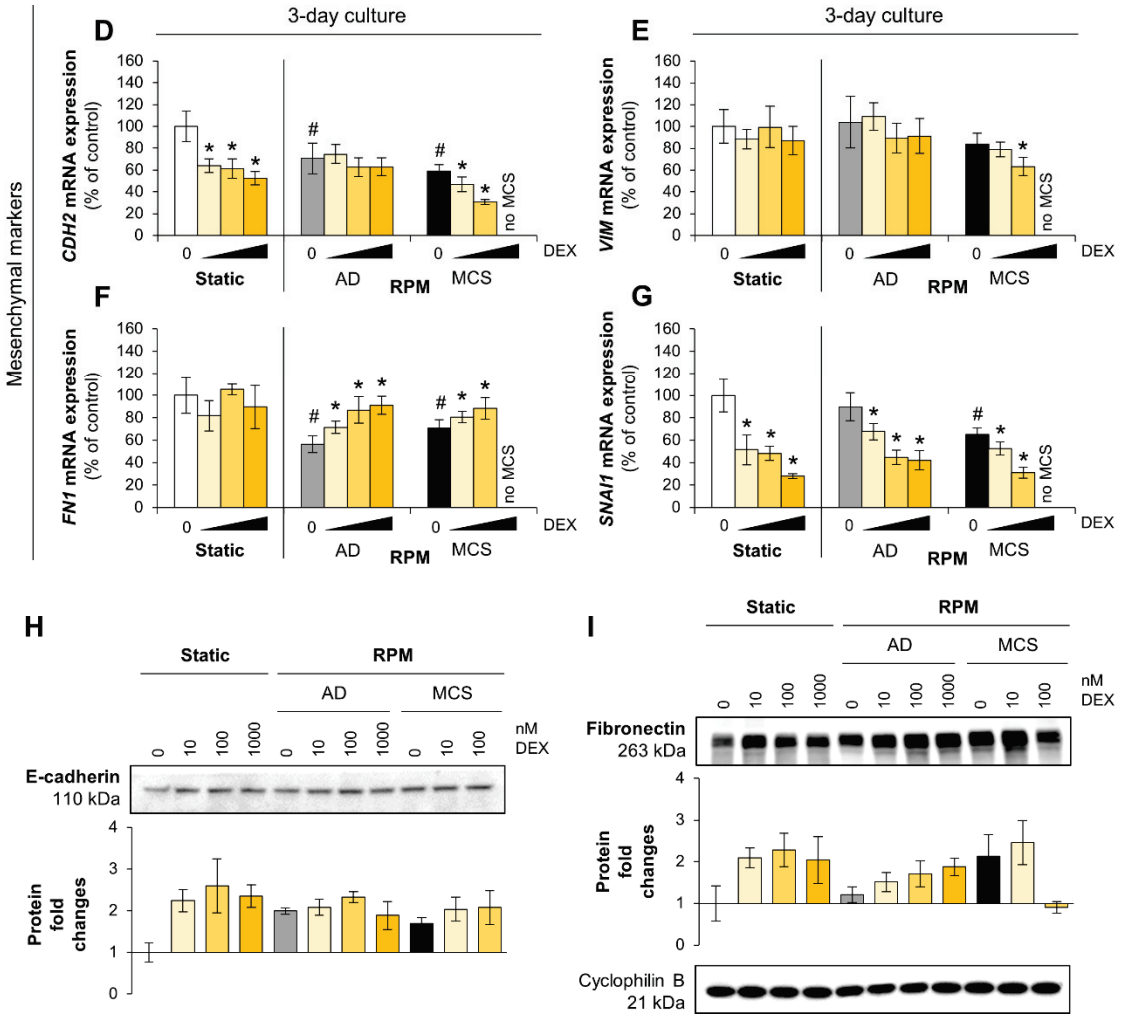


Figure 6. Effect of DEX on the mRNA synthesis of epithelial markers, mesenchymal markers, and other epithelial–mesenchymal transition (EMT) players in FTC-133 cells. (**A**) *CDH1* mRNA expression; (**B,C**) Immunofluorescence. White arrows show translocation of β-catenin (green) into the nucleus (blue; DAPI-stained) both in μ*g* and in the presence of DEX. Yellow arrows indicate an increased occurrence of β-catenin on the plasma membrane in the absence of DEX. Scale bars: 20 μm; (**D**) *CDH2* mRNA expression; (**E**) *VIM* mRNA expression; (**F**) *FN1* mRNA expression; (**G**) *SNAI1* mRNA expression. Depicted are means of relative mRNA levels ± standard deviations ($n = 5$). *: $p < 0.05$ vs. DEX-free samples. #: $p < 0.05$ vs. static cultures; (**H,I**) Western blots indicate protein levels of regulated genes after 3 days. Representatives of each of the three replicates is shown. Diagrams describe relative fold changes to control. AD: adherently growing cells; MCS: multicellular spheroids.

The amount of E-cadherin protein was slightly higher in cells exposed to the RPM than those from static cell cultures and was not influenced by DEX in μ*g*. Under normal culture conditions DEX seemed to increase E-cadherin levels (Figure 6H). Downstream of the cadherin complex, β-catenin mRNA (encoded by *CTNNB1*) was not influenced significantly by DEX (Figure S3). However, β-catenin was translocated from the plasma membrane into the nucleus in the presence of DEX (Figure 6B,C) suggesting an involvement of the Wnt/β-catenin pathway. This is supported by the fact that the transcription of the E-cadherin repressor Snail1 (encoded by *SNAI1*) was also downregulated after DEX treatment (Figure 6G).

N-cadherin (encoded by *CDH2*) and vimentin (encoded by *VIM*) were identified to promote thyroid tumorigenesis [56,57]. *CDH2* mRNA was upregulated in cells after short-term exposure (Figure S3C) and downregulated after long-term exposure to the RPM (Figure 6D). Similar to *CDH1*, *CDH2* expression

in spheroids was reduced by DEX supplementation (Figure 6D). Furthermore, DEX elicited the same reducing effects in control cells of a three-day culture. However, adherently growing cells on the RPM were not influenced by DEX. *VIM* expression was not altered by RPM-exposure, but slightly reduced by high DEX concentrations in MCS cells after three days (Figure 6E). RPM-exposure reduced *FN1* mRNA levels in three-day cultures. This effect could be reversed in the presence of DEX (Figure 6F). Protein levels of fibronectin were also slightly increased after DEX supplementation (Figure 6I).

3.4. Anoikis Factors

There is a further possibility that RPM-based spheroid formation of FTC-133 cells in the presence of DEX is abolished through anoikis of detached cells. Cells undergo apoptosis before aggregates are formed. Unfortunately, live/dead staining of detached cells inside the RPM is technically not possible. Adherent cells showed no signs of apoptosis after DEX treatment and after µ*g*-exposure as visualized by a TUNEL staining (Figure 7A). Caspase-3 cleavage tests were negative, both for adherent and spheroid cells in the presence of DEX (Figure 7B). Additionally, we investigated several factors involved in anoikis on the transcriptional level. The cysteine protease caspase-8 (encoded by *CASP8*) is implicated in apoptosis and involved in the induction of NF-κB nuclear translocation [58]. DEX had only a minor effect on *CASP8* gene expression in our experiments (Figure 7C).

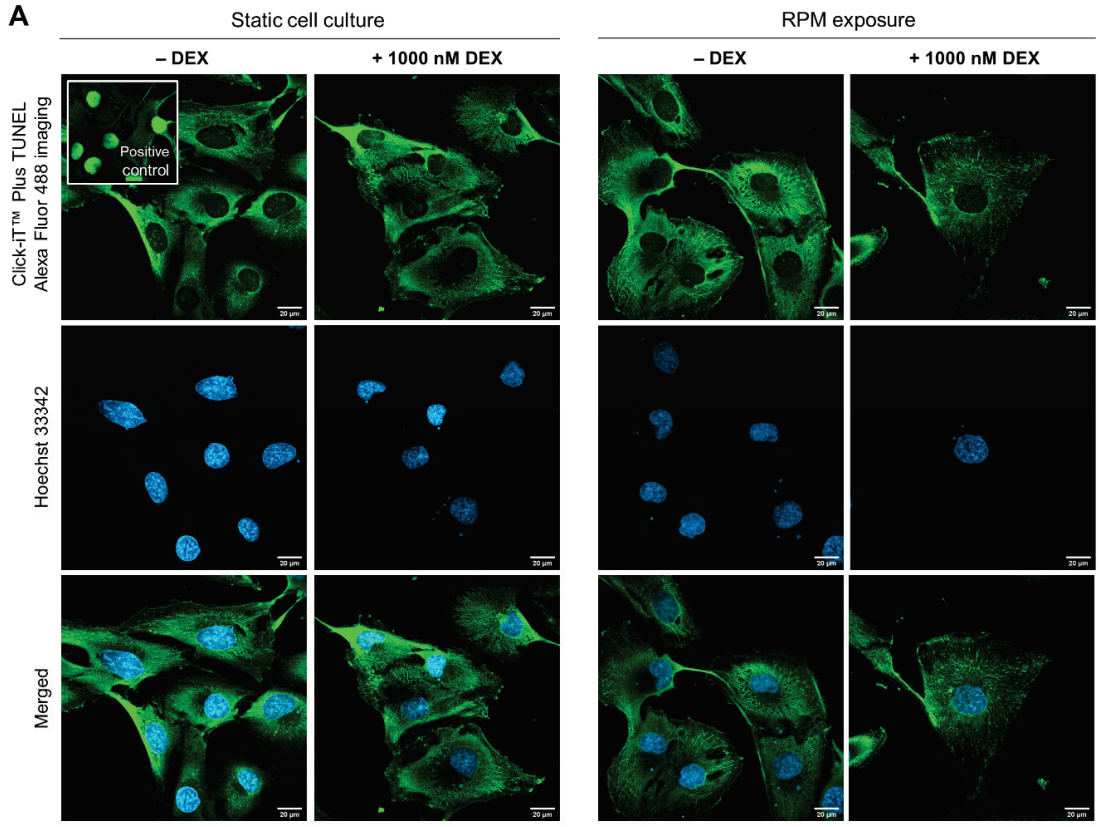


Figure 7. *Cont.*

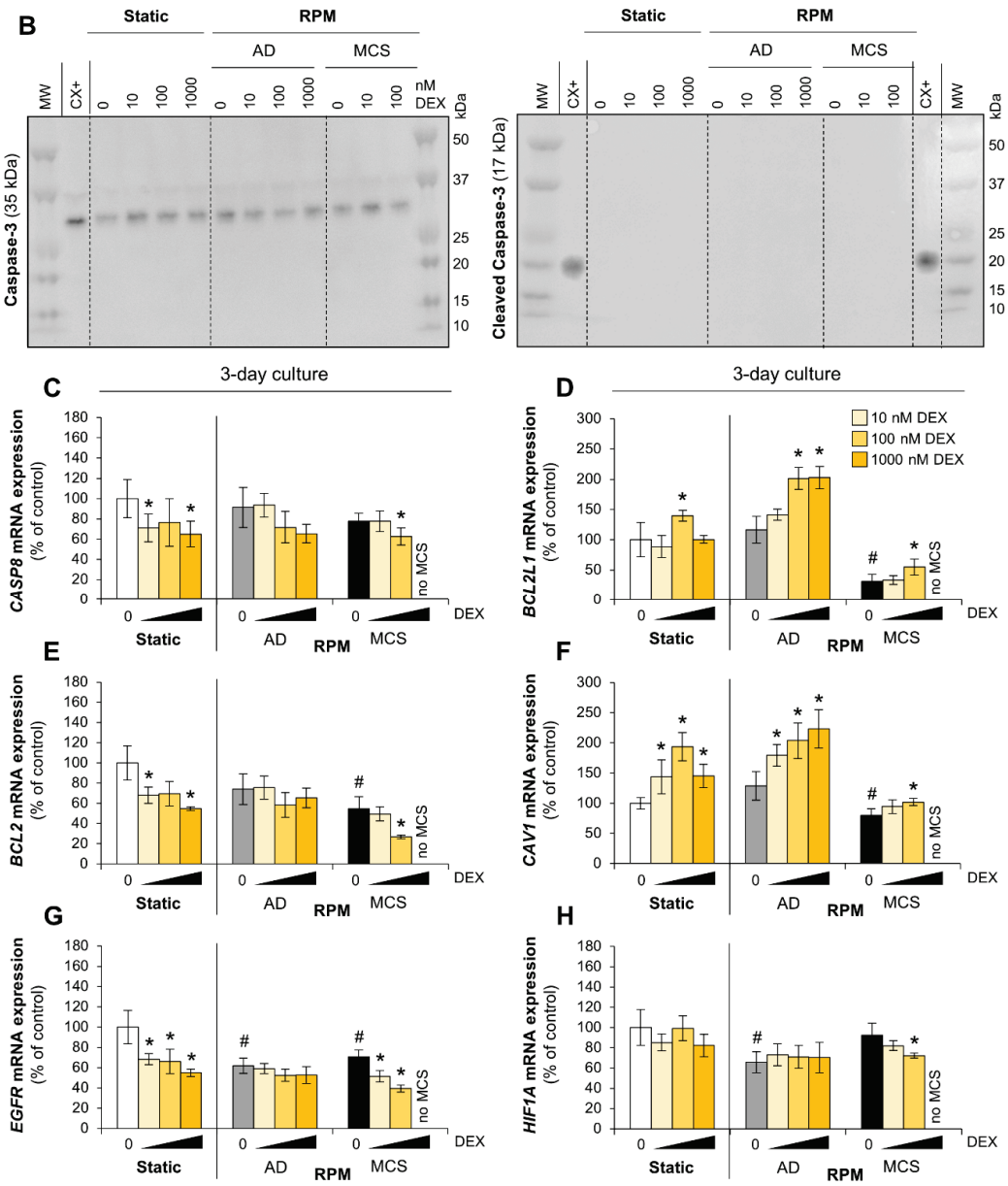


Figure 7. Effect of DEX on apoptosis and anoikis-related proteins in FTC-133 cells. (**A**) No apoptotic cells (green nuclei) were detected by transferase dUTP nick-end labeling (TUNEL) staining after three days. The staining indicates free fluorophores in the cytoplasm in all images except for the positive control. Scale bars: 20 µm; (**B**) Caspase-3 cleavage as an indicator of apoptosis; (**C**) *CASP8* mRNA expression; (**D**) *BCL2L1* mRNA expression; (**E**) *BCL2* mRNA expression; (**F**) *CAV1* mRNA expression; (**G**) *EGFR* mRNA expression; (**H**) *HIF1A* mRNA expression. Depicted are means of relative mRNA levels ± standard deviations ($n = 5$). *: $p < 0.05$ vs. DEX-free samples. $^{\#}$: $p < 0.05$ vs. static cultures. AD: adherently growing cells; MCS: multicellular spheroids.

The anti-apoptotic protein B-cell lymphoma-extra large (Bcl-xL; encoded by *BCL2L1*) has been implicated in the survival of cancer cells by inhibiting the function of the tumor suppressor p53 [59,60]. *BCL2L1* mRNA synthesis was upregulated in FTC-133 cells exposed to the RPM after four hours and reduced by DEX supplementation (Figure S4C). After three days, the *BCL2L1* mRNA synthesis was downregulated in MCS cells, but remained unchanged in adherently growing cells on the RPM. DEX increased *BCL2L1* mRNA after long-term exposure to the RPM (Figure 7D). In contrast, B-cell lymphoma 2 (Bcl-2; encoded by *BCL2*) was further downregulated by DEX in MCS cells (Figure 7E).

A further factor, caveolin-1 (encoded by *CAV1*), was shown to inhibit anchorage-independent growth, anoikis, and invasiveness in human breast cancer cells [61]. Indeed, µ*g* affected the *CAV1* gene expression during spheroid formation: in MCS cells, the *CAV1* mRNA level was reduced. DEX treatment led to an upregulation of caveolin-1 mRNA (Figure 7F).

The loss of coupling between normal integrin and EGF receptor (EGFR) signaling may be further cause for anoikis resistance in tumor cells [62]. We analyzed *EGFR* mRNA synthesis and found a downregulation of EGFR in RPM-grown cells. In addition, DEX decreased *EGFR* transcription in control cells and MCS after three days (Figure 7G).

Hypoxia inducible factor-1 alpha (HIF-1α; encoded by *HIF1A*) is abundantly expressed in most human carcinomas and their metastases. HIF-1α can be induced via EGFR activation and is known to control central metastasis-associated pathways such as angiogenesis, invasion, and resistance to anoikis [63]. Transcription of *HIF1A* was only downregulated in adherently growing cells in three-day RPM cultures and remained unaffected in MCS or by DEX supplementation (Figure 7H).

3.5. Dexamethasone vs. Microgravity—Elucidation of Spheroid Formation Capability

Comparing DEX-induced gene expression data of control cells and transcriptional adaption of FTC-133 cells to µ*g* revealed similar regulation patterns (Figure 8A). We performed an additional two-step RPM culture experiment to check if spheroid formation capability was lost after long-term exposure to µ*g*. Cells that were pre-incubated on the RPM for 48 h showed only marginally reduced spheroid formation during the following 24 h (Figure 8B,C).

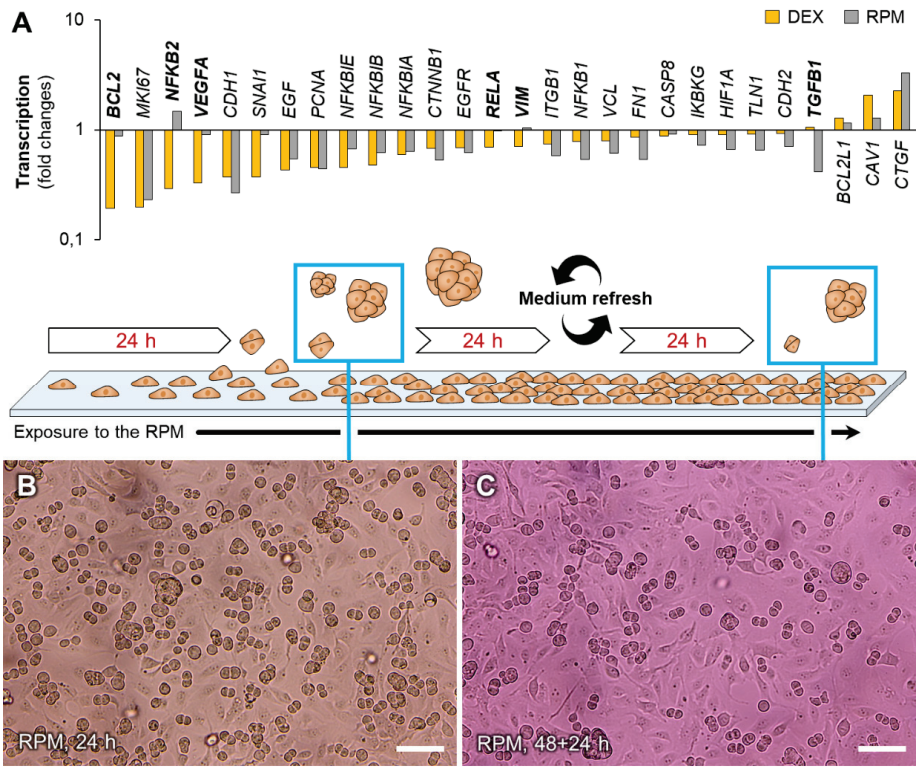


Figure 8. Spheroid formation capability of FTC-133 cells cultured on the RPM. (**A**) Comparison of transcription regulation patterns 4 h after DEX supplementation (yellow bars) and after a three-day RPM-exposure (grey bars). Bold gene symbols indicate fold changes >2.5 or regulation in opposite directions. (**B**) Cells 24 h after the RPM-experiment started; (**C**) Cells 24 h after an initial two-day RPM exposure. Medium was refreshed and spheroids were discarded after the first two days. Although many genes were similarly regulated after DEX supplementation and after a three-day-exposure to the RPM, in contrast to DEX treatment, cells did not lose the ability to form spheroids in µ*g*. Scale bars: 100 µm.

4. Discussion

We investigated the effects of DEX supplementation on the growth of follicular thyroid cancer cells exposed to simulated μ*g*. During a three-day culture on an RPM, cells grew into the form of a large MCS, as it was reported and studied earlier [28,52,64,65]. Previous research revealed that the addition of DEX to spinner flask cultures led to smaller, irregularly shaped spheroids of rat hepatocytes. Higher DEX concentrations inhibited MCS aggregation and promoted MCS disassembly in culture dishes [66]. Kopp et al. [34] described an inhibitory effect of DEX on the MCS formation rate of MCF-7 breast cancer cells cultured on the RPM. However, the authors did not perform any further analyses to elucidate the underlying effects of DEX on MCF-7 cells. After the current study we can confirm similar effects on FTC-133 cells. We found a dose-dependent inhibition of RPM-based spheroid formation by DEX, that was independent from RelA nuclear translocation which was described for DEX-treated breast cancer cells [34]. This finding agrees with the theory of Bauerle et al. [43] that global regulation of thyroid cancer cell growth is not achieved by NF-κB signaling alone and indicates that NF-κB (pathway) may not be the main target of DEX inhibiting the 3D growth of FTC-133 cells in μ*g*. Therefore, we used transcriptional and translational methods to find answers for the changed growth behavior. Interestingly, after DEX supplementation a couple of genes were regulated in the same direction as after a three-day exposure to the RPM. Since the ability of spheroid formation was not suppressed in the RPM-cultures, especially those genes that are of interest, which had a differential expression pattern (Table 1).

Table 1. Significant differences ($p < 0.05$) in mRNA synthesis of adherently growing FTC-133 cells in presence of DEX in static cell culture compared with cells grown without DEX on the RPM.

Process/Pathway	4-Hour Culture	Both Time Points	3-Day Culture
NF-κB pathway	*NFKB1*↑, *NFKBIA*↓, *NFKBIB*↓	*NFKB2*↓, *NFKBIE*↓	*NFKB1*↓, *RELA*↓, *NFKBIA*↑, *IKBKG*↓
Autocrine signaling	*EGF*↓, *TGFB1*↓	*VEGFA*↓	
EMT	*CDH1*↓, *CTNNB1*↓, *VIM*↓,	*CDH2*↓, *SNAI1*↓	*CDH1*↑
Anoikis	*CASP8*↓, *BCL2*↓, *BCL2L1*↓, *EFGR*↓, *HIF1A*↓		*HIF1A*↑
Proliferation	*MKI67*↓, *PCNA*↓		*MKI67*↑

↑: significant upregulation in DEX-treated cells; ↓: significant downregulation in DEX-treated cells.

4.1. Cell Detachment in Microgravity and Epithelial–Mesenchymal Transition

The EMT describes a fundamental process of cancer progression when carcinoma cells lose their epithelial characteristics and acquire a migratory behavior, indicated by mesenchymal markers. This alteration enables them to escape from their epithelial cell community and invade into surrounding tissues, even at distant locations, and contributes to the acquisition and maintenance of stem cell-like properties [49,67]. In previous studies, DEX proved to suppress cell invasion in bladder cancer [68], inhibited hypoxia-induced EMT in colon cancer cells [69], and reduced TGF-β-induced EMT in non-malignant cells [70].

The interaction of DEX-bound GRs with NF-κB affects the expression of several target genes, one of which is TGF-β [71]. TGF-β induces the upregulation mesenchymal markers such as vimentin and downregulation of the epithelial marker E-cadherin, which are considered critical prerequisites for metastasis in numerous human cancers [72]. Therefore, it is not surprising that the expression of E-cadherin and β-catenin in thyroid cancer is associated with better prognosis [73]. Among the set of analyzed genes, *TGFB1* was regulated differently in μ*g* and in the presence of DEX. Hinz [74] suggested that the TGF-β complex functions as an extracellular mechanosensory that can be activated by contractile forces that are transmitted by integrins. Indeed, μ*g* was identified as a possible cause changing TGF-β expression levels [75]. In four-hour cultures stacked on the RPM, the *TGFB1* mRNA was slightly elevated

whereas in three-day cultures the mRNA level was attenuated, maybe due to missing forces in μ*g*. DEX supplementation led to a slow downregulation of *TGFB1* expression in static cell cultures or in follicular thyroid cancer cells grown for four hours on the RPM (Figure S2C). This observation could be cell-type specific, as DEX increased *TGFB1* expression in prostate cancer and pancreatic ductal carcinoma cells [76,77]. TGF-β signaling is identified as one of the most altered pathways in ovarian tumor spheroids [78] and cell aggregation proved to be induced by TGF-β in ovarian cancer cells [79]. Therefore, *TGFB1* could be a possible target gene for DEX that may inhibit spheroid formation of FTC-133 cells in an early culture stage at least in part by downregulation of *TGFB1*.

The translocation of β-catenin into the nucleus as well as upregulation of *FN1* mRNAs suggest an activation of the Wnt/β-catenin pathway after DEX supplementation. On the other hand, expression of Snail1 is reduced in the presence of DEX. However, in ovarian adenocarcinoma cells Snail1 is downregulated when TGF-β and Wnt signaling pathways are co-activated [80]. Snail1 acts as an EMT inducer and a potent repressor of E-cadherin [81,82]. The finding that E-cadherin expression correlates with spheroid formation capability suggests that intercellular adhesion plays a key role in 3D growth [83, 84]. Sahana et al. [85] found that the blocking of E-cadherin activity with antibodies promoted μ*g*-driven spheroid formation of MCF-7 cells. Budding of ovarian cancer spheroids from monolayers correlated with the expression of vimentin and lack of cortical E-cadherin [86]. In our experiments the *CDH1* gene was downregulated in adherent cells but remained nearly unchanged in MCS cells of a three-day RPM culture. E-cadherin protein increased after DEX supplementation. This finding is consistent with the observations of Sahana et al. [85] and suggests a quantity-dependent influence of E-cadherin on cancer cell aggregation, that is not directly related to its mRNA synthesis. For renal cell carcinoma, N-cadherin was shown not to be an essential molecule for spheroid formation indicating a somewhat different role from cell–cell adhesion. However, anti-N-cadherin antibodies inhibit spheroid formation in a renal cell carcinoma cell line that expressed N-cadherin alone [87]. Tsai et al. [88] suggested that N-cadherin might play a role in the formation and maintenance of spheroid core structures. Due to a higher affinity of N-cadherin to form homodimers [89], cells with higher N-cadherin expression aggregate first. Indeed, in the spheroid-inducing environment of the RPM, the *CDH2* gene was upregulated after four hours (Figure S3B). DEX reduced *CDH2* expression in these cells as well as in spheroids after three days. This explains the reduced spheroid formation in the presence of DEX, but on the other hand, it suggests a destabilization of formed spheroids.

Fibronectin was downregulated in μ*g*, but upregulated by DEX, in three-day cultures. Thus, it was the only mesenchymal factor showing a significantly altered regulation after DEX supplementation. Abu-Absi et al. [66] previously reported an increase in fibronectin and collagen III mRNA when rat hepatocytes were cultured in spinner flasks in the presence of DEX and suggested that a modification of the extracellular matrix (ECM) contributes to the changes in morphology. It is further known that DEX treatment significantly increases the strength of cell–ECM adhesion in glioblastoma cells and thus decreases their motility [90]. Robinson et al. [91] confirmed in different experiments that fibronectin matrix assembly plays a key role in cell aggregation and spheroid formation. So, it is very likely that DEX alters the ECM composition of FTC-133 cells, including fibronectin, in a way that they are no longer susceptible to 3D aggregation in μ*g*.

Our data indicate that FTC-133 cells were not shifted to a typical mesenchymal phenotype during spheroid formation on the RPM and the phenotype was not strongly influenced by DEX. However, the results confirm the involvement of the Wnt/β-catenin axis and TGF-β-induced signaling in μ*g*-triggered spheroid formation ability. These pathways were affected by DEX and can regulate some individual adhesion and matrix proteins (e.g., E-cadherin and fibronectin) which are important for detachment and 3D aggregation.

4.2. Survival of Detached Cells

At least for adherently growing FTC-133 cells, a cell-based assay showed no apoptotic cells after DEX treatment. For osteoblasts it is known that DEX can cause anoikis, probably due to the decreased integrin

β1 expression [92]. In our experiments, indeed we found a downregulation of *ITGB1* transcription in DEX-treated cells as well as lower integrin β1 levels in MCS cells that grew in the presence of DEX (Figure S5).

The induction of anoikis occurs through an interplay of the two apoptotic pathways involving activation of caspase-8 and inhibition of Bcl-2 [26]. Caspase-8 expression was only marginally affected by μ*g* and DEX treatment. We observed a counter-regulation for enhanced *CASP8* mRNA synthesis by DEX in cells after four hours on the RPM (Figure S4A). DEX significantly reduced expression of the anti-apoptotic *BCL2* gene in FTC-133 cells but stimulated the expression of the anti-apoptotic Bcl-xL. An upregulation of Bcl-xL expression by DEX was reported earlier for follicular thyroid cancer cells where it promotes survival [93]. That Bcl-2 plays an important role in the efficacy of DEX was confirmed in a study with myeloma cells where Bcl-2 overexpression was associated with resistance to DEX [94]. Overexpression of Bcl-2 correlates with the progression and metastasis of prostate cancer [95] and was shown to inhibit anoikis at least in intestinal epithelial cells [96]. Looking at apoptosis signaling, there are a some, but not all, indications that anoikis can be induced in FTC-133 cells after DEX treatment.

Apart from the apoptotic pathways, there are other proteins playing important roles in the complex network of survival signaling. It has been reported that inhibition of E-cadherin binding prevented cell–cell aggregation and could induce anoikis in epithelial cells [97,98]. In addition, the overexpression of β-catenin, a downstream regulator of cadherin signaling, resulted in anoikis resistance [99]. Indeed, on the transcriptional level we saw a DEX-mediated downregulation of *CDH1* together with an upregulation of *CTNNB1* in MCS cells.

The integral membrane protein caveolin-1 was identified as an important factor in spheroid formation of thyroid cancer cells in an μ*g* environment [65,100] which further inhibits anchorage-independent growth and anoikis, obviously two independent processes, in MCF-7 breast cancer cells [61]. The *CAV1* gene was downregulated when FTC-133 cells formed MCS on an RPM [100]. We were able to confirm this effect in our experiments. The upregulation of *CAV1* expression in the presence of DEX may suppress caveolin's yet undefined effects on 3D aggregation of thyroid carcinoma cells. Interestingly, caveolin-1 is overexpressed in other metastatic carcinoma cells where it promotes growth [101,102] and resistance to anoikis [61]. Caveolin-1 controls the stability of focal adhesions and contributes to mechanosensing and adaptation in response to mechanical stimuli including cell detachment [103]. Moreno-Vicente et al. [104] demonstrated that caveolin-1 regulates yes-associated protein activity which in turn modulates pathophysiological processes such as ECM remodeling. The authors suggested that this regulation could determine the onset and progression of tumor development. A possible explanation for suppressed spheroid formation would be that a more rigid ECM inhibits the growth into 3D aggregates.

In summary, we found regulatory indications but no clear evidence of anoikis after DEX treatment, as both caspase-3 cleavage and TUNEL staining were negative. Therefore, we suggest that apoptosis does not play a (major) role in inhibition of FTC-133 spheroid formation by DEX.

4.3. Autocrine Signaling

Growth factors have been considered to be involved in spheroid formation of thyroid cancer cells for long time. During the Shenzhou-8 space experiment, extraordinarily large 3D aggregates were formed by FTC-133 cells which showed an altered expression of *EGF* and *CTGF* genes under real μ*g* [105]. A decreased expression of *CTGF* in MCS compared to an increased expression in adherent cells was observed after cultivation of FTC-133 on different μ*g*-devices suggesting an important role for CTGF in spheroid formation [65]. DEX supplementation resulted in an upregulation of *CTGF* mRNA synthesis. In vitro, CTGF was identified to stimulate ECM synthesis, proliferation, or integrin expression and has been implicated in different cancer-related processes, comprising migration, invasion, angiogenesis, and anoikis [46]. Elevated *CTGF* expression levels in primary papillary thyroid carcinoma samples were correlated with metastasis [106]. EGF acts as a strong mitogen for follicular thyroid cells [47] and has been shown to increase the spheroid size in various tumor cell lines [107–109]. Both, DEX and μ*g* reduced *EGF* expression. However, CTGF upregulation and EGF downregulation by DEX cannot explain the

inhibition of spheroid formation, especially since adherent cells on the RPM are able to form MCS but show the same gene regulations.

VEGF promotes tumor angiogenesis by stimulating proliferation and survival of endothelial cells and can directly modulate cancer cell behavior [110]. Studies have shown that VEGF expression is upregulated in most human tumors and correlates with the risk for the development of metastasis in papillary thyroid cancer [111,112]. VEGF expression can be upregulated in response to hypoxia and was found in the microenvironment of tumor spheroids formed by HT-29 human colon cancer cells [113]. Furthermore, spheroids formed by FTC-133 cells on an RPM showed an increase in *VEGFA* gene expression [52]. Inhibition of VEGF signaling significantly reduced cell viability of thyroid cancer cells and increased apoptosis in the NPA'87 tumor-derived cell line [114]. DEX was reported to reduce VEGF secretion in some head and neck cancer cells via STAT3 [115]. We can confirm a decreasing effect of DEX on *VEGFA* expression in FTC-133 cells, independently of their exposure to μ*g* or their growth behavior on the RPM. A decrease in VEGF-A by treatment using siRNA or anti-VEGF-A, reduced spheroid formation, proliferation, migration, and invasion of epidermal cancer stem cells [116]. This finding highlights the role of VEGF (signaling) in the formation of solid tumors and could also provide an explanation for the effect of DEX on FTC-133 cells. In T47D breast cancer cells, DEX was shown to affect the PI3K/AKT/mTOR pathway [117] that could also be a possible target in thyroid cancer cells responsible for the suppression of spheroid formation [118].

5. Conclusions

In our study, DEX suppressed spheroid formation of FTC-133 cells cultured on an RPM in a dose-dependent manner. Interestingly, DEX did not influence NF-κB in a way that would explain the inhibition of μ*g*-triggered spheroid formation indicating that NF-κB (pathway) may not be the main target of DEX in FTC-133 cells. However, transcriptional regulation of important individual factors in cancer cell biology, which were previously suggested to play a role in spheroid formation, was clearly affected by DEX. Thereby, our data indicate the presence of a more complex regulation network of spheroid formation also involving other signal pathways, such as Wnt/β-catenin and TGF-β, that regulate adhesion and matrix proteins which are important for cell detachment and 3D growth. According to our results, it will be necessary to carry out a broad transcriptome analysis in order to identify the exact influence of DEX on the growth behavior of follicular thyroid cancer cells. Furthermore, it needs to be clarified whether DEX not only inhibits formation of spheroids but also promotes their disassembly in μ*g*.

Supplementary Materials: The following materials are available online at http://www.mdpi.com/2073-4409/9/2/367/s1, Figure S1. Effect of 4 h DEX treatment on NF-κB family members and regulators in FTC-133 cells; Figure S2. Effect of 4 h DEX treatment on growth factors and proliferation markers in FTC-133 cells. Figure S3: Effect of 4 h DEX treatment on epithelial markers, mesenchymal markers and other EMT players in FTC-133 cells; Figure S4: Effect of 4 h DEX treatment on anoikis-related factors in FTC-133 cells; Figure S5: Effect of DEX on cell–cell contacts of FTC-133 cells.; Table S1: Primer sequences used in the quantitative real-time PCR; Table S2: Antibodies used for Western blot analyses.

Author Contributions: Conceptualization, D.M., M.K., and D.G.; methodology, D.M., J.S., and T.J.C.; software, D.M.; validation, D.M., M.K., and S.K.; formal analysis, D.M.; investigation, D.M., M.K., T.J.C., and M.Z.N.; resources, M.I. and T.J.C.; data curation, D.M., M.K., S.K., and D.G.; writing—original draft preparation, M.K. and D.M.; writing—review and editing, M.K., D.G., S.K., T.J.C., and M.W.; visualization, D.M. and M.K.; supervision, D.G. and M.K.; project administration, D.G.; funding acquisition, D.G. and M.I. All authors have read and agreed to the published version of the manuscript.

Funding: This research was funded by Deutsches Zentrum für Luft- und Raumfahrt (DLR), grant numbers 50WB1524 and 50WB1924.

Acknowledgments: The authors would like to thank the Institute of Anatomy (Otto von Guericke University), especially Stefan Kahlert and Andrea Kröber, for the technical support. We also acknowledge financial support by the Open Access Publication Fonds of the Otto von Guericke University Magdeburg.

Conflicts of Interest: The authors declare no conflicts of interest.

References

1. Kadmiel, M.; Cidlowski, J.A. Glucocorticoid receptor signaling in health and disease. *Trends Pharmacol. Sci.* **2013**, *34*, 518–530. [CrossRef] [PubMed]
2. Mangelsdorf, D.J.; Thummel, C.; Beato, M.; Herrlich, P.; Schütz, G.; Umesono, K.; Blumberg, B.; Kastner, P.; Mark, M.; Chambon, P.; et al. The nuclear receptor superfamily: The second decade. *Cell* **1995**, *83*, 835–839. [CrossRef]
3. Coutinho, A.E.; Chapman, K.E. The anti-inflammatory and immunosuppressive effects of glucocorticoids, recent developments and mechanistic insights. *Mol. Cell. Endocrinol.* **2011**, *335*, 2–13. [CrossRef]
4. Vandevyver, S.; Dejager, L.; Tuckermann, J.; Libert, C. New insights into the anti-inflammatory mechanisms of glucocorticoids: An emerging role for glucocorticoid-receptor-mediated transactivation. *Endocrinology* **2013**, *154*, 993–1007. [CrossRef]
5. Vandewalle, J.; Luypaert, A.; De Bosscher, K.; Libert, C. Therapeutic mechanisms of glucocorticoids. *Trends Endocrinol. Metab.* **2018**, *29*, 42–54. [CrossRef]
6. Herr, I.; Pfitzenmaier, J. Glucocorticoid use in prostate cancer and other solid tumours: Implications for effectiveness of cytotoxic treatment and metastases. *Lancet Oncol.* **2006**, *7*, 425–430. [CrossRef]
7. Wang, H.; Wang, Y.; Rayburn, E.R.; Hill, D.L.; Rinehart, J.J.; Zhang, R. Dexamethasone as a chemosensitizer for breast cancer chemotherapy: Potentiation of the antitumor activity of adriamycin, modulation of cytokine expression, and pharmacokinetics. *Int. J. Oncol.* **2007**, *30*, 947–953. [CrossRef]
8. Yennurajalingam, S.; Frisbee-Hume, S.; Palmer, J.L.; Delgado-Guay, M.O.; Bull, J.; Phan, A.T.; Tannir, N.M.; Litton, J.K.; Reddy, A.; Hui, D.; et al. Reduction of cancer-related fatigue with dexamethasone: A double-blind, randomized, placebo-controlled trial in patients with advanced cancer. *J. Clin. Oncol.* **2013**, *31*, 3076–3082. [CrossRef]
9. Wang, L.J.; Li, J.; Hao, F.R.; Yuan, Y.; Li, J.Y.; Lu, W.; Zhou, T.Y. Dexamethasone suppresses the growth of human non-small cell lung cancer via inducing estrogen sulfotransferase and inactivating estrogen. *Acta Pharmacol. Sin.* **2016**, *37*, 845–856. [CrossRef]
10. Lin, K.-T.; Sun, S.-P.; Wu, J.-I.; Wang, L.-H. Low-dose glucocorticoids suppresses ovarian tumor growth and metastasis in an immunocompetent syngeneic mouse model. *PLoS ONE* **2017**, *12*, e0178937. [CrossRef]
11. Gong, H.; Jarzynka, M.J.; Cole, T.J.; Lee, J.H.; Wada, T.; Zhang, B.; Gao, J.; Song, W.C.; DeFranco, D.B.; Cheng, S.Y.; et al. Glucocorticoids antagonize estrogens by glucocorticoid receptor-mediated activation of estrogen sulfotransferase. *Cancer Res.* **2008**, *68*, 7386–7393. [CrossRef] [PubMed]
12. Geng, Y.; Wang, J.; Jing, H.; Wang, H.W.; Bao, Y.X. Inhibitory effect of dexamethasone on lewis mice lung cancer cells. *Genet. Mol. Res.* **2014**, *13*, 6827–6836. [CrossRef] [PubMed]
13. Moon, E.Y.; Ryu, Y.K.; Lee, G.H. Dexamethasone inhibits in vivo tumor growth by the alteration of bone marrow cd11b(+) myeloid cells. *Int. Immunopharmacol.* **2014**, *21*, 494–500. [CrossRef] [PubMed]
14. Sau, S.; Banerjee, R. Cationic lipid-conjugated dexamethasone as a selective antitumor agent. *Eur. J. Med. Chem.* **2014**, *83*, 433–447. [CrossRef] [PubMed]
15. Komiya, A.; Shimbo, M.; Suzuki, H.; Imamoto, T.; Kato, T.; Fukasawa, S.; Kamiya, N.; Naya, Y.; Mori, I.; Ichikawa, T. Oral low-dose dexamethasone for androgen-independent prostate cancer patients. *Oncol. Lett.* **2010**, *1*, 73–79. [CrossRef] [PubMed]
16. Bray, F.; Ferlay, J.; Soerjomataram, I.; Siegel, R.L.; Torre, L.A.; Jemal, A. Global cancer statistics 2018: Globocan estimates of incidence and mortality worldwide for 36 cancers in 185 countries. *CA* **2018**, *68*, 394–424. [CrossRef]
17. Kim, J.; Gosnell, J.E.; Roman, S.A. Geographic influences in the global rise of thyroid cancer. *Nat. Rev. Endocrinol.* **2019**, *16*, 17–29. [CrossRef]
18. Pachmayr, E.; Treese, C.; Stein, U. Underlying mechanisms for distant metastasis—Molecular biology. *Visc. Med.* **2017**, *33*, 11–20. [CrossRef]
19. Yilmaz, M.; Christofori, G. Mechanisms of motility in metastasizing cells. *Mol. Cancer Res.* **2010**, *8*, 629–642. [CrossRef]
20. Paszek, M.J.; Zahir, N.; Johnson, K.R.; Lakins, J.N.; Rozenberg, G.I.; Gefen, A.; Reinhart-King, C.A.; Margulies, S.S.; Dembo, M.; Boettiger, D.; et al. Tensional homeostasis and the malignant phenotype. *Cancer Cell* **2005**, *8*, 241–254. [CrossRef]

21. Moore, S.W.; Roca-Cusachs, P.; Sheetz, M.P. Stretchy proteins on stretchy substrates: The important elements of integrin-mediated rigidity sensing. *Dev. Cell* **2010**, *19*, 194–206. [CrossRef] [PubMed]
22. Roussos, E.T.; Condeelis, J.S.; Patsialou, A. Chemotaxis in cancer. *Nat. Rev. Cancer* **2011**, *11*, 573–587. [CrossRef] [PubMed]
23. Brabletz, T.; Kalluri, R.; Nieto, M.A.; Weinberg, R.A. Emt in cancer. *Nat. Rev. Cancer* **2018**, *18*, 128–134. [CrossRef] [PubMed]
24. Yu, W.; Yang, L.; Li, T.; Zhang, Y. Cadherin signaling in cancer: Its functions and role as a therapeutic target. *Front. Oncol.* **2019**, *9*, 989. [CrossRef]
25. Taddei, M.L.; Giannoni, E.; Fiaschi, T.; Chiarugi, P. Anoikis: An emerging hallmark in health and diseases. *J. Pathol.* **2012**, *226*, 380–393. [CrossRef]
26. Paoli, P.; Giannoni, E.; Chiarugi, P. Anoikis molecular pathways and its role in cancer progression. *Biochim. Biophys. Acta* **2013**, *1833*, 3481–3498. [CrossRef]
27. Chang, T.T.; Hughes-Fulford, M. Molecular mechanisms underlying the enhanced functions of three-dimensional hepatocyte aggregates. *Biomaterials* **2014**, *35*, 2162–2171. [CrossRef]
28. Kopp, S.; Warnke, E.; Wehland, M.; Aleshcheva, G.; Magnusson, N.E.; Hemmersbach, R.; Corydon, T.J.; Bauer, J.; Infanger, M.; Grimm, D. Mechanisms of three-dimensional growth of thyroid cells during long-term simulated microgravity. *Sci. Rep.* **2015**, *5*, 16691. [CrossRef]
29. Kunz-Schughart, L.A. Multicellular tumor spheroids: Intermediates between monolayer culture and in vivo tumor. *Cell Biol. Int.* **1999**, *23*, 157–161. [CrossRef]
30. Martin, A.; Zhou, A.; Gordon, R.E.; Henderson, S.C.; Schwartz, A.E.; Schwartz, A.E.; Friedman, E.W.; Davies, T.F. Thyroid organoid formation in simulated microgravity: Influence of keratinocyte growth factor. *Thyroid* **2000**, *10*, 481–487. [CrossRef] [PubMed]
31. Bauer, J.; Grimm, D.; Gombocz, E. Semantic analysis of thyroid cancer cell proteins obtained from rare research opportunities. *J. Biomed. Inf.* **2017**, *76*, 138–153. [CrossRef] [PubMed]
32. Bauer, J.; Wehland, M.; Infanger, M.; Grimm, D.; Gombocz, E. Semantic analysis of posttranslational modification of proteins accumulated in thyroid cancer cells exposed to simulated microgravity. *Int. J. Mol. Sci.* **2018**, *19*, 2257. [CrossRef] [PubMed]
33. Krüger, M.; Melnik, D.; Kopp, S.; Buken, C.; Sahana, J.; Bauer, J.; Wehland, M.; Hemmersbach, R.; Corydon, T.J.; Infanger, M.; et al. Fighting thyroid cancer with microgravity research. *Int. J. Mol. Sci.* **2019**, *20*, 2553. [CrossRef] [PubMed]
34. Kopp, S.; Sahana, J.; Islam, T.; Petersen, A.G.; Bauer, J.; Corydon, T.J.; Schulz, H.; Saar, K.; Huebner, N.; Slumstrup, L.; et al. The role of nfkappab in spheroid formation of human breast cancer cells cultured on the random positioning machine. *Sci. Rep.* **2018**, *8*, 921. [CrossRef]
35. Corydon, T.J.; Mann, V.; Slumstrup, L.; Kopp, S.; Sahana, J.; Askou, A.L.; Magnusson, N.E.; Echegoyen, D.; Bek, T.; Sundaresan, A.; et al. Reduced expression of cytoskeletal and extracellular matrix genes in human adult retinal pigment epithelium cells exposed to simulated microgravity. *Cell. Physiol. Biochem.* **2016**, *40*, 1–17. [CrossRef]
36. Grosse, J.; Wehland, M.; Pietsch, J.; Ma, X.; Ulbrich, C.; Schulz, H.; Saar, K.; Hübner, N.; Hauslage, J.; Hemmersbach, R.; et al. Short-term weightlessness produced by parabolic flight maneuvers altered gene expression patterns in human endothelial cells. *Faseb J.* **2012**, *26*, 639–655. [CrossRef]
37. Ma, X.; Pietsch, J.; Wehland, M.; Schulz, H.; Saar, K.; Hübner, N.; Bauer, J.; Braun, M.; Schwarzwälder, A.; Segerer, J.; et al. Differential gene expression profile and altered cytokine secretion of thyroid cancer cells in space. *Faseb J.* **2014**, *28*, 813–835. [CrossRef]
38. Ma, X.; Wehland, M.; Schulz, H.; Saar, K.; Hubner, N.; Infanger, M.; Bauer, J.; Grimm, D. Genomic approach to identify factors that drive the formation of three-dimensional structures by ea.Hy926 endothelial cells. *PLoS ONE* **2013**, *8*, e64402. [CrossRef]
39. Ye, J.; Coulouris, G.; Zaretskaya, I.; Cutcutache, I.; Rozen, S.; Madden, T.L. Primer-blast: A tool to design target-specific primers for polymerase chain reaction. *BMC Bioinform.* **2012**, *13*, 134. [CrossRef]
40. Grosse, J.; Wehland, M.; Pietsch, J.; Schulz, H.; Saar, K.; Hübner, N.; Eilles, C.; Bauer, J.; Abou-El-Ardat, K.; Baatout, S.; et al. Gravity-sensitive signaling drives 3-dimensional formation of multicellular thyroid cancer spheroids. *Faseb J.* **2012**, *26*, 5124–5140. [CrossRef]
41. Pacifico, F.; Leonardi, A. Role of nf-kappab in thyroid cancer. *Mol. Cell. Endocrinol.* **2010**, *321*, 29–35. [CrossRef] [PubMed]

42. Giuliani, C.; Bucci, I.; Napolitano, G. The role of the transcription factor nuclear factor-kappa b in thyroid autoimmunity and cancer. *Front. Endocrinol.* **2018**, *9*, 471. [CrossRef] [PubMed]
43. Bauerle, K.T.; Schweppe, R.E.; Haugen, B.R. Inhibition of nuclear factor-kappa b differentially affects thyroid cancer cell growth, apoptosis, and invasion. *Mol. Cancer* **2010**, *9*, 117. [CrossRef] [PubMed]
44. Yamamoto, Y.; Gaynor, R.B. Therapeutic potential of inhibition of the nf-kappab pathway in the treatment of inflammation and cancer. *J. Clin. Investig.* **2001**, *107*, 135–142. [CrossRef]
45. Holbourn, K.P.; Acharya, K.R.; Perbal, B. The ccn family of proteins: Structure-function relationships. *Trends Biochem. Sci.* **2008**, *33*, 461–473. [CrossRef]
46. Chu, C.Y.; Chang, C.C.; Prakash, E.; Kuo, M.L. Connective tissue growth factor (ctgf) and cancer progression. *J. Biomed. Sci.* **2008**, *15*, 675–685. [CrossRef]
47. Asmis, L.M.; Gerber, H.; Kaempf, J.; Studer, H. Epidermal growth factor stimulates cell proliferation and inhibits iodide uptake of frtl-5 cells in vitro. *J. Endocrinol.* **1995**, *145*, 513–520. [CrossRef]
48. Colletta, G.; Cirafici, A.M.; Di Carlo, A. Dual effect of transforming growth factor beta on rat thyroid cells: Inhibition of thyrotropin-induced proliferation and reduction of thyroid-specific differentiation markers. *Cancer Res.* **1989**, *49*, 3457–3462.
49. Xu, J.; Lamouille, S.; Derynck, R. Tgf-β-induced epithelial to mesenchymal transition. *Cell Res.* **2009**, *19*, 156–172. [CrossRef]
50. Gugnoni, M.; Sancisi, V.; Manzotti, G.; Gandolfi, G.; Ciarrocchi, A. Autophagy and epithelial-mesenchymal transition: An intricate interplay in cancer. *Cell Death Dis.* **2016**, *7*, e2520. [CrossRef]
51. Bhatti, M.Z.; Pan, L.; Wang, T.; Shi, P.; Li, L. Reggamma potentiates tgf-beta/smad signal dependent epithelial-mesenchymal transition in thyroid cancer cells. *Cell Signal.* **2019**, *64*, 109412. [CrossRef]
52. Riwaldt, S.; Bauer, J.; Wehland, M.; Slumstrup, L.; Kopp, S.; Warnke, E.; Dittrich, A.; Magnusson, N.E.; Pietsch, J.; Corydon, T.J.; et al. Pathways regulating spheroid formation of human follicular thyroid cancer cells under simulated microgravity conditions: A genetic approach. *Int. J. Mol. Sci.* **2016**, *17*, 528. [CrossRef]
53. Chung, Y.J.; Lee, J.I.; Chong, S.; Seok, J.W.; Park, S.J.; Jang, H.W.; Kim, S.W.; Chung, J.H. Anti-proliferative effect and action mechanism of dexamethasone in human medullary thyroid cancer cell line. *Endocr. Res.* **2011**, *36*, 149–157. [CrossRef]
54. Scholzen, T.; Gerdes, J. The ki-67 protein: From the known and the unknown. *J. Cell. Physiol.* **2000**, *182*, 311–322. [CrossRef]
55. Chen, Z.Y.; Guo, S.; Li, B.B.; Jiang, N.; Li, A.; Yan, H.F.; Yang, H.M.; Zhou, J.L.; Li, C.L.; Cui, Y. Effect of weightlessness on the 3d structure formation and physiologic function of human cancer cells. *Biomed. Res. Int.* **2019**, *2019*, 4894083. [CrossRef]
56. Da, C.; Wu, K.; Yue, C.; Bai, P.; Wang, R.; Wang, G.; Zhao, M.; Lv, Y.; Hou, P. N-cadherin promotes thyroid tumorigenesis through modulating major signaling pathways. *Oncotarget* **2017**, *8*, 8131–8142. [CrossRef]
57. Vasko, V.; Espinosa, A.V.; Scouten, W.; He, H.; Auer, H.; Liyanarachchi, S.; Larin, A.; Savchenko, V.; Francis, G.L.; de la Chapelle, A.; et al. Gene expression and functional evidence of epithelial-to-mesenchymal transition in papillary thyroid carcinoma invasion. *Proc. Natl. Acad. Sci. USA* **2007**, *104*, 2803–2808. [CrossRef]
58. Su, H.; Bidere, N.; Zheng, L.; Cubre, A.; Sakai, K.; Dale, J.; Salmena, L.; Hakem, R.; Straus, S.; Lenardo, M. Requirement for caspase-8 in nf-kappab activation by antigen receptor. *Science* **2005**, *307*, 1465–1468. [CrossRef]
59. Schott, A.F.; Apel, I.J.; Nuñez, G.; Clarke, M.F. Bcl-xl protects cancer cells from p53-mediated apoptosis. *Oncogene* **1995**, *11*, 1389–1394.
60. Li, M.; Wang, D.; He, J.; Chen, L.; Li, H. Bcl-xl: A multifunctional anti-apoptotic protein. *Pharmacol. Res.* **2020**, *151*, 104547. [CrossRef]
61. Fiucci, G.; Ravid, D.; Reich, R.; Liscovitch, M. Caveolin-1 inhibits anchorage-independent growth, anoikis and invasiveness in mcf-7 human breast cancer cells. *Oncogene* **2002**, *21*, 2365–2375. [CrossRef] [PubMed]
62. Reginato, M.J.; Mills, K.R.; Paulus, J.K.; Lynch, D.K.; Sgroi, D.C.; Debnath, J.; Muthuswamy, S.K.; Brugge, J.S. Integrins and egfr coordinately regulate the pro-apoptotic protein bim to prevent anoikis. *Nat. Cell Biol.* **2003**, *5*, 733–740. [CrossRef] [PubMed]
63. Rohwer, N.; Welzel, M.; Daskalow, K.; Pfander, D.; Wiedenmann, B.; Detjen, K.; Cramer, T. Hypoxia-inducible factor 1alpha mediates anoikis resistance via suppression of alpha5 integrin. *Cancer Res.* **2008**, *68*, 10113–10120. [CrossRef] [PubMed]

64. Riwaldt, S.; Pietsch, J.; Sickmann, A.; Bauer, J.; Braun, M.; Segerer, J.; Schwarzwälder, A.; Aleshcheva, G.; Corydon, T.J.; Infanger, M.; et al. Identification of proteins involved in inhibition of spheroid formation under microgravity. *Proteomics* **2015**, *15*, 2945–2952. [CrossRef]
65. Warnke, E.; Pietsch, J.; Wehland, M.; Bauer, J.; Infanger, M.; Görög, M.; Hemmersbach, R.; Braun, M.; Ma, X.; Sahana, J.; et al. Spheroid formation of human thyroid cancer cells under simulated microgravity: A possible role of ctgf and cav1. *Cell Commun. Signal.* **2014**, *12*, 32. [CrossRef]
66. Abu-Absi, S.F.; Hu, W.-S.; Hansen, L.K. Dexamethasone effects on rat hepatocyte spheroid formation and function. *Tissue Eng.* **2005**, *11*, 415–426. [CrossRef]
67. Thiery, J.P. Epithelial–mesenchymal transitions in tumour progression. *Nat. Rev. Cancer* **2002**, *2*, 442–454. [CrossRef]
68. Zheng, Y.; Izumi, K.; Li, Y.; Ishiguro, H.; Miyamoto, H. Contrary regulation of bladder cancer cell proliferation and invasion by dexamethasone-mediated glucocorticoid receptor signals. *Mol. Cancer Ther.* **2012**, *11*, 2621–2632. [CrossRef]
69. Kim, J.H.; Hwang, Y.-J.; Han, S.H.; Lee, Y.E.; Kim, S.; Kim, Y.J.; Cho, J.H.; Kwon, K.A.; Kim, J.H.; Kim, S.-H. Dexamethasone inhibits hypoxia-induced epithelial-mesenchymal transition in colon cancer. *World J. Gastroenterol.* **2015**, *21*, 9887–9899. [CrossRef]
70. Jang, Y.H.; Shin, H.S.; Sun Choi, H.; Ryu, E.S.; Jin Kim, M.; Ki Min, S.; Lee, J.H.; Kook Lee, H.; Kim, K.H.; Kang, D.H. Effects of dexamethasone on the tgf-beta1-induced epithelial-to-mesenchymal transition in human peritoneal mesothelial cells. *Lab. Investig.* **2013**, *93*, 194–206. [CrossRef]
71. Parrelli, J.M.; Meisler, N.; Cutroneo, K.R. Identification of a glucocorticoid response element in the human transforming growth factor beta 1 gene promoter. *Int. J. Biochem. Cell Biol.* **1998**, *30*, 623–627. [CrossRef]
72. Huber, M.A.; Kraut, N.; Beug, H. Molecular requirements for epithelial-mesenchymal transition during tumor progression. *Curr. Opin. Cell Biol.* **2005**, *17*, 548–558. [CrossRef]
73. Ivanova, K.; Ananiev, J.; Aleksandrova, E.; Ignatova, M.M.; Gulubova, M. Expression of e-cadherin/beta-catenin in epithelial carcinomas of the thyroid gland. *Open Access Maced. J. Med. Sci.* **2017**, *5*, 155–159. [CrossRef]
74. Hinz, B. The extracellular matrix and transforming growth factor-β1: Tale of a strained relationship. *Matrix Biol.* **2015**, *47*, 54–65. [CrossRef]
75. Beheshti, A.; Ray, S.; Fogle, H.; Berrios, D.; Costes, S.V. A microrna signature and tgf-β1 response were identified as the key master regulators for spaceflight response. *PLoS ONE* **2018**, *13*, e0199621. [CrossRef]
76. Li, Z.; Chen, Y.; Cao, D.; Wang, Y.; Chen, G.; Zhang, S.; Lu, J. Glucocorticoid up-regulates transforming growth factor-β (tgf-β) type ii receptor and enhances tgf-β signaling in human prostate cancer pc-3 cells. *Endocrinology* **2006**, *147*, 5259–5267. [CrossRef]
77. Liu, L.; Aleksandrowicz, E.; Schonsiegel, F.; Groner, D.; Bauer, N.; Nwaeburu, C.C.; Zhao, Z.; Gladkich, J.; Hoppe-Tichy, T.; Yefenof, E.; et al. Dexamethasone mediates pancreatic cancer progression by glucocorticoid receptor, tgfbeta and jnk/ap-1. *Cell Death Dis.* **2017**, *8*, e3064. [CrossRef]
78. Ameri, W.A.; Ahmed, I.; Al-Dasim, F.M.; Mohamoud, Y.A.; AlAzwani, I.K.; Malek, J.A.; Karedath, T. Tgf-β mediated cell adhesion dynamics and epithelial to mesenchymal transition in 3d and 2d ovarian cancer models. *Biorxiv* **2018**, 465617. [CrossRef]
79. Sodek, K.L.; Ringuette, M.J.; Brown, T.J. Compact spheroid formation by ovarian cancer cells is associated with contractile behavior and an invasive phenotype. *Int. J. Cancer* **2009**, *124*, 2060–2070. [CrossRef]
80. Mitra, T.; Roy, S.S. Co-activation of tgfβ and wnt signalling pathways abrogates emt in ovarian cancer cells. *Cell. Physiol. Biochem.* **2017**, *41*, 1336–1345. [CrossRef]
81. Peinado, H.; Olmeda, D.; Cano, A. Snail, zeb and bhlh factors in tumour progression: An alliance against the epithelial phenotype? *Nat. Rev. Cancer* **2007**, *7*, 415–428. [CrossRef] [PubMed]
82. Yook, J.I.; Li, X.Y.; Ota, I.; Fearon, E.R.; Weiss, S.J. Wnt-dependent regulation of the e-cadherin repressor snail. *J. Biol. Chem.* **2005**, *280*, 11740–11748. [CrossRef]
83. Lin, R.Z.; Chou, L.F.; Chien, C.C.; Chang, H.Y. Dynamic analysis of hepatoma spheroid formation: Roles of e-cadherin and beta1-integrin. *Cell Tissue Res.* **2006**, *324*, 411–422. [CrossRef] [PubMed]
84. Smyrek, I.; Mathew, B.; Fischer, S.C.; Lissek, S.M.; Becker, S.; Stelzer, E.H.K. E-cadherin, actin, microtubules and fak dominate different spheroid formation phases and important elements of tissue integrity. *Biol. Open* **2019**, *8*, bio037051. [CrossRef]

85. Sahana, J.; Nassef, M.Z.; Wehland, M.; Kopp, S.; Krüger, M.; Corydon, T.J.; Infanger, M.; Bauer, J.; Grimm, D. Decreased e-cadherin in mcf7 human breast cancer cells forming multicellular spheroids exposed to simulated microgravity. *Proteomics* **2018**, *18*, e1800015. [CrossRef]
86. Pease, J.C.; Brewer, M.; Tirnauer, J.S. Spontaneous spheroid budding from monolayers: A potential contribution to ovarian cancer dissemination. *Biol. Open* **2012**, *1*, 622–628. [CrossRef]
87. Shimazui, T.; Schalken, J.A.; Kawai, K.; Kawamoto, R.; van Bockhoven, A.; Oosterwijk, E.; Akaza, H. Role of complex cadherins in cell-cell adhesion evaluated by spheroid formation in renal cell carcinoma cell lines. *Oncol. Rep.* **2004**, *11*, 357–360. [CrossRef]
88. Tsai, C.-W.; Wang, J.-H.; Young, T.-H. Core/shell multicellular spheroids on chitosan as in vitro 3d coculture tumor models. *Artif. Cells Nanomed. Biotechnol.* **2018**, *46*, S651–S660. [CrossRef]
89. Katsamba, P.; Carroll, K.; Ahlsen, G.; Bahna, F.; Vendome, J.; Posy, S.; Rajebhosale, M.; Price, S.; Jessell, T.M.; Ben-Shaul, A.; et al. Linking molecular affinity and cellular specificity in cadherin-mediated adhesion. *Proc. Natl. Acad. Sci. USA* **2009**, *106*, 11594–11599. [CrossRef]
90. Shannon, S.; Vaca, C.; Jia, D.; Entersz, I.; Schaer, A.; Carcione, J.; Weaver, M.; Avidar, Y.; Pettit, R.; Nair, M.; et al. Dexamethasone-mediated activation of fibronectin matrix assembly reduces dispersal of primary human glioblastoma cells. *PLoS ONE* **2015**, *10*, e0135951. [CrossRef]
91. Robinson, E.E.; Foty, R.A.; Corbett, S.A. Fibronectin matrix assembly regulates α5β1-mediated cell cohesion. *Mol. Biol. Cell* **2004**, *15*, 973–981. [CrossRef]
92. Naves, M.A.; Pereira, R.M.; Comodo, A.N.; de Alvarenga, E.L.; Caparbo, V.F.; Teixeira, V.P. Effect of dexamethasone on human osteoblasts in culture: Involvement of beta1 integrin and integrin-linked kinase. *Cell Biol. Int.* **2011**, *35*, 1147–1151. [CrossRef]
93. Petrella, A.; Ercolino, S.F.; Festa, M.; Gentilella, A.; Tosco, A.; Conzen, S.D.; Parente, L. Dexamethasone inhibits trail-induced apoptosis of thyroid cancer cells via bcl-xl induction. *Eur. J. Cancer* **2006**, *42*, 3287–3293. [CrossRef]
94. Gazitt, Y.; Fey, V.; Thomas, C.; Alvarez, R. Bcl-2 overexpression is associated with resistance to dexamethasone, but not melphalan, in multiple myeloma cells. *Int. J. Oncol.* **1998**, *13*, 397–405. [CrossRef]
95. Lin, Y.; Fukuchi, J.; Hiipakka, R.A.; Kokontis, J.M.; Xiang, J. Up-regulation of bcl-2 is required for the progression of prostate cancer cells from an androgen-dependent to an androgen-independent growth stage. *Cell Res.* **2007**, *17*, 531–536. [CrossRef]
96. Toruner, M.; Fernandez-Zapico, M.; Sha, J.J.; Pham, L.; Urrutia, R.; Egan, L.J. Antianoikis effect of nuclear factor-kappab through up-regulated expression of osteoprotegerin, bcl-2, and iap-1. *J. Biol. Chem.* **2006**, *281*, 8686–8696. [CrossRef]
97. Bergin, E.; Levine, J.S.; Koh, J.S.; Lieberthal, W. Mouse proximal tubular cell-cell adhesion inhibits apoptosis by a cadherin-dependent mechanism. *Am. J. Physiol. Renal Physiol.* **2000**, *278*, F758–F768. [CrossRef]
98. Kantak, S.S.; Kramer, R.H. E-cadherin regulates anchorage-independent growth and survival in oral squamous cell carcinoma cells. *J. Biol. Chem.* **1998**, *273*, 16953–16961. [CrossRef]
99. Orford, K.; Orford, C.C.; Byers, S.W. Exogenous expression of beta-catenin regulates contact inhibition, anchorage-independent growth, anoikis, and radiation-induced cell cycle arrest. *J. Cell. Biol.* **1999**, *146*, 855–868. [CrossRef]
100. Riwaldt, S.; Bauer, J.; Pietsch, J.; Braun, M.; Segerer, J.; Schwarzwälder, A.; Corydon, T.J.; Infanger, M.; Grimm, D. The importance of caveolin-1 as key-regulator of three-dimensional growth in thyroid cancer cells cultured under real and simulated microgravity conditions. *Int. J. Mol. Sci.* **2015**, *16*, 28296–28310. [CrossRef]
101. Liu, W.R.; Jin, L.; Tian, M.X.; Jiang, X.F.; Yang, L.X.; Ding, Z.B.; Shen, Y.H.; Peng, Y.F.; Gao, D.M.; Zhou, J.; et al. Caveolin-1 promotes tumor growth and metastasis via autophagy inhibition in hepatocellular carcinoma. *Clin. Res. Hepatol. Gastroenterol.* **2016**, *40*, 169–178. [CrossRef] [PubMed]
102. Chatterjee, M.; Ben-Josef, E.; Thomas, D.G.; Morgan, M.A.; Zalupski, M.M.; Khan, G.; Andrew Robinson, C.; Griffith, K.A.; Chen, C.-S.; Ludwig, T.; et al. Caveolin-1 is associated with tumor progression and confers a multi-modality resistance phenotype in pancreatic cancer. *Sci. Rep.* **2015**, *5*, 10867. [CrossRef] [PubMed]
103. Sinha, B.; Köster, D.; Ruez, R.; Gonnord, P.; Bastiani, M.; Abankwa, D.; Stan, R.V.; Butler-Browne, G.; Vedie, B.; Johannes, L.; et al. Cells respond to mechanical stress by rapid disassembly of caveolae. *Cell* **2011**, *144*, 402–413. [CrossRef] [PubMed]
104. Moreno-Vicente, R.; Pavon, D.M.; Martin-Padura, I.; Catala-Montoro, M.; Diez-Sanchez, A.; Quilez-Alvarez, A.; Lopez, J.A.; Sanchez-Alvarez, M.; Vazquez, J.; Strippoli, R.; et al. Caveolin-1 modulates mechanotransduction

responses to substrate stiffness through actin-dependent control of yap. *Cell Rep.* **2018**, *25*, 1622–1635.e1626. [CrossRef] [PubMed]
105. Pietsch, J.; Ma, X.; Wehland, M.; Aleshcheva, G.; Schwarzwälder, A.; Segerer, J.; Birlem, M.; Horn, A.; Bauer, J.; Infanger, M.; et al. Spheroid formation of human thyroid cancer cells in an automated culturing system during the shenzhou-8 space mission. *Biomaterials* **2013**, *34*, 7694–7705. [CrossRef]
106. Cui, L.; Zhang, Q.; Mao, Z.; Chen, J.; Wang, X.; Qu, J.; Zhang, J.; Jin, D. Ctgf is overexpressed in papillary thyroid carcinoma and promotes the growth of papillary thyroid cancer cells. *Tumour Biol.* **2011**, *32*, 721–728. [CrossRef]
107. Dufau, I.; Frongia, C.; Sicard, F.; Dedieu, L.; Cordelier, P.; Ausseil, F.; Ducommun, B.; Valette, A. Multicellular tumor spheroid model to evaluate spatio-temporal dynamics effect of chemotherapeutics: Application to the gemcitabine/chk1 inhibitor combination in pancreatic cancer. *BMC Cancer* **2012**, *12*, 15. [CrossRef]
108. Engebraaten, O.; Bjerkvig, R.; Pedersen, P.H.; Laerum, O.D. Effects of egf, bfgf, ngf and pdgf(bb) on cell proliferative, migratory and invasive capacities of human brain-tumour biopsies in vitro. *Int. J. Cancer* **1993**, *53*, 209–214. [CrossRef]
109. Mueller-Klieser, W. Three-dimensional cell cultures: From molecular mechanisms to clinical applications. *Am. J. Physiol.* **1997**, *273*, C1109–C1123. [CrossRef]
110. Lichtenberger, B.M.; Tan, P.K.; Niederleithner, H.; Ferrara, N.; Petzelbauer, P.; Sibilia, M. Autocrine vegf signaling synergizes with egfr in tumor cells to promote epithelial cancer development. *Cell* **2010**, *140*, 268–279. [CrossRef]
111. Klein, M.; Vignaud, J.M.; Hennequin, V.; Toussaint, B.; Bresler, L.; Plenat, F.; Leclere, J.; Duprez, A.; Weryha, G. Increased expression of the vascular endothelial growth factor is a pejorative prognosis marker in papillary thyroid carcinoma. *J. Clin. Endocrinol. Metab.* **2001**, *86*, 656–658. [CrossRef] [PubMed]
112. Karaca, Z.; Tanriverdi, F.; Unluhizarci, K.; Ozturk, F.; Gokahmetoglu, S.; Elbuken, G.; Cakir, I.; Bayram, F.; Kelestimur, F. Vegfr1 expression is related to lymph node metastasis and serum vegf may be a marker of progression in the follow-up of patients with differentiated thyroid carcinoma. *Eur. J. Endocrinol.* **2011**, *164*, 277–284. [CrossRef] [PubMed]
113. Waleh, N.S.; Brody, M.D.; Knapp, M.A.; Mendonca, H.L.; Lord, E.M.; Koch, C.J.; Laderoute, K.R.; Sutherland, R.M. Mapping of the vascular endothelial growth factor-producing hypoxic cells in multicellular tumor spheroids using a hypoxia-specific marker. *Cancer Res.* **1995**, *55*, 6222–6226. [PubMed]
114. Vieira, J.M.; Santos, S.C.; Espadinha, C.; Correia, I.; Vag, T.; Casalou, C.; Cavaco, B.M.; Catarino, A.L.; Dias, S.; Leite, V. Expression of vascular endothelial growth factor (vegf) and its receptors in thyroid carcinomas of follicular origin: A potential autocrine loop. *Eur. J. Endocrinol.* **2005**, *153*, 701–709. [CrossRef] [PubMed]
115. Shim, S.H.; Hah, J.H.; Hwang, S.Y.; Heo, D.S.; Sung, M.W. Dexamethasone treatment inhibits vegf production via suppression of stat3 in a head and neck cancer cell line. *Oncol. Rep.* **2010**, *23*, 1139–1143. [CrossRef]
116. Grun, D.; Adhikary, G.; Eckert, R.L. Vegf-a acts via neuropilin-1 to enhance epidermal cancer stem cell survival and formation of aggressive and highly vascularized tumors. *Oncogene* **2016**, *35*, 4379–4387. [CrossRef]
117. Meng, X.G.; Yue, S.W. Dexamethasone disrupts cytoskeleton organization and migration of t47d human breast cancer cells by modulating the akt/mtor/rhoa pathway. *Asian Pac. J. Cancer Prev.* **2014**, *15*, 10245–10250. [CrossRef]
118. Srivastava, A.; Kumar, A.; Giangiobbe, S.; Bonora, E.; Hemminki, K.; Forsti, A.; Bandapalli, O.R. Whole genome sequencing of familial non-medullary thyroid cancer identifies germline alterations in mapk/erk and pi3k/akt signaling pathways. *Biomolecules* **2019**, *9*, 605. [CrossRef]



© 2020 by the authors. Licensee MDPI, Basel, Switzerland. This article is an open access article distributed under the terms and conditions of the Creative Commons Attribution (CC BY) license (http://creativecommons.org/licenses/by/4.0/).

biomolecules

MDPI

Article

The Formation of Stable Lung Tumor Spheroids during Random Positioning Involves Increased Estrogen Sensitivity

Balkis Barkia [1], Viviann Sandt [1], Daniela Melnik [1], José Luis Cortés-Sánchez [1,†], Shannon Marchal [1], Bjorn Baselet [2], Sarah Baatout [2,3], Jayashree Sahana [4], Daniela Grimm [4], Markus Wehland [1,5], Herbert Schulz [1,5], Manfred Infanger [5,6], Armin Kraus [5,6,‡] and Marcus Krüger [1,5,*,‡]

1 Department of Microgravity and Translational Regenerative Medicine, Otto von Guericke University, 39106 Magdeburg, Germany; balkissbarkia@gmail.com (B.B.); viviann.sandt@med.ovgu.de (V.S.); daniela.melnik@med.ovgu.de (D.M.); jose.cortes@ovgu.de (J.L.C.-S.); shannon.marchal@med.ovgu.de (S.M.); markus.wehland@med.ovgu.de (M.W.); herbert.schulz@med.ovgu.de (H.S.)
2 Radiobiology Unit, Belgian Nuclear Research Centre SCK-CEN, 2400 Mol, Belgium; bjorn.baselet@sckcen.be (B.B.); sarah.baatout@sckcen.be (S.B.)
3 Department of Biotechnology, Faculty of Bioscience Engineering, Ghent University, 9000 Ghent, Belgium
4 Department of Biomedicine, Faculty of Health, Aarhus University, 8000 Aarhus, Denmark; jaysaha@biomed.au.dk (J.S.); dgg@biomed.au.dk (D.G.)
5 Research Group "Magdeburger Arbeitsgemeinschaft für Forschung unter Raumfahrt- und Schwerelosigkeitsbedingungen" (MARS), Otto von Guericke University, 39106 Magdeburg, Germany; manfred.infanger@med.ovgu.de (M.I.); armin.kraus@med.ovgu.de (A.K.)
6 Clinic for Plastic, Aesthetic and Hand Surgery, University Hospital Magdeburg, 39120 Magdeburg, Germany
* Correspondence: marcus.krueger@med.ovgu.de; Tel.: +49-391-67-57471
† Current address: Institute of Anatomy, University Hospital Magdeburg, 39120 Magdeburg, Germany.
‡ These authors contributed equally to this work.

Abstract: The formation of tumor spheroids on the random positioning machine (RPM) is a complex and important process, as it enables the study of metastasis ex vivo. However, this process is not yet understood in detail. In this study, we compared the RPM-induced spheroid formation of two cell types of lung carcinoma (NCI-H1703 squamous cell carcinoma cells and Calu-3 adenocarcinoma cells). While NCI-H1703 cells were mainly present as spheroids after 3 days of random positioning, Calu-3 cells remained predominantly as a cell layer. We found that two-dimensional-growing Calu-3 cells have less mucin-1, further downregulate their expression on the RPM and therefore exhibit a higher adhesiveness. In addition, we observed that Calu-3 cells can form spheroids, but they are unstable due to an imbalanced ratio of adhesion proteins (β_1-integrin, E-cadherin) and anti-adhesion proteins (mucin-1) and are likely to disintegrate in the shear environment of the RPM. RPM-exposed Calu-3 cells showed a strongly upregulated expression of the estrogen receptor alpha gene *ESR1*. In the presence of 17β-estradiol or phenol red, more stable Calu-3 spheroids were formed, which was presumably related to an increased amount of E-cadherin in the cell aggregates. Thus, RPM-induced tumor spheroid formation depends not solely on cell-type-specific properties but also on the complex interplay between the mechanical influences of the RPM and, to some extent, the chemical composition of the medium used during the experiments.

Keywords: lung cancer; tumor spheroids; simulated microgravity; cell signaling; phenol red

check for updates

Citation: Barkia, B.; Sandt, V.; Melnik, D.; Cortés-Sánchez, J.L.; Marchal, S.; Baselet, B.; Baatout, S.; Sahana, J.; Grimm, D.; Wehland, M.; et al. The Formation of Stable Lung Tumor Spheroids during Random Positioning Involves Increased Estrogen Sensitivity. *Biomolecules* **2024**, *14*, 1292. https://doi.org/10.3390/biom14101292

Academic Editor: Leonard B. Maggi Jr.

Received: 6 September 2024
Revised: 1 October 2024
Accepted: 10 October 2024
Published: 12 October 2024

Copyright: © 2024 by the authors. Licensee MDPI, Basel, Switzerland. This article is an open access article distributed under the terms and conditions of the Creative Commons Attribution (CC BY) license (https://creativecommons.org/licenses/by/4.0/).

1. Introduction

The random positioning machine (RPM) is a tool originally from gravitational biology and space medicine that can be used to research new ways of fighting cancer [1,2]. The RPM has already been used to study various types of cancer, including thyroid, pancreatic, breast and prostate cancer [3–11]. One effect that has been observed in all cancer cells examined on the RPM so far is the detachment of cells from the cell layer and the subsequent formation of three-dimensional tumor spheroids. This process, which shows molecular biological

similarity to metastasis in vivo, has recently led to the designation of the RPM culture of cancer cells as an in vitro metastasis model [12–14]. However, the morphology and quality of tumor spheroid formation depends on the cell type used and its response to the RPM cell culture environment. MCF-7 breast cancer cells, for example, form glandular spheroids [11], while FTC-133 thyroid tumor spheroids show compact aggregation [10]. The spheroids from PC-3 prostate carcinoma cells are somewhat unstable and loose during the first few days on the RPM [3]. The amount of expressed membrane glycoproteins such as the anti-adhesive mucin-1 also has an influence on the number of spheroids formed by random positioning from ML-1 thyroid carcinoma cells and LnCAP prostate carcinoma cells [14].

Lung carcinoma cells have rarely been examined on the RPM. However, lung cancer is one of the most common and deadliest type of cancer worldwide. According to the latest GLOBOCAN data, lung cancer now ranks first in both incidence (12.4% of all sites) and mortality (18.7% of all sites), ahead of breast, colorectal and prostate cancer [15]. New therapeutic strategies and in vitro approaches for more detailed research are therefore urgently needed, as the prognosis is particularly poor for non-small cell lung cancer (NSCLC) patients, who account for 85% of lung cancer cases [16]. Lung cancer usually only becomes noticeable when it has spread to a high degree in the lungs or metastasized to other parts of the body. When lung carcinomas are discovered, they are usually at metastatic stage IIIB or IV [16,17]. During metastasis, there are two different forms of lung tumor cell migration: the movement of single cells or small cell clusters, as seen in small cell carcinomas (SCLCs) and undifferentiated NSCLCs, and the movement of large clusters of organized cells, as typically seen in adenocarcinomas or some cases of squamous cell carcinomas (both NSCLCs) [17]. The organized cell clusters, which were similarly observed as tumor spheroids in RPM experiments for other types of cancer, suggest a more detailed investigation in the "in vitro metastasis model". Following the pilot study by Ahn et al. [18], which showed that the migration rate of two-dimensional-growing A549 cells under random positioning was faster than that of NCI-H1703, we are the second team to compare cells from a squamous cell carcinoma with cells from an adenocarcinoma on the RPM; this time focusing on tumor spheroids.

2. Materials and Methods

2.1. Cell Lines and Cell Culture

The NCI-H1703 lung squamous cell carcinoma cell line (passages 20–28) was purchased from ATCC (Manassas, VA, USA). The Calu-3 lung adenocarcinoma cell line (passages 16–25) was a kind gift from Prof. Heike Walles, University of Magdeburg. Both cell lines were cultured in phenol-red-free DMEM/F12 medium + 2.5 mM L-glutamine + 29 mM sodium bicarbonate (Life Technologies, Carlsbad, CA, USA) supplemented with 10% fetal calf serum (FCS; Sigma-Aldrich, St. Louis, MO, USA) and 1% penicillin/streptomycin (Life Technologies) at 37 °C, 5% CO_2 and a relative humidity of 95%. An identical DMEM/F12 medium with phenol red (Life Technologies) was used for comparative experiments to study the effects of phenol red. Cells were routinely checked microscopically and passaged at a maximum confluence of 90%. For the experiments, a cell density of 0.5×10^6 cells was seeded into uncoated T25 cell culture flasks (Sarstedt, Nümbrecht, Germany) and given 24 h for the cells to settle and adhere. For immunofluorescence staining, uncoated glass coverslips (Carl Roth, Karlsruhe, Germany) with sterilized Vaseline (Edeka, Hamburg, Germany) were placed in a T25 flask, which were then UV illuminated for at least one hour and allowed to dry overnight before seeding the cells.

2.2. Random Positioning

For most experiments, a desktop RPM 2.0 (Yuri, Meckenbeuren, Germany) was used in a HERAcell CO_2 incubator (Thermo Scientific, Waltham, MA, USA) at 37 °C, 5% CO_2 without humidification. An incubator RPM (iRPM 2.0; developed by Prof. Jörg Sekler, University of Applied Sciences and Arts Northwestern Switzerland [19]) was used for

comparison experiments, which offered a larger sample load for the analyses (e.g., gene expression analysis). Both devices led to the same phenotypic observations and are therefore comparable for this study. The medium was not specially pretreated. For random positioning, the RPM was operated in real random mode (two frames rotation) at an average speed of 60°/s (range: 50–70°/s). Before starting the rotation, the cell culture flasks were filled completely with medium, avoiding bubbles (any remaining bubbles were carefully removed using a pipette tip before closing the culture flask). Static controls were placed next to the desktop RPM or in the same environmental conditions (iRPM experiments).

2.3. Static Spheroid Formation

Cells were seeded in 96-well BIOFLOAT™ U-bottom plates (faCellitate, Mannheim, Germany) at a density of 8000 cells per well cultured in phenol red and phenol-red-free medium at 37 °C and 5% CO_2. Images were captured every 24 h over seven days using an Olympus CKX53 inverted microscope (Olympus, Tokyo, Japan).

2.4. Estrogen Treatment (Calu-3)

17β-estradiol (Sigma-Aldrich) was dissolved in 100% ethanol (Chemsolute; Th. Geyer, Renningen, Germany). To tests the effects of 17β-estradiol, we supplemented phenol-red-free DMEM/12 medium with 10 nM 17β-estradiol from the beginning of cell culture.

2.5. mRNA Isolation and Quantitative Real-Time PCR

The adherent cells were carefully washed once with DPBS (Life Technologies), fixed with RNAlater™ solution (Invitrogen, Life Technologies) and harvested with a cell scraper. The spheroids were centrifuged at 125× *g* for 5 min; the supernatant was discarded and then fixed with RNAlater™. Further processing of the samples was performed in the same way as described in [14]. The primer sequences used for the quantitative real-time PCR are listed in the Supplementary Materials (Table S1). The PCR reaction was performed on a QuantStudio™ 3 device (Thermo Fisher Scientific). Samples were measured in triplicate and evaluated by using the comparative threshold cycle ($\Delta\Delta C_T$) method with 18S rRNA as the housekeeper reference. QuantStudio™ Design & Analysis software (v1.5, Thermo Fisher Scientific) was used, which allows an internal check of the curve and result quality to detect misleading results that should be excluded. The individual data points are displayed in the graphs. Outliers in biological replicates were identified with the Grubbs'/ESD test using the GraphPad outlier calculator (Prism v9, GraphPad Software, Boston, MA, USA).

2.6. Luminex® Multiplex Assay

Multiplex bead arrays for TNF, IL-6, IL-8 and osteopontin protein levels in the cell culture supernatant were analyzed using a multiplex magnetic bead array (Human LXSAHM-06; R&D systems, Minneapolis, MN, USA). Assays were performed according to the manufacturer's instructions. Samples were run on a MAGPIX instrument (Luminex, Austin, TX, USA) and analyzed with Belysa Immunoassay Curve Fitting Software (v1.2, Sigma-Aldrich, St. Louis, MO, USA).

2.7. Phase Contrast Microscopy

Cells were monitored and imaged using an Olympus CKX53 inverted microscope (Olympus, Tokyo, Japan) in phase contrast mode with a magnification of 10× (NA: 0.25) or 20× (NA: 0.4). A Keyence BZ-X810 microscope (Keyence, Neu-Isenburg, Germany) in phase contrast mode at a magnification of 10× (NA: 0.45) was used to inspect and image the cells during the spheroid-formation experiment in 96-well plates. The image analysis was carried out with Fiji software (v1.54f, ImageJ, imagej.net).

2.8. Immunofluorescence Microscopy and Analysis

For fixation, the two-dimensional-growing cells were washed once with 0.1 M phosphate buffer (PB; Na_2HPO_4/NaH_2PO_4; Carl Roth, Karlsruhe, Germany) and fixed with

4% paraformaldehyde (PFA; Carl Roth). Spheroids were collected in centrifugation tubes (Sarstedt), centrifuged at 125× *g* for 5 min at 4 °C and fixed with 4% PFA. All samples were stored at 4 °C until the staining procedure (analyzed within 3 days). To remove the 4% PFA, the cells were washed three times with 0.1 PB. The cell membranes were permeabilized with 0.2% Triton X-100 (Carl Roth) in 0.1 M PB and washed three times with 0.1 M PB. To block non-specific binding sites, 3% bovine serum albumin (BSA, Carl Roth) in 0.1 M PB was used for 1 h at room temperature. Cells were then labeled with primary antibodies (Table S2) diluted in 0.1 M PB with 1% BSA overnight at 4 °C. The next day, the cells were washed three times with 0.1 M PB, incubated with the secondary antibodies (Table S2) for 1 h at room temperature and washed again three times with 0.1 M PB. For F-actin staining, Alexa Fluor™ 568 Phalloidin (Invitrogen #A12380, Life Technologies) was added at a dilution of 1:400 for 1 h. For nuclear DNA staining, the samples were incubated for 5–10 min with 100 ng/mL DAPI (4′,6-diamidino-2-phenylindole; Thermo Fisher Scientific) in 0.1 M PB, finally washed three times with 0.1 M PB and mounted with Fluoromount™ (Sigma-Aldrich). The spheroids were treated accordingly. For spheroid staining, however, the cell aggregates were incubated with both the primary and secondary antibodies for 24 h. For nuclear DNA staining, the samples were incubated for 2 h at 4 °C with 100 ng/mL DAPI in 0.1 M PB. Washing steps for spheroids were accompanied by soft centrifugation at 200 rpm for 1 min at 4 °C.

After staining, the slides were examined using a ZEISS LSM 800 confocal laser scanning microscope (Carl Zeiss, Jena, Germany). To ensure comparability of the images, all the images were acquired with the same settings using the ZEISS Airyscan detector and ZEN 3.4 software (Carl Zeiss). The Airyscan processing settings were optimized for each antibody–wavelength combination. To check for non-specific binding of the secondary antibody and thus a false negative signal, the secondary antibodies were applied to separate samples of the same condition without the primary antibody.

2.9. Statistical Analysis

Statistical evaluation was performed using SPSS Statistics (v29, IBM, Armonk, NY, USA). The non-parametric Mann–Whitney U test was used to compare samples (biological replicates) from different culture conditions. Outliers were omitted before analysis. All data are presented as the mean ± standard deviation (SD). In most plots, the individual data points are shown additionally. The sample size for each experiment is provided in the figure legends.

2.10. Interaction Networks of Chemicals and Proteins (STITCH Analysis)

The interactions between phenol red and proteins were determined using the STITCH ('search tool for interactions of chemicals') v5.0 database, available at http://stitch.embl.de/ (accessed on 17 July 2024) [20]. The search was performed for *Homo sapiens* with a high confidence interaction score.

3. Results

3.1. Different Lung Cancer Types Show Different Spheroid-Formation Ability When Exposed to the Random Positioning Machine

To compare the spheroid formation of carcinoma cells from different lung origin tissues, we cultured model cell lines of squamous cell carcinoma (NCI-H1703) and adenocarcinoma (Calu-3) for 3 days on the RPM (Figure 1A). At the beginning of the experiment, the cells were mounted as subconfluent 2D cultures. At the end of the experiment, the growth forms of the two dynamic cell cultures were very different: while the NCI-H1703 cells were mainly present as 3D spheroids, the Calu-3 cultures remained almost completely two-dimensional (Figure 1B).

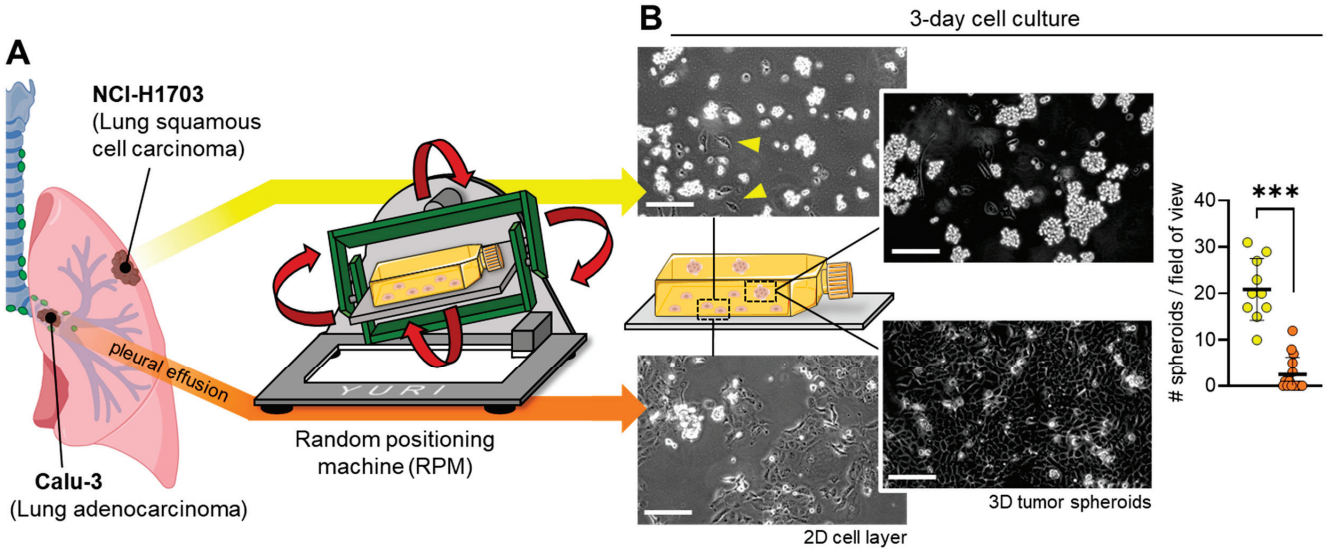


Figure 1. On the RPM, two-dimensional cultures of different lung carcinoma cell types resulted in different subpopulations. (**A**) While NCI-H1703 squamous cell carcinoma cells (yellow line, top) mainly formed 3D aggregates after 3 days of rotation (some of the few adherent cells are indicated by yellow arrows), Calu-3 adenocarcinoma cells (orange line, bottom) remained almost completely as a two-dimensional cell layer. (**B**) Microscopic images of the cell culture after 3 days of dynamic culture on the RPM. The bar chart shows the number of spheroids per microscopic image. Scale bar: 200 µm. Non-parametric Mann–Whitney U test *** $p \leq 0.001$. Parts of the figure were drawn using pictures from Biorender.com and Servier Medical Art.

3.2. Spheroid Stability Due to the Presence of Adhesion and Anti-Adhesion Proteins

To better understand the different spheroid-formation behaviors, the gene expression of different cell–cell, cell–extracellular matrix (ECM) and anti-adhesion molecules was investigated. We have already recognized in a previous RPM study that the balance between adhesion and anti-adhesion proteins can influence RPM-induced spheroid formation [14]. At the transcription level, these factors were already present in different amounts in the two cell lines studied. In static cell culture, Calu-3 cells showed a higher basal expression in adhesion proteins (*ITGB1*, *ICAM1*, *CDH1*, *GJA1*), and a lower expression of the anti-adhesion gene *MUC1* compared to NCI-H1703 cells (Figure 2A).

The one-day and three-day cultivation on the RPM resulted in only minor differences in the expression of the respective genes between the two cell lines (Figure 2B). There was a significant reduction in *MUC1* expression in Calu-3 cells after 72 h on the RPM (Figure 2B), which may indicate that the cell layer of Calu-3 may be more adhesive on the RPM. Immunofluorescence analysis confirmed the slightly lower mucin-1 level in Calu-3 cells compared to NCI-H1703 cells and a reduction in mucin-1 in Calu-3 cells after 72 h on the RPM at the protein level (Figure 2C).

Since we initially found no explanation for the different amounts of spheroids in the two cell types in the expression data, we next investigated the ability of the cells to form spheroids under static conditions by using a low-adhesion plate. Here, we observed that both cells are quite capable of forming 3D aggregates. While NCI-H1703 cells formed homogeneous spheroids in the plate, Calu-3 spheroids consisted of several small, "cauliflower-like" substructures (Figure 3A). When attempting to transfer the spheroids with a pipette, the instability of the Calu-3 spheroids quickly became apparent as they disintegrated into their substructures (Figure 3A). We assume that this also happened on the RPM, where higher shear forces occur inside the culture flasks [21–23].

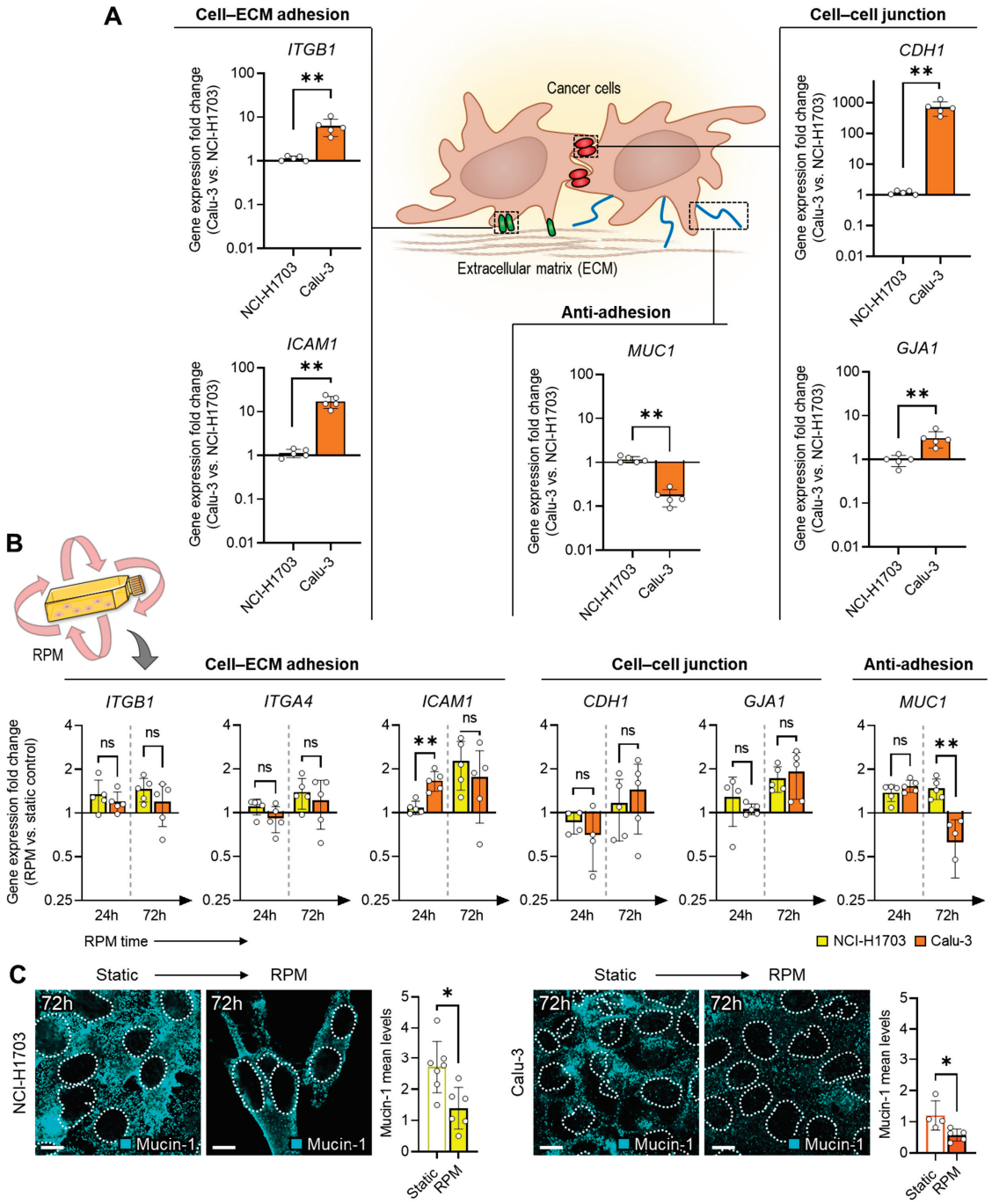


Figure 2. Gene expression differences of cell adhesion molecules in two-dimensional cell cultures of NCI-H1703 (orange) and Calu-3 cells (yellow). (**A**) Relative expression differences in Calu-3 vs. NCI-H1703 cells in a static cell culture after 24 h (n = 5). (**B**) Expression changes in a dynamic 2D RPM cell culture after 24 h and 72 h (n = 4–5). (**C**) Immunofluorescence of mucin-1 in a 3-day culture (n = 5 for each condition; one representative picture is shown). Outlines of the nuclei as indicated using DAPI staining depicted as dashed lines. The averaged mean values of mucin-1 fluorescence per cell for each microscopic image are shown in the bar graphs. Scale bar: 10 µm. Non-parametric Mann–Whitney U test * $p \leq 0.05$, ** $p \leq 0.01$, ^{ns} non-significant. Parts of the figure were drawn using pictures from Biorender.com and Servier Medical Art.

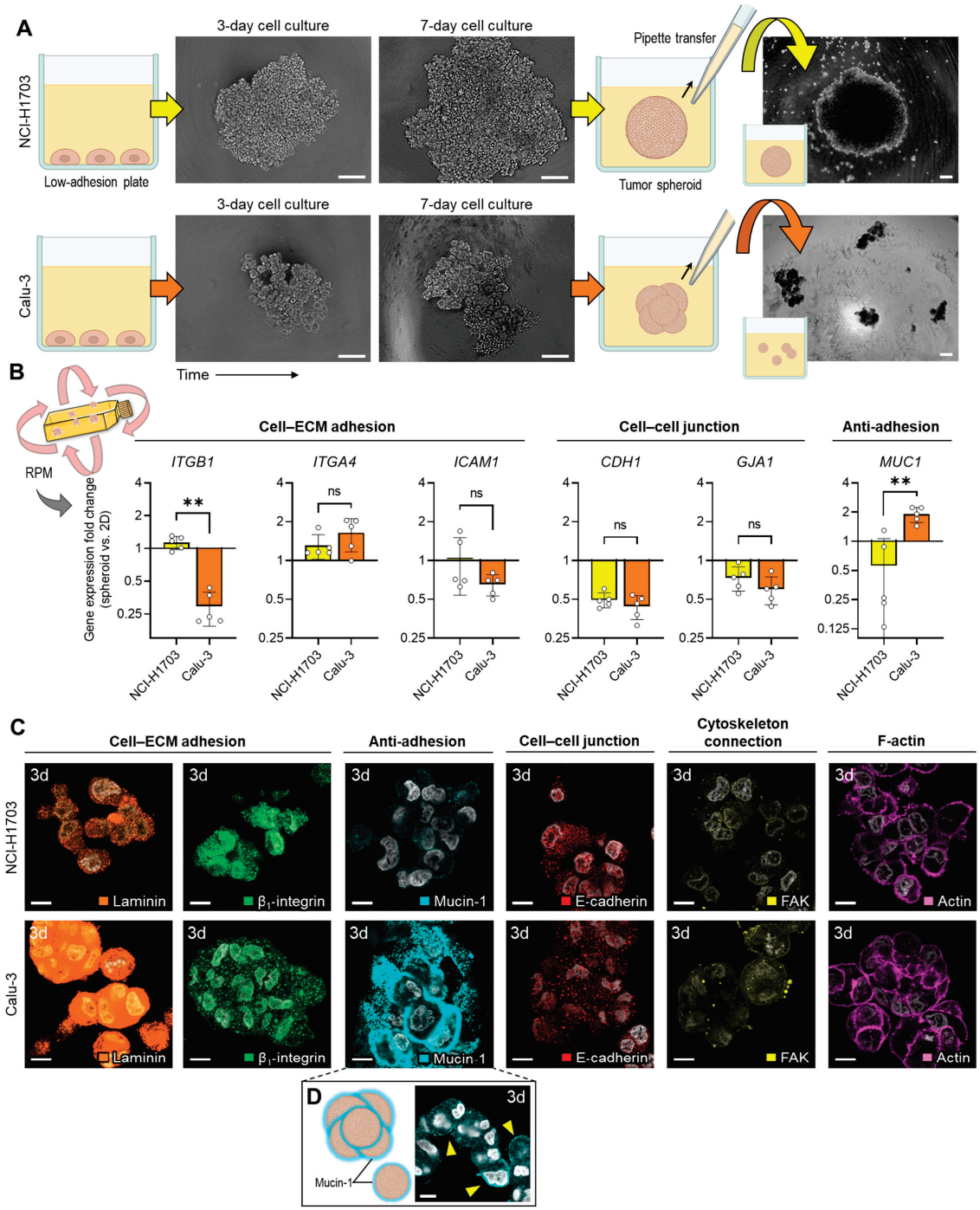


Figure 3. (**A**) Spheroid formation of NCI-H1703 and Calu-3 cells in low-adhesion plates within 7 days. The two cell lines show a different spheroid morphology. Mechanical influences (such as pipetting) led to the disintegration of 7-day Calu-3 tumor spheroids. Scale bar: 200 µm. (**B**) Gene expression changes in spheroid cells compared to 2D culture on RPM after 3 days ($n = 5$). (**C**) Immunofluorescence of laminin, β_1-integrin, mucin-1, E-cadherin, focal adhesion kinase (FAK) and F-actin combination in a 3-day culture ($n = 5$ for each condition; one representative picture is shown). Nuclei are stained with DAPI (gray). Scale bar: 10 µm. (**D**) Typical mucin-1 distribution in a Calu-3 spheroid structure around the subaggregates (yellow arrows). Scale bar: 10 µm. Non-parametric Mann–Whitney U test ** $p \leq 0.01$, ^{ns} non-significant. Parts of the figure were drawn using pictures from Biorender.com and Servier Medical Art.

Gene expression analysis of the spheroids showed that aggregated Calu-3 cells downregulate the adhesion-related genes *ITGB1* and *ICAM1*, while upregulating the anti-adhesion-related *MUC1* (Figure 3B). Consistent with the gene expression data, immunofluorescence staining of 3-day-old tumor spheroids from the RPM culture confirmed that Calu-3 spheroids are mainly characterized by less β_1-integrin and E-cadherin and much more mucin-1 and laminin compared to NCI-H1703 spheroids at this stage (Figure 3C). "Cauliflower-like" Calu-3 spheroid aggregates showed a mucin-1 distribution around the subaggregates (Figure 3D), which easily fell apart under mechanical impact.

3.3. RPM-Induced Secretion of Multifunctional Signaling Molecules

Possible stimuli that can affect the spheroid cells include mechanical (RPM, shear forces) and chemical (signaling molecules) influences. For the latter, a cell culture supernatant analysis was performed with a focus on (inflammatory) factors that have been associated with spheroid formation in previous RPM studies [13]. The cell culture supernatant of the Calu-3 culture generally contained much higher levels of the secreted proteins (including IL-6, IL-8, TNF, OPN) compared to the NCI-H1703 culture, which also increased over the culture period (Figure 4A). The supernatant of RPM-exposed Calu-3 cells showed even higher levels of the inflammatory markers IL-6 and TNF, while IL-8, which was elevated in most cell cultures with 3D growth, was more upregulated in the NCI-H1703 samples than in Calu-3 samples (Figure 4B). Secreted osteopontin (OPN) levels were not altered by the RPM. The increased secretion of IL-6 and TNF indicated involvement of NFκB signaling in Calu-3 cells exposed to the RPM. Indeed, we found early upregulation of the NFκB target gene *IL6* (24 h) and delayed upregulation of *BIRC2* and *BIRC3* (72 h) in Calu-3 cells from the RPM experiment (Figure 4C). This upregulation was induced by the RPM in the adherent cell population and did not change during spheroid formation (Figure 4C, gray box). However, no translocation of RelA into the nucleus of Calu-3 cells could be observed after 72 h on the RPM (Figure 4D), which rules out activation of the NFκB signaling pathway in Calu-3 cells on the RPM as a trigger for the secreted factors. Other transcription factors involved in mechanosignaling, such as STAT3 and p38, were also not increasingly translocated to the cell nucleus (Figure 4D). Therefore, the causative (mechano)signaling pathway for the observed gene regulation changes in Calu-3 cells remains unknown for now. Another observed transcriptional effect was the upregulation of *SPP1* (coding for osteopontin) in NCI-H1703 cells on the RPM (Figure 4E).

3.4. Calu-3 Cells Upregulate ESR1 Expression during Random Positioning

Since larger Calu-3 spheroids have already been described in previous RPM studies after a three-day-rotation culture [12], we next focused on the differences to the current experiments. The main difference in our experiments was the use of a phenol-red-free medium. A comparative experiment with phenol-red-containing medium of the same composition led to the formation of NCI-H1703 spheroids and of larger Calu-3 spheroids on the RPM (Figure 5A). Since phenol red has an estrogen-like structure and can therefore bind to the estrogen receptor ERα (Figure 5B) [24], we examined the expression of *ESR1* in the RPM-exposed cells. The expression of *ESR1* was undetectable in NCI-H1703 cells, and *ESR1* was only weakly expressed in Calu-3 cells. However, we found a very strong upregulation of *ESR1* in adherent Calu-3 cells after 3 days on the RPM (Figure 5C, boxes). Although *ESR1* was lower expressed in the cells of the Calu-3 spheroids, this expression was still higher than in normal cell cultures. A similar regulatory behavior, albeit much weaker, was observed for the growth factor receptor gene *EGFR* (Figure 5C).

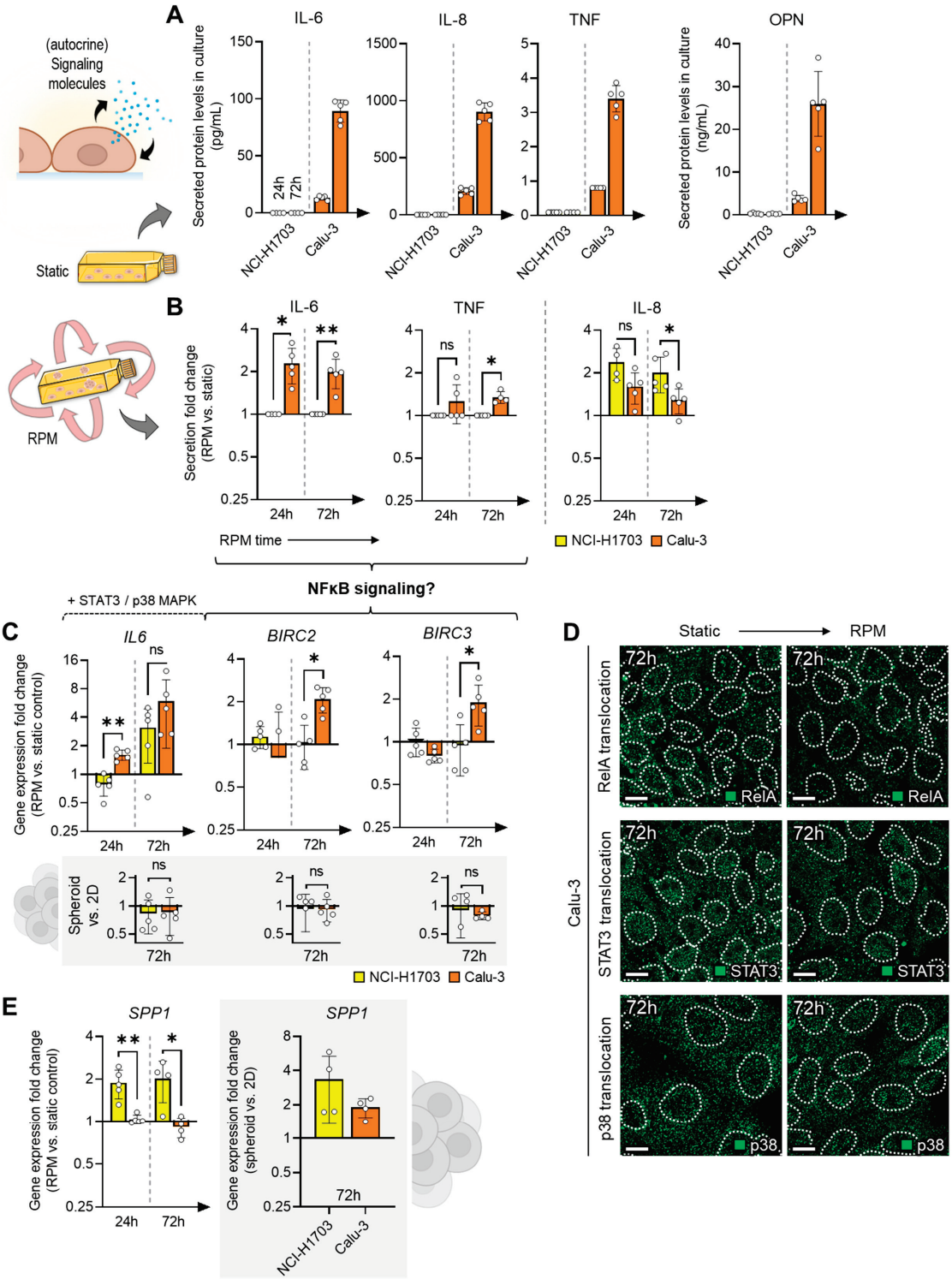


Figure 4. (**A**) Protein levels in the supernatant of static cell cultures of NCI-H1703 and Calu-3 after 24 and 72 h. (**B**) Effects of RPM cell culture on the content of secreted proteins. (**C**) Expression changes in NFκB target genes during RPM cell culture ($n = 5$). The small diagrams in the gray box describe the changes in gene expression in tumor spheroid cells. (**D**) Immunofluorescence of RelA, STAT3 and p38 in a 3-day culture ($n = 4$–5 for each condition; one representative picture is shown). Outlines of the nuclei as indicated using DAPI staining depicted as dashed lines. Scale bar: 10 µm. (**E**) Expression changes in *SPP1* during RPM cell culture ($n = 4$–5). Non-parametric Mann–Whitney U test * $p \leq 0.05$, ** $p \leq 0.01$, ^{ns} non-significant. Parts of the figure were drawn using pictures from Biorender.com and Servier Medical Art.

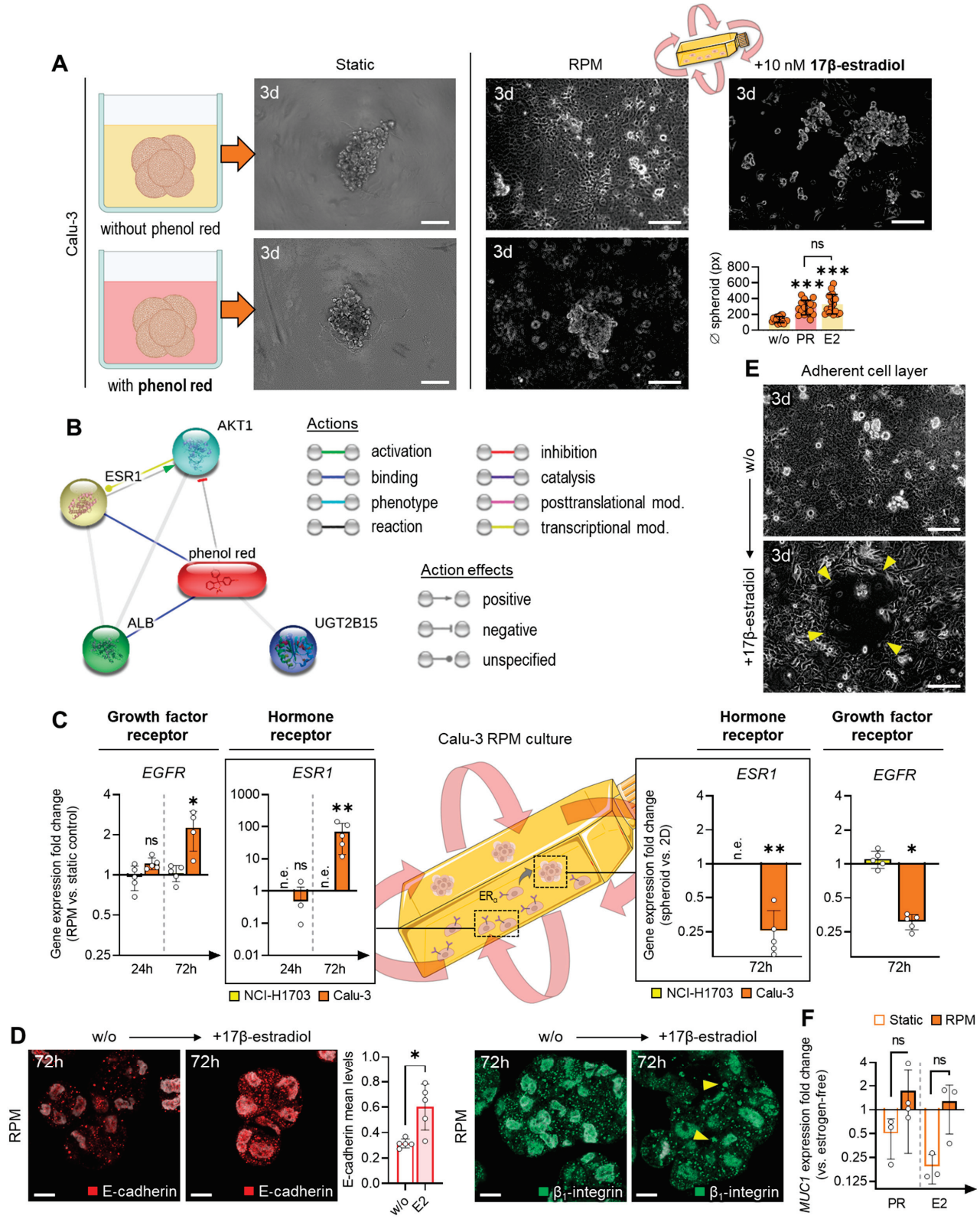


Figure 5. (**A**) Effect of phenol red on the spheroid formation of Calu-3 cells under static and RPM conditions after 72 h. The bar chart shows the spheroid size on the microscopic images in phenol-red-free medium (w/o), medium with phenol red (PR) and medium with 10 nM 17β-estradiol (E2). Scale bar: 200 µm. (**B**) STITCH v5.0 interaction network of phenol red in human cells. (**C**) Expression of *EGFR* and *ESR1* in two-dimensional-growing Calu-3 cells (left) and in Calu-3 spheroids (right) on the

RPM (n = 5). n.e., not expressed. (**D**) Immunofluorescence of E-cadherin and β_1-integrin in a 3-day culture (n = 5 for each condition; one representative picture is shown). Nuclei are stained with DAPI (gray). The increased formation of integrin clusters is indicated by yellow arrows. The averaged mean values of E-cadherin fluorescence per cell for each microscopic image are shown in the bar graph. Scale bar: 10 µm. (**E**) Adherent cell layer of Calu-3 cells after 3 days on an RPM without and with 10 nM 17β-estradiol. Scale bar: 200 µm. (**F**) Expression of *MUC1* in Calu-3 cells on the RPM in the presence of phenol red (PR) or 10 nM 17β-estradiol (E2) (n = 3–4). AKT1, Rho family-alpha serine/threonine-protein kinase; ALB, albumin; ESR1, estrogen receptor 1; ERα, estrogen receptor alpha; UGT2B15, UDP glucuronosyltransferase 2 family polypeptide B15. Non-parametric Mann–Whitney U test * $p \leq 0.05$, ** $p \leq 0.01$, *** $p \leq 0.001$, ^{ns} non-significant. Parts of the figure were drawn using pictures from Biorender.com and Servier Medical Art.

An immunofluorescence analysis of 3-day-old Calu-3 spheroids from the RPM showed a higher amount of E-cadherin in the presence of 10 nM 17β-estradiol (Figure 5D), which should contribute to an increased stability of the spheroids. β_1-integrin was more clustered in spheroids exposed to estradiol (Figure 5D, yellow arrows).

To test whether phenol red is indeed the cause of the more stable Calu-3 spheroids that were formed on the RPM, 10 nM 17β-estradiol was added to phenol-red-free medium in a further random positioning experiment. In the presence of estradiol, many larger spheroids also formed after 72 h in the RPM culture (Figure 5A, right column). In these samples, the effect of spheroid formation was even more pronounced than with phenol red. The adherent cell layer was thinner in the presence of estradiol and showed intermittent gaps (Figure 5E, arrows). A possible explanation would be the trend toward an increased expression of *MUC1* in the presence of estrogens (phenol red (p = 0.057) and 17β-estradiol (p = 0.100)) in the RPM-exposed cells compared to a static culture (Figure 5F).

4. Discussion

Cultivation of lung carcinoma cells on the RPM also leads to tumor spheroid formation. By using different types of lung cancer in this study, it was possible to gain new and deeper insights into the complex processes of "in vitro metastasis" using the RPM.

4.1. Spheroid Formation

The development of stable spheroids requires the temporally coordinated interaction of ECM components, cell–ECM and cell–cell connections (Figure 6A). Only if these conditions are met can spheroids be observed as a subpopulation of the cell culture at the end of an RPM experiment.

We observed a better spheroid-forming ability of NCI-H1703 squamous cell carcinoma cells compared to Calu-3 adenocarcinoma cells during normal RPM operation. This is an interesting result, as Ahn et al. [18] had previously observed a stronger proliferation and migration of A549 adenocarcinoma cells compared to NCI-H1703 cells on the RPM. It is quite possible that cancer cell migration in the RPM model does not correlate with spheroid formation. What we could confirm in our experiments was a different expression of adhesion and anti-adhesion proteins in both cell types, the "glue mixture" that holds them together. Compared to NCI-H1703 cells, Calu-3 cells exhibited higher levels of adhesion proteins and lower amounts of the anti-adhesion protein mucin-1, which also plays an important role in cancer metastasis [25,26]. The key role of mucin-1 in RPM-induced spheroid formation (Figure 6B) suggested in the work of Melnik et al. [14] was also confirmed in this study. Calu-3 cells in two-dimensional culture showed an even lower mucin-1 expression on the RPM, which may be related to their lower tendency to form spheroids during rotation (more pronounced 2D cell layer). Why Calu-3 cells downregulate mucin-1, while other cell types (such as Nthy-ori 3-1 thyrocytes) upregulate it during random positioning [14], cannot be answered at present.

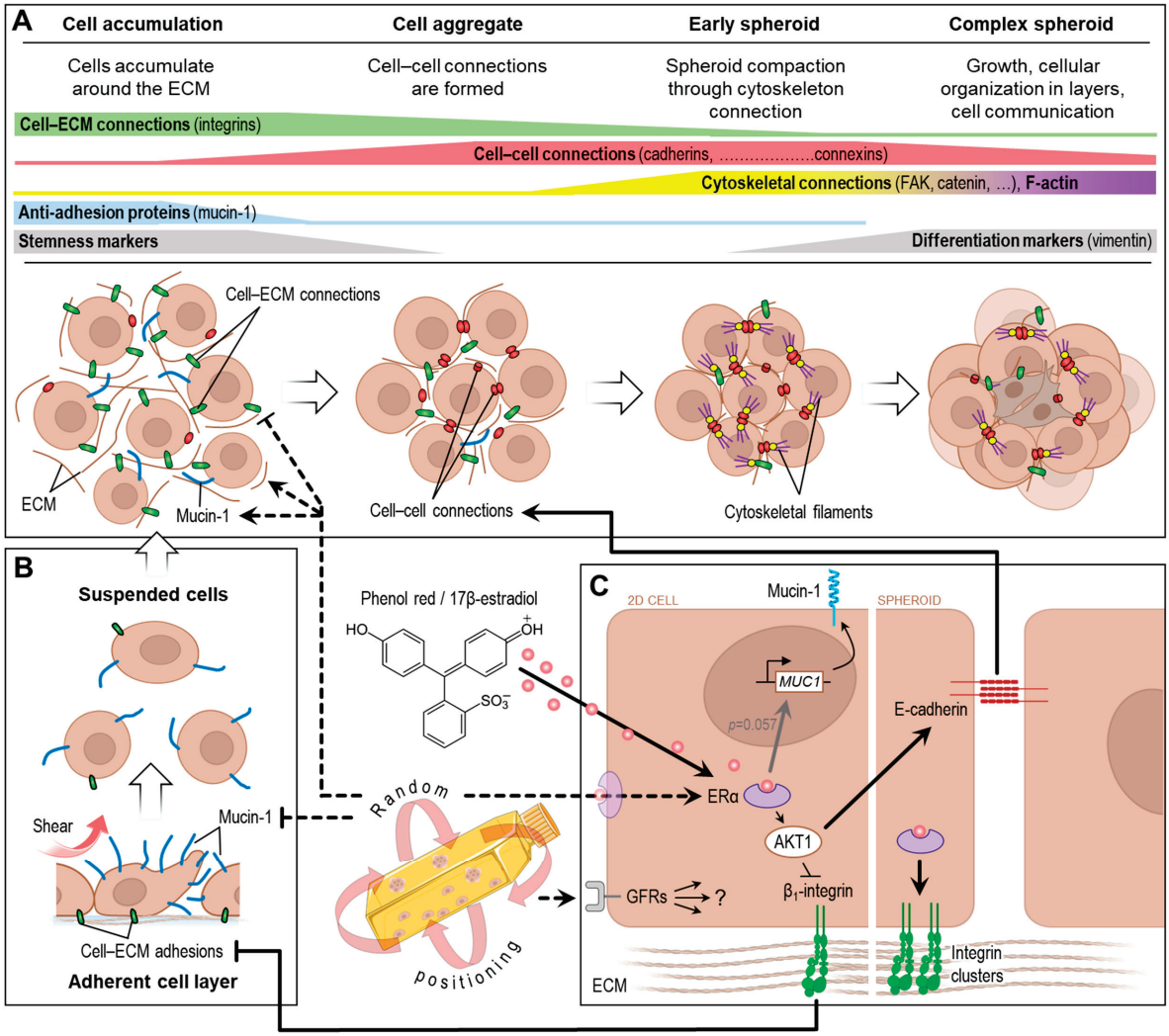


Figure 6. The current model of spheroid formation on a random positioning machine. (**A**) The aggregation of a loose accumulation of suspension cells into a compact, stable spheroid takes place in various stages, each of which focuses on different structural proteins. (**B**) The easy detachment of the cells from the adherent cell layer is dependent on the expression of anti-adhesive mucin-1 (blue). (**C**) Presumed molecular biological effects of ERα signaling on the formation of spheroids. Arrows indicate activation/increase, T-arrows inhibition/decrease. Dashed lines indicate the relationships that lead to few unstable Calu-3 spheroids in the RPM cell culture. Solid lines indicate the processes that lead to more and more stable Calu-3 spheroids in the presence of phenol red/estrogen on the RPM. ECM, extracellular matrix; ER, estrogen receptor; GFR, growth factor receptor. Parts of the figure were drawn using pictures from Biorender.com and Servier Medical Art.

During our studies, it became apparent that the stability of the Calu-3 spheroids formed was so low that they disintegrated due to the shear forces of the RPM. Consistent with this, we found an upregulation of *MUC1* and a strong downregulation of *ITGB1* expression in Calu-3 spheroid cells on the RPM. β_1-integrin is one of the most important factors mediating cohesion in early cell aggregates [27–30]. The cell aggregates are then stabilized by cell–cell junctions (cadherins, connexins and possibly also tight junction proteins). One stage later, the cytoskeleton is coupled to the cell–cell junctions via connecting proteins (focal adhesions, etc.) (Figure 6A). At the protein level, it was confirmed that Calu-3 tumor spheroids have fewer adhesion proteins (β_1-integrin, E-cadherin) and instead express much more mucin-1 and laminin. Since mucin-1 was found mainly around smaller subaggregates (Figure 3D), it is possible that these cell clusters aggregate through laminin but do not coalesce into larger stable spheroids due to the anti-adhesion effect of mucin-1

(in combination with lower-expressed β_1-integrin and E-cadherin). This could explain the cauliflower-like structure of Calu-3 spheroids.

In our 3-day experiments, we were only able to observe spheroid development up to the early aggregation phase, as we could not yet observe cytoskeletal linkage or mature focal adhesions. Looking at the most important proteins present in 3-day-old cell aggregates, the Calu-3 spheroids were probably still in the (first) aggregation phase, while the NCI-H1703 spheroids were already one developmental step further (see Figure 6A). Whether the spheroid formation (detachment) of the Calu-3 cells started later due to less mucin-1 or whether the aggregation process in Calu-3 cells generally takes longer remains to be investigated. An upregulation of *CDH1* over a period of 3 days was also described by Baghoum et al. [31] for clinorotated A549 cells. In addition, the levels of *TJP1* (tight junction protein 1, ZO-1) mRNA were increased after 3 days of rotation. Unfortunately, it is not clear from this study whether only the spheroids were analyzed (which would then have been in the aggregation phase) or whether it was a whole culture analysis.

We also found increased proinflammatory signaling molecules in the cell culture supernatant of Calu-3 cells exposed to the RPM. However, an involvement of the NFκB signaling pathway in the preparation of spheroid formation on the RPM, as described in breast cancer cells [32], can be excluded for the two lung carcinoma cell lines investigated.

NCI-H1703 cells also showed transcriptional upregulation of *SPP1* on the RPM. In breast cancer, osteopontin is known to promote 3D growth [33]. Therefore, *SPP1* expression is also often investigated in RPM studies (recently summarized in [34]). However, the extent to which it interferes with RPM-induced tumor spheroid formation is unclear, especially since no elevated levels of osteopontin were found in the NCI-H1703 randomly positioned cell cultures.

In RPM-cultured cancer cells, several factors are altered at the transcriptome, proteome and secretome level. Not all of them contribute to the phenomenon of spheroid formation. The assignment of RPM effects at the molecular level to the different biological and phenotypic processes is one of the challenges of the coming years.

4.2. Random Positioning and Estrogen Receptor

An interesting, albeit unexpected, result of this work was the influence of the *ESR1* expression of Calu-3 cells via the RPM. It is already known from breast cancer research that the transcriptional regulation of *ESR1* can also be controlled by various extrinsic factors [35]. Hormones are important signaling molecules in the body, and a change in hormone sensitivity has a major impact on the biology of cells. In cancer cells in particular, hormone dependency often determines the progression and treatability of the disease [36]. Laboratory results, for example, have indicated a carcinogenic effect of estrogens in female lung cancer [37]. Conversely, this finding also means that the RPM ("simulated microgravity"; s-µg) cell culture can influence the proliferation and drug sensitivity of cancer cells by increasing ER expression. This should be considered when ER-positive cells are used together with estrogen-like additives (e.g., phenol red in human cell culture medium) in RPM studies. Observations such as altered proliferation [38–43] and chemosensitivity [44–48] have often been described for rotating (s-µg) experiments with cancer cells and may be related to hormone receptor signaling pathways, among others. As a possible consequence of *ESR1* upregulation in this study, we were able to show that estrogens and phenol red have an influence on the spheroid stability (3D growth) of ERα-positive Calu-3 cells on the RPM. It has already been described for breast cancer cells that estrogens contribute to the increased formation of desmosomes via ERα and thus to cell–cell adhesion, making them less invasive [49]. An important step in this process is the AKT1-mediated downregulation of β_1-integrin and the upregulation of E-cadherin (Figure 6C) [50]. In the presence of 17β-estradiol, we indeed found more E-cadherin in the Calu-3 spheroids, as well as an increased clustering of β_1-integrin, which also indicates a more stable adhesion [51]. In addition, *MUC1* expression was increased in the presence of estrogens, as has already been described for breast cancer cells [52,53]. Upregulation of

ESR1 and *PGR1* was previously described only once by Kopp et al. [11] for MCF-7 cells in a 5-day RPM cell culture. In this study, in which a phenol-red-containing medium was also used, the formation of duct-like spheroids was observed. Increased ERα expression was also reported in MCF-7 cells exposed to a continuously spinning rotary cell culture system [54]. The authors found evidence that ERα may play an important role in protecting cells from oxidative stress damage under s-μg. However, it should be noted that the cells were encapsulated in a matrix and the approach is therefore not completely comparable to our experiments.

Due to the limited data available, it is not yet possible to assess the extent to which an RPM can simulate the effects of real (space) microgravity on the estrogen sensitivity of human cells. Estrogens are often described to change in vivo during space travel or microgravity analogy studies [55]. Some studies report a decrease of estrogen levels [56], which in turn could be compensated by an increased estrogen sensitivity of body cells. On the other hand, there is currently little research on how estrogen signaling and related pathways change during spaceflight. In humans, one study reported enriched estrogen signaling pathways and an upregulation of *ESR1* within 2 months postflight followed by a downregulation in the 3rd month [57]. The data on estrogen signaling in rodents are conflicting. One study reports a downregulation of *ESR1* and *ESR2* in the uterus of mice [58], with another study finding no alterations in estrogen receptor expression in the ovaries of mice after being flown to space [59]. Further studies are needed in this area.

4.3. Random Positioning and Growth Factor Receptors

We further observed an increase in *EGFR* transcription in two-dimensional-growing Calu-3 cells after 3 days on the RPM. The influence of random positioning on the transcription of growth factor receptor genes in cancer cells has already been mentioned in earlier RPM studies, but the literature of recent years does not provide a consistent picture here. Hybel et al. [3] found an increased expression of *KDR*/*FLK1* in RPM-exposed PC-3 prostate cells after 3 days and of *FLT1* after 5 days, which would be consistent with the increase in *EGFR* expression we observed. However, a decrease in *EGFR* expression was observed in MCF-7 breast cancer cells after 14 days on the RPM [60]. Melnik et al. [61] also found a reduction in *EGFR* expression after 3 days of rotation in FTC-133 thyroid cancer cells. Thus, the transcriptional control of growth factor receptor expression during random positioning appears to be cell-type dependent or subject to a more complex regulatory pattern, which requires further investigation. It is also unclear whether these growth factors and their signaling pathways contribute to the process of spheroid formation (Figure 6C, question mark), as tumor spheroids were clearly formed in all the studies mentioned above.

5. Conclusions

The comparison of the RPM-induced tumor spheroid formation of Calu-3 and NCI-H1703 lung carcinomas revealed the complex processes during random positioning. In agreement with previous work, mucin-1 again influenced the detachment of the adherent growing cancer cells by the flow shear occurring on the RPM and thus the quantitative ratio of the formed subpopulations (cell layer vs. spheroids) at the end of the experiment. Calu-3 data indicated that mucin-1 is not only an important factor in the initiation of spheroid formation (detachment) but also for the stability of the subsequently formed spheroids (mainly mediated via cell–cell junctions), a prerequisite for their integrity under the shear stress conditions on the RPM. We have now been able to show that random positioning can increase the estrogen sensitivity of a cell culture and that estrogens (as well as phenol red) affect the expression of E-cadherin and mucin-1, which in turn influences spheroid stability. Accordingly, the spheroid formation induced by the RPM depends not only on cell-type-specific properties and the mechanical influences of random positioning on the cells but also partly on the chemical composition of the medium used during the experiments.

Supplementary Materials: The following supporting information can be downloaded at https://www.mdpi.com/article/10.3390/biom14101292/s1, Table S1: Primer sequences for quantitative real-time PCR; Table S2: Antibodies used for immunofluorescence analyses.

Author Contributions: Conceptualization, M.K., D.G. and A.K.; methodology, V.S., B.B. (Balkis Barkia), D.M., J.L.C.-S., S.M. and B.B. (Bjorn Baselet); validation, M.K., J.L.C.-S., D.M. and V.S.; formal analysis, B.B. (Balkis Barkia), J.L.C.-S., D.M., B.B. (Bjorn Baselet), M.W. and M.K.; investigation, B.B. (Balkis Barkia), V.S., D.M., J.L.C.-S., S.M., M.K. and J.S.; resources, D.G., M.I. and S.B.; writing—original draft preparation, M.K., B.B. (Balkis Barkia) and S.M.; writing—review and editing, M.K., D.G., S.M., J.L.C.-S., D.M., B.B. (Bjorn Baselet), B.B. (Balkis Barkia), V.S., H.S. and S.B.; visualization, M.K.; supervision, M.K. and A.K.; funding acquisition, D.G. All authors have read and agreed to the published version of the manuscript.

Funding: This work was supported by the German Space Agency at DLR (Deutsches Zentrum für Luft- und Raumfahrt, grant number 50WB2219).

Institutional Review Board Statement: Not applicable.

Informed Consent Statement: Not applicable.

Data Availability Statement: The data presented in this study are available in the electronic Supplementary Materials. The complete raw data are available on request.

Acknowledgments: We would like to thank Anna Dittrich (Systems Biology, University of Magdeburg) for her support with the immunofluorescence staining and Klaudija Janic (Organic Chemistry, University of Magdeburg) for instructing us on the use of the Keyence BZ-X800 microscope.

Conflicts of Interest: The authors declare no conflicts of interest.

References

1. Topal, U.; Zamur, C. Microgravity, stem cells, and cancer: A new hope for cancer treatment. *Stem Cells Int.* **2021**, *2021*, 5566872. [CrossRef]
2. Sabbatini, M.; Bonetto, V.; Magnelli, V.; Lorusso, C.; Dondero, F.; Masini, M.A. Microgravity as an anti-metastatic agent in an in vitro glioma model. *Biophysica* **2023**, *3*, 636–650. [CrossRef]
3. Hybel, T.E.; Dietrichs, D.; Sahana, J.; Corydon, T.J.; Nassef, M.Z.; Wehland, M.; Krüger, M.; Magnusson, N.E.; Bauer, J.; Utpatel, K.; et al. Simulated microgravity influences VEGF, MAPK, and PAM signaling in prostate cancer cells. *Int. J. Mol. Sci.* **2020**, *21*, 1263. [CrossRef]
4. Masiello, M.G.; Cucina, A.; Proietti, S.; Palombo, A.; Coluccia, P.; D'Anselmi, F.; Dinicola, S.; Pasqualato, A.; Morini, V.; Bizzarri, M. Phenotypic switch induced by simulated microgravity on mda-mb-231 breast cancer cells. *BioMed Res. Int.* **2014**, *2014*, 652434. [CrossRef]
5. Sahana, J.; Corydon, T.J.; Wehland, M.; Krüger, M.; Kopp, S.; Melnik, D.; Kahlert, S.; Relja, B.; Infanger, M.; Grimm, D. Alterations of growth and focal adhesion molecules in human breast cancer cells exposed to the random positioning machine. *Front. Cell Dev. Biol.* **2021**, *9*, 672098. [CrossRef]
6. Chen, Z.Y.; Jiang, N.; Guo, S.; Li, B.B.; Yang, J.Q.; Chai, S.B.; Yan, H.F.; Sun, P.M.; Zhang, T.; Sun, H.W.; et al. Effect of simulated microgravity on metabolism of hgc-27 gastric cancer cells. *Oncol. Lett.* **2020**, *19*, 3439–3450. [CrossRef]
7. Masini, M.A.; Bonetto, V.; Manfredi, M.; Pastò, A.; Barberis, E.; Timo, S.; Vanella, V.V.; Robotti, E.; Masetto, F.; Andreoli, F.; et al. Prolonged exposure to simulated microgravity promotes stemness impairing morphological, metabolic and migratory profile of pancreatic cancer cells: A comprehensive proteomic, lipidomic and transcriptomic analysis. *Cell. Mol. Life Sci.* **2022**, *79*, 226. [CrossRef]
8. Kim, Y.J.; Jeong, A.J.; Kim, M.; Lee, C.; Ye, S.-K.; Kim, S. Time-averaged simulated microgravity (tasmg) inhibits proliferation of lymphoma cells, l-540 and hdlm-2, using a 3d clinostat. *Biomed. Eng. Online* **2017**, *16*, 48. [CrossRef]
9. Calvaruso, M.; Militello, C.; Minafra, L.; La Regina, V.; Torrisi, F.; Pucci, G.; Cammarata, F.P.; Bravatà, V.; Forte, G.I.; Russo, G. Biological and mechanical characterization of the random positioning machine (rpm) for microgravity simulations. *Life* **2021**, *11*, 1190. [CrossRef]
10. Kopp, S.; Warnke, E.; Wehland, M.; Aleshcheva, G.; Magnusson, N.E.; Hemmersbach, R.; Corydon, T.J.; Bauer, J.; Infanger, M.; Grimm, D. Mechanisms of three-dimensional growth of thyroid cells during long-term simulated microgravity. *Sci. Rep.* **2015**, *5*, 16691. [CrossRef]
11. Kopp, S.; Slumstrup, L.; Corydon, T.J.; Sahana, J.; Aleshcheva, G.; Islam, T.; Magnusson, N.E.; Wehland, M.; Bauer, J.; Infanger, M.; et al. Identifications of novel mechanisms in breast cancer cells involving duct-like multicellular spheroid formation after exposure to the random positioning machine. *Sci. Rep.* **2016**, *6*, 26887. [CrossRef]

12. Cortés-Sánchez, J.L.; Melnik, D.; Sandt, V.; Kahlert, S.; Marchal, S.; Johnson, I.R.D.; Calvaruso, M.; Liemersdorf, C.; Wuest, S.L.; Grimm, D.; et al. Fluid and bubble flow detach adherent cancer cells to form spheroids on a random positioning machine. *Cells* **2023**, *12*, 2665. [CrossRef]
13. Grimm, D.; Schulz, H.; Krüger, M.; Cortés-Sánchez, J.L.; Egli, M.; Kraus, A.; Sahana, J.; Corydon, T.J.; Hemmersbach, R.; Wise, P.M.; et al. The fight against cancer by microgravity: The multicellular spheroid as a metastasis model. *Int. J. Mol. Sci.* **2022**, *23*, 3073. [CrossRef]
14. Melnik, D.; Cortés-Sánchez, J.L.; Sandt, V.; Kahlert, S.; Kopp, S.; Grimm, D.; Krüger, M. Dexamethasone selectively inhibits detachment of metastatic thyroid cancer cells during random positioning. *Cancers* **2023**, *15*, 1641. [CrossRef]
15. Bray, F.; Laversanne, M.; Sung, H.; Ferlay, J.; Siegel, R.L.; Soerjomataram, I.; Jemal, A. Global cancer statistics 2022: Globocan estimates of incidence and mortality worldwide for 36 cancers in 185 countries. *CA Cancer J. Clin.* **2024**, *74*, 229–263. [CrossRef]
16. Araghi, M.; Mannani, R.; Heidarnejad Maleki, A.; Hamidi, A.; Rostami, S.; Safa, S.H.; Faramarzi, F.; Khorasani, S.; Alimohammadi, M.; Tahmasebi, S.; et al. Recent advances in non-small cell lung cancer targeted therapy; An update review. *Cancer Cell Int.* **2023**, *23*, 162. [CrossRef]
17. Popper, H.H. Progression and metastasis of lung cancer. *Cancer Metastasis Rev.* **2016**, *35*, 75–91. [CrossRef]
18. Ahn, C.B.; Lee, J.-H.; Han, D.G.; Kang, H.-W.; Lee, S.-H.; Lee, J.-I.; Son, K.H.; Lee, J.W. Simulated microgravity with floating environment promotes migration of non-small cell lung cancers. *Sci. Rep.* **2019**, *9*, 14553. [CrossRef]
19. Benavides Damm, T.; Walther, I.; Wüest, S.L.; Sekler, J.; Egli, M. Cell cultivation under different gravitational loads using a novel random positioning incubator. *Biotechnol. Bioeng.* **2014**, *111*, 1180–1190. [CrossRef]
20. Kuhn, M.; von Mering, C.; Campillos, M.; Jensen, L.J.; Bork, P. Stitch: Interaction networks of chemicals and proteins. *Nucleic Acids Res.* **2008**, *36*, D684–D688. [CrossRef]
21. Brungs, S.; Hauslage, J.; Hemmersbach, R. Validation of random positioning versus clinorotation using a macrophage model system. *Microgravity Sci. Technol.* **2019**, *31*, 223–230. [CrossRef]
22. Hauslage, J.; Cevik, V.; Hemmersbach, R. Pyrocystis noctiluca represents an excellent bioassay for shear forces induced in ground-based microgravity simulators (clinostat and random positioning machine). *NPJ Microgravity* **2017**, *3*, 12. [CrossRef]
23. Wuest, S.L.; Stern, P.; Casartelli, E.; Egli, M. Fluid dynamics appearing during simulated microgravity using random positioning machines. *PLoS ONE* **2017**, *12*, e0170826. [CrossRef]
24. Berthois, Y.; Katzenellenbogen, J.A.; Katzenellenbogen, B.S. Phenol red in tissue culture media is a weak estrogen: Implications concerning the study of estrogen-responsive cells in culture. *Proc. Natl. Acad. Sci. USA* **1986**, *83*, 2496–2500. [CrossRef]
25. Lan, Y.; Ni, W.; Tai, G. Expression of muc1 in different tumours and its clinical significance (review). *Mol. Clin. Oncol.* **2022**, *17*, 161. [CrossRef]
26. Horm, T.M.; Schroeder, J.A. Muc1 and metastatic cancer: Expression, function and therapeutic targeting. *Cell Adh. Migr.* **2013**, *7*, 187–198. [CrossRef]
27. Gionet-Gonzales, M.A.; Leach, J.K. Engineering principles for guiding spheroid function in the regeneration of bone, cartilage, and skin. *Biomed. Mater.* **2018**, *13*, 034109. [CrossRef]
28. Han, S.J.; Kwon, S.; Kim, K.S. Challenges of applying multicellular tumor spheroids in preclinical phase. *Cancer Cell Int.* **2021**, *21*, 152. [CrossRef]
29. Lin, R.-Z.; Chang, H.-Y. Recent advances in three-dimensional multicellular spheroid culture for biomedical research. *Biotechnol. J.* **2008**, *3*, 1172–1184. [CrossRef]
30. Kouroupis, D.; Correa, D. Increased mesenchymal stem cell functionalization in three-dimensional manufacturing settings for enhanced therapeutic applications. *Front. Bioeng. Biotechnol.* **2021**, *9*, 621748. [CrossRef]
31. Baghoum, H.; Alahmed, H.; Hachim, M.; Senok, A.; Jalaleddine, N.; Al Heialy, S. Simulated microgravity influences immunity-related biomarkers in lung cancer. *Int. J. Mol. Sci.* **2022**, *24*, 155. [CrossRef]
32. Kopp, S.; Sahana, J.; Islam, T.; Petersen, A.G.; Bauer, J.; Corydon, T.J.; Schulz, H.; Saar, K.; Huebner, N.; Slumstrup, L.; et al. The role of nfκb in spheroid formation of human breast cancer cells cultured on the random positioning machine. *Sci. Rep.* **2018**, *8*, 921. [CrossRef]
33. Tuck, A.B.; Chambers, A.F.; Allan, A.L. Osteopontin overexpression in breast cancer: Knowledge gained and possible implications for clinical management. *J. Cell Biochem.* **2007**, *102*, 859–868. [CrossRef]
34. Graf, J.; Schulz, H.; Wehland, M.; Corydon, T.J.; Sahana, J.; Abdelfattah, F.; Wuest, S.L.; Egli, M.; Krüger, M.; Kraus, A.; et al. Omics studies of tumor cells under microgravity conditions. *Int. J. Mol. Sci.* **2024**, *25*, 926. [CrossRef]
35. Lung, D.K.; Reese, R.M.; Alarid, E.T. Intrinsic and extrinsic factors governing the transcriptional regulation of esr1. *Horm. Cancer* **2020**, *11*, 129–147. [CrossRef]
36. Sherbet, G.V. Hormonal influences on cancer progression and prognosis. *Vitam. Horm.* **2005**, *71*, 147–200. [CrossRef]
37. Chakraborty, S.; Ganti, A.K.; Marr, A.; Batra, S.K. Lung cancer in women: Role of estrogens. *Expert. Rev. Respir. Med.* **2010**, *4*, 509–518. [CrossRef]
38. Morabito, C.; Guarnieri, S.; Catizone, A.; Schiraldi, C.; Ricci, G.; Mariggiò, M.A. Transient increases in intracellular calcium and reactive oxygen species levels in tcam-2 cells exposed to microgravity. *Sci. Rep.* **2017**, *7*, 15648. [CrossRef]
39. Tan, X.; Xu, A.; Zhao, T.; Zhao, Q.; Zhang, J.; Fan, C.; Deng, Y.; Freywald, A.; Genth, H.; Xiang, J. Simulated microgravity inhibits cell focal adhesions leading to reduced melanoma cell proliferation and metastasis via fak/rhoa-regulated mtorc1 and ampk pathways. *Sci. Rep.* **2018**, *8*, 3769. [CrossRef]

40. Taga, M.; Yamauchi, K.; Odle, J.; Furian, L.; Sundaresan, A.; Ramesh, G.T.; Pellis, N.R.; Andrassy, R.J.; Kulkarni, A.D. Melanoma growth and tumorigenicity in models of microgravity. *Aviat. Space Environ. Med.* **2006**, *77*, 1113–1116.
41. Ma, X.; Pietsch, J.; Wehland, M.; Schulz, H.; Saar, K.; Hübner, N.; Bauer, J.; Braun, M.; Schwarzwälder, A.; Segerer, J.; et al. Differential gene expression profile and altered cytokine secretion of thyroid cancer cells in space. *FASEB J.* **2014**, *28*, 813–835. [CrossRef]
42. Chang, D.; Xu, H.; Guo, Y.; Jiang, X.; Liu, Y.; Li, K.; Pan, C.; Yuan, M.; Wang, J.; Li, T.; et al. Simulated microgravity alters the metastatic potential of a human lung adenocarcinoma cell line. *Vitr. Cell. Dev. Biol.-Anim.* **2013**, *49*, 170–177. [CrossRef]
43. Chung, J.H.; Ahn, C.B.; Son, K.H.; Yi, E.; Son, H.S.; Kim, H.-S.; Lee, S.H. Simulated microgravity effects on nonsmall cell lung cancer cell proliferation and migration. *Aerosp. Med. Hum. Perform.* **2017**, *88*, 82–89. [CrossRef]
44. Vora, P.M.; Prabhu, S. Exploring the influence of microgravity on chemotherapeutic drug response in cancer: Unveiling new perspectives. *J. Cell Mol. Med.* **2024**, *28*, e18347. [CrossRef]
45. Rembiałkowska, N.; Baczyńska, D.; Dubińska-Magiera, M.; Choromańska, A.; Bieżuńska-Kusiak, K.; Gajewska-Naryniecka, A.; Novickij, V.; Saczko, J.; Przystupski, D.; Kulbacka, J. Rccs bioreactor-based modeled microgravity affects gastric cancer cells and improves the chemotherapeutic effect. *Membranes* **2022**, *12*, 448. [CrossRef]
46. McKinley, S.; Taylor, A.; Peeples, C.; Jacob, M.; Khaparde, G.; Walter, Y.; Ekpenyong, A. Simulated microgravity-induced changes to drug response in cancer cells quantified using fluorescence morphometry. *Life* **2023**, *13*, 1683. [CrossRef]
47. Prasanth, D.; Suresh, S.; Prathivadhi-Bhayankaram, S.; Mimlitz, M.; Zetocha, N.; Lee, B.; Ekpenyong, A. Microgravity modulates effects of chemotherapeutic drugs on cancer cell migration. *Life* **2020**, *10*, 162. [CrossRef]
48. Przystupski, D.; Górska, A.; Szewczyk, A.; Drąg-Zalesińska, M.; Kulbacka, J. 3d clinorotation affects drug sensitivity of human ovarian cancer cells. *Microgravity Sci. Technol.* **2021**, *33*, 42. [CrossRef]
49. Maynadier, M.; Chambon, M.; Basile, I.; Gleizes, M.; Nirde, P.; Gary-Bobo, M.; Garcia, M. Estrogens promote cell–cell adhesion of normal and malignant mammary cells through increased desmosome formation. *Mol. Cell Endocrinol.* **2012**, *364*, 126–133. [CrossRef]
50. Riggio, M.; Perrone, M.C.; Polo, M.L.; Rodriguez, M.J.; May, M.; Abba, M.; Lanari, C.; Novaro, V. Akt1 and akt2 isoforms play distinct roles during breast cancer progression through the regulation of specific downstream proteins. *Sci. Rep.* **2017**, *7*, 44244. [CrossRef]
51. Changede, R.; Sheetz, M. Integrin and cadherin clusters: A robust way to organize adhesions for cell mechanics. *BioEssays* **2017**, *39*, e201600123. [CrossRef] [PubMed]
52. Zaretsky, J.Z.; Barnea, I.; Aylon, Y.; Gorivodsky, M.; Wreschner, D.H.; Keydar, I. Muc1 gene overexpressed in breast cancer: Structure and transcriptional activity of the muc1 promoter and role of estrogen receptor alpha (erα) in regulation of the muc1 gene expression. *Mol. Cancer* **2006**, *5*, 57. [CrossRef] [PubMed]
53. Seregni, E.; Botti, C.; Bajetta, E.; Ferrari, L.; Martinetti, A.; Nerini-Molteni, S.; Bombardieri, E. Hormonal regulation of muc1 expression. *Int. J. Biol. Markers* **1999**, *14*, 29–35. [CrossRef] [PubMed]
54. Zheng, H.-X.; Tian, W.-M.; Yan, H.-J.; Jiang, H.-D.; Liu, S.-S.; Yue, L.; Han, F.; Wei, L.-J.; Chen, X.-B.; Li, Y. Expression of estrogen receptor α in human breast cancer cells regulates mitochondrial oxidative stress under simulated microgravity. *Adv. Space Res.* **2012**, *49*, 1432–1440. [CrossRef]
55. Tou, J.C.; Grindeland, R.E.; Wade, C.E. Effects of diet and exposure to hindlimb suspension on estrous cycling in sprague-dawley rats. *Am. J. Physiol. Endocrinol. Metab.* **2004**, *286*, E425–E433. [CrossRef]
56. Mark, S.; Scott, G.B.I.; Donoviel, D.B.; Leveton, L.B.; Mahoney, E.; Charles, J.B.; Siegel, B. The impact of sex and gender on adaptation to space: Executive summary. *J. Women Health* **2014**, *23*, 941–947. [CrossRef]
57. Mathyk, B.A.; Tabetah, M.; Karim, R.; Zaksas, V.; Kim, J.; Anu, R.I.; Muratani, M.; Tasoula, A.; Singh, R.S.; Chen, Y.-K.; et al. Spaceflight induces changes in gene expression profiles linked to insulin and estrogen. *Commun. Biol.* **2024**, *7*, 692. [CrossRef]
58. Holets, L.M.; Gupta, V.; Roby, K.F.; Tash, J.S. Spaceflight inhibits ovarian follicle development, induces down regulation of estrogen receptor alpha, and alters metabolic pathways and gene expression in mouse uterus. *Biol. Reprod.* **2012**, *87*, 18. [CrossRef]
59. Hong, X.; Ratri, A.; Choi, S.Y.; Tash, J.S.; Ronca, A.E.; Alwood, J.S.; Christenson, L.K. Effects of spaceflight aboard the international space station on mouse estrous cycle and ovarian gene expression. *NPJ Microgravity* **2021**, *7*, 11. [CrossRef]
60. Sahana, J.; Cortés-Sánchez, J.L.; Sandt, V.; Melnik, D.; Corydon, T.J.; Schulz, H.; Cai, Z.; Evert, K.; Grimm, D.; Wehland, M. Long-term simulation of microgravity induces changes in gene expression in breast cancer cells. *Int. J. Mol. Sci.* **2023**, *24*, 1181. [CrossRef]
61. Melnik, D.; Sahana, J.; Corydon, T.J.; Kopp, S.; Nassef, M.Z.; Wehland, M.; Infanger, M.; Grimm, D.; Krüger, M. Dexamethasone inhibits spheroid formation of thyroid cancer cells exposed to simulated microgravity. *Cells* **2020**, *9*, 367. [CrossRef]

Disclaimer/Publisher's Note: The statements, opinions and data contained in all publications are solely those of the individual author(s) and contributor(s) and not of MDPI and/or the editor(s). MDPI and/or the editor(s) disclaim responsibility for any injury to people or property resulting from any ideas, methods, instructions or products referred to in the content.

www.nature.com/scientificreports

SCIENTIFIC REPORTS

nature research

OPEN

Morphological and Molecular Changes in Juvenile Normal Human Fibroblasts Exposed to Simulated Microgravity

Received: 30 January 2019
Accepted: 5 August 2019
Published online: 15 August 2019

Christoph Buken[1,2], Jayashree Sahana[2], Thomas J. Corydon[2,3], Daniela Melnik[1], Johann Bauer[4], Markus Wehland[1], Marcus Krüger[1], Silke Balk[1], Nauras Abuagela[1], Manfred Infanger[1] & Daniela Grimm[1,2,5]

The literature suggests morphological alterations and molecular biological changes within the cellular milieu of human cells, exposed to microgravity (µ*g*), as many cell types assemble to multicellular spheroids (MCS). In this study we investigated juvenile normal human dermal fibroblasts (NHDF) grown in simulated µ*g* (s-µ*g*) on a random positioning machine (RPM), aiming to study changes in cell morphology, cytoskeleton, extracellular matrix (ECM), focal adhesion and growth factors. On the RPM, NHDF formed an adherent monolayer and compact MCS. For the two cell populations we found a differential regulation of fibronectin, laminin, collagen-IV, aggrecan, osteopontin, TIMP-1, integrin-β_1, caveolin-1, E-cadherin, talin-1, vimentin, α-SM actin, TGF-β_1, IL-8, MCP-1, MMP-1, and MMP-14 both on the transcriptional and/or translational level. Immunofluorescence staining revealed only slight structural changes in cytoskeletal components. Flow cytometry showed various membrane-bound proteins with considerable variations. *In silico* analyses of the regulated proteins revealed an interaction network, contributing to MCS growth via signals mediated by integrin-β_1, E-cadherin, caveolin-1 and talin-1. In conclusion, s-µ*g*-conditions induced changes in the cytoskeleton, ECM, focal adhesion and growth behavior of NHDF and we identified for the first time factors involved in fibroblast 3D-assembly. This new knowledge might be of importance in tissue engineering, wound healing and cancer metastasis.

With recently growing ambitions in human spaceflight endeavors, the pathophysiologic mechanisms of many health problems that individuals in space regularly face, require further investigation. Astronauts in space often suffer from problems with the skin. The dermis of crew members frequently develops extensive allergy-like rashes, a fluid shift, slowed wound healing, and an alteration in skin physiological properties[1]. In the epidermis, a significant thinning of this skin layer has been reported in a mouse model in space, lowering the mechanical barrier against environmental forces, such as radiation[2]. In the dermal skin layer, the composition and ratio of collagen and elastin have been shown to be altered after a six-month space mission of ISS-astronauts, thus decreasing the skin's overall elasticity[3]. These findings strongly suggest that morphology and structure of the skin are altered by microgravity (µ*g*). For this reason, the effects of µg on dermal cells need to be characterized. As the key regulatory cell type of dermal integrity, we focused on juvenile normal human dermal fibroblasts (NHDF) and their reaction to an extended period of simulated microgravity (s-µ*g*), created by a random positioning machine (RPM).

Most fibroblasts are of mesenchymal origin and represent the major cell type of the connective tissue. An important role of the fibroblasts is to synthesize the components of the extracellular matrix (ECM) and maintain

[1]Clinic for Plastic, Aesthetic and Hand Surgery, Otto von Guericke University Magdeburg, Leipziger Str. 44, 39120, Magdeburg, Germany. [2]Department for Biomedicine, Aarhus University, Høegh-Guldbergsgade 10, DK-8000, Aarhus C, Denmark. [3]Department of Ophthalmology, Aarhus University Hospital, 8200 Aarhus N, Palle Juul-Jensens Boulevard 99, DK-8200, Aarhus N, Denmark. [4]Max Planck Institute of Biochemistry, Am Klopferspitz 18, 82152, Planegg, Germany. [5]Gravitational Biology and Translational Regenerative Medicine, Faculty of Medicine and Mechanical Engineering, Otto von Guericke University Magdeburg, 39120, Magdeburg, Germany. Correspondence and requests for materials should be addressed to D.G. (email: dgg@biomed.au.dk)

the ECM homeostasis. They produce the structural network for mammalian tissues and are involved in wound repair[4,5]. Fibroblasts can acquire an activated and immunoregulatory phenotype[6]. Moreover, fibroblasts play an important role in biological processes like inflammation, angiogenesis, cancer progression, as well as in tissue fibrosis[6].

The first aim of this study is to focus on the morphology and the growth behavior of fibroblasts exposed to the RPM. Since several years, we have studied the behavior of benign and malignant cells with emphasis on proliferation, cellular differentiation, migration, apoptosis or with focus on the cytoskeleton, focal adhesion and ECM[7]. In this context we exposed human cells of various types to s-μ*g* and real microgravity (r-μ*g*)[8–13]. Normally, most cell types grow as a two-dimensional (2D) monolayer *in vitro*, when they are cultured in culture flasks and incubated in a standard cell culture incubator at 1*g* normal laboratory conditions on Earth. The cells leaving the monolayers in μ*g* assemble in a scaffold-free manner to three-dimensional (3D) multicellular spheroids (MCS) or to tubular structures, depending on the cell type[8–13]. This change in phenotype occurs during spaceflights as well as during exposure to μ*g*-simulators[14–16]. It is accompanied by alterations of the cytoskeletal network as well as by changes in the gene expression, protein synthesis and secretion patterns[7,17].

The second aim of this study is to study possible changes in the ECM (laminin, fibronectin, proteoglycans, osteopontin), the cytoskeleton (actin, tubulin, vimentin), and focal adhesion (FA) factors (vinculin, talin-1, E-cadherin, focal adhesion kinase 1) of NHDF exposed to the RPM. It is known that fibronectin is involved in spheroid formation of thyroid cancer cells[18].

It has been found earlier that spheroids generated from periodontal fibroblasts using the liquid overlay technique were able to adhere to biological membranes and might be used as an adjunct for periodontal regeneration[19]. Moreover, fibroblasts are often used for co-cultures with cancer cells as a model for epithelial–mesenchymal transition *in vitro*[20]. As a major component of the tumor microenvironment, cancer-associated fibroblasts are involved in cancer progression and drug resistance[21]. For these studies often scaffolds are used. Growing 3D constructs in space or using μ*g* provided by the RPM as a technology for tissue-engineering (TE) makes it possible to work without any scaffolds. This type of MCS has to be characterized. Therefore, it is necessary to investigate structure, morphology, ECM, cytoskeleton together with FA factors in NHDF in more detail.

Another objective is to investigate expectable changes in growth factors (connective tissue growth factor (CTGF), epidermal growth factor (EGF), vascular endothelial growth factor (VEGF), and cytokines (interleukin-6 (IL-6), interleukin 8 (IL-8). In addition, we focused on changes in the productive potential of fibroblasts by investigating their collagen synthesis (collagen type I, III and IV) and metabolism (tissue inhibitor of metalloproteinases 1 (TIMP1), matrix metalloproteinases (MMPs)). We studied these factors because some of them are known to promote growth of human cells. CTGF and EGF had shown to be involved in spheroid formation of thyroid cancer cells in space[16]. VEGF is known to be involved in 3D growth of endothelial cells[22] and the cytokines IL-6 and IL-8 improved spheroid formation of thyroid cancer cells under 1*g*-conditions using the liquid-overlay technique to engineer MCS[23].

Finally, we investigated possible interactions of the genes and proteins determined in NHDF exposed to the RPM and performed a pathway analysis.

Results and Discussion

Characterization and morphology of juvenile normal human dermal fibroblasts exposed to the RPM.

A main objective of this study was to examine structural alterations in juvenile NHDF exposed for three days (3d) to the RPM. We studied the morphology of adherent cells and of 3D MCS. Phase contrast microscopy showed that the NHDF cultured under static 1*g*-conditions grew as a normal two-dimensional (2D) monolayer, when the flasks were placed next to the RPM in a commercially available incubator (Fig. 1A). The cells revealed a spindle-shaped morphology. They were disjointed and scattered, when covering the cell culture flask bottom. However, after a three-day exposure of NHDF to the RPM, two phenotypes were found: one part of the fibroblasts grew as 3D MCS and the other one remained adherently and grew as a 2D monolayer (Fig. 1B,C). Both cellular phenotypes were investigated by qPCR, Western blotting, and immunofluorescence staining (IFS). The adherent cells were further studied by flow cytometry. Multianalyte Profiling (MAP) technology was used to measure the cytokine levels in the cell culture supernatants.

MCS formation after exposure to conditions of s-μ*g* had been repeatedly reported with various cell types, such as EA.hy926 endothelial cells, normal thyroid cells (Nthy-ori 3-1), FTC-133 follicular thyroid cancer cells and MCF-7 breast cancer cells[8–13]. Studies with NHDF exposed to a RPM can increase the current knowledge in TE. The RPM is an interesting device widely used for TE[24–26]. Fibroblasts can be used for co-culture experiments in order to e.g. trigger formation of vessels and other tissues and thus, it is important to know whether fibroblasts can grow as 3D MCS or remain growing adherently in the cell culture flasks.

In addition, future co-culture models of fibroblasts, endothelial cells and cancer cells using the RPM may allow a further understanding of metastasis and tumor progression. The interaction among heterotypic fibroblasts and cancer cells contributes to cancer progression. Therefore, understanding its complex microenvironment is important. NHDF can be used in co-cultures with various malignant cell types. Today MCS are cultured to examine the molecular mechanisms involved in tumorigenesis, cancer biology, angiogenesis and for drug testing of e.g. chemotherapeutic agents or tyrosine kinase inhibitors. In addition, MCS are studied in toxicology and radiation biology. Clarifying the mechanisms of μ*g*-dependent changes is an up-to-date topic for increasing the current knowledge in space medicine and developing new therapeutical options or countermeasures that can be translated to *in vivo* models, while sparing laboratory animals. In this regard, the science areas TE, cancer research and pharmacology merge smoothly.

As mentioned above, we observed that in the s-μ*g*-group one part of the cells grew in MCS floating in the medium, while another part grew in MCS that were still in connection with the adherent cell monolayer (AD). Hematoxylin-Eosin (HE; Fig. 1D–F) and Elastica van Gieson (EvG; Fig. 1G–I) staining showed these MCS

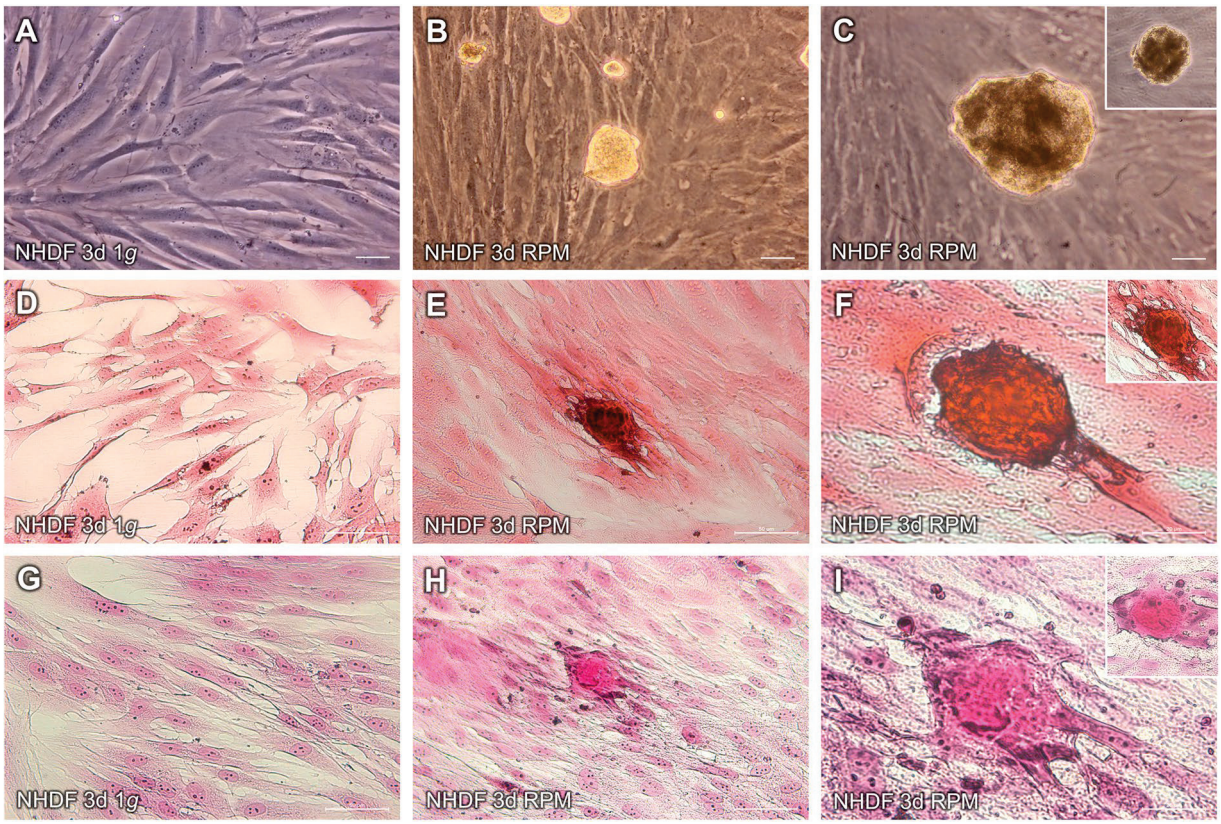


Figure 1. Characterization of morphological alterations in juvenile NHDF cells after a three-day RPM-exposure. Phase contrast microscopy images of 1*g*-control cells (**A**), RPM-AD (**B**) and RPM-MCS (**C**). Hematoxylin-Eosin staining of 1*g*-control cells (**D**), RPM-AD (**E**) and RPM-MCS (**F**). Elastica van Gieson staining of 1*g*-control cells (**G**), RPM-AD (**H**) and RPM-MCS (**I**). Scale bars: 50 µm.

(Fig. 1E,F,H,I), which were not observed in the 1*g*-control cells (Fig. 1D,G). Additionally, there was a group of pre-MCS (Fig. 1B). These initially unicellular configurations resemble an intermediate stage, which is still adherent to the bottom of the culture flask and will develop into fully developed MCS. Cell culture flasks of juvenile fibroblasts generally showed a large number of MCS after a 3-day RPM-exposure. An intermediate type was also detectable in endothelial cells (EC) exposed to an RPM. The EC grew either within a monolayer adhering to the culture flask bottom, or within an elongated cellular aggregate floating in the culture medium or within an assembly of cells consisting mainly of two cell rows still in contact with the plastic dish surface[27]. These double-row EC assemblies were considered to be progenitors of the elongated cylindrical structures (called tubular structures) tissue engineered on the RPM[27].

Also in cancer cell and EC lines, AD and MCS cells were found in each culture flask mounted on the RPM. This raised the question, why individual cells of one population behave differently. Until now, preliminary hints were observed, which could explain the different behavior of individual cells of a given population. Flow cytometric and electrophoretic studies revealed a considerable quantitative variation of distinct surface related biochemical components between the individual cells of a thyroid cancer cell line[28,29]. In addition, ASAP1, a protein whose overexpression destabilizes the interaction of focal adhesion kinase 1 and paxillin[30] was found only in FTC-133 MCS cells[31]. SRC that loosens E-cadherin-E-cadherin binding within the tight junctions by phosphorylation was lacking in MCF-7 AD cells[11]. Furthermore, FTC-133 follicular thyroid cancer cells formed more and larger spheroids during 3 days of culturing on the RPM than CGTH W-1 cells. By a proteome analysis of the two cell populations integrin-α5 and myosin-10 were only detected in the FTC-133 cells. Hence, currently, one may assume that some key proteins, responsible for spheroid formation, reach a critical accumulation threshold only in a part of the cells of a population. Therefore, we included flow cytometry in this study as an additional tool to quantify proteins.

Impact of simulated microgravity on extracellular matrix proteins, the cytoskeleton, and focal adhesion factors. In a next step, we first focused on the ECM proteins laminin, fibronectin, aggrecan, chondroitin sulfate and osteopontin. The ECM plays a key role in cell adhesion, migration, proliferation and growth and may be altered by gravitational unloading. The ECM is responsible for the structure of the tissues. Three groups of samples were collected at day 3: 1*g*-control group, RPM-AD group and RPM-MCS group. To investigate possible changes in the ECM composition after a 3-day RPM-exposure, we performed IFS of each group and investigated laminin (Fig. 2A–C) and fibronectin (Fig. 2D–F).

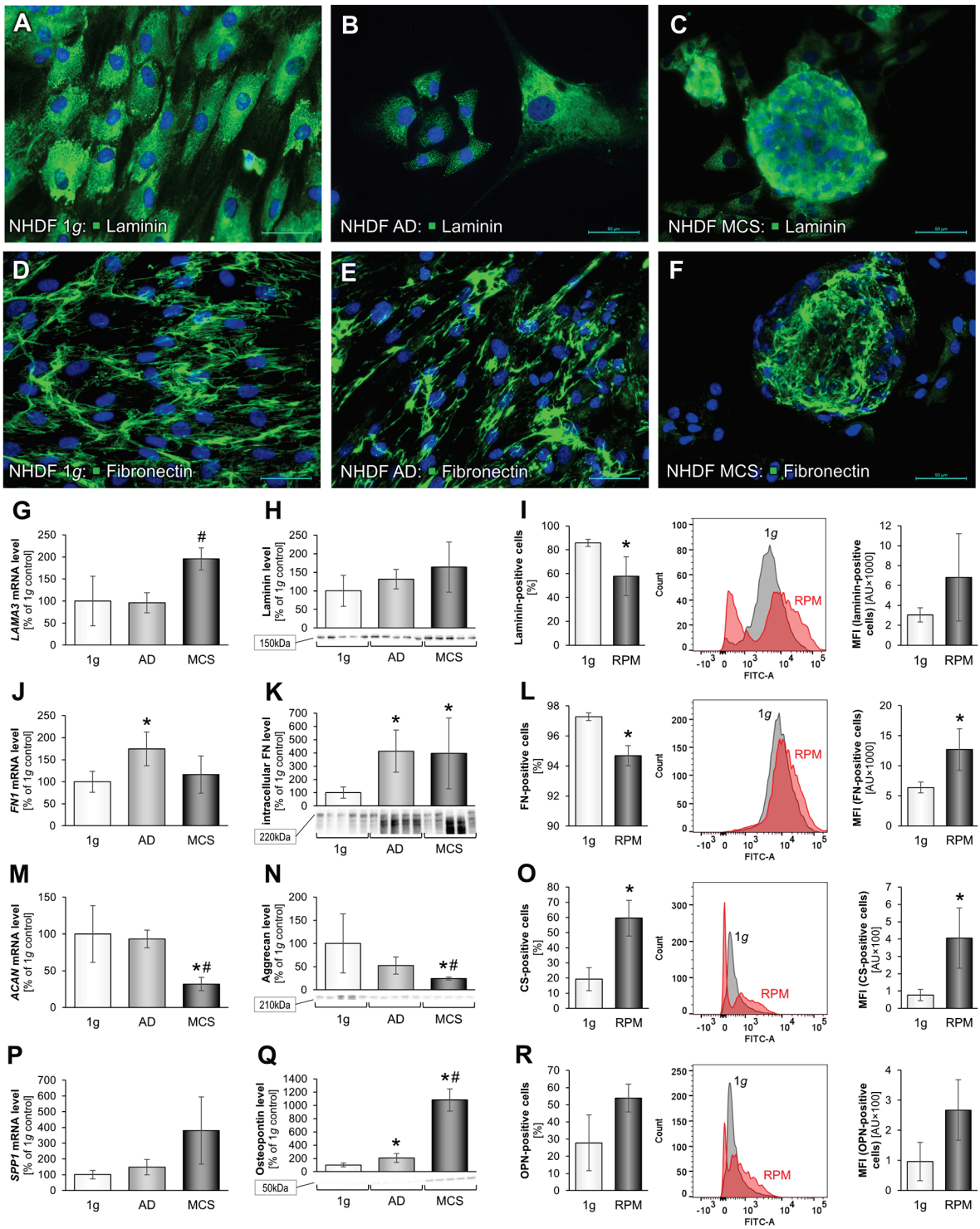


Figure 2. Changes in the ECM composition of NHDF after a three-day RPM-exposure: Immunofluorescence images of 1*g*-control cells, RPM-AD and RPM-MCS of laminin (**A**–**C**) and fibronectin (**D**–**F**). Transcriptional and translational laminin analysis: Quantitative gene expression levels of *LAMA3* (**G**), intracellular laminin levels (**H**) and flow cytometric analysis of laminin-labeled cells (**I**) displaying the percentage of laminin-positive cells as well as alteration of the median fluorescence intensity (MFI). Transcriptional and translational fibronectin analysis: Quantitative gene expression levels of *FN1* (**J**), intracellular fibronectin levels (**K**) and flow cytometric analysis of fibronectin-labeled cells (**L**). Transcriptional and translational aggrecan analysis: Quantitative gene expression level of *ACAN* (**M**), intracellular aggrecan levels (**N**) and flow cytometric analysis of chondroitin sulfate-labeled cells (**O**). Transcriptional and translational osteopontin analysis: Quantitative gene expression levels of *SPP1* (**P**), intracellular osteopontin levels (**Q**) and flow cytometric analysis of osteopontin-labeled cells (**R**). Full-length blots of cropped Western blot images are presented in Supplementary Fig. S1. $^{*}p < 0.05$ 1*g* vs. RPM; $^{\#}p < 0.05$ AD vs. MCS. Scale bars: 50 µm.

While a quantitative analysis of fluorescence intensities for laminin and all other IFS pictures was not made due to the fact that the 3D nature of the MCS results in a cumulative fluorescence signal caused by multiple cell layers, thus most certainly causing artifactual measurements, qualitative changes were assessable. Compared to the 1*g*-control, RPM-adherent (AD) cells seemed to exhibit a slightly smaller ratio of fibrous vs. granular laminin-positive structures. In addition, the fibres in AD cells were less organized (Fig. 2B). The highly packed MCS did not allow for a more detailed examination of laminin structures (Fig. 2C). In qPCR analyses we found a significant *LAMA3* mRNA increase in the MCS group (Fig. 2G). Western blotting revealed a slight increase in MCS, which was not significant compared to 1*g*-controls (Fig. 2H). The amount of laminin-positive AD cells was reduced, but they exerted a higher median fluorescence intensity (MFI) as determined by flow cytometry (Fig. 2I). Laminin and fibronectin were expressed in a lower number of cells, but laminin- and fibronectin-positive cells showed higher average protein levels as reflected by MFI (Fig. 2I,L).

Laminin is a glycoprotein and a substantial part of the basal laminae[32]. It is also a cell adhesion molecule and it became apparent that laminin is a gravi-sensitive protein. Changes in the amount of laminin in MCS had also been detected in earlier studies investigating cardiac fibroblasts, follicular thyroid cancer cells or endothelial cells after RPM-exposure[22,33,34]. These results are cell type-specific. Human adult retinal epithelium (ARPE-19) cells revealed a significant reduction of *LAMB2* mRNA and laminin protein after a 5-day and 10-day RPM-exposure[17].

The visualization of fibronectin by IFS showed no discernable differences in fibronectin structure and distribution between 1*g*-controls (Fig. 2D), AD cells (Fig. 2E), and MCS (Fig. 2F). qPCR analyses, revealed a significant 1.5-fold increase in the *FN1* gene expression in AD cells (Fig. 2J). Fibronectin is the main mediator of cell-ECM interaction[35] and an important factor involved in early wound repair[36,37]. In addition, the corresponding protein was elevated in RPM-AD and RPM-MCS (Fig. 2K). The number of fibronectin-positive RPM-AD cells was reduced compared to 1*g*-cells, but they exerted a significant higher MFI (Fig. 2L).

We further focused on the gene expression of the ECM components aggrecan (*ACAN*) and osteopontin (secreted phosphoprotein 1 (*SPP1*)). qPCR analyses revealed a significant decrease in the *ACAN* gene expression in MCS as compared to the other groups (Fig. 2M). This observation was coherent with the Western blot data (Fig. 2N). We also studied chondroitin sulfate (CS) by flow cytometric analysis and found an increase in CS-positive cells on the RPM (Fig. 2O). The proteoglycan aggrecan, best known for its water binding capacity via hydrated gel structures in hyaline- and fibrocartilage[38], acts as chondro-protective as well as anti-inflammatory agent and inhibitor of chondrocyte apoptosis[39]. Interestingly, this finding was reciprocal, when investigating osteopontin. Although not significant in qPCR data, the *SPP1* gene expression was almost 4-fold elevated in MCS cells as compared to 1*g*-control cells (Fig. 2P). In addition, the osteopontin protein was significantly elevated in MCS compared to the other groups (Fig. 2Q). We were further able to confirm this data with the results from flow cytometry (Fig. 2R). This supports our findings from previous studies[22].

Taken together, the enhancement of fibronectin proteins in MCS is no novel finding and is comparable with earlier results deriving from the TE of preliminary vessels[40]. Increases in fibronectin were also found in tube-like structures of EC after a 35-day RPM-exposure[41]. In addition, 3D human hair dermal papilla spheroids revealed an increase in ECM proteins compared to 1*g*-cultures[42]. Similar results were measured in MCS when thyroid cancer spheroids exposed to an RPM were investigated[43,44]. A key role of fibronectin is indicated for all phases of wound healing[36]. Furthermore, an enhanced fibronectin mRNA is detectable in abnormal wound healing when keloids are formed[45]. Astronauts suffer of an abnormal wound healing and thus, it is important to increase the current knowledge about the changes in fibroblasts cultured in µ*g* in regard to their ECM synthesis[35]. ECM proteins, adhesion molecules, and cytoskeletal proteins form a dynamic network interacting with signalling molecules as an adaptive response to µ*g*.

Therefore, secondly, we investigated the cytoskeletal factors vimentin, tubulin and actin in NHDF exposed to the RPM. IFS of the intermediate filament vimentin was performed to further characterize the morphological changes under s-µ*g*-influence with regard to the cytoskeleton, where we found no differences between 1*g*-controls, AD and MCS (Fig. 3A–C). The corresponding *VIM* gene expression was not changed in all groups (Fig. 3D). On the other hand, we found a highly significant increase of the RPM-AD protein content in comparison to the other groups (Fig. 3E). The occurrence of vimentin in NHDF cells is evident by their mesenchymal origin. As a type-3 intermediate filament it plays a major role in establishing the cytoskeletal framework of the cell[46]. In recent breast cancer cell studies vimentin was described as a mediator of cytoskeletal organization in epithelial to mesenchymal transition in metastasis, where it plays a role in altering cell shape and allowing motility and adhesion[47]. It is known that fibroblasts and other benign cells are used by a developing cancer to form its own tumor-specific stroma that is afterwards able to influence cancer progression and metastasis[48]. These cancer-associated fibroblasts (CAFs) can be obtained by the activation of normal fibroblasts with cancer cell conditioned fibroblast growth media using breast cancer cells or other cancer types. Activated human primary mammary fibroblasts HPMFs exerted an upregulation of vimentin and desmin among others[48].

CAFs will be investigated scaffold-free on an RPM to study the influence of µ*g* on these cells and were used for co-culture experiments. These studies will be performed in the future.

To further investigate the impact of an RPM-exposure on the cytoskeleton, we performed qPCR and Western blot analyses of various other components of the cytoskeleton. Investigating *TUBB* gene expression and its β-tubulin protein no significantly change was detectable (Fig. 3F,G).

In addition, we focused on the actin gene expression and protein content. Actin is a dynamic structural protein and microfilament with a diameter of about 7 nm, and is responsible for the stability of the cell, cell movement and among others for the formation of microvilli, pseudopodia, adherence junctions and tight junctions. First, we investigated the *ACTB* gene expression, which was not significantly changed (Fig. 3H). Pan-actin protein was also not changed in MCS compared to 1*g*-controls (Fig. 3I). There was a slight decrease in the alpha smooth muscle actin gene (*ACTA2*) in AD and MCS samples compared to 1*g*-control samples (Fig. 3J). Although the qPCR data did not show any significant changes, the Western blot results revealed a significant reduction in

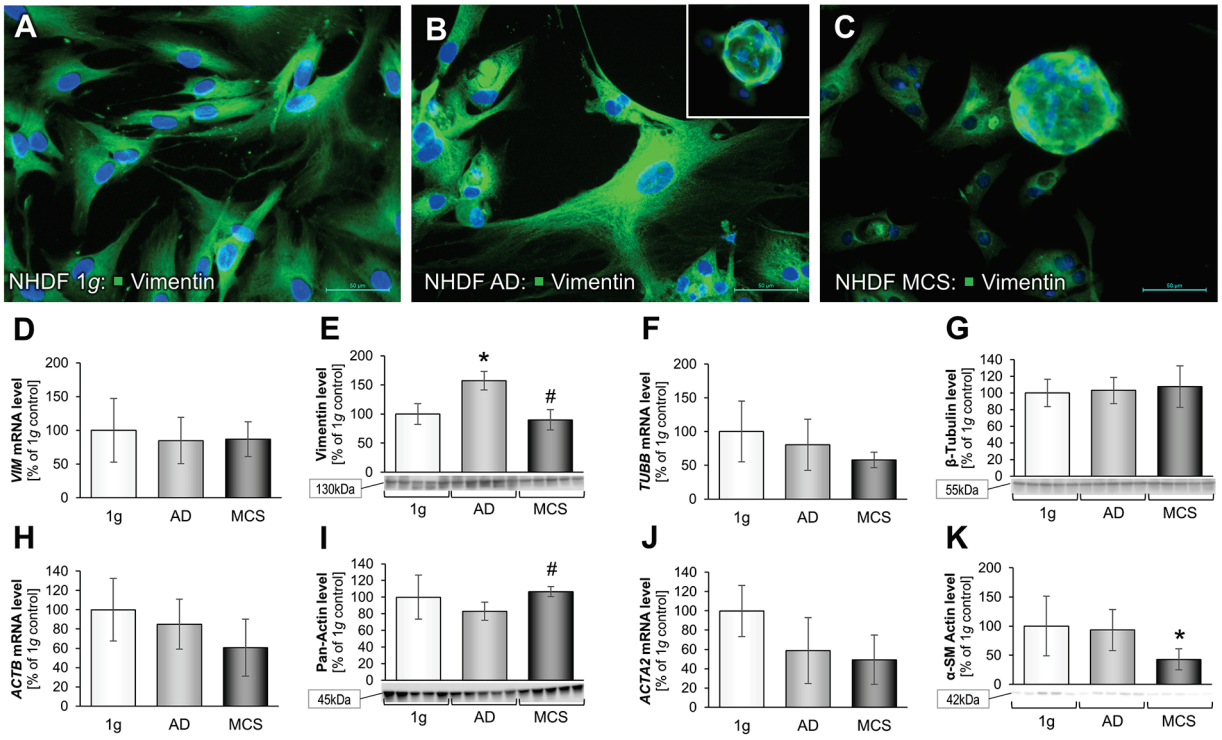


Figure 3. Cytoskeletal changes in NHDF cells after a 3-day s-μ*g*-exposure: Immunofluorescence images of 1*g*-control cells, RPM-AD and RPM-MCS of vimentin (**A**–**C**). Transcriptional and translational vimentin analysis: Quantitative gene expression levels of *VIM* (**D**) and intracellular vimentin levels (**E**). Transcriptional and translational β-tubulin analysis: Quantitative gene expression levels of *TUBB* (**F**) and intracellular β-tubulin levels (**G**). Quantitative gene expression levels of *ACTB* (**H**). Intracellular pan-actin levels (**I**). Transcriptional and translational alpha smooth muscle actin analysis: Quantitative gene expression levels of *ACTA2* (**J**) and intracellular alpha smooth muscle actin levels (**K**). Full-length blots of cropped Western blot images are presented in Supplementary Fig. S2. *$p < 0.05$ 1*g* vs. RPM; #$p < 0.05$ AD vs. MCS. Scale bars: 50 μm.

the MCS group compared to 1*g* (Fig. 3K). β-actin protein was not changed in all samples, and served as loading protein for the Western blot analyses. β-actin as major component of the cytoskeleton and β-tubulin as essential part of microtubules play major roles in the cytoskeletal integrity, cellular motility and migration[49–51]. This is a very interesting finding because these results demonstrate that the cytoskeletal genes and proteins are stable after a 3-day s-μ*g*-exposure of NHDF. This is noteworthy, as other cell types, such as chondrocytes, thyroid cancer cells or breast cancer cells exhibited more pronounced changes in the cytoskeletal conformation after exposure to both short- and long-term r- or s-μ*g*[38,46,52–54]. Moreover, earlier studies have shown that fibroblasts cultured in hypergravity of 20*g* for 8 days revealed only moderate cytoskeletal changes and that accelaration forces below 15*g* had no effect at all[55]. This is an indication that the extent of cellular changes in response to altered gravity conditions is cell type-specific and we speculate that fibroblasts are comparatively more resistant against this kind of mechanical challenge than other cells.

In summary, these observations are new and obviously the ECM and the cytoskeleton of fibroblasts are affected and altered in earlier phases by μ*g*. The cytoskeletal role in sensing gravitational changes was previously stated by the tensegrity model[56–59]. Subsequently, the cytoskeletal role on initiating cell signaling changes of NHDF under μ*g*-conditions, e.g. apoptotic behavior, has to be further investigated at earlier phases obtained during a parabolic flight campaign or sounding rocket mission.

Moreover, thirdly we focused on focal adhesions in NHDF exposed to the RPM. FAs, also called cell–matrix adhesions, are subcellular structures mediating cellular signaling in response to ECM adhesion and serve as mechanical linkages to the ECM. To further investigate the impact of a RPM-exposure to NHDF, we focused on FA proteins, as NHDF cells tend to grow three-dimensionally. FAs play an important role in this process, e.g. through sensing of the μ*g*-environment[60,61]. To further characterize alterations in FA proteins, we focused on vinculin as a major protein of interest. Vinculin is a protein with profound impact on cell-matrix adhesion and intercellular junctions and plays a major role in fibroblast-mediated wound healing[62]. Additionally, it has a vital role in mechanotransduction with integrins at focal adhesion sites[63]. Vinculin also directly interacts with talin, integrins and actin, hence allowing a proper cellular migration and orchestrating focal adhesion[64]. Vinculin is a component of the adherence junctions. It mediates cellular and extracellular signals.

Structural and morphological changes in vinculin were made visible by IFS (Fig. 4A–C). It became apparent, that there was a distinct reduction of the amount of micro-spiculae in the RPM-AD (Fig. 4B) and RPM-MCS groups (Fig. 4C), when comparing them to the 1*g*-control cells (Fig. 4A). Analysis of the *VCL* gene expression profile showed a tendency to decrease in the RPM- and AD-group (Fig. 4D). Furthermore, the protein content of

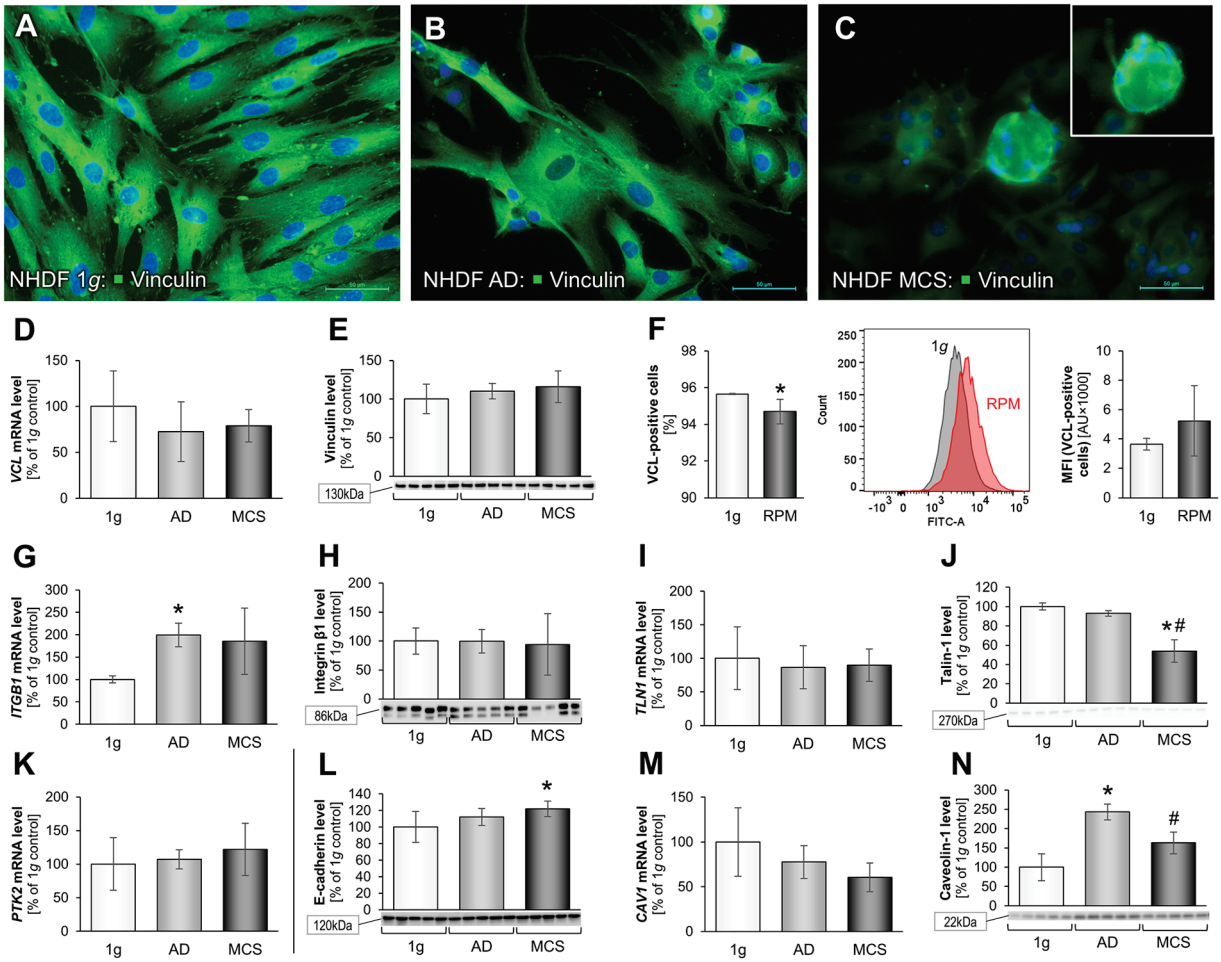


Figure 4. Alterations in focal adhesion-associated genes and proteins after a 3-day s-μ*g*-exposure: Immunofluorescence images of 1*g*-control cells, RPM-AD and RPM-MCS of vinculin (**A**–**C**). Transcriptional and translational vinculin analysis: Quantitative gene expression levels of *VCL* (**D**), intracellular vinculin levels (**E**) and flow cytometric analysis of vinculin-labeled cells (**F**). Transcriptional and translational integrin-β_1 analysis: Quantitative gene expression levels of *ITGB1* (**G**) and intracellular integrin-β_1 levels (**H**). Transcriptional and translational talin analysis: Quantitative gene expression levels of *TLN1* (**I**) and intracellular talin-1 levels (**J**). Quantitative gene expression levels of *FAK1*/*PTK2* (**K**). Intracellular E-cadherin levels (**L**). Transcriptional and translational caveolin-1 analysis: Quantitative gene expression levels of *CAV1* (**M**) and intracellular caveolin-1 levels (**N**). Full-length blots of cropped Western blot images are presented in Supplementary Fig. S3. *$p < 0.05$ 1*g* vs. RPM; $^{\#}p < 0.05$ AD vs. MCS. Scale bars: 50 μm.

vinculin was not changed in the MCS group (Fig. 4E). Flow cytometry reveled a significant reduction of vinculin in the RPM-AD group and an increase in MFI (Fig. 4F).

Another important component of the focal FAs is the cytosolic and mechanosensitive protein talin. It links integrin direct and indirect via vinculin to the cytoskeleton. Talin-1 plays a role in extravasation, cell adhesion, trans-endothelial migration and invasion. In addition, integrins bind to talin and talin binds to vinculin and thus they influence cell adhesion. The integrin receptors are involved in the attachment of adherent cells to the ECM. Talin connects the integrins to the actin cytoskeleton and acts as mechanotransductor. Our qPCR data for integrin-β_1 (*ITGB1*) showed a highly significant increase of the *ITGB1* gene expression in the AD group compared to the 1*g*-control group. *ITGB1* was not changed in MCS (Fig. 4G). The corresponding integrin-β_1 protein was not altered in all groups (Fig. 4H). The talin-1 (*TLN1*) gene expression was not changed in all cell samples (Fig. 4I). A clear reduction of talin-1 protein was measured in MCS (Fig. 4J).

Integrin-β_1 is a crucial cell surface receptor that mediates binding of the cell with its surrounding ECM. Additionally, it has a signaling function leading to modulation of gene expression within the cell[65], and plays an important role in processing mechanotransduction[66]. Talin, together with fibronectin, laminin, integrin-β_1 and vinculin, plays a major role in focal adhesion processes[12]. The same role applies to focal adhesion kinase (FAK/protein tyrosine kinase 2 (PTK2)) and E-cadherin, of which the latter is largely contributing to the formation of MCS[67]. In addition, FAK had been shown to play a crucial role in mechanosensing and -transduction[68]. It is also involved in migration, it links to the ECM and the cytoskeleton. After a three-day RPM-exposure, the *FAK1*/*PTK2* gene expression was not changed in all groups (Fig. 4K). FAs are composed of different functional

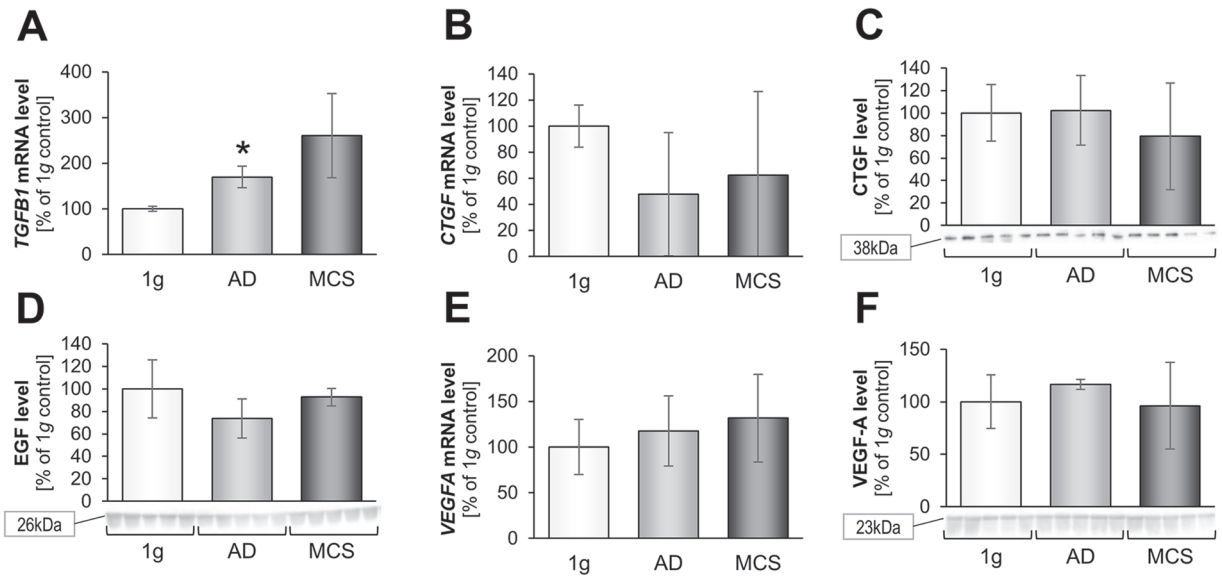


Figure 5. Investigation of selected growth factors after a 3-day s-μg-exposure of normal human dermal fibroblasts: Quantitative gene expression levels of *TGFB1* (**A**). Transcriptional and translational connective tissue growth factor (CTGF) analysis: Quantitative gene expression levels of *CTGF* (**B**) and intracellular CTGF protein levels (**C**). Intracellular EGF protein levels (**D**). Transcriptional and translational vascular endothelial growth factor A (VEGF-A) analysis: Quantitative gene expression levels of *VEGFA* (**E**) and intracellular VEGF-A protein levels (**F**). Full-length blots of cropped Western blot images are presented in Supplementary Fig. S4. *$p < 0.05$ 1*g* vs. RPM; #$p < 0.05$ AD vs. MCS.

modules separately controling mechanosensing and the cellular mechanoresponse. PTK2 (FAK) has shown to be involved in directing the cellular answer by controlling lamellipodial protrusions and cell migration[69]. FAK is involved in the regulation of adhesion, a process which occurs early. The unaltered gene expression after three days may be explained that the biological response of the cells to gravitational unloading occurred within minutes after starting the RPM and the exposure of the NHDF to μ*g*-conditions.

Moreover, we measured E-cadherin protein which is involved in cell-cell adhesion and necessary for wound healing[70]. E-cadherin protein was significantly enhanced in the MCS group vs. 1*g* and AD cells (Fig. 4L), which is an interesting finding and hints to its importance for 3D growth and MCS formation of fibroblasts. In contrast, in breast cancer cells exposed to r-μ*g* and s-μ*g* it was demonstrated that E-cadherin protein was significantly reduced and is involved in cell adhesion processes, and plays a significant role in tumorigenesis[11,71]. In addition, blockage of E-cadherin and a down-regulation of *CDH1* led to enhanced spheroid formation of MCF-7 breast cancer cells[11]. Changes in the E-cadherin protein synthesis can lead to tumor progression. Pathway analyses indicate that VCL protein has an activating effect on *CDH1*[71].

Another important group of proteins known to be involved in 3D growth of cells are the caveolins. Caveolin-1 is involved in the induction of apoptosis and inhibits the TGF-β_1-induced production of ECM. In contrast to previous data with thyroid cancer cells[13,72], caveolin-1 (*CAV1*) was not changed in AD and MCS cells (Fig. 4M). However, the caveolin-1 protein content in AD was counter-regulated and significantly elevated compared to 1*g* and MCS (Fig. 4N). This finding is different as compared to data obtained from cancer cells, where caveolin has demonstrated to be a key inhibiting regulator of 3D growth in malignant thyroid cancer cells[72]. Obviously caveolin-1 has different effects in normal cells, which has to be further examined in the future. CAV1 has been associated with the regulation of cell mechanics, including cell softening and loss of stiffness sensing ability in NIH3T3 fibroblasts[73]. CAV1 controls the hyperresponsiveness of fibroblasts to mechanical stimulation[73] and is involved in the progression of keloids during wound healing. The authors showed that an epigenetically decreased CAV1 elevated fibrogenesis-associated RUNX2 and influences the cell mechanics. Long-term studies of NHDF and NIH3T3 exposed to s-μ*g* and to vibrations using a Vibraplex device should be performed in the future.

Growth factors, cytokines and collagen metabolism. In a next step, we investigated growth factors known to be involved in growth and proliferation. CTGF, EGF, transforming growth factor beta (TGF-β) and VEGF-A all contribute to the stimulation of growth in different cell types. *CTGF* and *EGF* mRNAs were up-regulated in thyroid cancer cells exposed to r-μ*g* in space and are responsible among others for the formation of MCS[16].

We detected a significant up-regulation of *TGFB1* gene expression of AD and a slight, not significant elevation in MCS as compared to 1*g*-control cells (Fig. 5A). TGF-β_1 is a multifunctional cytokine and plays a major contextual role in cellular proliferation, adhesion and differentiation, consequently being a target in therapy of malignant diseases[74]. It is also stimulating adhesion, migration and influencing the growth behavior of normal cells.

CTGF gene expression and protein content were not significantly altered in AD and MCS cells (Fig. 5B,C). This is different compared to the results obtained from malignant cells like FTC-133 thyroid cancer cells. The

CTGF gene expression was down-regulated in MCS of thyroid cancer cells exposed for three days to the 2D clinostat and RPM, whereas in the AD group the *CTGF* mRNA was not changed compared with 1*g*-controls[13]. In addition, we found no change of the *EGF* mRNA in AD and MCS cells (Fig. 5D). The reason for this different behavior of the fibroblasts may be their mesenchymal origin. It may be speculated that CTGF and EGF are not involved in 3D formation of normal fibroblast spheroids. This contrasts findings obtained from the Sino-German Shenzhou-8 spaceflight mission, where the experimental findings revealed a scaffold-free formation of extraordinary large 3D MCS by FTC-133 cells with an increased expression of *EGF* and *CTGF* genes under r-μ*g* and on the RPM[16]. These differences might be explained by the longer experiment duration of 10 days. The impact of launch stress and the influence of cosmic radiation may not play a role because the accompanying RPM experiment revealed a comparable result[16].

In a further step, we focused on VEGF-A which plays a major role in cell growth and angiogenesis. Angiogenesis, the development of new vessels from existing vasculature, is important for tumor and normal cell growth, survival, and progression. On the molecular level, these biological processes are affected by a number of cytokines, among which the VEGF family and their related receptors, have an exceptional position[75]. A recent study showed a down-regulation of *VEGFA* in endothelial cells exposed to short-term r-μ*g* obtained during parabolic flight maneuvers and vibration[75]. VEGF-A has recently been described as an important regulatory protein in tube formation[12,76]. Our research group was able to show an elevated VEGF-A level in cellular supernatants of endothelial cells after a 35-day culture on the RPM[41]. In this study, the *VEGFA* gene expression and corresponding protein were not changed after a 3-day RPM-culture (Fig. 5E,F).

Moreover, we investigated the synthesis and release of gravi-sensitive cytokines (IL-6, IL-8, MCP-1) and the expression of *TNFA, RELA, ICAM1* and *JNK1*. Recently, we demonstrated the profound influence of interleukin-6 (IL-6) and interleukin-8 (IL-8) on spheroid formation in cancer cells, when cultured on the RPM and under 1*g*-conditions, applying the liquid-overlay technique[23]. Hence, we focused - among others - on these interleukins to further characterize the signaling pathways in NHDF. Additionally, an investigation of the cytokine levels in the supernatants of NHDF cells was performed using Multi-Analyte Profiling (MAP) technology (Human Cytokine MAP® A v1.0, Myriad RBM, Inc.). Of all investigated cytokines (GM-CSF, IFN-γ, IL-2, IL-3, IL-4, IL-5, IL-6, IL-7, IL-8, IL-10, IL-18, MIP-1α, MIP-1β, TNFα, TNF-β) only three (IL-6, IL-8, MCP-1) showed a substantial occurrence above the lower limit of quantification (LLOQ). The soluble proteins identified by MAP were measured regarding their mutual interactions and their influence on proteins, which were associated with the cells secreting the soluble proteins and had been identified in earlier studies[12,13,77].

The *IL6* gene expression and protein content were not changed (Fig. 6A,B). The IL-6 protein secretion was slightly reduced in RPM-samples (Fig. 6C). In contrast, we measured a significant increase in the *IL8* (*CXCL8*) gene expression (Fig. 6D) and the amount of IL-8 protein in MCS (Fig. 6E). This was paralleled by a tendentially higher secretion of IL-8 protein in the RPM group (Fig. 6F). However, the changes in IL-6 and IL-8 correspond with our findings from previous studies[12,23,41]. Interestingly, the obtained MAP analysis is coherent with the respective Western blot data. The interleukin IL-8 had been suggested to induce the expression of several proteins like β-actin, integrin-β_1 and talin, and support their key role in tumor progression, metastasis and angiogenesis[23,78]. Grosse *et al*. showed in 2012 that IL-6, IL-8, OPN, TLN1, CTGF, and NF-κB play a large contributory role in RPM-dependent thyroid carcinoma cell spheroid formation[79]. A direct influence of IL-8 protein on MCS engineered under normal 1*g*-conditions using the liquid-overlay technique was demonstrated on FTC-133 and ML-1 follicular thyroid cancer cell cultures[23].

In addition, we focused on monocyte chemoattractant protein-1 (MCP-1, C-C motif chemokine ligand 2 (CCL2)), which is a key member of the large family of chemokines regulating mainly cell trafficking. MCP-1 itself is associated with regulating migration and infiltration of monocytes/macrophages[80]. A large number of studies focused on MCP-1 and its involvement in various diseases. A high or constitutive expression level of CCL2 is often observed[81]. The human thyroid Nthy-ori 3-1 cells secrete MCP-1 after 24 h in a continually increasing amount, although no differences could be observed between normal gravity and s-μ*g*[12]. The gene expression of *CCL2* was not changed (Fig. 6G), but MCP-1 protein was significantly increased in MCS cells (Fig. 6H). Furthermore, the MAP analysis showed a clearly decreased MCP-1 level in RPM supernatants (Fig. 6I). An up-regulation of the *CCL2* mRNA was also measured in AD cells and a down-regulation of MCP1 was also found in UCLA RO-82-W-1 follicular thyroid cancer spheroids formed after a 24-hour RPM-exposure[77].

In addition, we investigated tumor necrosis factor alpha (TNFα) (Fig. 6J) and nuclear factor 'kappa-light-chain-enhancer' of activated B-cells (NF-κB) (Fig. 6K,L), which are both playing a role in apoptosis, cell survival and cell detachment[79]. *TNFA* was not altered in RPM samples, which indicate that it is not supporting the MCS formation of NHDF (Fig. 6J). It was earlier reported that FTC-133 thyroid cancer cells grown on the RPM showed higher levels of NF-κB p65 (RelA) protein and apoptosis than 1*g*-controls, a result also found earlier in endothelial cells[79]. The V-rel avian reticuloendotheliosis viral oncogene homolog A (*RELA*) mRNA remained unchanged in all groups (Fig. 6K). Furthermore, NF-κB p65 protein was not significantly altered (Fig. 6L). Therefore, NF-κB p65 seems not to be involved in the RPM-dependent NHDF spheroid formation, which is in contrast to tumor cells. In earlier studies, we had demonstrated the involvement of NF-κB p65 in MCS formation of thyroid cancer cells[79] and MCF-7 breast cancer cells[8]. To our knowledge this is the first report that NF-κB p65 is not influencing the 3D growth of NHDF.

Finally, we evaluated the *ICAM1* gene expression in this setting and could demonstrate that *ICAM1* in NHDF was not significantly altered by RPM-exposure (Fig. 6M). Other investigated cytokines were c-Jun N-terminal kinases (JNKs), known to be involved in apoptosis, neurodegeneration, cell differentiation and proliferation[31].

JNK1 or mitogen-activated protein kinase 8 is a mediator to cellular external stimuli that plays a contributory role in TNFα-mediated apoptosis through MAPK/JNK pathway[82] and ICAM-1, a surface protein contributing to cell-cell interaction and interacting with integrin-β_1 and believed to promote MCS formation[8]. However,

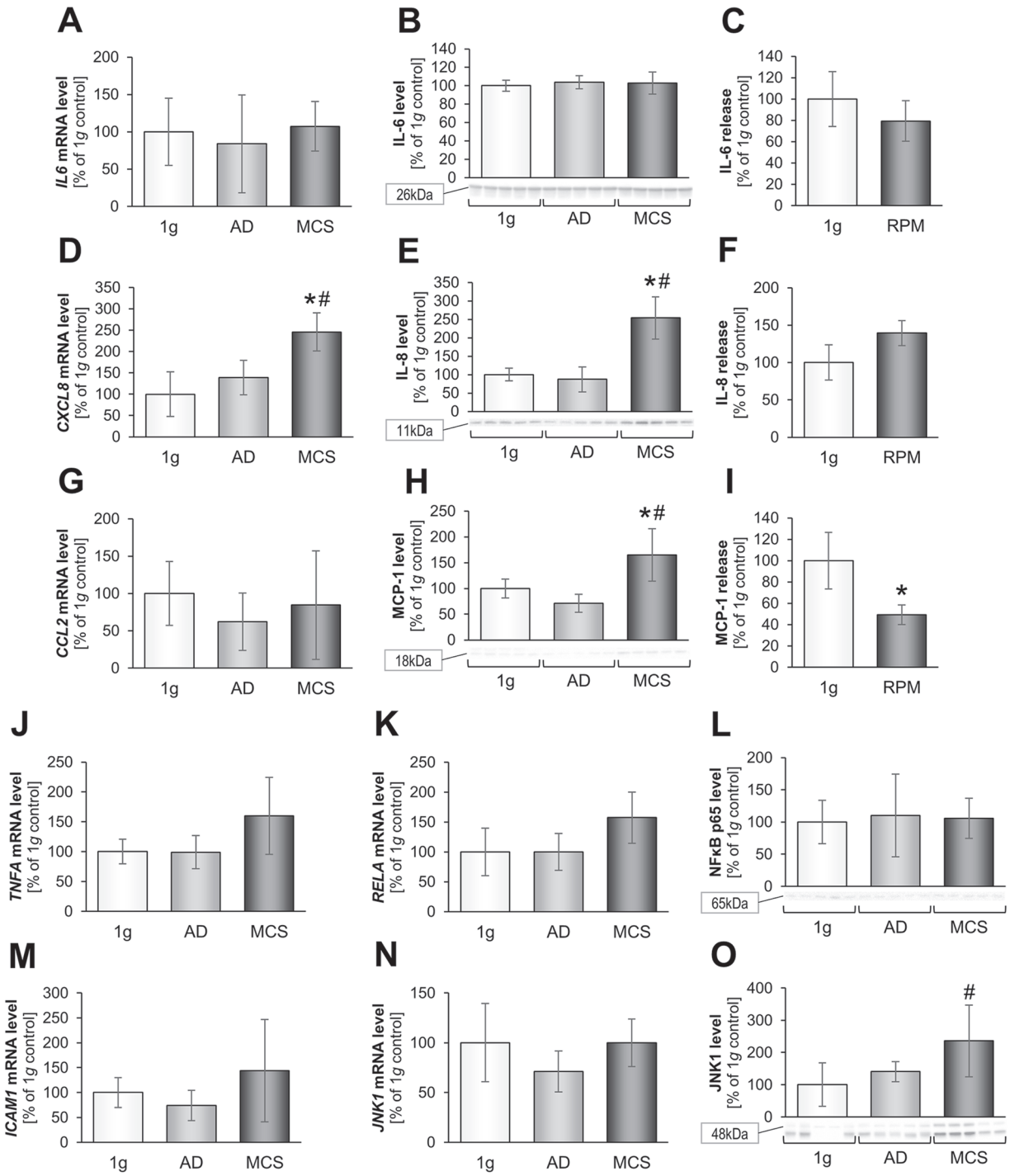


Figure 6. Analysis of selected cytokines after a 3-day s-μ*g*-exposure: Transcriptional and translational IL-6 analysis: Quantitative gene expression levels of *IL-6* (**A**) and intracellular IL-6 levels (**B**), release of IL-6 (**C**). Transcriptional and translational IL-8 analysis: Quantitative gene expression levels of *CXCL8* (**D**) and intracellular IL-8 levels (**E**), release of IL-8 (**F**). Transcriptional and translational MCP-1 analysis: Quantitative gene expression levels of *CCL2* (**G**), intracellular MCP-1 levels (**H**), release of MCP-1 (**I**). Quantitative gene expression levels of *TNFA* (**J**). Transcriptional and translational NF-κB p65 analysis: Quantitative gene expression levels of *RELA* (**K**) and intracellular NF-κB p65 levels (**L**). Quantitative gene expression levels of *ICAM1* (**M**). Transcriptional and translational JNK1 analysis: Quantitative gene expression levels of *JNK1* (**N**) and intracellular JNK1 protein levels (**O**). Full-length blots of cropped Western blot images are presented in Supplementary Fig. S5. *$p < 0.05$ 1*g* vs. RPM; #$p < 0.05$ AD vs. MCS.

JNK1 levels in MCS were not significantly changed compared to 1*g*, but significantly elevated compared to AD (Fig. 6N,O).

To our best knowledge this is the first report showing that IL-8 might be an important trigger of spheroid formation in dermal fibroblasts, while IL-6 and NF-κB p65 which are both important inducers of metastasis in cancer seem not to be involved in 3D growth in benign fibroblasts. Future functional tests will prove these observations.

Moreover, we studied the collagen synthesis and metabolism of NHDF and focused on collagen type I, III and IV, as well as on the expression of *TIMP1, MMP1, MMP3*, and *MMP14*. As previously mentioned, fibroblasts are the key cell type to maintain a proper dermal function. They synthesize collagen, the main structural component of the skin providing a structural framework and elasticity. Lack of collagen or improper collagen homeostasis (e.g. in the aging skin or after intensive UV-radiation photodamage) leads to a deficient dermal structure[83,84]. In general, the collagen homeostasis is maintained via collagen synthesis by fibroblasts and the modulation by matrix metalloproteinases (MMPs). These MMPs themselves are regulated by tissue inhibitors of metalloproteinases (TIMPs)[85]. Photoaged skin (e.g. through UV-radiation) is often characterized by a distinct damage of dermal connective tissue and a malfunction of the collagen-MMP-TIMP regulation[86,87]. MMP1 (interstitial collagenase) and MMP3 (stromelysin-1) have been shown to be elevated with UV-radiation damage to skin[84]. MMP1 levels have also been elevated in aged skin or been correlated with collagen fragmentation that resembles a malfunctioning dermal ECM microenvironment[88,89].

As astronauts in space encounter a variety of these environmental factors like UV radiation and vibration, it is of interest to investigate the fibroblast reaction, particularly with regard to s-μ*g*, where this interplay of environmental factors is reduced to only one.

IFS of collagen types I and IV revealed a relatively equal distribution within the three groups (Fig. 7A–F). The *COL1A1* gene expression (Fig. 7G) was not changed in all RPM samples, but the corresponding protein was reduced in MCS samples as measured by Western blot (Fig. 7H). In addition, the flow cytometry analyses showed a reduced amount of collagen type I-positive AD cells, but with a higher MFI (Fig. 7I).

Regarding the gene expression profile, the obtained data showed a highly significant up-regulation of *COL4A5* in MCS samples (Fig. 7J). This was confirmed by Western blot analysis (Fig. 7K). Flow cytometry revealed no change in the amount of collagen type IV-positive cells, but an increase in MFI (Fig. 7L). Collagen type IV is an essential contributory part to the cellular basal laminae, which it forms together with entactin, perlecan and laminin[90,91]. Comparing these results with those of laminin protein, this data hints towards a distinct influence on the cellular basal lamina configuration, when cells are exposed to s-μ*g*. In addition, we examined the cells concerning collagen type III positivity by flow cytometry and measured no changes in 1*g* and RPM samples, but the RPM cells showed an elevated MFI (Fig. 7M). Collagen types I and III are structural proteins of the dermal ECM[92,93]. As collagen type I is synthesized in its pro-collagen precursor state by fibroblasts it forms fibrils that are stabilized by cross-linkage[84].

Interestingly, in this study, there was also a significant up-regulation of the *TIMP1* and *MMP1* gene expression in MCS compared with the 1*g*-control group (Fig. 7N,O). In contrast, MMP1 and *MMP3* were both significantly up-regulated in AD samples. Tissue inhibitor of metalloproteinases inhibit metalloproteinases, which in turn are widely known to degrade the ECM and thus participate in remodeling the shape and composition of cell aggregates and tissues[12]. An overexpression of *TIMP1* was also implicated in several cancer types and correlated with a less-positive outcome for a patient after treatment[94]. An increase in TIMP1 might be a facilitator of cell-cell contacts during the rearrangement of the focal adhesion complex for 3D cell aggregate formation[12,95]. The matrix metalloproteinase 1 (MMP1) is also known as fibroblast collagenase, which is responsible for tissue remodeling and the breakdown of collagen type I, II and III. We also examined MMP3 which breaks down various collagen types (II, III, IV, IX), and other ECM proteins like proteoglycans, fibronectin, or laminin. In addition, MMP3 can activate MMP1, MMP7 or MMP9 revealing that MMP3 is essential in tissue remodeling. The *MMP3* gene was up-regulated in AD cells compared to 1*g* (Fig. 7P).

Finally, we focused on MMP14, which is important for the structural remodeling during aging processes. MMP14 expression in fibroblasts is important for the collagen remodeling in adult skin and supports the dermal homeostasis[96]. *MMP14* was clearly decreased in MCS compared to 1*g*-controls (Fig. 7Q).

Taken together, the expression and amount of the basal lamina component collagen type IV was significantly elevated in MCS, indicating its importance for the 3D growth of fibroblasts. In parallel, *TIMP1*, *MMP1* mRNAs were significantly up-regulated and *MMP14* down-regulated in MCS indicating their involvement in 3D growth. The meaning of these findings has to be studied in more detail in the future.

***In silico* analysis of relationships and interaction of studied genes and proteins.** After a cohort of 27 proteins and genes coding for them has been investigated regarding their accumulation and regulation, respectively, we focused on the proteins' cellular localization and their mutual relationships. The *in silico* analysis of the proteins mentioned above indicated 15 proteins, which are mainly active in the extracellular space, five proteins normally inserted in the membrane and seven proteins of the cytoplasm or the nucleus. They form an extended network of 48 direct interactions shown by solid lines or arrows and of another 60 ways of mutual influence as indicated by dashed arrows (Fig. 8A). In this system fibronectin and integrin-β_1 play a central role. When activated and forming a heterodimer with an appropriate integrin-alpha, integrin-β_1 can bind to fibronectin, laminin, osteopontin and various collagens via the extracellular domain[97,98]. Integrin-β_1 is activated by binding talin and kindlin via its cytoplasmic domain[99]. The signal of this binding is transferred to the cytoskeleton and the FA complex via vinculin and actin[100]. Vinculin binds to mitogen-activated protein kinase 8 (MAPK8)[101] and mechanosensing of E-cadherin[102]. Both components have an influence on NF-κB (RELA, Fig. 8A). Caveolin-1 regulates integrin-β_1 and SRC by forming complexes with both components of the focal FA system[103]. Production of fibronectin is stimulated by the epidermal growth factor[104]. EGF was slightly reduced in fibroblasts exposed to

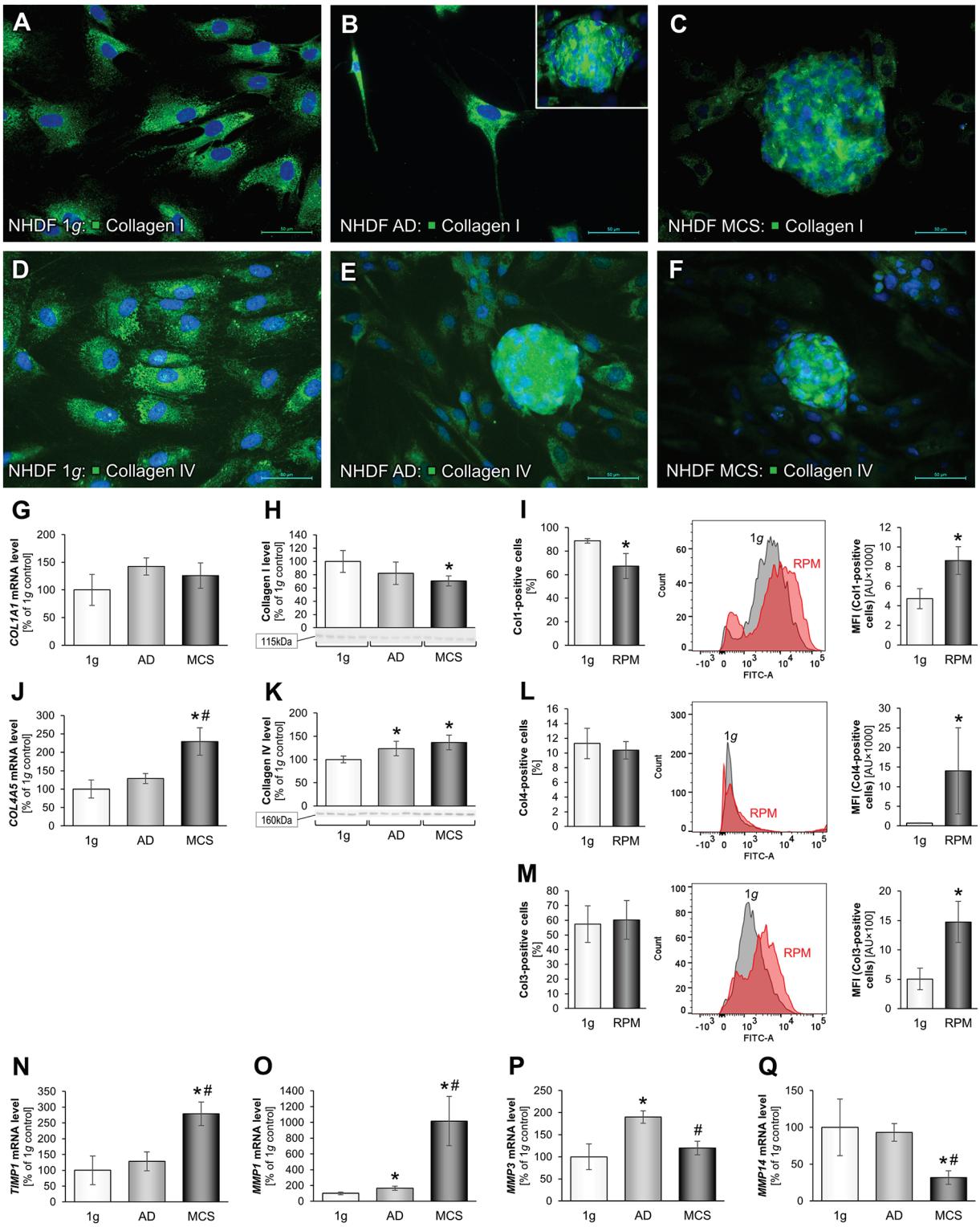


Figure 7. Alterations in collagen levels of juvenile NDHF cells following a 3-day exposure to microgravity: Immunofluorescence images of 1*g*-control cells, RPM-AD and RPM-MCS of collagen-I (**A**–**C**) and collagen-IV (**D**–**F**). Transcriptional and translational collagen type I analysis: Quantitative gene expression levels of *COL1A1* (**G**), intracellular collagen-I levels (**H**) and flow cytometric analysis of collagen type I-labeled cells (**I**). Quantitative gene expression levels of *COL4A5* (**J**), intracellular collagen-I levels (**K**) and flow cytometric analysis of fibronectin-labeled cells (**L**). Flow cytometric analysis of collagen type III-labeled cells (**M**). Quantitative gene expression levels of *TIMP1* (**N**), *MMP1* (**O**), *MMP3* (**P**) and *MMP14* (**Q**). Full-length blots of cropped Western blot images are presented in Supplementary Fig. S6. $^{*}p < 0.05$ 1*g* vs. RPM; $^{\#}p < 0.05$ AD vs. MCS. Scale bars: 50 µm.

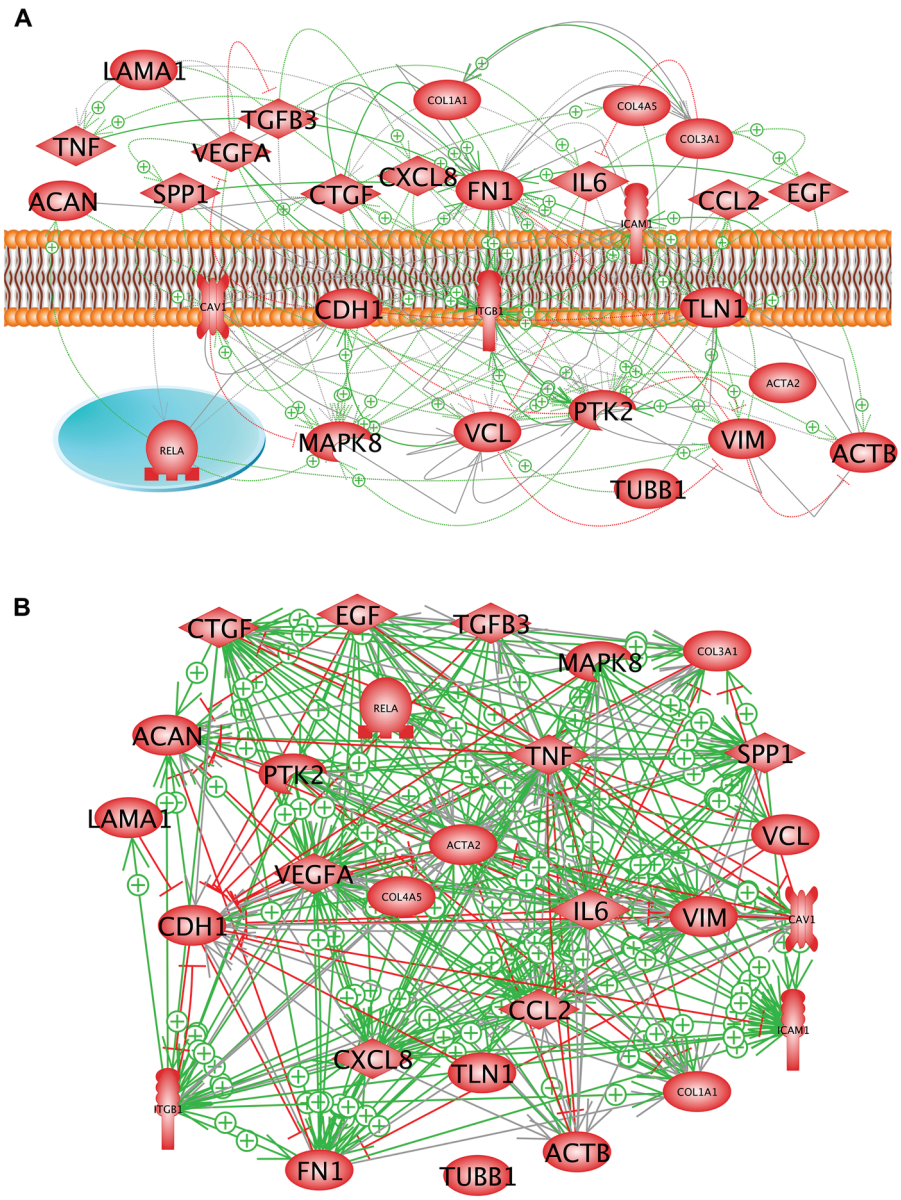


Figure 8. (**A**) Pathway studio analysis of investigated proteins. The figure shows all occurring protein-protein interactions. The color of shown lines indicates the type of interaction: green line: promotion of indicated partner; red line: inhibition of indicated partner. Grey solid lines indicate possible complex formation, solid arrows point to direct interaction and dashed arrows to indirect influence. Membrane and nucleus (blue circle) mark predominant localization of the proteins. (**B**) Pathway studio analysis on the expression of investigated genes. The color of shown lines indicates the type of interaction: green line: promotion of indicated partner; red line: inhibition of indicated partner. Arrows indicate the direction of influence.

the RPM (Fig. 5D). This could, according to the presented analysis, be a reason that E-cadherin is enhanced and integrin-β_1 remains unchanged. Figure 8B shows the influence of the proteins on the expression of the relevant genes. This network includes 244 relationships. Looking at the green arrows shown it can be seen that most of the arrows start at MAPK8 or EGF. This means that both are main up-regulators of the system. While, as indicated above, the EGF protein was slightly lowered in AD cells during incubation on the RPM (Fig. 5D), the expression of *MAPK8* (*JNK1*) remained stable under s-μ*g* compared to 1*g* (Fig. 6N,O). Both entities have equal and different targets, as shown by the arrowheads. A possible balance of both systems appears to be a topic of future research.

Conclusions

Juvenile NHDF, when exposed to s-μg, grew in form of two different phenotypes, as adherent monolayer and as cells in compact MCS (Fig. 1). A similar behavior is also shown by other cell types, when they are cultured in space or under s-μ*g* conditions on Earth. Benign cells (chondrocytes[105] or thyroid cells[12]) and thyroid cancer cells[13,106] also exhibited a comparable growth. As mentioned above and shown by the various flow cytometric

Structure	AD cells	MCS cells
Focal adhesions		
gene expression	*ITGB1*↑	
intracellular protein	Caveolin-1↑	E-cadherin↑, Talin-1↑
Extracellular matrix		
gene expression	*FN1*↑ *MMP1*↑, *MMP3*↑	*LAMA3*↑, *ACAN*↓, *COL4A5*↑, *TIMP1*↑, *MMP1*↑↑, *MMP14*↓
intracellular protein	Fibronectin↑ Osteopontin↑ Collagen IV↑	Fibronectin↑ Osteopontin↑↑ Aggrecan↓ Collagen I↓, Collagen IV↑
Cytoskeleton		
intracellular protein	Vimentin↑	Pan-Actin↑, α-SM Actin↓
Growth factors		
gene expression	*TGFB1*↑	
Cytokines		
gene expression		*CXCL8*↑
intracellular protein		IL-8↑, MCP-1↑, JNK1↑
protein release		MCP-1↓

Table 1. Biochemical differences between adherently growing (2D) and multicellular spheroid cells (3D growth) of NHDF in s-µ*g*.

measurements, the reason for this phenomenon is probably due to a different accumulation of distinct, for spheroid formation responsible proteins in the individual cells of a population. The differences between the individual cells appear to be more expressed in cell populations cultured on the RPM as compared to the 1*g*-cultures (Figs 2 and 7). Though, at the moment one can only speculate about that spreading of protein accumulation. It could be due to differences of localization of the cells in a culture flask or to a variation of protein production based on regulation of transcription and translation processes. Perhaps both factors play a role.

The differential regulation of several ECM proteins, growth factors, cytokines in connection with matrix metalloproteinases showed a picture of interacting proteins (positively or negatively) which clearly strengthens 3D growth of the cells exposed to s-µ*g*. The differences and similarities between the adherent population and MCS are summarized in Table 1. Major divergences occurring among these two clusters are measured for vimentin, laminin, collagen type IV, TIMP1, MMP1, MMP14, E-cadherin, and IL-8. A similar result of both phenotypes was found for TGF-β_1, ITGB1, FN1, SPP1, and CAV1. These data suggest to evaluate the functional effects of these proteins in future investigations. In addition, future studies will be performed to shed light on the mechanisms involved in the process of spheroid formation, such as genetic knock-outs or knock-ins in cell lines. The membrane components laminin and collagen type IV, fibronectin, IL-8, MMPs and TIMP1 in concert with TGF-β_1 and integrin-β_1 play a major role in our experimental setting.

These new findings with NHDF indicate what may possibly occur in space. The behavior of fibroblasts under space conditions is of high interest because the astronaut's skin is getting thinner (thinned stratum corneum, impaired barrier function, and loss of dermal elasticity)[3,107] with time. Research in this area is of high interest because of the planned space tourism adventures in the near future. Moreover, knowledge about the mechanisms of fibroblast spheroid formation helps to increase our understanding in the biofabrication of biological tissues or it can be used for co-culture experiments with cancer cells and following drug testing.

Material and Methods

Cell culture. Juvenile normal human dermal fibroblasts (NHDF, catalogue number C-12300; PromoCell GmbH, Heidelberg, Germany) were delivered in a cryo-conserved state and cultured in 75 cm^2 ventilated cell culture flasks (Sarstedt AG, Nürnbrecht, Germany). Roswell Park Memorial Institute Medium (RPMI 1640) (Gibco, Carlsbad, USA) supplemented with 10% fetal calf serum (FCS) (ThermoFisher, Waltham, USA), 100 IU penicillin and 100 µg streptomycin (Biochrom AG, Berlin, Germany) was used under standard conditions of 37 °C and 5% CO_2. The RPM experiments including control groups were performed by seeding juvenile fibroblasts in 25 cm^2 ventilated cell culture flasks (Sarstedt AG) and allowing 24 h for the cells to attach to the bottom of the flask. A day later, the experiment started. In order to reduce shear stress from air inclusions, flasks were filled completely with medium. After completion of experiments medium was centrifugated thoroughly for detection of multicellular spheroids (MCS).

Random positioning machine. All experiments for simulation of the microgravity conditions were performed using a desktop RPM (Airbus Defence and Space, former Dutch Space, Leiden, Netherlands). The RPM was described earlier in detail[13,108,109]. Briefly, the RPM consists of two perpendicular, independently motor-driven frames, with the innermost frame carrying the specimen to be exposed to s-µ*g*. Using a personal computer, the frames were operated in the 3D random mode, moving in random directions and speeds, maintaining a mean angular velocity of 60 °/s. Over time, this movement pattern will lead to an averaging of the gravitational vector to zero, effectively producing a state of s-µ*g*. The quality of the achieved s-µ*g* is best in the center of the two rotational axes while some residual acceleration forces are present outside of it. Cell cultures of the RPM-groups were seeded

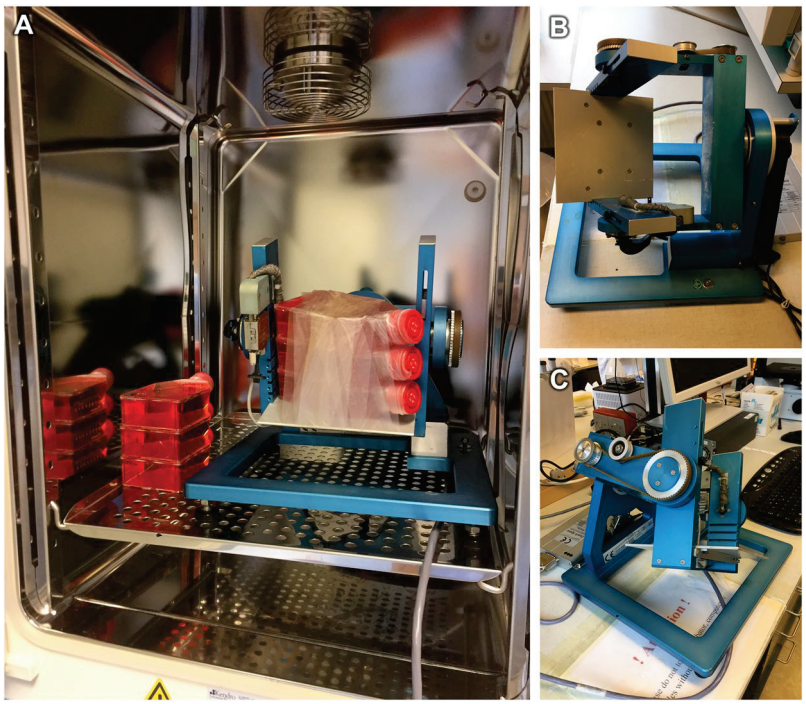


Figure 9. Table-top random positioning machine: Mounted cell culture flasks for RPM-experiments with adjacent 1*g*-control flasks in an incubator (**A**). RPM-frame without mounted flasks (**B**,**C**).

as described above and mounted to the RPM platform. The RPM was placed inside an incubator at 37 °C and 5% CO_2[13]. Cell cultures of the 1*g*-control groups were placed next to the RPM inside the same incubator (Fig. 9A).

Microscopy. Phase contrast microscopy was performed before and after the RPM-experiments to ensure cell viability and to detect possible morphological changes of the cell cultures. Phase contrast pictures were taken with a Leica DM IL LED microscope equipped with a Leica DFC310 FX digital CCD color camera (Leica Microsystems, Wetzlar, Germany). Immunofluorescence-stained cells were analyzed with a Leica DM2000 microscope with light source Leica EL6000. Excitation and emission wavelengths were $\lambda_{exc} = 488$ nm and $\lambda_{em} = 505$ nm for FITC. All samples were analyzed with the help of the image analysis program Leica Application Suite (Version 3.7; Leica Microsystems, Wetzlar, Germany).

Hematoxylin-Eosin and Elastica van Gieson staining. After the 3-day RPM-culture of NHDF, the 1*g*-cells, adherent s-µ*g*-cells and MCS were carefully washed three times in phosphate buffered saline (PBS) and fixed in 4% paraformaldehyde. HE- and EvG-staining procedures were performed to evaluate the cell morphology of the NHDF as previously described[53,110,111]. Briefly, for the HE stain, the cells were fixed with 2% PFA (Carl Roth) for 10 min. Following the fixation, the cells were incubated for 5 min with distilled water, then incubated for 10 min with an acidic Mayer's hematoxylin solution (Carl Roth) to stain the cell nuclei blue. The dye was removed by washing the sample three times with tapwater.The cytoplasm and other cell structures were stained with eosin G (Carl Roth) for 10 min and then washed three times with tapwater. The EvG staining was done according to standard procedures by the routine diagnostic laboratory of the Institute of Pathology, University Hospital of Regensburg. All samples were visualized by light microscopy, using the Leica DM IL LED microscope, as described above.

Immunofluorescence staining. The cells were fixed with a 4% paraformaldehyde solution for 20 min. Then they were subjected to membrane permeabilization with ice-cold methanol for 10 min and blocking with 1% (weight (w)/volume (v)) bovine serum albumin (BSA, Sigma-Aldrich, Steinheim, Germany) in PBS for 15 min. The slides were then released from the flasks and the cells were incubated with primary antibodies (listed in Table 2) in a PBS solution with 1% (w/v) BSA for 24 h at room temperature, followed by washing and incubation with secondary antibodies (Table 2) in PBS solution with 1% (w/v) BSA for an additional 24 h. Afterwards, the cells were washed three times with PBS and prepared for microscopy using Fluoroshield™ mounting media with DAPI (4',6-diamidino-2-phenylindole; Sigma-Aldrich). Slides were kept at 4 °C in a dark box for 2 days before microscopical investigation[41].

Flow cytometry. The staining procedure for flow cytometry was published earlier[14,112]. Briefly, PFA-fixed cells were carefully scraped off the bottom of the culture flasks, collected in 50-mL tubes and centrifuged for 5 min at 1500 × *g* at room temperature. The pelleted cells were resuspended in PBS, and 10^5 cells each were transferred into two round-bottom tubes and incubated with 0.1% Triton X-100 in PBS for 10 min. The cells in one tube were incubated for 90 min with the respective primary antibody, while the other was incubated with PBS. The cells in

Primary Antibody	Company	Dilution	Molecular Weight (kDa)	Catalogue Number
Collagen I	Invitrogen	1:250	115–120	PA1-26204
Collagen IV	Invitrogen	1:250	160	PA5-50939
Fibronectin	Sigma	1:400	220	F3648
Laminin	Sigma	1:200	250	L9393
Vimentin	Sigma	1:200	53	V5255
Vinculin	Sigma	1:400	116	V9131

Table 2. Antibodies used for immunofluorescence staining (IFS). The corresponding secondary antibodies – Anti-rabbit IgG (H + L), F(ab')$_2$ Fragment (Alexa Fluor®488 Conjugate) (Ref. 4412S) and Anti-mouse IgG (H + L), F(ab')$_2$ Fragment (Alexa Fluor®488 Conjugate) (Ref. 4408S, both CST, Danvers, MA, USA) – were used at a dilution of 1:500.

Primary Antibody	Company	Dilution	Molecular Weight (kDa)	Catalogue Number
Chondroitin sulfate	Invitrogen	1:100	210–250	MA3-16888
Collagen I	Invitrogen	1:100	115–120	PA1-26204
Collagen III	Invitrogen	1:100	140	PA5-27828
Collagen IV	Invitrogen	1:100	160	PA5-50939
Fibronectin	Invitrogen	1:100	220	PA5-29578
Laminin	Invitrogen	1:100	250	PA1-16730
Osteopontin	Sigma	1:100	50	SAB4200018
Vinculin	Abcam	1:100	116	Ab18058

Table 3. Antibodies used for Flow Cytometry. The corresponding secondary antibodies – Anti-rabbit IgG (H + L), F(ab')$_2$ Fragment (Alexa Fluor®488 Conjugate) (Ref. 4412S) and Anti-mouse IgG (H + L), F(ab')$_2$ Fragment (Alexa Fluor®488 Conjugate) (Ref. 4408S, both CST) – were used at a dilution of 1:1000.

both round-bottom tubes were then incubated with the secondary antibody (Cell Signaling; 1:1000) for 60 min. An overview of the used antibodies and their applied concentrations is given in Table 3. The final measurement of the single cells was performed with a FACSCanto™ II (Becton Dickinson, Franklin Lakes, NJ, USA). The analysis of the flow cytometry data was carried out with FlowJo 10.4 (FlowJo LLC, Ashland, OR, USA).

RNA isolation and quantitative real-time PCR. The method of RNA extraction and qPCR was published earlier in detail[8,10,13]. Briefly, the RNA isolation was done using the RNeasy Mini Kit (Qiagen, Hilden, Germany), with an additional DNase digestion step (Qiagen) in order to eliminate residual DNA contaminations. Afterwards, the amount of RNA was quantified using a Photometer Ultrospec2010 (Amersham Biosciences, Freiburg, Germany). The first strand cDNA synthesis kit (Thermo Fisher Scientific, Waltham, US) was applied for reverse transcription. qPCR was performed on the 7500 Fast Real-Time PCR System using the FAST SYBR Green Master Mix (both Applied Biosystems, Darmstadt, Germany) according to standard protocols[8,10,13]. In short, 1 µg of isolated RNA was reverse-transcribed in a total volume of 20 µL reaction mix. For the PCR, 1 µL of the resulting cDNA was mixed with water, primer stocks and 2x FAST SYBR Green Master Mix to yield a final reaction voume of 15 µL with an end concentration of 300 nM for the primers. For the actual PCR run we employed the default protocol for the FAST Master Mixes as implemented in the system software, complemented by a subsequent melting curve analysis to check for primer specificity. cDNA-selective-primers were synthesized by TIB Molbiol (Berlin, Germany) and are listed in Table 4. The primers were designed using Primer Express (Applied Biosystems) to have a T_m of ~60 °C and to span exon-exon boundaries. All samples were measured in triplicate. For normalization, 18S rRNA was used as a housekeeping gene. The comparative CT(ΔΔCT) method was used for relative quantification of transcription levels and 1*g* was defined as 100% for reference.

Western blot analysis. Western blotting and densitometry were performed as previously described[41]. The number of investigated samples/per group was n = 5. Equal amounts of 10 µL lysate containing 2 µg/µL protein were loaded and separated on precast TGX stain-free gels (Bio-Rad, Munich, Germany). Transturbo blot PVDF membranes (Bio-Rad) were used for blotting. An overview of the used antibodies and their applied concentrations is given in Table 5. The analysis was performed using ImageQuant™ LAS 4000 (GE Healthcare UK Limited, Buckinghamshire, UK). The membranes were analyzed using ImageJ software (U.S. National Institutes of Health, Bethesda, MD, USA; http://rsb.info.nih.gov/ij/), for densitometric quantification of the bands. Protein from the 3T3 Swiss Albino cell line (American Type Culture Collection, Manassas, VA, USA) was used as a positive control[113].

Multianalyte profiling (MAP) technology. Investigation of cellular supernatants for distribution of cytokines and proteins was performed by means of Multianalyte Profiling (MAP) technology. The analysis

Gene	Primer Name	Sequence
18S (HKG)	18S-F	GGAGCCTGCGGCTTAATTT
	18S-R	CAACTAAGAACGGCCATGCA
ACAN	ACAN-F	AGTCCAACTCTTCAAGGTGAACTA
	ACAN-R	ACTCAGCGAGTTGTCATGGT
ACTA2	ACTA2-F	GAGCGTGGCTATTCCTTCGT
	ACTA2-R	TTCAAAGTCCAGAGCTACATAACACAGT
ACTB	ACTB-F	TGCCGACAGGATGCAGAAG
	ACTB-R	GCCGATCCACACGGAGTACT
CAV1	CAV1-F	CCTCCTCACAGTTTTCATCCA
	CAV1-R	TGTAGATGTTGCCCTGTTCC
COL1A1	COL1A1-F	ACGAAGACATCCCACCAATCAC
	COL1A1-R	CGTTGTCGCAGACGCAGAT
COL4A5	COL4A5-F	GGTACCTGTAACTACTATGCCAACTCCTA
	COL4A5-R	CGGCTAATTCGTGTCCTCAAG
CTGF	CTGF-F	ACAAGGGCCTCTTCTGTGACTT
	CTGF-R	GGTACACCGTACCACCGAAGAT
FAK1/*PTK2*	FAK1-F	TGTGGGTAAACCAGATCCTGC
	FAK1-R	CTGAAGCTTGACACCCTCGT
FN1	FN1-F	AGATCTACCTGTACACCTTGAATGACA
	FN1-R	CATGATACCAGCAAGGAATTGG
ICAM1	ICAM1-F	CGGCTGACGTGTGCAGTAAT
	ICAM1-R	CTTCTGAGACCTCTGGCTTCGT
IL6	IL6-F	CGGGAACGAAAGAGAAGCTCTA
	IL6-R	GAGCAGCCCCAGGGAGAA
IL8/*CXCL8*	IL8-F	TGGCAGCCTTCCTGATTTCT
	IL8-R	GGGTGGAAAGGTTTGGAGTATG
ITGB1	ITGB1-F	GAAAACAGCGCATATCTGGAAATT
	ITGB1-R	CAGCCAATCAGTGATCCACAA
JNK1/*MAPK8*	JNK1-F	TCTCCTTTAGGTGCAGCAGTG
	JNK1-R	CAGAGGCCAAAGTCGGATCT
LAMA3	LAMA3-F	AAAGCAAGAAGTCAGTCCAGC
	LAMA3-R	TCCCATGAAGACCATCTCGG
MCP1/*CCL2*	MCP1-F	GCTATAGAAGAATCACCAGCAGCAA
	MCP1-R	TGGAATCCTGAACCCACTTCTG
MMP1	MMP1-F	GTCAGGGGAGATCATCGGG
	MMP1-R	GAGCATCCCCTCCAATACCTG
MMP3	MMP3-F	ACAAAGGATACAACAGGGACCAA
	MMP3-R	TAGAGTGGGTACATCAAAGCTTCAGT
MMP14	MMP14-F	ACTTTATGGGGGTGAGTCAGG
	MMP14-R	GATGTTGGGCCCATAGGTGG
NFκBP65/*RELA*	NFKBP65-F	CGCTTCTTCACACACTGGATTC
	NFKBP65-R	ACTGCCGGGATGGCTTCT
SPP1	SPP1-F	CGAGGTGATAGTGTGGTTTATGGA
	SPP1-R	CGTCTGTAGCATCAGGGTACTG
TGFB1	TGFB1-F	CACCCGCGTGCTAATGGT
	TGFB1-R	AGAGCAACACGGGTTCAGGTA
TIMP1	TIMP1-F	GCCATCGCCGCAGATC
	TIMP1-R	GCTATCAGCCACAGCAACAACA
TLN1	TLN1-F	GATGGCTATTACTCAGTACAGACAACTGA
	TLN1-R	CATAGTAGACTCCTCATCTCCTTCCA
TNFA	TNFA-F	ATCTTCTCGAACCCCGAGTGA
	TNFA-R	GGCCCGGCGGTTCA
TUBB	TUBB-F	CTGGACCGCATCTCTGTGTACTAC
	TUBB-R	GACCTGAGCGAACAGAGTCCAT
VCL	VCL-F	GTCTCGGCTGCTCGTATCTT
	VCL-R	GTCCACCAGCCCTGTCATTT

Continued

Gene	Primer Name	Sequence
VEGFA	VEGFA-F	GCGCTGATAGACATCCATGAAC
	VEGFA-R	CTACCTCCACCATGCCAAGTG
VIM	VIM-F	TTCAGAGAGAGGAAGCCGAAAAC
	VIM-R	AGATTCCACTTTGCGTTCAAGGT

Table 4. Primer sequences for qPCR. All sequences are given in 5′-3′ direction.

Primary Antibody	Company	Dilution	Molecular Weight (kDa)	Catalogue Number
Aggrecan	Abcam	1:1000	210-250	ab36861
α-actin 2	Abcam	1:1000	42	ab5694
β-Actin (HKP)	Sigma	1:1000	42	AC-74
Caveolin-1	Abcam	1:1000	22	ab2910
Collagen I	Abcam	1:500	115-120	ab21286
Collagen IV	Invitrogen	1:1000	160	PA5-50939
CTGF	Sigma	1:1000	38	C4871
E-Cadherin	Abcam	1:1000	120	ab15148
EGF	Sigma	1:1000	26	WH0001950M1
Fibronectin	Invitrogen	1:1000	220	PA5-29578
IL-6	Invitrogen	1:1000	26	AHC0762
IL-8	Abcam	1:1000	11	ab7747
Integrin-β_1	CST	1:1000	115,135	4706S
JNK1	Abcam	1:1000	48	ab110724
Laminin	Sigma	1:1000	250	L9393
MCP-1/CCL2	Sigma	1:500	18	Mabn712
NF-κB	CST	1:1000	65	C22B4
Osteopontin	Sigma	1:1000	50	o7264
Pan-Actin	CST	1:1000	45	D18C11
Talin	Sigma	1:1000	225-230	T3287
β-Tubulin	Santa Cruz	1:1000	55	sc-5274
VEGF	Abcam	1:1000	23	ab46154
Vimentin	Sigma	1:1000	53	V5255
Vinculin	Sigma	1:1000	116	V9131

Table 5. Antibodies applied for Western blot analysis. The corresponding secondary antibody HRP-linked anti-mouse IgG (Ref. P0260) was used at a dilution of 1:2000, the HRP-linked anti-rabbit IgG (Ref. P0399, both Dako, Carpinteria, CA, USA) was used at a dilution of 1:4000.

was carried out using Human Cytokine MAP A v1.0 by Myriad RBM, Inc., Austin, TX, USA. Supernatants of 1*g*-control and RPM-groups where stored at −80 °C and shipped to Myriad RBM.

Pathway analysis. To investigate and visualize the original localization and the mutual interactions of detected proteins, we entered relevant UniProt accession numbers in a Pathway Studio v.11 software (Elsevier Research Solutions, Amsterdam, The Netherlands)[31,77].

Statistical analysis. Statistical Analysis was performed using IBM SPSS Statistics 23.0 software (IBM Deutschland GmbH, Ehningen, Germany) in form of mean ± SD. Statistical deviations were evaluated using Mann-Whitney-U-test. All data is presented as mean ± standard deviation. $p < 0.05$ was considered as statistically significant.

References

1. Crucian, B. *et al*. Incidence of clinical symptoms during long-duration orbital spaceflight. *Int J Gen Med* **9**, 383–391, https://doi.org/10.2147/IJGM.S114188 (2016).
2. Neutelings, T. *et al*. Skin physiology in microgravity: a 3-month stay aboard ISS induces dermal atrophy and affects cutaneous muscle and hair follicles cycling in mice. *NPJ Microgravity* **1**, 15002, https://doi.org/10.1038/npjmgrav.2015.2 (2015).
3. Tronnier, H., Wiebusch, M. & Heinrich, U. Change in skin physiological parameters in space–report on and results of the first study on man. *Skin Pharmacol Physiol* **21**, 283–292, https://doi.org/10.1159/000148045 (2008).
4. Buckley, C. D. *et al*. Fibroblasts regulate the switch from acute resolving to chronic persistent inflammation. *Trends Immunol* **22**, 199–204 (2001).
5. Sriram, G., Bigliardi, P. L. & Bigliardi-Qi, M. Fibroblast heterogeneity and its implications for engineering organotypic skin models *in vitro*. *Eur J Cell Biol* **94**, 483–512, https://doi.org/10.1016/j.ejcb.2015.08.001 (2015).
6. Kendall, R. T. & Feghali-Bostwick, C. A. Fibroblasts in fibrosis: novel roles and mediators. *Front Pharmacol* **5**, 123, https://doi.org/10.3389/fphar.2014.00123 (2014).
7. Pietsch, J. *et al*. The effects of weightlessness on the human organism and mammalian cells. *Curr Mol Med* **11**, 350–364 (2011).

8. Kopp, S. *et al*. The role of NFkappaB in spheroid formation of human breast cancer cells cultured on the Random Positioning Machine. *Sci Rep* **8**, 921, https://doi.org/10.1038/s41598-017-18556-8 (2018).
9. Ma, X. *et al*. Proteomic differences between microvascular endothelial cells and the EA.hy926 cell line forming three-dimensional structures. *Proteomics* **14**, 689–698, https://doi.org/10.1002/pmic.201300453 (2014).
10. Ma, X. *et al*. Genomic approach to identify factors that drive the formation of three-dimensional structures by EA.hy926 endothelial cells. *PLoS One* **8**, e64402, https://doi.org/10.1371/journal.pone.0064402 (2013).
11. Sahana, J. *et al*. Decreased E-Cadherin in MCF7 Human Breast Cancer Cells Forming Multicellular Spheroids Exposed to Simulated Microgravity. *Proteomics* **18**, e1800015, https://doi.org/10.1002/pmic.201800015 (2018).
12. Warnke, E. *et al*. Cytokine Release and Focal Adhesion Proteins in Normal Thyroid Cells Cultured on the Random Positioning Machine. *Cell Physiol Biochem* **43**, 257–270, https://doi.org/10.1159/000480368 (2017).
13. Warnke, E. *et al*. Spheroid formation of human thyroid cancer cells under simulated microgravity: a possible role of CTGF and CAV1. *Cell Commun Signal* **12**, 32, https://doi.org/10.1186/1478-811X-12-32 (2014).
14. Pietsch, J. *et al*. Three-dimensional growth of human endothelial cells in an automated cell culture experiment container during the SpaceX CRS-8 ISS space mission - The SPHEROIDS project. *Biomaterials* **124**, 126–156, https://doi.org/10.1016/j.biomaterials.2017.02.005 (2017).
15. Pietsch, J. *et al*. Application of free-flow IEF to identify protein candidates changing under microgravity conditions. *Proteomics* **10**, 904–913, https://doi.org/10.1002/pmic.200900226 (2010).
16. Pietsch, J. *et al*. Spheroid formation of human thyroid cancer cells in an automated culturing system during the Shenzhou-8 Space mission. *Biomaterials* **34**, 7694–7705, https://doi.org/10.1016/j.biomaterials.2013.06.054 (2013).
17. Corydon, T. J. *et al*. Reduced Expression of Cytoskeletal and Extracellular Matrix Genes in Human Adult Retinal Pigment Epithelium Cells Exposed to Simulated Microgravity. *Cell Physiol Biochem* **40**, 1–17, https://doi.org/10.1159/000452520 (2016).
18. Pietsch, J. *et al*. A proteomic approach to analysing spheroid formation of two human thyroid cell lines cultured on a random positioning machine. *Proteomics* **11**, 2095–2104, https://doi.org/10.1002/pmic.201000817 (2011).
19. Berahim, Z., Moharamzadeh, K., Rawlinson, A. & Jowett, A. K. Biologic interaction of three-dimensional periodontal fibroblast spheroids with collagen-based and synthetic membranes. *J Periodontol* **82**, 790–797, https://doi.org/10.1902/jop.2010.100533 (2011).
20. Kim, S. A., Lee, E. K. & Kuh, H. J. Co-culture of 3D tumor spheroids with fibroblasts as a model for epithelial-mesenchymal transition *in vitro*. *Exp Cell Res* **335**, 187–196, https://doi.org/10.1016/j.yexcr.2015.05.016 (2015).
21. Jeong, S. Y., Lee, J. H., Shin, Y., Chung, S. & Kuh, H. J. Co-Culture of Tumor Spheroids and Fibroblasts in a Collagen Matrix-Incorporated Microfluidic Chip Mimics Reciprocal Activation in Solid Tumor Microenvironment. *PLoS One* **11**, e0159013, https://doi.org/10.1371/journal.pone.0159013 (2016).
22. Infanger, M. *et al*. Induction of three-dimensional assembly and increase in apoptosis of human endothelial cells by simulated microgravity: impact of vascular endothelial growth factor. *Apoptosis* **11**, 749–764, https://doi.org/10.1007/s10495-006-5697-7 (2006).
23. Svejgaard, B. *et al*. Common Effects on Cancer Cells Exerted by a Random Positioning Machine and a 2D Clinostat. *PLoS One* **10**, e0135157, https://doi.org/10.1371/journal.pone.0135157 (2015).
24. Mann, V. *et al*. Changes in Human Foetal Osteoblasts Exposed to the Random Positioning Machine and Bone Construct Tissue Engineering. *Int J Mol Sci* **20**, https://doi.org/10.3390/ijms20061357 (2019).
25. Grimm, D. *et al*. Growing tissues in real and simulated microgravity: new methods for tissue engineering. *Tissue Eng Part B Rev* **20**, 555–566, https://doi.org/10.1089/ten.TEB.2013.0704 (2014).
26. Grimm, D. *et al*. Tissue Engineering Under Microgravity Conditions-Use of Stem Cells and Specialized Cells. *Stem Cells Dev* **27**, 787–804, https://doi.org/10.1089/scd.2017.0242 (2018).
27. Grimm, D. *et al*. Different responsiveness of endothelial cells to vascular endothelial growth factor and basic fibroblast growth factor added to culture media under gravity and simulated microgravity. *Tissue Eng Part A* **16**, 1559–1573, https://doi.org/10.1089/ten.TEA.2009.0524 (2010).
28. Schönberger, J. *et al*. Establishment and characterization of the follicular thyroid carcinoma cell line ML-1. *J Mol Med* **78**, 102–110 (2000).
29. Weber, G., Grimm, D. & Bauer, J. Application of binary buffer systems to free flow cell electrophoresis. *Electrophoresis* **21**, 325–328, https://doi.org/10.1002/(sici)1522-2683(20000101)21:2<325::Aid-elps325>3.0.Co;2-p (2000).
30. Liu, Y., Loijens, J. C., Martin, K. H., Karginov, A. V. & Parsons, J. T. The association of ASAP1, an ADP ribosylation factor-GTPase activating protein, with focal adhesion kinase contributes to the process of focal adhesion assembly. *Mol Biol Cell* **13**, 2147–2156, https://doi.org/10.1091/mbc.e02-01-0018 (2002).
31. Bauer, J. *et al*. Proteome Analysis of Human Follicular Thyroid Cancer Cells Exposed to the Random Positioning Machine. *Int J Mol Sci* **18**, https://doi.org/10.3390/ijms18030546 (2017).
32. Timpl, R. *et al*. Laminin–a glycoprotein from basement membranes. *J Biol Chem* **254**, 9933–9937 (1979).
33. Grimm, D. *et al*. Simulated microgravity alters differentiation and increases apoptosis in human follicular thyroid carcinoma cells. *FASEB J* **16**, 604–606 (2002).
34. Ulbrich, C. *et al*. The impact of vascular endothelial growth factor and basic fibroblast growth factor on cardiac fibroblasts grown under altered gravity conditions. *Cell Physiol Biochem* **26**, 1011–1022, https://doi.org/10.1159/000323976 (2010).
35. Riwaldt, S. *et al*. Preparation of A Spaceflight: Apoptosis Search in Sutured Wound Healing Models. *Int J Mol Sci* **18**, https://doi.org/10.3390/ijms18122604 (2017).
36. Lenselink, E. A. Role of fibronectin in normal wound healing. *Int Wound J* **12**, 313–316, https://doi.org/10.1111/iwj.12109 (2015).
37. Zhang, Y. *et al*. Disentangling the multifactorial contributions of fibronectin, collagen and cyclic strain on MMP expression and extracellular matrix remodeling by fibroblasts. *Matrix Biol* **40**, 62–72, https://doi.org/10.1016/j.matbio.2014.09.001 (2014).
38. Aleshcheva, G. *et al*. Moderate alterations of the cytoskeleton in human chondrocytes after short-term microgravity produced by parabolic flight maneuvers could be prevented by up-regulation of BMP-2 and SOX-9. *FASEB J* **29**, 2303–2314, https://doi.org/10.1096/fj.14-268151 (2015).
39. Fioravanti, A. & Collodel, G. In *Adv Pharmacol* Vol. 53, 449–465 (Academic Press, 2006).
40. Grimm, D. *et al*. A delayed type of three-dimensional growth of human endothelial cells under simulated weightlessness. *Tissue Eng Part A* **15**, 2267–2275, https://doi.org/10.1089/ten.tea.2008.0576 (2009).
41. Dittrich, A. *et al*. Key Proteins Involved in Spheroid Formation and Angiogenesis in Endothelial Cells After Long-Term Exposure to Simulated Microgravity. *Cell Physiol Biochem* **45**, 429–445, https://doi.org/10.1159/000486920 (2018).
42. Gupta, A. C. *et al*. Establishment of an *in vitro* organoid model of dermal papilla of human hair follicle. *J Cell Physiol* **233**, 9015–9030, https://doi.org/10.1002/jcp.26853 (2018).
43. Grimm, D. *et al*. Effects of simulated microgravity on thyroid carcinoma cells. *J Gravit Physiol* **9**, P253–256 (2002).
44. Infanger, M. *et al*. Simulated weightlessness changes the cytoskeleton and extracellular matrix proteins in papillary thyroid carcinoma cells. *Cell Tissue Res* **324**, 267–277, https://doi.org/10.1007/s00441-005-0142-8 (2006).
45. Oliver, N., Babu, M. & Diegelmann, R. Fibronectin gene transcription is enhanced in abnormal wound healing. *J Invest Dermatol* **99**, 579–586 (1992).
46. Aleshcheva, G. *et al*. Changes in morphology, gene expression and protein content in chondrocytes cultured on a random positioning machine. *PLoS One* **8**, e79057, https://doi.org/10.1371/journal.pone.0079057 (2013).

47. Mendez, M. G., Kojima, S. & Goldman, R. D. Vimentin induces changes in cell shape, motility, and adhesion during the epithelial to mesenchymal transition. *FASEB J* **24**, 1838–1851, https://doi.org/10.1096/fj.09-151639 (2010).
48. Wessels, D. J. *et al*. Reciprocal signaling and direct physical interactions between fibroblasts and breast cancer cells in a 3D environment. *PLoS One* **14**, e0218854, https://doi.org/10.1371/journal.pone.0218854 (2019).
49. Bunnell, T. M., Burbach, B. J., Shimizu, Y. & Ervasti, J. M. beta-Actin specifically controls cell growth, migration, and the G-actin pool. *Mol Biol Cell* **22**, 4047–4058, https://doi.org/10.1091/mbc.E11-06-0582 (2011).
50. Cleveland, D. W. *et al*. Number and evolutionary conservation of alpha- and beta-tubulin and cytoplasmic beta- and gamma-actin genes using specific cloned cDNA probes. *Cell* **20**, 95–105 (1980).
51. Hammond, J. W., Cai, D. & Verhey, K. J. Tubulin modifications and their cellular functions. *Current opinion in cell biology* **20**, 71–76, https://doi.org/10.1016/j.ceb.2007.11.010 (2008).
52. Corydon, T. J. *et al*. Alterations of the cytoskeleton in human cells in space proved by life-cell imaging. *Sci Rep* **6**, 20043, https://doi.org/10.1038/srep20043 (2016).
53. Kopp, S. *et al*. Identifications of novel mechanisms in breast cancer cells involving duct-like multicellular spheroid formation after exposure to the Random Positioning Machine. *Sci Rep* **6**, 26887, https://doi.org/10.1038/srep26887 (2016).
54. Kopp, S. *et al*. Microgravity Affects Thyroid Cancer Cells during the TEXUS-53 Mission Stronger than Hypergravity. *Int J Mol Sci* **19**, 4001 (2018).
55. Croute, F., Gaubin, Y., Pianezzi, B. & Soleilhavoup, J. P. Effects of hypergravity on the cell shape and on the organization of cytoskeleton and extracelluar matrix molecules of *in vitro* human dermal fibroblasts. *Microgravity Sci Technol* **8**, 118–124 (1995).
56. Cogoli, A. Signal transduction in T lymphocytes in microgravity. *Gravit Space Biol Bull* **10**, 5–16 (1997).
57. Häder, D. P., Braun, M., Grimm, D. & Hemmersbach, R. Gravireceptors in eukaryotes-a comparison of case studies on the cellular level. *NPJ Microgravity* **3**, 13, https://doi.org/10.1038/s41526-017-0018-8 (2017).
58. Ingber, D. How cells (might) sense microgravity. *FASEB J* **13**(Suppl), S3–15 (1999).
59. Vorselen, D., Roos, W. H., MacKintosh, F. C., Wuite, G. J. & van Loon, J. J. The role of the cytoskeleton in sensing changes in gravity by nonspecialized cells. *FASEB J* **28**, 536–547, https://doi.org/10.1096/fj.13-236356 (2014).
60. Geiger, B., Spatz, J. P. & Bershadsky, A. D. Environmental sensing through focal adhesions. *Nat Rev Mol Cell Biol* **10**, 21–33, https://doi.org/10.1038/nrm2593 (2009).
61. Zhao, T. *et al*. Simulated Microgravity Reduces Focal Adhesions and Alters Cytoskeleton and Nuclear Positioning Leading to Enhanced Apoptosis via Suppressing FAK/RhoA-Mediated mTORC1/NF-κB and ERK1/2 Pathways. *Int J Mol Sci* **19**, https://doi.org/10.3390/ijms19071994 (2018).
62. Izard, T. & Brown, D. T. Mechanisms and Functions of Vinculin Interactions with Phospholipids at Cell Adhesion Sites. *J Biol Chem* **291**, 2548–2555, https://doi.org/10.1074/jbc.R115.686493 (2016).
63. Spanjaard, E. & de Rooij, J. Mechanotransduction: Vinculin Provides Stability when Tension Rises. *Curr Biol* **23**, R159–R161, https://doi.org/10.1016/j.cub.2013.01.020 (2013).
64. Humphries, J. D. *et al*. Vinculin controls focal adhesion formation by direct interactions with talin and actin. *J Cell Biol* **179**, 1043–1057, https://doi.org/10.1083/jcb.200703036 (2007).
65. Legate, K. R., Wickstrom, S. A. & Fassler, R. Genetic and cell biological analysis of integrin outside-in signaling. *Genes Dev* **23**, 397–418, https://doi.org/10.1101/gad.1758709 (2009).
66. Katsumi, A., Orr, A. W., Tzima, E. & Schwartz, M. A. Integrins in mechanotransduction. *J Biol Chem* **279**, 12001–12004, https://doi.org/10.1074/jbc.R300038200 (2004).
67. Cui, X., Hartanto, Y. & Zhang, H. Advances in multicellular spheroids formation. *J R Soc Interface* **14**, https://doi.org/10.1098/rsif.2016.0877 (2017).
68. Wang, H. B., Dembo, M., Hanks, S. K. & Wang, Y. Focal adhesion kinase is involved in mechanosensing during fibroblast migration. *Proc Natl Acad Sci USA* **98**, 11295–11300, https://doi.org/10.1073/pnas.201201198 (2001).
69. Stutchbury, B., Atherton, P., Tsang, R., Wang, D. Y. & Ballestrem, C. Distinct focal adhesion protein modules control different aspects of mechanotransduction. *J Cell Sci* **130**, 1612–1624, https://doi.org/10.1242/jcs.195362 (2017).
70. Matsuyoshi, N. & Imamura, S. Multiple cadherins are expressed in human fibroblasts. *Biochem Biophys Res Commun* **235**, 355–358, https://doi.org/10.1006/bbrc.1997.6707 (1997).
71. Nassef, M. Z. *et al*. Real Microgravity Influences the Cytoskeleton and Focal Adhesions in Human Breast Cancer Cells. *Int J Mol Sci* **20**, 3156 (2019).
72. Riwaldt, S. *et al*. The Importance of Caveolin-1 as Key-Regulator of Three-Dimensional Growth in Thyroid Cancer Cells Cultured under Real and Simulated Microgravity Conditions. *Int J Mol Sci* **16**, 28296–28310, https://doi.org/10.3390/ijms161226108 (2015).
73. Hsu, C. K. *et al*. Caveolin-1 Controls Hyperresponsiveness to Mechanical Stimuli and Fibrogenesis-Associated RUNX2 Activation in Keloid Fibroblasts. *J Invest Dermatol* **138**, 208–218, https://doi.org/10.1016/j.jid.2017.05.041 (2018).
74. Kingsley, D. M. The TGF-beta superfamily: new members, new receptors, and new genetic tests of function in different organisms. *Genes Dev* **8**, 133–146 (1994).
75. Wehland, M. *et al*. The impact of altered gravity and vibration on endothelial cells during a parabolic flight. *Cell Physiol Biochem* **31**, 432–451, https://doi.org/10.1159/000343380 (2013).
76. Grimm, D., Bauer, J. & Schoenberger, J. Blockade of neoangiogenesis, a new and promising technique to control the growth of malignant tumors and their metastases. *Curr Vasc Pharmacol* **7**, 347–357 (2009).
77. Riwaldt, S. *et al*. Pathways Regulating Spheroid Formation of Human Follicular Thyroid Cancer Cells under Simulated Microgravity Conditions: A Genetic Approach. *Int J Mol Sci* **17**, 528, https://doi.org/10.3390/ijms17040528 (2016).
78. Gopinathan, G. *et al*. Interleukin-6 Stimulates Defective Angiogenesis. *Cancer Res* **75**, 3098–3107, https://doi.org/10.1158/0008-5472.Can-15-1227 (2015).
79. Grosse, J. *et al*. Gravity-sensitive signaling drives 3-dimensional formation of multicellular thyroid cancer spheroids. *FASEB J* **26**, 5124–5140, https://doi.org/10.1096/fj.12-215749 (2012).
80. Deshmane, S. L., Kremlev, S., Amini, S. & Sawaya, B. E. Monocyte chemoattractant protein-1 (MCP-1): an overview. *J Interferon Cytokine Res* **29**, 313–326, https://doi.org/10.1089/jir.2008.0027 (2009).
81. Gerard, C. & Rollins, B. J. Chemokines and disease. *Nat Immunol* **2**, 108–115, https://doi.org/10.1038/84209 (2001).
82. Zhou, Y. Y., Li, Y., Jiang, W. Q. & Zhou, L. F. MAPK/JNK signalling: a potential autophagy regulation pathway. *Biosci Rep* **35**, https://doi.org/10.1042/bsr20140141 (2015).
83. Fisher, G. J., Varani, J. & Voorhees, J. J. Looking older: fibroblast collapse and therapeutic implications. *Arch Dermatol* **144**, 666–672, https://doi.org/10.1001/archderm.144.5.666 (2008).
84. Quan, T. *et al*. Matrix-degrading metalloproteinases in photoaging. *J Investig Dermatol Symp Proc* **14**, 20–24, https://doi.org/10.1038/jidsymp.2009.8 (2009).
85. Arpino, V., Brock, M. & Gill, S. E. The role of TIMPs in regulation of extracellular matrix proteolysis. *Matrix Biol* **44-46**, 247–254, https://doi.org/10.1016/j.matbio.2015.03.005 (2015).
86. Fligiel, S. E. *et al*. Collagen degradation in aged/photodamaged skin *in vivo* and after exposure to matrix metalloproteinase-1 *in vitro*. *J Invest Dermatol* **120**, 842–848, https://doi.org/10.1046/j.1523-1747.2003.12148.x (2003).
87. Quan, T. *et al*. Elevated matrix metalloproteinases and collagen fragmentation in photodamaged human skin: impact of altered extracellular matrix microenvironment on dermal fibroblast function. *J Invest Dermatol* **133**, 1362–1366, https://doi.org/10.1038/jid.2012.509 (2013).

88. Fisher, G. J. *et al*. Collagen fragmentation promotes oxidative stress and elevates matrix metalloproteinase-1 in fibroblasts in aged human skin. *Am J Pathol* **174**, 101–114, https://doi.org/10.2353/ajpath.2009.080599 (2009).
89. Xia, W. *et al*. Expression of catalytically active matrix metalloproteinase-1 in dermal fibroblasts induces collagen fragmentation and functional alterations that resemble aged human skin. *Aging Cell* **12**, 661–671, https://doi.org/10.1111/acel.12089 (2013).
90. Hohenester, E. & Yurchenco, P. D. Laminins in basement membrane assembly. *Cell Adh Migr* **7**, 56–63, https://doi.org/10.4161/cam.21831 (2013).
91. Laurie, G. W., Leblond, C. P. & Martin, G. R. Localization of type IV collagen, laminin, heparan sulfate proteoglycan, and fibronectin to the basal lamina of basement membranes. *J Cell Biol* **95**, 340–344 (1982).
92. Nimni, M. E. Collagen: structure, function, and metabolism in normal and fibrotic tissues. *Semin Arthritis Rheum* **13**, 1–86 (1983).
93. Uitto, J. & Bernstein, E. F. Molecular mechanisms of cutaneous aging: connective tissue alterations in the dermis. *J Investig Dermatol Symp Proc* **3**, 41–44 (1998).
94. Jackson, H. W., Defamie, V., Waterhouse, P. & Khokha, R. TIMPs: versatile extracellular regulators in cancer. *Nat Rev Cancer* **17**, 38–53, https://doi.org/10.1038/nrc.2016.115 (2017).
95. Verma, R. P. & Hansch, C. Matrix metalloproteinases (MMPs): chemical-biological functions and (Q)SARs. *Bioorg Med Chem* **15**, 2223–2268, https://doi.org/10.1016/j.bmc.2007.01.011 (2007).
96. Zigrino, P. *et al*. Fibroblast-Derived MMP-14 Regulates Collagen Homeostasis in Adult Skin. *J Invest Dermatol* **136**, 1575–1583, https://doi.org/10.1016/j.jid.2016.03.036 (2016).
97. Lessan, K., Aguiar, D. J., Oegema, T., Siebenson, L. & Skubitz, A. P. CD44 and beta1 integrin mediate ovarian carcinoma cell adhesion to peritoneal mesothelial cells. *Am J Pathol* **154**, 1525–1537 (1999).
98. Singh, M., Dalal, S. & Singh, K. Osteopontin: At the cross-roads of myocyte survival and myocardial function. *Life Sci* **118**, 1–6, https://doi.org/10.1016/j.lfs.2014.09.014 (2014).
99. Meves, A., Stremmel, C., Bottcher, R. T. & Fassler, R. beta1 integrins with individually disrupted cytoplasmic NPxY motifs are embryonic lethal but partially active in the epidermis. *J Invest Dermatol* **133**, 2722–2731, https://doi.org/10.1038/jid.2013.232 (2013).
100. Gingras, A. R. *et al*. Central region of talin has a unique fold that binds vinculin and actin. *J Biol Chem* **285**, 29577–29587, https://doi.org/10.1074/jbc.M109.095455 (2010).
101. Alapati, K., Kesanakurti, D., Rao, J. S. & Dasari, V. R. uPAR and cathepsin B-mediated compartmentalization of JNK regulates the migration of glioma-initiating cells. *Stem Cell Res* **12**, 716–729, https://doi.org/10.1016/j.scr.2014.02.008 (2014).
102. le Duc, Q. *et al*. Vinculin potentiates E-cadherin mechanosensing and is recruited to actin-anchored sites within adherens junctions in a myosin II-dependent manner. *J Cell Biol* **189**, 1107–1115, https://doi.org/10.1083/jcb.201001149 (2010).
103. Zhang, H. *et al*. Restoration of caveolin-1 expression suppresses growth and metastasis of head and neck squamous cell carcinoma. *Br J Cancer* **99**, 1684–1694, https://doi.org/10.1038/sj.bjc.6604735 (2008).
104. Ohji, M., SundarRaj, N. & Thoft, R. A. Transforming growth factor-beta stimulates collagen and fibronectin synthesis by human corneal stromal fibroblasts *in vitro*. *Curr Eye Res* **12**, 703–709 (1993).
105. Aleshcheva, G. *et al*. Tissue Engineering of Cartilage on Ground-Based Facilities. *Microgravity Sci Technol* **28**, 237–245, https://doi.org/10.1007/s12217-015-9479-0 (2016).
106. Kopp, S. *et al*. Mechanisms of three-dimensional growth of thyroid cells during long-term simulated microgravity. *Sci Rep* **5**, 16691, https://doi.org/10.1038/srep16691 (2015).
107. Burgdorf, W. H. & Hoenig, L. J. Dermatology and the American Experience in Space. *JAMA Dermatol* **151**, 877, https://doi.org/10.1001/jamadermatol.2014.2557 (2015).
108. Borst, A. G. & van Loon, J. J. W. A. Technology and Developments for the Random Positioning Machine, RPM. *Microgravity Sci Technol* **21**, 287–292, https://doi.org/10.1007/s12217-008-9043-2 (2008).
109. Wuest, S. L., Richard, S., Kopp, S., Grimm, D. & Egli, M. Simulated microgravity: critical review on the use of random positioning machines for mammalian cell culture. *Biomed Res Int* **2015**, 971474, https://doi.org/10.1155/2015/971474 (2015).
110. Infanger, M. *et al*. Vascular endothelial growth factor induces extracellular matrix proteins and osteopontin in the umbilical artery. *Ann Vasc Surg* **22**, 273–284, https://doi.org/10.1016/j.avsg.2007.11.002 (2008).
111. Infanger, M. *et al*. Intraluminal application of vascular endothelial growth factor enhances healing of microvascular anastomosis in a rat model. *J Vasc Res* **42**, 202–213, https://doi.org/10.1159/000085176 (2005).
112. Pietsch, J. *et al*. Metabolic enzyme diversity in different human thyroid cell lines and their sensitivity to gravitational forces. *Proteomics* **12**, 2539–2546, https://doi.org/10.1002/pmic.201200070 (2012).
113. Todaro, G. J. & Green, H. Quantitative studies of the growth of mouse embryo cells in culture and their development into established lines. *J Cell Biol* **17**, 299–313 (1963).

Acknowledgements

This project was supported by the German Space Agency (DLR, grants 50WB1524 and 50WB1924) and Aarhus University. We like to thank Ms. Christa Baumann, Institute of Pathology, University of Regensburg, Germany, for performing the histochemical staining.

Author Contributions

D.G., C.B., M.I. and N.A. designed the research. J.B., M.W., M.K., D.G. and C.B. analyzed the data. C.B., J.S., M.K., S.B., T.J.C., M.W., D.M. and J.B. performed the experiments: J.S. and M.W. Western blot analyses; C.B. and D.M. qPCR analyses; M.K. and S.B. flow cytometry, and J.S., C.B. and T.J.C. immunofluorescence staining. Pathway analyses were done by J.B., D.G., T.J.C., N.A. and M.I. supported the research. D.G., M.W., M.K., J.B., T.J.C. and C.B. wrote the paper.

Additional Information

Supplementary information accompanies this paper at https://doi.org/10.1038/s41598-019-48378-9.

Competing Interests: The authors declare no competing interests.

Publisher's note: Springer Nature remains neutral with regard to jurisdictional claims in published maps and institutional affiliations.


Open Access This article is licensed under a Creative Commons Attribution 4.0 International License, which permits use, sharing, adaptation, distribution and reproduction in any medium or format, as long as you give appropriate credit to the original author(s) and the source, provide a link to the Creative Commons license, and indicate if changes were made. The images or other third party material in this article are included in the article's Creative Commons license, unless indicated otherwise in a credit line to the material. If material is not included in the article's Creative Commons license and your intended use is not permitted by statutory regulation or exceeds the permitted use, you will need to obtain permission directly from the copyright holder. To view a copy of this license, visit http://creativecommons.org/licenses/by/4.0/.

© The Author(s) 2019

RESEARCH ARTICLE

Cellular Interactions

Proteomics

www.proteomics-journal.com

Decreased E-Cadherin in MCF7 Human Breast Cancer Cells Forming Multicellular Spheroids Exposed to Simulated Microgravity

*Jayashree Sahana, Mohamed Zakaria Nassef, Markus Wehland, Sascha Kopp, Marcus Krüger, Thomas J. Corydon, Manfred Infanger, Johann Bauer, and Daniela Grimm**

MCF7 human breast cancer cells were cultured under normal gravity (1 *g*) and on a random positioning machine (RPM) preventing sedimentation. After 2 weeks, adherent 1 *g*-control and adherent RPM cells (AD) as well as multicellular spheroids (MCS) were harvested. AD and MCS had been exposed to the RPM in the same culture flask. In a subsequent proteome analysis, the majority of the proteins detected showed similar label-free quantification (LFQ) scores in each of the respective subpopulations, but in both AD or MCS cultures, proteins were also found whose LFQs deviated at least twofold from their counterparts in the 1 *g*-control cells. They included the cell junction protein E-cadherin, which was diminished in MCS cells, where proteins of the E-cadherin autodegradation pathway were enhanced and c-Src (proto-oncogene tyrosine-protein kinase c-Src) was detected. Spheroid formation was prevented by inhibition of c-Src but promoted by antibodies blocking E-cadherin activity. An interaction analysis of the detected proteins that are involved in forming and regulating junctions or adhesion complexes and in E-cadherin autodegradation indicated connections between the two protein groups. This suggests that the balance of proteins that up- or downregulate E-cadherin mediates the tendency of MCF7 cells to form MCS during RPM exposure.

1. Introduction

Cell populations derived from human tissues such as the thyroid, the liver, the kidneys, the mammary gland, the cartilage, or the veins usually form monolayers when cultured in vitro under normal gravity conditions (1 *g*). If such monolayers are exposed to conditions similar to weightlessness that prevent their sedimentation, their growth behavior is altered. While some cells remain within the monolayer, many cells detach from the bottom of a culture flask and assemble to form 3D aggregates called spheroids.[1,2] This transition from 2D to 3D growth is accompanied by changes in a number of molecular and cellular characteristics, which may occur at the gene as well as at the gene product level. After 4 h of annulled gravity, cells begin to leave the monolayer.[3] After 24 h, a considerable number of 3D aggregates are observed. After 7 days of RPM exposure, cells adhering to the bottom of the culture flasks can still be observed as well as floating cell aggregates, which are rounded or show cellular structures resembling the organ from which the cells are derived.[4–7]

Cell sedimentation can be prevented by sending cells into space or by mounting culture flasks on a random positioning machine (RPM). Studying cells in vitro under these conditions may help to advance tissue engineering techniques,[2] to enhance learning about diseases that may affect astronauts or space tourists,[8] or allow investigation of mechanisms of metastasis of malignant cells.[9] Metastasis and spheroid formation under microgravity resemble each other, as

J. Sahana, Prof. T. J. Corydon, Prof. D. Grimm
Department of Biomedicine
Aarhus University
8000 Aarhus C, Denmark
E-mail: dgg@biomed.au.dk

M. Z. Nassef, Dr. M. Wehland, S. Kopp, Dr. M. Krüger, Prof. M. Infanger, Prof. D. Grimm
Clinic for Plastic, Aesthetic and Hand Surgery
Otto-von-Guericke-University Magdeburg
39120 Magdeburg, Germany

Prof. T. J. Corydon,
Department of Ophthalmology
Aarhus University Hospital
8000 Aarhus C, Denmark

Dr. J. Bauer
Max-Planck Institute of Biochemistry
82152 Martinsried, Germany

Prof. D. Grimm
Gravitational Biology and Translational Regenerative Medicine, Faculty of Medicine and Mechanical Engineering
Otto-von-Guericke-University Magdeburg
39120 Magdeburg, Germany

DOI: 10.1002/pmic.201800015

 © 2018 WILEY-VCH Verlag GmbH & Co. KGaA, Weinheim

Originale der Publikationen

Significance Statement

Cell exposure to a random positioning machine (RPM) mimics culturing cells in Space, where human tissue cancer cells split in a population, which continues to grow as a monolayer and another one forming multicellular spheroids (MCS). Investigating the proteome of MCF7 human breast cancer cells (BCC), in this study we expand the knowledge of proteins involved in triggering cells to leave the monolayer and grow within MCS subsequently. While ISG15 appears to play a role in the stabilization of MCS of BCC, like it was suggested earlier for thyroid cancer cells, ASAP1 is associated with the formation of MCS and BCAR1 and MAPK8 are enhanced in both types of cells, when they remain in a monolayer cultured on an RPM. In addition, SRC was detected in MCS but not in AD cells, while E-cadherin content was lower in MCS than in AD cells. Anti-E-cadherin antibodies reducing E-cadherin activity favor MCS formation, and PP2, blocking the E-cadherin regulator SRC, prevents MCS formation. As several authors have found a strict correlation between E-cadherin expression and metastatic activity of cancer cells in patients, studies on tumor cells exposed to an RPM can be considered to be a suitable model for studying metastatic mechanisms in vitro.

in both processes, a part of an existing cell population leaves its primary site of growth and moves to another one, where it joins or builds new 3D aggregates.[4,6] Spheroid formation has already been investigated in various types of cancer cells.[5] Microscopic observations clearly indicate a change of intercellular contacts, as spheroid cells are in contact with other cells that surround them in a 3D structure, while the adherent monolayer cells contact neighboring cells in one plane and the bottom of the culture flask, perpendicularly. Proteome analyses indicate a number of proteins that are differentially regulated during the change of these cell–cell contacts.[7,10–13] Regulated proteins include compounds of the extracellular matrix (ECM), of cell–cell adhesion complexes, and of apoptosis. But the exact mechanism of the transition from a 2D to a 3D kind of growth is not known yet. At the moment, it is thought that cells polarize before they leave a monolayer, but it is not sure, whether they subsequently pass through a period of lack of anchorage resembling the situation in a suspension culture.[6]

In recent studies, we have investigated the behavior of RPM-exposed breast cancer cells. Malignant breast cancer is still widespread with 1.7 million cases in 2012 with a high death rate, and urgently needs further research studies in this field.[6,14] Breast cancer is currently treated with several approved drugs, such as the tyrosine kinase inhibitor sorafenib, or with approved therapeutic antibodies such as bevacizumab, ramucirumab, or trastuzumab.[15,16] However, with the current state of technology, it is difficult to eliminate all of the cancer cells in any given patient in order to achieve healing. One solution could be to learn more about the proteins involved when cancer cells leave their primary site of growth and form new cell structures at another site.[5]

In this study, we identified proteins present in MCF7 breast cancer cells cultured under normal laboratory conditions or exposed to an RPM.[6] For this purpose, we applied a highly developed technique to determine a large number of cellular proteins.[17] In 2006, early approaches to identify the proteins in breast cancer cells were undertaken.[18,19] Later, the cellular proteins of breast cancer cells were determined focusing on special aspects, such as the differences between various breast cancer cell lines or cell clones[20,21] or on different types of proteins such as membrane proteins, mitochondrial proteins, glycolytic enzymes, or cell cycle promoting proteins.[22–25] In recent years, clear differences have been detected in the proteins of different breast cancer cell lines with different degrees of malignancy, and between proteins of cells derived from tumors from patients suffering from different grades of breast cancer.[26,27] In addition, protein differences were observed in cells treated with metformin, a drug that reduces blood glucose levels and is associated with a lower incidence of cancer.[28] In this study, we analyzed the proteins of the breast cancer cell line MCF7 and focused on quantitative differences in proteins detected in the cells of three MCF7 subpopulations, respectively. The subpopulations comprised adherent monolayer cells cultured under normal gravity (1 *g*-controls), as well as adherent monolayer cells (AD) and spheroid forming (multicellular spheroids [MCS]) cells, which were cultured on a RPM in the same culture flask. Evaluating these protein data, we focused on proteins involved in forming cell contacts with the cellular or noncellular environment, and on the pathways regulating these processes. We also tested the involved proteins' cell line specificity in comparison with previously investigated FTC-133 thyroid cancer cells[13,29,30] and found two agents influencing their behavior.

2. Experimental Section

2.1. Cell Culture and Harvest

MCF7 human breast adenocarcinoma cells were purchased from Sigma-Aldrich (order no. 86012803). Cells were cultivated in RPMI 1640 medium (Life Technologies) supplemented with 10% fetal calf serum (FCS; Biochrom, S0115) and 1% penicillin/streptomycin (Biochrom, A2213) at 37 °C and 5% CO_2. One day prior to the experimental run on the RPM, cells were seeded in T25 vented cell culture flasks (Sarstedt, Numbrecht, Germany). For microscopic investigations a second experiment was performed using slide flasks (Nunc™ Lab-Tek™ Flask on Slide; Thermo Fisher Scientific). When indicated, rat monoclonal antibodies against the ectodomain of E-cadherin (5 μl mL^{-1}, DECMA-1, U3254, Sigma-Aldrich)[31] or 5 × 10^6 mol L^{-1} PP2 (c-Src inhibitor, Calbiochem, San Diego, CA, USA) dissolved in DMSO were added.[32] Before starting the run, flasks were completely filled up with medium, ensuring that no air bubbles remained, as described by Kopp, et al.[6] After 2 weeks of culturing, the cells were harvested according to the protocol described by Bauer, et al.[13] First, the supernatant of each T25 culture flask from the RPM cultures was collected and centrifuged at 4 °C for MCS collection. After centrifugation, the supernatant was carefully aspirated, and the MCS were collected, washed in phosphate buffered saline (PBS, Life Technologies), and either stored in liquid nitrogen or prepared for microscopy. To harvest the adherent cells from the RPM AD and 1 *g* cultures, the supernatant was

 © 2018 WILEY-VCH Verlag GmbH & Co. KGaA, Weinheim

removed and 5 mL of ice-cold PBS was carefully added to each T25 flask after removal of the supernatant. The PBS was then aspirated and the cells were detached with a scraper. The cell suspension was collected and centrifuged at 4 °C. The PBS was discarded and the dry pellet was washed with PBS and either stored in liquid nitrogen or prepared for microscopy.

2.2. Acridine Orange/Ethidium Bromide Staining

MCF7 cells of all groups were stained with acridine orange/ethidium bromide (Molecular Probes, Darmstadt, Germany) after exposure to the RPM and their controls, respectively, as performed in previous studies.[33] The stained MCF7 cells were immediately investigated by using a Zeiss LSM 710 confocal laser scanning microscope (Zeiss, Jena, Germany). To check for cell death, the slides were left for drying and images were taken after 5 min.

2.3. Microscopy

The cells were observed and photographed using an Axiovert 25 Microscope (Carl Zeiss Microscopy, LLC, USA) and a Canon EOS 550D camera (Canon GmbH, Krefeld, Germany).

2.4. Random Positioning Machine

A desktop RPM (Airbus Defense and Space, former Dutch Space, Leiden, The Netherlands) was located in a standard incubator at 37 °C and 5% CO_2. The RPM was operated in real random mode with random directions and intervals and a maximum speed of 12.5 revolutions per minute. Sample flasks to be tested were placed onto the middle frame with a maximal distance of 7 cm from the center of rotation allowing a theoretical μg quality of between 10^{-4} and 10^{-2} g. The method has been extensively studied and described in other publications.[34,35] Static controls were placed beside the RPM in the same incubator.

2.5. RNA and Protein Isolation and Quantitative Real-Time PCR

RNA and protein isolation were performed according to routine protocols[4,36] using the AllPrep RNA/Protein Kit (Qiagen GmbH, Hilden, Germany) following the manufacturer's instructions. Biomolecule concentration determination was performed spectrophotometrically using an Ultrospec 2100 pro (Amersham Biosciences, Amersham, Great Britain). Complementary DNA was produced using the First Strand cDNA Synthesis Kit (Thermo Scientific, Waltham, Massachusetts, USA) following the manufacturer's instructions. Quantitative real-time PCR (qPCR) was performed using the SYBR Select Master Mix (Applied Biosystems, Darmstadt, Germany) and the 7500 Real-Time PCR System (Applied Biosystems) to determine the expression levels of *BCAR1*, *MAPK8 (JNK1)*, and *CDH1 (E-cadherin)* genes. Specific primers were designed to span exon–exon boundaries and to have a T_m of 60 °C using Primer Express software (Applied Biosystems), and were synthesized by TIB Molbiol (Berlin, Germany). Samples were measured in triplicate and were normalized to the housekeeper 18S rRNA.

The sequences of the primers used for qPCR were

BCAR1-F: CCAAGATGTCCGTGCCTATGAA; BCAR1-R: TGGCAGGCATGTTCTGTCTT; CDH1-F: GCTGGACCGAGAGAGTTTCC; CDH1-R: CAGCTGTTGCTGTTGTGCTT; MAPK8-F: TCTCCTTTAGGTGCAGCAGTG; MAPK8-R: CAGAGGCCAAAGTCGGATCT; as well as

18S-rRNA-F: GGAGCCTGCGGCTTAATTT; 18S-rRNA-R: CAACTAAGAACGGCCATGCA for the housekeeper gene. All sequences are given in the 5′-3′ direction.

The comparative threshold cycle ($\Delta\Delta$CT) method was used for relative quantification of transcription levels, with 1 g set as 100%.

2.6. Mass Spectrometry

Cells were lysed in a buffer containing 6 M guanidinium hydrochloride, 20 mM TCEP (tris(2-carboxyethyl)phosphine), and 40 mM chloroacetamide in 25 mM Tris pH 8.0. Lysis buffer preheated to 95 °C was added to the cells and the mixture was sonicated using a Bioruptor plus water bath sonicator (Diagnode, Seraing, Belgium). The lysates were again heated to 95 °C for 2 min followed by one more sonication at the maximum power setting for ten cycles. Following complete lysis, the sample was diluted tenfold with 25 mM Tris pH 8.0 and digested overnight at 37 °C with endoproteinase lysC (Wako Chemicals GmbH, Neuss, Germany) and mass spectrometry grade trypsin (V511, Promega) at a 1:50 enzyme:protein ratio. The digested peptides were then purified and concentrated on three plugged SDB-XC StageTips.[37]

For the liquid chromatography, mass spectrometry analysis of about 2 μg of peptides were loaded onto a 50 cm, 75 μm I.D. column packed with 1.9 μm C18 beads (Dr Maisch GmbH, Ammerbuch, Germany) using a Thermo EASY-nLC 1200 system (Thermo Scientific, Waltham, USA). The peptides were separated over a 215 min gradient with buffer A (0.1% formic acid) and buffer B (0.1% formic acid and 80% acetonitrile). The LC column was maintained at a constant temperature of 60 °C using a column oven (Sonation, Biberach, Germany). The peptides eluting from the column were directly sprayed into a Q Exactive HF mass spectrometer (Thermo Scientific) via a nano-electrospray ionization source (Thermo Scientific).[38]

The mass spectrometer was operated in a data-dependent top 15 mode. Survey scans and fragmentation scans were acquired at resolution of 60 000 and 15 000, respectively ($m/z = 200$). Fragmentation was performed on precursors isolated within a window of 1.4 m/z with a normalized collision energy setting of 27.

Raw data from the mass spectrometer were processed using the MaxQuant computational proteomics platform version 1.5.7.9[39] using the standard parameters. Relative protein quantification analysis was performed using the label-free quantitation (LFQ) algorithm as described elsewhere.[40]

2.7. Western Blot Analysis

Western blot analysis, gel electrophoresis, trans-blotting, and densitometry were carried out following routine protocols as

© 2018 WILEY-VCH Verlag GmbH & Co. KGaA, Weinheim

described previously.[12] Twenty microliters of lysate per sample containing 2 μg μL^{-1} protein were loaded onto SDS-Polyacrylamide gels. A total number of six samples per cell population plus one positive control CX+ were analyzed after 14 days of culturing. Primary antibodies were applied against BCAR1 (Abcam, dilution 1:1000), MAPK8 (Cell Signaling, dilution 1:1000), and E-cadherin (Abcam, dilution 1:1000). HRP-linked secondary antibody was used at a dilution of 1:2000 (Dako Denmark A/S). A final analysis was performed in a Clarity Western ECL Substrate (Bio Rad, Hercules, CA, USA). Ponceau S red staining was used as an alternative to housekeeping genes as loading controls. The membranes were analyzed using ImageJ software (U.S. National Institutes of Health, Bethesda, MD, USA; http://rsb.info.nih.gov/ij/), for densitometric quantification of the bands. Ponceau S was evaluated according to Bauer et al.[13]

2.8. Pathway Analysis

To investigate and visualize localizations and interactions of proteins, we entered relevant UniProtKB entry numbers into the Pathway Studio v.11 software (Elsevier Research Solutions, Amsterdam, The Netherlands).[13,30] To estimate the belonging of the detected proteins to known pathways, the Reactome pathway database was searched, also entering relevant UniProtKB entry numbers.[41]

2.9. Statistical Evaluation

Statistical evaluation was performed using SPSS 15.0 (SPSS, Inc., Chicago, IL, USA). The Mann–Whitney U test was used to compare the 1 g and RPM conditions, as well as AD cells and MCS cells. All data are presented as means ± standard deviation (SD) with a significance level of $p < 0.05$.

3. Results and Discussion

3.1. Harvest of Three Different MCF7 Subpopulations

After 2 weeks of incubation, three types of cells from the MCF7 cell line were harvested (**Figure 1**A,B). 1 g-control cells were grown under normal gravity and remained adherent until the day of harvest (Figure 1A). These cells were passaged once on the seventh day after a 1 to 5 dilution. Adherent cells and cells growing in MCS had been incubated on an RPM in the same culture flasks without any passaging (Figure 1B). Under the same culture conditions, the uniform MCF7 cell population had split in two different types of cells, which we call subpopulations in this

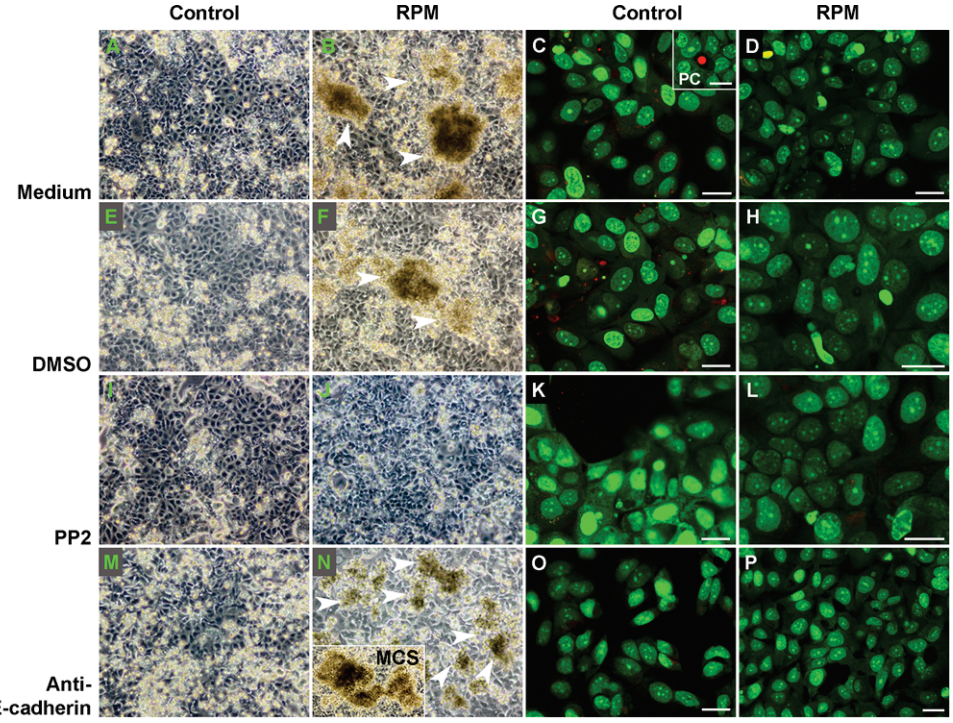


Figure 1. Morphology and viability of MCF7 cells incubated at 1 g (control) or on the RPM. Left side of the figure: phase contrast microscopy of MCF7 cells incubated at 1 g (A, E, I, M) or on the RPM (B, F, J, N) for 14 days. Representative examples of spheroids formed on the RPM are marked by white arrowheads (B, F, N). J) Notably, no spheroids were formed on the RPM in the presence of the Src inhibitor PP2, N) whereas anti-E-cadherin (DECMA-1) stimulated the formation of spheroids. Insert in (N) shows an example of a large spheroid observed in the presence of anti-E-cadherin. Right side of figure: acridine orange/ethidium bromide staining revealed a green fluorescence in all cells of all groups (C, D, G, H, K, L, O, P) which indicates viability of MCF7 cells incubated on the RPM or at static 1 g-conditions. Insert in (C) represents positive control (PC) of the acridine orange/ethidium bromide assay after approximately 5 min incubation. Scale bars 20 μm.

© 2018 WILEY-VCH Verlag GmbH & Co. KGaA, Weinheim

ADVANCED SCIENCE NEWS
www.advancedsciencenews.com

Proteomics
www.proteomics-journal.com

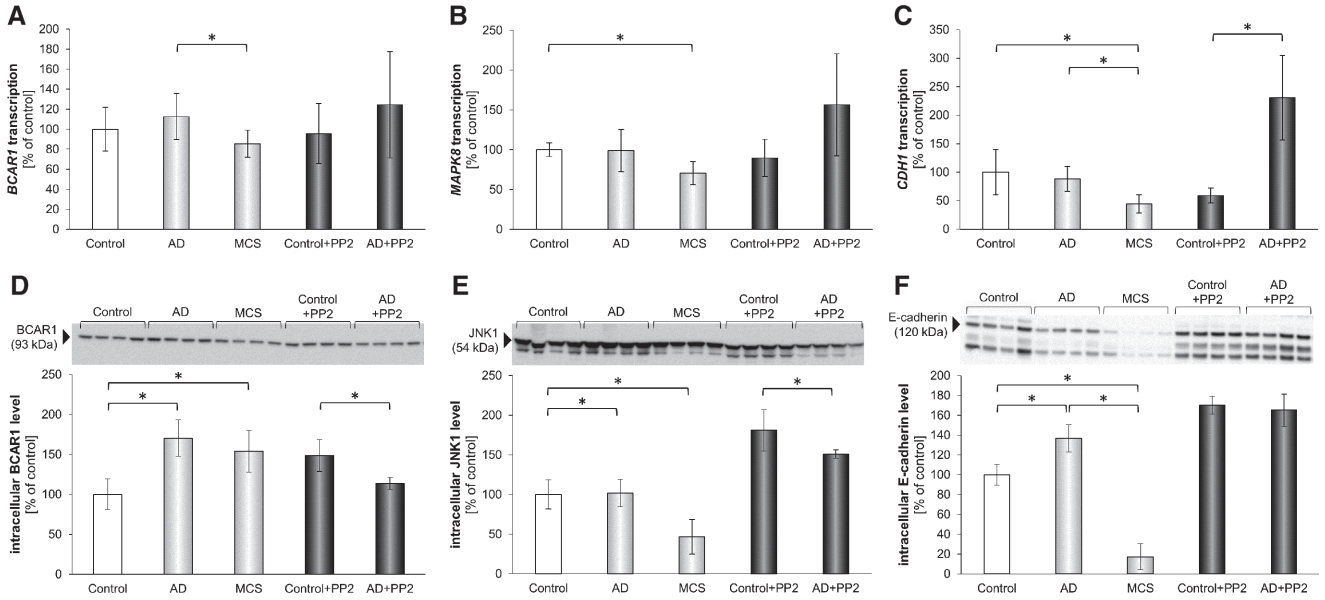


Figure 2. Relative expression of (A) *BCAR1*, B) *MAPK8*, and C) *CDH1*. Transcription was analyzed after 2 weeks at 1 *g* conditions or on the RPM in absence and presence of PP2. All values are given as mean ± standard deviation. Western blot analysis of (D) BCAR1, E) JNK1, and F) E-cadherin proteins. Intracellular levels were determined after 2 weeks of RPM exposure in the absence and presence of PP2. $*p < 0.05$. AD, adherent cells; MCS, multicellular spheroids, after RPM-exposure.

manuscript. The MCS comprised cells that had detached from the bottom of the culture flask and formed 3D aggregates, while the AD cells had remained adherent until harvest.

3.2. Proteome Analysis

After harvest, proteins present in the various subpopulations of MCF7 cells were identified by mass spectrometry. The analysis revealed 6580 different proteins in 1 *g*-control cells, 6464 proteins in AD cells, and 6261 in MCS cells. These proteins, which together represented 6968 unique human proteins, could be identified with LFQ scores above 10^7.[40] They were evaluated with regard to their LFQ values detectable in the different subpopulations of MCF7 cells, respectively. In a first approach, we focused on proteins involved in the cell contacts with their environment, that is, with neighboring cells or with the bottom of the culture flasks and compared the current results with recent observations made on thyroid cancer cells cultivated for 3 days according to an equal protocol.[13,42–44]

Arf-GAP with SH3 domain, ANK repeat, and PH domain-containing protein 1 (ASAP1), which had been found in thyroid MCS and control cells, but not in thyroid AD cells,[13] was detected in MCF7 control cells with an LFQ value of 14.68×10^8, in AD cells with a score of 19×10^8, and in MCS cells with a 22.5×10^8 LFQ score. Breast cancer anti-estrogen resistance protein 1 (BCAR1) and mitogen activated protein kinase 8 (MAPK8), which were absent in thyroid MCS cells and present in thyroid AD and control cells,[13] were detected with LFQ values for BCAR1 of 10.01×10^8 (1 *g*), 9.3×10^8 (AD), and 7.71×10^8 (MCS) and with LFQ scores for MAPK8 of 2.1×10^8 (1 *g*), 2.1×10^8 (AD), and 1.75×10^8 (MCS). Increased ASAP1 and simultaneously reduced BCAR1 and MAPK8 in MCS suggested that these proteins were changed in MCF7 cells after 2 weeks in a similar manner to the same proteins in thyroid cells switching from a 2D to a 3D growth during the first 72 h of culturing on the RPM.[13] This finding suggests that ASAP1 is associated with the formation of 3D aggregates of thyroid and breast cancer cells, while BCAR1 and MAPK8 are enhanced in both types of cells when their cells remain in a monolayer on a RPM. In order to verify the LFQ values, we performed western blot (WB) analyses. **Figure 2**D,E indicates a higher concentration of BCAR1 and MAPK8 (JNK1) in AD than in MCS cells. The protein changes correspond rather well to the LFQ values as well as to the corresponding mRNA expression in MCS cells (Figure 2A,B).

Comparing these 2 week long experiments with the recent study on 3 day old spheroids,[13] it has to be considered that spheroid formation progresses in a time-dependent manner.[3,45] Therefore, the current results were also compared with those obtained when FTC-133 thyroid cells were sent into space and incubated for more than 10 days, during which most of the cells formed spheroids.[46,47] At that time, we found that the interferon stimulated gene 15 (*ISG15*) was the highest upregulated of all genes investigated with the microarray technology,[29,46] while in the analysis of 3 day old FTC-133 spheroids, the ISG15 protein was found to be reduced in MCS.[13] In the current experiment on MCF7 cells, we again detected ISG15 protein. It was enhanced in MCS cells with an LFQ value of 126.1×10^8, when compared with AD (LFQ = 19.7×10^8) and 1 *g* cells (LFQ = 62.4×10^8). The role of ISG15 protein in spheroid formation is as yet unknown. The protein is normally induced by interferon and modifies a number of cellular proteins co-translationally by ISGylation. A proteome analysis has revealed ISG15 target proteins, including proteins involved in cell structure and motility.[48] The time course of its accumulation suggests a role of ISG15 in the stabilization rather than in the formation of the spheroids.[13,29,46]

© 2018 WILEY-VCH Verlag GmbH & Co. KGaA, Weinheim

Table 1. Number of proteins detected in AD and MCS cells with quantitative changes more than twofold compared with the corresponding proteins in 1 *g*-control cells. The number of proteins indicated in the right column was used for searching pathways in the Reactome database.

Proteins detected in A	Proteins of A compared with equal proteins in B	Twofold enhanced A versus B	Detected in A, not detected in B	Used for searching Reactome database
AD cells (group 1)	1 *g* cells	359	97	456
1 *g* cells (group 2)	AD cells	446	213	659
MCS cells (group 3)	1 *g* cells	458	109	567
1 *g* cells (group 4)	MCS cells	664	427	1091

In order to focus on additional proteins that could have an influence on the behavior of MCF7 cells exposed to the RPM, we compared the quantities of the various proteins found in each subpopulation. The majority of the human proteins detected in AD and MCS cells indicated LFQ values that were changed less than twofold in either direction compared with the corresponding proteins in 1 *g*-control cells. Only LFQ values for 359 proteins were found at levels twofold higher in AD cells than in 1 *g* cells, while 446 proteins were found to be twofold higher in 1 *g* cells than in AD cells. Ninety-seven of the AD cell proteins were not detected in 1 *g* cells, but 213 of the 1 *g* cell proteins were not detected in AD cells. Furthermore, LFQ values for 458 proteins were detected being twofold higher in MCS cells than in 1 *g* cells and 664 proteins were found to be twofold higher in 1 *g* cells than in MCS cells. One hundred and nine of the MCS cell proteins were not detected in 1 *g* cells, while 427 proteins of the 1 *g* cells were not seen in MCS cells (**Table 1**).

3.3. Pathway Identification

As shown in Figure 1, the way that cells contact their neighbors or the bottom of the culture flask is different in MCS and AD cells, although the gravitational forces acting on the cells are similar. Attachment of cells to their solid environment is either mediated by ECM proteins or occurs by direct cell–cell interaction via various types of so-called junctions.[49] Only three of the more than 300 ECM proteins were detected in MCS formed on the RPM with at least twofold enhanced LFQ values (**Table 2**). Therefore, we evaluated the junction proteins in more detail. Each of these junctions is linked to a set of proteins forming signaling pathways, which may be retrieved from the Reactome database.[41] Therefore, we searched the Reactome database using either all of the 6968 different proteins identified in this analysis or, for comparison, proteins of each of the four groups indicated in Table 1, right hand column individually. Subsequently, we depicted those proteins in our analysis, that were included at least once in the pathways R-HSA-196025, R-HSA-191650, R-HSA-191647, R-HSA-157858, R-HSA-190828, R-HSA-190861, R-HSA-420029, R-HSA-418990, R-HSA-421270, R-HSA-446728, and/or R-HSA-190873, because the proteins comprising these pathways are involved in the formation, regulation, or maintenance of junctions.[41]

When the whole set of detected proteins was matched against the Reactome database, 60 relevant proteins were found. Nineteen of these proteins were also recognized, when the four groups of proteins strongly affected by RPM exposure (Table 1) were matched individually. Fourteen were found to belong to junction-related pathways (Table 2), when the proteins of group 4 indicated in Table 1 were matched against Reactome. The LFQs of these proteins were at least halved in MCS cells compared with the 1 *g*-controls. Another five proteins were identified when the proteins of group 2 (Table 1) were used to search the Reactome database (Table 2). Three of them were present in MCS and control cells at similar concentrations but were not detectable in AD cells. Only the focal adhesion protein beta-parvin (PARVB), which was not detectable in AD cells, was more than doubled in MCS cells compared with 1 *g*-control cells.[50] Taken together, MCS cells appear to contain smaller amounts of distinct proteins that form and regulate junctions than control cells (Table 2).

E-cadherin is the most abundant of the 14 proteins detected in MCS cells with LFQ scores less than half of those in 1 *g*-controls (Table 2). Its decrease in MCS was also shown by WB analysis (Figure 2F) and corresponds with a slight reduction of mRNA expression (Figure 2C). E-cadherin is a multi-domain membrane protein. Its extracellular domain interacts with the same domain of another E-cadherin molecule belonging to another cell in a calcium-dependent manner establishing connections between neighboring cells.[51] Its intracellular domains are connected to the cytoskeleton and its stability is regulated by catenin D1.[52] Associating with the juxtamembrane domain of E-cadherin, catenin D1 affects cell–cell adhesion.[53] Catenin D1 was also detected in our preceding study on thyroid cancer cells. At that time, the catenin D1 content in MCS cells was reduced by 30% compared with 1 *g*-control cells. E-cadherin had not been detected in one of our preceding proteome analyses performed on thyroid cancer cells and endothelial cells.[7,12,13] According to the literature, E-cadherin is under the direct influence of proteins, which we earlier proposed to be involved in the regulation of MCS formation.[13] According to the literature, E-cadherin is upregulated by ISG15 as well as by CLDN3 and FERMT2 shown in Table 2,[54–56] which were all detected in MCS cells with higher LFQs than in controls. In addition, E-cadherin is downregulated by MAPK8 and BCAR1, which are accumulated to a higher level in AD than in MCS cells, as well as by PSMD10 and SRC, which are absent in AD but present in MCS cells (Table 2).[57–60] As our measurements clearly indicated a reduction of E-cadherin in MCS cells, it may be concluded that the proteins effecting lower amounts of E-cadherin are dominant.

The downregulation of E-cadherin could also be supported by members of the so-called "Autodegradation of Cdh1 by Cdh1:APC/C" (R-HSA-174084) pathway. They were identified when the Reactome database was searched using the proteins of group 3 (doubled in the MCS cells compared with the 1 *g*-controls) indicated in Table 1. The R-HSA-174084 pathway includes 63 proteins, of which 54 were found in the present

© 2018 WILEY-VCH Verlag GmbH & Co. KGaA, Weinheim

Table 2. Accumulated ECM proteins and proteins belonging either to junction-related pathways (upper part) or to the CDH1 autodegradation pathway (lower part).

Protein ID	Protein name	ΣLFQ (•10^8) of four independent experiments		
		1 *g*-control	AD	MCS
P02751	Fibronectin	5.8	0.6	196
P23142	Fibulin-1	0.62	0.19	13.9
P39060	Collagen alpha-1(XVIII) chain	13.8	22	32.8
P12830	Cadherin-1 (E-cadherin)	163	134	76
O60716	Catenin delta-1	158	158	77
P09497	Clathrin light chain B	79.7	60.9	28
P16144	Integrin beta 4	29.5	24.6	12.5
O15551	Claudin-3	12.6	3.15	1.8
Q96AC1	Fermitin family homolog 2	8.43	5.79	3.52
P15151	Poliovirus receptor	6.42	8.98	1.16
Q03001	Dystonin	5.35	4.97	1.42
Q96NY8	Nectin-4	5.06	7.87	2.04
P53675	Clathrin heavy chain 2	4.42	1.1	1.38
P22223	Cadherin-3	1.08	1.56	0.16
P56749	Claudin-12	0.71	0.79	0.18
Q9BY67	Cell adhesion molecule 1	3.4	2.04	n.d.
E9PEQ4	Dynamin-2	1.05	1.54	n.d.
Q7Z5N4	Protein sidekick-1	2.05	0.57	1.6
P12931	Proto-oncogene tyrosine-protein kinase Src	1.45	n.d.	1.49
Q3ZCM7	Tubulin beta-8 chain	1.74	n.d.	1.87
P48509	CD151 antigen; tetraspanin	0.98	n.d.	0.99
Q9HBI1	Beta-parvin	0.07	n.d.	1.48
P25788	Proteasome subunit alpha type-3	17.5	20.7	35.4
P60900	Proteasome subunit alpha type-6	10.1	7.88	34.6
O75832	26S proteasome non-ATPase regulatory subunit 10	5.7	4.02	13.5
P49720	Proteasome subunit beta type-3	4.2	2.48	10
Q9UJX3	Anaphase-promoting complex subunit 7	3.2	1.44	8.1
P51668	Ubiquitin-conjugating enzyme E2 D1	n.d.	n.d.	4.68
P40306	Proteasome subunit beta type-10	0.26	n.d.	2.43
Q13042	Cell division cycle protein 16 homolog	0.53	1.61	2.42
Q9UM13	Anaphase-promoting complex subunit 10	0.34	n.d.	1.73
Q9UJX2	Cell division cycle protein 23 homolog	4.56	1.92	6.03
P28070	Proteasome subunit beta type-4	3.49	7.45	6.16

analysis. Nine of the 54 proteins belonging to the pathway were twofold higher in MCS cells compared with 1 *g* cells (Table 2, lower part). Another two proteins (Q9UJX2, P28070) belonging to the E-cadherin autodegradation pathway were detected when proteins of group 1 and group 2 (Table 1) were used to search for pathways. These proteins were enhanced by 50% in MCS cells compared with 1 *g*-controls (Table 2). The R-HSA-174084 pathway comprises mainly proteasomes, ubiquitin, and cell cycle proteins including CDC23, CDC16, AnaPC10, and AnaPC7 (Table 2). In order to elucidate how the proteins of this pathway could diminish cellular E-cadherin, we made a closer examination of the interaction of the 60 junction-related proteins detected with the E-cadherin regulator proteins described above and with the R-HSA-174084 pathway proteins applying Pathway Studio.[30] A direct link between the CDC23/CDC16/Anapc7 and E-cadherin has been described for *Caenorhabditis elegans*.[61] However, the influence of the mentioned proteins appears to be mediated via the additional proteins CDC27, AnaPC2, and UBE2C, which were detected in this analysis with very similar LFQ values in all three MCF7 subpopulations (**Figure 3**). The CDC16 and CDC23 peptides assemble with CDC27[62] forming a sub-complex, which represents about 50% of the molecular mass of the whole APC-complex and bears a great a number of phosphorylation sites.[63] The pattern of phosphorylation of these sites has an influence on the activity of the complex.[64] CDC27 is required for UBE2C promoter activity[65] and UBE2C can suppress the expression of E-cadherin.[66] Since E-cadherin was diminished in MCS, we

© 2018 WILEY-VCH Verlag GmbH & Co. KGaA, Weinheim

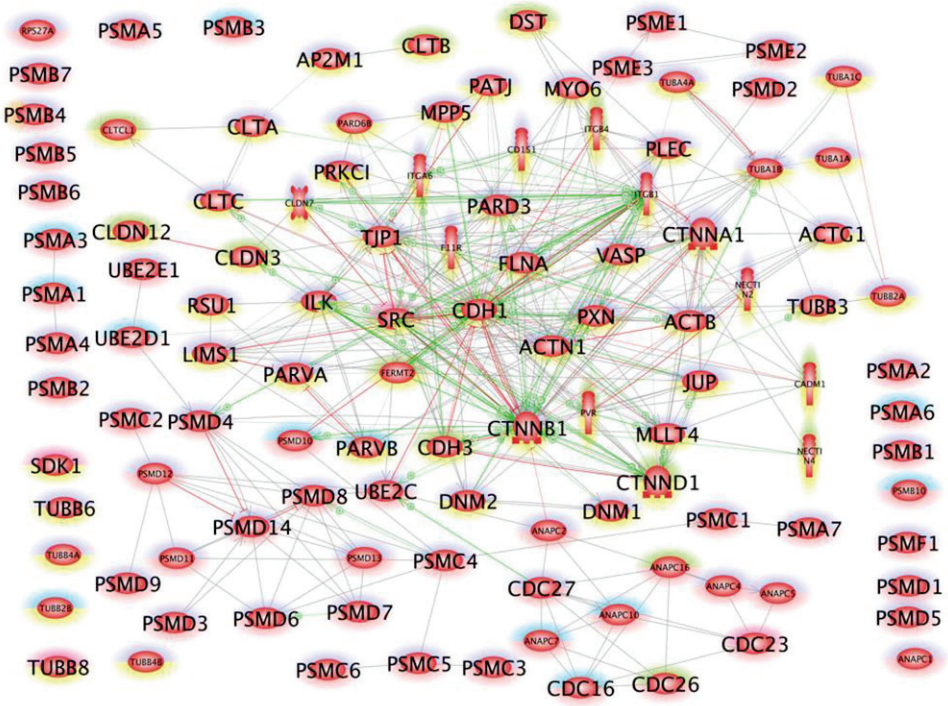


Figure 3. Pathway studio analysis of detected proteins involved in the formation and regulation of junctions and in CDH1 autodegradation. The belonging to the group of proteins involved in the formation and regulation of junctions is indicated by a yellow colored lower half-rim around the protein symbols, while the belonging to the group of proteins of the CDH1 autodegradation pathway is indicated by a red colored lower half-rim around the protein symbols. Blue upper half-rims indicate upregulation, green upper half-rims indicate downregulation, and violet upper half-rims show unregulated proteins. Regulation means that the LFQ of a protein in MCS is at least twofold enhanced or diminished as compared to controls. Grey, green, and red lines or arrows show the type of interaction. Green lines or arrows indicate supporting and red ones indicate inhibiting type of interaction. Grey lines and arrows show that an interaction is described but not yet clearly defined. The interactions are shown on the gene and gene product levels.

concluded that E-cadherin activity could counteract MCS formation. In order to prove this hypothesis, we performed cultivation experiments according to the same protocol as described for the proteome analysis but added anti-E-cadherin function-blocking antibodies or PP2, which blocks c-Src, a non-receptor tyrosine kinase that has been reported to inhibit the surface expression and function of E-cadherin[32] (Figure 1), to the culture medium. Microscopic analyses of the cultured cells show that the anti-E-cadherin antibodies promoted MCS formation (Figure 1M,N), while PP2 inhibited this process (Figure 1I,J). Simultaneously, PP2 enhanced MAPK8 and E-cadherin slightly in 1 *g*-controls and AD cells (Figure 2E,F). A significant upregulation was found for the *CDH1* gene of AD (Figure 2C). Addition of DMSO, the solvent of PP2, had no effect (Figure 1E,F). In all flasks, the cells remained viable, as demonstrated by acridine orange/ethidium bromide staining and shown by the green fluorescence in Figure 1C, D,G,H,K,L,O,P.

4. Concluding Remarks

Biological experiments supported the central role of E-cadherin in spheroid formation as it was concluded from the proteome analysis. A further study of E-cadherin regulation is important because several authors have found a strict correlation between E-cadherin expression and metastatic activity of cancer cells.[67–69] It is of interest to investigate the mechanism of E-cadherin activity in cells exposed to the microgravity in order to see if it depends on the level of E-cadherin expression[70] or if post-translational modifications such as phosphorylation play an additive role. Studies of cells changing their growth behavior under RPM exposure, revealed again to be a very suitable model to promote research on the metastatic activity of cancer cells in Earth-bound patients. It allows to combine biological and biochemical experiments to address questions on the mechanisms that enable the cells to leave a monolayer and to survive a possible anchorage free period.[71–75] As demonstrated in this study, the application of immunological or chemical agents will be of great help for future investigations on these questions.

Acknowledgements

J.S. and M.Z.N. contributed equally to this work. This study was supported by the German Space Agency DLR (D.G.) (BMWi grant 50WB1524), and Aarhus University, Denmark (D.G.). We thank Dr. Nagarjuna Nagaraj and the members of the biochemistry core facility at the Max-Planck Institute of Biochemistry for performing proteomic sample preparation and measurements. D.G. and J.B. designed the experiment. J.S. and M.Z.N. executed the RPM experiments, collected the material, and performed the western

 © 2018 WILEY-VCH Verlag GmbH & Co. KGaA, Weinheim

blot analyses. S.K., M.Z.N., and M.K. performed qrtPCR analyses. T.J.C. performed the viability tests. J.B. performed the pathway analyses. J.B., J.S., M.W., and D.G. wrote the manuscript. M.I. and D.G. contributed reagents, materials, and analysis tools. All authors reviewed the manuscript.

Conflict of Interest

The authors declare no conflict of interest.

Keywords

cell interaction, ISG15, proteome data, Reactome, signaling pathways, simulated microgravity

Received: January 12, 2018
Revised: April 27, 2018
Published online: May 21, 2018

[1] J. Pietsch, J. Bauer, M. Egli, M. Infanger, P. Wise, C. Ulbrich, D. Grimm, *Curr. Mol. Med.* **2011**, *11*, 350.
[2] D. Grimm, M. Wehland, J. Pietsch, G. Aleshcheva, P. Wise, J. van Loon, C. Ulbrich, N. E. Magnusson, M. Infanger, J. Bauer, *Tissue Eng. Part B Rev.* **2014**, *20*, 555.
[3] E. Warnke, J. Pietsch, M. Wehland, J. Bauer, M. Infanger, M. Gorog, R. Hemmersbach, M. Braun, X. Ma, J. Sahana, D. Grimm, *Cell Commun. Signal.* **2014**, *12*, 32.
[4] S. Kopp, E. Warnke, M. Wehland, G. Aleshcheva, N. E. Magnusson, R. Hemmersbach, T. J. Corydon, J. Bauer, M. Infanger, D. Grimm, *Sci. Rep.* **2015**, *5*, 16691.
[5] D. Grimm, J. Pietsch, M. Wehland, P. Richter, S. M. Strauch, M. Lebert, N. E. Magnusson, P. Wise, J. Bauer, *Expert Rev. Proteomics* **2014**, *11*, 465.
[6] S. Kopp, L. Slumstrup, T. J. Corydon, J. Sahana, G. Aleshcheva, T. Islam, N. E. Magnusson, M. Wehland, J. Bauer, M. Infanger, D. Grimm, *Sci. Rep.* **2016**, *6*, 26887.
[7] X. Ma, A. Sickmann, J. Pietsch, R. Wildgruber, G. Weber, M. Infanger, J. Bauer, D. Grimm, *Proteomics* **2014**, *14*, 689.
[8] R. J. White, M. Averner, *Nature* **2001**, *409*, 1115.
[9] J. L. Becker, G. R. Souza, *Nat. Rev. Cancer* **2013**, *13*, 315.
[10] D. Grimm, J. Bauer, P. Kossmehl, M. Shakibaei, J. Schoberger, H. Pickenhahn, G. Schulze-Tanzil, R. Vetter, C. Eilles, M. Paul, A. Cogoli, *FASEB J.* **2002**, *16*, 604.
[11] J. Pietsch, R. Kussian, A. Sickmann, J. Bauer, G. Weber, M. Nissum, K. Westphal, M. Egli, J. Grosse, J. Schonberger, R. Wildgruber, M. Infanger, D. Grimm, *Proteomics* **2010**, *10*, 904.
[12] J. Pietsch, J. Bauer, G. Weber, M. Nissum, K. Westphal, M. Egli, J. Grosse, J. Schönberger, C. Eilles, M. Infanger, D. Grimm, *Microgravity Sci. Technol.* **2011**, *23*, 381.
[13] J. Bauer, S. Kopp, E. M. Schlagberger, J. Grosse, J. Sahana, S. Riwaldt, M. Wehland, R. Luetzenberg, M. Infanger, D. Grimm, *Int. J. Mol. Sci.* **2017**, *18*, 546.
[14] J. Ferlay, I. Soerjomataram, R. Dikshit, S. Eser, C. Mathers, M. Rebelo, D. M. Parkin, D. Forman, F. Bray, *Int. J. Cancer* **2015**, *136*, E359.
[15] D. Grimm, M. Wehland, J. Pietsch, M. Infanger, J. Bauer, *Curr. Pharm. Des.* **2011**, *17*, 272
[16] M. Wehland, J. Bauer, M. Infanger, D. Grimm, *Curr. Pharm. Des.* **2012**, *18*, 4244.
[17] R. Aebersold, M. Mann, *Nature* **2016**, *537*, 347.
[18] H. A. Sarvaiya, J. H. Yoon, I. M. Lazar, *Rapid Commun. Mass Spectrom.* **2006**, *20*, 3039.
[19] J. Hardouin, L. Canelle, C. Vlieghe, J.-P. Lasserre, M. Caron, R. Joubert-Caron, *Cancer Genomics Proteomics* **2006**, *3*, 355.
[20] S. Nie, S. P. McDermott, Y. Deol, Z. Tan, M. S. Wicha, D. M. Lubman, *Proteomics* **2015**, *15*, 3772.
[21] A. Aka, S. X. Lin, *PLoS One* **2012**, *7*, e31532.
[22] C. Pionneau, L. Canelle, J. Bousquet, J. Hardouin, J. Bigeard, M. Caron, R. Joubert-Caron, *Cancer Genomics Proteomics* **2005**, *2*, 199.
[23] R. Lamb, H. Harrison, J. Hulit, D. L. Smith, M. P. Lisanti, F. Sotgia, *Oncotarget* **2014**, *5*, 11029.
[24] J. P. Murphy, D. M. Pinto, *J. Proteome. Res.* **2011**, *10*, 604
[25] M. J. Tenga, I. M. Lazar, *Proteomics* **2013**, *13*, 48.
[26] T. Geiger, S. F. Madden, W. M. Gallagher, J. Cox, M. Mann, *Cancer Res.* **2012**, *72*, 2428
[27] S. Tyanova, R. Albrechtsen, P. Kronqvist, J. Cox, M. Mann, T. Geiger, *Nat. Commun.* **2016**, *7*, 10259.
[28] F. Sacco, A. Silvestri, D. Posca, S. Pirro, P. F. Gherardini, L. Castagnoli, M. Mann, G. Cesareni, *Cell Syst.* **2016**, *2*, 159.
[29] J. Bauer, M. Wehland, J. Pietsch, A. Sickmann, G. Weber, D. Grimm, *Microgravity Sci. Technol.* **2016**, *28*, 357.
[30] J. Bauer, M. Bussen, P. Wise, M. Wehland, S. Schneider, D. Grimm, *Expert Rev. Proteomics* **2016**, *13*, 697.
[31] X. Qian, T. Karpova, A. M. Sheppard, J. McNally, D. R. Lowy, *EMBO J.* **2004**, *23*, 1739.
[32] P. Fan, F. A. Agboke, R. E. McDaniel, E. E. Sweeney, X. Zou, K. Creswell, V. C. Jordan, *Eur. J. Cancer* **2014**, *50*, 457.
[33] S. Kopp, J. Sahana, T. Islam, A. G. Petersen, J. Bauer, T. J. Corydon, H. Schulz, K. Saar, N. Huebner, L. Slumstrup, S. Riwaldt, M. Wehland, M. Infanger, R. Luetzenberg, D. Grimm, *Sci. Rep.* **2018**, *8*, 921.
[34] A. G. Borst, J. J. W. A. van Loon, *Microgravity Sci. Technol.* **2008**, *21*, 287.
[35] E. Warnke, S. Kopp, M. Wehland, R. Hemmersbach, J. Bauer, J. Pietsch, M. Infanger, D. Grimm, *Microgravity Sci. Technol.* **2016**, *28*, 247.
[36] E. Caló, V. V. Khutoryanskiy, *Eur. Polym. J.* **2015**, *65*, 252.
[37] J. Rappsilber, M. Mann, Y. Ishihama, *Nat. Protoc.* **2007**, *2*, 1896.
[38] N. Nagaraj, N. A. Kulak, J. Cox, N. Neuhauser, K. Mayr, O. Hoerning, O. Vorm, M. Mann, *Mol. Cell. Proteomics* **2012**, *11*, M111.013722.
[39] J. Cox, M. Mann, *Nat. Biotechnol.* **2008**, *26*, 1367.
[40] J. Cox, M. Y. Hein, C. A. Luber, I. Paron, N. Nagaraj, M. Mann, *Mol. Cell. Proteomics* **2014**, *13*, 2513.
[41] M. Milacic, R. Haw, K. Rothfels, G. Wu, D. Croft, H. Hermjakob, P. D'Eustachio, L. Stein, *Cancers* **2012**, *4*, 1180.
[42] J. Pietsch, A. Sickmann, G. Weber, J. Bauer, M. Egli, R. Wildgruber, M. Infanger, D. Grimm, *Proteomics* **2011**, *11*, 2095.
[43] S. Riwaldt, J. Pietsch, A. Sickmann, J. Bauer, M. Braun, J. Segerer, A. Schwarzwalder, G. Aleshcheva, T. J. Corydon, M. Infanger, D. Grimm, *Proteomics* **2015**, *15*, 2945
[44] S. Riwaldt, J. Bauer, J. Pietsch, M. Braun, J. Segerer, A. Schwarzwalder, T. J. Corydon, M. Infanger, D. Grimm, *Int. J. Mol. Sci.* **2015**, *16*, 28296.
[45] M. Infanger, C. Ulbrich, S. Baatout, M. Wehland, R. Kreutz, J. Bauer, J. Grosse, S. Vadrucci, A. Cogoli, H. Derradji, M. Neefs, S. Kusters, M. Spain, M. Paul, D. Grimm, *J. Cell Biochem.* **2007**, *101*, 1439.
[46] X. Ma, J. Pietsch, M. Wehland, H. Schulz, K. Saar, N. Hubner, J. Bauer, M. Braun, A. Schwarzwalder, J. Segerer, M. Birlem, A. Horn, R. Hemmersbach, K. Wasser, J. Grosse, M. Infanger, D. Grimm, *FASEB J.* **2014**, *28*, 813.
[47] J. Pietsch, X. Ma, M. Wehland, G. Aleshcheva, A. Schwarzwalder, J. Segerer, M. Birlem, A. Horn, J. Bauer, M. Infanger, D. Grimm, *Biomaterials* **2013**, *34*, 7694.
[48] N. V. Giannakopoulos, J. K. Luo, V. Papov, W. Zou, D. J. Lenschow, B. S. Jacobs, E. C. Borden, J. Li, H. W. Virgin, D. E. Zhang, *Biochem. Biophys. Res. Commun.* **2005**, *336*, 496.
[49] S. Sluysmans, E. Vasileva, D. Spadaro, J. Shah, F. Rouaud, S. Citi, *Biol. Cell* **2017**, *109*, 139.
[50] G. Rosenberger, I. Jantke, A. Gal, K. Kutsche, *Hum. Mol. Genet.* **2003**, *12*, 155.
[51] F. van Roy, G. Berx, *Cell Mol. Life Sci.* **2008**, *65*, 3756.

 © 2018 WILEY-VCH Verlag GmbH & Co. KGaA, Weinheim

[52] A. B. Reynolds, *Biochim. Biophys. Acta* **2007**, *1773*, 2.
[53] N. Ishiyama, M. Ikura, *Subcell Biochem.* **2012**, *60*, 39.
[54] Y. C. Tsai, S. Pestka, L. H. Wang, L. W. Runnels, S. Wan, Y. L. Lyu, L. F. Liu, *PLoS One* **2011**, *6*, e24291.
[55] X. Shang, X. Lin, E. Alvarez, G. Manorek, S. B. Howell, *Neoplasia* **2012**, *14*, 974.
[56] C. Ren, J. Du, C. Xi, Y. Yu, A. Hu, J. Zhan, H. Guo, W. Fang, C. Liu, H. Zhang, *Biochem. Biophys. Res. Commun.* **2014**, *446*, 187.
[57] C. Cellurale, G. Sabio, N. J. Kennedy, M. Das, M. Barlow, P. Sandy, T. Jacks, R. J. Davis, *Mol. Cell. Biol.* **2011**, *31*, 1565.
[58] N. Tikhmyanova, E. A. Golemis, *PLoS One* **2011**, *6*, e22102.
[59] L. Gao, H. Xie, L. Dong, J. Zou, J. Fu, X. Gao, L. Ou, S. Xiang, H. Song, *Mol. Med. Rep.* **2014**, *9*, 1032.
[60] F. Palacios, J. S. Tushir, Y. Fujita, C. D'Souza-Schorey, *Mol. Cell. Biol.* **2005**, *25*, 389.
[61] P. J. Brockie, A. V. Maricq, WormBook, ed. The C. elegans Research Community **2006**, WormBook, *1*, 1, https://doi.org/10.1895/wormbook.1.61.1, http://www.wormbook.org.
[62] A. Schreiber, F. Stengel, Z. Zhang, R. I. Enchev, E. H. Kong, E. P. Morris, C. V. Robinson, P. C. da Fonseca, D. Barford, *Nature* **2011**, *470*, 227.
[63] C. Kraft, F. Herzog, C. Gieffers, K. Mechtler, A. Hagting, J. Pines, J. M. Peters, *EMBO J.* **2003**, *22*, 6598.
[64] J. A. Steen, H. Steen, A. Georgi, K. Parker, M. Springer, M. Kirchner, F. Hamprecht, M. W. Kirschner, *Proc. Natl. Acad. Sci. U.S.A.* **2008**, *105*, 6069.
[65] S. Nath, T. Banerjee, D. Sen, T. Das, S. Roychoudhury,*J. Biol. Chem.* **2011**, *286*, 15666.
[66] S. Shuliang, C. Lei, J. Guangwu, L. Changjie, *Oncol. Res.* **2013**, *21*, 121.
[67] S. M. Siitonen, J. T. Kononen, H. J. Helin, I. S. Rantala, K. A. Holli, J. J. Isola, *Am. J. Clin. Pathol.* **1996**, *105*, 394.
[68] R. M. Bremnes, R. Veve, F. R. Hirsch, W. A. Franklin, *Lung Cancer* **2002**, *36*, 115.
[69] J. Peng, S. Qi, P. Wang, W. Li, L. Song, C. Liu, F. Li, *Future Oncol.* **2016**, *12*, 715.
[70] B. Angres, A. Barth, W. J. Nelson, *J. Cell Biol.* **1996**, *134*, 549.
[71] S. K. Wu, A. K. Lagendijk, B. M. Hogan, G. A. Gomez, A. S. Yap, *Cell Cycle* **2015**, *14*, 315.
[72] A. G. Grieve, C. Rabouille, *J. Cell Sci.* **2014**, *127*, 3331.
[73] P. Paoli, E. Giannoni, P. Chiarugi, *Biochim. Biophys. Acta* **2013**, *1833*, 3481.
[74] D. Grimm, M. Infanger, K. Westphal, C. Ulbrich, J. Pietsch, P. Kossmehl, S. Vadrucci, S. Baatout, B. Flick, M. Paul, J. Bauer, *Tissue Eng. Part A* **2009**, *15*, 2267.
[75] M. G. Masiello, A. Cucina, S. Proietti, A. Palombo, P. Coluccia, F. D'Anselmi, S. Dinicola, A. Pasqualato, V. Morini, M. Bizzarri, *Biomed. Res. Int.* **2014**, *2014*, 652434.

 © 2018 WILEY-VCH Verlag GmbH & Co. KGaA, Weinheim

Cellular Physiology and Biochemistry

Cell Physiol Biochem 2018;45:429-445
DOI: 10.1159/000486920
Published online: January 29, 2018
Accepted: December 10, 2017

© 2018 The Author(s)
Published by S. Karger AG, Basel
www.karger.com/cpb

Karger Open access

This article is licensed under the Creative Commons Attribution-NonCommercial-NoDerivatives 4.0 International License (CC BY-NC-ND) (http://www.karger.com/Services/OpenAccessLicense). Usage and distribution for commercial purposes as well as any distribution of modified material requires written permission.

Original Paper

Key Proteins Involved in Spheroid Formation and Angiogenesis in Endothelial Cells After Long-Term Exposure to Simulated Microgravity

Anita Dittrich[a,b] Daniela Grimm[a,c,d] Jayashree Sahana[a] Johann Bauer[e] Marcus Krüger[c,d] Manfred Infanger[d] Nils E. Magnusson[b]

[a]Institute of Biomedicine, Pharmacology, Aarhus University, Aarhus C, [b]Medical Research Laboratory, Department of Clinical Medicine, Aarhus University, Aarhus C, Denmark; [c]Gravitational Biology and Translational Regenerative Medicine, Otto-von-Guericke-University Magdeburg, Magdeburg, [d]Clinic for Plastic, Aesthetic and Hand Surgery, Otto-von-Guericke-University Magdeburg, Magdeburg, [e]Max-Planck-Institute of Biochemistry, Martinsried, Germany

Key Words
Microgravity • Endothelial cells • Angiogenesis • Endothelial dysfunction • Multicellular spheroids • Tube formation • Random Positioning Machine

Abstract
Background/Aims: Cardiovascular complications are common in astronauts returning from a prolonged spaceflight. These health problems might be driven by complex modulations of gene expression and protein synthesis in endothelial cells (ECs). Studies on the influence of microgravity on phenotype, growth pattern and biological processes of ECs can help to understand these complications. ***Methods:*** We exposed ECs (EA.hy926) to a Random Positioning Machine (RPM). Proteins associated with cell structure, angiogenesis and endothelial dysfunction were investigated in distinct pools of multicellular spheroids (MCS), adherent cells (AD) and tubular structures (TS) formed after a 35-day RPM-exposure. ***Results:*** Combining morphological and molecular approaches, we found AD, MCS and TS with changes in the synthesis and release of proteins involved in three-dimensional growth. Fibronectin and monocyte chemoattractant protein-1 (MCP-1) mRNAs and protein contents were elevated along with an increased secretion of vascular endothelial growth factor (VEGF), interleukin (IL)-6, IL-8, MCP-1, intercellular adhesion molecule 1 (ICAM-1), vascular cell adhesion molecule 1 (VCAM-1), neutrophil gelatinase-associated lipocalin (NGAL) and regulated on activation, normal T cell expressed and secreted (RANTES) proteins in the culture supernatant as determined by multianalyte profiling technology. Together they form a network of interaction. ***Conclusions:*** These results show that a prolonged RPM-exposure of ECs induced TS and MCS formation. The factors VEGF, NGAL, IL-6, IL-8, MCP-1, VCAM-1, ICAM-1, fibronectin and RANTES seem to be affected when gravity is omitted.

© 2018 The Author(s)
Published by S. Karger AG, Basel

Daniela Grimm
Gravitational Biology and Translational Regenerative Medicine,
Otto-von-Guericke-University Magdeburg, Zenit, Building 65, Magdeburg (Germany)
Tel. +45-871 67693, Fax +45-8612-8804, E-Mail dgg@biomed.au.dk

KARGER

Downloaded from http://karger.com/cpb/article-pdf/45/2/429/2448497/000486920.pdf by guest on 31 October 2024

Cellular Physiology and Biochemistry
Cell Physiol Biochem 2018;45:429-445
DOI: 10.1159/000486920
Published online: January 29, 2018
© 2018 The Author(s). Published by S. Karger AG, Basel
www.karger.com/cpb

Introduction

The impact of microgravity on different cell types is currently a topic of interest. Astronauts suffer of various health problems after a long-term space travel. Cardiovascular problems like hypotension and arrhythmias might occur. A recent study showed that a dysfunctional vestibular system induces a blood pressure drop in astronauts returning from a space mission [1]. Endothelial cells (ECs) play a key role in the pathogenesis of various diseases and are highly sensitive to microgravity. ECs were investigated in space on the International Space Station (ISS) [2, 3] and on Earth using techniques to simulate microgravity [4-7]. With the help of so-called ground-based facilities like clinostats or the RPM, which are devices constructed to simulate microgravity, some aspects of annulling gravity can be studied. Such devices trigger at least a part of the incubated cells to detach from the bottom of a culture flask and to form 3D aggregates like they are observed after spaceflights [2]. ECs have shown that they grow as three-dimensional (3D) aggregates in form of multicellular spheroids (MCS) or tubular structures (TS) without any scaffold when they were exposed to the RPM or had been cultured in space on the ISS [2, 8]. The morphology of these aggregates had been investigated earlier [8]. The TS exhibited a lumen and the walls consist of a single layer of ECs resembling a vascular intima. The process of tube formation started between the 5th and 7th day [9]. The cells had arranged themselves in line and formed a tube from accumulated extracellular matrix (ECM) proteins [8]. The mechanisms for this behavior are still not completely clear. A recent study showed that ras homolog gene family member A (RhoA) inactivation supports the actin rearrangement-associated angiogenic responses in human umbilical vein endothelial cells (HUVECs) during simulated microgravity [7]. Early cytoskeletal changes of microgravity-exposed ECs have previously been described in real and simulated microgravity [10, 11].

There is evidence of a direct correlation of the cytoskeletal changes upon microgravity and transcription alterations [12]. It is suggested that the interaction of the extracellular matrix (ECM), cell adhesion and connection to cytoskeleton are the basis of gravisensing in human cells [12].

In this study, we focused on long-term changes of ECs exposed to a RPM for 35 days and investigated proteins known to be involved in the process of angiogenesis as well as factors secreted into the culture supernatant. The relationship of factors driving the 3D growth of ECs in a microgravity-dependent system such as vascular endothelial growth factor (VEGF) and its receptors fetal liver kinase 1 (Flk1 or kinase insert domain receptor (KDR) or VEGFR-2) and Fms-related tyrosine kinase 1 (Flt1 or VEGFR-1), cytokines like the interleukins (IL)-6 and IL-8, plasminogen activator inhibitor 1 (PAI-1), monocyte chemoattractant protein 1 (MCP-1 or CCL2), the cell adhesion molecules vascular cell adhesion molecule 1 (VCAM-1) and intercellular adhesion molecule 1 (ICAM-1) were investigated.

In addition, we focused on ECM proteins and on inflammation factors released in the culture supernatant by the ECs.

The principal aim of these investigations was to find further reasons why simulated microgravity conditions are associated with a change in growth behavior and increased spheroid and tube formation (angiogenesis) of these ECs.

The results obtained suggested that the 3D growth of ECs in a microgravity-dependent system is driven via a network of genes and proteins involved in cell structure maintenance and intercellular signaling.

Materials and Methods

Cell culture

The permanent human cell line EA.hy926 expresses factor VIII-related antigen a marker of vascular endothelial function [13].

The cell line had been established by fusing HUVEC with the permanent cell line A549, which derived from a human lung carcinoma. EA.hy926 cells were grown in RPMI 1640 medium (Invitrogen, Eggenstein,

Downloaded from http://karger.com/cpb/article-pdf/45/2/429/2448497/000486920.pdf by guest on 31 October 2024

Cellular Physiology and Biochemistry
Cell Physiol Biochem 2018;45:429-445
DOI: 10.1159/000486920
Published online: January 29, 2018
© 2018 The Author(s). Published by S. Karger AG, Basel
www.karger.com/cpb

Germany) supplemented with 10% fetal bovine serum (Biochrom, Berlin, Germany), 100 units/mL penicillin and 100 µg/mL streptomycin (Invitrogen).

The cells were grown in 75-cm^2 culture flasks (Sarstedt, Nümbrecht, Germany) until subconfluent monolayers were formed. After reaching a subconfluency of 80%, the cells were subcultured into T-25 cell culture flasks (10^6 cells/flask). The next day the adherent monolayers were randomized into the following study groups: 35-day (d) 1*g*-group and 35-d RPM-group. T-25 cell culture flasks at 1*g* were subcultured and collected at days 7, 14, 21, 29 and 35. The flasks were filled completely with medium, to avoid air bubbles and were either mounted on the RPM (Fig. 1A), a device created to realize microgravity conditions on Earth (Airbus, Defense and Space, Leiden, the Netherlands), or kept in the same incubator next to the RPM at 1*g* with a constant temperature of 37 °C and 5% CO_2. The general behavior of cells on the RPM had been thoroughly investigated and previously published in detail [11, 14-19].

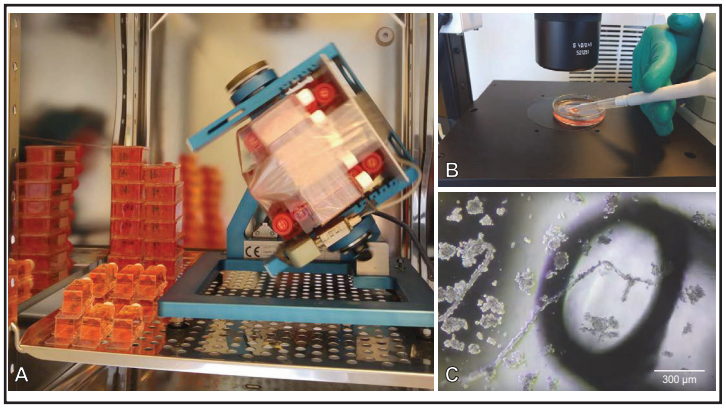


Fig. 1. Procedure of the experiments: Cultures of EA.hy926 cells on the RPM and collection of MCS and tubular structures. T-25 flasks and slideflasks are placed in the incubator under 1*g*-conditions or secured on the RPM (A), here seen while in motion. Collecting TS using a 1 mL pipette tip (B). TS collected with a pipette under the phase contrast microscope at day 35 (C).

Cells of T-25 cell culture flasks at the RPM were collected at day 35 (n=15) and used for Western blot analyses and quantitative PCR (qPCR). Adherently growing cells from the 1*g*- and µ*g* (microgravity)-conditions were collected by scraping off the cells from the bottom of the culture flasks in 5 mL ice-cold phosphate buffered saline (PBS). The MCS from the µ*g*-samples were collected by centrifugation (4°C) of the supernatants and followed by washing with PBS. TS were collected with a pipette under microscopy (Fig. 1B, C). They were pooled from 15 flasks for qPCR by transferring portions of the supernatant to a petri dish, using a standard pipette with a 1 mL tip to extract the TS under a phase contrast microscope (Fig. 1C). Dry pellets from all T25 samples were snap frozen in liquid nitrogen and kept at -80°C while the TS were preserved in TRIzol® reagent (Thermo Fischer Scientific, Waltham, MA USA) and kept at -20°C.

Slide flasks kept at 1*g* (n=20) and µ*g* (n=20) were all collected at day 35 and used directly for immunofluorescence staining. Every three days, starting at day 5 one third of the medium was replaced with fresh medium and the cells examined by phase contrast microscopy (Leica Microsystems GmbH, Wetzlar, Germany) and photographed using a Canon EOS 550D. Supernatant samples were collected from T-25 flasks, centrifuged at 4°C and kept at -20°C.

Immunofluorescence staining

Slideflasks were kept intact while the cells were fixed using a 4% paraformaldehyde solution for 20 min, then subjected to membrane permeabilization with ice-cold methanol for 10 min and blocking with 1% bovine serum albumin (BSA, Sigma-Aldrich, Steinheim, Germany) in PBS for 15 min. The slides were then released from the flasks and the cells incubated with primary antibodies in a PBS solution with 1% BSA for 24 h at room temperature (RT), followed by washing and incubation with secondary antibodies in PBS solution with 1% BSA for an additional 24 h. The used antibodies for these investigations are given in Table 1. The cells were washed and prepared for microscopy using Fluoroshield™ mounting media with DAPI (4',6-diamidino-2-phenylindole; Sigma-Aldrich-F6057). Slides were kept at 4°C in a dark box for 2 days before confocal laser scanning microscopy. The stained samples were examined using a Zeiss 510 META inverted confocal laser scanning microscope (Zeiss, Germany), equipped with a Plan-Apochromat 63×1.4 objective [20]. Excitation and emission wavelengths were: λ_{exc} = 488 nm and λ_{em} ≥505 nm for FITC. Afterwards, the samples were analyzed with the help of the image analysis program Scion Image (Version 1.63 MacOs, Scion Corporation, USA).

Downloaded from http://karger.com/cpb/article-pdf/45/2/429/2448497/000486920.pdf by guest on 31 October 2024

Cellular Physiology and Biochemistry
Cell Physiol Biochem 2018;45:429-445
DOI: 10.1159/000486920
Published online: January 29, 2018
© 2018 The Author(s). Published by S. Karger AG, Basel
www.karger.com/cpb

Western blot analyses

The method for Western blotting was published earlier in detail [21-23]. Cell pellets solubilized in lysis buffer were measured for total protein concentration using Bio-Rad DC™ protein assay (BioRad, USA), and samples for Western blot prepared accordingly with Laemmeli buffer with 5% β-mercaptoethanol for a final protein concentration of 2 µg/µL. Samples were denatured at 95°C for 15 min. 15 µL of each sample was loaded on TGX Stain-free precast gels and electrophoresis performed in Criterion electrophoresis chambers (BioRad). Gels were transferred to membranes (Trans-Blot Turbo™ PVDF membrane pack) using the Trans-Blot turbo transfer system (BioRad). Blocking of the membrane was done in 0.3% I-block in PBS (Applied Biosystems, USA) for 3 h at RT. The membranes were incubated with primary and secondary antibody solutions (PBS with 1% BSA) for 24 h and 2 h respectively. Super Signal™ West kit (Thermo Fisher) was used to develop the membranes for imaging with the ChemiDoc system (Bio-Rad). Total protein images of the gels were also taken with the ChemiDoc and used for normalization. A complete list of antibodies used in this study is shown in Table 1.

Table 1. Antibodies used for western blot analyses and immunofluorescence**.** AB, antibody; n.d. not done; sigma, Sigma Aldrich, HAF007, HAF008 are both from R&D systems; Sc, Santa Cruz Biotechnology, Mabn, Merck Millipore; Ab, Abcam; AF488, Alexa Fluor®488 Thermo Fisher Scientific; RHO, rhodamine conjugate, Thermo Fisher Scientific

Target protein	Western blot			Immunofluorescence		
	Primary AB	Dilution	Secondary AB	Primary AB	dilution	Secondary AB
Fibronectin	sigmaF3648	1:1000	HAF008	sigmaF3648	1:150	Goat anti-Rabbit IgG (H+L) AF488
VEGF	Sc7269	1:1000	HAF008	Ab46151	1:150	Goat anti-mouse IgG (H+L) RHO
MCP-1	Mabn712	1:500	HAF007	Mabn712	1:250	Goat anti-Mouse IgG (H+L) AF488
TGF-β	Ab92486	1:250	HAF008	Ab92486	1:250	Goat anti-rabbit IgG (H+L) AF488
PAI-1	Ab66705	1:500	HAF008	Ab66705	1:500	Goat anti-rabbit IgG (H+L) AF488
IL-6	n.d.			Sc28343	1:50	Goat anti-mouse IgG (H+L) RHO
IL-8	n.d.			Sc7922	1:50	Goat anti-rabbit IgG (H+L) AF488
NGAL	n.d.			Sc50350	1:50	Goat anti-rabbit IgG (H+L) AF488

Neutrophil gelatinase-associated lipocalin (NGAL) and VEGF 165 measurements

A time resolved immunofluorometric assay (TRIFMA) was used to measure the levels of NGAL (LCN2) and VEGF 165 in the supernatants collected at the days 5, 14, 23, 29 and 35 following previously described methods [24-26].

Cytokine measurements by multianalyte profiling (MAP) technology

The different cytokines and proteins released into the supernatants of the cell cultures, were analyzed by the company Myriad RBM (Austin, Texas, USA). The MAP analysis was performed using the Human Inflammation kit® as described previously [24]. Supernatants were taken after 35 d from 1*g*- (n = 5) and RPM-samples (n = 13) and stored at -80°C until shipment to Myriad RBM.

RNA isolation and quantitative real-time PCR

The RNA isolation and quantitative real-time PCR (qPCR) were performed as described earlier in detail [2, 25, 27]. RNA and proteins were isolated using the AllPrep RNA/Protein kit (Qiagen GmbH, Hilden, Germany) according to the manufacturer's recommendations. The RNA was determined with the SpectraMax M2 (Molecular Devices, California, USA). Reverse transcription was done using the First Strand cDNA Synthesis Kit (Thermo Scientific, Waltham, Massachusetts, USA) according to the manufacturer's protocol. With the qPCR we determined the expression levels of target genes listed in Table 2, using the SYBR® Select Master Mix (Applied Biosystems, Darmstadt, Germany) and the 7500 Real-Time PCR System (Applied Biosystems). cDNA-selective primers were designed to span exon-exon boundaries and to have a T_m of 60 °C using Primer Express software (Applied Biosystems), and were synthesized by TIB Molbiol (Berlin, Germany). All samples were measured in triplicate and normalized to the housekeeper 18S rRNA. Comparative CT (ΔΔCT) methods were used for relative quantification of transcription levels, with 1*g* set as 100%.

STRING Analysis

Interactions between proteins were determined using the STRING 10 platform [28]. For each protein, the UniProtKB entry number was inserted in the input form "multiple proteins" and "Homo sapiens" was

Downloaded from http://karger.com/cpb/article-pdf/45/2/429/2448497/000486920.pdf by guest on 31 October 2024

Cellular Physiology and Biochemistry
Cell Physiol Biochem 2018;45:429-445
DOI: 10.1159/000486920
Published online: January 29, 2018
© 2018 The Author(s). Published by S. Karger AG, Basel
www.karger.com/cpb

selected as organism. The resulting network view was downloaded in the molecular action view showing lines between interacting proteins and genes [29].

Statistical Evaluation

Statistical Evaluation was performed using SPSS 15.0 (SPSS, Inc., Chicago, IL, USA). The Mann-Whitney-U-Test (protein release) or a Student's *t*-tests (gene expression) were used to compare 1*g* and s-µ*g* conditions, as well as AD cells and MCS cells. All data is presented as mean ± standard deviation (SD) with a significance level of $p < 0.05$.

Table 2. Primers used for quantitative real-time PCR

Gene	Primer	Sequences (5'-3' direction)
CCL2	MCP1-F	GCTATAGAAGAATCACCAGCAGCAA
	MCP1-R	TGGAATCCTGAACCCACTTCTG
COL4A1	COL4A1-F	AAAGGGAGATCAAGGGATAG
	COL4A1-R	TCACCTTTTTCTCCAGGTAG
CXCL8	IL8-F	TGGCAGCCTTCCTGATTTCT
	IL8-R	GGGTGGAAAGGTTTGGAGTATG
FLK1	FLK1-F	TCTTCTGGCTACTTCTTGTCATCATC
	FLK1-R	GATGGACAAGTAGCCTGTCTTCAGT
FLT1	FLT1-F	CCCTCGCCGGAAGTTGTAT
	FLT1-R	GATAATTAACGAGTAGCCACGAGTCAA
FN1	FN1-F	TATGAGCAGGACCAGAAATAC
	FN1-R	CCACTTCATGTTGTCTCTTC
IL6	IL6-F	CGGGAACGAAAGAGAAGCTCTA
	IL6-R	GAGCAGCCCCAGGGAGAA
SERPINE1	PAI1-F	AGGCTGACTTCACGAGTCTTTCA
	PAI1-R	CACTCTCGTTCACCTCGATCTTC
TGFB1	TGFB1-F	CACCCGCGTGCTAATGGT
	TGFB1-R	AGAGCAACACGGGTTCAGGTA
VEGFA	VEGF-F	AATGTGAATGCAGACCAAAG
	VEGF-R	GACTTATACCGGGATTTCTTG
YWHAQ	YWHAQ-F	GGTACCTTGCTGAAGTTGCG
(housekeeper)	YWHAQ-R	GGGTGTGTGGGTTGCATCT

Results

Three phenotypes of endothelial cells after RPM-exposure

We had recently shown that after five and seven days in space and on the RPM, adherently growing cells (AD), multicellular spheroids (MCS) and small tubular structures (TS) can be observed [2, 8, 9, 15]. In 1*g*-cultures no 3D aggregates were detectable. The timeline of 3D aggregation was shown in previous experiments [8, 9, 15]. In this paper, we focused on 35-d spheroids and TS (Fig. 2A-C). At day 35 large numbers of TS could be collected. On average, each T-25 flask contained 12-15 TS with a length of approx. 500-800 µm and 3-5 larger TS with a length of about 2-3 mm, which could be seen with the naked eye in a petri dish (Fig. 1C). The TS were investigated by qPCR, and the MCS by qPCR, Western blotting, and immunofluorescence. The cell culture supernatants were measured by MAP technology.

Extracellular matrix proteins

For immunofluorescence staining (IFS) three groups of samples (1*g*, RPM-AD and RPM-MCS) were used and collected at day 35 (Fig. 3A).

Visualization of fibronectin protein by IFS revealed a decrease in AD cells and an elevated accumulation in the MCS cells at day 35 compared to the 1*g*-control cells (Fig. 3A). This result is supported by the gene expression of *FN1* determined by qPCR (Fig. 3B) and confirmed by Western blot analysis (Fig. 3F).

Moreover, we investigated transforming growth factor-beta1 (TGFB1) by IFS (Fig. 3D). Although a slightly more intensive staining of TGFB1 in ECs exposed to the RPM appeared, Western blotting did not reveal any

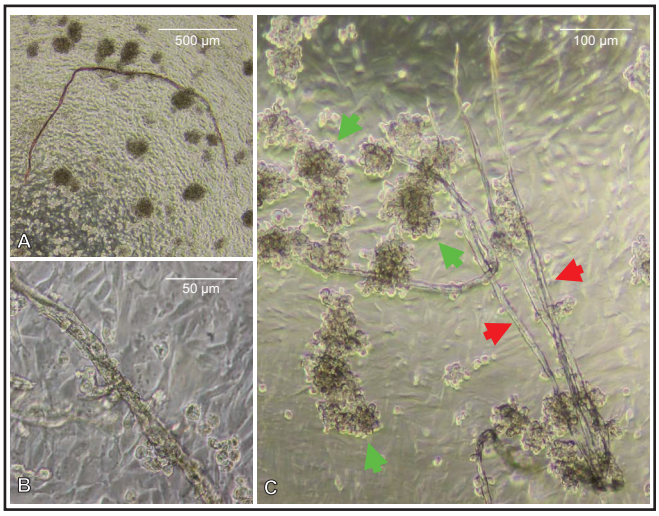


Fig. 2. Morphologic examination of the cells: Phase-contrast microscopy of EA.hy926 cells exposed to the RPM for 35 days. Samples cultured for 35 d on the RPM (A, B) revealed cells that stayed adherently as a monolayer (AD), MCS and large TS. Detailed view of TS and MCS on day 35 (C). Green arrowheads show MCS and red arrowheads mark TS.

KARGER

Downloaded from http://karger.com/cpb/article-pdf/45/2/429/2448497/000486920.pdf by guest on 31 October 2024

Cellular Physiology and Biochemistry
Cell Physiol Biochem 2018;45:429-445
DOI: 10.1159/000486920
Published online: January 29, 2018
© 2018 The Author(s). Published by S. Karger AG, Basel
www.karger.com/cpb

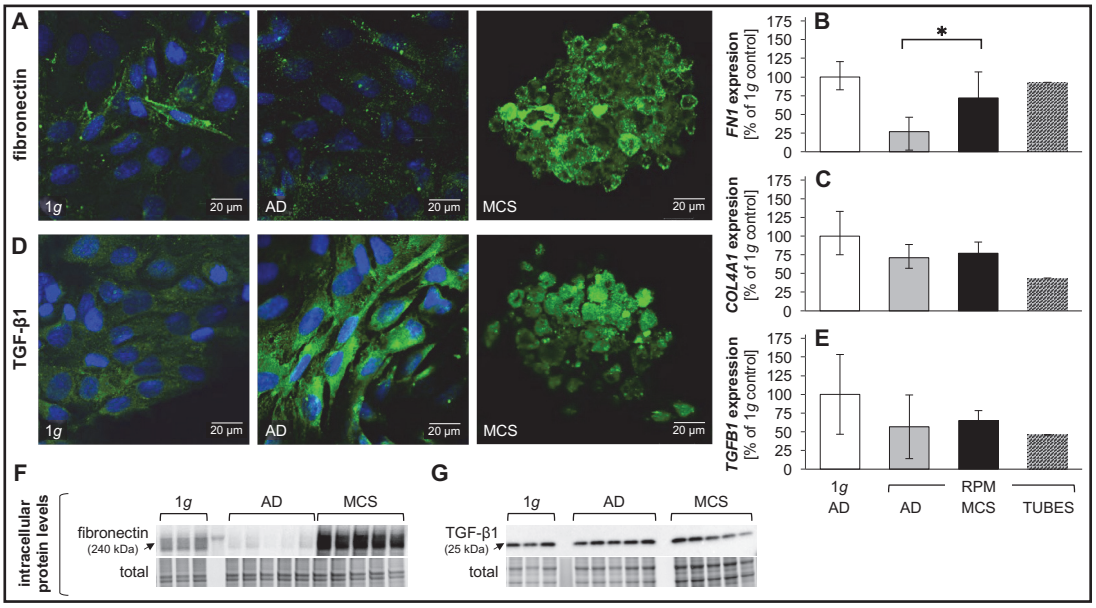


Fig. 3. Influence of RPM-exposure on the extracellular matrix of ECs: Quantitative alterations of protein content and gene expression of ECM-associated proteins after 35 d. Fibronectin. Immunofluorescence images of 1*g*-control cells, RPM-AD and RPM-MCS (A), Expression of *FN1* (B). Collagen-IV. Expression of *COL4A1* (C). TGF-β_1. Immunofluorescence images of 1*g*-control cells, RPM-AD and RPM-MCS (D). Expression of *TGFB1* (E). Intracellular levels of fibronectin (F) and TGF-β_1 determined via Western Blot (G). *p<0.05. Scale bars: 20 µm.

changes in the cellular protein content (Fig. 3G). In addition, the *TGFB1* gene expression was not altered in all groups (Fig. 3E). A similar result was detected for the mRNA expression of *COL4A1* (Fig. 3C).

Regulation of Vascular Endothelial Growth Factor in ECs exposed to the RPM

VEGF is an important regulator of angiogenesis and tube formation [11, 30]. We focused on the gene expression of *VEGFA*, on the VEGF protein level and the secretion of VEGF165 in the cell culture supernatant. This data is given in Fig. 4.

IFS of VEGF revealed that the amount of VEGF protein is subtly increased in the AD samples and more pronounced in the RPM-MCS cells compared to the 1*g*-controls (Fig. 4A). Interestingly, the qPCR data revealed that *VEGFA* is not differentially regulated (Fig. 4B).

Soluble VEGF protein was measured in the cell supernatants at different time points (5 d, 14 d, 23 d, 29 d and 35 d) (Fig. 4C). The concentration of secreted VEGF was significantly increased at day 35 and all other time points in µ*g*-supernatants.

In addition, we measured the gene expression of *FLT1* and *FLK1* (Fig. 4D, E). The mRNAs of both VEGF receptors were not significantly changed in all groups.

The cytokines interleukin-6 and interleukin-8 in spheroid formation

IFS revealed an accumulation of interleukin-6 (IL-6) in spheroids as compared to AD cells and 1*g* cells (Fig. 5A). There was a tendency of an increase in *IL6* mRNA in spheroids and tubes compared to 1*g*-samples (Fig. 5B). In addition, the release of IL-6 protein in the supernatant was significantly elevated in RPM-samples (Fig. 5E).

Interleukin-8 (IL-8) plays an important role in 3D growth and spheroid formation of cancer cells and benign cells [20, 31, 32]. Therefore, we focused on IL-8 in these experiments. IFS visualized a clear accumulation of IL-8 protein in the spheroids compared to AD and 1*g*-cells (Fig. 5C). These results were supported by the upregulated *CXCL8* mRNA level in the MCS group as compared to all other groups (Fig. 5D). Moreover, the secretion of IL-8 protein, as measured by MAP technology, was significantly enhanced in RPM-samples (Fig. 5E).

Downloaded from http://karger.com/cpb/article-pdf/45/2/429/2448497/000486920.pdf by guest on 31 October 2024

Cellular Physiology and Biochemistry
Cell Physiol Biochem 2018;45:429-445
DOI: 10.1159/000486920
Published online: January 29, 2018
© 2018 The Author(s). Published by S. Karger AG, Basel
www.karger.com/cpb

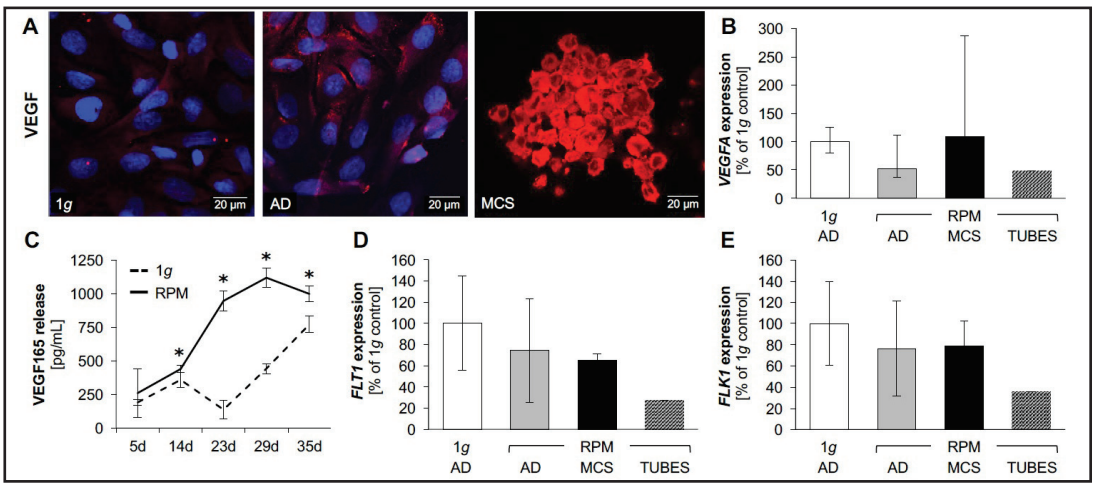


Fig. 4. Influence of RPM-exposure on Vascular Endothelial Growth Factor. Quantitative alterations of protein content and gene expression of VEGF and VEGF receptors after 35 d. VEGF. Immunofluorescence images of 1*g*-control cells, RPM-AD and RPM-MCS (A). Expression of *VEGFA* (B). Time course of VEGF165 release by the ECs (C). VEGF receptors. Expression of *FLT1* (D) und *FLK1* (E). *p<0.05. Scale bars: 20 µm.

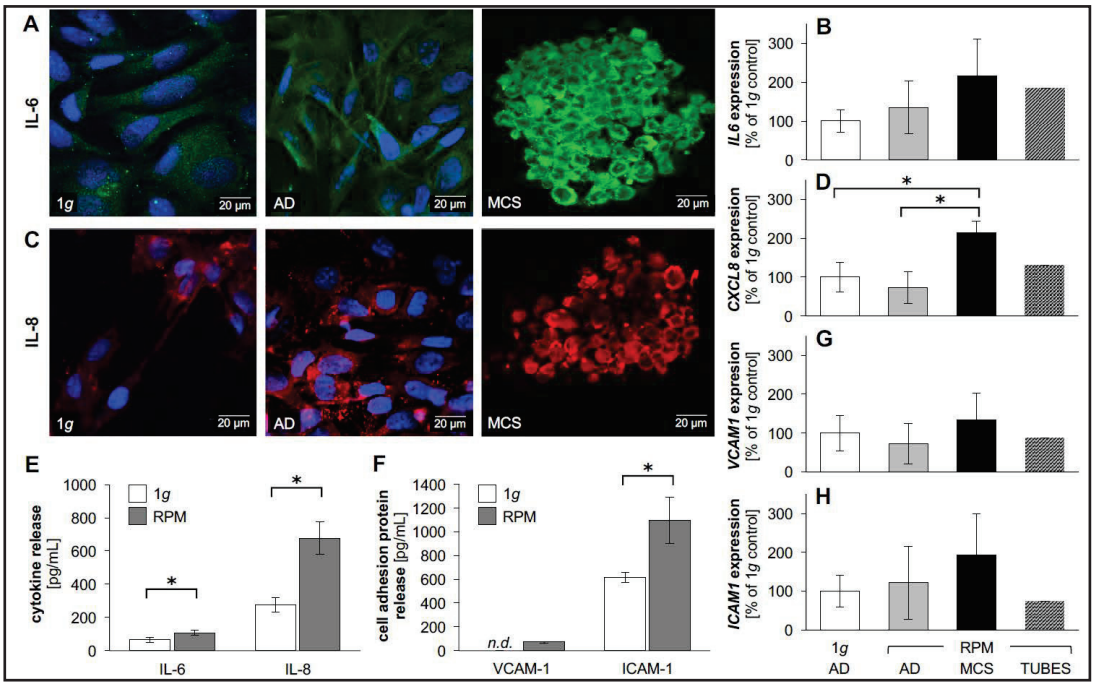


Fig. 5. Influence of RPM-exposure on interleukins and cell adhesion molecules: Quantitative alterations of protein content and gene expression of IL-6 and IL-8 after 35 d. IL-6. Immunofluorescence images of 1*g*-control cells, RPM-AD and RPM-MCS (A). Expression of *IL6* (B). IL-8. Immunofluorescence images of 1*g*-control cells, RPM-AD and RPM-MCS (C). Expression of *CXCL8* (D). Release of interleukins IL-6 and IL-8 (E). Release of the cell adhesion molecules VCAM-1 and ICAM-1 (F). Expression of *VCAM1* (G) and *ICAM1* (H). *p<0.05. Scale bars: 20 µm. n.d.: not detectable.

We also could detect an enhanced vascular cell adhesion molecule 1 (VCAM-1) and intercellular adhesion molecule 1 (ICAM-1) secretion after 35 d on the RPM (Fig. 5F), whereas the gene expressions of both cell adhesion molecules (*VCAM1* and *ICAM1*) were not significantly altered (Fig. 5G and 5H).

Downloaded from http://karger.com/cpb/article-pdf/45/2/429/2448497/000486920.pdf by guest on 31 October 2024

Cellular Physiology and Biochemistry
Cell Physiol Biochem 2018;45:429-445
DOI: 10.1159/000486920
Published online: January 29, 2018
© 2018 The Author(s). Published by S. Karger AG, Basel
www.karger.com/cpb

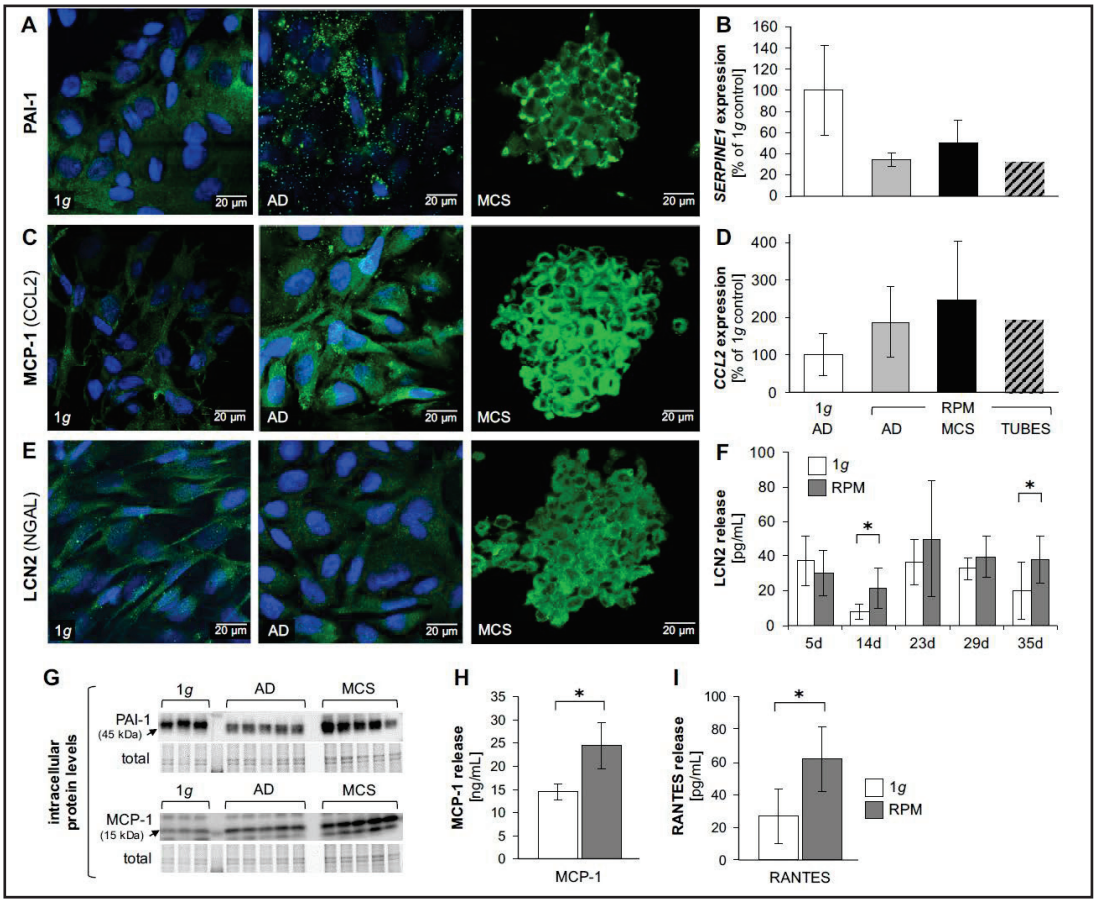


Fig. 6. Influence of RPM-exposure on soluble factors: Quantitative alterations of protein content and gene expression of PAI-1, MCP-1 (CCL2), and LCN2 (NGAL) after 35 d. PAI-1. Immunofluorescence images of 1*g*-control cells, RPM-AD and RPM-MCS (A). Expression of *SERPINE1* (B). MCP-1. Immunofluorescence images of 1*g*-control cells, RPM-AD and RPM-MCS after 35d (C). Expression of *CCL2* (D). LCN2. Immunofluorescence images of 1*g*-control cells, RPM-AD and RPM-MCS (E). Time course of LCN2 release (F). Intracellular levels of PAI-1 and MCP-1 determined via Western Blot (G) Release of MCP-1 (H) and RANTES (I). *p<0.05. Scale bars: 20 µm.

Selected factors involved in angiogenesis

Plasminogen activator inhibitor-1 (PAI-1) is also known as SERPINE1 and a risk factor for atherosclerosis and thrombosis. The immunofluorescence of PAI-1 revealed a concentration of the protein at the cellular membranes in MCS, possibly in connection with extracellular uPAR (Fig. 6A). PAI-1 is equally distributed in the cytoplasm of RPM-AD cells (Fig. 6A). The amount of the cellular protein is unchanged in all groups. *SERPINE1* mRNA levels were not changed in all groups (Fig. 6B). Western blotting revealed a slightly elevated amount of the PAI-1 protein in MCS compared to AD and 1*g*-cells (Fig. 6G).

IFS visualized an accumulation of monocyte chemoattractant protein 1 (MCP1, CCL2) protein in MCS (Fig. 6C). The release of MCP-1 protein was clearly increased in AD cells and MCS compared with 1*g*-samples (Fig. 6H). qPCR to measure the *CCL2* gene expression showed a tendency to an elevation in AD and MCS (Fig. 6D). A similar finding was seen in the Western Blot analysis (Fig. 6G).

The chemokine (C-C motif) ligand 5 (also CCL5) is also known as RANTES (regulated on activation, normal T cell expressed and secreted) [33]. It is of interest that the RANTES/CCL5-activity seems to be related to the *in vitro* promotion of endothelial cell migration, spreading and neo-vessel formation [33]. RANTES/CCL5-mediated angiogenesis depends

Downloaded from http://karger.com/cpb/article-pdf/45/2/429/2448497/000486920.pdf by guest on 31 October 2024

Cellular Physiology and Biochemistry
Cell Physiol Biochem 2018;45:429-445
DOI: 10.1159/000486920
Published online: January 29, 2018
© 2018 The Author(s). Published by S. Karger AG, Basel
www.karger.com/cpb

at least partly on VEGF secretion by ECs [33]. Here we could show that RANTES was clearly elevated in RPM-samples at day 35 compared to 1*g*-samples (Fig. 6I).

Neutrophil gelatinase-associated lipocalin (NGAL or LCN2) is detectable in activated neutrophils, kidney tubule cells, tumor cells, macrophages, vascular smooth muscle cells and endothelial cells. Recent studies have suggested that NGAL could also have pathophysiological importance in cardiovascular diseases [34]. We investigated NGAL by TRIFMA and found that its release in the supernatant is significantly elevated in RPM-samples at day 14 and day 35 (Fig. 6F). An accumulated NGAL in MCS was also detected by IFS (Fig. 6E).

Soluble factors released in the culture supernatant by the ECs

Concentrations of selected cytokines within 1*g* and RPM culture supernatants were determined by MAP analysis in order to measure the secretion behavior of the ECs. Table 3 shows all soluble factors of the InflammationMAP® v. 1.0, which were detectable.

C-reactive protein (CRP), eotaxin-1, factor VII, fibrinogen, haptoglobin, interferon gamma (IFN-gamma), interleukin-1 alpha (IL-1α), interleukin-1 beta (IL-1β), interleukin-1 receptor antagonist (IL-1ra), interleukin-2 (IL-2), interleukin-3 (IL-3), interleukin-4 (IL-4), interleukin-5 (IL-5), interleukin-7 (IL-7), interleukin-10 (IL-10), interleukin-12 subunit p40 (IL-12p40), interleukin-12 subunit p70 (IL-12p70), interleukin-15 (IL-15), interleukin-17 (IL-17), interleukin-18 (IL-18), interleukin-23 (IL-23), macrophage inflammatory protein-1 alpha (MIP-1α), macrophage inflammatory protein-1 beta (MIP-1β), matrix metalloprotein-

Table 3. Proteins released by EA.hy926 cells after a 35-day exposure to the RPM. The data was generated by Multi-Analyte Profiling using the Human Inflammation MAP® v1.0. Values are given as mean ± SD; *****, P <0.05 vs. 1*g*; LLOQ (Lower Limit of Quantitation, lowest concentration of an analyte in a sample that can be reliably detected). The values are determined as the mean of 5 (1*g* control) or 13 (RPM) blank readings. C-reactive Protein (CRP), eotaxin-1, factor VII, fibrinogen, haptoglobin, interferon gamma (IFN-gamma), interleukin-1 alpha (IL-1α), interleukin-1 beta (IL-1β), interleukin-1 receptor antagonist (IL-1ra), interleukin-2 (IL-2), interleukin-3 (IL-3), interleukin-4 (IL-4), interleukin-5 (IL-5), interleukin-7 (IL-7), interleukin-10 (IL-10), interleukin-12 subunit p40 (IL-12p40), interleukin-12 subunit p70 (IL-12p70), interleukin-15 (IL-15), interleukin-17 (IL-17), interleukin-18 (IL-18), interleukin-23 (IL-23), macrophage inflammatory protein-1 alpha (MIP-1α), macrophage inflammatory protein-1 beta (MIP-1β), matrix metalloproteinase-3 (MMP-3), matrix metalloproteinase-9 (MMP-9), stem cell factor (SCF), tumor necrosis factor alpha (TNF-α), tumor necrosis factor beta (TNF-β), and vitamin D-binding protein (VDBP) levels were below the LLOQ

Factors	1*g* control	RPM	LLOQ	Units
Alpha-1-Antitrypsin (AAT)	0.087 ± 0.014	0.246 ± 0.095	0.075	ng/mL
Alpha-2-Macroglobulin (A2Macro)	1.240 ± 0.152	1.423 ± 0.174	0.520	µg/mL
Beta-2-Microglobulin (B2M)	73.0 ± 33.6	124.1 ± 46.3	0.042	µg/mL
Brain-Derived Neurotrophic Factor (BDNF)	0.590 ± 0.090	0.671 ± 0.104	0.008	ng/mL
Complement C3 (C3)	0.076 ± 0.032	0.412 ± 0.095*	0.027	ng/mL
Ferritin (FRTN)	0.247 ± 0.144	0.425 ± 0.079*	0.034	ng/mL
Granulocyte-Macrophage Colony-Stimulating Factor (GM-CSF)	< 5.6	8.862 ± 2.047	5.6	pg/mL
Intercellular Adhesion Molecule 1 (ICAM-1)	0.617 ± 0.040	1.110 ± 0.194	0.570	ng/mL
Interleukin-6 (IL-6)	64.8 ± 14.4	108.2 ± 15.7*	0.580	pg/mL
Interleukin-8 (IL-8)	276.8 ± 44.5	678.5 ± 98.3*	1.600	pg/mL
Monocyte Chemotactic Protein 1 (MCP-1)	14.56 ± 1.71	24.49 ± 4.95*	0.022	ng/mL
T-Cell-Specific Protein RANTES (RANTES)	0.027 ± 0.017	0.062 ± 0.020*	0.001	ng/mL
Tissue Inhibitor of Metalloproteinases 1 (TIMP-1)	53.2 ± 22.7	59.5 ± 20.6	0.013	ng/mL
Tumor necrosis factor receptor 2 (TNFR2)	0.017 ± 0.001	0.032 ± 0.005*	0.010	pg/mL
Vascular Cell Adhesion Molecule-1 (VCAM-1)	< 0.062	0.072 ± 0.006	0.062	ng/mL
Vascular Endothelial Growth Factor (VEGF)	25.8 ± 5.63	55.8 ± 13.3*	8.800	pg/mL
von Willebrand Factor (vWF)	0.033 ± 0.017	0.019 ± 0.007	0.002	µg/mL

Downloaded from http://karger.com/cpb/article-pdf/45/2/429/2448497/000486920.pdf by guest on 31 October 2024

Cellular Physiology and Biochemistry
Cell Physiol Biochem 2018;45:429-445
DOI: 10.1159/000486920
Published online: January 29, 2018
© 2018 The Author(s). Published by S. Karger AG, Basel
www.karger.com/cpb

ase-3 (MMP-3), matrix metalloproteinase-9 (MMP-9), stem cell factor (SCF), tumor necrosis factor alpha (TNF-α), tumor necrosis factor beta (TNF-β), and vitamin D-binding protein (VDBP) levels were below the Lower Limit of Quantification (LLOQ).

Alpha$_2$-macroglobulin, beta$_2$-microglobulin, brain-derived neurotrophic factor (BDNF), tissue inhibitor of metalloproteinases 1 (TIMP-1), von Willebrand Factor (vWF) and intercellular adhesion molecule-1 (ICAM-1) were detectable in the supernatant, but not altered in RPM-samples compared with 1*g*.

Vascular Cell Adhesion Molecule-1 (VCAM-1), granulocyte-macrophage colony-stimulating factor (GM-CSF), was below the LLOQ in 1*g* samples but detectable in RPM-samples. Alpha$_1$-antitrypsin (SERPINA1), complement C3 (C3), ferritin (FRTN), and tumor necrosis factor receptor 2 (TNFR-2 were significantly elevated in RPM-samples (Table 3).

Pathway Analyses

In order to see whether the up- and down-regulations in gene expression and protein accumulation within the cells or in the cell supernatant described above were isolated processes or are linked within a network of mutual influences, we applied STRING. Overall, the analysis showed that besides the ferritin, all the components investigated were part of a network of interaction either at protein or at transcriptional level (Fig. 7). This is true for components, which were known from earlier studies to be involved in tube or MCS formation as well as for components detected by the current MAP analysis (Table 3; Fig. 3, 4, 5 and 6).

At a protein level indicated by blue, purple, and black lines, FN1, TGFB1, VEGF, TIMP-1, FLT1, KDR and PAI-1, which were known from earlier studies play central roles together with the newly detected vWF, SERPINA1, and CSF2. In addition, C3 and RANTES contribute to this network via IL-8 [35, 36].

IL-6 and IL-8 appear to be mainly interactive in this system on a transcriptional level (yellow lines, grey lines with green arrowhead). IL-8 can up-regulate *IL6* and *VEGFA* expression, while IL-6 exerts influence on VEGFA, VCAM-1, ICAM-1, TIMP-1 and CCL2 expression [37-39]. VEGFA is also regulated by BDNF, LCN2 and PAI-1, but has positive regulatory effects on *FN1* [40, 41].

Discussion

In this study, we cultured EA.hy926 cells on a RPM, which was constructed to simulate microgravity conditions on Earth. Randomizing the gravity vector by the RPM keeps human cells floating in the medium and allows to study aspects of annulling gravity. A part of the incubated cells detaches from the bottom of a culture flask and forms 3D aggregates like they are observed after spaceflights [2, 4, 5, 19]. Even though in contrast to a stay in space, sheer forces are produced on the RPM, multicellular spheroids and tubular structures are formed in both conditions [18-20].

After EA.hy926 cells remained viable during a 35-d RPM-exposure, we could study genes and proteins favoring the formation and existence of 3D structures *in vitro.* EA.hy926 cells are hybrid cells obtained by a fusion of HUVEC and A549 lung cancer cells [13] and differ in their protein content considerably from primary endothelial cells like microvascular ECs [42]. Regarding their tube formation behavior, they are very similar compared to primary ECs, but are more robust [2, 42]. Adherent EA.hy926 cells started to diverge after 12 h of incubation on the RPM [30], while 1*g*-cultures continued to grow as monolayers and exhibited overgrowth and a lower viability and had to be subcultured weekly during the experiment. Large amounts of 3D structures were formed after 5 days on the RPM [8, 9, 42]. They included MCS and convoluted TS and clusters not previously seen in similar short-term experiments (Fig. 2). These TS elongated and formed branches, but were maintained when imposing turbulent flow in the culture flask, indicating a high degree of structural integrity of the MCS and TS.

Downloaded from http://karger.com/cpb/article-pdf/45/2/429/2448497/000486920.pdf by guest on 31 October 2024

Cellular Physiology and Biochemistry
Cell Physiol Biochem 2018;45:429-445
DOI: 10.1159/000486920
Published online: January 29, 2018
© 2018 The Author(s). Published by S. Karger AG, Basel
www.karger.com/cpb

Mechanisms for spheroid and tube formation of ECs exposed to the RPM

The *in vitro* growth of TS resembles blood vessel growth, which is controlled by several growth factors (VEGF, fibroblast growth factor, TGF-β_1) and by cytokines, such as interleukins. VEGF signaling is involved in various processes of tube formation such as EC migration, proliferation, and differentiation [43-46].

After a 35-d RPM-exposure, VEGF was accumulated in MCS as determined by immunofluorescence (Fig. 4A), while the mRNAs of *VEGF*, *FLT1* and *FLK1* were not differentially expressed. This is in contrast to increased *VEGF* expression found in previous experiments of shorter durations [9, 10, 42]. This finding may be explained by the different sizes of the spheroids, which were collected after 35 days and their high amount of proteins. The signal for the synthesis of VEGF may have been released earlier and this process is already completed after 35 days. Still, a significantly increased amount of VEGF165 was observed in RPM culture supernatants as compared to 1*g*-cultures at different time points (Fig. 4C).

In contrast to VEGF, the impact of TGF-β_1 in angiogenesis is still unclear. TGF-β_1 signaling might be important for vascular morphogenesis and stability [47], as it seems to support VEGF expression, while the effect of interaction on a protein level is still unknown (Fig. 7, [48]). According to the literature TGF-β_1 can act as a promotor or as an inhibitor of angiogenesis *in vivo* and *in vitro* [49], depending on the experimental conditions. In our experiment, the amount of TGF-β_1 protein was constant in 1*g*, AD and RPM-samples after 35 days as measured by Western blot analysis. Immunofluorescence staining delivered a similar result. In addition, the gene expression of *TGFB1* was not altered. This indicates that the role of TGF-β_1 in spheroid and tube formation is more marginal.

Synthesis and maintenance of the ECM is important for the function of ECs. Here we measured the mRNA of collagen IV. The *COL4A1* gene expression was not altered in AD, MCS and TS cells after 35d. In addition, we focused on the ECM protein and cell adhesion molecule fibronectin, which plays an important role in wound healing and inflammation [21, 22]. Fibronectin is involved in migration, cell adhesion, differentiation processes and its expression is altered in various disorders such as diabetes, ischemia and reperfusion [50] as well as other cardiovascular disorders or cancers [50]. Anderson *et al* [51]. showed that an elevation in ECM synthesis in micropattern-elongated ECs is regulated by TGF-β_1 (see also Fig. 7), and that an elevated ECM might be important for the maintenance of a healthy endothelium *in vivo*. Its role in tissue engineering of TS might be more important in short-term studies. After a prolonged RPM-exposure, the measured increase in *FN1* mRNA and the accumulation of fibronectin may also play a key role in a healthy endothelium and relevant for the process of angiogenesis. We found a clear increase in fibronectin protein in MCS compared to µ*g*-AD cells and 1*g*-cells after 35 days. This is similar to previous findings at shorter durations [8, 10, 30]. Elevated fibronectin contributes to the activity of VEGF, and the combination of both proteins present at higher levels would likely contribute greatly to angiogenesis [52]. Furthermore, it is plausible that lower levels of fibronectin facilitate the detachment of cells from the monolayer, as fibronectin is involved in the adhesion cells to the culture flask. Earlier analyses with thyroid cancer cells expressing surface proteins that bind fibronectin, support the hypothesis concerning the role of fibronectin in 3D growth of human cells [53].

Enhanced amounts of IL-6 and IL-8 were detected in MCS and a significantly enhanced release of IL-6 and IL-8 was measured by MAP technology in RPM-cultures. This points to enhancement of IL-6 and IL-8 production under microgravity. Both cytokines play a role in wound repair and inflammation and increased amounts were secreted in the culture supernatant by the ECs. IL-6 is involved in angiogenesis and vascular remodeling [54]. IL-6 protein was elevated in the MCS. A similar result was detected for IL-8. In parallel, the *CXCL8* mRNA was significantly elevated in MCS compared to AD and 1*g*-cultures (Fig. 5D). In our system, both interleukins seem to exert their effects favoring angiogenesis via enhancement of expression of VCAM-1, ICAM-1 and VEGF165 (Fig. 7).

Downloaded from http://karger.com/cpb/article-pdf/45/2/429/2448497/000486920.pdf by guest on 31 October 2024

Cellular Physiology and Biochemistry
Cell Physiol Biochem 2018;45:429-445
DOI: 10.1159/000486920
Published online: January 29, 2018
© 2018 The Author(s). Published by S. Karger AG, Basel
www.karger.com/cpb

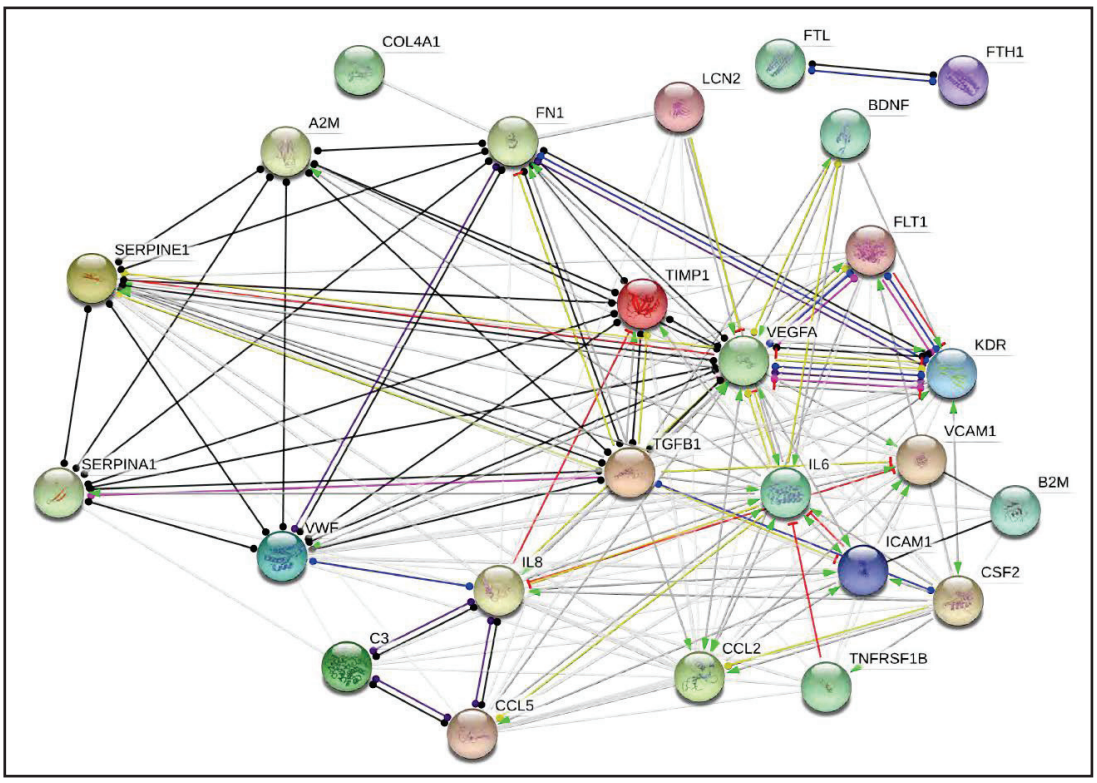


Fig. 7. STRING analysis of the proteins investigated in this study: FN1, VEGFA, MCP-1, TGF-β_1, PAI-1, IL-6, IL-8, COL4A1, FLK1, FLT1, VCAM-1, TNFR2, TIMP-1, ICAM-1, CCL2, A2M, B2M and LCN2 were used because earlier studies suggested their involvement in 3D structure formation. vWF, CCL5, C3, BDNF and SERPINA1 were detected in the current MAP analysis. The colors of the lines mean type of interaction: black line, undefined reactions, blue line, binding; purple line, posttranslational modification; red line, inhibition; yellow line, influence on expression; grey line with green arrow head, support of expression.

Multianalyte profiling also revealed an increase in the secretion of VCAM-1 in RPM-cultures, whereas VCAM-1 was not detectable in 1*g*-samples. In addition, the release of ICAM-1 was significantly elevated by long-term RPM-exposure of the ECs. Both adhesion molecules mediate the adhesion of several cell types such as lymphocytes, tumor cells and others to vascular endothelium [55]. In inflammation disorders the VCAM-1 expression is induced on the EC by cytokines or shear stress [56]. VCAM is detectable at the surface of the EC. Thereafter, the EC are activated to express adhesion molecules mediating leukocyte binding and to reveal a changed EC shape [56]. It has been shown that angiogenesis induced *in vivo* in rat cornea and dependent on IL-4 and IL-13, is mainly mediated through a soluble VCAM-1/α4 integrin pathway [57]. In addition, ICAM-1 is capable to induce angiogenesis and to increase the survival of microvessels [58]. Increased amounts of VCAM-1 and ICAM-1 in RPM-cultures might support 3D formation of ECs exposed to the RPM.

Plasminogen activator inhibitor-1 (PAI-1 or serpin E1) is normally known as the principal inhibitor of tissue plasminogen activator (tPA) and urokinase (uPA). PAI-1 is mainly produced by ECs, but is also secreted by other cells, e.g. thyroid cancer cells [59]. PAI-1 is involved in cancer angiogenesis, metastasis and promotes angiogenesis by stimulating EC migration toward fibronectin [60]. It also plays a role during retinal angiogenesis [61] and has been demonstrated to support angiogenesis in cancer. Geis *et al.* [62] showed that the HIF-2α-dependent PAI-1 induction contributes to angiogenesis in hepatocellular carcinoma. PAI-1 was already examined in microgravity studies and was reduced after a short-term RPM-exposure of ECs [15]. This is in line with our results showing a reduction in the AD cells after 35 days. A decrease in PAI-1 may initiate an increase in active plasmin, which

Downloaded from http://karger.com/cpb/article-pdf/45/2/429/2448497/000486920.pdf by guest on 31 October 2024

Cellular Physiology and Biochemistry
Cell Physiol Biochem 2018;45:429-445
DOI: 10.1159/000486920
Published online: January 29, 2018
© 2018 The Author(s). Published by S. Karger AG, Basel
www.karger.com/cpb

may be important for ECM remodeling and 3D formation. In addition, the inhibitory effect on VEGFA may be attenuated (see Fig. 7 red line, [40]). In clinical settings, increased plasma levels of plasmin are associated with an increased risk of atherosclerosis and myocardial infarction [63]. Moreover, in thyroid cancer cells exposed for 24 h to the RPM, the *PAI1* mRNA was reduced in the presence of elevated *VEGF*, while the *TGFB1* mRNA was not altered. In an earlier study, we had shown that increased plasminogen is relevant for the inhibition of spheroid formation [64]. These data support the thesis that downregulation of PAI-1 could help to form spheroids [65], because soluble PAI-1 is linked to inflammation, endothelium dysfunction and cardiovascular disease [66] and cancer metastasis.

Monocyte chemoattractant protein-1 (MCP-1)/CCL2 is synthesized and secreted by various cell types. ECs express functional CCR2, which is important for endothelial wound repair and inflammatory reactions. Consistent with previous research of shorter durations, we found MCP-1 protein to be elevated in both AD cells and MCS as determined by immunofluorescence and detected a similar trend in the Western blot analyses. The *MCP1* (*CCL2*) gene expression was not significantly changed, but MCS revealed a tendency of an increase in CCL2. Its role in the formation of spheroids or tubes remains to be investigated in future studies as a stimulatory effect on expression of VEGFA, ICAM-1 and VCAM-1 is suggested by the STRING analysis.

Additional soluble factors released in the supernatant

As detected by MAP technology several proteins were released by the EC in the culture supernatant after 35 days (Table 3). An increased secretion was measured for alpha-1-antitrypsin, GM-CSF, T-cell-specific protein RANTES, complement C3, ferritin, tumor necrosis factor receptor 2 in RPM-samples. In contrast, the release of alpha-2-macroglobulin, beta-2-microglobulin, brain-derived neurotrophic factor, tissue inhibitor of metalloproteinases 1 and von Willebrand Factor in ECs remained unchanged, when the cells were cultured for 35 days on the RPM. All of these factors are members of the network shown in Fig. 7. Although unknown so far in detail, SERPINA1 and vWF appear to play a significant role.

In addition, we measured NGAL by TRIFMA. Recent publications showed that NGAL, a biomarker for kidney disease has also a pathophysiological importance in cardiovascular diseases. It has negative regulatory influence on *VEGFA* transcription (Fig. 7 red cross bar, [67]). We had investigated the time course of NGAL secretion and found an increase with significance in RPM culture supernatants after 35 d (Fig. 6F). Furthermore, NGAL had been detected in different cancer types [25, 31]. Its role in 3D growth of ECs has to be studied in more detail in the future.

Conclusion

A long-term exposure of EA.hy926 cells to the RPM changed the growth behavior of the cells. Like observed on primary microvascular endothelial cells, three different phenotypes appeared: adherently growing cells at the bottom of the culture flasks, multicellular spheroids and 3D tubular structures, both in suspension in the culture supernatant. Consistent with earlier data [8, 9] and observations made during the ESA-SPHEROIDS space mission to the ISS [2], the MCS developed during the first two weeks [2]. Using EA.hy926 cells, we could expand this period and demonstrate that VEGF, IL-6, IL-8, PAI-1, ICAM-1 and VCAM-1 are interesting proteins involved in the changed growth behavior and the development of the three phenotypes. Especially MCP-1 and NGAL are interesting targets for future experiments.

Acknowledgements

The authors would like to thank the German Space Agency (DLR; (DG) BMWi project 50WB1524), and Aarhus University, Denmark. The funders had no role in study design, data collection and analysis, decision to publish, or preparation of the manuscript.

KARGER

Downloaded from http://karger.com/cpb/article-pdf/45/2/429/2448497/000486920.pdf by guest on 31 October 2024

Cellular Physiology and Biochemistry
Cell Physiol Biochem 2018;45:429-445
DOI: 10.1159/000486920
Published online: January 29, 2018
© 2018 The Author(s). Published by S. Karger AG, Basel
www.karger.com/cpb

D.G. and N.E.M. designed the experiments. A.D., and J.S. executed the experiments and collected the material. A.D. and N.E.M. performed western blot analyses. M.K., A.D. and N.E.M. performed qPCR analyses. J.B. performed the pathway analyses. D.G., J.B., N.E.M. and M.K. wrote the manuscript. M.I. contributed reagents, materials and analysis tools. All authors reviewed the manuscript.

Disclosure Statement

Competing financial interests: The authors declare no competing financial interests.

References

1 Hallgren E, Migeotte P-F, Kornilova L, Delière Q, Fransen E, Glukhikh D, Moore ST, Clément G, Diedrich A, MacDougall H, Wuyts FL: Dysfunctional vestibular system causes a blood pressure drop in astronauts returning from space. Sci Rep 2015;5:17627.
2 Pietsch J, Gass S, Nebuloni S, Echegoyen D, Riwaldt S, Baake C, Bauer J, Corydon TJ, Egli M, Infanger M, Grimm D: Three-dimensional growth of human endothelial cells in an automated cell culture experiment container during the SpaceX CRS-8 ISS space mission - The SPHEROIDS project. Biomaterials 2017;124:126-156.
3 Versari S, Longinotti G, Barenghi L, Maier JA, Bradamante S: The challenging environment on board the International Space Station affects endothelial cell function by triggering oxidative stress through thioredoxin interacting protein overexpression: the ESA-SPHINX experiment. Faseb j 2013;27:4466-4475.
4 Aleshcheva G, Bauer J, Hemmersbach R, Slumstrup L, Wehland M, Infanger M, Grimm D: Scaffold-free Tissue Formation Under Real and Simulated Microgravity Conditions. Basic Clin Pharmacol Toxicol 2016;119:S26-33.
5 Grimm D, Wehland M, Pietsch J, Aleshcheva G, Wise P, van Loon J, Ulbrich C, Magnusson NE, Infanger M, Bauer J: Growing tissues in real and simulated microgravity: new methods for tissue engineering. Tissue Eng Part B Rev 2014;20:555-566.
6 Janmaleki M, Pachenari M, Seyedpour SM, Shahghadami R, Sanati-Nezhad A: Impact of Simulated Microgravity on Cytoskeleton and Viscoelastic Properties of Endothelial Cell. Sci Rep 2016;6:32418.
7 Shi F, Wang YC, Hu ZB, Xu HY, Sun J, Gao Y, Li XT, Yang CB, Xie C, Li CF, Zhang S, Zhao JD, Cao XS, Sun XQ: Simulated Microgravity Promotes Angiogenesis through RhoA-Dependent Rearrangement of the Actin Cytoskeleton. Cell Physiol Biochem 2017;41:227-238.
8 Grimm D, Infanger M, Westphal K, Ulbrich C, Pietsch J, Kossmehl P, Vadrucci S, Baatout S, Flick B, Paul M, Bauer J: A delayed type of three-dimensional growth of human endothelial cells under simulated weightlessness. Tissue Eng Part A 2009;15:2267-2275.
9 Grimm D, Bauer J, Ulbrich C, Westphal K, Wehland M, Infanger M, Aleshcheva G, Pietsch J, Ghardi M, Beck M, El-Saghire H, de Saint-Georges L, Baatout S: Different responsiveness of endothelial cells to vascular endothelial growth factor and basic fibroblast growth factor added to culture media under gravity and simulated microgravity. Tissue Eng Part A 2010;16:1559-1573.
10 Grosse J, Wehland M, Pietsch J, Ma X, Ulbrich C, Schulz H, Saar K, Hubner N, Hauslage J, Hemmersbach R, Braun M, van Loon J, Vagt N, Infanger M, Eilles C, Egli M, Richter P, Baltz T, Einspanier R, Sharbati S, Grimm D: Short-term weightlessness produced by parabolic flight maneuvers altered gene expression patterns in human endothelial cells. Faseb j 2012;26:639-655.
11 Infanger M, Ulbrich C, Baatout S, Wehland M, Kreutz R, Bauer J, Grosse J, Vadrucci S, Cogoli A, Derradji H, Neefs M, Kusters S, Spain M, Paul M, Grimm D: Modeled gravitational unloading induced downregulation of endothelin-1 in human endothelial cells. J Cell Biochem 2007;101:1439-1455.
12 Häder DP, Braun M, Grimm D, Hemmersbach R: Gravireceptors in eukaryotes-a comparison of case studies on the cellular level. NPJ Microgravity 2017;3:13.
13 Edgell CJ, McDonald CC, Graham JB: Permanent cell line expressing human factor VIII-related antigen established by hybridization. Proc Natl Acad Sci U S A 1983;80:3734-3737.

Downloaded from http://karger.com/cpb/article-pdf/45/2/429/2448497/000486920.pdf by guest on 31 October 2024

Cellular Physiology and Biochemistry
Cell Physiol Biochem 2018;45:429-445
DOI: 10.1159/000486920
Published online: January 29, 2018
© 2018 The Author(s). Published by S. Karger AG, Basel
www.karger.com/cpb

14 Borst AG, van Loon JJWA: Technology and Developments for the Random Positioning Machine, RPM. Microgravity Sci Technol 2008;21:287.
15 Ma X, Wehland M, Schulz H, Saar K, Hubner N, Infanger M, Bauer J, Grimm D: Genomic approach to identify factors that drive the formation of three-dimensional structures by EA.hy926 endothelial cells. PLoS One 2013;8:e64402.
16 Ulbrich C, Westphal K, Baatout S, Wehland M, Bauer J, Flick B, Infanger M, Kreutz R, Vadrucci S, Egli M, Cogoli A, Derradji H, Pietsch J, Paul M, Grimm D: Effects of basic fibroblast growth factor on endothelial cells under conditions of simulated microgravity. J Cell Biochem 2008;104:1324-1341.
17 Ulbrich C, Westphal K, Pietsch J, Winkler HD, Leder A, Bauer J, Kossmehl P, Grosse J, Schoenberger J, Infanger M, Egli M, Grimm D: Characterization of human chondrocytes exposed to simulated microgravity. Cell Physiol Biochem 2010;25:551-560.
18 Wuest SL, Richard S, Kopp S, Grimm D, Egli M: Simulated microgravity: critical review on the use of random positioning machines for mammalian cell culture. Biomed Res Int 2015;2015:971474.
19 Warnke E, Pietsch J, Wehland M, Bauer J, Infanger M, Gorog M, Hemmersbach R, Braun M, Ma X, Sahana J, Grimm D: Spheroid formation of human thyroid cancer cells under simulated microgravity: a possible role of CTGF and CAV1. Cell Commun Signal 2014;12:32.
20 Svejgaard B, Wehland M, Ma X, Kopp S, Sahana J, Warnke E, Aleshcheva G, Hemmersbach R, Hauslage J, Grosse J, Bauer J, Corydon TJ, Islam T, Infanger M, Grimm D: Common Effects on Cancer Cells Exerted by a Random Positioning Machine and a 2D Clinostat. PLoS One 2015;10:e0135157.
21 Infanger M, Grosse J, Westphal K, Leder A, Ulbrich C, Paul M, Grimm D: Vascular endothelial growth factor induces extracellular matrix proteins and osteopontin in the umbilical artery. Ann Vasc Surg 2008;22:273-284.
22 Infanger M, Shakibaei M, Kossmehl P, Hollenberg SM, Grosse J, Faramarzi S, Schulze-Tanzil G, Paul M, Grimm D: Intraluminal application of vascular endothelial growth factor enhances healing of microvascular anastomosis in a rat model. J Vasc Res 2005;42:202-213.
23 Pietsch J, Kussian R, Sickmann A, Bauer J, Weber G, Nissum M, Westphal K, Egli M, Grosse J, Schonberger J, Wildgruber R, Infanger M, Grimm D: Application of free-flow IEF to identify protein candidates changing under microgravity conditions. Proteomics 2010;10:904-913.
24 Grosse J, Warnke E, Pohl F, Magnusson NE, Wehland M, Infanger M, Eilles C, Grimm D: Impact of sunitinib on human thyroid cancer cells. Cell Physiol Biochem 2013;32:154-170.
25 Kopp S, Warnke E, Wehland M, Aleshcheva G, Magnusson NE, Hemmersbach R, Corydon TJ, Bauer J, Infanger M, Grimm D: Mechanisms of three-dimensional growth of thyroid cells during long-term simulated microgravity. Sci Rep 2015;5:16691.
26 Magnusson NE, Hornum M, Jorgensen KA, Hansen JM, Bistrup C, Feldt-Rasmussen B, Flyvbjerg A: Plasma neutrophil gelatinase associated lipocalin (NGAL) is associated with kidney function in uraemic patients before and after kidney transplantation. BMC Nephrol 2012;13:8.
27 Rothermund L, Kreutz R, Kossmehl P, Fredersdorf S, Shakibaei M, Schulze-Tanzil G, Paul M, Grimm D: Early onset of chondroitin sulfate and osteopontin expression in angiotensin II-dependent left ventricular hypertrophy. Am J Hypertens 2002;15:644-652.
28 Snel B, Lehmann G, Bork P, Huynen MA: STRING: a web-server to retrieve and display the repeatedly occurring neighbourhood of a gene. Nucleic Acids Res 2000;28:3442-3444.
29 Pietsch J, Riwaldt S, Bauer J, Sickmann A, Weber G, Grosse J, Infanger M, Eilles C, Grimm D: Interaction of proteins identified in human thyroid cells. Int J Mol Sci 2013;14:1164-1178.
30 Infanger M, Kossmehl P, Shakibaei M, Baatout S, Witzing A, Grosse J, Bauer J, Cogoli A, Faramarzi S, Derradji H, Neefs M, Paul M, Grimm D: Induction of three-dimensional assembly and increase in apoptosis of human endothelial cells by simulated microgravity: impact of vascular endothelial growth factor. Apoptosis 2006;11:749-764.
31 Kopp S, Slumstrup L, Corydon TJ, Sahana J, Aleshcheva G, Islam T, Magnusson NE, Wehland M, Bauer J, Infanger M, Grimm D: Identifications of novel mechanisms in breast cancer cells involving duct-like multicellular spheroid formation after exposure to the Random Positioning Machine. Sci Rep 2016;6:26887.
32 Warnke E, Pietsch J, Kopp S, Bauer J, Sahana J, Wehland M, Krüger M, Hemmersbach R, Infanger M, Lutzenberg R, Grimm D: Cytokine Release and Focal Adhesion Proteins in Normal Thyroid Cells Cultured on the Random Positioning Machine. Cell Physiol Biochem 2017;43:257-270.

Downloaded from http://karger.com/cpb/article-pdf/45/2/429/2448497/000486920.pdf by guest on 31 October 2024

Cellular Physiology and Biochemistry
Cell Physiol Biochem 2018;45:429-445
DOI: 10.1159/000486920
Published online: January 29, 2018
© 2018 The Author(s). Published by S. Karger AG, Basel
www.karger.com/cpb

33 Suffee N, Hlawaty H, Meddahi-Pelle A, Maillard L, Louedec L, Haddad O, Martin L, Laguillier C, Richard B, Oudar O, Letourneur D, Charnaux N, Sutton A: RANTES/CCL5-induced pro-angiogenic effects depend on CCR1, CCR5 and glycosaminoglycans. Angiogenesis 2012;15:727-744.
34 Eilenberg W, Stojkovic S, Piechota-Polanczyk A, Kaun C, Rauscher S, Groger M, Klinger M, Wojta J, Neumayer C, Huk I, Demyanets S: Neutrophil Gelatinase-Associated Lipocalin (NGAL) is Associated with Symptomatic Carotid Atherosclerosis and Drives Pro-inflammatory State *In vitro*. Eur J Vasc Endovasc Surg 2016;51:623-631.
35 Lappegard KT, Bergseth G, Riesenfeld J, Pharo A, Magotti P, Lambris JD, Mollnes TE: The artificial surface-induced whole blood inflammatory reaction revealed by increases in a series of chemokines and growth factors is largely complement dependent. J Biomed Mater Res A 2008;87:129-135.
36 Lee TH, Avraham H, Lee SH, Avraham S: Vascular endothelial growth factor modulates neutrophil transendothelial migration via up-regulation of interleukin-8 in human brain microvascular endothelial cells. J Biol Chem 2002;277:10445-10451.
37 Heinrich PC, Behrmann I, Haan S, Hermanns HM, Muller-Newen G, Schaper F: Principles of interleukin (IL)-6-type cytokine signalling and its regulation. Biochem J 2003;374:1-20.
38 Xie K: Interleukin-8 and human cancer biology. Cytokine Growth Factor Rev 2001;12:375-391.
39 Zhang GJ, Crist SA, McKerrow AK, Xu Y, Ladehoff DC, See WA: Autocrine IL-6 production by human transitional carcinoma cells upregulates expression of the alpha5beta1 firbonectin receptor. J Urol 2000;163:1553-1559.
40 Wu J, Strawn TL, Luo M, Wang L, Li R, Ren M, Xia J, Zhang Z, Ma W, Luo T, Lawrence DA, Fay WP: Plasminogen activator inhibitor-1 inhibits angiogenic signaling by uncoupling vascular endothelial growth factor receptor-2-alphaVbeta3 integrin cross talk. Arterioscler Thromb Vasc Biol 2015;35:111-120.
41 Wu T, Zhang B, Ye F, Xiao Z: A potential role for caveolin-1 in VEGF-induced fibronectin upregulation in mesangial cells: involvement of VEGFR2 and Src. Am J Physiol Renal Physiol 2013;304:F820-830.
42 Ma X, Sickmann A, Pietsch J, Wildgruber R, Weber G, Infanger M, Bauer J, Grimm D: Proteomic differences between microvascular endothelial cells and the EA.hy926 cell line forming three-dimensional structures. Proteomics 2014;14:689-698.
43 Ferrara N, Gerber HP, LeCouter J: The biology of VEGF and its receptors. Nat Med 2003;9:669-676.
44 Kristensen TB, KnuTSon ML, Wehland M, Laursen BE, Grimm D, Warnke E, Magnusson NE: Anti-vascular endothelial growth factor therapy in breast cancer. Int J Mol Sci 2014;15:23024-23041.
45 Tammela T, Enholm B, Alitalo K, Paavonen K: The biology of vascular endothelial growth factors. Cardiovasc Res 2005;65:550-563.
46 Wehland M, Bauer J, Magnusson NE, Infanger M, Grimm D: Biomarkers for anti-angiogenic therapy in cancer. Int J Mol Sci 2013;14:9338-9364.
47 Pardali E, ten Dijke P: Transforming growth factor-beta signaling and tumor angiogenesis. Front Biosci (Landmark Ed) 2009;14:4848-4861.
48 Breier G, Blum S, Peli J, Groot M, Wild C, Risau W, Reichmann E: Transforming growth factor-beta and Ras regulate the VEGF/VEGF-receptor system during tumor angiogenesis. Int J Cancer 2002;97:142-148.
49 Goumans MJ, Liu Z, ten Dijke P: TGF-beta signaling in vascular biology and dysfunction. Cell Res 2009;19:116-127.
50 Kossmehl P, Schonberger J, Shakibaei M, Faramarzi S, Kurth E, Habighorst B, von Bauer R, Wehland M, Kreutz R, Infanger M, Schulze-Tanzil G, Paul M, Grimm D: Increase of fibronectin and osteopontin in porcine hearts following ischemia and reperfusion. J Mol Med (Berl) 2005;83:626-637.
51 Anderson DE, Hinds MT: Extracellular matrix production and regulation in micropatterned endothelial cells. Biochem Biophys Res Commun 2012;427:159-164.
52 Wijelath ES, Rahman S, Namekata M, Murray J, Nishimura T, Mostafavi-Pour Z, Patel Y, Suda Y, Humphries MJ, Sobel M: Heparin-II domain of fibronectin is a vascular endothelial growth factor-binding domain: enhancement of VEGF biological activity by a singular growth factor/matrix protein synergism. Circ Res 2006;99:853-860.
53 Pietsch J, Sickmann A, Weber G, Bauer J, Egli M, Wildgruber R, Infanger M, Grimm D: A proteomic approach to analysing spheroid formation of two human thyroid cell lines cultured on a random positioning machine. Proteomics 2011;11:2095-2104.

Downloaded from http://karger.com/cpb/article-pdf/45/2/429/2448497/000486920.pdf by guest on 31 October 2024

Cellular Physiology and Biochemistry
Cell Physiol Biochem 2018;45:429-445
DOI: 10.1159/000486920
Published online: January 29, 2018
© 2018 The Author(s). Published by S. Karger AG, Basel
www.karger.com/cpb

54 Yao JS, Zhai W, Fan Y, Lawton MT, Barbaro NM, Young WL, Yang GY: Interleukin-6 upregulates expression of KDR and stimulates proliferation of human cerebrovascular smooth muscle cells. J Cereb Blood Flow Metab 2007;27:510-520.
55 Eibl RH, Benoit M: Molecular resolution of cell adhesion forces. IEE Proc Nanobiotechnol 2004;151:128-132.
56 Cook-Mills JM, Marchese ME, Abdala-Valencia H: Vascular cell adhesion molecule-1 expression and signaling during disease: regulation by reactive oxygen species and antioxidants. Antioxid Redox Signal 2011;15:1607-1638.
57 Fukushi J, Ono M, Morikawa W, Iwamoto Y, Kuwano M: The activity of soluble VCAM-1 in angiogenesis stimulated by IL-4 and IL-13. J Immunol 2000;165:2818-2823.
58 Deng C, Zhang D, Shan S, Wu J, Yang H, Yu Y: Angiogenic effect of intercellular adhesion molecule-1. J Huazhong Univ Sci Technolog Med Sci 2007;27:9-12.
59 Riwaldt S, Bauer J, Pietsch J, Braun M, Segerer J, Schwarzwalder A, Corydon TJ, Infanger M, Grimm D: The Importance of Caveolin-1 as Key-Regulator of Three-Dimensional Growth in Thyroid Cancer Cells Cultured under Real and Simulated Microgravity Conditions. Int J Mol Sci 2015;16:28296-28310.
60 Isogai C, Laug WE, Shimada H, Declerck PJ, Stins MF, Durden DL, Erdreich-Epstein A, DeClerck YA: Plasminogen activator inhibitor-1 promotes angiogenesis by stimulating endothelial cell migration toward fibronectin. Cancer Res 2001;61:5587-5594.
61 Basu A, Menicucci G, Maestas J, Das A, McGuire P: Plasminogen activator inhibitor-1 (PAI-1) facilitates retinal angiogenesis in a model of oxygen-induced retinopathy. Invest Ophthalmol Vis Sci 2009;50:4974-4981.
62 Geis T, Doring C, Popp R, Grossmann N, Fleming I, Hansmann ML, Dehne N, Brune B: HIF-2alpha-dependent PAI-1 induction contributes to angiogenesis in hepatocellular carcinoma. Exp Cell Res 2015;331:46-57.
63 Ploplis VA: Effects of altered plasminogen activator inhibitor-1 expression on cardiovascular disease. Curr Drug Targets 2011;12:1782-1789.
64 Riwaldt S, Pietsch J, Sickmann A, Bauer J, Braun M, Segerer J, Schwarzwalder A, Aleshcheva G, Corydon TJ, Infanger M, Grimm D: Identification of proteins involved in inhibition of spheroid formation under microgravity. Proteomics 2015;15:2945-2952.
65 Liekens S, De Clercq E, Neyts J: Angiogenesis: regulators and clinical applications. Biochem Pharmacol 2001;61:253-270.
66 Verma S, Buchanan MR, Anderson TJ: Endothelial function testing as a biomarker of vascular disease. Circulation 2003;108:2054-2059.
67 Tong Z, Kunnumakkara AB, Wang H, Matsuo Y, Diagaradjane P, Harikumar KB, Ramachandran V, Sung B, Chakraborty A, Bresalier RS, Logsdon C, Aggarwal BB, Krishnan S, Guha S: Neutrophil gelatinase-associated lipocalin: a novel suppressor of invasion and angiogenesis in pancreatic cancer. Cancer Res 2008;68:6100-6108.

Downloaded from http://karger.com/cpb/article-pdf/45/2/429/2448497/000486920.pdf by guest on 31 October 2024

International Journal of
Molecular Sciences

MDPI

Article

Short-Term Microgravity Influences Cell Adhesion in Human Breast Cancer Cells

Mohamed Zakaria Nassef [1], Sascha Kopp [1,*], Daniela Melnik [1], Thomas J. Corydon [2,3], Jayashree Sahana [2], Marcus Krüger [1], Markus Wehland [1], Thomas J. Bauer [1], Christian Liemersdorf [4], Ruth Hemmersbach [4], Manfred Infanger [1] and Daniela Grimm [1,2,5,*]

1 Clinic for Plastic, Aesthetic and Hand Surgery, Otto von Guericke University Magdeburg, 39120 Magdeburg, Germany; mohamed.nassef@med.ovgu.de (M.Z.N.); daniela.melnik@med.ovgu.de (D.M.); marcus.krueger@med.ovgu.de (M.K.); markus.wehland@med.ovgu.de (M.W.); thomas.bauer@med.ovgu.de (T.J.B.); manfred.infanger@med.ovgu.de (M.I.)
2 Department of Biomedicine, Aarhus University, 8000 Aarhus C, Denmark; corydon@biomed.au.dk (T.J.C.); jaysaha@biomed.au.dk (J.S.)
3 Department of Ophthalmology, Aarhus University Hospital, 8200 Aarhus N, Denmark
4 Institute of Aerospace Medicine, Department of Gravitational Biology, German Aerospace Center, 51147 Cologne, Germany; christian.liemersdorf@dlr.de (C.L.); ruth.hemmersbach@dlr.de (R.H.)
5 Gravitational Biology and Translational Regenerative Medicine, Faculty of Medicine and Mechanical Engineering, Otto von Guericke University, 39120 Magdeburg, Germany
* Correspondence: sascha.kopp@med.ovgu.de (S.K.); dgg@biomed.au.dk (D.G.); Tel.: +49-391-6721267 (S.K.); +45-871-67693 (D.G.)

Received: 11 October 2019; Accepted: 12 November 2019; Published: 15 November 2019



Abstract: With the commercialization of spaceflight and the exploration of space, it is important to understand the changes occurring in human cells exposed to real microgravity (r-μ*g*) conditions. We examined the influence of r-μ*g*, simulated microgravity (s-μ*g*, incubator random positioning machine (iRPM)), hypergravity (hyper-*g*), and vibration (VIB) on triple-negative breast cancer (TNBC) cells (MDA-MB-231 cell line) with the aim to study early changes in the gene expression of factors associated with cell adhesion, apoptosis, nuclear factor "kappa-light-chain-enhancer" of activated B-cells (NF-κB) and mitogen-activated protein kinase (MAPK) signaling. We had the opportunity to attend a parabolic flight (PF) mission and to study changes in RNA transcription in the MDA-MB cells exposed to PF maneuvers (29th Deutsches Zentrum für Luft- und Raumfahrt (DLR) PF campaign). PF maneuvers induced an early up-regulation of *ICAM1*, *CD44* and *ERK1* mRNAs after the first parabola (P1) and a delayed upregulation of *NFKB1*, *NFKBIA*, *NFKBIB*, and *FAK1* after the last parabola (P31). ICAM-1, VCAM-1 and CD44 protein levels were elevated, whereas the NF-κB subunit p-65 and annexin-A2 protein levels were reduced after the 31st parabola (P31). The *PRKCA*, *RAF1*, *BAX* mRNA were not changed and cleaved caspase-3 was not detectable in MDA-MB-231 cells exposed to PF maneuvers. Hyper-*g*-exposure of the cells elevated the expression of *CD44* and *NFKBIA* mRNAs, iRPM-exposure downregulated *ANXA2* and *BAX*, whereas VIB did not affect the TNBC cells. The early changes in ICAM-1 and VCAM-1 and the rapid decrease in the NF-κB subunit p-65 might be considered as fast-reacting, gravity-regulated and cell-protective mechanisms of TNBC cells exposed to altered gravity conditions. This data suggest a key role for the detected gravity-signaling elements in three-dimensional growth and metastasis.

Keywords: breast cancer cells; microgravity; hypergravity; cell adhesion; apoptosis; NF-κB

1. Introduction

The GLOBOCAN statistics from 2018 showed that breast cancer is the most common cancer in women and the second leading cause of cancer deaths worldwide [1]. Breast cancer comprises multiple subtypes with characteristic histology, treatability and outcome [2]. Currently, seven molecular subtypes are known [3–6]: luminal A (estrogen receptor positive (ER+)/progesterone receptor positive (PR+)/androgen receptor positive (AR+)/human epidermal growth receptor 2 negative (HER2−)/antigen KI67 negative (KI67−)), luminal B (ER+/PR+/AR+/HER2−/KI67+), HER2 enriched (ER−/PR−/HER2+), molecular apocrine (ER−/PR−/AR+/HER2+/KI67+), basal-like/triple-negative (ER−/PR−/AR−/HER2−), normal breast-like (ER+/PR+/HER2−/KI67−) and claudin-low (ER−/PR−/HER2−). Survival of the patients is associated with prognostic factors like tumor size, hormone-receptor-profile and metastases at the time of diagnosis. An onset therapy is the surgical resection of the tumor tissue (lumpectomy or mastectomy). Tumor size and possible metastases to the sentinel lymph node are decisive for the choice of following therapy. Chemotherapy, radiation and anti-hormone therapy, targeted treatment against HER2 and anti-angiogenic therapy are often applied after surgery or in the case of advanced disease stages [7]. Despite the advanced therapy, it is estimated that about 626,679 deaths wordwide will occur from breast cancer per year [1]. Therefore, it is necessary to implement novel ideas to find drug targets and to test new treatment options. This study will focus on the well-described basal-like/triple-negative cancer (TNBC) and will study the TNBC cell line MDA-MB-231 exposed to short-term altered gravity conditions and vibration (VIB) [8]. Using altered gravity conditions in the field of cancer research is not typically the first method to search for target proteins [9], but more than 20 years ago it became clear that cells exposed to microgravity (μ*g*) opened an alternative view on cancer cells as they revealed numerous changes like an altered gene expression, protein synthesis and secretion. With the help of simulated microgravity (s-μ*g*) and mass spectrometry, we found novel protein targets involved in cancer [10–13]. A space journey and a longer stay on the International Space Station (ISS) provide altered gravity conditions, which are not found on Earth. On Earth, we can simulate μ*g* to some extent by applying rotating devices like a 2D or 3D clinostat, the National Aeronautics and Space Administration (NASA)-developed rotating wall vessel or a random positioning machine (RPM) [14]. Exposure of different cancer cells types to real (r-μ*g*) or simulated (s-)μ*g*-conditions influences various biological processes, which are of importance in cancer research. Other researchers reported about changes in the morphological phenotype, growth behavior, gene expression, protein content and release, cytoskeletal reorganization, extracellular matrix composition, cell adhesion and others [14,15]. One important finding was that in r- and s-μ*g* various cell types form three-dimensional (3D) aggregates also called multicellular spheroids (MCS), resembling the in vivo situation of tumors much closer than conventional cell cultures [14]. These MCS are of great interest in cancer research to test drugs and to find new treatment targets [16]. An activation of nuclear factor "kappa-light-chain-enhancer" of activated B-cells (NF-κB), a proinflammatory transcription factor, was often detected in breast cancer [17]. The "inhibitor of κB" (IκB) proteins include IκBα, IκBβ, IκBγ, IκBε, and others [18]. Among them, IκBα, IκBβ and IκBε are the most important regulators of NF-κB and are of high interest in cancer research and μ*g*-based research. Interestingly, the NF-κB-signaling pathway was significantly altered in FTC-133 cancer cells [19] as well as in MCF-7 breast cancer cells [20] exposed to s-μ*g* when MCS were formed. Grosse et al. described an increase in NF-κB p65 protein, when cells were exposed to s-μ*g* on an RPM [19]. This discovery was in concert with findings by Kopp et al., who described an activation and increase in NF-κB and associated molecules in MCF-7 cells exposed to the RPM [20]. Through drug-initiated NF-κB inhibition, they were able to reduce the formation of MCS. As it is not clear when NF-κB signaling is triggered during MCS formation, we exposed MDA-MB-231 breast cancer cells to r-μ*g* during a parabolic flight campaign (PFC).

The principal aim of this study was, first, to investigate the early phases of r-μ*g* achieved by PF maneuvers on TNBC cells and to test whether there is a link between factors of apoptosis, changes in NF-κB signaling and cell adhesion. The second aim was to study VIB and hyper-*g* (1.8 *g*) effects on the MDA-MB-231 cells. In a third approach, we exposed the MDA-MD-231 cells to an incubator RPM (iRPM)

for 2 h to compare the effects of s-μ*g* with those from r-μ*g*. Afterwards, we performed quantitative polymerase chain reaction (qPCR) focusing on genes involved in NF-κB signaling, cell adhesion and MAPK signaling as well as apoptosis. Furthermore, the molecular biological results were finally evaluated by STRING (Search Tool for the Retrieval of Interacting Genes/Proteins) analyses to visualize the mutual regulation and interactions of genes and proteins examined in this study.

2. Results

2.1. Viability Staining

To examine whether the MDA-MB-231 cells were viable after the VIB-, hyper-*g*-, and iRPM-exposure, a terminal deoxynucleotidyl transferase dUTP nick end labeling (TUNEL) assay for the detection of DNA fragmentation was performed to measure the amount of apoptotic cells (Figure 1). Comparing ground controls at Earth's normal gravity (1 *g*), VIB, 1.8 *g* hyper-*g* (comparable to the hyper-*g* exposure on the PFC), and iRPM cell samples, the cytoplasm was evenly stained green, while the nucleus showed no green staining. In contrast, the positive control, which was treated with DNase prior to the staining procedure, presents an intensive green staining of the nucleus. This finding shows, that altered gravity conditions or VIB did not induce apoptosis in MDA-MB-231 cells (Figure 1).

2.2. Nuclear Factor "Kappa-Light-Chain-Enhancer" of Activated B-Cells (NF-κB) Signaling Factors in Triple-Negative Breast Cancer Cells during Altered Gravity Conditions

To verify the influence of PF maneuvers on factors involved in the NF-κB-signaling pathway, the gene expression pattern of NF-κB signaling factors was determined in MDA-MB-231 cells (Figure 2). As a PF comprises different conditions beside microgravity like hyper-*g* (1.8 *g*), and VIB, these factors had been additionally tested to isolate the effects derived from the exposure to μ*g* (Figure 3).

The major factors of the NF-κB-signaling pathway are NF-κB subunits p105/50, p100/52 and p65 (*NFKB3*, *RELA*) of which their corresponding genes are *NFKB1*, *NFKB2* and *NFKB3*.

While the gene expression of *NFKB1* (P31, up-regulation) (Figure 2A) and *NFKB3*, (*RELA;* P1, up-regulation, Figure 2C) are significantly changed after the PF conditions, VIB-, 1.8 *g*- and iRPM-exposure had no significant impact on these genes. The *NFKB2* mRNA was not altered in any experimental condition (Figure 2B, Figure 3C,D). In contrast, the Western blot analyses of NF-κB p65 protein presented a significant reduction after P1 and P31 (Figure 2D).

The NF-κB-signaling pathway is modulated by its inhibitors NF-κB-inhibitor-alpha, -beta and -epsilon (*NFKBIA, NFKBIB, NFKBIE*) and the NF-κB essential modulator (*IKBKG*, *NEMO*). In the case of *NFKBIA*, *NFKBIB* and *NFKBIE* (Figure 2E,G,H) gene expression, a significant upregulation was only found for *NFKBIA* and *NFKBIB* after P31 compared to their corresponding controls. The *NFKBIA* mRNA was differentially expressed by hyper-*g* (Figure 3G). Protein analyses revealed no significant change in IκBα and NEMO (Figure 2F,J). The *NFKBIE* and *IKBKG* gene expressions (Figure 2H,I) were not altered in any of the experimental conditions (Figure 3K–N).

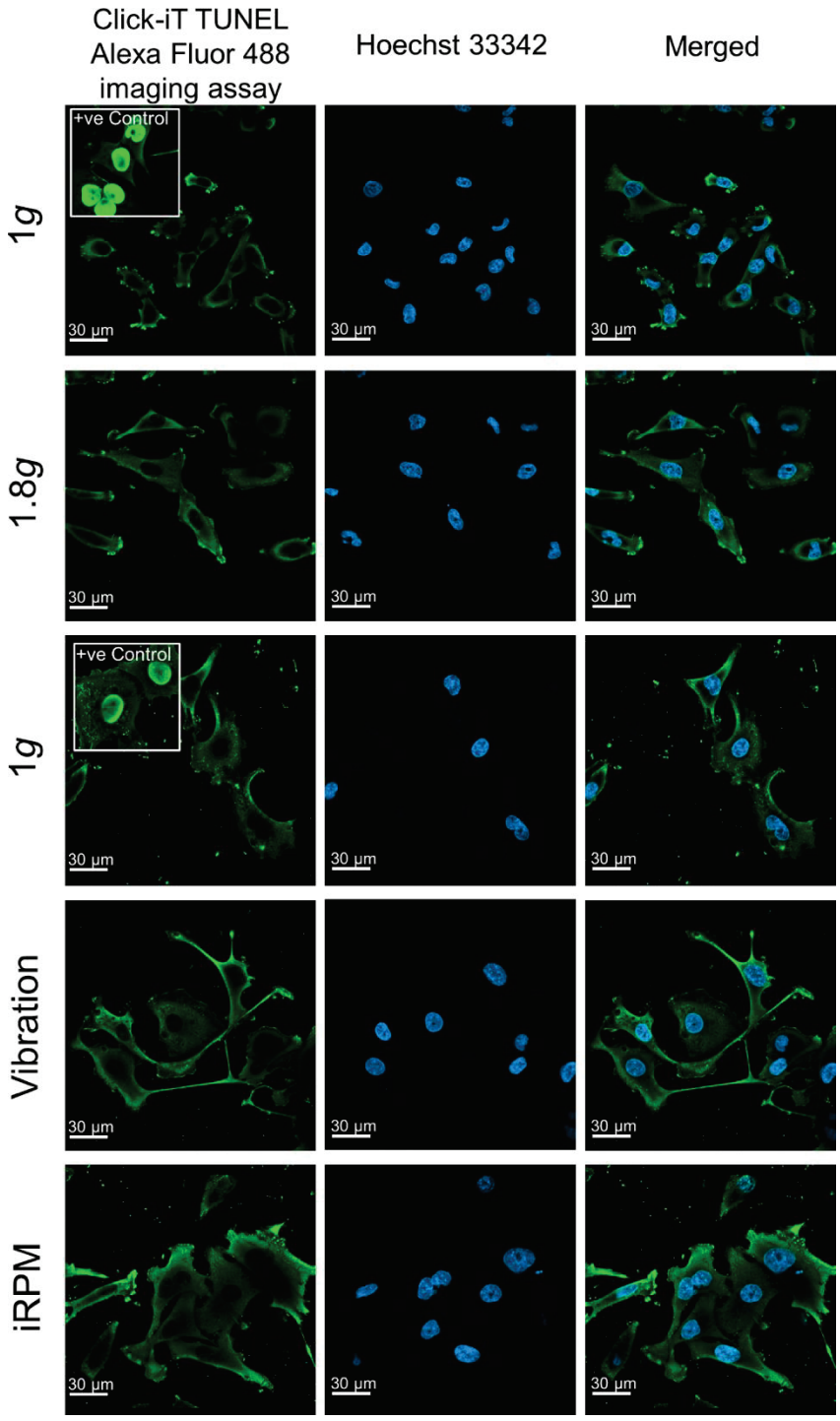


Figure 1. Click-IT terminal deoxynucleotidyl transferase dUTP nick end labeling (TUNEL) assay performed on MDA-MB-231 cells exposed to 1 *g*, 1.8 *g* hyper-*g*, vibration (VIB) and the incubator random positioning machine (iRPM). Green staining indicates free fluorophores in the cytoplasm in all images with the exception of the positive control. In the positive control, samples have been pretreated with DNase to induce DNA fragmentation, which is visualized by an enrichment of the fluorophores in the nucleus. Blue staining highlights the cells' nuclei. Green stained nuclei present apoptotic cells as shown in the inserted positive controls. None of the applied experimental approaches had induced apoptosis in the cells.

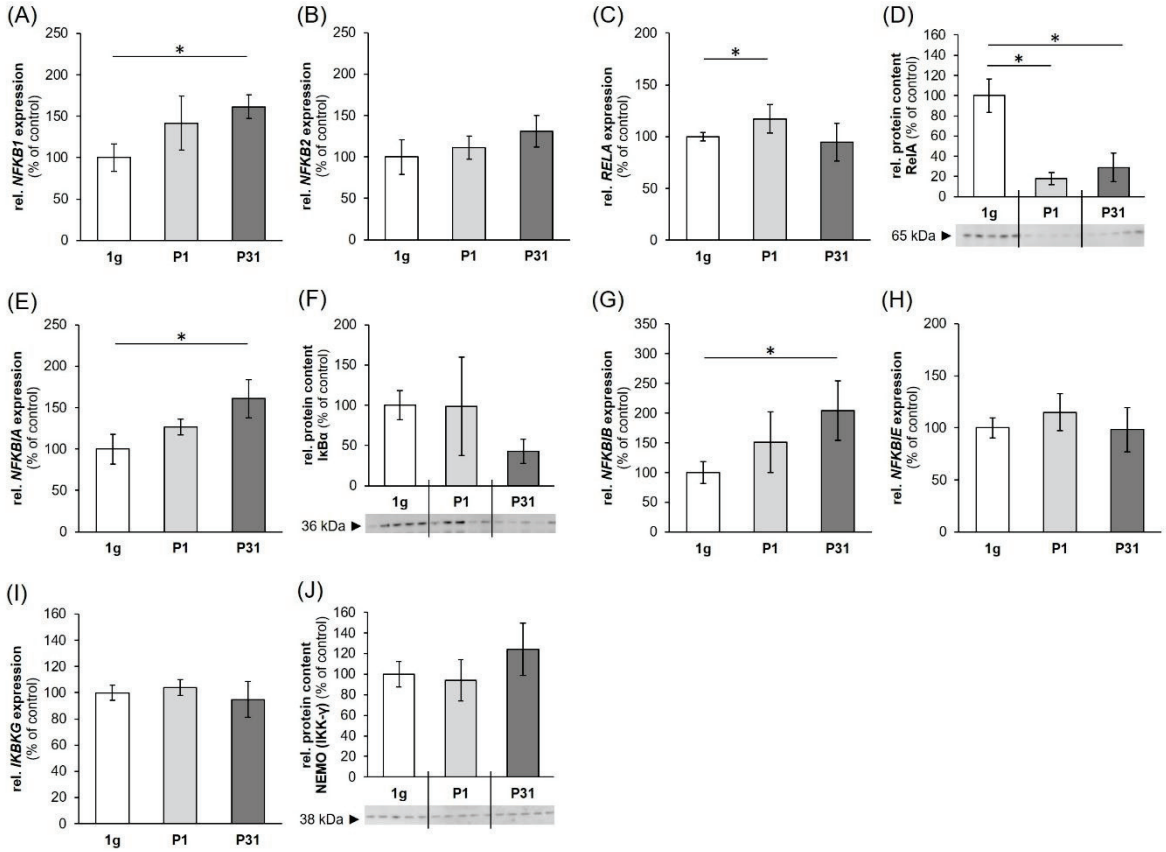


Figure 2. Influence of short-term microgravity on the gene expression: (**A**) *NFKB1*, (**B**) *NFKB2*, (**C**) *RELA*, (**E**) *NFKBIA*, (**G**) *NFKBIB*, (**H**) *NFKBIE*, (**I**) *IKBKG* and protein content: (**D**) RelA, (**F**) IκBα (**J**) NEMO; of NF-κB signaling factors. $n = 5$; The data are given as mean ± standard deviation. * $p < 0.05$ vs. 1 *g-control*.

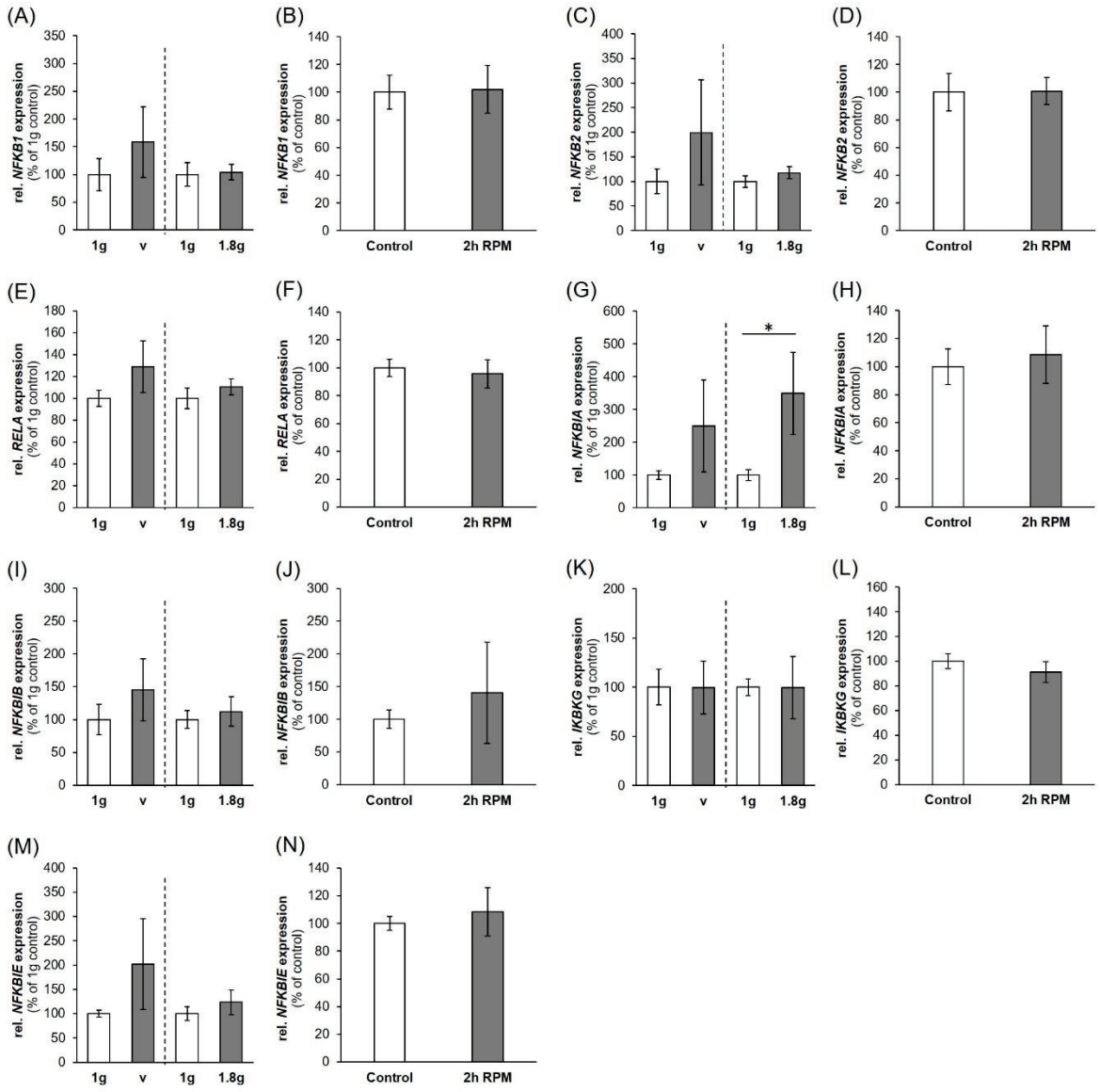


Figure 3. Influence of VIB (V), hyper-*g* and iRPM-exposure on the gene expression of NF-κB signaling factors: (**A**,**B**) *NFKB1*, (**C**,**D**) *NFKB2*, (**E**,**F**) *RELA*, (**G**,**H**) *NFKBIA*, (**I**,**J**) *NFKBIB*, (**K**,**L**) *IKBKG*, (**M**,**N**) *NFKBIE*. $n = 5$. The data are given as mean ± standard deviation. * $p < 0.05$ vs. corresponding 1 *g*-controls. The dashed vertical line seperates two independent experiments.

2.3. Expression of Factors Belonging to the Biological Process of Apoptosis

Caspase 3 is a major factor in apoptosis [21]. Gene expression of *CASP3* was significantly upregulated after P1 and P31 (Figure 4A) while being not regulated after exposure to vibration and the RPM (Figure 5A,B). Measuring the cleaved caspase-3 protein by Western blot analysis and could not detect any active caspase-3, whereas the positive control colon cancer cells CX+ exerted a strong positivity [21] (Figure 4B).

The gene expression of *ANXA1* (Figure 4C, Figure 5C,D) was not significantly changed during any of the experimental procedures. *ANXA2* mRNA expression showed a similar behavior (Figure 4D, Figure 5E) except a downregulation after 2h of RPM exposure (Figure 5F). ANXA2 (annexin A2) protein (Figure 4E) was first significantly increased after P1 and then re-adapted after P31, which is in agreement with the data obtained after a two-hour iRPM-exposure of the MDA-MB-231 cells (Figure 5F). In addition, the *BAX* mRNA was not differentially regulated (Figure 4F, Figure 5I,J), but *BCL2* mRNA

was reduced at both time points (Figure 4G). Finally, the *BAX* mRNA was not altered by VIB and hyper-*g*, but signicantly reduced in MDA-MB-231 cells exposed to the iRPM (Figure 5G,H).

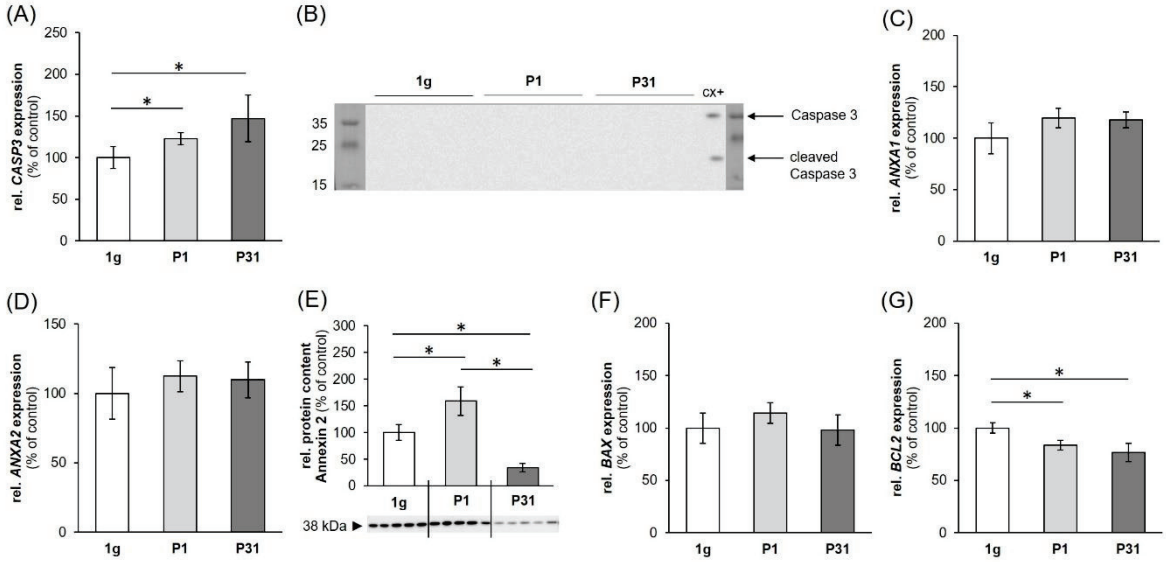


Figure 4. Influence of short-term microgravity on the gene expression: (**A**) *CASP3*, (**C**) *ANXA1*, (**D**) *ANXA2*, (**F**) *BAX*, (**G**) *BCL2*; and protein content (**B**) caspase 3, (**E**) annexin 2 regulators of apoptosis. The data are given as mean ± standard deviation. * $p < 0.05$ vs. 1 *g*-control. CX+ colon cancer cells served as positive control for programmed cell death.

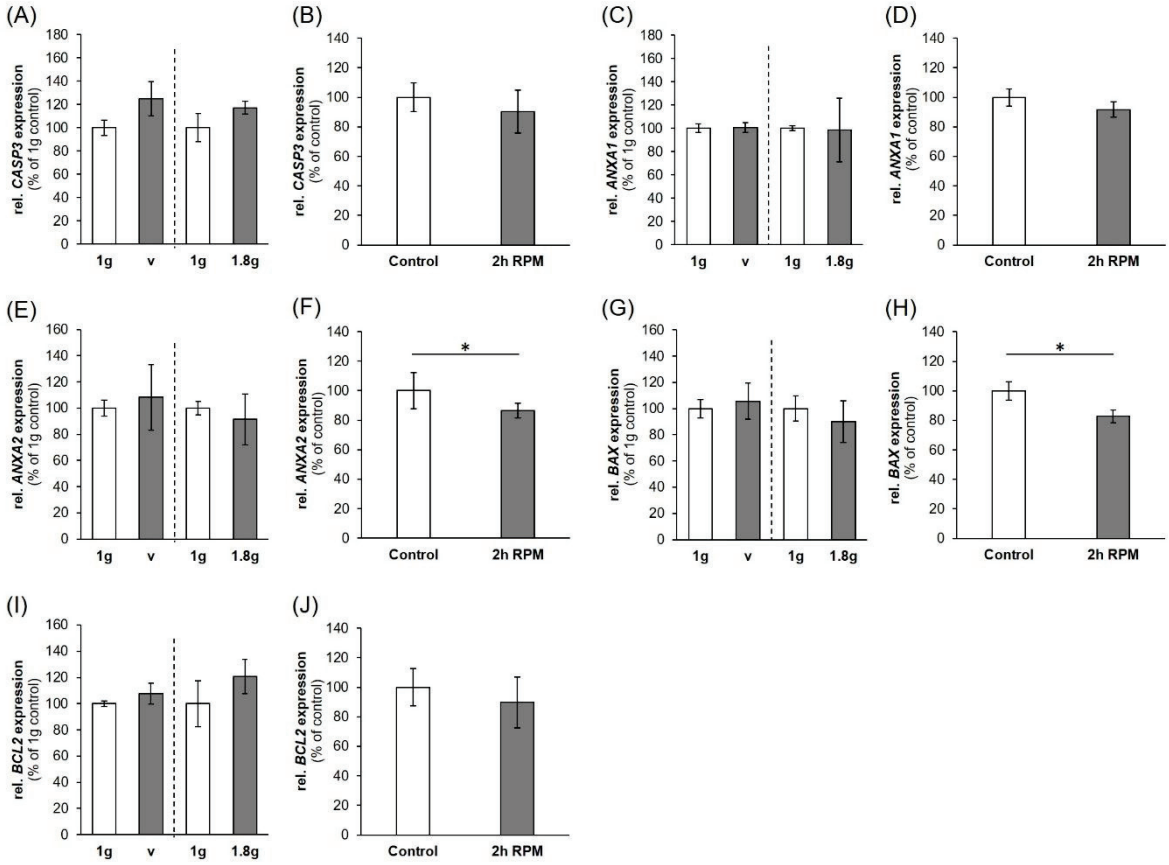


Figure 5. Influence of a VIB (V), hyper-*g* and iRPM-exposure on the gene expression of apoptosis signaling factors: (**A**,**B**) *CASP3*, (**C**,**D**) *ANXA1*, (**E**,**F**) *ANXA2*, (**G**,**H**) *BAX*, (**I**,**J**) *BCL2*. $n = 5$. The data are given as mean ± standard deviation. * $p < 0.05$ vs. 1 *g*-control.

2.4. Regulation of Cell Adhesion Molecules in Triple-Negative Breast Cancer (TNBC) Cells

The *ICAM1* gene expression was significantly upregulated after one parabola. Although our data seem to hint towards an additional upregulation after 31 parabolas, the high variability of the measurements interfered with the statistical analysis (Figure 6A). ICAM1 protein was significantly reduced after the first parabola and increased after 31 parabolas (Figure 6B). We did not observe changes in the *VCAM1* gene expression (Figure 6C), while VCAM-1 protein levels were significantly elevated after one and 31 parabolas compared to static 1 *g*-controls (Figure 6D).

SPP1 gene expression was found to be significantly enhanced compared to the levels after one parabola, but not to 1 *g*-controls (Figure 6E). Osteopontin protein expression on the other hand was significantly downregulated compared to static controls after both one and 31 parabolas (Figure 6F).

Finally, the *CD44* gene expression showed a constant increase over the course of the experiment, with significant rises after one parabola vs. 1 *g*-controls and 31 parabolas vs. 1 *g*-controls and levels after one parabola (Figure 6G). CD44 protein levels followed the same tendency with significant increases compared to static controls for both one and 31 parabola samples (Figure 6H).

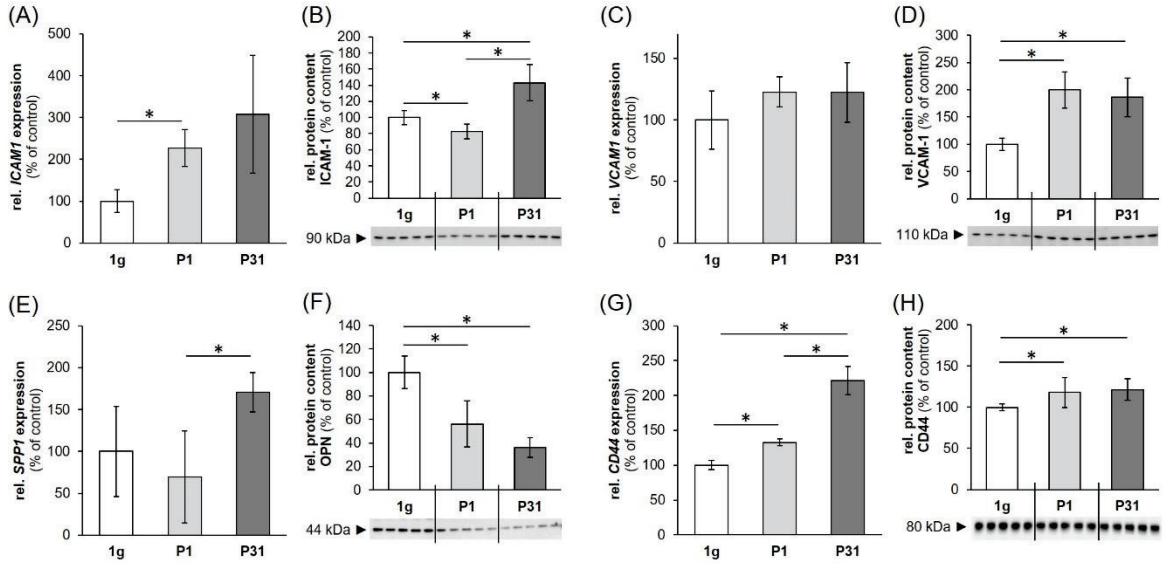


Figure 6. Expression of genes: (**A**) *ICAM1*, (**C**) *VCAM1*, (**E**) *SPP1*, (**G**) *CD44*; and proteins: (**B**) ICAM-1, (**D**) VCAM-1, (**F**) OPN, (**H**) CD44 involved in cell adhesion. 1 g: ground control; P1: parabola 1; P31: parabola 31. The data are given as mean ± standard deviation. * $p < 0.05$ vs. 1 *g*-control; ** $p < 0.01$ vs. 1 *g*-control.

ICAM1, *VCAM1*, and *SPP1* were not significantly regulated after VIB, hyper-*g*- or iRPM-exposure (Figure 7A–F). The *CD44* gene expression, on the other hand, was significantly enhanced under conditions of 1.8 *g* hyper-*g*, but remained unchanged by VIB- and iRPM-exposure (Figure 7G,H).

2.5. Factors of the Mitogen-Activated Protein Kinase (MAPK) Signaling Pathway Known to be Involved in Cancer Progression and Metastasis

First, we determined the gene expression of *PRKCA* (protein kinase C alpha, PKC α). The *PRKCA* mRNA was not significantly upregulated after the 31st parabola compared with corresponding 1 *g*-samples (Figure 8A).

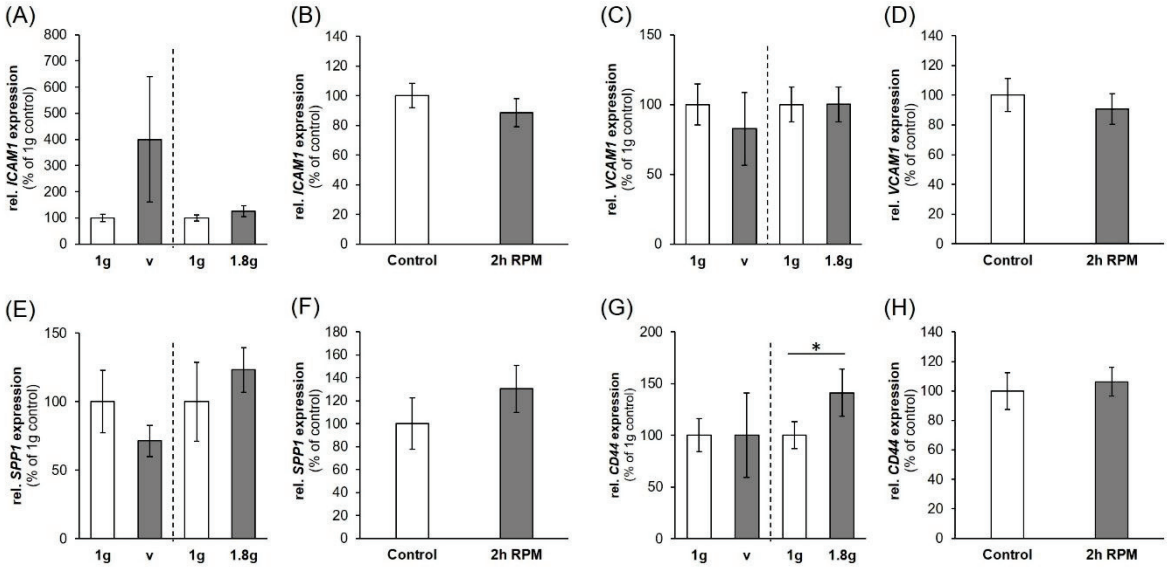


Figure 7. Influence of a VIB (V), hyper-*g* and iRPM-exposure on the gene expression of cell adhesion signaling factors: (**A**,**B**) *ICAM1*, (**C**,**D**) *VCAM1*, (**E**,**F**) *SPP1*, (**G**,**H**) *CD44*. 1 *g*: ground control; V: 2 h of vibration; 1.8 *g*: 2 h of hyper-*g*. The data are given as mean ± standard deviation. * $p < 0.05$ vs. 1 *g*-control.

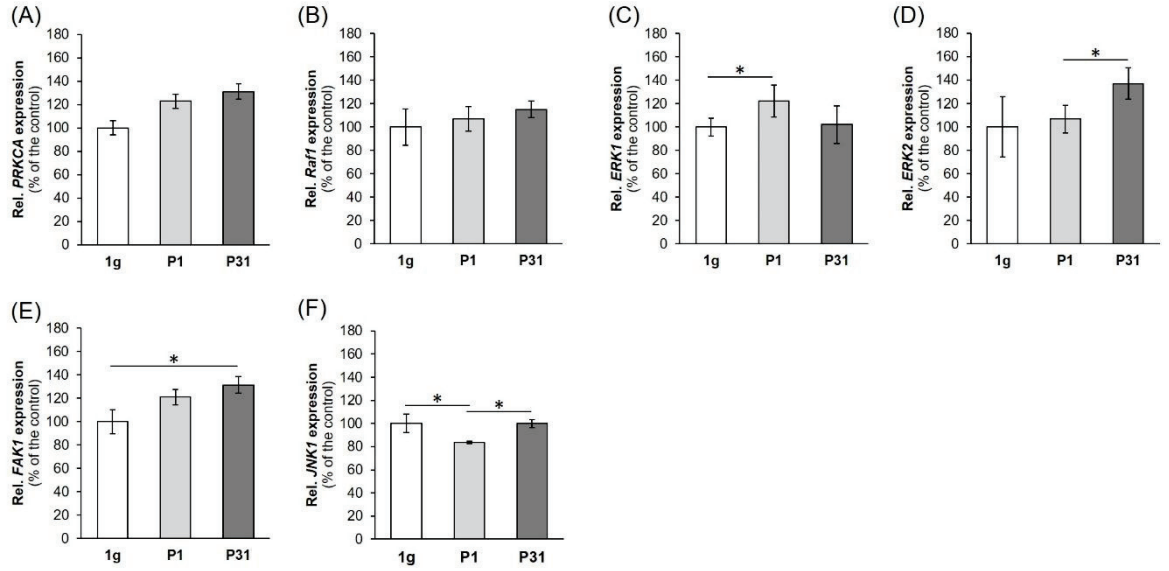


Figure 8. Expression of genes: (**A**) *PRKCA*, (**B**) *Raf1*, (**C**) *ERK1*, (**D**) *ERK2*, (**E**) *FAK1*, (**F**) *JNK1*, involved in cancer progression and metastasis. 1 *g*: ground control; P1: parabola 1; P31: parabola 31. The data are given as mean ± standard deviation. * $p < 0.05$ vs. 1 *g*-control.

Then we focused on *RAF1* (RAF proto-oncogene serine/threonine-protein kinase). *RAF1* remained unchanged by PF maneuvers (Figure 8B). Afterwards, we measured the *ERK1* (extracellular signal-regulated kinase 1) (Figure 8C) and *ERK2* (extracellular signal-regulated kinase 2) (Figure 8D) gene expression. The *ERK1* gene expression was significantly up-regulated after the first parabola compared to 1 *g*-samples (Figure 8C). The *ERK2* mRNA was significantly elevated after the 31st parabola compared with P1 r-μ*g*-samples (Figure 8D). There is a direct interaction between *ERK1,2* and *FAK1* (focal adhesion kinase 1 also known as PTK2 (protein tyrosine kinase 2)). The *FAK1* mRNA was significantly up-regulated after P31 compared to 1 *g*-samples (Figure 8E).

In a next step we measured the *MAPK8* (mitogen-activated protein kinase 8) mRNA also called *JNK1* (c-Jun N-Terminal Protein Kinase 1) (Figure 8F). *JNK1* was down-regulated after P1 and was not significantly changed after P31, indicating a rapid short-term effect of microgravity.

2.6. Search Tool for the Retrieval of Interacting Genes/Proteins (STRING) Analysis

The various genes analyzed by qPCR were investigated in regard to their possible interaction and mutual expression dependence. A STRING/EMBL analysis of these items represented in molecule action mode is shown in Figure 9. It can be seen that the nuclear factors, whose expression was analyzed, are regulating each other very strongly, while the remaining items form a loose network. *RELA*, *NFKB1* and *NFKB2*, which represent three of the five members of the transcription factor NF-κB family are strictly controlled at various levels [22]. Their activity is regulated by interaction with each other, with inhibitors such as NFKBIA, NFKBIB, NFKBIE and with kinases such as IKBKB (NEMO). The regulation occurs at various levels including the gene expression level. For example, NFKB1 and RELA form protein heterodimers and are also associated in the regulation of their expression [23]. Moreover, *RELA* and *VCAM1* are upregulated after an injury of an artery, while *NFKBIA* is down-regulated [24] and if annexin A1 is upregulated, it forms a complex with IKFKG that activates NFKB [25]. On the other hand, the nuclear factors control the transcription of other genes. A target of RELA is *ICAM* expression, which is also regulated by osteopontin [26,27]. Osteopontin is co-expressed with *CD44* [28], which co-localizes with annexin A2 [29]. Moreover, there are links between NFKB1 and the expression of *CASP3* [30,31]. *CASP3* and *BAX* are upregulated during apoptosis, while *BCL2* is downregulated [32]. After the PF maneuvers, we measured increases in *CASP3* and a reduction of *BCL2* mRNAs, but no changes in their protein products and no signs of apoptosis. In addition, we detected an upregulation of *ERK1* after P1 compared to 1 *g*, *ERK2* after P31 compared to P1 samples, and *FAK1* after P31 compared to 1 *g*, whereas PRKCA and RAF1 remained unchanged in short-term μ*g*. Moreover, the *JNK1* gene expression was down-regulated after the first parabola and unaltered after P31 compared to 1 *g*.

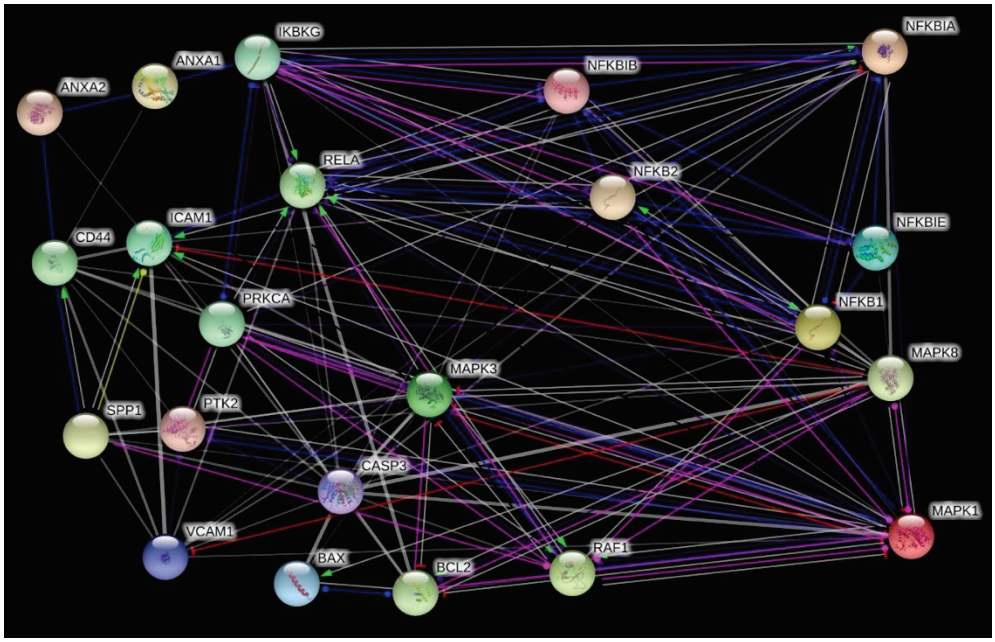


Figure 9. Network of the functional interaction of genes and their products analyzed in this study. The analysis was performed by STRING (Search Tool for the Retrieval of Interacting Genes/Proteins) v11.0) provided by the STRING Consortium (Available online: https://string-db.org/). The result is presented in the molecule action mode. Gene names are indicated.

3. Discussion

The basal-like or triple-negative form of breast cancer refers to tumors not expressing the *ER*, *PR*, *AR* and *HER2* genes [1]. This breast cancer type is very heterogeneous, which complicates treatment. The MDA-MB-231 cell line was isolated from a pleural effusion of a patient with invasive ductal carcinoma and is ER-, PR-, and E-cadherin negative and expresses mutated p53. Microarray profiling revealed that the MDA-MB-231 cell genome clusters with the basal subtype of breast cancer. In addition, MDA-MB-231 cell lack HER2 and thus this cell line is a good model of TNBC [8,33,34].

Gravity is permanently influencing the human body and all life on Earth. Gravitational unloading results in enormous changes in the organism, organs, tissues and cells [35,36].

Microgravity induces a large number of changes in thyroid and breast cancer cells, such as alterations of the cytoskeleton, extracellular matrix, focal adhesion, growth behavior, differentiation, proliferation, cell adhesion or an increased apoptosis [15,20,37–40].

We recently exposed MCF-7 breast cancer cells to the RPM and detected 3D MCS formation within 24 h [20]. The pathway analysis of 47 examined genes proposed that NF-κB variants are involved in the formation of MCS [20]. This finding was in agreement with data obtained earlier from thyroid cancer studies [19]. Poorly differentiated FTC-133 follicular thyroid cancer cells cultured on an RPM for 24 h showed higher levels of NF-κB-p65 protein and apoptosis than 1 *g*-controls [19]. Both studies indicated an involvement of NF-κB in 3D growth. No information exists about the early phases when cells are exposed to μ*g*.

We had the opportunity to attend the 29th Deutsches Zentrum für Luft- und Raumfahrt (DLR) PF mission in Bordeaux Merignac, France, and to study cells in r-μ*g* (Available online: https://www.dlr.de/rd/desktopdefault.aspx/tabid-2285/3423_read-47055/; https://www.dlr.de/rd/desktopdefault.aspx/tabid-2285/3423_read-50372/). We investigated MDA-MB-231 cells in r-μ*g* during PF maneuvers. The cells were fixed with RNA*later* after the first and the 31st parabola, keeping in mind that this last time point represents a mixture of alternated acceleration phases. Postflight we focused on NF-κB signaling, cell adhesion, and apoptosis. Furthermore, cells exposed to an iRPM, hyper-*g* cultures (1.8 *g*) and VIB samples were examined to evaluate the impact of these factors on the cells.

3.1. Influence of Altered Gravity Conditions and Vibration on Cell Survival

Apoptosis is involved in the pathogenesis of many diseases including among others ischemia, autoimmune and neurodegenerative diseases, as well as in tumor response to chemotherapy and/or radiotherapy [41].

It is known from earlier studies that cancer cells will become apoptotic when exposed to r-μ*g* and s-μ*g* and that apoptosis is involved in cell detachment and formation of spheroids [19]. Therefore, we investigated *CASP3*, *ANXA1*, *ANXA2*, *BAX* and *BCL2* mRNA expression patterns.

In our short-term experiments, after a 2-h exposure to s-μ*g*, hyper-*g* or vibration, TUNEL staining of TNBC cells revealed no signs of apoptosis and 100% viable cells. The gene expression of *CASP3* was elevated after the first and 31st parabola, but no uncleaved caspase-3 was detectable and no detectable cleavage of caspase-3 occurred. The *CASP3* gene expression was not changed in VIB-, hyper-*g*- and s-μ*g*-samples. This is in agreement with earlier findings obtained with endothelial cells exposed to PF maneuvers [42]. Furthermore, the gene expression of *CASP3* and *ANXA2* was reduced in endothelial cells exposed to a two-hour period of VIB or hyper-*g* conditions [43]. In MDA-MB-231 cells *ANXA1* mRNAs were not changed during the parabolic flight, hyper-*g*-, s-μ*g*- and VIB-exposure. However, ANXA2 protein after PFC as well as *ANXA2* mRNA expression after s-μ*g* exposure was significantly altered. Thus, μ*g* has an impact on cell survival that is highly dependent on the cell type as well as on the duration of exposure.

3.2. Impact of Real Microgravity on NF-κB Signalling in TNBC

NF-κB is an interesting factor because it is associated with spaceflight-related health problems. Activation of NF-κB is frequently observed in breast cancer as well. An *NFKB3* overexpression indicates increased aggressiveness of breast cancer and a poor prognosis [44]. In addition, NF-κB is involved in endocrine therapy resistance [45]. Activation of NF-κB promotes the survival of tumor cells. Several gene products that negatively regulate apoptosis in tumor cells are controlled by NF-κB activation.

The NF-κB proteins include the different variants NF-κB-p50, -p52 and -p65, which are encoded by the gene loci *NFKB1*, *2* and *3* [45]. These proteins are bound and inhibited by IκB proteins. The effectors and inhibitors are activated by external triggers and, thus, interesting in μ*g*-based research.

Human adherent cells exposed to s-μ*g* on a RPM showed elevated levels of NF-κB p65 protein compared with 1 *g*-controls, a result found earlier in endothelial cells and in FTC-133 follicular thyroid cancer cells [19,46].

NF-κB exerts several transcriptional regulatory functions important for programmed cell death [47] and is inactivated by binding to IκB (inhibitor of NFκB).

The *NFKB1* (Nuclear Factor Kappa B Subunit 1) mRNA was significantly elevated after the 31st parabola compared to 1 *g*, no changes were measured for the *NFKB2* (Nuclear Factor Kappa B Subunit 2) mRNA at each time point and an upregulated gene was found for *NFKB3* (*RELA* Proto-Oncogene (V-Rel Avian Reticuloendotheliosis Viral Oncogene Homolog A), Nuclear Factor NF-Kappa-B P65 Subunit) after the first parabola. *NFKB3* mRNA was unaltered after the last parabola (P31). Despite this result, the corresponding protein NF-κB p65 was down-regulated after the first and 31st parabola. This counterregulatory effect was not due to VIB or hyper-*g* occurring during the PF (Figure 3E,F), as the *NFKB3* gene expression was unchanged in VIB and 1.8 *g* samples. The normalization of *NFKB3* after 31 parabolas and the down-regulation of NF-κB p65 protein in short-term r-μ*g* (after one parabola, that means 22 s of r-μ*g*) is in agreement with earlier microarray data obtained from activated T cells cultured in space, which showed a suppressed expression of c-REL and NF-κB gene targets after 1.5 h [48]. In addition, a four-hour exposure on the RPM of activated T cells revealed a suppressed expression of NF-κB gene targets [49].

In many cell types, NF-κB dimers are located in the cytoplasm in an inactive form through association with any of several IκB inhibitor proteins (IκBα, -β, -ε, -γ, p105 and p100) [50].

The NF-κB signaling pathway is mainly regulated by inhibitor κB (IκB) proteins and the IκB kinase complex through two major pathways: the canonical and non-canonical NF-κB pathways [50]. We measured significantly elevated *NFKBIA* and *NFKBIB* mRNAs after the 31st parabola, whereas the *NFKBIE* and *IKBKG* gene expression were not altered by r-μ*g* (Figure 2). VIB did not affect the family of cellular IκB proteins inhibiting the NF-κB transcription factors, but hyper-*g* elevated the *NFKBIA* mRNA expression indicating that the measured elevation may be due to the hyper-*g* phase of the parabola, because an iRPM-exposure of the MDA-MB-231 cells demonstrated no changes in NF-κB signaling. On the iRPM all investigated genes remained stably expressed. The RPM aims to simulate near weightlessness, but one should take note of increased fluid movements—and thus shear forces—occurring in the flasks,when the device is used for cell cultures experiments [51]. First, it is important to place the sample as close as possible to the center of rotation in order to minimize residual g-artifacts and second, the cell culture flasks have to be completely filled with medium without air bubbles to minimize shear stress. The RPM is used to prepare spaceflight missions and for tissue engineering purposes. It has proven to be a useful device for long-term cultures of cancer cells and benign cells [14]. Postflight data revealed that genes and proteins involved in the regulation of thyroid cancer cell proliferation and metastasis were similarly regulated under RPM and spaceflight conditions [52].

3.3. Parabolic Flight Maneuvers Changed Cell Adhesion Factors

It is known that s-μ*g* conditions induced changes in the cytoskeleton, ECM, and focal adhesion factors in various cell types [53,54]. Long-term RPM-exposure of human endothelial cells induced the

formation of 3D tubular structures and spheroids [55]. In parallel, secretion of the factors ICAM-1, and VCAM-1 were both increased, when the influence of gravity is minimized for 35 days [55]. In MDA-MB-231 cells exposed to short-term μ*g* on a parabolic flight, an increased synthesis of ICAM-1 protein was found after the P31. A similar result was measured for VCAM-1 protein as given in Figure 6.

The adhesion molecules ICAM-1 and VCAM-1 are mediating the cell adhesion of cancer cells, lymphocytes and other cells to the vascular endothelium [56]. Moreover, ICAM-1 is involved in angiogenesis and is able to increase the survival of microvessels [57].

Primary human macrophages differentiated from monocytes exposed to 11 days r-μ*g* in space on the ISS revealed a reduced surface expression of ICAM-1, defucosylation of surface proteins and an altered metabolite spectrum [58]. Another study examined the ICAM-1 protein synthesis and *ICAM1* gene expression in cells of the monocyte/macrophage system exposed to r- and s-μ*g* obtained during 2D clinostat, parabolic flight, sounding rocket, and orbital experiments [59]. Murine BV-2 microglial cells showed a downregulated *ICAM1* expression, when exposed to a 2D clinostat and a rapid and reversible downregulation in the μ*g*-phase of PF maneuvers [59].

Interestingly, an elevated *ICAM1* mRNA was measured in macrophage-like differentiated human U937 cells during the μ*g*-phase of PFs. In non-differentiated U937 cells, no effect of μ*g* was observed [59].

In addition, we studied the early effects of hyper-*g*, and VIB comparable to the conditions that occur during PFs on the gene expression of *ICAM1* and *VCAM1*. Both vibration and hypergravity had no effect on *VCAM1* expression. Hyper-*g* did not change the *ICAM1* mRNA expression, while VIB-exposure of the MDA-MB-231 cells revealed a non-significant result due to the high variation. Furthermore, the *SPP1* gene expression was not altered by VIB and hyper-*g*, whereas *CD44* was unchanged by VIB, but significantly elevated by hyper-*g*. Therefore, it can be assumed that the elevated *CD44* gene and protein expression after P31 (Figure 6G,H) is mainly due to hyper-*g* (Figure 7G). Comparable results were obtained when poorly differentiated ML-1 follicular thyroid cancer cells were investigated during a PFC. The *SPP1* mRNA was significantly elevated after P31 [60]. The *SPP1* gene expression was not changed by VIB and hyper-*g* in ML1 follicular thyroid cancer cells [60]. Corresponding data were obtained when human chondrocytes were studied during PF maneuvers [61]. No significant changes in the gene expression levels were observed during VIB and hyper-*g* experiments [61].

In a next step, we focused on the cell-surface glycoprotein CD44 antigen, which is involved in cell adhesion, migration and cell-cell interactions. The CD44 is a receptor for hyaluronic acid and interacts with osteopontin. The mRNA expression of *CD44* and the corresponding protein content were both significantly elevated after P1 and P31 compared to 1 *g*. Similar results were obtained earlier, when cells were exposed to a NASA rotary cell culture system (RCCS) grown as 3D spheroids and were CD44-positive [62]. The CD44-positivity of the cells grown in 3D MCS was determined by immunocytochemistry and was elevated in bladder cancer, prostate cancer, and glioma cell lines compared with 1 *g*-cultures [62].

Rat osteoblasts cultured for 4 or 5 days aboard the Space Shuttle and solubilized during spaceflight revealed strongly elevated *CD44* mRNA levels in the flight cultures [63]. In addition, FTC-133 follicular thyroid cancer cells exposed to an RPM for 24 h expressed a *CD44* mRNA which was significantly up-regulated in adherent cells but not significantly altered in MCS [19]. In addition, an increase in *SPP1* mRNA was measured in adherent FTC-133 cells cultured on the RPM. *CD44* can also interact with *SPP1*. The *SPP1* mRNA was elevated in MDA-MB-231 cells after P31 compared with P1 and 1 *g*-samples. The synthesis of the protein was reduced during the PF maneuvers (Figure 6F), whereas both hyper-*g* and VIB stress had no effect on *SPP1*. These results are in concert with data obtained from thyroid cancer cells exposed to the RPM. Simulated μ*g* reduced the amount of osteopontin in adherent cells and MCS. Based on the role of osteopontin as a mediator of cell-matrix adhesion and communication, it is influencing tumorigenesis and invasion [64]. Osteopontin seems to be involved in motility regulation by interaction with CD44 in colon cancer cells, which suggests a role for osteopontin

in cancer progression [65]. Osteopontin is a potential cancer biomarker [66] and is involved in biological processes such as cell proliferation, survival, angiogenesis, progression and metastasis [66].

Another study demonstrated that in MDA-MB-231 cells, the inhibition of NF-kB via the chemical compound Bay-11-7082 results in a CD44 suppression [67]. The NF-kB inhibition and subsequent CD44 suppression reduced the cell proliferation and invasiveness of breast cancer cells. In contrast in μ*g*, the cells reacted with a down-regulation of NF-kB p65 protein and an increase in CD44, a finding which has to be investigated in long-term μ*g*-studies in the future.

3.4. Interaction Network of Selected Genes Evaluated by STRING Analysis

The interaction between CD44 and osteopontin as a potential basis for cancer progression and metastasis formation is known for a long time [68]. In this study, the up-regulation of the *CD44* mRNA seems to be induced by the hyper-*g* phases of the PF maneuvers, whereas *SPP1* is mainly elevated by r-μ*g*. Interestingly, the synthesis of osteopontin is reduced, a finding only observed in r-μ*g*.

Furthermore, osteopontin regulates the *ICAM-1* and *VEGFA* expression mainly in triple-negative/basal-like breast cancer, supporting its role in tumor progression in TNBC [27]. Osteopontin protein was reduced in P31 samples, whereas the ICAM-1 protein synthesis was elevated after 31 parabolas which may allow for both proteins to conclude a counterregulatory interaction mechanism in short-term μ*g*.

Another group demonstrated that purified native OPN induces NF-κB activation and NF-κB-dependent ICAM-1 expression in breast cancer cells [69]. We measured a reduced amount of NF-κB after P1 and P31 which may be due to the reduced osteopontin content (Figure 2D, Figure 6F).

Both cell adhesion molecules ICAM-1 and VCAM-1 are increased in patients with advanced breast cancer and the increase in VCAM-1 is of prognostic significance [70]. In our study the VCAM-1 protein synthesis was elevated after P1 and P31. *VCAM1* is one of five genes (*CXCL12*, *MMP2*, *MMP11*, *VCAM1*, and *MME*), which were associated with tumor progression, angiogenesis, and metastasis [71].

There is also an interaction between *CD44* and *ANXA2*. *ANXA1* together with *ANXA2* are both associated with the aggressive behavior of TNBC [72]. The prognostic impact of *ANXA1* relies on a high *ANXA2* expression and both are preferential for TNBC [72]. The MDA-MB-231 cells exhibited a high expression of *ANXA1* and *ANXA2*. *ANXA1* remained stable under all gravity conditions and VIB. Both, r- and s-μ*g* induced a reduction of ANXA2 protein after 31 parabolas and *ANXA2* expression after 2h RPM exposure. This response seems to be due to altered gravity.

ANXA1 is known to constitutively activate NF-κB in breast cancer cells by interacting with the IKK complex [25], an interaction that might not to be relevant in μ*g*.

ANXA2 is upregulated in many cancer types and is involved in cancer cell migration, adhesion, invasion, and metastasis [73]. Intracellular annexin A2 regulates NF-κB signaling by binding to the p50 subunit in a calcium-independent manner [73]. The ANXA2-p50 complex translocated into the nucleus [73]. After the first parabola annexin A2 protein synthesis was elevated and then after the 31st parabola reduced. The *NFKB1* mRNA was upregulated after P31, but was not altered under all other experimental conditions (Figure 2A, Figure 3A,B).

MAPK3 (*ERK1*) was upregulated after the first parabola and is interacting with *RELA*, *CASP3* and *BCL2*. It is known that NF-κB inhibits ERK activation to enhance cell survival during the development of tumor adaptive radioresistance in breast cancer cells [74]. In addition, ERK1/2 play a key role in controlling the BCL2-regulated, cell-intrinsic apoptotic pathway [75]. Other interactions are found for OPN, FAK and ERK1/2 as well as RELA. Integrin αvβ3 binding with OPN mediates the signaling pathways of FAK, ERK1/2, and NF-κB to activate cellular migration [66], which is important for the dissemination of cancer cells to distant tissues.

3.5. MAPK Signaling Factors Involved in Cancer Progression and Metastasis

We investigated further factors known to enhance cancer growth and spreading. The protein kinase C alpha (PKCα) is implicated in cancer progression and associated with a poor prognosis in

breast cancer patients [76]. There is evidence that PKCα is a key regulator of migration and invasion in endocrine resistant ER+ breast cancer and basal A TNBC, but not in other subtypes such as endocrine sensitive ER+ [76]. In this study, we found a slight increase in *PRKCA* in TNBP exposed to short-term μ*g* after 31 parabolas. This result was not significant, and thus it may be speculated that *PRKCA* is upregulated later, when the cell detachment starts as well as the 3D aggregation of breast cancer cells [40]. In addition, *PRKCA* is also a key candidate gene in melanoma metastasis [77]. An important step for metastasis is that protein kinase C alpha activates RAF-1 by direct phosphorylation [78].

The biological process of the epithelial-mesenchymal transition (EMT) is known to increase migration and spreading of cancer cells, progression of the cell cycle, and resistance to apoptosis and chemotherapy. It supports tumor progression. One important signaling pathway involved in progression and metastasis is the MAPK pathway [79]. Therefore, we determined the *RAF1* mRNA expression. RAF1 works as a regulatory link between the membrane-associated Ras GTPases and the MAPK/ERK cascade and functions as a switch determining proliferation, differentiation, apoptosis, survival and oncogenic transformation of human cells [80]. RAF1 activation initiates a mitogen-activated protein kinase (MAPK) cascade [80]. The fact that it remained unaltered might explain that we did not find any apoptosis in TNBC exposed to short-term microgravity (Figure 8B).

Furthermore, we measured the expression of *ERK1* and *ERK2*. The ERK subfamily consists of typical (ERK 1/2/5), and atypical (ERK 3/4/7/8) members. ERKs are involved in the regulation of EMT and are thus promoting tumor progression. The *ERK1* gene expression was significantly up-regulated after the first parabola compared to 1 *g*-samples, and *ERK 2* after the 31st parabola compared with P1 r-μ*g*-samples (Figure 8D). ERK1 seems to give an initial signal to start 3D aggregation in μ*g*.

Moreover, we focused on the focal adhesion kinase 1 (FAK1), which is also called PTK2 protein tyrosine kinase 2 (PTK2) and known to increase cancer cell migration and promote metastatic dissemination to distant sites [81]. Blocking of FAK revealed that breast cancer cells became less metastatic due to decreased mobility [81]. The *FAK1* mRNA was significantly up-regulated after P31 compared to 1 *g*-samples. This is an interesting result indicating its importance for 3D aggregation, breast cancer progression and invasion. Chan et al. [82] had demonstrated that the depletion of FAK induced the formation of active invadopodia and impaired invasive cell migration.

Finally, we measured the *MAPK8*/*JNK1* mRNA in our experimental μ*g*-dependent approach. The *JNK1* gene was down-regulated after the first parabola in the μ*g*-exposed TNBP cells.

It has been shown that *JNK1* promotes cell survival in Her2/neu-positive breast cancer [83]. Human studies have shown the relevance of JNK activation to various human cancers [84]. These kinases are involved in the prevention of malignant transformation via the induction of apoptosis and in promoting cell survival in established tumors [85]. In addition, there is a potential to monitor JNK activity as an early biomarker of response to chemotherapy [85]. Therefore, the decrease in *JNK1* mRNA expression seems to promote a following 3D formation of the TNBC cells in real μ*g*-conditions.

Taken together, TNBC cells exposed to short-term μ*g* obtained by PF maneuvers kept all signs of a more aggressive phenotype as elevations of ICAM1 and VCAM1 proteins occurred soon.

MDA-MB-231 cells exposed to short-term r-μ*g* were relatively stable to this external stressor, vibration and hyper-*g*.

In summary, an early up-regulation of *NFKB1* (P1), *NFKB3* (*RELA*) (P1), *ERK1* (P1), *ICAM1* (P1), *NFKBIA* (P31), *NFKBIB* (P31), *FAK1* (P31), *SPP1* (P31) and *CD44* (P1, P31) gene expression as well as a reduced protein content of NF-κB p65 and osteopontin were found after the PF maneuvers. *CD44* and *NFKBIA* were upregulated in hyper-*g*, showing that the hyper-*g*-phase seems to influence both factors. For all other genes, our data indicate that the microgravity phase is the driving factor of most of these changes in gene expression. These results are very important because apoptosis is needed for cell detachment together with an activation of NF-κB-p65 to form 3D growth (spheroids) of cancer cells when they were exposed to μ*g*. Changes in osteopontin protein suggest a role in survival, angiogenesis, invasion, and metastasis of TNBC cells.

4. Materials and Methods

4.1. Cell Culture

MDA-MB-231 cells were purchased from the American Type Culture Collection (ATCC® HTB26™, Manassas, Virginia, USA)). They were cultured in RPMI 1640 (Life Technologies, Paisley, UK), 10 % FCS (Sigma Aldrich, Steinheim, Germany) and 1% penicillin/streptomycin (Life Technologies, New York, USA). The cells were cultured in vented T75 cm^2 flasks (Sarstedt, Nümbrecht, Germany) and were split every 4–5 days to prevent confluence.

4.2. 29th. Parabolic Flight Campaign

The PFs were organized by the DLR in cooperation with Novespace, Bordeaux-Mérignac Airport, France. The cells were transferred on board of the Airbus A310 (Figure 10A) into a pre-warmed 37 °C incubator shortly before take-off and they were incubated at 37 °C for the whole time during the flight. The flight rack is shown in Figure 10B. Each parabola had an initial phase of hyper-*g* (1.8 *g*) for 22 s during pull-up and a final phase of hypergravity for 22 s during pull-out (Figure 10C). The two hyper-*g*-phases framed a 22-s long µ*g*-phase. The flight maneuver was repeated 31 times per flight day. During the PFs, the MDA-MB-231 cells were fixed with RNA*later* (Invitrogen by Thermo Fischer Scientific, Vilnius, Lithuania) at the end of the first parabola (P1) and the end of the last parabola (P31). The cells were cultured in T75cm^2 cell culture flasks (Sarstedt, Nümbrecht, Germany) with 10 mL medium in each flask. Each flask had a fixed three-way connector on the lid which was connected with 140 cm tubing to a 50 mL syringe filled with RNA*later*. The RNA*later* was injected manually into the flasks at the designated times. Additional MDA-MB-231 cells were incubated on ground to serve as static 1 *g*-controls. The ground control cells were fixed with RNA*later* in parallel to the samples on board of the flight. After landing, the medium and RNA*later* mixture was removed and replaced with 5 mL of fresh RNA*later*. The cells were harvested with a 25 cm scraper (Sarstedt, Nümbrecht, Germany) and stored suspended in RNA*later* at 4 °C in 15 mL tubes until RNA isolation [54].

4.3. Vibration Experiments

As a PF implements different stressors, vibration was tested on the cells using the Vibraplex device (DLR, Cologne, Germany) [61,86]. MDA-MB-231 cells were seeded on µ-Slide VI ibiTreat channel slides (Ibidi, Gräfelfing, Germany) for immunostaining and in T25 cm^2 cell culture flasks for RNA isolation. The flasks and the slides were attached to the Vibraplex platform. The Vibraplex was transferred into a 37 °C incubator. Frequencies between 0.2 to 14 Hz were produced via the Vibraplex for a two-hour duration. These frequencies resemble the VIB produced during the PF. After the vibration procedure, the cells were fixed with either 4% PFA for immunostaining or RNA*later* for RNA isolation. Ground control slides and flasks were cultured in parallel for comparison.

4.4. Hyper-g Experiments

MDA-MB-231 cells were counted and seeded into µ-Slide VI ibiTreat channel slides (Ibidi, Gräfelfing, Germany) comparable to [87] for immunostaining. For RNA isolation T 75 cm^2 flasks were used with a confluence of 90%. The flasks and the slides were fixed on swing-out gondolas inside the DLR multi-sample incubator centrifuge (MuSIC) located inside a 37 °C incubator. The centrifuge was rotating at a constant speed to produce 1.8 *g* for 2 h which is comparable to the hypergravity phases produced during the parabolic flight. The device designed by the DLR, Department of Gravitational Biology, is shown in Figure 10D. At the end of the run, the cells were fixed with either 4% PFA for immunostaining or RNA*later* for RNA isolation. All slides and cell culture flasks were randomly assigned to centrifugation or 1 *g*-ground controls.

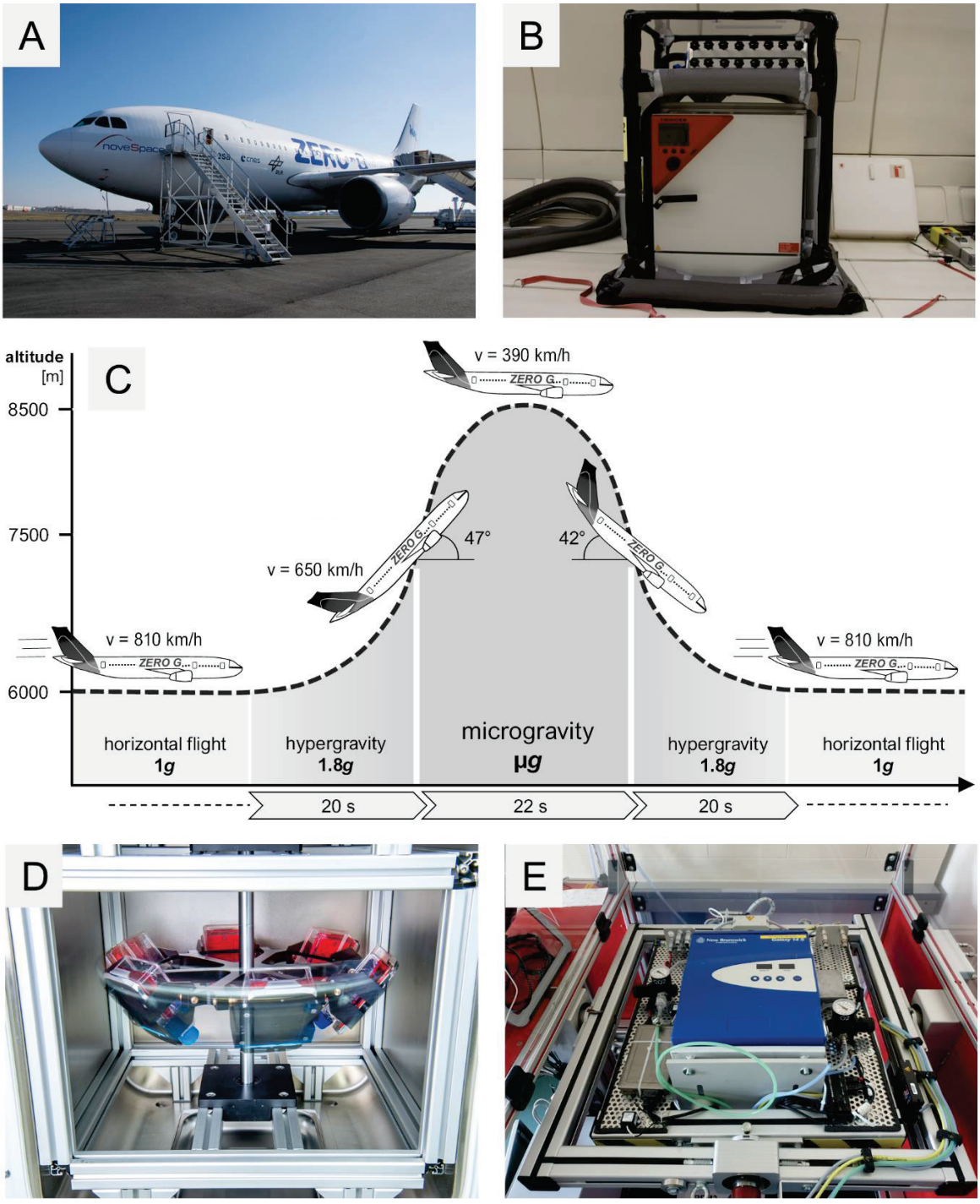


Figure 10. (**A**) Airbus A310 ZERO-G; (**B**) Deutsches Zentrum für Luft- und Raumfahrt (DLR) Flight rack; (**C**) Different phases of a parabolic flight; (**D**) DLR Multi-sample incubator centrifuge (MuSIC); (**E**) Incubator random positioning machine (iRPM).

4.5. Incubator Random Positioning Machine (iRPM)

The iRPM (Figure 10E) was designed and constructed by Prof. Jörg Sekler-Fachhochschule Nordwestschweiz. Details of the device were published in [88].

MDA-MB-231 cells were seeded in µ-Slide VI ibiTreat channel slides (Ibidi, Gräfelfing, Germany) for immunostaining and T25cm^2 flasks for RNA isolation. The slides and the flasks were placed inside a 37 °C pre-warmed iRPM. At the end of the 2 h, the cells were fixed with either 4% PFA for

immunostaining or RNA*later* for RNA isolation. The RNA was isolated as mentioned earlier. All the slides and flasks were put in comparison to 1 *g*-ground control.

4.6. RNA Isolation and Quantitative Polymerase Chain Reaction (qPCR)

All falcon tubes were centrifuged (2500× *g* for 10 min at 4 °C), followed by discarding the supernatant. The RNA was isolated afterwards using the RNeasy Mini Kit (Qiagen, Hilden, Germany) according to the manufacturer's protocol. The quality of the RNA was evaluated with a spectrophotometer. Afterwards, RNA was converted to cDNA with the High Capacity cDNA reverse Transcription Kit according to the manufacturer's protocol (Applied Biosystems, Darmstadt, Germany). 1 µg total RNA in 20 µL reaction mix was prepared as stock for qPCR. The primers were designed using Primer Blast (primer designing tool from NCBI).

A total volume of 13 µL SYBR green reaction mix (Applied Biosystems, Darmstadt, Germany) was pipetted in each well in a 96 well plate. 1 µL of cDNA was added to each reaction mix with a concentration of 100 µM forward and reverse primers. The 7500 Fast Real-Time PCR System (Applied Biosystems, Darmstadt, Germany) was used to determine the transcription level of targeted genes (see Table 1). The program consisted of an initial 20 s long holding stage of 95 °C followed by the cycling stage. The cycling stage consisted of 40 cycles of 3 s at 95 °C and 30 s at 60 °C. A melting curve was implemented at the end of each run to verify the primer specificity. The data was collected and analyzed by the $\Delta\Delta C_T$ method. 18S rRNA and TBP were used as reference genes.

Table 1. List of primer used during the study. Primer sequences are given in 5′ to 3′ direction.

Factor	Primer Name	Sequence 5′–3′
18S rRNA	18s-F	GGAGCCTGCGGCTTAATTT
	18s-R	CAACTAAGAACGGCCATGCA
Annexin A1; ANXA1	ANXA1-F	GCCAAAGACATAACCTCAGACACAT
	ANXA1-R	GAATCAGCCAAGTCTTCATTCACA
Annexin A2; ANXA2	ANXA2-F	GGTACAAGAGTTACAGCCCTTATGACA
	ANXA2-R	CATGGAGTCATACAGCCGATCA
BCL2 Associated X, Apoptosis Regulator; BAX	Bax-F	GTCAGCTGCCACTCGGAAA
	Bax-R	AGTAACATGGAGCTGCAGAGGAT
B-cell lymphoma 2; BCL2	Bcl2-F	TCAGAGACAGCCAGGAGAAATCA
	Bcl2-R	CCTGTGGATGACTGAGTACCTGAA
Caspase 3; CASP3	Casp3-F	CTCCAACATCGACTGTGAGAAGTT
	Casp3-R	GCGCCAGCTCCAGCAA
CD44	CD44-F	ACCCTCCCCTCATTCACCAT
	CD44-R	GTTGTACTACTAGGAGTTGCCTGGATT
Extracellular signal-regulated kinases 1; ERK1	ERK1-F	ACCTGCGACCTTAAGATTTGTGA
	ERK1-R	AGCCACATACTCCGTCAGGAA
Extracellular signal-regulated kinases 2; ERK2	ERK2-F	TTCCAACCTGCTGCTCAACA
	ERK2-R	TCTGTCAGGAACCCTGTGTGAT
Focal adhesion kinase 1 (Protein-tyrosine kinase 2); pan-FAK1	FAK1-F	TGTGGGTAAACCAGATCCTGC
	FAK1-R	CTGAAGCTTGACACCCTCGT
Intercellular adhesion molecule 1; ICAM1	ICAM1-F	CGGCTGACGTGTGCAGTAAT
	ICAM1-R	CTTCTGAGACCTCTGGCTTCGT

Table 1. *Cont.*

Factor	Primer Name	Sequence 5′–3′
Mitogen-activated protein kinase 8 (MAPK8) (JNK1-a2); MAPK8/JNK1	JNK1-F	TCTCCTTTAGGTGCAGCAGTG
	JNK1-R	CAGAGGCCAAAGTCGGATCT
NF-kappa-B transcription complex P105/P50; NFKB1	NFkB1-F	CTTAGGAGGGAGAGCCCAC
	NFkB1-R	TGAAACATTTGTTCAGGCCTTC
NF-kappa-B transcription complex P100/P52; NFKB2	NFkB2-F	GTACAAAGATACGCGGACCC
	NFkB2-R	CCAGACCTGGGTTGTAGCA
NF-kappa-B transcription complex P65; NFKB P65	NFkB P65-F	CGCTTCTTCACACACTGGATTC
	NFkB P65-R	ACTGCCGGGATGGCTTCT
NF-kappa-B essential modulator (NEMO); IKBKG	IkBKG-F	AACTGGGACTTTCTCGGAGC
	IkBKG-R	GGCAAGGGCTGTCAGCAG
NF-kappa-B inhibitor alpha; NFKBIA	NFkBIa-F	AATGCTCAGGAGCCCTGTAAT
	NFkBIa-R	CTGTTGACATCAGCCCCACA
NF-kappa-B inhibitor beta; NFKBIB	NFkBIb-F	CCCGGAGGACCTGGGTT
	NFkBIb-R	GCAGTGCCGTGTCCCC
NF-kappa-B inhibitor epsilon; NFKBIE	NFkBIe-F	TGGGCATCTCATCCACTCTG
	NFkBIe-R	ACAAGGGATTCCTCAGTCAGGT
Protein kinase C alpha type; PRKCA	PRKCA-F	TGGGTCACTGCTCTATGGACTTATC
	PRKCA-R	CGCCCCCTCTTCTCAGTGT
TATA-box binding protein; TBP	TBP-F	GTGACCCAGCATCACTGTTTC
	TBP-R	GCAAACCAGAAACCCTTGCG
Raf-1 Proto-Oncogene, Serine/Threonine Kinase; Raf1	Raf1-F	GGGAGCTTGGAAGACGATCAG
	Raf1-R	ACACGGATAGTGTTGCTTGTC
Osteopontin (OPN); SPP1	SPP1-F	CGAGGTGATAGTGTGGTTTATGGA
	SPP1-R	CGTCTGTAGCATCAGGGTACTG
Vascular cell adhesion protein 1; VCAM1	VCAM1-F	CATGGAATTCGAACCCAAACA
	VCAM1-R	GGCTGACCAAGACGGTTGTATC

4.7. Western Blotting

Western blot analysis, gel electrophoresis, trans-blotting, and densitometry were carried out following routine protocols as described previously [21,54,61]. Following lysis and centrifugation, aliquots of 30 μ*g* were subjected to sodium dodecyl sulphate-polyacrylamide gel electrophoresis (SDS-PAGE) and Western blotting. The samples were collected at the end of the P1 and P31 and were compared to 1 *g* control samples. Each condition is represented with 5 samples with a total number of 15 samples for all the conditions per cell line. The samples were loaded onto Criterion XT 4–12% precast gels (Bio-Rad, Hercules, CA, USA) and run for 1 h at 150 V. Proteins were then transferred with a TurboBlot (Bio-Rad) (100 V, 30 min) to a PVDF membrane. Cofilin-1 was used as a loading control. Membranes were then blocked for 2 h in TBS-T containing 0.3% I Block (Applied Biosystems, Foster City, CA, USA). For the detection of the selected antigens (see Table 2), the membranes were incubated overnight at room temperature in TBS-T and 0.3% I Block solutions of the antibodies. Following three washing steps of 5 min, the membranes were incubated for a further 2 h at room temperature with the secondary antibody Horseradish peroxidase (HRP)-linked antibody (Cell Signaling Technology Inc., Danvers, MA, USA) diluted 1:4000 in TBS-T and 0.3% I-Block. The respective protein bands were

visualized using Bio-Rad Clarity Western ECL (Bio-Rad) and images were captured with Image Quant LAS 4000 mini (GE Healthcare Life Science, Freiburg, Germany). Images of stained membranes were captured on Syngene PXi 4EZ image analysis system (Synoptics, Cambridge, UK) and analyzed using the ImageJ software for densitometric quantification of the respective bands and total protein load.

Table 2. List of the names, sources, companies, molecular weight and dilutions of all the antibodies that were used for Western blots.

Antibody	kDa	Dilution	Company	Source
Annexin 2	38	1:1000	Abcam #ab41802	Rb
NFkBp65	65	1:1000	Thermo Fisher #PA1-186	Rb
IKBKG	38	1:500	Origene #TA812460	MS
IkBα/NFKBIA	36	1:1000	Invitrogen #MA5-15132	MS
Cofilin-1	20	1:2000	Abcam #ab 42824	Rb
CD44	80	1:500	CST#5640	MS
VCAM1	110	1:500	Sc80431	MS
Casp 3	35	1:800	CST#9662	Rb
ICAM1	90	1:500	CST#4915	Rb
Osteopontin	44	1:1000	SAB4200018	MS

4.8. Terminal Deoxynucleotidyl Transferase dUTP Nick End Labeling (TUNEL) Staining

The MDA-MB-231 cells were cultured in µ-Slide VI 0.4 ibiTreat Ibidi slides (IBIDI GmbH, Martinsried, Planegg, Germany), exposed to VIB, hyper-*g* and iRPM and subsequently collected for the detection of apoptosis. The method was published earlier in Lützenberg et al. [89].

TUNEL staining was performed according to the manufacturer's recommendation (Thermo Fisher Scientific, Waltham, Massachusetts, USA; Click-iT TUNEL Alexa Fluor 488 (cat# C10245)).

The stained cell samples (VIB, hyper-*g*, iRPM and corresponding static 1 *g*-controls) were examined utilizing a Leica DM 2000 microscope equipped with an objective with a calibrated magnification of 400× and connected to an external light source, Leica EL 6000 (Leica Microsystems GmbH, Wetzlar, Germany). To obtain positive controls the cells were treated with DNAase before the TUNEL staining.

4.9. STRING Analysis

Interactions between proteins were determined using the STRING 10 platform [90]. For each protein, the UniProtKB entry number was inserted in the input form "multiple proteins" and "Homo sapiens" was selected as organism. The resulting network view was downloaded in the molecular action view showing lines between interacting proteins and genes [91].

4.10. Statistical Analyses

GraphPad prism 7.01 (GraphPad Software, Inc., California, USA) was used to analyze the data. The nonparametric Mann-Whitney U test was used as a statistical test of significance. The difference between groups was considered significant when the *p*-value was less than 0.05 (* $p < 0.05$).

5. Conclusions

Short-term r-µ*g* produced by PF maneuvers induced the gene expression of cell adhesion molecules in triple-negative breast cancer cells. This finding is in agreement with long-term µ*g* (s- and r-µ*g*) data with other cell types grown on the NASA-developed high-aspect ratio vessel (HARV) or on the Space Shuttle in space for 4–5 days [62,63,92]. The CD44 upregulation in the r-µ*g*- and hyper-*g*-cultures may be involved in the compensative regulation to counteract cellular apoptosis occurring in µ*g* [93,94].

Cell adhesion molecules and factors of the MAPK pathway are involved in the adaptive response to perturbation of mechanical stress under short-term real microgravity. Overall, our study suggests that a fine balance between NF-κB-p65 and osteopontin gene dosage is required to regulate metastasis, survival and angiogenesis of TNBC cells.

Author Contributions: Parabolic flight campaign: M.Z.N., D.M., T.J.C., S.K., and M.K.; VIB experiment: T.J.B. and M.Z.N.; iRPM experiment: M.Z.N., T.J.B., and hyper-*g* experiment: C.L., R.H., M.Z.N., S.K., M.K., T.J.B.; Conceptualization, D.G., T.J.C. and S.K.; methodology, S.K., M.Z.N., D.M., T.J.B., and J.S.; Software, T.J.B., M.W., and S.K.; Validation, D.G., T.J.C., S.K., M.K. and D.M.; Formal analysis, M.Z.N., S.K., J.S., and M.W.; Investigation, M.Z.N., and S.K.; Resources, M.I. and R.H.; Writing—Original draft preparation, M.Z.N., S.K., D.G., and M.W.; Project administration, D.G.; funding acquisition, D.G. and M.I.

Funding: This research was funded by the German Space Agency (DLR; BMWi projects 50WB1524; 50WB1924).

Acknowledgments: We would like to thank Katrin Stang, Michael Becker and Markus Braun (German Aerospace Center DLR, Bonn) for their support and for giving us the possibility to attend the 29th DLR Parabolic Flight Campaign in Bordeaux-Mérignac, France.

Conflicts of Interest: The authors declare no conflict of interest.

Abbreviations

2D	Two-dimensional
3D	Three-dimensional
ANXA1	Annexin A1
ANXA2	Annexin A2
AR	Androgen receptor
ATCC	American Type Culture Collection
BAX	BCL2 Associated X, Apoptosis Regulator
BCL2	B-cell lymphoma 2
CASP3	Caspase3
CD44	Cell surface glycoprotein CD44
Cx+	Connexin positive
CXCL12	C-X-C Motif Chemokine Ligand 12
CYC1	Cytochrome c1
DLR	Deutsches Zentrum für Luft- und Raumfahrt
ECM	Extracellular matrix
ER	Estrogen receptor
ERK1,2	Extracellular Signal-Regulated Kinase 1, 2
FAK1	Focal adhesion kinase 1
FCS	Fetal calf serum
FTC-133	Human follicular thyroid carcinoma cell line
GLOBOCAN	Global Cancer Observatory
HARV	High-aspect ratio vessel
HER2	Human epidermal growth receptor 2
hyper-*g*	Hypergravity
ICAM1	Intercellular adhesion molecule 1
IKBKG	NF-kappa-B essential modulator (NEMO)
IKK	IκB kinase
iRPM	Incubator random positioning machine
ISS	International Space Station
IκB	Inhibitor of κB
IκBα	Inhibitor of κB alpha
IκBβ	Inhibitor of κB beta
IκBγ	Inhibitor of κB gamma
IκBε	Inhibitor of κB epsilon
JNK1	Mitogen-activated protein kinase 8
KI67	Antigen KI67

μ*g*	Microgravity
MAPK	Mitogen-Activated Protein Kinase
MCF-7	Michigan Cancer Foundation-7 cell line
MCS	Multicellular spheroids
MDA-MB-231	M.D. Anderson-Metastasis Breast cancer cell line
ML1	Human thyroid carcinoma cell line
MME	Membrane Metalloendopeptidase
MMP11	Matrix Metallopeptidase 11
MMP2	Matrix Metallopeptidase 2
MuSIC	Multi-sample incubator centrifuge
NFKB1	NF-kappa-B transcription complex P105/P50
NFKB2	NF-kappa-B transcription complex P100/P52
NFKB3/NFKB P65	NF-kappa-B transcription complex P65
NFKBIA	NF-κB-inhibitor-alpha
NFKBIB	NF-κB-inhibitor-beta
NFKBIE	NF-κB-inhibitor-epsilon
NFκB	Nuclear factor-kappaB
P	Parabola
PF	Parabolic flight
PFA	Paraformaldehyde
PR	Progesterone receptor
PRKCA	Protein kinase C alpha
PTK2	Protein tyrosine kinase 2 (known as FAK1)
qPCR	Quantitative polymerase chain reaction
RAF1	RAF proto-oncogene serine/threonine-protein kinase
r-μ*g*	Real microgravity
RELA	V-Rel Avian Reticuloendotheliosis Viral Oncogene Homolog A
RPM	Random positioning machine
s-μ*g*	Simulated microgravity
SPP1/OPN	Osteopontin
STRING	Search Tool for the Retrieval of Interacting Genes/Proteins
TBP	TATA-box binding protein
TNBC	Triple-negative breast cancer
TUNEL	Terminal deoxynucleotidyl transferase dUTP nick end labeling
VCAM1	Vascular cell adhesion protein 1
VIB	Vibration

References

1. Bray, F.; Ferlay, J.; Soerjomataram, I.; Siegel, R.L.; Torre, L.A.; Jemal, A. Global cancer statistics 2018: GLOBOCAN estimates of incidence and mortality worldwide for 36 cancers in 185 countries. *CA Cancer J. Clin.* **2018**, *68*, 394–424. [CrossRef]
2. Van't Veer, L.J.; Dai, H.; van de Vijver, M.J.; He, Y.D.; Hart, A.A.; Mao, M.; Peterse, H.L.; van der Kooy, K.; Marton, M.J.; Witteveen, A.T.; et al. Gene expression profiling predicts clinical outcome of breast cancer. *Nature* **2002**, *415*, 530–536. [CrossRef]
3. Soliman, N.A.; Yussif, S.M. Ki-67 as a prognostic marker according to breast cancer molecular subtype. *Cancer Biol. Med.* **2016**, *13*, 496–504. [CrossRef] [PubMed]
4. Dai, X.; Li, T.; Bai, Z.; Yang, Y.; Liu, X.; Zhan, J.; Shi, B. Breast cancer intrinsic subtype classification, clinical use and future trends. *Am. J. Cancer Res.* **2015**, *5*, 2929–2943. [PubMed]
5. Farmer, P.; Bonnefoi, H.; Becette, V.; Tubiana-Hulin, M.; Fumoleau, P.; Larsimont, D.; Macgrogan, G.; Bergh, J.; Cameron, D.; Goldstein, D.; et al. Identification of molecular apocrine breast tumours by microarray analysis. *Oncogene* **2005**, *24*, 4660–4671. [CrossRef] [PubMed]

6. Prat, A.; Parker, J.S.; Karginova, O.; Fan, C.; Livasy, C.; Herschkowitz, J.I.; He, X.; Perou, C.M. Phenotypic and molecular characterization of the claudin-low intrinsic subtype of breast cancer. *Breast Cancer Res.* **2010**, *12*, R68. [CrossRef] [PubMed]
7. Kristensen, T.B.; Knutsson, M.L.; Wehland, M.; Laursen, B.E.; Grimm, D.; Warnke, E.; Magnusson, N.E. Anti-vascular endothelial growth factor therapy in breast cancer. *Int. J. Mol. Sci.* **2014**, *15*, 23024–23041. [CrossRef]
8. Cailleau, R.; Young, R.; Olive, M.; Reeves, W.J., Jr. Breast tumor cell lines from pleural effusions. *J. Natl. Cancer Inst.* **1974**, *53*, 661–674. [CrossRef]
9. Becker, J.L.; Souza, G.R. Using space-based investigations to inform cancer research on Earth. *Nat. Rev. Cancer* **2013**, *13*, 315–327. [CrossRef]
10. Obermaier, C.; Jankowski, V.; Schmutzler, C.; Bauer, J.; Wildgruber, R.; Infanger, M.; Kohrle, J.; Krause, E.; Weber, G.; Grimm, D. Free-flow isoelectric focusing of proteins remaining in cell fragments following sonication of thyroid carcinoma cells. *Electrophoresis* **2005**, *26*, 2109–2116. [CrossRef]
11. Pietsch, J.; Kussian, R.; Sickmann, A.; Bauer, J.; Weber, G.; Nissum, M.; Westphal, K.; Egli, M.; Grosse, J.; Schonberger, J.; et al. Application of free-flow IEF to identify protein candidates changing under microgravity conditions. *Proteomics* **2010**, *10*, 904–913. [CrossRef] [PubMed]
12. Bauer, J.; Kopp, S.; Schlagberger, E.M.; Grosse, J.; Sahana, J.; Riwaldt, S.; Wehland, M.; Luetzenberg, R.; Infanger, M.; Grimm, D. Proteome Analysis of Human Follicular Thyroid Cancer Cells Exposed to the Random Positioning Machine. *Int. J. Mol. Sci.* **2017**, *18*, 546. [CrossRef] [PubMed]
13. Sahana, J.; Nassef, M.Z.; Wehland, M.; Kopp, S.; Kruger, M.; Corydon, T.J.; Infanger, M.; Bauer, J.; Grimm, D. Decreased E-Cadherin in MCF7 Human Breast Cancer Cells Forming Multicellular Spheroids Exposed to Simulated Microgravity. *Proteomics* **2018**, *18*, e1800015. [CrossRef] [PubMed]
14. Grimm, D.; Egli, M.; Kruger, M.; Riwaldt, S.; Corydon, T.J.; Kopp, S.; Wehland, M.; Wise, P.; Infanger, M.; Mann, V.; et al. Tissue Engineering Under Microgravity Conditions-Use of Stem Cells and Specialized Cells. *Stem Cells Dev.* **2018**, *27*, 787–804. [CrossRef]
15. Masiello, M.G.; Cucina, A.; Proietti, S.; Palombo, A.; Coluccia, P.; D'Anselmi, F.; Dinicola, S.; Pasqualato, A.; Morini, V.; Bizzarri, M. Phenotypic switch induced by simulated microgravity on MDA-MB-231 breast cancer cells. *BioMed Res. Int.* **2014**, *2014*, 652434. [CrossRef]
16. Kruger, M.; Melnik, D.; Kopp, S.; Buken, C.; Sahana, J.; Bauer, J.; Wehland, M.; Hemmersbach, R.; Corydon, T.J.; Infanger, M.; et al. Fighting Thyroid Cancer with Microgravity Research. *Int. J. Mol. Sci.* **2019**, *20*, 2553. [CrossRef]
17. Wang, W.; Nag, S.A.; Zhang, R. Targeting the NFkappaB signaling pathways for breast cancer prevention and therapy. *Curr. Med. Chem.* **2015**, *22*, 264–289. [CrossRef]
18. Zhang, Q.; Lenardo, M.J.; Baltimore, D. 30 Years of NF-kappaB: A Blossoming of Relevance to Human Pathobiology. *Cell* **2017**, *168*, 37–57. [CrossRef]
19. Grosse, J.; Wehland, M.; Pietsch, J.; Schulz, H.; Saar, K.; Hubner, N.; Eilles, C.; Bauer, J.; Abou-El-Ardat, K.; Baatout, S.; et al. Gravity-sensitive signaling drives 3-dimensional formation of multicellular thyroid cancer spheroids. *FASEB J.* **2012**, *26*, 5124–5140. [CrossRef]
20. Kopp, S.; Sahana, J.; Islam, T.; Petersen, A.G.; Bauer, J.; Corydon, T.J.; Schulz, H.; Saar, K.; Huebner, N.; Slumstrup, L.; et al. The role of NFkappaB in spheroid formation of human breast cancer cells cultured on the Random Positioning Machine. *Sci. Rep.* **2018**, *8*, 921. [CrossRef]
21. Murakami, N.; Kuhnel, A.; Schmid, T.E.; Ilicic, K.; Stangl, S.; Braun, I.S.; Gehrmann, M.; Molls, M.; Itami, J.; Multhoff, G. Role of membrane Hsp70 in radiation sensitivity of tumor cells. *Radiat. Oncol.* **2015**, *10*, 149. [CrossRef]
22. Oeckinghaus, A.; Hayden, M.S.; Ghosh, S. Crosstalk in NF-kappaB signaling pathways. *Nat. Immunol.* **2011**, *12*, 695–708. [CrossRef]
23. Huang, T.; Kang, W.; Zhang, B.; Wu, F.; Dong, Y.; Tong, J.H.; Yang, W.; Zhou, Y.; Zhang, L.; Cheng, A.S.; et al. miR-508-3p concordantly silences NFKB1 and RELA to inactivate canonical NF-kappaB signaling in gastric carcinogenesis. *Mol Cancer* **2016**, *15*, 9. [CrossRef]
24. Lindner, V. The NF-kappaB and IkappaB system in injured arteries. *Pathobiology* **1998**, *66*, 311–320. [CrossRef]
25. Bist, P.; Leow, S.C.; Phua, Q.H.; Shu, S.; Zhuang, Q.; Loh, W.T.; Nguyen, T.H.; Zhou, J.B.; Hooi, S.C.; Lim, L.H. Annexin-1 interacts with NEMO and RIP1 to constitutively activate IKK complex and NF-kappaB: Implication in breast cancer metastasis. *Oncogene* **2011**, *30*, 3174–3185. [CrossRef]

26. Anwar, K.N.; Fazal, F.; Malik, A.B.; Rahman, A. RhoA/Rho-associated kinase pathway selectively regulates thrombin-induced intercellular adhesion molecule-1 expression in endothelial cells via activation of I kappa B kinase beta and phosphorylation of RelA/p65. *J. Immunol.* **2004**, *173*, 6965–6972. [CrossRef]
27. Ortiz-Martinez, F.; Sanmartin, E.; Pomares-Navarro, E.; Perez-Balaguer, A.; Andres, L.; Sanchez-Paya, J.; Aranda, F.I.; Lerma, E.; Peiro, G. Osteopontin Regulates VEGFA and ICAM-1 mRNA Expression in Breast Carcinoma. *Am. J. Clin. Pathol.* **2015**, *143*, 812–822. [CrossRef]
28. Ue, T.; Yokozaki, H.; Kitadai, Y.; Yamamoto, S.; Yasui, W.; Ishikawa, T.; Tahara, E. Co-expression of osteopontin and CD44v9 in gastric cancer. *Int. J. Cancer* **1998**, *79*, 127–132. [CrossRef]
29. Chintagari, N.R.; Jin, N.; Wang, P.; Narasaraju, T.A.; Chen, J.; Liu, L. Effect of cholesterol depletion on exocytosis of alveolar type II cells. *Am. J. Respir. Cell Mol. Biol.* **2006**, *34*, 677–687. [CrossRef]
30. Tiys, E.S.; Ivanisenko, T.V.; Demenkov, P.S.; Ivanisenko, V.A. FunGeneNet: A web tool to estimate enrichment of functional interactions in experimental gene sets. *BMC Genom.* **2018**, *19*, 76. [CrossRef]
31. Zaczynska, E.; Kochanowska, I.; Kruzel, M.; Zimecki, M. Lactoferrin Prevents Susceptibility of WEHI 231 Cells to Anti-Ig-Induced Cell Death Promoting Cell Differentiation. *Folia Biol. (Praha)* **2018**, *64*, 16–22.
32. Reza, A.; Choi, Y.J.; Yasuda, H.; Kim, J.H. Human adipose mesenchymal stem cell-derived exosomal-miRNAs are critical factors for inducing anti-proliferation signalling to A2780 and SKOV-3 ovarian cancer cells. *Sci. Rep.* **2016**, *6*, 38498. [CrossRef]
33. Cailleau, R.; Olive, M.; Cruciger, Q.V. Long-term human breast carcinoma cell lines of metastatic origin: Preliminary characterization. *In Vitro* **1978**, *14*, 911–915. [CrossRef]
34. Brinkley, B.R.; Beall, P.T.; Wible, L.J.; Mace, M.L.; Turner, D.S.; Cailleau, R.M. Variations in cell form and cytoskeleton in human breast carcinoma cells in vitro. *Cancer Res.* **1980**, *40*, 3118–3129.
35. White, R.J.; Averner, M. Humans in space. *Nature* **2001**, *409*, 1115–1118. [CrossRef]
36. Hader, D.P.; Braun, M.; Grimm, D.; Hemmersbach, R. Gravireceptors in eukaryotes-a comparison of case studies on the cellular level. *NPJ Microgravity* **2017**, *3*, 13. [CrossRef]
37. Grimm, D.; Bauer, J.; Kossmehl, P.; Shakibaei, M.; Schoberger, J.; Pickenhahn, H.; Schulze-Tanzil, G.; Vetter, R.; Eilles, C.; Paul, M.; et al. Simulated microgravity alters differentiation and increases apoptosis in human follicular thyroid carcinoma cells. *FASEB J.* **2002**, *16*, 604–606. [CrossRef]
38. Qian, A.; Zhang, W.; Xie, L.; Weng, Y.; Yang, P.; Wang, Z.; Hu, L.; Xu, H.; Tian, Z.; Shang, P. Simulated weightlessness alters biological characteristics of human breast cancer cell line MCF-7. *Acta Astronaut.* **2008**, *63*, 947–958. [CrossRef]
39. Kopp, S.; Warnke, E.; Wehland, M.; Aleshcheva, G.; Magnusson, N.E.; Hemmersbach, R.; Corydon, T.J.; Bauer, J.; Infanger, M.; Grimm, D. Mechanisms of three-dimensional growth of thyroid cells during long-term simulated microgravity. *Sci. Rep.* **2015**, *5*, 16691. [CrossRef]
40. Kopp, S.; Slumstrup, L.; Corydon, T.J.; Sahana, J.; Aleshcheva, G.; Islam, T.; Magnusson, N.E.; Wehland, M.; Bauer, J.; Infanger, M.; et al. Identifications of novel mechanisms in breast cancer cells involving duct-like multicellular spheroid formation after exposure to the Random Positioning Machine. *Sci. Rep.* **2016**, *6*, 26887. [CrossRef]
41. Schoenberger, J.; Bauer, J.; Moosbauer, J.; Eilles, C.; Grimm, D. Innovative strategies in in vivo apoptosis imaging. *Curr. Med. Chem.* **2008**, *15*, 187–194. [CrossRef]
42. Grosse, J.; Wehland, M.; Pietsch, J.; Ma, X.; Ulbrich, C.; Schulz, H.; Saar, K.; Hubner, N.; Hauslage, J.; Hemmersbach, R.; et al. Short-term weightlessness produced by parabolic flight maneuvers altered gene expression patterns in human endothelial cells. *FASEB J.* **2012**, *26*, 639–655. [CrossRef]
43. Wehland, M.; Ma, X.; Braun, M.; Hauslage, J.; Hemmersbach, R.; Bauer, J.; Grosse, J.; Infanger, M.; Grimm, D. The impact of altered gravity and vibration on endothelial cells during a parabolic flight. *Cell Physiol. Biochem.* **2013**, *31*, 432–451. [CrossRef]
44. Sarkar, D.K.; Jana, D.; Patil, P.S.; Chaudhari, K.S.; Chattopadhyay, B.K.; Chikkala, B.R.; Mandal, S.; Chowdhary, P. Role of NF-kappaB as a Prognostic Marker in Breast Cancer: A Pilot Study in Indian Patients. *Indian J. Surg. Oncol.* **2013**, *4*, 242–247. [CrossRef]
45. Khongthong, P.; Roseweir, A.K.; Edwards, J. The NF-KB pathway and endocrine therapy resistance in breast cancer. *Endocr. Relat. Cancer* **2019**, *26*, 369–380. [CrossRef]
46. Ulbrich, C.; Westphal, K.; Baatout, S.; Wehland, M.; Bauer, J.; Flick, B.; Infanger, M.; Kreutz, R.; Vadrucci, S.; Egli, M.; et al. Effects of basic fibroblast growth factor on endothelial cells under conditions of simulated microgravity. *J. Cell Biochem.* **2008**, *104*, 1324–1341. [CrossRef]

47. Ghobrial, I.M.; Witzig, T.E.; Adjei, A.A. Targeting apoptosis pathways in cancer therapy. *CA Cancer J. Clin.* **2005**, *55*, 178–194. [CrossRef]
48. Chang, T.T.; Walther, I.; Li, C.F.; Boonyaratanakornkit, J.; Galleri, G.; Meloni, M.A.; Pippia, P.; Cogoli, A.; Hughes-Fulford, M. The Rel/NF-kappaB pathway and transcription of immediate early genes in T cell activation are inhibited by microgravity. *J. Leukoc. Biol.* **2012**, *92*, 1133–1145. [CrossRef]
49. Boonyaratanakornkit, J.B.; Cogoli, A.; Li, C.F.; Schopper, T.; Pippia, P.; Galleri, G.; Meloni, M.A.; Hughes-Fulford, M. Key gravity-sensitive signaling pathways drive T cell activation. *FASEB J.* **2005**, *19*, 2020–2022. [CrossRef]
50. Gilmore, T.D. Introduction to NF-kappaB: Players, pathways, perspectives. *Oncogene* **2006**, *25*, 6680–6684. [CrossRef]
51. Wuest, S.L.; Stern, P.; Casartelli, E.; Egli, M. Fluid Dynamics Appearing during Simulated Microgravity Using Random Positioning Machines. *PLoS ONE* **2017**, *12*, e0170826. [CrossRef] [PubMed]
52. Ma, X.; Pietsch, J.; Wehland, M.; Schulz, H.; Saar, K.; Hubner, N.; Bauer, J.; Braun, M.; Schwarzwalder, A.; Segerer, J.; et al. Differential gene expression profile and altered cytokine secretion of thyroid cancer cells in space. *FASEB J.* **2014**, *28*, 813–835. [CrossRef] [PubMed]
53. Buken, C.; Sahana, J.; Corydon, T.J.; Melnik, D.; Bauer, J.; Wehland, M.; Kruger, M.; Balk, S.; Abuagela, N.; Infanger, M.; et al. Morphological and Molecular Changes in Juvenile Normal Human Fibroblasts Exposed to Simulated Microgravity. *Sci. Rep.* **2019**, *9*, 11882. [CrossRef] [PubMed]
54. Nassef, M.Z.; Kopp, S.; Wehland, M.; Melnik, D.; Sahana, J.; Kruger, M.; Corydon, T.J.; Oltmann, H.; Schmitz, B.; Schutte, A.; et al. Real Microgravity Influences the Cytoskeleton and Focal Adhesions in Human Breast Cancer Cells. *Int. J. Mol. Sci.* **2019**, *20*, 3456. [CrossRef]
55. Dittrich, A.; Grimm, D.; Sahana, J.; Bauer, J.; Kruger, M.; Infanger, M.; Magnusson, N.E. Key Proteins Involved in Spheroid Formation and Angiogenesis in Endothelial Cells After Long-Term Exposure to Simulated Microgravity. *Cell Physiol. Biochem.* **2018**, *45*, 429–445. [CrossRef]
56. Eibl, R.H.; Benoit, M. Molecular resolution of cell adhesion forces. *IEE Proc. Nanobiotechnol.* **2004**, *151*, 128–132. [CrossRef]
57. Deng, C.; Zhang, D.; Shan, S.; Wu, J.; Yang, H.; Yu, Y. Angiogenic effect of intercellular adhesion molecule-1. *J. Huazhong Univ. Sci. Technol. Med. Sci.* **2007**, *27*, 9–12. [CrossRef]
58. Tauber, S.; Lauber, B.A.; Paulsen, K.; Layer, L.E.; Lehmann, M.; Hauschild, S.; Shepherd, N.R.; Polzer, J.; Segerer, J.; Thiel, C.S.; et al. Cytoskeletal stability and metabolic alterations in primary human macrophages in long-term microgravity. *PLoS ONE* **2017**, *12*, e0175599. [CrossRef]
59. Paulsen, K.; Tauber, S.; Dumrese, C.; Bradacs, G.; Simmet, D.M.; Golz, N.; Hauschild, S.; Raig, C.; Engeli, S.; Gutewort, A.; et al. Regulation of ICAM-1 in cells of the monocyte/macrophage system in microgravity. *BioMed Res. Int.* **2015**, *2015*, 538786. [CrossRef]
60. Ulbrich, C.; Pietsch, J.; Grosse, J.; Wehland, M.; Schulz, H.; Saar, K.; Hubner, N.; Hauslage, J.; Hemmersbach, R.; Braun, M.; et al. Differential gene regulation under altered gravity conditions in follicular thyroid cancer cells: Relationship between the extracellular matrix and the cytoskeleton. *Cell Physiol. Biochem.* **2011**, *28*, 185–198. [CrossRef]
61. Aleshcheva, G.; Wehland, M.; Sahana, J.; Bauer, J.; Corydon, T.J.; Hemmersbach, R.; Frett, T.; Egli, M.; Infanger, M.; Grosse, J.; et al. Moderate alterations of the cytoskeleton in human chondrocytes after short-term microgravity produced by parabolic flight maneuvers could be prevented by up-regulation of BMP-2 and SOX-9. *FASEB J.* **2015**, *29*, 2303–2314. [CrossRef]
62. Ingram, M.; Techy, G.B.; Saroufeem, R.; Yazan, O.; Narayan, K.S.; Goodwin, T.J.; Spaulding, G.F. Three-dimensional growth patterns of various human tumor cell lines in simulated microgravity of a NASA bioreactor. *In Vitro Cell Dev. Biol. Anim.* **1997**, *33*, 459–466. [CrossRef] [PubMed]
63. Kumei, Y.; Morita, S.; Katano, H.; Akiyama, H.; Hirano, M.; Oyha, K.; Shimokawa, H. Microgravity signal ensnarls cell adhesion, cytoskeleton, and matrix proteins of rat osteoblasts: Osteopontin, CD44, osteonectin, and alpha-tubulin. *Ann. N. Y. Acad. Sci.* **2006**, *1090*, 311–317. [CrossRef] [PubMed]
64. Weber, G.F. The cancer biomarker osteopontin: Combination with other markers. *Cancer Genom. Proteom.* **2011**, *8*, 263–288.
65. Irby, R.B.; McCarthy, S.M.; Yeatman, T.J. Osteopontin regulates multiple functions contributing to human colon cancer development and progression. *Clin. Exp. Metastasis* **2004**, *21*, 515–523. [CrossRef]

66. Wei, R.; Wong, J.P.C.; Kwok, H.F. Osteopontin—A promising biomarker for cancer therapy. *J. Cancer* **2017**, *8*, 2173–2183. [CrossRef]
67. Smith, S.M.; Lyu, Y.L.; Cai, L. NF-kappaB affects proliferation and invasiveness of breast cancer cells by regulating CD44 expression. *PLoS ONE* **2014**, *9*, e106966. [CrossRef]
68. Weber, G.F.; Ashkar, S.; Cantor, H. Interaction between CD44 and osteopontin as a potential basis for metastasis formation. *Proc. Assoc. Am. Physicians* **1997**, *109*, 1–9.
69. Ahmed, M.; Kundu, G.C. Osteopontin selectively regulates p70S6K/mTOR phosphorylation leading to NF-kappaB dependent AP-1-mediated ICAM-1 expression in breast cancer cells. *Mol. Cancer* **2010**, *9*, 101. [CrossRef]
70. O'Hanlon, D.M.; Fitzsimons, H.; Lynch, J.; Tormey, S.; Malone, C.; Given, H.F. Soluble adhesion molecules (E-selectin, ICAM-1 and VCAM-1) in breast carcinoma. *Eur. J. Cancer* **2002**, *38*, 2252–2257. [CrossRef]
71. Lee, J.Y.; Park, K.; Lee, E.; Ahn, T.; Jung, H.H.; Lim, S.H.; Hong, M.; Do, I.G.; Cho, E.Y.; Kim, D.H.; et al. Gene Expression Profiling of Breast Cancer Brain Metastasis. *Sci. Rep.* **2016**, *6*, 28623. [CrossRef] [PubMed]
72. Gibbs, L.D.; Vishwanatha, J.K. Prognostic impact of AnxA1 and AnxA2 gene expression in triple-negative breast cancer. *Oncotarget* **2018**, *9*, 2697–2704. [CrossRef] [PubMed]
73. Jung, H.; Kim, J.S.; Kim, W.K.; Oh, K.J.; Kim, J.M.; Lee, H.J.; Han, B.S.; Kim, D.S.; Seo, Y.S.; Lee, S.C.; et al. Intracellular annexin A2 regulates NF-kappaB signaling by binding to the p50 subunit: Implications for gemcitabine resistance in pancreatic cancer. *Cell Death Dis.* **2015**, *6*, e1606. [CrossRef] [PubMed]
74. Ahmed, K.M.; Dong, S.; Fan, M.; Li, J.J. Nuclear factor-kappaB p65 inhibits mitogen-activated protein kinase signaling pathway in radioresistant breast cancer cells. *Mol. Cancer Res.* **2006**, *4*, 945–955. [CrossRef]
75. Cook, S.J.; Stuart, K.; Gilley, R.; Sale, M.J. Control of cell death and mitochondrial fission by ERK1/2 MAP kinase signalling. *FEBS J.* **2017**, *284*, 4177–4195. [CrossRef]
76. Pham, T.N.D.; Perez White, B.E.; Zhao, H.; Mortazavi, F.; Tonetti, D.A. Protein kinase C alpha enhances migration of breast cancer cells through FOXC2-mediated repression of p120-catenin. *BMC Cancer* **2017**, *17*, 832. [CrossRef]
77. Chen, J.; Wu, F.; Shi, Y.; Yang, D.; Xu, M.; Lai, Y.; Liu, Y. Identification of key candidate genes involved in melanoma metastasis. *Mol. Med. Rep.* **2019**, *20*, 903–914. [CrossRef]
78. Kolch, W.; Heidecker, G.; Kochs, G.; Hummel, R.; Vahidi, H.; Mischak, H.; Finkenzeller, G.; Marme, D.; Rapp, U.R. Protein kinase C alpha activates RAF-1 by direct phosphorylation. *Nature* **1993**, *364*, 249–252. [CrossRef]
79. Olea-Flores, M.; Zuniga-Eulogio, M.D.; Mendoza-Catalan, M.A.; Rodriguez-Ruiz, H.A.; Castaneda-Saucedo, E.; Ortuno-Pineda, C.; Padilla-Benavides, T.; Navarro-Tito, N. Extracellular-Signal Regulated Kinase: A Central Molecule Driving Epithelial-Mesenchymal Transition in Cancer. *Int. J. Mol. Sci.* **2019**, *20*, 2885. [CrossRef]
80. Eblen, S.T. Extracellular-Regulated Kinases: Signaling From Ras to ERK Substrates to Control Biological Outcomes. *Adv. Cancer Res.* **2018**, *138*, 99–142. [CrossRef]
81. Crapoulet, N.; O'Brien, P.; Ouellette, R.J.; Robichaud, G.A. Coordinated expression of Pax-5 and FAK1 in metastasis. *Anticancer Agents Med. Chem.* **2011**, *11*, 643–649. [CrossRef] [PubMed]
82. Chan, K.T.; Cortesio, C.L.; Huttenlocher, A. FAK alters invadopodia and focal adhesion composition and dynamics to regulate breast cancer invasion. *J. Cell Biol.* **2009**, *185*, 357–370. [CrossRef] [PubMed]
83. Han, J.S.; Crowe, D.L. Jun amino-terminal kinase 1 activation promotes cell survival in ErbB2-positive breast cancer. *Anticancer Res.* **2010**, *30*, 3407–3412. [PubMed]
84. Zhang, J.Y.; Selim, M.A. The role of the c-Jun N-terminal Kinase signaling pathway in skin cancer. *Am. J. Cancer Res.* **2012**, *2*, 691–698.
85. Ashenden, M.; van Weverwijk, A.; Murugaesu, N.; Fearns, A.; Campbell, J.; Gao, Q.; Iravani, M.; Isacke, C.M. An In Vivo Functional Screen Identifies JNK Signaling As a Modulator of Chemotherapeutic Response in Breast Cancer. *Mol. Cancer Ther.* **2017**, *16*, 1967–1978. [CrossRef]
86. Lutzenberg, R.; Solano, K.; Buken, C.; Sahana, J.; Riwaldt, S.; Kopp, S.; Kruger, M.; Schulz, H.; Saar, K.; Huebner, N.; et al. Pathway Analysis Hints Towards Beneficial Effects of Long-Term Vibration on Human Chondrocytes. *Cell Physiol. Biochem.* **2018**, *47*, 1729–1741. [CrossRef]
87. Corydon, T.J.; Kopp, S.; Wehland, M.; Braun, M.; Schutte, A.; Mayer, T.; Hulsing, T.; Oltmann, H.; Schmitz, B.; Hemmersbach, R.; et al. Alterations of the cytoskeleton in human cells in space proved by life-cell imaging. *Sci. Rep.* **2016**, *6*, 20043. [CrossRef]

88. Benavides Damm, T.; Walther, I.; Wuest, S.L.; Sekler, J.; Egli, M. Cell cultivation under different gravitational loads using a novel random positioning incubator. *Biotechnol. Bioeng.* **2014**, *111*, 1180–1190. [CrossRef]
89. Lutzenberg, R.; Wehland, M.; Solano, K.; Nassef, M.Z.; Buken, C.; Melnik, D.; Bauer, J.; Kopp, S.; Kruger, M.; Riwaldt, S.; et al. Beneficial Effects of Low Frequency Vibration on Human Chondrocytes in Vitro. *Cell Physiol. Biochem.* **2019**, *53*, 623–637. [CrossRef]
90. Snel, B.; Lehmann, G.; Bork, P.; Huynen, M.A. STRING: A web-server to retrieve and display the repeatedly occurring neighbourhood of a gene. *Nucleic Acids Res.* **2000**, *28*, 3442–3444. [CrossRef]
91. Pietsch, J.; Riwaldt, S.; Bauer, J.; Sickmann, A.; Weber, G.; Grosse, J.; Infanger, M.; Eilles, C.; Grimm, D. Interaction of proteins identified in human thyroid cells. *Int. J. Mol. Sci.* **2013**, *14*, 1164–1178. [CrossRef] [PubMed]
92. Li, N.; Wang, C.; Sun, S.; Zhang, C.; Lu, D.; Chen, Q.; Long, M. Microgravity-Induced Alterations of Inflammation-Related Mechanotransduction in Endothelial Cells on Board SJ-10 Satellite. *Front. Physiol.* **2018**, *9*, 1025. [CrossRef] [PubMed]
93. Fedorchenko, O.; Stiefelhagen, M.; Peer-Zada, A.A.; Barthel, R.; Mayer, P.; Eckei, L.; Breuer, A.; Crispatzu, G.; Rosen, N.; Landwehr, T.; et al. CD44 regulates the apoptotic response and promotes disease development in chronic lymphocytic leukemia. *Blood* **2013**, *121*, 4126–4136. [CrossRef] [PubMed]
94. Lewis, M.L.; Reynolds, J.L.; Cubano, L.A.; Hatton, J.P.; Lawless, B.D.; Piepmeier, E.H. Spaceflight alters microtubules and increases apoptosis in human lymphocytes (Jurkat). *FASEB J.* **1998**, *12*, 1007–1018. [CrossRef]



© 2019 by the authors. Licensee MDPI, Basel, Switzerland. This article is an open access article distributed under the terms and conditions of the Creative Commons Attribution (CC BY) license (http://creativecommons.org/licenses/by/4.0/).

Cellular Physiology and Biochemistry

Cell Physiol Biochem 2017;43:257-270
DOI: 10.1159/000480368
Published online: August 30, 2017
Accepted: Juni 23, 2017

© 2017 The Author(s)
Published by S. Karger AG, Basel
www.karger.com/cpb

Karger Open access

This article is licensed under the Creative Commons Attribution-NonCommercial-NoDerivatives 4.0 International License (CC BY-NC-ND) (http://www.karger.com/Services/OpenAccessLicense). Usage and distribution for commercial purposes as well as any distribution of modified material requires written permission.

Original Paper

Cytokine Release and Focal Adhesion Proteins in Normal Thyroid Cells Cultured on the Random Positioning Machine

Elisabeth Warnke[a] Jessica Pietsch[a] Sascha Kopp[a] Johann Bauer[b] Jayashree Sahana[c] Markus Wehland[a] Marcus Krüger[a] Ruth Hemmersbach[d] Manfred Infanger[a] Ronald Lützenberg[a] Daniela Grimm[a,c]

[a]Clinic for Plastic, Aesthetic and Hand Surgery, Otto-von-Guericke-University Magdeburg, Magdeburg, Germany; [b]Max-Planck Institute of Biochemistry, Martinsried, Germany; [c]Institute of Biomedicine, Pharmacology, Aarhus University, Aarhus, Denmark; [d]DLR, German Aerospace Centre, Institute of Aerospace Medicine, Gravitational Biology, Cologne, Germany

Key Words
Thyroid • Multicellular spheroids • Cytokines • Focal adhesion • Extracellular matrix proteins • Pathway analyses

Abstract
Background/Aims: Spaceflight impacts on the function of the thyroid gland *in vivo*. *In vitro* normal and malignant thyrocytes assemble in part to multicellular spheroids (MCS) after exposure to the random positioning machine (RPM), while a number of cells remain adherent (AD). We aim to elucidate possible differences between AD and MCS cells compared to 1*g*-controls of normal human thyroid cells. ***Methods:*** Cells of the human follicular epithelial thyroid cell line Nthy-ori 3-1 were incubated for up to 72 h on the RPM. Afterwards, they were investigated by phase-contrast microscopy, quantitative real-time PCR and by determination of cytokines released in their supernatants. ***Results:*** A significant up-regulation of *IL6*, *IL8* and *CCL2* gene expression was found after a 4h RPM-exposure, when the whole population was still growing adherently. MCS and AD cells were detected after 24 h on the RPM. At this time, a significantly reduced gene expression in MCS compared to 1*g*-controls was visible for *IL6*, *IL8*, *FN1*, *ITGB1*, *LAMA1*, *CCL2*, and *TLN1*. After a 72 h RPM-exposure, IL-6, IL-8, and TIMP-1 secretion rates were increased significantly. ***Conclusion:*** Normal thyrocytes form MCS within 24 h. Cytokines seem to be involved in the initiation of MCS formation via focal adhesion proteins.

© 2017 The Author(s)
Published by S. Karger AG, Basel

Introduction

Long-term space missions are a challenge for the health of crewmembers. There are reports about various health concerns such as dysfunctions of the musculoskeletal and cardiovascular system, a down-regulation of the immune system, and visual problems [1-3]. In space, the thyroid gland *in vivo* revealed a variety of changes such as follicles with

E. Warnke and J. Pietsch contributed equally to this manuscript.

Daniela Grimm
Department of Biomedicine, Space Medicine, Aarhus University, Wilhelm Meyers Allé 4, DK-8000 Aarhus C, (Denmark)
Tel. +45-871 67693, Fax +45-8612 8804, E-Mail dgg@biomed.au.dk

KARGER

Downloaded from http://karger.com/cpb/article-pdf/43/1/257/2444310/000480368.pdf by guest on 31 October 2024

Cellular Physiology and Biochemistry
Cell Physiol Biochem 2017;43:257-270
DOI: 10.1159/000480368
Published online: August 30, 2017
© 2017 The Author(s). Published by S. Karger AG, Basel
www.karger.com/cpb

larger thyrocytes and increases in cAMP, thyrotropin-receptors (TSHR), and caveolin-1 [4, 5]. On the cellular level, it is known that both real (r-μ*g*) and simulated microgravity (s-μ*g*) influence growth behaviour, gene expression pattern, protein synthesis and secretion in thyroid cancer cells [6-11]. In addition, thyroid hormone production is decreased, while a TSHR up-regulation was detected in follicular thyroid cancer cells after exposure for 24 h to a random positioning machine (RPM) [12] - a device designed to simulate microgravity conditions [13, 14]. As thyroid hormones produced by the thyroid gland are influencing the function of nearly every cell and organ of the human body [15, 16], thyroid cells cultured under microgravity justify a thorough investigation. Therefore, the research was extended to normal thyrocytes.

Culturing normal thyroid cells in a rotary cell culture system (RCCS), three-dimensional (3D) cell aggregates resembling thyroid follicles were observed exhibiting the ability to produce thyroglobulin [17]. Rat FRTL-5 thyroid cells were investigated in r-μ*g* during a TEXUS rocket flight. The cells did not respond to thyrotropin (TSH) treatment and exhibited an irregular shape with condensed chromatin, shedding of the TSHR in the supernatant, and elevated protein levels of sphingomyelin-synthase and Bax [18]. Mice exposed to hypergravity treatment revealed up-regulation of the TSHR and caveolin-1 as well as a down-regulation of STAT3 without changes in cAMP [19].

Earlier experiments have shown that human thyroid cancer cells exhibit changes in the secretion of growth factors and cytokines, as well as alterations in the factors involved in 3D growth, in the cytoskeleton, and in the extracellular matrix composition when cultured in a an RPM [10, 20, 21]. Furthermore, human thyroid cells may exhibit two phenotypes in s-μ*g* either in the form of multicellular spheroids (MCS) or as adherent monolayer (AD) cells [20, 21].

For the present study, the human follicular epithelial thyroid cell line Nthy-ori 3-1 was exposed for 4 h, 24 h and 72 h to the RPM. MCS and AD cells were investigated in comparison to static 1*g*-controls. For this purpose, phase-contrast images were taken to monitor expected changes in the morphology of the thyrocytes. Furthermore, quantitative real-time PCR (qPCR) and multi-analyte profiling (MAP) analyses were performed. The chosen genes and cytokines were detected previously to have changed in cells of this cell line in s-μ*g* after RPM-exposure of 7 and 14 days [21]. The principal aim of these experiments was to close the knowledge gap concerning the impact of microgravity on the behaviour of normal thyroid cells exposed for a short time to s-μ*g* generated by an RPM.

Materials and Methods

Culture of Nthy-ori 3-1 cells

The Nthy-ori 3-1 cell line (Sigma-Aldrich, Munich, Germany) is a primary human thyroid follicular epithelial cell line. The immortalised cell line exhibits thyroid specific functions, such as iodide-trapping and thyroglobulin synthesis and reveals no signs of tumorigenesis, when transplanted into nude mice [22].

The Nthy-ori 3-1 cells were cultured under standard cell culture conditions (37°C and 5% CO_2). The cells grew in RPMI 1640 medium (Life Technologies, Naerum, Denmark), supplemented with 1 % penicillin/streptomycin (Life Technologies) and 10 % (v/v) fetal calf serum (FCS) (Biochrom, Berlin, Germany). The cells were cultured in T25 cm^2 vented cell culture flasks (Sarstedt, Newton, USA) for one day prior to RPM-exposure. Each flask was seeded with 1×10^6 cells. The culture flasks were filled completely with medium without any air bubbles. The flasks (n = 60 per time point) were assigned randomly to use as static controls (1*g*; n = 30) or as RPM-samples (n = 30). The 1*g*-controls were positioned next to the RPM in the same incubator. Supernatants and cells were harvested after 4 h, 24 h or 72 h according to the protocol.

Random positioning machine (RPM)

The Desktop RPM manufactured by Airbus Defense & Space (ADS, Leyden, The Netherlands) was used for the simulation of microgravity [23]. The device was stored in an incubator at 37°C and 5 % CO_2, operated in real random direction mode at 60 degrees/s and equipped with T25 flasks. The flasks were fixed to the ground plate, giving a maximum distance of 7.5 cm from the centre of rotation.

Downloaded from http://karger.com/cpb/article-pdf/43/1/257/2444310/000480368.pdf by guest on 31 October 2024

Cellular Physiology and Biochemistry
Cell Physiol Biochem 2017;43:257-270
DOI: 10.1159/000480368
Published online: August 30, 2017
© 2017 The Author(s). Published by S. Karger AG, Basel
www.karger.com/cpb

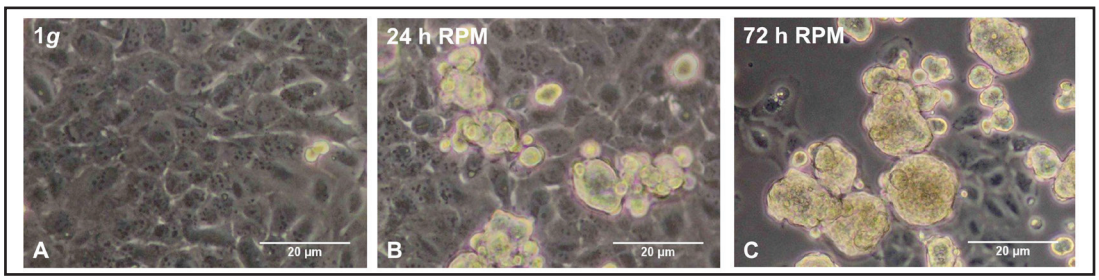


Fig. 1. Phase-contrast microscopy images of Nthy-ori 3-1 cells under 1*g*-conditions and after 24 h and 72 h of exposure to the RPM. Human thyrocytes of the cell line Nthy-ori 3-1 were exposed to the RPM for up to 72 h. Compared to 1*g*-controls (A), which showed only cells growing as adherent monolayers, cells exposed to s-µ*g* generated by the RPM showed no morphological differences after 4 h (data not shown), but started to detach and form 3D aggregates after a 24 h RPM-exposure (B). The MCS increased in number and size over time (72 h), while adherent cells decreased (C).

After the experimental run, cells and supernatants were harvested according to the protocol. The supernatants were collected and centrifuged at 4°C and 3000 rpm. Samples of 1.5 mL were transferred from the supernatants to 2 mL Eppendorf tubes (Eppendorf, Wesseling-Berzdorf, Germany) and frozen at -80°C for MAP analyses. The pellet resulting from centrifugation contained the MCS. After removal of the supernatant, the MCS pellets were snap frozen in liquid nitrogen. AD cells were washed twice with PBS on ice, scraped off the bottom surface and transferred into a tube. After a centrifugation for 10 min at 3000 rpm and 4°C, the supernatant was discarded. The pellets were resuspended in 1 mL PBS and again centrifuged for 10 min at 3000 rpm and 4°C. The remaining supernatant was discarded carefully and the pellets with AD cells snap frozen in liquid nitrogen. Finally, the cells were stored at -80°C.

Phase-contrast microscopy

Phase-contrast microscopy was performed for visual observation of the cellular morphology, using the Leica Microscope (Leica Microsystems CMS GmbH, Germany). Pictures of RPM and control samples were taken after 4 h and 24 h (Fig. 1).

Cytokine measurements by multianalyte profiling (MAP) technology

Cytokines and proteins released into the supernatant were analysed by the company Myriad RBM (Austin, Texas, USA). The MAP analysis was performed using the Human CytokineMAP A and the KidneyMAP® as described previously [24-29]. Supernatants were taken after 4 h, 24 h and 72 h from 1*g*- and RPM-samples (n = 9-10; each group) and stored at -80°C until shipment to Myriad RBM.

RNA isolation and quantitative real-time PCR (qPCR)

RNA isolation was performed using the RNeasy Mini Kit (Qiagen, Hilden, Germany), with an additional DNase digestion step (Qiagen) in order to eliminate residual DNA contaminations. Subsequently, the amount of RNA was quantified via a Photometer Ultrospec2010 (Amersham Biosciences, Freiburg, Germany). The first strand cDNA synthesis kit (Thermo Fisher Scientific, Waltham, US) was used for reverse transcription. qPCR was performed using the 7500 Real-Time PCR System (Applied Biosystems, Darmstadt, Germany) according to routine protocols [30-32]. cDNA-selective-primers were synthesized by TIB Molbiol (Berlin, Germany) and are listed in Table 1. The primers were designed using Primer Express (Applied Biosystems, Darmstadt, Germany) to have a T_m of ~ 60°C and to span exon-exon boundaries. All samples were measured in triplicate. For normalization, 18S rRNA

Table 1. Primers used for quantitative real-time PCR. All sequences are given in 5'-3' direction

Gene	Primer Name	Sequence
18S rRNA	18S-F	GGAGCCTGCGGCTTAATTT
	18S-R	GGAGCCTGCGGCTTAATTT
FN1	FN1-F	AGATCTACCTGTACACCTTGAATGACA
	FN1-R	CATGATACCAGCAAGGAATTGG
IL6	IL6-F	CGGGAACGAAAGAGAAGCTCTA
	IL6-R	GAGCAGCCCCAGGGAGAA
CXCL8	CXCL8-F	TGGCAGCCTTCCTGATTTCT
	CXCL8-R	GGGTGGAAAGGTTTGGAGTATG
CCL2	CCL2-F	GCTATAGAAGAATCACCAGCAGCAA
	CCL2-R	TGGAATCCTGAACCCACTTCTG
LAMA1	LAMA1-F	TGCTCATGGTCAATGCTAATCTG
	LAMA1-R	TCTATCAATCCTCTTCCTTGGACAA
ITGB1	ITGB1-F	GAAAACAGCGCATATCTGGAAAT
	ITGB1-R	CAGCCAATCAGTGATCCACAA
TLN1	TLN1-F	GATGGCTATTACTCAGTACAGACAACTGA
	TLN1-R	CATAGTAGACTCCTCATCTCCTTCCA

All sequences are given in 5'-3' direction

KARGER

Downloaded from http://karger.com/cpb/article-pdf/43/1/257/2444310/000480368.pdf by guest on 31 October 2024

Cellular Physiology and Biochemistry
Cell Physiol Biochem 2017;43:257-270
DOI: 10.1159/000480368
Published online: August 30, 2017
© 2017 The Author(s). Published by S. Karger AG, Basel
www.karger.com/cpb

was used as a housekeeping gene. The comparative C_T ($\Delta\Delta C_T$) method was used for relative quantification of transcription levels and 1*g* was defined as 100 % for reference.

Western blot analyses

Whole cell lysates were used for Western blotting following routine protocols for gel electrophoresis and trans-blotting, as described earlier [31, 33]. Equal amounts of 10 µL lysate containing 2 µg/µL protein were loaded on precast TGX stain-free gels (Bio-Rad, Munich, Germany). Transturbo blot PVDF membranes (Bio-Rad) were used for blotting. Each Western blot contained 5 samples for each group: 4 h 1*g*, 4 h RPM-AD cells, 24 h 1*g*, 24 h RPM AD cells and 24 h RPM MCS.

The following primary antibodies were used at a dilution of 1:1000: fibronectin (F3648), laminin (L9393) and talin (T3287) (all Sigma-Aldrich) and vascular endothelial growth factor (VEGFA; ab46154, Abcam, Cambridge, United Kingdom). The corresponding secondary antibodies were used at a dilution of 1:3000: HRP-linked anti-mouse IgG (#7076) and anti-rabbit IgG (#7074, both Cell Signaling Technology, Massachusetts, USA). The analysis was performed in ChemiDoc XRS+ (Bio-Rad), and the densitometric quantification was performed using ImageLab (BioRad).

Pathway Studio analysis

The commercially available Pathway Studio v.11 (Elsevier Research Solutions, Amsterdam, The Netherlands) was applied for the investigation of mutual regulation networks. For the analysis, SwissProt numbers of the investigated proteins were entered and networks built by the software based on relationships and processes from the literature, PubMed, databases and experimental data [9, 10, 33].

Statistical evaluation

Statistical evaluation was performed with SPSS 15.0 (SPSS, Inc., Chicago, IL, USA) using the Mann-Whitney-U-Test. All data are presented as mean ± standard deviation (SD) values and differences between groups were considered significant at $p < 0.05$.

Results

Multicellular spheroid (MCS) formation

Subconfluent monolayers of the human follicular epithelial thyroid cell line Nthy-ori 3-1 were exposed to the RPM or to 1*g*-control conditions. Both groups were located in parallel in the same incubator. After 4 h, the cells of both RPM and 1*g*-controls groups showed solely adherent growth. MCS formation occurred within 24 h on the RPM (Fig. 1) while cells of the 1*g*-controls continued to grow as a 2D cell monolayer attached to the bottom of the culture flask. In RPM cultures, the mixture of AD cells and MCS remained for up to 72 h of RPM-exposure, although the number of AD cells appeared to decrease slightly. The two cell populations could be harvested separately from the RPM-samples according to the method described above.

Cytokine release of Nthy-ori 3-1 cells after RPM-exposure

Concentrations of selected cytokines within the various culture supernatants were determined by MAP analysis in order to estimate the secretion activities of the cells (Human CytokineMAP A and Human KidneyMAP®, carried out by Myriad RBM). Table 2 shows all of the cytokines of these two MAPs, which could be detected.

Interleukin 6 (IL-6; *IL6*), interleukin 8 (IL-8; *CXCL8*), cystatin-c (*CST3*), tissue inhibitor of metalloproteinase (TIMP-1; *TIMP1*) and VEGF (*VEGF*) could be detected after 4 h, whereas monocyte chemoattractant protein (MCP-1; *CCL2*) could only be detected after 24 h and 72 h and interleukin 7 (IL-7; *IL7*) could only be detected after 72 h and even then only in the RPM-samples.

Although these cytokines have been identified, only five of them revealed significant differences between 1*g* and the respective RPM sample. Cystatin-c (*CST3*) and tissue inhibitor of metalloproteinase-1 (*TIMP1*) were reduced significantly in s-µ*g* compared to 1*g* after 4 h.

Downloaded from http://karger.com/cpb/article-pdf/43/1/257/2444310/000480368.pdf by guest on 31 October 2024

Cellular Physiology and Biochemistry
Cell Physiol Biochem 2017;43:257-270
DOI: 10.1159/000480368
Published online: August 30, 2017
© 2017 The Author(s). Published by S. Karger AG, Basel
www.karger.com/cpb

Table 2. Cytokines released by Nthy-ori 3-1 cells after a 4 h-, 24 h- and 72 h-RPM-exposure, detected by Multi-Analyte Profiling using human CytokineMAP A® and human KidneyMAP®

		4h		24h		72h	
Factors	LDD (pg/mL)	1*g* (pg/mL)	RPM (pg/mL)	1*g* (pg/mL)	RPM (pg/mL)	1*g* (pg/mL)	RPM (pg/mL)
Human CytokineMAP A							
IL-6 (*IL6*)	1.0	15.72 ± 9.12	13.00 ± 4.31	107.78 ± 39.98	102.70 ± 17.06	180.00 ± 26.45	267.22 ± 34.13 *
IL-7 (*IL7*)	6.1	n.d.	n.d.	n.d.	n.d.	n.d.	8.54 ± 0.72
IL-8 (*CXCL8*)	0.56	37.9 ± 19.47	30.4 ± 10.02	324.6 ± 177.32	224.8 ± 54.84	468.4 ± 92.08	642.3 ± 176.16 *
MCP-1 (*CCL2*)	15	n.d.	n.d.	112.22 ± 53.42	66.89 ± 20.09	433.56 ± 82.27	441.1 ± 67.67
Human KidneyMAP®							
Cystatin-c (*CST3*)	20	358.00 ± 87.6	185.56 ± 35.00 *	3,022.2 ± 739.04	2,680.0 ± 727.74	9,755.56 ± 1,101.63	11,190.00 ± 1,781.2
TIMP-1 (*TIMP1*)	6.1	177.00 ± 44.73	102.7 ± 20.78 *	2,410.0 ± 811.73	2,030.0 ± 376.96	6,344.44 ± 869.36	8,366.67 ± 1,531.89*
VEGF (*VEGFA*)	3.9	12.07 ± 2.45	10.85 ± 2.39	110.00 ± 36.33	124.6 ± 38.71	328.56 ± 56.35	359.5 ± 72.24

The gene names of the proteins are given in brackets. Values are given as mean ± SD; 1*g*, ground control; n.d., not detectable; *, P <0.05 vs. 1*g*; LDD (Least Detectable Dose) determined as the mean of 20 blank readings.

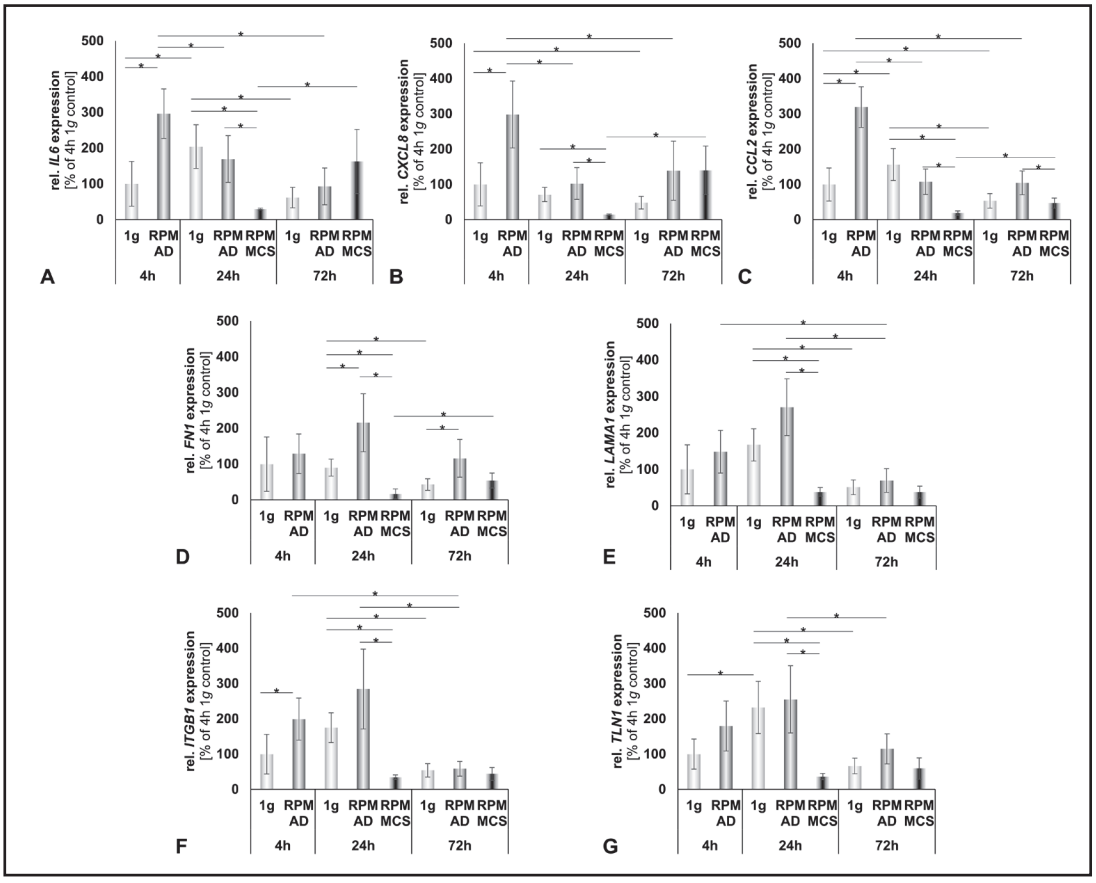


Fig. 2. Quantitative real-time PCR (qPCR) was used to determine the gene expression. The gene expression levels of *IL6* (A), *CXCL8* (B), *CCL2* (C), *FN1* (D), *LAMA1* (E), *ITGB1* (F), and *TLN1* (G) were measured after 4 h, 24 h and 72 h RPM-exposure and in corresponding 1*g*-controls. All values were expressed relative to the value for 4 h of 1*g*, which was set to 100 % and all other values are expressed relative to this value. 1*g* – static control; RPM – random positioning machine; AD – adherent cells; MCS – multicellular spheroids; n = 5-6; * - p<0.05.

After 24 h RPM-exposure, no significant changes could be observed. However, after 72 h, IL-6 (*IL6*), IL-8 (*CXCL8*) as well as TIMP-1 (*TIMP1*) were elevated significantly in s-µ*g* compared to 1*g*-controls.

KARGER

Downloaded from http://karger.com/cpb/article-pdf/43/1/257/2444310/000480368.pdf by guest on 31 October 2024

Cellular Physiology and Biochemistry
Cell Physiol Biochem 2017;43:257-270
DOI: 10.1159/000480368
Published online: August 30, 2017
© 2017 The Author(s). Published by S. Karger AG, Basel
www.karger.com/cpb

Altered gene expression in Nthy-ori 3-1 cells exposed to the RPM

Changes in the mRNA expression levels of *IL6*, *CXCL8* and *CCL2* were investigated by qPCR (Fig. 2A-C). This revealed a significant increase between 1*g*- control cells and RPM-AD cells that had been exposed for 4 h. However, these increases in gene expression were already equalized after 24 h. Interestingly, the gene expression was decreased significantly after 24 h in RPM-MCS samples compared to 1*g*-controls as well as RPM-AD samples. For *IL6* and *CXCL8* no significant alterations were detectable after RPM-exposure for 72 h. *CCL2* gene expression was only reduced significantly compared to RPM-AD samples, but not compared to 1*g*-controls.

Furthermore, we focused on the genes coding for fibronectin (*FN1*), laminin (*LAMA1*), β_1-integrin (*ITGB1*), and talin (*TLN1*), as these are involved in focal adhesion processes. Only *ITGB1* showed a significantly increased gene expression in RPM-AD samples compared to 1*g*-controls after 4 h (Fig. 2F). The other three genes revealed no significant changes at this time point (Fig. 2D, E and G). However, 24 h of RPM exposure triggered a significantly elevated expression in *FN1* in RPM-AD samples compared to 1*g*-controls and MCS, while *TLN1, ITGB1* and *LAMA1* were up-regulated significantly in RPM-AD samples compared to RPM-MCS samples only, but were expressed similarly in 1*g*-control samples. After RPM-exposure for 72 h, only a significant increase in RPM-AD samples compared to 1*g* controls could be detected for *FN1* expression level (Fig. 2D).

Content of selected proteins after RPM-exposure

After focusing on gene expression changes, we studied the ECM and cell adhesion molecules laminin, fibronectin and talin-1 (Fig. 3A, B, and D). The amount of laminin was similar in cells exposed for 4 h to the RPM, but increased after 24 h. There was no significant difference in the laminin protein content after a 24 h-exposure (Fig. 3A). Also, the fibronectin accumulation was approximately equal in samples incubated for 4 h. After 24 h, both, the RPM-AD cells and the RPM-MCS cells exhibited increased amounts of fibronectin (Fig. 3B). Talin-1, which links integrins to the actin cytoskeleton has been shown to be increased slightly in MCS compared to 1*g* and AD cells after RPM-exposure for 24 h. VEGF was released into the supernatant and was unaltered in 1*g*-control cells of thyrocytes cultured for 4 h on the RPM, while RPM-AD cells that had been exposed for 24 h exhibited a lower VEGF content. There was no difference in VEGF content between MCS and 1*g*-control cells (Fig. 3C).

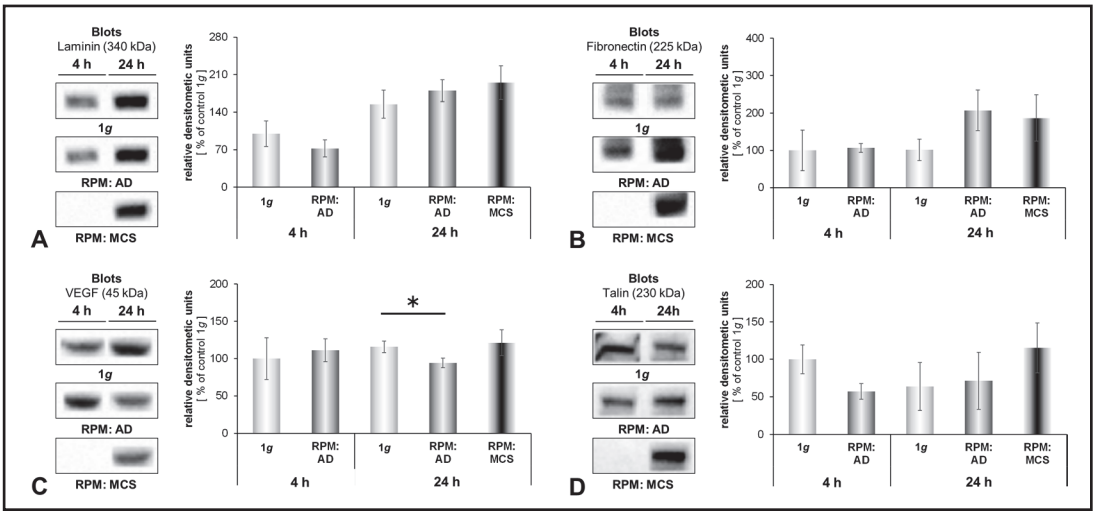


Fig. 3. Content of cell adhesion proteins, VEGF and talin. Nthy-ori 3-1 cells were harvested after 4 h and 24 h of exposure to the RPM or as corresponding 1*g*-controls. The protein contents of laminin (A), fibronectin (B), VEGF (C) and talin (D) were detected by Western blot analyses. Static 1*g*-control (1*g*); random positioning machine (RPM); adherent cells (AD); multicellular spheroids (MCS); n =5; * $p < 0.05$ vs. 1*g*-control.

Downloaded from http://karger.com/cpb/article-pdf/43/1/257/2444310/000480368.pdf by guest on 31 October 2024

Cellular Physiology and Biochemistry
Cell Physiol Biochem 2017;43:257-270
DOI: 10.1159/000480368
Published online: August 30, 2017
© 2017 The Author(s). Published by S. Karger AG, Basel
www.karger.com/cpb

Pathway Analyses

Searching related information via Pathway Studio, proteins of differentially expressed genes and proteins detected in the supernatant of Nthy-ori 3-1 cells were investigated with respect to their cellular localization and their interaction on the protein level (Fig. 4) as well as in regard to their mutual influence on the genetic level (Fig. 5). The cohort of proteins analysed includes the extracellular proteins laminin A1 and fibronectin, the membrane proteins integrin-β_1 and talin-1. These four proteins can bind to each other as shown by the solid lines in Fig. 4 [34, 35]. Their stability is enhanced by a direct interaction with TIMP1 [36] and via an indirect positive action by IL-8 [37]. IL-7 and VEGF also have an influence on the ITGB1, LAMA1, FN1, TLN1 complex [38-40], while IL-6, MCP-1 and cystatin c do not appear to make contact with this complex.

On the gene level *LAMA1* is isolated from the genes of the other soluble and membrane-bound proteins investigated (Fig. 5). Like VEGFA, IL-6 and MCP-1 have positive regulatory effects on the genes of *ITGB1* and *FN1* [41-45]. IL-8 can up-regulate *FN1* expression [46]. *CXCL8* and *CCL2* genes are also up-regulated by VEGF and IL-6 [47, 48], while *TLN1* is down-regulated by IL-6 and IL-8 [49]. In addition, cystatin c affects turnover of fibronectin [50] and IL-7 regulates the expression of *CCL2* and *CXCL8* [51].

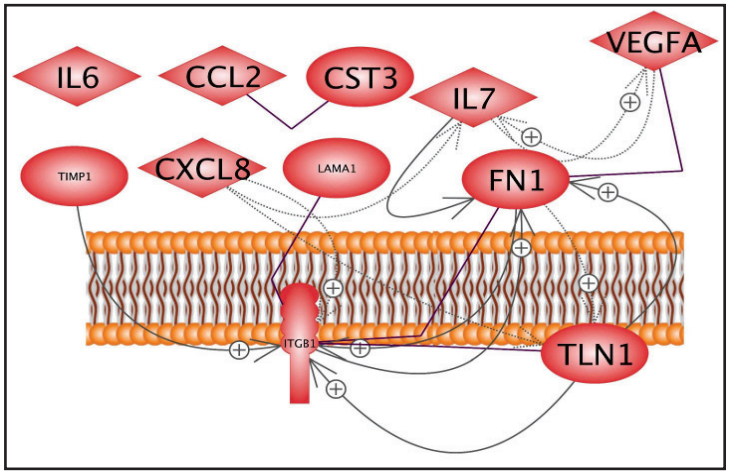


Fig. 4. Mutual interaction and localization of the 11 investigated proteins. Interaction and localization of cytokines observed in cell culture supernatants (Table 2) and of proteins whose genes were sensitive to exposure to the RPM (Fig. 2). Solid lines indicate binding, solid arrows show directed interaction, dashed arrows show influence. + signs point to an activity enhancing effect. The interaction network was built up using Pathway Studio v.11.

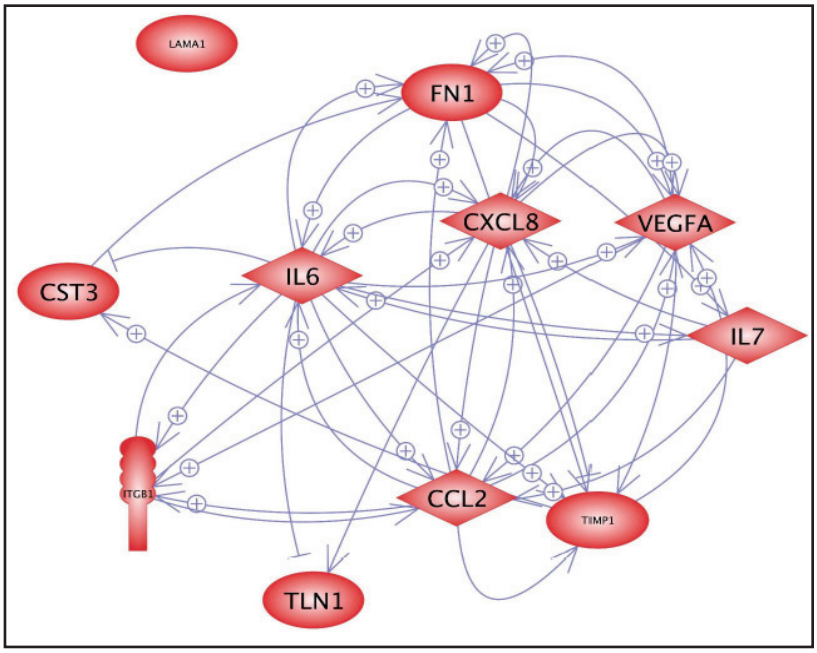


Fig. 5. Mutual interaction of selected genes at the gene expression level. Selected genes, whose up- or down-regulation were analysed by qPCR after RPM-exposure as shown in Fig. 2 together with the genes of the proteins secreted into the supernatant as shown in Table 2. The arrows indicate influence. Arrows with + sign indicate up-regulation, while lines with crossbars at the end show down-regulation. The interaction network was built up using Pathway Studio v.11.

KARGER

Downloaded from http://karger.com/cpb/article-pdf/43/1/257/2444310/000480368.pdf by guest on 31 October 2024

Cellular Physiology and Biochemistry
Cell Physiol Biochem 2017;43:257-270
DOI: 10.1159/000480368
Published online: August 30, 2017
© 2017 The Author(s). Published by S. Karger AG, Basel
www.karger.com/cpb

Discussion

In this study, we investigated the morphological and molecular biological changes of normal human thyrocytes (Nthy-ori 3-1 cell line) exposed for 4 h, 24 h and 72 h to a an RPM. The objective of this project was to monitor changes occurring during short-term RPM-exposure in normal human thyrocytes with respect to the influence of soluble factors on proteins involved in focal adhesion. These findings might help to further understand the observed impact of microgravity on the formation of 3D aggregates of normal human thyrocytes and other cells [4, 5].

MCS formation

One part of the RPM-exposed normal human thyroid cells of the Nthy-ori 3-1 cell line formed MCS, while the other part continued to grow adherently. The MCS became visible after 24 h. This observation broadens the observation made by Kopp et al., who investigated MCS after 7 and 14 days [21]. This early 3D growth is in agreement with the formation of cancer MCS by the thyroid cancer cells lines ML-1, FTC-133 and RO82-W-1 [12, 21, 28, 49]. Like the thyroid cancer cells FTC-133, the normal Nthy-ori 3-1 cells required a lag time of several hours of RPM-exposure, before some of the cells started to detach from the bottom of the culture flask and to assemble to 3D aggregates [28], while others remained adherent. Hence, regarding the morphological changes triggered by s-μ*g*, a striking difference between normal and cancer cells could not be detected.

Genes and proteins altered by RPM-exposure

Investigating cytokines, we found an influence of s-μ*g* on IL-6 (*IL6*) and IL-8 (*CXCL8*) at gene and protein secretion levels (Table 2, Fig. 2). The cytokines IL-6 and IL-8 are involved in angiogenesis and progression in different cancer types [52-54]. On the RPM, their genes were up-regulated significantly after 4 h in RPM-AD cells. However, after 24 h both were un-regulated again in RPM-AD cells, but were down-regulated significantly in MCS cells (Fig. 2). During the next 48 h a slight tendency of up-regulation in AD as well as MCS cells was observed although this was not significant (Fig. 2A, B). In parallel, the secretion of IL-6 and IL-8 into the supernatant did not reveal any alteration due to s-μg until 72 h when both proteins were up-regulated significantly in RPM-exposed cells (Table 2).

IL-6 and IL-8 play a key role in angiogenesis and 3D growth in cancer [55, 56]. IL-6 induces the production of VEGF [57] and a similar function is assumed for IL-8 (Fig. 5). When secreted by U937 cells IL-8 induces the fibronectin expression by inflammatory breast cancer cells (SUM149 cell line) via interaction with IL-8 specific receptors and stimulation of the PI3K/Akt signalling pathway [46].

IL-6 and IL-8 influence the formation and growth of MCS established under 1*g*-conditions [49, 58]. Recently, we demonstrated their direct impact using the liquid-overlay technique [49]. The cytokines IL-6 and IL-8 are strong regulators controlling *FN1* and *ITGB1* expression (Fig. 5). Furthermore, both cytokines were increased significantly in space samples of human thyroid cancer FTC-133 cells cultured in r-μ*g* conditions for 12 days on the International Space Station compared with 1*g*-controls [9]. However, in this case no MCS formation could be observed whereas during another spaceflight on which FTC-133 cells were grown for 10 days in μ*g* and MCS were formed, no differences between ground and space samples could be observed for IL-6 and only a slight decrease was observed for IL-8 [7]. How these findings can be explained regarding the role of IL-6 and IL-8 in 3D growth has to be elucidated in future space experiments.

An important finding was the detection of IL-7 in the supernatant after RPM-exposure for 72 h (Table 2). Interestingly, control samples did not secrete IL-7. IL-7 is considered a powerful pro-inflammatory cytokine, which can induce tumorigenesis [59]. A variety of cells, for example intestinal epithelial cells, keratinocytes, hepatic tissue, endothelial cells, smooth muscle cells, fibroblasts, thyroid cancer cells and others, have proven to produce IL-7 [21, 60]. IL-6 interacts with IL-7 and vice versa (Fig. 5). Together they have a regulatory influence on

Downloaded from http://karger.com/cpb/article-pdf/43/1/257/2444310/000480368.pdf by guest on 31 October 2024

Cellular Physiology and Biochemistry
Cell Physiol Biochem 2017;43:257-270
DOI: 10.1159/000480368
Published online: August 30, 2017
© 2017 The Author(s). Published by S. Karger AG, Basel
www.karger.com/cpb

cell-cell adhesion of melanocytes [61], but no data exist concerning the interaction between IL-6 and IL-7 for normal thyroid cells. In our experiments the cells secreted IL-7 only after 72 h on the RPM, while the corresponding 1*g*-control cells did not secrete this cytokine at all. However, it could be shown that Nthy-ori 3-1 cells secrete IL-7 after 7 days when cultured under normal 1*g*-conditons and on the RPM [21].

In addition, IL-7 can influence ECM production and decrease fibronectin expression. This was shown in human subconjunctival fibroblasts [62]. In our experiments the *FN1* gene expression was elevated in Nthy-ori 3-1 AD cells after RPM-exposure for 24 h compared with 1*g*-control cells, while the *FN1* mRNA was down-regulated in MCS cells (Fig. 2A). After a 72 h RPM-exposure, the *FN1* expression was still down-regulated in Nthy-ori 3-1 MCS compared to AD cells. This finding was paralleled by the secretion of IL-7 by the RPM-mounted thyroid cells after 72 h and might demonstrate a regulatory interaction of IL-7 with fibronectin (Fig. 4). In addition, these data suggest that the cytokine IL-7 might be a very likely key candidate involved in regulating MCS formation [21].

Integrins are transmembrane α- and β-subunit forming receptors for distinct ECM proteins, such as fibronectin, or laminin [63]. They mediate the cell adhesion to ECM components supporting adhesion of cells grown on two-dimensional surfaces and within three-dimensional matrices [64]. Although integrins consist of α- and β-subunit, incorporated β_1-integrin seems to play a special role increasing cell migration and invasion, and decreasing sensitivity to anti-cancer drug in triple-negative breast cancer [65]. Overexpression of β_1-integrin has been demonstrated to improve the activities and functions of several benign cell types [66]. For example, r-μ*g* during a parabolic flight induced β_1-integrin expression in human chondrocytes [67].

The role that laminin plays in MCS formation remains to be elucidated. However, it is a fact that laminins interact with several integrin isoforms and are involved in migration and development [35, 68]. Moreover, since the gene expression of *LAMA1* was down-regulated in MCS cells, an impact of this gene or protein seems to be very likely. Interestingly, laminin A1 was not detected in a recent proteome study, which revealed more than 5000 proteins of thyroid cancer cells [69]. Therefore, the presence of laminin A1 could be a sign of normal cell differentiation as was shown for human mesenchymal stem cells [70].

Talin (*TLN1*) is found in high concentrations in focal adhesions and links integrins to the actin cytoskeleton [71]. Due to its direct interaction with β_1-integrin (Fig. 4), we analysed the gene expression of *TLN1*. In Nthy-ori 3-1 cells, the *TLN1* mRNA was found to be down-regulated significantly in MCS after RPM-exposure for 24 h, but without differences to normal gravity after 4 and 72 h. It has been shown that TLN1 is involved in RPM-dependent thyroid carcinoma MCS formation [8]. Regarding the findings described above, the *TLN1* gene expression might point to the time frame in which the detachment and subsequent formation of MCS occurs.

VEGF was detectable in Nthy-ori 3-1 cells and the secretion of VEGF increased over time in the supernatant (Table 2). No difference between 1*g*-controls and RPM-samples could be observed up until 72 h. VEGF plays an important role in neoangiogenesis, proliferation and migration, mainly of endothelial cells but also of various other cells types [72-74]. VEGF seems to be affected considerably in thyroid cancer cells exposed to s-μ*g* [72, 75]. Furthermore, there might be a delayed response in Nthy-ori 3-1 cells, when exposed to s-μ*g*. It could be shown that VEGF secretion was decreased after RPM-exposure for 7d [21].

The secretion of TIMP-1 was significantly lower after 4 h in RPM-samples compared with 1*g*-controls, whereas a 1.32-fold elevated amount of TIMP-1 was measured after 72 h in the supernatant of RPM-samples. TIMPs inhibit metalloproteinases, which in turn are widely known to degrade the ECM and thus participate in remodelling the shape and composition of cell aggregates and tissues [76, 77]. An overexpression of TIMP-1 was also implicated in several cancer types and correlated with a less-positive outcome for a patient after treatment [76]. A decreased expression of TIMP-1 seems to facilitate the detachment of the thyroid Nthy-ori 3-1 cells from the bottom of cell culture flasks in the early hours of RPM-exposure (Table 2) due to a failure to stabilize integrin-β_1 activity [36]. The later increase might be a

Downloaded from http://karger.com/cpb/article-pdf/43/1/257/2444310/000480368.pdf by guest on 31 October 2024

Cellular Physiology and Biochemistry
Cell Physiol Biochem 2017;43:257-270
DOI: 10.1159/000480368
Published online: August 30, 2017
© 2017 The Author(s). Published by S. Karger AG, Basel
www.karger.com/cpb

facilitator of cell-cell contacts during the rearrangement of the focal adhesion complex for 3D cell aggregate formation [69]. A similar influence could be observed in endothelial cells. Even after 7 d and 14 d of RPM-exposure, the amount of TIMP-1 was reduced significantly in s-µ*g* [24]. These data indicate the involvement of TIMP-1 in 3D formation of MCS, which contain a high amount of ECM proteins.

Cystatin-c is secreted as an extracellular polypeptide and functions biologically as a protease inhibitor. Dysregulated cystatin-c levels are implicated in various clinical diseases [78]. The secretion of cystatin-c was decreased significantly after 4 h of RPM-exposure. Later on, no differences between the different groups were evident. As cystatin-c was down-regulated together with TIMP-1 a general inhibition of ECM degradation seems to be a result of microgravity. Further experiments should be conducted to verify this hypothesis.

MCP-1 is a key member of the large family of chemokines which regulate mainly cell trafficking. MCP-1 itself is associated with regulating migration and infiltration of monocytes/macrophages [79]. Many experiments were conducted focusing on MCP-1 and its involvement in various diseases like hypertension, inflammatory or neuronal diseases and cancer. A high or constitutive expression level of *CCL2* is often observed [80-82]. The human thyroid Nthy-ori 3-1 cells secrete MCP-1 after 24 h in a continually increasing amount of MCP-1 although no differences could be observed between normal gravity and s-µ*g*. These findings are in accordance with the earlier results regarding MCP-1 in the supernatant of Nthy-ori 3-1 cells cultivated on the RPM for 7 d [21]. Whether this expression has an impact on the signal transduction or if the MCP-1 specific receptor CCR2 [83] is even expressed, remains to be elucidated.

Conclusion

The normal human thyroid cell line Nthy-ori 3-1 was shown to form MCS as early as 24 h after RPM-exposure. The secretion of several cytokines in connection with focal adhesion proteins paint a picture of entangled and positively or negatively interacting proteins which might strengthen the onset of the MCS formation. Further analyses will have to be performed to elucidate in more detail how these cytokines exert their effect. Though MCS formation is induced by exposing cells to an RPM, which is comparable to their behaviour in r-µ*g*, our results indicate what might happen during a spaceflight. However, they have to be verified under this condition.

Acknowledgements

The authors would like to thank the German Space Agency (DLR; (DG) BMWi projects 50WB1124 and 50WB1524), Aarhus University, Denmark, and DGLRM (Young Fellow Program for EW). We would like to thank the team of PRS & EJE Hertfordshire, UK, for academic proofreading of the manuscript. The funders had no role in study design, data collection and analysis, decision to publish, or preparation of the manuscript. EW is a doctoral candidate of the Helmholtz Space Life Sciences Research School, German Aerospace Centre Cologne, Germany. We like to thank the PhD school for support.

Disclosure Statement

The authors declare no competing financial interest.

References

1 White RJ, Averner M: Humans in space. Nature 2001;409:1115-1118.
2 Grimm D, Wise P, Lebert M, Richter P, Baatout S: How and why does the proteome respond to microgravity? Expert Rev Proteomics 2011;8:13-27.

Downloaded from http://karger.com/cpb/article-pdf/43/1/257/2444310/000480368.pdf by guest on 31 October 2024

Cellular Physiology and Biochemistry
Cell Physiol Biochem 2017;43:257-270
DOI: 10.1159/000480368
Published online: August 30, 2017
© 2017 The Author(s). Published by S. Karger AG, Basel
www.karger.com/cpb

3 Rea G, Cristofaro F, Pani G, Pascucci B, Ghuge SA, Corsetto PA, Imbriani M, Visai L, Rizzo AM: Microgravity-driven remodeling of the proteome reveals insights into molecular mechanisms and signal networks involved in response to the space flight environment. J Proteomics 2016;137:3-18.
4 Albi E, Curcio F, Lazzarini A, Floridi A, Cataldi S, Lazzarini R, Loreti E, Ferri I, Ambesi-Impiombato FS: How microgravity changes galectin-3 in thyroid follicles. Biomed Res Int 2014;2014:652863.
5 Masini MA, Albi E, Barmo C, Bonfiglio T, Bruni L, Canesi L, Cataldi S, Curcio F, D'Amora M, Ferri I, Goto K, Kawano F, Lazzarini R, Loreti E, Nakai N, Ohira T, Ohira Y, Palmero S, Prato P, Ricci F, Scarabelli L, Shibaguchi T, Spelat R, Strollo F, Ambesi-Impiombato FS: The impact of long-term exposure to space environment on adult mammalian organisms: a study on mouse thyroid and testis. PLoS One 2012;7:e35418.
6 Pietsch J, Ma X, Wehland M, Aleshcheva G, Schwarzwalder A, Segerer J, Birlem M, Horn A, Bauer J, Infanger M, Grimm D: Spheroid formation of human thyroid cancer cells in an automated culturing system during the Shenzhou-8 Space mission. Biomaterials 2013;34:7694-7705.
7 Ma X, Pietsch J, Wehland M, Schulz H, Saar K, Hubner N, Bauer J, Braun M, Schwarzwalder A, Segerer J, Birlem M, Horn A, Hemmersbach R, Wasser K, Grosse J, Infanger M, Grimm D: Differential gene expression profile and altered cytokine secretion of thyroid cancer cells in space. FASEB J 2014;28:813-835.
8 Grosse J, Wehland M, Pietsch J, Schulz H, Saar K, Hubner N, Eilles C, Bauer J, Abou-El-Ardat K, Baatout S, Ma X, Infanger M, Hemmersbach R, Grimm D: Gravity-sensitive signaling drives 3-dimensional formation of multicellular thyroid cancer spheroids. FASEB J 2012;26:5124-5140.
9 Riwaldt S, Pietsch J, Sickmann A, Bauer J, Braun M, Segerer J, Schwarzwalder A, Aleshcheva G, Corydon TJ, Infanger M, Grimm D: Identification of proteins involved in inhibition of spheroid formation under microgravity. Proteomics 2015;15:2945-2952.
10 Riwaldt S, Bauer J, Pietsch J, Braun M, Segerer J, Schwarzwalder A, Corydon TJ, Infanger M, Grimm D: The Importance of Caveolin-1 as Key-Regulator of Three-Dimensional Growth in Thyroid Cancer Cells Cultured under Real and Simulated Microgravity Conditions. Int J Mol Sci 2015;16:28296-28310.
11 Bauer J, Wehland M, Pietsch J, Sickmann A, Weber G, Grimm D: Annotated Gene and Proteome Data Support Recognition of Interconnections Between the Results of Different Experiments in Space Research. Microgravity Sci Technol 2016;28:357-365.
12 Grimm D, Bauer J, Kossmehl P, Shakibaei M, Schoberger J, Pickenhahn H, Schulze-Tanzil G, Vetter R, Eilles C, Paul M, Cogoli A: Simulated microgravity alters differentiation and increases apoptosis in human follicular thyroid carcinoma cells. FASEB J 2002;16:604-606.
13 Brungs S, Egli M, Wuest SL, M. Christianen PC, W. A. van Loon JJ, Ngo Anh TJ, Hemmersbach R: Facilities for Simulation of Microgravity in the ESA Ground-Based Facility Programme. Microgravity Sci Technol 2016;28:191-203.
14 Warnke E, Kopp S, Wehland M, Hemmersbach R, Bauer J, Pietsch J, Infanger M, Grimm D: Thyroid Cells Exposed to Simulated Microgravity Conditions – Comparison of the Fast Rotating Clinostat and the Random Positioning Machine. Microgravity Sci Technol 2016;28:247-260.
15 Hanley P, Lord K, Bauer AJ: Thyroid Disorders in Children and Adolescents: A Review. JAMA Pediatr 2016;170:1008-1019.
16 Ito K, Kagaya Y, Shimokawa H: Thyroid hormone and chronically unloaded hearts. Vascul Pharmacol 2010;52:138-141.
17 Martin A, Zhou A, Gordon RE, Henderson SC, Schwartz AE, Schwartz AE, Friedman EW, Davies TF: Thyroid organoid formation in simulated microgravity: influence of keratinocyte growth factor. Thyroid 2000;10:481-487.
18 Albi E, Ambesi-Impiombato FS, Peverini M, Damaskopoulou E, Fontanini E, Lazzarini R, Curcio F, Perrella G: Thyrotropin receptor and membrane interactions in FRTL-5 thyroid cell strain in microgravity. Astrobiology 2011;11:57-64.
19 Albi E, Curcio F, Lazzarini A, Floridi A, Cataldi S, Lazzarini R, Loreti E, Ferri I, Ambesi-Impiombato FS: A firmer understanding of the effect of hypergravity on thyroid tissue: cholesterol and thyrotropin receptor. PLoS One 2014;9:e98250.
20 Pietsch J, Sickmann A, Weber G, Bauer J, Egli M, Wildgruber R, Infanger M, Grimm D: A proteomic approach to analysing spheroid formation of two human thyroid cell lines cultured on a random positioning machine. Proteomics 2011;11:2095-2104.

Downloaded from http://karger.com/cpb/article-pdf/43/1/257/2444310/000480368.pdf by guest on 31 October 2024

Cellular Physiology and Biochemistry
Cell Physiol Biochem 2017;43:257-270
DOI: 10.1159/000480368
Published online: August 30, 2017
© 2017 The Author(s). Published by S. Karger AG, Basel
www.karger.com/cpb

21 Kopp S, Warnke E, Wehland M, Aleshcheva G, Magnusson NE, Hemmersbach R, Corydon TJ, Bauer J, Infanger M, Grimm D: Mechanisms of three-dimensional growth of thyroid cells during long-term simulated microgravity. Sci Rep 2015;5:16691.
22 Lemoine NR, Mayall ES, Jones T, Sheer D, McDermid S, Kendall-Taylor P, Wynford-Thomas D: Characterisation of human thyroid epithelial cells immortalised *in vitro* by simian virus 40 DNA transfection. Br J Cancer 1989;60:897-903.
23 Borst AG, van Loon JJWA: Technology and Developments for the Random Positioning Machine, RPM. Microgravity Sci Technol 2008;21:287-292.
24 Grimm D, Infanger M, Westphal K, Ulbrich C, Pietsch J, Kossmehl P, Vadrucci S, Baatout S, Flick B, Paul M, Bauer J: A delayed type of three-dimensional growth of human endothelial cells under simulated weightlessness. Tissue Eng Part A 2009;15:2267-2275.
25 Grimm D, Bauer J, Ulbrich C, Westphal K, Wehland M, Infanger M, Aleshcheva G, Pietsch J, Ghardi M, Beck M, El-Saghire H, de Saint-Georges L, Baatout S: Different responsiveness of endothelial cells to vascular endothelial growth factor and basic fibroblast growth factor added to culture media under gravity and simulated microgravity. Tissue Eng Part A 2010;16:1559-1573.
26 Grosse J, Warnke E, Pohl F, Magnusson NE, Wehland M, Infanger M, Eilles C, Grimm D: Impact of sunitinib on human thyroid cancer cells. Cell Physiol Biochem 2013;32:154-170.
27 Infanger M, Ulbrich C, Baatout S, Wehland M, Kreutz R, Bauer J, Grosse J, Vadrucci S, Cogoli A, Derradji H, Neefs M, Kusters S, Spain M, Paul M, Grimm D: Modeled gravitational unloading induced downregulation of endothelin-1 in human endothelial cells. J Cell Biochem 2007;101:1439-1455.
28 Warnke E, Pietsch J, Wehland M, Bauer J, Infanger M, Gorog M, Hemmersbach R, Braun M, Ma X, Sahana J, Grimm D: Spheroid formation of human thyroid cancer cells under simulated microgravity: a possible role of CTGF and CAV1. Cell Commun Signal 2014;12:32.
29 Grosse J, Warnke E, Wehland M, Pietsch J, Pohl F, Wise P, Magnusson NE, Eilles C, Grimm D: Mechanisms of apoptosis in irradiated and sunitinib-treated follicular thyroid cancer cells. Apoptosis 2014;19:480-490.
30 Infanger M, Faramarzi S, Grosse J, Kurth E, Ulbrich C, Bauer J, Wehland M, Kreutz R, Kossmehl P, Paul M, Grimm D: Expression of vascular endothelial growth factor and receptor tyrosine kinases in cardiac ischemia/reperfusion injury. Cardiovasc Pathol 2007;16:291-299.
31 Kossmehl P, Kurth E, Faramarzi S, Habighorst B, Shakibaei M, Wehland M, Kreutz R, Infanger M, AH JD, Grosse J, Paul M, Grimm D: Mechanisms of apoptosis after ischemia and reperfusion: role of the renin-angiotensin system. Apoptosis 2006;11:347-358.
32 Rothermund L, Kreutz R, Kossmehl P, Fredersdorf S, Shakibaei M, Schulze-Tanzil G, Paul M, Grimm D: Early onset of chondroitin sulfate and osteopontin expression in angiotensin II-dependent left ventricular hypertrophy. Am J Hypertens 2002;15:644-652.
33 Kopp S, Slumstrup L, Corydon TJ, Sahana J, Aleshcheva G, Islam T, Magnusson NE, Wehland M, Bauer J, Infanger M, Grimm D: Identifications of novel mechanisms in breast cancer cells involving duct-like multicellular spheroid formation after exposure to the Random Positioning Machine. Sci Rep 2016;6:26887.
34 Green JA, Berrier AL, Pankov R, Yamada KM: beta1 integrin cytoplasmic domain residues selectively modulate fibronectin matrix assembly and cell spreading through talin and Akt-1. J Biol Chem 2009;284:8148-8159.
35 Ichikawa-Tomikawa N, Ogawa J, Douet V, Xu Z, Kamikubo Y, Sakurai T, Kohsaka S, Chiba H, Hattori N, Yamada Y, Arikawa-Hirasawa E: Laminin alpha1 is essential for mouse cerebellar development. Matrix Biol 2012;31:17-28.
36 Jung KK, Liu XW, Chirco R, Fridman R, Kim HR: Identification of CD63 as a tissue inhibitor of metalloproteinase-1 interacting cell surface protein. EMBO J 2006;25:3934-3942.
37 Xie K: Interleukin-8 and human cancer biology. Cytokine Growth Factor Rev 2001;12:375-391.
38 Shao B, Yago T, Coghill PA, Klopocki AG, Mehta-D'souza P, Schmidtke DW, Rodgers W, McEver RP: Signal-dependent slow leukocyte rolling does not require cytoskeletal anchorage of P-selectin glycoprotein ligand-1 (PSGL-1) or integrin alphaLbeta2. J Biol Chem 2012;287:19585-19598.
39 Ariel A, Hershkoviz R, Cahalon L, Williams DE, Akiyama SK, Yamada KM, Chen C, Alon R, Lapidot T, Lider O: Induction of T cell adhesion to extracellular matrix or endothelial cell ligands by soluble or matrix-bound interleukin-7. Eur J Immunol 1997;27:2562-2570.

KARGER

Downloaded from http://karger.com/cpb/article-pdf/43/1/257/2444310/000480368.pdf by guest on 31 October 2024

Cellular Physiology and Biochemistry
Cell Physiol Biochem 2017;43:257-270
DOI: 10.1159/000480368
Published online: August 30, 2017
© 2017 The Author(s). Published by S. Karger AG, Basel
www.karger.com/cpb

40 Mitsi M, Hong Z, Costello CE, Nugent MA: Heparin-mediated conformational changes in fibronectin expose vascular endothelial growth factor binding sites. Biochemistry 2006;45:10319-10328.
41 Zhang GJ, Crist SA, McKerrow AK, Xu Y, Ladehoff DC, See WA: Autocrine IL-6 production by human transitional carcinoma cells upregulates expression of the alpha5beta1 firbonectin receptor. J Urol 2000;163:1553-1559.
42 Suhr KB, Tsuboi R, Seo EY, Piao YJ, Lee JH, Park JK, Ogawa H: Sphingosylphosphorylcholine stimulates cellular fibronectin expression through upregulation of IL-6 in cultured human dermal fibroblasts. Arch Dermatol Res 2003;294:433-437.
43 Giunti S, Tesch GH, Pinach S, Burt DJ, Cooper ME, Cavallo-Perin P, Camussi G, Gruden G: Monocyte chemoattractant protein-1 has prosclerotic effects both in a mouse model of experimental diabetes and *in vitro* in human mesangial cells. Diabetologia 2008;51:198-207.
44 Ashida N, Arai H, Yamasaki M, Kita T: Distinct signaling pathways for MCP-1-dependent integrin activation and chemotaxis. J Biol Chem 2001;276:16555-16560.
45 Ancelin M, Chollet-Martin S, Herve MA, Legrand C, El Benna J, Perrot-Applanat M: Vascular endothelial growth factor VEGF189 induces human neutrophil chemotaxis in extravascular tissue via an autocrine amplification mechanism. Lab Invest 2004;84:502-512.
46 Mohamed MM: Monocytes conditioned media stimulate fibronectin expression and spreading of inflammatory breast cancer cells in three-dimensional culture: A mechanism mediated by IL-8 signaling pathway. Cell Commun Signal 2012;10:3.
47 Lee TH, Avraham H, Lee SH, Avraham S: Vascular endothelial growth factor modulates neutrophil transendothelial migration via up-regulation of interleukin-8 in human brain microvascular endothelial cells. J Biol Chem 2002;277:10445-10451.
48 Heinrich PC, Behrmann I, Haan S, Hermanns HM, Muller-Newen G, Schaper F: Principles of interleukin (IL)-6-type cytokine signalling and its regulation. Biochem J 2003;374:1-20.
49 Svejgaard B, Wehland M, Ma X, Kopp S, Sahana J, Warnke E, Aleshcheva G, Hemmersbach R, Hauslage J, Grosse J, Bauer J, Corydon TJ, Islam T, Infanger M, Grimm D: Common Effects on Cancer Cells Exerted by a Random Positioning Machine and a 2D Clinostat. PLoS One 2015;10:e0135157.
50 Nikitovic D, Juranek I, Wilks MF, Tzardi M, Tsatsakis A, Tzanakakis GN: Anthracycline-dependent cardiotoxicity and extracellular matrix remodeling. Chest 2014;146:1123-1130.
51 Damas JK, Waehre T, Yndestad A, Otterdal K, Hognestad A, Solum NO, Gullestad L, Froland SS, Aukrust P: Interleukin-7-mediated inflammation in unstable angina: possible role of chemokines and platelets. Circulation 2003;107:2670-2676.
52 Kobawala TP, Trivedi TI, Gajjar KK, Patel DH, Patel GH, Ghosh NR: Significance of Interleukin-6 in Papillary Thyroid Carcinoma. J Thyroid Res 2016;2016:6178921.
53 Kumari N, Dwarakanath BS, Das A, Bhatt AN: Role of interleukin-6 in cancer progression and therapeutic resistance. Tumour Biol 2016;9: 11553-11572.
54 Shi J, Wei PK: Interleukin-8: A potent promoter of angiogenesis in gastric cancer. Oncol Lett 2016;11:1043-1050.
55 Mihara M, Hashizume M, Yoshida H, Suzuki M, Shiina M: IL-6/IL-6 receptor system and its role in physiological and pathological conditions. Clin Sci (Lond) 2012;122:143-159.
56 Singh JK, Simoes BM, Howell SJ, Farnie G, Clarke RB: Recent advances reveal IL-8 signaling as a potential key to targeting breast cancer stem cells. Breast Cancer Res 2013;15:210.
57 Tartour E, Pere H, Maillere B, Terme M, Merillon N, Taieb J, Sandoval F, Quintin-Colonna F, Lacerda K, Karadimou A, Badoual C, Tedgui A, Fridman WH, Oudard S: Angiogenesis and immunity: a bidirectional link potentially relevant for the monitoring of antiangiogenic therapy and the development of novel therapeutic combination with immunotherapy. Cancer Metastasis Rev 2011;30:83-95.
58 Provatopoulou X, Georgiadou D, Sergentanis TN, Kalogera E, Spyridakis J, Gounaris A, Zografos GN: Interleukins as markers of inflammation in malignant and benign thyroid disease. Inflamm Res 2014;63:667-674.
59 Zarogoulidis P, Lampaki S, Yarmus L, Kioumis I, Pitsiou G, Katsikogiannis N, Hohenforst-Schmidt W, Li Q, Huang H, Sakkas A, Organtzis J, Sakkas L, Mpoukovinas I, Tsakiridis K, Lazaridis G, Syrigos K, Zarogoulidis K: Interleukin-7 and interleukin-15 for cancer. J Cancer 2014;5:765-773.
60 Jiang Q, Li WQ, Aiello FB, Mazzucchelli R, Asefa B, Khaled AR, Durum SK: Cell biology of IL-7, a key lymphotrophin. Cytokine Growth Factor Rev 2005;16:513-533.

Downloaded from http://karger.com/cpb/article-pdf/43/1/257/2444310/000480368.pdf by guest on 31 October 2024

Cellular Physiology and Biochemistry
Cell Physiol Biochem 2017;43:257-270
DOI: 10.1159/000480368
Published online: August 30, 2017
© 2017 The Author(s). Published by S. Karger AG, Basel
www.karger.com/cpb

61 Kirnbauer R, Charvat B, Schauer E, Kock A, Urbanski A, Forster E, Neuner P, Assmann I, Luger TA, Schwarz T: Modulation of intercellular adhesion molecule-1 expression on human melanocytes and melanoma cells: evidence for a regulatory role of IL-6, IL-7, TNF beta, and UVB light. J Invest Dermatol 1992;98:320-326.
62 Yamanaka O, Saika S, Ikeda K, Miyazaki K, Ohnishi Y, Ooshima A: Interleukin-7 modulates extracellular matrix production and TGF-beta signaling in cultured human subconjunctival fibroblasts. Curr Eye Res 2006;31:491-499.
63 Hynes RO: Integrins: bidirectional, allosteric signaling machines. Cell 2002;110:673-687.
64 Kubow KE, Horwitz AR: Reducing background fluorescence reveals adhesions in 3D matrices. Nat Cell Biol 2011;13:3-5.
65 Yin HL, Wu CC, Lin CH, Chai CY, Hou MF, Chang SJ, Tsai HP, Hung WC, Pan MR, Luo CW: beta1 Integrin as a Prognostic and Predictive Marker in Triple-Negative Breast Cancer. Int J Mol Sci 2016;17: 1432.
66 Liang W, Zhu C, Liu F, Cui W, Wang Q, Chen Z, Zhou Q, Xu S, Zhai C, Fan W: Integrin beta1 Gene Therapy Enhances *in Vitro* Creation of Tissue-Engineered Cartilage Under Periodic Mechanical Stress. Cell Physiol Biochem 2015;37:1301-1314.
67 Aleshcheva G, Wehland M, Sahana J, Bauer J, Corydon TJ, Hemmersbach R, Frett T, Egli M, Infanger M, Grosse J, Grimm D: Moderate alterations of the cytoskeleton in human chondrocytes after short-term microgravity produced by parabolic flight maneuvers could be prevented by up-regulation of BMP-2 and SOX-9. FASEB J 2015;29:2303-2314.
68 Savino W, Mendes-da-Cruz DA, Golbert DC, Riederer I, Cotta-de-Almeida V: Laminin-Mediated Interactions in Thymocyte Migration and Development. Front Immunol 2015;6:579.
69 Bauer J, Kopp S, Schlagberger EM, Grosse J, Sahana J, Riwaldt S, Wehland M, Luetzenberg R, Infanger M, Grimm D: Proteome Analysis of Human Follicular Thyroid Cancer Cells Exposed to the Random Positioning Machine. Int J Mol Sci 2017;18: 546.
70 Kim TO, Park SH, Kim HS, Ahuja N, Yi JM: DNA methylation changes in extracellular remodeling pathway genes during the transformation of human mesenchymal stem cells. Genes Genomics 2016;38:611-619.
71 Vignoud L, Albiges-Rizo C, Frachet P, Block MR: NPXY motifs control the recruitment of the alpha5beta1 integrin in focal adhesions independently of the association of talin with the beta1 chain. J Cell Sci 1997;110:1421-1430.
72 Grimm D, Bauer J, Schoenberger J: Blockade of neoangiogenesis, a new and promising technique to control the growth of malignant tumors and their metastases. Curr Vasc Pharmacol 2009;7:347-357.
73 Hu K, Olsen BR: Vascular endothelial growth factor control mechanisms in skeletal growth and repair. Dev Dyn 2017;246:227-234.
74 Pożarowska D, Pożarowski P: The era of anti-vascular endothelial growth factor (VEGF) drugs in ophthalmology, VEGF and anti-VEGF therapy. Cent Eur J Immunol 2016;41:311-316.
75 Wehland M, Bauer J, Magnusson NE, Infanger M, Grimm D: Biomarkers for anti-angiogenic therapy in cancer. Int J Mol Sci 2013;14:9338-9364.
76 Jackson HW, Defamie V, Waterhouse P, Khokha R: TIMPs: versatile extracellular regulators in cancer. Nat Rev Cancer 2017;17:38-53.
77 Verma RP, Hansch C: Matrix metalloproteinases (MMPs): Chemical–biological functions and (Q)SARs. Bioorg Med Chem 2007;15:2223-2268.
78 Jurczak P, Groves P, Szymanska A, Rodziewicz-Motowidlo S: Human cystatin C monomer, dimer, oligomer, and amyloid structures are related to health and disease. FEBS Lett 2016;590:4192-4201.
79 Deshmane SL, Kremlev S, Amini S, Sawaya BE: Monocyte Chemoattractant Protein-1 (MCP-1): An Overview. J Interferon Cytokine Res 2009;29:313-326.
80 Gerard C, Rollins BJ: Chemokines and disease. Nat Immunol 2001;2:108-115.
81 Rudemiller NP, Crowley SD: The role of chemokines in hypertension and consequent target organ damage. Pharmacol Res 2017;119:404-411.
82 Yoshimura T: The production of monocyte chemoattractant protein-1 (MCP-1)/CCL2 in tumor microenvironments. Cytokine DOI:10.1016/j.cyto.2017.02.001.
83 Vakilian A, Khorramdelazad H, Heidari P, Sheikh Rezaei Z, Hassanshahi G: CCL2/CCR2 signaling pathway in glioblastoma multiforme. Neurochem Int 2017;103:1-7.

KARGER

Downloaded from http://karger.com/cpb/article-pdf/43/1/257/2444310/000480368.pdf by guest on 31 October 2024

frontiers in Cell and Developmental Biology

ORIGINAL RESEARCH
published: 30 June 2021
doi: 10.3389/fcell.2021.672098

Alterations of Growth and Focal Adhesion Molecules in Human Breast Cancer Cells Exposed to the Random Positioning Machine

*Jayashree Sahana[1], Thomas J. Corydon[1,2], Markus Wehland[3,4], Marcus Krüger[3,4], Sascha Kopp[3,4], Daniela Melnik[3], Stefan Kahlert[5], Borna Relja[6], Manfred Infanger[3,4] and Daniela Grimm[1,3,4]**

[1] Department of Biomedicine, Aarhus University, Aarhus, Denmark, [2] Department of Ophthalmology, Aarhus University Hospital, Aarhus, Denmark, [3] Department of Microgravity and Translational Regenerative Medicine, Clinic for Plastic, Aesthetic and Hand Surgery, Otto von Guericke University, Magdeburg, Germany, [4] Research Group "Magdeburger Arbeitsgemeinschaft für Forschung unter Raumfahrt- und Schwerelosigkeitsbedingungen" (MARS), Otto von Guericke University, Magdeburg, Germany, [5] Institute of Anatomy, Otto von Guericke University, Magdeburg, Germany, [6] Department of Radiology and Nuclear Medicine, Experimental Radiology, Otto von Guericke University, Magdeburg, Germany

OPEN ACCESS

Edited by:
Christine Mehner,
Mayo Clinic Florida, United States

Reviewed by:
Mariano Bizzarri,
Sapienza University of Rome, Italy
Ruth Hemmersbach,
Helmholtz Association of German Research Centers (HZ), Germany

***Correspondence:**
Daniela Grimm
Daniela.grimm@med.ovgu.de

Specialty section:
This article was submitted to Cell Adhesion and Migration, a section of the journal Frontiers in Cell and Developmental Biology

Received: 25 February 2021
Accepted: 27 May 2021
Published: 30 June 2021

Citation:
Sahana J, Corydon TJ, Wehland M, Krüger M, Kopp S, Melnik D, Kahlert S, Relja B, Infanger M and Grimm D (2021) Alterations of Growth and Focal Adhesion Molecules in Human Breast Cancer Cells Exposed to the Random Positioning Machine. Front. Cell Dev. Biol. 9:672098. doi: 10.3389/fcell.2021.672098

In this study, we evaluated changes in focal adhesions (FAs) in two types of breast cancer cell (BCC) lines (differentiated MCF-7 and the triple-negative MDA-MB-231 cell line) exposed to simulated microgravity (s-μ*g*) created by a random positioning machine (RPM) for 24 h. After exposure, the BCC changed their growth behavior and exhibited two phenotypes in RPM samples: one portion of the cells grew as a normal two-dimensional monolayer [adherent (AD) BCC], while the other portion formed three-dimensional (3D) multicellular spheroids (MCS). After 1 h and 30 min (MDA-MB-231) and 1 h 40 min (MCF-7), the MCS adhered completely to the slide flask bottom. After 2 h, MDA-MB-231 MCS cells started to migrate, and after 6 h, a large number of the cells had left the MCS and continued to grow in a scattered pattern, whereas MCF-7 cells were growing as a confluent monolayer after 6 h and 24 h. We investigated the genes associated with the cytoskeleton, the extracellular matrix and FAs. *ACTB, TUBB, FN1, FAK1*, and *PXN* gene expression patterns were not significantly changed in MDA-MB-231 cells, but we observed a down-regulation of *LAMA3, ITGB1* mRNAs in AD cells and of *ITGB1, TLN1* and *VCL* mRNAs in MDA-MB-231 MCS. RPM-exposed MCF-7 cells revealed a down-regulation in the gene expression of *FAK1, PXN, TLN1, VCL* and *CDH1* in AD cells and *PXN, TLN* and *CDH1* in MCS. An interaction analysis of the examined genes involved in 3D growth and adhesion indicated a central role of fibronectin, vinculin, and E-cadherin. Live cell imaging of eGFP-vinculin in MCF-7 cells confirmed these findings. β-catenin-transfected MCF-7 cells revealed a nuclear expression in 1*g* and RPM-AD cells. The target genes *BCL9, MYC* and *JUN* of the Wnt/β-catenin signaling pathway were differentially expressed in RPM-exposed MCF-7 cells. These findings suggest that vinculin and β-catenin are key mediators of BCC to form MCS during 24 h of RPM-exposure.

Keywords: microgravity, breast cancer, multicellular spheroids, focal adhesions, cytoskeleton, extracellular matrix

Originale der Publikationen

INTRODUCTION

Tumor diseases are a heavy burden for people around the world with high morbidity and mortality. The second leading cause of death worldwide is cancer (Sung et al., 2021). According to data published by the WHO Global Cancer Observatory (GLOBOCAN) in 2020, tumor diseases were responsible for an estimated 10 million deaths in 2020 (Sung et al., 2021).

In this study, we focused on breast cancer cells. Breast cancer (BC) is the most commonly diagnosed malignant tumor with an estimated 2.3 million new cases (11.7%) (Sung et al., 2021). BC is a very heterogeneous disease, as tumor cells can show different gene expression patterns (van't Veer et al., 2002). An individualized therapy for patients is therefore necessary. BC shows seven molecular subtypes with typical histology, treatment options, and outcomes (van't Veer et al., 2002; Nassef et al., 2019a). Patient survival rates are associated with the size of the tumor, the hormone receptor profile, and metastases at the time of diagnosis. Standard therapy is the surgical resection of the cancer. Depending on tumor type, size, staging, and metastasis to sentinel lymph nodes, strategies like chemotherapy, radiation and anti-hormone therapy, targeted treatment against HER2, and anti-angiogenic therapy are often applied after surgery or in cases of advanced disease stage (Kristensen et al., 2014). Despite advanced therapy, it is estimated that about 684,996 deaths worldwide will occur from BC per year (Sung et al., 2021). Therefore, novel therapeutic strategies with the help of new technologies are required.

Microgravity (μg)-based cancer research currently generates major interest (Becker and Souza, 2013; Krüger et al., 2019). Gravitational biology and space medicine are growing areas of research worldwide. It is known today that cells cultivated in real and simulated μg show changes in proliferation, transcription factors, gene expression patterns, and in the content of various proteins (Lewis et al., 1998; Boonyaratanakornkit et al., 2005; Chang and Hughes-Fulford, 2009; Pietsch et al., 2010; Chang et al., 2012; Svejgaard et al., 2015; Kopp et al., 2016, 2018; Buken et al., 2019; Grimm et al., 2020). Exposure of cells to real μg and the random positioning machine (RPM) leads to changes in the cytoskeleton, focal adhesion components, extracellular matrix proteins, and differentiation, as well as to an increase in apoptosis and changes in growth behavior (Lewis et al., 1998; Svejgaard et al., 2015; Kopp et al., 2018; Buken et al., 2019; Nassef et al., 2019a,b).

In earlier investigations, MCF-7 cells (Soule et al., 1973) showed variable growth behavior when exposed to the RPM for one and 5 days: one portion of the cells remained adherent, while the second portion grew in the form of spheroids with and without gland-like structures (Kopp et al., 2016). In contrast, MCF-7 cells only formed compact spheroids when cultured for 24 h under conditions of simulated μg created by an RPM (Kopp et al., 2016).

Our second cell line of interest is the well-described basal-like triple-negative MDA-MB-231 cell line, which has also been investigated in real μg and on an RPM (Masiello et al., 2014; Nassef et al., 2019a). Exposure to simulated (s-) μg resulted in three-dimensional (3D) growth and demonstrated a fundamental role in shaping form and function in human BCC (Masiello et al., 2014). These cell cultures in μg can be performed scaffold-free to engineer 3D aggregates, including multicellular spheroids (MCS), tissues, and tubular structures (Grimm et al., 2020). The organoids can be used for research in space medicine and for testing the delivery and efficacy of drugs (Grimm et al., 2020). Cancer cells are sensitive to mechanical stress. The regulation of focal adhesions (FAs) and cytoskeletal dynamics are important for cell maintenance, cell adherence, cell movement, and migration (Hughes-Fulford, 2003; Li et al., 2009). It has been demonstrated that s-μg reduces FAs and alters the cytoskeleton and nuclear positioning, leading to enhanced apoptosis in B16 melanoma cells (Zhao et al., 2018). Another study showed that the inhibition of FAs leads to reduced melanoma cell proliferation and metastasis (Tan et al., 2018).

Therefore, the objective of this study was to (i) investigate the changes and growth of BC cells exposed to s-μg created by an RPM, (ii) and to test, based on previous findings, the hypothesis that 24 h of exposure to s-μg cells induces the formation of MCS and alters the expression of genes related to the cytoskeleton, cell adhesion, and focal adhesions (FAs) in BC. Finally, we focused on the migration behavior and invasion potential of the MCS of both BC cell types.

MATERIALS AND METHODS

Cell Culturing and Microgravity Simulation on the RPM

MDA-MB-231 human breast adenocarcinoma cells (MDA-MB-231; ATCC® HTB-26^{TM}) and the MCF-7 human breast adenocarcinoma cell line MCF7 (ATCC® HTB-22TM) were purchased from the American Type Culture Collection (Manassas, Virginia, United States). The cells were cultured in RPMI 1640 (Life Technologies, Naerum, Denmark) in complete medium supplemented with 10% fetal calf serum (Sigma-Aldrich St. Louis, MO, United States) and 1% penicillin/streptomycin (Life Technologies, Carlsbad, CA, United States) under standard cell culture conditions (37°C and 5% CO_2). Three days prior to the experiment, 2×10^6 cells were counted and seeded into T75 cm^2 vented cap cell culture flasks (Sarstedt, Nümbrecht, Germany). A total number of 24 T25 cm^2 cell culture flasks was prepared for the RPM experiments. Twelve flasks were kept under normal gravity conditions in the same incubator where the RPM was situated and used as ground controls (1g), and 12 flasks were mounted on the RPM. In addition, 2×24 slide flasks (NuncTM, ThermoFisher Scientific, Denmark) were prepared for each condition, and 1×10^5 cells were seeded in each 9 cm^2 slide flask for immunofluorescence staining. Each flask was completely filled with medium, in a complete air bubble-free condition. The flasks were installed on the center frame of the RPM and run for 24 h. The 1g controls were stored inside the device in the same incubator at 37°C and with 5% CO_2.

After 24 h, the RPM was stopped, and the BC cells were examined and photographed by phase contrast microscopy. For qPCR investigations, the medium from RPM flasks was transferred into 50 mL tubes and centrifuged at 4°C to collect

the MCS. The MCS were washed in phosphate buffered saline (PBS) (Life Technologies), centrifuged again and after removal of the PBS stored in liquid nitrogen. For harvesting the adherent cells from 1*g* control and RPM cultures from the cell culture flask bottom, 10 mL ice-cold PBS was added to each T75 cm^2 flask, and the cells were scraped off with a scraper. The cell suspension was collected and centrifuged at 4°C. The PBS was discarded, and the dry pellet was washed twice with PBS and afterward stored in liquid nitrogen for protein extraction and RNA isolation. For immunofluorescence staining, the medium was discarded and the cells were washed twice with PBS. Afterward, 2 mL 4% PFA (paraformaldehyde solution) was added to fix the cells for 45 min at room temperature. Then, the PFA was discarded, and 2 mL of PBS was added to the slide flasks, which were then stored in a refrigerator for future staining.

Simulated Microgravity Conditions Created by a Random Positioning Machine

The RPM was purchased from Airbus, Defense, and Space (former Dutch Space, Leiden, the Netherlands) and used to simulate microgravity. The method was published earlier in detail (Borst and van Loon, 2008; Wuest et al., 2015). In short, the RPM attempts to nullify the gravity vector by continuously rotating the central frame (where samples are mounted) around two perpendicular axes. The degree of rotation was in between 60°/s and 75°/s and randomized around both axes by continuously changing the direction; thus, the net magnitude of gravity vector toward the sample approaches zero, resulting in simulated microgravity. Twelve T25 cm^2 flasks (12 each run) were fixed on the central frame of the RPM. After 24 h, the device was stopped, and the samples were collected and investigated by phase contrast microscopy. Three different groups were collected from the RPM experiments: 1*g*, AD, and MCS.

Phase Contrast Imaging

The morphology of the 1*g* control and RPM BC cells before, during, and after the experiment were photographed using phase contrast microscopy. The images were taken with a Canon EOS550D camera (Canon GmbH, Krefeld, Germany) through a Leica DM IL LED inverted microscope (Leica Microsystems, Brønshøj, Denmark).

Proliferation, Migration, and Invasion

Ki-67 immunofluorescence staining was performed to visualize the proliferating cells in MCS after 24 h. The immunofluorescence method is described in Section "Immunofluorescence Staining and Confocal Laser Scanning Microscopy." To demonstrate the migration behavior of the MCS, the spheroids were collected after 24 h, pipetted in slide flasks and studied for adherence and migration by phase contrast microscopy (Leica Microsystems).

To test the invasion potential of the MCS of both cell lines, we cultured a confluent monolayer of human endothelial cells [EA.hy926 cell line (ATCC CRL-2922)] in slide flasks [detailed cell culture method published in reference (Dittrich et al., 2018)], pipetted MCF-7 or MDA-MB-231 BC MCS cells on the endothelial cells, and studied the invasion potential of the MCS cells. The examination was performed by phase contrast microscopy.

Immunofluorescence Staining and Confocal Laser Scanning Microscopy

The BC cells investigated in slide flasks were fixed with 4% PFA solution for 30 min. Then, they were subjected to membrane permeabilization with 0.1% Triton X for 10 min and blocking with 1% [weight (w)/volume (v)] bovine serum albumin (BSA, Sigma-Aldrich, Steinheim, Germany) in PBS for 30 min. The slides were then released from the flasks, and the cells were incubated with primary antibodies (listed in **Table 1**) in a PBS solution with 1% (w/v) BSA overnight at room temperature. The next day, the cells were washed three times with PBS before incubation with the secondary Alexa Fluor 488 (AF488)-conjugated anti-rabbit (Cell Signaling Technology, Danvers, MA, United States) or anti-mouse antibody (Invitrogen) at a dilution of 1:1,000 for 2 h at ambient temperature. Afterward, the slides were washed with PBS three times and prepared and covered for microscopy using Fluoroshield™ mounting media with DAPI (4′,6-diamidino-2-phenylindole; Sigma-Aldrich). The covered slides were kept at 4°C in a dark box until confocal microscopy was performed (Buken et al., 2019).

Fluorescence staining was analyzed using a ZEISS LSM 710 CLSM (ZEISS, Jena, Germany) and a 40 × oil-immersion objective with a NA of 1.3 (Nyegaard et al., 2015; Corydon et al., 2016b). The quantification of the fluorescence intensity was performed with the FIJI image processing software (available from[1]). Briefly, data in.czi-format was imported using the Bio-Formats plugin and all color channels were split into separate grayscale images. In the green channel, individual cells were outlined with the freehand ROI tool and both area and integrated density was measured. Subsequently, background and secondary antibody control intensities were subtracted to yield the corrected total cell fluorescence. For each experimental condition, at least five different fields of view with a mean number of five cells were analyzed.

[1]https://fiji.sc/

TABLE 1 | List of antibodies used for immunofluorescence.

Antibody	Immunofluorescence	
E-cadherin	CST#2500S	Rb
Fibronectin	Millipore Sigma/F3648	Rb
Ki 67	Abcam# ab15580	Rb
Laminin	Sigma/L9393	Rb
Talin	Millipore Sigma/T3287	Ms
Vinculin	Millipore Sigma/V9131	Ms

Ms, mouse; Rb, rabbit; Sigma (now by MERCK, Darmstadt, Germany); ABCAM (Cambridge, United Kingdom); Cell Signaling Technology (CST, BioNordika Denmark A/S, Herlev, Denmark); and MERCK Millipore (Burlington, Massachusetts, United States).

RNA Isolation and Quantitative Real-Time Polymerase Chain Reaction

The method was published earlier in detail (Ma et al., 2013; Kopp et al., 2015). RNA isolation was performed using a RNeasy Mini Kit (Qiagen, Hilden, Germany) with an additional DNase digestion step (Qiagen) in order to eliminate residual DNA contamination. Afterward, the amount of RNA was quantified using a Photometer Ultrospec2010 (Amersham Biosciences, Freiburg, Germany). A first strand cDNA synthesis kit (Thermo Fisher Scientific, Waltham, MA, United States) was applied for reverse transcription. qPCR was performed on a 7,500 Fast Real-Time PCR System using the FAST SYBR Green Master Mix (both Applied Biosystems, Darmstadt, Germany) according to standard protocols (Kopp et al., 2016, 2018; Buken et al., 2019; Nassef et al., 2019a).

All samples were measured in triplicate. For normalization, 18S rRNA was used as a housekeeping gene. The comparative Ct ($\Delta\Delta$Ct) method was used for relative quantification of transcription levels, and the 1*g* control group was defined as 100% for reference. Before performing qPCR, primers were designed using NCBI Primer Blast, and they were selective for cDNA by spanning exon–exon junctions and had a melting temperature of around 60°C. The primers were synthesized by TIB Molbiol (Berlin, Germany) and are listed in **Table 2**:

TABLE 2 | List of all the primers' sequences used in the quantitative PCR. All the sequences are listed in the 5′-3′-direction.

Factor	Primer Name	Sequence 5′–3′
18S	18S-F	GGAGCCTGCGGCTTAATTT
	18S-R	CAACTAAGAACGGCCATGCA
ACTB	ACTB-F	TGCCGACAGGATGCAGAAG
	ACTB-R	GCCGATCCACACGGAGTACT
BCL9	BCL9-F	CAGAGCAGACAATAGGCCCC
	BCL9-R	AGACCCTTTTCCCGCAATCC
CCND1	CCND1-F	CCCTGACGGCCGAGAAG
	CCND1-R	AGGTTCCACTTGAGCTTGTTCAC
CDH1	CDH1-F	GCTGGACCGAGAGAGTTTCC
	CDH1-R	CAGCTGTTGCTGTTGTGCTT
CTNNA1	CTNNA1-F	AATTTAGCGCTCGCCCAG
	CTNNA1-R	ACAAGGGTTGTAACCTGTGTAA
CTNNB1	CTNNB1-F	GAAACAGCTCGTTGTACCGC
	CTNNB1-R	ATCCACTGGTGAACCAAGCA
FAK1/PTK2	FAK1-F	TGTGGGTAAACCAGATCCTGC
	FAK1-R	CTGAAGCTTGACACCCTCGT
FN1	FN1-F	AGATCTACCTGTACACCTTGAATGACA
	FN1-R	CATGATACCAGCAAGGAATTGG
ITGB1	ITGB1-F	GAAAACAGCGCATATCTGGAAATT
	ITGB1-R	CAGCCAATCAGTGATCCACAA
JUN	JUN-F	GAGCTGGAGCGCCTGATAAT
	JUN-R	CCCTCCTGCTCATCTGTCAC
LAMA3	LAMA3-F	AAAGCAAGAAGTCAGTCCAGC
	LAMA3-R	TCCCATGAAGACCATCTCGG
MYC	MYC-F	GGATTCTCTGCTCTCCTCGAC
	MYC-R	CTTCTTGTTCCTCCTCAGAGTC
NFATC2	NFATC2-F	CAAGACGAGCTTGACTTCTCCA
	NFATC2-R	GCATTCGGCTCTTCTTCGTTC
PXN	PXN-F	CATGGACGACCTCGACGC
	PXN-R	CAAGAACACAGGCCGTTTGG
TBP	TBP-F	GTGACCCAGCATCACTGTTTC
	TBP-R	GCAAACCAGAAACCCTTGCG
TLN1	TLN1-F	GATGGCTATTACTCAGTACAGACAACTGA
	TLN1-R	CATAGTAGACTCCTCATCTCCTTCCA
TUBB	TUBB-F	CTGGACCGCATCTCTGTGTACTAC
	TUBB-R	GACCTGAGCGAACAGAGTCCAT
VCL	VCL-F	GTCTCGGCTGCTCGTATCTT
	VCL-R	GTCCACCAGCCCTGTCATTT

STRING Analysis

The interactions between proteins were determined using the STRING v10 platform (Snel et al., 2000). For each protein, the UniProtKB entry number was inserted in the input form "multiple proteins," and "Homo sapiens" was selected as the organism. The resulting network view was downloaded in the molecular action view showing lines between interacting proteins and genes (Nassef et al., 2019a).

Transfection of the MCF-7 Cell Line to Visualize Vinculin and β-Catenin

The MCF-7 BCC cells were stably transfected using a Sleeping Beauty (SB) transposon-based vector containing the eGFP-hVCL1 cassette for the visualization of vinculin as described in Nassef et al. (2019b). In brief, an eGFP-hVCL fragment containing NotI and XbaI restriction sites in the 5′ and 3′ ends, respectively, was sub-cloned into a Sleeping Beauty (SB) transposon-based vector pT2/CMV-linker-SV40-Neo (Staunstrup et al., 2011; Pihlmann et al., 2012) containing a linker, enabling insertion of the *Not*I-eGFP-hVCL1-*Xba*1 fragment. The resulting plasmid, pT2/CMV-eGFP-hVCL1-SV40-Neo, was entitled pSB-eGFP-vinculin. In order to provide stable expression of the eGFP-vinculin expression cassette, MCF-7 cells were co-transfected with pSB-eGFP-vinculin and pCMV−SB100X (Pihlmann et al., 2012) using X-tremeGENE 9 transfection reagent (Roche, Mannheim, Germany) according to the manufacturer's protocol (Askou et al., 2015). An inactive SB transposase (mSB) was included as negative control. Transfected cells were cultured in medium containing G418 (geneticin) to allow for growth of stably transfected cells only. A fluorescence microscope was used to validate the efficiency of the transfection.

To visualize catenin in MCF-7 BCC cells, a cDNA fragment encoding human β-catenin N-terminally tagged with the mCherry marker protein was cloned into the piggyBac plasmid pPBT-CMV-MCS-IRES-Puro (Sharma et al., 2012). The resulting plasmid, entitled pPBT-mCherry-catenin, was transiently transfected into MCF-7 cells using X-tremeGENE 9 transfection reagent (Roche) according to manufacturer's protocol (Askou et al., 2015). Following transfection, the cells were maintained for 24 h at 1*g* conditions and then transferred to either 1*g* or to the RPM for additional 24 h.

Images of MCF-7 BCC cells expressing eGFP-vinculin were captured by a confocal scanning microscope (CLSM) 710 (Zeiss, Jena, Germany). Images of MCF-7 BCC cells expressing mCherry-catenin were captured 48 h post-transfection by a CLSM 800 (Zeiss).

Originale der Publikationen

Statistical Analysis

All statistical evaluations were performed using IBM SPSS Statistics 23 (IBM Deutschland GmbH, Ehningen, Germany). The Mann–Whitney U-Test was utilized to evaluate the statistical significance in the changes in expression levels following RPM exposure, thus comparing the 1g control to AD and MCS. A significance level of 0.05 was used. The standard deviation was calculated and presented together with the mean values as percentages in bar plots.

RESULTS

Morphology, Cell Growth, Migration and Invasion Behavior of the BCC

MCF-7 and MDA-MB-231 BCC cultured under normal standard cell culture conditions at 1*g* grew as a two-dimensional (2D) monolayer (**Figures 1A,D**). MCF-7 revealed their characteristic epithelial growth behavior at 1*g* (**Figure 1A**). MDA-MB-231 cells exhibited an epithelial-like morphology and appeared phenotypically as spindle-shaped cells under normal 1*g* static conditions (**Figure 1D**). In contrast, both BCC types, the MCF-7 and MDA-MB-231 cells exposed to an RPM for 24 h showed two different phenotypes: adherent cells and multiple multicellular spheroids floating in the medium (**Figures 1B,E**).

The proliferation marker Ki-67 was determined to indicate the active phases of the cell cycle (G1, S, G2, and mitosis), because the Ki-67 protein is absent in resting G0 cells. The Ki-67 immunofluorescence showed various proliferating cells on the surface of the MCS of both cell types (**Figures 1C,F**).

In addition, we tested the migration behavior of the MCS. After 20 min 50% of the MCF-7 spheroids and 30% of the MDA-MB-231 spheroids were adherent to the slide flask bottom. All MDA-MB-231 MCS had attached after 1.5 h, and all MCF-7 MCS stayed adherent on the slide flask bottom after 1 h 40 min. **Figures 1H,L** show the MCS of both cell types at 2 h. The MDA-MB-231 cells started to migrate (**Figure 1L**), whereas the MCF-7 MCS exhibited an outer membrane (yellow arrows, **Figure 1H**). After 6 h, a large number of MDA-MB-231 BCC had migrated out of the MCS (**Figure 1M**) and only some remaining 3D aggregates are visible. In contrast, the MCF-7 MCS were still compact and only a few cells started to leave the MCS (red arrows, **Figure 1I**). In these areas, the membrane around the cells growing three-dimensionally was destroyed. After 24 h, MDA-MB-231 cells grew in form of a monolayer and the cells had lost their intercellular contacts (**Figure 1N**), whereas MCF-7 cells still grew as a more compact cell monolayer, but with a broader interstitial space (**Figure 1J**).

To evaluate the invasion behavior of both BC types, spheroids were seeded out on a confluent monolayer of EA.hy926 endothelial cells (ECs) (**Figures 1O–V**). After 3 h, MCF-7 spheroids exhibited an outer membrane (yellow arrows) at the contact area to the ECs. The ECs changed their orientation and provided more space for the tumor cells, which started their invasion (**Figure 1P**). The blue arrow shows the invasive MCF-7 cells, and the black arrow indicates the looser EC layer (**Figure 1P**). Three hours later, the MCF-7 MCS were invasive growing in between the ECs, providing space to the cancer cells (**Figure 1Q**). The overview given in **Figure 1R** shows the invasiveness of the MCF-7 tumor cells after a 24 h co-culture and their growth between the EC monolayer.

MDA-MB-231 spheroids seeded on ECs very rapidly attached and spread out onto the EC monolayer (**Figure 1T**). After a 6-h co-culture, all cells of the MCS had migrated out of the spheroid and progressed growing between the EC monolayer (**Figure 1U**). After 24 h, mostly single tumor cells were detectable between the ECs (**Figure 1V**).

Changes in Cytoskeletal Factors in MDA-MB-231 Cells Exposed to the RPM

We measured the gene expression of β-actin in MDA-MB-231 cells exposed to the RPM. The *ACTB* mRNA expression was not altered in 1*g*, adherent (AD) and MCS samples (**Figure 2A**). In parallel, the *TUBB* mRNA expression was not changed in all groups (**Figure 2B**). The cytoskeletal components of MCF-7 cells were examined in an earlier study (Kopp et al., 2016).

Changes in Cell Adhesion Molecules of MDA-MB-231 Cells Exposed to the RPM

We investigated the cell adhesion molecules fibronectin and laminin. There was no significant change in the gene expression of *FN1* in MCS after 24 h (**Figure 3A**). The fibronectin immunofluorescence was significantly elevated in RPM-AD cells and MCS compared with 1*g* cells (**Figures 3B–E**). In addition, the mRNA expression of *LAMA3* was not changed in MCS vs. 1*g*, but significantly down-regulated in AD cells in comparison to 1*g* static control cells (**Figure 3F**). The laminin immunofluorescence was increased in RPM-AD cells and MCS (**Figures 3G–J**). Both cell adhesion molecules and extracellular matrix proteins were investigated earlier in MCF-7 cells (Kopp et al., 2016).

The Impact of RPM-Exposure on Focal Adhesions and Interacting Factors in MDA-MB-231 Cells

We investigated integrin-β1 and measured a significantly down-regulated *ITGB1* gene expression in RPM-exposed AD and MCS samples (**Figure 4A**). The gene expression of focal adhesion kinase 1 (*FAK1*), also known as PTK2 protein tyrosine kinase 2 (*PTK2*), was not changed by RPM exposure in MDA-MB-231 cells (**Figure 4B**). In addition, the *PXN* mRNA was not altered in RPM-exposed MDA-MB-231 cells compared to 1*g* controls (**Figure 4C**).

Furthermore, the *TLN1* gene expression was not significantly altered in RPM-AD cells cultured under s-μ*g* conditions, but significantly reduced in MCS (**Figure 4D**). IFS revealed a cytoplasmic staining of talin-1. RPM-exposed AD cells exhibited an increase in talin-1 compared to 1*g* and MCS (**Figures 4E–H**). Furthermore, the MCS expressed talin-1 in an intensity comparable to 1*g* cells (**Figure 4H**).

In addition, the *VCL* gene expression was significantly down-regulated in MCS compared to 1*g* (**Figure 4I**). The IFS of vinculin showed a similar fluorescence intensity in the cytoplasm of the

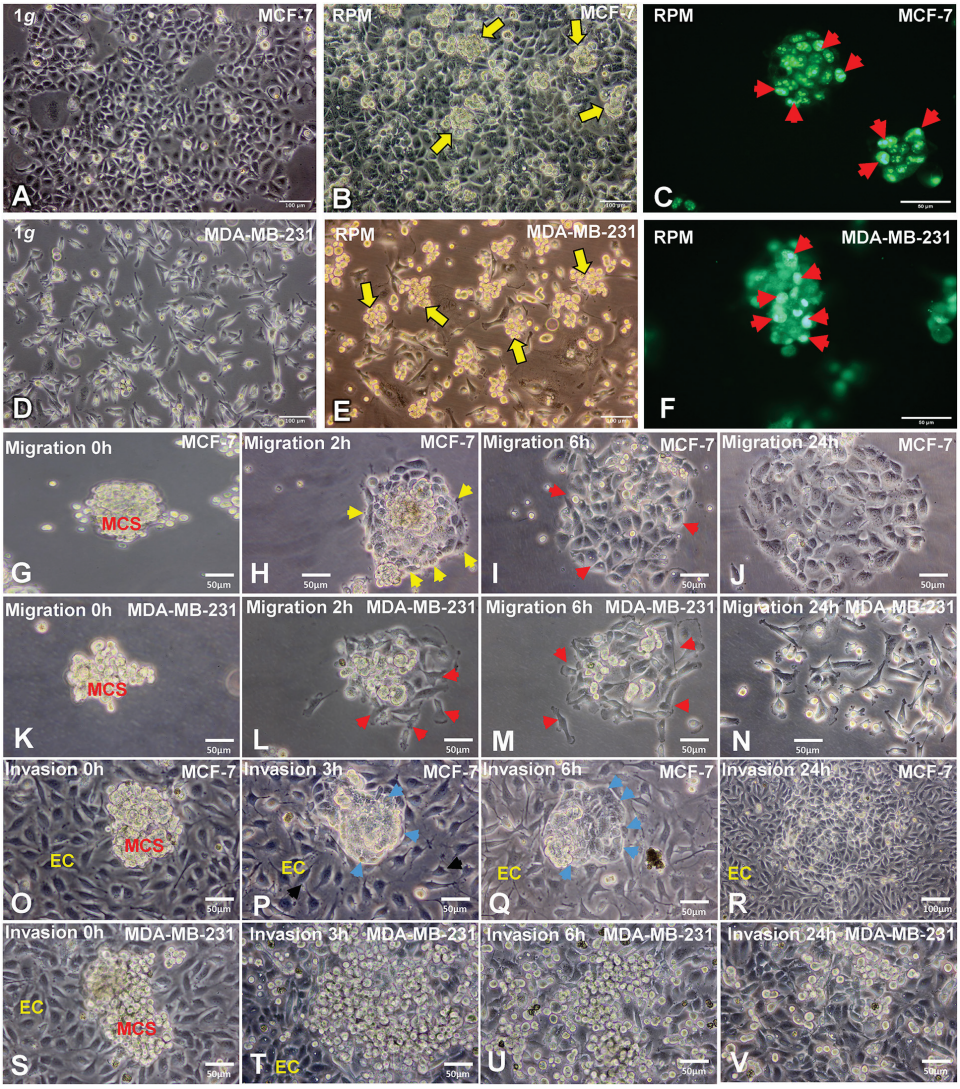


FIGURE 1 | Phase contrast microscopy of MCF-7 and MDA-MB-231 breast cancer cells (BCC). **(A)** Characteristic epithelial morphology of the MCF-7 cell line cultured at 1*g*. **(B)** Adherent MCF-7 cells and multiple compact multicellular spheroids (MCS, yellow arrows) were visible when the MCF-7 cells were exposed to the random positioning machine (RPM) for 24 h. **(C)** Ki-67 immunofluorescence staining (IFS) of MCF-7 MCS. The red arrows show Ki-67 positive nuclei. **(D)** MDA-MB-231 cell line cultured under static 1*g* control conditions at 24 h. **(E)** MDA-MB-231 cells exposed to the RPM for 24 h. Multiple multicellular spheroids (yellow arrows) are visible as well as adherent cells. Magnification × 100. The yellow arrows indicate MCS floating in the supernatant of the cell cultures. **(F)** Ki-67 IFS of MDA-MB-231 MCS. The red arrows show Ki-67 positive nuclei. **(G)** Migration behavior of the MCF-7 cells in spheroids at 0 h, **(H)** 2h, the yellow arrows indicate the attachment of the MCS on the slide flask bottom and the cell membrane. **(I)** 6 h, the red arrows show areas of migration and **(J)** 24 h. **(K)** Migration behavior of MDA-MB-231 cells in spheroids at 0 h, **(L)** 2 h, the red arrows show the attached MCS and migration **(M)** 6 h, red arrows indicate migrated cells and after **(N)** 24 h. No MCS were visible at this time point. Invasion test: co-cultures of EA.hy926 endothelial cells and MCF-7 MCS. **(O)** 0 h, **(P,Q)** 3 h and 6h, the blue arrows show the formation of a cellular membrane. **(R)** After 24 h the MCF-7 BCC had invaded the endothelial cells. Invasion test: co-cultures of EA.hy926 endothelial cells and MDA-MB-231 MCS. **(S)** 0 h, **(T)** 3 h, at this time point the MDA-MB-231 cells had already migrated out of the MCS and showed an invasive growth. **(U)** 6 h and **(V)** 24 h.

MDA-MB-231 MCS compared to 1*g*, but a significant increase in AD cells exposed to s-µ*g* (**Figures 4J–M**).

The Impact of RPM-Exposure on Focal Adhesions in MCF-7 Cells

The next step was to examine focal adhesion molecules in MCF-7 BCC exposed to s-µ*g* conditions. The results are presented in **Figure 5**. *PTK2* mRNA expression was reduced in the AD group (**Figure 5A**). Furthermore, the gene expression of *PXN* was significantly down-regulated in both RPM groups (**Figure 5B**). Moreover, we focused on talin-1. The *TLN1* mRNA expression was significantly decreased in AD and MCS cells (**Figure 5C**). The IFS revealed a significant increase in the cytoplasmic fluorescence of talin in AD samples compared to MCS and 1*g* samples (**Figures 5D–G**). In MCS, the talin IF is significantly reduced compared with 1*g* (**Figure 5G**). Finally, the gene expression of

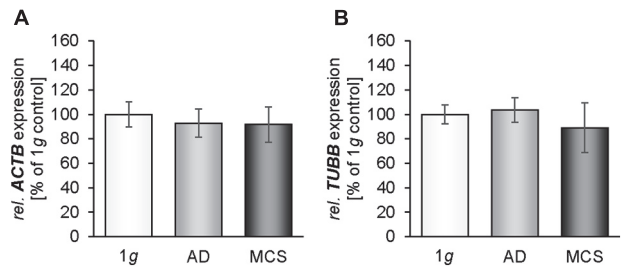


FIGURE 2 | Gene expression [*ACTB* **(A)**, *TUBB* **(B)**] of MDA-MB-231 cells exposed to the RPM. * $p < 0.05$ 1*g* vs. adherent (AD) and/or MCS and #$p < 0.05$ AD vs. MCS.

VCL was not differentially displayed in MCS vs. 1*g*, but down-regulated in RPM-AD cells vs. 1*g* (**Figure 5H**). The IFS of vinculin is significantly reduced in AD cells compared to 1*g* cells, whereas the vinculin IF was elevated in MCS compared to 1*g* and AD (**Figures 5I–L**).

The Impact of RPM-Exposure on E-Cadherin in MCF-7 Cells

MCF-7 BCC exposed to the RPM showed a down-regulation of the *CDH1* gene in AD and MCS samples (**Figure 6A**). IFS revealed an elevated fluorescence intensity in AD cells compared to normal 1*g* control BCC (**Figures 6B–E**).

Results of Gene/Protein Interactions (STRING Analysis)

The various genes analyzed by qPCR were investigated with regard to their possible interactions and mutual expression dependence. A STRING/EMBL (European Molecular Biology Laboratory) analysis of these items represented in molecule action mode is shown in **Figure 7A**. It can be seen that the FA factors for which the expression pattern was analyzed regulate each other very strongly. The genes of interest (**Figures 7B,C**) were differentially regulated in s-μ*g* samples (AD and MCS). **Figures 7B,C** present a summary of the qPCR data, already described in **Figures 2–6**, and provide a comparable overview on the results. A closer look at the 24 h samples revealed that most genes involved in the focal adhesion molecule complex, especially the *CDH1* mRNA, were highly down-regulated in both AD and MCS groups of MCF-7 BCC. The cell adhesion molecule and extracellular matrix protein fibronectin was slightly elevated in AD and MCS. A down-regulation was observed for *LAMA3* in MDA-MB-231 cells.

Vinculin/β-Catenin Signaling in MCF-7 Cells

For stable expression and amenable live-cell visualization of vinculin in MCF-7 BCC, a Sleeping Beauty (SB) transposon-based vector containing a CNV-driven eGFP-hVCL1 cassette was constructed according to Nassef et al., 2019b; **Figure 8A**. This

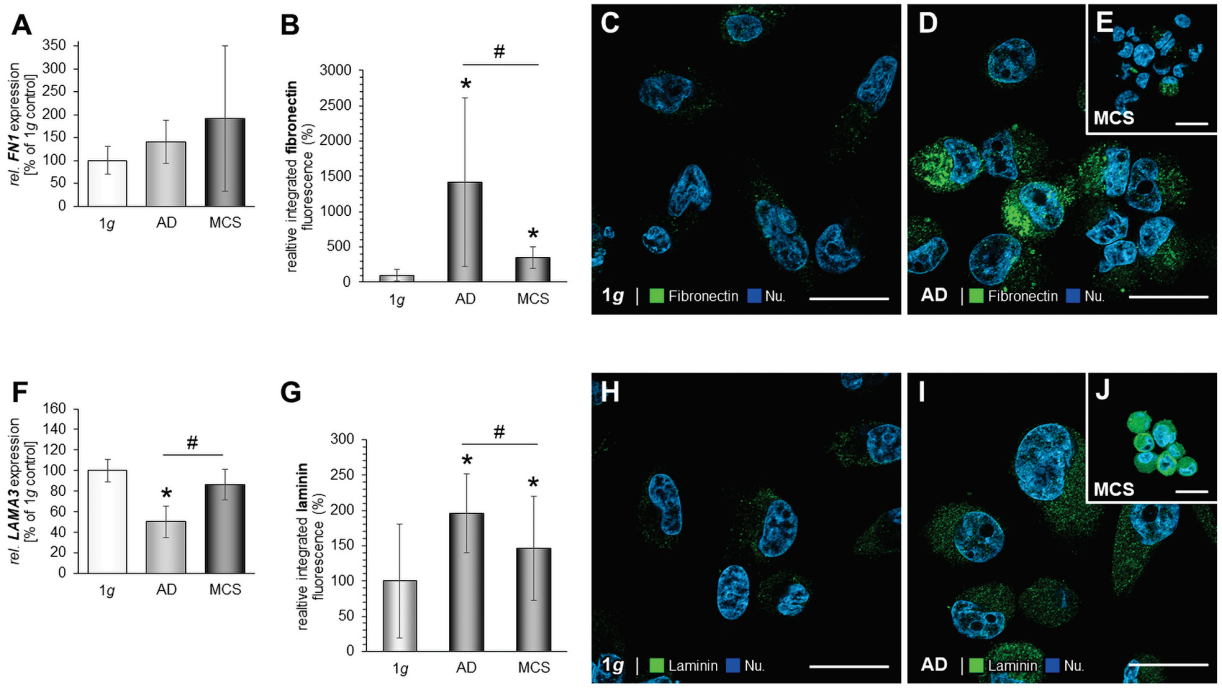


FIGURE 3 | Investigation of fibronectin **(A–E)** and laminin **(F–J)**: The gene expression of *FN1* **(A)**, analysis of the fluorescence intensity of fibronectin **(B)** and immunofluorescence staining (IFS) of fibronectin in 1*g* samples of MDA-MB-231 cells: **(C)**, RPM-AD samples **(D)** and MCS **(E)**; the *LAMA3* mRNA expression **(F)** as well as analysis of the fluorescence intensity of fibronectin **(G)**, the IFS of laminin in 1*g* samples **(H)**, RPM-AD samples **(I)** and MCS **(J)** of MDA-MB-231 cells exposed to the RPM. *$p < 0.05$ 1*g* vs. AD and/or MCS and #$p < 0.05$ AD vs. MCS.

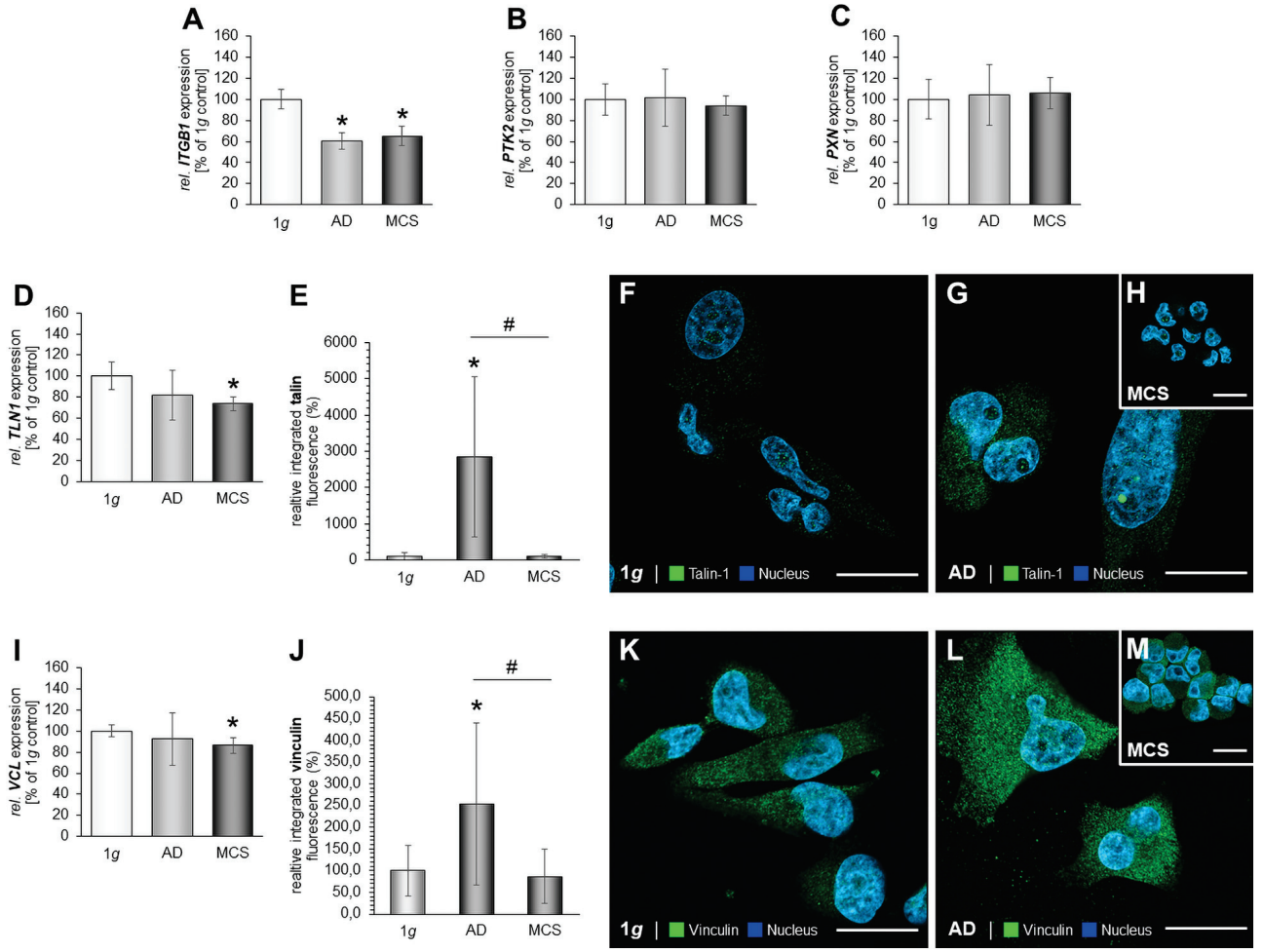


FIGURE 4 | Focal adhesions in MDA-MB-231 cells. The gene expression of *ITGB1* **(A)**, *PTK2* mRNA expression **(B)**, *PXN* mRNA expression **(C)** of MDA-MB-231 cells exposed to the RPM. In addition, the gene expression of *TLN1* **(D)** and analysis of the fluorescence intensity of talin **(E)**, IFS of 1*g* control cells **(F)** and RPM-exposed MDA-MB-231 cells [AD cells: **(G)** and MCS: **(H)**] is given. Moreover, the *VCL* mRNA **(I)** and analysis of the fluorescence intensity of vinculin **(J)**, the IFS of vinculin are shown in 1*g* control cells **(K)** and RPM-exposed AD cells **(L)** and MCS **(M)**. $^*p < 0.05$ 1*g* vs. AD and/or MCS and $\#p < 0.05$ AD vs. MCS.

construct enables the synthesis of a fusion-protein containing the eGFP marker protein N-terminally tagged to vinculin. Following co-transfections with pSB-eGFP-vinculin and pCMV-SB100X, cells were incubated in medium containing G418 for selection of clones. Several colonies were obtained after inspection by fluorescence microscopy for validation of the expression level of eGFP-vinculin. Only few colonies were obtained when using an inactive SB transposase, showing that the eGFP-vinculin-positive clones results from SB-mediated insertion of the eGFP-hVCL1 cassette.

eGFP-vinculin is strongly expressed at 1*g* in transfected MCF-7 BCC. Stress fibers and lamellipodia are visible (**Figure 8B**, white arrows). A similar expression pattern was detected in RPM-exposed AD cells (**Figure 8C**). A prominent formation of stress fibers (see right side of the cells shown to the right in **Figure 8C**) is detectable. A uniform expression of eGFP-vinculin is seen in MCS (**Figure 8D**). Interestingly, the stress fibers had disappeared in BCC MCS (**Figure 8D**). **Figure 8E** gives the results of the analysis of the fluorescence intensity of eGFP-vinculin. The highest fluorescence intensity was measured in MCS and at 1*g*.

To visualize catenin in MCF7 BCC cells the cDNA fragment encoding human β-catenin N-terminally tagged with the mCherry marker protein were cloned into the pPBT-CMV-MCS-IRES-Puro plasmid (**Figure 8F**). Following transient transfection, the mCherry-catenin was expressed in the cytoplasm and the nucleus of MCF-7 cells grown under normal gravity conditions (**Figure 8G**). β-catenin is less located in the nuclei of MCS cells than of adherent cells after RPM exposure (**Figures 8H,I**). A non-uniform expression of mCherry-catenin is found in MCS (**Figure 8I**). The protein is accumulated at the outer cell membrane (**Figure 8I**). **Figure 8J** gives the results of the analysis of the fluorescence intensity of mCherry-catenin.

The *CTNNB1* mRNA was not significantly expressed in all three groups (**Figure 8K**). In addition, the gene expression of *CTNNA1* was not significantly altered (**Figure 8L**). The Wnt/β-catenin target gene *JUN* was down-regulated in AD

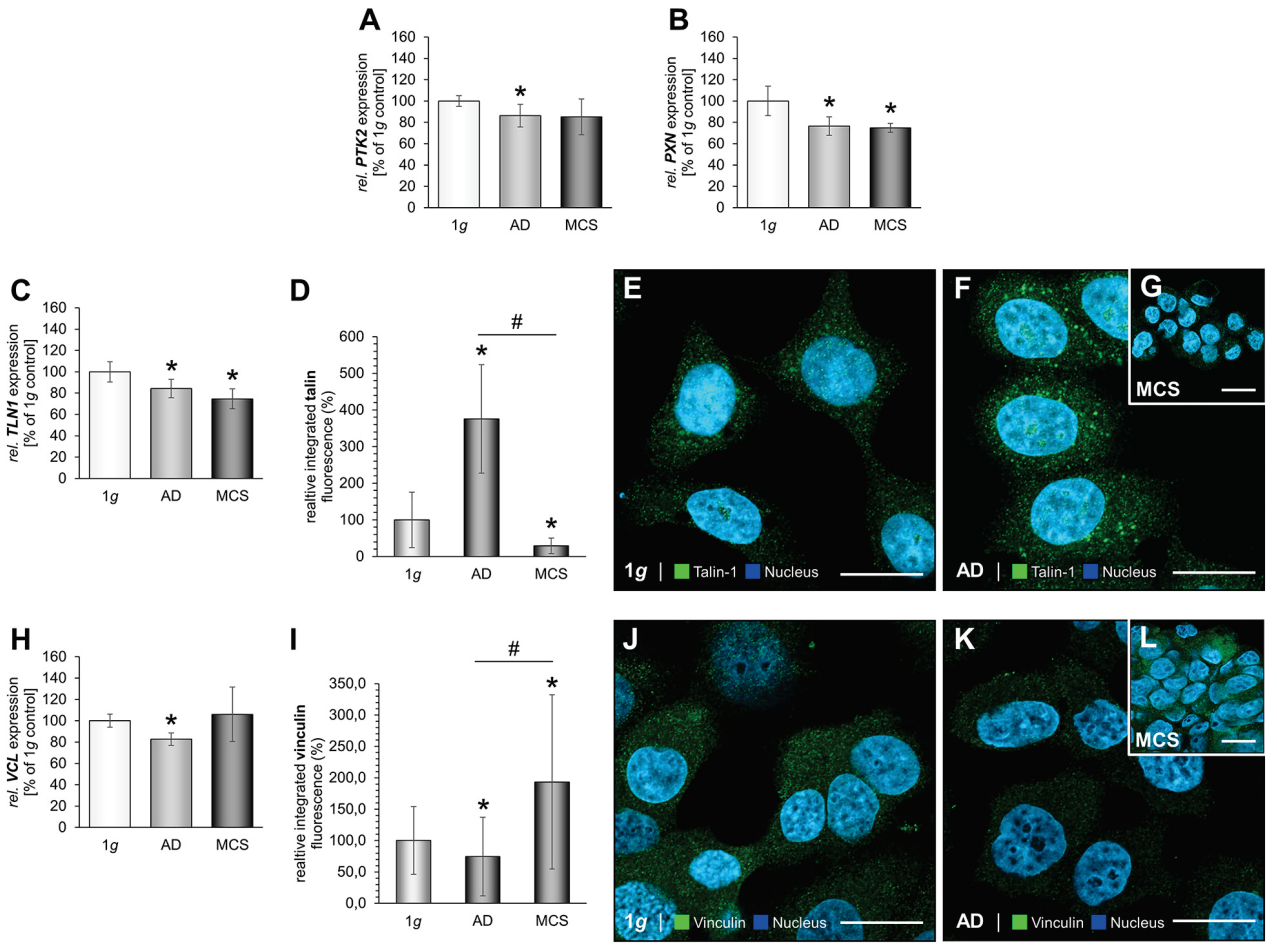


FIGURE 5 | Focal adhesions in MCF-7 BCC. The *PTK2* mRNA expression **(A)**, *PXN* mRNA expression **(B)** of MCF-7 cells exposed to the RPM. In addition, the gene expression of *TLN1* **(C)** and analysis of the fluorescence intensity of talin **(D)**, IFS of 1*g* control cells **(E)** and RPM-exposed MCF-7 BCC [AD: **(F),** MCS: **(G)**] is given. *VCL* mRNA **(H)** and analysis of the fluorescence intensity of vinculin **(I)**, the IFS of vinculin are shown in 1*g* control cells **(J)** and RPM-exposed cells [AD: **(K),** MCS: **(L)**]. $*p < 0.05$ 1*g* vs. AD and/or MCS and $\#p < 0.05$ AD vs. MCS.

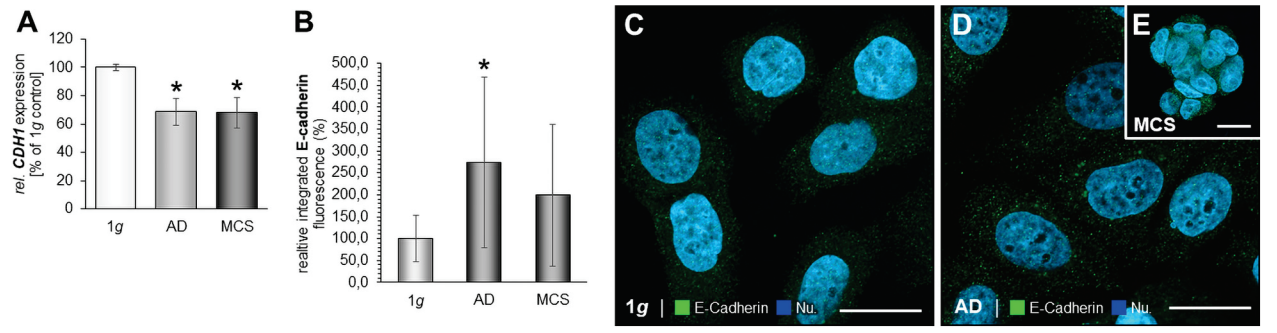


FIGURE 6 | E-cadherin in microgravity-exposed MCF-7 BCC. **(A)** *CDH1* gene expression in MCF-7 BCC exposed to s-μ*g*. **(B)** Analysis of the fluorescence intensity of E-cadherin **(C)**, IFS of E-cadherin of 1*g* MCF-7 BCC RPM-exposed BCC [AD: **(D),** MCS: **(E)**]. $*p < 0.05$ 1*g* vs. AD and/or MCS.

samples and up-regulated in MCS (**Figure 8M**). The *CCND1* mRNA was not changed (**Figure 8N**). Furthermore, the *NFATC2* mRNA was not significantly altered after RPM exposure (**Figure 8O**).

The Wnt/β-catenin target genes *BCL9* and *MYC* were differentially expressed in RPM-exposed BCC (**Figures 8P,Q**). *BCL9* was significantly up-regulated in MCS compared to AD and 1*g* samples (**Figure 8P**). The *MYC* mRNA was

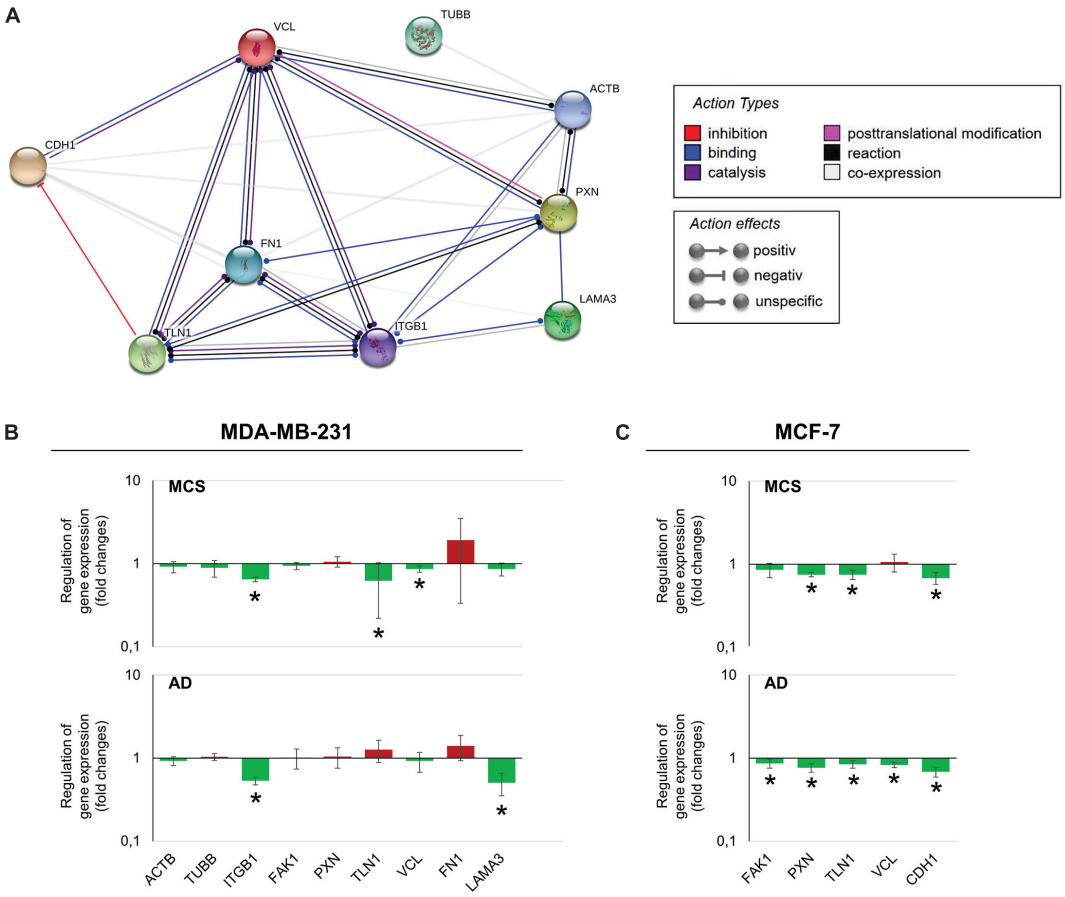


FIGURE 7 | (A) Network of the functional interaction of genes and their products analyzed in this study. The analysis was performed by STRING (Search Tool for the Retrieval of Interacting Genes/Proteins, v11.0) provided by the STRING Consortium (available online: https://string-db.org/). The result is presented in the molecule action mode. Gene names are indicated. **(B)** Summary of the gene expression fold change measured by qPCR of 24 h RPM-exposed MDA-MB-231 samples. Results determined in AD and MCS in relation to 1*g* were given. The red color indicates up-regulated genes and the green color down-regulated genes. **(C)** Summary of the gene expression fold change measured by qPCR of 24-h RPM-exposed MCF-7 samples. The * indicates a significant change in fold change.

significantly elevated in AD cells compared to 1*g* and MCS samples (**Figure 8Q**).

DISCUSSION

In this study, we focused on the changes induced in MDA-MB-231 and MCF-7 BCC when they were cultured under s-μ*g* conditions created by an RPM. The RPM, suggested also as ground-based facility by the European Space Agency, was chosen for our experiments because effects on various cells with respect to behavior and morphology seen in r-μ*g* are reproduced with good agreement (Wuest et al., 2015). Nevertheless, a final validation of our data is necessary in r-μ*g* to justify the term s-μ*g* in the context of our experimental approach. The MDA-MB-231 cell line is a good model for the basal-like or triple-negative form of BC (Chavez et al., 2010). This cell line was established from a pleural effusion of a patient with invasive ductal carcinoma and is E-cadherin-negative and expresses mutated p53. In contrast, the MCF-7 cell line is estrogen receptor (ER)-, progesterone receptor (PR)-, and E-cadherin-positive (Soule et al., 1973; Kopp et al., 2016), and it represents a model of a well-differentiated BC type.

The dynamic biological process of cell adhesion plays an important role in cell detachment and aggregation into 3D spheroids (Gumbiner, 1996). It has long been known that μ*g* influences cell-to-cell interactions and alters the cytoskeleton, integrins, and ECM components of mammalian cells (Buravkova et al., 2005; Aleshcheva et al., 2016; Hader et al., 2017).

Various researchers have demonstrated that the adherence behavior of human cells changes when they are exposed to μ*g* conditions (Dittrich et al., 2018; Zhao et al., 2018; Deng et al., 2019; Nassef et al., 2019a; Romswinkel et al., 2019). In particular, cell adhesion changes are involved in the scaffold-free formation of MCS (Riwaldt et al., 2015a; Svejgaard et al., 2015; Dittrich et al., 2018; Buken et al., 2019). The two cell adhesion molecules ICAM-1 and VCAM-1 are significantly altered by μ*g* in different mammalian cells (Paulsen et al., 2015; Riwaldt et al., 2015b; Tauber et al., 2017; Buken et al., 2019). Their specific involvement in 3D growth was suggested for thyroid cancer cells after the CellBox-1 space mission (Riwaldt et al., 2015a).

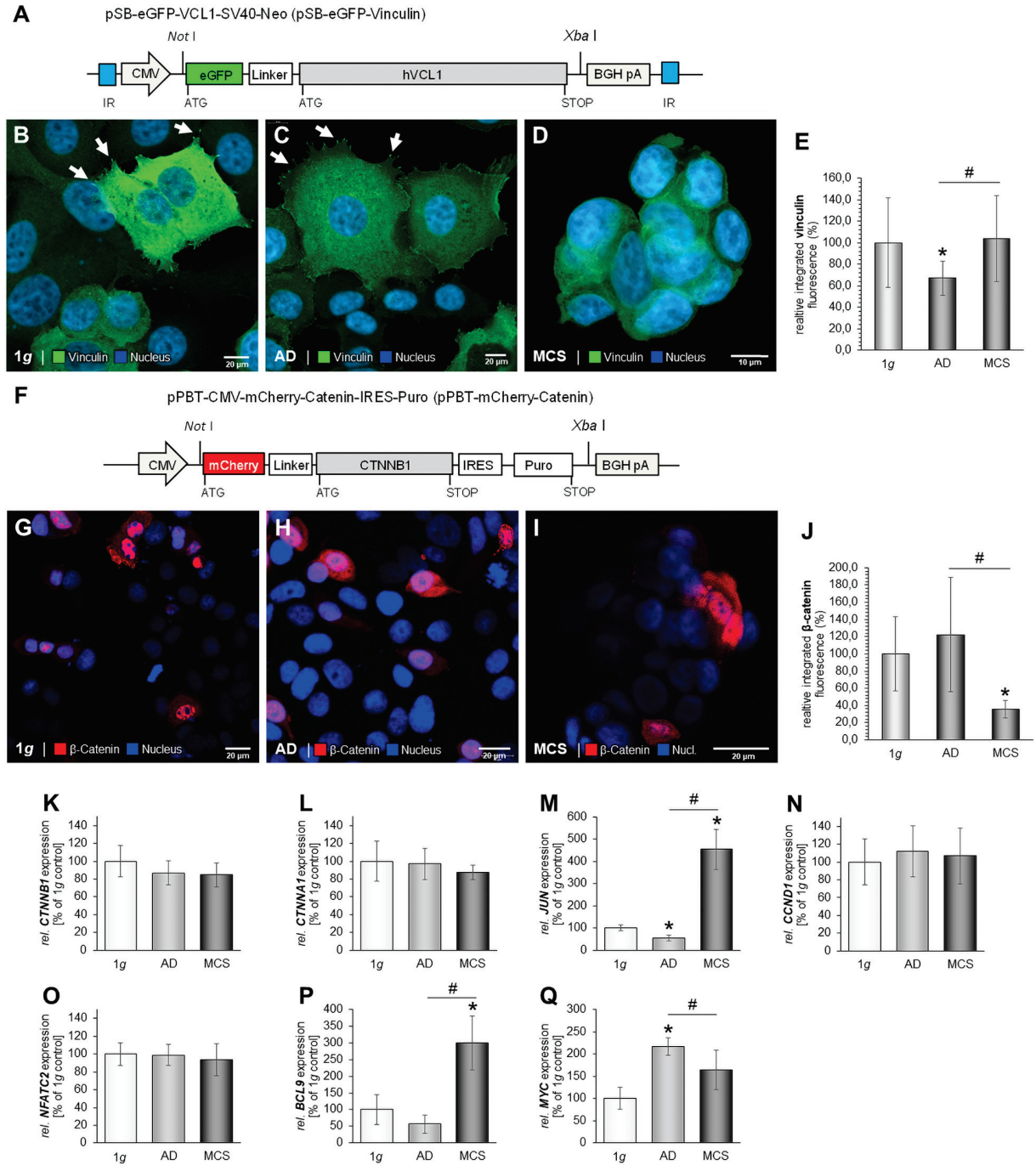


FIGURE 8 | Stable expression of eGFP-vinculin in MCF-7 cells. Following co-transfection of pSB-eGFP-vinculin and pCMV-SB100X cells were cultured in medium containing G418 to allow growth of stably transfected cells only. **(A)** Graphic illustration of the pSB-eGFP-vinculin plasmid containing the coding sequence of the eGFP-vinculin fusion protein encoded from a CMV promoter. Restrictions used for cloning are indicated. BGH pA, bovine growth hormone polyadenylation site; CMV, cytomegalovirus promoter; IR, internal repeats. **(B)** Image of eGFP-vinculin in MCF-7 cells subjected to 1*g*. The white arrows show lamellipodia and vinculin focal adhesion dots. **(C)** Image of eGFP-vinculin in MCF-7 cells after RPM exposure. The white arrows indicate vinculin dots **(D)** Image of eGFP-vinculin in MCF-7 MCS following RPM-exposure. Scale bars 10 μm. Expression of mCherry-catenin in MCF-7 cells. MCF-7 cells were transfected with pPBT-mCherry-catenin and images were captured 48 h post transfection. **(E)** Analysis of the fluorescence intensity of eGFP-vinculin. **(F)** Graphic illustration of the pSB-eGFP-vinculin plasmid containing the coding sequence of the eGFP-vinculin fusion protein encoded from a CMV promoter. Restrictions used for cloning are indicated. BGH pA, bovine growth hormone polyadenylation site; CMV, cytomegalovirus promoter. **(G)** Image of MCF-7 cells expressing mCherry-catenin at 1*g*. **(H)** Image of RPM-exposed adherent MCF-7 cells expressing mCherry-catenin following incubation at μ*g*. **(I)** Image of MCF-7 MCS expressing mCherry-catenin following incubation at μ*g*. Scale bars 20 μm. **(J)** Analysis of the fluorescence intensity of mCherry-catenin. Gene expressions of *CTNNB1* **(K)**; *CTNNA1* **(L)**; JUN **(M)**; *CCND1* **(N)**; *NFATC2* **(O)**; *BCL9* mRNA **(P)** and *MYC* **(Q)**, MCF-7 cells exposed to the RPM. *$p < 0.05$ 1*g* vs. AD and/or MCS and #$p < 0.05$ AD vs. MCS.

Originale der Publikationen

Changes in the Cytoskeleton and Extracellular Matrix

It is well known that μ*g* induces a disorganization in the network of microfilaments, intermediate filaments, and microtubules in various cell types (Vorselen et al., 2014). Several studies have revealed that the formation of the cytoskeleton is highly sensitive to alterations in gravity and shown that altered gravity conditions have an enormous impact on the cytoskeleton and the differential expression of genes related to it (Vassy et al., 2001; Uva et al., 2002; Ulbrich et al., 2011; Aleshcheva et al., 2013, 2015; Corydon et al., 2016a).

In this study, we observed that the gene expression of *ACTB* was not differentially altered in MDA-MB-231 cells after 24 h of RPM exposure. This is in accordance with earlier results obtained from MCF-7 BCC cultured for 24 h on the RPM (Kopp et al., 2016). In parallel, the *TUBB* gene expression was not altered in adherently growing RPM-exposed MDA-MB-231 cells compared with 1*g* samples. *TUBB* remained unchanged in MCS samples. This finding is different to the *TUBB* gene expression of MCF-7 BCC, FTC-133 thyroid cancer cells, and normal thyroid cells exposed to s-μ*g* (Kopp et al., 2015, 2016), where a downregulation of the *TUBB* gene was observed in MCS of these cell types. This difference may be explained by the low differentiation of the MDA-MB-231 BC type.

In addition, we studied the expression of fibronectin. In general, we found a slight but insignificant trend for an increase in *FN1* at the mRNA level when MDA-MB-231 cells were exposed to the RPM. Interestingly, the IIF staining revealed an increase of fibronectin protein in AD and MCS cells. In general protein and mRNA abundance, although derived from the same tissue or cell type, is usually in a non-linear relationship as multiple processes beyond transcript concentration contribute to protein abundance. Protein abundance modulation through the binding to regulatory elements (e.g., micro-RNAs), protein's half-life, autophagy, protein synthesis delay by physical distance, availability of involved actors and feedback regulatory mechanisms usually leading to a reduced correlation between mRNA and protein levels.

This protein data fits with the results of an earlier study on human fetal osteoblasts exposed to the RPM, where the cells showed elevated *FN1* gene expression and fibronectin protein content after a seven-day period of RPM exposure (Mann et al., 2019). In addition, the *FN1* gene expression was not changed in MCF-7 spheroids after 24 h of RPM-exposure (Kopp et al., 2016).

LAMA3 mRNA was reduced in AD samples, but not differentially expressed in MDA-MB-231 MCS samples compared with 1*g* controls. This is in contrast to the data obtained from MCF-7 cells, where *LAMA3* was significantly up-regulated in MCS (Kopp et al., 2016). This finding may be due to the formation of gland-like MCS when MCF-7 cells were exposed to the RPM for 5 days (Kopp et al., 2016). Laminin is a component of the basal lamina of a cell and influences the biological processes differentiation, migration and adhesion. This might explain the high amount of *LAMA3* mRNA in MCS, where a high grade of differentiation and changes in the extracellular matrix components occur to form the 3D glandular structures.

The Focal Adhesions of BCC Grown in Simulated Microgravity

Furthermore, we focused on the FAs of MDA-MB-231 and MCF-7 BCC exposed to the RPM. FAs are subcellular structures mediating cellular signaling processes as a reaction to ECM adhesion and are known as mechanical linkages to the ECM. FAs are key players in gravisensing and the detachment of cells and following aggregation into 3D assemblies. This aggregation occurs through changes in the mechanical loading conditions in an s-μ*g* environment, among other pathways (Geiger et al., 2009; Romswinkel et al., 2019).

Vinculin has an impact on cell–matrix adhesion and intercellular junctions and plays an important role in mechanotransduction with integrins at FA sites (Spanjaard and de Rooij, 2013). Vinculin interacts with talin, integrins, and actin, and thus influences cellular migration and focal adhesion. Vinculin is a mediator of cellular and extracellular signals. The gene expression of *VCL* was reduced in the MCS of MDA-MB-231 cells compared to 1*g* (**Figure 4I**). IFS of vinculin revealed an increase of the fluorescence intensity in AD samples and no change in MDA-MB-231 MCS.

The other important FA component investigated in this study is the cytosolic and mechanosensitive protein talin. Its major task is to link integrins directly and indirectly *via* vinculin to the cytoskeleton. Talin-1 is involved in cell adhesion, progression, extravasation, and *trans*-endothelial migration in cancer. Integrins bind to talin, and then talin connects to vinculin to influence the process of cell adhesion. Finally, integrin receptors promote the attachment of adherent growing cells to the ECM. In this context, talin acts as mechanotransductor. In triple-negative MDA-MB-231 BCC, the *TLN1* gene expression in AD was not significantly changed, but reduced in MCS. The IFS of talin-1 revealed an increase in talin-1 protein in AD samples compared to 1*g* and MCS in TNBC (**Figure 4E**). In MCF-7 cells, the *TLN1* gene expression was significantly reduced in AD and MCS cells compared to 1*g* (**Figure 5C**). As talin carries the mechanical force in ECM and cell adhesion, the reduced expression of talin would indicate less cell adhesion and cell detachment in the s-μ*g* environment.

The cell surface receptor and cell adhesion molecule integrin-β1 is encoded by the *ITGB1* gene. We found a down-regulation of *ITGB1* in MDA-MB-231 cells exposed to s-μ*g* (**Figure 4A**). Integrin-β1 links the actin cytoskeleton with the ECM, and, thus, signaling transduction is possible between the ECM and the cytoplasm. In addition, integrin-β1 modulates gene expression within the cell and is a key player in mechanotransduction (Katsumi et al., 2004; Legate et al., 2009). Integrin-β1, talin, vinculin, fibronectin, and laminin play key roles in focal adhesion processes and can give hint that focal adhesion is less in MCS. These findings are in agreement with the results of a recently published paper (Monti et al., 2021). The adhesion process is very important for the survival strategy of cancer cells to antagonize cell death when the cells are exposed to the RPM. The cytoskeleton, integrins and focal adhesion factors are involved in anti-apoptotic strategies, depending on the cell type (Monti et al., 2021). No signs of apoptosis were

Originale der Publikationen

found in MCF-7 cells after a 24-h RPM-exposure, which was paralleled by a reduction of vinculin and integrin-β1 in MCS (Monti et al., 2021).

Furthermore, the focal adhesion kinase [FAK/protein tyrosine kinase 2 (PTK2)] is involved in mechanosensing and transduction, proliferation, and migration; it links the ECM and the cytoskeleton (McLean et al., 2005). *FAK1/PTK2* gene expression was not changed in all MDA-MB-231 groups (**Figure 4B**). The protein paxillin is encoded by the *PXN* gene. Paxillin is expressed at FA and its function is to adhere human cells to the ECM. Other FA proteins can bind to paxillin, like FAK1 or vinculin. In MCF-7 cells, the *PXN* mRNA in AD and MCS and the corresponding proteins were reduced as compared to 1*g* (**Figure 5B**). In MDA-MB-231 cells, *PXN* gene expression was unchanged (**Figure 4C**). These findings fit to the results obtained for integrin-β1, which were similarly regulated. This underlines their close interaction when BCCs were exposed to s-μ*g*, leading to cell detachment and the formation of 3D spheroids, where the expression level of FA components can regulate migration and 3D aggregation.

Interaction Network of Selected Genes Evaluated by STRING Analysis

The STRING analysis revealed several interactions between the selected factors. *FN1, VCL, TLN1*, and *ITGB1* are indicated as dominant target genes, as many arrows point to their icons (**Figure 7A**). Fibronectin was found to be the central target gene. There exist interactions between vinculin and fibronectin. The *FN1* gene expression was unaltered in MDA-MB-231 cells (**Figure 3A**). The *FN1* gene expression was also not changed in MCF-7 BCC as published earlier (Kopp et al., 2016). The *VCL* mRNA was down-regulated in RPM-exposed MDA-MB-231 MCS cells (**Figure 4I**). In MCF-7 cells, the *VCL* mRNA was significantly reduced in AD cells. Differences between BC cell types may be due to the different characteristic features of the two breast BC types.

Fibronectin is elevated in podocytes by mechanical stress (Kliewe et al., 2019). Fibronectin KO podocytes showed significantly down-regulated FA molecules (talin, vinculin, and paxillin) as well as a reduction in cell spreading, indicating an important role of fibronectin in adhesion (Kliewe et al., 2019). Fibronectin plays a key role in the adaptation of podocytes to mechanical stress. This finding supports the hypothesis that the interaction of FN1 with vinculin is an adaptive mechanism to protect μ*g*-exposed BCC from mechanical stress. FN1 also interacts with talin and paxillin. Talin links intracellular networks with the ECM *via* its connection with the actin cytoskeleton and membrane integrins (Haining et al., 2016). Talin exposes new recognition sites when undergoing force-induced mechanical unfolding, and it can bind to and recruit cytoskeletal proteins that are involved in mechanotransduction and MCS formation (Haining et al., 2016). Moreover, paxillin and fibronectin are involved in embryonic developmental events, possibly due to paxillin-mediated modulation of fibronectin-regulated focal adhesion dynamics and organization of the membrane cytoskeletal structures. Thus, paxillin regulates cell migration and spreading of BCC (Hagel et al., 2002). In addition, VCL interacts with CDH1. The cell adhesion glycoprotein E-cadherin (CDH1) is commonly inactivated and reduced in progressive breast tumors. In MCS of MCF-7 cells, it was down-regulated after 14 days of RPM exposure (Sahana et al., 2018). Vinculin is involved in the establishment or regulation of the cadherin-based cell adhesion complex. This process is mediated by a direct interaction with β-catenin (Hazan et al., 1997). The loss of cell–cell adhesion is involved in cancer invasion and metastasis. It has been shown that vinculin impacts metastasis and prognosis in several tumors (Li et al., 2014; Zhang et al., 2019).

As demonstrated in **Figure 4I**, the *VCL* gene expression levels were reduced in MCS of MDA-MB-231. In addition, *VCL* mRNA was significantly down-regulated in MCF-7 AD cells. These findings were also confirmed in highly metastatic CRC cell lines and metastatic tissues (Li et al., 2014).

The *ITGB1* gene expression was significantly reduced in MCS of MCF-7 cells (Kopp et al., 2016). This was also measured in MDA-MB-231 cells, where the *ITGB1* mRNA was clearly down-regulated in AD and MCS cells (**Figure 4A**). Integrin-β1 is a membrane protein and is linked to the ECM with the cytoskeleton; it is also capable of transmitting signals (Yeh et al., 2012).

The STRING analysis revealed an interaction between fibronectin and integrin-β1, both playing a central role in 3D formation (Buken et al., 2019). When integrin-β1 is activated and forms a heterodimer with an appropriate integrin-α, integrin-β1 can bind to fibronectin, laminin, and other ECM components *via* the extracellular domain (Lessan et al., 1999). In addition, integrin-β1 can be activated by binding talin and kindlin *via* its cytoplasmic domain (Meves et al., 2013). This binding signal will be transferred to the cytoskeleton and the FA complex *via* vinculin and actin (Gingras et al., 2010).

Vinculin and β-Catenin Signaling in RPM-Exposed MCF-7 Cells

It is known that vinculin regulates the cell surface E-cadherin expression by regulating β-catenin (Peng et al., 2010). In addition, the loss of vinculin and membrane-bound β-catenin promotes metastasis in colorectal cancer (Li et al., 2014) and may also play a role in progression of other cancer types. The loss of cell adhesion is important for spheroid formation and also for metastasis. Vinculin is a key adhesion-related protein and is involved in metastasis in various tumors (Li et al., 2014).

As shown in **Figure 6**, RPM-exposure of MCF-7 cells resulted in a down-regulation of *CDH1*. Therefore, we focused in detail on vinculin and β-catenin signaling in MCF-7 cells. Unfortunately, MDA-MB-231 cells do not express E-cadherin (Eslami Amirabadi et al., 2019), and, therefore, we used the MCF-7 cell line for this study.

Live cell imaging of vinculin/β-catenin transfected MCF-7 cells exposed to the RPM revealed that vinculin was distributed throughout the cytoplasm. The protein was detectable at adhesive membrane areas. It is known to mediate the interactions of integrins and the actin cytoskeleton (Bays and DeMali, 2017).

Vinculin regulates the adhesion process by interacting with actin. The connection of vinculin to F-actin is important in regard to its role in cell–matrix adhesion. Changes in the vinculin–F-actin interaction can impact morphology, stiffness, adhesion and migration of the cells (Ezzell et al., 1997).

β-catenin (mCherry) was located in the nucleus and cytoplasm in all adherent cells (**Figure 8**; 1*g*, RPM-AD). In MCS, β-catenin was detectable in the membranes. β-catenin is a known cadherin-associated protein and an important cell adhesion regulator. Furthermore, β-catenin is a transcriptional co-activator in the nucleus and involved the canonical Wnt signal transduction pathways. Therefore, we have focused on Wnt/β-catenin signaling and on the gene expression of several target genes such as *BCL9, MYC, JUN* and *CCND1* (cyclin D1). Both, *CTNNA1* and *CTNNB1,* mRNAs were not significantly altered by gravitational unloading using the RPM. A similar result for the *CTNNB1* gene expression was obtained when low-differentiated follicular thyroid cancer cells (FTC-133 cell line) were exposed for 4 h or 3 days to the RPM (Melnik et al., 2020). Additional studies using cells providing stable expression of β-catenin may further support the results obtained in transiently transfected MCF-7 cells.

It was reported that mechanical unloading of wildtype mice caused a decrease in Wnt/β-catenin signaling activity accompanied by upregulation of Sost, and it is involved in osteoporosis (Lin et al., 2009). Furthermore, the β-catenin location is sensitive to s-μ*g* in osteoblasts (Yin et al., 2018). The nuclear factor of activated T cells (NFAT) is involved in proliferation, angiogenesis, migration in various cancer types (Werneck et al., 2011) and is associated with epithelial–mesenchymal transition (EMT) in breast cancer (Quang et al., 2015). Therefore, we studied the expression of *NFATC2* in our experimental setting. We measured that both *NFATC2* and *CCND1* (cyclin D) were not significantly changed after RPM exposure in MCF-7 cells. An earlier study investigated endothelial cells (EA.hy926 cell line) during a parabolic flight mission (Wehland et al., 2013). The gene expression of *CCND1* was reduced when EA.hy926 cells were studied under vibration (Wehland et al., 2013). No change in the gene expression was measurable when the cells were exposed to hypergravity conditions (Wehland et al., 2013). After one parabola (P) and 31P (real microgravity), the *CCND1* gene was up-regulated (Wehland et al., 2013).

Interestingly, we measured a significant increase in the *BCL9* (B-cell lymphoma 9) and *JUN/c-JUN* (Jun proto-oncogene, AP-1 transcription factor subunit) gene expression of the MCS compared to the 1*g* and the RPM-AD group. The oncogene *BCL9* functions as a transcriptional co-activator of the Wnt/β-catenin signaling pathway in cancer. *BCL9* plays a key role in tumor progression and remodeling of the tumor microenvironment (Jiang et al., 2020). Its upregulation in RPM-exposed samples hints to its involvement in spheroid formation. Little is known about *JUN* in microgravity-exposed cells. A recent study (Shi et al., 2021) investigated the effects of μ*g* on macrophage differentiation from hematopoietic progenitor cells (HPCs) and demonstrated that a 12-day RCCS exposure of these cells reduced the amount of p-JUN in the RCCS-exposed group.

Furthermore, we investigated the *MYC* (c-myc) gene expression. *MYC* was significantly elevated in RPM-AD cells as compared to the 1*g* and MCS group. This is an interesting finding which was also observed *in vivo* in mice exposed to a 30-day spaceflight (Radugina et al., 2018). Radugina et al. demonstrated the nuclear immunolocalization of c-Jun and c-Myc proteins, indicating their sensitivity to μ*g*. Future research is necessary to gain more information about the impact of μ*g* on cancer growth and the involvement of the Wnt/β-catenin signaling pathway.

In summary, a 24 h RPM exposure of triple-negative MDA-MB-231 and MCF-7 BCC induced changes in growth, the cytoskeleton, the extracellular matrix, and focal adhesions. As demonstrated in **Figure 1**, multicellular tumor spheroids of both cell lines showed a fast migration behavior and clear invasion potential when co-cultured with EA.hy926 endothelial cells. After a 24 h RPM-cultivation, multiple round compact MCS and in parallel adherent cells were visible in the cell culture supernatant of both cell types. The 3D aggregates will be used in future studies to examine the effects of anticancer drugs. MCS closely mimic the form and micromilieu of a metastasis. In this study, MDA-MB-231 BC MCS cells grown under conditions of s-μ*g* exhibited a differential regulation of the expression of ECM, and FA genes, such as *ITGB1, VCL* and *TLN1*. RPM exposure of MCF-7 BC MCS cells resulted in significant changes in the gene expression of *PXN, TLN1,* and *CDH1*, and the WNT-β-catenin target genes *BCL9, JUN* and *MYC*. The focal adhesion complex as well as cell adhesion molecules and the cytoskeleton are important gravisensors in μ*g*.

Taken together, the overall gene expression pattern is only slightly modified by RPM-exposure as previously evidenced (Po et al., 2019). Facing an essential maintenance of an overall coherence in gene expression pattern, the only few genes that are modified by microgravity are those involved in growth, the cytoskeleton and mechanotransduction.

In conclusion, BCC (MCF-7 and MDA-MB-231 cells) were exposed to s-μ*g* conditions generated by an RPM. During cell culture on the RPM, the cells transformed from a 2D monolayer into tissue specific multicellular *in vitro* 3D spheroids. The RPM-exposed cells revealed alterations in cytoskeletal proteins, as well as changes in ECM components and FA factors. A 24-h RPM-exposure induced a significant down-regulation of *ITGB* and *LAMA3* mRNAs in adherent cells and in MCS of the MDA-MB-231 cell line. Moreover, the *VCL* mRNA was significantly reduced in MDA-MB-231 MCS cells. In contrast, the gene expression of *FAK1, PXN, TLN1, VCL,* and *CDH1* was significantly down-regulated in adherent MCF-7 cells cultured for 24 h on the RPM. In addition, *PXN, TLN1* and *CDH1* were down-regulated in MCS, whereas *VCL* and *LAMA3* mRNAs were not changed in MCF-7 cells.

Overall, this study provides novel knowledge about the complexity of adherence, migration and invasion behavior of human BCC spheroids engineered with s-μ*g* technology. Further investigations targeting FA proteins and genes in BCC cultured on an RPM will hopefully, indicate novel targets that are interesting future candidates for cancer therapy.

DATA AVAILABILITY STATEMENT

The datasets analyzed for this study can be provided by contacting the corresponding author.

AUTHOR CONTRIBUTIONS

DG and TC: conceptualization. SKo and JS: methodology. SKo: software. DG, TC, MW, SKo, and MK: validation. DM, SKa, SKo, JS, and MK: formal analysis. JS: investigation. BR, MI, and DG: resources. DG, JS, and TC: writing—original draft preparation. DG, TC, MK, and MW: writing—review and editing. MK and SKa: visualization. DG: supervision and project administration. DG and MI: funding acquisition. All authors have read and agreed to the published version of the manuscript.

FUNDING

This research was funded by Deutsches Zentrum für Luft- und Raumfahrt (DLR), BMWi project 50WB1924.

REFERENCES

Aleshcheva, G., Bauer, J., Hemmersbach, R., Slumstrup, L., Wehland, M., Infanger, M., et al. (2016). Scaffold-free tissue formation under real and simulated microgravity conditions. *Basic Clin. Pharmacol. Toxicol.* 119(Suppl. 3), 26–33. doi: 10.1111/bcpt.12561

Aleshcheva, G., Sahana, J., Ma, X., Hauslage, J., Hemmersbach, R., Egli, M., et al. (2013). Changes in morphology, gene expression and protein content in chondrocytes cultured on a random positioning machine. *PLoS One* 8:e79057. doi: 10.1371/journal.pone.0079057

Aleshcheva, G., Wehland, M., Sahana, J., Bauer, J., Corydon, T. J., Hemmersbach, R., et al. (2015). Moderate alterations of the cytoskeleton in human chondrocytes after short-term microgravity produced by parabolic flight maneuvers could be prevented by up-regulation of BMP-2 and SOX-9. *FASEB J.* 29, 2303–2314. doi: 10.1096/fj.14-268151

Askou, A. L., Aagaard, L., Kostic, C., Arsenijevic, Y., Hollensen, A. K., Bek, T., et al. (2015). Multigenic lentiviral vectors for combined and tissue-specific expression of miRNA- and protein-based antiangiogenic factors. *Mol. Ther. Methods Clin. Dev.* 2:14064. doi: 10.1038/mtm.2014.64

Bays, J. L., and DeMali, K. A. (2017). Vinculin in cell-cell and cell-matrix adhesions. *Cell Mol. Life Sci.* 74, 2999–3009. doi: 10.1007/s00018-017-2511-3

Becker, J. L., and Souza, G. R. (2013). Using space-based investigations to inform cancer research on Earth. *Nat. Rev. Cancer* 13, 315–327. doi: 10.1038/nrc3507

Boonyaratanakornkit, J. B., Cogoli, A., Li, C. F., Schopper, T., Pippia, P., Galleri, G., et al. (2005). Key gravity-sensitive signaling pathways drive T cell activation. *FASEB J.* 19, 2020–2022. doi: 10.1096/fj.05-3778fje

Borst, A. G., and van Loon, J. J. W. A. (2008). Technology and developments for the random positioning machine, RPM. *Micrograv. Sci. Technol.* 21:287. doi: 10.1007/s12217-008-9043-2

Buken, C., Sahana, J., Corydon, T. J., Melnik, D., Bauer, J., Wehland, M., et al. (2019). Morphological and molecular changes in juvenile normal human fibroblasts exposed to simulated microgravity. *Sci. Rep.* 9:11882. doi: 10.1038/s41598-019-48378-9

Buravkova, L., Romanov, Y., Rykova, M., Grigorieva, O., and Merzlikina, N. (2005). Cell-to-cell interactions in changed gravity: ground-based and flight experiments. *Acta Astronaut.* 57, 67–74. doi: 10.1016/j.actaastro.2005.03.012

Chang, T. T., and Hughes-Fulford, M. (2009). Monolayer and spheroid culture of human liver hepatocellular carcinoma cell line cells demonstrate distinct global gene expression patterns and functional phenotypes. *Tissue Eng. Part A* 15, 559–567. doi: 10.1089/ten.tea.2007.0434

Chang, T. T., Walther, I., Li, C. F., Boonyaratanakornkit, J., Galleri, G., Meloni, M. A., et al. (2012). The Rel/NF-kappaB pathway and transcription of immediate early genes in T cell activation are inhibited by microgravity. *J. Leukoc. Biol.* 92, 1133–1145. doi: 10.1189/jlb.0312157

Chavez, K. J., Garimella, S. V., and Lipkowitz, S. (2010). Triple negative breast cancer cell lines: one tool in the search for better treatment of triple negative breast cancer. *Breast Dis.* 32, 35–48. doi: 10.3233/BD-2010-0307

Corydon, T. J., Kopp, S., Wehland, M., Braun, M., Schutte, A., Mayer, T., et al. (2016a). Alterations of the cytoskeleton in human cells in space proved by life-cell imaging. *Sci. Rep.* 6:20043. doi: 10.1038/srep20043

Corydon, T. J., Mann, V., Slumstrup, L., Kopp, S., Sahana, J., Askou, A. L., et al. (2016b). Reduced expression of cytoskeletal and extracellular matrix genes in human adult retinal pigment epithelium cells exposed to simulated microgravity. *Cell Physiol. Biochem.* 40, 1–17. doi: 10.1159/000452520

Deng, B., Liu, R., Tian, X., Han, Z., and Chen, J. (2019). Simulated microgravity inhibits the viability and migration of glioma via FAK/RhoA/Rock and FAK/Nek2 signaling. *Vitro Cell Dev. Biol. Anim.* 55, 260–271. doi: 10.1007/s11626-019-00334-7

Dittrich, A., Grimm, D., Sahana, J., Bauer, J., Kruger, M., Infanger, M., et al. (2018). Key Proteins involved in spheroid formation and angiogenesis in endothelial cells after long-term exposure to simulated microgravity. *Cell Physiol. Biochem.* 45, 429–445. doi: 10.1159/000486920

Eslami Amirabadi, H., Tuerlings, M., Hollestelle, A., SahebAli, S., Luttge, R., van Donkelaar, C. C., et al. (2019). Characterizing the invasion of different breast cancer cell lines with distinct E-cadherin status in 3D using a microfluidic system. *Biomed. Microdev.* 21:101. doi: 10.1007/s10544-019-0450-5

Ezzell, R. M., Goldmann, W. H., Wang, N., Parashurama, N., and Ingber, D. E. (1997). Vinculin promotes cell spreading by mechanically coupling integrins to the cytoskeleton. *Exp. Cell Res.* 231, 14–26. doi: 10.1006/excr.1996.3451

Geiger, B., Spatz, J. P., and Bershadsky, A. D. (2009). Environmental sensing through focal adhesions. *Nat. Rev. Mol. Cell Biol.* 10, 21–33. doi: 10.1038/nrm2593

Gingras, A. R., Bate, N., Goult, B. T., Patel, B., Kopp, P. M., Emsley, J., et al. (2010). Central region of talin has a unique fold that binds vinculin and actin. *J. Biol. Chem.* 285, 29577–29587. doi: 10.1074/jbc.M109.095455

Grimm, D., Bauer, J., Wise, P., Kruger, M., Simonsen, U., Wehland, M., et al. (2020). The role of SOX family members in solid tumours and metastasis. *Semin. Cancer Biol.* 67(Pt 1), 122–153. doi: 10.1016/j.semcancer.2019.03.004

Gumbiner, B. M. (1996). Cell adhesion: the molecular basis of tissue architecture and morphogenesis. *Cell* 84, 345–357. doi: 10.1016/s0092-8674(00)81279-9

Hader, D. P., Braun, M., Grimm, D., and Hemmersbach, R. (2017). Gravireceptors in eukaryotes-a comparison of case studies on the cellular level. *NPJ Micrograv.* 3:13. doi: 10.1038/s41526-017-0018-8

Hagel, M., George, E. L., Kim, A., Tamimi, R., Opitz, S. L., Turner, C. E., et al. (2002). The adaptor protein paxillin is essential for normal development in the mouse and is a critical transducer of fibronectin signaling. *Mol. Cell Biol.* 22, 901–915. doi: 10.1128/mcb.22.3.901-915.2002

Haining, A. W., Lieberthal, T. J., and Del Rio Hernandez, A. (2016). Talin: a mechanosensitive molecule in health and disease. *FASEB J.* 30, 2073–2085. doi: 10.1096/fj.201500080R

Hazan, R. B., Kang, L., Roe, S., Borgen, P. I., and Rimm, D. L. (1997). Vinculin is associated with the E-cadherin adhesion complex. *J. Biol. Chem.* 272, 32448–32453. doi: 10.1074/jbc.272.51.32448

Hughes-Fulford, M. (2003). Function of the cytoskeleton in gravisensing during spaceflight. *Adv. Space Res.* 32, 1585–1593. doi: 10.1016/S0273-1177(03)90399-1

Jiang, M., Kang, Y., Sewastianik, T., Wang, J., Tanton, H., Alder, K., et al. (2020). BCL9 provides multi-cellular communication properties in colorectal cancer by interacting with paraspeckle proteins. *Nat. Commun.* 11:19. doi: 10.1038/s41467-019-13842-7

Katsumi, A., Orr, A. W., Tzima, E., and Schwartz, M. A. (2004). Integrins in mechanotransduction. *J. Biol. Chem.* 279, 12001–12004. doi: 10.1074/jbc.R300038200

Kliewe, F., Kaling, S., Lotzsch, H., Artelt, N., Schindler, M., Rogge, H., et al. (2019). Fibronectin is up-regulated in podocytes by mechanical stress. *FASEB J.* 33, 14450–14460. doi: 10.1096/fj.201900978RR

Kopp, S., Sahana, J., Islam, T., Petersen, A. G., Bauer, J., Corydon, T. J., et al. (2018). The role of NFkappaB in spheroid formation of human breast cancer cells cultured on the random positioning machine. *Sci. Rep.* 8:921. doi: 10.1038/s41598-017-18556-8

Kopp, S., Slumstrup, L., Corydon, T. J., Sahana, J., Aleshcheva, G., Islam, T., et al. (2016). Identifications of novel mechanisms in breast cancer cells involving duct-like multicellular spheroid formation after exposure to the Random Positioning Machine. *Sci. Rep.* 6:26887. doi: 10.1038/srep26887

Kopp, S., Warnke, E., Wehland, M., Aleshcheva, G., Magnusson, N. E., Hemmersbach, R., et al. (2015). Mechanisms of three-dimensional growth of thyroid cells during long-term simulated microgravity. *Sci. Rep.* 5:16691. doi: 10.1038/srep16691

Kristensen, T. B., Knutsson, M. L., Wehland, M., Laursen, B. E., Grimm, D., Warnke, E., et al. (2014). Anti-vascular endothelial growth factor therapy in breast cancer. *Int. J. Mol. Sci.* 15, 23024–23041. doi: 10.3390/ijms151223024

Krüger, M., Melnik, D., Kopp, S., Buken, C., Sahana, J., Bauer, J., et al. (2019). Fighting thyroid cancer with microgravity research. *Int. J. Mol. Sci.* 20:2553. doi: 10.3390/ijms20102553

Legate, K. R., Wickstrom, S. A., and Fassler, R. (2009). Genetic and cell biological analysis of integrin outside-in signaling. *Genes Dev.* 23, 397–418. doi: 10.1101/gad.1758709

Lessan, K., Aguiar, D. J., Oegema, T., Siebenson, L., and Skubitz, A. P. (1999). CD44 and beta1 integrin mediate ovarian carcinoma cell adhesion to peritoneal mesothelial cells. *Am. J. Pathol.* 154, 1525–1537. doi: 10.1016/s0002-9440(10)65406-5

Lewis, M. L., Reynolds, J. L., Cubano, L. A., Hatton, J. P., Lawless, B. D., and Piepmeier, E. H. (1998). Spaceflight alters microtubules and increases apoptosis in human lymphocytes (Jurkat). *FASEB J.* 12, 1007–1018. doi: 10.1096/fasebj.12.11.1007

Li, J., Zhang, S., Chen, J., Du, T., Wang, Y., and Wang, Z. (2009). Modeled microgravity causes changes in the cytoskeleton and focal adhesions, and decreases in migration in malignant human MCF-7 cells. *Protoplasma* 238, 23–33. doi: 10.1007/s00709-009-0068-1

Li, T., Guo, H., Song, Y., Zhao, X., Shi, Y., Lu, Y., et al. (2014). Loss of vinculin and membrane-bound beta-catenin promotes metastasis and predicts poor prognosis in colorectal cancer. *Mol. Cancer* 13:263. doi: 10.1186/1476-4598-13-263

Lin, C., Jiang, X., Dai, Z., Guo, X., Weng, T., Wang, J., et al. (2009). Sclerostin mediates bone response to mechanical unloading through antagonizing Wnt/beta-catenin signaling. *J. Bone Miner. Res.* 24, 1651–1661. doi: 10.1359/jbmr.090411

Ma, X., Wehland, M., Schulz, H., Saar, K., Hubner, N., Infanger, M., et al. (2013). Genomic approach to identify factors that drive the formation of three-dimensional structures by EA.hy926 endothelial cells. *PLoS One* 8:e64402. doi: 10.1371/journal.pone.0064402

Mann, V., Grimm, D., Corydon, T. J., Kruger, M., Wehland, M., Riwaldt, S., et al. (2019). Changes in human foetal osteoblasts exposed to the random positioning machine and bone construct tissue engineering. *Int. J. Mol. Sci.* 20:1357. doi: 10.3390/ijms20061357

Masiello, M. G., Cucina, A., Proietti, S., Palombo, A., Coluccia, P., D'Anselmi, F., et al. (2014). Phenotypic switch induced by simulated microgravity on MDA-MB-231 breast cancer cells. *Biomed. Res. Int.* 2014:652434. doi: 10.1155/2014/652434

McLean, G. W., Carragher, N. O., Avizienyte, E., Evans, J., Brunton, V. G., and Frame, M. C. (2005). The role of focal-adhesion kinase in cancer - a new therapeutic opportunity. *Nat. Rev. Cancer* 5, 505–515. doi: 10.1038/nrc1647

Melnik, D., Sahana, J., Corydon, T. J., Kopp, S., Nassef, M. Z., Wehland, M., et al. (2020). Dexamethasone inhibits spheroid formation of thyroid cancer cells exposed to simulated microgravity. *Cells* 9:367. doi: 10.3390/cells9020367

Meves, A., Stremmel, C., Bottcher, R. T., and Fassler, R. (2013). beta1 integrins with individually disrupted cytoplasmic NPxY motifs are embryonic lethal but partially active in the epidermis. *J. Invest. Dermatol.* 133, 2722–2731. doi: 10.1038/jid.2013.232

Monti, N., Masiello, M. G., Proietti, S., Catizone, A., Ricci, G., Harrath, A. H., et al. (2021). Survival pathways are differently affected by microgravity in normal and cancerous breast cells. *Int. J. Mol. Sci.* 22:862. doi: 10.3390/ijms22020862

Nassef, M. Z., Kopp, S., Melnik, D., Corydon, T. J., Sahana, J., Kruger, M., et al. (2019a). Short-Term microgravity influences cell adhesion in human breast cancer cells. *Int. J. Mol. Sci.* 20:5730. doi: 10.3390/ijms20225730

Nassef, M. Z., Kopp, S., Wehland, M., Melnik, D., Sahana, J., Kruger, M., et al. (2019b). Real microgravity influences the cytoskeleton and focal adhesions in human breast cancer cells. *Int. J. Mol. Sci.* 20:3156. doi: 10.3390/ijms20133156

Nyegaard, M., Rendtorff, N. D., Nielsen, M. S., Corydon, T. J., Demontis, D., Starnawska, A., et al. (2015). A novel locus harbouring a functional CD164 nonsense mutation identified in a large danish family with nonsyndromic hearing impairment. *PLoS Genet.* 11:e1005386. doi: 10.1371/journal.pgen.1005386

Paulsen, K., Tauber, S., Dumrese, C., Bradacs, G., Simmet, D. M., Golz, N., et al. (2015). Regulation of ICAM-1 in cells of the monocyte/macrophage system in microgravity. *Biomed. Res. Int.* 2015:538786. doi: 10.1155/2015/538786

Peng, X., Cuff, L. E., Lawton, C. D., and DeMali, K. A. (2010). Vinculin regulates cell-surface E-cadherin expression by binding to beta-catenin. *J. Cell Sci.* 123(Pt 4), 567–577. doi: 10.1242/jcs.056432

Pietsch, J., Kussian, R., Sickmann, A., Bauer, J., Weber, G., Nissum, M., et al. (2010). Application of free-flow IEF to identify protein candidates changing under microgravity conditions. *Proteomics* 10, 904–913. doi: 10.1002/pmic.200900226

Pihlmann, M., Askou, A. L., Aagaard, L., Bruun, G. H., Svalgaard, J. D., Holm-Nielsen, M. H., et al. (2012). Adeno-associated virus-delivered polycistronic microRNA-clusters for knockdown of vascular endothelial growth factor in vivo. *J. Gene Med.* 14, 328–338. doi: 10.1002/jgm.2623

Po, A., Giuliani, A., Masiello, M. G., Cucina, A., Catizone, A., Ricci, G., et al. (2019). Phenotypic transitions enacted by simulated microgravity do not alter coherence in gene transcription profile. *NPJ Micrograv.* 5:27. doi: 10.1038/s41526-019-0088-x

Quang, C. T., Leboucher, S., Passaro, D., Fuhrmann, L., Nourieh, M., Vincent-Salomon, A., et al. (2015). The calcineurin/NFAT pathway is activated in diagnostic breast cancer cases and is essential to survival and metastasis of mammary cancer cells. *Cell Death Dis.* 6:e1658. doi: 10.1038/cddis.2015.14

Radugina, E. A., Almeida, E. A. C., Blaber, E., Poplinskaya, V. A., Markitantova, Y. V., and Grigoryan, E. N. (2018). Exposure to microgravity for 30 days onboard Bion M1 caused muscle atrophy and impaired regeneration in murine femoral Quadriceps. *Life Sci. Space Res.* 16, 18–25. doi: 10.1016/j.lssr.2017.08.005

Riwaldt, S., Bauer, J., Pietsch, J., Braun, M., Segerer, J., Schwarzwalder, A., et al. (2015a). The importance of Caveolin-1 as key-regulator of three-dimensional growth in thyroid cancer cells cultured under real and simulated microgravity conditions. *Int. J. Mol. Sci.* 16, 28296–28310. doi: 10.3390/ijms161226108

Riwaldt, S., Pietsch, J., Sickmann, A., Bauer, J., Braun, M., Segerer, J., et al. (2015b). Identification of proteins involved in inhibition of spheroid formation under microgravity. *Proteomics* 15, 2945–2952. doi: 10.1002/pmic.201500067

Romswinkel, A., Infanger, M., Dietz, C., Strube, F., and Kraus, A. (2019). The Role of C-X-C chemokine receptor Type 4 (CXCR4) in cell adherence and spheroid formation of human Ewing's sarcoma cells under simulated microgravity. *Int. J. Mol. Sci.* 20:6073. doi: 10.3390/ijms20236073

Sahana, J., Nassef, M. Z., Wehland, M., Kopp, S., Kruger, M., Corydon, T. J., et al. (2018). Decreased E-Cadherin in MCF7 human breast cancer cells forming multicellular spheroids exposed to simulated microgravity. *Proteomics* 18:e1800015. doi: 10.1002/pmic.201800015

Sharma, N., Hollensen, A. K., Bak, R. O., Staunstrup, N. H., Schroder, L. D., and Mikkelsen, J. G. (2012). The impact of cHS4 insulators on DNA transposon vector mobilization and silencing in retinal pigment epithelium cells. *PLoS One* 7:e48421. doi: 10.1371/journal.pone.0048421

Shi, L., Tian, H., Wang, P., Li, L., Zhang, Z., Zhang, J., et al. (2021). Spaceflight and simulated microgravity suppresses macrophage development via altered RAS/ERK/NFÎžB and metabolic pathways. *Cell. Mol. Immunol.* 18, 1489–1502. doi: 10.1038/s41423-019-0346-6

Snel, B., Lehmann, G., Bork, P., and Huynen, M. A. (2000). STRING: a web-server to retrieve and display the repeatedly occurring neighbourhood of a gene. *Nucleic Acids Res.* 28, 3442–3444. doi: 10.1093/nar/28.18.3442

Soule, H. D., Vazguez, J., Long, A., Albert, S., and Brennan, M. (1973). A human cell line from a pleural effusion derived from a breast carcinoma. *J. Natl. Cancer Inst.* 51, 1409–1416. doi: 10.1093/jnci/51.5.1409

Spanjaard, E., and de Rooij, J. (2013). Mechanotransduction: vinculin provides stability when tension rises. *Curr. Biol.* 23, R159–R161. doi: 10.1016/j.cub.2013.01.020

Staunstrup, N. H., Sharma, N., Bak, R. O., Svensson, L., Petersen, T. K., Aarenstrup, L., et al. (2011). A Sleeping Beauty DNA transposon-based genetic sensor for functional screening of vitamin D3 analogues. *BMC Biotechnol.* 11:33. doi: 10.1186/1472-6750-11-33

Sung, H., Ferlay, J., Siegel, R. L., Laversanne, M., Soerjomataram, I., Jemal, A., et al. (2021). Global cancer statistics 2020: GLOBOCAN estimates of incidence and mortality worldwide for 36 cancers in 185 countries. *CA Cancer J. Clin.* 71, 209–249. doi: 10.3322/caac.21660

Svejgaard, B., Wehland, M., Ma, X., Kopp, S., Sahana, J., Warnke, E., et al. (2015). Common effects on cancer cells exerted by a random positioning machine and a 2D clinostat. *PLoS One* 10:e0135157. doi: 10.1371/journal.pone.0135157

Tan, X., Xu, A., Zhao, T., Zhao, Q., Zhang, J., Fan, C., et al. (2018). Simulated microgravity inhibits cell focal adhesions leading to reduced melanoma cell proliferation and metastasis via FAK/RhoA-regulated mTORC1 and AMPK pathways. *Sci. Rep.* 8:3769. doi: 10.1038/s41598-018-20459-1

Tauber, S., Lauber, B. A., Paulsen, K., Layer, L. E., Lehmann, M., Hauschild, S., et al. (2017). Cytoskeletal stability and metabolic alterations in primary human macrophages in long-term microgravity. *PLoS One* 12:e0175599. doi: 10.1371/journal.pone.0175599

Ulbrich, C., Pietsch, J., Grosse, J., Wehland, M., Schulz, H., Saar, K., et al. (2011). Differential gene regulation under altered gravity conditions in follicular thyroid cancer cells: relationship between the extracellular matrix and the cytoskeleton. *Cell Physiol. Biochem.* 28, 185–198. doi: 10.1159/000331730

Uva, B. M., Masini, M. A., Sturla, M., Prato, P., Passalacqua, M., Giuliani, M., et al. (2002). Clinorotation-induced weightlessness influences the cytoskeleton of glial cells in culture. *Brain Res.* 934, 132–139. doi: 10.1016/s0006-8993(02)02415-0

van't Veer, L. J., Dai, H., van de Vijver, M. J., He, Y. D., Hart, A. A., Mao, M., et al. (2002). Gene expression profiling predicts clinical outcome of breast cancer. *Nature* 415, 530–536. doi: 10.1038/415530a

Vassy, J., Portet, S., Beil, M., Millot, G., Fauvel-Lafeve, F., Karniguian, A., et al. (2001). The effect of weightlessness on cytoskeleton architecture and proliferation of human breast cancer cell line MCF-7. *FASEB J.* 15, 1104–1106. doi: 10.1096/fj.00-0527fje

Vorselen, D., Roos, W. H., MacKintosh, F. C., Wuite, G. J., and van Loon, J. J. (2014). The role of the cytoskeleton in sensing changes in gravity by nonspecialized cells. *FASEB J.* 28, 536–547. doi: 10.1096/fj.13-236356

Wehland, M., Ma, X., Braun, M., Hauslage, J., Hemmersbach, R., Bauer, J., et al. (2013). The impact of altered gravity and vibration on endothelial cells during a parabolic flight. *Cell Physiol. Biochem.* 31, 432–451. doi: 10.1159/000343380

Werneck, M. B., Vieira-de-Abreu, A., Chammas, R., and Viola, J. P. (2011). NFAT1 transcription factor is central in the regulation of tissue microenvironment for tumor metastasis. *Cancer Immunol. Immunother.* 60, 537–546. doi: 10.1007/s00262-010-0964-4

Wuest, S. L., Richard, S., Kopp, S., Grimm, D., and Egli, M. (2015). Simulated microgravity: critical review on the use of random positioning machines for mammalian cell culture. *Biomed. Res. Int.* 2015:971474. doi: 10.1155/2015/971474

Yeh, Y. C., Lin, H. H., and Tang, M. J. (2012). A tale of two collagen receptors, integrin beta1 and discoidin domain receptor 1, in epithelial cell differentiation. *Am. J. Physiol. Cell Physiol.* 303, C1207–C1217. doi: 10.1152/ajpcell.00253.2012

Yin, C., Zhang, Y., Hu, L., Tian, Y., Chen, Z., Li, D., et al. (2018). Mechanical unloading reduces microtubule actin crosslinking factor 1 expression to inhibit beta-catenin signaling and osteoblast proliferation. *J. Cell Physiol.* 233, 5405–5419. doi: 10.1002/jcp.26374

Zhang, M., Liu, P., Xu, F., He, Y., Xie, X., and Jiang, X. (2019). Vinculin promotes gastric cancer proliferation and migration and predicts poor prognosis in patients with gastric cancer. *J. Cell Biochem.* 120, 14107–14115. doi: 10.1002/jcb.28686

Zhao, T., Li, R., Tan, X., Zhang, J., Fan, C., Zhao, Q., et al. (2018). Simulated microgravity reduces focal adhesions and alters cytoskeleton and nuclear positioning leading to enhanced Apoptosis via Suppressing FAK/RhoA-mediated mTORC1/NF-kappaB and ERK1/2 pathways. *Int. J. Mol. Sci.* 19:1994. doi: 10.3390/ijms19071994

Conflict of Interest: The authors declare that the research was conducted in the absence of any commercial or financial relationships that could be construed as a potential conflict of interest.

The reviewer RH declared a past co-authorship with one of the authors, DG.

Copyright © 2021 Sahana, Corydon, Wehland, Krüger, Kopp, Melnik, Kahlert, Relja, Infanger and Grimm. This is an open-access article distributed under the terms of the Creative Commons Attribution License (CC BY). The use, distribution or reproduction in other forums is permitted, provided the original author(s) and the copyright owner(s) are credited and that the original publication in this journal is cited, in accordance with accepted academic practice. No use, distribution or reproduction is permitted which does not comply with these terms.

frontiers in Cell and Developmental Biology

ORIGINAL RESEARCH
published: 17 February 2022
doi: 10.3389/fcell.2022.841017

Three-Dimensional Growth of Prostate Cancer Cells Exposed to Simulated Microgravity

Dorothea Dietrichs[1], Daniela Grimm[1,2,3], Jayashree Sahana[3], Daniela Melnik[1], Thomas J. Corydon[3,4], Markus Wehland[1,2], Marcus Krüger[1,2], Randy Vermeesen[5], Bjorn Baselet[5], Sarah Baatout[5,6], Trine Engelbrecht Hybel[3], Stefan Kahlert[7], Herbert Schulz[1,2], Manfred Infanger[1,2] and Sascha Kopp[1,2†]*

[1]*Department of Microgravity and Translational Regenerative Medicine, Otto von Guericke University Magdeburg, Magdeburg, Germany,* [2]*Research Group "Magdeburger Arbeitsgemeinschaft für Forschung unter Raumfahrt- und Schwerelosigkeitsbedingungen" (MARS), Otto von Guericke University Magdeburg, Magdeburg, Germany,* [3]*Department of Biomedicine, Aarhus University, Aarhus, Denmark,* [4]*Department of Ophthalmology, Aarhus University Hospital, Aarhus, Denmark,* [5]*Radiobiology Unit, SCK CEN, Belgian Nuclear Research Centre, Mol, Belgium,* [6]*Department of Molecular Biotechnology, Ghent University, Ghent, Belgium,* [7]*Institute of Anatomy, Otto von Guericke University Magdeburg, Magdeburg, Germany*

OPEN ACCESS

Edited by:
Xiaohua Lei, Shenzhen Institutes of Advanced Technology (CAS), China

Reviewed by:
Lucia Morbidelli, University of Siena, Italy
Giulia Ricci, University of Campania Luigi Vanvitelli, Italy

***Correspondence:**
Daniela Grimm
dgg@biomed.au.dk

†Present Address:
Sascha Kopp, Core Facility Tissue Engineering, Otto von Guericke University Magdeburg, Magdeburg, Germany

Specialty section:
This article was submitted to Cell Growth and Division, a section of the journal Frontiers in Cell and Developmental Biology

Received: *21 December 2021*
Accepted: *25 January 2022*
Published: *17 February 2022*

Citation:
Dietrichs D, Grimm D, Sahana J, Melnik D, Corydon TJ, Wehland M, Krüger M, Vermeesen R, Baselet B, Baatout S, Hybel TE, Kahlert S, Schulz H, Infanger M and Kopp S (2022) Three-Dimensional Growth of Prostate Cancer Cells Exposed to Simulated Microgravity. Front. Cell Dev. Biol. 10:841017. doi: 10.3389/fcell.2022.841017

Prostate cancer metastasis has an enormous impact on the mortality of cancer patients. Factors involved in cancer progression and metastasis are known to be key players in microgravity (μ*g*)-driven three-dimensional (3D) cancer spheroid formation. We investigated PC-3 prostate cancer cells for 30 min, 2, 4 and 24 h on the random positioning machine (RPM), a device simulating μ*g* on Earth. After a 24 h RPM-exposure, the cells could be divided into two groups: one grew as 3D multicellular spheroids (MCS), the other one as adherent monolayer (AD). No signs of apoptosis were visible. Among others, we focused on cytokines involved in the events of metastasis and MCS formation. After 24 h of exposure, in the MCS group we measured an increase in *ACTB, MSN, COL1A1, LAMA3, FN1, TIMP1, FLT1, EGFR1, IL1A, IL6, CXCL8*, and *HIF1A* mRNA expression, and in the AD group an elevation of *LAMA3, COL1A1, FN1*, *MMP9*, *VEGFA, IL6,* and *CXCL8* mRNAs compared to samples subjected to 1 *g* conditions. Significant downregulations in AD cells were detected in the mRNA levels of *TUBB, KRT8*, *IL1B, IL7, PIK3CB, AKT1 and MTOR* after 24 h. The release of collagen-1α1 and fibronectin protein in the supernatant was decreased, whereas the secretion of IL-6 was elevated in 24 h RPM samples. The secretion of IL-1α, IL-1β, IL-7, IL-2, IL-8, IL-17, TNF-α, laminin, MMP-2, TIMP-1, osteopontin and EGF was not significantly altered after 24 h compared to 1 *g* conditions. The release of soluble factors was significantly reduced after 2 h (IL-1α, IL-2, IL-7, IL-8, IL-17, TNF-α, collagen-1α1, MMP-2, osteopontin) and elevated after 4 h (IL-1β, IL-2, IL-6, IL-7, IL-8, TNF-α, laminin) in RPM samples. Taken together, simulated μ*g* induced 3D growth of PC-3 cancer cells combined with a differential expression of the cytokines IL-1α, IL-1β, IL-6 and IL-8, supporting their involvement in growth and progression of prostate cancer cells.

Keywords: prostate cancer, cytokines, interleukins, cytoskeleton, extracellular matrix, PAM signaling, prostate cancer cells and microgravity

INTRODUCTION

As estimated by GLOBOCAN (Global Cancer Observatory) in 2020, prostate cancer (PC) comprises an incidence of almost 1.4 million new cases and 375,000 deaths worldwide (Sung et al., 2021). PC was the second most frequent cancer and the fifth leading cause of cancer death among men in 2020 (Sung et al., 2021). Adenocarcinomas are the most common types of PC, and in general PC progresses very slowly. The 5-years survival rate for most men with local or regional PC is nearly 100%, but if diagnosed with PC metastasis, the 5-years survival rate is reduced to 31% (Gandaglia et al., 2014).

This shows that metastasis of PC has a vast impact on the mortality and the overall quality of life of patients. Compared to other cancer types, PC metastasizes predominantly to the skeleton (84%) and the lymph nodes (10.6%) (Gandaglia et al., 2014). Additionally, spreading to the liver (10.2%) and thorax (9.1%) is also common (Gandaglia et al., 2014). Metastatic PC is mostly terminal even after intensive multimodal treatment. Therefore, there is an urgent need to increase the knowledge of PC biology, genomics, proteomics and advanced profiling technologies in order to find new drug development targets.

In context of PC expansion, proteins released by the PC cells (PCC) into the interstitial space are of high interest. Secreted factors such as cytokines and chemokines are released into the tumor microenvironment and play a key role in cancer progression. Cytokines are released in response to immune reactions like infection, inflammation and immunity in order to inhibit tumor development and progression. The tumor cells can respond just as well to cytokines that induce cancer growth, reduce programmed cell death and facilitate invasion and metastasis (Dranoff, 2004). Thus, cytokines, their receptors and specific signaling pathways are key factors in driving the specific events leading to metastasis of PC (Dranoff, 2004; Adekoya and Richardson, 2020).

Moreover, cytokines are key players in all events of the metastatic process and hence, they remodel the extracellular matrix, influence the epithelial-mesenchymal-transition, invasion, angiogenesis, and the processes involved in the establishment of tumor cells in the secondary organs (Adekoya and Richardson, 2020).

An extraordinary and novel approach to investigate tumor cell processes is using microgravity (μ*g*), either with real (r-) μ*g* in space or simulated (s-) μ*g* by ground-based devices like the random positioning machine (RPM) (Becker and Souza, 2013). Space provides special physical conditions which cannot be reproduced on Earth, as well as μ*g* conditions which are used to investigate molecular mechanisms and signaling processes controlling cell growth and function (Becker and Souza, 2013). Cancer research in space and molecular biological studies on cells exposed to r- and/or s-μ*g* are therefore a hot topic in space medicine (Krüger et al., 2019; Grimm et al., 2020; Nassef et al., 2020).

Previous research revealed that r- and s-μ*g* have a large impact on the biochemistry and physiology of human cells. This comprises various changes, such as alterations of the extracellular matrix (ECM), the focal adhesion complex, the cytoskeleton, growth behavior, as well as changes in differentiation and proliferation (Nassef et al., 2019). Moreover, Häder *et al.* (Häder et al., 2017) suggested a direct correlation of the μ*g*-induced cytoskeletal changes and transcriptional alterations. They concluded that the interaction of the ECM, cell adhesion and the cytoskeleton is of great importance for gravisensing in human cells. Cytoskeletal alterations detected in human cells exposed to μ*g* were described as follows: microtubules are regularly localized more around the nucleus and might lose their radial organization, are shortened, as well as more curved and bent. The F-actin network is altered and the number of stress fibers reduced. F-actin is redistributed and is situated more perinuclear or is localized more cortical. Intermediate filaments (vimentin, cytokeratin) form clusters, reveal larger meshes and are localized more perinuclear (Vorselen et al., 2014). These findings obtained from fixed cells were recently confirmed by live-cell imaging in r-μ*g* (Corydon et al., 2016a; Nassef et al., 2019).

Moreover, s- and r-μ*g* influenced ECM proteins in a time-dependent manner (Infanger et al., 2006) and cell-type dependent, resulting in increases or decreases of ECM components (Infanger et al., 2006; Marrero et al., 2009; Zhivodernikov et al., 2020). In addition, PC MCS engineered on the RPM revealed a decrease in *COL1A1* after 3 days and an increase after 5 days, whereas basement components like *COL4A5* and *LAMA3* as well as the cell adhesion molecule *FN1* were elevated in MCS at both time points (Hybel et al., 2020). These findings indicate that the cells try to expand the ECM in MCS to stabilize themselves and to resist the s-μ*g* conditions, as the ECM provides structural support for the cells (Bonnans et al., 2014).

In addition, lack of gravity and/or RPM exposure of various cell types was shown to promote cell growth in a scaffold-free three-dimensional (3D) way, forming MCS (Riwaldt et al., 2016; Grimm et al., 2020). MCS are 3D aggregates exhibiting complex cell-to-cell and cell-to-matrix interactions. These interactions have been reported to induce gradients for nutrients, gases, growth factors and signal factors. This 3D structure reflects the natural microenvironment of cells more accurately than 2D monocultures and also resembles the microenvironment of real tissues (Mehta et al., 2012; Cui et al., 2017). Several cancer cell-types like thyroid and breast cancer cells exposed to an RPM formed MCS within 24 h (Kopp et al., 2016; Riwaldt et al., 2016).

3D PC aggregates (PC-3, LNCaP and DU-145 cell lines) engineered on microgravity simulators and the subsequent formation of 3D spheroids was demonstrated on both, the NASA rotary cell culture system and the RPM (Ingram et al., 1997; Hybel et al., 2020).

Understanding the biology of spheroids is very important for a more complete appreciation of *in vivo* tissue formation and function. MCS are frequently used to study molecular mechanisms involved in angiogenesis, cancer development, and biology and for pharmacological testing. Unveiling the mechanisms of microgravity-dependent molecular and cellular changes is an up-to-date requirement for improving space medicine and cancer research (Becker and Souza, 2013; Krüger et al., 2019; Nassef et al., 2020). A clear advantage of microgravity is that it enables the engineering of MCS without any scaffolds. Moreover, long-term experiments using thyroid cancer cells show

that FTC-133 spheroids and EA.hy926 spheroids or intima constructs did not develop a central necrosis, when exposed to an RPM (Kopp et al., 2015; Dittrich et al., 2018).

Therefore, spheroids formation in μ*g* is an innovative approach to study the early phases of tumor progression and metastasis. The PI3K/AKT/mTOR (PAM) signaling pathway is frequently mutated in prostate cancer and thus a good candidate for the involvement in tumor progression (Tee et al., 2018). It is regulating growth, metabolism, and migration of PCC.

In this study we investigated the impact of short-term (30 min, 2, 4 and 24 h) s-μ*g*-exposure via RPM on PC-3 prostate cancer cells, which were established from an adenocarcinoma. The principal aim of this study was to measure the gene expression and secretion rate of cytokines in PCC. Secondly, we focused on the altered gene expression of cytoskeletal factors and the extracellular matrix (ECM). Third, a special focus was placed on the PAM signaling pathway, which is proposed to be the underlying mechanism of spheroid formation in PC. Fourth, we engineered 3D spheroids under 1*g*-conditions by the liquid-overlay technique to use them as a control for the 3D spheroids in simulated microgravity and studied the gene expression of selected factors in 1*g*-MCS.

MATERIALS AND METHODS

Cell Cultures

The PC-3 cell line (ECACC 90112714) was purchased from the European Collection of Authenticated Cell Cultures (ECACC). The cells originated from a 62-year-old male Caucasian suffering from grade 4 prostatic adenocarcinoma.

$3{\cdot}10^6$ cells were seeded into T75 cm^2 flasks (Sarstedt, Nümbrecht, Germany) and cultured using RPMI 1640 medium (Gibco, Fisher Scientific, Schwerte, Germany), supplemented with 10% FCS (Sigma Aldrich, Steinheim, Germany) and 1% penicillin/streptomycin (Life Technologies, New York, United States). Every 3 days the medium was changed, and upon reaching 70–80% confluence, the cells were split at a 1:10 ratio.

Simulated Microgravity on the iRPM and Sample Collection

In preparation for the experiments in s-μ*g* on the incubator RPM (iRPM), 10 T25 cm^2 flasks (Sarstedt, Nümbrecht, Germany; order nr. 83.3910.002 vented caps) per group were filled each with $2{\cdot}10^6$ cells in 13 ml RPMI 1640 medium (Life Technologies, Paisley, United Kingdom), complemented with 10% FCS (Sigma Aldrich, Steinheim, Germany) and 1% penicillin/streptomycin (Life Technologies, New York, United States), and kept in 1 *g* conditions (37°C, 5% CO_2) for 1 day to let the cells adhere. Afterwards, the flasks were filled entirely with growth medium, avoiding the formation of air bubbles. Furthermore, the bottle caps were secured at the edges with parafilm, sparing the ventilated area. Five flasks of each group were placed and fixed inside the incubator on the iRPM, while the other five remained under 1*g* standard conditions (both 37°C, 5% CO_2). After the duration of 30 min, 2 h, and 4 h, respectively, the cell culture supernatants were collected in 50 ml tubes and stored at −150°C. Then 2 ml RNA*later* Stabilization Solution (Invitrogen by Thermo Fischer Scientific, Waltham, MA, United States) was added to the flasks and the cells mechanically detached with cell scrapers. The resulting cell suspensions were collected in 15-ml tubes and stored at 4°C until further processing.

For the immunofluorescence staining, $0.2{\cdot}10^5$ cells were seeded into 4 slideflasks (Thermo Scientific) and incubated for 36 h. At this timepoint the culture medium was discarded, the slideflasks completely filled with fresh RPMI 1640 medium (Life Technologies, Paisley, United Kingdom) containing 10% FCS (Sigma Aldrich, Steinheim, Germany) and 1% penicillin/streptomycin (Life Technologies, New York, United States), and sealed with parafilm air bubble-free. Following, two flasks were cultured on the iRPM for 24 h, while two were left in the incubator under standard conditions as controls. After the experiment, the medium was discarded and the slides were fixed with 4% Paraformaldehyde (PFA, Sigma-Aldrich, St. Louis, Missouri, United States) in phosphate-buffered saline (PBS; Gibco, Life Technologies, Paisley, United Kingdom).

The iRPM was constructed by the group of Professor Jörg Sekler at the Fachhochschule Nordwestschweiz (Windisch AG, Switzerland). Details on the iRPM are described in (Benavides Damm et al., 2014).

Liquid Overlay

The liquid-overlay technique is an established method to generate 3D cell aggregates in static culture (Svejgaard et al., 2015). In short, 96-well plates are coated with 40 μl of 1% agarose in RPMI 1640 medium. After hardening of the gel, 4,000 cells/200 μl in RPMI 1640 supplemented with 10% FCS and 1% Pen/Strep were incubated as described in 4.1 for 24 h. This step was followed by microscopic evaluation of cell viability using Ready Probes for live cell imaging (Thermo Scientific, Waltham, Massachusetts, United States) and cell aggregate collection for quantitative real-time PCR. Five 96-well plates were seeded and spheroids of one plate were collected to make up one PCR sample. As a control, adherently growing cells were cultured for 24 h in five standard T25 cm^2 cell culture flasks.

Quantitative Real-Time Polymerase Chain Reaction (qPCR)

The expression levels of the genes of interest were determined via qPCR. Primer Express software (Applied Biosystems) was used to design appropriate primers with a T_m of ~60°C (**Table 1**). The primers were synthesized by TIB Molbiol (Berlin, Germany) and all assays were run on a 7,500 Fast Real-Time PCR System using the FAST SYBR™ Green Master Mix (both Applied Biosystems, Darmstadt, Germany). The reaction volume was 15 μL including 1 μL of template cDNA and a final primer concentration of 500 nM. PCR conditions were as follows: 20 s at 95°C, 40 cycles of 30 s at 95°C and 30 s at 60°C, followed by a melting curve analysis step (temperature gradient from 60 to 95°C with +0.3°C/cycle).

If all amplicons showed one single T_m similar to the one predicted by the Primer Express software, the PCR reactions were considered specific. Every sample was measured in triplicates, and relative quantification was performed by means of the comparative C_T ($\Delta\Delta C_T$) method. *18S rRNA* was used as a housekeeping gene to normalize the expression data.

TABLE 1 | Primers used for qPCR analyses.

Gene	Primer name	Sequence 5′–3′
18S rRNA	18s-F	GGAGCCTGCGGCTTAATTT
	18s-R	CAACTAAGAACGGCCATGCA
ACTB	ACTB-F	TGCCGACAGGATGCAGAAG
	ACTB-R	GCCGATCCACACGGAGTACT
AKT1	AKT1-F	CTTCTATGGCGCTGAGATTGTG
	AKT1	CAGCATGAGGTTCTCCAGCTT
CASP3	CASP3-F	CTCCAACATCGACTGTGAGAAGTT
	CASP3-R	GCGCCAGCTCCAGCAA
CASP8	CASP8-F	TGCAAAAGCACGGGAGAAAG
	CASP8-R	CTCTTCAAAGGTCGTGGTCAAAG
CASP9	CASP9-F	CTCCAACATCGACTGTGAGAAGTT
	CASP9-R	GCGCCAGCTCCAGCAA
COL1A1	COL1A1-F	ACGAAGACATCCCACCAATCAC
	COL1A1-R	CGTTGTCGCAGACGCAGAT
CXCL8	CXCL8-F	TGGCAGCCTTCCTGATTTCT
	CXCL8-R	GGGTGGAAAGGTTTGGAGTATG
EGF	EGF-F	TGCCAGCTGCACAAATACAGA
	EGF-R	TCTTACGGAATAGTGGTGGTCATC
EGFR	EGFR-F	TTGCCGCAAAGTGTGTAACG
	EGFR-R	GAGATCGCCACTGATGGAGG
EZR	EZR-F	GCAATCCAGCCAAATACAACTG
	EZR-R	CCACATAGTGGAGGCCAAAGTAC
FLT1	FLT1-F	CCCTCGCCGGAAGTTGTAT
	FLT1-R	GATAATTAACGAGTAGCCACGAGTCAA
FN1	FN1-F	AGATCTACCTGTACACCTTGAATGACA
	FN1-R	CATGATACCAGCAAGGAATTGG
HIF1A	HIF1A-F	TGCTTTAACTTTGCTGGCCC
	HIF1A-R	AGTTTCTGTGTCGTTGCTGC
IL1A	IL1A-F	AGTAGCAACCAACGGGAAGG
	IL1A-R	AGGCTTGATGATTTCTTCCTCTGA
IL1B	IL1B-F	TTCGAGGCACAAGGCACAA
	IL1B-R	TGGCTGCTTCAGACACTTGAG
IL6	IL6-F	CGGGAACGAAAGAGAAGCTCTA
	IL6-R	GAGCAGCCCCAGGGAGAA
IL7	IL7-F	CCAGTTGCGGTCATCATGACTA
	IL7-R	TGATGCTACTGGCAACAGAACA
KDR	KDR-F	TCTTCTGGCTACTTCTTGTCATCATC
	KDR-R	GATGGACAAGTAGCCTGTCTTCAGT
KRT8	KRT8-F	GATCTCTGAGTGAACCGGAACA
	KRT8-R	GCTCGGCATCTGCAATGG
LAMA3	LAMA3-F	AAAGCAAGAAGTCAGTCCAGC
	LAMA3-R	TCCCATGAAGACCATCTCGG
MMP9	MMP9-F	CCTGGAGACCTGAGAACCAATC
	MMP9-R	TTCGACTCTCCACGCATCTCT
MSN	MSN-F	GAAATTTGTCATCAAGCCCATTG
	MSN-R	CCATGCACAAGGCCAAGAT
MTOR	MTOR-F	ATCTTGGCCATAGCTAGCCTC
	MTOR-R	ACAACTGGGTCATTGGAGGG
PIK3CB	PIK3CB-F	AGAAAAGTTTGGCCGGTTCC
	PIK3CB-R	GCAGTCAACATCAGCGCAAA
RDX	RDX-F	GAAAATGCCGAAACCAATCAA
	RDX-R	GTATTGGGCTGAATGGCAAATT
SPP1	SPP1-F	CGAGGTGATAGTGTGGTTTATGGA
	SPP1-R	CGTCTGTAGCATCAGGGTACTG
TGFB1	TGFB1-F	CACCCGCGTGCTAATGGT
	TGFB1-R	AGAGCAACACGGGTTCAGGTA
TIMP1	TIMP1-F	GCCATCGCCGCAGATC
	TIMP1-R	GCTATCAGCCACAGCAACAACA
TUBB	TUBB-F	CTGGACCGCATCTCTGTGTACTAC
	TUBB-R	GACCTGAGCGAACAGAGTCCAT
VEGFA	VEGFA-F	CTACCTCCACCATGCCAAGTG
	VEGFA-R	GCGCTGATAGACATCCATGAAC

TABLE 2 | Materials used for immunofluorescence.

Antibody/Probe	Species	Order number	Manufacturer	Dilution in PBS
Fibronectin	mouse monoclonal	sc-18827	Santa Cruz Biotechnology	(1:100)
anti-mouse IgG (H + L)	goat secondary antibody	A11001	Invitrogen by Thermo Fischer Scientific	(1:500)

Immunofluorescence

Following the removal of PFA, the cells were washed twice with PBS and permeabilized with 0.2% Triton. After blocking with 3% bovine serum albumin (BSA) in PBS for 1 h, the primary antibody was added and incubated at 4°C overnight. The next day, the cells were washed twice with PBS, the secondary antibody was added and incubated for 1 h. Afterwards, the cells were rinsed three times with PBS and mounted with DAPI fluoroshield and a cover slip. A list of antibodies and probes used for immunofluorescence staining is given in **Table 2**.

Multiplex Bead Array

Collagen I alpha I, fibronectin, interleukin (IL)-1α/1F1, IL-1β/1F2, IL-2, IL-6, IL-7, IL-8/CXCL8, IL-17/17-A, tumor necrosis factor alpha (TNF-α), matrix metalloproteinase-2 (MMP-2), epidermal growth factor (EGF), serpin E1/plasminogen activator inhibitor-1 (PAI-1), osteopontin (OPN), chemokine (C-C motif) ligand 2 (CCL2)/ monocyte chemoattractant protein 1 (MCP-1), tissue inhibitor metalloproteinases metallopeptidase inhibitor 1 (TIMP-1) and laminin levels in cell culture supernatant were analyzed using a multiplex magnetic bead array (R&D systems, Minneapolis, United States). Assays were performed according to manufacturer's instructions. Samples were run on a MAGPIX instrument (Luminex, s-Hertogenbosch, Netherlands) and analyzed with MILLIPEX analyst standard version 5.1 (Merck, Darmstadt, Germany).

Microscopy

After immunofluorescence staining, the slides were investigated using confocal laser scanning microscopy. The observations were made with a Leica DM 2000 microscope equipped with a 40x objective and an external light source Leica EL 6000 (Leica Microsystems GmbH, Wetzlar, Germany).

Statistical Analysis

The statistics were performed using the GraphPad Prism 7.01 software (GraphPad Software, Inc., California, United States). Differences between s-μ*g* samples and related controls were assessed with the Mann-Whitney U-test, p-values < 0.05 were considered significant.

RESULTS

Cell Growth, Morphology and Cell Viability

Culture flasks containing 70% sub-confluent PC-3 cells were mounted on the RPM for 30 min, 2, 4 and 24 h. The 1*g* control samples were placed next to the RPM and cultured in parallel. PC-3 cells cultured under 1*g*-conditions grew as 2D monolayer cultures (**Figure 1A**). PC-3 cells exposed to the RPM for 30 min, 2 and 4 h showed no three-dimensional (3D) growth and grew adherently on the cell culture flask bottom (not shown). Phase contrast microscopy showed normal epithelial PC-3 cells exhibiting numerous microvilli, abnormal nuclei and nucleoli. The cells subjected to short-term exposure (30 min, 2 h, and 4 h) to the RPM compared to 1*g* samples revealed no visible morphological changes. No dead cells were detectable. 3D multicellular spheroids could be detected in the supernatant after a 24 h RPM exposure. Thus, there are two different phenotypes of PC-3 cells visible: adherently growing cells (AD) and detached 3D MCS (**Figures 1B,C**) We used a "terminal deoxynucleotidyl transferase dUTP nick end labeling" (TUNEL) assay to detect DNA breaks formed during the final phase of apoptosis, when DNA fragmentation takes place. No apoptotic cells were visible in all AD cell samples irrespective of RPM exposure or not. Sporadic apoptotic cells were detected in MCS (**Figure 1D**). In addition, we focused on apoptosis signaling. Genes associated with apoptosis such as *CASP3*, *CASP8,* and *CASP9* mRNAs were not significantly changed after short-term incubation (30 min, 2 h, and 4 h) as well as after 24 h on the RPM compared to 1*g* (**Figures 1E–G**). We studied the gene expression of *HIF1A* (hypoxia inducible factor 1) in PC-3 cells exposed for 24 h to s-μ*g* conditions. The *HIF1A* mRNA in AD cells was not altered, but significantly elevated in MCS (**Figure 1H**).

Spheroids Engineered Under 1*g*-Conditions

The liquid-overlay technique was used to obtain MCS under 1*g*-conditions within 24 h. We microscopically investigated the MCS formation and their viability. **Figure 2A** presents a representative cell aggregate formed within 24 h. In comparison to the MCS built on the RPM, the cells are loosely united. **Figure 2B** presents the cell viability staining. While all nuclei are stained blue, compromised nuclei, representing non-viable cells, are stained green. Compared to the MCS engineered on the RPM, the cell viability of MCS formed under 1*g*-conditions (**Figure 2B**) seems to be lower. The gene expression of *CASP3*, *CASP8* and *CASP9* (**Figures 2C–E**) was significantly upregulated in 1*g*-MCS compared to control samples.

The Cytoskeleton

The cytoskeletal protein β-actin (ACTB) is widely distributed in all eukaryotic cells and is involved in cell migration, cell division, cell structure, cell integrity and immune response. After 24 h RPM exposure an increase in the *ACTB* gene expression was measured in MCS, but not in the adherent cells compared to 1*g* (**Figure 3A**). MCS built under 1*g*-conditions showed a significant upregulation of *ACTB* in comparison to control samples. A short-term (30 min, 2 h, and 4 h) RPM exposure of PC-3 cells did not change the gene expression level of *ACTB*.

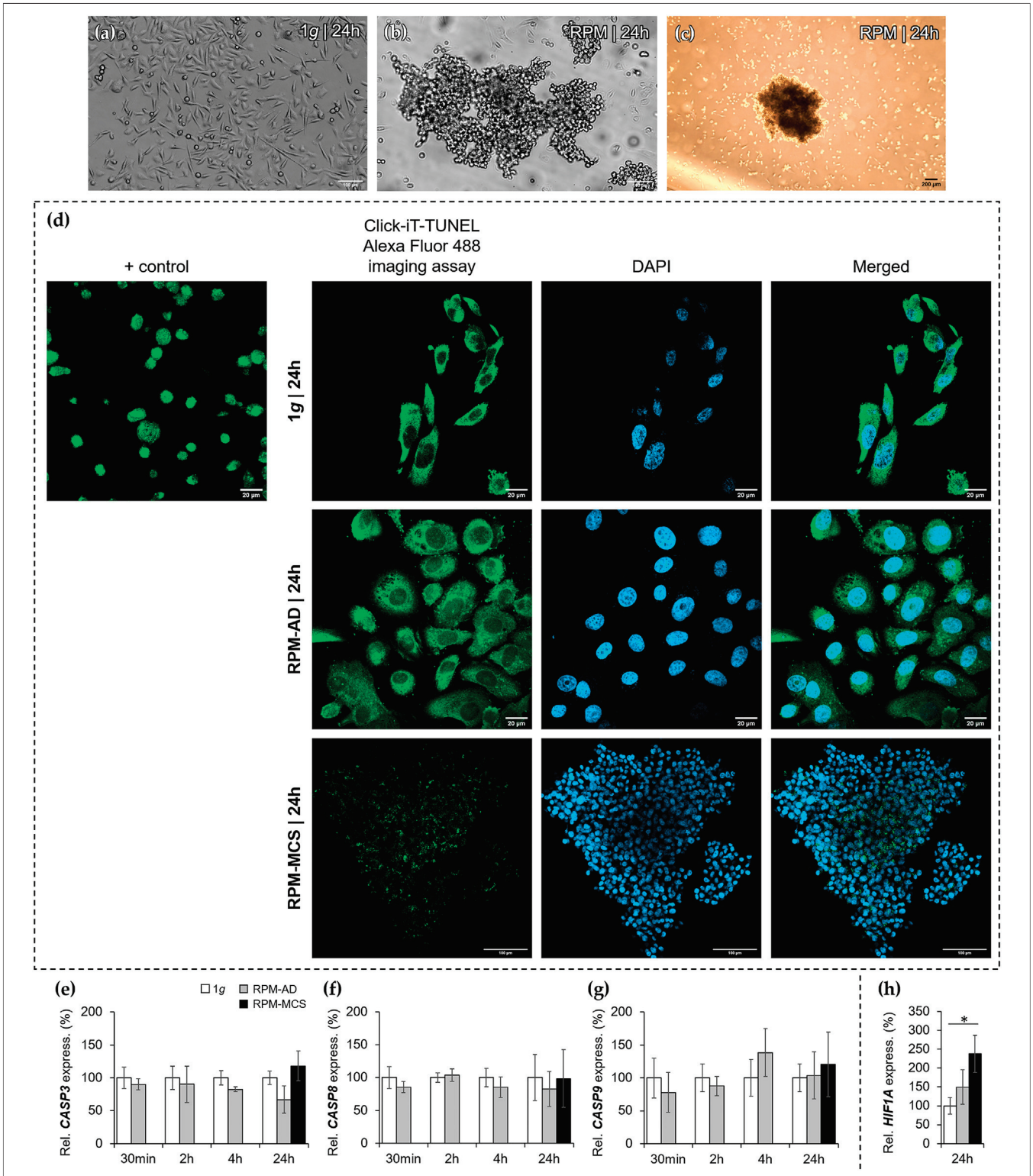


FIGURE 1 | Phase contrast microscopy of PC-3 cells: **(A)** static 1*g* control cells (Scale bar 100 µm) and **(B,C)** 24 h RPM-exposed samples showing detached spheroids swimming above adherently growing cells (scale bar **(B)** 100 µm and **(C)** 200 µm). **(D)** Terminal deoxynucleotidyl transferase dUTP nick end labeling (TUNEL) assay and 4′,6-diamidino-2-phenylindole (DAPI) staining revealed no apoptotic cells in 1*g* controls (scale bar 20 µm) and also no apoptosis in RPM-exposed AD (scale bar 20 µm and MCS cells (scale bar 100 µm). The positive control, induced by DNase, is given in the first row (Scale bar 20 µm). **(E,F,G)** The *CASP3, CASP8* and *CASP9* (30 min, 2, 4 and 24 h) gene expression was not significantly altered at all time points. **(H)** The gene expression of *HIF1A* after 24 h was not changed in AD cells, but significantly elevated in MCS compared to 1*g* (n = 5).

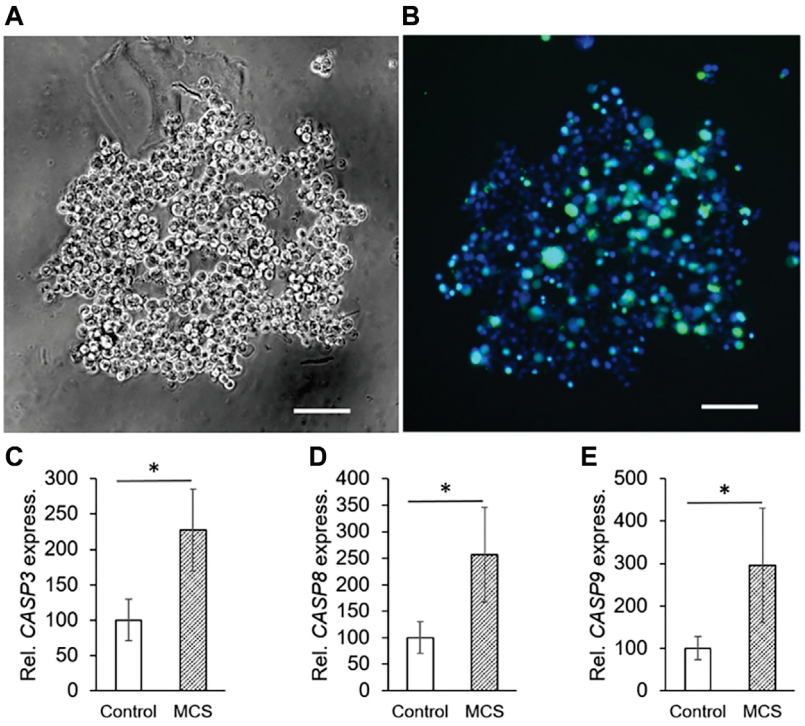


FIGURE 2 | Phase contrast microscopy of PC-3 cells: **(A)** static 1*g*-MCS after 24 h using the liquid overlay technique (scale bar 100 µm) and **(B)** same sample using the live cell viability assay, where the blue color indicates the nuclei of all cells while the green color demonstrates compromised cells. **(C,D,E)** The *CASP3, CASP8* and *CASP9* (24 h) gene expression was significantly altered in 1*g*-MCS after 24 h (n = 5).

The *TUBB* gene expression did not change when PC-3 cells were exposed to short-term s-µ*g* (**Figure 3B**). In contrast, AD cells exhibited a downregulated *TUBB* expression after 24 h compared to 1*g* cells. PC-3 cells growing in MCS did not show a change in *TUBB* expression. No significant differential *EZR* and *RDX* gene expression could be observed over the experiment duration (**Figure 3C**, **Figure 3D** respectively). Interestingly, the MSN mRNA was downregulated after a 30-min RPM exposure, whereas the gene was upregulated in MCS after 24 h compared to corresponding static 1*g* samples (**Figure 3E**). In addition, the *KRT8* mRNA was significantly downregulated in AD after 24 h compared to 1*g* (**Figure 3F**). While in RPM samples were only marginal expression changes visible, the investigations of these genes in 1*g*-MCS showed a significant upregulation of the cytoskeletal genes (**Figures 3A–F**).

The Extracellular Matrix

The mRNA expression of *FN1* was significantly upregulated in PC-3 cells growing in the AD monolayer and in MCS when cultured under conditions of s-µ*g* for 24 h. Short-term s-µ*g* did not induce changes in the *FN1* gene expression of PC-3 cells. In addition, MCS grown under 1*g*-conditions revealed no expression changes of *FN1* (**Figure 4A**). The immunofluorescence staining revealed a similar amount of fibronectin in the cytoplasm of the PC-3 cells exposed for 24 h to the RPM compared to static control cells (**Figure 4A**, right image). MCS cells revealed a loose connection between neighboring cells and an uneven distribution of fibronectin within the cells which is in contrast to the 1*g* AD and RPM AD cells. In parallel, the PC-3 cells exposed to the RPM secreted a significantly reduced amount of fibronectin into the supernatant within 24 h (**Table 3**). The amount of secreted fibronectin was similar in all groups after 2 and 4 h of RPM exposure (**Table 3**).

Moreover, the *COL1A1* gene expression was not significantly changed when exposed to short-term (30 min, 2 h, 4 h) s-µ*g*. In contrast, after a 24 h RPM exposure there was a significant upregulation of *COL1A1* detectable in both AD and MCS samples while 1*g*-MCS revealed a significantly reduced expression of *COL1A1* (**Figure 4B**). In addition, collagen-1α1 was released by the PC-3 cells in a significant lower amount after a 2 and 24 h RPM exposure compared to control samples (**Table 3**).

A similar result in respect to the gene expression was found for *LAMA3* in 24 h RPM-exposed cells. *LAMA3* was significantly upregulated in AD and MCS after 24 h. No expression change was detected in 1*g*-MCS (**Figure 4C**). The secretion of laminin by the cells was significantly elevated after 2 and 4 h in RPM samples, but the release was not significantly altered in 24 h cultures (**Table 3**).

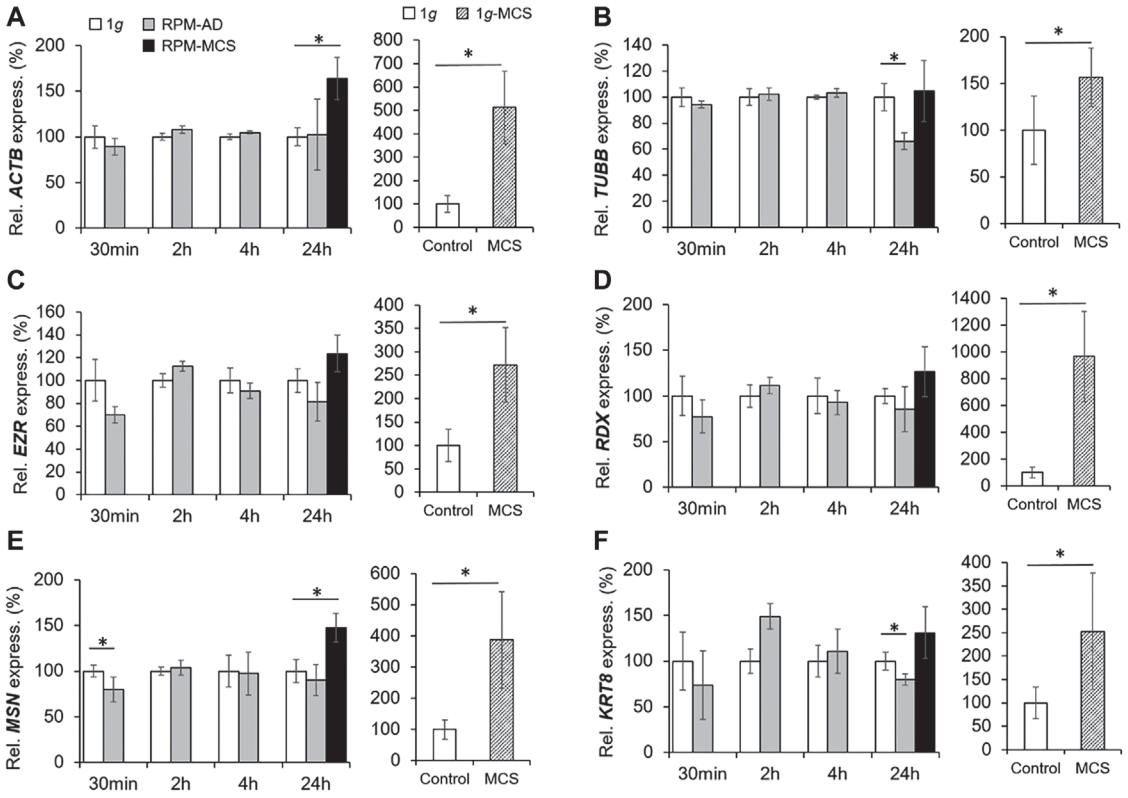


FIGURE 3 | Gene expression of **(A)** *ACTB*, **(B)** *TUBB*, **(C)** *EZR*, **(D)** *RDX*, **(E)** *MSN* and **(F)** *KRT8* of PC-3 cells exposed to the RPM for 30 min, 2, 4 and 24 h and 1*g*-MCS after 24 h. n = 5; *$p < 0.05$ vs. 1*g*.

Furthermore, the *SPP1* mRNA was not changed when the cells were exposed to the RPM and was not detectable by qPCR in 1*g*-MCS (**Figure 4D**). The release of osteopontin into the cell supernatant was reduced early, but remained later unchanged compared to 1*g* samples (**Table 3**).

Finally, the gene expression of *MMP9* was significantly increased in AD cells after a 24 h-RPM-exposure and was not detectable in 1*g*-MCS (**Figure 4E**), whereas *TIMP1* was elevated in RPM-MCS as well as in 1*g*-MCS (**Figure 4F**). The secretion of TIMP1 was not changed at any timepoint (**Table 1**). After 2 h, the release of MMP-2 protein in the supernatant was significantly lower in RPM cultures but remained unchanged in 4 and 24 h cell cultures exposed to 1*g*- or RPM-conditions (**Table 3**).

The Impact of Simulated Microgravity on Proinflammatory Cytokines

We focused on the expression and secretion of proliferation of proinflammatory cytokines known to be involved in tumor progression and metastasis. A significant upregulation of *IL6* was found already after 2 h in RPM samples. The *IL6* gene expression remained elevated after 4 and 24 h in RPM samples (**Figure 5A**). The release of IL-6 in the supernatant was significantly enhanced in all RPM samples after 2, 4 and 24 h (**Table 3**).

In parallel, the *CXCL8* mRNA was significantly upregulated already after 2 and 4 h in PC-3 cells exposed to the RPM. In addition, *CXCL8* was elevated in AD after 24 h compared to 1*g* cells (**Figure 5B**). The amount of released IL-8 protein in the supernatant was reduced after 2 h, but clearly elevated after 4 h in RPM samples compared to corresponding 1*g* samples (**Table 3**). After 24 h the cells secreted an equal amount of IL-8 in the supernatant, irrespective of RPM exposure or static 1*g* culture conditions (**Table 3**).

The *IL1B* mRNA expression was downregulated in RPM samples after 30 min, then upregulated after 2 and 4 h and finally downregulated in AD and MCS samples after 24 h (**Figure 5C**). The IL-1β protein release in the cell supernatant by the PC-3 cells was not significantly altered in this time course (**Table 3**).

In contrast to these findings, *TGFB1* was not differentially expressed in 1*g* and RPM samples at all time points (**Figure 5D**). IL-17 protein was secreted in a significantly reduced amount in RPM-exposed PC-3 cells compared with 1*g* samples after 2 h (**Table 3**). In addition, TNF-α was also released in a significantly decreased amount by RPM-exposed PC-3 cells after 2 h but was elevated after 4 h (**Table 3**). The expression of proinflammatory cytokines in 1*g*-MCS was, with the exception of *TGFB1*, highly upregulated (**Figures 5A–D**).

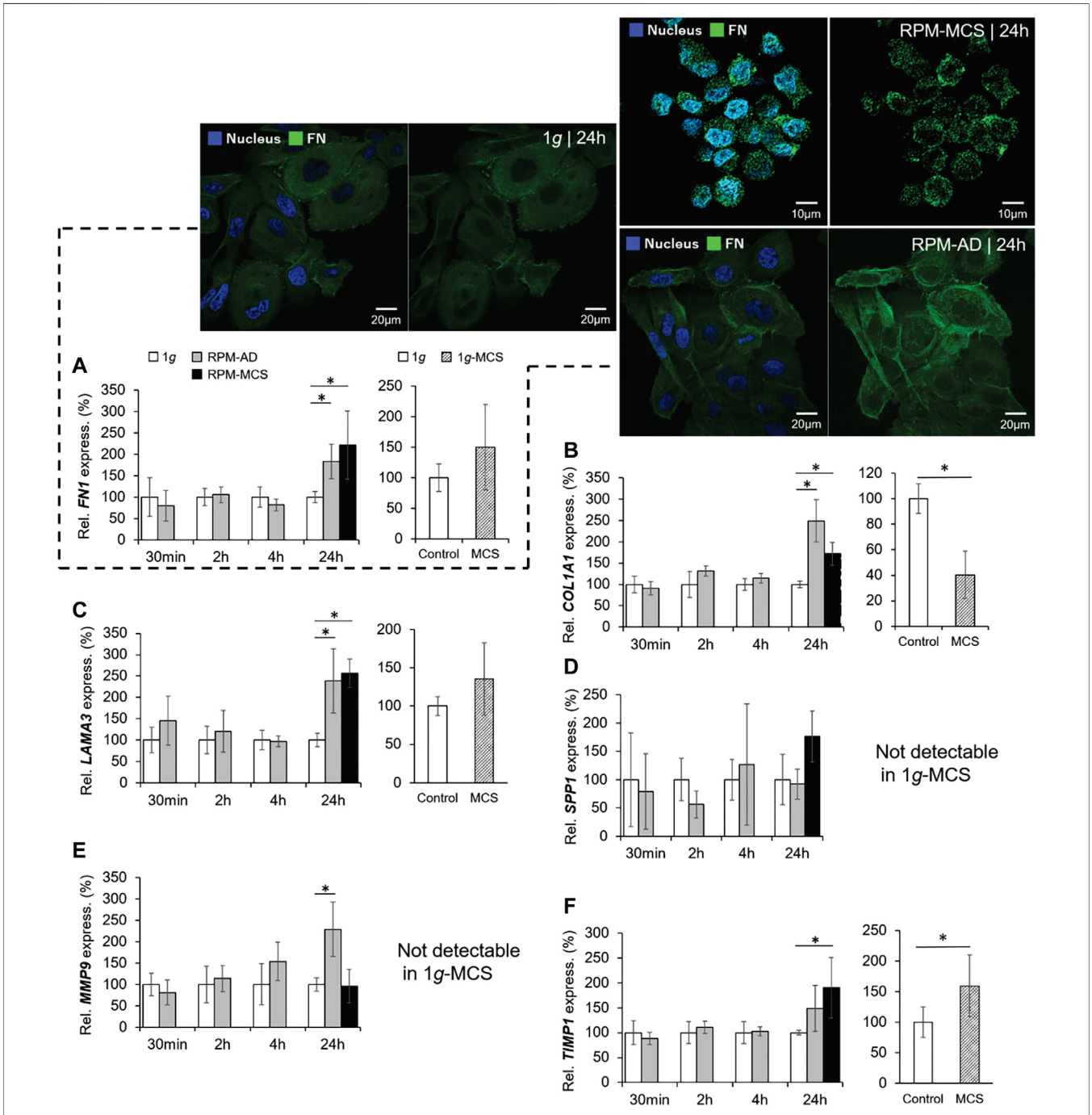


FIGURE 4 | Extracellular matrix: Gene expression of **(A)** *FN1* and immunofluorescence of fibronectin: left two images of the 1*g*/24 h sample (merged left picture and fibronectin (Alexa Fluor 488) right picture), top right two images of the RPM/24 h MCS samples (merged left picture and fibronectin right picture) and lower right two images of the RPM/24 h AD samples (merged left picture and fibronectin right picture), DAPI-stained nucleus (blue), **(B)** *COL1A1*, **(C)** *LAMA3*, **(D)** *SPP1*, **(E)** *MMP9,* and **(F)** *TIMP1* of PC-3 cells exposed to the RPM for 30 min, 2, 4 and 24 h and 1*g*-MCS after 24 h. n = 5; **p* < 0.05 vs. 1*g*.

Impact of Simulated Microgravity on Anti-inflammatory Cytokines

The gene expression of *IL1A* was elevated after 2 and 4 h in adherently growing cells exposed to the RPM compared to static control cells (**Figure 6A**). After 24 h, *IL1A* was significantly upregulated in MCS, but not in AD cells compared to 1*g* samples. The secretion of IL-1α in the cell supernatant was reduced in 2 h RPM-exposed samples compared to 1*g* (**Table 3**). In 1*g*-MCS a significant upregulation of *IL1A* was measured (**Figure 6A**).

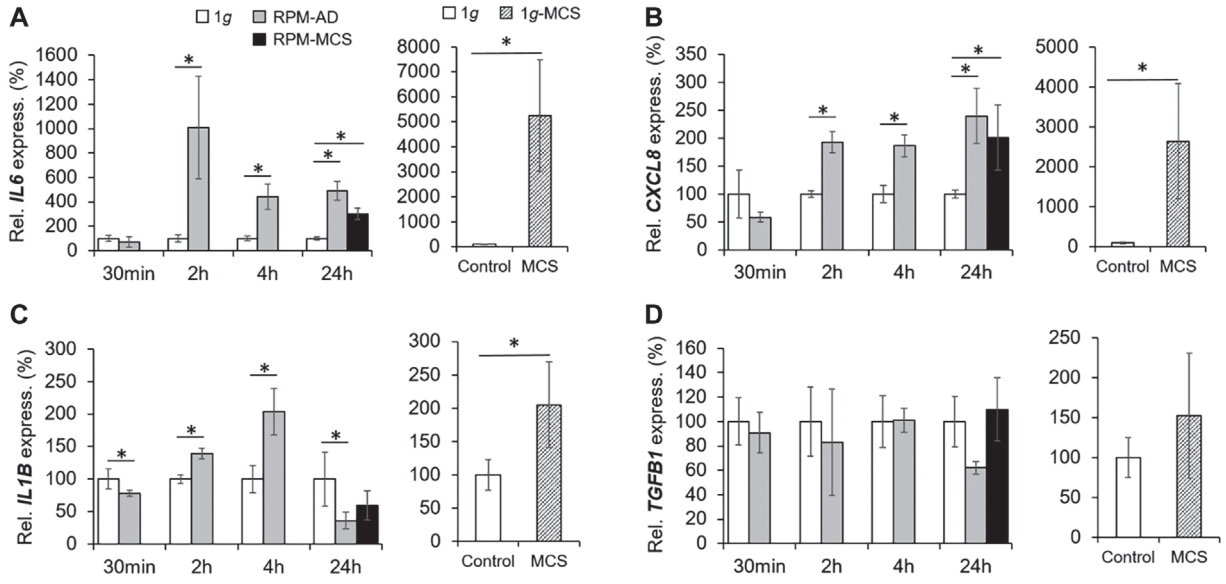


FIGURE 5 | Proinflammatory cytokines: Gene expression of **(A)** *IL6* and **(B)** *CXCL8* mRNA, **(C)** *IL1B*, and **(D)** *TGFB1* of PC-3 cells exposed to the RPM for 30 min, 2, 4 and 24 h and 1*g*-MCS after 24 h. n = 5; **p* < 0.05 vs. 1*g*.

TABLE 3 | Secreted proteins of PC-3 cells [pg/mL]. n = 5; **p* < 0.05 vs. 1*g*.

Protein	2 h		4 h		24 h	
	1*g*	RPM	1*g*	RPM	1*g*	RPM
IL-1α	22 ± 1	18 ± 2*	23 ± 2	25 ± 1	49 ± 8	42 ± 3
IL-1β	11 ± 1	10 ± 1	12 ± 2	15 ± 2*	22 ± 5	20 ± 2
IL-2	144 ± 2	132 ± 3*	146 ± 3	154 ± 3*	191 ± 13	184 ± 6
IL-6	13 ± 1	21 ± 3*	12 ± 3	58 ± 11*	59 ± 23	169 ± 42*
IL-7	14 ± 0	12 ± 0*	13 ± 1	15 ± 1*	21 ± 3	19 ± 2
IL-8	434 ± 65	195 ± 44*	519 ± 147	1,154 ± 208*	2,190 ± 1,059	3,097 ± 765
IL-17	39 ± 1	32 ± 4*	37 ± 5	40 ± 6	51 ± 7	48 ± 6
TNF-α	14 ± 1	11 ± 1*	14 ± 1	16 ± 1*	26 ± 4	23 ± 4
Fibronectin [ng/mL]	69 ± 2	58 ± 12	65 ± 13	65 ± 9	136 ± 31	97 ± 2*
Collagen I α1	125 ± 12	65 ± 11*	135 ± 33	138 ± 25	285 ± 101	163 ± 30*
Laminin	95 ± 9	145 ± 15*	88 ± 7	217 ± 34*	178 ± 17	233 ± 48
MMP-2	1854 ± 30	1786 ± 36*	1847 ± 39	1876 ± 45	2,149 ± 93	2068 ± 46
TIMP-1	1703 ± 208	1,334 ± 329	2,174 ± 695	1783 ± 372	9,245 ± 3,972	6,579 ± 1,086
Osteopontin	6,010 ± 154	5,441 ± 400*	5,928 ± 356	6,193 ± 260	7,287 ± 551	6,914 ± 537
EGF	13 ± 0	12 ± 2	12 ± 2	13 ± 2	15 ± 2	15 ± 2

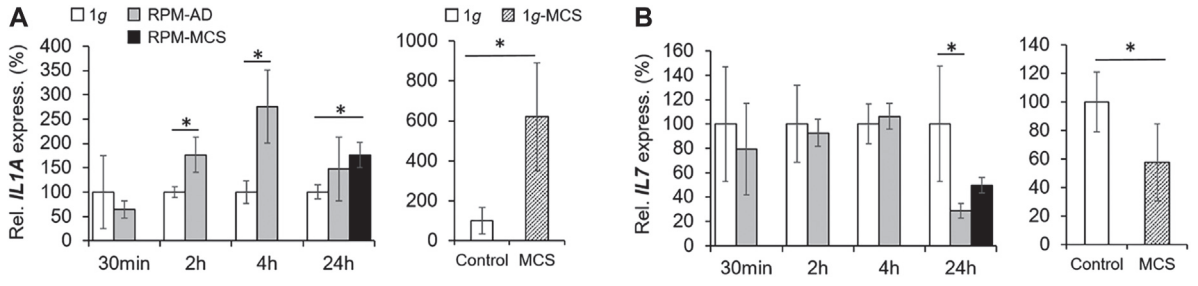


FIGURE 6 | Anti-inflammatory cytokines: Gene expression of **(A)** *IL1A* and **(B)** *IL17* of PC-3 cells exposed to the RPM for 30 min, 2, 4 and 24 h and 1*g*-MCS after 24 h. n = 5; **p* < 0.05 vs. 1*g*.

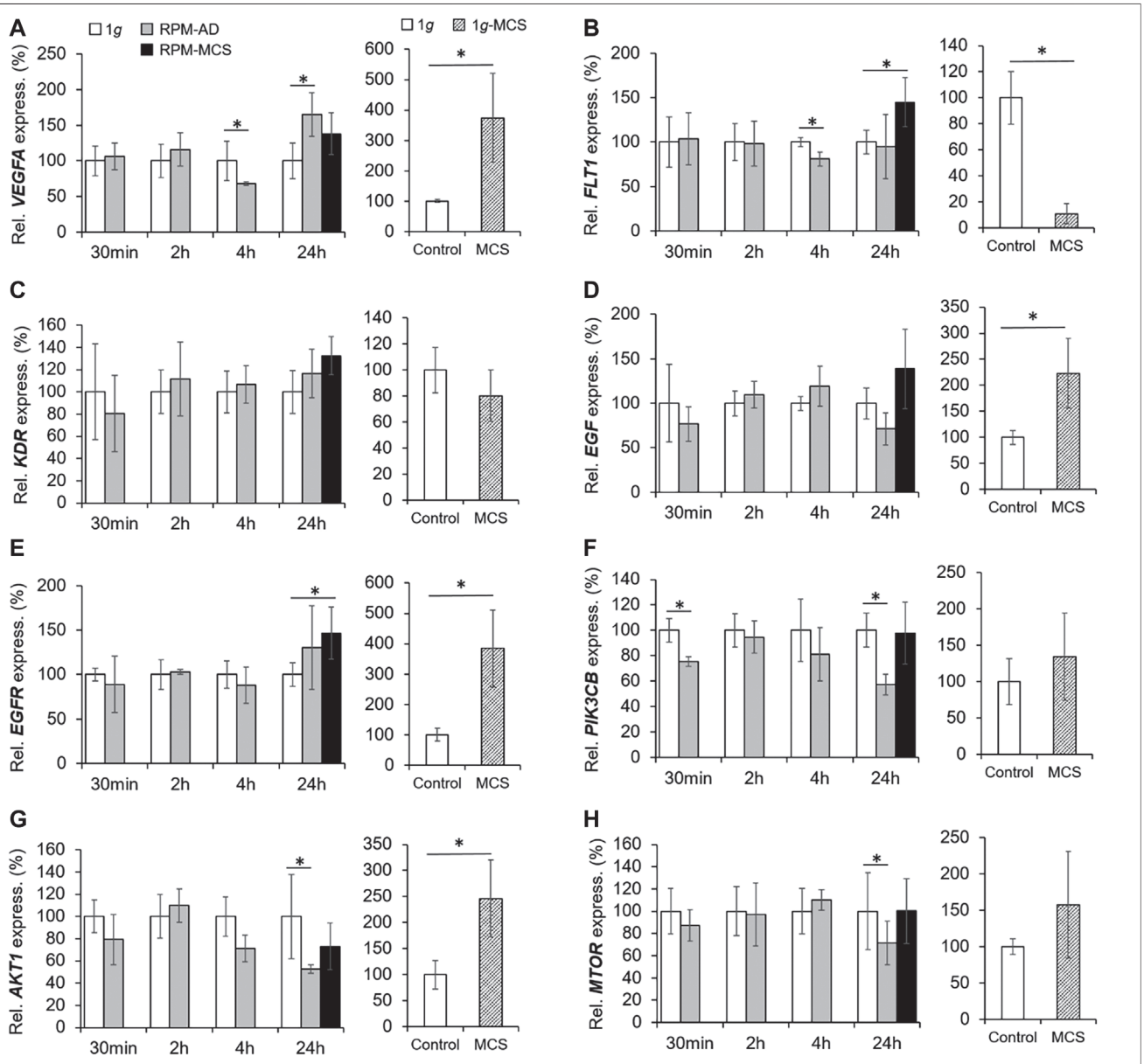


FIGURE 7 | VEGF, EGF and PAM signaling: Gene expression of **(A)** *VEGFA*, **(B)** *FLT1*, **(C)** *KDR*, **(D)** *EGF*, **(E)** *EGFR*, **(F)** *PIK3CB*, **(G)** *AKT1,* and **(H)** *MTOR* of PC-3 cells exposed to the RPM for 30min, 2, 4 and 24 h and 1*g*-MCS after 24 h. n = 5 **p* < 0.05 vs. 1*g*.

Furthermore, we measured the release of IL-2 and detected a reduced amount of this protein after a 2 h RPM exposure of the cells, whereas after 4 h the secretion was elevated in the RPM samples (**Table 3**). In contrast, the *IL7* gene expression was not changed in short-term cultures (30 min, 2 and 4 h). Interestingly, in 24 h RPM cultures the *IL7* mRNA was significantly downregulated in AD and MCS cells compared to the control group, which is similar in 1*g*-MCS (**Figure 6B**). The secretion of the IL-7 protein was reduced after 2 h and enhanced after 4 h of RPM exposure of the cells (**Table 3**). After 24 h, the secretion of IL-7 was similar in both groups.

Influence of Simulated Microgravity on VEGF, EGF and PI3K/AKT/mTOR (PAM) Signaling Pathways

The mRNA level of *VEGFA* was not changed in PC-3 cells exposed to the RPM for 30 min and 2 h. After 4 h the *VEGFA* mRNA was significantly downregulated in the AD group.

In contrast, the 24 h AD samples showed an increased level of *VEGFA* mRNA compared to 1*g*. RPM-MCS exhibited no change in *VEGFA*. In contrast, the gene expression of VEGF-A was elevated in 1*g*-MCS (**Figure 7A**). In parallel, we focused on the VEGF receptors *FLT1* and *KDR*. *FLT1* was significantly

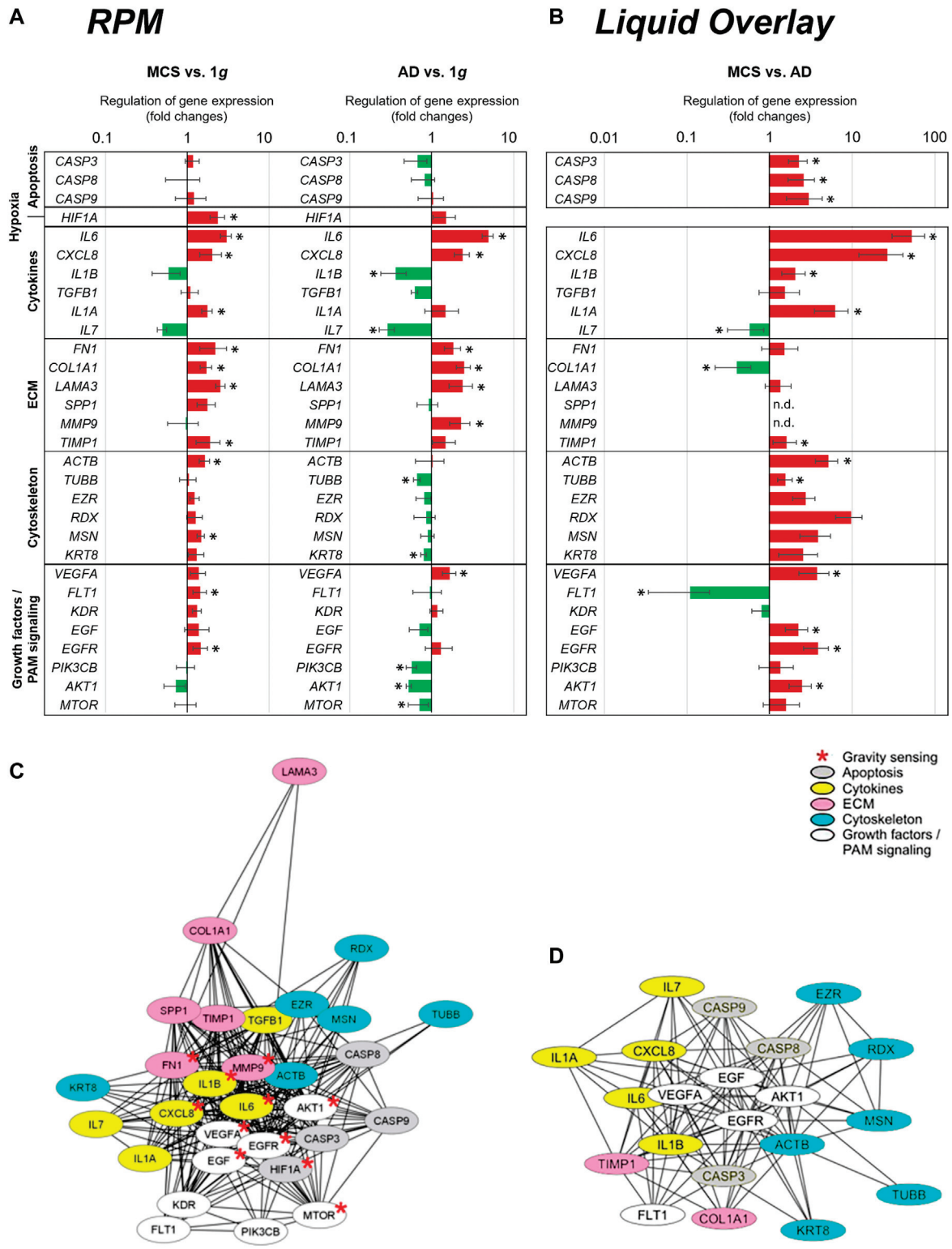


FIGURE 8 | qPCR expression changes of selected genes and their relationship in STRING protein-protein interaction networks. **(A)** qPCR gene expression fold changes of the 24 h RPM-exposed PC-3 samples (AD and MCS) in relation to 1*g*. The red and green colors indicate upregulated and downregulated genes in RPM-exposed samples respectively. Significant regulations are indicated by black asterisks ($p < 0.05$). **(B)** qPCR gene expression fold changes of liquid overlay derived MCS cell aggregates in relation to controls. **(C,D)** Network of the functional interaction of genes and their products **(C)** analyzed in this study and **(D)** differtially regulated in liquid overlay derived MCS cell aggregates. The analysis was performed by STRING 11.0 (https://string-db.org/) and combined scores are visualized by Cytoscape 3.8.2. Affiliation to functional gene groups is color-coded. Red asterisks indicate genes known to be involved in prostate cancer gravity sensing.

Originale der Publikationen

downregulated in AD cells after 4h, whereas after 24 h the *FLT1* mRNA was only upregulated in MCS. Contrary, *FLT1* is significantly downregulated in 1*g*-MCS (**Figure 7B**). The *KDR* mRNA expression was not altered over the entire time course using both methods (**Figure 7C**).

In addition, we investigated the *EGF* and *EGFR* gene expression in PC-3 cells exposed to s-μ*g* and in 1*g*-MCS. The *EGF* mRNA was not differentially displayed in PC-3 cells exposed to short-term microgravity. After 24 h, a non-significant increase in *EGF* was measured in MCS while a significant upregulation of *EGF* was measured in 1*g*-MCS (**Figure 7D**). After 24 h, a significant upregulation of the *EGFR* was detected in PC-3 cells growing in form of MCS using both methods (**Figure 7E**). The secretion of EGF protein was not changed in all groups (**Table 3**).

Furthermore, we studied key factors of the PAM pathway. The *PIK3CB* (Phosphatidylinositol-4,5-Bisphosphate 3-Kinase Catalytic Subunit Beta) gene was downregulated early in 30 min RPM exposed PC-3 cells (**Figure 7F**). After 24 h, RPM-exposed adherently growing PC-3 cells exhibited a downregulated *PIK3CB* mRNA expression. No expression changes were detectable in 1*g*-MCS (**Figure 7F**).

In parallel, the *AKT1* (RAC-alpha Serine/threonine-protein kinase 1) gene showed no altered expression in short-term samples but a significantly downregulated expression in 24 h AD RPM samples compared to 1*g*. Using the liquid overlay technique, the MCS group revealed a significantly upregulated *AKT1* (**Figure 7G**).

Finally, we studied the *MTOR* gene expression. The results were similar to the findings obtained for *AKT1*. *MTOR* was not differentially expressed in the short-term study, but the gene was downregulated in AD cells after a 24 h RPM exposure. In 1*g*-MCS no expression changes were measured for *MTOR* (**Figure 7H**).

Search Tool for the Retrieval of Interacting Genes/Proteins Analysis

Figure 8A presents a summary of the qPCR data, already demonstrated in **Figures 1**, **3**–**7**, and gives an interpretation of the results. The genes of interest were differentially regulated in RPM samples (AD and RPM).

The results indicate several interactions for VEGFA, EGF, EGFR, IL1B, CXCL8, IL6, MTOR, AKT1, MMP9, and FN1, which are known to be involved in gravisensing of PC-3 prostate cancer cells exposed to short-term r-μ*g* (**Figure 8C**). It became clear that these selected factors for which the expression pattern was measured are regulating each other very strongly.

The majority of the genes quantified in this study were upregulated in MCS with the exception of the downregulated *IL1B*, *IL7*, and *AKT1* mRNAs and *CASP3, CASP9, CASP8, MMP9, TUBB, EZR, RDX, KRT8, TGFB, SPP1, VEGFA, KDR, EGF, PIK3CB,* and *MTOR* which were not differentially displayed. A closer look at the 24 h AD samples revealed that the majority of cytoskeletal genes and PAM signaling factors were downregulated. In contrast, significant upregulations were found for ECM genes and proinflammatory cytokines such as among others *IL6*, *CXCL8*, and *VEGFA* and *FLT1*.

Figure 8B shows the summary of the qPCR data of the 1*g*-MCS vs. AD control cells (liquid-overlay engineered MCS), already given in **Figures 2**–**7**. The 1*g*-liquid overlay generated MCS cell aggregates show a different picture of gene regulation. Significant upregulations were measured for the following genes: *CASP3, CASP8, CASP9, IL6, CXCL8, IL1B, IL1A, TIMP1, ACTB, TUBB, EZR, RDX, MSN, KRT8, VEGFA, EGF, EGFR,* and *AKT1*. Significant downregulations were measured for *IL7, COL1A1,* and *FLT1*. In contrast to the RPM experiment, an upregulation of apoptosis-associated cysteine-aspartic acid proteases and a strong downregulation of the growth factor receptor FLT1 catch the eye (**Figure 8B**).

The various genes analyzed by qPCR were investigated with regard to possible interactions and mutual expression dependence of their corresponding proteins. A STRING/EMBL (European Molecular Biology Laboratory) analysis of the 30 qPCR items represented in this study are shown in **Figure 8C**. **Figure 8D** visualizes interactions of 21 proteins whose genes are significantly regulated in 1*g*-MCS compared to corresponding adherent controls. The STRING network shows a clear demarcation of cytokines from cytoskeletal genes.

DISCUSSION

For many years, it has been known that various cells exposed to r- and s-μ*g* exhibit a large number of morphological and molecular changes (Grimm et al., 2018; Grimm et al., 2020). Ingram et al. showed in 1997 that various tumor cell types, among them PC-3 cells, when exposed to s-μ*g* created by a NASA bioreactor grew in form of 3D aggregates (Ingram et al., 1997). The authors had used a NASA rotary cell culture system for the different spheroid cultures. They reported that the cell adhesion molecules CD44 and E-cadherin were upregulated in the 3D spheroids (Ingram et al., 1997). Furthermore, another group demonstrated the application of an s-μ*g* culture system to study growth and differentiation during a coculture of prostate stromal and epithelial cells on microcarrier beads (Zhau et al., 1997). The authors investigated the effects of an androgen (dihydrotestosterone) on growth and PSA expression by LNCaP prostate cancer cells grown alone or as coculture with prostate fibroblasts under s-μ*g* conditions (Zhau et al., 1997). The response was similar to that observed *in vivo*. Margolis et al. demonstrated that *ex vivo* integral prostatic tissue could be successfully cultured for 28 days on the NASA-designed Rotating Wall Vessel (RWV) (Margolis et al., 1999). The prostate tissue was still suitable for further investigations (Margolis et al., 1999). Another group used the high aspect rotating-wall vessel (HARV) to study the behavior of DU-145 human prostate carcinoma cells (Clejan et al., 2001). DU-145 cells exposed to HARV cultivation showed 3D growth as well as a less aggressive, slower growing, low proliferative, higher differentiated and less pliant cell than other techniques (Clejan et al., 2001).

The project Biotechnology Demonstration System-0, one of the 80 scientific experiments aboard Space Shuttle Columbia on flight STS-107, could show that in less than 1 day in space PCC had formed a tumor larger than one inch in diameter (Twombly,

2003). In a ground-based study under s-μ*g* conditions, the PCC and bone stroma formed small tissue aggregates (Twombly, 2003). On the space shuttle Columbia, the aggregates grew to the size of a golf ball by day 6. This data is in accordance with results obtained after the Shenzhou-8/SimBox Chinese-German space mission where follicular thyroid cancer cells (FTC-133 cell line) had been studied in space for 10 days (Pietsch et al., 2013). Interestingly, FTC-133 MCS grown in the flight sample in space ranged from 5 to 10 mm in diameter, while spheroids cultured on the RPM were significantly smaller at 2–3 mm in diameter, as observed in earlier experiments (Pietsch et al., 2010; Pietsch et al., 2013).

In a recent study, we investigated PC-3 cells for 3 and 5 days under s-μ*g* conditions using a desktop RPM without any scaffold (Hybel et al., 2020). The cells revealed changes in morphology, cytoskeleton, ECM, focal adhesion complex and growth behavior. In addition, a significant upregulation of genes belonging to the PAM pathway was demonstrated (Hybel et al., 2020).

PC-3 Cells Exposed to the RPM Exhibit Changes in Morphology, Cytoskeleton and Extracellular Matrix

PC-3 cells cultured under conditions of s-μ*g* showed changes in growth within 24 h. One part grew in form of 3D multicellular spheroids and the other one continued growing as adherent cells in a 2D monolayer. This is in accordance with other cell types, including human thyroid cancer cells and breast cancer cells (Pietsch et al., 2010; Pietsch et al., 2013; Masiello et al., 2014). We focused on signs of apoptosis and could show that the TUNEL staining revealed no apoptotic cells after 24 h. In addition, the *CASP3, CASP8,* and *CASP9* genes were not differentially displayed. These findings demonstrated in **Figure 1** show viable PC-3 after RPM exposure.

In addition, we have measured the gene expression of *HIF1A* after a 24-h exposure. Interestingly, there was no significant change in the adherently growing cells, but an increase in MCS (**Figure 1H**).

A significant *HIF1A* expression has been detected in a large number of cancers, which include among others prostate tumors (Zhong et al., 1999). Elevated HIF1A levels in several cancers have been associated with aggressive tumor progression, and thus has been implicated as a predictive and prognostic marker for resistance to therapy and increased mortality (Semenza, 2003). We do not expect hypoxia in the completely filled cell culture flasks because they have vented caps. The cells are viable and no apoptosis is detectable. The gas exchange has been studied earlier (Pietsch et al., 2012).

It is known that HIF1A is initiating angiogenesis through interactions with pro-angiogenic factors like VEGF-A (Birner et al., 2001). VEGF-A is elevated in RPM-exposed PC-3 cells after 24 h. HIF1A has a regulatory role in promoting tumor progression, likely through hypoxia-induced VEGF-A expression pathways (Powis and Kirkpatrick, 2004). HIF1A overexpression in tumors may also occur in a hypoxia-independent pathway. In hemangioblastoma, *HIF1A* expression is found in most cell samples from the well-vascularized tumor (Krieg et al., 2000). It will be of high interest to perform future long-term studies investigating this finding in detail.

A large number of studies have shown that r-μ*g* as well as s-μ*g* generated by an RPM has a major impact on the cytoskeleton (Vorselen et al., 2014; Corydon et al., 2016a; Chen et al., 2019; Nassef et al., 2019; Strube et al., 2020). Thereby it reacts on alterations of gravity with a bunch of rearrangements in the structure of the cytoskeleton. Moreover, it is suggested that the cytoskeleton may act as a direct sensor of gravity and displays the initial response to changed gravity levels (Vorselen et al., 2014; Häder et al., 2017). The cytoskeleton acts as a shape-giving structure providing the mechanical strength of cells. Thus, it works as a continuous pre-stressed lattice keeping cellular structural stability. It is composed of the actin and microtubule network, as well as intermediate filaments (Vorselen et al., 2014). F-actin belongs to the microfilaments and forms a large part of the cytoskeleton. In this study, we focused on the gene expression of β-actin (*ACTB*). β-actin is involved in forming the cell structure, cell motility and cell integrity. Short-term s-μ*g*-exposure induced no significant changes in the mRNA expression level (**Figure 3**). Remarkably, after 24 h an upregulation of *ACTB* was detectable in MCS samples but not in AD. This is in line with earlier studies finding that the mRNA level of ACTB was increased after cultivating PC-3 cells for 5 days on an RPM (Hybel et al., 2020). This supports the assumption that the actin-network is influenced by gravity changes and plays a critical role in 3D growth. Moreover, it is also suggested that actin itself can work as a mechanosensitive structure (Vorselen et al., 2014). The cytoskeleton of various cell types influenced by μ*g* reacts in a similar way, thus it can be assumed that the cytoskeleton acts as the general sensor of gravity and that the changes in the cytoskeleton become important for 3D growth (Grimm et al., 2018). Together with further morphogenetic events, these changes in the actin cytoskeleton promote the emergence of ordered structures and finally they result in the formation of MCS (Cui et al., 2017).

Moreover, we focused on the *TUBB* gene expression. β-tubulin belongs to the tubulin superfamily, that in turn contains six families (α, β, γ, δ, ε, and ζ tubulins). The most important families are the α- and β-tubulins as they form the major components of the microtubules. Short-term (30 min, 2 h, 4 h) RPM exposure showed no significant changes in the mRNA expression level compared to 1*g*. After a 24 h-exposure a significant downregulation was observed in AD samples but not in MCS samples. Previous research has clearly shown that microtubule self-organization is sensitive to the direction and the magnitude of gravity. The microtubules can respond to alteration of gravity by rearranging their structure and formation. Accordingly, they lose their radial organization, can be shortened, and can be more curved and bent (Lewis et al., 1998). But it was shown that these alterations are dependent on the type of cell and differ from cell to cell (Vorselen et al., 2014).

Furthermore, we investigated changes in the ECM. The ECM acts as a kind of sensor of alterations in gravity force. It is known that s-μ*g* exposure generated by an RPM, results in

changes in the ECM like the formation of long-chain fibers with multiple RGD motifs. The RGD motif is a tripeptide that consists of arginine, glycine, and aspartate and mediates cell attachment. These motifs can bind tightly to the integrins on the cell membrane surface and interact with the cytoskeleton in the way that dispersed cells in the cell culture flask initially are drawn closer to form loose aggregates (Cui et al., 2017). In this manner the ECM is also early involved in spheroid formation of different tumor types (Grimm et al., 2002; Marrero et al., 2009; Lin et al., 2020).

To investigate the ECM components, we measured the *FN1*, *COL1A1*, *LAMA3, SPP1, MMP9* and *TIMP1* gene expression. Short-term s-μ*g* exposure (30 min, 2 h, 4 h) did not alter the expression of the selected ECM genes. In contrast, after a 24-h RPM-exposure, the *FN1*, *COL1A1* and *LAMA3* genes were elevated in both AD and MCS samples (**Figures 4A–C**). This is in line with earlier studies on different cell types demonstrating that there is a general tendency of elevated ECM components when cancer cells but also stem cells and specialized cells were exposed to long-term s-μ*g* (Grimm et al., 2002; Kraus et al., 2017; Ebnerasuly et al., 2018). It has to be noted that this increase is dependent on the cell type. There were opposite results detectable when adult retinal epithelium cells (ARPE-19) were exposed to the RPM (Corydon et al., 2016b). The *FN1* expression and *LAMB2* expression was reduced after RPM exposure in AD and MCS of ARPE-19 cells (Corydon et al., 2016b).

When analyzing the presence of fibronectin in MCS obtained in s-μ*g*, a slightly different cytoplasmic distribution, exemplified by a dotted pattern, compared to 1*g* samples was observed. A likely explanation could be that the cells of the MCS are significantly smaller. The apparent shrinking of the cells and the accompanying compression of the cytoplasm may collectively result in an altered cytoplasmic distribution and reduced secretion of fibronectin, despite the increased expression of *FN1*. However, reduced gravitational conditions may also impact the cytoplasmic appearance of fibronectin in RPM-MCS (**Figure 4A**).

In addition, human mesenchymal stem cells exposed to 10 days s-μ*g* showed a decrease in collagen production, as well as a reduced expression of *TIMP1*, *TIMP3,* and *MMP11* genes, together with an elevated expression of tenascin and laminin subunit (Zhivodernikov et al., 2020).

The *SPP1* gene expression was not significantly changed in all groups of PC-3 exposed to s-μ*g* conditions. The expression of osteopontin is known to be cell type-dependent. Rat osteoblasts cultured for 4 or 5 days aboard the Space Shuttle revealed a reduced (30%) *SPP1* mRNA (osteopontin) in the flight samples (Kumei et al., 2006). In contrast, the *SPP1* mRNA was elevated in human fetal osteoblasts exposed to the RPM (Mann et al., 2019). A similar result was obtained for human primary chondrocytes (Wehland et al., 2020).

Simulated Microgravity Influences the Expression and Release of Inflammatory Cytokines in PC-3 Cells

We focused on the cytokine release pattern of PC-3 cells when exposed to the RPM. It is assumed that some cytokines play a major role in spheroid formation. *IL6* for example exhibits a higher expression in PC-3 cells as well as in other prostate cancer cell lines and plays a major role as a proliferative autocrine and paracrine factor in prostate cancer (Azevedo et al., 2011). Furthermore, Gopinathan et al. (Gopinathan et al., 2015) showed that *IL6* can directly generate the development of new blood vessels, the proliferation and migration of endothelial cells and has thereby a tumor promoting activity.

In the present study, the *IL6* gene expression increased very early with a 10-fold peak after 2 h of RPM-exposure. Afterwards, within 4 and 24 h (AD and MCS) it slightly decreased but still showed an about 5-fold elevation compared to 1*g* samples. This is in line with Grosse et al. (Grosse et al., 2012), who performed similar experiments with FTC-133 thyroid cancer cells and demonstrated that the tumor cells on the RPM released IL-6 in the supernatant. Svejgaard et al. (Svejgaard et al., 2015) demonstrated that both cytokines IL-6 and IL-8 improve 3D aggregation of the human thyroid cancer cell lines (ML-1 and RO-82-W-1) using the liquid overlay technique and that these cytokines induced the protein expression of β-actin, β_1-integrin, talin-1, and Ki-67. These findings implicate that IL-6 as well as IL-8 are involved in spheroid formation. The detailed mechanisms are still unknown and have to be investigated more precisely in future studies. Interestingly, the IL-6 release was significantly elevated in all RPM samples at all time points (**Table 3**).

Taken together, all these findings indicate that interleukin-6 might be an important factor for tumor cell growth, angiogenesis, metastasis and spheroid formation. The expression of *CXCL8* showed a similar pattern as *IL6* indicating a similar reaction of the anti-inflammatory cytokines to microgravity.

Singh et al. (Singh and Lokeshwar, 2009) showed that IL-8 is acting as a survival factor of cancer cells and in this context IL-8 interacts with Akt and NF-κB, and has thereby a control function on the apoptotic pathway. Moreover, IL-8 plays a role in PC-3 survival, invasion, and resistance to chemotherapeutic drugs in PC-3 cells. Wilson et al. (Waugh and Wilson, 2008) mentioned that IL-8 signaling is involved in PC-3 survival and acts as an intrinsic factor of chemoresistance in advanced prostate cancer. Besides, Waugh et al. (Waugh and Wilson, 2008) showed that *CXCL8* signaling regulates, among others, the transcriptional activity of the androgen receptor of PC-3 so that PC-3 proliferate androgen-independently. Therefore, taken these findings together, IL-8 is of special interest as it has an impact on PC-3 cells in many ways.

In the present study, we measured an upregulation of *CXCL8* in AD cells and 3D PC-3 MCS. The secretion of IL-8 was significantly elevated after 4 h, but similar after 24 h between the RPM and 1*g* group (**Table 3**). It is known that IL-8 increases the expression of several proteins of the cytoskeleton and focal adhesion complex. These proteins in turn play a major role in tumor progression and metastasis (Desiniotis and Kyprianou, 2011). Remarkably, these proteins belonging to the cytoskeleton and focal adhesion complex also

Originale der Publikationen

can sense gravity changes and therefore have a great impact on spheroid formation.

Simulated Microgravity has Impact on VEGF, EGF, and PAM Signaling

We studied factors of signaling pathways known to be involved in 3D growth (Krüger et al., 2019; Nassef et al., 2020). The expression of genes belonging to the *VEGF* signaling pathway were analyzed, showing that the gene expression of *VEGFA* was downregulated after 4 h and in contrast upregulated after 24 h of RPM exposure in AD samples compared to 1*g* (**Figure 7A**). In MCS samples, however, the *VEGFA* mRNA showed no significant change. One potential explanation for this finding could be that a less-aggressive phenotype developed when the cells merged into spheroid formation, which was found earlier in follicular thyroid cancer cells cultured in space (Ma et al., 2014). Furthermore, VEGF-A has various well-known effects in cancer. It is mediating increased vascular permeability, inducing angiogenesis, vasculogenesis and growth. In addition, VEGF-A promotes migration and progression. Within 24 h, the prostate cancer cells exposed to the RPM start to detach and to form MCS. A high amount of VEGF-A promotes spheroid formation which might explain the elevated level of *VEGFA* mRNA in 24 h AD samples.

The *KDR* gene was not differentially expressed in all groups, whereas *FLT1* was downregulated after 4 h in AD, unchanged after 24 h in AD, but elevated in MCS. As the VEGF-A pathway has been implicated in pathological angiogenesis and tumor development (Nagy et al., 2007), a lower expression of the pathway points towards a less-aggressive cancer growth behavior.

Furthermore, we investigated the gene expression of *EGF*. The EGF protein is a key player in cancer by enhancing cell proliferation, survival, invasion, and metastasis (Bhat et al., 2014). The expression of epidermal growth factor receptor (EGFR) in cancer is often associated with a more aggressive phenotype and predictive of poor prognosis (Bhat et al., 2014). The *EGFR* mRNA is upregulated in MCS compared to 1*g* control cells indicating its involvement in 3D spheroid formation (**Figure 7E**).

The PAM pathway is of special interest because it is often mutated in prostate cancer (Tee et al., 2018) and therefore involved in cancer growth and progression. It is also a frequent reason of drug-resistance especially to androgen-deprivation therapy in prostate cancer (Park et al., 2018). Regarding the PAM signaling pathway, the *PIK3CB* gene was downregulated after 30 min and finally, after 24 h also in AD samples. A similar result was obtained for the *AKT1* and *MTOR* mRNAs, which were both reduced in 24 h AD cells. In addition, these genes were not altered in MCS. This is an interesting result because downregulation of the PAM pathway can activate apoptosis in cancer (Yang et al., 2019). Apoptosis was not detected after RPM exposure, which is an interesting result and it can therefore be concluded that other signaling factors exhibited anti-apoptotic effects on the PC exposed to short-term μ*g*. Long-term s-μ*g*-exposure of PC-3 cells (5 days) resulted in a significant upregulation of *AKT* and *MTOR* mRNAs in both AD and MCS (Hybel et al., 2020).

Interaction Network of Selected Genes Evaluated by STRING Analysis and Cytoscape 3.8.2

The STRING analysis revealed an interaction network of VEGFA, FLT1, EGF, EGFR, IL1B, IL6, CXCL8, MTOR, AKT1, MMP9, and FN1. The interaction between the VEGF and EGFR pathway is well known and the rationale for a multi-target anticancer therapy (Ciardiello et al., 2006). EGF application is able to enhance VEGF-A production and to induce PI3K-dependent positive feedback on AKT and ERK via VEGFR2 in hematological malignancies (human monocytic leukemia THP1 cell line and Burkitt's lymphoma Raji cell line (Saryeddine et al., 2016). Both pathways are key players in cancer cell growth, progression, metastasis and angiogenesis. Multikinase inhibitor therapy targeting among other factors VEGF-A is applied today in different types of advanced metastatic cancers (Wehland et al., 2012; Ancker et al., 2017; Randrup Hansen et al., 2017; Sarkar et al., 2020). EGF mediates cellular proliferation, differentiation, and survival (Herbst, 2004) and is involved in spheroid formation of cancer cells exposed to r-μ*g* in space. The *EGF* gene expression was clearly upregulated in AD and MCS of FTC-133 follicular thyroid cancer cells in space during the Shenzhou-8 space mission (Pietsch et al., 2013). These results indicate the importance of EGF signaling for spheroid formation.

A further factor involved in spheroid formation and spreading of cancer cells is fibronectin. Proteome analyses revealed that surface proteins are binding fibronectin, and thus strengthening the 3D spheroid formation of thyroid cancer cells (Pietsch et al., 2011). This might be also important for other cancer types. Bioinformatic analyses have demonstrated that EGFR, KDR, FN1, TGFB1 as well as PCNA are interacting with VEGF-A and are involved in non-small cell lung cancer tumorigenesis (Wang et al., 2015). FN1 is involved in the occurrence and development of various tumors and is upregulated in multiple cancer types. *FN1* is able to promote cell proliferation and migration in gastric cancer cell lines (Sun et al., 2020). A recent study showed that both cell adhesion molecules and ECM components OPN (SPP1) and FN1 might work as biological markers of progression and prognosis in esophageal cancer (Li et al., 2020).

The functional roles of VEGF and OPN in angiogenesis and their clinical significance in tumor biology are well-described (Shijubo et al., 2000). In PC metastasis both protein synthesis and gene expression of *SPP1* were remarkably upregulated in metastatic castration-resistant PC (Pang et al., 2019).

Pro-inflammatory cytokines such as IL-1, IL-6, IL-17, and TNF-α promote proliferation and differentiation of cancer cells (Vendramini-Costa and Carvalho, 2012). The cytokines IL-6 and IL-8 (CXCL-8) are further key elements which are able to enhance 3D growth in PC-3 and have both already shown to

induce 3D growth in thyroid tumor cells grown under 1*g*-conditions using the liquid overlay technique (Svejgaard et al., 2015). Both cytokines were clearly elevated in PC-3 exposed to the RPM and may serve as key players for 3D aggregation. IL-6 is a key factor in the tumor microenvironment. IL-6 overexpression was demonstrated in almost all cancer types (Kumari et al., 2016). High levels of IL-6 advance tumorigenesis and regulate among others metabolism, angiogenesis, invasiveness, metastasis, apoptosis, and survival (Kumari et al., 2016). IL-6 can induce cell growth and VEGF synthesis in malignant mesotheliomas or gastric cancer (Huang et al., 2004; Adachi et al., 2006). Furthermore, EGFR signaling promotes induction of the IL-6 receptor controlled by mTOR (Garbers et al., 2013). An aberrant EGFR activation triggered IL-6 synthesis (Garbers et al., 2013).

The PI3K-AKT-mTOR signaling network is activated and during prostate tumorigenesis, PC progression and recurrence (Shorning et al., 2020). The mTOR pathway is involved in VEGF biosynthesis, and disruption of the VEGF/Neuroplin-1 (NRP1) axis. VEGF/NRP1 are promoting angiogenesis and pro-tumorigenic signaling in both endothelial and cancer cells (Pal et al., 2019). The *VEGFA* gene expression is enhanced in AD cells indicating signaling towards 3D formation of PC-3.

Even though there are various more convenient techniques to produce spheroids like the hanging drop technique (Timmins et al., 2004) or the liquid-overlay technique (Svejgaard et al., 2015), these methods introduce unfavorable aspects which are low quantity, poor nutrition exchange among others. In addition, the transition from 2D growth to 3D growth cannot be monitored in these experimental setups. We used the liquid-overlay technique and engineered MCS under 1*g*-conditions. After 24 h, the PC-3 cells formed loose 3D aggregates on agarose. Unfortunately, more dead cells were detected compared to RPM-engineered MCS (**Figure 2B**). The qPCR analysis revealed a strong up-regulation for proinflammatory cytokines like among others *IL6* and *CXCL8*. This finding might be explained by the higher amount of dead cells in 1*g*-engineered MCS. The opposite result was obtained for the expression of *VEGFA* and *FLT1* in 1*g*-MCS. *VEGFA* and *KDR* were both not differentially altered and *FLT1* was significantly elevated in RPM-MCS, whereas *VEGFA* was upregulated and *FLT1* down-regulated in 1*g*-MCS.

In addition, the ECM genes *FN1, COL1A1,* and *LAMA3* were all significantly up-regulated in RPM-MCS and differentially regulated in 1*g*-MCS. Taken together the results involving 1*g*-MCS engineered with the liquid-overlay technique are not suitable to study the early phases of tumor progression and metastasis in PC. The MCS formed with an RPM are rounder and compact, are created without agarose or a scaffold, do not show an increase in apoptosis and can grow for a longer time under s-μ*g* conditions as shown in an earlier study (Hybel et al., 2020).

Comparison Between Short-Term and Long-Term Changes in PC-3 Cells Exposed to the RPM

COL1A1, which encodes one part of the fibril-forming pro-alpha1 chains of type I collagen, *LAMA3,* encoding the alpha part of the heterotrimeric laminin molecule, and *FN1,* encoding fibronectin, which is involved in RET signaling and is part of the integrin pathway, are substantial components of the ECM. All three genes are upregulated in PC-3 after a 24-h RPM-exposure in AD as well as in MCS. In a previous study with long-term RPM-exposure of PC-3 cells, we found that the upregulation of *LAMA3* and *FN1* expression persists after 3 days of RPM exposure in AD and MCS but turns to depletion in AD at day five (Hybel et al., 2020). In contrast, the *COL1A1* gene is up-regulated after 5 days of RPM-exposure (Hybel et al., 2020).

ACTB and *TUBB* are encoding the β-actin and β-tubulin class I proteins, respectively. Both factors are substantial proteins of the cytoskeleton. While the *ACTB* expression is upregulated in PC-3 cells after a 24-h RPM-exposure only in MCS, the *TUBB* expression is depleted after 24 h in RPM-AD samples. However, after 5 days under RPM-conditions, both genes are upregulated in AD as well as in MCS samples (Hybel et al., 2020).

AKT1 encodes one of the three AKT serine-threonine protein kinases and participates in mTOR signaling. Both, *AKT1* and *MTOR* are depleted in AD under 24 h in s-μ*g,* but upregulated after 5 days in s-μ*g* (AD & MCS) (Hybel et al., 2020).

In contrast, *FLT1* and *VEGFA,* encoding the angiogenesis proteins vascular endothelial growth factor receptor 1 and the vascular endothelial growth factor 1, are both upregulated after 24 h s-μ*g*. The up-regulation of *FLT1* takes place in MCS and the up-regulation of *VEGFA* in AD. After 5 days of μg exposure *FLT1* is upregulated in AD and MCS and *VEGFA* expression is depleted in MCS (Hybel et al., 2020).

In general, compared to a short-term s-μ*g*-experiment, substantial changes in AD and MCS expression of cytoskeletal genes, extracellular matrix and PAM signaling can still be detected after three and 5 days of RPM-exposure, respectively. This suggests that in the future extended time course experiments may be appropriate. Recent studies have highlighted the existence of an integrated signaling network connecting mechanosensitive pathways to circadian gene regulation in *e.g.* human keratinocytes (Ranieri et al., 2015). Whether this is also the case in PC-3 prostate cancer cells awaits further studies.

In summary, this study focused on the early effects of s-μ*g* on PC-3 cells. Short-term s-μ*g* influenced the growth behavior of PC-3 cells towards a 3D phenotype. No signs of apoptosis were detectable. Changes in the expression of genes belonging to the cytoskeleton, ECM, cytokines, VEGF, EGFR, and PAM signaling were measured. This was accompanied by alterations of the secretion of the cytokines and ECM components. We observed significant increases in *IL6* and *CXCL8* gene expression after 2, 4 and 24 h in MCS, which hints towards a more aggressive phenotype in short-term microgravity. After 24 h *TIMP1* was elevated in MCS and *MMP9* in AD cells (**Figures 4E,F**). In addition, the release of IL-6 in the supernatant was elevated at all time points in RPM samples. These results fit to earlier short-term studies (parabolic flight experiments) which have already shown that thyroid cancer cells exhibit a more aggressive phenotype when cultured under r-μ*g* (Ma et al., 2014). This is a finding which should be studied in more detail in the future.

PC-3 exposed to s-μ*g* created by an RPM grew in form of two phenotypes: an adherent monolayer and as 3D aggregates. The

PC-3 cells started to aggregate 24 h following subjection to s-μ*g* conditions. Moreover, the 24 h RPM exposure of PC-3 cells resulted in an early activation of the VEGF pathway, EGFR1 and a downregulation of PAM signaling. Moreover, the secretion and gene expression of proinflammatory cytokines *IL1B*, *IL6* and *CXCL8* were markedly upregulated and closely involved in the first phases of spheroid formation of PC-3 cultivated under conditions of s-μ*g*. This makes them interesting targets for a possible suppression of the development of metastases. In fact, HuMax-IL-8 (BMS-986253), a novel fully human monoclonal anti-IL-8 antibody has recently been introduced in different phase I trials testing its anti-cancer potential [NCT02536469, NCT03689699] (Bilusic et al., 2019). These trials, however, were done on patients with advanced, already metastasized stages of cancer. Our results suggest that IL-6 or IL-8 inhibition might already be beneficial in early stages of cancer by preventing or slowing down metastasis. Both factors will be targeted in future short- and long-term experiments. Liquid-overlay engineered PC-3 MCS revealed apoptotic cells after 24 h, which may influence the expression of cytokines, cytoskeletal genes and other factors. Taken these findings together, multicellular spheroids engineered by microgravity represent a novel model for studying the early phases of metastasis *in vitro*. The present findings may thus provide additional insights in selecting new targets to impair prostate cancer progression.

DATA AVAILABILITY STATEMENT

The raw data supporting the conclusion of this article will be made available by the authors, without undue reservation.

AUTHOR CONTRIBUTIONS

Conceptualization, DG and SKo; methodology, DD, JS, TEH, DM, SB, BB, and RV; software, HS, and SKo; validation, MW, HS, DG, and MK; formal analysis, DD; investigation, DD, DM, TEH, JS, RV, and SKa; resources, DG; data curation, DD, DM, HS, and MW; writing—original draft preparation, DD, DG; writing—review and editing, DG, TJC, MK, BB, and SKo; visualization, MK, SKa; supervision, DG, MI, SB, and TJC; project administration, DG; funding acquisition, DG and SB; All authors have read and agreed to the published version of the manuscript.

FUNDING

This research was funded by Deutsches Zentrum für Luft-und Raumfahrt (DLR), BMWi project 50WB 1924. The research was supported by BELSPO PRODEX (IMPULSE Grant 4000109861).

REFERENCES

Adachi, Y., Aoki, C., Yoshio-Hoshino, N., Takayama, K., Curiel, D. T., and Nishimoto, N. (2006). Interleukin-6 Induces Both Cell Growth and VEGF Production in Malignant Mesotheliomas. *Int. J. Cancer* 119, 1303–1311. doi:10.1002/ijc.22006

Adekoya, T. O., and Richardson, R. M. (2020). Cytokines and Chemokines as Mediators of Prostate Cancer Metastasis. *Ijms* 21, 4449. doi:10.3390/ijms21124449

Ancker, O., Wehland, M., Bauer, J., Infanger, M., and Grimm, D. (2017). The Adverse Effect of Hypertension in the Treatment of Thyroid Cancer with Multi-Kinase Inhibitors. *Ijms* 18, 625. doi:10.3390/ijms18030625

Azevedo, A., Cunha, V., Teixeira, A. L., and Medeiros, R. (2011). IL-6/IL-6R as a Potential Key Signaling Pathway in Prostate Cancer Development. *Wjco* 2, 384–396. doi:10.5306/wjco.v2.i12.384

Becker, J. L., and Souza, G. R. (2013). Using Space-Based Investigations to Inform Cancer Research on Earth. *Nat. Rev. Cancer* 13, 315–327. doi:10.1038/nrc3507

Benavides Damm, T., Walther, I., Wüest, S. L., Sekler, J., and Egli, M. (2014). Cell Cultivation under Different Gravitational Loads Using a Novel Random Positioning Incubator. *Biotechnol. Bioeng.* 111, 1180–1190. doi:10.1002/bit.25179

Bhat, F. A., Sharmila, G., Balakrishnan, S., Singh, P. R., Srinivasan, N., and Arunakaran, J. (2014). Epidermal Growth Factor-Induced Prostate Cancer (PC3) Cell Survival and Proliferation Is Inhibited by Quercetin, a Plant Flavonoid through Apoptotic Machinery. *Biomed. Prev. Nutr.* 4, 459–468. doi:10.1016/j.bionut.2014.07.003

Bilusic, M., Heery, C. R., Collins, J. M., Donahue, R. N., Palena, C., Madan, R. A., et al. (2019). Phase I Trial of HuMax-IL8 (BMS-986253), an anti-IL-8 Monoclonal Antibody, in Patients with Metastatic or Unresectable Solid Tumors. *J. Immunotherapy Cancer* 7, 240. doi:10.1186/s40425-019-0706-x

Birner, P., Schindl, M., Obermair, A., Breitenecker, G., and Oberhuber, G. (2001). Expression of Hypoxia-Inducible Factor 1alpha in Epithelial Ovarian Tumors: its Impact on Prognosis and on Response to Chemotherapy. *Clin. Cancer Res.* 7, 1661–1668.

Bonnans, C., Chou, J., and Werb, Z. (2014). Remodelling the Extracellular Matrix in Development and Disease. *Nat. Rev. Mol. Cell Biol.* 15, 786–801. doi:10.1038/nrm3904

B. Vendramini-Costa, D., and E. Carvalho, J. (2012). Molecular Link Mechanisms between Inflammation and Cancer. *Cpd* 18, 3831–3852. doi:10.2174/138161212802083707

Chen, Z.-Y., Guo, S., Li, B.-B., Jiang, N., Li, A., Yan, H.-F., et al. (2019). Effect of Weightlessness on the 3D Structure Formation and Physiologic Function of Human Cancer Cells. *Biomed. Res. Int.* 2019, 1–17. doi:10.1155/2019/4894083

Ciardiello, F., Troiani, T., Bianco, R., Orditura, M., Morgillo, F., Martinelli, E., et al. (2006). Interaction between the Epidermal Growth Factor Receptor (EGFR) and the Vascular Endothelial Growth Factor (VEGF) Pathways: a Rational Approach for Multi-Target Anticancer Therapy. *Ann. Oncol.* 17 (Suppl. 7), vii109–vii114. doi:10.1093/annonc/mdl962

Clejan, S., O'connor, K., and Rosensweig, N. (2001). Tri-dimensional Prostate Cell Cultures in Simulated Microgravity and Induced Changes in Lipid Second Messengers and Signal Transduction. *J. Cell. Mol. Med.* 5, 60–73. doi:10.1111/j.1582-4934.2001.tb00138.x

Corydon, T. J., Kopp, S., Wehland, M., Braun, M., Schütte, A., Mayer, T., et al. (2016a). Alterations of the Cytoskeleton in Human Cells in Space Proved by Life-Cell Imaging. *Sci. Rep.* 6, 20043. doi:10.1038/srep20043

Corydon, T. J., Mann, V., Slumstrup, L., Kopp, S., Sahana, J., Askou, A. L., et al. (2016b). Reduced Expression of Cytoskeletal and Extracellular Matrix Genes in Human Adult Retinal Pigment Epithelium Cells Exposed to Simulated Microgravity. *Cell Physiol Biochem* 40, 1–17. doi:10.1159/000452520

Cui, X., Hartanto, Y., and Zhang, H. (2017). Advances in Multicellular Spheroids Formation. *J. R. Soc. Interf.* 14, 20160877. doi:10.1098/rsif.2016.0877

Desiniotis, A., and Kyprianou, N. (2011). Significance of Talin in Cancer Progression and Metastasis. *Int. Rev. Cell Mol. Biol.* 289, 117–147. doi:10.1016/B978-0-12-386039-2.00004-3

Dittrich, A., Grimm, D., Sahana, J., Bauer, J., Krüger, M., Infanger, M., et al. (2018). Key Proteins Involved in Spheroid Formation and Angiogenesis in Endothelial Cells after Long-Term Exposure to Simulated Microgravity. *Cell Physiol Biochem* 45, 429–445. doi:10.1159/000486920

Dranoff, G. (2004). Cytokines in Cancer Pathogenesis and Cancer Therapy. *Nat. Rev. Cancer* 4, 11–22. doi:10.1038/nrc1252

Ebnerasuly, F., Hajebrahimi, Z., Tabaie, S. M., and Darbouy, M. (2018). Simulated Microgravity Condition Alters the Gene Expression of Some ECM and Adhesion Molecules in Adipose Derived Stem Cells. *Int. J. Mol. Cell Med* 7, 146–157. doi:10.22088/IJMCM.BUMS.7.3.146

Gandaglia, G., Abdollah, F., Schiffmann, J., Trudeau, V., Shariat, S. F., Kim, S. P., et al. (2014). Distribution of Metastatic Sites in Patients with Prostate Cancer: A Population-Based Analysis. *Prostate* 74, 210–216. doi:10.1002/pros.22742

Garbers, C., Kuck, F., Aparicio-Siegmund, S., Konzak, K., Kessenbrock, M., Sommerfeld, A., et al. (2013). Cellular Senescence or EGFR Signaling Induces Interleukin 6 (IL-6) Receptor Expression Controlled by Mammalian Target of Rapamycin (mTOR). *Cell Cycle* 12, 3421–3432. doi:10.4161/cc.26431

Gopinathan, G., Milagre, C., Pearce, O. M. T., Reynolds, L. E., Hodivala-Dilke, K., Leinster, D. A., et al. (2015). Interleukin-6 Stimulates Defective Angiogenesis. *Cancer Res.* 75, 3098–3107. doi:10.1158/0008-5472.CAN-15-1227

Grimm, D., Bauer, J., Kossmehl, P., Shakibaei, M., Schönberger, J., Pickenhahn, H., et al. (2002). Simulated Microgravity Alters Differentiation and Increases Apoptosis in Human Follicular Thyroid Carcinoma Cells. *FASEB j.* 16, 604–606. doi:10.1096/fj.01-0673fje

Grimm, D., Egli, M., Krüger, M., Riwaldt, S., Corydon, T. J., Kopp, S., et al. (2018). Tissue Engineering under Microgravity Conditions-Use of Stem Cells and Specialized Cells. *Stem Cell Development* 27, 787–804. doi:10.1089/scd.2017.0242

Grimm, D., Wehland, M., Corydon, T. J., Richter, P., Prasad, B., Bauer, J., et al. (2020). The Effects of Microgravity on Differentiation and Cell Growth in Stem Cells and Cancer Stem Cells. *Stem Cell Transl Med* 9, 882–894. doi:10.1002/sctm.20-0084

Grosse, J., Wehland, M., Pietsch, J., Schulz, H., Saar, K., Hübner, N., et al. (2012). Gravity-sensitive Signaling Drives 3-dimensional Formation of Multicellular Thyroid Cancer Spheroids. *FASEB j.* 26, 5124–5140. doi:10.1096/fj.12-215749

Häder, D.-P., Braun, M., Grimm, D., and Hemmersbach, R. (2017). Gravireceptors in Eukaryotes-A Comparison of Case Studies on the Cellular Level. *NPJ Microgravity* 3, 13. doi:10.1038/s41526-017-0018-8

Herbst, R. S. (2004). Review of Epidermal Growth Factor Receptor Biology. *Int. J. Radiat. Oncology*Biology*Physics* 59, S21–S26. doi:10.1016/j.ijrobp.2003.11.041

Huang, S.-P., Wu, M.-S., Shun, C.-T., Wang, H.-P., Lin, M.-T., Kuo, M.-L., et al. (2004). Interleukin-6 Increases Vascular Endothelial Growth Factor and Angiogenesis in Gastric Carcinoma. *J. Biomed. Sci.* 11, 517–527. doi:10.1007/BF02256101

Hybel, T. E., Dietrichs, D., Sahana, J., Corydon, T. J., Nassef, M. Z., Wehland, M., et al. (2020). Simulated Microgravity Influences VEGF, MAPK, and PAM Signaling in Prostate Cancer Cells. *Ijms* 21, 1263. doi:10.3390/ijms21041263

Infanger, M., Kossmehl, P., Shakibaei, M., Bauer, J., Kossmehl-Zorn, S., Cogoli, A., et al. (2006). Simulated Weightlessness Changes the Cytoskeleton and Extracellular Matrix Proteins in Papillary Thyroid Carcinoma Cells. *Cell Tissue Res* 324, 267–277. doi:10.1007/s00441-005-0142-8

Ingram, M., Techy, G. B., Saroufeem, R., Yazan, O., Narayan, K. S., Goodwin, T. J., et al. (1997). Three-dimensional Growth Patterns of Various Human Tumor Cell Lines in Simulated Microgravity of a NASA Bioreactor. In Vitro *Cell.Dev.Biol.-Animal* 33, 459–466. doi:10.1007/s11626-997-0064-8

Kopp, S., Slumstrup, L., Corydon, T. J., Sahana, J., Aleshcheva, G., Islam, T., et al. (2016). Identifications of Novel Mechanisms in Breast Cancer Cells Involving Duct-like Multicellular Spheroid Formation after Exposure to the Random Positioning Machine. *Sci. Rep.* 6, 26887. doi:10.1038/srep26887

Kopp, S., Warnke, E., Wehland, M., Aleshcheva, G., Magnusson, N. E., Hemmersbach, R., et al. (2015). Mechanisms of Three-Dimensional Growth of Thyroid Cells during Long-Term Simulated Microgravity. *Sci. Rep.* 5, 16691. doi:10.1038/srep16691

Kraus, A., Luetzenberg, R., Abuagela, N., Hollenberg, S., and Infanger, M. (2017). Spheroid Formation and Modulation of Tenocyte-specific Gene Expression under Simulated Microgravity. *Mltj* 7, 411–417. doi:10.11138/mltj/2017.7.3.411

Krieg, M., Haas, R., Brauch, H., Acker, T., Flamme, I., and Plate, K. H. (2000). Up-regulation of hypoxia-inducible factors HIF-1α and HIF-2α under normoxic conditions in renal carcinoma cells by von Hippel-Lindau tumor suppressor gene loss of function. *Oncogene* 19, 5435–5443. doi:10.1038/sj.onc.1203938

Krüger, M., Melnik, D., Kopp, S., Buken, C., Sahana, J., Bauer, J., et al. (2019). Fighting Thyroid Cancer with Microgravity Research. *Ijms* 20, 2553. doi:10.3390/ijms20102553

Kumari, N., Dwarakanath, B. S., Das, A., and Bhatt, A. N. (2016). Role of Interleukin-6 in Cancer Progression and Therapeutic Resistance. *Tumor Biol.* 37, 11553–11572. doi:10.1007/s13277-016-5098-7

Kumei, Y., Morita, S., Katano, H., Akiyama, H., Hirano, M., Oyha, K., et al. (2006). Microgravity Signal Ensnarls Cell Adhesion, Cytoskeleton, and Matrix Proteins of Rat Osteoblasts: Osteopontin, CD44, Osteonectin, and -Tubulin. *Ann. New York Acad. Sci.* 1090, 311–317. doi:10.1196/annals.1378.034

Lewis, M. L., Reynolds, J. L., Cubano, L. A., Hatton, J. P., Lawless, B. D., and Piepmeier, E. H. (1998). Spaceflight Alters Microtubules and Increases Apoptosis in Human Lymphocytes (Jurkat). *FASEB j.* 12, 1007–1018. doi:10.1096/fasebj.12.11.1007

Li, M., Wang, K., Pang, Y., Zhang, H., Peng, H., Shi, Q., et al. (2020). SPP1 and FN1 Associated with Progression and Prognosis of Esophageal Cancer Identified by Integrated Expression Profiles Analysis. *Med. Sci. Monit.* 26, e920355. doi:10.12659/MSM.920355

Lin, X., Zhang, K., Wei, D., Tian, Y., Gao, Y., Chen, Z., et al. (2020). The Impact of Spaceflight and Simulated Microgravity on Cell Adhesion. *Ijms* 21, 3031. doi:10.3390/ijms21093031

Ma, X., Pietsch, J., Wehland, M., Schulz, H., Saar, K., Hübner, N., et al. (2014). Differential Gene Expression Profile and Altered Cytokine Secretion of Thyroid Cancer Cells in Space. *FASEB j.* 28, 813–835. doi:10.1096/fj.13-243287

Mann, V., Grimm, D., Corydon, T., Krüger, M., Wehland, M., Riwaldt, S., et al. (2019). Changes in Human Foetal Osteoblasts Exposed to the Random Positioning Machine and Bone Construct Tissue Engineering. *Ijms* 20, 1357. doi:10.3390/ijms20061357

Margolis, L., Hatfill, S., Chuaqui, R., Vocke, C., Emmert-Buck, M., Linehan, W. M., et al. (1999). Long Term Organ Culture of Human Prostate Tissue in a NASA-Designed Rotating wall Bioreactor. *J. Urol.* 161, 290–297. doi:10.1016/s0022-5347(01)62134-7

Marrero, B., Messina, J. L., and Heller, R. (2009). Generation of a Tumor Spheroid in a Microgravity Environment as a 3D Model of Melanoma. In Vitro *Cell.Dev.Biol.-Animal* 45, 523–534. doi:10.1007/s11626-009-9217-2

Masiello, M. G., Cucina, A., Proietti, S., Palombo, A., Coluccia, P., D'Anselmi, F., et al. (2014). Phenotypic Switch Induced by Simulated Microgravity on MDA-MB-231 Breast Cancer Cells. *Biomed. Res. Int.* 2014, 1–12. doi:10.1155/2014/652434

Mehta, G., Hsiao, A. Y., Ingram, M., Luker, G. D., and Takayama, S. (2012). Opportunities and Challenges for Use of Tumor Spheroids as Models to Test Drug Delivery and Efficacy. *J. Controlled Release* 164, 192–204. doi:10.1016/j.jconrel.2012.04.045

Nagy, J. A., Dvorak, A. M., and Dvorak, H. F. (2007). VEGF-A and the Induction of Pathological Angiogenesis. *Annu. Rev. Pathol. Mech. Dis.* 2, 251–275. doi:10.1146/annurev.pathol.2.010506.134925

Nassef, M. Z., Kopp, S., Wehland, M., Melnik, D., Sahana, J., Krüger, M., et al. (2019). Real Microgravity Influences the Cytoskeleton and Focal Adhesions in Human Breast Cancer Cells. *Ijms* 20, 3156. doi:10.3390/ijms20133156

Nassef, M. Z., Melnik, D., Kopp, S., Sahana, J., Infanger, M., Lützenberg, R., et al. (2020). Breast Cancer Cells in Microgravity: New Aspects for Cancer Research. *Ijms* 21, 7345. doi:10.3390/ijms21197345

Pal, K., Madamsetty, V. S., Dutta, S. K., Wang, E., Angom, R. S., and Mukhopadhyay, D. (2019). Synchronous Inhibition of mTOR and VEGF/NRP1 axis Impedes Tumor Growth and Metastasis in Renal Cancer. *Npj Precis. Onc.* 3, 31. doi:10.1038/s41698-019-0105-2

Pang, X., Xie, R., Zhang, Z., Liu, Q., Wu, S., and Cui, Y. (2019). Identification of SPP1 as an Extracellular Matrix Signature for Metastatic Castration-Resistant Prostate Cancer. *Front. Oncol.* 9, 924. doi:10.3389/fonc.2019.00924

Park, S., Kim, Y. S., Kim, D. Y., So, I., and Jeon, J.-H. (2018). PI3K Pathway in Prostate Cancer: All Resistant Roads lead to PI3K. *Biochim. Biophys. Acta (Bba) - Rev. Cancer* 1870, 198–206. doi:10.1016/j.bbcan.2018.09.001

Pietsch, J., Kussian, R., Sickmann, A., Bauer, J., Weber, G., Nissum, M., et al. (2010). Application of Free-Flow IEF to Identify Protein Candidates Changing under Microgravity Conditions. *Proteomics* 10, 904–913. doi:10.1002/pmic.200900226

Pietsch, J., Ma, X., Wehland, M., Aleshcheva, G., Schwarzwälder, A., Segerer, J., et al. (2013). Spheroid Formation of Human Thyroid Cancer Cells in an Automated Culturing System during the Shenzhou-8 Space mission. *Biomaterials* 34, 7694–7705. doi:10.1016/j.biomaterials.2013.06.054

Pietsch, J., Sickmann, A., Weber, G., Bauer, J., Egli, M., Wildgruber, R., et al. (2011). A Proteomic Approach to Analysing Spheroid Formation of Two Human Thyroid Cell Lines Cultured on a Random Positioning Machine. *Proteomics* 11, 2095–2104. doi:10.1002/pmic.201000817

Pietsch, J., Sickmann, A., Weber, G., Bauer, J., Egli, M., Wildgruber, R., et al. (2012). Metabolic Enzyme Diversity in Different Human Thyroid Cell Lines and Their Sensitivity to Gravitational Forces. *Proteomics* 12, 2539–2546. doi:10.1002/pmic.201200070

Powis, G., and Kirkpatrick, L. (2004). Hypoxia Inducible Factor-1alpha as a Cancer Drug Target. *Mol. Cancer Ther.* 3, 647–654.

Randrup Hansen, C., Grimm, D., Bauer, J., Wehland, M., and Magnusson, N. (2017). Effects and Side Effects of Using Sorafenib and Sunitinib in the Treatment of Metastatic Renal Cell Carcinoma. *Ijms* 18, 461. doi:10.3390/ijms18020461

Ranieri, D., Cucina, A., Bizzarri, M., Alimandi, M., and Torrisi, M. R. (2015). Microgravity Influences Circadian Clock Oscillation in Human Keratinocytes. *FEBS Open Bio* 5, 717–723. doi:10.1016/j.fob.2015.08.012

Riwaldt, S., Bauer, J., Wehland, M., Slumstrup, L., Kopp, S., Warnke, E., et al. (2016). Pathways Regulating Spheroid Formation of Human Follicular Thyroid Cancer Cells under Simulated Microgravity Conditions: A Genetic Approach. *Ijms* 17, 528. doi:10.3390/ijms17040528

Sarkar, C., Goswami, S., Basu, S., and Chakroborty, D. (2020). Angiogenesis Inhibition in Prostate Cancer: An Update. *Cancers* 12, 2382. doi:10.3390/cancers12092382

Saryeddine, L., Zibara, K., Kassem, N., Badran, B., and El-Zein, N. (2016). EGF-induced VEGF Exerts a PI3K-dependent Positive Feedback on ERK and AKT through VEGFR2 in Hematological *In Vitro* Models. *PLoS One* 11, e0165876. doi:10.1371/journal.pone.0165876

Semenza, G. L. (2003). Targeting HIF-1 for Cancer Therapy. *Nat. Rev. Cancer* 3, 721–732. doi:10.1038/nrc1187

Shijubo, N., Uede, T., Kon, S., Nagata, M., and Abe, S. (2000). Vascular Endothelial Growth Factor and Osteopontin in Tumor Biology. *Crit. Rev. Oncog* 11, 135–146.

Shorning, B. Y., Dass, M. S., Smalley, M. J., and Pearson, H. B. (2020). The PI3K-AKT-mTOR Pathway and Prostate Cancer: At the Crossroads of AR, MAPK, and WNT Signaling. *Ijms* 21, 4507. doi:10.3390/ijms21124507

Singh, R. K., and Lokeshwar, B. L. (2009). Depletion of Intrinsic Expression of Interleukin-8 in Prostate Cancer Cells Causes Cell Cycle Arrest, Spontaneous Apoptosis and Increases the Efficacy of Chemotherapeutic Drugs. *Mol. Cancer* 8, 57. doi:10.1186/1476-4598-8-57

Strube, F., Infanger, M., Wehland, M., Delvinioti, X., Romswinkel, A., Dietz, C., et al. (2020). Alteration of Cytoskeleton Morphology and Gene Expression in Human Breast Cancer Cells under Simulated Microgravity. *Cell J* 22, 106–114. doi:10.22074/cellj.2020.6537

Sun, Y., Zhao, C., Ye, Y., Wang, Z., He, Y., Li, Y., et al. (2020). High Expression of Fibronectin 1 Indicates Poor Prognosis in Gastric Cancer. *Oncol. Lett.* 19, 93–102. doi:10.3892/ol.2019.11088

Sung, H., Ferlay, J., Soerjomataram, I., Siegel, R. L., Laversanne, M., Soerjomataram, I., Jemal, A., et al. (2021). Global Cancer Statistics 2018: GLOBOCAN Estimates of Incidence and Mortality Worldwide for 36 Cancers in 185 Countries. *CA: A Cancer J. Clinicians* 71, 209–249. doi:10.3322/caac.21660

Svejgaard, B., Wehland, M., Ma, X., Kopp, S., Sahana, J., Warnke, E., et al. (2015). Common Effects on Cancer Cells Exerted by a Random Positioning Machine and a 2D Clinostat. *PLoS One* 10, e0135157. doi:10.1371/journal.pone.0135157

Tee, S. S., Suster, I., Truong, S., Jeong, S., Eskandari, R., Digialleonardo, V., et al. (2018). Targeted AKT Inhibition in Prostate Cancer Cells and Spheroids Reduces Aerobic Glycolysis and Generation of Hyperpolarized [1-13C] Lactate. *Mol. Cancer Res.* 16, 453–460. doi:10.1158/1541-7786.MCR-17-0458

Timmins, N., Dietmair, S., and Nielsen, L. (2004). Hanging-drop Multicellular Spheroids as a Model of Tumour Angiogenesis. *Angiogenesis* 7, 97–103. doi:10.1007/s10456-004-8911-7

Twombly, R. (2003). Prostate Modeling experiment success Becomes Part of Legacy of Shuttle Astronauts. *JNCI J. Natl. Cancer Inst.* 95, 505–507. doi:10.1093/jnci/95.7.505

Vorselen, D., Roos, W. H., Mackintosh, F. C., Wuite, G. J. L., and Loon, J. J. W. A. (2014). The Role of the Cytoskeleton in Sensing Changes in Gravity by Nonspecialized Cells. *FASEB j.* 28, 536–547. doi:10.1096/fj.13-236356

Wang, Y., Huang, L., Wu, S., Jia, Y., Yang, Y., Luo, L., et al. (2015). Bioinformatics Analyses of the Role of Vascular Endothelial Growth Factor in Patients with Non-small Cell Lung Cancer. *PLoS One* 10, e0139285. doi:10.1371/journal.pone.0139285

Waugh, D. J. J., and Wilson, C. (2008). The Interleukin-8 Pathway in Cancer. *Clin. Cancer Res.* 14, 6735–6741. doi:10.1158/1078-0432.CCR-07-4843

Wehland, M., Bauer, J., Infanger, M., and Grimm, D. (2012). Target-based Anti-angiogenic Therapy in Breast Cancer. *Curr. Pharm. Des.* 18, 4244–4257. doi:10.2174/138161212802430468

Wehland, M., Steinwerth, P., Aleshcheva, G., Sahana, J., Hemmersbach, R., Lützenberg, R., et al. (2020). Tissue Engineering of Cartilage Using a Random Positioning Machine. *Ijms* 21, 9596. doi:10.3390/ijms21249596

Yang, J., Nie, J., Ma, X., Wei, Y., Peng, Y., and Wei, X. (2019). Targeting PI3K in Cancer: Mechanisms and Advances in Clinical Trials. *Mol. Cancer* 18, 26. doi:10.1186/s12943-019-0954-x

Zhau, H. E., Goodwin, T. J., Chang, S.-M., Baker, T. L., and Chung, L. W. K. (1997). Establishment of a Three-Dimensional Human Prostate Organoid Coculture under Microgravity-Simulated Conditions: Evaluation of Androgen-Induced Growth and PSA Expression. In Vitro *Cell.Dev.Biol.-Animal* 33, 375–380. doi:10.1007/s11626-997-0008-3

Zhivodernikov, I. V., Ratushnyy, A. Y., Matveeva, D. K., and Buravkova, L. B. (2020). Extracellular Matrix Proteins and Transcription of Matrix-Associated Genes in Mesenchymal Stromal Cells during Modeling of the Effects of Microgravity. *Bull. Exp. Biol. Med.* 170, 230–232. doi:10.1007/s10517-020-05040-z

Zhong, H., De Marzo, A. M., Laughner, E., Lim, M., Hilton, D. A., Zagzag, D., et al. (1999). Overexpression of Hypoxia-Inducible Factor 1alpha in Common Human Cancers and Their Metastases. *Cancer Res.* 59, 5830–5835.

Conflict of Interest: The authors declare that the research was conducted in the absence of any commercial or financial relationships that could be construed as a potential conflict of interest.

Publisher's Note: All claims expressed in this article are solely those of the authors and do not necessarily represent those of their affiliated organizations, or those of the publisher, the editors and the reviewers. Any product that may be evaluated in this article, or claim that may be made by its manufacturer, is not guaranteed or endorsed by the publisher.

Copyright © 2022 Dietrichs, Grimm, Sahana, Melnik, Corydon, Wehland, Krüger, Vermeesen, Baselet, Baatout, Hybel, Kahlert, Schulz, Infanger and Kopp. This is an open-access article distributed under the terms of the Creative Commons Attribution License (CC BY). The use, distribution or reproduction in other forums is permitted, provided the original author(s) and the copyright owner(s) are credited and that the original publication in this journal is cited, in accordance with accepted academic practice. No use, distribution or reproduction is permitted which does not comply with these terms.

GLOSSARY

μg Microgravity
2D Two-dimensional
3D Three-dimensional
ACTB Beta-actin
AD Adherent Monolayer
AKT1 RAC-alpha Serine/Threonine-protein kinase 1
CASP3 Caspase-3
CASP8 Caspase-8
CASP9 Caspase-9
COL1A1 Collagen-1a1
CXCL8/IL-8 Interleukin-8
ECM Extracellular matrix
EGF Epidermal Growth Factor
EGFR1 Epidermal Growth Factor Receptor 1
EZR Ezrin
FLT1 Tyrosine kinase 1
FN1 Fibronectin
HARV High aspect rotating-wall vessel
HIF1A Hypoxia inducible factor 1A
IL-17 Interleukin-17
IL-1A Interleukin-1 Alpha
IL1B Interleukin-1 Beta
IL-2 Interleukin-2
IL-6 Interleukin-6
IL-7 Interleukin-7
KDR Kinase Insert Domain Receptor
KRT8 Kreatin 8
LAMA3 Laminin Subunit Alpha 3
LNCaP Lymph Node Carcinoma of the Prostate
MCP-1 Monocyte Chemoattractant Protein 1
MCS Multicellular Spheroid(s)
MMP11 Matrix Metalloproteinase-11
MMP2 Matrix Metallopeptidase-2
MMP9 Matrix Metalloproteinase-9
MSN Moesin
MTOR Mechanistic Target of Rapamycin kinase
NFKB Nuclear Factor kappa B
NRP1 Neuroplin-1
OPN/SPPI Osteopontin/Secreted Phosphoprotein 1
PAI-1 Plasminogen Activator Inhibitor-1
PCC Prostate Cancer Cells
PCNA Proliferating Cell Nuclear Antigen
PFA Paraformaldehyde
PIK3CB Phosphatidylinositol-4,5-bisphosphate 3-kinase Catalytic Subunit Beta
r-μg Real Microgravity
RDX Radixin
RPM Random Positioning Machine
RWV Rotating Wall Vessel
s-μg Simulated Microgravity
TGFB1 Transforming Growth Factor Beta 1
TIMP1 Tissue Inhibitor of Metalloproteinases/metallopeptidase Inhibitor 1
TIMP3 TIMP metallopeptidase Inhibitor 3
TNF-a Tumor Necrosis Factor Alpha
TUBB Tubulin Beta
VEGFA Vascular Endothelial Growth Factor A

International Journal of
Molecular Sciences

MDPI

Article

Changes in Human Foetal Osteoblasts Exposed to the Random Positioning Machine and Bone Construct Tissue Engineering

Vivek Mann [1], Daniela Grimm [2,3], Thomas J Corydon [2,4], Marcus Krüger [3], Markus Wehland [3], Stefan Riwaldt [2,3], Jayashree Sahana [2], Sascha Kopp [3], Johann Bauer [5], Janne E. Reseland [6], Manfred Infanger [3], Aina Mari Lian [6], Elvis Okoro [1] and Alamelu Sundaresan [1,*]

1 Osteoimmunology and Integrative Physiology Laboratory, Department of Biology, Texas Southern University, Cleburne, Houston, TX 77004, USA; vivekmann7@gmail.com (V.M.); okoro_elvis@yahoo.com (E.O.)
2 Department for Biomedicine, Aarhus University, Wilhelm Meyers Allé 4, DK-8000 Aarhus C, Denmark; dgg@biomed.au.dk (D.G.); corydon@biomed.au.dk (T.J.C.); stefan.riwaldt@med.ovgu.de (S.R.); jaysaha@biomed.au.dk (J.S.)
3 Clinic for Plastic, Aesthetic and Hand Surgery, Otto von Guericke University Magdeburg, Leipziger Str. 44, 39120 Magdeburg, Germany; marcus.krueger@med.ovgu.de (M.K.); markus.wehland@med.ovgu.de (M.W.); sascha.kopp@med.ovgu.de (S.K.); manfred.infanger@med.ovgu.de (M.I.)
4 Department of Ophthalmology, Aarhus University Hospital, Palle Juul-Jensens Boulevard 99, DK-8200 Aarhus N, Denmark
5 Max Planck Institute of Biochemistry, Martinsried, Am Klopferspitz 18, 82152 Planegg, Germany; jbauer@biochem.mpg.de
6 Clinical Oral Research Laboratory, Institute of Clinical Dentistry, UiO, University of Oslo, Geitmyrsveien 71 0455 Oslo, Norway; j.e.reseland@odont.uio.no (J.E.R.); a.m.lian@odont.uio.no (A.M.L.)
* Correspondence: alamelu.sundaresan@tsu.edu; Tel.: +1-713-313-7926; Fax: +1-713-313-7032

Received: 14 February 2019; Accepted: 13 March 2019; Published: 18 March 2019



Abstract: Human cells, when exposed to both real and simulated microgravity (s-μ*g*), form 3D tissue constructs mirroring in vivo architectures (e.g., cartilage, intima constructs, cancer spheroids and others). In this study, we exposed human foetal osteoblast (hFOB 1.19) cells to a Random Positioning Machine (RPM) for 7 days and 14 days, with the purpose of investigating the effects of s-μ*g* on biological processes and to engineer 3D bone constructs. RPM exposure of the hFOB 1.19 cells induces alterations in the cytoskeleton, cell adhesion, extra cellular matrix (ECM) and the 3D multicellular spheroid (MCS) formation. In addition, after 7 days, it influences the morphological appearance of these cells, as it forces adherent cells to detach from the surface and assemble into 3D structures. The RPM-exposed hFOB 1.19 cells exhibited a differential gene expression of the following genes: transforming growth factor beta 1 (*TGFB1*, bone morphogenic protein 2 (*BMP2*), SRY-Box 9 (*SOX9*), actin beta (*ACTB*), beta tubulin (*TUBB*), vimentin (*VIM*), laminin subunit alpha 1 (*LAMA1*), collagen type 1 alpha 1 (*COL1A1*), phosphoprotein 1 (*SPP1*) and fibronectin 1 (*FN1*). RPM exposure also induced a significantly altered release of the cytokines and bone biomarkers sclerostin (SOST), osteocalcin (OC), osteoprotegerin (OPG), osteopontin (OPN), interleukin 1 beta (IL-1β) and tumour necrosis factor 1 alpha (TNF-1α). After the two-week RPM exposure, the spheroids presented a bone-specific morphology. In conclusion, culturing cells in s-μ*g* under gravitational unloading represents a novel technology for tissue-engineering of bone constructs and it can be used for investigating the mechanisms behind spaceflight-related bone loss as well as bone diseases such as osteonecrosis or bone injuries.

Keywords: osteoblasts; bone; tissue engineering; simulated microgravity; biomarker; cytoskeleton

1. Introduction

Real microgravity in space can affect the health of astronauts after an extended period of time on the international space station (ISS) or other future platforms allowing a sojourn in orbit [1]. Therefore, space life-science research has been initiated, with hopes to enable humans to undertake long-term space explorations. Studies of terrestrial organisms exposed to real (r-μ*g*) or simulated microgravity (s-μ*g*) face multiple challenges, as even experiments with cells under r-μ*g* conditions are rather rare and expensive. For this reason, researchers have developed simulation devices, such as the 2D clinostat (CN), the NASA-developed rotating wall vessel (RWV) bioreactor, the random positioning machine (RPM) and the magnetic levitator, among others, to prepare for spaceflights and to conduct ground-based space research on stem cells and specialized cells [1–3]. RPMs are like clinostats or rotating wall vessel bioreactors, ground-based facilities constructed to simulate microgravity on the Earth's surface (1 *g*). Their working principle is based on a gravity vector averaging to zero over time [4]. The cell samples are placed on the inner frame, where they are constantly reoriented; meanwhile, 1 *g* is always acting on the samples. The gravity vector needs to point in a specific direction for a short time period only, without acceleration of cell sedimentation. As the gravity vector averages to zero, the cells experience a state similar to microgravity. Mesland [5] proposed that the frame rotations should be faster than the investigated biological processes. Moreover, the rotation cannot be too fast, as centrifugal forces will become effective [6]. It is known that the use of an RPM induces additional forces on the cells, through the special moving pattern. It is important to mention that, when the RPM is operated within certain boundaries, these forces can be attenuated to a minimum [7]. The RPM is used worldwide for tissue-engineering purposes for various cell types and is an accepted model in preparing for future spaceflight missions [1,8].

In vitro studies on different types of human renal cortical cells or mouse MC3T3 osteoblasts in space or on microgravity simulating devices, have demonstrated significant changes in gene expression patterns [9,10], increased apoptosis (ML1 follicular thyroid cancer cells, glial cells, MDA-MB231 breast cancer cells and human lymphocytes (Jurkat)) [11–14] and induction of autophagy (human umbilical vein endothelial cells, HEK293 cells) [15,16], as well as changes in differentiation (FTC-133 follicular thyroid cancer cells) [17], migration, cell adhesion, extracellular matrix composition (ML1 cells) [11] and alterations in the cytoskeleton (FTC-133 cells, A431 epidermoid carcinoma cells) [18,19].

Magnetic levitation of mouse calvarial MC3T3 osteoblast cells was used as a ground-based simulation of microgravity [10]. The cells were grown on cytodex-3 beads and cultured in a superconducting magnet for 2 days, which resulted in marked alterations in gene expression. Gravitational stress leads to up- and down-regulation of hundreds of genes [10]. Random rotation and magnetic levitation induced similar changes in the actin cytoskeleton of A431 cells, which were also described in r-μ*g* [19].

Interestingly, it was found that tissue cells switch, in space, from a two-dimensional (2D) monolayer growth to a three-dimensional (3D) growth, into a tissue-like construct [20]. Tissue engineering in space and the application of microgravity simulation techniques is a new topic in translational regenerative medicine. Knowledge of the mechanisms of 3D growth in human cells is very important for advancing the processes of tissue engineering. Various cells exposed to the special environment of r-μ*g* and s-μ*g* conditions have already been characterized. Some examples of growing tissues from specialized cells in microgravity are: Multicellular tumour spheroids from various tumour types (MDA-MB231 and MCF-7 breast cancer cells, as well as FTC-133, ML1 and RO82-W-1 follicular thyroid cancer cells) [13,21–25], artificial vessel constructs (EA.hy926 endothelial cells) [26,27], regenerated cartilage (primary human chondrocytes) [28,29] or bone tissues (human pre-osteoblastic cells, human mesenchymal pre-osteoblastic cells) [30,31].

Tissue engineering of bone tissue is of high importance in regenerative medicine. The incidence of bone disorders worldwide is continuously increasing, due to aging populations combined with obesity and reduced physical activity [32]. The loss of skeletal tissue can accompany trauma, injury and disease. Treatment strategies include the use of stem cells, specialized cells, novel scaffolds and growth factors to improve the bone formation process [1]. Tissue-engineered bone fragments from

new-born rat calvarial cells might serve as a potential alternative to the conventional use of bone grafts, as pioneered by Su et al. [33] and Hidaka et al. [34] in animal models.

By the application of s-μ*g* methods, several preliminary studies suggested the use of osteoblast precursor or stem cells to be most suitable for the engineering of bone fragments [35]. Pre-osteoblasts, from HEPM-1460 cells, cultured in an RWV could be engineered into osseous-like tissue [30,31]. Clarke et al. designed a new method for engineering bone constructs by culturing primary osteoblasts and osteoclast precursors on a special bioreactor. This high-aspect ratio vessel (HARV) culture system provided randomized gravity vector conditions and a low-shear stress environment [36].

This study aims to tissue-engineer bone constructs by exposing the fast-growing foetal human osteoblasts of the hFOB 1.19 cell line—a well-characterized, stable osteoprogenitor and a widely used model for normal osteoblast differentiation [37,38]—to the RPM. Using this new method, we intend to increase our knowledge about the biology of foetal osteoblasts and to understand the effects of RPM-exposure on hFOB 1.19 cells, as indicated by differentially expressed genes and changes in protein secretion, as compared to the static 1 *g* conditions. The next step is to develop ideal bone grafts for future applications in translational studies and, subsequently, in clinical applications.

2. Results

2.1. Morphological Examination of RPM-Exposed hFOB 1.19 Cells Reveal Signs of Organoid Formation

We detected two distinct growth patterns of hFOB 1.19 cells, exposed to simulated microgravity on an RPM for 7 days and 14 days, respectively. Human foetal osteoblasts grow in adherent monolayers (AD) during exposure to static 1 *g* conditions (for 7 days and 14 days) as shown by standard phase-contrast imaging (see Figure 1A,B). In contrast, two different hFOB 1.19 populations are distinguishable in s-μ*g*. Within the same culture flask, one group of the cells developed in the form of an adherent monolayer and the other group formed several 3D bone constructs or multicellular spheroids (MCS). These cells had detached from the monolayer and assembled into bone-like cell aggregates (see Figure 1C,D). The MCS presented an increase in size and number after 14 days of RPM exposure (see Figure 1D), as compared to 7 days RPM samples (see Figure 1C). While the bone-like constructs were observed in sizes up to 0.5 mm in length and 0.4 mm in width after 14 days, the biggest MCS was 0.2 mm in diameter after 7 days (see Figure 1F). Furthermore, using phase contrast microscopy (at magnification ×100), three times more MCS per field of view were seen on day 14, as compared to day 7 (the numbers in the inserts in Figure 1E–G). The MCS were either distributed anchorage-independently throughout the cultivation medium or found to be partially attached to the adherent monolayer. There were no MCS detectable at 7 days (Figure 1A) and 14 days (Figure 1B) in the 1 *g* control samples.

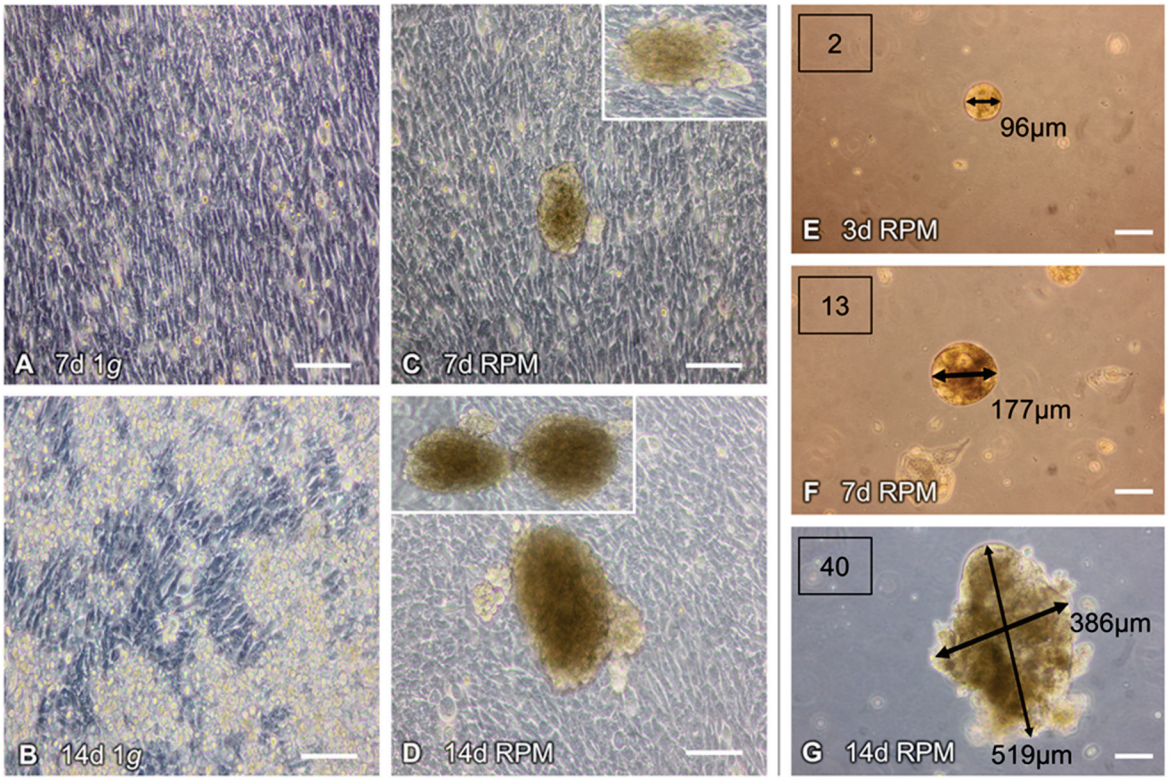


Figure 1. Random Positioning Machine (RPM)-induced formation of 3D multicellular spheroids (MCS) of human foetal osteoblasts (hFOB 1.19): Under static 1 *g* conditions, the cells grew adherently and remained in confluent monolayer cultures, when incubated for (**A**) 7 days and (**B**) 14 days. (**C**,**D**) Exposed to an RPM, the cells assembled into 3D aggregates, with the MCS increasing, over time, in size and number. (**E**) Microscopic analyses showed 2 MCS in the field of view, with an average diameter of 96 µm, after 3 days. After 7 days (**F**) and 14 days (**G**) cultivation on the RPM, the numbers of the spheroids increased from 13 to 40 MCS per field of view. The spheroids were 386 × 519 µm tall, after 14 days. The white squares in (**C**) and (**D**) show other examples of MCS. Scale bars: 100 µm; d, days.

Haematoxylin–Eosin (HE)- and Sirius red-staining show the differences between the 7 days (Figure 2A,C) and 14 days RPM samples (Figure 2B,D). HE-stained MCS cross-sections are displayed at 20× (Figure 2A,B) and 10× (inserts) magnification. Numerous osteoblasts were visible in the constructs; they had produced an extracellular matrix. After 14 days, some resorption zones were detectable, where the organic matrix had broken down (Figure 2B).

Sirius red staining of the 14 days RPM samples (Figure 2D) revealed an increased deposition of collagen fibres, in contrast to the 7 days RPM samples (Figure 2C). Collagen is the most abundant organic molecule in the extracellular matrix of bone tissue [39]. Von Kossa and Alcian blue stains strongly suggested calcium deposits in the 14 days cultures (Figure 2F,H) but not after day 7 (Figure 2E,G). These stains indicate mineralization and differentiation of the cells after 14 days.

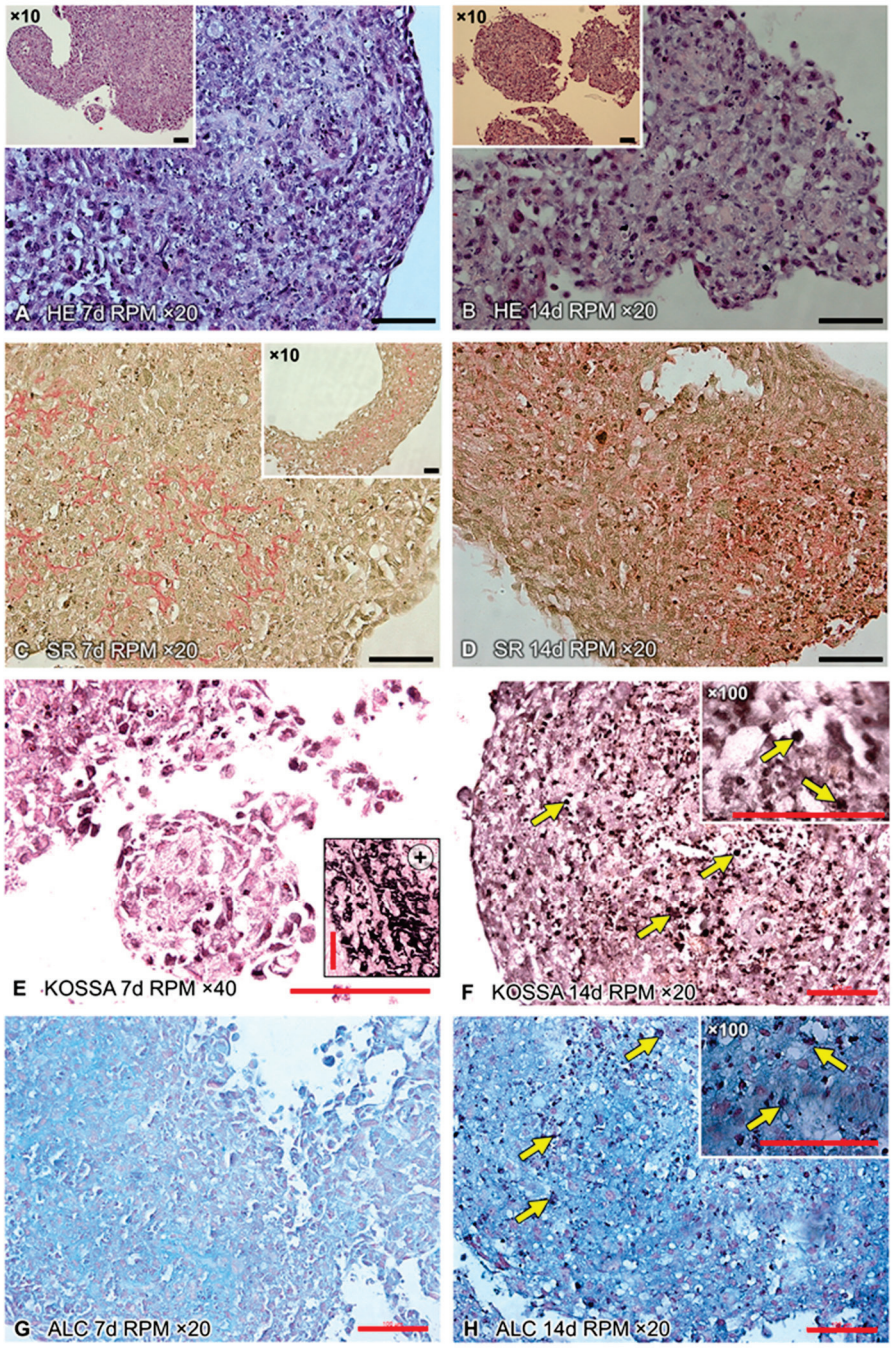


Figure 2. Histological assessment of paraffin-embedded cross-sections. The hFOB 1.19 cells were cultured for 7 days and 14 days on the RPM. 3D constructs were collected and, subsequently, paraffin-embedded. (**A**,**B**) HE staining shows the substantial aggregation of cells after 7 days and 14 days. (**C**,**D**) Sirius red-stained samples reveal a substantial collagen deposition. A clear increase is visible after 14 days, compared to 7 days. The black arrows indicate collagen deposition (red). Two stains were used to analyse biological mineralization within the MCS. (**E**,**F**) The von Kossa stain (KOSSA) is widely used for the detection of calcinosis in tissues. The small picture in (**E**) shows a positive control. (**G**,**H**) The Alcian blue (ALC) dye labels anionic tissue components, such as hyaluronate or chondroitin sulphate. The yellow arrows in (**F**) and (**H**) indicate regions of early calcification after 14 days. Scale bars: 100 µm, d, days.

2.2. Alterations of the Cytoskeleton and the Extracellular Matrix

Changes in cell morphology depend on foregoing alterations in cytological architecture. Cytoskeletal changes are broadly acknowledged as the cause of bone loss in microgravity [40] and for organoid formation in bone tissue engineering [41].

Immunofluorescence was performed to elucidate the cytoskeletal changes of β-tubulin. F-actin was visualized by means of rhodamine-phalloidin staining. Well-organized F-actin filaments were observed under static 1 *g* conditions, for 7 days and 14 days of cultivation (Figure 3A,C). Following RPM exposure, a decrease in F-actin filaments was observed (Figure 3B,D). A shift in the microfilament distribution towards F-actin accumulation at the cell boundaries was clearly noticeable in both the 7 days and 14 days RPM samples. The 3D aggregates contained outer cell membranes with F-actin deposits (Figure 3B,D). MCS formation was visible. Filopodia and lamellipodia were detectable in the RPM-exposed samples. *ACTB* mRNA expression was significantly elevated in both 7 days RPM samples and further enhanced in the 14 days MCS samples (Figure 3I, Table 1).

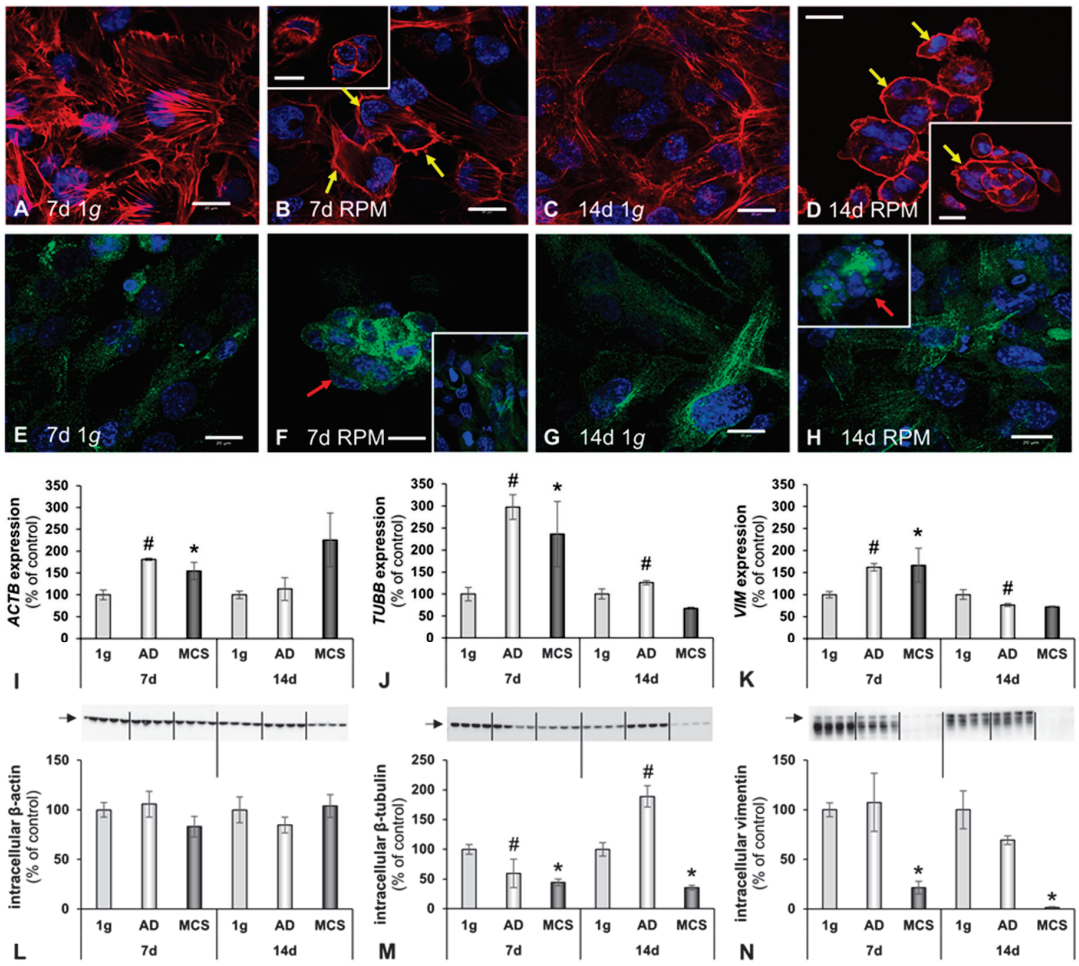


Figure 3. Influence of simulated microgravity on the cytoskeleton of human osteoblasts. Phalloidin–rhodamine staining visualized the F-actin distribution in the 1 *g* control cells (**A**,**C**) and RPM-exposed cells (**B**,**D**). The yellow arrows indicate filopodia and lamellipodia, as well as the accumulation of F-actin at the outer cellular membranes. (**E**–**H**) Tubulin immunofluorescence: Red arrows indicate holes in the tubulin network in spheroids. Gene expression of selected cytoskeletal genes: (**I**) β-actin (*ACTB*), (**J**) β-tubulin (*TUBB*) and (**K**) vimentin (*VIM*). Intracellular protein levels. (**L**) β-actin, (**M**) β-tubulin and (**N**) vimentin. All values are given as mean ± standard deviation. # $p < 0.05$ 1 *g* vs. AD; * $p < 0.05$ 1 *g* vs. MCS. Scale bars: 20 µm, d, days.

Table 1. Changes in gene expression, protein levels and secretion behaviour.

mRNA Levels [% of 1 *g* Control]												
		Gene										
Sample		***ACTB***	***BMP2***	***COL1A1***	***FN1***	***SPP1***	***LAMA1***	***MKI67***	***SOX9***	***TGFB1***	***TUBB***	***VIM***
7 days	**1 *g***	100.0 ± 11.0	100.0 ± 6.7	100.0 ± 24.3	100.0 ± 10.8	100.0 ± 14.8	100.0 ± 3.6	100.0 ± 20.6	100.0 ± 20.8	100.0 ± 12.1	100.0 ± 15.1	100.0 ± 7.2
	AD	**▲181.2 ± 2.9**	**▼45.6 ± 9.7**	124.0 ± 6.0	**▲127.8 ± 6.2**	**▲1094.0 ± 89.0**	**▲197.3 ± 18.4**	111.4 ± 10.3	**▲160.1 ± 10.1**	123.2 ± 3.5	**▲297.4 ± 27.8**	**▲162.3 ± 8.5**
	MCS	**▲154.7 ± 19.7**	**▲207.2 ± 69.9**	112.6 ± 41.7	218.5 ± 73.9	**▲1719.2 ± 709.5**	**▲244.4 ± 67.0**	89.0 ± 35.9	140.1 ± 51.6	147.1 ± 32.3	**▲236.2 ± 74.5**	**▲166.7 ± 38.5**
14 days	**1 *g***	100.0 ± 8.6	100.0 ± 32.1	100.0 ± 8.6	100.0 ± 3.6	100.0 ± 3.4	100.0 ± 11.5	100.0 ± 9.6	100.0 ± 8.1	100.0 ± 3.8	100.0 ± 11.3	100.0 ± 11.1
	AD	113.1 ± 25.8	**▼28.8 ± 6.5**	**▲234.0 ± 5.3**	**▲119.8 ± 2.7**	**▲813.4 ± 22.2**	127.9 ± 8.1	132.1 ± 9.5	**▲151.2 ± 5.9**	**▲133.8 ± 4.0**	**▲125.7 ± 4.8**	**▼76.1 ± 3.5**
	MCS	225.2 ± 61.7	100.1 ± 43.8	225.7 ± 11.4	107.7 ± 7.0	1098.2 ± 11.3	148.9 ± 17.6	109.7 ± 5.8	108.0 ± 4.3	87.7 ± 0.7	67.3 ± 2.7	72.1 ± 1.7
Intracellular Protein Levels [% of 1 *g* Control]												
		Protein										
Sample		**β-actin**	**BMP2**	**Col 1**	**FN**	**OPN**	**laminin**	**Ki-67**	**SOX9**	**TGF-β1**	**β-tubulin**	**vimentin**
7 days	**1 *g***	100.0 ± 7.5	100.0 ± 13.6	100.0 ± 10.4	100.0 ± 18.8	100.0 ± 16.6	100.0 ± 13.2	100.0 ± 14.8	100.0 ± 27.3	100.0 ± 20.1	100.0 ± 8.2	100.0 ± 6.9
	AD	105.8 ± 12.9	86.5 ± 5.4	91.4 ± 5.2	139.2 ± 19.2	**▲154.4 ± 13.2**	110.7 ± 11.1	107.8 ± 9.1	75.3 ± 17.0	**▲312.1 ± 41.4**	**▼59.7 ± 23.9**	107.4 ± 29.3
	MCS	83.2 ± 10.4	**▼55.7 ± 3.2**	**▼68.8 ± 1.1**	**▲186.9 ± 19.1**	**▼19.4 ± 7.5**	**▼72.1 ± 7.7**	**▼67.5 ± 6.5**	80.9 ± 3.7	**▲345.9 ± 30.4**	**▼44.3 ± 5.6**	**▼21.5 ± 6.3**
14 days	**1 *g***	100.0 ± 13.1	100.0 ± 8.8	100.0 ± 9.8	100.0 ± 13.2	100.0 ± 24.6	100.0 ± 7.6	100.0 ± 7.5	100.0 ± 9.6	100.0 ± 27.3	100.0 ± 11.3	100.0 ± 19.2
	AD	84.8 ± 8.0	**▲196.9 ± 13.6**	**▲148.1 ± 11.1**	**▲146.9 ± 18.0**	**▲2852.2 ± 964.4**	83.5 ± 7.6	**▼75.3 ± 12.0**	79.6 ± 10.8	**▼15.5 ± 2.4**	**▲188.8 ± 18.0**	69.3 ± 4.3
	MCS	103.9 ± 11.7	**▼16.9 ± 1.0**	**▼25.5 ± 2.1**	**91.0 ± 34.3**	**▼14.8 ± 17.3**	**▲266.4 ± 44.4**	**▲300.8 ± 15.9**	**▲125.4 ± 12.8**	39.8 ± 26.0	**▼35.7 ± 3.8**	**▼1.6 ± 0.8**

Table 1. *Cont.*

Protein Secretion [% of 1 *g* Control]								
		Protein						
Sample		**DKK1**	**IL-1β**	**OC**	**OPG**	**OPN**	**SOST**	**TNF-α**
7 days	**1 *g***	100.0 ± 1.4	100.0 ± 13.0	100.0 ± 32.6	100.0 ± 15.3	100.0 ± 14.7	100.0 ± 7.8	100.0 ± 8.7
	RPM	98.8 ± 2.5	**▼34.8 ± 5.7**	112.0 ± 47.8	**▼42.6 ± 19.0**	**▲206.7 ± 38.1**	**▼49.4 ± 16.9**	**▼46.2 ± 12.2**
14 days	**1 *g***	100.0 ± 6.6	100.0 ± 11.2	100.0 ± 24.9	100.0 ± 26.2	100.0 ± 14.8	100.0 ± 32.6	100.0 ± 7.5
	RPM	102.1 ± 6.0	125.6 ± 13.5	**▲148.9 ± 28.0**	**▲154.1 ± 22.5**	**▲579.2 ± 20.8**	74.4 ± 21.4	96.0 ± 11.0

▲ significant increase/up-regulation ($p < 0.05$); ▼ significant decrease/down-regulation ($p < 0.05$).

In accordance with F-actin, the tubulin distribution was well-organized, as expected, in the 1 *g* samples (Figure 3E). In the 7 days RPM samples, an elevated amount of tubulin protein was found in the 3D aggregates and a more intense fluorescence in the RPM-AD samples (Figure 3F).

In addition, the tubulin microtubule expression was similar in the 1 *g* controls (Figure 3G). The 14 days MCS revealed holes in the tubulin cytoskeleton of the MCS samples (Figure 3H). The *TUBB* mRNA levels were significantly increased in both 7 days RPM samples; whereas, after 14 days, *TUBB* remained significantly elevated in the RPM-AD samples (Figure 3J, Table 1). Moreover, we determined the *VIM* mRNA expression by qRT-PCR (Figure 3K), which mirrored the *TUBB* gene expression. A significant elevation of *VIM* mRNA was measured in all 7 days RPM samples; whereas, after 14 days, *VIM* was up-regulated in RPM-AD samples (Figure 3K, Table 1). Similar data were obtained by Western blot analyses of the corresponding proteins (Figure 3L–N; Table 1).

The cell adhesion and extracellular matrix protein laminin connects the cytoskeletal filaments, through transmembrane integrin receptors, with the extracellular matrix [42]. As expected, the majority of the anti-laminin positive ECM material was detectable in the cellular membranes of the hFOB 1.19 cells (Figure 4A–D). A moderate increase in laminin deposition was noticeable after 7 days RPM exposure (Figure 4B). The qRT-PCR data for *LAMA1* revealed a significant increase in both 7 days RPM samples. After 14 days, *LAMA1* gene expression did not significantly change, in comparison to the 7 days RPM samples (Figure 4E, Table 1).

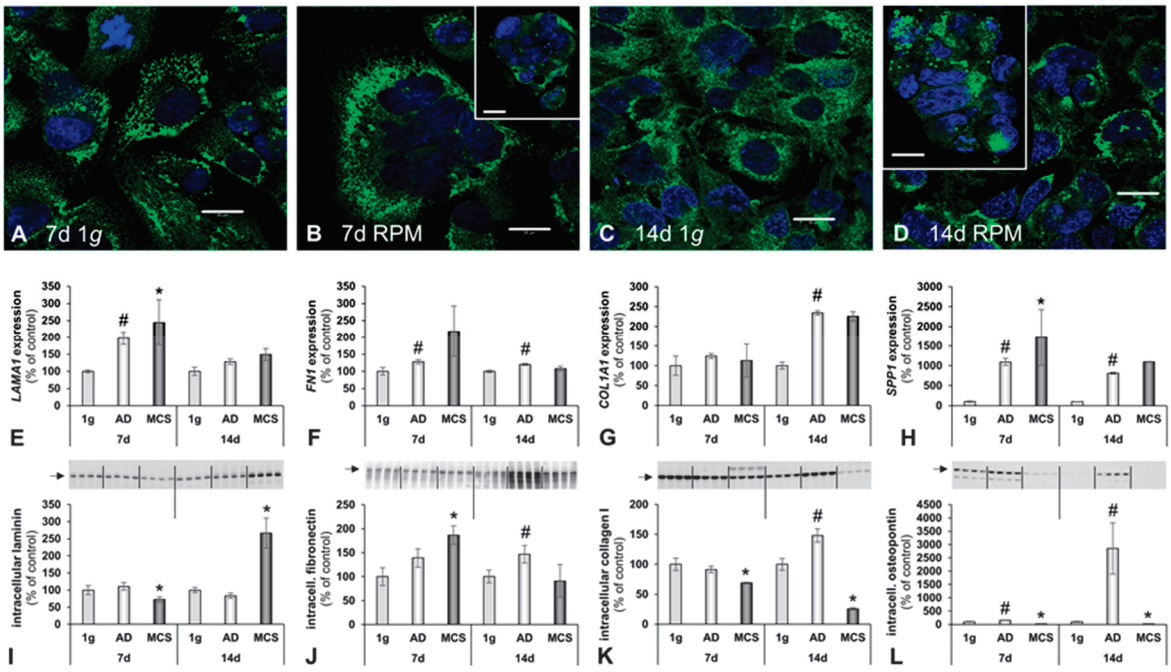


Figure 4. The influence of simulated microgravity on the extracellular matrix (ECM) of human osteoblasts. Laminin immunofluorescence. (**A**) 7 days 1 *g* control cells, (**B**) 7 days RPM exposed cells, (**C**) 14 days 1 g control cells and (**D**) 14 days RPM exposed cells. Gene expression of selected ECM genes: (**E**) Laminin α1 (*LAMA1*); (**F**) fibronectin (*FN1*); (**G**) collagen I subunit α1 (*COL1A1*); and (**H**) osteopontin (*SPP1*). Intracellular ECM protein levels: (**I**) Laminin; (**J**) fibronectin; (**K**) collagen type I; and (**L**) osteopontin. All values are given as mean ± standard deviation. # $p < 0.05$ 1 g vs. AD; * $p < 0.05$ 1 *g* vs. MCS. Scale bars: 20 µm, d, days.

The modulating influence of fibronectin on osteoblast function is well described in the literature [43]. In this study, the *FN1* gene expression was significantly elevated in adherent RPM samples at 7 days and 14 days. No change was detectable in the MCS samples (Figure 4F, Table 1).

In accordance with the morphological data, *COLA1A* gene expression was up-regulated in cells exposed to the RPM for 14 days. After 7 days RPM exposure, no significant change was detectable, compared with the 1 *g* controls (Figure 4G, Table 1).

To investigate alterations in the ECM secretion of the hFOB 1.19 cells more deeply, we assessed the *SPP1* gene expression and the intracellular amount of protein, respectively (Figure 4H,L). The *SPP1* (i.e., the osteopontin coding gene) gene expression was significantly up-regulated in both the 7 days RPM samples and 14 days RPM samples, compared to corresponding 1 *g* controls. (Figure 4H, Table 1).

2.3. Changes in BMP2/TGF-β Signalling Pathways

TGF-β/BMP2 signalling has an effect on several different cellular processes. Their important functions for osteogenesis in mammals are widely accepted [44]. TGF-β_1 promotes bone matrix synthesis, as well as differentiation of osteoblast progenitors [44].

The *TGFB1* gene expression was not significantly changed but showed a tendency to increase after 7 days. It was significantly up-regulated in the 14 days RPM-AD samples (Figure 5A, Table 1). The TGF-β_1 protein was elevated in both AD and MCS after 7 days but not elevated in MCS after 14 days (Figure 5E, Table 1).

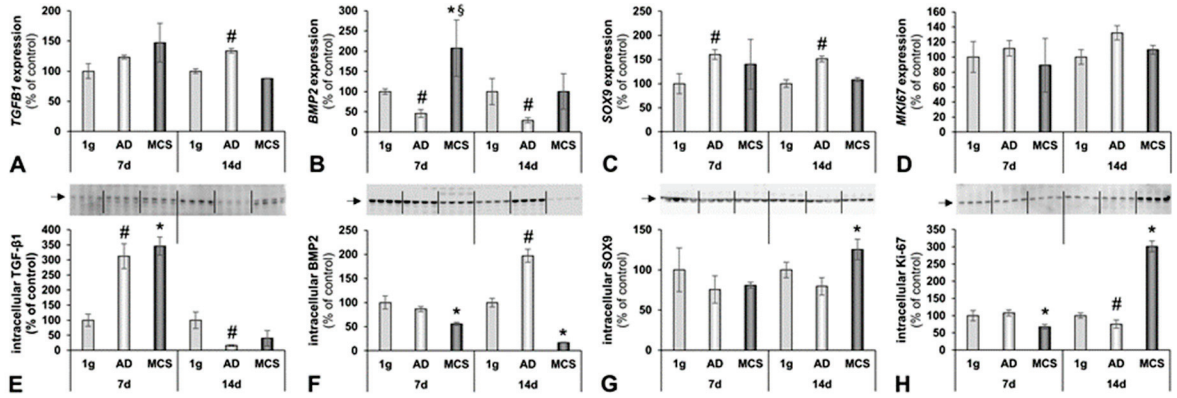


Figure 5. Bone-specific factors influenced by simulated microgravity. Gene expression of selected genes: (**A**) TGF-β_1 (*TGFB1*); (**B**) BMP2 (*BMP2*); (**C**) SOX9 (*SOX9*); and (**D**) Ki-67 (*MKI67*). Intracellular ECM protein levels: (**E**) TGF-β1; (**F**) BMP2; (**G**) SOX9; and (**H**) Ki-67. All values are given as mean ± standard deviation. # $p < 0.05$ 1 *g* vs. AD; * $p < 0.05$ 1 *g* vs. MCS; § AD vs. MCS, $p < 0.05$, d, days.

The *BMP2* expression was contrarily regulated. We detected a significantly decreased *BMP2* gene expression level in both the 7 days and 14 days RPM-AD samples, compared to the corresponding 1 *g* controls. The *BMP2* expression was clearly up-regulated in the 7 days MCS (Figure 5B, Table 1). The BMP2 protein levels showed a counter-regulatory behaviour (Figure 5F).

As published earlier, hFOB 1.19 cells are able to differentiate to a chondrogenic state [45]. *SOX9* is an acknowledged marker for proliferating chondrocytes and it is recognized as a crucial transcription factor for differentiation of precursor cells into chondrocytes [46]. Our studies revealed a significant increase in *SOX9* expression levels of RPM-exposed adherent foetal osteoblasts in both 7 days and 14 days-experiments (Figure 5C, Table 1). In addition, we measured the mRNA of the proliferation marker Ki-67 (*MKI67*) in all groups but did not detect an altered gene expression (Figure 5D, Table 1). However, the Ki-67 antigen varied and was three-fold higher expressed in the constructs, compared to the control cells, after 2 weeks of culturing on the RPM (Figure 5H, Table 1).

It is known that BMPs influence Wnt signalling in bone remodelling through Dkk1 and SOST [44]. A negatively regulated bone mass, through increased osteoclastogenesis caused by increased RANKL-signalling, due to reduced Wnt-signalling by increased Sost concentrations, has already been elucidated in an animal model [47].

2.4. Secretion of Soluble Factors in the Supernatant

Differentiation of osteoblast precursor cells to osteoblasts is inhibited by TNF-α [48]. Additionally, TNF-α acts as an inflammatory cytokine in several skeletal diseases [49]. In our study, the TNF-α secretion was reduced in 7 days RPM samples but remained stable after 14 days (Figure 6A, Table 1).

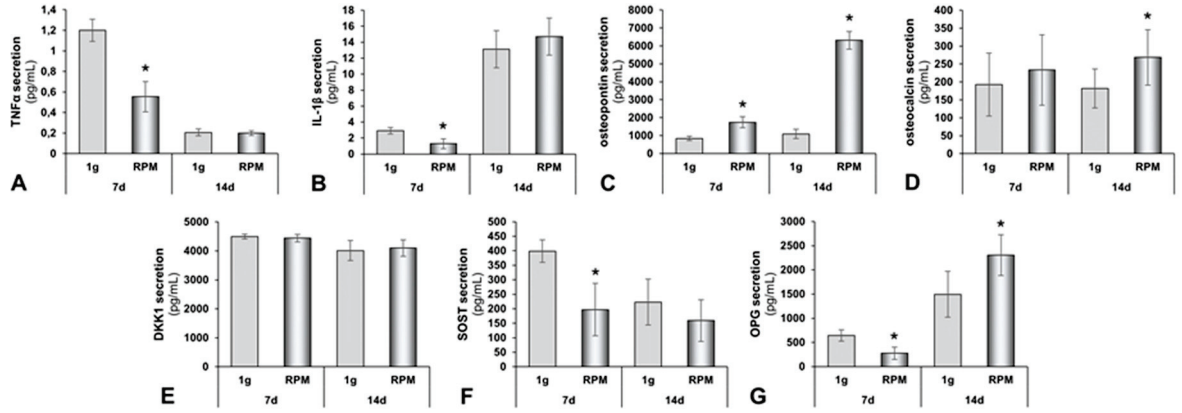


Figure 6. Protein secretion of human osteoblasts exposed to the RPM. (**A**) Tumour necrosis factor α (TNF-α); (**B**) interleukin-1β (IL-1β); (**C**) osteopontin; (**D**) osteocalcin; (**E**) dickkopf-1 (DKK1); (**F**) sclerostin (SOST); and (**G**) osteoprotegerin (OPG). All values are given as mean ± standard deviation. * $p < 0.05$ 1 *g* vs. RPM, d, days.

Besides TNF-α, IL-1β is known as a classical mediator of acute inflammation. In general, IL-1β is known to attenuate bone formation and reduce osteoblastogenesis [50]. IL-1β secretion was significantly decreased in the supernatant of osteoblasts exposed for 7 days to the RPM, compared to the 1 *g* controls. In contrast, a 14 days RPM exposure induced the release of IL-1β, as compared to the 14 days 1 *g* controls (Figure 6B, Table 1).

In addition, osteopontin secretion in the supernatants was significantly up-regulated in the supernatant of RPM samples after both 7 days and 14 days, compared to corresponding controls (Figure 6C, Table 1). Osteocalcin (OC), which, in particular, is synthesized by osteoblasts, maintains a central role in bio-mineralization [51]. OC concentrations of the secreted proteins were significantly elevated in the 14 days RPM samples, as compared with the corresponding control (Figure 6D, Table 1).

The release of Dkk1 remained unchanged in all study groups (Figure 6E, Table 1), whereas the SOST concentration was significantly reduced in the 7 days RPM samples (Figure 6F, Table 1); after 14 days, a lower amount of SOST was released by the osteoblasts in the supernatant. A 14 days RPM exposure did not change the release of SOST by the cells (Figure 6F, Table 1).

Osteoprotegerin (OPG) skews the balance between osteoclastogenesis and osteoblastogenesis towards increased bone formation by decreasing RANK activation. The RANKL decoy receptor, OPG, is a Wnt-pathway target gene. Wnt-activation leads to up-regulated OPG synthesis [52]. In the 7 days experiment, OPG secretion was significantly reduced by RPM exposure; whereas, after 14 days, a clear elevated OPG release in RPM-exposed cultures was detectable (Figure 6G, Table 1). The HBNMAG-51K (MILLIPLEX MAP) bone metabolism multiplex assay also investigated ACTH, IL-6, insulin, leptin, PTH and FGF-23. None of the six proteins were released in detectable amounts by the foetal osteoblasts.

2.5. Interactions of Proteins Involved in Bone Formation

We employed Pathway studio v11 to probe the linkage between the proteins detected experimentally, either in the supernatant (by Luminex technology) or within the cells (measured by Western blotting). Figure 7A represents the interaction analysis as a network of interacting proteins, such as the bone markers OPG (TNFRSF11B). In vivo OPG binds RANKL and blocks its interaction with RANK [53]. The binding may be inhibited by collagen 1α1 [54], while TNF-α enhances the

concentration of both proteins [55]. In addition, sclerostin (SOST) and the bone morphogenic protein 2 (BMP2) have an influence on the RANKL/OPG system. However, SOST inhibits vimentin and β-actin through DKK1 [56], while elevating the expression of *SOX9* [57]. Additional central points of the overall network are laminin α, fibronectin and TGF-β_1 [58]; as well as osteopontin, which interacts with vimentin [59] and fibronectin [60]. Figure 7B presents a mutual interaction of the expression of the genes, investigated by qRT-PCR and shown in Figure 3I–K, Figure 4E–H, Figure 5A–D and in Table 1.

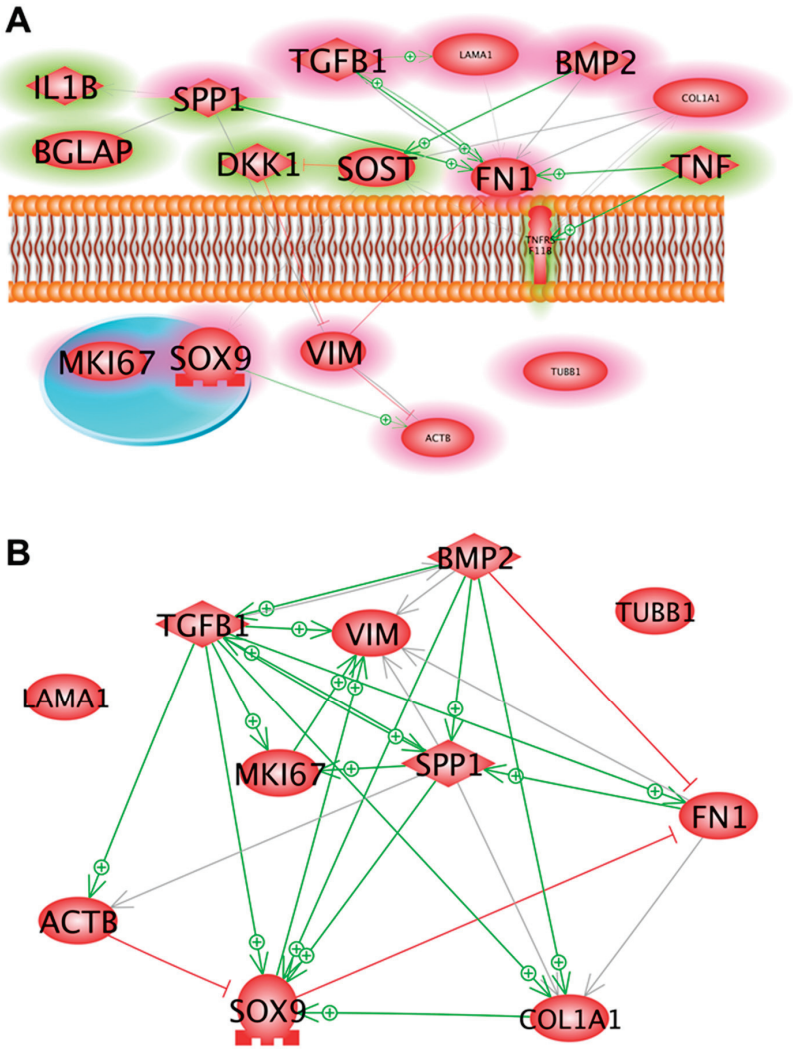


Figure 7. (**A**) Interaction and localization of proteins detected either in the supernatant by Luminex technology (green rims) or within the cells by Western blotting (red rims). Solid lines indicate binding, solid arrows show directed interaction and dashed arrows show influence. + signs point to an activity enhancing effect and red lines indicate inhibition. (**B**) Mutual interactions of the expression of the genes, investigated by qRT-PCR and shown in Figure 3I–K, Figure 4E–H, Figure 5A–D and in Table 1. + signs point to an activity-enhancing effect and red lines indicate inhibition. Each interaction network was built using Pathway Studio v.11.

3. Discussion

In the present study, we investigated human foetal osteoblasts (hFOB 1.19 cell line), either exposed to the RPM or cultivated under static 1 *g* conditions for 7 days and 14 days, respectively.

The objective of this study was to examine the potential of the osteoblast constructs as suitable biomaterial to support human osteogenesis, with potential application in bone tissue engineering. Manifold attempts to engineer tissue substitutes by exposing cells to simulated microgravity,

using different methods, such as the RPM, RWV, 2D-clinostat or magnetic levitation, have been made [1,24,27–32,61–63]. These techniques had been applied to culture multicellular cancer spheroids from thyroid cancer cells (FTC-133 [17,25], ML-1 [11,24] and RO82-W-1 [24] cells), breast cancer cells (MDA-MB-231 [13,61,63] or MCF7 [22,23,64]), cartilage tissue pieces (human chondrocytes [28,29], primary sheep chondrocytes [62]) and 3D aggregates from stem cells [1,61,63], endothelial cells [26,27,61] and others [61]. These new methods offer new applications in tissue engineering and 3D bioprinting, are important for drug targeting and discovery and show potential in the field of cancer research [1,20,35].

Practical applications need further improvement, however, which may be achieved by discovering possibilities for intervening the process, as we have shown for the cells of the MCF7 cell line [23,64]. Therefore, we investigated the underlying mechanisms involved in the development of the spheroids. We focused on cytoskeletal changes (F-actin microfilaments and tubulin microtubules), the ECM and the growth and multicellular spheroid formation of the hFOB 1.19 cells when subjected to the RPM or to 1 *g* conditions. In addition, we studied the expression of genes coding for proteins involved in cell structure, shape, migration, adhesion or angiogenesis and hence which might play a role in the cellular capacity to sense gravitational alterations and the development of MCS, demonstrated with FTC-133 follicular thyroid cancer cells or MCF-7 breast cancer cells [17,21,22].

Interestingly, we observed that a minor fraction of the hFOB 1.19 cells grew in the form of 3D constructs or MCS after 7 days RPM exposure.

Applying the experimental design, described in the material and methods section, which was based on recent experience with culturing the FTC-133 thyroid and MCF7 breast cancer cells, as well as endothelial cells under real and simulated microgravity [17,21,22,26,27], we repeatedly detected that hFOB 1.19 cells developed into two phenotypically different populations; one subpopulation remaining adherent to the bottom of the culture flask (the RPM-AD monolayer) and another subpopulation that formed MCS, freely floating in the cultivation medium. The number and size of the MCS increased after 14 days RPM exposure (Figure 1), suggesting that the reduced gravity conditions provided by the RPM promoted the development of MCS and 3D growth, even if no scaffold was present—as demonstrated earlier with the help of an RCC, using human embryonic palatal mesenchymal pre-osteoblasts [65]. The MCS contained numerous cells and ECM deposition was evident at both 7 days and 14 days, along the surface of the tissue-engineered construct. The construct (MCS) size and number changed with time, particularly between 7 days and 14 days (see Figure 1). Constructs appeared to be confluent with cells at 14 days, both at the periphery and centre of the construct. As demonstrated in Figure 2, an accumulation of ECM proteins was detectable with time, as well as calcification areas, which were visible after 14 days (as demonstrated by the von Kossa and Alcian blue stains).

F-actin staining revealed increases in F-actin at the cellular membranes of the MCS after 7 days and 14 days. Actin, tubulin and vimentin are key components of the cytoskeleton and have various functions [66,67]. They play an important role in the perception of exterior signals, including the gravitational force [66]. Notably, cytoskeletal alterations have been detected in cell lines derived from various cell types, such as lymphocytes, glial cells, endothelial cells, cancer cells and others [11,12,14,21–23,26,28]. Unfortunately, studies investigating the cytoskeleton in r-μ*g* and s-μ*g*, so far, are based on the analysis of fixed cells. Live cell imaging of FTC-133 cancer cells expressing the Lifeact-GFP marker protein for the visualization of F-actin under real microgravity during a TEXUS sounding rocket mission and a parabolic flight mission using a compact fluorescence microscope (FLUMIAS) confirmed the results obtained with fixed cells [18].

During the TEXUS rocket flight, well-structured filament bundles were found in FTC-133 thyroid cells, as well as stress fibres, together with filopodia- and lamellipodia-like structures and cell detachment [18]. These experiments, performed in s-μ*g* and r-μ*g*, revealed clear changes in morphology, cytoskeleton and function. Studies on microtubules in altered gravity conditions have shown that they are also gravity-sensitive [67].

In this study, we detected similar cytoskeletal changes of F-actin at the outer cellular membrane after both 7 days and 14 days (see Figure 3). Moreover, we found up-regulated *ACTB, TUBB and VIM*

in the AD and MCS samples after 7 days RPM exposure. *VIM* was significantly down-regulated after 14 days in the RPM-AD samples. The *TUBB* gene expression level of the 1 *g* samples was similar to that of the MCS group (Figure 3).

The 1 *g* control samples, grown in T25 culture flasks, multiplied as a monolayer and never formed any MCS. In contrast, hFOB 1.19 cells exposed to the RPM presented 3D growth. Histological investigation of these constructs showed both round and irregularly-formed structures, with a uniform cellular distribution throughout the constructs at 7 days and 14 days (Figures 1 and 2). An external layer (or capsule) of cells developed on the surface of the constructs, becoming more prominent with time. There was no histological difference between 7 days or 14 days-RPM exposure. Sirius red staining revealed an ECM deposition in the MCS, detectable at both 7 days and 14 days. The ECM was composed of ECM proteins secreted by the cells, thereby providing important structural, mechanical and biochemical support to the surrounding cells [68]. We observed several alterations in the components of the ECM. The gene expression of *SPP1* was clearly up-regulated in all RPM samples. The *FN1* mRNA expression was significantly elevated in AD cells, compared to 1 *g*, whereas no changes were found in MCS. Collagen type 1 is a marker for early stage osteogenesis, which was expressed in all cultured constructs. The *COL1A1* mRNA was not significantly altered in the 7 days samples but was significantly elevated in the 14 days samples. In contrast, *LAMA1* was significantly up-regulated in all 7 days RPM samples but was not altered in the 14 days samples.

In accordance with these findings, CLSM analysis revealed an apparent increase in laminin in the cells exposed to the RPM, compared to the 1 *g* controls. Even though CLSM is not a quantitative method, the obtained images indicated an overall increase in anti-laminin-positive signals in the RPM samples, compared with the 1 g controls. Moreover, the CLSM images also demonstrated that F-actin and laminin were accumulated at the cell boundaries and in the extracellular space around the MCS, which corresponds well to earlier findings on different types of cells such as glial cells, lymphocytes (Jurkat) and FTC-133 thyroid cancer cells [12,14,18].

Bone morphogenetic protein 2 (BMP-2) belongs to the TGF-β superfamily; it is involved in cartilage and bone development and has demonstrated an osteo-inductive effect [69,70]. Patients receiving exogenous BMP-2 to treat bone fractures or defects exhibited elevated sera levels of TNF-α and IL-1β, which may affect the outcome of bone regeneration [50]. *BMP2* gene expression was significantly reduced in RPM AD cells after both 7 days and 14 days. In 7 days samples, BMP2 was elevated in MCS, compared to 1 *g*, indicating BMP2 playing a role in early bone formation, in this experimental setting.

Transforming Growth Factor β1 (TGF-β1) has been shown to influence cell attachment of bone cells of the line MG-63 [71]. TGF-β1 is involved in the regulation of cell proliferation, differentiation and growth [44]. In addition, it is linked with embryogenesis, tissue repair and bone regulation [44].

There was a trend of increased *TGFB1* mRNA levels in the 7 days RPM samples. We measured a significantly elevated *TGFB1* mRNA level in the 14 days RPM-AD cells, compared to the 1 *g* samples. Pathway analyses (Figure 7) revealed interactions between TGFB1 and LAMA1, as well as between TGFB1 and FN1. TGF-β_1 is known to enhance ECM deposition in several tissues.

The SRY HMG box-related gene 9 (*SOX9*), which plays an important role in normal skeletal development, was up-regulated in both the 7 days- and 14 days-RPM-AD cell samples, as compared to the 1 *g* samples. No change was found in the MCS. The BMP2, TGFB1 and SOX9 proteins are involved in chondrogenic and osteogenic differentiation [72].

In summary, the mRNAs of *BMP2*, *TGFB1* and *SOX9* were affected in foetal osteoblasts exposed to s-μ*g*. This was similar to earlier studies, which demonstrated the positive influence of these factors on human chondrocytes exposed to parabolic flight manoeuvres [73]. The relevant proteins, such as BMP-2, represent growth and differentiation factors regulating the chondrocyte development through a complex mutual regulation [74]. The products of TGFB1 and SOX9, together with BMP-2, drive development from mesenchymal stem cells toward cartilage-forming chondrocytes [75]. This progress

appears to be supported, because BMP-2, TGFB1 and SOX9 gene expression and protein content were enhanced after 31 parabolic manoeuvres [73].

We also focused on the *MKI67* mRNA expression, which was not significantly altered in all samples, while the Ki-67 antigen was clearly enhanced in the 14 days RPM-MCS cell samples (Figure 5H) indicating that this group had an enhanced proliferation behaviour in the experimental setting.

We further investigated the secretion of the cytokines involved in bone formation from hFOB cells. The release of dickkopf-related protein 1 (DKK1) in the cell supernatant was unchanged after 7 days and 14 days, between both control and RPM samples but the hFOB cells revealed a time-dependent reduction of the protein after 14 days, compared to 7 days. DKK1 is a secreted Wnt inhibitor that binds LRP5 and LRP6 during embryonic development. There is evidence that a reduction in DKK1 elevates Wnt activity and induces a high bone mass phenotype. Reduced levels of DKK1 remove suppression of bone formation and prevent the development of osteolytic bone diseases. Targeting DKK1 might have therapeutic significance for the treatment of low bone-mass diseases [76].

Furthermore, a key signalling factor controlling bone resorption and bone formation is the receptor activator of nuclear factor-κB (RANK)/RANK ligand/osteoprotegerin [77]. Osteoprotegerin (OPG) is a cytokine receptor, which also belongs to the tumour necrosis factor (TNF) receptor superfamily.

Pro-inflammatory cytokines, extracellular matrix proteins and bone-regulating cytokines of the RANKL/OPG and Wnt/β-catenin pathways are mandatory for normal bone repair [78].

The OPG level was reduced after 7 days in RPM samples, as compared to the controls. In contrast, after 14 days, the secretion of OPG was significantly elevated and further enhanced by RPM exposure.

Osteocalcin (OC), also called bone gamma-carboxyglutamic acid-containing protein (BGLAP), is synthesized by osteoblasts and is involved in the metabolic regulation. OC acts as a pro-osteoblastic (anabolic) factor and is important for bone formation. Furthermore, it has also been implicated in bone mineralization and calcium ion homeostasis [79].

OC secretion remained stable after a 7 days exposure to the RPM and in the 1 *g* control osteoblasts. In contrast, the release of OC was significantly elevated in 14 days RPM-exposed osteoblasts, as compared to static controls. These results fit well to the finding that, after 14 days, the bone tissue constructs were increased in both number and size. The pathway analysis revealed that OC interacted with *SPP1*.

Osteopontin is also known as secreted phosphoprotein 1 (SPP1). It is an extracellular structural protein and, therefore, an organic bone component. It is also detectable in various cell types (e.g., FTC-133 follicular thyroid cancer cells and EA.hy926 endothelial cells) and has been shown to be altered by microgravity conditions [25,27,80].

We measured the osteopontin (*SPP1*) gene expression and found that *SPP1* mRNA was significantly elevated after both 7 days and 14 days in the RPM samples, as compared to the static controls. This finding is in agreement with data obtained from thyroid cancer cells and endothelial cells, which both showed elevated *SPP1* mRNAs after RPM exposure [25,27,80].

Sclerostin (SOST) is produced by osteocytes and has anti-anabolic effects on bone formation; inhibition of SOST can stimulate bone formation [81]. The SOST secretion was significantly reduced after 7 days in the RPM samples, as compared to the 1 *g* controls.

After 14 days, the cells secreted unaltered levels of SOST in the supernatant. This indicates that, initially, microgravity inhibits SOST and stimulates bone formation, but, after 14 days, microgravity did not support bone formation through this mechanism any longer.

Pro-inflammatory cytokines are important for bone formation and bone repair [78] and, therefore, we measured the secretions of IL-1β and TNF-α in the supernatant.

The cytokine interleukin-1β (IL-1β) is an important mediator of the inflammatory response and is involved in several biological processes, such as proliferation, differentiation and apoptosis [82]. The induction of cyclooxygenase-2 (PTGS2/COX2) by this cytokine in the central nervous system is found to contribute to inflammatory pain hypersensitivity [83]. The release of IL-1β decreased significantly after 7 days in RPM samples, as compared to the 1 *g* controls. After 14 days, foetal

osteoblasts in the RPM samples released increased amounts of the IL-1β protein, as compared to the 1 *g* controls. The amount of released IL-1β was significantly higher after 14 days, compared to the amounts after 7 days.

Furthermore, we investigated the release of tumour necrosis factor alpha (TNF-α), which is a cytokine involved in the regulation of a wide spectrum of biological processes, including cell proliferation, differentiation, apoptosis, lipid metabolism and coagulation [84].

The release of TNF-α decreased after 7 days in RPM samples, as compared to the static 1 *g* controls. After 14 days, the hFOB cells of both groups only secreted a low and unaltered amount of TNF-α in the supernatant.

Taken together, these in vitro tissue-engineered bone constructs provide an accurate system for investigating the molecular signaling pathways involved in normal bone formation and remodeling processes and could be also used for co-cultures with osteoclasts. Additionally, as an in vitro system, it has the potential of reducing animal experiments, for instance as an alternative method for testing the effects of pharmaceutical agents or biochemical stimuli. Moreover, these bone constructs can be used for investigating bone-related diseases. Patients having plastic and/or reconstructive surgery with traumatic bone defects or osteonecrosis could benefit from this approach in the future.

4. Materials and Methods

4.1. Cell Culture

The cell culture model used was represented by a human foetal osteoblast cell line, hFOB 1.19 (catalogue number CRL-11372; American Type Culture Collection, Manassas, VA, USA), which is a conditionally-immortalized clonal cell line [37]. hFOB 1.19 is immortalized with a gene encoding for a temperature-sensitive mutant of the SV40 large T antigen (tsA58).

We cultured hFOB 1.19 in a 1:1 mixture of DMEM and Ham's F12 media (Lonza, Verviers, Belgium) supplemented with 2.5 mM L-glutamine (without phenol red), 10% foetal bovine serum (Biochrom AG, Berlin, Germany) and 0.3 mg/mL G418 (Gibco, Life Technologies, Naerum, Denmark). The cells were seeded in 75 cm^2 ventilated cell culture flasks (Sarstedt AG, Nümbrecht, Germany) under the standard conditions of 37 °C and 5% CO_2, as previously described [21–23].

Cells in the third to fifth passage were used in the subsequent experiments. For RPM experiments, hFOB 1.19 cells were seeded into 25 cm^2 ventilated cell culture flasks (Sarstedt AG) and given at least 24 h to properly attach to the bottom of the flasks, forming an adherent monolayer (AD). Subsequently, the flasks were completely filled with the supplemented medium. The experiment ended with the fixation of cells assigned to s-μ*g* or controls, as described earlier [21–23]. For 14 days experiments, a 50% medium exchange by aspiration was necessary after 7 days, to ensure proper concentrations of nutrients and waste products. The remaining MCS were retrieved by upright positioning of flasks, leading to MCS sedimentation.

4.2. Random Positioning Machine

Microgravity conditions were simulated using a desktop RPM (Airbus Defence and Space, former Dutch Space, Leiden, The Netherlands) [2]. The RPM rotates a central frame around two perpendicular axes, randomly changing the direction of rotation and the angular velocity, in the range between 60°/s and 75°/s, in both axes (Figure 8). It was used in the real random mode. Thereby, the direction of the gravitational acceleration affecting the samples was continuously randomized and the magnitude of the net gravitational vector approached zero over time, producing a simulated state of microgravity [4,7]. The RPM was placed inside a commercial incubator, under standard conditions at 37°C and 5% CO_2, with up to twelve 25 cm^2 flasks fixed to the central frame. The flasks were placed no further than 7.5 cm from the centre of rotation.

All 25 cm^2 flasks were completely filled with medium, minimizing shear stress. The samples were run on the RPM for 7 days and 14 days, while an equivalent number of 25 cm^2 flasks, also

completely filled with medium, were placed in the same incubator, to serve as 1 *g* controls to the RPM samples [21–23].

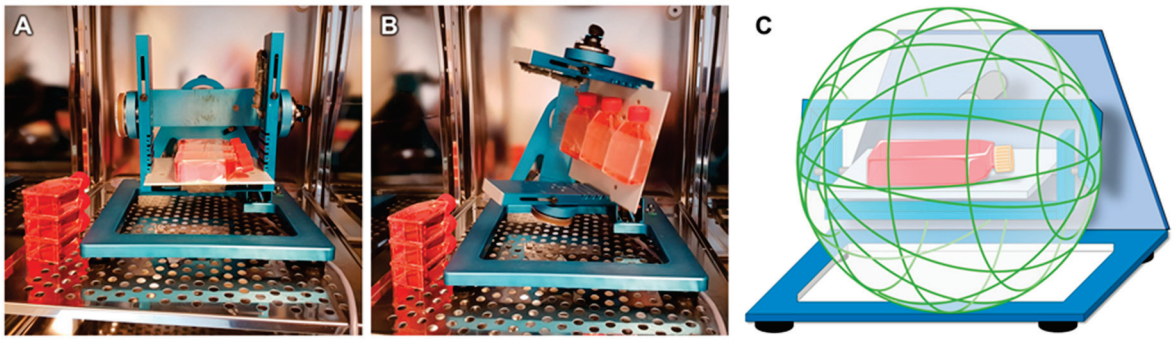


Figure 8. Experimental setup with the Random Positioning Machine (RPM). (**A**) The desktop-RPM (developed by AIRBUS Defence & Space, former: Dutch Space) is placed inside a standard incubator and was loaded with cells in bubble-free filled cell culture flasks. (**B**) After starting, it simulates microgravity by random rotation around two axes. The 1 g controls were placed next to the RPM. (**C**) The working principle of the RPM in real random mode. Parts of the figure were drawn by using pictures from Servier Medical Art. Servier Medical Art by Servier is licensed under a Creative Commons Attribution 3.0 Unported License (https://creativecommons.org/licenses/by/3.0/).

4.3. F-Actin, Tubulin and Laminin Staining

For F-actin, laminin and tubulin staining, 5×10^5 cells were seeded in 60 Nunc™ LAB-TEK™ slide flasks (nr. 170920, material: polystyrene, Fisher Scientific, Roskilde, Denmark).

The attached cells were cultured for 7 days or 14 days, respectively, on the RPM ($n = 30$) or next to the RPM, acting as 1 g controls ($n = 30$) in the same incubator. The slide flasks were filled completely and made air bubble free with medium.

For the 14 days experiment, 50% of the medium in the cultivation flasks was carefully aspirated and exchanged with fresh medium after 7 days. After 7 days or 14 days of cultivation, the cells were washed twice with DPBS (Life Technologies™, Carlsbad, CA, USA) and fixed, with 4% paraformaldehyde and 70% methanol, for 30 min. After fixation, the cells were permeabilized with a Triton-X-100 (Merck, Darmstadt, Germany) and, subsequently, washed twice with DPBS.

Laminin and tubulin were visualized by immunofluorescence, using primary antibodies against laminin (1:25, L9393, Merck) and tubulin (1:500, T5293, Merck).

After the primary antibody incubation for 24 hours at room temperature, the cells were washed twice with DPBS. Subsequently, the samples were incubated with anti-rabbit (laminin) or anti-mouse (tubulin) secondary antibodies, conjugated to an Alexa Fluor 488 (1:500, 4412S and 4408S, both Cell Signalling Technology, Danvers, MA, USA).

F-actin was visualized by means of rhodamine-phalloidin staining (Molecular Probes®, Eugene, OR, USA). For the detailed method, see [26]. Fluoro-shielding with 4′, 6-diamidino-2-phenylindole, DAPI, (Sigma) was used for nuclear counterstaining and mounting in all samples, before subsequent imaging by confocal laser scanning microscopy (CLSM) [26,85].

4.4. Microscopy

Phase contrast microscopy was performed before and after the RPM experiments, to ensure viability and determine the morphological changes of the cells. Pictures were taken using a Canon EOS 550D camera (Canon GmbH, Krefeld, Germany) through a Leica DM IL LED inverted microscope (Leica Microsystems, Wetzlar, Germany). Fluorescence staining was analysed using a Zeiss LSM 710 CLSM (Zeiss, Jena, Germany) fitted with a Plan-Apochromat 63 × 1.4 objective, as previously described [26,85]. Excitation and emission wavelengths for the Alexa Fluor 488 were $\lambda_{ex} = 488$ nm and $\lambda_{em} = 525$ nm, respectively. Correspondingly, for the TRITC: $\lambda_{ex} = 532$ nm and $\lambda_{em} = 576$ nm.

4.5. RNA Isolation

The cells were removed from the culture flasks with scrapers and transferred immediately to tubes for isolation by centrifugation at 3400× *g* for 10 min at 4 °C. Total RNA was extracted using an AllPrep RNA/Protein Kit (Qiagen GmbH, Hilden, Germany), according to the manufacturer's instructions. RNA concentrations and quality were determined spectrophotometrically at 260 nm with a SpectraMax M2 Microplate Reader (Molecular Devices, Sunnyvale, CA, USA).

The isolated RNA had an A260/A280 ratio of >1.5. The cDNA for quantitative PCR was obtained using a First-Strand cDNA Synthesis Kit (Fisher Scientific), according to the manufacturer's instructions.

4.6. Quantitative Real Time PCR

Quantitative real-time PCR (qRT-PCR) was used to determine the expression levels of target genes [21–23,26]. Appropriate primers (overview given in Table 2) were designed using the Primer express software (Applied Biosystems, Darmstadt, Germany) with a T_m of 60°C, taking care of the exon-exon boundaries. All primers were synthesized by TIB Molbiol (Berlin, Germany). The cDNA analysis was performed using a 7500 Fast Real-Time PCR System with Fast SYBR Master Mix (both from Applied Biosystems). The final reaction volume was 12.5 µL, including 1 µL template cDNA and a primer concentration of 500 nM. PCR conditions were as follows: 20 s at 95 °C, 40 cycles of 3 s at 95 °C, 1 min at 60 °C, followed by a melting curve analysis, with a temperature gradient from 60 °C to 95 °C in 0.3 °C increments. If all amplicons showed a T_m similar to the one predicted by the Primer Express software, the PCR reaction was considered to be specific. Each sample was measured in triplicate. Relative transcription levels were quantified using the comparative C_T ($\Delta\Delta C_T$) method. The transcription level of the housekeeping gene *18S rRNA* was used as a reference gene for data normalization.

Table 2. Primers used for qRT-PCR.

Gene	Primer Name	Sequence
18S rRNA	18S-F	GGAGCCTGCGGCTTAATTT
	18S-R	CAACTAAGAACGGCCATGCA
ACTB	ACTB-F	TGCCGACAGGATGCAGAAG
	ACTB-R	GCCGATCCACACGGAGTACT
BMP2	BMP2-F	GACCTGTATCGCAGGCACTCA
	BMP2-R	TCGTTTCTGGTAGTTCTTCCAAAGA
COL1A1	COL1A1-F	ACGAAGACATCCCACCAATCAC
	COL1A1-R	CGTTGTCGCAGACGCAGAT
FN1	FN1-F	TGAGGAGCATGGTTTTAGGAGAA
	FN1-R	TCCTCATTTACATTCGGCGTATAC
LAMA1	LAMA1-F	TGCTCATGGTCAATGCTAATCTG
	LAMA1-R	TCTATCAATCCTCTTCCTTGGACAA
MKI67	MKI67-F	TGGGGAAAGTAGGTGTGAAAGAAG
	MKI67-R	CTCCTTAAACGTTCTGATGCTCTTG
SOX9	SOX9-F	TTGAGACCTTCGACGTCAATGAG
	SOX9-R	TCTGGCCACGAGTGGCC
SPP1	SPP1-F	CGAGGTGATAGTGTGGTTTATGGA
	SPP1-R	CGTCTGTAGCATCAGGGTACTG
TBP	TATA-F	GTGACCCAGCATCACTGTTTC
	TATA-R	GCAAACCAGAAACCCTTGCG
TGFB1	TGFB1-F	CACCCGCGTGCTAATGGT
	TGFB1-R	AGAGCAACACGGGTTCAGGTA
TUBB	TUBB-F	CTGGACCGCATCTCTGTGTACTAC
	TUBB-R	GACCTGAGCGAACAGAGTCCAT
VIM	VIM-F	TTCAGAGAGAGGAAGCCGAAAAC
	VIM-R	AGATTCCACTTTGCGTTCAAGGT

All sequences are given in 5′–3′ direction.

All samples were measured in triplicate and normalized to the housekeepers 18S mRNA and TBP. The 7 days 1 *g* samples were set as 100%.

4.7. Determination of Intracellular Protein Levels

Western blot analyses, including gel electrophoresis, trans-blotting and densitometry, were performed following routine protocols, as described previously [64,86]. Primary antibodies for protein detection and used dilutions are listed in Table 3. All samples were normalized to the housekeeper protein cyclophilin.

Table 3. Antibodies used for Western blot analyses.

Antibody Target	Company/No	Host	Size (kDa)	Used Dilution
β-actin	Sigma/A5316	Ms	42	1:2000
BMP2	Novus biological/	Rb	44	1:500
Collagen I	Sigma/C2456	Ms	~130	1:500
Cyclophilin	Abcam/AB178397	Rb	20	1:2000
Fibronectin	Invitrogen/MA1198	Ms	250	1:1000
Ki-67	Santa cruz/c-15402	Rb	250	1:200
Laminin	Invitrogen/PA1-1673	Rb	~200	1:1000
Osteopontin	Sigma/07264	Rb	50	1:1000
SOX9	Abcam/ab26414	Rb	56	1:1000
TGF-β1	Abcam/ab92486	Rb	44	1:500
TNF-α	Abcam/ab9739	Rb	26	1:500
β-tubulin	Sigma/T5293	Ms	50	1:1000
Vimentin	Sigma/WH0007431	Ms	~53	1:1000

Ms: mouse, Rb: rabbit.

4.8. Measurement of Secreted Bone Biomarkers

Multi-analyte profiling of the protein levels in the cell culture medium of primary human osteoblasts was performed on the Luminex 200 system (Luminex, Austin, TX, USA), using xMAP technology. Acquired fluorescence data were analysed by the xPONENT 3.1 software (Luminex). The effect of adiponectin on the secretion of bone markers in the culture medium was measured using the Milliplex Human. The effects of RPM on the secretion of bone markers in the culture medium was measured using the Milliplex Human Bone Panel (HBNMAG-51K, MILLIPORE Corporation, Billerica, MA, USA). The assay included analysis of the following secreted biomarkers; adrenocorticotrophic hormone (ACTH), Dickkopf-1 (Dkk1), interleukin-6 (IL-6), insulin, leptin, tumour necrosis factor alpha (TNF-α), osteoprotegerin (OPG), osteocalcin (OC), osteopontin (SPP1), sclerostin (SOST), parathyroid hormone (PTH) and fibroblast growth factor-23 (FGF-23). Multi-analyte profiling of the protein levels of these factors in the cell culture medium was performed using the Luminex 200 system (Luminex, Austin, TX, USA), using xMAP technology. Acquired fluorescence data were analysed by applying the Luminex xPONENT version 3.1.871 or MILLIPLEX™ Analyst version 5.1 software (Luminex).

4.9. Histological Staining

After the 7 days and 14-days RPM culture of the hFOB 1.19 cells, the MCS were collected, three times carefully washed in PBS and fixed in 4% paraformaldehyde. After paraffin embedding, the MCS were sectioned with a microtome into 3 µm sections. Haematoxylin and eosin stains were applied, as described earlier [22]. Sirius red staining was performed to evaluate qualitative collagen content, as described earlier [87]. All sections were visualized by light microscopy, using an oil-immersion objective with calibrated magnifications of ×100 and ×200.

4.10. Determination of Calcification of the MCS

The multicellular spheroids were stained with the von Kossa silver staining technique [88]. The von Kossa stain was used to quantify mineralization in the 3D constructs. In addition, the MCS were stained with Alcian blue [89] (Sigma, Taufkirchen, Germany) and, subsequently, examined. For this purpose, the MCS were fixed, for 10 min, with 4% paraformaldehyde (PFA in DPBS), washed twice with DPBS, stained with a drop of the diluted staining solution (diluted according to the manufacturer's instructions), washed twice with DPBS again and mounted with Entellan®(Merck, Darmstadt, Germany) for further microscopic analysis.

4.11. Pathway Analysis

To investigate the mutual regulation between genes and to visualize the localization and interactions between proteins, we entered the relevant UniProtKB entry numbers in the Pathway Studio v.11 software (Elsevier Research Solutions, Amsterdam, The Netherlands). Graphs were generated for gene expression, protein regulation and binding. The method was described previously [22].

4.12. Statistical Analysis

All statistical analyses were performed using the SPSS 24.0 software (SPSS, Inc., Chicago, IL, USA). Data are presented as the mean ± SD. Due to the number of samples per group, an estimation of the data distribution characteristics was not feasible. We, therefore, employed the assumption-less, non-parametric Mann-Whitney-U test to assess the differences between the experimental groups. $p < 0.05$ was considered statistically significant.

5. Conclusions

The hFOB 1.19 cell line has been described as a model cell line for osteogenesis, with an ability to form mineralized nodules [37]. However, not all studies using the hFOB 1.19 cell line have published histological investigations [38,90]. Our histological staining identified cell distribution, including alterations of the cytoskeleton and the extracellular matrix and mineralization in the 3D constructs, having had up to 14 days of RPM exposure.

The human foetal osteoblasts exposed to the RPM grew as adherent monolayer, as well as in the form of RPM-derived bone constructs. We have successfully demonstrated the ability of the modelled microgravity analogue RPM to form 3D constructs and to support human osteogenesis in vitro. Given these findings, we conclude that hFOB 1.19 constructs show an excellent potential as biomaterial for human bone-tissue engineering applications.

Author Contributions: A.S., V.M. and D.G. designed the research. V.M., A.S., J.S., D.G., T.J.C., J.B., M.K., M.W., J.R., A.M.L. and S.K. performed the research. J.B., S.R., S.K., J.R., M.K., M.W., A.M.L., A.S., and V.M. analysed data. T.J.C., V.M. and J.S. performed the CLSM studies. J.B. performed the pathway analyses. J.S. and M.K. performed the Western blot analyses. A.M.L. and J.R. measured the bone markers in the supernatants. D.G., V.M., A.S., J.B., S.R. and E.O wrote the paper. M.I. supported the research.

Funding: This research was funded by NASA grant no. NNX09AV17A, "Development of technologies for elucidation and mitigation of bone loss in microgravity, osteoporosis and inflammatory disease. P.I Alamelu Sundaresan, Mickey Leland study abroad scholarship awarded to Vivek Mann (2015, 2016); This research was also funded by the German Space Agency (DLR, 'Deutsches Zentrum für Luft- und Raumfahrt'; grant no. DLR/BMWi project 50WB1524 (DG)), Texas Southern University, Houston, Texas, U.S.A and Aarhus University, Aarhus, Denmark.

Acknowledgments: We would like to thank Petra Wise from the Charles Drew University, Los Angeles, CA, USA for the English Editing of the manuscript. We thank Christa Baumann for preparing the paraffin-slides and histochemical staining.

Conflicts of Interest: The authors declare no competing financial and non-financial interests.

Abbreviations

μg	Microgravity
2D	Two- dimensional
3D	Three- dimensional
ACTB	Actin beta
ACTH	Adrenocorticotrophic hormone
AD	Adherent monolayers
ALC	Alcian blue
BMP2	Bone morphogenic protein 2
CLSM	Confocal laser scanning microscopy
CN	Clinostat
COL1A1	Collagen type 1 alpha 1
Dkk1	Dickkopf- related protein 1
ECM	Extra cellular matrix
FGF-23	Fibroblast growth factor-23
FN1	Fibronectin 1
HE	Haematoxylin–Eosin
hFOB	Human foetal osteoblast
IL-1β	Interleukin 1 beta
ISS	International space station
LAMA1	Laminin subunit alpha 1
MCS	Multicellular spheroid
MKI67	Marker of proliferation Ki-67
OC	Osteocalcin
OPG	Osteoprotegerin
OPN	Osteopontin
PTH	Parathyroid hormone
qRT-PCR	Quantitative real-time PCR
r-	Real
RANK	Receptor activator of nuclear factor-κB
RANKL	Receptor activator of nuclear factor-κB ligand
RCC	Rotating Cell Culture
RPM	Random Positioning Machine
RWV	Rotating wall vessel
s-	Simulated
SOST	Sclerostin
SOST	Sclerostin
SOX9	SRY-Box 9
SPP1	Secreted Phosphoprotein 1
TGF-β1	Transforming growth factor beta 1
TNF-1α	Tumour necrosis factor 1 alpha
TUBB	Beta tubulin
VIM	Vimentin

References

1. Grimm, D.; Egli, M.; Krüger, M.; Riwaldt, S.; Corydon, T.J.; Kopp, S.; Wehland, M.; Wise, P.; Infanger, M.; Mann, V.; et al. Tissue engineering under microgravity conditions-use of stem cells and specialized cells. *Stem Cells Dev.* **2018**, *27*, 787–804. [CrossRef]
2. Herranz, R.; Anken, R.; Boonstra, J.; Braun, M.; Christianen, P.C.; de Geest, M.; Hauslage, J.; Hilbig, R.; Hill, R.J.; Lebert, M.; et al. Ground-based facilities for simulation of microgravity: Organism-specific recommendations for their use, and recommended terminology. *Astrobiology* **2013**, *13*, 1–17. [CrossRef] [PubMed]

3. Qian, A.; Yin, D.; Yang, P.; Jia, B.; Zhang, W.; Shang, P. Development of a ground-based simulated experimental platform for gravitational biology. *IEEE Trans. Appl. Supercond.* **2009**, *19*, 42–46. [CrossRef]
4. Borst, A.G.; van Loon, J.J.W.A. Technology and developments for the random positioning machine, rpm. *Microgravity Sci. Technol.* **2008**, *21*, 287. [CrossRef]
5. Mesland, D. Novel ground-based facilities for research in the effects of weight. *ESA Microgravity News* **1996**, *9*, 5–10.
6. van Loon, J.J.W.A. Some history and use of the random positioning machine, rpm, in gravity related research. *Adv. Space Res.* **2007**, *39*, 1161–1165. [CrossRef]
7. Wuest, S.L.; Richard, S.; Kopp, S.; Grimm, D.; Egli, M. Simulated microgravity: Critical review on the use of random positioning machines for mammalian cell culture. *Biomed. Res. Int.* **2015**, *2015*, 971474. [CrossRef]
8. Strauch, S.M.; Grimm, D.; Corydon, T.J.; Krüger, M.; Bauer, J.; Lebert, M.; Wise, P.; Infanger, M.; Richter, P. *Current knowledge about the impact of microgravity on the proteome. Expert Review of Proteomics*; Taylor & Francis: Thames, UK, 2018; pp. 1–12.
9. Hammond, T.G.; Lewis, F.C.; Goodwin, T.J.; Linnehan, R.M.; Wolf, D.A.; Hire, K.P.; Campbell, W.C.; Benes, E.; O'Reilly, K.C.; Globus, R.K.; et al. Gene expression in space. *Nat. Med.* **1999**, *5*, 359. [CrossRef] [PubMed]
10. Hammer, B.E.; Kidder, L.S.; Williams, P.C.; Xu, W.W. Magnetic levitation of mc3t3 osteoblast cells as a ground-based simulation of microgravity. *Microgravity Sci. Technol.* **2009**, *21*, 311–318. [CrossRef] [PubMed]
11. Grimm, D.; Bauer, J.; Kossmehl, P.; Shakibaei, M.; Schoberger, J.; Pickenhahn, H.; Schulze-Tanzil, G.; Vetter, R.; Eilles, C.; Paul, M.; et al. Simulated microgravity alters differentiation and increases apoptosis in human follicular thyroid carcinoma cells. *FASEB J.* **2002**, *16*, 604–606. [CrossRef]
12. Uva, B.M.; Masini, M.A.; Sturla, M.; Bruzzone, F.; Giuliani, M.; Tagliafierro, G.; Strollo, F. Microgravity-induced apoptosis in cultured glial cells. *Eur. J. Histochem.* **2002**, *46*, 209–214. [CrossRef]
13. Masiello, M.G.; Cucina, A.; Proietti, S.; Palombo, A.; Coluccia, P.; D'Anselmi, F.; Dinicola, S.; Pasqualato, A.; Morini, V.; Bizzarri, M. Phenotypic switch induced by simulated microgravity on mda-mb-231 breast cancer cells. *Biomed. Res. Int.* **2014**, *2014*, 652434. [CrossRef] [PubMed]
14. Lewis, M.L.; Reynolds, J.L.; Cubano, L.A.; Hatton, J.P.; Lawless, B.D.; Piepmeier, E.H. Spaceflight alters microtubules and increases apoptosis in human lymphocytes (jurkat). *FASEB J.* **1998**, *12*, 1007–1018. [CrossRef] [PubMed]
15. Li, C.F.; Sun, J.X.; Gao, Y.; Shi, F.; Pan, Y.K.; Wang, Y.C.; Sun, X.Q. Clinorotation-induced autophagy via hdm2-p53-mtor pathway enhances cell migration in vascular endothelial cells. *Cell Death Dis.* **2018**, *9*, 147. [CrossRef] [PubMed]
16. Ryu, H.W.; Choi, S.H.; Namkoong, S.; Jang, I.S.; Seo, D.H.; Choi, I.; Kim, H.S.; Park, J. Simulated microgravity contributes to autophagy induction by regulating amp-activated protein kinase. *DNA Cell Biol.* **2014**, *33*, 128–135. [CrossRef] [PubMed]
17. Ma, X.; Pietsch, J.; Wehland, M.; Schulz, H.; Saar, K.; Hubner, N.; Bauer, J.; Braun, M.; Schwarzwalder, A.; Segerer, J.; et al. Differential gene expression profile and altered cytokine secretion of thyroid cancer cells in space. *FASEB J.* **2014**, *28*, 813–835. [CrossRef]
18. Corydon, T.J.; Kopp, S.; Wehland, M.; Braun, M.; Schutte, A.; Mayer, T.; Hulsing, T.; Oltmann, H.; Schmitz, B.; Hemmersbach, R.; et al. Alterations of the cytoskeleton in human cells in space proved by life-cell imaging. *Sci. Rep.* **2016**, *6*, 20043. [CrossRef]
19. Moes, M.J.A.; Gielen, J.C.; Bleichrodt, R.-J.; van Loon, J.J.W.A.; Christianen, P.C.M.; Boonstra, J. Simulation of microgravity by magnetic levitation and random positioning: Effect on human a431 cell morphology. *Microgravity Sci. Technol.* **2011**, *23*, 249–261. [CrossRef]
20. Unsworth, B.R.; Lelkes, P.I. Growing tissues in microgravity. *Nat. Med.* **1998**, *4*, 901–907. [CrossRef]
21. Kopp, S.; Warnke, E.; Wehland, M.; Aleshcheva, G.; Magnusson, N.E.; Hemmersbach, R.; Corydon, T.J.; Bauer, J.; Infanger, M.; Grimm, D. Mechanisms of three-dimensional growth of thyroid cells during long-term simulated microgravity. *Sci. Rep.* **2015**, *5*, 16691. [CrossRef]
22. Kopp, S.; Slumstrup, L.; Corydon, T.J.; Sahana, J.; Aleshcheva, G.; Islam, T.; Magnusson, N.E.; Wehland, M.; Bauer, J.; Infanger, M.; et al. Identifications of novel mechanisms in breast cancer cells involving duct-like multicellular spheroid formation after exposure to the random positioning machine. *Sci. Rep.* **2016**, *6*, 26887. [CrossRef]

23. Kopp, S.; Sahana, J.; Islam, T.; Petersen, A.G.; Bauer, J.; Corydon, T.J.; Schulz, H.; Saar, K.; Huebner, N.; Slumstrup, L.; et al. The role of nfkappab in spheroid formation of human breast cancer cells cultured on the random positioning machine. *Sci. Rep.* **2018**, *8*, 921. [CrossRef]
24. Svejgaard, B.; Wehland, M.; Ma, X.; Kopp, S.; Sahana, J.; Warnke, E.; Aleshcheva, G.; Hemmersbach, R.; Hauslage, J.; Grosse, J.; et al. Common effects on cancer cells exerted by a random positioning machine and a 2d clinostat. *PLoS ONE* **2015**, *10*, e0135157. [CrossRef]
25. Grosse, J.; Wehland, M.; Pietsch, J.; Schulz, H.; Saar, K.; Hubner, N.; Eilles, C.; Bauer, J.; Abou-El-Ardat, K.; Baatout, S.; et al. Gravity-sensitive signaling drives 3-dimensional formation of multicellular thyroid cancer spheroids. *FASEB J.* **2012**, *26*, 5124–5140. [CrossRef]
26. Dittrich, A.; Grimm, D.; Sahana, J.; Bauer, J.; Krüger, M.; Infanger, M.; Magnusson, N.E. Key proteins involved in spheroid formation and angiogenesis in endothelial cells after long-term exposure to simulated microgravity. *Cell Physiol. Biochem.* **2018**, *45*, 429–445. [CrossRef]
27. Grimm, D.; Bauer, J.; Ulbrich, C.; Westphal, K.; Wehland, M.; Infanger, M.; Aleshcheva, G.; Pietsch, J.; Ghardi, M.; Beck, M.; et al. Different responsiveness of endothelial cells to vascular endothelial growth factor and basic fibroblast growth factor added to culture media under gravity and simulated microgravity. *Tissue Eng. Part A* **2010**, *16*, 1559–1573. [CrossRef]
28. Ulbrich, C.; Westphal, K.; Pietsch, J.; Winkler, H.D.; Leder, A.; Bauer, J.; Kossmehl, P.; Grosse, J.; Schoenberger, J.; Infanger, M.; et al. Characterization of human chondrocytes exposed to simulated microgravity. *Cell Physiol. Biochem.* **2010**, *25*, 551–560. [CrossRef]
29. Aleshcheva, G.; Bauer, J.; Hemmersbach, R.; Egli, M.; Wehland, M.; Grimm, D. Tissue engineering of cartilage on ground-based facilities. *Microgravity Sci. Tech.* **2016**, *28*, 237–245. [CrossRef]
30. Boehrs, J.; Zaharias, R.S.; Laffoon, J.; Ko, Y.J.; Schneider, G.B. Three-dimensional culture environments enhance osteoblast differentiation. *J. Prosthodont.* **2008**, *17*, 517–521. [CrossRef]
31. Schneider, G.B.; Boehrs, J.K.; Hoopes, J.V.; Seabold, D.A. Use of 3-dimensional environments to engineer osseous-like tissue. *J. Dev. Biol. Tissue Eng.* **2011**, *3*, 42–47.
32. Amini, A.R.; Laurencin, C.T.; Nukavarapu, S.P. Bone tissue engineering: Recent advances and challenges. *Crit. Rev. Biomed. Eng.* **2012**, *40*, 363–408. [CrossRef]
33. Su, G.N.; Hidaka, M.; Kimura, Y.; Yamamoto, G. In situ collagen gelation: A new method for constructing large tissue in rotary culture vessels. *In Vitro Cell Dev. Biol. Anim.* **2003**, *39*, 368–374. [CrossRef]
34. Hidaka, M.; Su, G.N.; Chen, J.K.; Mukaisho, K.; Hattori, T.; Yamamoto, G. Transplantation of engineered bone tissue using a rotary three-dimensional culture system. *In Vitro Cell Dev. Biol. Anim.* **2007**, *43*, 49–58. [CrossRef]
35. Ulbrich, C.; Wehland, M.; Pietsch, J.; Aleshcheva, G.; Wise, P.; van Loon, J.; Magnusson, N.; Infanger, M.; Grosse, J.; Eilles, C.; et al. The impact of simulated and real microgravity on bone cells and mesenchymal stem cells. *Biomed. Res. Int.* **2014**, *2014*, 928507. [CrossRef]
36. Clarke, M.S.; Sundaresan, A.; Vanderburg, C.R.; Banigan, M.G.; Pellis, N.R. A three-dimensional tissue culture model of bone formation utilizing rotational co-culture of human adult osteoblasts and osteoclasts. *Acta Biomater.* **2013**, *9*, 7908–7916. [CrossRef]
37. Harris, S.A.; Tau, K.R.; Enger, R.J.; Toft, D.O.; Riggs, B.L.; Spelsberg, T.C. Estrogen response in the hfob 1.19 human fetal osteoblastic cell line stably transfected with the human estrogen receptor gene. *J. Cell. Biochem.* **1995**, *59*, 193–201. [CrossRef]
38. Subramaniam, M.; Jalal, S.M.; Rickard, D.J.; Harris, S.A.; Bolander, M.E.; Spelsberg, T.C. Further characterization of human fetal osteoblastic hfob 1.19 and hfob/er alpha cells: Bone formation in vivo and karyotype analysis using multicolor fluorescent in situ hybridization. *J. Cell. Biochem.* **2002**, *87*, 9–15. [CrossRef]
39. Maniatopoulos, C.; Sodek, J.; Melcher, A.H. Bone formation in vitro by stromal cells obtained from bone marrow of young adult rats. *Cell Tissue Res.* **1988**, *254*, 317–330. [CrossRef]
40. Xu, H.; Wu, F.; Zhang, H.; Yang, C.; Li, K.; Wang, H.; Yang, H.; Liu, Y.; Ding, B.; Tan, Y.; et al. Actin cytoskeleton mediates bmp2-smad signaling via calponin 1 in preosteoblast under simulated microgravity. *Biochimie* **2017**, *138*, 184–193. [CrossRef]
41. Aisha, M.D.; Nor-Ashikin, M.N.; Sharaniza, A.B.; Nawawi, H.; Froemming, G.R. Orbital fluid shear stress promotes osteoblast metabolism, proliferation and alkaline phosphates activity in vitro. *Exp. Cell Res.* **2015**, *337*, 87–93. [CrossRef]

42. Viale-Bouroncle, S.; Gosau, M.; Morsczeck, C. Laminin regulates the osteogenic differentiation of dental follicle cells via integrin-alpha2/-beta1 and the activation of the fak/erk signaling pathway. *Cell Tissue Res.* **2014**, *357*, 345–354. [CrossRef]
43. Bentmann, A.; Kawelke, N.; Moss, D.; Zentgraf, H.; Bala, Y.; Berger, I.; Gasser, J.A.; Nakchbandi, I.A. Circulating fibronectin affects bone matrix, whereas osteoblast fibronectin modulates osteoblast function. *J. Bone Miner. Res.* **2010**, *25*, 706–715.
44. Wu, M.; Chen, G.; Li, Y.P. Tgf-beta and bmp signaling in osteoblast, skeletal development, and bone formation, homeostasis and disease. *Bone Res.* **2016**, *4*, 16009. [CrossRef]
45. Yen, M.L.; Chien, C.C.; Chiu, I.M.; Huang, H.I.; Chen, Y.C.; Hu, H.I.; Yen, B.L. Multilineage differentiation and characterization of the human fetal osteoblastic 1.19 cell line: A possible in vitro model of human mesenchymal progenitors. *Stem Cells* **2007**, *25*, 125–131. [CrossRef]
46. Bi, W.; Deng, J.M.; Zhang, Z.; Behringer, R.R.; de Crombrugghe, B. Sox9 is required for cartilage formation. *Nat. Genet.* **1999**, *22*, 85–89. [CrossRef]
47. Kamiya, N.; Ye, L.; Kobayashi, T.; Mochida, Y.; Yamauchi, M.; Kronenberg, H.M.; Feng, J.Q.; Mishina, Y. Bmp signaling negatively regulates bone mass through sclerostin by inhibiting the canonical wnt pathway. *Development* **2008**, *135*, 3801–3811. [CrossRef]
48. Gilbert, L.; He, X.; Farmer, P.; Boden, S.; Kozlowski, M.; Rubin, J.; Nanes, M.S. Inhibition of osteoblast differentiation by tumor necrosis factor-alpha. *Endocrinology* **2000**, *141*, 3956–3964. [CrossRef]
49. Abbas, S.; Zhang, Y.H.; Clohisy, J.C.; Abu-Amer, Y. Tumor necrosis factor-alpha inhibits pre-osteoblast differentiation through its type-1 receptor. *Cytokine* **2003**, *22*, 33–41. [CrossRef]
50. Huang, R.L.; Yuan, Y.; Tu, J.; Zou, G.M.; Li, Q. Opposing tnf-alpha/il-1beta- and bmp-2-activated mapk signaling pathways converge on runx2 to regulate bmp-2-induced osteoblastic differentiation. *Cell Death Dis.* **2014**, *5*, e1187. [CrossRef]
51. Neve, A.; Corrado, A.; Cantatore, F.P. Osteocalcin: Skeletal and extra-skeletal effects. *J. Cell. Physiol.* **2013**, *228*, 1149–1153. [CrossRef]
52. Glass, D.A., 2nd; Bialek, P.; Ahn, J.D.; Starbuck, M.; Patel, M.S.; Clevers, H.; Taketo, M.M.; Long, F.; McMahon, A.P.; Lang, R.A.; et al. Canonical wnt signaling in differentiated osteoblasts controls osteoclast differentiation. *Dev. Cell* **2005**, *8*, 751–764. [CrossRef]
53. Luan, X.; Lu, Q.; Jiang, Y.; Zhang, S.; Wang, Q.; Yuan, H.; Zhao, W.; Wang, J.; Wang, X. Crystal structure of human rankl complexed with its decoy receptor osteoprotegerin. *J. Immunol.* **2012**, *189*, 245–252. [CrossRef]
54. Wu, X.; Guo, S.; Shen, G.; Ma, X.; Tang, C.; Xie, K.; Liu, J.; Guo, W.; Yan, Y.; Luo, E. Screening of osteoprotegerin-related feature genes in osteoporosis and functional analysis with DNA microarray. *Eur. J. Med. Res.* **2013**, *18*, 15. [CrossRef]
55. Saidenberg-Kermanac'h, N.; Cohen-Solal, M.; Bessis, N.; De Vernejoul, M.C.; Boissier, M.C. Role for osteoprotegerin in rheumatoid inflammation. *Jt. Bone Spine* **2004**, *71*, 9–13. [CrossRef]
56. Bae, D.; Moon, S.H.; Park, B.G.; Park, S.J.; Jung, T.; Kim, J.S.; Lee, K.B.; Chung, H.M. Nanotopographical control for maintaining undifferentiated human embryonic stem cell colonies in feeder free conditions. *Biomaterials* **2014**, *35*, 916–928. [CrossRef]
57. Yamaguchi, Y.; Kumagai, K.; Imai, S.; Miyatake, K.; Saito, T. Sclerostin is upregulated in the early stage of chondrogenic differentiation, but not required in endochondral ossification in vitro. *PLoS ONE* **2018**, *13*, e0201839. [CrossRef]
58. Gattazzo, F.; Urciuolo, A.; Bonaldo, P. Extracellular matrix: A dynamic microenvironment for stem cell niche. *Biochim. Biophys. Acta* **2014**, *1840*, 2506–2519. [CrossRef]
59. Dong, Q.; Zhu, X.; Dai, C.; Zhang, X.; Gao, X.; Wei, J.; Sheng, Y.; Zheng, Y.; Yu, J.; Xie, L.; et al. Osteopontin promotes epithelial-mesenchymal transition of hepatocellular carcinoma through regulating vimentin. *Oncotarget* **2016**, *7*, 12997–13012. [CrossRef]
60. Mukherjee, B.B.; Nemir, M.; Beninati, S.; Cordella-Miele, E.; Singh, K.; Chackalaparampil, I.; Shanmugam, V.; DeVouge, M.W.; Mukherjee, A.B. Interaction of osteopontin with fibronectin and other extracellular matrix molecules. *Ann. N. Y. Acad. Sci.* **1995**, *760*, 201–212. [CrossRef]
61. Tocchio, A.; Durmus, N.G.; Sridhar, K.; Mani, V.; Coskun, B.; El Assal, R.; Demirci, U. Magnetically guided self-assembly and coding of 3d living architectures. *Adv. Mater.* **2018**, *30*, 1705034. [CrossRef]

62. Parfenov, V.A.; Koudan, E.V.; Bulanova, E.A.; Karalkin, P.A.; Pereira, F.D.; Norkin, N.E.; Norkin, N.E.; Knyazeva, A.D.; Gryadunova, A.A.; Petrov, O.F.; et al. Scaffold-free, label-free and nozzle-free biofabrication technology using magnetic levitational assembly. *Biofabrication* **2018**, *10*, 034104. [CrossRef]
63. Anil-Inevi, M.; Yaman, S.; Yildiz, A.A.; Mese, G.; Yalcin-Ozuysal, O.; Tekin, H.C.; Ozcivici, E. Biofabrication of in situ self assembled 3d cell cultures in a weightlessness environment generated using magnetic levitation. *Sci. Rep.* **2018**, *8*, 7239. [CrossRef]
64. Sahana, J.; Nassef, M.Z.; Wehland, M.; Kopp, S.; Krüger, M.; Corydon, T.J.; Infanger, M.; Bauer, J.; Grimm, D. Decreased e-cadherin in mcf7 human breast cancer cells forming multicellular spheroids exposed to simulated microgravity. *Proteomics* **2018**, *18*, e1800015. [CrossRef]
65. Ko, Y.J.; Zaharias, R.S.; Seabold, D.A.; Lafoon, J.; Schneider, G.B. Osteoblast differentiation is enhanced in rotary cell culture simulated microgravity environments. *J. Prosthodont.* **2007**, *16*, 431–438. [CrossRef]
66. Vorselen, D.; Roos, W.H.; MacKintosh, F.C.; Wuite, G.J.; van Loon, J.J. The role of the cytoskeleton in sensing changes in gravity by nonspecialized cells. *FASEB J.* **2014**, *28*, 536–547. [CrossRef]
67. Hader, D.P.; Braun, M.; Grimm, D.; Hemmersbach, R. Gravireceptors in eukaryotes-a comparison of case studies on the cellular level. *NPJ Microgravity* **2017**, *3*, 13. [CrossRef]
68. Frantz, C.; Stewart, K.M.; Weaver, V.M. The extracellular matrix at a glance. *J. Cell Sci.* **2010**, *123*, 4195–4200. [CrossRef]
69. Egashira, K.; Sumita, Y.; Zhong, W.; Takashi, I.; Ohba, S.; Nagai, K.; Asahina, I. Bone marrow concentrate promotes bone regeneration with a suboptimal-dose of rhbmp-2. *PLoS ONE* **2018**, *13*, e0191099. [CrossRef]
70. Qian, X.; Zhang, C.; Chen, G.; Tang, Z.; Liu, Q.; Chen, J.; Tong, X.; Wang, J. Effects of bmp-2 and fgf2 on the osteogenesis of bone marrow-derived mesenchymal stem cells in hindlimb-unloaded rats. *Cell Biochem. Biophys.* **2014**, *70*, 1127–1136. [CrossRef]
71. Sefat, F.; Khaghani, S.A.; Nejatian, T.; Genedy, M.; Abdeldayem, A.; Moghaddam, Z.S.; Denyer, M.C.; Youseffi, M. Transforming growth factor beta (tgf-beta) isomers influence cell detachment of mg-63 bone cells. *Tissue Cell* **2015**, *47*, 567–574. [CrossRef]
72. Zhou, N.; Li, Q.; Lin, X.; Hu, N.; Liao, J.Y.; Lin, L.B.; Zhao, C.; Hu, Z.M.; Liang, X.; Xu, W.; et al. Bmp2 induces chondrogenic differentiation, osteogenic differentiation and endochondral ossification in stem cells. *Cell Tissue Res.* **2016**, *366*, 101–111. [CrossRef] [PubMed]
73. Aleshcheva, G.; Wehland, M.; Sahana, J.; Bauer, J.; Corydon, T.J.; Hemmersbach, R.; Frett, T.; Egli, M.; Infanger, M.; Grosse, J.; et al. Moderate alterations of the cytoskeleton in human chondrocytes after short-term microgravity produced by parabolic flight maneuvers could be prevented by up-regulation of bmp-2 and sox-9. *FASEB J.* **2015**, *29*, 2303–2314. [CrossRef]
74. Gao, L.; Sheu, T.J.; Dong, Y.; Hoak, D.M.; Zuscik, M.J.; Schwarz, E.M.; Hilton, M.J.; O'Keefe, R.J.; Jonason, J.H. Tak1 regulates sox9 expression in chondrocytes and is essential for postnatal development of the growth plate and articular cartilages. *J. Cell Sci.* **2013**, *126*, 5704–5713. [CrossRef]
75. Weber, M.; Sotoca, A.M.; Kupfer, P.; Guthke, R.; van Zoelen, E.J. Dynamic modelling of microrna regulation during mesenchymal stem cell differentiation. *BMC Syst. Biol.* **2013**, *7*, 124. [CrossRef] [PubMed]
76. MacDonald, B.T.; Joiner, D.M.; Oyserman, S.M.; Sharma, P.; Goldstein, S.A.; He, X.; Hauschka, P.V. Bone mass is inversely proportional to dkk1 levels in mice. *Bone* **2007**, *41*, 331–339. [CrossRef]
77. Kenkre, J.S.; Bassett, J. The bone remodelling cycle. *Ann. Clin. Biochem.* **2018**, *55*, 308–327. [CrossRef]
78. Cassuto, J.; Folestad, A.; Gothlin, J.; Malchau, H.; Karrholm, J. The key role of proinflammatory cytokines, matrix proteins, rankl/opg and wnt/beta-catenin in bone healing of hip arthroplasty patients. *Bone* **2018**, *107*, 66–77. [CrossRef]
79. Wei, J.; Karsenty, G. An overview of the metabolic functions of osteocalcin. *Rev. Endocr. Metab. Disord.* **2015**, *16*, 93–98. [CrossRef]
80. Infanger, M.; Kossmehl, P.; Shakibaei, M.; Baatout, S.; Witzing, A.; Grosse, J.; Bauer, J.; Cogoli, A.; Faramarzi, S.; Derradji, H.; et al. Induction of three-dimensional assembly and increase in apoptosis of human endothelial cells by simulated microgravity: Impact of vascular endothelial growth factor. *Apoptosis* **2006**, *11*, 749–764. [CrossRef]
81. Tamplen, M.; Fowler, T.; Markey, J.; Knott, P.D.; Suva, L.J.; Alliston, T. Treatment with anti-sclerostin antibody to stimulate mandibular bone formation. *Head Neck* **2018**, *40*, 1453–1460. [CrossRef]

82. Veeriah, V.; Zanniti, A.; Paone, R.; Chatterjee, S.; Rucci, N.; Teti, A.; Capulli, M. Interleukin-1beta, lipocalin 2 and nitric oxide synthase 2 are mechano-responsive mediators of mouse and human endothelial cell-osteoblast crosstalk. *Sci. Rep.* **2016**, *6*, 29880. [CrossRef]
83. Samad, T.A.; Moore, K.A.; Sapirstein, A.; Billet, S.; Allchorne, A.; Poole, S.; Bonventre, J.V.; Woolf, C.J. Interleukin-1beta-mediated induction of cox-2 in the cns contributes to inflammatory pain hypersensitivity. *Nature* **2001**, *410*, 471–475. [CrossRef]
84. Azuma, Y.; Kaji, K.; Katogi, R.; Takeshita, S.; Kudo, A. Tumor necrosis factor-alpha induces differentiation of and bone resorption by osteoclasts. *J. Biol. Chem.* **2000**, *275*, 4858–4864. [CrossRef]
85. Corydon, T.J.; Mann, V.; Slumstrup, L.; Kopp, S.; Sahana, J.; Askou, A.L.; Magnusson, N.E.; Echegoyen, D.; Bek, T.; Sundaresan, A.; et al. Reduced expression of cytoskeletal and extracellular matrix genes in human adult retinal pigment epithelium cells exposed to simulated microgravity. *Cell Physiol. Biochem.* **2016**, *40*, 1–17. [CrossRef]
86. Pietsch, J.; Bauer, J.; Weber, G.; Nissum, M.; Westphal, K.; Egli, M.; Grosse, J.; Schönberger, J.; Eilles, C.; Infanger, M.; et al. Proteome analysis of thyroid cancer cells after long-term exposure to a random positioning machine. *Microgravity Sci. Technol.* **2011**, *23*, 381–390. [CrossRef]
87. Grimm, D.; Jabusch, H.C.; Kossmehl, P.; Huber, M.; Fredersdorf, S.; Griese, D.P.; Kramer, B.K.; Kromer, E.P. Experimental diabetes and left ventricular hypertrophy: Effects of beta-receptor blockade. *Cardiovasc. Pathol.* **2002**, *11*, 229–237. [CrossRef]
88. Meloan, S.N.; Puchtler, H. Chemical mechanisms of staining methods: Von kossa's technique: What von kossa really wrote and a modified reaction for selective demonstration of inorganic phosphates. *J. Histotechnol.* **1985**, *8*, 11–13. [CrossRef]
89. Aleshcheva, G.; Sahana, J.; Ma, X.; Hauslage, J.; Hemmersbach, R.; Egli, M.; Infanger, M.; Bauer, J.; Grimm, D. Changes in morphology, gene expression and protein content in chondrocytes cultured on a random positioning machine. *PLoS ONE* **2013**, *8*, e79057. [CrossRef]
90. Dhurjati, R.; Liu, X.; Gay, C.V.; Mastro, A.M.; Vogler, E.A. Extended-term culture of bone cells in a compartmentalized bioreactor. *Tissue Eng.* **2006**, *12*, 3045–3054. [CrossRef]



© 2019 by the authors. Licensee MDPI, Basel, Switzerland. This article is an open access article distributed under the terms and conditions of the Creative Commons Attribution (CC BY) license (http://creativecommons.org/licenses/by/4.0/).

International Journal of
Molecular Sciences

MDPI

Article

Changes in Exosome Release in Thyroid Cancer Cells after Prolonged Exposure to Real Microgravity in Space

Petra M. Wise [1], Paolo Neviani [1], Stefan Riwaldt [2], Thomas Juhl Corydon [3,4], Markus Wehland [2,5], Markus Braun [6], Marcus Krüger [2,5], Manfred Infanger [2,5] and Daniela Grimm [2,3,5,*]

1 The Saban Research Institute, Children's Hospital Los Angeles, University of Southern California, 4650 Sunset Blvd, Los Angeles, CA 90027, USA; wisepetra@gmail.com (P.M.W.); pneviani@chla.usc.edu (P.N.)
2 Department of Microgravity and Translational Regenerative Medicine, Clinic for Plastic, Aesthetic and Hand Surgery, Otto von Guericke University, Universitätsplatz 2, 39106 Magdeburg, Germany; stefan.riwaldt@med.ovgu.de (S.R.); markus.wehland@med.ovgu.de (M.W.); marcus.krueger@med.ovgu.de (M.K.); manfred.infanger@med.ovgu.de (M.I.)
3 Department of Biomedicine, Aarhus University, Ole Worms Allé 4, 8000 Aarhus C, Denmark; corydon@biomed.au.dk
4 Department of Ophthalmology, Aarhus University Hospital, Palle Juul-Jensens Blvd. 99, 8200 Aarhus N, Denmark
5 Research Group "Magdeburger Arbeitsgemeinschaft für Forschung unter Raumfahrt- und Schwerelosigkeitsbedingungen" (MARS), Otto von Guericke University, 39106 Magdeburg, Germany
6 Deutsches Zentrum für Luft- und Raumfahrt (DLR), Raumfahrtmanagement Bonn-Oberkassel, 53227 Bonn, Germany; m.braun@dlr.de
* Correspondence: dgg@biomed.au.dk; Tel.: +45-21379702

check for updates

Citation: Wise, P.M.; Neviani, P.; Riwaldt, S.; Corydon, T.J.; Wehland, M.; Braun, M.; Krüger, M.; Infanger, M.; Grimm, D. Changes in Exosome Release in Thyroid Cancer Cells after Prolonged Exposure to Real Microgravity in Space. *Int. J. Mol. Sci.* **2021**, *22*, 2132. https://doi.org/10.3390/ijms22042132

Academic Editor: Riccardo Alessandro

Received: 4 February 2021
Accepted: 18 February 2021
Published: 21 February 2021

Publisher's Note: MDPI stays neutral with regard to jurisdictional claims in published maps and institutional affiliations.

Copyright: © 2021 by the authors. Licensee MDPI, Basel, Switzerland. This article is an open access article distributed under the terms and conditions of the Creative Commons Attribution (CC BY) license (https://creativecommons.org/licenses/by/4.0/).

Abstract: Space travel has always been the man's ultimate destination. With the ability of spaceflight though, came the realization that exposure to microgravity has lasting effects on the human body. To counteract these, many studies were and are undertaken, on multiple levels. Changes in cell growth, gene, and protein expression have been described in different models on Earth and in space. Extracellular vesicles, and in particular exosomes, are important cell-cell communicators, being secreted from almost all the cells and therefore, are a perfect target to further investigate the underlying reasons of the organism's adaptations to microgravity. Here, we studied supernatants harvested from the CellBox-1 experiment, which featured human thyroid cancer cells flown to the International Space Station during the SpaceX CRS-3 cargo mission. The initial results show differences in the number of secreted exosomes, as well as in the distribution of subpopulations in regards to their surface protein expression. Notably, alteration of their population regarding the tetraspanin surface expression was observed. This is a promising step into a new area of microgravity research and will potentially lead to the discovery of new biomarkers and pathways of cellular cross-talk.

Keywords: thyroid cancer; cell culture; exosomes; microgravity; spaceflight; transmembrane proteins; tetraspanins

1. Introduction

Man has always looked to the stars, and throughout history has been on the pursuit to reach them. As the technology evolved, mankind took step after step towards this quest, and today space travel for research missions is a reality, with commercial travel and exploration of other planets on the horizon [1–4]. In addition to the technical challenges space travelers face, the human body itself suffers negative effects from a prolonged lack of exposure to gravitational forces, which can lead to various impairments in multiple physiological systems [5–10]. Since the early days of spaceflight, researchers have investigated the effects of weightlessness on the human body [11–13].

As spaceflights are rare and require extensive preparation and funding, most of the initial cell biological experiments are conducted under simulated microgravity conditions. Various devices have been developed to successfully simulate weightlessness on Earth, such as the random positioning machine (RPM) and clinostats [14–18]. The observed changes after cell incubation within these devices often predict cellular changes during spaceflight, but by direct comparison simulated and real microgravity do not cause identical effects [19]. Therefore, our team took the opportunity to conduct experiments under prolonged microgravity as part of a joint enterprise by the German Aerospace Center (Deutsches Zentrum für Luft- und Raumfahrt, DLR) and the Chinese Manned Space Engineering Office (CMSEO) [20] during the Shenzhou-8/SimBox Spaceflight mission in 2011. The planning and execution of cell culture experiments on the unmanned Shenzhou-8 spacecraft was a major challenge. The cell culture equipment had to be created to withstand the physical forces during the mission, as well as being adapted to small, automated modules to enable fluid exchanges [21,22].

Based on hardware tests prior to and during the Shenzhou-8 mission, the results and insights gained through the analysis of the harvested samples provided us with the requisite knowledge to set up another experiment under prolonged exposure to microgravity. We previously demonstrated changes of cancer cells from two- to three-dimensional growth after exposure to simulated microgravity on the RPM [21,22]. Concurrently, genomic adaptations in pathways involved in the cytoskeletal composition were identified [23–25]. As described in Section 4.2., the human follicular thyroid cancer cell line FTC-133 was flown to the International Space Station (ISS) on the SpaceX CRS-3 cargo mission in newly designed, automated CellBox-1 modules. Incubation aboard the ISS proceeded for 12 days, following a pre-determined feeding and fixation schedule (flight module, FM). Concurrently, cells from the same passage were grown under the exact same conditions considering the hardware, temperature, and fluid exchange schedule in a laboratory on Earth (ground module, GM). The harvested cells and supernatant were analyzed to determine the growth behavior, adaptations in gene and protein expression, and protein interactions.

To further explore the underlying processes of any differential protein expression, we decided to investigate the cell culture supernatants as to their content of extracellular vesicles (EVs). EVs have evolved into a fast-growing focal point in biomedical research over the last decade, as they show a high potential as biomarkers and in clinical applications due to their emerging roles in disease, as well as normal physiology. EVs are a family of membrane vesicles containing a phospholipid bilayer, which are secreted into the extracellular environment by the majority of (if not all) cells [26–28]. These vesicles can be categorized into three major types: Exosomes, microvesicles, and apoptotic bodies. They are found in circulating body fluids, including blood, saliva, and urine [26,29–32]. EVs reflect their cell of origin with respect to protein, nucleic acid, and lipid content, functionally they mediate cell-cell communication. EVs have the potential to serve as biomarkers for a wide array of diseases in clinical diagnosis, and may lead the way to a variety of future therapeutic approaches. Hence, the role of EVs in the tumor environment has been studied extensively over the last decade. They are transferred from tumors to the surrounding extracellular environment and thus, modulate the immune and therapy response, and promote matrix remodeling as well as angiogenesis [33–36]. Conversely, the transfer of EVs from the tumor microenvironment to tumor cells enhances tumorigenesis by increasing tumor cell proliferation, resistance to chemotherapy, and migration [36–41]. Furthermore, EVs can travel to distant areas of the organism, where they can be involved in the preparation of the pre-metastatic niche [42–47].

This research paper will focus particularly on exosomes, which can be distinguished from the remaining EVs by their biogenesis and size. Exosomes range in size from roughly 30 to 150 nm and are further defined by the presence of specific transmembranes, extracellular, and cytosolic proteins, as well as the absence of some intracellular proteins present in other EVs. The International Society for Extracellular Vesicles (ISEV) has detailed the minimal experimental requirements for a definition of exosomes and other EVs [48,49].

Additionally, exosomes are defined by their release mechanism to the extracellular environment via fusion of late endosomes/multivesicular bodies (MVBs) with the plasma membrane (Figure 1) [50,51]. The study and the development of applications of exosomes has so far been challenging, as the initial isolation and enrichment methods resulted in low yields and/or co-precipitation of aggregated and bound proteins, as well as due to their small size. Therefore, finding new ways to characterize these promising vesicles is a focus of researchers worldwide. One of the most common methods of determining the size distribution and concentration of exosomes is nanoparticle tracking analysis (NTA), where the particle size of isolated EVs is calculated by the Brownian motion [52,53]. However, conventional NTA reaches its limit when it comes to determining the cell origin and distinguishing between different EVs. The Western blot analysis is frequently used to verify that isolated vesicles are in fact exosomes, but this requires a rather large number of vesicles. The immunocapture of exosomes on antibody-coated beads followed by the analysis via flow cytometry enhances the specificity of the characterization, but has a slow throughput and is quite costly, particularly with multiplexing for several markers [53–55]. Here, we have employed a method based on the single particle interferometric reflectance imaging sensor (SP-IRIS) (ExoView™, NanoView Biosciences, Boston, MA, USA) which allows multiplexed phenotyping and digital counting of various populations of individual exosomes captured on a microarray-based chip. This method allows the characterization of exosomes directly from human biofluids without the need of prior vesicle isolation or concentration, and so allows a detailed analysis with a very small sample size [53,55]. In this paper, we are reporting the results of the characterization of the cell supernatants from samples that were grown under prolonged microgravity on the ISS, as well as their control counterparts incubated on Earth. Given the growing body of knowledge regarding the role of exosomes as biomarkers, as well as their potential in disease diagnostics and therapy, these initial investigations could be the start of a new area of research into understanding adaptations and changes of an organism in space on the level of cellular cross-talk. Additionally, through exosomes we may gain further insights into the mechanisms of cell regulation via EVs.

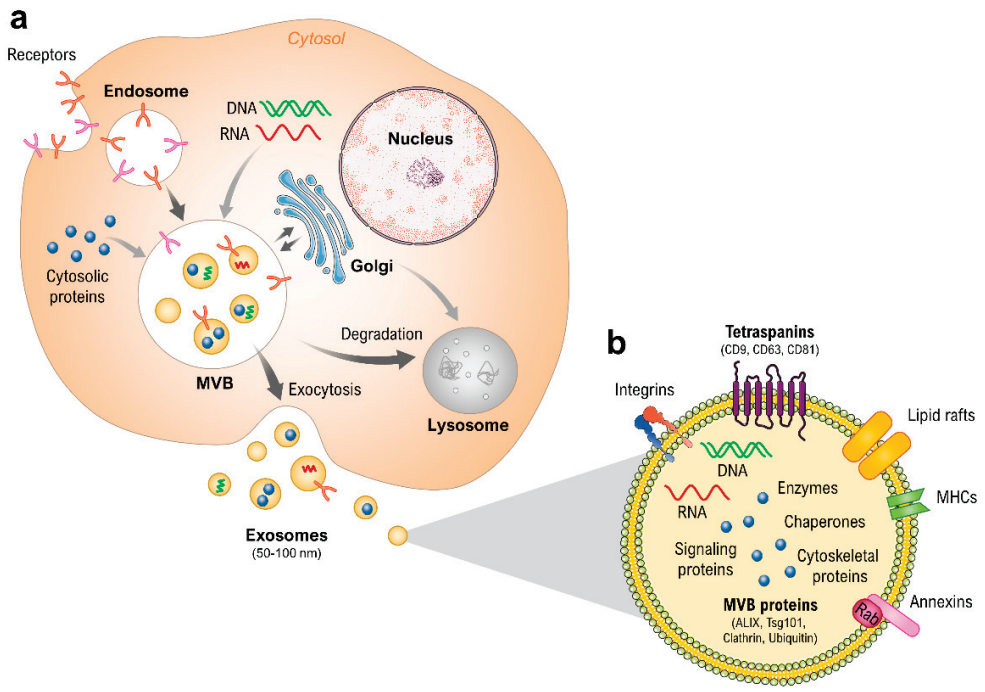


Figure 1. (**a**) Schematic overview of exosome biogenesis, cargo loading, and release. (**b**) Typical molecular contents of an exosome. Parts of the figure are drawn using pictures from Servier Medical Art (https://smart.servier.com (accessed on 20 February 2021)), licensed under a Creative Commons Attribution 3.0 Unported License (https://creativecommons.org/licenses/by/3.0 (accessed on 20 February 2021)).

2. Results

Since the first description of secreted membrane vesicles, there has been rapid growth in the number of studies on EVs [56,57]. Over the years, the functional roles of these vesicles have been explored, and with rising interest in the implications and possibilities of EVs many isolation methods have been developed, with the specific method depending on the source material, as well as the requirements needed to explore the given hypothesis [49,54,58,59]. For example, differential centrifugation protocols, as well as methods for both filtration and polymer precipitation have been shown to drastically differ in yield, purity, and functionality of the harvested EVs [58,60,61]. Similarly, the definition and description of EVs has varied greatly and proved overwhelming at times. Therefore, the ISEV suggested that investigators report the amount of several proteins (three or more) in at least a semi-quantitative manner in any EV preparation, including EV isolates obtained from body fluids or from secreting cells in vitro. The proteins described and characterized should be proteins expected to be present in the EVs of interest, especially transmembrane proteins and cytosolic proteins with membrane-binding capacity. In addition, the level of presence of proteins not expected to be enriched in EVs of endosomal origin should also be determined [48]. Transmembrane proteins expected to be present in exosomal preparations include, among others, tetraspanins (CD9, CD63, CD81), integrins, and growth factor receptors. The group of expected or enriched cytosolic proteins includes endosome or membrane-binding proteins (TSG101) and signal transduction or scaffolding proteins (syntenin). Intracellular proteins that are absent or under-represented in exosomes, but present in other types of EVs, are proteins found in the endoplasmic reticulum (ER) (calnexin) or the Golgi apparatus (GM130) [48].

The method of this study was SP-IRIS, using the ExoView™ system (NanoView Biosciences, Boston, MA, USA). With this method, human exosomes can be selectively captured on a chip plate directly from biofluids without prior need to isolate and concentrate EVs. Additionally, the method is suitable for even very small sample sizes, as high as 20 µL for unprocessed not concentrated samples. To assess the amount and population distribution of exosomes in the cell supernatants harvested from the CellBox-1 experiment, we used EV-TETRA-C ExoView Tetraspanin chip plates (NanoView Biosciences, Boston, MA, USA), which capture exosomes via pre-loaded antibodies (ABs) to the tetraspanins CD9, CD63, and CD81. The interferometric analysis enables the researcher to investigate the particle count and the size distribution of a given sample [53,55]. By counter-staining the captured exosomes with fluorescent ABs to the three tetraspanins it is possible to characterize the EVs according to their transmembrane protein expression, and identify different populations present in the sample. Here, we describe the results gained from the GM and FM cell culture supernatants harvested from the CellBox-1 experiment on the ISS.

2.1. Interferometric Analysis

2.1.1. Particle Concentration

The absolute number of captured particles was measured via interferometric analyses, by scanning the tetraspanin spots (CD9, CD63, and CD81) as well as the IgG control, all in triplicate experiments. As pictured in Figure 2, the majority of EVs were bound to the DC9 spots in both the GM and FM samples (GM: 4256/3038/3715.33 particles; FM: 4380.5/3915/3331 particles), followed by particles bound to CD63 (GM: 268/355/205.66 particles; FM: 1479.5/2121.5/1245 particles), and CD81 (GM: 98.33/239/87.33 particles; FM: 75/386.5/196.33 particles). The number of CD9 particles is fairly similar in all the samples regardless of the exposure to microgravity, but the numbers of CD63 and CD81 is elevated in FM samples roughly 10-fold (CD63) to 20-fold (CD81), respectively, compared to the GM samples. The total concentration in FM samples averages at 7235.2 particles, and in GM samples at 4094.4 particles, which indicates an average increase in EVs of 74% (Figure 2a, Figure S1). The statistical analysis using an unpaired t-test revealed a significant change in between one group, the comparison of captured particles on the CD63 spot with a p-value of 0.011 (Figure 2b).

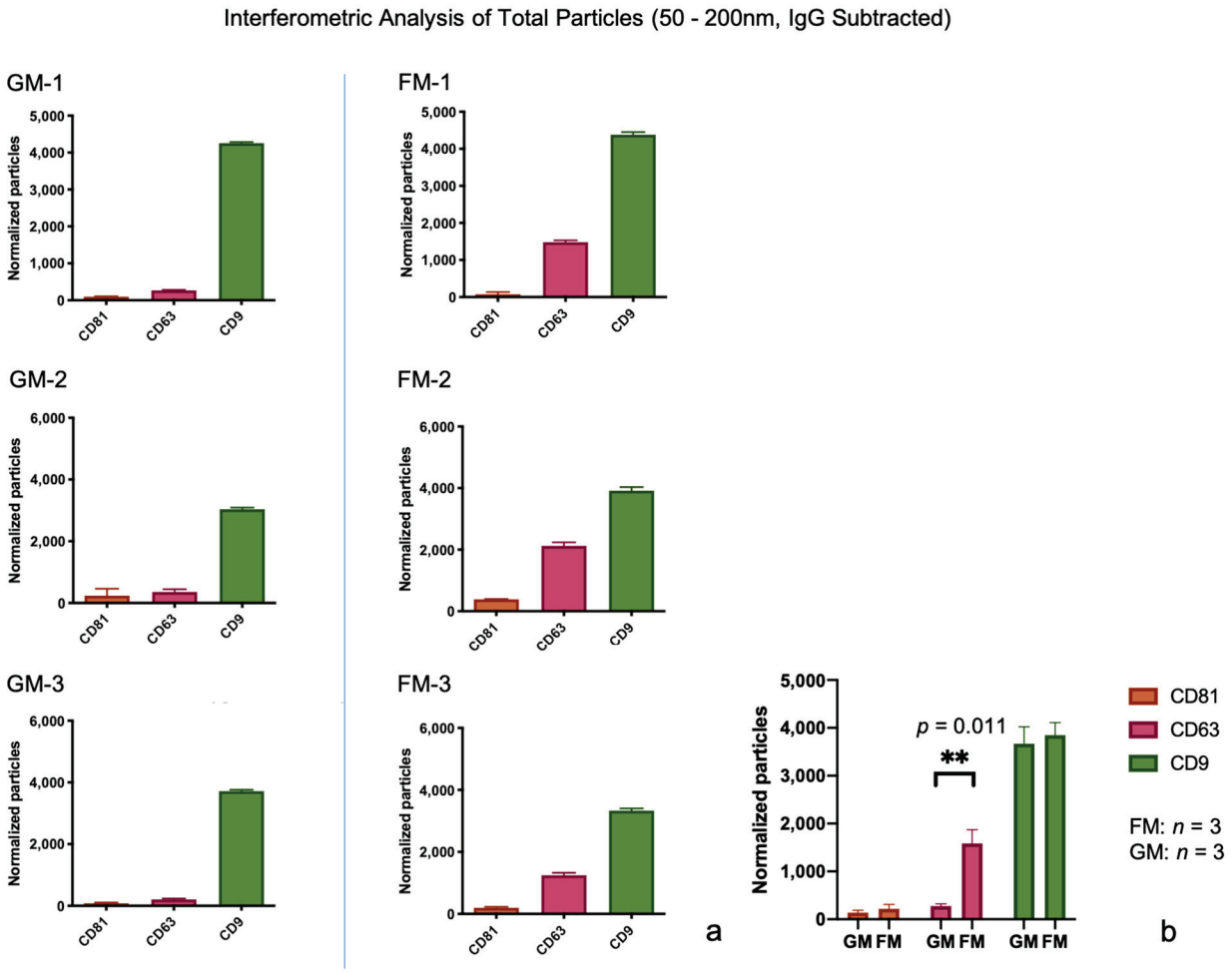


Figure 2. (**a**) Total count of captured particles via the interferometric analysis, from both sample sets, ground module (GM) and flight module (FM). Measurements were taken in triplicates, values are shown with the standard deviation (SD). (**b**) The statistical analysis via the unpaired *t*-test was performed to compare the GM group to the FM group on different card spots. Statistical significance is displayed as ** ($p \leq 0.01$).

2.1.2. Particle Size Distribution

The size distribution of the captured EVs was determined by interferometry, as well. Currently, the ExoView interferometric analysis is limited to the size range of 50–200 nm. As shown in Figure 3, the majority of particles captured by the tetraspanins are well within the size range of 30–100 nm, which is the defined size of exosomes [48,54] in all GM and FM samples alike. This size range covers an average of 5742 particles in the GM group and 8368 particles in the FM group. Only very few particles were found in sizes larger than 100 nm: On average, 314 particles in GM samples and 252 particles in FM samples. The mode size of exosomes is 60 nm, with an average of 2592 particles in the FM samples and 1520 particles in the GM samples (Tables 1 and 2). The size distribution on all six analyzed samples shows that the analyzed particles can be considered exosomes, both due to their size and the presence of the tetraspanins CD9, CD63, and CD81 (Figure 3).

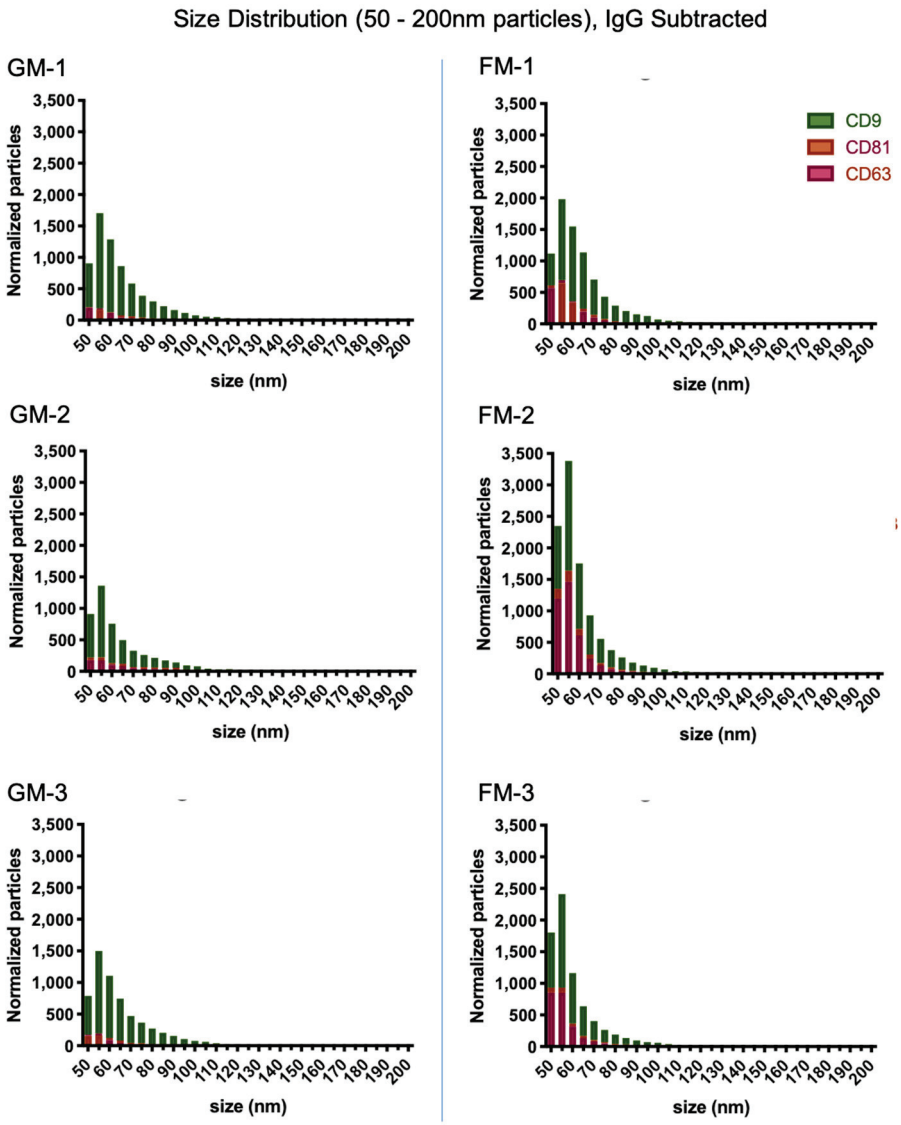


Figure 3. Particle size distribution by the interferometric analysis of both samples sets. Measurements were taken in triplicates; the results were normalized with the IgG control, the size range spans from 50–200 nm.

Table 1. Particle size distribution baseline corrected, GM sample set.

	CD81			CD63			CD9		
Size (nm)	**GM-1**	**GM-2**	**GM-3**	**GM-1**	**GM-2**	**GM-3**	**GM-1**	**GM-2**	**GM-3**
50	4.3	41.7	−16.7	204	179	172.3	696.7	690.3	633.6
55	−18	48.4	−32.3	187	175	193	1536	1136.7	1335.7
60	5.4	26.3	32.4	120.7	103	92	1162.7	628.6	983.7
65	31	38.7	37.7	45	83.7	44.7	784.7	376.3	663.4
70	33.4	15	27.6	30.2	54.3	17.6	520	259.7	426
75	22.7	23.7	23	19.2	44	16	348	194	327
80	17	20.3	15.7	11.3	38.7	9.7	271.6	156.3	248.4
85	13.7	22.3	13.3	9	30.3	7	199	121	184.3
90	13	27.7	9.3	5.3	28.3	8.7	142.6	85	138
95	7.3	10	9	4.5	19.4	5	102	65	92.3
100	8.7	10.3	6	5.5	18.3	7.4	64.3	52.3	64.4
105	6.7	6.7	3.3	6.5	4.3	3.6	42.3	30	56.3

Table 1. *Cont.*

	CD81			CD63			CD9		
Size (nm)	**GM-1**	**GM-2**	**GM-3**	**GM-1**	**GM-2**	**GM-3**	**GM-1**	**GM-2**	**GM-3**
110	5.6	9	3	3.8	6.6	2.3	41	18.3	35
115	6	14.6	3.4	3.3	7.3	1.4	22	14.6	21
120	5	7.3	3.3	0.8	6.3	3.3	18.3	8.7	17.7
125	2	6.7	2.4	1.8	7.4	1.4	10.3	7	12.4
130	3.4	6.7	2.3	0.2	6.4	1.7	7.7	5.4	9
135	1.7	3	1.3	1	1	−0.3	6	6	8.3
140	3	7	0.4	0.5	5	1	5.7	3	3.7
145	1.3	2.6	0.7	0	−1.7	1	4.7	0.6	4.4
150	1	1.3	0.3	0	2.7	0.7	3.7	2	3
155	1	3.6	1	−0.7	0.3	0.3	1	0.3	4.3
160	0.3	2.3	0.3	0	2.3	0.3	1.3	1	1.7
165	0.3	3	0.3	1.5	3.3	0	1.7	2.3	1
170	0.3	3.4	1.7	0.8	1	0.3	1.6	2.4	1.7
175	1	1.3	0.7	0	1	0	0.3	1.3	0.7
180	0	2	0.7	−0.3	1.3	0	0.7	2	0
185	0.3	2.7	0	0	1.7	0	0	1.4	1
190	0	3	0.3	0	1.6	0	0	0.6	0.7
195	0.4	−0.3	0	−0.3	1.4	0	−0.3	−0.3	0.3
200	−0.3	1.3	1	−0.3	1	0.7	0.4	0.3	0.7

Table 2. Particle size distribution baseline corrected, FM sample set.

	CD81			CD63			CD9		
Size (nm)	**GM-1**	**GM-2**	**GM-3**	**GM-1**	**GM-2**	**GM-3**	**GM-1**	**GM-2**	**GM-3**
50	4.3	41.7	−16.7	204	179	172.3	696.7	690.3	633.6
55	−18	48.4	−32.3	187	175	193	1536	1136.7	1335.7
60	5.4	26.3	32.4	120.7	103	92	1162.7	628.6	983.7
65	31	38.7	37.7	45	83.7	44.7	784.7	376.3	663.4
70	33.4	15	27.6	30.2	54.3	17.6	520	259.7	426
75	22.7	23.7	23	19.2	44	16	348	194	327
80	17	20.3	15.7	11.3	38.7	9.7	271.6	156.3	248.4
85	13.7	22.3	13.3	9	30.3	7	199	121	184.3
90	13	27.7	9.3	5.3	28.3	8.7	142.6	85	138
95	7.3	10	9	4.5	19.4	5	102	65	92.3
100	8.7	10.3	6	5.5	18.3	7.4	64.3	52.3	64.4
105	6.7	6.7	3.3	6.5	4.3	3.6	42.3	30	56.3
110	5.6	9	3	3.8	6.6	2.3	41	18.3	35
115	6	14.6	3.4	3.3	7.3	1.4	22	14.6	21
120	5	7.3	3.3	0.8	6.3	3.3	18.3	8.7	17.7
125	2	6.7	2.4	1.8	7.4	1.4	10.3	7	12.4
130	3.4	6.7	2.3	0.2	6.4	1.7	7.7	5.4	9
135	1.7	3	1.3	1	1	−0.3	6	6	8.3
140	3	7	0.4	0.5	5	1	5.7	3	3.7
145	1.3	2.6	0.7	0	−1.7	1	4.7	0.6	4.4
150	1	1.3	0.3	0	2.7	0.7	3.7	2	3
155	1	3.6	1	−0.7	0.3	0.3	1	0.3	4.3
160	0.3	2.3	0.3	0	2.3	0.3	1.3	1	1.7
165	0.3	3	0.3	1.5	3.3	0	1.7	2.3	1
170	0.3	3.4	1.7	0.8	1	0.3	1.6	2.4	1.7
175	1	1.3	0.7	0	1	0	0.3	1.3	0.7
180	0	2	0.7	−0.3	1.3	0	0.7	2	0
185	0.3	2.7	0	0	1.7	0	0	1.4	1
190	0	3	0.3	0	1.6	0	0	0.6	0.7
195	0.4	−0.3	0	−0.3	1.4	0	−0.3	−0.3	0.3
200	−0.3	1.3	1	−0.3	1	0.7	0.4	0.3	0.7

2.2. Fluorescent Analysis

2.2.1. Total Fluorescent Particle Counts

The analysis of the chip plate captured exosomes counterstained with fluorescent antibodies to the tetraspanins offers deeper insights into the varying population of EVs in a given sample, as well as their distribution and changes under different conditions and the ability to detect vesicles below the detection limit of 50 nm. The results of our examination of the total fluorescent particle counts with all three ABs on all capture spots can be seen in Figure 4. The figure displays the combined values of all three fluorescent tetraspanin ABs. It can be observed that in the GM samples, the majority of the particles are found at the CD9 slot (on average 7107/6917/6890 particles), followed by the particles on the CD63 slot (on average 4556/4296/4549 particles), and lastly by CD81 (on average 3470/3368/3416 particles). Contrary to this, the results in the FM samples point to the highest count of bound particles on the CD63 spot (on average 9216/9136/9277 particles), which is a 103% increase compared to the averaged GM samples. The particles on the CD9 spot (on average 8461/8546/8230 particles) display a 21% increase, and the particles on CD81 (on average 5179/5189/5035 particles) a 50% increase in comparison to GM. Looking at the sum of particles, this is a 53% increase over all three spots in the samples that were subjected to prolonged microgravity (Figure 4a). A comparison of all the samples from the GM and FM group via unpaired *t*-tests revealed significant changes in the particles captured on the CD81 spot ($p \leq 0.026$) and the CD63 spot ($p < 0.0001$) (Figure 4b).

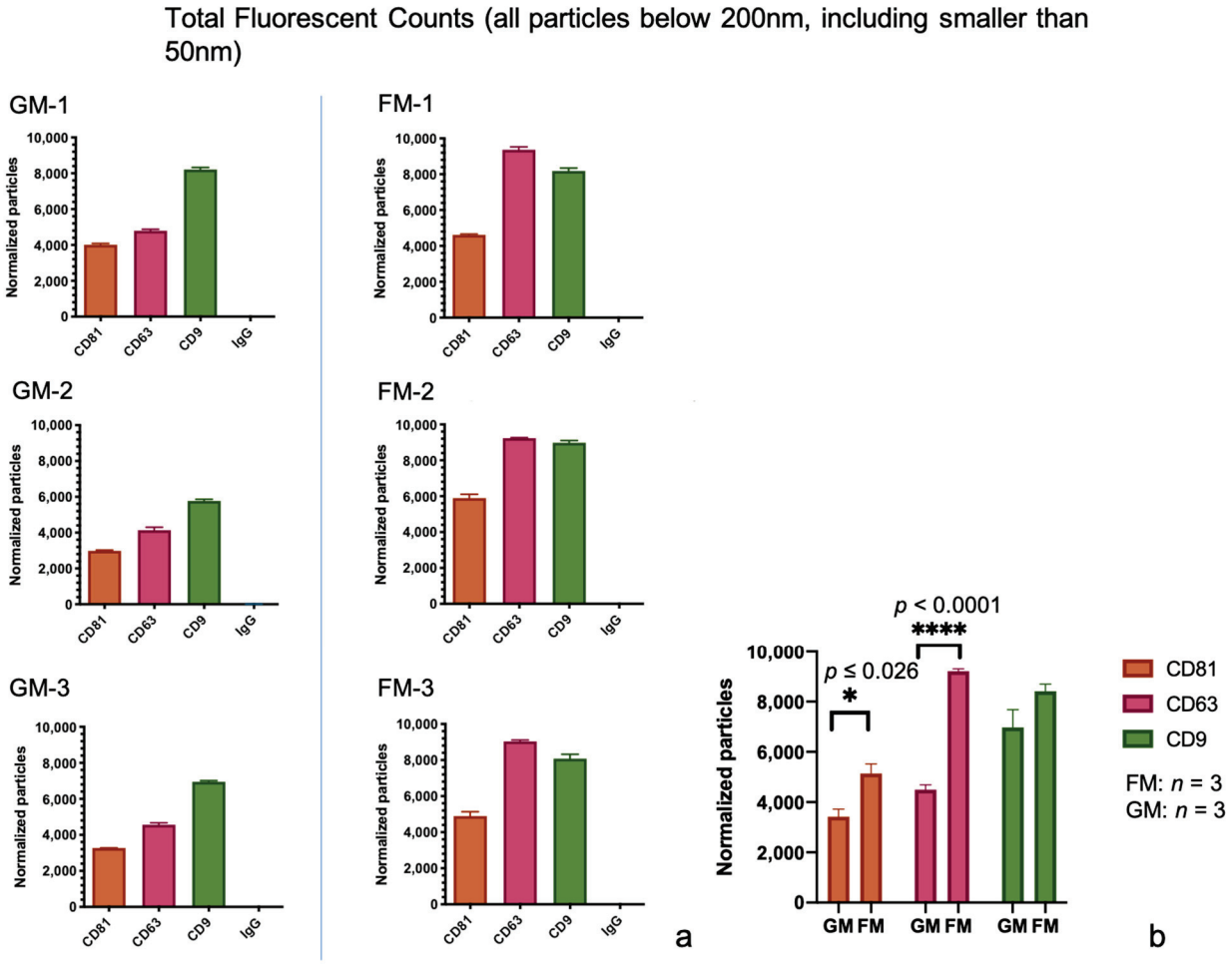


Figure 4. (**a**) Absolute particle counts by fluorimetric scans. Included are all the size particles up to 200 nm, values are shown with SD. (**b**) The statistical analysis via the unpaired t-test was performed to compare the GM group to the FM group on different card spots. Statistical significance is displayed as * ($p \leq 0.05$) and **** ($p \leq 0.0001$).

One might expect to find the highest particle counts where the AB concurs with the coating of a spot, due to a higher affinity of a particle to a specific slot depending on the surface expression of the protein in question. This only seems to hold true for CD63 in our samples. In both sets, GM and FM, CD63 shows the most prominent count on its own spot on the chip plate and shows lower counts on the remaining spots. CD81, on the other hand, shows the most prominent counts on the CD9 spots in both the FM and GM sample sets. In both sample sets, CD81 shows more particles on the CD9 spot than on the other two, even the CD81 spot itself (Figure 5). A proposed explanation of this discrepancy may be due to the low antigen density on single vesicles (e.g., less than three epitopes available for recognition by the fluorescently conjugated antibody or due to steric hindrance (low epitope accessibility due to the small size of the vesicles).

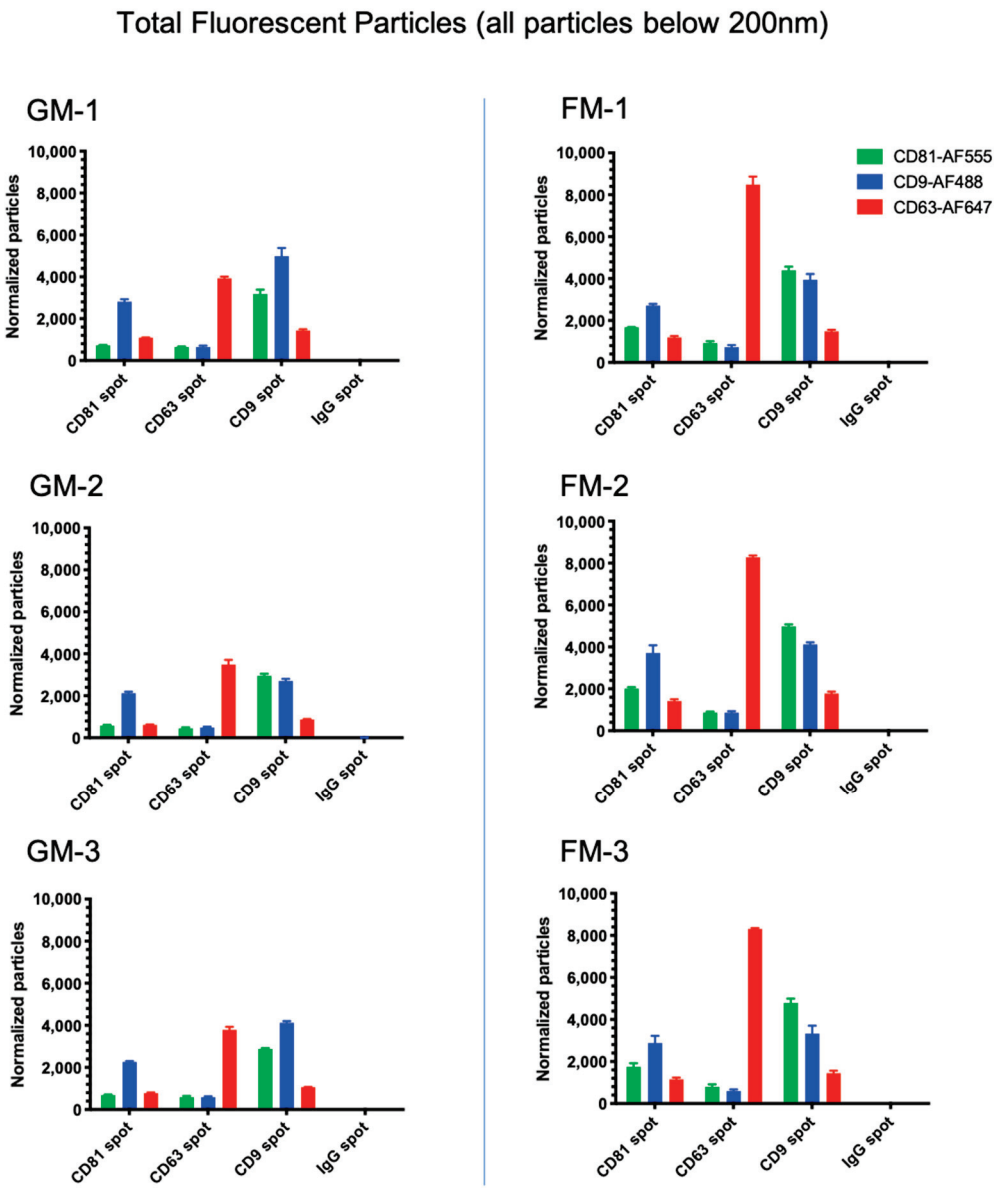


Figure 5. Total particle counts by the fluorimetric analysis up to 200 nm, including particles smaller than 50 nm. Particles were counted for all three counterstains, CD9, CD63, and CD81 separately on the specific spots on the chip plates in triplicates. Values are shown with SD.

2.2.2. Colocalization Analysis

Single Tetraspanin Surface Expression—CD9, CD63, and CD81

The number of particles with CD9 surface expression only is slightly elevated in the GM sample set (3169 particles on average) in comparison to the FMs (2696 particles on average, Figure 6a,b; Tables S1 and S2). The population of CD63 only expressing exosomes is by far the largest in both experimental groups, with an average of 3491 particles in the GM sample set and 7856 particles in the FM samples. The statistical analysis of the GM and FM group via unpaired t-tests revealed significant changes in the particles expressing CD63 only ($P < 0.0001$) (Figure 6b). CD81 as a single expressed tetraspanin describes the smallest of the single expression populations with an average of 448 (GMs), respectively and 1198 particles (FMs) on average.

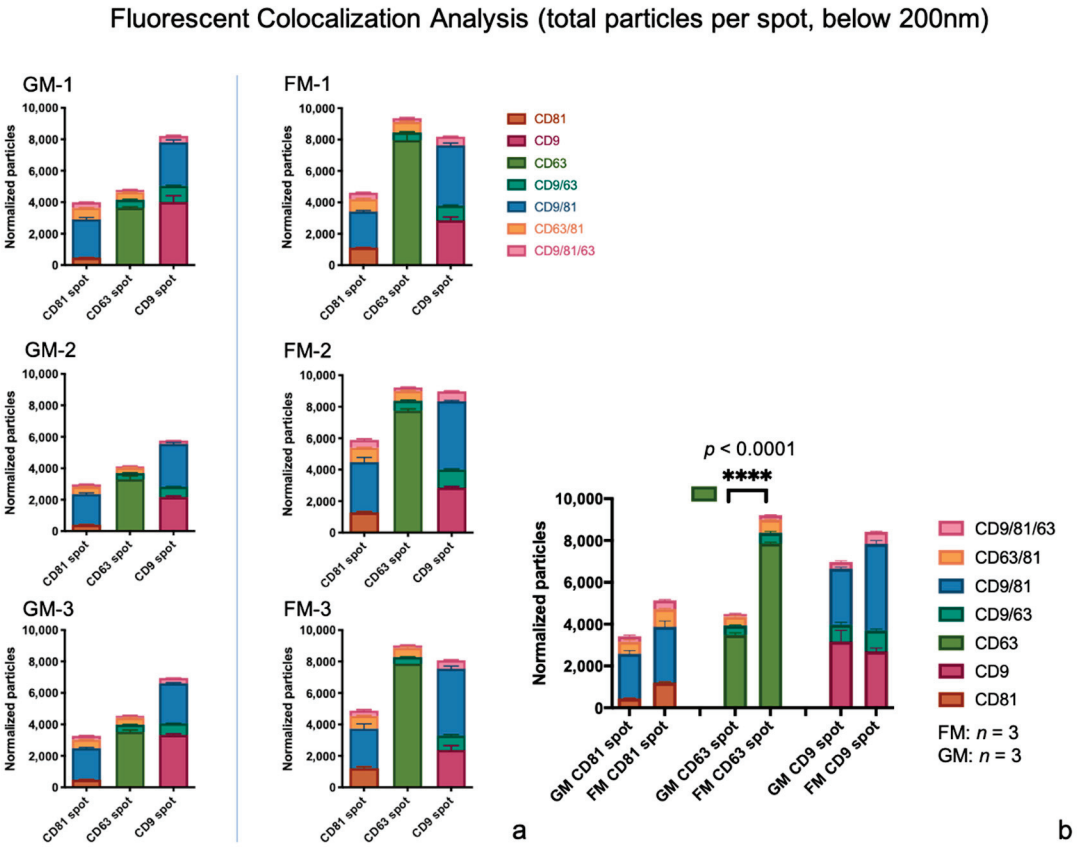


Figure 6. (**a**,**b**) The colocalization analysis of all captured particles. The particles were scanned for single expression of CD9, CD63, and CD81, as well the co-expression of two or all three tetraspanins, values are shown with SD. (**a**) The total particles by spot and per sample, displayed as actual counts. (**b**) The total fluorescent count of particles displayed as a comparison of the two sample groups combined, the displayed median of actual counts. Statistical significance is displayed as **** ($p \leq 0.0001$).

Co-expression of two Tetraspanins – CD9/CD63, CD9/CD81, and CD63/CD81

Exosomes co-expressing the tetraspanins CD9 and CD63 only differ slightly in the two experimental sets (GM and FM). In the GMs, 1243 particles were counted, in the FMs 1504 particles. Not unexpectedly, the CD9/CD81 co-expressing exosomes are the largest population of this group, with counts of 4820 particles in the GMs on average, and 6826 particles in the FMs. The CD63/CD81 population is the smallest in this group, averaging 1007 particles in GM and 1476 particles in FM (Figure 6a,b and Figure 7a,b; Tables S1 and S2).

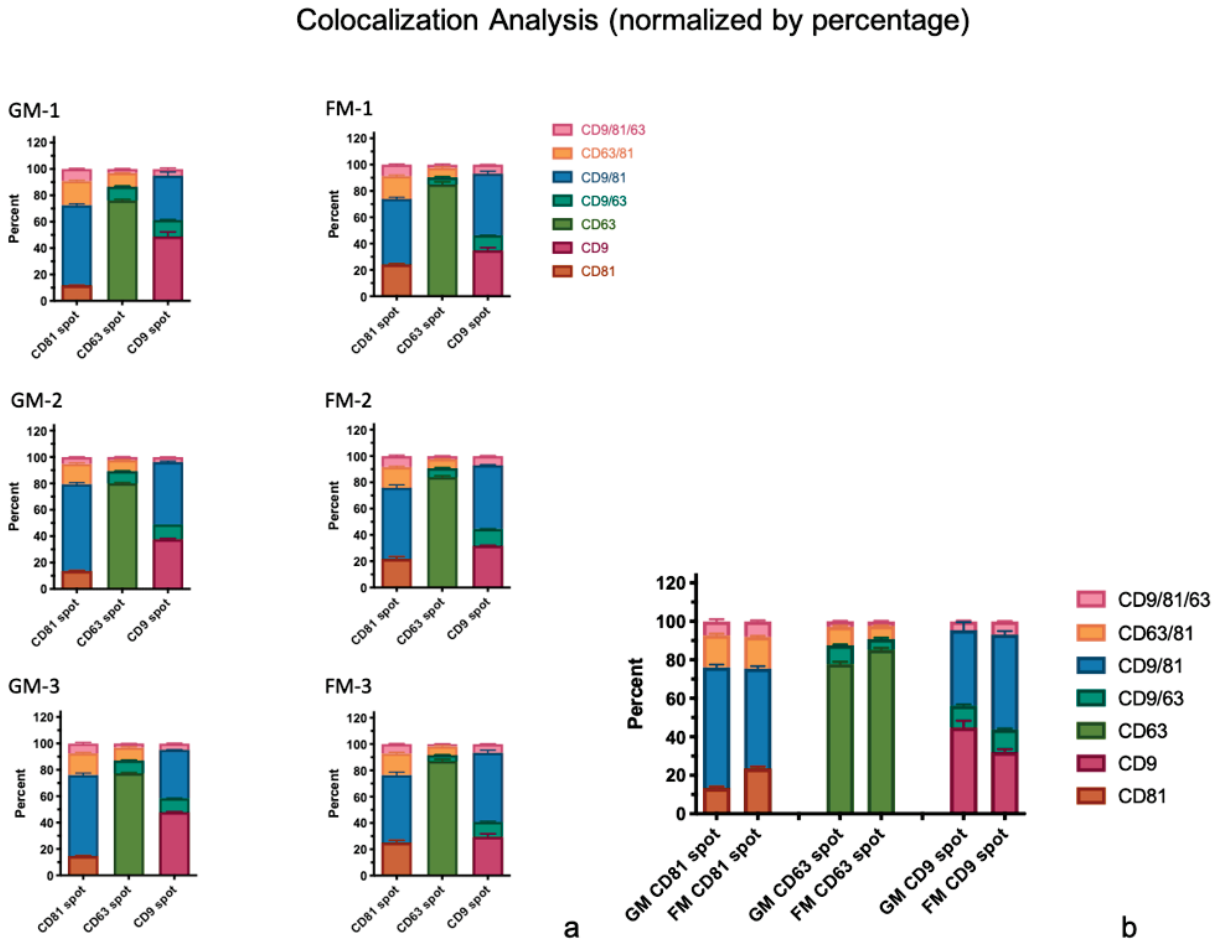


Figure 7. (**a**,**b**) The colocalization analysis of all captured particles. The particle scanned was for a single expression of CD9, CD63, and CD81, as well the co-expression of two or all three tetraspanins, values are shown with SD. (**a**) Total particles by spot and per sample, displayed as a percentage. (**b**) The total fluorescent count of particles displayed in comparison of the two sample groups combined, displayed as a median percentage.

Co-Expression of all three Tetraspanins – CD9/CD63/CD81

Exosomes found with all three tetraspanins make up the second smallest population of all, with 704 (GMs) and 1202 (FMs) counted exosomes (Figure 6a,b and Figure 7a,b; Tables S1 and S2).

3. Discussion

Since the dawn of manned spaceflight, particular attention has been given to the effects of microgravity on the human organism. These effects are extensive and span from physiological changes and adaptations all the way to altered gene expression and cellular modifications. Physiological adaptations to the cardiovascular, musculoskeletal, and sensorimotor systems and the implications of varying durations of spaceflight thereon have been studied extensively, as well as methods for the preparation and reconditioning of space travelers [62–64]. Muscle and bone loss are commonly experienced even with regular exercise prior to and during flights, and these changes can be demonstrated on both the physiological and cellular level [6,8,16].

In recent years, the importance of EVs in intercellular communication and post-transcriptional proteomic regulation, as well as disease biomarkers has been described in detail in various settings [29,65–68]. The analysis of surface markers has emerged as one defining part of EV and exosome definition and nomenclature [48,49]. With the evolving development of new analytical methods, the possibilities to study in-depth changes in EV

secretion, cargo, and population setup have increased significantly. Hence, we took this opportunity to get a view of the results of the CellBox-1 experiments from a different angle. Here, we describe initial experiments to evaluate possible changes in exosomal secretion and populations under prolonged exposure to microgravity in a human follicular thyroid cancer cell line (FTC-133), in which our group has previously studied in various conditions of weightlessness [22–24,69,70]. Through our knowledge of the genomic and proteomic changes of this particular cell line, as well as its phenotypical behavior, we are perfectly equipped to classify all the observations in this new research area.

The primary focus of these preliminary experiments on the exosomal secretion was to determine the number of secreted vesicles, their size distribution, and their population regarding the tetraspanin surface expression. These parameters would be a first indication of changes in cellular cross-talk under microgravity, and hence, would point to an adaptation of the cells to the change in environment. The broad majority of captured particles are exosomes per size definition, in the range of 50–100 nm [48,49,54]. Comparing the two sample sets, we can see a definite increase in the overall particle number in the FMs in reaction to the microgravity exposure. The relative size distribution stays comparatively the same, and the mode of particle sizes is still 60 nm, even though the total number on all the levels rose in the flight samples. The logical assumption is that, at a minimum, the amount of transferred cargo from the tumor cell to the target cell increases proportionally to the larger number of secreted vesicles, even though the actual content of exosomes can depend on various other intra- and extracellular conditions [67,71,72]. In consequence, our working hypothesis was that the change in gravitational forces should have a distinct effect on the exosome number, as well as their surface protein and cargo composition mirroring the adaptions of the cells, we have observed in this and previous experiments. This study in fact showed that the number of vesicles and the composition of sub-populations regarding their surface tetraspanin composition does considerably change under the influence of real microgravity.

The analysis by fluorescence of the EVs counterstained with the tetraspanins CD9, CD63, and CD81 further supports the previous interferometric results and allows for the detection of vesicles that fall below the lower detection limit of 50 nm allowed by the interferometric measurement. Here, though, the changes in the surface proteins expressed on the captured exosomes also exhibit a change in the sub-populations present in the GM and FM sample sets. Tetraspanins are not only valuable biomarkers that are enriched in the membranes of exosomes, they are a superfamily of proteins involved in a multitude of biological processes. Those processes include cell adhesion, motility, invasion, and membrane fusion, as well as signaling and protein trafficking [73,74]. Tetraspanins form a network with exosomal and other proteins regulating signaling transduction pathways and the formation of premetastatic sites in the tumor microenvironment (TME) [75]. Tetraspanins also play a critical role in the target cell selection for exosome uptake and, therefore, the reprogramming of the target cell. CD9, CD63, and CD81, in conjunction with other tetraspanins, promote (in association with exosomes) cancer cell motility, invasion, metastasis, tumor initiation, promotion, progression, and angiogenesis [74,75].

In the TME, CD9 suppresses motility and promotes adherence to the surrounding matrix which subsequently leads to a suppression of tumor progression. The CD9 downregulation has been correlated with tumor progression, and is often found in late-stage tumors [76]. On the other hand, CD9 has been observed to display converse activity, and therefore, it is difficult to pinpoint a specific role to this tetraspanin in regards to an increase or decrease of tumorigenicity as a result of exposure to real microgravity [76]. Additionally, CD9 is emerging as an important regulator controlling the expression and activity of different adhesion molecules, among them several metalloproteinases [77–80]. Riwaldt et al. described the gene alterations of the matrix metalloproteinases MMP3 and MMP9 and the resulting phenotypical changes in another human thyroid cancer cell line (UCLA RO 82-W-1). In this article, the authors discuss a study of pathways involved in

the transition from a two-dimensional to a three-dimensional cell growth as a result of the simulated microgravity [25].

CD63 and CD81 have been shown to be important contributors in the sorting of protein cargo to EVs. Wnt11 aids cell migration and metastasis in breast cancer cells, and the sorting of the Wnt11 cargo to EVs is supported by CD81, but not other tetraspanins [40,73]. Similarly, CD63 is a key contributor to the protein loading of intraluminal vesicles (ILVs) in the MVBs during the exosome biogenesis [73,81]. In cancer, the surface expression of CD63 is linked to tumor cell motility, and a decrease of this tetraspanin is linked to the increased malignancy and higher chances of metastasis [82,83]. The results of the CellBox-1 experiments show a high expression of CD63, with an additional increase with exposure to microgravity. Whether this leads to changes in the tumorigenic behavior of FTC-133 or in the cargo of the secreted exosomes will have to be determined in further studies. Further, CD81 has been found to contribute to tumor progression and an enhanced metastatic phenotype [84–87]. As with CD63, at this stage of the investigation, one cannot attribute a particular change in function to the observed changes without further experimentation.

Co-expression of CD9/CD81 was shown to regulate TGF-β1 signaling in melanoma by providing critical support for the TGFβR2-TGFβR1 association, which in turns favors epithelial to mesenchymal transition-like changes, invasion, and metastases [87]. In this study, we have shown an increase in the CD9/CD81 population in the FMs compared to GMs, but whether this could point to a transition of a more aggressive stage in the FTC-133 cells is another hypothesis that requires further data in order to be adequately discussed.

To conclude, it would certainly be very interesting to evaluate the changes in the exosomal proteomic cargo following prolonged exposure to microgravity in comparison to the results gained from the proteomic analysis of the FTC-133 cells of the CellBox-1 mission [23,24]. This would give an even deeper insight into the cellular regulation post-transcription and could not only enhance our knowledge of these pathways, but also point towards a direction for future treatment regimens. This demonstrates the vast possibilities promised by EVs in the medical field, and is surely worth further exploration.

4. Materials and Methods

4.1. Cell Cultures

Human follicular thyroid cancer cells (FTC-133), purchased from the Health Protection Agency Culture Collections (HPACC, Salisbury, UK), were cultured in RPMI-1640 (Invitrogen, Eggenstein, Germany), supplemented with 10% fetal calf serum (FCS, Biochrom, Berlin, Germany), penicillin (100 U/mL; Merck Millipore), and streptomycin (100 µg/mL; Merck Millipore) at 37 °C and 5% CO_2, as described previously. Prior to the start of the experiment, 10^6 cells were loaded into an automated cell culture system, the FM hardware [22], or alternatively seeded in T-25 culture flasks for the ground control experiments. The medium exchange and cell fixation at the experimental endpoint occurred automatically as scheduled [23].

4.2. CellBox-1 Spaceflight Experiment

The CellBox-1 spaceflight experiment was part of the SpaceX CRS-3 Commercial Resupply Service mission, launched on 18 April, 2014 (https://www.dlr.de/content/de/bilder/2014/2/start-des-des-cellbox-experiments_15157.html (accessed on 20 February 2021)) and is reported in detail by Riwaldt et al. [23]. In brief, 1×10^6 FTC-133 was seeded in nine cell containers (FM) and incubated at 37 °C and 5% CO_2. 24 h prior to launch, three FMs were transferred to an incubation chamber at 23 °C at Cape Canaveral to serve as ground controls (GM). The remaining six FMs were moved to the Dragon capsule and flown to the International Space Station (ISS). Upon arrival at the ISS, the FMs were incubated continuously at 23 °C at a *g*-force oscillating around ± 0.005 g. After 12 days of microgravity, the cells of three FMs were fixed using RNA*later* via an automated process [22], collecting the aspirated media. The remaining three FMs were continuously incubated at 23 °C for the remainder of the spaceflight and therefore, not included in this

analysis. The GMs were treated identically and simultaneously on the ground. 48 h post-fixation, both the FMs and GMs were cooled to 4 °C. After the return of the Dragon vessel on 20 May 2014, all the containers were returned to the lab for cell and cell supernatant harvest (Figure 8).

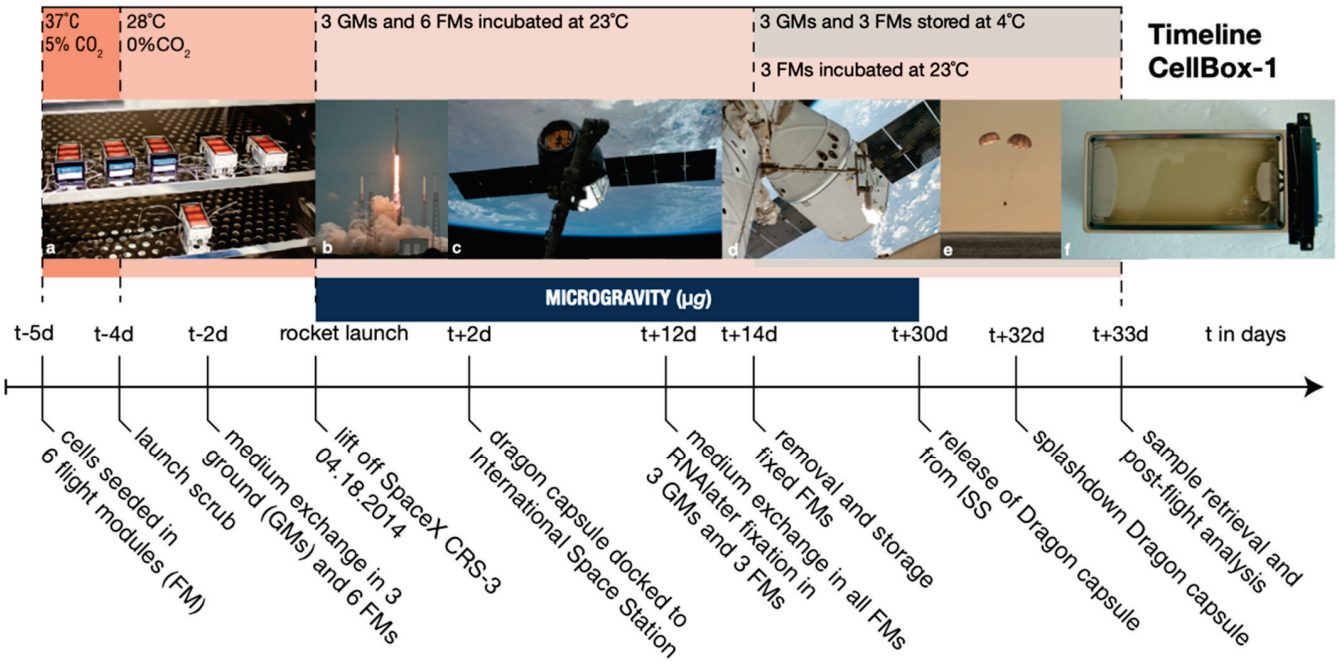


Figure 8. Timeline of the CellBox-1 experiment. (**a**) Six flight modules (FMs) incubated at 37 °C, 5% CO_2. Each container filled with 1×10^6 FTC-133 thyroid cancer cells. (**b**) Falcon-9 lift-off within Cargo Resupply Services mission 3 (SpaceX CRS-3). (**c**) SpaceX Dragon capsule arrives at the International Space Station (ISS). (**d**) Dragon capsule docked to ISS. (**e**) Dragon capsule splashdown into the Pacific Ocean. (**f**) Flight module prior to sample collection and post-flight analysis. (Picture a courtesy of RaisFoto, pictures **b**–**e** photo credit SpaceX).

4.3. Exosome Harvest and Isolation

After the harvest, the cell supernatants of the FMs and GMs were subjected to an adjusted differential centrifugation protocol [88] using a swinging bucket rotor, consisting of two consecutive spins at 300× *g* (10 min, 4 °C) followed by centrifugation at 2500× *g* (15 min, 4 °C, twice) to pellet cells, cell debris, and large vesicles. High speed centrifugation was not necessary as the analysis via ExoView®does not require a preceding particle isolation. The collected supernatants were divided into 2 mL aliquots and stored at −80 °C until further analysis.

4.4. ExoView® Kit Assay Procedure

For the capture and analysis of the CellBox-1 supernatants, the EV-TETRA-C ExoView Tetraspanin Kit (NanoView Biosciences, Boston, MA, USA) was used, with all samples processed and stained according to the manufacturer's protocol. The spots on the chip plates were coated with antibodies for the tetraspanins CD9, CD81, and CD63, as well as an IgG negative control, all in triplicates. In short, the samples were diluted 1:2 and incubated ON at RT on the sealed chip plate in order to capture the exosomes present. The incubation was followed by three wash steps prior to the surface membrane immunofluorescence staining. An antibody mixture containing fluorescently labeled anti-CD9 (CF® 488A), anti-CD81 (CF® 555), and anti-CD63 (CF® 647) was pipetted onto the chip and incubated for 1 h on an orbital shaker, blocked from light exposure. Three wash steps with the supplied wash buffer and two washes with DI water for 3 min each (RT, shaking, light omitted) followed this incubation. Subsequently, the chip plates were dried and scanned as described below.

4.5. Digital Detection of Exosomes

The chip plates were scanned using the ExoView R100 (NanoView Biosciences, Boston, MA, USA) in combination with the ExoScan software. All the chip plates used were pre-scanned prior to the exosome capture to obtain a baseline signal, then the exosome-laden chips were scanned identically positioned on the stage platform. The analysis was visualized with the ExoView software, resulting in the EV count, size distribution, and colocalization of EV subpopulations.

4.6. Statistical Analysis

The total counts of numbers were analyzed via the unpaired *t*-test, comparing all the samples from either the GM or FM group respective to the capture spot on the chip plate, CD9, CD63, or CD81. The analysis was conducted using the GraphPad Prism 9 software (GraphPad Software, San Diego, CA, USA).

5. Conclusions

This initial analysis of secreted EVs harvested from human follicular thyroid cells that were either subjected to real microgravity on the ISS or grown on Earth is a first step towards evaluating the feasibility of future experiments with exosomes, and the range of questions that such experiments could answer. The changes and adaptations we have observed promise to enhance our understanding of the changes and adaptations of the human organism to microgravity exposure on a cellular level. Additionally, these studies may offer new biomarkers and therapeutic approaches for multiple clinical pictures.

Supplementary Materials: The following are available online at https://www.mdpi.com/1422-0067/22/4/2132/s1. Figure S1: Total count of captured particles via the interferometric analysis; Table S1: Absolute values of colocalization analysis; Table S2: Colocalization analysis calculated as percentages.

Author Contributions: Conceptualization, P.M.W. and D.G.; methodology, P.M.W. and P.N.; software, P.M.W. and P.N.; validation, D.G., P.M.W. and M.W.; formal analysis, P.M.W. and P.N.; investigation, P.M.W., P.N., S.R., M.W. and M.B.; resources, M.B., M.I. and D.G.; writing—original draft preparation, P.M.W.; writing—review and editing, D.G., T.J.C., M.K. and M.W.; visualization, P.M.W. and M.K.; supervision, D.G. and P.M.W.; project administration, D.G.; funding acquisition, D.G. and M.I. All authors have read and agreed to the published version of the manuscript.

Funding: This research was funded by Deutsches Zentrum für Luft- und Raumfahrt (DLR), BMWi projects 50WB1524 and 50WB1924 (D.G.).

Institutional Review Board Statement: Not applicable.

Informed Consent Statement: Not applicable.

Data Availability Statement: Not applicable.

Acknowledgments: The authors would like to thank Jessica Pietsch, Berlin, Germany, for her contributions and support for the CellBox-1 mission. We would also like to thank Guenter Ruyters and Peter Preu from the DLR Space Administration, Bonn, Germany, for giving us the opportunity to participate in the SpaceX CRS-3 Mission. Finally, we would like to thank NASA, the companies SpaceX and Airbus Defence and Space for bringing our cells to the International Space Station.

Conflicts of Interest: The authors declare no conflict of interest.

Abbreviations

AB	Antibody
EMT	Epithelial to Mesenchymal Transition
EV	Extracellular Vesicle
GM	Ground Module
FM	Flight Module
ILV	Intraluminal Vesicle

MVBs	Multivesicular Bodies
NTA	Nanoparticle Tracking Analysis
ON	Overnight
RPM	Random Positioning Machine
RT	Room temperature
SD	Standard Deviation
SP-IRIS	Single Particle Interferometric Reflectance Imaging Sensor
TME	Tumor Microenvironment

References

1. NASA. First Human-Made Object to Enter Space. Available online: https://www.nasa.gov/mission_pages/explorer/bumper.html (accessed on 7 August 2020).
2. NASA. Space Programs. Available online: http://adc.gsfc.nasa.gov/adc/education/space_ex/probes.html (accessed on 2 July 2020).
3. Mann, A. The Vostok Program: The Soviet's First Crewed Spaceflight Program. Available online: https://www.space.com/vostok-program.html (accessed on 28 July 2020).
4. SpaceX. Space Station—Transporting Humans to the Orbiting Laboratory. Available online: https://www.spacex.com/human-spaceflight/iss/index.html (accessed on 28 July 2020).
5. Baldwin, K.M. Effect of spaceflight on the functional, biochemical, and metabolic properties of skeletal muscle. *Med. Sci. Sports Exerc.* **1996**, *28*, 983–987. [CrossRef]
6. Baldwin, K.M.; White, T.P.; Arnaud, S.B.; Edgerton, V.R.; Kraemer, W.J.; Kram, R.; Raab-Cullen, D.; Snow, C.M. Musculoskeletal adaptations to weightlessness and development of effective countermeasures. *Med. Sci. Sports Exerc.* **1996**, *28*, 1247–1253. [CrossRef]
7. Stampi, C. Sleep and circadian rhythms in space. *J. Clin. Pharmacol.* **1994**, *34*, 518–534. [CrossRef]
8. Strollo, F. Hormonal changes in humans during spaceflight. *Adv. Space Biol. Med.* **1999**, *7*, 99–129. [CrossRef]
9. Taylor, G.R. Overview of spaceflight immunology studies. *J. Leukoc. Biol.* **1993**, *54*, 179–188. [CrossRef] [PubMed]
10. White, R.J.; Averner, M. Humans in space. *Nature* **2001**, *409*, 1115–1118. [CrossRef]
11. White, R.J. Weightlessness and the human body. *Sci. Am.* **1998**, *279*, 58–63. [CrossRef] [PubMed]
12. Garrett-Bakelman, F.E.; Darshi, M.; Green, S.J.; Gur, R.C.; Lin, L.; Macias, B.R.; McKenna, M.J.; Meydan, C.; Mishra, T.; Nasrini, J.; et al. The NASA Twins Study: A multidimensional analysis of a year-long human spaceflight. *Science* **2019**, *364*. [CrossRef]
13. Battista, N.; Meloni, M.A.; Bari, M.; Mastrangelo, N.; Galleri, G.; Rapino, C.; Dainese, E.; Agrò, A.F.; Pippia, P.; Maccarrone, M. 5-Lipoxygenase-dependent apoptosis of human lymphocytes in the International Space Station: Data from the ROALD experiment. *FASEB J.* **2012**, *26*, 1791–1798. [CrossRef] [PubMed]
14. Herranz, R.; Anken, R.; Boonstra, J.; Braun, M.; Christianen, P.C.; de Geest, M.; Hauslage, J.; Hilbig, R.; Hill, R.J.; Lebert, M.; et al. Ground-based facilities for simulation of microgravity: Organism-specific recommendations for their use, and recommended terminology. *Astrobiology* **2013**, *13*, 1–17. [CrossRef] [PubMed]
15. Hoson, T.; Kamisaka, S.; Masuda, Y.; Yamashita, M.; Buchen, B. Evaluation of the three-dimensional clinostat as a simulator of weightlessness. *Planta* **1997**, *203 Suppl*, S187–S197. [CrossRef]
16. Pietsch, J.; Bauer, J.; Egli, M.; Infanger, M.; Wise, P.; Ulbrich, C.; Grimm, D. The effects of weightlessness on the human organism and mammalian cells. *Curr. Mol. Med.* **2011**, *11*, 350–364. [CrossRef]
17. van Loon, J. Some history and use of the random positioning machine, RPM, in gravity related research. *Adv. Space Res.* **2007**, *39*, 1161–1165. [CrossRef]
18. Maccarrone, M.; Battista, N.; Meloni, M.; Bari, M.; Galleri, G.; Pippia, P.; Cogoli, A.; Finazzi-Agrò, A. Creating conditions similar to those that occur during exposure of cells to microgravity induces apoptosis in human lymphocytes by 5-lipoxygenase-mediated mitochondrial uncoupling and cytochrome c release. *J. Leukoc. Biol.* **2003**, *73*, 472–481. [CrossRef]
19. Schwarzenberg, M.; Pippia, P.; Meloni, M.A.; Cossu, G.; Cogoli-Greuter, M.; Cogoli, A. Signal transduction in T lymphocytes–a comparison of the data from space, the free fall machine and the random positioning machine. *Adv. Space Res.* **1999**, *24*, 793–800. [CrossRef]
20. German Aerospace Center (DLR). Germany and China—Joint Experiments in Space. Available online: https://www.dlr.de/content/en/downloads/news-archive/2011/20111101_germany-and-china---joint-experiments-in-space_1805.pdf?__blob=publicationFile&v=10 (accessed on 1 November 2011).
21. Kramer, C.D.; Kalla, E.M. The challenge of designing biomedical equipment during human research for long duration low-gravity NASA missions. In Proceedings of the 1997 16 Southern Biomedical Engineering Conference, Biloxi, MS, USA, 4–6 April 1997; pp. 30–37. [CrossRef]
22. Pietsch, J.; Ma, X.; Wehland, M.; Aleshcheva, G.; Schwarzwälder, A.; Segerer, J.; Birlem, M.; Horn, A.; Bauer, J.; Infanger, M.; et al. Spheroid formation of human thyroid cancer cells in an automated culturing system during the Shenzhou-8 Space mission. *Biomaterials* **2013**, *34*, 7694–7705. [CrossRef]

23. Riwaldt, S.; Pietsch, J.; Sickmann, A.; Bauer, J.; Braun, M.; Segerer, J.; Schwarzwälder, A.; Aleshcheva, G.; Corydon, T.J.; Infanger, M.; et al. Identification of proteins involved in inhibition of spheroid formation under microgravity. *Proteomics* **2015**, *15*, 2945–2952. [CrossRef] [PubMed]
24. Riwaldt, S.; Bauer, J.; Pietsch, J.; Braun, M.; Segerer, J.; Schwarzwälder, A.; Corydon, T.J.; Infanger, M.; Grimm, D. The Importance of Caveolin-1 as Key-Regulator of Three-Dimensional Growth in Thyroid Cancer Cells Cultured under Real and Simulated Microgravity Conditions. *Int. J. Mol. Sci.* **2015**, *16*, 28296–28310. [CrossRef]
25. Riwaldt, S.; Bauer, J.; Wehland, M.; Slumstrup, L.; Kopp, S.; Warnke, E.; Dittrich, A.; Magnusson, N.E.; Pietsch, J.; Corydon, T.J.; et al. Pathways Regulating Spheroid Formation of Human Follicular Thyroid Cancer Cells under Simulated Microgravity Conditions: A Genetic Approach. *Int. J. Mol. Sci.* **2016**, *17*, 528. [CrossRef] [PubMed]
26. Colombo, M.; Raposo, G.; Théry, C. Biogenesis, secretion, and intercellular interactions of exosomes and other extracellular vesicles. *Annu. Rev. Cell Dev. Biol.* **2014**, *30*, 255–289. [CrossRef]
27. Quek, C.; Hill, A.F. The role of extracellular vesicles in neurodegenerative diseases. *Biochem. Biophys. Res. Commun.* **2017**, *483*, 1178–1186. [CrossRef]
28. Bank, I.E.; Timmers, L.; Gijsberts, C.M.; Zhang, Y.N.; Mosterd, A.; Wang, J.W.; Chan, M.Y.; De Hoog, V.; Lim, S.K.; Sze, S.K.; et al. The diagnostic and prognostic potential of plasma extracellular vesicles for cardiovascular disease. *Expert Rev. Mol. Diagn.* **2015**, *15*, 1577–1588. [CrossRef] [PubMed]
29. Abels, E.R.; Breakefield, X.O. Introduction to Extracellular Vesicles: Biogenesis, RNA Cargo Selection, Content, Release, and Uptake. *Cell. Mol. Neurobiol.* **2016**, *36*, 301–312. [CrossRef] [PubMed]
30. Orozco, A.F.; Lewis, D.E. Flow cytometric analysis of circulating microparticles in plasma. *Cytometry A* **2010**, *77*, 502–514. [CrossRef]
31. Gonzales, P.A.; Pisitkun, T.; Hoffert, J.D.; Tchapyjnikov, D.; Star, R.A.; Kleta, R.; Wang, N.S.; Knepper, M.A. Large-scale proteomics and phosphoproteomics of urinary exosomes. *J. Am. Soc. Nephrol.* **2009**, *20*, 363–379. [CrossRef] [PubMed]
32. Sharma, S.; Gillespie, B.M.; Palanisamy, V.; Gimzewski, J.K. Quantitative nanostructural and single-molecule force spectroscopy biomolecular analysis of human-saliva-derived exosomes. *Langmuir* **2011**, *27*, 14394–14400. [CrossRef]
33. Al-Nedawi, K.; Meehan, B.; Micallef, J.; Lhotak, V.; May, L.; Guha, A.; Rak, J. Intercellular transfer of the oncogenic receptor EGFRvIII by microvesicles derived from tumour cells. *Nat. Cell Biol.* **2008**, *10*, 619–624. [CrossRef]
34. Andreola, G.; Rivoltini, L.; Castelli, C.; Huber, V.; Perego, P.; Deho, P.; Squarcina, P.; Accornero, P.; Lozupone, F.; Lugini, L.; et al. Induction of lymphocyte apoptosis by tumor cell secretion of FasL-bearing microvesicles. *J. Exp. Med.* **2002**, *195*, 1303–1316. [CrossRef] [PubMed]
35. Huber, V.; Fais, S.; Iero, M.; Lugini, L.; Canese, P.; Squarcina, P.; Zaccheddu, A.; Colone, M.; Arancia, G.; Gentile, M.; et al. Human colorectal cancer cells induce T-cell death through release of proapoptotic microvesicles: Role in immune escape. *Gastroenterology* **2005**, *128*, 1796–1804. [CrossRef] [PubMed]
36. Skog, J.; Würdinger, T.; van Rijn, S.; Meijer, D.H.; Gainche, L.; Sena-Esteves, M.; Curry, W.T.; Carter, B.S.; Krichevsky, A.M.; Breakefield, X.O. Glioblastoma microvesicles transport RNA and proteins that promote tumour growth and provide diagnostic biomarkers. *Nat. Cell Biol.* **2008**, *10*, 1470–1476. [CrossRef]
37. Richards, K.E.; Zeleniak, A.E.; Fishel, M.L.; Wu, J.; Littlepage, L.E.; Hill, R. Cancer-associated fibroblast exosomes regulate survival and proliferation of pancreatic cancer cells. *Oncogene* **2017**, *36*, 1770–1778. [CrossRef] [PubMed]
38. Au Yeung, C.L.; Co, N.N.; Tsuruga, T.; Yeung, T.L.; Kwan, S.Y.; Leung, C.S.; Li, Y.; Lu, E.S.; Kwan, K.; Wong, K.K.; et al. Exosomal transfer of stroma-derived miR21 confers paclitaxel resistance in ovarian cancer cells through targeting APAF1. *Nat. Commun.* **2016**, *7*, 11150. [CrossRef] [PubMed]
39. Leca, J.; Martinez, S.; Lac, S.; Nigri, J.; Secq, V.; Rubis, M.; Bressy, C.; Sergé, A.; Lavaut, M.N.; Dusetti, N.; et al. Cancer-associated fibroblast-derived annexin A6+ extracellular vesicles support pancreatic cancer aggressiveness. *J. Clin. Investig.* **2016**, *126*, 4140–4156. [CrossRef] [PubMed]
40. Luga, V.; Zhang, L.; Viloria-Petit, A.M.; Ogunjimi, A.A.; Inanlou, M.R.; Chiu, E.; Buchanan, M.; Hosein, A.N.; Basik, M.; Wrana, J.L. Exosomes mediate stromal mobilization of autocrine Wnt-PCP signaling in breast cancer cell migration. *Cell* **2012**, *151*, 1542–1556. [CrossRef] [PubMed]
41. Whiteside, T.L. Tumor-Derived Exosomes and Their Role in Tumor-Induced Immune Suppression. *Vaccines* **2016**, *4*, 35. [CrossRef] [PubMed]
42. Peinado, H.; Alečković, M.; Lavotshkin, S.; Matei, I.; Costa-Silva, B.; Moreno-Bueno, G.; Hergueta-Redondo, M.; Williams, C.; García-Santos, G.; Ghajar, C.; et al. Melanoma exosomes educate bone marrow progenitor cells toward a pro-metastatic phenotype through MET. *Nat. Med.* **2012**, *18*, 883–891. [CrossRef]
43. Somasundaram, R.; Herlyn, M. Melanoma exosomes: Messengers of metastasis. *Nat. Med.* **2012**, *18*, 853–854. [CrossRef]
44. Alderton, G.K. Metastasis. Exosomes drive premetastatic niche formation. *Nat. Rev. Cancer* **2012**, *12*, 447. [CrossRef]
45. Hood, J.L.; San, R.S.; Wickline, S.A. Exosomes released by melanoma cells prepare sentinel lymph nodes for tumor metastasis. *Cancer Res.* **2011**, *71*, 3792–3801. [CrossRef]
46. Costa-Silva, B.; Aiello, N.M.; Ocean, A.J.; Singh, S.; Zhang, H.; Thakur, B.K.; Becker, A.; Hoshino, A.; Mark, M.T.; Molina, H.; et al. Pancreatic cancer exosomes initiate pre-metastatic niche formation in the liver. *Nat. Cell Biol.* **2015**, *17*, 816–826. [CrossRef]
47. Nogués, L.; Benito-Martin, A.; Hergueta-Redondo, M.; Peinado, H. The influence of tumour-derived extracellular vesicles on local and distal metastatic dissemination. *Mol. Aspects Med.* **2018**, *60*, 15–26. [CrossRef] [PubMed]

48. Lötvall, J.; Hill, A.F.; Hochberg, F.; Buzás, E.I.; Di Vizio, D.; Gardiner, C.; Gho, Y.S.; Kurochkin, I.V.; Mathivanan, S.; Quesenberry, P.; et al. Minimal experimental requirements for definition of extracellular vesicles and their functions: A position statement from the International Society for Extracellular Vesicles. *J. Extracell. Vesicles* **2014**, *3*, 26913. [CrossRef]
49. Théry, C.; Witwer, K.W.; Aikawa, E.; Alcaraz, M.J.; Anderson, J.D.; Andriantsitohaina, R.; Antoniou, A.; Arab, T.; Archer, F.; Atkin-Smith, G.K.; et al. Minimal information for studies of extracellular vesicles 2018 (MISEV2018): A position statement of the International Society for Extracellular Vesicles and update of the MISEV2014 guidelines. *J. Extracell. Vesicles* **2018**, *7*, 1535750. [CrossRef]
50. Hessvik, N.P.; Llorente, A. Current knowledge on exosome biogenesis and release. *Cell Mol. Life Sci.* **2018**, *75*, 193–208. [CrossRef] [PubMed]
51. Hartjes, T.A.; Mytnyk, S.; Jenster, G.W.; van Steijn, V.; van Royen, M.E. Extracellular Vesicle Quantification and Characterization: Common Methods and Emerging Approaches. *Bioengineering* **2019**, *6*, 7. [CrossRef]
52. Filipe, V.; Hawe, A.; Jiskoot, W. Critical evaluation of Nanoparticle Tracking Analysis (NTA) by NanoSight for the measurement of nanoparticles and protein aggregates. *Pharm Res.* **2010**, *27*, 796–810. [CrossRef] [PubMed]
53. Daaboul, G.G.; Gagni, P.; Benussi, L.; Bettotti, P.; Ciani, M.; Cretich, M.; Freedman, D.S.; Ghidoni, R.; Ozkumur, A.Y.; Piotto, C.; et al. Digital Detection of Exosomes by Interferometric Imaging. *Sci. Rep.* **2016**, *6*, 37246. [CrossRef]
54. Lässer, C.; Eldh, M.; Lötvall, J. Isolation and characterization of RNA-containing exosomes. *J. Vis. Exp.* **2012**, *59*, e3037. [CrossRef] [PubMed]
55. Avci, O.; Ünlü, N.L.; Özkumur, A.Y.; Ünlü, M.S. Interferometric Reflectance Imaging Sensor (IRIS)–A Platform Technology for Multiplexed Diagnostics and Digital Detection. *Sensors* **2015**, *15*, 17649–17665. [CrossRef] [PubMed]
56. Harding, C.; Stahl, P. Transferrin recycling in reticulocytes: pH and iron are important determinants of ligand binding and processing. *Biochem. Biophys. Res. Commun.* **1983**, *113*, 650–658. [CrossRef]
57. Pan, B.T.; Johnstone, R.M. Fate of the transferrin receptor during maturation of sheep reticulocytes in vitro: Selective externalization of the receptor. *Cell* **1983**, *33*, 967–978. [CrossRef]
58. Lane, R.E.; Korbie, D.; Trau, M.; Hill, M.M. Purification Protocols for Extracellular Vesicles. *Methods Mol. Biol.* **2017**, *1660*, 111–130. [CrossRef] [PubMed]
59. Gardiner, C.; Di Vizio, D.; Sahoo, S.; Théry, C.; Witwer, K.W.; Wauben, M.; Hill, A.F. Techniques used for the isolation and characterization of extracellular vesicles: Results of a worldwide survey. *J. Extracell. Vesicles* **2016**, *5*, 32945. [CrossRef] [PubMed]
60. Shu, S.; Yang, Y.; Allen, C.L.; Hurley, E.; Tung, K.H.; Minderman, H.; Wu, Y.; Ernstoff, M.S. Purity and yield of melanoma exosomes are dependent on isolation method. *J. Extracell. Vesicles* **2020**, *9*, 1692401. [CrossRef]
61. Brown, P.N.; Yin, H. Polymer-Based Purification of Extracellular Vesicles. *Methods Mol. Biol.* **2017**, *1660*, 91–103. [CrossRef]
62. Lambrecht, G.; Petersen, N.; Weerts, G.; Pruett, C.; Evetts, S.; Stokes, M.; Hides, J. The role of physiotherapy in the European Space Agency strategy for preparation and reconditioning of astronauts before and after long duration space flight. *Musculoskelet Sci. Pract.* **2017**, *27 Suppl 1*, S15–S22. [CrossRef]
63. Barratt, M.R.P.; Pool, S.L. (Eds.) *Principles of Clinical Medicine for Space Flight*, 1st ed.; Springer-Verlag: New York, NY, USA, 2008; p. 596. [CrossRef]
64. Petersen, N.; Lambrecht, G.; Scott, J.; Hirsch, N.; Stokes, M.; Mester, J. Postflight reconditioning for European Astronauts—A case report of recovery after six months in space. *Musculoskelet. Sci. Pract.* **2017**, *27 Suppl 1*, S23–S31. [CrossRef]
65. Claridge, B.; Kastaniegaard, K.; Stensballe, A.; Greening, D.W. Post-translational and transcriptional dynamics—regulating extracellular vesicle biology. *Expert Rev. Proteom.* **2019**, *16*, 17–31. [CrossRef]
66. Challagundla, K.B.; Fanini, F.; Vannini, I.; Wise, P.; Murtadha, M.; Malinconico, L.; Cimmino, A.; Fabbri, M. microRNAs in the tumor microenvironment: Solving the riddle for a better diagnostics. *Expert Rev. Mol. Diagn.* **2014**, *14*, 565–574. [CrossRef]
67. Challagundla, K.; Wise, P.; Fabbri, M. Exosomic microRNAs and Drug Resistance in the Neuroblastoma Environment. Poster Presentation, 2013.
68. Barile, L.; Vassalli, G. Exosomes: Therapy delivery tools and biomarkers of diseases. *Pharmacol. Ther.* **2017**, *174*, 63–78. [CrossRef]
69. Grosse, J.; Wehland, M.; Pietsch, J.; Schulz, H.; Saar, K.; Hübner, N.; Eilles, C.; Bauer, J.; Abou-El-Ardat, K.; Baatout, S.; et al. Gravity-sensitive signaling drives 3-dimensional formation of multicellular thyroid cancer spheroids. *FASEB J.* **2012**, *26*, 5124–5140. [CrossRef]
70. Ma, X.; Pietsch, J.; Wehland, M.; Schulz, H.; Saar, K.; Hübner, N.; Bauer, J.; Braun, M.; Schwarzwälder, A.; Segerer, J.; et al. Differential gene expression profile and altered cytokine secretion of thyroid cancer cells in space. *FASEB J.* **2014**, *28*, 813–835. [CrossRef] [PubMed]
71. Fabbri, M.; Paone, A.; Calore, F.; Galli, R.; Gaudio, E.; Santhanam, R.; Lovat, F.; Fadda, P.; Mao, C.; Nuovo, G.J.; et al. MicroRNAs bind to Toll-like receptors to induce prometastatic inflammatory response. *Proc. Natl. Acad. Sci. USA* **2012**, *109*, E2110–E2116. [CrossRef] [PubMed]
72. Murtadha, M.; Wise, P.; Neviani, P.; Challagundla, K.; Frediani, J.; Fabbri, M. TLR8 dependent economic miR0192 secreted by tumor associated macrophages (TAMs) modulates MYC and induces chemoresistance in neuroblastoma (NB). TSRI Poster Presentation, 2016.
73. Andreu, Z.; Yáñez-Mó, M. Tetraspanins in extracellular vesicle formation and function. *Front. Immunol.* **2014**, *5*, 442. [CrossRef] [PubMed]

74. French, K.C.; Antonyak, M.A.; Cerione, R.A. Extracellular vesicle docking at the cellular port: Extracellular vesicle binding and uptake. *Semin. Cell Dev. Biol.* **2017**, *67*, 48–55. [CrossRef] [PubMed]
75. Malla, R.R.; Pandrangi, S.; Kumari, S.; Gavara, M.M.; Badana, A.K. Exosomal tetraspanins as regulators of cancer progression and metastasis and novel diagnostic markers. *Asia Pac. J. Clin. Oncol.* **2018**, *14*, 383–391. [CrossRef] [PubMed]
76. Zöller, M. Tetraspanins: Push and pull in suppressing and promoting metastasis. *Nat. Rev. Cancer* **2009**, *9*, 40–55. [CrossRef]
77. Reyes, R.; Cardeñes, B.; Machado-Pineda, Y.; Cabañas, C. Tetraspanin CD9: A Key Regulator of Cell Adhesion in the Immune System. *Front. Immunol.* **2018**, *9*, 863. [CrossRef] [PubMed]
78. Scheller, J.; Chalaris, A.; Garbers, C.; Rose-John, S. ADAM17: A molecular switch to control inflammation and tissue regeneration. *Trends Immunol.* **2011**, *32*, 380–387. [CrossRef] [PubMed]
79. Reiss, K.; Saftig, P. The "a disintegrin and metalloprotease" (ADAM) family of sheddases: Physiological and cellular functions. *Semin. Cell Dev. Biol.* **2009**, *20*, 126–137. [CrossRef] [PubMed]
80. Edwards, D.R.; Handsley, M.M.; Pennington, C.J. The ADAM metalloproteinases. *Mol. Aspects Med.* **2008**, *29*, 258–289. [CrossRef]
81. Simons, M.; Raposo, G. Exosomes—Vesicular carriers for intercellular communication. *Curr. Opin. Cell Biol.* **2009**, *21*, 575–581. [CrossRef]
82. Pols, M.S.; Klumperman, J. Trafficking and function of the tetraspanin CD63. *Exp. Cell Res.* **2009**, *315*, 1584–1592. [CrossRef]
83. Zhijun, X.; Shulan, Z.; Zhuo, Z. Expression and significance of the protein and mRNA of metastasis suppressor gene ME491/CD63 and integrin alpha5 in ovarian cancer tissues. *Eur. J. Gynaecol. Oncol.* **2007**, *28*, 179–183. [PubMed]
84. Vences-Catalán, F.; Levy, S. Immune Targeting of Tetraspanins Involved in Cell Invasion and Metastasis. *Front Immunol.* **2018**, *9*, 1277. [CrossRef]
85. Vences-Catalán, F.; Rajapaksa, R.; Srivastava, M.K.; Marabelle, A.; Kuo, C.C.; Levy, R.; Levy, S. Tetraspanin CD81 promotes tumor growth and metastasis by modulating the functions of T regulatory and myeloid-derived suppressor cells. *Cancer Res.* **2015**, *75*, 4517–4526. [CrossRef] [PubMed]
86. Hong, I.K.; Byun, H.J.; Lee, J.; Jin, Y.J.; Wang, S.J.; Jeoung, D.I.; Kim, Y.M.; Lee, H. The tetraspanin CD81 protein increases melanoma cell motility by up-regulating metalloproteinase MT1-MMP expression through the pro-oncogenic Akt-dependent Sp1 activation signaling pathways. *J. Biol. Chem.* **2014**, *289*, 15691–15704. [CrossRef]
87. Wang, H.X.; Sharma, C.; Knoblich, K.; Granter, S.R.; Hemler, M.E. EWI-2 negatively regulates TGF-β signaling leading to altered melanoma growth and metastasis. *Cell Res.* **2015**, *25*, 370–385. [CrossRef]
88. Théry, C.; Amigorena, S.; Raposo, G.; Clayton, A. Isolation and characterization of exosomes from cell culture supernatants and biological fluids. *Curr. Protoc. Cell Biol.* **2006**, *30*, 3–22. [CrossRef] [PubMed]

International Journal of
Molecular Sciences

MDPI

Article

Changes in Exosomal miRNA Composition in Thyroid Cancer Cells after Prolonged Exposure to Real Microgravity in Space

Petra M. Wise [1], Paolo Neviani [1], Stefan Riwaldt [2], Thomas J. Corydon [3,4], Markus Wehland [2,5], Markus Braun [6], Marcus Krüger [2,5], Manfred Infanger [2,5] and Daniela Grimm [2,3,5,*]

1 The Saban Research Institute, Children's Hospital Los Angeles, University of Southern California, 4650 Sunset Blvd., Los Angeles, CA 90027, USA; wisepetra@gmail.com (P.M.W.); pneviani@chla.usc.edu (P.N.)
2 Department of Microgravity and Translational Regenerative Medicine, Clinic for Plastic, Aesthetic and Hand Surgery, Otto von Guericke University, Universitätsplatz 2, 39106 Magdeburg, Germany; stefan.riwaldt@med.ovgu.de (S.R.); markus.wehland@med.ovgu.de (M.W.); marcus.krueger@med.ovgu.de (M.K.); manfred.infanger@med.ovgu.de (M.I.)
3 Department of Biomedicine, Aarhus University, Ole Worms Allé 4, 8000 Aarhus C, Denmark; corydon@biomed.au.dk
4 Department of Ophthalmology, Aarhus University Hospital, 8200 Aarhus N, Denmark
5 Research Group "Magdeburger Arbeitsgemeinschaft für Forschung unter Raumfahrt- und Schwerelosigkeitsbedingungen" (MARS), Otto von Guericke University, 39106 Magdeburg, Germany
6 Deutsches Zentrum für Luft- und Raumfahrt (DLR), Raumfahrtagentur im DLR, Bonn-Oberkassel, 53227 Bonn, Germany; m.braun@dlr.de
* Correspondence: dgg@biomed.au.dk; Tel.: +45-21379702

check for updates

Citation: Wise, P.M.; Neviani, P.; Riwaldt, S.; Corydon, T.J.; Wehland, M.; Braun, M.; Krüger, M.; Infanger, M.; Grimm, D. Changes in Exosomal miRNA Composition in Thyroid Cancer Cells after Prolonged Exposure to Real Microgravity in Space. *Int. J. Mol. Sci.* **2021**, *22*, 12841. https://doi.org/10.3390/ijms222312841

Academic Editor: Alfred King-Yin Lam

Received: 4 November 2021
Accepted: 25 November 2021
Published: 27 November 2021

Publisher's Note: MDPI stays neutral with regard to jurisdictional claims in published maps and institutional affiliations.

Copyright: © 2021 by the authors. Licensee MDPI, Basel, Switzerland. This article is an open access article distributed under the terms and conditions of the Creative Commons Attribution (CC BY) license (https://creativecommons.org/licenses/by/4.0/).

Abstract: As much as space travel and exploration have been a goal since humankind looked up to the stars, the challenges coming with it are manifold and difficult to overcome. Therefore, researching the changes the human organism undergoes following exposure to weightlessness, on a cellular or a physiological level, is imperative to reach the goal of exploring space and new planets. Building on the results of our CellBox-1 experiment, where thyroid cancer cells were flown to the International Space Station, we are now taking advantage of the newest technological opportunities to gain more insight into the changes in cell–cell communication of these cells. Analyzing the exosomal microRNA composition after several days of microgravity might elucidate some of the proteomic changes we have reported earlier. An array scan of a total of 754 miRNA targets revealed more than 100 differentially expressed miRNAs in our samples, many of which have been implicated in thyroid disease in other studies.

Keywords: thyroid cancer; cell culture; exosomes; microgravity; spaceflight; miRNA

1. Introduction

Space, the final frontier, is the ultimate goal for humans to explore. The fascination of the stars and the longing to reach them is as old as humankind itself. Through technological advancement combined with the age of information, space travel has become part of our reality. Multiple programs, manned or unmanned, have broadened our knowledge about space and the planets of our solar system; exploration of its planets and even commercial travel seems possible in the near future [1–6]. Still, research must find solutions to overcome multiple challenges to advance to these goals, not only on a technical level but also to prevent the rather dramatic effects the space environment wields over the human organism. The fact is that prolonged lack of exposure to gravitational forces can lead to numerous impairments in multiple physiological systems [7–12]. Therefore, researchers have started investigating the effects of weightlessness on the human body early in the history of spaceflight [13–15].

Even with the addition of several new enterprises in the field of interstellar travel, spaceflights are still rare and require extensive preparation and funding. Hence, most of

the initial cell biological experiments are conducted on Earth under simulated microgravity (s-μ*g*) conditions. To adequately simulate weightlessness in a laboratory setting, disparate devices have been developed over the years, such as the random positioning machine (RPM) and clinostats [16–20].

The changes observed after cell incubation within these devices often predict cellular changes during spaceflight, but by direct comparison, s-μg and real microgravity (r-μ*g*) do not cause identical effects [21]. When our team was presented with the opportunity to conduct experiments under prolonged microgravity as part of a joint enterprise with the German Aerospace Center (Deutsches Zentrum für Luft- und Raumfahrt, DLR) (Bonn, Germany) and the Chinese Manned Space Engineering Office (CMSEO) (Beijing, PR China) [22] during the Shenzhou-8/SimBox Spaceflight mission in 2011, we took on the challenge. Both the planning and execution of cell culture experiments on the unmanned Shenzhou-8 spacecraft was a major undertaking. The cell culture equipment had to be developed to withstand the physical forces during the mission and had to be adapted to small, automated modules to enable fluid exchanges [23,24].

Extensive hardware tests prior to and during the Shenzhou-8 mission and the results and insights gained through the following analysis of the harvested samples provided us with the essential knowledge to equip a follow-up experiment under prolonged exposure to r-μ*g* conditions (r-μ*g*). Our team described changes of cancer cells from two to three-dimensional growth after exposure to simulated microgravity on the RPM before [24]. Moreover, genomic adaptations in pathways involved in the cytoskeletal composition were identified [25–27]. For the above-mentioned follow-up investigation, the human follicular thyroid cancer cell line FTC-133 was flown to the International Space Station (ISS) on the SpaceX CRS-3 cargo mission in newly designed, automated CellBox-1 modules, as described in more detail in Section 4.2. Incubation aboard the ISS proceeded for 12 days, following a pre-determined feeding and fixation schedule (flight module, FM). Concurrently, cells from the same passage were grown under the exact same conditions considering the hardware, temperature, and fluid exchange schedule in a laboratory on Earth (ground module, GM). The harvested cells and supernatant were analyzed to determine the growth behavior, adaptations in gene and protein expression, and protein interactions [26].

In an attempt to gain more knowledge on the underlying cellular changes of the differential protein expression following exposure to microgravity, we decided to reanalyze the CellBox-1 sample supernatants, this time regarding their exosome content. Exosomes are a group of extracellular vesicles (EVs), which have gained increasing interest and attention over the last decade. EVs are a family of lipid bilayer-delimited particles, which are naturally released into the extracellular environment by the majority of (if not all) cells and do not replicate [28–30]. Over the last decade, their high potential as biomarkers, as well as therapeutic vessels in clinical applications became apparent, due to their emerging roles in normal physiology, as well as various diseases. Diverse subtypes of EVs have been defined, but the three major types are categorized in exosomes, microvesicles, and apoptotic bodies. They are found in circulating body fluids, including blood, saliva, and urine [28,31–34]. EVs reflect their cell of origin with respect to their cargo, which consists of proteins, nucleic acids, lipids, metabolites, and even organelles from the parent cell. Initially thought to solely be a means of cellular waste disposal, more and more functional roles of EVs have been elucidated over the years, and concurrently, the interest in their implications and possible uses have led to the development of various methods of isolation and analysis [35–38]. Transfer of functional proteins and RNA, molecular recycling, creation of a metastatic niche for cancer and pathfinding through the environment, and quorum sensing are only a few [39–46]. EVs facilitate the horizontal transfer of information between different cells and are most likely the organism's most important tool in cell–cell communication. With their potential to serve as biomarkers for a wide array of diseases in clinical diagnosis, the role of EVs in the tumor microenvironment has been studied extensively over the last decade. EVs are transferred from tumors to the surrounding extracellular environment and, thus, modulate the immune and therapy

response, and promote matrix remodeling, as well as angiogenesis [47–50]. Conversely, the transfer of EVs from the tumor microenvironment to tumor cells enhances tumorigenesis by increasing tumor cell proliferation, resistance to chemotherapy, and migration [50–55]. As mentioned above, EVs can travel to distant areas of the organism, where they can be involved in the preparation of the pre-metastatic niche [39–44].

Our groups' interest is focused on exosomes, also known as small EVs, vesicles of endosomal origin defined by their size, biogenesis, and multiple well-defined markers. Exosomes range in size from roughly 30 to 150 nm and are further defined by the presence of specific transmembrane, extracellular, and cytosolic proteins, as well as the absence of some intracellular proteins present in other EVs. The International Society for Extracellular Vesicles (ISEV) has detailed the minimal experimental requirements for a definition of exosomes and other EVs [37,56]. Additionally, exosomes can be distinguished by their release mechanism to the extracellular environment via fusion of late endosomes/multivesicular bodies (MVBs) with the plasma membrane (Figure 1) [57,58]. The challenges of studying exosomes—their small size, low yields and/or co-precipitation of aggregated and bound proteins during isolation and enrichment—have been met by the research community with the development of new methods to characterize these promising particles. The most common methods of determining the size distribution and concentration of exosomes, along with the determination of cell origin and distinguishing between different EVs have been described in detail [59–61]. Previously, we have used a method based on the single-particle interferometric reflectance imaging sensor (SP-IRIS) (ExoView™, NanoView Biosciences, Boston, MA, USA), which permits multiplexed phenotyping and digital counting of various populations of individual exosomes captured on a microarray-based chip. This method allows the characterization of exosomes directly from human biofluids without the need for prior vesicle isolation or concentration and so grants a detailed analysis with a very small sample size [60,62,63].

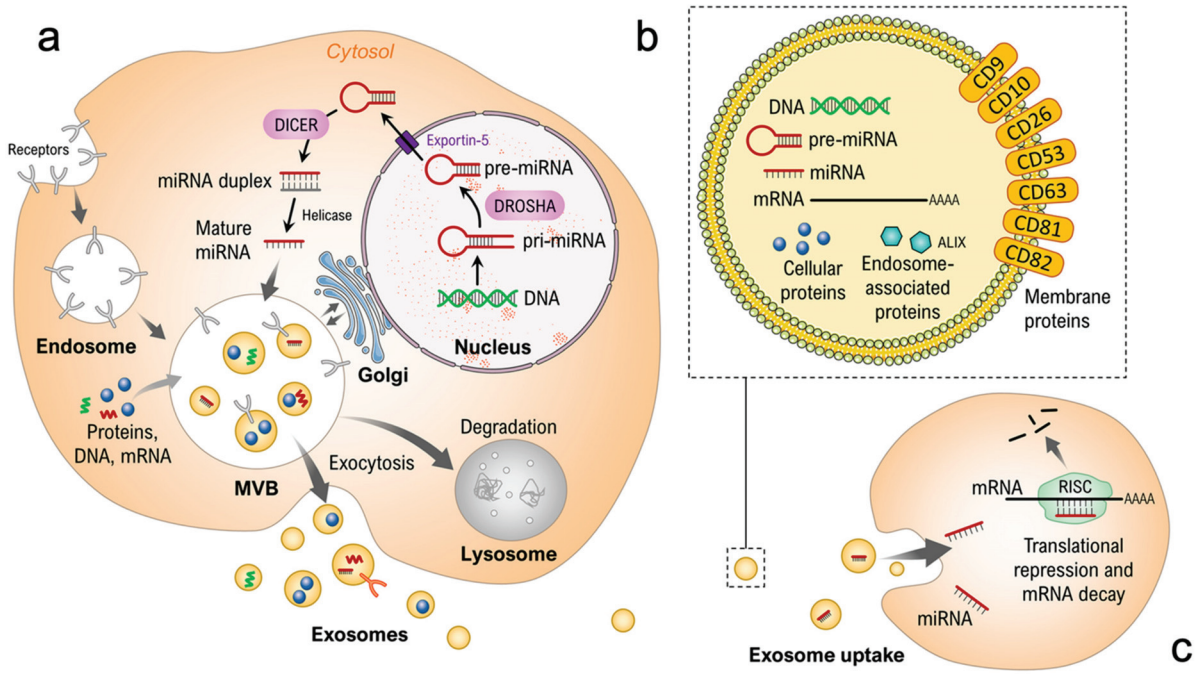


Figure 1. (**a**) Schematic overview of exosome biogenesis, cargo loading, and release and miRNA maturation. (**b**) Typical molecular contents of an exosome. (**c**) Exosomal uptake and post-translational protein regulation via miRNAs. Parts of the figure are drawn using pictures from the Servier Medical Art (https://smart.servier.com), licensed under a Creative Commons Attribution 3.0 Unported License (https://creativecommons.org/licenses/by/3.0).

Here, we are presenting the results of our continuative analysis of the exosomal composition of the CellBox-1 samples for integration with the entirety of our previous findings. To delve deeper into the regulatory changes of protein expression after prolonged exposure to r-μg, we opted to analyze potential changes in the exosomal microRNA (miRNA) content. miRNAs are small, non-coding RNA molecules found in animals, plants and some viruses and are involved mainly in the post-transcriptional regulation of gene expression [64,65]. First discovered in 1993, their regulatory function was not elucidated until the early 2000s [66–69]. The majority of miRNA "genes" are located in intergenic regions or in antisense orientation in annotated genes [65,67,70]. They are transcribed as fairly long primary transcripts, the pri-miRNA, then transformed into the hairpin-shaped pre-miRNA by the RNase III Drosha [71,72]. After being transported into the cytoplasm, the pre-miRNA is cleaved to the mature miRNA by Dicer, a critical member of the RISC complex (RNA-induced silencing complex), with a length of 19–25 nucleotides [65,73–75] (Figure 1). miRNAs pair with mRNAs to direct post-transcriptional repression (mainly) by way of either direct translational repression, mRNA destabilization or both [66,76]. Another member of the RISC complex, Ago2, is activated by the miRNA/mRNA pairing and cleaves the mRNA [77]. The various molecular processes involved in miRNA-directed translational repression and mRNA destabilization, which include inhibition of translation initiation and poly(A) shortening, are reviewed in detail by Filipowicz et al. [78]. The number of defined miRNAs has passed 1200 and is rising continuously. With the large quantity of reported miRNAs in cancer research, our interest in this group of protein regulators was easily triggered, and our prospects were to find some common links between changes in the exosomal miRNA cargo and our previously reported genomic and proteomic cellular changes following extended exposure to r-μg. Optimizing for source material, as well as the given hypotheses, is crucial, as the different protocols differ drastically in yield, purity, and functionality of the harvested EVs, as shown in comparative studies [35,79,80].

Likewise, the definition and description of EVs have varied greatly and proved overwhelming at times. As a result, the ISEV set the minimal required standard in defining the different vesicles to the report of amounts of several proteins (three or more) in at least a semi-quantitative manner in any EV preparation, including EV isolates obtained from body fluids or from secreting cells in vitro. The proteins described and characterized should be proteins expected to be present in the EVs of interest, especially transmembrane proteins and cytosolic proteins with membrane-binding capacity. In addition, the level of presence of proteins not expected to be enriched in EVs of endosomal origin should also be determined [56]. Transmembrane proteins expected to be present in exosomal preparations include, among others, tetraspanins (CD9, CD63, CD81), integrins, and growth factor receptors. The group of expected or enriched cytosolic proteins includes endosome or membrane-binding proteins (TSG101) and signal transduction or scaffolding proteins (syntenin). Intracellular proteins that are absent or under-represented in exosomes but present in other types of EVs are proteins found in the endoplasmic reticulum (ER) (calnexin) or the Golgi apparatus (GM130) [56].

2. Results

Exosomal miRNAs are instrumental in post-transcriptional regulation of protein expression and have earned recognition, particularly in tumorigenic pathways, including thyroid cancer [81–84]. With methods in place to engineer either cell-secreted or artificial exosomes loaded with a cargo of choice, as well as the possibility to target the recipient cell of choice precisely via surface protein presentation, the choice to scan our samples for differential miRNA expression was easy. The application of the TaqMan system is widely used and standardized, and therefore, offers numerous options for a thorough analysis. The EVs isolated from the CellBox-1 samples have been defined as exosomes in our previous publication [63]; hence we were able to use these EVs directly for any follow-up analyses.

2.1. Particle Concentration and Size Distribution Analysis by NanoSight

Following the exosome isolation via size exclusion chromatography (SEC) the concentration and size distribution of the harvested particles was evaluated by nanoparticle tracking analysis (NTA) using a NanoSight instrument. Since the EVs present in all samples were already characterized as exosomes previously, this single analysis is sufficient to validate the harvested particles. The two fractions per sample containing the desired particles were analyzed; for the GMs, the mean size ranged from 92.1 to 129.6 nm with an average of 107.3 nm. The mode, meaning the size of the majority of particles, ranged from 64 to 117.8 nm, averaging 86.9 nm. The FM mean particle size ranged from 94.3 to 114.9 nm with an average of 106.8 nm, and the mode ranged from 68.7 to 98.3 nm, averaging 83.8 nm.

The concentration of the FM samples was determined at an average of 2.7×10^{10} particles/mL, ranging from 1.31×10^{10} to 4.99×10^{10} particles/mL; the GM samples averaged at a concentration of 2.0×10^{10} particles/mL in the range from 1.15×10^{10} to 2.65×10^{10} particles/mL. Figure 2 displays the size graphs for one fraction per sample, and the entire reports can be found in Supplementary Figure S1.

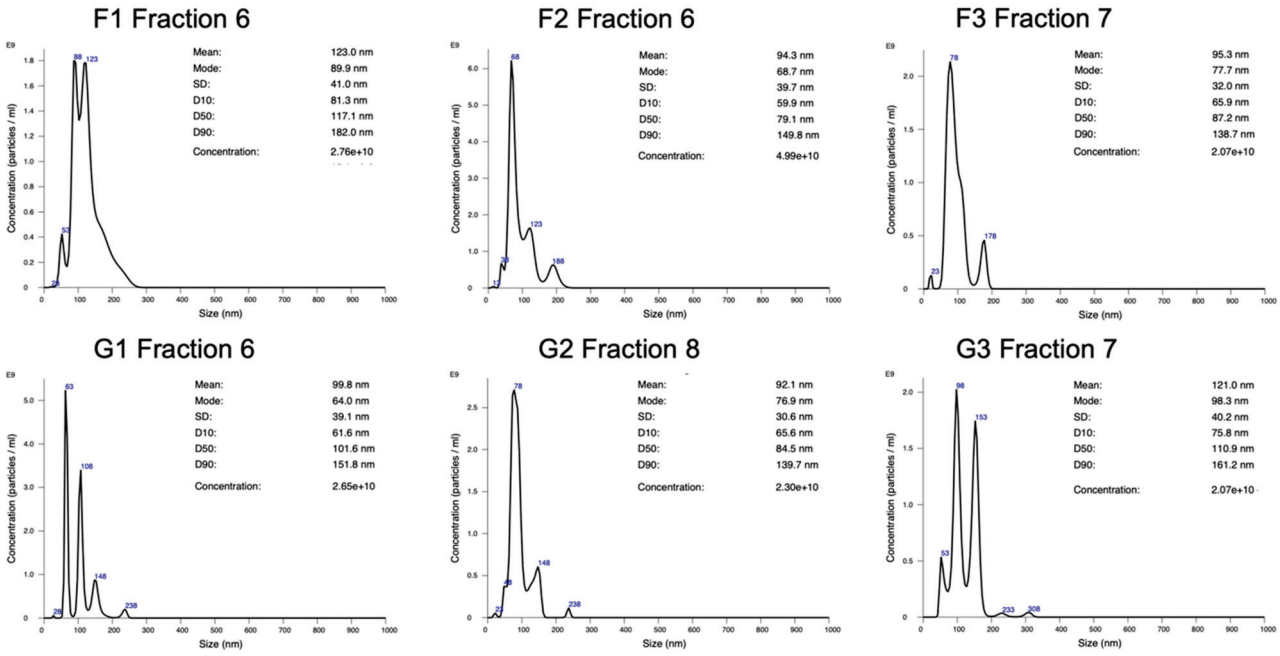


Figure 2. Size and concentration graphs of one of two fractions per sample. On display is the fraction with the higher particle concentration.

2.2. TaqMan™ Advanced miRNA Human Array Cards

The TaqMan™ Advanced miRNA Arrays offer a valuable first insight into any different expression patterns of any given samples, as the investigator is able to scan 754 targets in a streamlined and validated experimental setup. The human array cards have been developed to screen for miRNAs that have been reported as valuable markers in cancer and other relevant diseases. The analysis of total RNA cargo isolated from exosomes following our scan of one FM and GM CellBox-1 sample each disclosed a surprisingly large amount of differentially expressed miRNAs.

A total of 119 miRNAs were either elevated or decreased in the FM in comparison to the GM (Table 1). A total of 19 miRNAs displayed a higher relative quantification (RQ) value in FM, the percent increase ranging from 7% to 48%, with hsa-miR-553 leading the list. Hsa-miR-941 (138% increase), hsa-miR-1286 (132% increase), and hsa-miR-548d-5p (119% increase) also revealed more than double the expression compared to the GM. Expression of another four miRNAs was increased in the range of 94–81%: hsa-miR-154-3p

(94%), hsa-miR-548g-3p (91%), hsa-miR-500a-3p (83%), and hsa-miR-583 (81%); the adjacent 11 miRNAs displayed expressional elevations between 52% and 7%.

Table 1. Differentially expressed microRNAs in FM compared to GM.

Target	RQ	% Change	Target	RQ	% Change
hsa-miR-553	5.476	448%	hsa-miR-28-5p	0.331	−67%
hsa-miR-941	2.382	138%	hsa-miR-1302	0.328	−67%
hsa-miR-1286	2.321	132%	hsa-miR-208b-3p	0.323	−68%
hsa-miR-548d-5p	2.191	119%	hsa-miR-30c-2-3p	0.320	−68%
hsa-miR-154-3p	1.944	94%	hsa-miR-367-3p	0.312	−69%
hsa-miR-548g-3p	1.913	91%	hsa-miR-1-3p	0.304	−70%
hsa-miR-500a-3p	1.827	83%	hsa-miR-452-5p	0.287	−71%
hsa-miR-583	1.814	81%	hsa-miR-197-3p	0.282	−72%
hsa-miR-221-5p	1.523	52%	hsa-miR-214-3p	0.276	−72%
hsa-miR-626	1.433	43%	hsa-miR-208a-3p	0.272	−73%
hsa-miR-16-5p	1.401	40%	hsa-miR-199a-5p	0.259	−74%
hsa-miR-1203	1.337	34%	hsa-miR-100-5p	0.259	−74%
hsa-miR-378a-3p	1.287	29%	hsa-miR-103a-3p	0.249	−75%
hsa-miR-452-3p	1.268	27%	hsa-miR-625-5p	0.247	−75%
hsa-miR-144-3p	1.180	18%	hsa-miR-376a-3p	0.246	−75%
hsa-miR-200a-5p	1.097	10%	hsa-miR-380-3p	0.242	−76%
hsa-miR-302d-3p	1.093	9%	hsa-miR-429	0.236	−76%
hsa-miR-646	1.084	8%	hsa-miR-125b-5p	0.235	−77%
hsa-miR-34b-3p	1.067	7%	hsa-miR-7-1-3p	0.231	−77%
hsa-miR-633	0.977	−2%	hsa-miR-128-3p	0.231	−77%
hsa-miR-1255a	0.952	−5%	hsa-miR-374b-5p	0.229	−77%
hsa-miR-524-3p	0.885	−11%	hsa-miR-323b-5p	0.229	−77%
hsa-miR-606	0.883	−12%	hsa-miR-653-5p	0.228	−77%
hsa-miR-1260a	0.875	−12%	hsa-miR-199a-3p_	0.219	−78%
hsa-let-7b-3p	0.859	−14%	hsa-miR-199b-3p		
hsa-miR-133b	0.842	−16%	hsa-miR-448	0.218	−78%
hsa-miR-645	0.841	−16%	hsa-miR-501-5p	0.217	−78%
hsa-miR-576-3p	0.839	−16%	hsa-miR-423-5p	0.197	−80%
hsa-miR-182-3p	0.823	−18%	hsa-miR-487a-3p	0.197	−80%
hsa-miR-548j-5p	0.816	−18%	hsa-miR-378a-5p	0.191	-81%
hsa-miR-27a-5p	0.806	−19%	hsa-miR-9-5p	0.191	−81%
hsa-miR-765	0.799	−20%	hsa-miR-374a-5p	0.191	−81%
hsa-miR-361-3p	0.787	−21%	hsa-miR-548a-3p	0.189	−81%
hsa-miR-628-3p	0.778	−22%	hsa-miR-325	0.186	−81%
hsa-miR-21-3p	0.761	−24%	hsa-miR-134-5p	0.184	−82%
hsa-miR-181c-3p	0.751	−25%	hsa-let-7d-5p	0.182	−82%
hsa-miR-770-5p	0.729	−27%	hsa-miR-31-5p	0.178	−82%
hsa-miR-34a-3p	0.725	−27%	hsa-miR-2110	0.170	−83%
hsa-miR-593-3p	0.660	−34%	hsa-miR-92a-3p	0.165	−83%
hsa-miR-548k	0.620	−38%	hsa-miR-148b-3p	0.164	−84%
hsa-miR-552-3p	0.612	−39%	hsa-miR-384	0.157	−84%
hsa-miR-562	0.594	−41%	hsa-miR-502-3p	0.155	−85%
hsa-miR-10b-3p	0.562	−44%	hsa-miR-148a-3p	0.149	−85%
hsa-miR-548n	0.544	−46%	hsa-miR-342-5p	0.145	−86%
hsa-miR-564	0.541	−46%	hsa-miR-200a-3p	0.138	−86%
hsa-miR-551a	0.521	−48%	hsa-miR-490-3p	0.138	−86%
hsa-miR-196a-5p	0.511	−49%	hsa-miR-200c-3p	0.136	−86%
hsa-miR-516b-5p	0.480	−52%	hsa-miR-744-5p	0.135	−87%
hsa-miR-190a-5p	0.467	−53%	hsa-miR-25-3p	0.122	−88%
hsa-miR-133a-3p	0.449	−55%	hsa-miR-450b-3p	0.118	−88%
hsa-miR-181b-5p	0.444	−56%	hsa-miR-27b-3p	0.108	−89%
hsa-miR-153-3p	0.417	−58%	hsa-miR-485-5p	0.100	−90%
hsa-miR-101-3p	0.417	−58%	hsa-miR-483-5p	0.098	−90%
hsa-miR-18a-3p	0.411	−59%	hsa-miR-518f-3p	0.097	−90%
hsa-miR-548e-3p	0.402	−60%	hsa-miR-525-3p	0.091	−91%
hsa-miR-147a	0.397	−60%	hsa-miR-567	0.089	−91%
hsa-miR-338-3p	0.368	−63%	hsa-miR-324-5p	0.084	−92%
hsa-miR-660-5p	0.346	−65%	hsa-miR-339-3p	0.070	−93%
hsa-miR-518c-3p	0.335	−66%	hsa-miR-518d-3p	0.069	−93%
hsa-miR-137	0.332	−67%	hsa-miR-501-3p	0.066	−93%

Of the 100 scanned miRNA targets with decreased RQ values, the percentage ranged from 2% to 93%; the detailed list can be found in Table 1. Briefly, 12 miRNAs displayed expression decreases below 20% (2–19%), and 16 ranged between 20% and 49%. The largest group could be found in the range between 50% and 80%, namely 39 of all scanned targets. A total of 24 miRNAs could be found grouped together with an expression decrease between 81% and 89%. Lastly, the nine remaining targets with the largest decrease in expression were the following: hsa-miR-485-5p, hsa-miR-483-5p, hsa-miR-518f-3p (all −90%), hsa-miR-525-3p, hsa-miR-567 (both −91%), hsa-miR-324-5p (−92%), and hsa-miR-339-3p, hsa-miR-518d-3p, hsa-miR-501-3p (all −93%).

Following another thorough in silico investigation, we discovered that a total of 23 of these differentially expressed miRNAs have been described in the pathogenesis of various thyroid cancers previously [84]. Hence, we decided to focus on these oncomiRs and tumor suppressors for further verification. Only two of the overexpressed miRNAs in the FM compared to the GM were found in this group, namely hsa-miR-221-5p (52% increase) and hsa-miR-144-3p (18% increase). The remaining 21 miRNAs were downregulated in varying degrees, starting from an 11% decrease up to an 85% decrease in the case of hsa-miR-148a-3p, as displayed in detail in Figure 3.

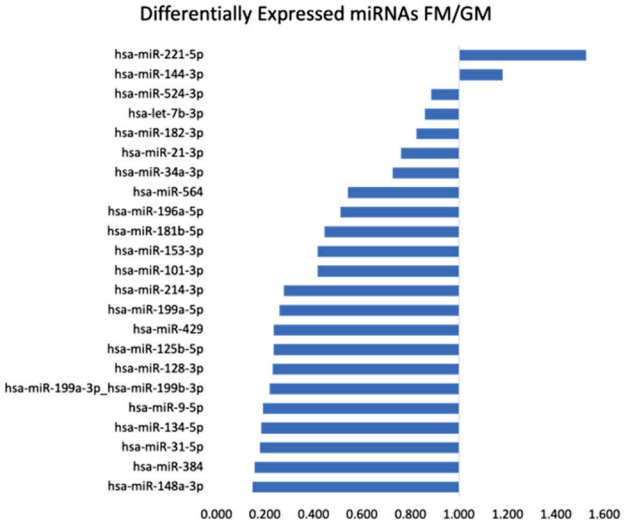


Figure 3. Differentially expressed miRNAs comparing FM with GM with TaqMan™ Advanced miRNA with the relevant impact in thyroid cancer.

2.3. TaqMan™ Advanced miRNA Single Target Assays

Even though an application as a biomarker usually comes to mind first and would be easiest to utilize, two facts discouraged us from choosing this route: (a) the number of overexpressed miRNAs in our FM sample was distinctly lower compared to the GM, and (b) only two of these were reported as oncomiRs in thyroid cancer. Namely, hsa-miR-221-5p was upregulated most, but the 3p-strand is the one described in papillary thyroid carcinoma (PTC) previously [81,82,84–86]. The second oncomiR overexpressed in FM, hsa-miR-144-3p, is the lower expressed strand of the hairpin; hence most of the reports regarding hsa-miR-144 in PTC and MTC (medullary thyroid carcinoma) were evaluating the 5p strand [83,87]. Therefore, we decided to focus on the more intriguing tumor suppressors.

Three of these tumor-suppressor miRNAs were chosen to be validated using TaqMan™ Advanced Single Target assays: hsa-miR-429 (decreased by 76%), hsa-miR-128-3p (77% decrease), and hsa-miR-199a-5p (downregulated 78%). All three have been described in thyroid tumors previously [88–91].

2.3.1. hsa-miR-429

In the initial TaqMan™ Advanced miRNA Array scan, the hsa-miR-429 expression was decreased by 76% in FM compared to GM. In a follow-up single assay, all FM and GM samples were analyzed, resulting in an increased expression across the board of varying degrees. The C_t values in all triplicates of FM1 and FM2 were at around 37 to 38 and averaged 38.23 in GM1 and GM1. Normalization with C39 led to relative quantification values of 0.0004 and 0.00025 (FM1, FM2) vs. 0.00032 and 0.00014. FM3 though displayed a much more dominant increase in miR-429 expression, at C_t values of 30 to 31 (FM3) compared to 35.1 (GM1) with a resulting relative quantification of 0.022 (FM3) vs. 0.0021 (GM3) (Figure 4).

hsa-miR-429

Ct Values

	C39			hsa-miR-429		
FM1	25.85158	26.51918	26.44772	38.34598	37.01517	
FM2		25.59104	25.63623	37.65828	37.64675	37.4042
FM3	25.34388	25.05793	24.86713	30.68106	30.67476	30.36722
GM1	25.54179	25.80831	25.30381	39.9313	38.00795	35.92782
GM2	25.18294	25.62094	25.3523	38.38113	37.19382	39.94162
GM3	26.36722	25.90043	25.79144	36.08803	34.91956	34.19653

Relative Quantification

FM1	0.000232	0.000584	
FM2	0.000237	0.000239	0.000282
FM3	0.02074	0.020831	0.025781
GM1	4.69E-05	0.000178	0.000752
GM2	0.000122	0.000279	4.15E-05
GM3	0.000931	0.002094	0.003456

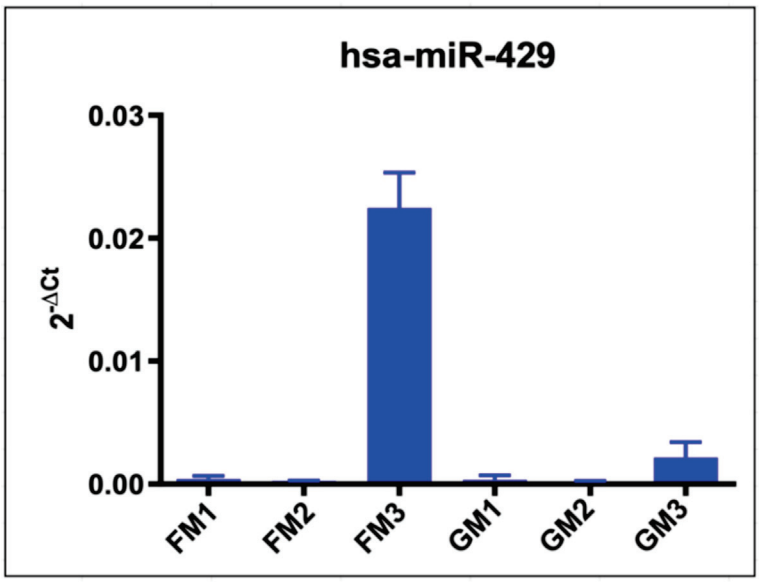


Figure 4. Results of the single assay analysis of hsa-miR-429, including Ct values, relative quantification, and the graphical representation of the results. Empty spots in the listed Ct values did not produce any measurable amplification.

2.3.2. hsa-miR-128-3p

Based on a 77% decrease in miR-128-3p expression in the array scan, the results of the single assay analysis delivered mixed results. As depicted in Figure 5, FM2 and FM3 supported this trend amplifying at C_t values between 37.4 and 38.2, compared to the GM values ranging at an average of 34.1, leading to a relative quantification of 0.0002 and 0.0001 vs. 0.0046 and 0.0018 on average. FM1, on the other hand, showed an increase in expression at C_t values from 30.4 to 31 vs. GM at values at around 38, with the respective average in relative quantification of 0.049 (FM1) and 0.00015 (GM1). These inconsistent results may have various underlying reasons, as the positioning of the modules on the racks may have subjected these samples to varying extents of different in-flight stressors, such as space radiation or acceleration forces, as described in the discussion.

hsa-miR-128-3p

Ct Values

	C39			hsa-miR-128-3p		
FM1	25.85158	26.51918	26.44772	31.02007	30.47569	30.41649
FM2		25.59104	25.63623	37.41007	37.61737	38.63999
FM3	25.34388	25.05793	24.86713	37.87515	38.22082	38.51696
GM1	25.54179	25.80831	25.30381	38.50281	37.984	
GM2	25.18294	25.62094	25.3523	32.98102	33.30802	33.1186
GM3	26.36722	25.90043	25.79144	34.31579	36.99346	

Relative Quantification

FM1	0.037234	0.054301	0.056576
FM2	0.000281	0.000244	0.00012
FM3	0.000142	0.000111	9.08E-05
GM1	0.000126	0.000181	
GM2	0.00517	0.004121	0.0047
GM3	0.003181	0.000497	

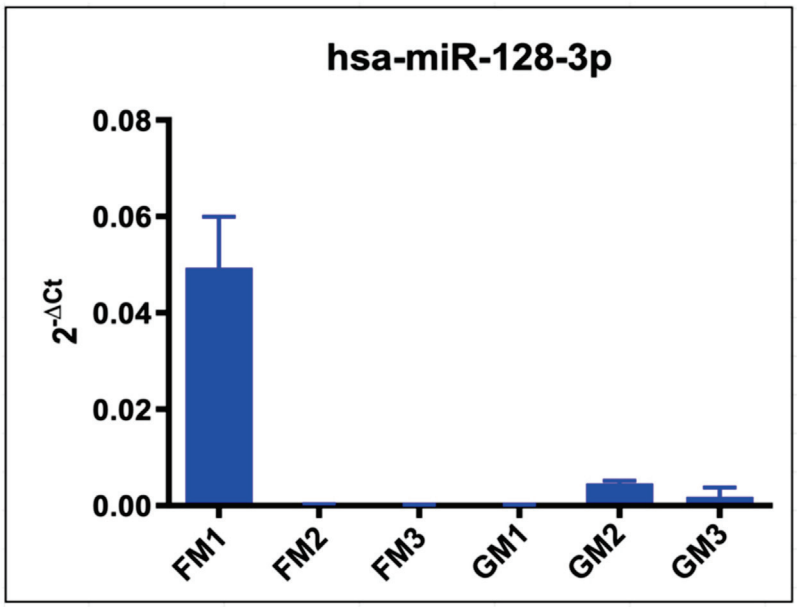


Figure 5. Results of the single assay analysis of hsa-miR-128-3p, including Ct values, relative quantification, and the graphical representation of the results. Empty spots in the listed Ct values did not produce any measurable amplification.

2.3.3. hsa-miR-199a-3p_hsa-miR199b-3p

The last miR chosen for validation via single assay was hsa-miR-199a-3p_hsa-199b-3p. The expression decrease in the array scan was 78% in FM vs. GM, and this trend could be validated across all three sample sets, as shown in Figure 6. With average relative quantification values of 0.07 vs. 0.31 (FM1 vs. GM1), 0.004 vs. 0.05 (FM2 vs. GM2), and 0.03 vs. 0.04 (FM3 vs. GM3), all exosomes isolated from FM contained a lower amount of miR-199. The underlying C_t values were in the range from 29.64 to 33.52, with an average of 31.12 (FMs) and 26.99 to 30.99 with an average of 29.09 (GMs).

hsa-miR-199a-3p_hsa-miR-199b-3p

Ct Values

	C39			hsa-miR-199		
FM1	25.8516	26.51918	26.44772	30.2234	30.36885	29.64577
FM2		25.59104	25.63623	32.91386	33.44229	33.5204
FM3	25.3439	25.05793	24.86713	29.95817	29.919	30.13116
GM1	25.5418	25.80831	25.30381	26.99282	27.41952	27.23264
GM2	25.1829	25.62094	25.3523	29.3444	29.67277	29.459
GM3	26.3672	25.90043	25.79144	30.27337	30.99472	30.47641

Relative Quantification

FM1	0.06468	0.058475	0.096526
FM2	0.00634	0.004399	0.004167
FM3	0.03423	0.035174	0.030364
GM1	0.36818	0.273912	0.311793
GM2	0.0643	0.051212	0.059391
GM3	0.05242	0.031796	0.04554

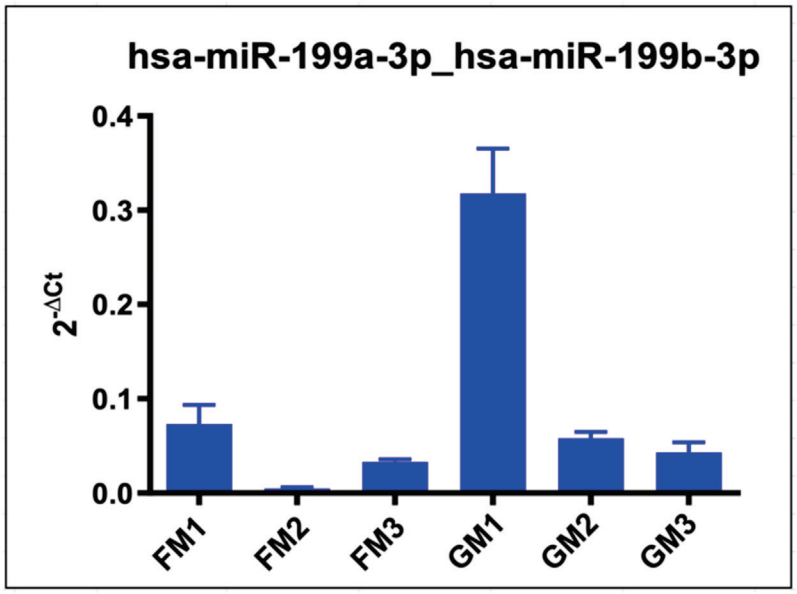


Figure 6. Results of the single assay analysis of hsa-miR-199a-3p_hsa-miR-199b-3p, including Ct values, relative quantification, and the graphical representation of the results. Empty spots in the listed Ct values did not produce any measurable amplification.

3. Discussion

Ever since the first manned space missions, the experienced effects of microgravity on the human organism have been a focal point of space research. Overcoming these extensive changes and adaptations, which span from gene expression alterations and cellular modifications to physiological adjustments, is mandatory to successfully continue the quest of space exploration and travel. Extensive studies on the occurrent physiological adaptations to the cardiovascular, musculoskeletal, and sensorimotor systems and the implications of varying durations of spaceflight were undertaken, and processes to prepare and recondition space travelers were developed [92–94]. Still, despite all efforts and scientific advances, many questions remain unanswered and are challenging space explorers, so the search for further insights continues.

In recent years, our group has studied multiple cell culture systems regarding their genomic and proteomic adaptations resulting from exposure to various conditions of weightlessness [25,26,95,96]. One of these systems we have explored is thyroid cancer, an endocrine tumor of continuously increasing incidence over the last decades [97,98]. To expand our knowledge further and to better understand the underlying cellular pathways leading to the demonstrated changes, we decided to re-evaluate the CellBox-1 samples in regard to their EV content and composition. EVs have taken a prominent place in the rankings of intercellular communication and post-transcriptional proteomic regulation over the last decade, and their significance as disease biomarkers and potential pharmaceuticals should not be underestimated [31,99–102]. Recently, we described the changes in exosomal secretion and populations under prolonged exposure to microgravity in the

human follicular thyroid cancer cell line FTC-133, which our group has studied in various conditions of weightlessness before [24,63,103]. In these preliminary experiments on the exosomal secretion, we determined the number of secreted vesicles, their size distribution, and their population regarding the tetraspanin surface expression to evaluate the influence of microgravity on changes in the cellular cross-talk [63].

The impact of non-coding RNAs on regulatory processes in cells has been found to be more and more prominent, particularly in tumor networks [104–107]. Small non-coding RNAs, or miRNAs, have been described as highly adaptable cargo in tumor-associated exosomes, secreted from not only tumor cells but also from tumor-associated cells or immune cells. Given the ever-growing, vast pool of knowledge in this field, as well as the availability of new methods to re-analyze the samples from our prior experiments, miRNAs suggested themselves as the next logical targets. To get an initial overview of any given changes in our flight samples compared to the ground controls, we set up an initial screen over a total of 754 miRNA targets using the TaqMan™ array methodology. Surprisingly, we found almost 120 miRNAs differentially expressed in our samples. To narrow the selection of targets of interest for further validation, we analyzed the list filtering for miRNAs previously reported in thyroid cancer. This resulted in a pool of 23 miRNAs, 2 of them overexpressed in FM compared to GM; the remaining 21 were downregulated (Figure 3). From this group, we selected three miRNAs to be validated in all CellBox-1 samples via TaqMan™ single assays.

Before discussing these miRNAs, we would like to direct the reader's attention to one miRNA, which was neither part of the list of previously described in thyroid cancer targets and hence, was not further evaluated in this study. We would like to include and point out hsa-miR-553 in our discussion, particularly because of its extraordinary high expression difference in the array screening. As recorded in Table 1, the RQ value of the FM was 5.476, which corresponds to the quite astonishing increase of 448% compared to our calibrator, GM. hsa-miR-553 was first specified by Cummins et al. [108] in 2006 as part of the colorectal miRNAome, which was determined via an extensive screening of non-coding RNAs tags in human colorectal cells. Ever since this miRNA has been reported on only one more time in relation to a malignant disease: Liang et al. revealed that miR-553 promoted proliferation, metastasis, and tumor-associated macrophage (TAM) resistance in MCF-7 and MCF-7/TAMR breast cancer cells; and high expression levels of miR-599 was correlated with poor prognosis. The circular RNA circBMPR2 served as a miR-553 sponge and decreased the abundance of miR-553 in the cytoplasm, according to the authors. Vice versa, miR-553 overexpression could partly reverse the effects of circBMPR2 on breast cancer cells. Moreover, circBMPR2 and miR-553 could regulate the expression of each other, forming a negative-feedback loop [109]. Therefore, despite the impressive increase of hsa-miR-553, we decided to not further investigate this miRNA at this time but rather shift our focus on several of the tumor suppressors described in thyroid cancers, as this might offer valuable insights to pathways we have described in FTC-133 prior, and which could be targeted in an effort to reduce tumorigenicity or even point towards possible therapeutic approaches.

As mentioned previously, the oncomiRs are a promising and logical target in tumor and exosome research. Significantly in EVs, upregulated miRNAs can be easily measured via liquid biopsies, and with possible specificity to any particular cancer, can easily serve as biomarkers and for disease staging. However, in view of the possibilities that exosomes offer regarding cargo loading and targeted delivery, tumor suppressors are a much more fascinating topic to explore. The prospects in developing and using tumor suppressor-laden exosomes to specifically target tumor cells and to circumvent their adaptations to the tumor environment and the organism's immune response are worth the efforts. Hence, we were focusing on three miRNAs previously distinguished as tumor suppressors in thyroid cancer and additionally downregulated in our FM sample. This downregulation would be consistent with an increase in malignancy as a result of the extended exposure to microgravity, which supports our previous results within this cell line and other cell systems we have worked with [24,26,27,103,110].

3.1. hsa-miR-429

hsa-miR-429 is a member of the miR-200 family, along with miR-200a, miR-200b, miR-200c, and miR-141, and its genetic location can be found on chromosome 1 [111]. The evidence points to an involvement of miR-429 dysregulation in EMT, progression, development, invasion, metastasis, apoptosis, and drug resistance [112–114]. Similar to many other miRNAs, miR-429 has been characterized in multiple different tissues and types of cancers and has been portrayed as a relevant contributor to tumorigenesis as either a tumor suppressor or promoter in very tumor-specific patterns [88,115–117]. Aside from thyroid cancer, tumor-suppressive properties have been reported for miR-429 in breast cancer, cervical cancer, gastric cancer, glioblastoma, and osteosarcoma, to only name a few. An association of miR-429 in tumor progression, proliferation, migration, invasion, and metastasis has been discussed in this regard, as well as the induction of apoptosis, cell cycle arrest, and drug resistance in instances [118]. Contrastingly, miR-429 has displayed oncogenic characteristics in lung cancer, prostate cancer, and endometrial carcinoma. Here also, the miR is correlated with tumor development, progression, proliferation, and drug resistance. In certain tumors, namely colorectal cancer, bladder cancer, and hepatocellular carcinomas, miR-429 still has a quite paradoxical role—it has been reported as up and downregulated in the same tissues with the concurrent results. The type of involvement is consistent with the previously described conditions [118].

In thyroid cancer, miR-429 was evaluated in clinical samples and cell lines alike. The study authors found miR-429 significantly decreased studying 59 pairs of primary tumors and nontumorous control tissues, and transfection of miR-429 in thyroid cancer cell lines substantially inhibited cell proliferation, migration, and invasion ability. Moreover, miR-429 upregulation-induced apoptosis in several cell lines. Zinc finger E-box-binding homeobox 1 (ZEB1) was identified as a direct target of miR-429, and miR-429 transfection could inhibit ZEB1 by direct binding to its 3′-untranslated region (3′-UTR). ZEB1 is a well-known player in cancer, driving EMT, metastasis, and therapy resistance in many human cancers [119–121]. ZEB1 owes its pivotal role to the downregulation of E-cadherin and the regulation of further proteins involved in tumor progression, such as Crumbs3, HUGL2, and PATJ (Pals1-associated tight junction). Therapy resistance is not only limited to chemotherapy resistance but is also reported to influence radioresistance [120,122]. Further, ZEB1 reportedly regulates the development of an inflammatory phenotype and the activation of macrophages towards TAMs [122,123]. These data clearly suggest a role as a tumor suppressor in this disease pattern; our recent results substantiate these findings. We found that hsa-miR-429 was downregulated 76% in FM compared to GM in our initial scan, but we could not solidly validate these results with the following single target assay.

3.2. hsa-miR-128-3p

Cleaved from the stem-loop hsa-miR-128-2, miR-128-3p is the main mature strand with reports in more than 150 published experiments. It has been described—besides cancer—in various diseases physiological processes, such as rheumatoid arthritis, multiple sclerosis, atrial fibrosis, and vascular disease, response to sepsis and acute kidney injury, osteogenesis and bone healing, to name a few [124–129]. Mets et al. reported miR-128-3p as a candidate for an oncomiR in T-cell acute lymphoblastic leukemia as it downregulates PHF6, which plays an important tumor-suppressive role in this disorder. Other than that, miR-128-3p is mainly described in cancer as a tumor suppressor by inhibiting most processes during tumor development and progression, and the examples are manifold. Downregulating this miR accelerates progression in prostate, ovarian, and breast cancer, and in cervical cancer proliferation, migration, and invasion increases with diminishing miR-129-3p levels [130–134]. Additionally, miR-128-3p has been shown to increase chemosensitivity in colorectal cancer after transmission via exosomes or nanoparticles, making it a prime target in the attempt to overcome therapy resistance.

In a study examining papillary thyroid cancer (PTC) and follicular thyroid carcinoma (FTC) tissues and various thyroid carcinoma cell lines, miR-128 expression was markedly

downregulated. Functionally over-expressing the miR markedly inhibited cancer cell migration and invasion, and these processes were reversible by silencing miR-128 expressions in thyroid tumor cells, leading to reduced apoptosis, enhanced proliferation, and metastasis. These results were supported by an in vivo xenograft tumor model where the overexpression of miR-128 reduced the tumor growth rate and tumor weight [89]. Interestingly, miR-128 also seems to target ZEB1 in a tumor-suppressive manner. The circular RNA circ-ABCB10 is a strong promoter of tumorigenesis in breast and cervical cancer. Circ-ABCB10 acts as a sponge for miR-128, which in turn results in an increase in its direct target ZEB1, leading to augmented cell proliferation, migration, invasion, and inhibition of apoptosis in cervical cancer [135]. In esophageal squamous-cell cancer (ESCC), ZEB1 is a crucial mediator of epithelial-mesenchymal transition and induces malignant progression. In their study, Zhao et al. found that miR-128-3p was downregulated in ESCC tissues and cells and downregulated expression of miR-128-3p was testified to be associated with poor prognosis of ESCC patients. In vitro and in vivo, the authors demonstrated that miR-128-3p could suppress cell migration, invasion, and metastasis [136]. As with miR-429, our array scan shows a downregulation of miR-128-3p, and we were able to verify this in two samples during the single assay analysis. This is in accordance with a rise in tumorigenicity in the FM samples in FTC-133 and a development towards a more aggressive phenotype, which has been observed in previous studies.

3.3. hsa-miR-199

The hsa-miR-199 family consists of three stem-loops, which all are cleaved into two mature miRNAs: hsa-miR-199b, hsa-miR-199a-1, and hsa-miR-199a-2. As listed in Table 1, in our initial screening array, we found three mature miRs of this family downregulated, miR-199a-3p, miR-199b-3p, and miR-199a-5p, and all three of these have been previously described in thyroid cancers as tumor suppressors [84]. The selection to validate miR-199a-5p was made due to mechanical advantages. As all previously-discussed miRs, hsa-miR-199a-5p has been reported as an oncomiR in a few malignancies, but mostly the mature l miRs of the entire family has been associated with tumor suppression. Our chosen target inhibits proliferation, migration, and invasion in colorectal cancer by negatively regulating integrin α3β1 (ITGA3), which has been linked to intercellular communication and serves an important role in the signaling among cells and the extracellular matrix. In addition, it was suggested that miR-199a-5p overexpression suppresses the EMT of colorectal cancer cells, whereas the overexpression of ITGA3 restores this effect [137]. The same holds true by looking at another miR199a-5p direct target, ROCK1 (Rho-associated coiled coil-containing protein kinase 1), Zhu and colleagues demonstrated in their study that microRNA-199a-5p was significantly downregulated in colorectal cancer cell lines and tissue samples and was associated with a poor prognostic phenotype. MicroRNA-199a-5p suppressed colorectal cancer cell proliferation, migration, and invasion and induced cell apoptosis [138]. Contrastingly, in cervical cancer, miR-199a-5p promotes the same aspects—proliferation, migration, and EMT—via direct targeting of protein inhibitors of activated signal transducer and activators of transcription 3 (PIAS3). PIAS3 is a regulator protein of other key transcription factors, including MITF, NFκB, SMAD, and estrogen receptors [139,140].

Looking at thyroid tumors, the miR-199 family has been reported as aiding in the suppression of cell proliferation, invasion, metastasis, and enhancing apoptosis. The ectopic expression level of miR-199b-5p in papillary thyroid carcinoma cell B-CPAP could inhibit growth, migration, and invasion, as well as epithelial-mesenchymal transition (EMT) and decreased cell metastasis in vivo, and alongside it improved the sensitivity of thyroid carcinoma cells to chemotherapy. Silencing miR-199b-5p caused contradictory outcomes [84,141]. miR-199a-3p also seems to play an important role in tumor inhibition. A link between miR-199a-3p expression in thyroid tissues and clinicopathologic features was evaluated by Liu and colleagues, as well as its potential usefulness in prediction for invasion and metastasis of PTC [84,90]. Lastly, miR-199a-5p has been depicted as an inhibitor of progression, cell proliferation, migration, and invasion and a promoter of

apoptosis in PTC [91,142]. In addition, it was identified as a potential diagnostic biomarker in this disease [143]. Turning our attention to follicular thyroid carcinoma, the tumor type corresponding with our CellBox-1 samples, mir-199a-5p, has been reported to act via suppressing connective tissue growth factor (CTGF). Through comparison of clinical FTC samples and physiological controls, an under-expression of miR-199a-5p in FTC tissue samples combined with overexpression of CTGF was identified, proving a negatively correlated relationship between CTGF and miR-199a-5p [144]. In this miR, our study results clearly demonstrate a reduction in expression across the array scan, as well as the individual single assay analysis, which explains a development towards a more tumorigenic state of the FM samples in deactivating the tumor-suppressive potency of this group of miRs. With a decrease of miR-199 expression, the aggressiveness and invasiveness of the tumor cells should increase, and previous studies have pointed to such a development after exposure to microgravity conditions due to the various stressors the cells are subjected to [145].

To tie in this miR with the two previously discussed, miR-199a-5p also targets ZEB1 in multiple malignancies. It confers a tumor-suppressive role in triple-negative breast cancer (TNBC), in retarding proliferation, migration, invasion, and stem cell-like characteristics. The authors demonstrated modulation of EMT genes and stem cancer markers and suspect that miR-199a-5p may be involved in chemotherapy sensitivity in TNBC [146]. Further, through targeting ZEB1, miR-199a-5p inhibits EMT of ovarian ectopic endometrial stromal cells via the PI3K/Akt/mTOR signal pathway and in human renal tubular epithelial cells [147,148].

All in all, our studies show solid support for the hypothesis that these miRs have a role in reducing tumorigenesis in thyroid cancer. Their decrease in FM samples, as shown in the scan and the majority of single assays, match the previously-described intensification of oncogenic properties in thyroid cancer cells after subjection to s- and r-μg. The variance in some samples could be due to the exact positioning of the FMs during the spaceflight, which would subject the cells to different intensities of various other stressors besides microgravity, such as space irradiation, to just name one. This study shows once more the difficulties one is facing in space research since every change in the external conditions may lead to unexpected or never-before observed adaptations.

It has been amply demonstrated that post-transcriptional protein regulation through miRNAs is manifold but also very specific in regard to the particular tissues and environments. However, with this in mind, the possibilities of finding common denominators within the vast number of targets are always abounded. As shown in this publication, microRNA research is a great starting point to find new angles and viewpoints to an otherwise well-known picture. This holds true for the additional angle of microgravity research. Our group has demonstrated the benefit of utilizing real or s-μg in solving some of the riddles of tumor biology despite the challenges. With the aid of recently-developed methods and technical advances in exosome and miRNA research, we are opening another door to a better understanding of cancer and to the development of new therapeutic routes to battle this devastating disease.

4. Materials and Methods

4.1. Cell Cultures

Human follicular thyroid cancer cells (FTC-133), purchased from the Health Protection Agency Culture Collections (HPACC, Salisbury, UK), were cultured in RPMI-1640 (Invitrogen, Eggenstein, Germany), supplemented with 10% fetal calf serum (FCS, Biochrom, Berlin, Germany), penicillin (100 U/mL; Merck Millipore, Burlington, MA, USA), and streptomycin (100 µg/mL; Merck Millipore) at 37 °C and 5% CO_2, as described previously [26]. Prior to the start of the experiment, 10^6 cells were loaded into an automated cell culture system, the FM hardware [24], or alternatively seeded in T-25 culture flasks for the ground control experiments. The medium exchange and cell fixation at the experimental endpoint were automated following a preset schedule [25].

4.2. CellBox-1 Spaceflight Experiment

The CellBox-1 spaceflight experiment was conducted as part of the SpaceX CRS-3 Commercial Resupply Service mission, launched on 18 April 2014 (https://www.dlr.de/content/de/bilder/2014/2/start-des-des-cellbox-experiments_15157.html), Riwaldt et al. reported methods and results in detail [25]. In short, 1×10^6 FTC-133 were seeded in nine cell containers (FM) and incubated at 37 °C and 5% CO_2. Twenty-four hours prior to launch, three FMs were transferred to an incubation chamber at 23 °C at Cape Canaveral to serve as ground controls (GM). The remaining six FMs were moved to the Dragon capsule and flown to the International Space Station (ISS). Upon arrival at the ISS, the FMs were incubated continuously at 23 °C at a *g*-force oscillating around ± 0.005 *g*. After 12 days of microgravity, the cells of three FMs were fixed using RNA*later* via an automated process [24], collecting the aspirated media. The remaining three FMs were continuously incubated at 23 °C for the remainder of the spaceflight and, therefore, were not included in this analysis. The GMs were treated identically and simultaneously on the ground. Forty-eight hours post-fixation, both the FMs and GMs were cooled to 4 °C. After the return of the Dragon vessel on 20 May 2014, all containers were returned to the lab for cell and cell supernatant harvest (Figure 7).

4.3. Exosome Harvest and Isolation

Following harvest, the cell supernatants of the FMs and GMs underwent an adjusted differential centrifugation protocol [149]. Two consecutive spins at 300× *g* (10 min, 4 °C) using a swinging bucket rotor, followed by centrifugation at 2500× *g* (15 min, 4 °C, twice) pelleted cells, cell debris, and large vesicles. Additional high-speed centrifugation was not necessary as the analysis via ExoView® does not require preceding particle isolation. The collected supernatants were divided into 2 mL aliquots and stored at −80 °C until further analysis.

4.4. TaqMan™ Advanced miRNA Arrays

As previously reported, we have analyzed the CellBox-1 samples regarding their exosome number, size distribution and tetraspanin colocalization pattern via ExoView using the EV-TETRA-C ExoView Tetraspanin Kit (NanoView Biosciences, Boston, MA, USA) [63]. One sample each was used for further analysis of the miRNA content and to scan for expression changes. The method of choice was the TaqMan™ Advanced miRNA Array, using the Human A and B Cards (ThermoFisher Scientific, Waltham, MA, USA) according to the manufacturer's protocol. In summary, following the exosome harvest, the total RNA cargo was isolated, and the miRNA present was transcribed into cDNA via a TaqMan™ Advanced miRNA cDNA Synthesis Kit (ThermoFisher Scientific, Waltham, MA, USA). The resulting cDNA template was diluted 1:10 and mixed with the remaining reaction components (TaqMan® Fast Advanced Master Mix (2x), ThermoFisher Scientific, Waltham, MA, USA, RNase-free water) and applied onto the array cards. The sealed cards were loaded into the 7900HT Fast Real-Time PCR System with 384-Well Block Module (ThermoFisher Scientific, Waltham, MA, USA) and amplified with the following thermal protocol (Table 2).

Table 2. TaqMan™ Advanced miRNA Array Thermal Protocol.

Step	Temperature	Time	Cycles
Enzyme activation	92 °C	10 min	1
Denature	95 °C	1 s	40
Anneal/Extend	60 °C	20 s	

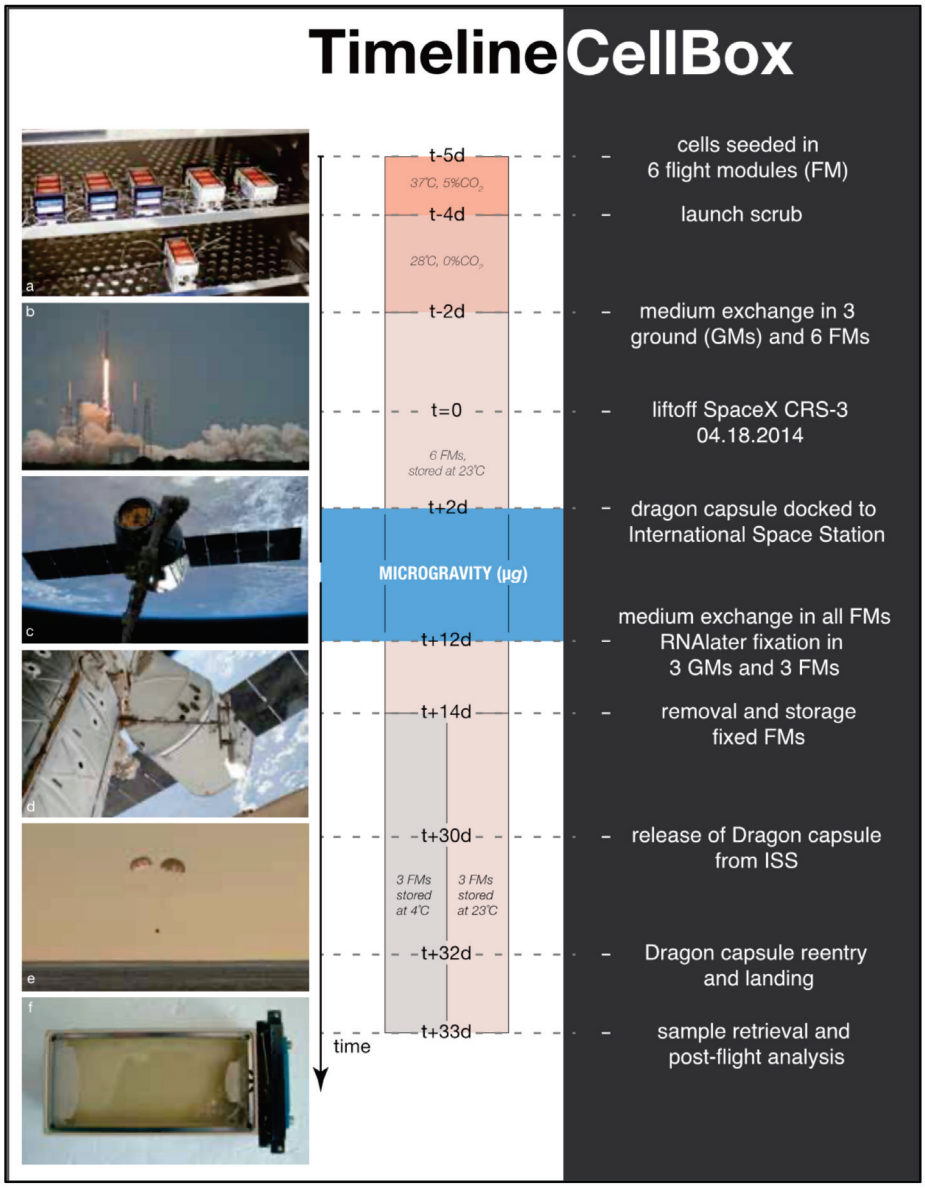


Figure 7. Timeline CellBox-1 experiment. (**a**) $1x10^6$ FTC-133 thyroid cancer cells seeded in six flight modules (FMs) incubated at 37 °C, 5%CO_2. (**b**) Falcon-9 launches within Cargo Resupply Services mission 3 (SpaceX CRS-3). (**c**) Dragon capsule adjacent to International Space Station (ISS). (**d**) SpaceX capsule docked to ISS. (**e**) Capsule reentry and Pacific Ocean landing. (**f**) Flight module inspection before post-flight analysis (picture a courtesy RaisFoto, pictures b-e photo credit SpaceX).

The analysis of the results was carried out with ThermoFisher's ExpressionSuite™ Software and displayed as a Comparative C_t ($\Delta\Delta C_t$).

4.5. Exosome Isolation by Size Exclusion Chromatography

The samples were centrifuged at 300× *g* for 10 min, followed by centrifugation at 3000× *g* for 10 min. The clarified supernatant was then concentrated to approximately 500 µL on a 100 KD Amicon Ultra Centrifugal filter (Millipore, Temecula, CA, USA). The exosomes were then isolated from the concentrated supernatant by size exclusion chromatography (SEC). Sephacryl S-300 High Resolution (GE Healthcare, Chicago, IL, USA) was packed on a glass econo-column chromatography column (BioRad, Hercules, CA, USA) (10 cm height, 1.5 cm diameter). The column was washed with 0.32% Sodium Citrate in PBS, and the supernatant was loaded onto the column and allowed to enter the resin by gravity flow. The eluate was collected in 23 fractions of 15 drops (~500 µL) on a Model 2110 Fraction

Collector (BioRad, Hercules, CA, USA). For each fraction, the presence of exosomes was determined by nanoparticle tracking analysis as described below. The exosome-containing fractions were then further concentrated to 1/100th of the original supernatant.

4.6. Exosome Characterization by Nanoparticle Tracking Analysis

The isolated exosomes were analyzed with a NanoSight NS300 (Malvern Panalytical Inc., Westborough, MA, USA). The NS300 allows rapid analysis of the size distribution and concentration of all types of nanoparticles from 0.01 to 1 µm in diameter. Particles in liquid suspension were loaded into a sample chamber, which is illuminated by a laser beam. Particles in the path of the beam scatter the laser light and is viewed with a digital camera, which captures a video of the particles moving under Brownian motion. The Nanoparticle Tracking Analysis (NTA) software analyses the particles individually and simultaneously (particle-by-particle), and by using the Stokes Einstein equation, calculates their hydrodynamic diameters [150].

4.7. TaqMan™ Advanced Single-Tube miRNA Assays

The validation of our selected miRNA target followed the protocol described above in Section 4.4., differing in the use of single-tube assays for hsa-miR-429, hsa-miR-128-3p, and hsa-miR-199a-5p rather than array cards and the use of C. elegans miR-39 as a normalizer (C39). Exosomes, and subsequently the contained RNA, were isolated from the remaining FM and GM as described above. After transcription of the received miRNA to cDNA (TaqMan™ Advanced miRNA cDNA Synthesis Kit, ThermoFisher Scientific, Waltham, MA, USA), the targets were quantitatively amplified using the thermal protocol below (Table 3) using a CFX96 Touch Real-Time PCR System and analyzed with the CFX Maestro Software (Bio-Rad Laboratories, Inc., Hercules, CA, USA).

Table 3. TaqMan™ Advanced *Single-tube miRNA Assay* Thermal Protocol.

Step	Temperature	Time	Cycles
Enzyme activation	95 °C	20 s	1
Denature	95 °C	3 s	40
Anneal/Extend	60 °C	30 s	

5. Conclusions

Our study results emphasize that exosomes and exosomal miRNAs can be critical tools to tie together the knowledge the microgravity research community has gathered so far. Even though this report focuses solely on thyroid cancers, the importance of the roles of exosomes and miRNAs in understanding and validating phenomena previously described is eminent. The use of cutting-edge technologies enabled us to further describe the cellular changes space travelers are subjected to, even years after the actual mission. Additionally, these analyses once again show how adaptable tumor cells react to even the slightest changes in the surrounding environment, be it microgravity or other related stressors. Further studies will certainly unravel and solidify necessary links on the path to finding a cure for cancer.

Supplementary Materials: Supplementary materials can be found at https://www.mdpi.com/article/10.3390/ijms222312841/s1.

Author Contributions: Conceptualization, P.M.W. and D.G.; methodology, P.M.W. and P.N.; software, P.M.W. and P.N.; validation, D.G., P.M.W. and M.W.; formal analysis, P.M.W. and P.N.; investigation, P.M.W., P.N., S.R., M.W. and M.B.; resources, M.B., M.I. and D.G.; writing—original draft preparation, P.M.W.; writing—review and editing, D.G., T.J.C., M.K. and M.W.; visualization, P.M.W. and M.K.; supervision, D.G. and P.M.W.; project administration, D.G.; funding acquisition, D.G. and M.I. All authors have read and agreed to the published version of the manuscript.

Funding: This research was funded by Deutsches Zentrum für Luft- und Raumfahrt (DLR), BMWi projects 50WB1524 and 50WB1924 (D.G.).

Institutional Review Board Statement: Not applicable.

Informed Consent Statement: Not applicable.

Data Availability Statement: Not applicable.

Acknowledgments: The authors like to thank the DLR Space Administration, Bonn, Germany, for giving us the opportunity to participate in the SpaceX CRS-3 Mission. Finally, we would like to thank NASA, the companies SpaceX, and Airbus Defense and Space for bringing our cells to the International Space Station. This work was performed with the support of the ExtraCellular Vesicle Core at The Saban Research Institute of Children's Hospital Los Angeles.

Conflicts of Interest: The authors declare no conflict of interest.

Abbreviations

AB	Antibody
CTGF	Connective Tissue Growth Factor
C39	C. elegans miR-39
EMT	Epithelial to Mesenchymal Transition
ESCC	Esophageal Squamous-Cell Cancer
EV	Extracellular Vesicle
GM	Ground Module
FM	Flight Module
FTC	Follicular Thyroid Carcinoma
ILV	Intraluminal Vesicle
MVBs	Multivesicular Bodies
ITGA3	Integrin α3β1
MTC	Medullary Thyroid Carcinoma
NTA	Nanoparticle Tracking Analysis
ON	Overnight
PTC	Papillary Thyroid Cancer
RISC	RNA-induced Silencing Complex
ROCK1	Rho-associated Coiled Coil-containing Protein Kinase 1
RPM	Random Positioning Machine
RQ	Relative Quantification
RT	Room Temperature
r-μg	Real Microgravity
s-μg	Simulated Microgravity
SEC	Size Exclusion Chromatography
SD	Standard Deviation
SP-IRIS	Single-Particle Interferometric Reflectance Imaging Sensor
TAM	Tumor Associated Macrophage
TME	Tumor Microenvironment
TNBC	Triple-negative Breast Cancer
ZEB1	Zinc Finger E-box-binding Homeobox 1

References

1. NASA. First Human-Made Object to Enter Space. Available online: https://www.nasa.gov/mission_pages/explorer/bumper.html (accessed on 6 September 2021).
2. NASA. Space Programs. Available online: http://adc.gsfc.nasa.gov/adc/education/space_ex/probes.html (accessed on 6 September 2021).
3. Mann, A. The Vostok Program: The Soviet's First Crewed Spaceflight Program. Available online: https://www.space.com/vostok-program.html (accessed on 6 September 2021).
4. SpaceX Space Station. Transporting Humans to the Orbiting Laboratory. Available online: https://www.spacex.com/human-spaceflight/iss/index.html (accessed on 6 September 2021).
5. Davenport, J. Virgin Galactic Successfully Flies Six Person Crew Including Founder Sir Richard Branson. Available online: https://www.nasaspaceflight.com/2021/07/virgin-galactic-fly-founder-branson/ (accessed on 6 September 2021).

6. Davenport, J. Blue Origin Launches First Crewed Flight with Four Crew, Including Founder Jeff Bezos and "Mercury 13" Aviatrix Wally Funk. Available online: https://www.nasaspaceflight.com/2021/07/blue-origin-first-crew/ (accessed on 6 September 2021).
7. Baldwin, K.M. Effect of spaceflight on the functional, biochemical, and metabolic properties of skeletal muscle. *Med. Sci. Sports Exerc.* **1996**, *28*, 983–987. [CrossRef]
8. Baldwin, K.M.; White, T.P.; Arnaud, S.B.; Edgerton, V.R.; Kraemer, W.J.; Kram, R.; Raab-Cullen, D.; Snow, C.M. Musculoskeletal adaptations to weightlessness and development of effective countermeasures. *Med. Sci. Sports Exerc.* **1996**, *28*, 1247–1253. [CrossRef] [PubMed]
9. Stampi, C. Sleep and Circadian Rhythms in Space. *J. Clin. Pharmacol.* **1994**, *34*, 518–534. [CrossRef] [PubMed]
10. Strollo, F. Hormonal changes in humans during spaceflight. *Adv. Space Biol. Med.* **1999**, *7*, 99–129. [PubMed]
11. Taylor, G.R. Overview of spaceflight immunology studies. *J. Leukoc. Biol.* **1993**, *54*, 179–188. [CrossRef] [PubMed]
12. White, R.J. Averner, M. Humans in space. *Nature* **2001**, *409*, 1115–1118. [CrossRef]
13. White, R.J. Weightlessness and the human body. *Sci. Am.* **1998**, *279*, 58–63. [CrossRef] [PubMed]
14. Garrett-Bakelman, F.E.; Darshi, M.; Green, S.J.; Gur, R.C.; Lin, L.; Macias, B.R.; McKenna, M.J.; Meydan, C.; Mishra, T.; Nasrini, J.; et al. The NASA Twins Study: A multidimensional analysis of a year-long human spaceflight. *Science* **2019**, *364*, 6436. [CrossRef]
15. Battista, N.; Meloni, M.A.; Bari, M.; Mastrangelo, N.; Galleri, G.; Rapino, C.; Dainese, E.; Agrò, A.F.; Pippia, P.; Maccarrone, M. 5-Lipoxygenase-dependent apoptosis of human lymphocytes in the International Space Station: Data from the ROALD experiment. *FASEB J.* **2012**, *26*, 1791–1798. [CrossRef]
16. Hoson, T.; Kamisaka, S.; Masuda, Y.; Yamashita, M.; Buchen, B. Evaluation of the three-dimensional clinostat as a simulator of weightlessness. *Planta* **1997**, *203*, S187–S197. [CrossRef]
17. Maccarrone, M.; Battista, N.; Meloni, M.; Bari, M.; Galleri, G.; Pippia, P.; Cogoli, A.; Finazzi-Agrò, A. Creating conditions similar to those that occur during exposure of cells to microgravity induces apoptosis in human lymphocytes by 5-lipoxygenase-mediated mitochondrial uncoupling and cytochrome c release. *J. Leukoc. Biol.* **2003**, *73*, 472–481. [CrossRef]
18. Van Loon, J. Some history and use of the random positioning machine, RPM, in gravity related research. *Adv. Space Res.* **2007**, *39*, 1161–1165. [CrossRef]
19. Herranz, R.; Anken, R.; Boonstra, J.; Braun, M.; Christianen, P.C.; de Geest, M.; Hauslage, J.; Hilbig, R.; Hill, R.J.; Lebert, M.; et al. Ground-based facilities for simulation of microgravity: Organism-specific recommendations for their use, and recommended terminology. *Astrobiology* **2013**, *13*, 1–17. [CrossRef]
20. Pietsch, J.; Bauer, J.; Egli, M.; Infanger, M.; Wise, P.; Ulbrich, C.; Grimm, D. The effects of weightlessness on the human organism and mammalian cells. *Curr. Mol. Med.* **2011**, *11*, 350–364. [CrossRef] [PubMed]
21. Schwarzenberg, M.; Pippia, P.; Meloni, M.A.; Cossu, G.; Cogoli-Greuter, M.; Cogoli, A. Signal transduction in T lymphocytes–a comparison of the data from space, the free fall machine and the random positioning machine. *Adv. Space Res.* **1999**, *24*, 793–800. [CrossRef]
22. German Aerospace Center, DLR. Germany and China—Joint Experiments in Space. Available online: https://www.dlr.de/content/en/downloads/news-archive/2011/20111101_germany-and-china---joint-experiments-in-space_1805.pdf?__blob=publicationFile&v=10 (accessed on 6 September 2021).
23. Kramer, C.D.; Kalla, E.M. The challenge of designing biomedical equipment during human research for long duration low-gravity NASA missions. In Proceedings of the 1997 16th South Biomed Engineer Conference, Biloxi, MS, USA, 4–6 April 1997; pp. 30–37.
24. Pietsch, J.; Ma, X.; Wehland, M.; Aleshcheva, G.; Schwarzwälder, A.; Segerer, J.; Birlem, M.; Horn, A.; Bauer, J.; Infanger, M.; et al. Spheroid formation of human thyroid cancer cells in an automated culturing system during the Shenzhou-8 Space mission. *Biomaterials* **2013**, *34*, 7694–7705. [CrossRef]
25. Riwaldt, S.; Pietsch, J.; Sickmann, A.; Bauer, J.; Braun, M.; Segerer, J.; Schwarzwälder, A.; Aleshcheva, G.; Corydon, T.J.; Infanger, M.; et al. Identification of proteins involved in inhibition of spheroid formation under microgravity. *Proteomics* **2015**, *15*, 2945–2952. [CrossRef]
26. Riwaldt, S.; Bauer, J.; Pietsch, J.; Braun, M.; Segerer, J.; Schwarzwälder, A.; Corydon, T.J.; Infanger, M.; Grimm, D. The Importance of Caveolin-1 as Key-Regulator of Three-Dimensional Growth in Thyroid Cancer Cells Cultured under Real and Simulated Microgravity Conditions. *Int. J. Mol. Sci.* **2015**, *16*, 28296–28310. [CrossRef] [PubMed]
27. Riwaldt, S.; Bauer, J.; Wehland, M.; Slumstrup, L.; Kopp, S.; Warnke, E.; Dittrich, A.; Magnusson, N.E.; Pietsch, J.; Corydon, T.J.; et al. Pathways Regulating Spheroid Formation of Human Follicular Thyroid Cancer Cells under Simulated Microgravity Conditions: A Genetic Approach. *Int. J. Mol. Sci.* **2016**, *17*, 528. [CrossRef] [PubMed]
28. Colombo, M.; Raposo, G.; Thery, C. Biogenesis, secretion, and intercellular interactions of exosomes and other extracellular vesicles. *Annu. Rev. Cell Dev. Biol.* **2014**, *30*, 255–289. [CrossRef]
29. Quek, C.; Hill, A.F. The role of extracellular vesicles in neurodegenerative diseases. *Biochem. Biophys. Res. Commun.* **2017**, *483*, 1178–1186. [CrossRef] [PubMed]
30. Bank, I.E.; Timmers, L.; Gijsberts, C.M.; Zhang, Y.N.; Mosterd, A.; Wang, J.W.; Chan, M.Y.; De Hoog, V.; Lim, S.K.; Sze, S.K.; et al. The diagnostic and prognostic potential of plasma extracellular vesicles for cardiovascular disease. *Expert Rev. Mol. Diagn.* **2015**, *15*, 1577–1588. [CrossRef] [PubMed]
31. Abels, E.R.; Breakefield, X.O. Introduction to Extracellular Vesicles: Biogenesis, RNA Cargo Selection, Content, Release, and Uptake. *Cell. Mol. Neurobiol.* **2016**, *36*, 301–312. [CrossRef] [PubMed]

32. Orozco, A.F.; Lewis, D.E. Flow cytometric analysis of circulating microparticles in plasma. *Cytometry A* **2010**, *77*, 502–514. [CrossRef] [PubMed]
33. Gonzales, P.A.; Pisitkun, T.; Hoffert, J.D.; Tchapyjnikov, D.; Star, R.A.; Kleta, R.; Wang, N.S.; Knepper, M.A. Large-scale proteomics and phosphoproteomics of urinary exosomes. *J. Am. Soc. Nephrol.* **2009**, *20*, 363–379. [CrossRef]
34. Sharma, S.; Gillespie, B.M.; Palanisamy, V.; Gimzewski, J.K. Quantitative nanostructural and single-molecule force spectroscopy biomolecular analysis of human-saliva-derived exosomes. *Langmuir* **2011**, *27*, 14394–14400. [CrossRef] [PubMed]
35. Lane, R.E.; Korbie, D.; Trau, M.; Hill, M.M. Purification Protocols for Extracellular Vesicles. *Methods Mol. Biol.* **2017**, *1660*, 111–130.
36. Lässer, C.; Eldh, M.; Lötvall, J. Isolation and characterization of RNA-containing exosomes. *J. Vis. Exp.* **2012**, *59*, e3037. [CrossRef] [PubMed]
37. Théry, C.; Witwer, K.W.; Aikawa, E.; Alcaraz, M.J.; Anderson, J.D.; Andriantsitohaina, R.; Antoniou, A.; Arab, T.; Archer, F.; Atkin-Smith, G.K.; et al. Minimal information for studies of extracellular vesicles 2018 (MISEV2018): A position statement of the International Society for Extracellular Vesicles and update of the MISEV2014 guidelines. *J. Extracell. Vesicles* **2018**, *7*, 1535750. [CrossRef]
38. Gardiner, C.; Di Vizio, D.; Sahoo, S.; Théry, C.; Witwer, K.W.; Wauben, M.; Hill, A.F. Techniques used for the isolation and characterization of extracellular vesicles: Results of a worldwide survey. *J. Extracell. Vesicles* **2016**, *5*, 32945. [CrossRef]
39. Peinado, H.; Alečković, M.; Lavotshkin, S.; Matei, I.; Costa-Silva, B.; Moreno-Bueno, G.; Hergueta-Redondo, M.; Williams, C.; García-Santos, G.; Ghajar, C.; et al. Melanoma exosomes educate bone marrow progenitor cells toward a pro-metastatic phenotype through MET. *Nat. Med.* **2012**, *18*, 883–891. [CrossRef]
40. Somasundaram, R.; Herlyn, M. Melanoma exosomes: Messengers of metastasis. *Nat. Med.* **2012**, *18*, 853–854. [CrossRef] [PubMed]
41. Alderton, G.K. Metastasis. Exosomes drive premetastatic niche formation. *Nat. Rev. Cancer* **2012**, *12*, 447. [CrossRef]
42. Hood, J.L.; San, R.S.; Wickline, S.A. Exosomes released by melanoma cells prepare sentinel lymph nodes for tumor metastasis. *Cancer Res.* **2011**, *71*, 3792–3801. [CrossRef]
43. Costa-Silva, B.; Aiello, N.M.; Ocean, A.J.; Singh, S.; Zhang, H.; Thakur, B.K.; Becker, A.; Hoshino, A.; Mark, M.T.; Molina, H.; et al. Pancreatic cancer exosomes initiate pre-metastatic niche formation in the liver. *Nat. Cell Biol.* **2015**, *17*, 816–826. [CrossRef] [PubMed]
44. Nogués, L.; Benito-Martin, A.; Hergueta-Redondo, M.; Peinado, H. The influence of tumour-derived extracellular vesicles on local and distal metastatic dissemination. *Mol. Asp. Med.* **2018**, *60*, 15–26. [CrossRef]
45. Hendricks, M.R.; Lane, S.; Melvin, J.A.; Ouyang, Y.; Stolz, D.B.; Williams, J.V.; Sadovsky, Y.; Bomberger, J.M. Extracellular vesicles promote transkingdom nutrient transfer during viral-bacterial co-infection. *Cell Rep.* **2021**, *34*, 108672. [CrossRef]
46. Maas SL, N.; Breakefield, X.O.; Weaver, A.M. Extracellular Vesicles: Unique Intercellular Delivery Vehicles. *Trends Cell Biol.* **2017**, *27*, 172–188. [CrossRef] [PubMed]
47. Al-Nedawi, K.; Meehan, B.; Micallef, J.; Lhotak, V.; May, L.; Guha, A.; Rak, J. Intercellular transfer of the oncogenic receptor EGFRvIII by microvesicles derived from tumour cells. *Nat Cell Biol* **2008**, *10*, 619–624. [CrossRef]
48. Andreola, G.; Rivoltini, L.; Castelli, C.; Huber, V.; Perego, P.; Deho, P.; Squarcina, P.; Accornero, P.; Lozupone, F.; Lugini, L.; et al. Induction of lymphocyte apoptosis by tumor cell secretion of FasL-bearing microvesicles. *J. Exp. Med.* **2002**, *195*, 1303–1316. [CrossRef]
49. Huber, V.; Fais, S.; Iero, M.; Lugini, L.; Canese, P.; Squarcina, P.; Zaccheddu, A.; Colone, M.; Arancia, G.; Gentile, M.; et al. Human colorectal cancer cells induce T-cell death through release of proapoptotic microvesicles: Role in immune escape. *Gastroenterology* **2005**, *128*, 1796–1804. [CrossRef]
50. Skog, J.; Würdinger, T.; van Rijn, S.; Meijer, D.H.; Gainche, L.; Sena-Esteves, M.; Curry, W.T.; Carter, B.S.; Krichevsky, A.M.; Breakefield, X.O. Glioblastoma microvesicles transport RNA and proteins that promote tumour growth and provide diagnostic biomarkers. *Nat. Cell Biol.* **2008**, *10*, 1470–1476. [CrossRef]
51. Richards, K.E.; Zeleniak, A.E.; Fishel, M.L.; Wu, J.; Littlepage, L.E.; Hill, R. Cancer-associated fibroblast exosomes regulate survival and proliferation of pancreatic cancer cells. *Oncogene* **2017**, *36*, 1770–1778. [CrossRef]
52. Au Yeung, C.L.; Co, N.N.; Tsuruga, T.; Yeung, T.L.; Kwan, S.Y.; Leung, C.S.; Li, Y.; Lu, E.S.; Kwan, K.; Wong, K.K.; et al. Exosomal transfer of stroma-derived miR21 confers paclitaxel resistance in ovarian cancer cells through targeting APAF. *Nat. Commun.* **2016**, *7*, 11150. [CrossRef] [PubMed]
53. Leca, J.; Martinez, S.; Lac, S.; Nigri, J.; Secq, V.; Rubis, M.; Bressy, C.; Sergé, A.; Lavaut, M.N.; Dusetti, N.; et al. Cancer-associated fibroblast-derived annexin A6+ extracellular vesicles support pancreatic cancer aggressiveness. *J. Clin. Investig.* **2016**, *126*, 4140–4156. [CrossRef] [PubMed]
54. Luga, V.; Zhang, L.; Viloria-Petit, A.M.; Ogunjimi, A.A.; Inanlou, M.R.; Chiu, E.; Buchanan, M.; Hosein, A.N.; Basik, M.; Wrana, J.L. Exosomes mediate stromal mobilization of autocrine Wnt-PCP signaling in breast cancer cell migration. *Cell* **2012**, *151*, 1542–1556. [CrossRef] [PubMed]
55. Whiteside, T.L. Tumor-Derived Exosomes and Their Role in Tumor-Induced Immune Suppression. *Vaccines* **2016**, *4*, 4. [CrossRef]
56. Lötvall, J.; Hill, A.F.; Hochberg, F.; Buzás, E.I.; Di Vizio, D.; Gardiner, C.; Gho, Y.S.; Kurochkin, I.V.; Mathivanan, S.; Quesenberry, P.; et al. Minimal experimental requirements for definition of extracellular vesicles and their functions: A position statement from the International Society for Extracellular Vesicles. *J. Extracell. Vesicles* **2014**, *3*, 26913. [CrossRef]
57. Hessvik, N.P.; Llorente, A. Current knowledge on exosome biogenesis and release. *Cell Mol. Life Sci.* **2018**, *75*, 193–208. [CrossRef]
58. Hartjes, T.A.; Mytnyk, S.; Jenster, G.W.; van Steijn, V.; van Royen, M.E. Extracellular Vesicle Quantification and Characterization: Common Methods and Emerging Approaches. *Bioengineering* **2019**, *6*, 1. [CrossRef]

59. Filipe, V.; Hawe, A.; Jiskoot, W. Critical evaluation of Nanoparticle Tracking Analysis (NTA) by NanoSight for the measurement of nanoparticles and protein aggregates. *Pharm. Res.* **2010**, *27*, 796–810. [CrossRef]
60. Daaboul, G.G.; Gagni, P.; Benussi, L.; Bettotti, P.; Ciani, M.; Cretich, M.; Freedman, D.S.; Ghidoni, R.; Ozkumur, A.Y.; Piotto, C.; et al. Digital Detection of Exosomes by Interferometric Imaging. *Sci. Rep.* **2016**, *6*, 37246. [CrossRef]
61. Avci, O.; Ünlü, N.L.; Özkumur, A.Y.; Ünlü, M.S. Interferometric Reflectance Imaging Sensor (IRIS)—A Platform Technology for Multiplexed Diagnostics and Digital Detection. *Sensors* **2015**, *15*, 17649–17665. [CrossRef]
62. Yang, Y.; Shen, G.; Wang, H.; Li, H.; Zhang, T.; Tao, N.; Ding, X.; Yu, H. Interferometric plasmonic imaging and detection of single exosomes. *Proc. Natl. Acad. Sci. USA* **2018**, *115*, 10275–10280. [CrossRef]
63. Wise, P.M.; Neviani, P.; Riwaldt, S.; Corydon, T.J.; Wehland, M.; Braun, M.; Krüger, M.; Infanger, M.; Grimm, D. Changes in Exosome Release in Thyroid Cancer Cells after Prolonged Exposure to Real Microgravity in Space. *Int. J. Mol. Sci.* **2021**, *22*, 2132. [CrossRef] [PubMed]
64. Bartel, D.P. Metazoan MicroRNAs. *Cell* **2018**, *173*, 20–51. [CrossRef] [PubMed]
65. Lee, Y.; Kim, M.; Han, J.; Yeom, K.H.; Lee, S.; Baek, S.H.; Kim, V.N. MicroRNA genes are transcribed by RNA polymerase II. *EMBO J.* **2004**, *23*, 4051–4060. [CrossRef] [PubMed]
66. Lee, R.C.; Feinbaum, R.L.; Ambros, V. The, *C. elegans* heterochronic gene lin-4 encodes small RNAs with antisense complementarity to lin-14. *Cell* **1993**, *75*, 843–854. [CrossRef]
67. Lagos-Quintana, M.; Rauhut, R.; Lendeckel, W.; Tuschl, T. Identification of novel genes coding for small expressed RNAs. *Science* **2001**, *294*, 853–858. [CrossRef]
68. Reinhart, B.J.; Slack, F.J.; Basson, M.; Pasquinelli, A.E.; Bettinger, J.C.; Rougvie, A.E.; Horvitz, H.R.; Ruvkun, G. The 21-nucleotide let-7 RNA regulates developmental timing in *Caenorhabditis elegans*. *Nature* **2000**, *403*, 901–906. [CrossRef]
69. Pasquinelli, A.E.; Reinhart, B.J.; Slack, F.; Martindale, M.Q.; Kuroda, M.I.; Maller, B.; Hayward, D.C.; Ball, E.E.; Degnan, B.; Müller, P.; et al. Conservation of the sequence and temporal expression of let-7 heterochronic regulatory RNA. *Nature* **2000**, *408*, 86–89. [CrossRef]
70. Lee, R.C.; Ambros, V. An extensive class of small RNAs in *Caenorhabditis elegans*. *Science* **2001**, *294*, 862–864. [CrossRef]
71. Lee, Y.; Ahn, C.; Han, J.; Choi, H.; Kim, J.; Yim, J.; Lee, J.; Provost, P.; Rådmark, O.; Kim, S.; et al. The nuclear RNase III Drosha initiates microRNA processing. *Nature* **2003**, *425*, 415–419. [CrossRef] [PubMed]
72. Kim, V.N. MicroRNA precursors in motion: Exportin-5 mediates their nuclear export. *Trends Cell Biol.* **2004**, *14*, 156–159. [CrossRef]
73. Bernstein, E.; Caudy, A.A.; Hammond, S.M.; Hannon, G.J. Role for a bidentate ribonuclease in the initiation step of RNA interference. *Nature* **2001**, *409*, 363–366. [CrossRef] [PubMed]
74. Ketting, R.F.; Fischer, S.E.; Bernstein, E.; Sijen, T.; Hannon, G.J.; Plasterk, R.H. Dicer functions in RNA interference and in synthesis of small RNA involved in developmental timing in *C. elegans*. *Genes Dev.* **2001**, *15*, 2654–2659. [CrossRef] [PubMed]
75. Hutvágner, G.; McLachlan, J.; Pasquinelli, A.E.; Bálint, E.; Tuschl, T.; Zamore, P.D. A cellular function for the RNA-interference enzyme Dicer in the maturation of the let-7 small temporal RNA. *Science* **2001**, *293*, 834–838. [CrossRef] [PubMed]
76. Wightman, B.; Ha, I.; Ruvkun, G. Posttranscriptional regulation of the heterochronic gene lin-14 by lin-4 mediates temporal pattern formation in *C. elegans*. *Cell* **1993**, *75*, 855–862. [CrossRef]
77. McKenzie, A.J.; Hoshino, D.; Hong, N.H.; Cha, D.J.; Franklin, J.L.; Coffey, R.J.; Patton, J.G.; Weaver, A.M. KRAS-MEK Signaling Controls Ago2 Sorting into Exosomes. *Cell Rep.* **2016**, *15*, 978–987. [CrossRef]
78. Filipowicz, W.; Bhattacharyya, S.N.; Sonenberg, N. Mechanisms of post-transcriptional regulation by microRNAs: Are the answers in sight? *Nat. Rev. Genet.* **2008**, *9*, 102–114. [CrossRef]
79. Shu, S.; Yang, Y.; Allen, C.L.; Hurley, E.; Tung, K.H.; Minderman, H.; Wu, Y.; Ernstoff, M.S. Purity and yield of melanoma exosomes are dependent on isolation method. *J. Extracell. Vesicles* **2020**, *9*, 1692401. [CrossRef]
80. Brown, P.N.; Yin, H. Polymer-Based Purification of Extracellular Vesicles. *Methods Mol. Biol.* **2017**, *1660*, 91–103. [PubMed]
81. Cong, D.; He, M.; Chen, S.; Liu, X.; Liu, X.; Sun, H. Expression profiles of pivotal microRNAs and targets in thyroid papillary carcinoma: An analysis of The Cancer Genome Atlas. *OncoTargets Ther.* **2015**, *8*, 2271–2277.
82. Rosignolo, F.; Sponziello, M.; Giacomelli, L.; Russo, D.; Pecce, V.; Biffoni, M.; Bellantone, R.; Lombardi, C.P.; Lamartina, L.; Grani, G.; et al. Identification of Thyroid-Associated Serum microRNA Profiles and Their Potential Use in Thyroid Cancer Follow-Up. *J. Endocr. Soc.* **2017**, *1*, 3–13. [PubMed]
83. Shabani, N.; Razaviyan, J.; Paryan, M.; Tavangar, S.M.; Azizi, F.; Mohammadi-Yeganeh, S.; Hedayati, M. Evaluation of miRNAs expression in medullary thyroid carcinoma tissue samples: miR-34a and miR-144 as promising overexpressed markers in MTC. *Hum. Pathol.* **2018**, *79*, 212–221. [CrossRef] [PubMed]
84. Ghafouri-Fard, S.; Shirvani-Farsani, Z.; Taheri, M. The role of microRNAs in the pathogenesis of thyroid cancer. *Noncoding RNA Res.* **2020**, *5*, 88–98. [CrossRef]
85. Diao, Y.; Fu, H.; Wang, Q. MiR-221 Exacerbate Cell Proliferation and Invasion by Targeting TIMP3 in Papillary Thyroid Carcinoma. *Am. J. Ther.* **2017**, *24*, e317–e328. [CrossRef]
86. Wei, Z.L.; Gao, A.B.; Wang, Q.; Lou, X.E.; Zhao, J.; Lu, Q.J. MicroRNA-221 promotes papillary thyroid carcinoma cell migration and invasion via targeting RECK and regulating epithelial-mesenchymal transition. *OncoTargets Ther.* **2019**, *12*, 2323–2333. [CrossRef]
87. Sun, J.; Shi, R.; Zhao, S.; Li, X.; Lu, S.; Bu, H.; Ma, X.; Su, C. E2F8, a direct target of miR-144, promotes papillary thyroid cancer progression via regulating cell cycle. *J. Exp. Clin. Cancer Res.* **2017**, *36*, 40. [CrossRef]

88. Wu, G.; Zheng, H.; Xu, J.; Guo, Y.; Zheng, G.; Ma, C.; Hao, S.; Liu, X.; Chen, H.; Wei, S.; et al. miR-429 suppresses cell growth and induces apoptosis of human thyroid cancer cell by targeting ZEB. *Artif. Cells Nanomed. Biotechnol.* **2019**, *47*, 548–554. [CrossRef]
89. Cao, X.Z.; Bin, H.; Zang, Z.N. MiR-128 suppresses the growth of thyroid carcinoma by negatively regulating SPHK. *Biomed. Pharmacother.* **2019**, *109*, 1960–1966. [CrossRef]
90. Liu, C.; Xing, M.; Wang, L.; Zhang, K. miR-199a-3p downregulation in thyroid tissues is associated with invasion and metastasis of papillary thyroid carcinoma. *Br. J. Biomed. Sci.* **2017**, *74*, 90–94. [CrossRef] [PubMed]
91. Ma, S.; Jia, W.; Ni, S. miR-199a-5p inhibits the progression of papillary thyroid carcinoma by targeting SNAI. *Biochem. Biophys. Res. Commun.* **2018**, *497*, 181–186. [CrossRef]
92. Lambrecht, G.; Petersen, N.; Weerts, G.; Pruett, C.; Evetts, S.; Stokes, M.; Hides, J. The role of physiotherapy in the European Space Agency strategy for preparation and reconditioning of astronauts before and after long duration space flight. *Musculoskelet. Sci. Pract.* **2017**, *27* (Suppl. S1), S15–S22. [CrossRef]
93. Barratt, M.R.; Baker, E.S.; Pool, S.L. *Principles of Clinical Medicine for Space Flight*, 1st ed.; Springer: New York, NY, USA, 2008; p. 596.
94. Petersen, N.; Lambrecht, G.; Scott, J.; Hirsch, N.; Stokes, M.; Mester, J. Postflight reconditioning for European Astronauts—A case report of recovery after six months in space. *Musculoskelet. Sci. Pract.* **2017**, *27* (Suppl. S1), S23–S31. [CrossRef]
95. Grosse, J.; Wehland, M.; Pietsch, J.; Schulz, H.; Saar, K.; Hübner, N.; Eilles, C.; Bauer, J.; Abou-El-Ardat, K.; Baatout, S.; et al. Gravity-sensitive signaling drives 3-dimensional formation of multicellular thyroid cancer spheroids. *FASEB J.* **2012**, *26*, 5124–5140. [CrossRef] [PubMed]
96. Ma, X.; Pietsch, J.; Wehland, M.; Schulz, H.; Saar, K.; Hübner, N.; Bauer, J.; Braun, M.; Schwarzwälder, A.; Segerer, J.; et al. Differential gene expression profile and altered cytokine secretion of thyroid cancer cells in space. *FASEB J.* **2014**, *28*, 813–835. [CrossRef]
97. Cramer, J.D.; Fu, P.; Harth, K.C.; Margevicius, S.; Wilhelm, S.M. Analysis of the rising incidence of thyroid cancer using the Surveillance, Epidemiology and End Results national cancer data registry. *Surgery* **2010**, *148*, 1147–1152, discussion 1152–1153. [CrossRef] [PubMed]
98. Rossi, E.D.; Pantanowitz, L.; Hornick, J.L. A worldwide journey of thyroid cancer incidence centred on tumour histology. *Lancet Diabetes Endocrinol.* **2021**, *9*, 193–194. [CrossRef]
99. Claridge, B.; Kastaniegaard, K.; Stensballe, A.; Greening, D.W. Post-translational and transcriptional dynamics—Regulating extracellular vesicle biology. *Expert Rev. Proteom.* **2019**, *16*, 17–31. [CrossRef]
100. Challagundla, K.B.; Fanini, F.; Vannini, I.; Wise, P.; Murtadha, M.; Malinconico, L.; Cimmino, A.; Fabbri, M. microRNAs in the tumor microenvironment: Solving the riddle for a better diagnostics. *Expert Rev. Mol. Diagn.* **2014**, *14*, 565–574. [CrossRef]
101. Challagundla, K.; Wise, P.; Fabbri, M. *Exosomic microRNAs and Drug Resistance in the Neuroblastoma Environment*; Poster for Annual Symposium; The Saban Research Institute: Los Angeles, CA, USA, 2013.
102. Barile, L.; Vassalli, G. Exosomes: Therapy delivery tools and biomarkers of diseases. *Pharmacol. Ther.* **2017**, *174*, 63–78. [CrossRef] [PubMed]
103. Kopp, S.; Krüger, M.; Feldmann, S.; Oltmann, H.; Schütte, A.; Schmitz, B.; Bauer, J.; Schulz, H.; Saar, K.; Huebner, N.; et al. Thyroid cancer cells in space during the TEXUS-53 sounding rocket mission—The THYROID Project. *Sci. Rep.* **2018**, *8*, 10355. [CrossRef]
104. Romano, G.; Veneziano, D.; Acunzo, M.; Croce, C.M. Small non-coding RNA and cancer. *Carcinogenesis* **2017**, *38*, 485–491. [CrossRef]
105. Anastasiadou, E.; Jacob, L.S.; Slack, F.J. Non-coding RNA networks in cancer. *Nat. Rev. Cancer* **2018**, *18*, 5–18. [CrossRef] [PubMed]
106. Slack, F.J.; Chinnaiyan, A.M. The Role of Non-coding RNAs in Oncology. *Cell* **2019**, *179*, 1033–1055. [CrossRef] [PubMed]
107. Panni, S.; Lovering, R.C.; Porras, P.; Orchard, S. Non-coding RNA regulatory networks. *Biochim. Biophys. Acta Gene Regul. Mech.* **2020**, *1863*, 194417. [CrossRef]
108. Cummins, J.M.; He, Y.; Leary, R.J.; Pagliarini, R.; Diaz LA, J.r.; Sjoblom, T.; Barad, O.; Bentwich, Z.; Szafranska, A.E.; Labourier, E.; et al. The colorectal microRNAome. *Proc. Natl. Acad. Sci. USA* **2006**, *103*, 3687–3692. [CrossRef]
109. Liang, Y.; Song, X.; Li, Y.; Ma, T.; Su, P.; Guo, R.; Chen, B.; Zhang, H.; Sang, Y.; Liu, Y.; et al. Targeting the circBMPR2/miR-553/USP4 Axis as a Potent Therapeutic Approach for Breast Cancer. *Mol. Ther. Nucleic Acids* **2019**, *17*, 347–361. [CrossRef]
110. Kopp, S.; Sahana, J.; Islam, T.; Petersen, A.G.; Bauer, J.; Corydon, T.J.; Schulz, H.; Saar, K.; Huebner, N.; Slumstrup, L.; et al. The role of NFκB in spheroid formation of human breast cancer cells cultured on the Random Positioning Machine. *Sci. Rep.* **2018**, *8*, 921. [CrossRef]
111. Hu, X.; Macdonald, D.M.; Huettner, P.C.; Feng, Z.; El Naqa, I.M.; Schwarz, J.K.; Mutch, D.G.; Grigsby, P.W.; Powell, S.N.; Wang, X. A miR-200 microRNA cluster as prognostic marker in advanced ovarian cancer. *Gynecol. Oncol.* **2009**, *114*, 457–464. [CrossRef]
112. Chen, J.; Wang, L.; Matyunina, L.V.; Hill, C.G.; McDonald, J.F. Overexpression of miR-429 induces mesenchymal-to-epithelial transition (MET) in metastatic ovarian cancer cells. *Gynecol. Oncol.* **2011**, *121*, 200–205. [CrossRef] [PubMed]
113. Liu, X.; Liu, Y.; Wu, S.; Shi, X.; Li, L.; Zhao, J.; Xu, H. Tumor-suppressing effects of miR-429 on human osteosarcoma. *Cell Biochem. Biophys.* **2014**, *70*, 215–224. [CrossRef]
114. Guo, C.; Zhao, D.; Zhang, Q.; Liu, S.; Sun, M.-Z. miR-429 suppresses tumor migration and invasion by targeting CRKL in hepatocellular carcinoma via inhibiting Raf/MEK/ERK pathway and epithelial-mesenchymal transition. *Sci. Rep.* **2018**, *8*, 2375. [CrossRef]
115. Li, J.; Du, L.; Yang, Y.; Wang, C.; Liu, H.; Wang, L.; Zhang, X.; Li, W.; Zheng, G.; Dong, Z. MiR-429 is an independent prognostic factor in colorectal cancer and exerts its anti-apoptotic function by targeting SOX. *Cancer Lett.* **2013**, *329*, 84–90. [CrossRef] [PubMed]

116. Snowdon, J.; Zhang, X.; Childs, T.; Tron, V.A.; Feilotter, H. The microRNA-200 family is upregulated in endometrial carcinoma. *PLoS ONE* **2011**, *6*, e22828. [CrossRef]
117. Wu, C.L.; Ho, J.Y.; Chou, S.C.; Yu, D.S. MiR-429 reverses epithelial-mesenchymal transition by restoring E-cadherin expression in bladder cancer. *Oncotarget* **2016**, *7*, 26593–26603. [CrossRef] [PubMed]
118. Guo, C.M.; Liu, S.Q.; Sun, M.Z. miR-429 as biomarker for diagnosis, treatment and prognosis of cancers and its potential action mechanisms: A systematic literature review. *Neoplasma* **2020**, *67*, 215–228. [CrossRef] [PubMed]
119. Larsen, J.E.; Nathan, V.; Osborne, J.K.; Farrow, R.K.; Deb, D.; Sullivan, J.P.; Dospoy, P.D.; Augustyn, A.; Hight, S.K.; Sato, M.; et al. ZEB1 drives epithelial-to-mesenchymal transition in lung cancer. *J. Clin. Investig.* **2016**, *126*, 3219–3235. [CrossRef]
120. Zhang, P.; Sun, Y.; Ma, L. ZEB1: At the crossroads of epithelial-mesenchymal transition, metastasis and therapy resistance. *Cell Cycle* **2015**, *14*, 481–487. [CrossRef] [PubMed]
121. Wu, H.T.; Zhong, H.T.; Li, G.W.; Shen, J.X.; Ye, Q.Q.; Zhang, M.L.; Liu, J. Oncogenic functions of the EMT-related transcription factor ZEB1 in breast cancer. *J. Transl. Med.* **2020**, *18*, 51. [CrossRef] [PubMed]
122. Cortés, M.; Sanchez-Moral, L.; de Barrios, O.; Fernández-Aceñero, M.J.; Martínez-Campanario, M.C.; Esteve-Codina, A.; Darling, D.S.; Győrffy, B.; Lawrence, T.; Dean, D.C.; et al. Tumor-associated macrophages (TAMs) depend on ZEB1 for their cancer-promoting roles. *EMBO J.* **2017**, *36*, 3336–3355. [CrossRef] [PubMed]
123. Katsura, A.; Tamura, Y.; Hokari, S.; Harada, M.; Morikawa, M.; Sakurai, T.; Takahashi, K.; Mizutani, A.; Nishida, J.; Yokoyama, Y.; et al. ZEB1-regulated inflammatory phenotype in breast cancer cells. *Mol. Oncol.* **2017**, *11*, 1241–1262. [CrossRef] [PubMed]
124. Xia, Z.; Meng, F.; Liu, Y.; Fang, Y.; Wu, X.; Zhang, C.; Liu, D.; Li, G. Decreased MiR-128–3p alleviates the progression of rheumatoid arthritis by up-regulating the expression of TNFAIP. *Biosci. Rep.* **2018**, *38*, 4. [CrossRef]
125. Cao, F.; Li, Z.; Ding, W.M.; Yan, L.; Zhao, Q.Y. LncRNA PVT1 regulates atrial fibrosis via miR-128–3p-SP1-TGF-β1-Smad axis in atrial fibrillation. *Mol. Med.* **2019**, *25*, 7. [CrossRef]
126. Xie, L.B.; Chen, B.; Liao, X.; Chen, Y.F.; Yang, R.; He, S.R.; Pei, L.J.; Jiang, R. LINC00963 targeting miR-128–3p promotes acute kidney injury process by activating JAK2/STAT1 pathway. *J. Cell Mol. Med.* **2020**, *24*, 5555–5564. [CrossRef]
127. Xu, T.; Luo, Y.; Wang, J.; Zhang, N.; Gu, C.; Li, L.; Qian, D.; Cai, W.; Fan, J.; Yin, G. Exosomal miRNA-128–3p from mesenchymal stem cells of aged rats regulates osteogenesis and bone fracture healing by targeting Smad. *J. Nanobiotechnol.* **2020**, *18*, 47. [CrossRef]
128. Farina, F.M.; Hall, I.F.; Serio, S.; Zani, S.; Climent, M.; Salvarani, N.; Carullo, P.; Civilini, E.; Condorelli, G.; Elia, L.; et al. miR-128–3p Is a Novel Regulator of Vascular Smooth Muscle Cell Phenotypic Switch and Vascular Diseases. *Circ. Res.* **2020**, *126*, e120–e135. [CrossRef]
129. Zanoni, M.; Orlandi, E.; Rossetti, G.; Turatti, M.; Calabrese, M.; Gomez Lira, M.; Gajofatto, A. Upregulated serum miR-128–3p in progressive and relapse-free multiple sclerosis patients. *Acta Neurol. Scand.* **2020**, *142*, 511–516. [CrossRef]
130. Hao, S.D.; Ma, J.X.; Liu, Y.; Liu, P.J.; Qin, Y. Long non-coding TUG1 accelerates prostate cancer progression through regulating miR-128–3p/YES1 axis. *Eur. Rev. Med. Pharmacol. Sci.* **2020**, *24*, 619–632.
131. Zhu, L.; Wang, A.; Gao, M.; Duan, X.; Li, Z. LncRNA MIR4435–2HG triggers ovarian cancer progression by regulating miR-128–3p/CKD14 axis. *Cancer Cell Int.* **2020**, *20*, 145. [CrossRef] [PubMed]
132. Zhao, J.; Li, D.; Fang, L. MiR-128–3p suppresses breast cancer cellular progression via targeting LIMK. *Biomed. Pharmacother.* **2019**, *115*, 108947. [CrossRef] [PubMed]
133. Wang, B.; Hang, J.; Li, W.; Yuan, W. Knockdown of LncRNA DLEU2 Inhibits Cervical Cancer Progression via Targeting miR-128–3p. *OncoTargets Ther.* **2020**, *13*, 10173–10184. [CrossRef] [PubMed]
134. Wang, R.; Liu, L.; Jiao, J.; Gao, D. Knockdown of MIR4435–2HG Suppresses the Proliferation, Migration and Invasion of Cervical Cancer Cells via Regulating the miR-128–3p/MSI2 Axis In Vitro. *Cancer Manag. Res.* **2020**, *12*, 8745–8756. [CrossRef]
135. Feng, W.; Guo, R.; Zhang, D.; Zhang, R. Circ-ABCB10 knockdown inhibits the malignant progression of cervical cancer through microRNA-128–3p/ZEB1 axis. *Biol. Proc. Online* **2021**, *23*, 17. [CrossRef]
136. Zhao, L.; Li, R.; Xu, S.; Li, Y.; Zhao, P.; Dong, W.; Liu, Z.; Zhao, Q.; Tan, B. Tumor suppressor miR-128–3p inhibits metastasis and epithelial-mesenchymal transition by targeting ZEB1 in esophageal squamous-cell cancer. *Acta Biochim. Biophys. Sin.* **2018**, *50*, 171–180. [CrossRef]
137. Tian, L.; Chen, M.; He, Q.; Yan, Q.; Zhai, C. MicroRNA-199a-5p suppresses cell proliferation, migration and invasion by targeting ITGA3 in colorectal cancer. *Mol. Med. Rep.* **2020**, *22*, 2307–2317. [CrossRef]
138. Zhu, Q.D.; Zhou, Q.Q.; Dong, L.; Huang, Z.; Wu, F.; Deng, X. MiR-199a-5p Inhibits the Growth and Metastasis of Colorectal Cancer Cells by Targeting ROCK. *Technol. Cancer Res. Treat.* **2018**, *17*, 1533034618775509. [CrossRef]
139. Qu, D.; Yang, Y.; Huang, X. miR-199a-5p promotes proliferation and metastasis and epithelial-mesenchymal transition through targeting PIAS3 in cervical carcinoma. *J. Cell Biochem.* **2019**, *120*, 13562–13572. [CrossRef]
140. Yagil, Z.; Nechushtan, H.; Kay, G.; Yang, C.M.; Kemeny, D.M.; Razin, E. The enigma of the role of protein inhibitor of activated STAT3 (PIAS3) in the immune response. *Trends Immunol.* **2010**, *31*, 199–204. [CrossRef]
141. Ren, L.; Xu, Y.; Qin, G.; Liu, C.; Yan, Y.; Zhang, H. miR-199b-5p-Stonin 2 axis regulates metastases and epithelial-to-mesenchymal transition of papillary thyroid carcinoma. *IUBMB Life* **2019**, *71*, 28–40. [CrossRef]
142. Wang, D.; Zheng, Y. Silencing long non-coding RNAs nicotinamide nucleotide transhydrogenase antisense RNA 1 inhibited papillary thyroid cancer cell proliferation, migration and invasion and promoted apoptosis via targeting miR-199a-5p. *Endocr. J.* **2021**, *68*, 583–597. [CrossRef]

143. Wei, S.; Yun, X.; Ruan, X.; Wei, X.; Zheng, X.; Gao, M. Identification of potential pathogenic candidates or diagnostic biomarkers in papillary thyroid carcinoma using expression and methylation profiles. *Oncol. Lett.* **2019**, *18*, 6670–6678. [CrossRef] [PubMed]
144. Sun, D.; Han, S.; Liu, C.; Zhou, R.; Sun, W.; Zhang, Z.; Qu, J. Microrna-199a-5p Functions as a Tumor Suppressor via Suppressing Connective Tissue Growth Factor (CTGF) in Follicular Thyroid Carcinoma. *Med. Sci. Monit.* **2016**, *22*, 1210–1217. [CrossRef] [PubMed]
145. Taga, M.; Yamauchi, K.; Odle, J.; Furian, L.; Sundaresan, A.; Ramesh, G.T.; Pellis, N.R.; Andrassy, R.J.; Kulkarni, A.D. Melanoma growth and tumorigenicity in models of microgravity. *Aviat. Space Environ. Med.* **2006**, *77*, 1113–1116.
146. Chen, J.; Shin, V.Y.; Siu, M.T.; Ho, J.C.; Cheuk, I.; Kwong, A. miR-199a-5p confers tumor-suppressive role in triple-negative breast cancer. *BMC Cancer* **2016**, *16*, 887. [CrossRef]
147. Zhang, L.C.; Wei, Z.B.; Tang, S.F. Knockdown of the Long Noncoding RNA LUCAT1 Inhibits High-Glucose-Induced Epithelial-Mesenchymal Transition through the miR-199a-5p-ZEB1 Axis in Human Renal Tubular Epithelial Cells. *Biomed. Res. Int.* **2020**, *2020*, 8895003. [CrossRef]
148. Liu, Y.; Lu, C.; Fan, L.; Wang, J.; Li, T.; Liu, Z.; Sheng, J.; Qian, R.; Duan, A.; Lu, D. MiR-199a-5p Targets ZEB1 to Inhibit the Epithelial-Mesenchymal Transition of Ovarian Ectopic Endometrial Stromal Cells Via PI3K/Akt/mTOR Signal Pathway In Vitro and In Vivo. *Reprod. Sci.* **2020**, *27*, 110–118. [CrossRef] [PubMed]
149. Théry, C.; Amigorena, S.; Raposo, G.; Clayton, A. Isolation and characterization of exosomes from cell culture supernatants and biological fluids. *Curr. Protoc. Cell Biol.* **2006**, *30*, 3–22. [CrossRef] [PubMed]
150. Dragovic, R.A.; Gardiner, C.; Brooks, A.S.; Tannetta, D.S.; Ferguson, D.J.; Hole, P.; Carr, B.; Redman, C.W.; Harris, A.L.; Dobson, P.J.; et al. Sizing and phenotyping of cellular vesicles using Nanoparticle Tracking Analysis. *Nanomedicine* **2011**, *7*, 780–788. [CrossRef] [PubMed]

Cellular Physiology and Biochemistry

Cell Physiol Biochem 2019;52:1039-1060
DOI: 10.33594/000000071
Published online: 13 April 2019
Accepted: 17 January 2019

© 2019 The Author(s)
Published by Cell Physiol Biochem Press GmbH&Co. KG, Duesseldorf
www.cellphysiolbiochem.com

This article is licensed under the Creative Commons Attribution-NonCommercial-NoDerivatives 4.0 International License (CC BY-NC-ND). Usage and distribution for commercial purposes as well as any distribution of modified material requires written permission.

Original Paper

Growth of Endothelial Cells in Space and in Simulated Microgravity – a Comparison on the Secretory Level

Marcus Krüger[a] Jessica Pietsch[a] Johann Bauer[b] Sascha Kopp[a] Daniel T. O. Carvalho[a] Sarah Baatout[c,d] Marjan Moreels[c] Daniela Melnik[a] Markus Wehland[a] Marcel Egli[e] Jayashree Sahana[f] Sara Dam Kobberø[f] Thomas J. Corydon[f,g] Stefano Nebuloni[h] Samuel Gass[h] Matthias Evert[i] Manfred Infanger[a] Daniela Grimm[a,f]

[a]Clinic for Plastic, Aesthetic and Hand Surgery, Otto von Guericke University Magdeburg, Magdeburg, Germany, [b]Max Planck Institute of Biochemistry, Martinsried, Germany, [c]Radiobiology Unit, Belgian Nuclear Research Centre, Mol, Belgium, [d]Molecular Biotechnology, Ghent University, Ghent, Belgium, [e]Institute of Medical Engineering, Space Biology Group, Lucerne University of Applied Sciences and Arts, Hergiswil, Switzerland, [f]Department of Biomedicine, Aarhus University, Aarhus, Denmark, [g]Department of Ophthalmology, Aarhus University Hospital, Aarhus, Denmark, [h]RUAG Slip Rings SA, Nyon, Switzerland, [i]Institute for Pathology, University of Regensburg, Regensburg, Germany

Key Words
Spaceflight • Microgravity • Cytokines • Extracellular matrix • Spheroids

Abstract
Background/Aims: Endothelial cells exposed to the Random Positioning Machine (RPM) reveal three different phenotypes. They grow as a two-dimensional monolayer and form three-dimensional (3D) structures such as spheroids and tubular constructs. As part of the ESA-SPHEROIDS project we want to understand how endothelial cells (ECs) react and adapt to long-term microgravity. ***Methods:*** During a spaceflight to the International Space Station (ISS) and a subsequent stay onboard, human ECs (EA.hy926 cell line) were cultured for 12 days in real microgravity inside an automatic flight hardware, specially designed for use in space. ECs were cultivated in the absence or presence of vascular endothelial growth factor, which had demonstrated a cell-protective effect on ECs exposed to an RPM simulating microgravity. After cell fixation in space and return of the samples, we examined cell morphology and analyzed supernatants by Multianalyte Profiling technology. ***Results:*** The fixed samples comprised 3D multicellular spheroids and tube-like structures in addition to monolayer cells, which are exclusively observed during growth under Earth gravity (1*g*). Within the 3D aggregates we detected enhanced collagen and laminin. The supernatant analysis unveiled alterations in secretion of several growth factors, cytokines, and extracellular matrix components as

Prof. Daniela Grimm
Department of Biomedicine, Aarhus University
Wilhelm Meyers Allé 4, DK-8000 Aarhus C (Denmark)
Tel. +45-871 67693, Fax +45-8612-8804, E-Mail dgg@biomed.au.dk

Cellular Physiology and Biochemistry
Cell Physiol Biochem 2019;52:1039-1060
DOI: 10.33594/000000071
Published online: 13 April 2019
© 2019 The Author(s). Published by Cell Physiol Biochem Press GmbH&Co. KG

compared to cells cultivated at 1*g* or on the RPM. This confirmed an influence of gravity on interacting key proteins and genes and demonstrated a flight hardware impact on the endothelial secretome. ***Conclusion:*** Since formation of tube-like aggregates was observed only on the RPM and during spaceflight, we conclude that microgravity may be the major cause for ECs' 3D aggregation.

© 2019 The Author(s). Published by Cell Physiol Biochem Press GmbH&Co. KG

Introduction

Humans are adapted to the Earth's constant gravity, an important physical force significantly contributing to the normal function of our cardiovascular system. Astronauts returning from space have, among others, shown cardiovascular problems such as arrhythmias, cardiac atrophy, low blood pressure or orthostatic intolerance, accredited to endothelium injury [1-4]. Like other vascular cells, endothelial cells (ECs) are mechanoresponsive and react to physiological mechanical cues such as fluid shear stress, cyclic stretch, or hydrostatic pressure [5]. Therefore, it is not surprising that ECs are also sensitive to variations in gravity. During the last decade, several studies demonstrated significant modifications in ECs after exposure to altered gravity conditions [6-12]. It is assumed that they convert gravitational stimuli via gene regulation into biochemical signals [13]. Indeed, ECs showed alterations of secretory functions [14] as well as gravity-dependent modulation of EC processes, such as cellular proliferation, apoptosis, cytoskeletal organization, intracellular signaling mechanisms, and growth behavior [15-18]. Most interestingly, the exposure to microgravity (μ*g*) generated a scaffold-free formation of three-dimensional (3D) cell aggregates called multicellular spheroids (MCS) [7, 19]. Small MCS with diameters of about 0.3 mm can be observed after a few days [20]. During an extended exposure, MCSs start to grow into tube-like structures reaching lengths of up to 2-3 mm [21]. Supplementation of vascular endothelial growth factor (VEGF) was shown to have cell-protective effects on ECs [8], but obviously does not affect the expression of adhesion molecules in MCS [22].

As the opportunities to perform long-term experiments on space crafts or space laboratories in real μ*g* (r-μ*g*) are rare due to high costs and a limited number of missions, most of the previous studies were conducted at 'ground-based facilities' such as the clinostat or the Random Positioning Machine (RPM), simulating some aspects of μ*g* (simulated μ*g*, s-μ*g*). RPM-based studies showed that s-μ*g* modifies the transcriptional [23] and translational [24] levels of gene expression in ECs. Recently, a long-term RPM experiment identified some key proteins involved in spheroid formation and angiogenesis [21].

Here, the ESA-SPHEROIDS project aimed to investigate the effects of r-μ*g* on EC function, with respect to formation of blood vessel-like structures, cell proliferation, and apoptosis. Thus, the results of the SPHEROIDS project could help develop potential countermeasures to prevent cardiovascular deconditioning in astronauts and improve knowledge of endothelial function on Earth. For this purpose, we performed an experiment onboard the International Space Station (ISS) in 2016 to observe human ECs remaining in space for 5 d and 12 d [25] in order to increase our knowledge in the behavior of human ECs exposed to r-μ*g*. The objective of this study was three-fold. First, we focused on the growth behavior of cells treated without or with vascular endothelial growth factor (VEGF) in space. Second, we studied the secretion behavior of ECs applying MAP technology and third, we performed an RPM experiment exactly copying the time and temperature protocols of the ISS mission and compared these results with the data received from the space samples. After completion of the experiments we analyzed the release of cytokines and extracellular matrix (ECM) proteins involved in 3D growth and cell adhesion such as laminin and fibronectin.

Cellular Physiology and Biochemistry
Cell Physiol Biochem 2019;52:1039-1060
DOI: 10.33594/000000071
Published online: 13 April 2019
© 2019 The Author(s). Published by Cell Physiol Biochem Press GmbH&Co. KG

Materials and Methods

Cell culture

We used the permanent human cell line EA.hy926 (CRL-2922; ATCC, Manassas, VA, USA), which had been established by fusing human umbilical vein endothelial cells (HUVECs) with the permanent cell line A549, derived from a human lung carcinoma. Although a hybrid, EA.hy926 cells still exhibit characteristic EC features [26, 27]. The cells were cultivated in RPMI-1640 medium (Invitrogen, Eggenstein, Germany) containing 100 µM sodium pyruvate and 2 µM L-glutamine (Thermo Fisher Scientific, Waltham, MA, USA) and 10% Fetal Calf Serum (FCS), 100 U/mL penicillin and 100 µg/mL streptomycin (all Biochrom, Berlin, Germany).

The cells were maintained in 75-cm^2 tissue culture flasks (Sarstedt, Nümbrecht, Germany) until monolayers were formed, reaching a confluency of approximately 80%. One day prior to the experiments, the EA.hy926 cells were suspended in RPMI-1640 medium so that the cells could be seeded in cultivation chambers (RUAG Space, Nyon, Switzerland) or in slide flasks (Nunc™ Lab-Tek™ SlideFlask; Thermo Fisher Scientific) for a preliminary 24 h-period of adherence. In this stage the cultures were used in the different experimental scenarios.

Flight hardware

The flight hardware was designed, developed and manufactured by RUAG Space (Nyon, Switzerland). SPHEROIDS received 8 experimental units each containing two independent cultivation chambers (CC) with adhesion surfaces made of polyether ether ketone (PEEK). Materials were intensely tested for biocompatibility [25]. For each experimental unit, one CC was filled with RPMI-1640 medium, the other one was filled with RPMI-1640 supplemented with 10 µg/mL VEGF-A (Sigma-Aldrich, Deisenhofen, Germany; further referred as VEGF). The assembly procedure preceding the spaceflight and the cell harvest after the mission has been previously described by Pietsch and coworkers [25]. 5×10^5 and 4×10^5 cells were seeded in the cultivation chambers for the 7-day experiment or the 14-day experiment respectively before handover to NASA. A timeline for automatic medium exchange and fixation had to be programmed prior to the spaceflight. Therefore, all worst-case scenarios (launch scrubs, delays until berthing at the ISS, until installation in KUBIK, and until turning-on power supply) had to be considered. Ultimately, we collected µ*g*-phases of 5 d and 12 d in our experiments. If a delay had occurred, it could have been longer. If all delays occurred, we would have got the maximum of 7 d and 14 d of r-µ*g*.

Dragon spaceflight with SpaceX CRS-8

SpaceX CRS-8 was a commercial resupply service mission transporting a total cargo load of over 3,100 kg to the ISS, including multiple experiments. On April 8th, 2016 at 20:43 UTC SPHEROIDS was launched in a Dragon capsule on board SpaceX CRS-8 from NASA's Kennedy Space Center in Florida. After 41 h and 14 min Dragon was berthed at the ISS. After completion of the mission, the flight hardware returned to Earth on May 11th, 2016 and was subsequently shipped to our laboratories.

Time and temperature were logged continuously via temperature sensing iButtons (iButtonLink, Whitewater, WI, USA; accuracy ±0.5°C) on top of the experimental units. The protocols for both, the 7-day and the 14-day experiments are shown in Fig. 1. The same protocols were subsequently used for the ground control and the RPM experiment.

Random Positioning Machine (RPM)

The RPM was developed as a '3D clinostat' to simulate µ*g* [28]. Our device was manufactured by Airbus Defence and Space and is used routinely in our laboratory. Cell culture experiments on the RPM had been investigated thoroughly and previously published in detail [18, 20, 29-32]. For the SPHEROIDS RPM experiment 10^6 cells were seeded in slide flasks (n = 5/group). After sub-confluent monolayers had formed, the slide flasks were filled completely with medium (air bubble-free), subsequently positioned on the inner frame of the RPM and the rotation was started at a speed of 60°/s using real random mode (random speed and random direction) according to the spaceflight timescale. For the experiment, the RPM was positioned in a standard incubator using the spaceflight temperature protocol (Fig. 1). In parallel, slide flasks were placed next to the RPM in the incubator as 1*g*-controls (n = 5/group).

Cellular Physiology and Biochemistry
Cell Physiol Biochem 2019;52:1039-1060
DOI: 10.33594/000000071
Published online: 13 April 2019
© 2019 The Author(s). Published by Cell Physiol Biochem Press GmbH&Co. KG

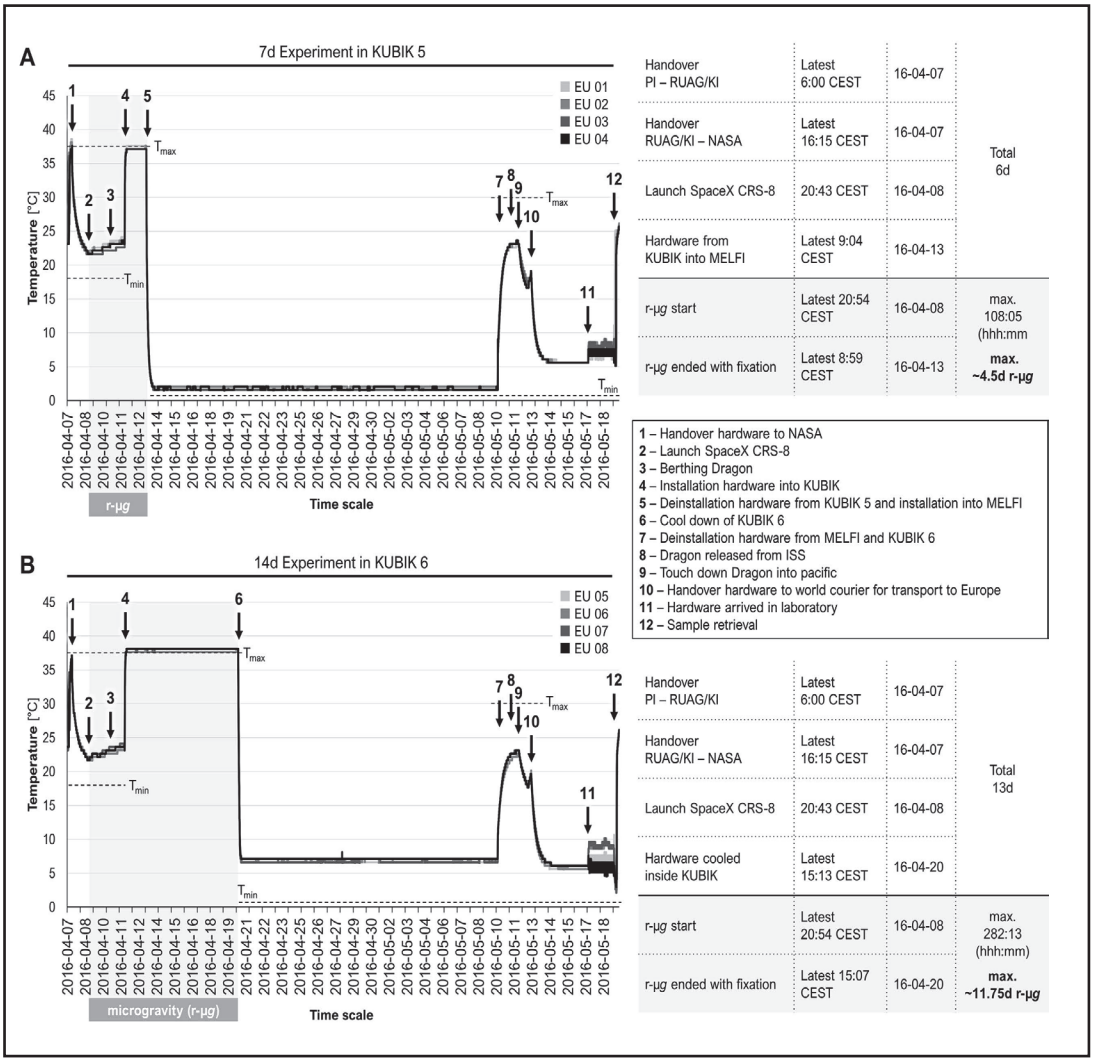


Fig. 1. Temperature profiles of the complete mission starting from shortly before handover of the flight hardware until the retrieval of the samples. Temperature was logged by thermosensors every 10 min on the top of every experimental unit. A) Four units were installed in KUBIK 5 for the 7-day experiment. B) Another four units were installed in KUBIK 6 for the 14-day experiment. The phase when living cells were exposed to r-µ*g* is drawn in grey. It ended with fixation. Dashed lines at 37.5°C and 0.5°C represent the maximum and minimal required temperature, respectively. EU: Experimental unit.

Morphology and cytochemistry

We used the hematoxylin/eosin (HE) staining method, which has been described earlier in detail [25, 33]. Multicellular spheroids and tubular structures had been PFA-fixed in space. They were paraffin-embedded, sectioned and mounted on object slides, deparaffinized and after rehydration stained with HE or Sirius red. All sections were visualized by light microscopy using a LEICA DM2000 microscope equipped with a Leica DFC310 FX digital CCD color camera.

Immunofluorescence microscopy (IFM)

To visualize laminin, the slides were incubated using a laminin-specific primary antibody (Sigma-Aldrich) followed by a peroxidase-labeled secondary antibody. Antigen-antibody complexes were visualized by the indirect immunoperoxidase technique [34].

Cellular Physiology and Biochemistry
Cell Physiol Biochem 2019;52:1039-1060
DOI: 10.33594/000000071
Published online: 13 April 2019
© 2019 The Author(s). Published by Cell Physiol Biochem Press GmbH&Co. KG

Cytokine measurements by Multianalyte Profiling (MAP) technology

The altered cytokines and proteins released into the cell culture supernatants were analyzed by the company Myriad RBM (Austin, TX, USA). The MAP analysis was performed using the Human InflammationMAP® as described previously [35]. Supernatants were collected from 1*g*- and µ*g*-samples after the 7 d and 14 d timepoints (flight hardware: n = 4, slide flasks: n = 5) and stored at -80°C prior to the analysis at Myriad RBM.

Collagen type I, laminin and fibronectin measurements from cell culture supernatants

Protein levels were determined using a commercial ELISA kits according to the manufacturer's instructions (LifeSpan BioSciences, Seattle, WA, USA; Cusabio Biotech, Houston, TX, USA). Supernatant samples harvested from the flight hardware were used undiluted. Supernatants of the cell culture flasks were diluted 1:1 (laminin, collagen type I 1*g*) or 1:10 (fibronectin, collagen type I RPM). 96-well plates were read using a SpectraMax M2 Microplate Reader (Molecular Devices, San José, CA, USA). Data was analyzed via elisaanalysis.com (Elisakit.com, Melbourne, Australia) with a 4-parameter logistic regression algorithm for standard curve equation.

Table 1. Primers used for qPCR

Gene	Primer	Sequence (5'-3' direction)
18S	18S-F	GGAGCCTGCGGCTTAATTT
	18S-R	CAACTAAGAACGGCCATGCA
B2M	B2M-F	CACTGAATTCACCCCCACTGA
	B2M-R	GCTTACATGTCTCGATCCCAC
CCL2	MCP1-F	GCTATAGAAGAATCACCAGCAGCAA
	MCP1-R	TGGAATCCTGAACCCACTTCTG
CCL11	CCL11-F	CCAACCACCTGCTGCTTTAAC
	CCL11-R	GTCTTGAAGATCACAGCTTTCTG
CDH5	CDH5-F	GTCCTGCAGATCTCCGCAAT
	CDH5-R	TGTTGGCCGTGTTATCGTGA
COL1A1	COL1A1-F	ACGAAGACATCCCACCAATCAC
	COL1A1-R	CGTTGTCGCAGACGCAGAT
CXCL8	IL8-F	TGGCAGCCTTCCTGATTTCT
	IL8-R	GGGTGGAAAGGTTTGGAGTATG
FTL	FTL-F	CTTGCCAACCAACCATGAGC
	FTL-R	AGAAGCCCAGAGAGAGGTAGG
IL6	IL6-F	CGGGAACGAAAGAGAAGCTCTA
	IL6-R	GAGCAGCCCCAGGGAGAA
FN1	FN1-F	TGAGGAGCATGGTTTTAGGAGAA
	FN1-R	TCCTCATTTACATTCGGCGTATAC
LAMA1	LAMA1-F	TGACTGACCTGGGTTCAGGA
	LAMA1-R	TGCTAGCACTCCTTGCTTCC
LAMB2	LAMB2-F	TGCTCATGGTCAATGCTAATCTG
	LAMB2-R	TCTATCAATCCTCTTCCTTGGACAA
TIMP1	TIMP1-F	GCCATCGCCGCAGATC
	TIMP1-R	GCTATCAGCCACAGCAACAACA
VEGFA	VEGFA-F	GCGCTGATAGACATCCATGAAC
	VEGFA-R	GCGCTGATAGACATCCATGAAC

RNA isolation and quantitative real-time PCR

RNA isolation and quantitative real-time PCR (qPCR) were performed as described earlier in detail [25, 36, 37]. ECs had been fixed with RNA*later*® (Sigma-Aldrich) at the end point of the experiments. RNA and protein were isolated using the RNeasy® Kit (Qiagen, Hilden, Germany) according to the manufacturer's recommendations. Concentrations were determined via optical density at 260 and 280 nm with a NanoDrop™ 2000 (Thermo Fisher Scientific, Waltham, MA, USA). Complementary DNA (cDNA) was produced using the First Strand cDNA Synthesis Kit (Thermo Fisher Scientific) following manufacturer's instructions. The expression levels of the following target genes were determined via qPCR: *B2M*, *CCL2*, *CCL11*, *CDH5*, *COL1A1*, *CXCL8*, *FN1*, *FTL*, *IL6*, *LAMA1*, *LAMB2*, *TIMP1*, *VEGFA*, and *18S*, using the SYBR® Select Master Mix (Applied Biosystems, Darmstadt, Germany) and the 7500 Fast Real-Time PCR System (Applied Biosystems). cDNA-selective primers were designed to span exon-exon boundaries and to have a T_m of 60°C using Primer Express software (Applied Biosystems), and were synthesized by TIB Molbiol (Berlin, Germany). The sequences of the forward and reverse primers are listed in Table 1. All samples were measured in triplicate and normalized against 18S rRNA as a housekeeping gene. Comparative C_T ($\Delta\Delta C_T$) methods were used for relative quantification of transcription levels, with 1*g* set as 100%.

Pathway analysis

To investigate and visualize interactions between selected proteins and genes, we input relevant UniProtKB entry numbers into the Pathway Studio v.11 software (Elsevier Research Solutions, Amsterdam, the Netherlands). The identified genes were analyzed according to their mutual regulation. The proteins were evaluated in regard to their cellular localization and their interaction.

Cellular Physiology and Biochemistry
Cell Physiol Biochem 2019;52:1039-1060
DOI: 10.33594/000000071
Published online: 13 April 2019
© 2019 The Author(s). Published by Cell Physiol Biochem Press GmbH&Co. KG

Statistical Evaluation

The statistical evaluation was performed using SPSS 15.0 (SPSS Inc., Chicago, IL, USA). The Mann-Whitney-U-Test was used to compare 1*g* and μ*g* conditions, 7 d and 14 d samples, samples with/without supplemented VEGF, as well as AD cells and MCS cells. All data is presented as mean ± standard deviation (SD) with a significance level of $p < 0.05$.

Results

The SPHEROIDS experiment

After all materials had been extensively tested for biocompatibility in our laboratory [25], a novel and enhanced flight hardware was available for the space experiment in early 2016. It consisted of eight experimental units, each containing two cell culture chambers, two separate medium chambers, two supernatant chambers, and one fixation chamber. The medium compartments (Fig. 2A) were filled with culture medium (Fig. 2B), the fixation compartments (Fig. 2C) with fixation fluid (half of the units with PFA for investigation of cell structures and cytochemistry, the other half with RNA*later* for transcriptional analyses; Fig. 2D). Next, the compartments were assembled (Fig. 2E) and connected with the cell culture chamber via pumps for automatic medium exchange and cell fixation (Fig. 2F, G). Last, two cell cultivation chambers (Fig. 2H, CC (E1) and CC (E2)) were added on top of the experimental unit (Fig. 2G) and filled with cells and medium. In each experimental unit, one cell cultivation chamber was filled with cells suspended in plain medium, the other one was filled with cells suspended in medium supplemented with VEGF (c = 10 μg/mL). During the space experiment four experimental units were incubated for a 7 d timeframe, the remaining four for the length of 14 d.

Two days before the launch on April 8th, the entire flight hardware was handed over to the NASA engineers, who placed it into the rocket at a temperature of 22°C. 10 minutes after launch the cells had already entered microgravity. After a two-day flight to the ISS at 22-23°C, astronauts placed the hardware inside the KUBIK incubator facility [38] in the European Columbus Laboratory (Fig. 3A). The cells continued proliferating under r-μ*g* conditions. Cells of four experimental units were automatically chemically fixed on the day 7 after handover (7 d samples ≈ 5 d in r-μ*g*). A medium exchange was executed on the remaining 4 experimental units. Then the cells were allowed to proliferate on the ISS for another seven days before fixation (14 d samples ≈ 12 d in r-μ*g*). Afterwards, the fixed EA.hy926 cells were stored at 4°C and remained in space, before returning to Earth on May 11th for subsequent analysis in the home laboratory (Fig. 3B). The flight hardware was cleaned, refilled and used for the ground control experiments, repeating the exact spaceflight protocol under normal 1*g* conditions (ground control; Fig. 3A). Furthermore, to study the effects of s-μ*g* in the laboratory, an additional experiment was performed on an RPM. Slide flasks offering a similar growth area and volume as the cultivation chambers (CCs) used as flight hardware, but could be installed on a desktop RPM were used for this additional experiment. The ground control as well as the RPM experiments were performed copying the exact time and temperature protocols of the space experiment (Fig. 1).

Growth behavior of EA.hy926 cells in microgravity

When cells returned from space, we were able to harvest the three different types of EA.hy926 cells. One part of the ECs stayed adherent (AD) over the course of 7 and 14 days (Fig. 3C). In addition, we recognized a scaffold-free formation of different 3D aggregates. Some of the formations were 3D structures with spherical appearance, called multicellular spheroids (MCS) (Fig. 3D), others were detected as tube-like structures (Fig. 3E, F). This demonstrates that ECs exhibit 3D growth in space similarly to their growth on the RPM (Fig. 3G).

Cellular Physiology and Biochemistry
Cell Physiol Biochem 2019;52:1039-1060
DOI: 10.33594/000000071
Published online: 13 April 2019
© 2019 The Author(s). Published by Cell Physiol Biochem Press GmbH&Co. KG

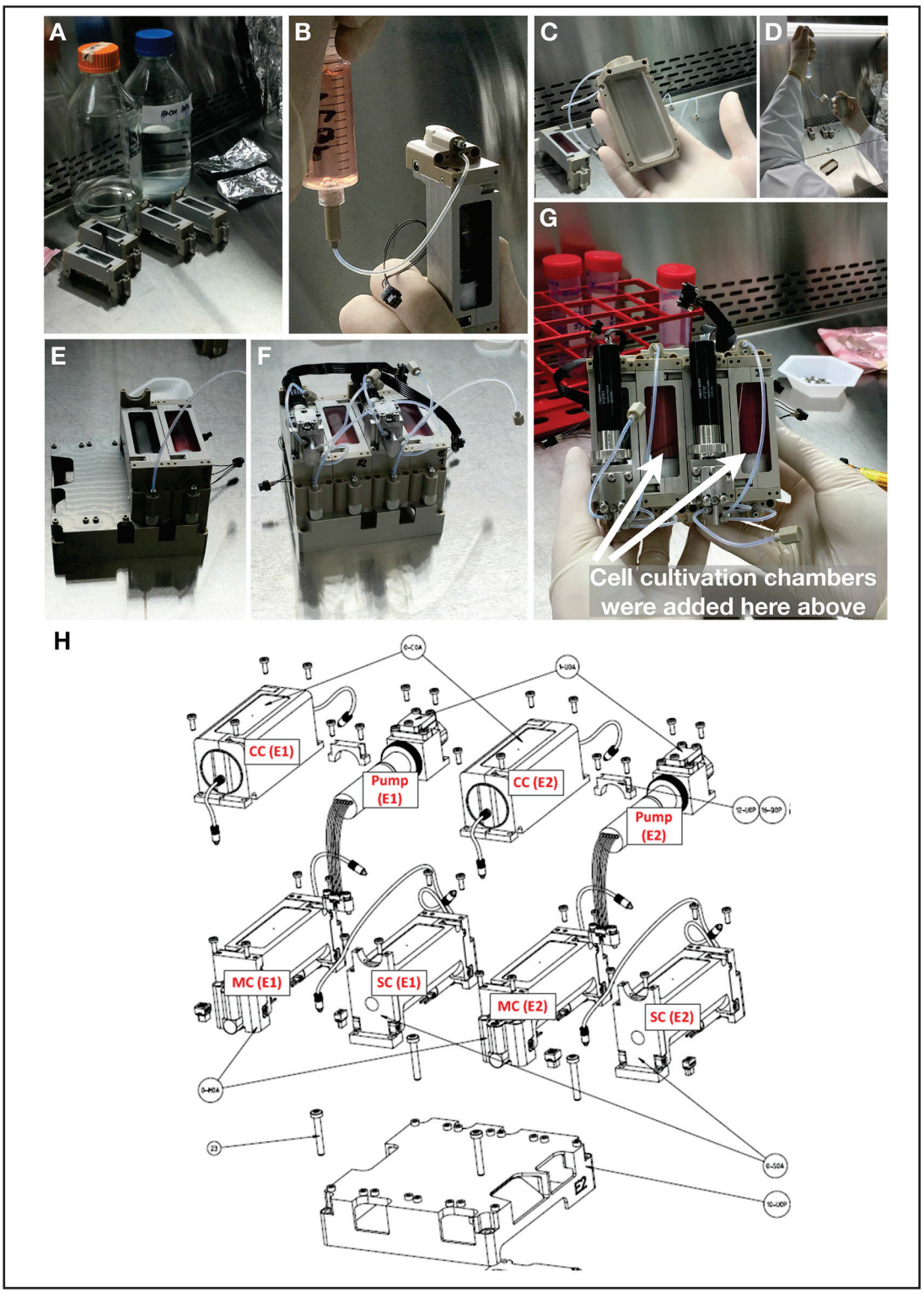


Fig. 2. Assembly and preparation of the SPHEROIDS flight hardware. A, B) The medium chambers were filled with cell culture medium. C, D) The fixation chamber was filled with fixation fluid, PFA or RNAlater. E, F) Medium chambers and supernatant chambers were assembled. G) The experimental unit before adding the cultivation chambers. H) Assembly of modules onto main support. The dimensions of one assembled hardware unit are 10 × 10 × 10 cm. CC: Cultivation chamber, E1: Experiment 1 (–VEGF), E2: Experiment 2 (+VEGF), MC: Medium chamber, SC: Supernatant chamber.

Cellular Physiology and Biochemistry
Cell Physiol Biochem 2019;52:1039-1060
DOI: 10.33594/000000071
Published online: 13 April 2019
© 2019 The Author(s). Published by Cell Physiol Biochem Press GmbH&Co. KG

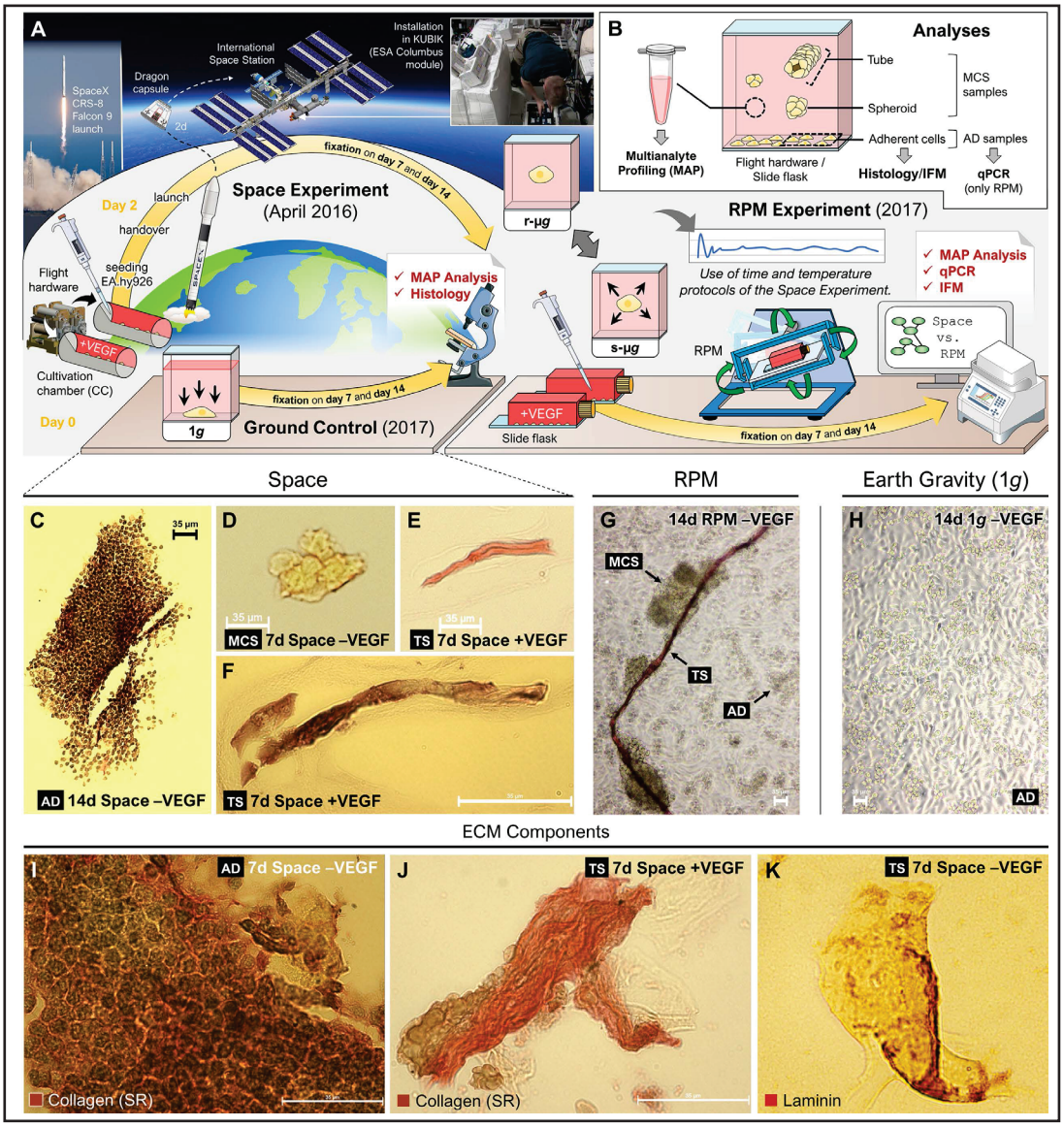


Fig. 3. Overview of the SPHEROIDS experiments. A) The SPHEROIDS study consisted of a space experiment that was conducted for two weeks on the ISS, a ground control, and an additional RPM experiment. B) Set of analyses that were done after the experiments. C-F) Morphology of space-grown EA.hy926 cells harvested from the flight hardware: Adherent cells (AD) after 14 d (C), multicellular spheroids (MCS) (D) and tube-like structures (TS) after 7d (E,F). G) Morphology of EA.hy926 cells cultured for 12 d on the RPM and (H) under 1*g* conditions. I) Adherently growing EA.hy926 cells after 5 d in space. J) A multicellular tube harvested from the 7-day space samples. ECs were stained with Sirius Red (showing collagen in red). K) Laminin staining of a tubular structure, grown for 5 d in space. Scale bars: 35 µm. Parts of the Fig. were drawn by using pictures from Servier Medical Art. Servier Medical Art by Servier is licensed under a Creative Commons Attribution 3.0 Unported License (https://creativecommons.org/licenses/by/3.0/).

The ECs stayed viable during the spaceflight and continued to produce ECM components. Collagen production occurred in AD cells and in 3D aggregates. This was visualized by Sirius red staining of paraffin-embedded ECs, collected from the flight hardware after the spaceflight (Fig. 3I, J). Laminin was also found occluded in the 3D structures (Fig. 3K).

Cellular Physiology and Biochemistry
Cell Physiol Biochem 2019;52:1039-1060
DOI: 10.33594/000000071
Published online: 13 April 2019
© 2019 The Author(s). Published by Cell Physiol Biochem Press GmbH&Co. KG

Table 2. Extracellular matrix proteins released by EA.hy926 cells after space-exposure compared with 1*g* controls. The cells were cultured in CCs of the flight hardware. The data was generated by using ELISA. Values are given as mean ± SD; LLOQ: Lower Limit of Quantitation, lowest concentration of an analyte in a sample that can be reliably detected

Factor	Earth gravity (1*g*)				Space (ISS mission)				LLOQ	Unit
	7 d		14 d		7 d		14 d			
	– VEGF	+ VEGF	– VEGF	+ VEGF	– VEGF	+ VEGF	– VEGF	+ VEGF		
Fibronectin	4.734 ± 0.095	4.847 ± 0.328	5.463 ± 0.638	4.951 ± 0.538	5.218 ± 1.469	5.126 ± 1.939	5.027 ± 0.167	5.205 ± 0.307	0.156	ng/mL
Laminin A / Laminin B	0.371 ± 0.058	0.342 ± 0.185	0.314 ± 0.187	0.187 ± 0.130	0.676 ± 0.423	0.764 ± 0.386	0.465 ± 0.036	0.434 ± 0.078	0.156	ng/mL
Collagen Type I	0.350 ± 0.582	<1.560	0.990 ± 0.868	0.003 ± 0.006	11.67 ± 5.74	15.70 ± 13.23	4.776 ± 0.240	4.649 ± 2.264	1.560	ng/mL

Table 3. Extracellular matrix proteins released by EA.hy926 cells after exposure to the RPM compared with 1*g* controls. Cells were cultured in slide flasks. The data was generated by using ELISA. Values are given as mean ± SD; *: P <0.05 vs. 1*g*; ▼|▲: P <0.05 vs. 7d; §: P <0.05 vs. –VEGF; LLOQ: Lower Limit of Quantitation, lowest concentration of an analyte in a sample that can be reliably detected

Factor	Earth gravity (1*g*)				RPM (s-µ*g*)				LLOQ	Unit
	7 d		14 d		7 d		14 d			
	– VEGF	+ VEGF	– VEGF	+ VEGF	– VEGF	+ VEGF	– VEGF	+ VEGF		
Fibronectin	23.31 ± 2.52	21.21 ± 1.80	23.69 ± 1.76	▲27.12 ± 4.04	22.37 ± 1.74	22.42 ± 1.90	26.19 ± 4.24	24.44 ± 2.20	0.156	ng/mL
Laminin A / Laminin B	7.079 ± 0.723	7.629 ± 1.086	▲13.34 ± 1.41	▲11.54 ± 1.10	9.92* ± 1.361	9.321 ± 1.139	12.05 ± 1.11	10.42 ± 1.07	0.156	ng/mL
Collagen Type I	6.686 ± 1.197	7.277 ± 1.235	▲28.85 ± 2.73	▲23.57§ ± 1.41	16.64 ± 8.42	14.62 ± 7.97	▲34.68 ± 12.80	▲39.07* ± 14.89	1.560	ng/mL

Release of extracellular matrix components

As shown above, collagen was secreted and incorporated into the ECM. In addition, together with several growth factors and cytokines, collagen and some other components of the ECM were released into the supernatant. Using MAP technology and ELISA, a number of proteins released into the supernatant under microgravity and control conditions were quantified (Tables 2-5).

Tables 2 and 3 indicate that much more fibronectin and laminin were produced, when the ECs were incubated in normal polystyrene slide flasks than during incubation in the newly developed CC suitable for culturing cells in space. This was true, even if the flasks or chambers were incubated under normal laboratory conditions according to equal protocols. However, under laboratory conditions, much more collagen I was secreted in slide flasks than in CCs. Though, similar amounts of collagen were found when the cells had been incubated under simulated or real microgravity independent of the material of the culture dish.

Release of matrix regulators, growth factors and cytokines

When the Human InflammationMAP® was applied to search for cellular proteins released into the supernatant, only part of the antibodies deployed indicated the presence of their targets (Tables 4, 5). In addition, the detection of specific proteins in the supernatant depended on the type of culture dish, wherein the cells were suspended. Differences of secretion, which depended on the type of culture dish were also found when the growth

Cellular Physiology and Biochemistry
Cell Physiol Biochem 2019;52:1039-1060
DOI: 10.33594/000000071
Published online: 13 April 2019
© 2019 The Author(s). Published by Cell Physiol Biochem Press GmbH&Co. KG

Table 4. Proteins released by EA.hy926 cells after space-exposure compared with 1*g* controls. The cells were cultured in CCs of the flight hardware. The data was generated by Multi-Analyte Profiling using the Myriad RBM Human Inflammation MAP® v1.0. Values are given as mean ± SD; *: P <0.05 vs. 1*g*; ▼|▲: P <0.05 vs. 7d;§: P <0.05 vs. –VEGF; LLOQ: Lower Limit of Quantitation, lowest concentration of an analyte in a sample that can be reliably detected. The values are determined as the mean of 5 (1*g* control) or 13 (RPM) blank readings. C-Reactive Protein (CRP), Factor VII, Granulocyte-Macrophage Colony-Stimulating Factor (GM-CSF), Haptoglobin, Intercellular Adhesion Molecule 1 (ICAM-1), Interferon γ (IFN-γ), Interleukin-1 beta (IL-1β), Interleukin-1 receptor antagonist (IL-1ra), Interleukin-2 (IL-2), Interleukin-3 (IL-3), Interleukin-4 (IL-4), Interleukin-5 (IL-5), Interleukin-7 (IL-7), Interleukin-10 (IL-10), Interleukin-12 Subunit p70 (IL-12p70), Interleukin-15 (IL-15), Interleukin-17 (IL-17), Interleukin-18 (IL-18), Interleukin-23 (IL-23), Macrophage Inflammatory Protein-1α (MIP-1α), Macrophage Inflammatory Protein-1β (MIP-1β), Matrix Metalloproteinase-3 (MMP-3), Matrix Metalloproteinase-9 (MMP-9), Stem Cell Factor (SCF), T-Cell-Specific Protein RANTES (RANTES), Tumor Necrosis Factor α (TNF-α), Tumor Necrosis Factor β (TNF-β), Tumor Necrosis Factor Receptor 2 (TNFR2), Vascular Cell Adhesion Molecule-1 (VCAM-1), Vitamin D-Binding Protein (VDBP), and von Willebrand Factor (vWF) levels were below the LLOQ

Factor	Earth gravity (1*g*)				Space (ISS mission)				LLOQ	Unit
	7 d		14 d		7 d		14 d			
	– VEGF	+ VEGF	– VEGF	+ VEGF	– VEGF	+ VEGF	– VEGF	+ VEGF		
α1-Antitrypsin (AAT)	<0.075	<0.075	<0.075	0.183 ± 0.365	<0.075	<0.075	<0.075	<0.075	0.075	ng/mL
α2-Macroglobulin (A2M)	1.225 ± 0.150	1.150 ± 0.058	1.148 ± 0.196	1.125 ± 0.050	1.055 ± 0.090	1.250 ± 0.191	1.350 ± 0.071	1.400 ± 0.141	0.520	µg/mL
β2-Microglobulin (B2M)	1.455 ± 0.369	1.825 ± 0.512	▼0.417 ± 0.237	▼0.093 ± 0.027	2.100* ± 0.283	2.025 ± 0.776	0.705 ± 0.021	0.730 ± 0.014	0.042	ng/mL
Brain-Derived Neurotrophic Factor (BDNF)	<0.008	<0.008	<0.008	<0.008	0.010 ± 0.012	0.012 ± 0.014	<0.008	<0.008	0.008	ng/mL
Complement C3 (C3)	<0.027	<0.027	<0.027	0.126 ± 0.224	<0.027	<0.027	<0.027	<0.027	0.027	ng/mL
Eotaxin-1	9.50 ± 10.96	5.75 ± 11.50	<16	▲38.50§ ± 8.19	<16	<16	<16	<16	16	pg/mL
Ferritin (FRTN)	0.151 ± 0.066	0.170 ± 0.058	▼0.028 ± 0.019	▼ <0.034	0.185 ± 0.040	0.129 ± 0.069	0.039 ± 0.004	0.047 ± 0.002	0.034	ng/mL
Fibrinogen	<0.065	<0.065	<0.065	0.788 ± 1.413	<0.065	<0.065	<0.065	<0.065	0.065	ng/mL
Interleukin-1α (IL-1 alpha)	0.165 ± 0.195	0.185 ± 0.226	0.080 ± 0.160	0.368§ ± 0.015	0.155 ± 0.186	0.175 ± 0.206	<0.280	0.280	0.280	pg/mL
Interleukin-6 (IL-6)	1.650 ± 0.443	1.950 ± 0.985	▼ <0.580	▼ <0.580	4.150 ± 2.829	4.400 ± 4.311	0.700 ± 0.990	1.700 ± 0.000	0.580	pg/mL
Interleukin-8 (IL-8)	80.25 ± 22.94	90.75 ± 25.62	▼18.23 ± 9.65	▼8.58 ± 3.95	104.25 ± 103.1	113.13 ± 120.4	66.50 ± 9.19	59.00 ± 5.66	1.600	pg/mL
Interleukin-12 Subunit p40	0.066 ± 0.047	0.068 ± 0.057	0.067 ± 0.047	0.156 ± 0.071	<0.047	<0.047	<0.047	<0.047	0.047	ng/mL
Monocyte Chemotactic Protein 1 (MCP-1)	0.241 ± 0.062	0.279 ± 0.083	▼0.025 ± 0.017	▼ <0.022	0.154 ± 0.033	0.169 ± 0.066	0.034 ± 0.007	0.029 ± 0.014	0.022	ng/mL
Tissue Inhibitor of Metalloproteinases 1 (TIMP-1)	1.095 ± 0.342	1.323 ± 0.407	0.507 ± 0.306	▼0.096 ± 0.034	0.825 ± 0.318	0.765 ± 0.448	0.255 ± 0.007	0.280 ± 0.014	0.013	ng/mL
Vascular Endothelial Growth Factor (VEGF)	15.8 ± 2.1	1883 ± 229	19.1 ± 9.8	▲7905 ± 679	<8.8	824 ± 686	<8.8	1430 ± 99	8.8	pg/mL

Cellular Physiology and Biochemistry
Cell Physiol Biochem 2019;52:1039-1060
DOI: 10.33594/000000071
Published online: 13 April 2019
© 2019 The Author(s). Published by Cell Physiol Biochem Press GmbH&Co. KG

Table 5. Proteins released by EA.hy926 cells after exposure to the RPM compared with 1*g* controls. The cells were cultured in slide flasks. The data was generated by Multi-Analyte Profiling using the Myriad RBM Human Inflammation MAP® v1.0. Values are given as mean ± SD, *: P <0.05 vs. 1*g*; ▼|▲: P <0.05 vs. 7d; §: P <0.05 vs. −VEGF; LLOQ: Lower Limit of Quantitation, lowest concentration of an analyte in a sample that can be reliably detected. The values are determined as the mean of 5 (1*g* control) or 13 (RPM) blank readings. C-Reactive Protein (CRP), Factor VII, Fibrinogen, Granulocyte-Macrophage Colony-Stimulating Factor (GM-CSF), Haptoglobin, Interferon γ (IFN-γ), Interleukin-1β (IL-1β), Interleukin-1 receptor antagonist (IL-1ra), Interleukin-2 (IL-2), Interleukin-3 (IL-3), Interleukin-4 (IL-4), Interleukin-5 (IL-5), Interleukin-7 (IL-7), Interleukin-10 (IL-10), Interleukin-12 Subunit p40 (IL-12p40), Interleukin-12 Subunit p70 (IL-12p70), Interleukin-15 (IL-15), Interleukin-17 (IL-17), Interleukin-18 (IL-18), Interleukin-23 (IL-23), Macrophage Inflammatory Protein-1α (MIP-1α), Macrophage Inflammatory Protein-1β (MIP-1β), Matrix Metalloproteinase-9 (MMP-9), Stem Cell Factor (SCF), Tumor Necrosis Factor alpha (TNF-α), Tumor Necrosis Factor β (TNF-β), Vascular Cell Adhesion Molecule-1 (VCAM-1), and Vitamin D-Binding Protein (VDBP) levels were below the LLOQ

Factor	Earth gravity (1*g*)				RPM (s-µ*g*)				LLOQ	Unit
	7 d		14 d		7 d		14 d			
	− VEGF	+ VEGF	− VEGF	+ VEGF	− VEGF	+ VEGF	− VEGF	+ VEGF		
α1-Antitrypsin (AAT)	<0.075	<0.075	▲0.205 ± 0.017	▲0.178 ± 0.019	<0.075	0.017 ± 0.038	▲0.248 ± 0.066	▲0.272* ± 0.041	0.075	ng/mL
α2-Macroglobulin (A2M)	1.113 ± 0.118	0.965 ± 0.052	1.175 ± 0.171	0.965 ± 0.090	0.974 ± 0.021	1.018 ± 0.078	1.015 ± 0,103	1.102 ± 0.136	0.520	µg/mL
β2-Microglobulin (B2M)	18.75 ± 5.44	18.75 ± 4.65	▲75.25 ± 6.34	▲73.75 ± 4.27	23.40 ± 8.20	24.80 ± 6.34	▲74.25 ± 12.09	▲85.60 ± 15.71	0.042	ng/mL
Brain-Derived Neurotrophic Factor (BDNF)	0.140 ± 0.027	0.103 ± 0.039	0.260 ± 0.174	▲0.378 ± 0.082	0.170 ± 0.040	0.156 ± 0.041	▲0.418 ± 0.123	▲0.506 ± 0.103	0.008	ng/mL
Complement C3 (C3)	<0.027	<0.027	▲0.173 ± 0.021	▲0.193 ± 0.021	0.012 ± 0.036	0.029 ± 0.033	▲0.203 ± 0.039	▲0.200 ± 0.080	0.027	ng/mL
Eotaxin-1	4.50 ± 9.00	27.75§ ± 3.40	4.50 ± 9.00	20.25 ± 3.30	7.20 ± 9.86	28.40§ ± 4.16	<16	31.60§ ± 6.84	16	pg/mL
Ferritin (FRTN)	0.140 ± 0.020	0.165 ± 0.013	▲0.343 ± 0.106	▲0.303 ± 0.026	0.228* ± 0.102	0.252* ± 0.052	▲0.508 ± 0.078	▲0.594§ ± 0.096	0.034	ng/mL
Intercellular Adhesion Molecule 1 (ICAM-1)	<0.570	<0.570	0.455 ± 0.308	▲0.640 ± 0.052	0.114 ± 0.255	0.114 ± 0.255	0.455 ± 0.308	▲0.822* ± 0.120	0.570	ng/mL
Interleukin-1α (IL-1 alpha)	<0.280	<0.280	0.090 ± 0.180	0.170 ± 0.197	0.064 ± 0.143	0.296 ± 0.173	▲0.585* ± 0.163	▲0.726* ± 0.138	0.280	pg/mL
Interleukin-6 (IL-6)	5.90 ± 0.54	5.60 ± 1.47	▲35.00 ± 1.41	▲38.25 ± 4.92	18.24* ± 16.13	18.40* ± 7.83	▲157.0* ± 44.80	▲185.0* ± 77.39	0.580	pg/mL
Interleukin-8 (IL-8)	50.25 ± 10.59	43.25 ± 11.18	▲192.0 ± 18.67	▲192.0 ± 25.74	93.20* ± 28.26	97.60* ± 22.07	▲297.3* ± 65.07	▲322.4* ± 97.82	1.600	pg/mL
Matrix Metalloproteinase-3 (MMP-3)	<0.010	<0.010	0.003 ± 0.006	0.004 ± 0.008	<0.010	0.002 ± 0.005	▲0.021* ± 0.006	▲0.031* ± 0.010	0.010	ng/mL
Monocyte Chemotactic Protein 1 (MCP-1)	3.06 ± 1.43	3.84 ± 0.40	▲9.72 ± 1.60	▲10.99 ± 1.02	6.97* ± 1.71	6.03* ± 1.25	▲19.88* ± 4.72	▲24.78* ± 5.81	0.022	ng/mL
T-Cell-Specific Protein RANTES (RANTES)	14.00 ± 2.94	11.60 ± 2.33	▲38.75 ± 3.10	▲38.50 ± 2.65	23.00* ± 4.06	22.80* ± 2.49	▲67.00 ± 24.93	▲76.40* ± 22.15	1.1	pg/mL
Tissue Inhibitor of Metalloproteinases 1 (TIMP-1)	23.25 ± 10.05	27.00 ± 6.32	▲77.00 ± 5.48	▲69.75 ± 8.22	29.80 ± 8.93	33.00 ± 9.27	▲66.50 ± 8.27	▲71.40 ± 23.84	0.013	ng/mL
Tumor Necrosis Factor Receptor 2 (TNFR2)	2.50 ± 5.00	7.75 ± 5.19	▲18.75 ± 5.56	▲18.50 ± 1.91	20.40* ± 15.65	28.20* ± 10.99	26.25 ± 7.41	18.20 ± 6.87	10	pg/mL
Vascular Endothelial Growth Factor (VEGF)	<8.8	3990 ± 1234	▲17.0 ± 2.8	▼1998 ± 249	2.0 ± 4.5	3804 ± 911	▲388* ± 376	4156* ± 689	8.8	pg/mL
von Willebrand Factor (vWF)	4.03 ± 0.83	1.43§ ± 1.66	▲29.00 ± 3.16	▲21.00 ± 3.46	1.46 ± 2.04	1.58 ± 1.45	▲8.03* ± 1.51	▲7.46* ± 2.06	2.3	ng/mL

Cellular Physiology and Biochemistry
Cell Physiol Biochem 2019;52:1039-1060
DOI: 10.33594/000000071
Published online: 13 April 2019
© 2019 The Author(s). Published by Cell Physiol Biochem Press GmbH&Co. KG

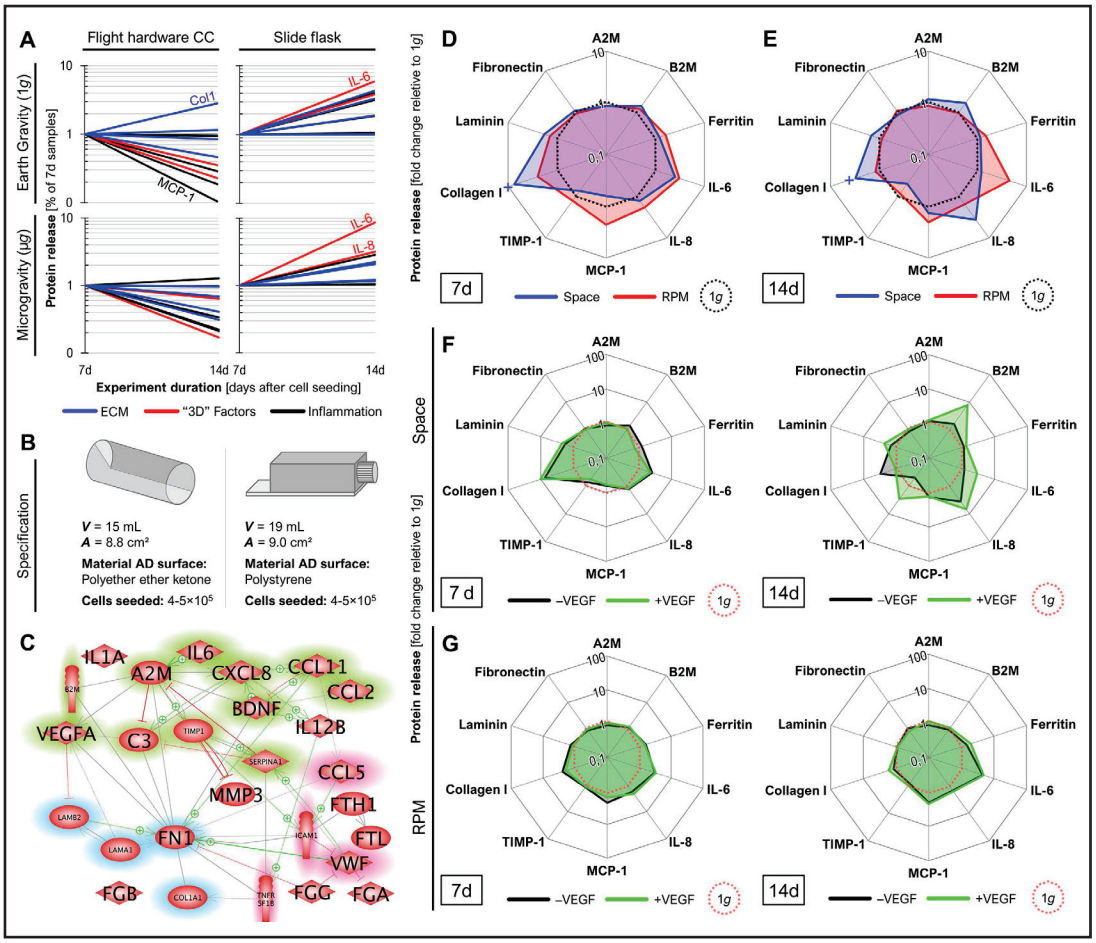


Fig. 4. Effects of microgravity on EC secretion behavior. A) Time courses of protein releases in the different cultivation chambers between day 7 and day 14. B) Specification of the constructed cultication chamber and commercial slide flasks. C) Mutual interaction of proteins analyzed by MAP technology (InflammationMAP®). Green background indicates released factors both in the hardware and in slide flasks, red background shows factors only released in slide flasks. ECM components are highlighted in blue. The green arrows indicate activating and the red one inhibiting effects. The interaction network was built up using Elsevier Pathway Studio v.11. D, E) Protein release profiles of ECs cultured for 5 d and 12 d under r- and s-µ*g* conditions. Fold changes of protein secretion compared to 1*g* controls are shown in blue (space samples) or in red (RPM samples). + marks the minimum fold change, as protein levels were below the LLOQ. The LLOQ was used for comparison. The black dotted lines indicate the secretion levels under 1*g* (control) conditions. F, G) Protein release profiles of ECs cultured for 5 d and 12 d in space (F) and on the RPM (G). Fold changes of protein secretion in presence of supplemented VEGF are shown in green, without additional VEGF in black. The red dotted lines indicate the secretion levels under 1*g* (control) conditions. * P <0.05 vs. 1*g*.

factors and cytokines were investigated (Fig. 4A). α1-Antitrypsin (AAT), α2-Macroglobulin (A2M), β2-Microglobulin (B2M), Brain-Derived Neurotrophic Factor (BDNF), Complement C3, Eotaxin-1, Ferritin (FRTN), interleukins (IL)-1α, -6, -8, Monocyte Chemotactic Protein 1 (MCP-1), Tissue Inhibitor of Metalloproteinases 1 (TIMP-1), and VEGF could be determined in both types of cell containers. But detectable amounts of Intercellular Adhesion Molecule 1 (ICAM-1), Matrix Metalloproteinase-3 (MMP-3), T-Cell-Specific Protein RANTES, Tumor Necrosis Factor Receptor 2 (TNFR2), and von Willebrand Factor (vWF) were only found in slide flasks, while fibrinogen and IL-12 were detected in CC only. Regarding the amount of secreted proteins found in both types of chambers, it is obvious that higher amounts of B2M, IL-6, MCP-1 and TIMP-1 were secreted in slide flasks. But IL-8 (also called CXCL8, CXC-

Cellular Physiology and Biochemistry
Cell Physiol Biochem 2019;52:1039-1060
DOI: 10.33594/000000071
Published online: 13 April 2019
© 2019 The Author(s). Published by Cell Physiol Biochem Press GmbH&Co. KG

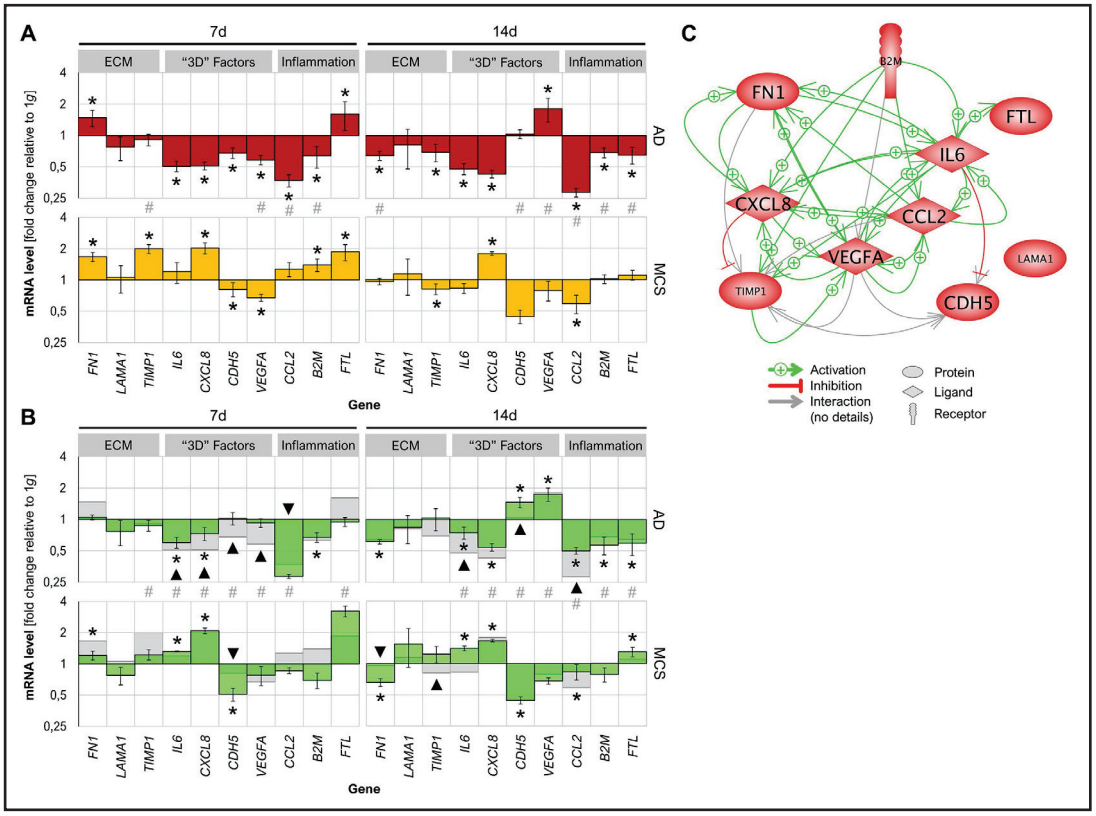


Fig. 5. Effects of s-μ*g* on the gene expression of EA.hy926 cells. A) Changes of mRNA levels after exposure to the RPM. Fold changes of AD cells are shown in red, fold changes of MCS are shown in yellow B) Changes of mRNA levels after VEGF supplementation (green bars) compared to samples without additional VEGF (grey bars). C) Mutual interaction of selected genes at gene expression level. We selected 10 genes, whose up- or down-regulation were analysed by qPCR after 14 d culturing on the RPM. The green arrows indicate activating and the red one inhibiting effects. The interaction network was built up using Elsevier Pathway Studio v.11. * P <0.05 vs. 1*g* control; # P <0.05 AD vs. MCS; ▼|▲ P <0.05 vs. –VEGF.

Motiv-Chemokine 8) appeared to be higher concentrated in CC (Table 4 and 5). Taking the various values together, it was obvious that the different materials of CC (Fig. 4B, left side) and of slide flasks (Fig. 4B, right side) influenced the release of biological factors differently, although both kinds of material did not have any influence on viability or apoptosis of the cells [25]. Their interaction was given in Fig. 4C.

Fold changes of secreted proteins

For better visualization of further results shown within the tables, spider charts were generated, which give an overview on the culture condition dependent variation of the influence of μ*g* and VEGF (Fig. 4D-G).

Selected components are compared regarding their release during one (Fig. 4D) or two weeks of spaceflight and RPM-culture (Fig. 4E). During the first week differences arose for MCP-1 and collagen I, while after a second week IL-6, IL-8 and collagen I differed in the amount of appearance within the culture supernatant, when their concentrations in the supernatant of spaceflight or RPM cultures were compared with those in the corresponding 1*g* controls. VEGF supplementation had little influence on the cells during the first week in space. During the second week in space, however, it boosted the release of B2M, IL-6, IL-8, and TIMP-1 but reduced collagen I secretion (Fig. 4F). When the cell cultures were incubated on the RPM, a significant influence of the presence of VEGF could not be detected (Fig. 4G).

Cellular Physiology and Biochemistry
Cell Physiol Biochem 2019;52:1039-1060
DOI: 10.33594/000000071
Published online: 13 April 2019
© 2019 The Author(s). Published by Cell Physiol Biochem Press GmbH&Co. KG

Interaction of proteins released into the supernatant

In order to see whether there is a linkage between the proteins secreted into the culture supernatant, we performed an interaction analysis. Fig. 4C shows that most of the factors detected in the culture supernatants form a network of interaction. In this network ECM components (blue rim) determined by ELISA are embedded together with biological factors detected by the Human InflammationMAP®. Furthermore, the compounds secreted in the supernatant during culturing in both kinds of culture dish showed far branched relationships as indicated by the icons with a green rim for SERPINA1, A2M, B2M BDNF, C3, CCL11 (eotaxin-1), IL-6, IL-8, CCL2 (MCP-1), TIMP-1, and VEGF-A. ICAM-1, MMP-3, TNFR2, CCL5 (RANTES) and vWF were detected only in supernatants of slide flasks. Of these factors ICAM-1, TNFR2, CCL5 (RANTES) and vWF are netted as indicated by icons with red rims. It is of interest that fibronectin (FN1), which is rather resistant to the influence of μ*g* and VEGF-A, binds to Col1A1, that is up-regulated especially in space. But further explanations about the cells' μ*g* dependent secretion behavior cannot be derived from their interaction network. Therefore, we also investigated the underlying network of genes.

Changes in gene expression

Unfortunately, the cell concentration found in the flight hardware after return was too low for transcriptional analysis by qPCR. Therefore, we investigated only the cells cultured on the RPM. Fig. 5A and 5B show that a number of genes (*TIMP1*, *IL6*, *CXCL8*, *CCL2*, *B2M*) are differently regulated in AD and MCS cells. While most of the investigated genes are down-regulated in AD cells, there is a considerable number of them up- or un-regulated in MCS cells (Table 6). This effect may be due to the kind of mutually up-building gene interaction shown in Fig. 5C. There is also an effect of duration of exposure to the RPM (*FN1*, *TIMP1*, *VEGFA*) and of the presence of supplemented VEGF. Only *LAMA1* was not significantly regulated under all culture conditions, but VEGF supplementation exerted its influence on the regulation of *FN1* already after 7 d (Table 6). There is little effect of the external VEGF on the *VEGFA* gene. Also IL-6 and IL-8 are regulated very similarly irrespective of the duration of RPM exposure or the presence of external VEGF. Most interesting are the effect of time of incubation and of VEGF on the regulation of *CDH5*, which may be important for spheroid formation. While after 7 d a divergence of regulation is visible in the presence of VEGF only, the divergence is enforced after 14 d. It is also interesting that *IL6*, which has an inhibitory influence on *CDH5* is up-regulated when *CDH5* is down-regulated (Fig. 5C, Table 6).

Discussion

In this study we investigated the influence of r-μ*g* on EA.hy926 cells. For this purpose, we cultured cells for 5 d and 12 d (previous studies in s-μ*g* suggested that these two time points are most interesting to observe μ*g*-dependent changes in phenotype/growth behavior [7, 19]) under r-μ*g* in space either in plain culture medium or in medium containing VEGF. Subsequently, we determined the growth pattern and quantities of growth factors/cytokines secreted and performed comparative experiments using the same timeline and temperature protocols as in the space experiment, but keeping the cells either on an RPM or under normal 1*g* laboratory conditions.

Three-dimensional growth in real (r-μg) and simulated microgravity (s-μg)

In space we observed similar 3D growth as observed in several studies using s-μ*g* before. Examining the cells subjected to r-μ*g* in space we detected three different populations of EA.hy926 cells. Some ECs remained adherent (Fig. 3C), but others had assembled to 3D structures either with spherical or with tube-like appearance (Fig. 3D-F). This demonstrates that EA.hy926 cells exhibit 3D growth in space, where r-μ*g* is a long-term condition that cannot be found on Earth. Hence, they behave similarly like human FTC-133 thyroid cells [39], bovine articular chondrocytes [40], or pig liver stem cells [41] which already showed

Cellular Physiology and Biochemistry
Cell Physiol Biochem 2019;52:1039-1060
DOI: 10.33594/000000071
Published online: 13 April 2019
© 2019 The Author(s). Published by Cell Physiol Biochem Press GmbH&Co. KG

Table 6. Gene expression of EA.hy926 cells after exposure to the RPM compared with 1*g* controls. Cells were cultured in slide flasks. The data was generated by using qPCR. Values are given as mean ± SD; *: P <0.05 vs. 1*g*; ▼|▲: P <0.05 vs. 7d; §: P <0.05 vs. –VEGF; #: P <0.05 vs. AD; AD: Adherently growing cells; MCS: Multicellular spheroids; n.d.: not detectable. *18S* was used as housekeeper. *LAMB2* (Laminin Subunit β2), *COL1A1* (Collagen Type I α1 Chain), and *CCL11* (Eotaxin-1) mRNA levels were below the LLOQ

Function	Gene Symbol	Encoded Protein	Earth gravity (1*g*) 7 d – VEGF	Earth gravity (1*g*) 7 d + VEGF	Earth gravity (1*g*) 14 d – VEGF	Earth gravity (1*g*) 14 d + VEGF	RPM (s-μ*g*) 7 d – VEGF	RPM (s-μ*g*) 7 d + VEGF	RPM (s-μ*g*) 14 d – VEGF	RPM (s-μ*g*) 14 d + VEGF	Morphology
Extracellular Matrix (ECM)	*FN1*	Fibronectin					167.2* ± 16.85	150.2*# ± 14.78	▼137.5# ± 10.08	▼110.5*§ ± 9.61	MCS
			100.0 ± 10.70	124.5§ ± 8.49	▲143.6 ± 8.42	▲168.0 ± 24.06	148.0* ± 26.25	130.2 ± 6.85	▼91.96* ± 8.95	▼102.8* ± 5.11	AD
	LAMA1	Laminin Subunit α1					105.9 ± 31.45	87.66 ± 16.73	▼31.47 ± 11.96	▼36.46# ± 14.77	MCS
			100.0 ± 26.46	112.9 ± 20.34	▼27.59 ± 5.38	▼23.61 ± 5.83	77.38 ± 19.86	86.65 ± 23.45	▼22.48 ± 9.26	▼19.80 ± 5.95	AD
	TIMP1	Tissue Inhibitor of Metallo-proteinases 1					199.9*# ± 19.81	199.6# ± 22.85	▼67.54* ± 8.10	▼93.75§ ± 16.97	MCS
			100.0 ± 19.25	162.5§ ± 10.50	83.12 ± 10.06	▼75.83 ± 12.06	91.12 ± 11.48	141,8§ ± 16.83	▼57.54* ± 11.04	▼77.85§ ± 18.78	AD
"3D" Factors	*IL6*	Interleukin-6					119.8# ± 26.70	201.7*# ± 1.81	▲174.0# ± 19.56	▲273.7*§# ± 15.22	MCS
			100.0 ± 22.57	152.8§ ± 16.63	▲210.5 ± 43.73	▲195.5 ± 28.29	50.68* ± 5.84	91.55*§ ± 11.00	▲100.7* ± 12.22	▲146.0*§ ± 19.13	AD
	CXCL8	Interleukin-8					202.5*# ± 26.37	314.5*§# ± 20.41	▲710.0*# ± 31.05	▲654.7*# ± 19.78	MCS
			100.0 ± 12.26	151.1§ ± 6.50	▲398.4 ± 54.49	▲393.1 ± 7.82	51.10* ± 4.35	110.2*§ ± 15.75	▲170.3* ± 14.19	▲212.7* ± 17.90	AD
	CDH5	VE-Cadherin					81.23* ± 12.45	62.56*§# ± 8.66	65.20*# ± 9.79	52.53*§# ± 4.14	MCS
			100.0 ± 11.17	123.0 ± 19.18	▲147.6 ± 26.05	119.0 ± 25.54	67.89* ± 7.72	126.0§ ± 17.28	▲152.8 ± 15.27	▲173.8* ± 20.09	AD
	VEGFA	Vascular Endothelial Growth Factor A					67.39*# ± 5.17	77.92*# ± 16.18	▲121.4# ± 25.96	▲104.8*# ± 7.64	MCS
			100.0 ± 14.70	131.9 ± 22.85	▲153.8 ± 44.46	▲188.6± 23.48	58.15* ± 5.79	92.41*§ ± 8.66	▲278.1* ± 71.17	▲268.0* ± 39.0	AD
	B2M	β2-Microglobulin					139.4*# ± 9.72	97.20 ± 16.32	▲356.2# ± 34.81	▲301.6# ± 46.12	MCS
			100.0 ± 17.67	140.0§ ± 18.85	▲351.1 ± 28.46	▲383.7 ± 84.58	63.54* ± 15.02	94.19*§ ± 9.86	▲240.6* ± 26.01	▲217.6* ± 41.83	AD
Inflammation	*CCL2*	Monocyte Chemotactic Protein 1 (MCP-1)					127.2# ± 19.20	144.9# ± 9.64	▼40.05*# ± 8.00	▼47.76# ± 8.08	MCS
			100.0 ± 14.38	167.9§ ± 13.54	▼68.08 ± 17.08	▼57.48 ± 8.18	37.05* ± 4.94	47.79*§ ± 2.28	▼19.33* ± 1.86	▼28.80*§ ± 2.06	AD
	FTL	Ferritin Light Chain					186.3* ± 32.54	402.4# ± 47.19	▲320.2# ± 35.14	344.9*# ± 36.86	MCS
			100.0 ± 20.05	124.9 ± 11.66	▲290.1 ± 62.73	▲266.1 ± 42.59	161.2* ± 49.54	118.1 ± 11.42	188.2* ± 33.70	157.2* ± 36.99	AD

Cellular Physiology and Biochemistry
Cell Physiol Biochem 2019;52:1039-1060
DOI: 10.33594/000000071
Published online: 13 April 2019
© 2019 The Author(s). Published by Cell Physiol Biochem Press GmbH&Co. KG

organoid formation during space missions. On Earth long-term s-µ*g* can be simulated with the help of instruments like the 2D-clinostat, the Rotating Wall Vessel, and the RPM or by using magnetic levitation [42-44]. We used the RPM as it provides high quality s-µ*g* inside the whole cell culture flask, for both adherent and floating cells as well as for spheroids. Even the simulation triggers ECs to exhibit 3D growth (Fig. 3G), when cells are exposed to a random change in direction of the gravitational pull preventing sedimentation which over time corresponds to a 'quasi-microgravity' [28], reaching a calculated quality of 10^{-3} to 10^{-4} *g* with our RPM [29]. This reduction of gravity forces not only changed the growth behavior of ECs, but triggers also 3D growth of thyroid (cancer) cells [36], breast cancer cells [45] or chondrocytes [46].

In addition to µ*g*, a space experiment is accompanied by multiple other factors, such as cosmic radiation, mechanical stress at the rocket launch, temperature fluctuations during the transport to the ISS and special CCs consisting of PEEK instead of polystyrene [25, 39]. Even vibration and hyper-*g* during the rocket launch can affect ECs on the transcriptional and translational level [11, 47, 48]. These factors, however, do not prevent 3D growth. Hence, prevention of sedimentation is the major cause that allows at least a group of cells to leave the monolayer and to assemble to 3D structures. This holds true in space as well as on suitable ground-based devices like the RPM. As the latter technology is cheaper and more often applicable than spaceflights, still inducing 3D growth similar to a stay in space, it can now be used with more confidence to learn about the mechanism of scaffold-free tissue formation under µ*g*.

Protein secretion and the influence of the hardware

Little is known about the proteins involved in µ*g*-dependent formation of tube-like structures by ECs [7, 8]. In human cancer cells we have already recognized several growth factors and proteins of the focal adhesion complex and of tight junctions playing a role in MCS formation [49, 50]. In these experiments we focused on components of the ECM (Tables 2, 3) as well as growth factors and cytokines released into the supernatant (Tables 4, 5). We studied their release by cells enclosed in flight hardware CCs or in polystyrene slide flasks as used for RPM experiments. Both types of cell containers were either kept under µ*g* (flight hardware in r-µ*g*, polystyrene flask in s-µ*g* on the RPM) as well as under 1*g* control conditions, respectively. Although 3D structures were found in both containers (Fig. 3), when cultured under µ*g*, we recognized container dependent differences in the release of proteins.

Significantly higher quantities of the ECM components fibronectin, laminin, and collagen I were detected in the supernatants of slide flasks than in those of space hardware CCs, independently whether the samples had been incubated under gravity or under µ*g*. (Tables 2, 3). Interestingly, a clear influence of gravity on the amounts of soluble ECM is only detected for collagen I. Type I collagen is the most abundant collagen of the human body [51]. Collagen metabolism in the ECM is related to the pathogenesis of cardiovascular stiffness [52, 53]. Astronauts returning from space do suffer from an increased arterial stiffness [54]. In addition, an increased procollagen level was found in the skin of mice living for 3 months on the ISS [55]. Hence, our *in vitro* result could represent a space-dependent effect. The ECM plays a crucial role in 3D growth and angiogenesis [56-58]. Infanger *et al.* have reported previously that s-µ*g* can enhance the expression of collagen I, laminin, and fibronectin in EA.hy926 cells [8]. In their experiments VEGF supplementation showed some effect during the first 4 h, but then the VEGF influence ceased and seemed to suppress the µ*g*-dependent amounts of ECM proteins [8].

As ECM components secreted by tissue cells are at least in part adsorbed by the CC material to form an anchorage possibility for the cells or incorporated in 3D structures, it is difficult to decide whether the different quantities of the components dissolved in the supernatant are due to a different production activity of the cells or to different adsorption by the chamber material. For example, intracellular levels of ECM proteins determined after long-term experiments on the RPM indicated significant increases of laminin and fibronectin

Cellular Physiology and Biochemistry
Cell Physiol Biochem 2019;52:1039-1060
DOI: 10.33594/000000071
Published online: 13 April 2019
© 2019 The Author(s). Published by Cell Physiol Biochem Press GmbH&Co. KG

in tube-like structures after 28 d [7] and a significant increase of fibronectin was found in MCS after 35 d [21]. In any case, our experiments suggest a relationship between the dissolved ECM components and cytokines. A clear cell container material-dependent difference was found in quantities of a number of cytokines/growth factors released into supernatant by ECs (Fig. 4A, B). This is corroborated by a recent study by Cazzaniga and coworkers, who reported that hardware designed for spaceflights can impact cell behavior [59]. But it is not clear which cytokine is directly affected by the chamber material and which is regulated by the network of interaction shown in Fig. 4C. Only the A2M quantities detected were similar under all incubation conditions.

Impact of VEGF supplementation

We observed a low VEGF production in space hardware and polystyrene flasks under 1*g*. This may be explained as VEGF is an important growth and survival factor for ECs [60], which is secreted by a variety of cell types, but not by ECs themselves [61]. Significantly enhanced amounts of VEGF were only found in supernatants of RPM cultures. This observation could be due to the nature of EA.hy926 cells, which are hybrid cells consisting of endothelial and of cancer cells [62] as well as due to mechanical stimuli, whose effects on VEGF have been demonstrated for different cell types [63-65].

In vivo, VEGF takes part in promoting angiogenesis by stimulation of survival, permeability, migration, and proliferation [66]. In flight hardware samples, VEGF supplementation made C3, eotaxin-1, fibrinogen, and IL-1a detectable and decreased B2M, IL-8 and TIMP-1 levels under 1*g*, while IL-6 was increased under µ*g* (Table 4, Fig. 4F). In polystyrene chambers, VEGF supplementation made eotaxin-1 visible after 7 d and 14 d but ICAM-1 after 14 d under 1*g* and under µ*g* (Table 5, Fig. 4G). A relationship between enhancement of VEGF, collagen I and eotaxin-1 has been described for airway smooth muscle cells [67]. Although a role of eotaxin-1 in *in vitro* scaffold-free tube formation has not been described yet, it appears to support cancer dependent angiogenesis [68].

IL-6 and IL-8

Interleukins 6 and 8 are well known candidates in analyses of µ*g* studies. Enhancement of IL-6 and IL-8 production under µ*g* conditions has been reported before for EA.hy926 cells [21, 23], and different malignant and non-malignant human cell lines [45, 69, 70]. IL-8 was identified to be a potent autocrine growth and survival factor for ECs [71]. It regulates angiogenesis and modulates endothelial cell-cell-connections by temporarily down-regulation of tight junctions but not by integrin-mediated focal adhesions [72]. In our experiments, after a 7 day culture the IL-8 concentration was found higher in the supernatants of flight hardware cultures than in those of polystyrene cultures (Tables 4, 5). During the second week the IL-8 concentration declined in the first type of cell containers, while it increased in polystyrene cultures. At that time the µ*g* effect was most prominent in the flight hardware chamber (Fig. 4D, E), resembling that of B2M, a protein which is expressed at a constant level in many cells [73]. B2M was described as a common γ radiation responder [74]. Its response to space conditions may therefore be contributed to an irradiation effect, while the role of IL-8 needs further investigation. In these experiments, the IL-6 secretion was clearly enhanced under r-µ*g* in flight hardware CCs as well as in polystyrene culture flasks, when 3D structures were formed. However, the µ*g* effect was time shifted. It was most prominent after 7 d on the flight hardware and after 14 d on the RPM (Fig. 4D, E). Time shifts in tube formation were already observed when microvascular ECs and EA.hy926 cells were investigated comparatively [24]. IL-6 has also been reported to induce ferritin synthesis [75]. This fits very well with the results of tables 4 and 5.

Source of cytokines/growth factors

Two other interesting proteins observed were MCP-1 and TIMP-1. Their secretion depended on the cell container material, similar to the one of IL-8 and B2M. However, these proteins did not show any response to µ*g*. Therefore, combining the cell culture supernatants

Cellular Physiology and Biochemistry
Cell Physiol Biochem 2019;52:1039-1060
DOI: 10.33594/000000071
Published online: 13 April 2019
© 2019 The Author(s). Published by Cell Physiol Biochem Press GmbH&Co. KG

analysis, one may conclude that considering the influence of the material of the culture dishes, the IL-6 concentration in the culture supernatants are most closely related to 3D structure formation. However, proteins detected in a culture supernatant may be released by both, the adherent and the 3D structure cells (Fig. 3C-F). In order to get an impression which cell type is responsible for a current concentration of a cytokine, growth factor or ECM component, we performed qPCR analyses on ten selected genes of which 9 form an interaction network (Fig. 5). As mentioned above, the analyses were performed only on RPM samples, due to a lack of the space sample material. At a first glance it can be seen that only *FN1*, *CDH5*, *VEGFA* and *FTL* genes share a similar activation status in adherent and 3D structure cells after 7 d, while *TIMP1*, *IL6* and *CCL2* showed these features after two weeks. Addition of VEGF to the culture medium changed the gene expression for *LAMA1*, *CDH5*, *CCL2*, *B2M* and *FTL* after 7 d and for *FN1*, *TIMP1*, *IL6*, *CDH5* and *B2M* after two weeks. The qPCR analyses clearly show that further work is required to identify the source of the various cytokines, growth factors and ECM components.

Conclusion

Using an automatic flight hardware, specially designed for space experiments, we demonstrated for the first time that ECs exhibit 3D growth in space. This indicates that μ*g* may be the major cause for the formation of tube-like aggregates of ECs and justifies the use of RPM for studies on scaffold free 3D structure formation, when the importance of the material of cell containers is considered. In this study it was clearly demonstrated that the material of the cell containers influences the protein secretion of ECs. A further influence on 3D formation cannot be excluded, as very large spheroids were detected when thyroid cancer cells had been sent to space [76]. IL-6 is more and more emerging as a key protein in μ*g* dependent 3D formation. It is up-regulated, when 3D structures are formed and down-regulate VE-cadherin weakening tight junctions, like E-cadherin in breast cancer cells [49]. Taken together, the SPHEROIDS experiments increased our knowledge of EC behavior in space. Aiming to better understand *in vitro* angiogenesis and to improve tissue engineering with ECs, it will be of interest to study the interplay of cells leaving the monolayer for 3D structure formation with those remaining in the monolayer.

Abbreviations

μ*g* (Microgravity); 1*g* (Earth gravity); 3D (Three-dimensional); CC (Cell cultivation chamber (flight hardware)); EC (Endothelial cell); ECM (Extracellular matrix); IL (Interleukin); ISS (International Space Station); MAP (Multi-Analyte Profiling); MCS (Multicellular spheroid); PEEK (Polyether ether ketone); RPM (Random Positioning Machine); VEGF (Vascular endothelial growth factor A).

Acknowledgements

The authors would like to thank Jason Hatton, Nadine Boersma and Andrea Koehler from ESA, Raimondo Fortezza from Telespazio, Stefan Riwaldt, Christin Baake, Daniel Echegoyen, and Lasse Slumstrup for their support of the space experiment. We like to thank Christa Baumann (University of Regensburg) for performing the paraffin embedding and histochemical stains of the space spheroids. The research was supported by the German Space Agency (DLR, grants 50BW1124 and 50BW1524), the European Space Agency (ESA, grant ESA-AO-2004-PCP-006) as well as BELSPO PRODEX (IMPULSE 2 grant 4000109861).

Cellular Physiology and Biochemistry
Cell Physiol Biochem 2019;52:1039-1060
DOI: 10.33594/000000071
Published online: 13 April 2019
© 2019 The Author(s). Published by Cell Physiol Biochem Press GmbH&Co. KG

Disclosure Statement

Competing financial interests: The authors declare no competing financial interests. The views expressed herein can in no way be taken to reflect the official opinion of the European Space Agency.

References

1 White RJ, Averner M: Humans in space. Nature 2001;409:1115.
2 Buckey JC, Jr., Lane LD, Levine BD, Watenpaugh DE, Wright SJ, Moore WE, Gaffney FA, Blomqvist CG: Orthostatic intolerance after spaceflight. J Appl Physiol 1996;81:7-18.
3 Delp MD, Charvat JM, Limoli CL, Globus RK, Ghosh P: Apollo Lunar Astronauts Show Higher Cardiovascular Disease Mortality: Possible Deep Space Radiation Effects on the Vascular Endothelium. Sci Rep 2016;6:29901.
4 Nicogossian AE, Charles JB, Bungo MW, Leach-Huntoon CS, Nicgossian AE: Cardiovascular function in space flight. Acta Astronaut 1991;24:323-328.
5 Sato M, Ohashi T: Biorheological views of endothelial cell responses to mechanical stimuli. Biorheology 2005;42:421-441.
6 Maier JA, Cialdai F, Monici M, Morbidelli L: The impact of microgravity and hypergravity on endothelial cells. Biomed Res Int 2015;2015:434803.
7 Grimm D, Infanger M, Westphal K, Ulbrich C, Pietsch J, Kossmehl P, Vadrucci S, Baatout S, Flick B, Paul M, Bauer J: A delayed type of three-dimensional growth of human endothelial cells under simulated weightlessness. Tissue Eng Part A 2009;15:2267-2275.
8 Infanger M, Kossmehl P, Shakibaei M, Baatout S, Witzing A, Grosse J, Bauer J, Cogoli A, Faramarzi S, Derradji H, Neefs M, Paul M, Grimm D: Induction of three-dimensional assembly and increase in apoptosis of human endothelial cells by simulated microgravity: impact of vascular endothelial growth factor. Apoptosis 2006;11:749-764.
9 Janmaleki M, Pachenari M, Seyedpour SM, Shahghadami R, Sanati-Nezhad A: Impact of Simulated Microgravity on Cytoskeleton and Viscoelastic Properties of Endothelial Cell. Sci Rep 2016;6:32418.
10 Versari S, Longinotti G, Barenghi L, Maier JA, Bradamante S: The challenging environment on board the International Space Station affects endothelial cell function by triggering oxidative stress through thioredoxin interacting protein overexpression: the ESA-SPHINX experiment. FASEB J 2013;27:4466-4475.
11 Wehland M, Ma X, Braun M, Hauslage J, Hemmersbach R, Bauer J, Grosse J, Infanger M, Grimm D: The impact of altered gravity and vibration on endothelial cells during a parabolic flight. Cell Physiol Biochem 2013;31:432-451.
12 Li N, Wang C, Sun S, Zhang C, Lü D, Chen Q, Long M: Microgravity-Induced Alterations of Inflammation-Related Mechanotransduction in Endothelial Cells on Board SJ-10 Satellite. Front Physiol 2018;9:1025.
13 Ingber DE: Tensegrity: the architectural basis of cellular mechanotransduction. Annu Rev Physiol 1997;59:575-599.
14 Griffoni C, Di Molfetta S, Fantozzi L, Zanetti C, Pippia P, Tomasi V, Spisni E: Modification of proteins secreted by endothelial cells during modeled low gravity exposure. J Cell Biochem 2011;112:265-272.
15 Versari S, Villa A, Bradamante S, Maier JAM: Alterations of the actin cytoskeleton and increased nitric oxide synthesis are common features in human primary endothelial cell response to changes in gravity. Biochim Biophys Acta 2007;1773:1645-1652.
16 Morbidelli L, Monici M, Marziliano N, Cogoli A, Fusi F, Waltenberger J, Ziche M: Simulated hypogravity impairs the angiogenic response of endothelium by up-regulating apoptotic signals. Biochem Biophys Res Commun 2005;334:491-499.
17 Carlsson SIM, Bertilaccio MTS, Ballabio E, Maier JAM: Endothelial stress by gravitational unloading: effects on cell growth and cytoskeletal organization. Biochim Biophys Acta 2003;1642:173-179.
18 Infanger M, Ulbrich C, Baatout S, Wehland M, Kreutz R, Bauer J, Grosse J, Vadrucci S, Cogoli A, Derradji H, Neefs M, Kusters S, Spain M, Paul M, Grimm D: Modeled gravitational unloading induced downregulation of endothelin-1 in human endothelial cells. J Cell Biochem 2007;101:1439-1455.

Cellular Physiology and Biochemistry
Cell Physiol Biochem 2019;52:1039-1060
DOI: 10.33594/000000071
Published online: 13 April 2019
© 2019 The Author(s). Published by Cell Physiol Biochem Press GmbH&Co. KG

19 Grimm D, Bauer J, Ulbrich C, Westphal K, Wehland M, Infanger M, Aleshcheva G, Pietsch J, Ghardi M, Beck M, El-Saghire H, de Saint-Georges L, Baatout S: Different responsiveness of endothelial cells to vascular endothelial growth factor and basic fibroblast growth factor added to culture media under gravity and simulated microgravity. Tissue Eng Part A 2010;16:1559-1573.
20 Ulbrich C, Westphal K, Baatout S, Wehland M, Bauer J, Flick B, Infanger M, Kreutz R, Vadrucci S, Egli M, Cogoli A, Derradji H, Pietsch J, Paul M, Grimm D: Effects of basic fibroblast growth factor on endothelial cells under conditions of simulated microgravity. J Cell Biochem 2008;104:1324-1341.
21 Dittrich A, Grimm D, Sahana J, Bauer J, Krüger M, Infanger M, Magnusson NE: Key Proteins Involved in Spheroid Formation and Angiogenesis in Endothelial Cells After Long-Term Exposure to Simulated Microgravity. Cell Physiol Biochem 2018;45:429-445.
22 Gapizov SS, Petrovskaya LE, Shingarova LN, Svirschevskaya EV, Dolgikh DA, Kirpichnikov MP: The Effect of TNF and VEGF on the Properties of Ea.hy926 Endothelial Cells in a Model of Multi-Cellular Spheroids. Acta Naturae 2018;10:34-42.
23 Ma X, Wehland M, Schulz H, Saar K, Hübner N, Infanger M, Bauer J, Grimm D: Genomic Approach to Identify Factors That Drive the Formation of Three-Dimensional Structures by EA.hy926 Endothelial Cells. PLoS ONE 2013;8:e64402.
24 Ma X, Sickmann A, Pietsch J, Wildgruber R, Weber G, Infanger M, Bauer J, Grimm D: Proteomic differences between microvascular endothelial cells and the EA.hy926 cell line forming three-dimensional structures. Proteomics 2014;14:689-698.
25 Pietsch J, Gass S, Nebuloni S, Echegoyen D, Riwaldt S, Baake C, Bauer J, Corydon TJ, Egli M, Infanger M, Grimm D: Three-dimensional growth of human endothelial cells in an automated cell culture experiment container during the SpaceX CRS-8 ISS space mission - The SPHEROIDS project. Biomaterials 2017;124:126-156.
26 Edgell CJ, McDonald CC, Graham JB: Permanent cell line expressing human factor VIII-related antigen established by hybridization. Proc Natl Acad Sci U S A 1983;80:3734-3737.
27 Ahn K, Pan S, Beningo K, Hupe D: A permanent human cell line (EA.hy926) preserves the characteristics of endothelin converting enzyme from primary human umbilical vein endothelial cells. Life Sci 1995;56:2331-2341.
28 van Loon JJWA: Some history and use of the random positioning machine, RPM, in gravity related research. Adv Space Res 2007;39:1161-1165.
29 Borst AG, van Loon JJWA: Technology and Developments for the Random Positioning Machine, RPM. Microgravity Sci Technol 2008;21:287.
30 Ma X, Wehland M, Schulz H, Saar K, Hübner N, Infanger M, Bauer J, Grimm D: Genomic approach to identify factors that drive the formation of three-dimensional structures by EA.hy926 endothelial cells. PLoS One 2013;8:e64402.
31 Ulbrich C, Westphal K, Pietsch J, Winkler HD, Leder A, Bauer J, Kossmehl P, Grosse J, Schoenberger J, Infanger M, Egli M, Grimm D: Characterization of human chondrocytes exposed to simulated microgravity. Cell Physiol Biochem 2010;25:551-560.
32 Wüest SL, Richard S, Kopp S, Grimm D, Egli M: Simulated microgravity: critical review on the use of random positioning machines for mammalian cell culture. Biomed Res Int 2015;2015:971474.
33 Riwaldt S, Monici M, Graver Petersen A, Birk Jensen U, Evert K, Pantalone D, Utpatel K, Evert M, Wehland M, Krüger M, Kopp S, Frandsen S, Corydon T, Sahana J, Bauer J, Lützenberg R, Infanger M, Grimm D: Preparation of A Spaceflight: Apoptosis Search in Sutured Wound Healing Models. Int J Mol Sci 2017;18(12):2604.
34 Grimm D, Jabusch HC, Kossmehl P, Huber M, Fredersdorf S, Griese DP, Kramer BK, Kromer EP: Experimental diabetes and left ventricular hypertrophy: effects of beta-receptor blockade. Cardiovasc Pathol 2002;11:229-237.
35 Grosse J, Warnke E, Pohl F, Magnusson NE, Wehland M, Infanger M, Eilles C, Grimm D: Impact of sunitinib on human thyroid cancer cells. Cell Physiol Biochem 2013;32:154-170.
36 Kopp S, Warnke E, Wehland M, Aleshcheva G, Magnusson NE, Hemmersbach R, Corydon TJ, Bauer J, Infanger M, Grimm D: Mechanisms of three-dimensional growth of thyroid cells during long-term simulated microgravity. Sci Rep 2015;5:16691.

Cellular Physiology and Biochemistry
Cell Physiol Biochem 2019;52:1039-1060
DOI: 10.33594/000000071
Published online: 13 April 2019
© 2019 The Author(s). Published by Cell Physiol Biochem Press GmbH&Co. KG

37 Rothermund L, Kreutz R, Kossmehl P, Fredersdorf S, Shakibaei M, Schulze-Tanzil G, Paul M, Grimm D: Early onset of chondroitin sulfate and osteopontin expression in angiotensin II-dependent left ventricular hypertrophy. Am J Hypertens 2002;15:644-652.
38 ESA. Kubik Description. Available online: http://esamultimedia.esa.int/docs/hsf_research/Kubik_description.pdf.
39 Pietsch J, Ma X, Wehland M, Aleshcheva G, Schwarzwälder A, Segerer J, Birlem M, Horn A, Bauer J, Infanger M, Grimm D: Spheroid formation of human thyroid cancer cells in an automated culturing system during the Shenzhou-8 Space mission. Biomaterials 2013;34:7694-7705.
40 Freed LE, Langer R, Martin I, Pellis NR, Vunjak-Novakovic G: Tissue engineering of cartilage in space. Proc Natl Acad Sci U S A 1997;94:13885-13890.
41 Talbot NC, Caperna TJ, Blomberg L, Graninger PG, Stodieck LS: The effects of space flight and microgravity on the growth and differentiation of PICM-19 pig liver stem cells. *In vitro* Cell Dev Biol Anim 2010;46:502-515.
42 Herranz R, Anken R, Boonstra J, Braun M, Christianen PCM, de Geest M, Hauslage J, Hilbig R, Hill RJA, Lebert M, Medina FJ, Vagt N, Ullrich O, van Loon JJWA, Hemmersbach R: Ground-Based Facilities for Simulation of Microgravity: Organism-Specific Recommendations for Their Use, and Recommended Terminology. Astrobiology 2013;13:1-17.
43 Wüest SL, Richard S, Kopp S, Grimm D, Egli M: Simulated Microgravity: Critical Review on the Use of Random Positioning Machines for Mammalian Cell Culture. Biomed Res Int 2015;2015:971474.
44 Becker JL, Souza GR: Using space-based investigations to inform cancer research on Earth. Nat Rev Canc 2013;13:315-327.
45 Kopp S, Slumstrup L, Corydon TJ, Sahana J, Aleshcheva G, Islam T, Magnusson NE, Wehland M, Bauer J, Infanger M, Grimm D: Identifications of novel mechanisms in breast cancer cells involving duct-like multicellular spheroid formation after exposure to the Random Positioning Machine. Sci Rep 2016;6:26887.
46 Aleshcheva G, Bauer J, Hemmersbach R, Slumstrup L, Wehland M, Infanger M, Grimm D: Scaffold-free Tissue Formation Under Real and Simulated Microgravity Conditions. Basic Clin Pharmacol Toxicol 2016;119:26-33.
47 Costa-Almeida R, Carvalho DTO, Ferreira MJS, Aresta G, Gomes ME, van Loon JJWA, Van der Heiden K, Granja PL: Effects of hypergravity on the angiogenic potential of endothelial cells. J R Soc Interface 2016;13:pii:20160688.
48 Morbidelli L, Marziliano N, Basile V, Pezzatini S, Romano G, Conti A, Monici M: Effect of Hypergravity on Endothelial Cell Function and Gene Expression. Microgravity Sci Technol 2009;21:135-140.
49 Sahana J, Nassef MZ, Wehland M, Kopp S, Krüger M, Corydon TJ, Infanger M, Bauer J, Grimm D: Decreased E-Cadherin in MCF7 Human Breast Cancer Cells Forming Multicellular Spheroids Exposed to Simulated Microgravity. Proteomics 2018:e1800015.
50 Bauer J, Kopp S, Schlagberger EM, Grosse J, Sahana J, Riwaldt S, Wehland M, Luetzenberg R, Infanger M, Grimm D: Proteome Analysis of Human Follicular Thyroid Cancer Cells Exposed to the Random Positioning Machine. Int J Mol Sci 2017;18:pii:E546.
51 Shoulders MD, Raines RT: Collagen structure and stability. Annu Rev Biochem 2009;78:929-958.
52 Kohn JC, Lampi MC, Reinhart-King CA: Age-related vascular stiffening: causes and consequences. Front Genet 2015;6:112.
53 McNulty M, Mahmud A, Spiers P, Feely J: Collagen type-I degradation is related to arterial stiffness in hypertensive and normotensive subjects. J Hum Hypertens 2006;20:867-873.
54 Hughson RL, Robertson AD, Arbeille P, Shoemaker JK, Rush JW, Fraser KS, Greaves DK: Increased postflight carotid artery stiffness and inflight insulin resistance resulting from 6-mo spaceflight in male and female astronauts. Am J Physiol Heart Circ Physiol 2016;310:H628-638.
55 Neutelings T, Nusgens BV, Liu Y, Tavella S, Ruggiu A, Cancedda R, Gabriel M, Colige A, Lambert C: Skin physiology in microgravity: a 3-month stay aboard ISS induces dermal atrophy and affects cutaneous muscle and hair follicles cycling in mice. Npj Microgravity 2015;1:15002.
56 Mongiat M, Andreuzzi E, Tarticchio G, Paulitti A: Extracellular Matrix, a Hard Player in Angiogenesis. Int J Mol Sci 2016;17:pii:1822.
57 Hynes RO: The extracellular matrix: not just pretty fibrils. Science 2009;326:1216-1219.

Cellular Physiology and Biochemistry
Cell Physiol Biochem 2019;52:1039-1060
DOI: 10.33594/000000071
Published online: 13 April 2019
© 2019 The Author(s). Published by Cell Physiol Biochem Press GmbH&Co. KG

58 Sottile J: Regulation of angiogenesis by extracellular matrix. Biochim Biophys Acta 2004;1654:13-22.
59 Cazzaniga A, Moscheni C, Maier JAM, Castiglioni S: Culture of human cells in experimental units for spaceflight impacts on their behavior. Exp Biol Med 2017;242:1072-1078.
60 Ferrara N, Henzel WJ: Pituitary follicular cells secrete a novel heparin-binding growth factor specific for vascular endothelial cells. Biochem Biophys Res Commun 1989;161:851-858.
61 Berse B, Brown LF, Water LVd, Dvorak HF, Senger DR: Vascular permeability factor (vascular endothelial growth factor) gene is expressed differentially in normal tissues, macrophages, and tumors. Mol Biol Cell 1992;3:211-220.
62 Lieber M, Smith B, Szakal A, Nelson-Rees W, Todaro G: A continuous tumor-cell line from a human lung carcinoma with properties of type II alveolar epithelial cells. Int J Cancer 1976;17:62-70.
63 dela Paz NG, Walshe TE, Leach LL, Saint-Geniez M, D'Amore PA: Role of shear-stress-induced VEGF expression in endothelial cell survival. J Cell Sci 2012;125:831-843.
64 Milkiewicz M, Brown MD, Egginton S, Hudlicka O: Association between shear stress, angiogenesis, and VEGF in skeletal muscles *in vivo*. Microcirculation 2001;8:229-241.
65 Corydon TJ, Mann V, Slumstrup L, Kopp S, Sahana J, Askou AL, Magnusson NE, Echegoyen D, Bek T, Sundaresan A, Riwaldt S, Bauer J, Infanger M, Grimm D: Reduced Expression of Cytoskeletal and Extracellular Matrix Genes in Human Adult Retinal Pigment Epithelium Cells Exposed to Simulated Microgravity. Cell Physiol Biochem 2016;40:1-17.
66 Infanger M, Grosse J, Westphal K, Leder A, Ulbrich C, Paul M, Grimm D: Vascular endothelial growth factor induces extracellular matrix proteins and osteopontin in the umbilical artery. Ann Vasc Surg 2008;22:273-284.
67 Chan V, Burgess JK, Ratoff JC, O'Connor B J, Greenough A, Lee TH, Hirst SJ: Extracellular matrix regulates enhanced eotaxin expression in asthmatic airway smooth muscle cells. Am J Respir Crit Care Med 2006;174:379-385.
68 Wagsater D, Lofgren S, Hugander A, Dienus O, Dimberg J: Analysis of single nucleotide polymorphism in the promoter and protein expression of the chemokine eotaxin-1 in colorectal cancer patients. World J Surg Oncol 2007;5:84.
69 Kopp S, Warnke E, Wehland M, Aleshcheva G, Magnusson NE, Hemmersbach R, Juhl Corydon T, Bauer J, Infanger M, Grimm D: Mechanisms of three-dimensional growth of thyroid cells during long-term simulated microgravity. Sci Rep 2015;5:16691.
70 Gershovich YG, Buravkova LB: Effects of microgravity simulation on the production of interleukins in culture of human mesenchymal stromal cells. Hum Physiol 2011;37:860-865.
71 Li A, Dubey S, Varney ML, Dave BJ, Singh RK: IL-8 directly enhanced endothelial cell survival, proliferation, and matrix metalloproteinases production and regulated angiogenesis. J Immunol 2003;170:3369-3376.
72 Yu H, Huang X, Ma Y, Gao M, Wang O, Gao T, Shen Y, Liu X: Interleukin-8 Regulates Endothelial Permeability by Down-regulation of Tight Junction but not Dependent on Integrins Induced Focal Adhesions. Int J Biol Sci 2013;9:966-979.
73 Li L, Dong M, Wang X-G: The Implication and Significance of Beta 2 Microglobulin: A Conservative Multifunctional Regulator. Chin Med J 2016;129:448-455.
74 Khodarev NN, Park JO, Yu J, Gupta N, Nodzenski E, Roizman B, Weichselbaum RR: Dose-dependent and independent temporal patterns of gene responses to ionizing radiation in normal and tumor cells and tumor xenografts. Proc Natl Acad Sci U S A 2001;98:12665-12670.
75 Rogers JT: Ferritin translation by interleukin-1and interleukin-6: the role of sequences upstream of the start codons of the heavy and light subunit genes. Blood 1996;87:2525-2537.
76 Ma X, Pietsch J, Wehland M, Schulz H, Saar K, Hübner N, Bauer J, Braun M, Schwarzwälder A, Segerer J, Birlem M, Horn A, Hemmersbach R, Waßer K, Grosse J, Infanger M, Grimm D: Differential gene expression profile and altered cytokine secretion of thyroid cancer cells in space. FASEB J 2014;28:813-835.

Acta Astronautica 159 (2019) 267–272

Contents lists available at ScienceDirect

Acta Astronautica

journal homepage: www.elsevier.com/locate/actaastro

Growing blood vessels in space: Preparation studies of the SPHEROIDS project using related ground-based studies

Marcus Krüger[a,*,1], Sascha Kopp[a,1], Markus Wehland[a], Johann Bauer[b], Sarah Baatout[c,d], Marjan Moreels[c], Marcel Egli[e], Thomas J. Corydon[f,g], Manfred Infanger[a], Daniela Grimm[a,f,h]

[a] Clinic for Plastic, Aesthetic and Hand Surgery, Otto von Guericke University Magdeburg, Leipziger Str. 44, D-39120, Magdeburg, Germany
[b] Max Planck Institute of Biochemistry, Am Klopferspitz 18, D-82152, Martinsried, Germany
[c] Radiobiology Unit, Belgian Nuclear Research Centre, Boeretang 200, B-2400, Mol, Belgium
[d] Department of Molecular Biotechnology, Ghent University, Coupure Links 653, B-9000, Ghent, Belgium
[e] Institute of Medical Engineering, Space Biology Group, Lucerne University of Applied Sciences and Arts, Obermattweg 9, CH-6052, Hergiswil, Switzerland
[f] Department of Biomedicine, Aarhus University, Bartholins Allé 6, DK-8000, Aarhus C, Denmark
[g] Department of Ophthalmology, Aarhus University Hospital, Palle Juul-Jensens Boulevard 99, DK-8200, Aarhus N, Denmark
[h] Gravitational Biology and Translational Regenerative Medicine, Faculty of Medicine and Mechanical Engineering, Otto von Guericke University Magdeburg, D-39120, Magdeburg, Germany

ARTICLE INFO

Keywords:
Microgravity
Spaceflight
Random positioning machine
3D growth
Spheroids
Tubular structures

ABSTRACT

Endothelial cells (ECs) grow as single layers on the bottom surface of cell culture flasks under normal (1g) culture conditions. In numerous experiments using simulated microgravity we noticed that the ECs formed three-dimensional, tube-like cell aggregates resembling the intima of small, rudimentary blood vessels. The SPHEROIDS project has now shown that similar processes occur in space. For the first time, we were able to observe scaffold-free growth of human ECs into multicellular spheroids and tubular structures during an experiment in real microgravity. With further investigation of the space samples we hope to understand endothelial 3D growth and to improve the *in vitro* engineering of biocompatible vessels which could be used in surgery.

1. Introduction

A few years ago, we detected that some types of endothelial cells (ECs) form tube-like structures when cultured on a random positioning machine (RPM) [1,2]. This observation was of great interest, because it opened up new possibilities to study neovascularization, which plays a crucial role for instance in tumor development. Gaining a deeper understanding of the underlying mechanisms in neovascularization further helps to engineer blood vessels that can be used in hand surgeries, plastic reconstructive surgeries and transplantations for example. RPMs represent one of several tools available to simulate microgravity (μg) on ground (1g). The working principle of the RPM is based on gravity vector averaging to zero [3]. The typical RPM system comprises two gimbal-mounted frames, which are each driven independently by motors. Through dedicated algorithms, the samples placed on the inner frame are constantly reoriented, such that the gravity vector is distributed in all directions over time. Thus, from the sample's point of view, the constantly reorienting gravity vector's trajectory converge toward zero over time. However, 1g is always acting on the sample at any given instant. It is assumed that the gravity vector needs to point in a specific direction for a minimal period of time in order to allow biological systems, like cells, to adapt to the gravity vector. But if the gravity vector constantly changes its orientation, the cells will lose the sense of direction and thus experience a state similar to μg (removed gravity vector). Therefore, the frame rotations shall be faster than the biological process studied [4]. However, the rotation cannot be too fast,

Abbreviations: Clinostat, (CN); endothelial cell, (EC); extracellular matrix, (ECM); Gene Ontology, (GO); human microvascular endothelial cell, (HMVEC); human saphenous vein endothelial cell, (HSVEC); human umbilical vein endothelial cell, (HUVEC); International Space Station, (ISS); microgravity, (μg); paraformaldehyde, (PFA); Periodic acid-Schiff, (PAS); Random Positioning Machine, (RPM); Rotating Wall Vessel, (RWV); three-dimentional, (3D); vascular endothelial growth factor, (VEGF)

* Corresponding author.
E-mail addresses: marcus.krueger@med.ovgu.de (M. Krüger), sascha.kopp@med.ovgu.de (S. Kopp), markus.wehland@med.ovgu.de (M. Wehland), jbauer@biochem.mpg.de (J. Bauer), sarah.baatout@sckcen.be (S. Baatout), marjan.moreels@sckcen.be (M. Moreels), marcel.egli@hslu.ch (M. Egli), corydon@biomed.au.dk (T.J. Corydon), manfred.infanger@med.ovgu.de (M. Infanger), dgg@biomed.au.dk (D. Grimm).
[1] Authors contributed equally.

https://doi.org/10.1016/j.actaastro.2019.03.074
Received 12 December 2018; Received in revised form 27 February 2019; Accepted 26 March 2019
Available online 28 March 2019
0094-5765/ © 2019 IAA. Published by Elsevier Ltd. All rights reserved.

as centrifugal forces will become effective [5]. Therefore, the RPM is typically used to examine slow processes, which are observed at least on the timescale of hours. It is obvious that an RPM treatment introduces additional forces to the samples through the unique moving pattern. If the RPMs are operated within certain boundaries however, these disturbing forces can be reduced to a minimum [6]. We therefore belive that an RPM treatment, applied with caution, can be called "simulated microgravity". The question remains, whether real μg can induce the same tube-like structure formation of ECs that were cultivated on the RPM. To answer this question, the ESA-SPHEROIDS project was launched. This project included an extensive phase of preparation regarding the selection of the type of ECs capable of tube-like structure formation even under the stressful situation and special cell culture conditions during a spaceflight. In addition, a hardware was prepared that guaranteed a proper culturing of human cells in space.

Two independently engineered hardware types were available in our team for a space mission to the ISS or a space experiment on an unmanned satellite/spacecraft. The first hardware (SimBox/CellBox), developed by Airbus Defence and Space (Friedrichshafen, Germany), holds a cell culture chamber with a volume of 13.5 mL. Below the cell culture chamber, two fluid tanks are mounted. One of them acts as a reservoir for fresh media in concert with being a waste compartment, the other one stores the fixative and is the compartment for the waste media of the second pumping procedure. Both, the fresh media compartment and the fixative compartment can hold up to 10 mL of a liquid and are used to exchange the fluid in the cell culture chamber [7]. The special feature of the tank is an internal silicon membrane, which very effectively allowed the storage of different fluids inside the same compartment without any cross-contamination. When the fresh media is pumped into the cell culture chamber, the waste fluid is simultaneously guided into the empty space on the other side of the membrane. In this way dead volume was avoided. Besides the fixed cells, the supernatant can be used for analyses.

The other hardware (now called SPHEROIDS hardware) was designed and constructed by RUAG Space (Nyon, Switzerland). One unit holds one fixative chamber, two cell culture chambers, two fresh media compartments and two waste compartments. Each cell culture chamber has a growth area of 9 cm^2 providing a total of 18 cm^2 per unit. The completed unit, including electronics, has a dimension of 10 × 10 × 10 cm [8] (Fig. 1).

Both hardware types are built of biocompatible materials and can be handled easily by the experimentators. However, the CellBox hardware is more compact. It provides a larger growth area but lacks the possibility of a complete media exchange. It has proven to be suitable for cancer cell cultures in space [7,9,10]. The SPHEROIDS hardware is designed with supernatant chambers, which are empty during the missions start. A complete exchange of media and also a complete flushing with fixative is possible. As these characteristics appeared important for tissue engineering of tubular structures in space, the SPHEROIDS hardware was chosen for this experiment.

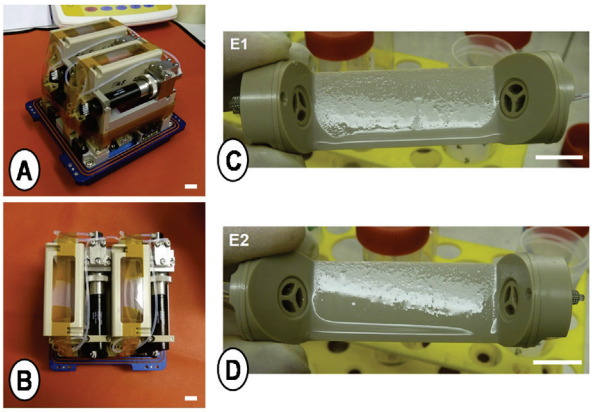


Fig. 1. Sample retrieval from the SPHEROIDS hardware. (A) Side view and (B) top view on one hardware unit removal of the cover. The two cultivation chambers (E1 and E2) are installed at the top of the unit. Samples in both chambers are fixed with PFA. (C + D) View onto the growth area of the cultivation chambers. The 'goose pimples-like' structures on the material surfaces are adherent EA.hy926 cells. Scale bars: 1 cm.

2. Material and methods

2.1. Cells

EA.hy926 [11] cells were cultivated in RPMI 1640 medium (Invitrogen, Eggenstein, Germany) containing 2 mM L-glutamine (Thermo Fisher Scientific, Waltham, US-MA) and 10% FCS, 100 U/mL penicillin and 100 μg/mL streptomycin (all Biochrom, Berlin, Germany).

Human saphenous vein endothelial cells (HSVECs) and human microvascular endothelial cells (HMVECs) were grown in advanced EC growth medium purchased from Provitro (Berlin, Germany).

All cell types grew in 75-cm^2 tissue culture flasks (Sarstedt, Nümbrecht, Germany) at 37 °C and 5% humidity.

2.2. Tube formation test on the RPM

In order to test the tube formation capability of the three cell types, the monolayer cells were scrapped off the bottom of the culture flask and suspended in RPMI 1640 medium. Subsequently, 10^6 cells were added to each of sixteen 25 cm^2 tissue culture flasks, respectively and incubated under normal gravity conditions at 37 °C until they reached 70% confluence. Afterwards, eight culture flasks, completely filled air-bubble-free with culture medium, were either mounted on a table top RPM [6] kept within a commercially available incubator or set in the incubator next to RPM. The cell culture procedure was continued as indicated below.

2.3. Spaceflight experiment

For preparing the spaceflight experiment, EA.hy926 cells were detached from the bottom of the culture flask, and suspended in RPMI 1640 medium. Then, 10^6 cells were seeded in each of the 16 cultivation chambers (RUAG Space, Nyon, Switzerland) of the SPHEROIDS hardware recently described [8] (Fig. 1). VEGF-A was added to one half of the culture chambers. As fixatives either paraformaldehyde (PFA) or RNA*later* (for RNA-sequencing at a later time) were used. During the 7-day-experiment, the nutrient solution was not refreshed, whereas it was changed for the 14-day-experiment.

2.4. Cell characterization

Cells cultured on the RPM were studied by phase contrast microscopy. For visualization of the three-dimensional (3D) aggregates, tube-like structures fixed with 4% PFA at the end of the culture period, indicated below, were collected from spaceflight cultures. Afterwards, they were embedded in paraffin and subjected to Periodic acid-Schiff (PAS) staining, performed according to routine protocols [12]. Then the coverslips were mounted and the structures were evaluated using a Zeiss Axiovert wide field microscope (Oberkochen, Germany).

2.5. Pathway analysis

To investigate and visualize the original localization and the mutual interactions of proteins coded by genes which were more than 4-fold up or down-regulated, we used the relevant UniProtKB entry numbers in the Elsevier Pathway Studio® v.11 software (Elsevier Research Solutions, Amsterdam, The Netherlands). The method was described earlier [13,14]. A STRING analysis was performed entering the names/

Table 1
Selected articles addressing the mechanisms of 3D growth of human ECs exposed to simulated μg.

Cells	Device, Duration	Findings	Ref.
HUVECs	CN, 1 d	Angiogenesis is mediated through PI3K-Akt-eNOS signalling pathway	[15]
HUVECs	CN, 1 d	iNOS up-regulation AP-1↓, NF-κB↓	[16]
HUVECs	CN, 1 d	Enhanced autophagosome formation, LC3↑, beclin-1↑	[17]
HUVECs	CN, 2 d	Induction of autophagy via HDM2-p53-mTOR pathway	[18]
HUVECs	CN, 1–2 d	eNOS↑, posttranslational modifications of caveolin-1	[19]
HUVECs	RWV, 1 d	Angiogenesis through RhoA-dependent rearrangement of the actin cytoskeleton	[20]
HUVECs	RWV, 3 d	hsp70↑, IL-1α↓, rapid remodelling of the cytoskeleton, actin↓	[21]
HUVECs	RWV/RPM, 2–4 d	Alterations of the actin cytoskeleton, NO synthesis	[22]
HUVECs/ HMVECs	RWV, 4 d	Up-regulation of hsp70	[23]
HUVECs	RWV, 8 d	Prostacyclin↑, NO↑	[24]
HUVECs	RPM, 1 h-3 d	Increased cell migration	[25]
HUVECs	RPM, 1 d	*ICAM1*↑	[26]
HUVECs	RPM, 1 d	*ICAM1*↑ in TNF-α-stimulated ECs	[27]
HUVECs	RPM, 1–2 d	"Anti-inflammatory phenotype", *NOS3*↑, *CAV1*↑, *CAV2*↑	[28]
HUVECs	RPM, 1–3 d	Alteration in cytoskeleton structure and mechanical properties	[29]
HUVECs	RCCS[a], 1–4 d	Increase of mTOR and Apaf-1, *miR-22*↑, *SRF*↓, *LAMC1*↓	[30]
HUVECs	RPM, 4 d	Secretome analysis: RANTES↑, eotaxin-1↑, IL-1α↓, IL-8↓, bFGF↓	[31]
EA.hy926	RPM, 2 h	Angiogenesis via the cGMP-PKG-dependent pathway	[32]
EA.hy926	RPM, 2 h	Increased migration caused by actin modulation and NO release	[33]
EA.hy926	RPM, 4–24 h	Induction of apoptosis, ECM proteins, ET-1, TGF-β. *NOS3*↓. IL-6↑, IL-8↑ NF-κB p50↑ and p65↑. bFGF protects ECs from apoptosis.	[34]
EA.hy926	RPM, 4–72 h	Increase of ECM protein (collagen type I, fibronectin, osteopontin, laminin, Flk-1), altered cytoskeletal components. Cell-protective influence of VEGF.	[35]
EA.hy926	RPM, 1–15 d	3D growth, increase of ECM proteins (osteopontin↑, fibronectin↑)	[36]
EA.hy926	RPM, 5–7 d	Secretome analysis: VEGF↓, bFGF↓, TNFRSF5↓, TNFSF5↓, ICAM-1↓, TNFR-2↓, IL-18↓, C3↓, VWF↓. PKCα plays a key role in tube formation	[37]
EA.hy926	RPM, 5–7 d	Gene array analysis: 1625 differentially expressed genes (*VWF*↑, *CXCL8*↑, *IL6*↑, *HMOX1*↑)	[38]
EA.hy926	RPM, 5–28 d	Tubes: integrin β1↑, α-tubulin↑, laminin↑, fibronectin↑	[1]
EA.hy926	RPM, 35 d	Secretome analysis: Suggested key proteins of spheroid formation (VEGF↑, LCN2↑, IL-6↑, IL-8↑, MCP-1↑, VCAM-1↑, ICAM-1↑, fibronectin↑, RANTES↑)	[39]
EA.hy926/ HMVECs	RPM, 5–7 d	Proteome analysis: Proteasomes and ribosomal proteins may play a role in tube formation	[2]

↑ = up-regulation/increase, ↓ = down-regulation/decrease.
[a] RCCS = rotary cell culture system.

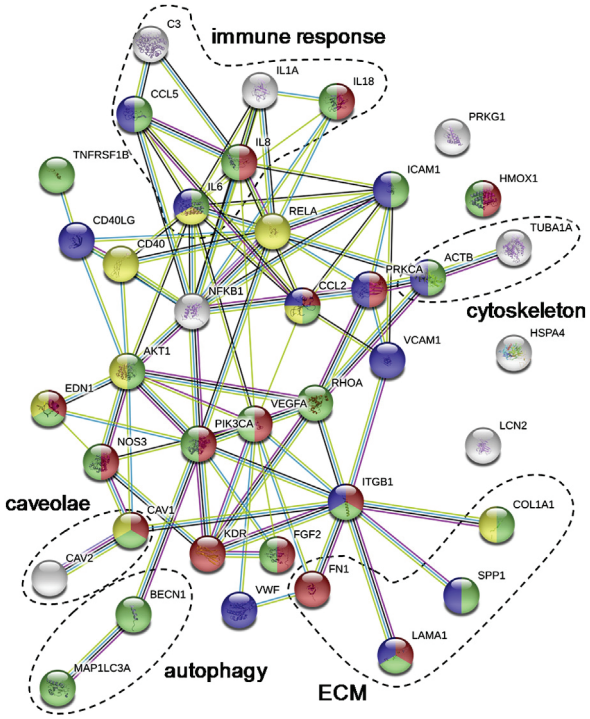


Fig. 2. Interactions of proteins influenced in ECs under μg conditions (STRING analysis). Contributions to biological processes (GO) such as blood vessel development (red), cell adhesion (blue), response to mechanical stimulus (yellow) and response to external stimulus (green) are indicated with different colours. (For interpretation of the references to colour in this figure legend, the reader is referred to the Web version of this article.)

entry numbers of proteins found in the literature references [10–34] using the STRING platform (https://string-db.org/).

3. Current knowledge from ground-based studies

Experiments using ground-based devices such as clinostats (CNs), rotating wall vessels (RWVs), or the RPM provide the basis for research in real μg and pave the way for rare and cost-intensive spaceflight projects like SPHEROIDS. Table 1 summarizes the previous research that was performed with human ECs on μg simulation devices.

The exact mechanism of endothelial 3D growth in simulated μg is still unknown. Fig. 2 shows a STRING analysis of EC proteins that are known to be affected by μg according to the literature summarized in Tab. 1. Alterations of the actin cytoskeleton were reported often and corroborate the theory of cytoskeletal gravisensing in eukaryotic cells [40]. Taking into account their corresponding Gene Ontology (GO) biological processes, proteins such as RelA, ET-1, CD40, Akt, caveolin-1, MCP-1, or interleukin (IL)-6 are modulated as reaction to mechanical stimuli (Fig. 2, yellow). They are metabolically connected to factors for cell adhesion (Fig. 2, blue) and blood vessel formation/angiogenesis (Fig. 2, red). Studies with human umbilical endothelial cells (HUVECs) indicated, that angiogenesis could be mediated via the PI3K-Akt-eNOS pathway and Rho signalling [15,18]. Possible key proteins of endothelial spheroid formation that were identified in EA.hy926 cells in RPM experiments build an interaction network between extracellular matrix (ECM), cytoskeleton, immune response and other cellular processes. It seems that μg intervenes deeply into cell function and metabolism finally resulting in an altered growth behaviour and the formation of tubular structures.

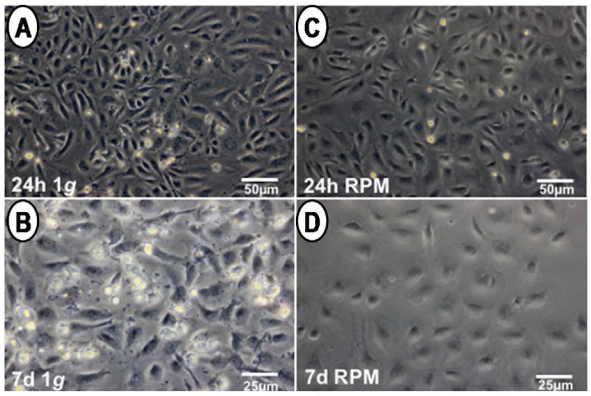


Fig. 3. HSVECs cultured under 1*g*-conditions for (A) 24 h and (B) 7 d or on the RPM for (C) 24 h and (D) 7 d.

4. Results

4.1. Selection of the most suitable cell line

We were looking for the cells, which could be expected to give the most appropriate answers in our experimental setup. According to the literature, a number of studies investigating ECs exposed to simulated µg have been published (as shown in Table 1). They were performed on HUVECs (Table 1, [15–31]) and EA.hy926 cells (Table 1, [1,2,32–39]). The studies have accumulated profound data about the behaviour of these cells under simulated µg conditions. In addition, they indicated various proteins and cellular factors playing a role in adjustment of ECs to randomization of the gravity vector. However, it should be kept in mind that HUVECs are cells derived from the endothelium of veins of the umbilical cord and EA.hy926 are hybrid cells generated by fusing HUVECs with the cancer cell line A432 [11]. As mentioned above, we were interested in studying normal adult ECs. We thus investigated human saphenous vein endothelial cells (HSVECs) and human microvascular endothelial cells (HMVECs). HSVECs are normal adult ECs. Hence, they appeared to be most appropriate to gain relevant knowledge. However, these cells are very sensitive (see Fig. 3).

Already after 24 h dead cells became visible in the culture flask incubated under static 1*g*-conditions (Fig. 3A). Their number increased up to the 7th day (Fig. 3B). On the RPM, the cells remained adherent during the first 24 h (Fig. 3C). After 7 d only adherent cells were seen, but no floating 3D aggregates (Fig. 3D). In addition, their number had decreased considerably. Hence, the data of the culturing of HSVECs showed that these cells do not form 3D aggregates and may be too sensitive for the stress of a spaceflight.

Afterwards, we searched for an alternative cell type representing adult healthy ECs and studied the EA.hy926 cell line and HMVECs. Both formed tube-like structures [2]. The formation was fast and the tubes were completed after 7 d (Fig. 4). However, HMVECs were also very sensitive. After 7 d under static 1*g*-conditions, a considerable number of dead or apoptotic cells can be found. In addition, HMVECs constantly need a temperature of 37 °C and die quickly when the temperature falls below 30 °C. Therefore, they are not suitable for a longer culture under ambient temperature in the Dragon capsule traveling to the ISS. In contrast, EA.hy926 cells appeared very tough without much apoptosis and presented some resistance to lower temperature, which made them the tool of choice.

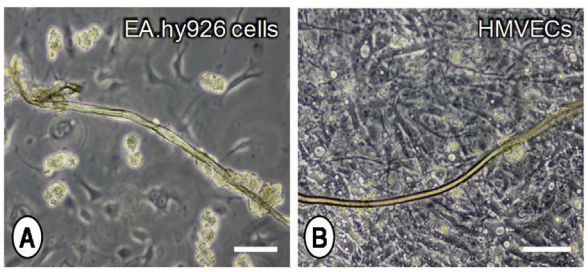


Fig. 4. Tubular structures formed by (A) EA.hy926 cells and (B) human microvascular endothelial cells after 7 d on an RPM. Scale bars: 100 µm.

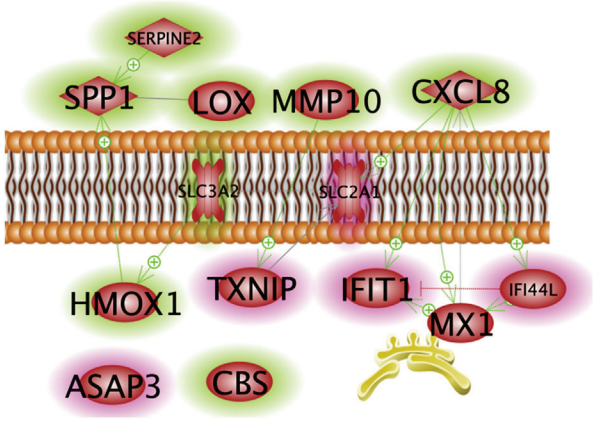


Fig. 5. Mutual interaction of proteins coded by genes which had been up- (green rim) or down-regulated (red rim) during a 5- or 7-day-exposure to the RPM. The icons at the upper edge indicate genes coding for extracellular proteins. The icons at the lower edge indicate cytoplasmic proteins. The yellow one indicates the endoplasmatic reticulum. (For interpretation of the references to colour in this figure legend, the reader is referred to the Web version of this article.)

4.2. In silico analysis

After the preparatory experiments we decided to use the EA.hy926 cell line for a first approach. These cells form tube-like structures (Fig. 4A) and survive a few days of ambient temperature below 30 °C [1,8,37]. We had characterized these cells very well [2,38]. From a genetic point of view 26 genes were of high interest, because they were either down- or up-regulated more than 4-fold. In addition, a few of them were genes whose products were known to be involved in the formation of 3D aggregates of human ECs as wells as of human cancer cells. Fig. 5 shows that the genes of the interacting osteopontin, protein-lysine 6-oxidase, and heme oxygenase 1 [37,41,42], were up-regulated, while those of interferon-induced proteins (IFIT1, IFI44L, MX1) were down-regulated. The latter proteins contribute to the activity of ISG15, which we recently found to be involved in breast cancer spheroid formation [43].

4.3. Tube-like aggregate formation during spaceflight

The cells seeded in the flight hardware were flown to the ISS and stayed there for 2 and 9 d at 37 °C as described in Ref. [8], before they were fixed and stored for the return. All eight experimental units were returned successfully. After the sample collection from the flight hardware units (Fig. 1), we detected 3D cell aggregates, which assembled after the launch of the experiment until their fixation approximately 5 and 12 d later (Fig. 6).

We investigated these aggregates emphasizing the morphology of the single cells. Fig. 5 shows a representative tube-like structure. It looks similar to the intima constructs, which we had detected in a preparatory study on the RPM [1] and confirmed these results obtained using a device designed to create conditions of µg on Earth.

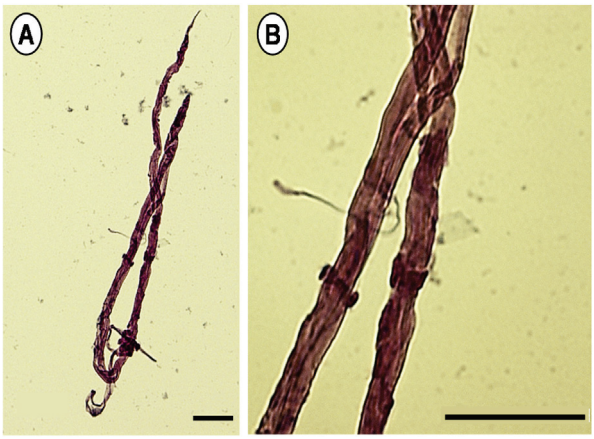


Fig. 6. Tube-like structure of human ECs harvested from the SPHEROIDS hardware after 12 d in space. (A) Periodic acid-Schiff (PAS) staining (× 200) (B) The enlarged detail view of the same tube (× 200) with subcellular structures. Scale bars: 35 µm.

5. Discussion

Extensive studies were performed on cultured ECs over the last years using the RPM (Table 1). These studies have shown that ECs are highly sensitive to random positioning, which induced 3D cell aggregation as well as an up-regulation of several growth factors and ECM components [38], but also initiated apoptosis in the EA.hy926 human endothelial cell line [35]. Further, it has been reported that $CD34^+$ human umbilical cord blood progenitors trans-differentiated into a vascular endo-thelial cell phenotype and continued growing into 3D structures inside a RWV [44].

Based on the data collected during the preparation of the spaceflight, we decided to use the EA.hy926 cell line for this study, although they may not be the optimal model to obtain the desired information in a first approach. At least, these cells form tube-like structures (Fig. 4A) and survive a few day period of ambient temperature below 30 °C. Hence, we expected that the cells show whether they behaved in space like they did on the RPM, forming tube like structures.

Especially the 3D growth behaviour is of interest, as it could be a versatile tool for angiogenesis studies *in vitro*. SPHEROIDS was not the first experiment culturing human ECs in real µg [45–47], but 3D growth was observed for the first time. The flight hardware enabled growth of EA.hy926 cells as tube-like structures in space, similar to previous results using an RPM. This suggests that among other environmental difference between space and the RPM, µg may be the main trigger for 3D growth. The lack of sedimentation and convection phenomena in µg enables cells to arrange themselves in 3D aggregates, that allow simulating the way cells are organized *in vivo*. This has provided more insights into the morphological and functional behaviour of ECs and allowed to collect valuable results on the pathophysiological morphologies and functions of ECs that could not be obtained through experiments in a normal terrestrial lab.

6. Conclusion

SPHEROIDS was not the first EC experiment in space, but 3D growth in real µg was observed for the first time. A specially developed hardware enabled growth of EA.hy926 cells as tube-like structures, which resemble the aggregates formed on the RPM. This confirms that µg may be the main trigger for 3D growth, although there are other environmental differences between space and the RPM. Hence, it appears that the lack of sedimentation facilitates the formation of 3D aggregates, simulating the way cells organize themselves inside the human body.

Acknowledgements

The research was supported by the German Space Agency (Deutsches Zentrum für Luft- und Raumfahrt, DLR, grants 50BW1124 and 50BW1524), the European Space Agency (ESA, grant ESA-AO-2004-006), by Aarhus University, and by BELSPO PRODEX (IMPULSE 2 grant 4000109861).

The authors would like to thank Jason Hatton, Nadine Boersma and Andrea Koehler from ESA, Raimondo Fortezza from Telespazio, and Markus Braun from DLR for their support of the space experiment. In addition, we like to thank the engineers Samuel Gass and Stefano Nebuloni (RUAG Space) as well as Christian Bruderrek and Jürgen Segerer (Airbus Defence and Space) for the development of the hardwares and their great help during the experiments. Finally, we would like to express our thanks to Christa Baumann (Institute of Pathology, University of Regensburg) for performing the paraffin embedding and histochemical stainings of the space spheroids.

References

[1] D. Grimm, M. Infanger, K. Westphal, C. Ulbrich, J. Pietsch, P. Kossmehl, S. Vadrucci, S. Baatout, B. Flick, M. Paul, J. Bauer, A delayed type of three-dimensional growth of human endothelial cells under simulated weightlessness, Tissue Eng. 15 (2009) 2267–2275 https://doi.org/10.1089/ten.tea.2008.0576.

[2] X. Ma, A. Sickmann, J. Pietsch, R. Wildgruber, G. Weber, M. Infanger, J. Bauer, D. Grimm, Proteomic differences between microvascular endothelial cells and the EA.hy926 cell line forming three-dimensional structures, Proteomics 14 (2014) 689–698 https://doi.org/10.1002/pmic.201300453.

[3] A.G. Borst, J.J.W.A. van Loon, Technology and developments for the random positioning machine, RPM, Microgravity Sci. Technol. 21 (2008) 287–292 https://doi.org/10.1007/s12217-008-9043-2.

[4] D. Mesland, Novel ground-based facilities for research in the effects of weight, ESA Microgravity News 9 (1996) 5–10.

[5] J.J.W.A. van Loon, Some history and use of the random positioning machine, RPM, in gravity related research, Adv. Space Res. 39 (2007) 1161–1165 https://doi.org/10.1016/j.asr.2007.02.016.

[6] S.L. Wuest, S. Richard, S. Kopp, D. Grimm, M. Egli, Simulated microgravity: critical review on the use of random positioning machines for mammalian cell culture, BioMed Res. Int. 2015 (2015) 971474 https://doi.org/10.1155/2015/971474.

[7] J. Pietsch, X. Ma, M. Wehland, G. Aleshcheva, A. Schwarzwälder, J. Segerer, M. Birlem, A. Horn, J. Bauer, M. Infanger, D. Grimm, Spheroid formation of human thyroid cancer cells in an automated culturing system during the Shenzhou-8 Space mission, Biomaterials 34 (2013) 7694–7705 https://doi.org/10.1016/j.biomaterials.2013.06.054.

[8] J. Pietsch, S. Gass, S. Nebuloni, D. Echegoyen, S. Riwaldt, C. Baake, J. Bauer, T.J. Corydon, M. Egli, M. Infanger, D. Grimm, Three-dimensional growth of human endothelial cells in an automated cell culture experiment container during the SpaceX CRS-8 ISS space mission - the SPHEROIDS project, Biomaterials 124 (2017) 126–156 https://doi.org/10.1016/j.biomaterials.2017.02.005.

[9] S. Riwaldt, J. Pietsch, A. Sickmann, J. Bauer, M. Braun, J. Segerer, A. Schwarzwälder, G. Aleshcheva, T.J. Corydon, M. Infanger, D. Grimm, Identification of proteins involved in inhibition of spheroid formation under microgravity, Proteomics 15 (2015) 2945–2952 https://doi.org/10.1002/pmic.201500067.

[10] S. Riwaldt, J. Bauer, J. Pietsch, M. Braun, J. Segerer, A. Schwarzwälder, T.J. Corydon, M. Infanger, D. Grimm, The importance of caveolin-1 as key-regulator of three-dimensional growth in thyroid cancer cells cultured under real and simulated microgravity conditions, Int. J. Mol. Sci. 16 (2015) 28296–28310 https://doi.org/10.3390/ijms161226108.

[11] C.J. Edgell, C.C. McDonald, J.B. Graham, Permanent cell line expressing human factor VIII-related antigen established by hybridization, Proc. Natl. Acad. Sci. U.S.A. 80 (1983) 3734–3737.

[12] S. Kopp, L. Slumstrup, T.J. Corydon, J. Sahana, G. Aleshcheva, T. Islam, N.E. Magnusson, M. Wehland, J. Bauer, M. Infanger, D. Grimm, Identifications of novel mechanisms in breast cancer cells involving duct-like multicellular spheroid formation after exposure to the Random Positioning Machine, Sci. Rep. 6 (2016) 26887 https://doi.org/10.1038/srep26887.

[13] J. Bauer, S. Kopp, E.M. Schlagberger, J. Grosse, J. Sahana, S. Riwaldt, M. Wehland, R. Luetzenberg, M. Infanger, D. Grimm, Proteome analysis of human follicular thyroid cancer cells exposed to the random positioning machine, Int. J. Mol. Sci. 18 (2017) 546 https://doi.org/10.3390/ijms18030546.

[14] J. Bauer, M. Wehland, M. Infanger, D. Grimm, E. Gombocz, Semantic analysis of posttranslational modification of proteins accumulated in thyroid cancer cells exposed to simulated microgravity, Int. J. Mol. Sci. 19 (2018) 2257 https://doi.org/10.3390/ijms19082257.

[15] F. Shi, Y.-C. Wang, T.-Z. Zhao, S. Zhang, T.-Y. Du, C.-B. Yang, Y.-H. Li, X.-Q. Sun, Effects of simulated microgravity on human umbilical vein endothelial cell angiogenesis and role of the PI3K-Akt-eNOS signal pathway, PLoS One 7 (2012) e40365https://doi.org/10.1371/journal.pone.0040365.

[16] Y.C. Wang, S. Zhang, T.Y. Du, B. Wang, X.Q. Sun, Clinorotation upregulates

inducible nitric oxide synthase by inhibiting AP-1 activation in human umbilical vein endothelial cells, J. Cell. Biochem. 107 (2009) 357–363 https://doi.org/10.1002/jcb.22134.
[17] Y.C. Wang, D.Y. Lu, F. Shi, S. Zhang, C.B. Yang, B. Wang, X.S. Cao, T.Y. Du, Y. Gao, J.D. Zhao, X.Q. Sun, Clinorotation enhances autophagy in vascular endothelial cells, Biochem. Cell Biol. 91 (2013) 309–314 https://doi.org/10.1139/bcb-2013-0029.
[18] C.F. Li, J.X. Sun, Y. Gao, F. Shi, Y.K. Pan, Y.C. Wang, X.Q. Sun, Clinorotation-induced autophagy via HDM2-p53-mTOR pathway enhances cell migration in vascular endothelial cells, Cell. Death Dis. 9 (2018) 147 https://doi.org/10.1038/s41419-017-0185-2.
[19] E. Spisni, M. Toni, A. Strillacci, G. Galleri, S. Santi, C. Griffoni, V. Tomasi, Caveolae and caveolae constituents in mechanosensing: effect of modeled microgravity on cultured human endothelial cells, Cell. Biochem. Biophys. 46 (2006) 155–164 https://doi.org/10.1385/cbb:46:2:155.
[20] F. Shi, Y.C. Wang, Z.B. Hu, H.Y. Xu, J. Sun, Y. Gao, X.T. Li, C.B. Yang, C. Xie, C.F. Li, S. Zhang, J.D. Zhao, X.S. Cao, X.Q. Sun, Simulated microgravity promotes angiogenesis through RhoA-dependent rearrangement of the actin cytoskeleton, Cell. Physiol. Biochem. 41 (2017) 227–238 https://doi.org/10.1159/000456060.
[21] S.I.M. Carlsson, M.T.S. Bertilaccio, E. Ballabio, J.A.M. Maier, Endothelial stress by gravitational unloading: effects on cell growth and cytoskeletal organization, Biochim. Biophys. Acta 1642 (2003) 173–179 https://doi.org/10.1016/j.bbamcr.2003.08.003.
[22] S. Versari, A. Villa, S. Bradamante, J.A.M. Maier, Alterations of the actin cytoskeleton and increased nitric oxide synthesis are common features in human primary endothelial cell response to changes in gravity, Biochim. Biophys. Acta 1773 (2007) 1645–1652 https://doi.org/10.1016/j.bbamcr.2007.05.014.
[23] M. Mariotti, J.A.M. Maier, Human micro- and macrovascular endothelial cells exposed to simulated microgravity upregulate hsp70, Microgravity Sci. Technol. 21 (2009) 141–144 https://doi.org/10.1007/s12217-008-9066-8.
[24] S.I.M. Carlsson, M.T.S. Bertilaccio, I. Ascari, S. Bradamante, J.A.M. Maier, Modulation of human endothelial cell behaviour in simulated microgravity, J. Gravitational Physiol. 9 (2002) P273–P274.
[25] L.B. Buravkova, Y.A. Romanov, The role of cytoskeleton in cell changes under condition of simulated microgravity, Acta Astronaut. 48 (2001) 647–650.
[26] L. Buravkova, Y. Romanov, M. Rykova, O. Grigorieva, N. Merzlikina, Cell-to-cell interactions in changed gravity: ground-based and flight experiments, Acta Astronaut. 57 (2005) 67–74.
[27] L.B. Buravkova, E.G. Rudimov, E.R. Andreeva, A.I. Grigoriev, The ICAM-1 expression level determines the susceptibility of human endothelial cells to simulated microgravity, J. Cell. Biochem. 119 (2018) 2875–2885 https://doi.org/10.1002/jcb.26465.
[28] S.M. Grenon, M. Jeanne, J. Aguado-Zuniga, M.S. Conte, M. Hughes-Fulford, Effects of gravitational mechanical unloading in endothelial cells: association between caveolins, inflammation and adhesion molecules, Sci. Rep. 3 (2013) 1494 https://doi.org/10.1038/srep01494.
[29] M. Janmaleki, M. Pachenari, S.M. Seyedpour, R. Shahghadami, A. Sanati-Nezhad, Impact of simulated microgravity on cytoskeleton and viscoelastic properties of endothelial cell, Sci. Rep. 6 (2016) 32418 https://doi.org/10.1038/srep32418.
[30] D. Xu, Y.B. Guo, M. Zhang, Y.Q. Sun, The subsequent biological effects of simulated microgravity on endothelial cell growth in HUVECs, Chin. J. Traumatol. 21 (2018) 229–237 https://doi.org/10.1016/j.cjtee.2018.04.004.
[31] C. Griffoni, S. Di Molfetta, L. Fantozzi, C. Zanetti, P. Pippia, V. Tomasi, E. Spisni, Modification of proteins secreted by endothelial cells during modeled low gravity exposure, J. Cell. Biochem. 112 (2011) 265–272 https://doi.org/10.1002/jcb.22921.
[32] J.H. Siamwala, S. Majumder, K.P. Tamilarasan, A. Muley, S.H. Reddy, G.K. Kolluru, S. Sinha, S. Chatterjee, Simulated microgravity promotes nitric oxide-supported angiogenesis via the iNOS–cGMP–PKG pathway in macrovascular endothelial cells, FEBS Lett. 584 (2010) 3415–3423 https://doi.org/10.1016/j.febslet.2010.06.039.
[33] J.H. Siamwala, S.H. Reddy, S. Majumder, G.K. Kolluru, A. Muley, S. Sinha, S. Chatterjee, Simulated microgravity perturbs actin polymerization to promote nitric oxide-associated migration in human immortalized Ea.hy926 cells, Protoplasma 242 (2010) 3–12 https://doi.org/10.1007/s00709-010-0114-z.
[34] C. Ulbrich, K. Westphal, S. Baatout, M. Wehland, J. Bauer, B. Flick, M. Infanger, R. Kreutz, S. Vadrucci, M. Egli, A. Cogoli, H. Derradji, J. Pietsch, M. Paul, D. Grimm, Effects of basic fibroblast growth factor on endothelial cells under conditions of simulated microgravity, J. Cell. Biochem. 104 (2008) 1324–1341 https://doi.org/10.1002/jcb.21710.
[35] M. Infanger, P. Kossmehl, M. Shakibaei, S. Baatout, A. Witzing, J. Grosse, J. Bauer, A. Cogoli, S. Faramarzi, H. Derradji, M. Neefs, M. Paul, D. Grimm, Induction of three-dimensional assembly and increase in apoptosis of human endothelial cells by simulated microgravity: impact of vascular endothelial growth factor, Apoptosis 11 (2006) 749–764 https://doi.org/10.1007/s10495-006-5697-7.
[36] M. Infanger, P. Kossmehl, M. Shakibaei, A. Cogoli, A. Witzing, S. Faramarzi, W. Wittfoht, M. Paul, D. Grimm, Vascular endothelial growth factor inhibits programmed cell death of endothelial cells induced by clinorotation, J. Gravitational Physiol. 11 (2004) P199–P200.
[37] D. Grimm, J. Bauer, C. Ulbrich, K. Westphal, M. Wehland, M. Infanger, G. Aleshcheva, J. Pietsch, M. Ghardi, M. Beck, H. El-Saghire, L. de Saint-Georges, S. Baatout, Different responsiveness of endothelial cells to vascular endothelial growth factor and basic fibroblast growth factor added to culture media under gravity and simulated microgravity, Tissue Eng. 16 (2010) 1559–1573 https://doi.org/10.1089/ten.TEA.2009.0524.
[38] X. Ma, M. Wehland, H. Schulz, K. Saar, N. Hübner, M. Infanger, J. Bauer, D. Grimm, Genomic approach to identify factors that drive the formation of three-dimensional structures by EA.hy926 endothelial cells, PLoS One 8 (2013) e64402https://doi.org/10.1371/journal.pone.0064402.
[39] A. Dittrich, D. Grimm, J. Sahana, J. Bauer, M. Krüger, M. Infanger, N.E. Magnusson, Key proteins involved in spheroid formation and angiogenesis in endothelial cells after long-term exposure to simulated microgravity, Cell. Physiol. Biochem. 45 (2018) 429–445 https://doi.org/10.1159/000486920.
[40] D. Vorselen, W.H. Roos, F.C. MacKintosh, G.J. Wuite, J.J. van Loon, The role of the cytoskeleton in sensing changes in gravity by nonspecialized cells, FASEB J. 28 (2014) 536–547 https://doi.org/10.1096/fj.13-236356.
[41] S. Kopp, M. Krüger, S. Feldmann, H. Oltmann, A. Schütte, B. Schmitz, J. Bauer, H. Schulz, K. Saar, N. Huebner, M. Wehland, M.Z. Nassef, D. Melnik, S. Meltendorf, M. Infanger, D. Grimm, Thyroid cancer cells in space during the TEXUS-53 sounding rocket mission - the THYROID Project, Sci. Rep. 8 (2018) 10355 https://doi.org/10.1038/s41598-018-28695-1.
[42] J. Bauer, M. Wehland, J. Pietsch, A. Sickmann, G. Weber, D. Grimm, Annotated gene and proteome data support recognition of interconnections between the results of different experiments in space research, Microgravity Sci. Technol. 28 (2016) 357–365 https://doi.org/10.1007/s12217-015-9451-z.
[43] J. Sahana, M.Z. Nassef, M. Wehland, S. Kopp, M. Krüger, T.J. Corydon, M. Infanger, J. Bauer, D. Grimm, Decreased E-cadherin in MCF7 human breast cancer cells forming multicellular spheroids exposed to simulated microgravity, Proteomics 18 (2018) e1800015 https://doi.org/10.1002/pmic.201800015.
[44] B. Chiu, J.Z. Wan, D. Abley, J. Akabutu, Induction of vascular endothelial phenotype and cellular proliferation from human cord blood stem cells cultured in simulated microgravity, Acta Astronaut. 56 (2005) 918–922.
[45] N. Li, C. Wang, S. Sun, C. Zhang, D. Lü, Q. Chen, M. Long, Microgravity-induced alterations of inflammation-related mechanotransduction in endothelial cells on board SJ-10 satellite, Front. Physiol. 9 (2018), https://doi.org/10.3389/fphys.2018.01025.
[46] S. Versari, G. Longinotti, L. Barenghi, J.A. Maier, S. Bradamante, The challenging environment on board the International Space Station affects endothelial cell function by triggering oxidative stress through thioredoxin interacting protein overexpression: the ESA-SPHINX experiment, FASEB J. 27 (2013) 4466–4475 https://doi.org/10.1096/fj.13-229195.
[47] M.Y. Kapitonova, S. Muid, G.R. Froemming, W.N. Yusoff, S. Othman, A.M. Ali, H.M. Nawawi, Real space flight travel is associated with ultrastructural changes, cytoskeletal disruption and premature senescence of HUVEC, Malays. J. Pathol. 34 (2012) 103–113.

WISSENSCHAFTLICHER LEBENSLAUF

Anstellungen

	Otto-von-Guericke-Universität Magdeburg (OVGU)
seit 06/2020	Leiter der Arbeitsgruppe Umweltzellbiologie in der neu gegründeten Abteilung für Mikrogravitation und Translationale Regenerative Medizin
10/2016 – 05/2020	Wissenschaftlicher Mitarbeiter an der Universitätsklinik für Plastische, Ästhetische und Handchirurgie, AG Weltraummedizin
	Friedrich-Alexander-Universität Erlangen-Nürnberg (FAU)
06/2012 – 09/2016	Wissenschaftlicher Mitarbeiter der Naturwissenschaftlichen Fakultät
02/2011 – 07/2013	Wissenschaftlicher Mitarbeiter und Dozent am Department Biologie
04/2010 – 03/2017	Lehrbeauftragter am Department Fachdidaktiken (Biologiedidaktik)
11/2009 – 12/2009	Wissenschaftlicher Mitarbeiter im Studienbüro Biologie
01/2006 – 12/2009	Wissenschaftlicher Mitarbeiter am Lehrstuhl für Mikrobiologie (Prof. Dr. W. Hillen)
07/2002 – 12/2005	Studentische Hilfskraft an den Lehrstühlen für Mikrobiologie (Prof. Dr. W. Hilllen), Molekulare Pflanzenphysiologie (Prof. Dr. W. Nezadal), Zoologie II/Tierphysiologie (Prof. Dr. O. von Helversen), Ökophysiologie der Pflanzen (Prof. Dr. G. Kreimer)

Ausbildung

Promotion	in Mikrobiologie bei Prof. Dr. W. Hillen (03/2006 – 12/2009) – Disputation (12/2009) „*Informationsübertragung im Tetrazyklin-Repressor als Grundlage für den allosterischen Induktionsmechanismus*“
Studium	der Biologie an der Friedrich-Alexander-Universität Erlangen-Nürnberg (10/2000 – 10/2005) – Diplomarbeit in Mikrobiologie: „*Ein Tet-Repressor mit neuer Operator-Spezifität*“
	Fachdidaktische Ausbildung im Fach Biologie (10/2005 – 07/2007)
Schule	Grundschule und Gymnasium (1986 – 2000)
	Abitur am Ehrenbürg-Gymnasium Forchheim (06/2000)

Drittmittel

07/2021 – 12/2023	Einfluss der Bindung an Albumin auf die zellbiologische und molekulare Wirkungsweise von Curcumin bei benignen und malignen humanen Zellen (Dr. Hans Feith und Dr. Elisabeth Feith-Stiftung)

Akademische Selbstverwaltung

02/2011 – 03/2013	Studiengangskoordinator Biologie / Integrated Life Sciences

Gutachtertätigkeiten

Fachzeitschriften	Peer-Reviewer: Acta Astronautica, Acta Biomaterialia, Applied Sciences, Biology, Biomedical and Environmental Sciences, Biomedicines, BMC Cancer, Cancers, Catalysts, Cells, Current Oncology, Diseases, European Journal of Cell Biology, The FASEB Journal, Foundations, General Physiology and Biophysics, International Journal of Molecular Sciences, Life, Life Sciences in Space Research, Marine Drugs, Metabolites,

	Microgravity Science and Technology, Molecules, Pharmaceutics, Photonics, Phytomedicine, Scientific Reports, Surfaces
Forschungsförderung	Deutsche Forschungsgemeinschaft (DFG), Dutch Cancer Society (KWF Kankerbestrijding)

Mitgliedschaften

seit 2020	Mitglied der Magdeburger Arbeitsgemeinschaft für Forschung unter Raumfahrt- und Schwerelosigkeitsbedingungen (MARS)
seit 2018	Mitglied der International Society of Gravitational Physiology (ISGP)

Sprachkenntnisse

Latinum
Englisch sehr gut in Wort und Schrift

Magdeburg, im November 2024